Ion Vişa
Editor

SYROM 2009

Proceedings of the 10th IFToMM International Symposium on Science of Mechanisms and Machines, held in Braşov, Romania, October 12–15, 2009

IFToMM

Springer

SYROM 2009

Ion Vişa
Editor

SYROM 2009

Proceedings of the 10th IFToMM International Symposium on Science of Mechanisms and Machines, held in Brasov, Romania, October 12–15, 2009

Springer

Editor
Ion Vişa
Transilvania University of Brasov
Fac. Technological Engineering
Bdul. Eroilor 29
500036 Brasov
Romania
visaion@unitbv.ro

ISBN: 978-90-481-3521-9 e-ISBN: 978-90-481-3522-6
DOI 10.1007/978-90-481-3522-6
Springer Dordrecht Heidelberg London New York

Library of Congress Control Number: 2009942258

Cover design: eStudio Calamar S.L.

Printed on acid-free paper

Springer is part of Springer Science+Business Media (www.springer.com)

Preface

The International Symposium on Science of Mechanisms and Machines, SYROM 2009, at its 10th edition, continues the tradition of scientific events devoted to the specific problems of the design, modelling, simulation, optimization and control of the mechanical systems. These events were organized every 4 years, since 1973, by the Romanian Association for the Mechanisms and Machine Science ARoTMM, aiming from the very beginning to gather international researchers, academics, professionals and students working in the field of mobile mechanical and mechatronic systems and to support scientific dissemination and experience exchange.

The initiator and organizer of the first 6 editions of the SYROM symposium was prof.dr.doc.st.eng. Nicolae I. Manolescu, internationally recognized scientists, founding member of the International Federation for the Promotion of Mechanisms and Machine Science IFToMM and of ARoTMM. For the first time outside the Politehnica University of Bucharest, SYROM is hosted this year by the Transilvania University of Brasov, and will take place during 12–15 October 2009. Keeping track with the scientific development, the SYROM topics enlarged during time by including the novel trends and research directions and the areas addressed now are including, besides Mechanisms and Machines, also Command and Control, Applications in High-Tech Products along with Current Trends in Education.

Recognizing the actuality and viability of the proposed topics, IFToMM included SYROM Symposium on the list of 2009 prestigious events (http://130.15.85.212/indexa.html).

At the 10th edition we received 79 papers, and after review 61 papers have been accepted for presentation and publication in the Symposium Proceedings. The papers topic aim, particularly to the mechanisms approached as multibody systems (MBS), applicable in the conceptual design of mechanisms, kinematics and dynamic analysis, modelling and simulation, synthesis and optimization. Current research in this area combines techniques as modelling – Digital modelling – Virtual Prototyping in the sustainable development concept, thus enabling the simultaneous evaluation of the shape, mounting/assembly, functionality and sustainability of the

systems and their impact on the environment. The modern concepts lately developed are mirrored by the symposium topics, focusing on the overall approach and relationship with the environment (and not separate components and subsystems). The integrated approach of the mechanical, electrical, hydraulic, electronic systems open the way to analysing and optimizing the functionality of the entire product. Good examples are the mechatronic systems which in addition to the mechanics involve the actuation, command/control and the eco-design; they can be found in high-tech products, in advanced applications like renewable energy and robotics.

We would like to express our thanks to the members of the International Scientific Committee, who had reviewed the papers, for the full support in assuring the quality of this event.

We would also like to thank the authors for their high level contribution at the tenth SYROM Edition.

Transilvania University of Brasov
July 2009

Ion VIŞA
SYROM 2009 Chairman

SYROM 2009 SCIENTIFIC COMMITTEE

Gyorgy ABRAHAM	University of Technology & Economics, Budapest, Hungary
Cătălin ALEXANDRU	Transilvania University of Braşov, Romania
Petre ALEXANDRU	Transilvania University of Braşov, Romania
Păun ANTONESCU	Politehnica University of Bucharest, Romania
Virgil ATANASIU	"Gh. Asachi" Technical University of Iaşi, Romania
Ioan ARDELEAN	Technical University of Cluj-Napoca, Romania
Yvan BAUDOIN	Royal Military Academy of Brussels, Belgium
Marco CECCARELLI	University of Cassino, Italy
Vencel CSIBI	Technical University of Cluj-Napoca, Romania
Thomas G. CHONDROS	University of Patras, Greece
Burkhard. CORVES	RWTH Aachen University, Germany
Javier CUADRADO	Universidad da Coruna, Spain
Juan S. DAI	King's College, University of London, United Kingdom
Dorin DIACONESCU	Transilvania University of Braşov, Romania
Ioan DOROFTEI	"Gh. Asachi" Technical University of Iaşi, Romania
Valeriu DULGHERU	Technical University of Chişinău, Moldavia
Grigore GOGU	IFMA, Clermond Ferrand, France
Manfred HILLER	University Duisburg – Essen, Germany
Chintien HUANG	National Cheng Kung University, Taiwan
Tian HUANG	Tianjin University, China
Manfred HUSTY	University of Innsbruck, Austria
Codruţa JALIU	Transilvania University of Braşov, Romania
Dirk LEFEBER	Free University of Brussels, Belgium
Song LIN	Technical University of Dresden, Germany
Erwin LOVASZ	Politehnica University of Timişoara, Romania
Vistrian MATIES	Technical University of Cluj-Napoca, Romania
Jean-Pierre MERLET	INRIA, France
Karl-Heinz MODLER	Technical University of Dresden, Germany
Mircea NEAGOE	Transilvania University of Brasov, Romania
Dumitru NICOLAE	University of Craiova, Romania
Nicolae ORLANDEA	Ann Arbor University, Michigan, USA

Contents

Contributors

A. Adîr Politehnica University of Bucharest, Romania, e-mail: adirancuta@yahoo.com

G. Adîr Politehnica University of Bucharest, Romania

V. Adîr Politehnica University of Bucharest, Romania

V.G. Adîr Politehnica University of Bucharest, Romania

S. Alaci Faculty of Mechanical Engineering, Mechatronics and Management, University "Stefan cel Mare" Suceava, Romania, e-mail: stalaci@yahoo.com

C. Alexandru Department of Product Design and Robotics, Transilvania University of Brasov, Romania, e-mail: calex@unitbv.ro

P. Alexandru Department of Product Design and Robotics, Transilvania University of Brasov, Romania, e-mail: alex.p@unitbv.ro

O. Altuzarra University of Basque Country Bilbao, Spain

A. Alutei Technical University of Cluj Napoca, Romania

D. Amarandei Faculty of Mechanical Engineering, Mechatronics and Management, University "Stefan cel Mare" Suceava, Romania

A. Antal Technical University of Cluj Napoca, Romania

T. Antal Technical University of Cluj Napoca, Romania, e-mail: antaljr@bavaria.utcluj.ro

F.D. Anton University Politehnica of Bucharest, Romania

S. Anton University Politehnica of Bucharest, Romania

O. Antonescu Politehnica University of Bucharest, Romania, e-mail: panton38@hotmail.com

P. Antonescu Politehnica University of Bucharest, Romania

I. Ardelean Department Mechanisms, Fine Mechanics and Mechatronics, Technical University of Cluj Napoca, Romania, e-mail: ioan_ardelean@yahoo.com

V. Atanasiu Technical University "Gh. Asachi" Iasi, Romania

J. Awrejcewicz Poznan University of Technology, Poland

M. Bara Technical University of Cluj Napoca, Romania, e-mail: bmvbara@yahoo.com

S. Berian Technical University of Cluj Napoca, Romania, e-mail: sergiuberian@yahoo.com

N. Bizdoaca University of Craiova, Romania

N. Bolotnik Fakultät für Maschinenbau, TU Ilmenau, Germany

T. Borangiu Politehnica University of Bucharest, Romania, e-mail: borangiu@cimr.pub.ro

C. Bozan Department of Product Design and Robotics, Transilvania University of Brasov, Romania

C. Brisan Technical University of Cluj Napoca, Romania

A. Bruja Technical University of Civil Engineering Bucharest, Romania, e-mail: brujaadrian@yahoo.fr

B. Burduhos Department of Product Design and Robotics, Transilvania University of Brasov, Romania, e-mail: bogdan.burduhos@unitbv.ro

J. Buskiewicz Poznan University of Technology, Poland, e-mail: jacek.buskiewicz@put.poznan.pl

S. Butnariu Department of Product Design and Robotics, Transilvania University of Brasov, Romania, e-mail: Butnariu@unitbv.ro

B. Butuc Department of Product Design and Robotics, Transilvania University of Brasov, Romania

A. Capustiac Technical University of Cluj Napoca, Romania

C. Carbone Laboratory of Robotics and Mechatronics DiMSAT – University of Cassino,Via Di Biasio 43, 03043 Cassino (Fr), Italy, e-mail: carbone@unicas.it

M. Ceccarelli Laboratory of Robotics and Mechatronics DiMSAT – University of Cassino, Via Di Biasio 43, 03043 Cassino (Fr), Italy, e-mail: ceccarelli@unicas.it

D.A. Cerlinca "Stefan cel Mare" University of Suceava, Romania

F.C. Ciornei Faculty of Mechanical Engineering, Mechatronics and Management, "Stefan cel Mare" University of Suceava, Romania

F. Cismaru University of Craiova, Romania

G. Ciubucciu-Ionete GMT Department, Dunarea de Jos University of Galati, Romania

V. Ciupe Politehnica University of Timisoara, Romania

B. Corves Department of Mechanisms Theory and Dynamics of Machines, RWTH Aachen University, Germany

I.A. Cosma Technical University of Cluj Napoca, Romania, e-mail: Ioan. Cosma@mmfm.utcluj.ro

I. Daj Department of Product Design and Robotics, Transilvania University of Brasov, Romania, e-mail: daj@unitbv.ro

N.M. Dehelean Politehnica University of Timisoara, Romania, e-mail: dehelean@mec.utt.ro

O.A. Detesan Technical University of Cluj Napoca, Romania

D. Diaconescu Department of Product Design and Robotics, Transilvania University of Brasov, Romania, e-mail: dvdiaconescu@unitbv.ro

M. Dima Technical University of Civil Engineering Bucharest, Romania

I. Doroftei "Gh. Asachi" Technical University of Iasi, Theory of Mechanisms and Robotics Department, Romania

A. Duca Technical University of Cluj Napoca, Romania

V.F. Duma Aurel Vlaicu University of Arad, Romania, e-mail: dumavirgil@yahoo.co.uk

N. Dumitru University of Craiova, Romania, e-mail: nicolae_dtru@yahoo.com

S. Dumitru University of Craiova, Romania

C. Francu Technical University of Civil Engineering Bucharest, Romania

B. Gherman Technical University of Cluj Napoca, Romania

G. Gogu French Institut of Advanced Mechanics, Clermont Ferrand, France

B. Grecu Politehnica University of Bucharest, Romania

A. Gronowicz Wroclaw University of Technology, Poland, e-mail: antoni.gronowicz@pwr.wroc.pl

Hao Gu University of Cassino, Italy, e-mail: hao.gu@unicas.it

R.M. Gui Technical University of Cluj Napoca, Romania

B. Gyurka Technical University of Cluj Napoca, Romania

G. Haraga Politehnica University of Bucharest, Romania

I. Hermenean Transilvania University of Brasov, Romania

A. Hernández University of Basque Country Bilbao, Spain

A.C. Horvat Technical University of Cluj Napoca, Romania

W. Hufenbach Technische Universität, Dresden

L. Irimescu "Stefan cel Mare" University of Suceava, Romania

V. Ispas Faculty of Machine Building, Technical University of Cluj Napoca, Romania, e-mail: ispasviorel@yahoo.com

Vrg. Ispas Technical University of Cluj Napoca, Romania

T.P. Itul Technical University of Cluj Napoca, Romania

C. Jaliu Department of Product Design and Robotics, Transilvania University of Brasov, Romania, e-mail: cjaliu@unitbv.ro

S. Jatsun Mechanical Department Kursk State Technical University 50 let Oktyabrya 94, 305040 Kursk, Russia, e-mail: jatsun@kursknet.ru

K. Kacso Technical University of Cluj Napoca, Romania

E. Kraritonov Bauman Moscow State Technical University, Moscow, Russia

M. Lates Department of Product Design and Robotics, Transilvania University of Brasov, Romania

D. Leohchi Technical University "Gh. Asachi" Iasi, Romania

E-C Lovasz Politehnica University of Timisoara, Romania

E. Macho University of Basque Country Bilbao, Spain

A. Malchikov University of Cassino, Italy

D. Mândru Technical University of Cluj Napoca, Romania

D. Mărgineanu Politehnica University of Timisoara, Romania

V. Măties̨ Technical University of Cluj Napoca, Romania

E. Mereuţă Dunarea de Jos University Galati, Romania,
e-mail: Elena.mereuta@ugal.ro

L.C. Mic Technical University of Cluj Napoca, Romania

L. Mihăescu Dunarea de Jos University Galati, Romania

K.H. Modler Technische Universität Dresden, Germany,
e-mail: karl-heinz.modler@tu-dresden.de

N. Modler Technische Universität Dresden, Germany

Gh. Moldovean Department of Product Design and Robotics, Transilvania University of Brasov, Romania, e-mail: ghmoldovean@unitbv.ro

M. Neagoe Department of Product Design and Robotics, Transilvania University of Brasov, Romania, e-mail: mneagoe@unitbv.ro

C. Negrean Technical University of Cluj Napoca, Romania

I. Negrean Technical University of Cluj Napoca, Romania,
e-mail: Iuliu.Negrean@mep.utcluj.ro

M. Negru University of Craiova, Romania

M. Nicolov Aurel Vlaicu University of Arad, Romania

N. Orlandea 2868 Sorrento Avenue, Ann Arbor, MI 48104 USA,
e-mail: orlanico@umich.edu

V. Pătruşel Aurel Vlaicu University of Arad, Romania

D. Perju Politehnica University of Timisoara, Romania

V. Petuya University of Basque Country Bilbao, Spain

C. Pinto University of Basque Country Bilbao, Spain

A. Pisla Technical University of Cluj Napoca, Romania

D.L. Pisla Technical University of Cluj Napoca, Romania, e-mail: doinapisla @yahoo.com

N. Plitea Technical University of Cluj Napoca, Romania

A.G. Podoleanu University of Kent at Canterbury

M.V. Popa Department of Product Design and Robotics, Transilvania University of Brasov, Romania

A. Pozdîrcă CAD-CAM Department, "Petru Maior" University of Târgu Mureş, Romania, e-mail: alexandru.pozdirca@yahoo.com

L. Racila University of Craiova, Romania, e-mail: racila_laurentiu@yahoo.com

N. Raţ Department of Product Design and Robotics, Transilvania University of Brasov, Romania, e-mail: ncretescu@unitbv.ro

C. Rozmarin Technical University "Gh. Asachi" Iasi, Romania

M. Rus Dunarea de Jos University Galati, Romania, e-mail: Madalina.Rus@ ugal.ro

C. Rusu Technical University of Cluj Napoca, Romania

O. Salgado University of Basque Country Bilbao, Spain

B. Sandru University of Basque Country Bilbao, Spain, e-mail: sandru.bogdan@ehu.es

R. Săulescu Department of Product Design and Robotics, Transilvania University of Brasov, Romania, e-mail: rsaulescu@unitbv.ro

M. Simion Technical University of Cluj Napoca, Romania

P. Sperzynski Wroclaw University of Technology, Poland

S. Stan Technical University of Cluj Napoca, Romania

I. Staretu Department of Product Design and Robotics, Transilvania University of Brasov, Romania, e-mail: staretu@unitbv.ro

R. Starosta Poznan University of Technology, Poland, e-mail: roman.starosta@put.poznan.pl

I. Stroe Department of Product Design and Robotics, Transilvania University of Brasov, Romania, e-mail: stroei@unitbv.ro

J. Szrek Wroclaw University of Technology, Poland

M.O. Tătar Technical University of Cluj Napoca, Romania, e-mail: Olimpiu.Tatar@mmfm.utcluj.ro

C.E. Tarniţă University of Craiova, Romania

D. Tarniţă University of Craiova, Romania, e-mail: dtarnita@yahoo.com

D.N. Tarniţă University of Medicine and Pharmacy Craiova, Romania

E. Teutan Technical University of Cluj Napoca, Romania

M. Urízar University of Basque Country Bilbao, Spain, e-mail: monica.urizar@ehu.es

C. Vaida Technical University of Cluj Napoca, Romania

V. Văcărescu Politehnica University of Timisoara, Romania

M. Vătăşescu Transilvania University of Brasov, Romania

R. Velicu Department of Product Design and Robotics, Transilvania University of Brasov, Romania, e-mail: rvelicu@unitbv.ro

S. Vereşiu Dunarea de Jos University Galati, Romania, e-mail: Silvia.veresiu@ugal.ro

A. Vidrean Technical University of Cluj Napoca, Romania

I. Vişa Department of Product Design and Robotics, Transilvania University of Brasov, Romania, e-mail: visaion@unitbv.ro

A. Vukolov Bauman Moscow State Technical University, Moscow, Russia, e-mail: andrei.vukolov@gmail.com

E.S. Zabava Politehnica University of Timisoara, Romania

I. Zeidis Fakultät für Maschinenbau, TU Ilmenau, Germany, e-mail: igor.zeidis@tu-ilmenau.de

K. Zimmermann Fakultät für Maschinenbau, TU Ilmenau, Germany

Challenges for Mechanism Design

Marco Ceccarelli

Abstract Mechanism Design has been the core of mechanical engineering and indeed of industrial engineering since the beginning of engineering practice and particularly in modern times. This has been motivated by the mechanical nature of tasks and interactions with machines that will be still fundamental in human-machine operations, although new and new technologies will be available. This will identify new interests and solutions as challenges for Mechanism Design, even in reconsidering and updating past achievements. Even the role of mechanical engineering can be reconsidered when discussing those challenges. This paper presents and outlines topics and considerations that can be considered for future activity in Mechanism Design both in research and teaching towards a service for the Society development. The significance of IFToMM, the International Federation for the Promotion of MMS is also stressed as the worldwide community that is focused on common views and developments for future improvements in the fields of Mechanism Design.

Keywords Mechanism and machine science · Mechanism design · Trends

1 Introduction

Mechanics of systems has been a main concern for system developments and mechanisms have been used since the beginning of a growth of the Society. In the past changes of needs and task requirements in Society and Technology have required continuous evolution of mechanisms and their uses, with or without a

M. Ceccarelli
LARM: Laboratory of Robotics and Mechatronics, University of Cassino, Cassino, Italy

I. Vişa (ed.), *SYROM 2009*,
DOI 10.1007/978-90-481-3522-6_1,

rational technical consciousness. Today it seems that we have reached a saturation and a very high level of knowledge on mechanisms so that several professionals and even researchers from other fields think that there is nothing else to be discovered or conceived in Mechanism Design. Most of the arguments concern with the fact that a lot of new systems can be designed and operated when problems are solved mainly in the other components than mechanical ones. This is due also to the recent developments of those subsystems. But nevertheless, if mechanical aspects are not considered properly, a new system fails. As an emblematic example let's refer to robots that still need a lot of research even in mechanical aspects with the aim to fully exploit the possibility that the other subsystems can provide for the mechanical functionality.

Attention must be addressed to the evolution of engineering frames and possibilities to properly direct efforts for future developments. Some specific emphasis has been yet addressed on historical trends for research activity in papers like [16, 17]. Even the author has attempted to outline historical developments with the aim to track the past for directions of future work in [3–9, 19].

In this survey a vision is outlined in order to show that, although many new issues in Mechanism Design can be still based on basic concepts that have been developed in the past, we have still several challenging issues to give proper solutions for new and updated problems in the evolving Technology and Society. New systems and updated performance are asked for mechanism applications that deserve attention starting from theoretical bases before to update or conceive algorithms for design and/or operation with optimal characteristics.

Two main considerations can be observed in order to claim that Mechanism Design is still a discipline with necessary strong activity in teaching, research, and practice. Namely they are:

- Human beings operate and interact with environment and systems on the basis of actions of mechanical nature; therefore mechanisms will be always an essential part of systems that help or substitute human beings in their operations and other manipulations.
- There is a continuous need to update problems and solutions in Technology, and specifically in Mechanism Design, since Society continuously evolves with new and updated needs and requirements; thus, even mechanisms are asked for new and updated problems that require a continuous evolution and update of knowledge and means for proper applications of mechanisms.

2 Mechanism Design and IFToMM Activity

The identity of a person and even a Community can be indicated by a name giving a synthetic description of the personality and its main capability or characteristics.

The names of IFToMM (the International Federation for the Promotion of MMS), TMM (Theory of Machines and Mechanisms), and MMS (Machine and Mechanism Science) identify IFToMM Community who refers to MMS at large.

The names of IFToMM, TMM, and MMS are related to fields of Mechanical Engineering concerning with Mechanism Design in broad sense.

The meaning of TMM, now MMS, can be clarified by looking at terminology. IFToMM terminology [11, 12] gives:

- Machine: mechanical system that performs a specific task, such as the forming of material, and the transference and transformation of motion and force.
- Mechanism: system of bodies designed to convert motions of, and forces on, one or several bodies into constrained motions of, and forces on, other bodies.

The meaning for the word "Theory" needs further explanation. The Greek word for Theory comes from the corresponding verb, whose main semantic meaning is related both with examination and observation of existing phenomena. But, even in the Classic language the word theory includes practical aspects of observation as experiencing the reality of the phenomena, so that theory means also practice of analysis results. In fact, this last aspect is what was included in the discipline of modern TMM when Gaspard Monge (1746–1818) established it in the Ecole Polytechnique at the beginning of nineteenth century [10] (see for example the book by [14], whose text include early synthesis procedures and hints for practical applications). Later (see for example [15]) and up today (see for example [18]) many textbooks have been entitled Theory of Mechanisms since they describe both fundamentals and applications of mechanisms in machinery.

The term MMS has been adopted within the IFToMM Community since the year 2000 [13] after a long discussion (see [2] in the IFToMM Bulletin), with the aim to give a better identification of the modern enlarged technical content and broader view of knowledge and practice with mechanisms. Indeed, the use of the term MMS has also stimulated an in-depth revision in the IFToMM terminology since the definition of MMS has been gives as [12]:

- Mechanism and Machine Science: Branch of science, which deals with the theory and practice of the geometry, motion, dynamics, and control of machines, mechanisms, and elements and systems thereof, together with their application in industry and other contexts, e.g. in Biomechanics and the environment. Related processes, such as the conversion and transfer of energy and information, also pertain to this field.

Summarizing, since the modern assessment, TMM has been considered as a discipline, which treats analysis, design and practice of mechanisms and machines. This will be also in the future for the area today named as MMS, since modern and futures systems will still include mechanisms and machines with mechanical designs and operations as related with life and working of human beings. These mechanical devices need to be designed and enhanced with approaches from mechanical engineering because of the mechanical reality of the environment where the human beings will always live, although new technologies will substitute some components or facilitate the operation of mechanical devices.

Technically, MMS can be seen as an evolution of TMM as having a broad content and view of a Science, including new disciplines. Historically, TMM has

included as main disciplines: History of TMM; Mechanism Analysis and Synthesis; Theoretical Kinematics; Mechanics of Rigid Bodies; Mechanics of Machinery; Machine Design; Experimental Mechanics; Teaching of TMM; Mechanical Systems for Automation; Control and Regulation of Mechanical Systems; RotorDynamics; Human-Machine Interfaces; Bio-Mechanics. The modernity of MMS has augmented TMM with new vision and means but also with many new disciplines, whose the most significant can be recognized in: Robotics; Mechatronics; Computational Kinematics; Computer Graphics; Computer Simulation; CAD/CAM for TMM; Tribology; Multibody Dynamics.

Mechanism Design can be understood as the group of disciplines in MMS that are specifically related to the design of the several aspects of machines in order to define the fundamental characteristics of geometry, motion capability, and functionality of a multi-body system. However, in modern terms Mechanism Design can be also considered within a design frame in which the features of mechanisms are only a part of a design process of systems as a multi-body systems. Therefore, the term Mechanism Design can often be so wide like MMS.

The evolution of the name from TMM to MMS, that has brought also a change in the denomination of the IFToMM Federation from "IFToMM International Federation of TMM" to "IFToMM, the International Federation for the Promotion of MMS", can be considered as due both to an enlargement of technical fields to an Engineering Science but even to a great success in research and practice of TMM with a worldwide engineer community.

The developments in TMM have stimulated cooperation all around the world at any level. One of the most relevant results has been the foundation of IFToMM in 1969, Figs. 1 and 2. IFToMM was founded as a Federation but as based on the

Fig. 1 A historical moment of the foundation of IFToMM, the International Federation for the Theory of Machines and Mechanisms, in Zakopane (Poland) on 27 September 1969 (Courtesy of IFToMM Archive): 1 – prof. Ivan I.Artobolevskii (USSR); 2 – prof. Adam Morecki (Poland); 5 – prof. Nicolae I. Manolescu (Romania); 6 – prof. Erskine F. Crossley (USA); 7 – prof. Giovanni Bianchi (Italy); 8 – prof. Aron E. Kobrinskii (USSR); 9 – prof. Werner Thomas (Germany); 10 – prof. Jan Oderfeld (Poland)

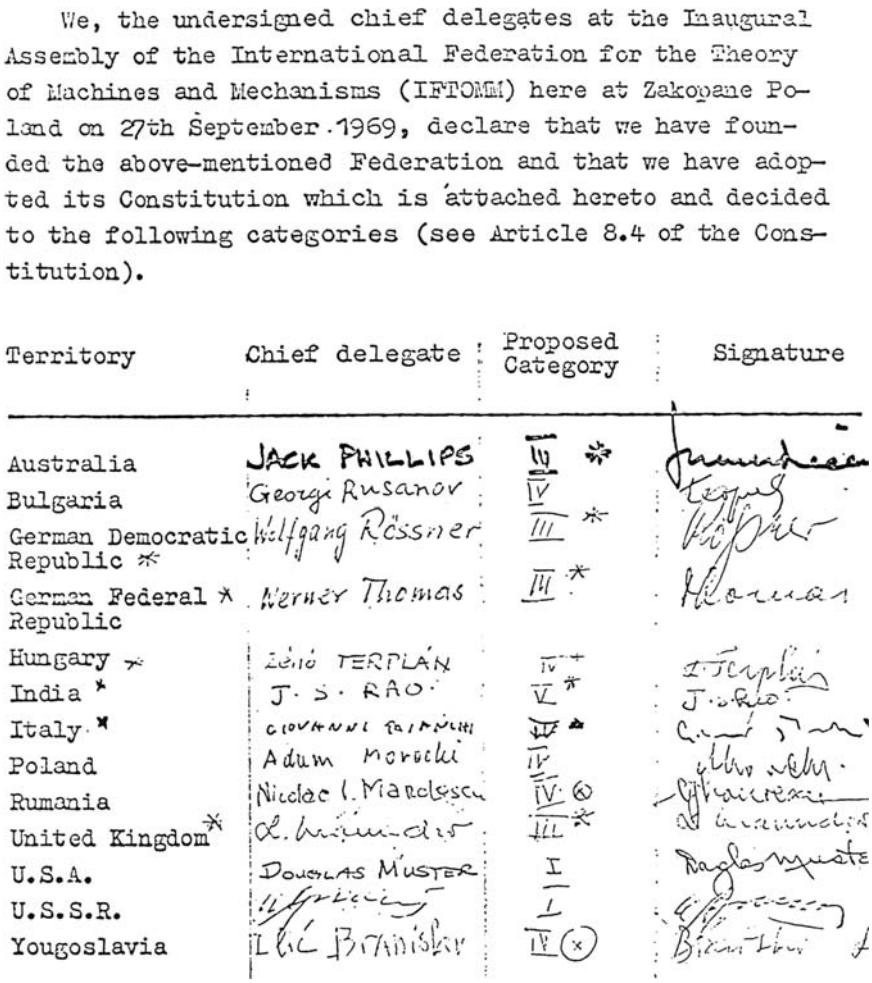

We, the undersigned chief delegates at the Inaugural Assembly of the International Federation for the Theory of Machines and Mechanisms (IFTOMM) here at Zakopane Poland on 27th September 1969, declare that we have founded the above-mentioned Federation and that we have adopted its Constitution which is attached hereto and decided to the following categories (see Article 8.4 of the Constitution).

Territory	Chief delegate	Proposed Category	Signature
Australia	JACK PHILLIPS	III *	
Bulgaria	Georgi Rusanov	IV	
German Democratic Republic *	Wolfgang Rössner	III *	
German Federal Republic *	Werner Thomas	III *	
Hungary *	Zénó TERPLÁN	IV *	
India *	J. S. RAO	V *	
Italy *	GIOVANNI [illegible]	III *	
Poland	Adam Morecki	IV	
Rumania	Nicolae I. Manolescu	IV ⊗	
United Kingdom *	[illegible]	III *	
U.S.A.	Douglas Muster	I	
U.S.S.R.	[illegible]	I	
Yougoslavia	[illegible]	IV ⊗	

Fig. 2 IFToMM foundation act (Courtesy of IFToMM Archive)

activity of individuals within a family frame with the aim to facilitate co-operation and exchange of opinions and research results in all the fields of TMM. Many individuals have contributed and still contribute to the success of IFToMM and related activity (see IFToMM webpage: www.iftomm.org) under a vision coordination of IFToMM Presidents over time, Fig. 3.

The modernity and relevance of IFToMM activity can be recognized in the common frame of views and results on MMS, in the many different technical fields. Thus, the role of IFToMM can be still recognized, like stated in its constitution, as instrumental in stimulating enhancements and giving common frames and views for the evolution of MMS both with technical aims and benefits for the Society.

Fig. 3 IFToMM Presidents at the Symposium HMM2000 in Cassino on May 2000 (from left to right): Giovanni Bianchi (1984–1987 and 1988–1991), Arcady Bessonov in substitution of Ivan I. Artobolevsky (1969–1971 and 1972–1975), Bernard Roth (1980–1983), Jorge Angeles (1996–2000), Kenneth J. Waldron (2000–2003 and 2004–2007), Leonard Maunder (1976–1979), Adam Morecki (1992–1995), and Marco Ceccarelli (2008–2011; at the time of the photo Chairman of HMM2000 IFToMM Symposium on History of Machines and Mechanisms) (years in the brackets indicate the President term)

3 Future Challenges

The main new research lines in Mechanism Design can be summarized in the following topics:

- 3D Kinematics and its application in practical new systems and methodologies
- Modeling and its mathematization
- Multi-d.o.f. multibody systems
- Spatial mechanisms and manipulators
- Unconventional mechanisms
- Scaled mechanisms
- Creative design
- Mechatronic designs
- Reconsideration and reformulation of theories and mechanism solutions

Those topics are also motivated by needs for formation and activity of professionals who will be able to conceive and transmit innovation and/or updated approaches both into production and service frames.

Teaching in MMS requires attention on modern methodologies that can use efficiently computer and software means, which are still evolving rapidly. Thus, there is a need to update also the teaching means that makes use of simulations and computer oriented formulation. In addition, mechatronic lay out of modern machinery suggest to teach mechanisms as integrated with other components like actuators and sensors since the beginning of the formation curricula.

Activity by professionals asks for novel applications and high performance designs of machines as they are continuously needed in evolving/updating systems and engineering tasks. In addition, there is a need to make understandable the new methodologies to professionals for practical implementation both of their use and results. New solutions and innovation is continuously asked not only for technical needs but even for political and strategic goals of company success (as even with an unreasonable obsession for novelty).

Are the above-mentioned topics really new arguments in the History of MMS? What challenges are still facing the MMS community?

It is quite clear that modern developments in Technology and Science have stimulated and required developments and novelties in machines and mechanisms too, since the growth of new and updated needs, but also because of current practical possibilities for mechanism solutions that were utopist just in a recent past.

Past solutions and efforts can be helpful to understand situations and developments that are still needed to reach successful achievements fulfilling today and even future requirements as outlined with few emblematic historical examples in a trend perspective in [9].

Lot of today activity is addressed to new models and new mathematizations for mechanisms. This attention is not new, but procedures and means can be considered new since they are related to goals of using modern means of calculus both in term of numerical algorithms and computer facilities. Today a high level of abstraction is used in treating design features and motion characteristics of mechanisms, mainly with the aim to obtain more comprehensive solutions and using efficiently new calculus means. This attention does not refer directly to any practical application and seems to be a pure academic exercise, but one can easily recognize that results of such a theoretical analysis can be implemented to improve successfully machinery operations both in terms of theoretical capabilities and mechanical design characteristics.

Today dualistic viewpoints are proposed as based on graphical and mathematical approaches yet. Thus, for examples graphs and algebraic groups are used to describe kinematic chains of mechanisms and their functionalities. Similarly, Graph Theory with a matrix algebra and Group Theory are introduced to formulate the operation of mechanisms and then new design algorithms. Lot of work is addressed to a suitable mathematization of mechanism aspects that can be efficiently treated through computer means. This issue, indeed, is an old need, i.e. designers and researchers worked on engineering views as a function of computational issues with available means of the time and therefore, theories and algorithms are today needed to be formulated or re-formulated accordingly to the capacity of those new available means. Computer means can make available mathematical means for practical engineering purposes with great computational accuracy, when they are properly adjusted to each other. An example from the past is the Algebra of matrices that today is commonly used in Robotics. It was not used until computer calculation since the end of 1950s made it feasible and more efficient than traditional graphical procedures. New attention is addressed today to other algebras and even using quaternions and biquaternions in a considerable growing literature.

Today computational issues seem to motivate also basic research and re-formulation regarding problems that were considered as definitively solved even in a recent past. This is because a new mathematization and related computational algorithms can give further insight both in solutions and design algorithms.

Issues on mathematization are still of current interest non only for computational purposes, but even for further investigation fields as for example for 3D kinematics. The great attention on 3D kinematics has been motivated from engineering viewpoint since when there has been the possibility to operate and regulate spatial mechanisms in practical applications. This has happened when it has been possible to control and to sensor spatial motion by using electronic components. Indeed, even the increase of spatial tasks for manipulations and industrial processes have made of practical interest mechanisms that were studied since the second half of nineteenth century, but mainly for pure academic interests. Screw systems are today extensively modeled and formulated to design and operate manipulators and spatial mechanisms in practical applications in several fields other than industry, like for example in medical engineering. Schemes from Screw Theory are used and although they are presented in new algorithms, basic concepts were conceived in the past. But, a useful mathematization and consequent practical implementation of Screw Theory have been developed in modern terms and are still under development as function of mathematical and informatics means through several approaches.

Spatial mechanisms are thought to be conceived in the last 5 decades. But the possibility to use them is not new. Nevertheless, there is great attention in conceiving new spatial mechanisms and manipulators both for theoretical investigations in reaching new and wider possibilities and for practical applications. New architectures can be searched by using the previously mentioned mathematical means as well as through intensive ingenuity approaches with experimental activity. Recent relevant attention is focused on parallel manipulator architectures and probably this will be a fecundus field for new conceptions in a near future yet. But even the multibody analysis can give possibilities in discovering but applying properly spatial mechanisms with new and old designs.

Problems that are related to manipulation mechanisms such as for grasping, are today of fundamental relevance, and considerable attention is addressed to the variety of grasps and to general models and formulation of the mechanics of grasp. Those needs have been determined by a large variety of tasks and objects that can be grasped in today applications both in industry and diary life. Today, we have very powerful technology for sensors and force control, but still the mechanics of the grasp is fundamental and even more influential on the grasp success is the mechanism design and its functionality. The grasp versatility of human hand with its compact design is still a challenge both for robotic applications and prosthesis implementation.

3D kinematics has been deepened and abstraction has reached good results so that is it used also in many other fields. Today one of the most successful field of novel applications is considered Computer Vision and Graphics, since when vision

systems are available with suitable advanced capabilities. The topic can be specifically addressed to enhance technical drawing towards its standardization. This is again the case today as related to user-oriented CAD techniques that can give results useful also for Vision applications.

This is to stress with an example that approaches and solutions in mechanism Design can be extended also to other files of Engineering, and this can be a further challenge when extension possibility is full understood.

Nowadays automatic machinery requires multi-d.o.f. mechanisms that have been possible only with the advent of modern control engineering and advanced electric motors. With the terms multi-d.o.f and multi-body its usually intended systems that have the core in mechanical parts but whose fucntionaluty string depends of several other components. Indeed, those systems are characterized by a complexity and sophistication that make their functionality are not easy to be understood and to be properly used in their practical operation. Thus, challenges can be still considered developments of analysis procedures both for design and operation purposes, mainly with characteristics of user-oriented features for professional activity.

Mechatronics is usually considered a last achievement of modern engineering by which modern systems are designed and operated because of integration of several components of different natures with a multi-disciplinary engineering approach, Fig. 4. The significant role of mechanisms in Mechatronics can be understood since it is fundamental to have a mechanical system to interact with the environment or to perform the task. However, for a mechanical system, but even for a mechatronic one within mechanics aspects mechanism can be considered together with material, mechanical design, and manufacturing as main aspects to be considered for a proper design and functionality. Although engineer formation was and is still achieved by teaching separately courses on specific disciplinary subjects, nevertheless machines have been always treated by looking at the integration of different aspects. Of course, nowadays the multitude and sophistication of those multi-disciplinary aspects require to emphasize on the multi-disciplinarity by asking expertise in specific fields but in a wider and wider context.

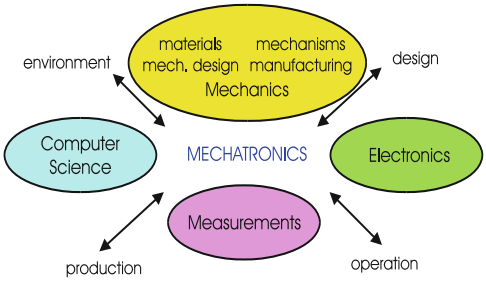

Fig. 4 A scheme for definition of Mechatronics

Another challenging trend in MMS can be identified in scaled mechanisms/machines and their applications both to very small and very large sizes.

Miniaturization has been experienced in the last decades and today micro-mechanisms are almost usual machines (as for example micro-grippers) so that research is now directed even to molecular scales. On the other hand the increase of power needs has required larger and larger size of mechanical devices. Even spatial exploration and exploitation have stimulated a great consideration of very large mechanism with deployable mechanism structures. The miniaturization at today levels is indeed a novelty in the history of engineering, but the scaling need is not new and engineering approaches were developed to adapt the mechanism size to the application requirements even by considering peculiarities of the scaling in terms of actions and relative significance.

In particular, the history of Mechanism Design is mainly related to an increase of tasks by enlarging mechanisms in terms of power, motion, and productivity. Thus once more, the new scaling of design and operation has required and still require to re-consider the basic principles of mechanisms. Similarly, the challenge of micro-mechanisms and even more nano-mechanisms can be considered in adapting and therefore in redesigning known mechanisms by considering the different new situations and environments at the very small scale applications.

One of the greatest attention for novelties in Mechanism Design can be considered the conception of new mechanisms and systems that can fulfill (optimally) new identified problems. Today is very difficult to conceive new mechanisms from theoretical viewpoint, after that in the past, efforts have obtained mechanism classifications with exhaustive listing of kinematic chains (see for example [1]). However, new architectures of mechanisms have been attempted even in the past by using different concepts from traditional mechanism design like for example with compliance or underactuated and overconstrained mobility. Indeed they are extensively used only in modern times, even if in the past we can find pioneering solutions. Unconventional mechanisms can be searched both with new kinematic chains and hybrid solutions with mechatronic solutions. The functionality needs to be properly investigated both for design characterization and operation feasibility. Thus, new solutions are more and more attempted by combining the traditional rigid body mechanism layout with other components of different nature and operation outputs (like springs with non-linear outputs, plastic joints, tribological actuators, and so on).

In the last decade, mechanism design has been revitalized as central role for machine design by a development of so-called Creative Design in which the creative skill of a designer is considered together with technical methodologies and computational algorithms in a well defined design process by which all the possibilities are explored for a given task. Indeed, Creative Design is still understood in a wider concept but always considering as central the intellectual creativity, which can be also independent of a strong technical background. The challenge can be recognized in the possibility to be free from the well defined schemes of the well established technical frames for mechanism design with the aim to discover both new systems or simple efficient solutions even from the large

existing variety. Indeed, most of the inventions of the past have been based on the ingenuity of inventors, who first attempted the construction and operation of their inventions and then they or even others studied and systematized a related theoretical background for further designs and enhancements.

A fundamental aspect, which is in common to new ideas from the past and challenges for real today novelties, can be identified in issues that are related to mathematization and computation of theories and mechanism solutions. Challenging problems, like in the past, are related to derive methodologies (i.e. knowledge) that can be used in practical engineering at current modern levels of efficiency, and are feasible for conceiving and updating tasks and requirements.

A great challenge can be understood in developing those new methodologies and mathematizations in formulation and procedures that can be understood and used really by professionals with the aim to improve both the mechanism technique and its understanding. This aspect is, indeed, connected with the continuous demand of novelty both in the Academic World and by the national governments. This seems to be like a diary obsession that often brings to unnecessary sophistication and complexity in the research activity and its results, even in the filed of practical applications. In addition, do we really need novelties in human-machine interactions? Or is it more challenging (convenient or reasonable) to optimize and adjust successful solutions? The obsession of novelty could be also fulfilled in directing efforts in updating and enhancing solutions regarding the evolving needs in technology and society, as previously mentioned, without making not understandable the novelties and the novelty obsession to large public (who are the contributors for the research funding).

From general viewpoint the role of Mechanism Design in a design process can be stressed as fundamental like in the example in Fig. 5 in which the features of mechanism operation are indicated as necessary consideration since the first stages of design consideration and they are still to be considered in the iterative-optimization cycles towards a final solution.

A final remark is necessary as to point out the role of engineers in the Society, as an important aspect for motivating activity in developing but enhancing engineering means and solutions, as outlined specifically on Mechanism Design in the paper. The role of engineers and engineering (mainly mechanical engineering and more specifically Mechanism Design) in the modern Society seems to have decreased in the last decades so that today the large public and even more particularly the governors have not an awareness of its significance as to be fundamental for not only the further development but even to maintain the current status of the Society. This weakness or even lack of an influent role of mechanical engineering, and even more specifically of Mechanism Design, can be seen in poor funding (or even lack) for research activity and in the decreasing of significance of mechanical engineers with Mechanism Design expertise even in the productive world (this is demonstrated by the decreasing of salary of industrial engineers!). Is that the Academic world (and particularly the IFToMM community) is not able to demonstrate such a role or the Society does not need engineering development? Answering to this amletic question is perhaps a primary challenge.

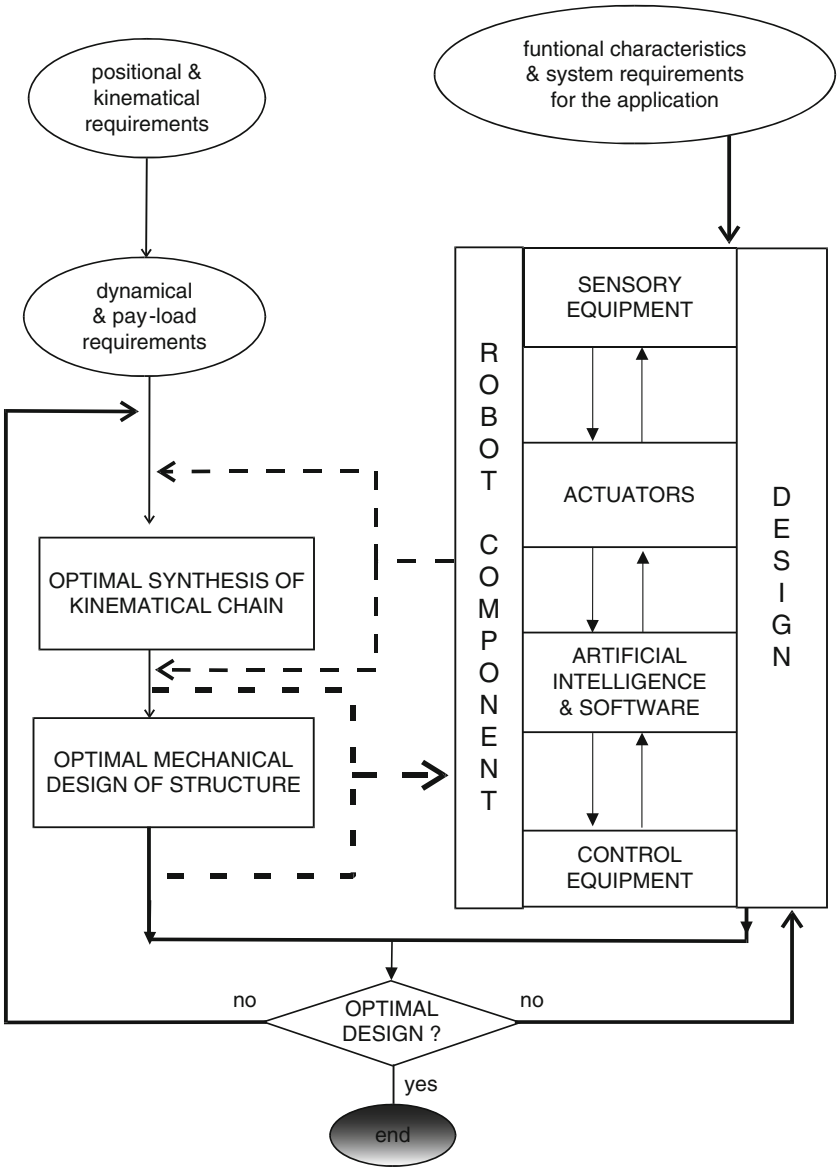

Fig. 5 The role of mechanism features in the design process of a mechatronic system like a robot

4 Conclusions

Not everything is new or recently developed in MMS and specifically in Mechanism Design. But this does not mean that there is not interest and even no need to work on developing and enhancing knowledge and applications in Mechanism

Design. New challenges are determined for Mechanism Design in the new Technology and Society needs both in term of new solutions and updating past systems. Many of today new issues in MMS have been conceived in the past in terms of basic principles that are often forgotten. But the rapidly evolving needs of Technology and Society will require a continuous re-thinking and re-conceiving of methodologies and solutions in suitable updated applications. Thus, main challenges for future success in Mechanism Design can be recognized in the capability of being able to keep updated the field and therefore in being ready to solve new and updated problems with new ideas or refreshing past solutions, like it has been done successfully in the past.

References

1. Artobolevsky, I.I.: Mechanisms in Modern Engineering, vols. 5. Mir Publishers, Moscow (1975–1980)
2. Ceccarelli, M.: On the meaning of TMM over time. Bull. IFToMM Newsl. **8**(1) (http://www.iftomm.org) (1999)
3. Ceccarelli, M.: From TMM to MMS: a vision of IFToMM. Bull. IFToMM Newsl. **10**(1) (http://www.iftomm.org) (2001a)
4. Ceccarelli, M.: The challenges for machine and mechanism design at the beginning of the third millennium as viewed from the past. In: Proceedings of Brazilian Congress on Mechanical Engineering COBEM2001, Uberlandia, Invited Lectures, vol. 20, pp. 132–151 (2001b)
5. Ceccarelli, M.: A historical perspective of robotics toward the future. Fuji Int. J. Robot. Mechatronics **13**(3), 299–313 (2001)
6. Ceccarelli, M.: IFToMM activity and its visibility. Bull. IFToMM Newsl. **13**(1) (http://www.iftomm.org) (2004a)
7. Ceccarelli, M.: Classifications of mechanisms over time. In: Proceedings of International Symposium on History of Machines and Mechanisms HMM2004, pp. 285–302. Kluwer, Dordrecht (2004)
8. Ceccarelli, M.: Evolution of TMM (Theory of Machines and Mechanisms) to MMS (Machine and Mechanism Science): an illustration survey. Keynote Lecture, 11th IFToMM World Congress in Mechanism and Machine Science 2004, Tianjin, vol. 1, pp. 13–24 (2004c)
9. Ceccarelli, M.: History and challenges of mechanism and machine science within IFToMM community. Special Issue on Jubilee of Budapest Technical University, Springer (2009)
10. Chasles, M.: Exposé historique concernant le cours de machines dans l'enseignement de l'Ecole Polytechinique. Gauthier-Villars, Paris (1886)
11. IFToMM: IFToMM Commission A. Standard for terminology. Mechanism and Machine Theory, **26**(5 Special issue) (1991)
12. IFToMM: Standardization and terminology. Mechanism and Machine Theory, **38**(7–10 Special issue) (2003)
13. IFToMM: IFToMM constitution and by-laws 2007. http://www.iftomm.org (2007)
14. Lanz, J.M., Betancourt, A.: Essai sur la composition des machines. Paris (1808)
15. Masi, F.: Teoria dei meccanismi. Zanichelli, Bologna (1888)
16. Roth, B.: Robots – state of art in regard to mechanisms theory. ASME J. Mech. Transm. Automation in Des. **105**, 11–12 (1983)
17. Shah, J.J. (ed.): Research opportunities in engineering design – final report to NSF. NSF Strategic Planning Workshop. ASME DETC, Irvine (1996)
18. Uicker, J.J., Pennock, G.R., Shigley, J.E.: Theory of machines and mechanisms. Oxford University Press, New York (2003)
19. Ceccarelli M.: What is old in what is new in MMS research, Special Lecture. In: Proceedings of 13-th Symposium on MMM, Japan Council of IFToMM, Tokyo, pp. 1–11 (2007)

Mechatronics and Mechanisms: From Drive to Process

B. Corves

Abstract Selected mechatronic design solutions that have been developed at the Department of Mechanism Design and Machine Dynamics at RWTH Aachen University will be presented. These mechatronic systems are taken from the field of glass machinery, textile machinery and robotics. It will be shown that for a proper design process modelling, simulation and optimization are indispensable.

Keyords Mechatronics · Simulation · Optimization · Topological and dimensional synthesis

1 Introduction

This paper shows a selected number of mechatronic design solutions that have been developed at the Department of Mechanism Design and Machine Dynamics at RWTH Aachen University. With these mechatronic design solutions which have already been presented in detail in previous papers that can be found in the reference list the author intends to show that in order to design a mechatronic machine architecture, a sound understanding not only of the mechanism itself but also of the drive system, be it pneumatic, hydraulic or servo-electric and of the technological process is indispensable. Only if the drive system, mechanism and the process are modelled and simulated properly, will it be possible to come up with optimal mechatronic design solution.

B. Corves
Department of Mechanisms Theory and Dynamics of Machines, RWTH Aachen University, Germany

I. Vişa (ed.), *SYROM 2009*,
DOI 10.1007/978-90-481-3522-6_2,

2 Mechatronic Machine Architecture

In this paper the focus will be on the systematic, mechatronic approach for the layout and design of active motion devices, i.e., planar and spatial mechanisms with non-uniform transfer characteristics.

Due to these non-uniform motions of the active motion devices together with the non-linear dynamic behavior of the drive systems, time variant inertia forces and inertia torques may lead to undesired stresses, strains and vibrations. In order to counteract these effects by applying suitable design solutions, it is necessary to simulate the behavior of the complete mechatronic system as exactly as possible in a multidisciplinary approach. This means that the modelling must include the dynamic behavior of the drive system, the nonlinear mechanism behavior and the reactive process effects.

3 Mechatronics in Glass Machinery

In modern glass forming machines the forming of container glass starts with a drop of molten glass with a honey-like viscosity at a temperature well above 1200°C. In order to shape the glass into a bottle, a considerable number of different mechanisms driven either by pneumatic or electric drive systems are used.

The IS-Machine consists of 6–16 parallel sections (Fig. 1) which are all of the same design and perform the same glass forming task. Therefore the glass forming process is no longer a completely serial process as on a round table machine but a parallel process with increased productivity and easier serviceability due to the individual section layout.

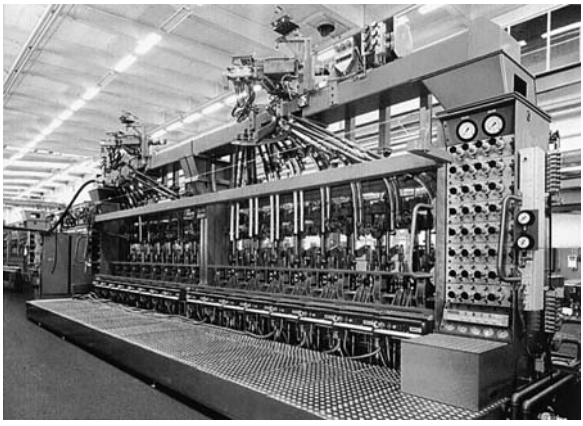

Fig. 1 2 × 8 Section IS-machine

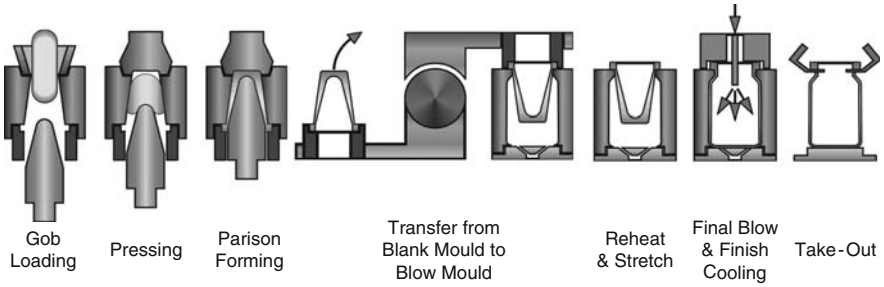

Fig. 2 Press & blow process

Figure 2 shows a typical Press & Blow process where after gob loading through the funnel into the blank mould, the parison is pressed and formed upside down by placing the baffle on top and moving the plunger from its loading position upwards. After the plunger and baffle have been removed and the mould halves have been opened, the parison is inverted from blank to blow side for parison reheat and final blow. After closing the blow molds and parison reheat the container is finally formed by applying final blow air. Finally the container is picked up by the take out and placed on the dead plate for additional cooling and final delivery into the cooling oven.

Precision and repeatability of the section mechanisms is of vital importance for a precise container forming process [1]. In order to properly realize the above described forming process on blank and blow side, it is necessary to synchronize the motion of all section mechanisms in a coordinated and precise manner [2]. Obviously a stable and repetitive glass forming process is the key to a high quality glass container. This process stability and precision has a lot to do with the section mechanisms, whose motion under high cycle rate and high precision must be optimally coordinated.

3.1 Pneumatic Actuation

Most of the mechanisms used in conventional machines are actuated by pneumatic cylinders. This is especially true for the plunger mechanism that is used on the blank side of the IS-Machine in order to press the molten gob of glass into a parison.

The physical model of the pneumatic cylinder, which is the basis for the simulation of the dynamic behavior of the pneumatic actuation is displayed in Fig. 3.

It shows all important parameters which influence the dynamic behavior of the pressure inside both cylinder chambers. This model not only considers the flow characteristics for inlet and outlet but also the leakage of both cylinder chambers. Also pneumatic end position damping can be simulated by means of piston position

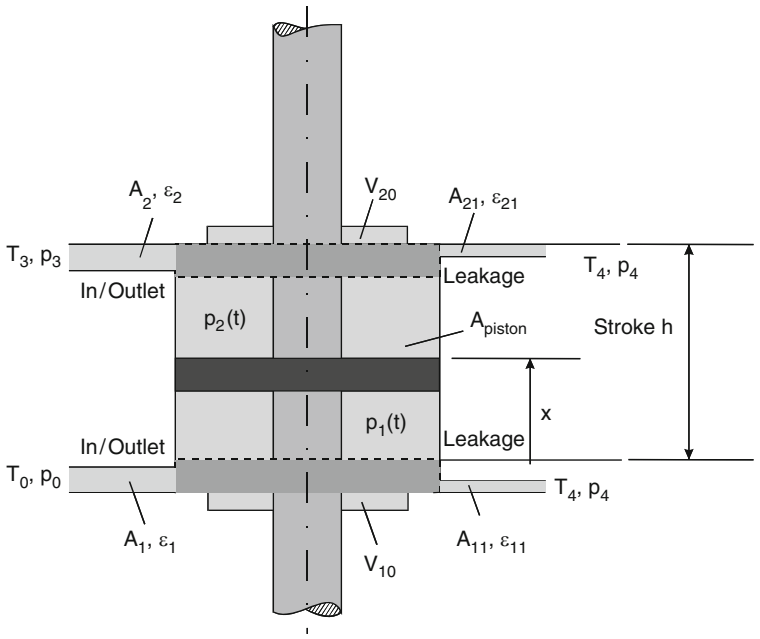

Fig. 3 Pneumatic cylinder model

dependant inlet and outlet cross sections. As an additional, optional feature, also hydraulic end position damping with stepped hydraulic constraints has been modelled.

Considering the time dependant mass flow, the dynamic behavior of the pressure inside the cylinder chambers can be derived from the first fundamental equation for stationary flow processes leading to the following non linear first order differential equations [2]:

$$\frac{dp_1}{dt} = \frac{n}{V_{10} + x \cdot A_{Kolben}} \begin{bmatrix} \varepsilon_1 \cdot A_1 \cdot p_0 \cdot \sqrt{2 \cdot R \cdot T_0} \cdot \left(\frac{p_1}{p_0}\right)^{\frac{\kappa-1}{\kappa}} \cdot \psi_{10} \\ -\varepsilon_{11} \cdot A_{11} \cdot p_4 \cdot \sqrt{2 \cdot R \cdot T_4} \cdot \left(\frac{p_1}{p_4}\right)^{\frac{3\kappa-1}{2\kappa}} \cdot \psi_{41} \\ -\dot{x} \cdot A_{Kolben} \cdot p_1 \end{bmatrix} \tag{1}$$

$$\frac{dp_2}{dt} = \frac{n}{V_{20} + (h - x) \cdot A_{Kolben}} \begin{bmatrix} -\varepsilon_2 \cdot A_2 \cdot p_3 \cdot \sqrt{2 \cdot R \cdot T_3} \cdot \left(\frac{p_2}{p_3}\right)^{\frac{3\kappa-1}{2\kappa}} \cdot \psi_{32} \\ -\varepsilon_{21} \cdot A_{21} \cdot p_4 \cdot \sqrt{2 \cdot R \cdot T_4} \cdot \left(\frac{p_2}{p_4}\right)^{\frac{3\kappa-1}{2\kappa}} \cdot \psi_{42} \\ +\dot{x} \cdot A_{Kolben} \cdot p_2 \end{bmatrix} \tag{2}$$

The dimensionless function $\psi_{i,\ j}$ describes the flow through an ideal nozzle dependant from the pressure ratio p_i/p_j, where a distinction must be made between subcritical and supercritical flow. Of course for a practical application inlet and outlet flow of a pneumatic cylinder very seldom can be modelled as an ideal nozzle. This effect is covered through a certain penalty function.

3.2 Servo Electric Actuation

As an alternative for the pneumatic drive generally used today for IS-section mechanisms, also a servo electric drive has been considered and modeled as a configuration with a rotational servo electric motor that drives a screw through an elastic coupling and a nut which is connected to the translation ally moving rod. After setting up a dynamic model of the servo electric motor together with the screw and nut combination, this model can simply replace the model of the pneumatic drive in order to have a complete model of the servo electric drive and mechanism and thus be able to compare the two drive concepts.

Figure 4 shows the Simulink© representation of the simulation model used for the servo electric drive. The dynamic behavior of the motor has been modelled as a DC-motor with the parameters coil resistance R and the inductivity L. Furthermore the self-induction of the motor has also been considered through the electro magnet flux constant K_{EMF}. This leads to the following differential equation:

$$\frac{dI}{dt} = -\frac{R}{L} \cdot I + \frac{1}{L} \cdot (U - U_{EMF}) \quad \text{with } U_{EMF} = K_{EMF} \cdot n \tag{3}$$

Figure 5 shows the model of the current controller which is based on an analogue PI-controller, described through the parameters K_p and T_I. Additionally a current saturation with an anti-wind-up loop has been modelled.

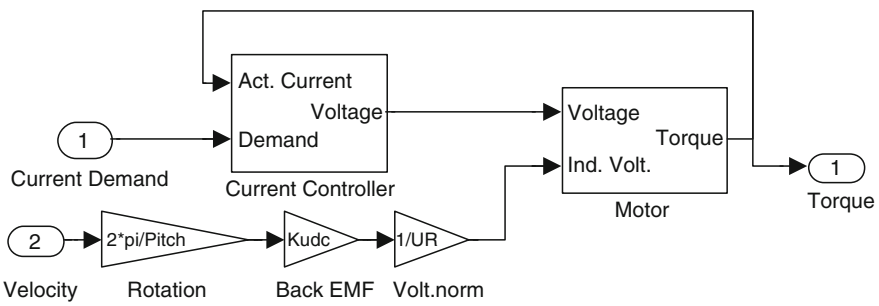

Fig. 4 Servo electric drive model

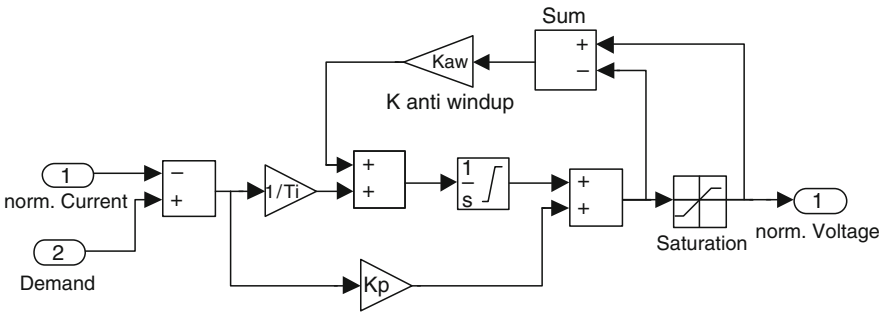

Fig. 5 Current controller model

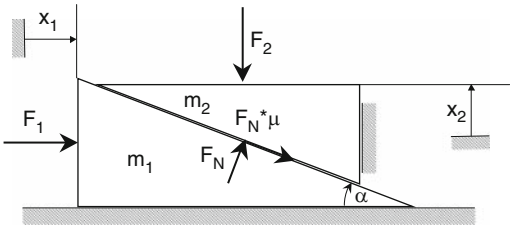

Fig. 6 Model of friction situation between screw and nut (contact forces shown as acting from m_1 to m_2)

Obviously the pneumatic cylinder described in Section 3.1. cannot simply be replaced by a rotational servo electric motor but a mechanical transmission is required to transform the rotary motion of the drive into a translational movement of the plunger. A custom designed brushless DC motor drives the outside nut of a hollow roller screw. The axially stationary nut forces the roller screw to move up and down and thereby actuates the plunger movement. The rotational degree of freedom of the screw is locked by two keys sliding in keyways.

The most important parts of the plunger mechanism model is the contact force dependant friction force model of the screw and nut assembly. The situation between screw and nut is dominated by the friction force, which depends on the normal force between screw and nut. Figure 6 shows all parameters that are needed for proper modeling.

The mass m_1 can be determined from the total moment of inertia of all rotational parts and the effective pitch radius of the screw:

$$m_1 = \frac{J_{rot}}{{r_{screw}}^2} \tag{4}$$

The parameter m_2 represents the total mass of all translation ally moving parts such as spindle and plunger itself.

The force F_1 is the sum of the driving force from the servo motor and the counteracting rotational friction torque from the motor and nut bearings.

$$F_1 = \frac{\left(T_{motor} - sign(\dot{x}_2) T_{fric}\right)}{r_{screw}} \tag{5}$$

The force F_2 apart from the friction term also contains a spring force F_{spring}, caused by a spring, which keeps the plunger in the gob loading position, the gravitational force from the mass m_2 and most important the glass forming force F_{Glass}:

$$\begin{aligned} F_2 = F_{Glass} + sign(\dot{x}_2) F_{fric} \\ + m_2 \cdot g - F_{spring} \end{aligned} \tag{6}$$

Now according to Fig. 6 the dynamic equilibrium can be formulated for masses m_1 and m_2:

$$\begin{aligned} m_1 \cdot \ddot{x}_1 = & - F_N \sin(\alpha) \\ & - \mu \cdot sign(\dot{x}_2) |F_N| \cdot \cos(\alpha) + F_1 \end{aligned} \tag{7}$$

$$\begin{aligned} m_2 \cdot \ddot{x}_2 = & - F_N \cos(\alpha) \\ & - \mu \cdot sign(\dot{x}_2) |F_N| \cdot \sin(\alpha) - F_2 \end{aligned} \tag{8}$$

At first glance these two equations seem to contain three unknowns, but since the two coordinates x_1 and x_2 are geometrically linked together by

$$x_1 = \frac{x_2}{\tan(\alpha)} \text{ with } \tan(\alpha) = \frac{pitch}{2 \cdot \pi \cdot r_{screw}} \tag{9}$$

it is possible to eliminate x_1 and in a further step also F_N. The only problem is the appearance of $|F_N|$. Therefore it is necessary to distinguish between Case A: $F_N 0$

$$\begin{aligned} \left(m_2 + m_1 \frac{1}{\tan(\alpha)} \left(\frac{1 - \mu \cdot sign(\dot{x}_2) \tan(\alpha)}{\tan(\alpha) + \mu \cdot sign(\dot{x}_2)}\right)\right) \cdot \\ \cdot \ddot{x}_2 = F_1 \left(\frac{1 - \mu \cdot sign(\dot{x}_2) \tan(\alpha)}{\tan(\alpha) + \mu \cdot sign(\dot{x}_2)}\right) - F_2 \end{aligned} \tag{10}$$

and Case B: $F_N < 0$:

$$\begin{aligned} \left(m_2 + m_1 \frac{1}{\tan(\alpha)} \left(\frac{1 + \mu \cdot sign(\dot{x}_2) \tan(\alpha)}{\tan(\alpha) - \mu \cdot sign(\dot{x}_2)}\right)\right) \cdot \\ \cdot \ddot{x}_2 = F_1 \left(\frac{1 + \mu \cdot sign(\dot{x}_2) \tan(\alpha)}{\tan(\alpha) - \mu \cdot sign(\dot{x}_2)}\right) - F_2 \end{aligned} \tag{11}$$

In order to determine whether Case A or Case B applies it is inevitable to introduce an algebraic loop in the simulation model. Since the simulation is based on numerically solving a system of non-linear differential equations, this can be done quite easily by using a unit delay for the "feed back" of F_N.

$$F_N = ((m_2 - m_1) \cdot \ddot{x}_2 + F_2)\cos(\alpha) + F_1 \cdot \sin(\alpha) \tag{12}$$

3.3 Pressing Process

In order to simulate the dynamic behavior of the plunger not only the actuation system but also the actual glass forming process, i.e., the pressing of the plunger shaping the glass gob into the final parison shape has to be simulated. In order to determine the reaction force between the plunger and the glass, it is necessary to develop a model for the glass forming process which is ruled by the following parameters:

- Parison and plunger geometry
- Plunger position and velocity
- Glass temperature and viscosity
- Heat transfer between glass and molds

Considering that the glass temperature and hence the glass viscosity, which exhibits a very progressive increase for decreasing glass temperature will not be constant during the forming process [3,4] it is clear, that the process simulation will not be trivial. In the past a lot of effort has been put into simulation models and programs for forming analysis [5], but these simulation programs are too detailed and thus require an excessive computational effort, which is not acceptable for the simulation of the dynamic motion behavior of the plunger. Therefore, a very simple axis-symmetric model of the plunger and parison as shown in Fig. 7 has been chosen in order to simulate the glass forming process. It shows (a) the start of parison forming, (b) parison forming and (c) end of parison forming. With this model, the forming process can be explained as pressing the glass through a ring of varying length with simultaneously varying inner and outer diameter [6].

Looking at an infinitesimal small ring element, force equilibrium can be formulated taking pressure and shear forces into account. By assuming Newtonian viscosity, it is possible to derive an equation, which describes the reaction force between plunger and glass:

$$F_{glass} = \eta(T) \cdot K_{glass}(x) \cdot \dot{x} \tag{13}$$

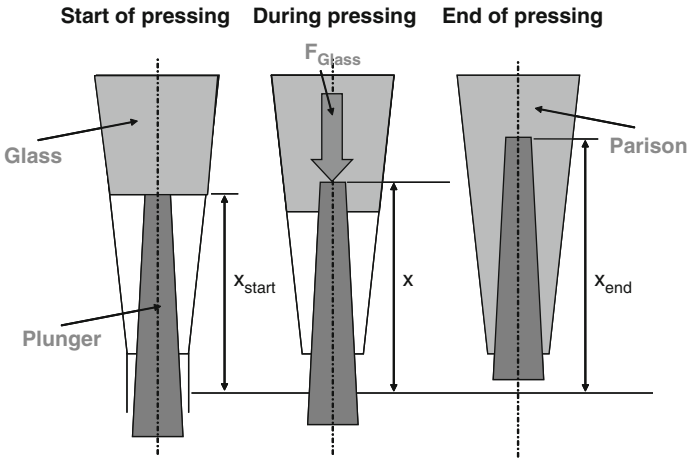

Fig. 7 Simple glass forming model

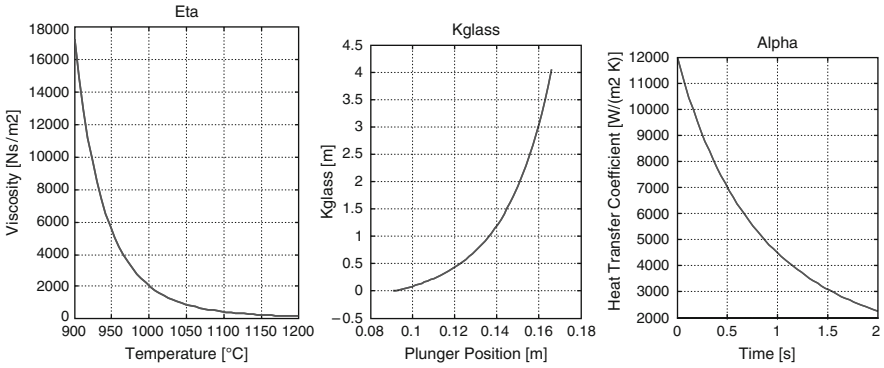

Fig. 8 Diagrams related to equation (13)

where $\eta(T)$ describes the temperature dependant glass viscosity, $K_{glass}(x)$ a non-linear geometry dependant force coefficient, which can be determined from the geometrical model shown in Fig. 7, and $\dot{x}$ the plunger velocity [6]. Figure 8a depicts a diagram of $K_{glass}(x)$for a typical parison geometry.

In order to determine the actual viscosity of the glass, it is not only necessary to apply the Vogel-Fulcher-Tammann-Equation [3]

$$\eta = \eta_0 \cdot e^{\left(\frac{b}{T - T_0}\right)} \tag{14}$$

which describes the dependency between glass temperature and viscosity (Fig. 8b), but also to develop a model of the heat transfer between glass and mould equipment.

Assuming a time dependent heat flux the following differential equation can be derived:

$$\frac{dT}{dt} = -\frac{\alpha \cdot A}{m_{glass} \cdot c_p} \cdot (T - T_m) \tag{15}$$

According to [7] the heat transfer coefficient α must be considered time dependant (Fig. 8c). Additional parameters in this equation are the contact surface A between glass and mould equipment, the mass of the glass m_{glass}, the mould temperature T_m, here considered constant and the specific heat capacity of the glass c_p.

3.4 Intelligent Control Scheme

To design a servo controller that satisfies the challenging demands, a very good understanding of the overall system including the glass pressing process is indispensable. In contrast to purely error driven PID controllers, the approach in the present case is to base the controller design partly on physical models describing the forming process. Model based controllers have the advantage that they can "look ahead" in time and cause a system to behave in a desired manner at the outset, not having to wait until driving errors enforce that certain behavior. Heart of the control system is the PC-based controller. The real time control program generates a current demand for the individual motors to control the plunger motion in every state of the system. The controller can be in three individual modes: position, velocity or force control, which is activated and coordinated by an intelligent selection algorithm. The structure is shown in Fig. 9.

The main controller is a PID position controller with position and force feedback. Additionally, a PI velocity controller acts as a limiting controller to ensure that the velocity demand is not exceeded. Likewise the force controller ensures that the given force demand, which can either be stepped or profiled, is not exceeded during glass forming. This includes a model based approach in order to compute the actual glass force from the current signal and the computed acceleration signal in order to eliminate the need for an additional glass force sensor. The output of the three controllers is fed into an intelligent selector block for model based coordination. As a result the controller acts as a pure position controller at the start of the motion with maximum possible acceleration.

Only after the programmed velocity is almost reached does the velocity controller take over. Likewise the force controller takes over the regime during the critical glass forming process.

On top of the above described control strategy a force demand controller compensating for long term changes in glass viscosity, gob weight, wear or friction of the mechanism is active.

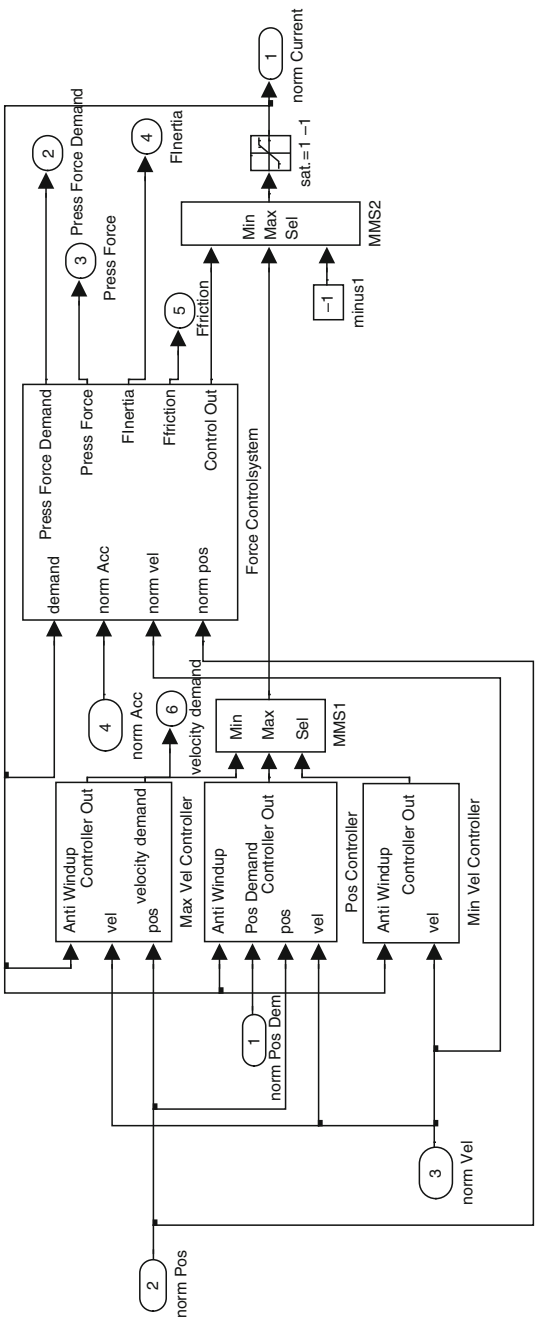

Fig. 9 Combined position, velocity or force controller

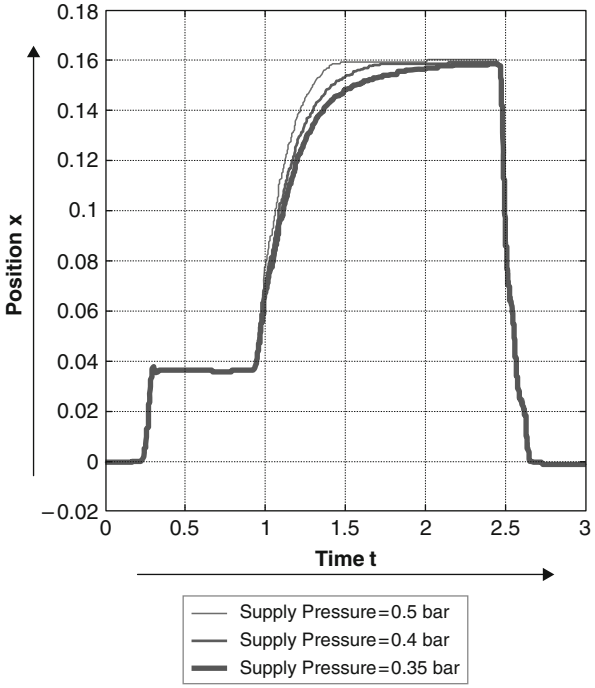

Fig. 10 Simulation results for different settings of pneumatic pressure

3.5 Simulation and Verification

Simulation results of the dynamic behavior of the conventional plunger mechanism for different settings of pneumatic plunger pressure are presented in Fig. 10. These diagrams show consistent results which also reflect that the pneumatic pressure has quite an influence on the motion of the plunger.

Since the conventional pneumatic plunger does not allow to perform direct measurements of the motion behavior the simulation results shown in Fig. 10 could not directly be verified. Therefore starting from the results of the simulation model of the pneumatically driven plunger mechanism, a mechanism with servo electric drive has been developed [8].

Using this prototype servo plunger, the verification of the model has been carried out both with and without glass. Measurements without glass allow to verify and eventually adjust and tune the parameters describing the electromechanical part of the system. Once that part describes the real physical system behavior with the desired precision, tests in a real production environment under glass are used to verify the overall model including the glass forming force.

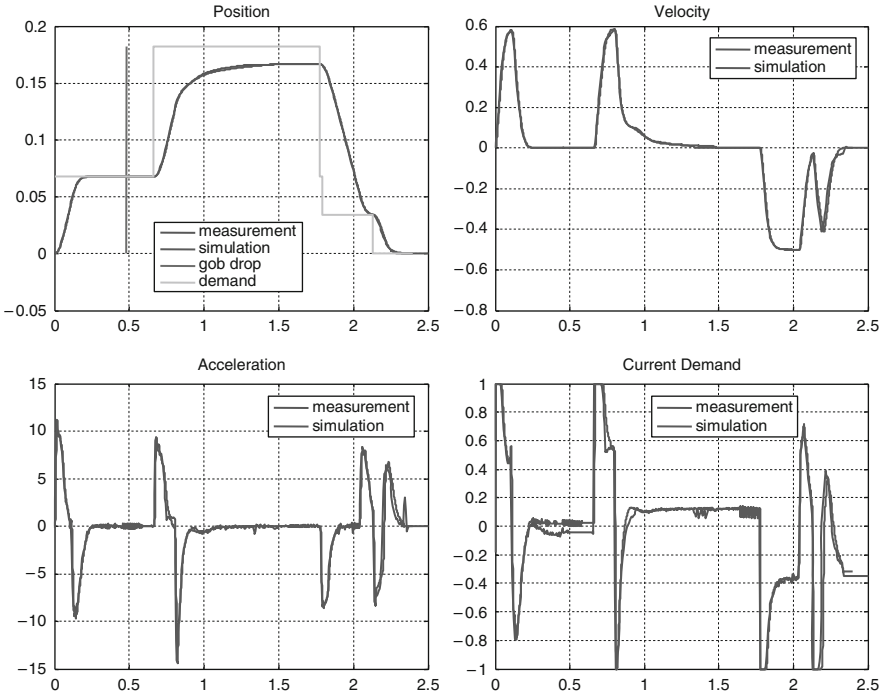

Fig. 11 Simulation results for different settings of pneumatic pressure

A comparison between the measured and the calculated plunger displacement, velocity and acceleration over a cycle for operation with glass is displayed in Fig. 11.

The plunger moves from the down position to the servo controlled loading position, then at maximum speed to the point where the pressing starts, from there it decelerates towards a lower pressing speed and finally it is retracted and moved back to the starting point. The agreement between measurement and calculation is excellent. The difference between measurement and calculation of position, velocity and current demand is virtually not visible.

4 Mechatronic Sewing Plant

In this chapter, a worldwide unique sewing plant "PARASEW1000" for fibre reinforced composite materials (FRC-materials) based on parallel kinematic manipulator (PKM) is presented [9,10]. Both the kinematic modelling of the sewing plant along with its different components is addressed as well as the establishment of a kinetostatic model that can be used for optimal design and control of "PARASEW1000."

4.1 Kinematic and Dynamic Modelling of the Parallel Manipulator

The goal of the kinematic and dynamic analysis is to determine the required actuators' lengths, velocities, accelerations and forces to guide the sewing machine with the specified stitching speed along a prescribed seam line.

The hybrid robot used to guide the sewing machine is composed of a fully parallel manipulator with five-dof and a serially attached servo motor. The parallel manipulator consists of five kinematic chains (legs) connecting a fixed base to a moving platform, as shown in Fig. 12. Four legs have the same topology "UPS" and are composed of a universal joint centered on point A_i attached to the base, an actuated prismatic joint and a spherical joint centered on point B_i attached to the platform, as shown in Fig. 13. The fifth kinematic chain "UPU" consists of a

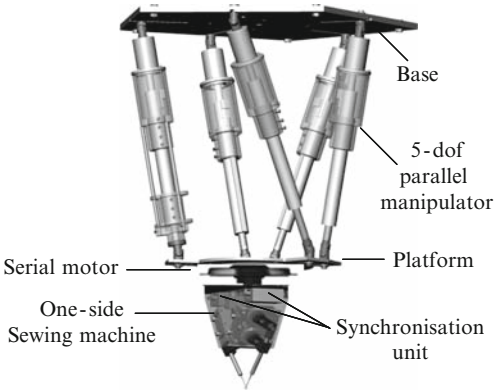

Fig. 12 PARASEW1000: A sewing plant based on a parallel manipulator

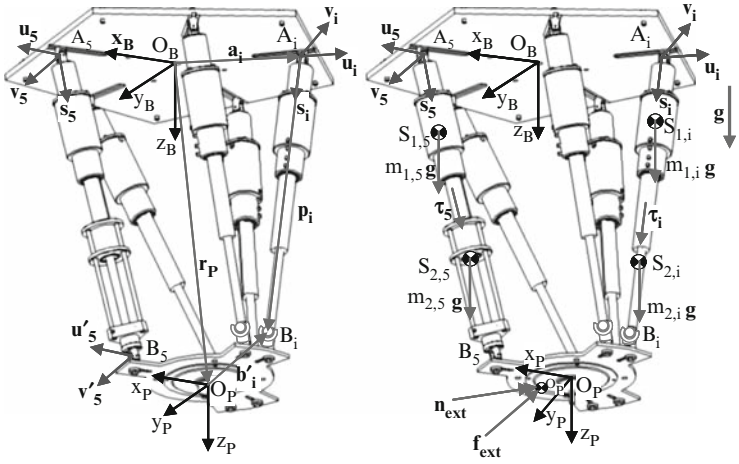

Fig. 13 Kinematic and dynamic parameters of the PKM

universal joint centered on point A_5 attached to the base, an actuated prismatic joint and a universal joint centered on point B_5 attached to the platform. The servo motor consists of a stator and a rotor. The former will be modelled as a single mass attached to the platform, the latter as a rotating mass and will be considered within the dynamic model of the sewing machine.

Since the platform has only five-dof, only five of the six Cartesian coordinates can be prescribed independently. For the tasks at hand, three translational (x, y, z) and two rotational (ϕ , θ) coordinates are required. Therefore as the first step in kinematic analysis the remaining rotational coordinate ψ can be computed in dependence of the other five coordinates (x, y, z, ϕ, θ). The coordinate ψ can be computed but cannot be controlled [9,10]. Of course the angle ψ also serves as input-data for the servo motor, which has to rotate the sewing head in accordance with the prescribed seam line taking into account the coercive rotation ψ about the axis perpendicular to the platform.

In order to describe the position of the manipulator, two different coordinate frames are specified: $\mathbf{R_B}$ (O_B, x_B, y_B, z_B) is attached to the base and $\mathbf{R_P}$ (O_P, x_P, y_P, z_P) is attached to the platform, as shown on the left hand side of Fig. 13. Now a vector-loop equation for the *i*th leg of the mechanism can be written as

$$\begin{cases} \mathbf{p_i} = \mathbf{r_P} + \mathbf{b_i} - \mathbf{a_i} \\ \mathbf{b_i} = {}^{\mathbf{B}}\mathbf{T_P}\left[\mathbf{b_i'}\right]_{\mathbf{R_P}} \end{cases}; i = 1..5 \tag{16}$$

where the matrix ${}^{\mathbf{B}}\mathbf{T_P}$ denotes the Euler transformation matrix from coordinate frame $\mathbf{R_P}$ to $\mathbf{R_B}$.

As shown in [10] this allows not only to determine the angle ψ

$$\psi = -\arctan\left[\frac{z_P \sin(\phi)\cos(\theta) - z_{B_5}\sin(\phi) + y_P \sin(\theta)}{(z_P - z_{B_5}\cos(\theta))\cos(\phi)}\right] \tag{17}$$

but also the actuator length of the *i*th leg as the norm of the vector $\mathbf{p_i}$ from the vector loop (16):

$$\begin{aligned} l_i &= ||\mathbf{p_i}|| \\ &= \sqrt{(\mathbf{r_P} + \mathbf{b_i} - \mathbf{a_i})^T \cdot (\mathbf{r_P} + \mathbf{b_i} - \mathbf{a_i})}; \; i = 1..5 \end{aligned} \tag{18}$$

Furthermore with $\dot{\mathbf{r}}_\mathbf{P}$ and $\omega_\mathbf{P}$ representing the linear and angular velocities of the moving platform.

$$\dot{\mathbf{r}}_\mathbf{P} = (\dot{x}_P, \dot{y}_P, \dot{z}_P)^t; \omega_\mathbf{p} = \begin{pmatrix} 0 & -\sin(\varphi) & \cos(\varphi)\sin(\theta) \\ 0 & \cos(\varphi) & \sin(\varphi)\sin(\theta) \\ 1 & 0 & \cos(\theta) \end{pmatrix} \begin{pmatrix} \dot{\varphi} \\ \dot{\theta} \\ \dot{\psi} \end{pmatrix} \tag{19}$$

also actuator velocities and acceleration can be determined:

$$\begin{aligned} \dot{l}_i = \dot{\mathbf{p}}_\mathbf{i} \cdot \mathbf{s}_\mathbf{i} &= \left(\dot{\mathbf{r}}_\mathbf{p} + \omega_\mathbf{p} \times \mathbf{b}_\mathbf{i}\right) \cdot \mathbf{s}_\mathbf{i} \\ &= \dot{\mathbf{r}}_\mathbf{p} \cdot \mathbf{s}_\mathbf{i} + \left(\mathbf{b}_\mathbf{i} \times \mathbf{s}_\mathbf{i}\right) \cdot \omega_\mathbf{p} \end{aligned} \tag{20}$$

$$\ddot{l}_i = \ddot{\mathbf{p}}_\mathbf{i} \cdot \mathbf{s}_\mathbf{i} + l_i \cdot \omega_i^2 \tag{21}$$

With regards to the dynamic modelling of we refer to the inverse dynamics. For the inverse dynamics problem, a prescribed trajectory of the platform under effect of applied and inertia forces is given and the task is to determine the actuators' forces required to produce that motion. As shown in [10] the inverse dynamics problem can be formulated using the principle of virtual work. For more details and the corresponding equations please refer to [10].

4.2 Kinematic and Dynamic Modelling of the Sewing Head

The sewing head which is attached to the above mentioned parallel manipulator is based on the ITA-sewing technique [11], which is based on the formation of a two-thread chain pass with two needles from only one side of the work piece. This technique requires a mechanism that leads the needles alternatively into the work piece such that a sewing thread loop formed by the first needle is than taken up by the second one. For this purpose a new sewing machine was developed at the IGM, as shown in Fig. 14. The needles' movements are realized with two separate mechanisms featuring identical kinematic structure, and are located on two planes that are arranged dihedral to each other with a specified apex angle α.

To ensure the generation of the sewing pattern, the needle laces are guided along an asymmetric eight-shaped coupler curve (Fig.15).

The needle guidance can be divided into the following sub-tasks: a vertical stroke movement between the horizontal level A and the horizontal level B, as shown in Fig. 15. The second one is a pivoting motion from tilt level C to tilt level D, and vice-versa.

Different mechanisms types such as cam, gear and crank mechanisms can be selected that are capable of generating the movement as mentioned above [12]. A selection of principle solutions for the overall function, needle guidance mechanism, is listed in Fig. 16.

In the next step, the principal solutions are evaluated taking into account the criteria stemming from the requirement specifications, i. e., the form of the eight-shaped coupler curve, approximated straight-line guidance between the positions 1 and 2 and between the positions 3 and 4 respectively, a variable setting stitch length as well as low inertia forces, a small design envelope, low weight, low costs and low construction complexity. The mechanism shown in Fig. 17 turned out to be the best suitable mechanism for the guidance of the sewing needle. This mechanism consists

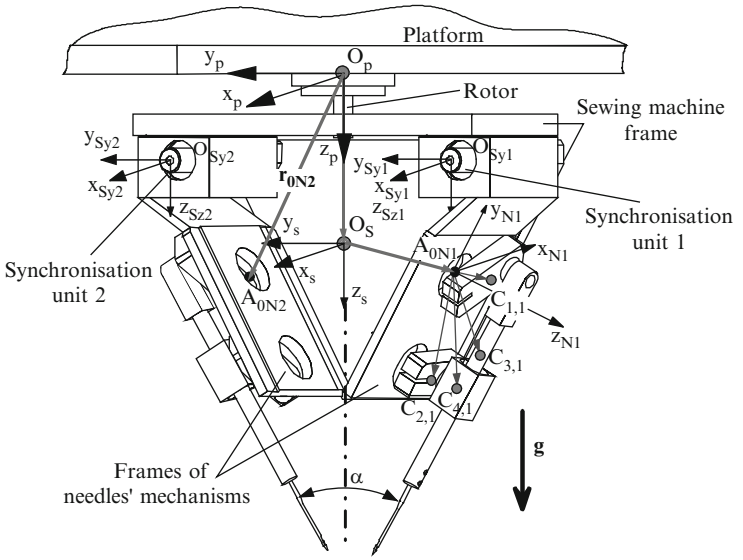

Fig. 14 Scheme of the one-side sewing head

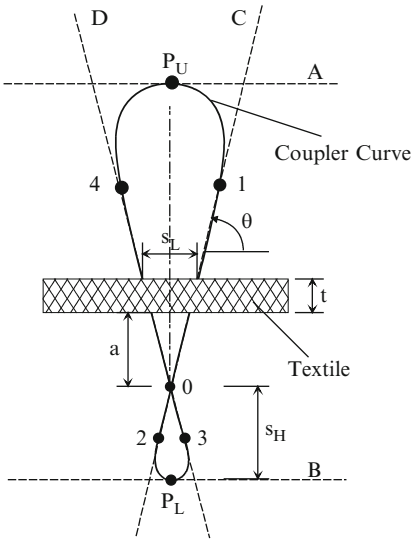

Fig. 15 Coupler curve of needle tip

of a five-bar linkage with four revolute joints and a prismatic joint attached to the link, which represents the needle holder.

The kinematic analysis is the basis for the further analysis of the mechanism, especially regarding motion design. The mathematical model of the mechanism is also used for the dimensional synthesis of the mechanism, when the needle tip has

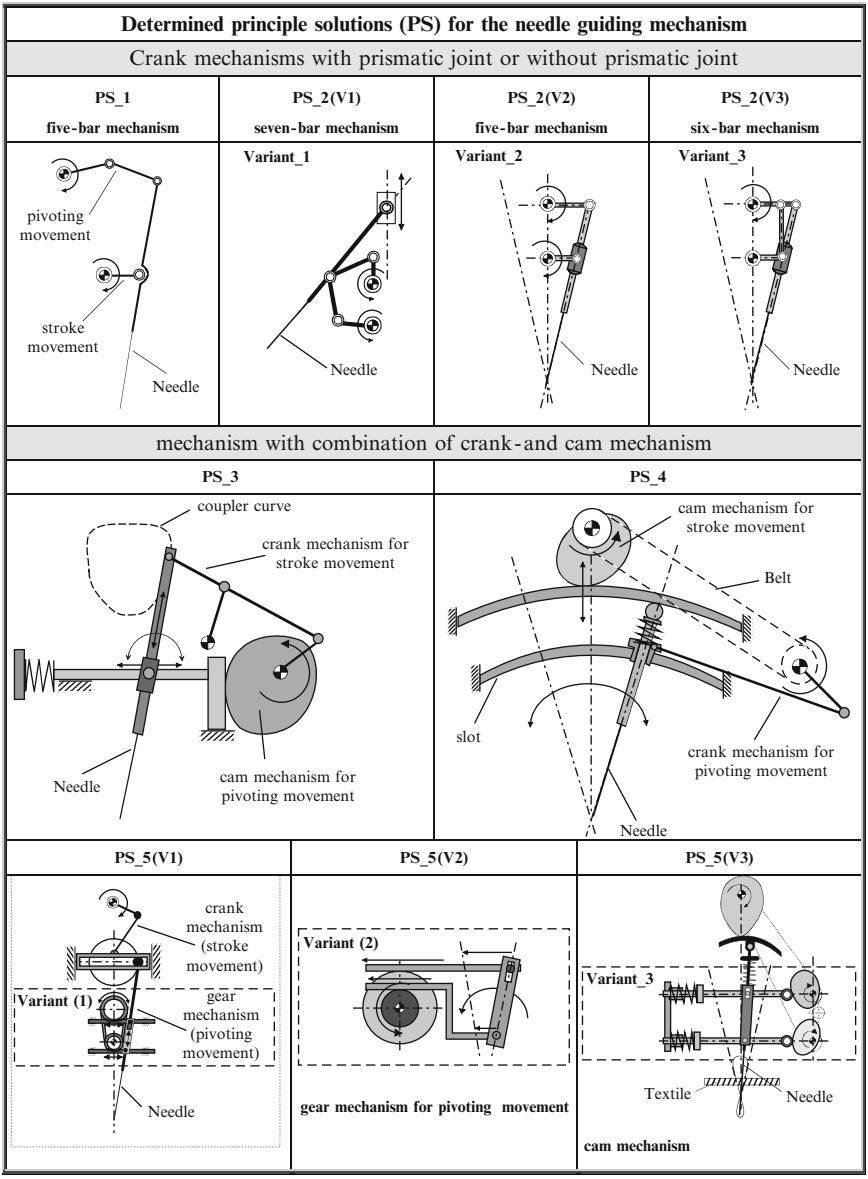

Fig. 16 Selection of principle solutions for the needle guidance mechanism

to satisfy a prescribed coupler curve. In order to describe the position of the needle tip and the orientation of the needle holder for each link a coordinate frame [R_i ($\mathbf{e}_{i,\,1}$, $\mathbf{e}_{i,\,2}$), i = 1…3] attached at the origin A_0, B_0 and A is defined together with the absolute coordinate frame R_0 ($\mathbf{e}_{0,\,1}$, $\mathbf{e}_{0,\,2}$) with the origin at A_0, as shown in Fig. 17.

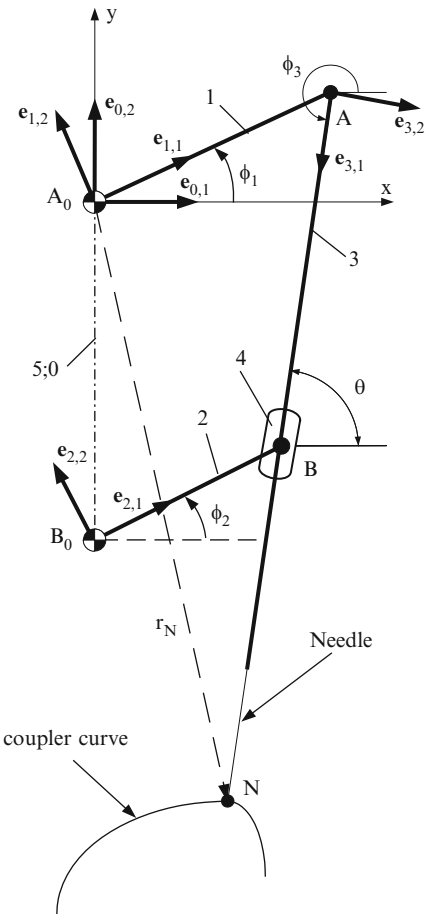

Fig. 17 Kinematic schematic of the new needle guiding mechanism

By writing the vector-loop equations as described in [12] the input angles of the 2two-dof five-bar mechanism can be determined.

4.3 Motion Design

In order to properly trace the desired coupler curve with regards to time synchronization a specific motion design is necessary. Since the coupler curve of the needle lace is already specified as an asymmetric eight-shaped curve, the motion design of the needle guiding mechanism will be confined to the trajectory planning with the trajectory being defined in the joint space. The first objective is to determine the motion segments φ_s and φ_f to assure the transfer of the thread loops underneath

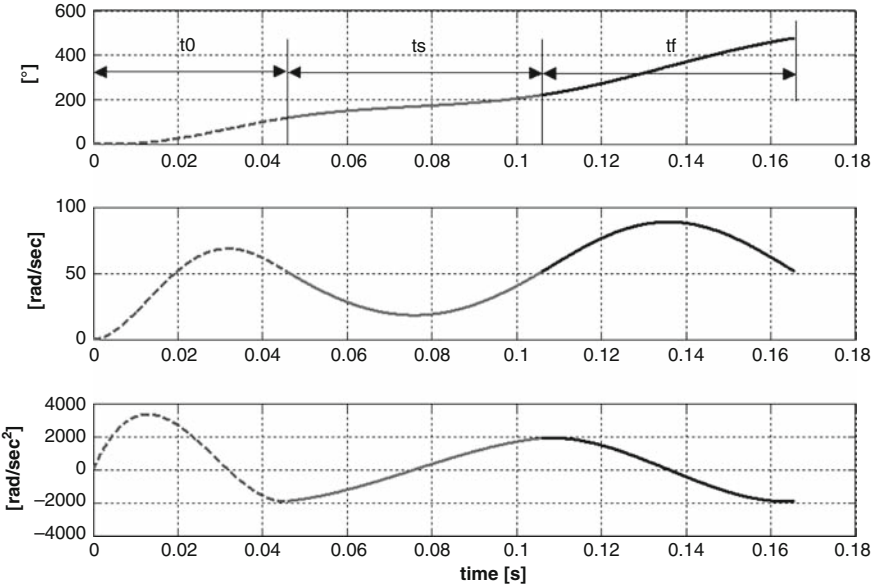

Fig. 18 Crank angle and its first and second derivatives

the sewing material. Thus, the initial and final joint positions ϕ_A and ϕ_B, as well as the times t_s and t_f to cover the segments φ_s and φ_f must be specified. The second objective is to generate a trajectory between initial and final joint positions for both motion segments, which guarantees a smooth motion of the needle laces along the coupler curves. Details of the trajectory planning can be found in [13]. Figure 18 depicts the profiles of crank angle ϕ and its first and second derivatives for one period.

4.4 Simulation Model

In order to verify the integrative approach for the design of the robot based sewing system, two simulation models of the sewing plant "PARASEW1000" have been created. Figure 19 shows the first model, that was implemented within MATLAB/SIMULINK© and can be used for the kinematic and dynamic analysis. Additionally, this model also serves as a base for the control of "PARASEW1000" via XPC-target©.

To visualize the motion of the sewing head and to detect possible mechanical interferences of the manipulator's legs, a second model has been implemented in the environment of the Multi-Body system visualNastran4D© (Fig. 20).

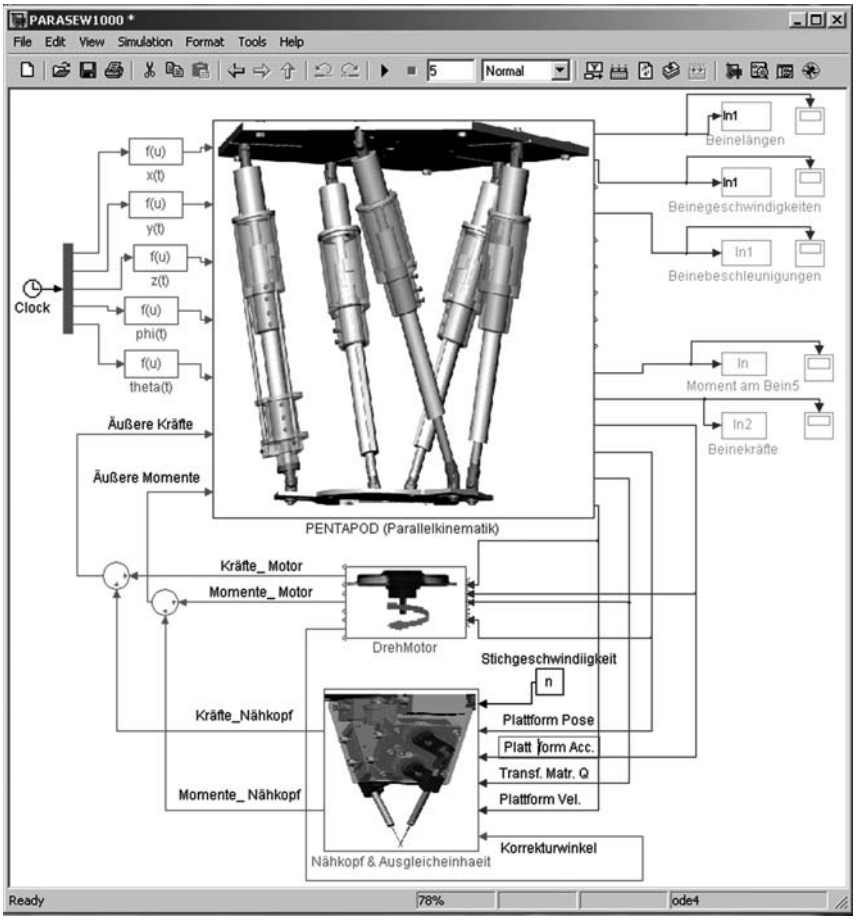

Fig. 19 Model of PARASEW1000 using MatLab/Simulink©

5 An Adjustable Gripper as a Reconfigurable Robot

In this chapter, a robot system will be presented, which combines a parallel manipulator with an adjustable gripper. The robot is able to grasp objects with different sizes and shapes without using an additional gripper. It consists of several fingers with contact elements which can be moved independently from each other to grasp the object [14]. After grasping, adhesion forces, provided, e.g., by an electromagnet or a vacuum cup, ensure that the fingertips remain connected to the object to be manipulated. The resulting closed-loop mechanism, formed by the fingers of the robot and the object, features a kinematic structure similar to that of parallel manipulators. The robot is now able to achieve manipulation of objects with six degrees of freedom by actuating exactly six joints.

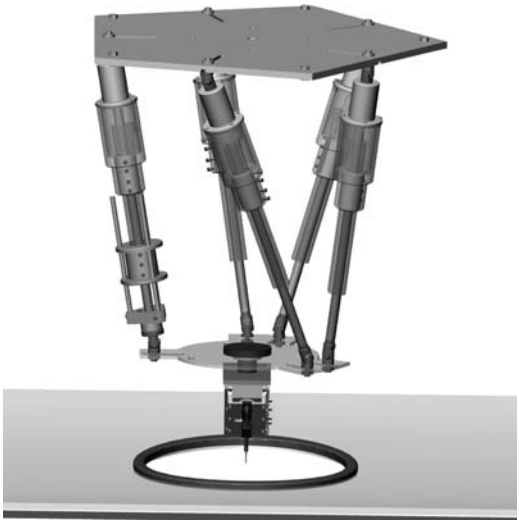

Fig. 20 Model of PARASEW1000 using visualNastran4D ©

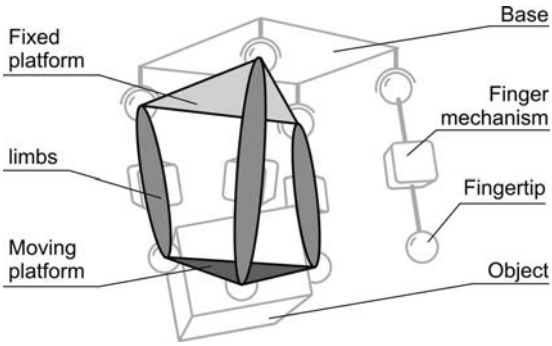

Fig. 21 The basic idea: Analogy with a parallel manipulator

5.1 New Manipulation Concept

The new design intends to bridge the gap between the performance and range of applications of human hands and industrial grippes in order to profit from their advantages and overcome their drawbacks. Hence the target is to design a handling device that is multifunctional and can be customized to match the requirements of changing tasks. In order to suit these needs the design should also be reconfigurable like the human hand but its efficiency and performance should be similar to industrial grippers.

The key idea is to generate a closed-loop kinematic chain formed by the robot's fingers and the object similar to the kinematic structure of a parallel manipulator, see Fig. 21. The grasped object and the fingers correspond, respectively, to the moving platform and the legs of a parallel manipulator.

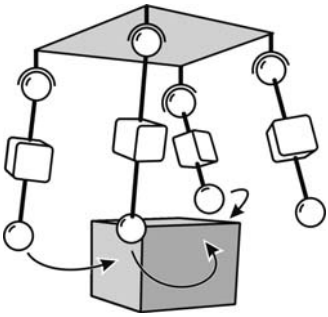

Fig. 22 The grasping phase

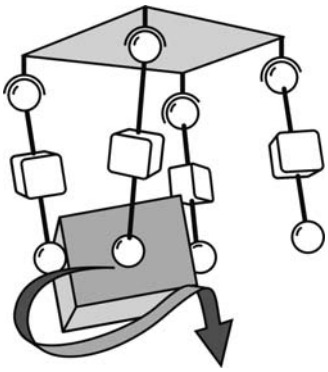

Fig. 23 The manipulation phase

Before grasping the object, the fingers are able to position their fingertips independently from each other, see Fig. 22.

The number of actuated joints per finger must be chosen accordingly, e.g., positioning fingertips in 3D space requires three actuators per finger.

After grasping, the fingers are connected to the object, and the grasped object is now part of a parallel kinematic structure, see Fig. 23. The appropriate number of constraints imposed by the connection between the fingers and the object depends on the connectivity number of each finger, i.e., the sum of the degrees of freedom in all the joints including the contact point, see [15].

It should be noted that before grasping the number of actuators can differ from the number of actuators during the manipulation phase. For example, a three-fingered hand has three actuators per finger before the grasping phase, but only two actuators per finger when the fingers grasp and manipulate the object. The remaining actuators are not necessary and can be disconnected or run passively.

Still, their encoders can be used to solve the forward kinematics problem and to determine the actual position of each fingertip. Moreover, the actuators can be used as redundant actuators to overcome singularities or to improve the stiffness and the payload of the mechanism.

A major advantage of a multi-fingered hand is that it can re-grasp objects, e.g., when large rotation angles are needed.

5.2 Topology Synthesis

The constraints, which have to be taken into account prior to the structural synthesis and design of the finger mechanisms, are [14]:

1. Only six actuators are required for manipulation
2. The connectivity number of each finger is equal to 6
3. Three fingers are simultaneously in contact with the object
4. One finger can be used for regrasping
5. Three controlled joints per finger are needed for positioning finger tips
6. The contact-joint DOF between the finger and the object is 3

The kinematic topology of each finger should satisfy the above conditions The topology synthesis consists now on the one hand in generating finger mechanisms with three DOF and one the other hand in finding joint configurations for the fingertip with three DOF in rotation.

Finger mechanisms can be classified into three groups according to their topologies: fingers with an open-loop kinematic chain, a closed-loop kinematic chain and a hybrid kinematic chain. Due to the high number of feasible kinematic topologies in each group, additional constraints to pre-select candidate structures are required. Finally, these candidate topologies are compared according to weighted evaluation criteria, and the most promising kinematic topologies with the highest score are selected. Figure 24 shows a small selection of feasible finger architectures.

Through an assessment of the generated finger architectures the most appropriate design solution F_4 has been selected.

Additionally a selection of feasible fingertip architectures has been set up in order to select the most appropriate (Fig. 25).

Figure 26 shows the complete selected kinematic topology of the manipulator. It is composed of three five bar mechanisms that are mounted on the base by the base pivot. The three DOF fingertip joint is designed in a spherical configuration of three revolute joints. This features many advantages, like a large pivoting angle ($\pm 90°$) and satisfactory adaptation behavior during the grasping phase.

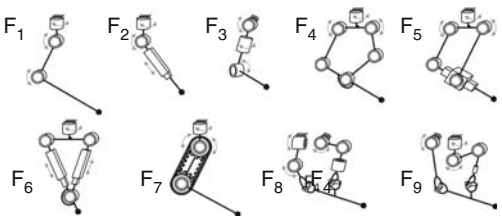

Fig. 24 Selection of feasible finger architectures

Fig. 25 Selection of feasible finger architectures

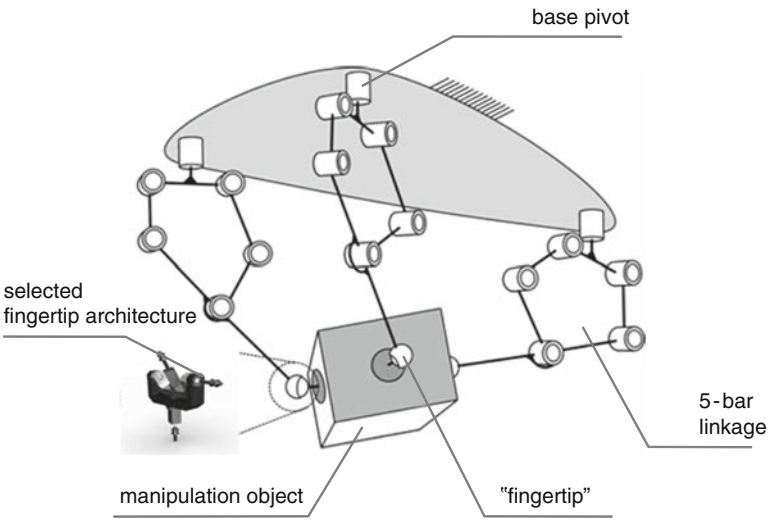

Fig. 26 Complete kinematic topology of the manipulator

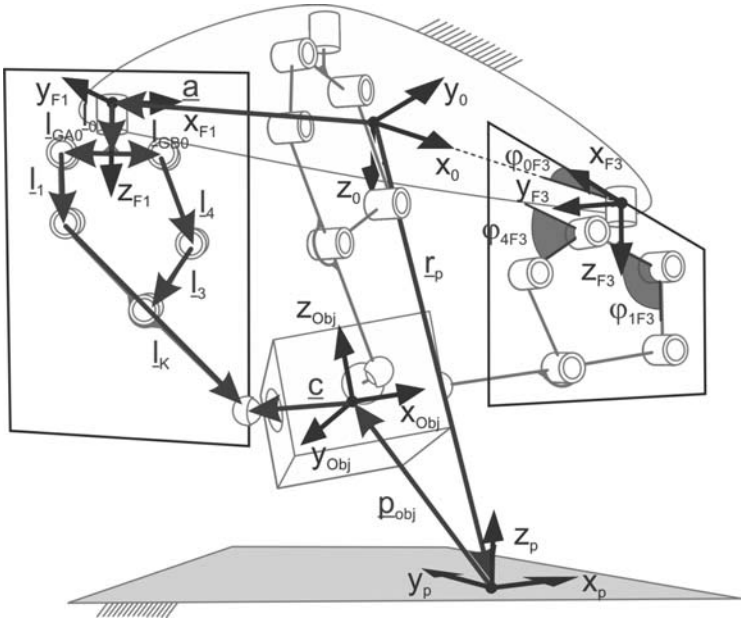

Fig. 27 Kinematic model of the manipulator

5.3 Dimensional Synthesis

In order to be able to properly perform the dimensional synthesis, a proper kinematic model has to be set up. Figure 27 shows that this has general similarity with a kinematic model of any parallel manipulator.

By setting up the loop closure equations the appropriate equations for the kinematic analysis can be set up. In this case the subsequent dimensional synthesis has been carried out by applying an optimization strategy such that certain criteria have to be fulfilled with regards to

(a) *Velocities*

$$\forall \vec{\chi} \in \mathbf{W},\ \left|\dot{\phi}_{\max}\right| \leq \dot{\phi}_{\text{zul}} \tag{22}$$

$$\text{with } \left|\dot{\phi}_{\max}\right| = \max_{i=1}^{6}\left(\sum_{j=1}^{6}\left|J_{Pij}\dot{\chi}_{jSoll}\right|\right)$$

(b) *Forces*

$$\forall \vec{\chi} \in \mathbf{W},\ \left|\mathrm{T}_{\max}\right| \leq \mathrm{T}_{\text{zul}} \tag{23}$$

$$\text{with } |\mathrm{T}_{\max}| = \max_{i=1}^{6} \left(\sum_{j=1}^{6} \left| J_{Pij}^{-T} F_{jSoll} \right| \right)$$

(c) *Precision*

$$\forall \vec{\chi} \in \mathbf{W},\ |\delta\chi_{\mathrm{Tmax}}| \leq \delta\chi_{\mathrm{Tzul}} \tag{24}$$

$$\text{with } |\delta\chi_{\max}| = \max_{u=1}^{64} \left\| \left(J_P^{-1} \cdot \underline{\delta\rho}_{uSoll} \right) \right\|_{(2,T)}$$

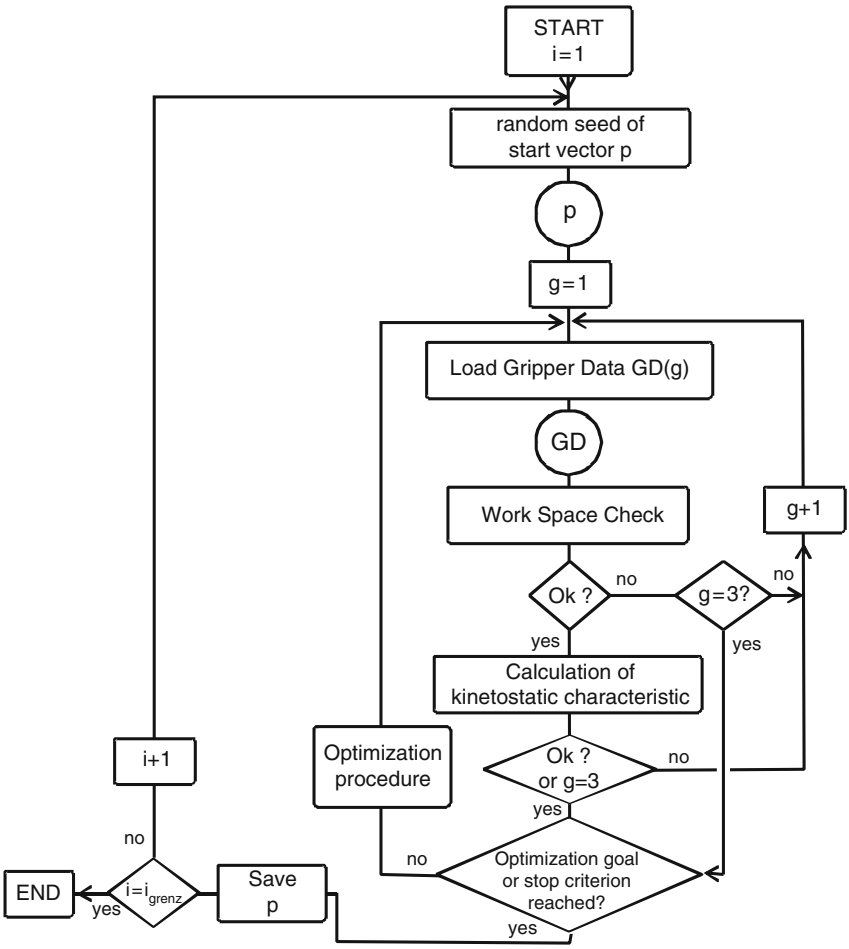

Fig. 28 General optimization plan

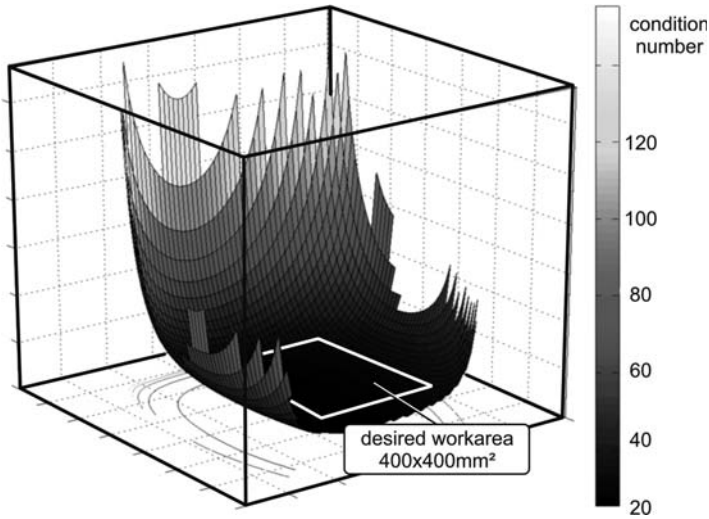

Fig. 29 Selection of feasible finger architectures

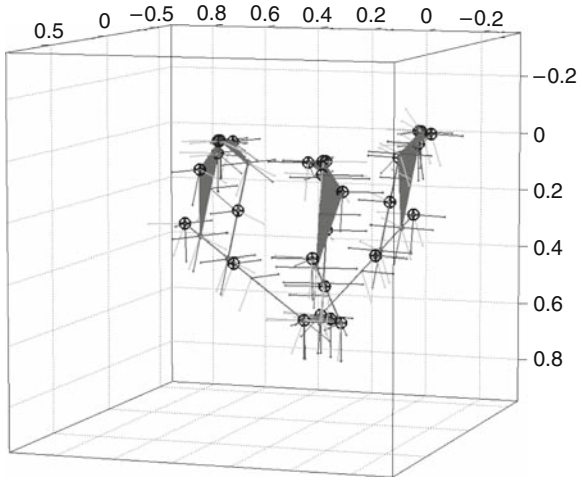

Fig. 30 Graphical representation of SimMechanics© simulation model

$$\text{and } \underline{\delta\rho}_{uSoll} = \begin{pmatrix} \pm\delta\rho_{Soll} \\ \vdots \\ \pm\delta\rho_{Soll} \end{pmatrix}$$

(d) *Condition Number*

$$\forall\vec{\chi} \in \mathbf{W},\ K \leq K_{\text{zul}} \tag{25}$$

Fig. 31 Prototype design of three fingers

with $K = cond(J_{P\_normiert})$

The above mentioned optimization criteria have to be fulfilled for all poses within the desired workspace $\forall \vec{\chi} \in \mathbf{W}$ such that the drive angles of all drives i are kept within given limits

$$\phi_{\min} < \phi_{\mathrm{i}} < \phi_{\max} \wedge imag(\phi_{\mathrm{i}}) = 0 \tag{26}$$

and the same be true for the passive joints

$$\gamma_{\min} < \gamma_{\mathrm{ij}} < \gamma_{\max} \tag{27}$$

Figure 28 shows the general structure of the optimization procedure realized within MATLAB/SIMULINK© in order to come up with a dimensional kinematic synthesis of the gripper fingers. It should be noted that the dimensioning of the manipulator is primarily achieved for a sample object.

The validity of the obtained results has been checked by computing the workspace and the distribution of the condition number of the manipulator over the workspace.

Figure 29 depicts the distribution of the condition number for a given plane of the resulting workspace in a height of 0.5 m. The figure shows that the requirement concerning the singularity free condition throughout the workspace is satisfied for the slice shown.

Additionally a SimMechanics© simulation model for three fingers has been created (Fig. 30) with expected masses of links, joints and other elements of the power train for object motions along given sample paths. This simulation model allows to distinguish between rigid reference model and elastic model in order to determine path and position errors due to elastic deformation thus enabling proper

stiffness design of the fingers. Finally Fig. 31 depicts a 3D-representation of the prototype design of three fingers.

6 Conclusion

In this paper different mechatronic motion devices have been presented. In any case, a systematic, mechatronic approach for the layout and design of such motion devices must include not only methods for the topological or dimensional synthesis of mechanisms but also a proper simulation model including the dynamics of the actuation device, such as pneumatic or servo electric actuation. The examples taken from glass machinery, textile industry or robotics showed that if a reliable simulation model, which properly reflects the characteristics and properties not only of the mechanism but also of the drive and the underlying process is available, then a tool and methodology can be created that allows to optimize an existing system for the requirement at hand.

References

1. Corves, B.: IS-Machine performance – requirements and developments. Parma: XII Convegno A.T.I.V 1996. Int. Glas. J. 91, 37–42 (1997)
2. Corves, B.: Modelling of mechanisms in container glass forming machines. Conference on interdisciplinary applications of Kinematics. Lima, Peru, 9–11 January 2008
3. Nölle, G.: Technik der Glasherstellung. Stuttgart: Dt. Verl. für Grundstoffindustrie (1997)
4. Ferrero, C.: Optimizing the workability of soda lime glass used in the production of containers. Int. Glas. J. 98, 41–45 (1998)
5. Liu, G.Q., Owen, D.R.J., Anderson, H.J.: Computational modelling for glass container forming processes. Proceedings of the colloquium on modelling of glass forming processes. Valenciennes, France (1998)
6. Corves, B.: Prozesssimulation und Reglerauslegung für einen Glaspressstempel. In: Tagung Verarbeitungsmaschinen und Verpackungstechnik, Dresden (2006)
7. McGraw, D.A.: Transfer of heat in glass during forming. J. Am. Ceram. Soc. 7, 353–363 (1961)
8. Grüninger, W., Kümmerle, M., Anheyer, W., Corves, B.: Modelling, design and implementation of a servoelectric plunger mechanism for glass container forming machines. Glas. Technol. 43(3), 89–94 (2002)
9. Mbarek, T., Nefzi, M., Corves, B.: Prototypische Entwicklung und Konstruktion eines neuartigen Parallelmanipulators mit dem Freiheitsgrad fünf. VDI-Berichte Nr. 1892,VDI Verlag Düsseldorf (2005)
10. Mbarek, T., Nefzi, M., Kordi, M., Corves, B.: Kinematics and kinetics of a high-dynamic sewing plant for FRC-materials based on parallel manipulator. In: Second international congress design and modelling of mechanical systems. Monastir, Tunisia, 19–21 March 2007
11. Moll, K.-U., Pickel, J., Wulfhorst, B.: Nähen mit einseitigem Nähgutzugriff Technische Textilien 41, H. 11, 216–217 (1998)

12. Corves, B., Mbarek, T., Riedel, M., Nefzi, M., Kordi, T.: A high dynamic robot based sewing system. Proceedings of 6th polish-German workshop "System Integration," Ilmenau, 5–8 July 2007. Wissenschaftsverlag Thüringen, Langewiesen, 97–108 (2008)
13. Mbarek, T., Kordi, M., Hüsing, M., Corves, B.: Robot-supported one-sided stitching technique for fibre reinforced composite materials. In: CIFMA01 IFCAM01, 1st International francophone congress for advanced mechanics. Aleppo (Syria), 2–4 May 2006
14. Riedel, M., Nefzi, M., Hüsing, M., Corves, B.: An adjustable gripper as a reconfigurable robot with a parallel structure. Second international workshop on fundamental issues and future research directions for parallel mechanisms and manipulators. Montpellier, France, 21–22 September 2008
15. Tsai, L.-W.: Robot analysis: The mechanics of serial and parallel manipulators, Chap. 3. Wiley, New York (1999)

Comparative Study of Two Index Two Methods Applied to Original ADAMS Computer Program

N. Orlandea

Abstract Improving the quality of the results by lowering the numerical integration index requires that the velocity constraints be used together with the corresponding geometrical constraints. An STF (Sparse Tableaux Formulation) implemented in the original ADAMS increases the size of the problem, and therefore, the size of the Dynamic Jacobean Matrix in a BDF (Backwards Difference Formula) scheme. The sparse matrix technique increases the number of operations by $N^{1.3–1.7}$, where N is the number of rows, of the structured Dynamic Jacobeans. Hence, reducing the number of equations, at the same time maintaining a reasonable sparsity and ignoring some small value terms, will improve the computation speed during numerical integration.

The method that is used to accomplish this task is the one described by Fuhrer and Leimkuhler. It suggests a partition of the Dynamic Jacobeans and two solving steps of two BDF corrector formulas. This idea fits into STF only if two sparse matrix symbolic codes are generated. Here the method is called. Using a real example, this paper compares the results of the 2-Steps method with the results obtained by means of the I2 (index 2) having stabilization as needed.

Keywords Jacobean · Corrector formula · 2-steps · I2 · SI2

1 Introduction

ADAMS (Automatic Dynamic Analysis of Mechanical Systems) was born in 1973, as a result of Orlandea's Ph.D. thesis [1] at the University of Michigan. It is based upon Sparse Tableaux Formulation (STF) and Backward Difference Formula

N. Orlandea
The University of Michigan, Ann Arbor, MI 48109, USA
e-mail: orlanico@umich.edu

I. Vişa (ed.), *SYROM 2009*,
DOI 10.1007/978-90-481-3522-6_3,

(BDF), [2]. The reasoning behind these formulas started with the idea of numerical stability during numerical integration that was thought to be insured by the BDF. BDF being a predictor corrector implicit integration method requires the Jacobean matrix $\tilde{\Im}$of the equations of motion F_e, geometrical and kinematic constraints F_c, as well as of the dynamic and force definition relations F_d.

Another important consideration was to keep all of the states and variables, without eliminating any of them. By letting the computer "just solve" the entire system, the number of human errors made during the process will be reduced. By keeping all of these variables, the size of $\tilde{\Im}$ becomes large, although very sparse. As a result, sparse matrix techniques have to be employed to improve the computation speed. The sparse matrix solver used, [3], was developed by Prof. Don Calahan, at the University of Michigan. It solves the system of equations by generating "symbolic codes," and then, as long as the pivots necessary to solve iteratively the nonlinear system have finite values other than zero, the computer simply executes this symbolic code. An additional way to increase the computation speed is to evaluate $\tilde{\Im}$ only when a change of the equation structure and/or a change in the time step takes place. $\tilde{\Im}$ does not have to be exact, but it cannot have wrong derivatives or terms. Hence the STF uses the following known formulas that have to be solved iteratively:

$$\begin{aligned} \tilde{\Im}^{m-1}\,\Delta\underline{\aleph}^{m} &= -\underline{\Re}^{m-1}, \\ \underline{\aleph}^{m} &= \underline{\aleph}^{m-1} + \Delta\underline{\aleph}^{m} \end{aligned} \tag{1}$$

where $\Delta\underline{\aleph}$ is the Newton difference vector and $\underline{\Re}$ is the residual vector. The iteration number is indicated by m.

Equations (1) that solve iteratively nonlinear problems can be recognized as a Newton-Raphson iteration method.

In 1972, Orlandea performed experiments where the quantity of computer operations were considered for different size Jacobeans generated in two ways: randomly and using the STF structured Jacobeans for mechanical systems. The sparsity of the STF structured Jacobeans have higher sparsity when the same size Jacobeans were considered for both situations. These results are given in [1] where it has been also shown that for STF the number of the computer operations is given by:

$$N_o = N_{\Im}^{1.3-1.7}, \tag{2}$$

where N_o is the number of operations and $N_{\Im}$ is the Jacobean size (i.e., the number of equations). It is well known that the number of operations for a Gauss elimination method is $N_{\Im}^3$. These results have shown that STF and the sparse matrix algorithms are efficient in solving large but sparse systems. However, relationship (2), also shows that the size of the Jacobean matrix matters but with lower sensitivity than in the case of the full matrix algorithms.

Over the years, the BDF gave confusing results. It worked well for some problems, but it did not work at all for other problems. This may happen when dealing with nonlinear systems. Nevertheless, this was not satisfactory.

In the middle of 1980, W. Gear in reference [4] tried to solve this problem by introducing the concept of index of a BDF numerical integration method.

Basically, the interpretation of the index concept is that "it measure how far a DAE (Differential and Algebraic Equations) system is from an ODE (Ordinary Differential Equations) system." This seems very general and abstract. However, if specifically in the case of the STF there are r constraint functions and k independent coordinates, the result is:

$$\Phi_p = 0,\ p = 1, ..., r \tag{3}$$

Therefore, if only the displacement constraints (3) are attached to the equations of motion, the method has index three.

$$\frac{\partial \Phi_p}{\partial q_j}\dot{q}_j = 0;\ \mathrm{j} = 1, \ldots .., \mathrm{k} \tag{4}$$

By including the displacement, (3), and the velocity constraints, (4), the method has index two.

$$\begin{gathered}\frac{\partial \Phi_p}{\partial q_j}\ddot{q}_j + \frac{\partial \Phi_p^2}{\partial q_j \partial q_l}\dot{q}_j\dot{q}_l = 0; \\ j = 1, ..., k\,;\quad l = 1, ..., k\end{gathered} \tag{5}$$

By considering the displacement, velocity and acceleration constraints, (3), (4) and (5), the method has index 1.

Finally, if the formulation is an ODE [5], then the method has index 0.

Index 3 methods, depending on the problems, introduce errors in the Lagrange multipliers and accelerations for constrained mechanical systems.

The dilemma is that ODE formulations are much harder to implement numerically; many times they are slower to solve due to the variable elimination process – especially, for large practical problems. At the same time they may give higher quality results. The DAE or STF are faster for large problems and they are easier to implement. However, for some problems, by using index three BDF the quality of the results are not as accurate for accelerations and forces. It logically follows that reducing the index of the STF will be a reasonable solution for improving the quality of the results. For this reason, more than the displacement constraints must be considered. The size of $\tilde{\Im}$ will increase and therefore will slow down the simulation speeds.

In 1989, Orlandea introduced index 2 and index 1 for STF formulation into a computer program called MCADA (Mechanical Computer Dynamic Analysis) [6]. The experiments done with MCADA have shown very little differences, if at all,

between index 2 and index 1 methods. Another important result was that index 3 STF gives reliable results for the displacements of the constrained mechanical systems.

Fuhrer and Leimkuhler [7] made an attempt to improve the computation speed for index 2 methods. They derived a method that reduces the size of $\tilde{\Im}$ by using partitions of $\tilde{\Im}$ and approximations based on the idea that an approximate $\tilde{\Im}$ is sufficient for good results as long as $\underline{\Re}$ is perfect. They had shown that these methods give different results for stiff and non-stiff equations, but in both situations some computational speed advantages can be obtained. They also mention that the sparsity of the Jacobeans remains the main factor in gaining computer simulation speed.

These ideas, including the explicit and the implicit equations of motion and the numerical stiffness of the equations of motion, will be discussed in the next chapter.

In the following discussions, the author will refer more to the formulations found in the original ADAMS program, and MCADA 3D and 2D. He will not discuss the capabilities of MSC.ADAMS, DADS, or Alter's MOTION. Essentially, these programs contain parts from the original ADAMS or, the author believes, were influenced by STF, the use of the sparse matrix techniques, formulation of the constraints based on links and the type of joints and using BDF and lower index methods.

2 Theoretical Considerations

The most general form of the equation of motion can be written in tensor form using the generalized mass matrix $\tilde{Y}$ and the applied generalized forces or torques $\underline{Q}$, corresponding to the generalized coordinateq_j or $\underline{q}$.

$$\tilde{Y}\,\underline{\ddot{q}} = -\begin{bmatrix} l & \\ & j \end{bmatrix}^{p} \underline{\dot{q}}_l \underline{\dot{q}}_p - \underline{Q} \tag{6}$$

where,

$$\begin{bmatrix} l & \\ & j \end{bmatrix}^{p} = \frac{1}{2}\left[\frac{\partial Y_{lj}}{\partial q_p} + \frac{\partial Y_{jp}}{\partial q_l} - \frac{\partial Y_{lp}}{\partial q_j}\right], \quad l,p,j = (1,2,....,k) \tag{7}$$

is the Christofel symbol of the first kind, dependent in general, on the generalized coordinates and velocities respectively $\underline{q}$ and $\underline{\dot{q}}$. They are the general form of Coriolis and other inertial forces. The terms Y_{lj}, Y_{jp}, Y_{lp} are the reduced generalized mass matrices.

Q_j are the generalized forces depending on the displacement, velocity, and time. The indices l and p in the Cristofel symbols are the summation indices. j refers to the number of generalized coordinates or the number of differential equations.

The form (6), although very general, is not necessarily the final form. It is an implicit form which means that the accelerations are not explicitly represented. To express the accelerations explicitly, the assumption that the matrix $\tilde{Y}^{-1}$exists, has to be made.

Then,

$$\underline{\ddot{q}} = -\tilde{Y}^{-1} \begin{bmatrix} l & & p \\ & j & \end{bmatrix} \underline{\dot{q}}_l \underline{\dot{q}}_p - \tilde{Y}^{-1} \underline{Q}, \tag{8}$$

and the final form of the equation of motion is:

$$\underline{\ddot{q}} = -\begin{Bmatrix} l & & p \\ & j & \end{Bmatrix} \underline{\dot{q}}_l \underline{\dot{q}}_p - \tilde{Y}^{-1} \underline{Q} \tag{9}$$

Where,

$$\begin{Bmatrix} l & & p \\ & j & \end{Bmatrix} = \tilde{Y}^{-1} \begin{bmatrix} l & & p \\ & j & \end{bmatrix},$$

represents the Cristofel symbol of the second kind.

The equations (9) are of index zero formulation. They are the most general form and they can always be written in an explicit acceleration form. To formulate and to solve numerically these kinds of equations for large systems (e.g., large number of bodies, joints and forces) is a nightmare.

The equation (9) can be used for constrained systems. In this case, the constraints and their corresponding forces are eliminated. For this formulation, the number of the differential equations is equal to the number of degrees of freedom of the mechanical system.

The purpose of this paper is to maintain the generality of the equations and to bring them to a practical form that can be interpreted and solved numerically.

Modularization is one good vehicle for maintaining generality and for simplifying the equations. For the first time, such a modularization was done in 1971 for STF and the ADAMS computer program. Any mechanism or mechanical system was decomposed in its component links or bodies, joints by type, and applied external forces compatible with a given field.

For instance, the auto industry primordial forces were engine characteristics, gravitational forces, linear and nonlinear springs and dampers as well as the tire traction equations. Aerospace required a different library of forces, such as drag, etc.

The analytical mapping for links or bodies is the equation of motion. Each body is considered in free motion, hence the number of degrees of freedom for all bodies

will be $6n$, where n is the number of links in the system. The six generalized coordinates for each body i,

are:

$$\begin{aligned} \underline{q_i} &= [q_{1i}, q_{2i}, q_{3i}, q_{4i}, q_{5i}, q_{6i}]^t \\ &= [x_i, y_i, z_i, \psi_i, \theta_i, \phi_i]^t \\ & \qquad i = 1, ..., n. \end{aligned} \tag{10}$$

The six coordinates for each body are the coordinates of the origin of a mobile body fixed system of reference and the Euler angles with respect to an inertial reference system. The origin of the system is preferably, but not necessarily to be the body's CG. The three Euler angles define the rotational position between the inertial system and body fixed system of reference. The body fixed system, again, is preferred to be the principal inertia system. However, this is not a requirement.

The set of equations of motion in an implicit form that contains the accelerations, the Cristofel symbols and the generalized forces is:

$$F_{ei}\left(\underline{\ddot{q}_i}, \underline{\dot{q}_i}, \underline{q_i}, t\right) = 0. \tag{11}$$

The constraints functions $\underline{\Phi}$ are organized into a library based upon the joint types. For example, they are written for spherical joint, revolute joint, translational joint, cylindrical joint, screw joint, etc. Hence, equation (3) together with equation (11) forms the following system of equations:

$$\begin{aligned} F_{si}\left(\underline{\ddot{q}_i}, \underline{\dot{q}_i}, \underline{q_i}, t\right) - \sum \frac{\partial \underline{\Phi}^t}{\partial \underline{q}} \underline{\lambda} = \underline{0}, \\ \underline{\Phi} = \underline{0} \end{aligned} \tag{12}$$

where, $\underline{\lambda} = [\lambda_1, ..., \lambda_r]$, are the Lagrange multipliers and r is the number of the scalar constraints.

The relation:

$$\underline{u} - \underline{\dot{q}} = \underline{0}, \tag{13}$$

is reducing the order of the differential equation of motion to one. $\underline{u}$ is equal to the velocity vector when the system is iterated to converge.

The force definition functions have the advantage of allowing the equation of motion to accept different forces without modifying their structure. This allows building force libraries for different fields of activity such as aerospace, auto, agricultural machinery, etc. Assuming that there are "s" definition functions for body "i," the result is:

$$\underline{F}_{di} - \underline{f}_i(\underline{u}_i, \underline{q}_i, t) = \underline{0},\ \underline{F}_{di} = [F_{d1}, ..., F_{ds}]^t \tag{14}$$

Combining the equations (3), (12), (13) and (14), yields:

$$\begin{aligned} \underline{\xi}_1 &= F_{ei}\left(\dot{\underline{u}}_i, \underline{u}_i, \underline{q}_i, t\right) - \sum \frac{\partial \underline{\Phi}_i^{\,t}}{\partial \underline{q}} \underline{\lambda} = \underline{0} \\ \underline{\xi}_2 &= u_i - \dot{\underline{q}}_i = \underline{0} \\ \underline{\xi}_3 &= \underline{\Phi}_i = \underline{0} \\ \underline{\xi}_4 &= \underline{F}_{di} - \underline{f}_i(\underline{u}_i, \underline{q}_i, t) = \underline{0} \end{aligned} \tag{15}$$

The system (15) written in matrix form, is an index three formulation. The fact that the position constraints $\underline{\Phi}$ are satisfied does not guarantee that the velocity constraints and acceleration constraints are satisfied. One of the advantages of the index three methods is that, if convergent, the system is perfect from a positional point of view. The joint drift will be minimized in accordance with the error control. This computation speed is the fastest of all methods because having the error control determined by only the position coordinates allows large time steps. The results can be used mainly for animations of the mechanical system's motion. A substantial number of computer runs were unsuccessful when the error control was extended on velocities and Lagrange multipliers.

Rewriting the system of equations (15) in a simplified vector form:

$$\underline{\xi} = \left[\underline{\xi}_1, \underline{\xi}_2, \underline{\xi}_3, \underline{\xi}_4\right]^t, \tag{16}$$

Equation (16) will be solved later after a few words about the BDF. The Backward Difference Formula [2] is derived from a Hermit interpolation method where the majority of the derivatives are ignored. Thus, a BDF interpolation is:

$$\sum_{i=0}^{k} (\beta_i h \dot{y}_{n-i} + \alpha_i y_{n-i}) = 0$$

where,$\beta_1 = \beta_2 = ... = \beta_k = 0, \alpha_0 = 1$. The α_i and β_0 are coefficients that depend on k. "k" represents the order of the numerical integration method. It also represents the maximum degree of the polynomial that approximates the solution. *"h"* is the time step. $y_n, y_{n-1}, ..., y_{n-k}$ represent the integration solutions at n, $n-1,. . ...,n-k$ time steps. Hence, this numerical integration algorithm is defined to be a multi-step method. Based upon the value of the coefficients, α_i andβ_0, the above equation can be written:

$$y_n = -\beta_0 h \dot{y}_n - \sum_{i=1}^{k} \alpha_i y_{n-i} \tag{17}$$

This form is the one that is frequently used. According to the formula (17), the problem that has to be solved is that the solutiony_n depends on$\dot{y}_n$. Because of this, the method of numerical integration is defined to be implicit. However, the relationship between $\dot{y}_n$ and y_n can be of the form $\dot{y}_n = f(y_n)$ that is an explicit function or of the form $F(\dot{y}_n, y_n) = 0$ that is an implicit function. The fact that this dependency is an explicit or an implicit function does not modify the definition of the integration method of being implicit. However, this dependency calls for a numerical algorithm that is capable of solving it in a general manner. Such a method is a Newton-Raphson type of iteration.

Solving the equation (16) using the Newton-Raphson algorithm yields:

$$\left(\frac{\partial \underline{\xi}}{\partial \underline{\dot{u}}}\Delta\underline{\dot{u}} + \frac{\partial \underline{\xi}}{\partial \underline{u}}\Delta\underline{u} + \frac{\partial \underline{\xi}}{\partial \underline{q}}\Delta\underline{q} + \frac{\partial \underline{\xi}}{\partial \lambda}\Delta\lambda\right)^m = -\underline{\xi}^{m-1} \tag{18}$$

Discretizing equation (17) for iteration m and $m-1$:

$$-(\Delta y_n + \beta_0 h \Delta \dot{y}_n)^m = \left(y_n + \beta_0 h \dot{y}_n + \sum_{i=1}^{k} \alpha_i y_{n-i}\right)^{m-1}$$

$$-(\Delta y_n + \beta_0 h \Delta \dot{y}_n)^{m-1} = \left(y_n + \beta_0 h \dot{y}_n + \sum_{i=1}^{k} \alpha_i y_{n-i}\right)^{m-2}$$

and making the difference of the two relationships, the result is

$$\Delta \dot{y}_n^m = \frac{\Delta y_n^m}{\beta_0 h} \tag{19}$$

Relation (19) is the fundamental BDF law. It shows the connection between function and its derivative in a discrete environment.

The formula (19) leads also to a relationship between velocities and accelerations expressed by:

$$\Delta \underline{\dot{u}}_n = \frac{\Delta \underline{u}_n}{\beta_0 h} \tag{20}$$

Then the solution vector has the form: $\underline{y}_n = \left[\underline{u}, \underline{q}, \underline{\lambda}\right]^t$

Substituting (20) in (18) yields

$$\left[\left(\frac{\partial \underline{\xi}}{\partial \underline{\dot{u}}}\frac{1}{\beta_0 h} + \frac{\partial \underline{\xi}}{\partial \underline{u}}\right)\Delta\underline{u} + \frac{\partial \underline{\xi}}{\partial \underline{q}}\Delta\underline{q} + \frac{\partial \underline{\xi}}{\partial \underline{\lambda}}\Delta\underline{\lambda}\right] = -\underline{\xi}$$

or in a matrix form:

$$\begin{bmatrix} \left(\frac{\partial \underline{\xi}_1}{\partial \underline{\dot{u}}} \frac{1}{\beta_0 h} + \frac{\partial \underline{\xi}_1}{\partial \underline{u}}\right) & \frac{\partial \underline{\xi}_1}{\partial \underline{q}} & \frac{\partial \underline{\xi}_1}{\partial \underline{\lambda}} & \tilde{D} \\ \frac{1}{\beta_0 h} & \tilde{I} & \tilde{0} & \tilde{0} \\ \tilde{0} & \frac{\partial \underline{\xi}_3}{\partial \underline{q}} & \tilde{0} & \tilde{0} \\ \frac{\partial \underline{\xi}_4}{\partial \underline{u}} & \frac{\partial \underline{\xi}_4}{\partial \underline{q}} & \tilde{0} & \tilde{I} \end{bmatrix} \begin{bmatrix} \Delta \underline{u} \\ \Delta \underline{q} \\ \Delta \underline{\lambda} \\ \Delta F_d \end{bmatrix} = - \begin{bmatrix} \underline{\xi}_1 \\ \underline{\xi}_2 \\ \underline{\xi}_3 \\ \underline{\xi}_4 \end{bmatrix} \tag{21}$$

$\tilde{I}$ is a unit matrix and $\tilde{D}$ is a matrix that connects the external forces to the corresponding equation of motion. It has all entries equaling 1; however, it is not a unity matrix. Equation (21) represents the corrector formula for index 3 ADAMS formulation.

Although it has a bad reputation, the index 3 formulation has the advantages of being fast, giving good results for unconstrained mechanical systems, and it requires the minimum size Jacobean for simulations.

It does have substantial disadvantages for constrained mechanical systems. It works reliably with highly accurate results only with constant time step. For constrained mechanical systems and variable time step, it accumulates errors in the Lagrange multipliers, velocities, and accelerations. For these systems, lower index methods such as 2, 1, and 0 are suggested.

Orlandea and Coddington [6] have shown that there is not a substantial difference in the quality of the results between index 2 and index 1 methods. The index 0 method, such as [8], is derived from STF by applying Sheth's rank definition [9] for the kinematic Jacobean. The fact that the rank should be computed and an extra matrix inversion is involved at each iteration, slows the integration substantially.

Using STF condition to implement the index 2 method, the equation (4), in a matrix form, must be attached to equation (21)

$$\underline{\xi}_5 = \frac{\partial \underline{\Phi}_i}{\partial \underline{q}} \dot{\underline{q}} = \underline{0} \tag{22}$$

Also, a new set of Lagrange multipliers
v_i , $i = 1,\ldots, m$, must be attached to $\underline{\xi}_2$

$$\underline{\xi}_2 = \underline{u}_i - \dot{\underline{q}}_i + \sum \frac{\partial \underline{\Phi}_i^{\,t}}{\partial \underline{q}} \underline{v} = \underline{0} \tag{23}$$

Hence, for index 2, the BDF corrector formula is:

$$\begin{bmatrix} \left(\frac{\partial \underline{\xi}_1}{\partial \underline{\dot{u}}}\frac{1}{\beta_0 h}+\frac{\partial \underline{\xi}_1}{\partial \underline{u}}\right) & \frac{\partial \underline{\xi}_1}{\partial \underline{q}} & \frac{\partial \underline{\xi}_1}{\partial \underline{\lambda}} & \underline{0} & \tilde{D} \\ \frac{1}{\beta_0 h} & \tilde{I} & \tilde{0} & \frac{\partial \underline{\xi}_1}{\partial \underline{v}} & \tilde{0} \\ \tilde{0} & \frac{\partial \underline{\xi}_3}{\partial \underline{q}} & \tilde{0} & \tilde{0} & \tilde{0} \\ \frac{\partial \underline{\xi}_5}{\partial \underline{u}} & \frac{\partial \underline{\xi}_5}{\partial \underline{q}} & \tilde{0} & \tilde{0} & \tilde{0} \\ \frac{\partial \underline{\xi}_4}{\partial \underline{u}} & \frac{\partial \underline{\xi}_4}{\partial \underline{q}} & \tilde{0} & \tilde{0} & \tilde{I} \end{bmatrix} \begin{bmatrix} \Delta \underline{u} \\ \Delta \underline{q} \\ \Delta \underline{\lambda} \\ \Delta \underline{v} \\ \Delta F_d \end{bmatrix} = - \begin{bmatrix} \underline{\xi}_1 \\ \underline{\xi}_2 \\ \underline{\xi}_3 \\ \underline{\xi}_5 \\ \underline{\xi}_4 \end{bmatrix} \tag{24}$$

The difference between (21) and (24) is a new row and column in the Jacobean matrix in position 4. There are also new entries in position 4 of the Newton differences and residual vectors. The supplementary Lagrange multipliers are necessary for making equation (24) solvable under dynamic conditions in the Newton-Raphson context. Based upon physical considerations, it is clear that when $\underline{u}$ is iterated to be equal to $\dot{q}$, the summation in equation (23) must be zero. This can always be satisfied if and only if, $\underline{v} \equiv \underline{0}$. These Lagrange multipliers do not have any physical meaning. There are a series of ways to treat these auxiliary multipliers during iterations.

Table 1, shows the STF Jacobean matrix assembled for a system of n links or bodies. In the first row of the table are represented the Newton differences vectors. For example, $\Delta \underline{w}_i = [\Delta \underline{u}_i, \Delta \underline{q}_i]^t$

Here, $\Delta \underline{u}_i$ is the generalized velocity vector for body i and is equal to

$\Delta \underline{u}_i = [\Delta ux_i, \Delta uy_i, \Delta uz_i, \Delta ws_i, \Delta wt_i, \Delta wp_i]^t$. *ux, uy,* and *uz* are the projections of the linear velocity of the origin of the body fixed reference system on the axis of the inertial system. *ws, wt*, and *wp* are the angular velocities corresponding to the Euler angles ψ , θ andϕ, already discussed above. The Newton differences for the generalized coordinates are

$\Delta \underline{q}_i = [\Delta x_i \,, \Delta y_i \,, \Delta z_i \,, \Delta \psi_i \,, \Delta \theta_i \,, \Delta \phi_i]^t$. These coordinates have the same structure for each body for

$i = 1, \ldots\ldots\ldots, n$. Again, all of these lead to the result that each rigid body is defined by 12 coordinates. Six are velocity coordinates and six are position coordinates.

After all of the $\Delta \underline{w}_i$, the solution vector should have all of the Newton differences of the Lagrange Multipliers and forces. In order all $\Delta \underline{\lambda}$, then all $\Delta \underline{v}$, and the last should be the definition forces $\Delta \underline{F}_d$.

Although equation (9) shows that the accelerations always can be expressed explicitly in the STF case; many times it will be more efficient to leave the equations in an implicit form. The derivatives of the Cristofel symbols of the second kind will become part of the Jacobean matrix. They can have very complicated functional forms that lead to a substantial increase in the number of computer

Table 1 Assembled Jacobean matrix for ADAMS index 2 with stabilization

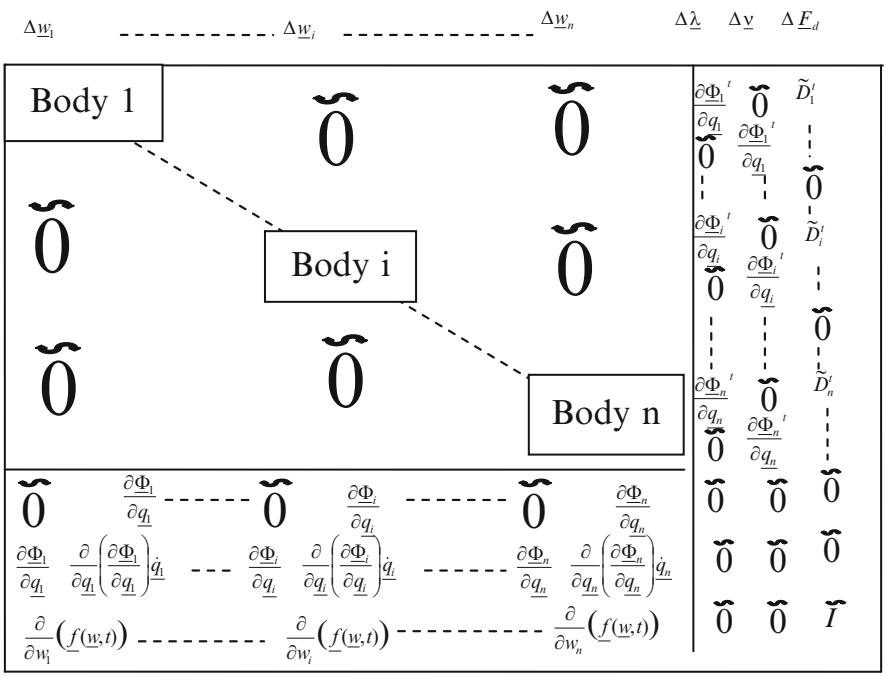

operations, especially for very large systems. Such examples are the rotational differential equations for each rigid body. Hence, the preference for these equations corresponding to ψ , θ and ϕ is to let them be an implicit form.

Another point that must be made is that the following derivatives $\frac{\partial}{\partial \underline{q}}\left(\frac{\partial \underline{\Phi}_p}{\partial \underline{q}}\underline{\lambda}\right)$ and $\frac{\partial}{\partial \underline{q}}\left(\frac{\partial \underline{\Phi}_p}{\partial \underline{q}}\underline{v}\right)$ are tensor valuations that require a substantial number of computer operations.

The first function will be very hard to avoid because the λ Lagrange multipliers are the main contributors to the computation of the reaction forces. The evaluation of the second function can be modified for numerical efficiency using two criteria: first we know the correct solution of$v$, it must be zero. Secondly, they are empty of any physical meaning. Hence, they can be used to reduce computer labor during iteration.

Figure 1 represents the Flow Chart of the original ADAMS and MCADA computer programs. They are identical programs. MCADA is used to test the program improvements, so it does not have a lot of bells and whistles.

The Flow Chart shows that after the input is read, the sparse matrix algorithm generates the symbolic code. This code contains the positions of the pivots, and the matrix fills in a $\tilde{L}\tilde{U}$ factorization scheme. Also, it contains numerical optimizations for gain in computational speed.

The input data contains, also, the initial conditions. The Jacobean matrix $\tilde{\Im}$ and the right side vector $\underline{\Re}$ (see (1), (24) and Table (1)) are iterated until the system

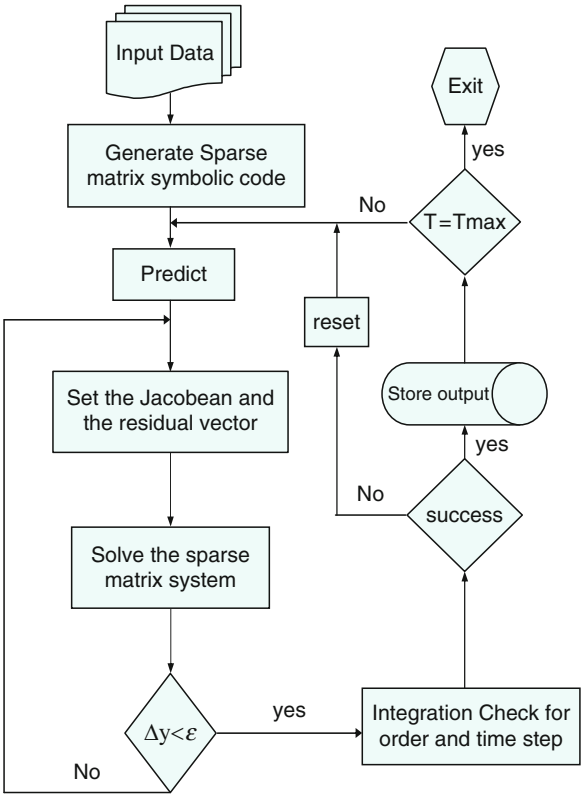

Fig. 1 Flow chart for "Original ADAMS and MCADA"

satisfies the error control for the Newton differences. When convergence is achieved, the process passes to the numerical integration routine that will recommend maintaining the time step and order or increasing them for higher productivity and accuracy of the next step. If the error control is not successful, the control again passes to the numerical integration routine. Depending on the situation, it will reduce the time step and/or the order. In this case, it will reset the values of the solution vector to the predicted values and will try a new iteration process with reduced time step and/or order.

If the time value is equal to Tmax, take the exit; otherwise, repeat the process until this value is reached.

3 The 2-Steps Method

To improve the computational efficiency and the quality of the results, the index must be lowered. Gear in [4] has shown that an index 2 method is convergent up to the 7th order of a BDF numerical integration method. Following through with this

idea, Fuhrer and Leimkuhler [7] introduced a partition method capable of efficiently solving index two with stabilization systems. They also observed that some blocks of the Jacobean matrix for the BDF corrector formula remained the same in both steps.

The suggested partitions are:

- Partition 1: contains equations (3) and (23). This partition is called the displacement or position partition.
- Partition 2: contains equations (4), (12), and (14). This partition is called the velocity-force partition. Solving these two partitions constitute the 2-Steps method.

The advantages brought by the first partition are a reduction with six equations for each body, the elimination of the velocity constraints and the force definition equations. This partition contains nonlinear equations; hence, it must be solved iteratively.

The second partition also eliminates six equations for each body and the position constraints. However, there are two issues with this partition. The first issue is that in the case of the STF formulation, the equations of motion are nonlinear functions of the velocity as suggested by the Cristofel symbols of the first kind. The second issue is that the force definition equations may also be nonlinear functions of the velocities and the Lagrange multipliers. Examples of this issue are the friction forces in joints. Hence, this partition will also be solved iteratively.

To start the program based on the initial conditions and the input data, the sparse matrix code is generated for both partitions. This operation can be parallelized for even more efficiency. The sparse matrix codes remain the same until a pivot becomes equal to zero. At that time, if the problem is physically possible, the system will find another pivot and will generate a new code that will be further executed. This regeneration of the sparse matrix code will be done specifically to the partition that needs it. Further, the Jacobean matrix and the residual vectors are generated for the position partition (Fig. 2).

After solving the positions and the $\underline{\nu}$ Lagrange multipliers, an error control is performed to check the convergence and the validity of the results.

The position data is passed to the second partition for evaluation of its Jacobean matrix and the residual vector. After solving, if successful, the results for velocities and Lagrange multipliers $\underline{\lambda}$, are combined with the position results in the same vector. Then this vector is passed to the numerical integration error control that defines the time step and the order.

The corrector formula required by the first step and partition is represented by equation (25). The function $\underline{\xi_2}$ used is the one given by equation (23).

$$\begin{bmatrix} \tilde{I} & \beta_0 h \dfrac{\partial \underline{\Phi}_p}{\partial \underline{q}}^t \\ \dfrac{\partial \underline{\Phi}_p}{\partial \underline{q}} & \tilde{0} \end{bmatrix} \begin{bmatrix} \Delta \underline{q} \\ \Delta \underline{\nu} \end{bmatrix} = - \begin{bmatrix} \beta_0 h \underline{\xi_2} \\ \underline{\xi_3} \end{bmatrix} \tag{25}$$

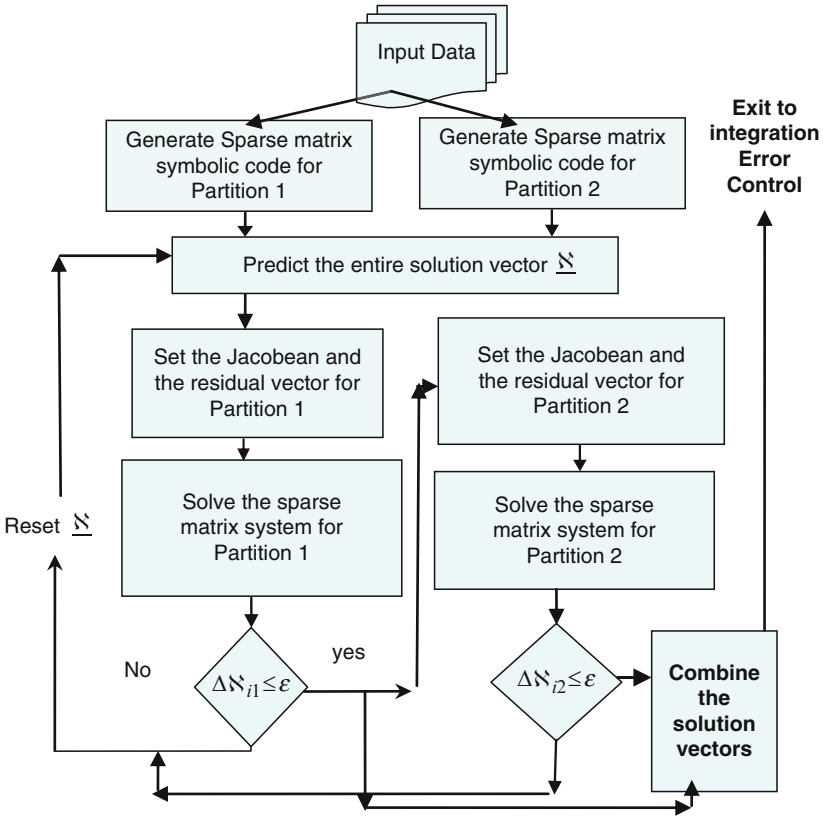

Fig. 2 Flow chart for stabilized index 2 with partitions

There are some observations to be made. The simplified form of the Jacobean of formula (25) is obtained because the time step is considered to be very small and the value $\beta_0 h \left[\frac{\partial}{\partial \underline{q}} \left(\frac{\partial \underline{\Phi}_p}{\partial \underline{q}} \underline{v}\right)\right]$ can be ignored. This may also be stressed by the fact that $\underline{v}$ is converging toward zero as well as β_0 which has small values for higher order. This idea is promoted also in [7] and is based on the statement that the Jacobean does not have to be perfect but the residual vector has to be accurate. However, the inaccuracies in the Jacobean matrix do increase the number of iterations.

All of these things may happen; however, there is not a warranty that they will be so. One idea is to iterate toward the $\underline{v}$ equal to zero starting with the initial value of zero. To maintain this value during iterations the following relationship must be solved together with equation (25). $\underline{v} - \underline{\delta} = \underline{0}$ where $\underline{\delta} \equiv \underline{0}$. This will add a number of columns and rows to the Jacobean of the corrector formula (25). The number is equal to the number of the equations of constraints. This seems to contradict the idea of reducing the size of the systems. Specifically, it adds only two unit matrices and, in this way, everything will be theoretically correct. The user has to make a

judgment as to which road he wants to pursue: to accept an approximate system, to perform the tensor evaluation that may be more time consuming and more difficult to achieve, or to increase the system in size and sparsity.

For the second step or partition, the equations of motion, the velocity constraints, and the definition forces are iterated together. The constraints and the equations of motions are linear in Lagrange multipliers λ and velocities. However, the Cristofel symbols and the force definition equations such as the friction in joints, in many situations, are nonlinear functions of velocity. For instance, the translational equations of motion are linear in velocities if the CG is elected as the origin of the body fixed system. However, the rotational differential equations are not explicit equations, even though, the fixed body system of coordinate is the principal system of inertia. All of these suggest that the system has to be iterated. If everything is linear, one solving step will be enough to obtain the desired results.

The corrector formula for this partition is given by first and last parts of the equations (15) and equation (22).

$$\begin{bmatrix} \left(\frac{\partial \underline{\xi}_1}{\partial \underline{\dot{u}}} + \frac{\partial \underline{\xi}_1}{\partial \underline{u}}\right) & \beta_0 h \frac{\partial \underline{\Phi}_p}{\partial \underline{q}}^t & \beta_0 h \tilde{D} \\ \frac{\partial \underline{\Phi}_p}{\partial \underline{q}} & \tilde{0} & \tilde{0} \\ \frac{\partial \underline{\xi}_4}{\partial \underline{u}} & \tilde{0} & \tilde{I} \end{bmatrix} \begin{bmatrix} \Delta \underline{u} \\ \Delta \underline{\lambda} \\ \Delta F_d \end{bmatrix} = - \begin{bmatrix} \beta_0 h \underline{\xi}_1 \\ \underline{\xi}_5 \\ \underline{\xi}_4 \end{bmatrix} \tag{26}$$

Some observations are needed. Without the force definition functions, this system of equations as well as the equations (25) will be an upper triangular block matrix. By comparing equation (26) with (25), it is clear why it is necessary to generate two sparse matrix symbolic codes. The topology of the Jacobean matrix for the two situations is different. As a matter of fact, it is nothing wrong to generate two sparse matrix symbolic codes if there is enough computer memory. It will be convenient and almost necessary to store these codes in the internal arrays accessible at any time by the CPU. Of course the codes can be stored on files and read in succession when the specific system is solved, (25) or (26). This will slow the process significantly and it is not recommended by this writer.

For I2 (index 2), method equation (25) can be used to stabilize the drift in the displacement constraints. Under I2 conditions, for tough problems, drift in the displacement constraints may take place. This drift must be monitored and when it surpasses a prescribed error, the system (25) should be iterated to close the constraints. Then, the data should be passed back to I2 algorithm and the simulation can continue. This method works very well in MCADA. The advantage of this method is shown by the fact that the drift does not happen all the time and only in sporadically tough situations.

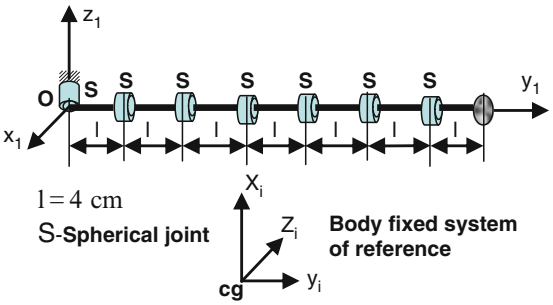

Fig. 3 The physical pendulum with 7 spherical joints

Table 2 Mechanical parameters of the physical pendulum

Body no.	M (g)	Ixx (g cm s^2)	Iyy (g cm s^2)	Izz (g cm s^2)
2–7	90	165	90	165
8	900	1,650	90	1,650

4 Numerical Example

For a numerical example, a kinematic chain was chosen that is a physical pendulum that has 8 links (bodies) and 7 spherical joints. This system may seem a well behaved dynamic system, which it is, as long as it approximates a mathematical pendulum. However, when the 21 free degrees of freedom become dynamically significant, the motion may become chaotic with some gyroscopic and crack-the-whip effects.

The kinematic chain is represented in Fig. 3. The last link has a weight that is 10 times greater than the weight of the other links. The mechanical parameters of the system for a physical pendulum are given in Table 2. The links are made of steel and they are cylindrical with a radius R=1 cm. Because of the cylindrical shape, the mass moments of inertia I_{xx} , $I_{yy}$and I_{zz} are also the principal moments of inertia. This implies that the mass products of inertia are zero.

For the mathematical pendulum approximations, the link cylinders are considered to have very thin walls, and they are made of light Titanium (Table 3).

The simulations were run for 5 s of real time. The pendulum executed four complete periods during this time.

Figure 4 portrays a half period animation of the mathematical pendulum. Although its behavior is very close to a periodic motion, it must be stressed again that this pendulum is approximating the mathematical pendulum by reducing the masses of the connecting links.

Eight simulations were performed for the physical pendulum having seven spherical joints and eight links. The first link is the ground. The simulations were run for different EPS (Error Per Step) that defined the boundary BND shown in Table 4. Two simulations were run for each value of the error. The first simulation

Table 3 Mechanical parameters of the mathematical pendulum

Body no.	M (g)	Ixx (g cm s^2)	Iyy (g cm s^2)	Izz (g cm s^2)
2–7	1	1.833	1	1.833
8	900	1,650	90	1,650

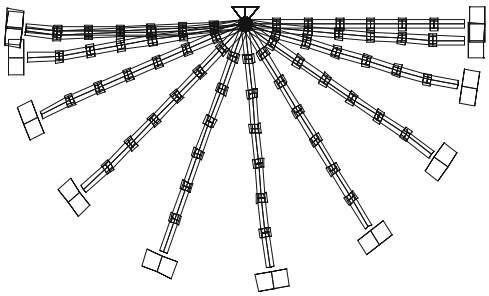

Fig. 4 Half period animation of the Kinematic Chain with 6 spherical joints

Table 4 The efficiency results. Comparison of the 2 Steps and I2 Simulations

Error BND		CPU (s)	No. of time steps
1^{-5}	2 Steps	42.55	4,297
	I2	46.25	4,691
1^{-6}	2 Steps	56.09	5,863
	I2	59.34	6,198
1^{-7}	2 Steps	69.79	7,437
	I2	78.51	8,258
1^{-8}	2 Steps	93.11	10,143
	I2	101.56	11,076

was for the 2-Steps BDF method and the second was an I2 (Index 2) with intermittent stabilization. The last one was chosen as a reference point for the computation efficiency.

The results from Table 4 show that the 2-Steps method compares very well with I2. Actually, it is faster. Over the years, I2 proved to be the most efficient method. The measures of the computation efficiency are the CPU (Central Processing Unit) time and the number of function evaluations or integration steps. There are substantial differences and trade-offs between the two methods. For instance, the I2 has 42 extra equations for this example. Also, I2 makes the tensor evaluation as discussed before. In contrast, the two steps method has two steps to solve and it uses two sparse matrix codes. For a thorough comparison, more eval uations on simulations of other mechanical systems must be made. However, this work started the comparison study.

An interesting aspect of the results is the chaotic behavior of the physical pendulum, as shown in Fig. 5. This motion is a result of the mass or weight of all of the links. When link 8 reaches the horizontal maximum vertical position, the tension created by the centrifugal forces is zero because of the reversing velocity of the pendulum. A slack effect is formed in the kinematic chain, because of the

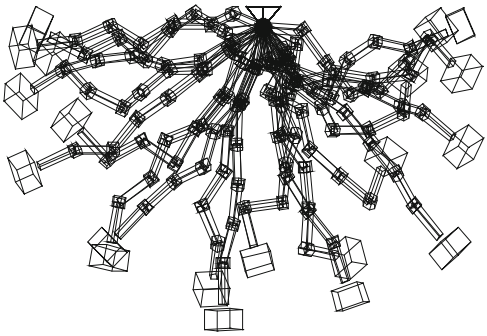

Fig. 5 An animation sequence of the physical pendulum

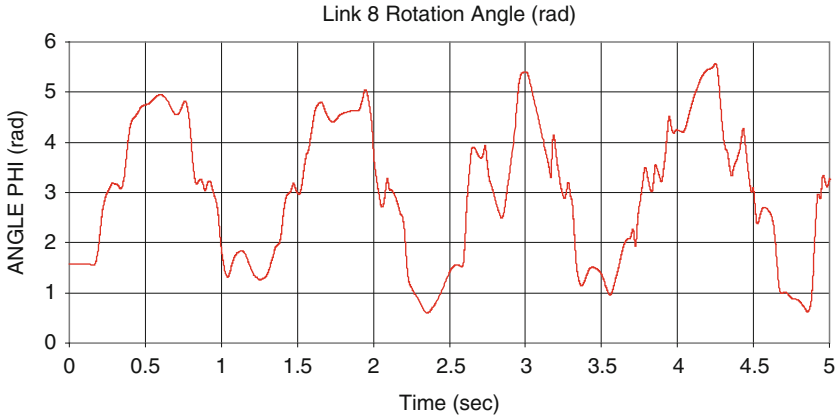

Fig. 6 Link 8's rotation Angle phi

combined weight of all the links. Hence, link 8 starts moving downward under the gravity effect. By moving downward, after a short time, its weight eliminates the slack in the chain by tensioning it. The last link suddenly starts moving on a circle which creates a sudden centrifugal force that associates itself directly with the gravitational force. All of these events create a snap in the chain, thereby increasing reaction forces in the joints. Consequently, the links start moving in different directions. The 21 degrees of freedom of the system have their motion determined by the initial conditions and forces. For large EPS, these initial conditions may change from time step to time step. Although the changes are very small, they may influence the results of the simulations when different errors are imposed. The lesson here is that the mechanisms must be designed desmodromoic without letting the degrees of freedom float along uncontrollably.

Figure 6 shows that the motion disorganization is increasing in time. The motion starts with small disturbances for first and second periods of the pendulum. They continue to grow in the third and fourth periods.

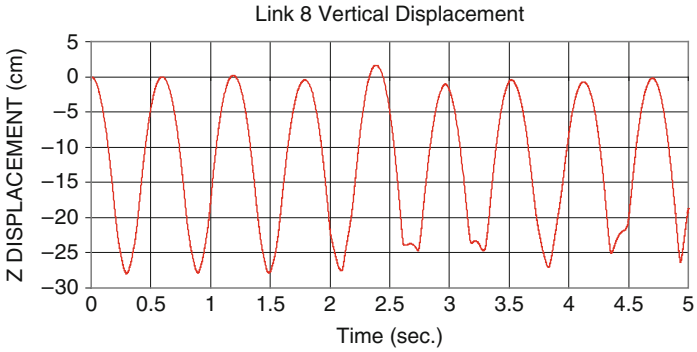

Fig. 7 Link 8's cg vertical displacement Z

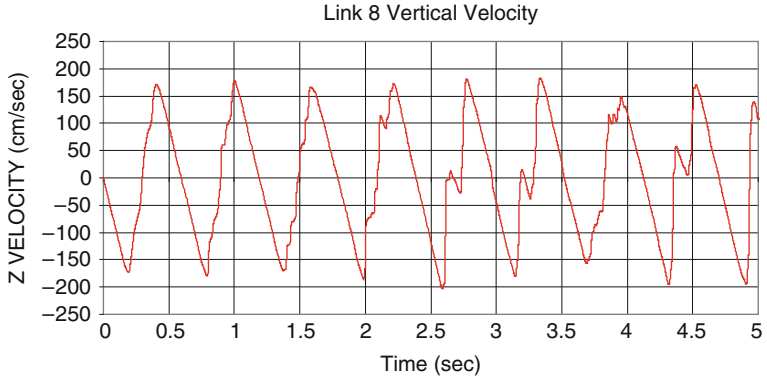

Fig. 8 Link 8 cg vertical velocity $\dot{Z}$

In Fig. 7, the frequency of the vertical coordinate Z of the link 8's CG has double frequency in comparison with the frequency of the rotation angle of the link. This is correct because the last link of the pendulum moves two times up and down for each period of the pendulum. As suggested by Fig. 8, the velocities are more sensitive to the motion disturbances than the displacements. After 2 s simulation time, the disturbances become more and more visible.

This example was chosen because of large number of degrees of freedom and difficult dynamics of the physical pendulum. Perhaps the behavior of a system having a closed loop topology will be more difficult dynamically. In reality, for ADAMS and MCADA, this will not make much difference. These programs have simulated thousands of systems with open loop, close loop and combined.

5 Conclusion

This work has shown that the 2-Step method works well and gives similar results to the BDF index 2 and BDF stabilized index 2. The main conclusions are:

- The structure of the Jacobean in step 2, of the 2-Steps method, does not necessarily have to be the same as the structure of the Jacobean in step 1. Of course, it is convenient for them to be the same. However, the approximations required for this to happen can create numerical problems.
- Two different sparse matrix symbolic codes can be generated for the two steps. This allows for introduction of the definition torques and forces that can be used only in step 2. The advantage of solving the definition forces separately, is the simplicity of their formulations with very little degradation of the sparsity.
- Generating two sparse matrix codes requires greater computation resources such as computer memory and, if possible, software parallelization.
- The simulations have shown that in the case of the physical pendulum with seven spherical joints, the 2-Steps method has a small advantage in CPU and function evaluation over I2. The computation speed advantages of the 2-Steps method, with respect to the usual SI2, are in the order of 5–20 times faster.

This work started with specific ideas to satisfy the needs of the original ADAMS and MCADA. Also, it can be viewed as a partial generalization of the ideas described in [7]. However, to draw complete conclusions, the 2-Steps method must be used in simulating other systems with different kinematic structure and simulation requirements.

References

1. Orlandea, N.: Node analogus and sparsity oriented methods for simulations of mechanical systems. Ph.D. thesis, The University of Michigan, Ann Arbor (1973)
2. Gear, C.W.: Numerical initial value problems in ordinary differential equations. Prentice-Hall, Upper Saddle River, NJ (1971)
3. Calahan, D.A.: Computer-aided network design. McGraw-Hill, New York (1973)
4. Gear, C.W.: Differential-algebraic equation index transformation. SIAM J. Sci. Stast. Comp. 9, 39–47 (1998)
5. Orlandea, N.V.: An index zero formulation of the general dynamic differential equations using the transmission functions. Proceedings of IMechE. Part K: J. Multi-body Dyn. 219, 159–171 (2005)
6. Orlandea, N., Coddington, R.: Reduced index sparse tableaux formulation for improved error control of the original ADAMS program, Mechanics in Design, University of Toronto, Toronto, Canada (1996)
7. Fuhrer, C., Leimkuhler, B.: Formulation and numerical solution of the equations of constrained mechanical motion. Technical Report FB-08, DFVLR, Koeln (1989)
8. Wehage, R.A.: Generalized coordinate partitioning in dynamic analysis of mechanical systems. Ph.D. thesis, The University of Iowa, Iowa City (1980)
9. Sheth, P.N., Ucker, J.J., Jr.: IMP (Integrated Mechanism Program) A computer-aided design analysis system for mechanism and linkages. J. Eng. Ind. ASME Trans. 94, 454–464 (1972)

Structural Synthesis of the Planar Cam-Linkage Mechanisms as Multibody Systems

Ion Vişa

Abstract The modern product design requires the use of commercial software that allows an unitary modelling of the mechanical systems, part in the final product. The paper proposes the multibody system method. There are proposed algorithms for defining and designing the mechanical systems as multibody systems, further applied for the cam-linkage mechanisms. Based on the different types of geometrical restrictions identified, the design method of the cam-linkage mechanisms is developed using graphs and is then applied on concrete applications. The multibody system methods can successfully replace the traditional mechanisms design methods.

Keywords Cam-linkage mechanisms · Multibody system method · Structural synthesis

1 Introduction

Industrial companies are developing and promoting innovative, quality products, able to satisfy the increasing demands of the customers, delivered in time, at an accessible price. Thus, product design and development must be organized based on software platforms for virtual prototyping and optimization, [1]. This is now a prerequisite for reducing the time and the costs in the production steps, including manufacturing, testing and physical prototype optimization.

Considering these, the products including mobile mechanical systems need a unitary model that can be applied to all the mechanisms involved, regardless their

I. Vişa
Department of Product Design and Robotics, Transilvania University of Braşov, Braşov, Romania

I. Vişa (ed.), *SYROM 2009*,
DOI 10.1007/978-90-481-3522-6_4,

type (linkages type, cams, gear mechanisms, etc.), allowing the study and optimization of the dynamic behavior in the entire product. A possible solution is to define and model the mechanisms in a product as multibody systems, [5, 15, 18, 24, 25, 27, 29, 31–33]. This needs a structural, kinematical and dynamic redefinition of the models used in the classical approach, so that the mission of the designer should focus on defining the mechanical system, interpreting and optimizing the results. The steps involving writing the equations, writing the algorithm for solving the resulted equation systems, implementing the adequate numerical algorithm are now transferred to the software, [2, 21, 22, 30, 43, 46].

In the modern product design, the multibody approach, applied to the conception of the mechanical systems, becomes a must. It is fundamental for a unitary approach of all the steps (analysis and optimization) in the design of the mechanical systems in a product. For the complex products (e.g., automotives, aircrafts, agricultural machines, airspace installations, bio systems, etc.) the design and development of the mechanical systems as multibody systems with a reduced number of bodies allow the real-time simulation of the dynamic behavior of the product.

Starting with 2001, plenty of work has been devoted to defining, modelling and studying the mechanisms as multibody systems in the research department "Product Design for Sustainable Development," in the Transilvania University of Brasov, Romania. The research results were presented in prestigious scientific events, [4, 7, 13, 19, 20, 34–44], were part of Ph.D. thesis (2005, Design and Kinematical – dynamic Study of the Transversal Mobile Coupling Using the Multibody System Method; 2007, Tracking Mechanisms for Solar Energy Conversion Systems; 2009, Modeling Cam-linkage Mechanisms Using the Multibody System Method), and were used in developing novel applications as tracking systems for PV modules and solar-thermal collectors, [1, 7–13], as car suspensions, [4], as couplings, [20].

The mechanical systems based on linkages and cams are often used in the structure of various products. Therefore, their integrated modelling as multibody systems represents an intensively studied topic and will be further detailed.

2 Defining a Mechanical System as Multibody System

In a product, a mechanical system transmits, in a determinate mode, the mechanical power for certain functionality. That implies the determined transmission of both components of the mechanical power: motion and forces.

In defining a mechanical system as multibody system both components of the mechanical power are considered. In defining the structural model, the notions of *body* and *restrictions between bodies* are considered, because the multibody system consists of bodies under geometrical and kinematical constrains.

In a given mechanisms, there must be considered as bodies: the fix or considered fix element, the input – output elements, elements with applied external driving and/or resistant forces, elements with more than two connections (ternary, quaternary,

etc.). A mechanism can be modelled as a multibody system considering a number n_b of bodies which is between the minimum number $n_{b,\ \min}$ and the maximum number $n_{b,\ \max}$. The maximum number of bodies is given by the number of elements $n_{b,\ \text{el}}$ in the mechanism, so that:

$$n_{b,\ \min} < n_b < n_{b,\ \max} = n_{b,\ \text{el}}. \tag{1}$$

For defining a mechanism as a multibody system with a minimum number of bodies, i.e., $n_b = n_{b,\ \min}$, the steps are according to the following algorithm:

Step 1: the fix body or the body considered fix
Step 2: the input body (bodies)
Step 3: the output body (bodies)
Step 4: bodies with applied external forces
Step 5: complex bodies (with more than two connections)
Step 6: other bodies (if necessary)

Defining the multibody systems with a minimum number of bodies is necessary in modelling the complex products involving mobile mechanical systems, for the real-time study of the dynamic behavior.

In the case of the planar motion, there are three degrees of freedom (L = 3) between two bodies considered independent. The geometrical restrictions between the two bodies can reduce the number of degrees of freedom to L = 2 (for one restriction, r = 1) or L = 1 (when r = 2).

The classical methods usually operate with notions like kinematical chains, type Assur groups (the Russian school), or closed kinematical mono- or poly-contour chains (the German school), each of these approaches having the well-known advantages and drawbacks, [3, 6, 14–17, 21, 23, 26, 28].

In a multibody system, the bodies can be in direct contact through a kinematical joint, or indirectly through a binary element with joints at both ends. Figure 1 presents an example of link through rotation joints between two bodies in direct and indirect contact.

For all the configurations corresponding to planar cam and linkages mechanisms, the following connections between the bodies can be identified, Fig. 2.

By combining the c. . ..f variants in Fig. 2, theoretically the following restrictions for two bodies can be defined, Fig. 3.

Based on the geometrical restrictions from Figs. 2 and 3, all the planar linkages and cams mechanisms can be described as multibody systems, by defining the minimum of bodies according to the algorithm already described and the type of

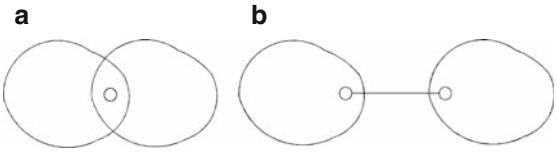

Fig. 1 Degrees of freedom and restriction between two bodies in direct (**a**) and indirect (**b**) contact

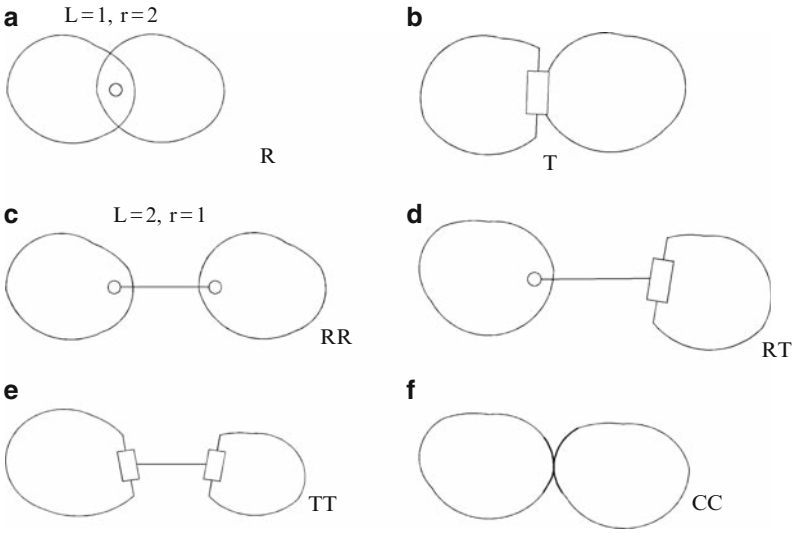

Fig. 2 Direct and indirect links between bodies in planar cam and linkage mechanisms

restrictions between the bodies, in the order 1–2, 1–3, . . . 1–$n_{b,\,min}$; 2–3, 2–$n_{b,\,min}$, etc. The number of possible combinations between the bodies is $C^2_{nb,min}$. As examples, Fig. 4 presents well-known mechanisms described as multibody systems.

The mechanism in the lifting system presented in Fig. 4a, has six elements and seven joints, corresponding to mobility M = 1 and driven by a hydraulic cylinder. It can be modelled as multibody system with a minimum number of two bodies: the fix/considered fix element 1 and element 2 which are both input and output element. The geometrical restrictions are presented in the associated table. In this case the number of combinations is $C^2_2 = 1$. According to the table, between the two bodies there are two restrictions of RR type, corresponding to $\sum r = 1 + 1$; according to (2), mobility of the multibody system is M = 3(2−1) – 2 = 1.

The mechanism corresponding to the undercarriage, Fig. 4b also consists of six elements and seven joints, mobility M = 1 and a driving hydraulic cylinder and can be modelled as multibody system with a minimum number of three bodies: the body considered fix – 1, the input bodies 2 and 3, body 2 also being the output body. In this case $C^2_3 = 3$. According to the associated table $\sum r = 5$, and as result, M = 3(3−2) – 5 = 1.

The mechanisms for the mechanical saw in Fig. 4c has seven elements, eight monomobile joints and the joint H with mobility 2; the mechanism mobility is 1 and the drive is insured by an electrical motor, rotating body 2. It can be modelled as a multibody system with a minimum number of four bodies: the fix body 1, the input body 2, the output body 3, the intermediate body 4 with three connections (ternary) and the geometrical restrictions presented in the associated table. In this case $C^2_4 = 6$ and $\sum r = 8$.The table has five lines because between bodies 2 and 3 there is no connection. For the multibody system M = 3(4–1) – 8 = 1.

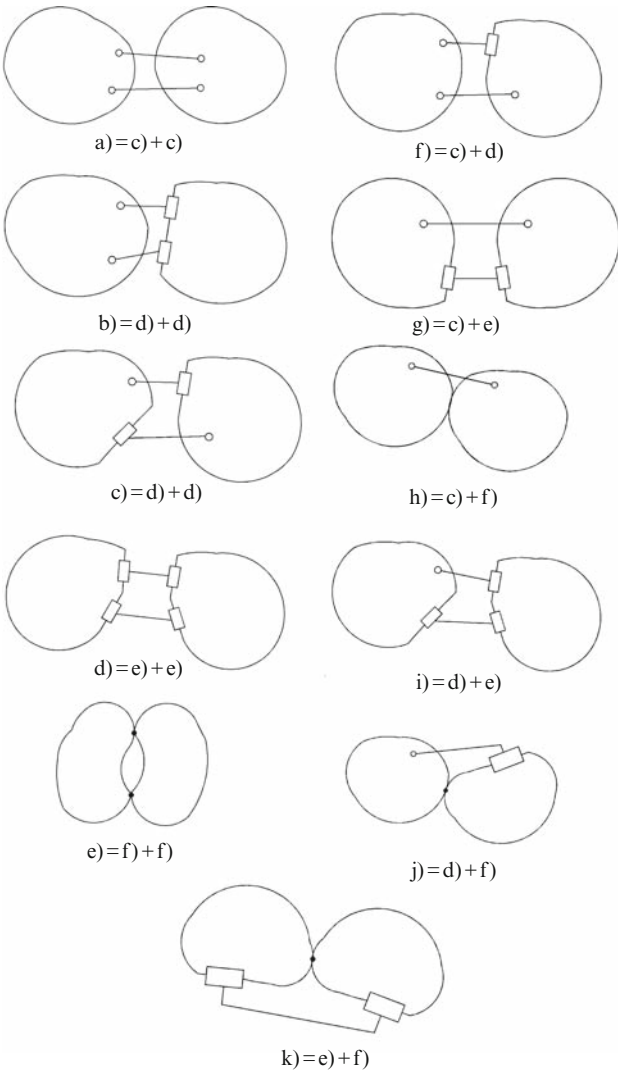

Fig. 3 Restrictions between two bodies

The mechanism of the loader presented in Fig. 4d has 11 elements and 14 kinematical joints, mobility 2 and is driven by two hydraulic cylinders. As a multibody system it can be modelled with a minimum number of five bodies: body 1 – the foundation, the input bodies 2, 3, 4 and the output body 5 and the geometrical restrictions presented in the associated table. In this case, $C_5^2 = 10$, but only six combinations are valid, the other four do not exist and $\sum r = 10$. The mobility of the multibody system is M = 3(5–1) − 10 = 2.

The example in Fig. 4e also corresponds to a multibody system with five bodies, with the geometric restrictions detailed in the table ($\sum r = 11, C_5^2 = 10, M = 1$).

a

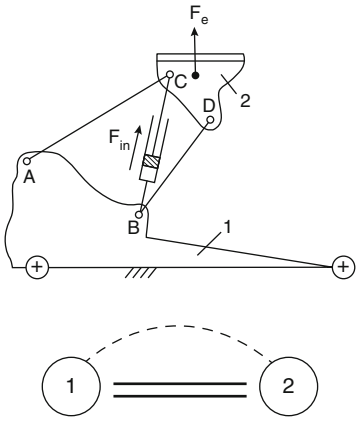

Body i – Body j	Type	Location	r
1 – 2	RR, RR	AC, DB	1+1

b

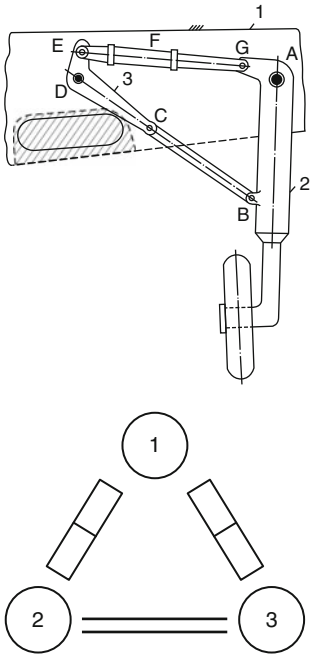

Body i – Body j	Type	Location	r
1 – 2	R	A	2
1 – 3	R	D	2
2 – 3	RR	BC	1

Fig. 4 (**a**) Jackscrew (Number of bodies $n_b = 2$). (**b**) Undercarriage (Number of bodies $n_b = 3$). (**c**) Mechanical saw (Number of bodies $n_b = 4$). (**d**) Loader (Number of bodies $n_b = 5$). (**e**) Textile machine (Number of bodies $n_b = 5$)

The method presented can be applied to any planar mechanism regardless the type and configuration, by associating one single multibody system with a minimum number of bodies, with well defined geometrical restrictions (Fig. 2) or combinations of restrictions as presented in Fig. 3.

c

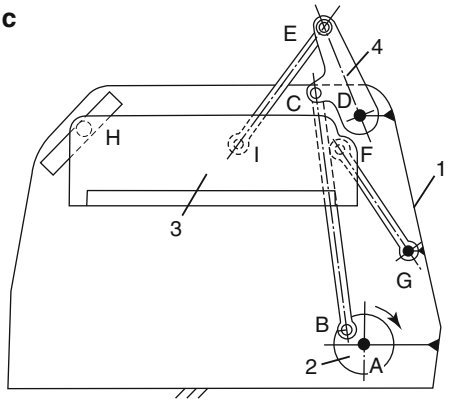

Body i – Body j	Type	Location	r
1 – 2	R	A	2
1 – 3	RR, RT	FG, H	1+1
1 - 4	R	D	2
2 – 4	RR	BC	1
3 - 4		EI	1

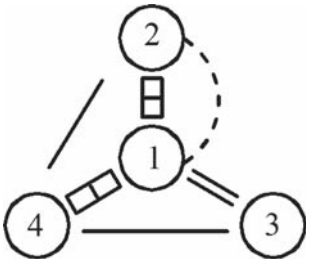

d

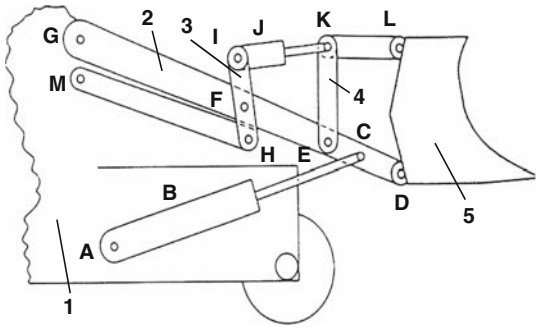

Body i – Body j	Type	Location	r
1 – 2	R	G	2
1 – 3	RR	MH	1
2 – 3	R	F	2
2 – 4	R	E	2
2 - 5	RR	D	2
4 - 5		KL	1

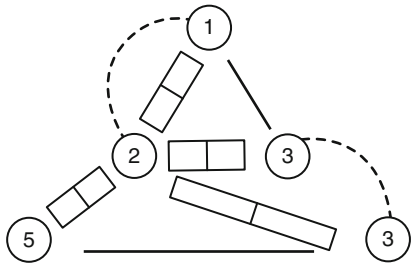

Fig. 4 (continued)

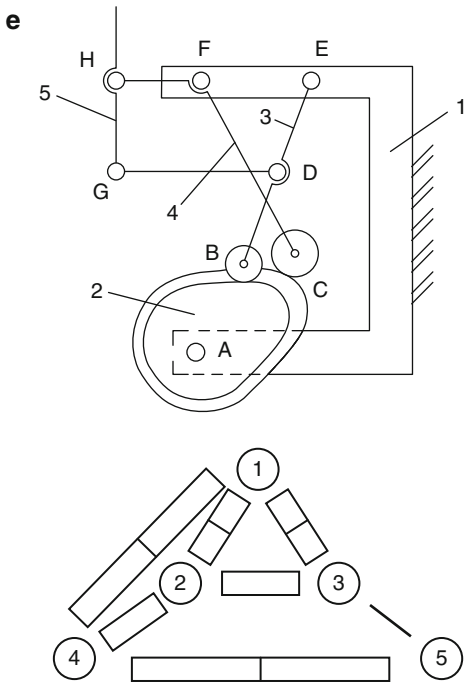

Body i – Body j	Type	Location	r
1 - 2	R	A	2
1 – 3	R	E	2
1 – 4	R	F	2
2 – 3	CC	B	1
2 – 4	CC	C	1
3 – 5	RR	DG	1
4 - 5	R	H	2

Fig. 4 (continued)

3 Designing a Mechanical System as a Multibody System with a Minimum Number of Bodies

The following initial data are required for defining a mechanical system as multibody system:

- The minimum number of bodies, $n_{b,\,min} \geq 2$
- The mobility of the multibody system, $M \geq 1$
- The types of the geometrical restrictions between the bodies: simple geometrical restrictions (direct contact between the bodies) type R(rotation), T (translation), CC (curve-curve); composed geometrical restrictions (indirect contact between the bodies), type RR, RT, TT

Between the number of bodies, the mobility and the sum of the geometrical restrictions there is the relation:

$$M = 3\left(n_{b,\,min} - 1\right) - \sum r \tag{2}$$

and the correlation from Table 1.

The sum of the geometrical restrictions $\sum r$ results from the geometrical restrictions r = 1 (RR, RT, TT – indirect contact between the bodies, CC – direct

Table 1 Mobility correlated with the sum of the geometrical restrictions

$n_{b,\ min} = 2$		$n_{b,\ min} = 3$		$n_{b,\ min} = 4$	
M	$\sum r$	M	$\sum r$	M	$\sum r$
1	2	1	5	1	8
2	1	2	4	2	7
3	0	3	3	3	6
		4	2	4	5
		5	1	5	4
		6	0	6	3
				7	2
				8	1
				9	0

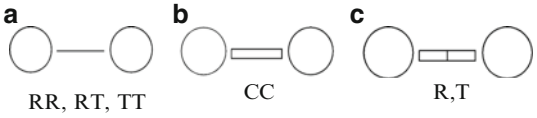

Fig. 5 Symbolic representation of the geometrical restrictions

contact between the bodies) and, respectively, r =2 (R, T) – direct contact between the bodies. Thus, depending on the r value and the body direct/indirect contact, three situations can be identified:

- r = 1, indirect contact between the bodies
- r = 1, direct contact between the bodies
- r = 2, direct contact between the bodies

For the three cases, the symbolic representations between two bodies are proposed in Fig. 5.

Using these representations, the associated graphs were developed for each multibody system presented in Figs. 4a–e. Based on the initial data and the graphical representations, Fig. 5, the algorithm for designing the mechanical systems as multibody systems is defined, with the following steps:

Step 1: Developing all the possible distinctive graphs, using the initial data: $n_{b,\ min}$, M and the distinct cases in Fig. 5 (all the cases can be considered or only part of them)

Step 2: Transforming the graphs in concrete mechanisms, considering the types of geometrical restrictions between the bodies

Step 3: Identifying the driving possibilities, by considering the motion between bodies (number of independent motions, M)

Step 4: Selecting the solutions that are complying with the application field.

The algorithm described is detailed for four concrete cases.

Case 1: $n_{b,\ min} = 2$, M = 1; variants a, b, c in Fig. 5

According to Table 1, $\sum r = 2$, thus the possible graphs are presented in Fig. 6.

Considering the composed restriction of RR type and joint R type, the mechanisms possible to be obtained are presented in Fig. 7, where the motion is introduced between the two bodies (Fig. 7a).

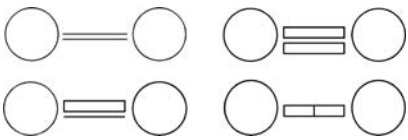

Fig. 6 Graphs corresponding to $n_{b,\ min} = 2$, M = 1

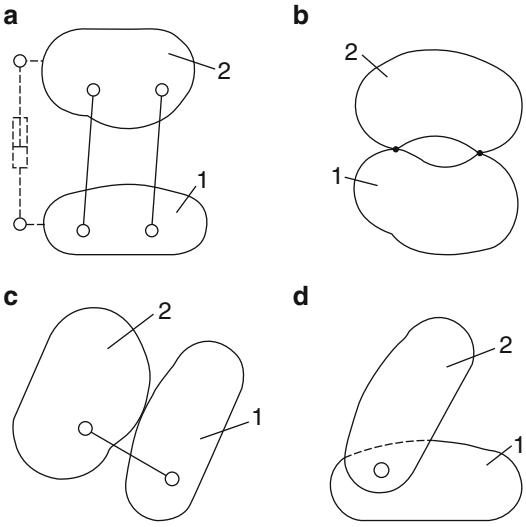

Fig. 7 The mechanisms with: $n_{b,\ min} = 2$, M = 1

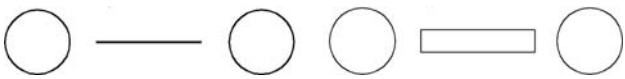

Fig. 8 Graphs corresponding to $n_{b,\ min} = 2$, M = 2

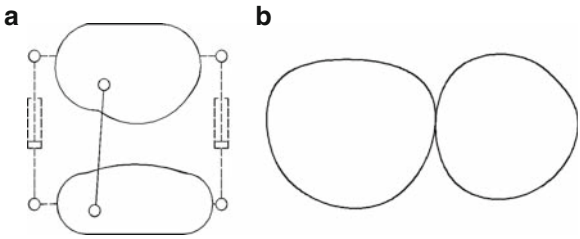

Fig. 9 The mechanisms with $n_{b,\ min} = 2$, M = 2

Case 2: $n_{b,\ min} = 2$, M = 2; variants a, b, c in Fig. 5

According to Table 1, $\sum r = 1$, so the possible graphs are (Fig. 8):

For the composed restriction RR, there is obtained the mechanisms in Fig. 9a. Driving motions are introduced between the two bodies.

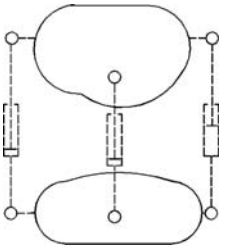

Fig. 10 The planar platform ($n_{b,\ min} = 2$, M = 3)

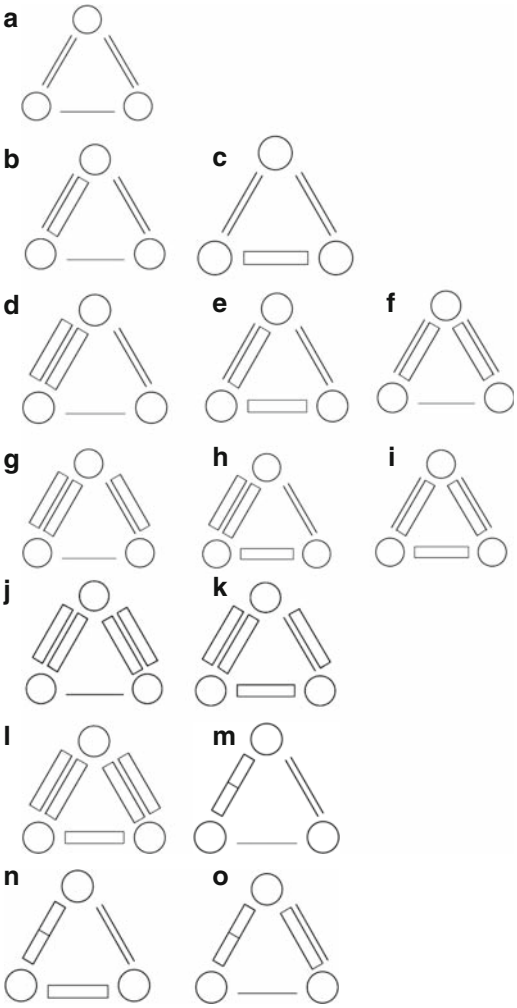

Fig. 11 Graphs corresponding to $n_{b,\ min} = 3$, M = 1

Fig. 11 (continued)

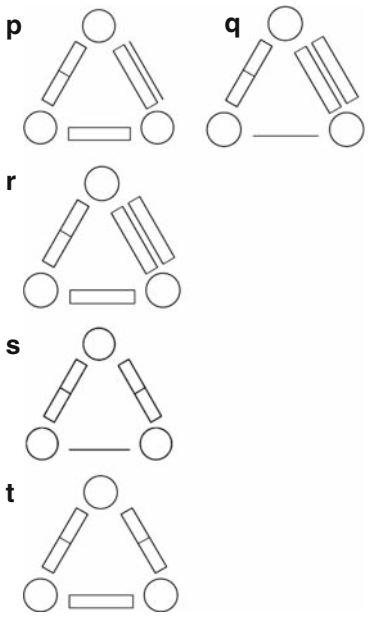

Case 3: $n_{b,\ min} = 2$, M = 3;

This situation corresponds to $\sum r = 0$, thus between the two bodies there are no geometrical restrictions. This corresponds to the planar platforms, where the three independent motions are introduced between the two bodies (Fig. 10).

Case 4: $n_{b,\ min} = 3$, M = 1; variants a, b, c in Fig. 5

According to Table 1 the sum $\sum r = 5$ and the possible graphs are in Fig. 11.

The general graph is presented in Fig. 11a, with $\sum r = (1 + 1) + (1 + 1) + 1$, meaning three groups because between three bodies C_3^2 connections are possible. These connections could be of types: RR, RT, TT. The graphs from Figs. 11b–c are obtained from the graph (a) where one connection is replaced by a CC type connection. All the graphs from (d) to (k) are obtained similarly; thus, the graphs (d) to (f) have two CC type connections, graphs (g) to (i) have three CC type connections, graphs (j) and (k) have four CC type connections. The graph (m) is obtained from (a), by replacing two composed connections by a single connection (R or T). The next graphs are obtained from (m) by replacing the composite joints by one CC (graphs (n) and (o)), by two CC (graphs (p) and (q)) or by three CC (graph (r)). The graph (s), is obtained from (m) by introducing a new simple restriction (type R or T) and the graph (t) from (n).

Based on the above graphs, concrete mechanisms are obtained, Fig. 12. The mechanisms in Figs. 12a, d and g correspond to the graphs presented in Figs. 11a, m, and s respectively and represent the fundamental structures with three bodies and M = 1. They are driven by an external independent motion, between the two bodies (e.g., Fig. 12a). Any of the three bodies can be the mechanism basis.

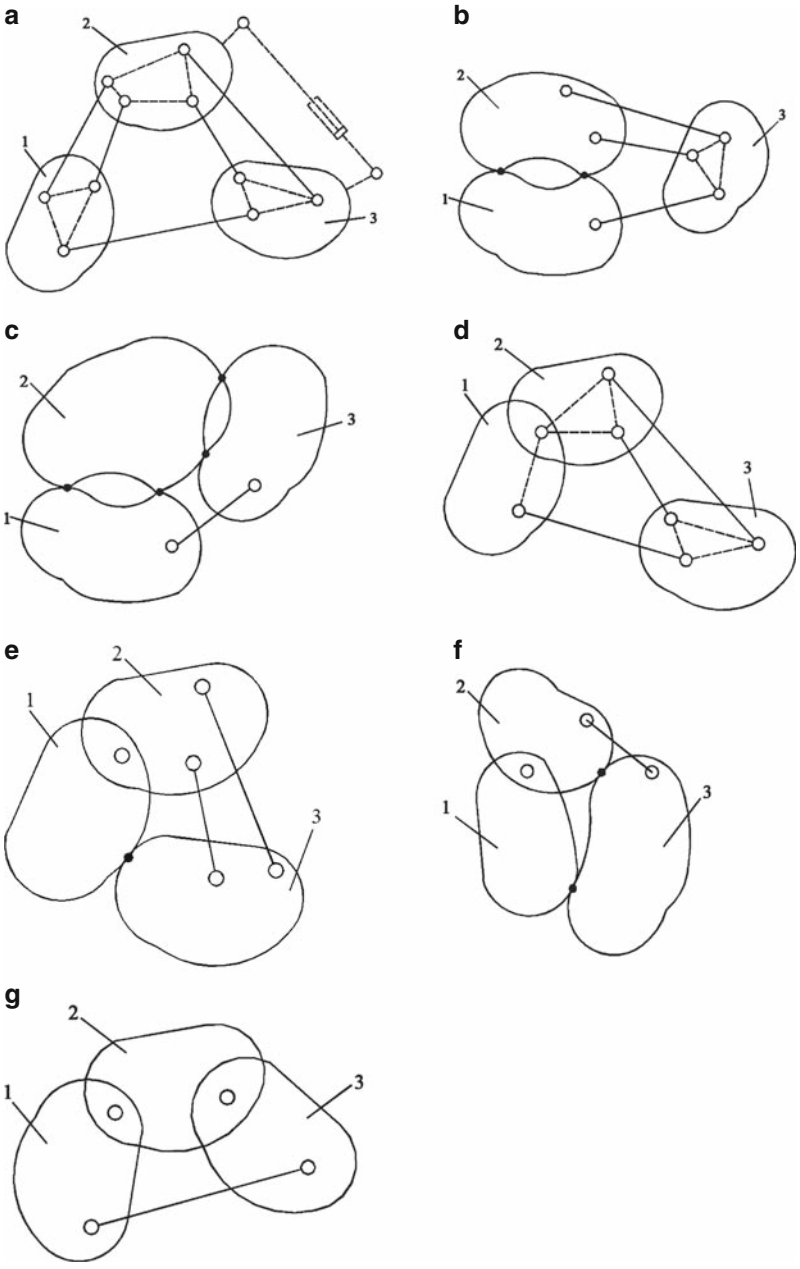

Fig. 12 The mechanisms with $n_{b,\,min} = 3$, M = 1

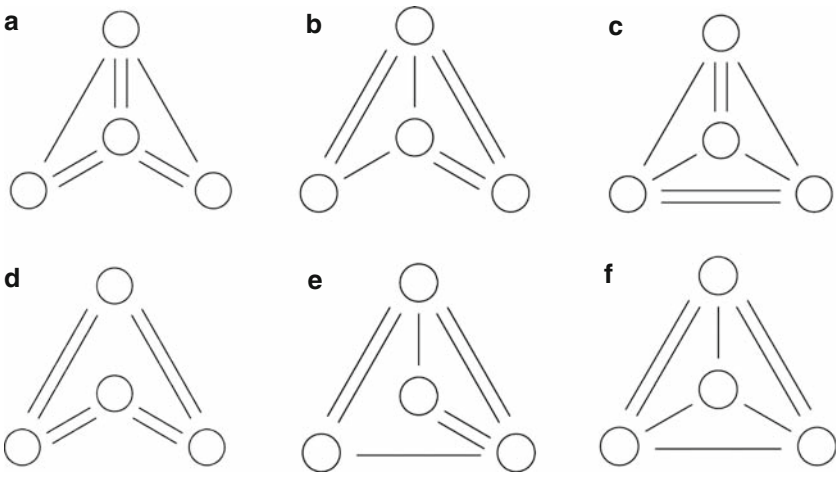

Fig. 13 Graphs corresponding to $n_{b,\ min} = 4$, M = 1

The mechanisms in Figs. 12b, c, e and f correspond to the graphs in Figs. 11d, j, n, and p respectively.

In the same way there can be obtained mechanisms with linkages and cams, with a minimum number of three bodies and mobilities higher than one (according to Table 1), and mechanisms with a minimum number of bodies higher than three, [39]. As example, for $n_{b,\ min} = 4$ and M = 1, six fundamental structures can be obtained having only geometrical composed restrictions between the bodies as Fig. 13 presents, [36]:

According to the algorithm for developing the mechanical multibody systems, considering the geometrical restrictions and the specific applications, solutions for concrete mechanisms are obtained. As example, in Fig. 14 there are presented the mechanisms obtained by considering the geometrical restrictions of types R, T, RR, RT, starting from the graph in Fig. 11m and considering the condition that between the wheel and the car body there is no direct link, i.e., between the bodies 1 and 2 there is a composed geometrical restriction.

Many other concrete mechanisms, applied in specific fields can be described by applying the method in couplings [20] or the mechanisms used for the solar tracking systems, [10, 12, 45], etc.

4 Conclusions

1. The design of the mobile mechanical systems using the multibody system method allows the unitary modelling, using an algorithm based on the minimum number of bodies, the mechanism mobility and the type of the geometrical restrictions between the bodies.

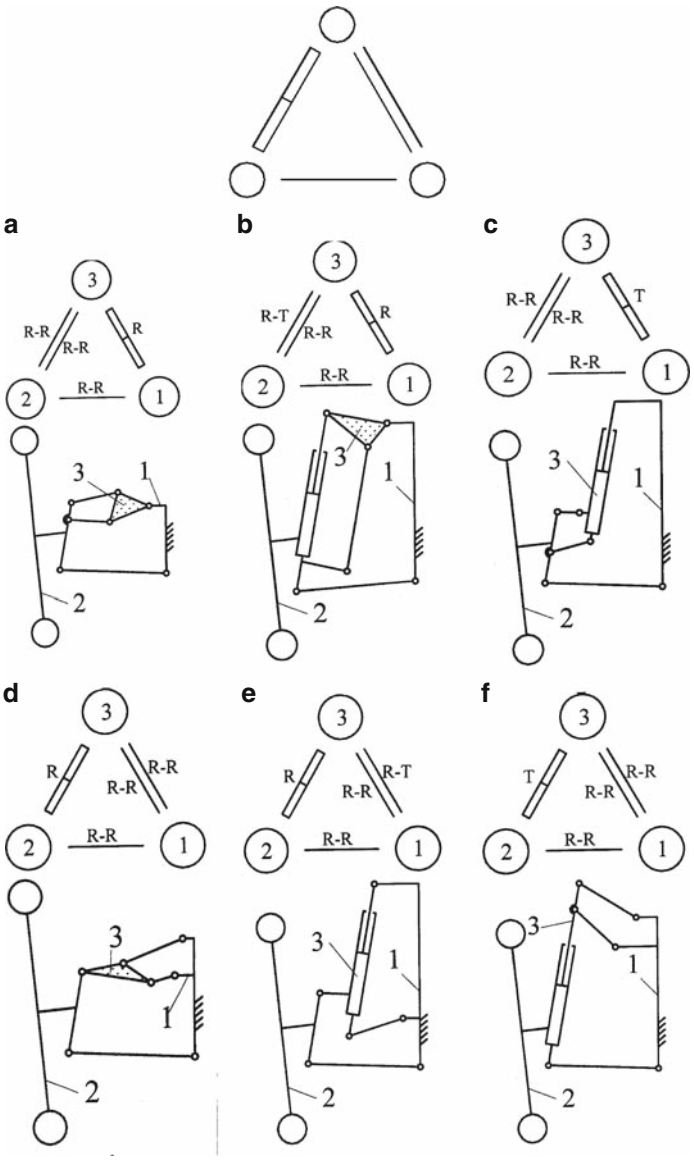

Fig. 14 The mechanisms derived from the graph in Fig. 11m

2. Using the types of geometrical restrictions identified between two bodies in the cam-linkage mechanisms and the associated graphs, there are obtained all the fundamental mechanisms structures with a minimum number of bodies and given mobility.
3. The method can be successfully applied both to planar or spatial mechanism types.

Fig. 14 (continued)

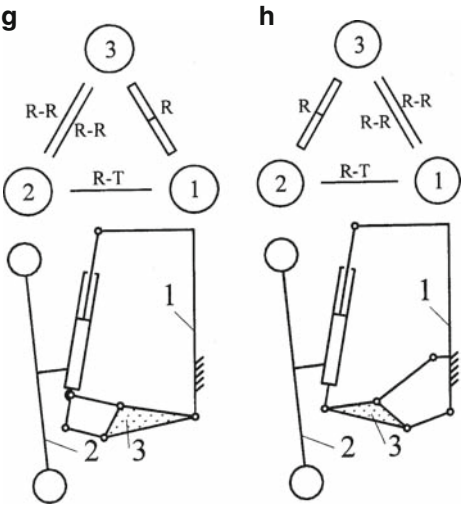

4. The method can be subject of automatization by developing the adequate software for the generation and selection of the graphs/mechanisms variants, fulfilling a given set of conditions.
5. The design of the mechanisms by using the multibody systems method insures obtaining all the possible variants of mechanisms, for a concrete application, from which the designer can chose the optimal ones, from the kinematical and dynamic points of view.
6. The multibody systems method creates an efficient interface between the user and the commercial software.
7. The method described in this paper can successfully replace the traditional analysis and design methods of the linkage and cam mechanisms.

References

1. Alexandru, C., Pozna, C., Comsit, M.: Evaluating the energetic efficiency of a dual-axis tracking system by using virtual prototyping tools. 21st European photovoltaic solar energy conference – EUPVSEC. Milano, Italy (2007), CD based
2. Angels, J., Zakkariev, E.: Computational methods in mechanical systems. NATO ASI Series F 161. Springer-Verlag, Heidelberg (1998)
3. Antonescu, P. (ed.): Mechanisms (in Romanian). Printech, Bucuresti (2003). ISBN 973-652-788-3
4. Antonya, C.S., Vişa, I.: Conceperea mecanismelor plane de suspensie a rotilor automobilelor prin metoda sistemelor multicorp. Proceedings of PRASIC'02, vol. I. Brasov, Romania (2002), CD based
5. Arponen, T., Piipponen, S., Tuomela, J.: Kinematic analysis of Bricard's mechanism. Nonlinear dynam. 56(1–2), 85–99 (2009)
6. Bagepalli, B.S., Haskins, T.L., Imam, I.: Generalized modeling of dynamic cam-follower pairs in mechanisms. J. Mech. Transm-T. ASME. 13(2), 102–109 (1991)

7. Ciobanu, D., Vişa, I.: Modeling and kinematic annalysis of cam mechanics as multibody systems. Proceedings of the ninth IFTOMM international symposium on theory of machines and mechanisms. Bucharest, Romania, 21–26 (2005)
8. Ciobanu, D.: Modeling cam-linkage mechanisms using the multibody system method. Ph.D. thesis, Transilvania University of Brasov (2009)
9. Ciobanu, D.: Strucral synthesis of complex cam-linakage mechanisms as multibody systems, vol. 1. Proceedings of PRASIC'02. Brasov, Romania (2002), CD based
10. Ciobanu, D., Vişa, I., Diaconescu, D.: Optimizing of a new tracking systems for small parabolic trough collectors. International conference EUROSUN (2008), CD based
11. Ciobanu, D., Vişa, I.: Sinteza structurală a mecansimelor complexe de tip came-pârghii considerate sisteme multicorp cu patru corpuri. Proceedings of PRASIC'06, vol. III, pp. 141–146. Brasov, Romania (2006)
12. Comsit, M.: Tracking mechanisms for solar energy conversion systems. Ph.D. thesis, Transilvania University of Brasov (2007)
13. Comsit, M., Vişa, I.: Structural synthesis of mechanisms for solar radiation devices. Proceedings of the Symposium MTM. Cluj Napoca, Romania (2005)
14. Dudita, F.L., Diaconescu, D.V., Gogu, G.R.: Linkagese.Design. Kinematics (Romaian language). Editura Tehnică, Bucureşti (1989). ISBN 973-31-0119-2
15. Erdman, G.A.: Modern kinematics. Developments in the last forty years. Willey, New York (1998). ISBN 0471554596
16. Erdmann, A.G., Sandor, G.N.: Mechanism design. Analysis and synthesis, vol. I. Prentice-Hall, Englewood Cliffs, NJ (1990). ISBN 978-0135698723
17. Galabor, V.B., Nicolov, N.L., Yordanov, A.S.: Systematics and synthesis of various types of co-axial function generator mechanisms of six-bar topological structure. Proceedings of the tenth world congress on the theory of machine and mechanism. Oulu, Finland**,** 358–363 (1999)
18. Garcia de Jalon, J., Bayo, E.: Kinematics and dynamics simulation of multibody systems. The real-time Challenge. Springer-Verlag, New York (1993)
19. Gavrila, C.: Structural analysis of the mechanisms for mobile couplings as multibody systems. Proceedings of PRASIC'02, vol. 1. Brasov, Romania (2002), CD based
20. Gavrila, C.: Design and kinematical – dynamic Study of the transversal mobile coupling using the multibody system method. Ph.D. thesis, Transilvania University of Brasov (2005)
21. Gogu, G.R.: Mobility of mechanisms: A critical review. Mecha. Mach. Theo. 40, 1068–1097 (2005)
22. Gonzales, M., Dpoico, D., Lugris, U., Cuadrado, J.: A benchmarking system for MBS simulation software: Problem standardization and performance measurement. Multibody Syst. Dyn. 16(2), 179–190 (2006)
23. Hain, K.: Beispiele und Ubungen zur Getriebsystematik. Düsseldorf (1967)
24. Haug, J.E.: Computer aided knematics and dynamics of mechanical systems. Allyn and Bacon, Boston, MA (1989). ISBN 0205116698
25. Huston, R.L., Liu, C.Q., Li, F.: Equivalent control of constrained multibody systems. Multibody Syst. Dyn. 10(3), 313–321 (2003)
26. Manolescu, N.: s.a., Mechanisms and machines theory (Romanian language), Editura Didactica si Pedagogica (1972)
27. Nikravesh, E.P.: Computer – aided analysis of mechanical systems. Prentice-Hall, Englewood Clifs, NJ (1988). ISBN 978-0131642201
28. Norton, R.L.: Design of machinery. McGraw Hill, New York (1992). ISBN 9780079097026
29. Roberson, R.E., Schwertassek, R.: Dynamics of multibody systems. Springer-Verlag, Berlin Heidelberg (1988). ISBN 038 717 4478
30. Sancibrian, R., Garcia, P., Viadero, F., Fernandez, A.: A general procedure based on exact gradient determination in dimensional synthesis of planar mechanisms. Mecha. Mach. Theo. 41(2), 212–229 (2006)
31. Schielen, W.: Multibody system handbook. Springer-Verlag, Berlin Heidelberg (1999). ISBN 038 7519467

32. Shabana, A.: Dynamics of multibody systems. Cambridge University Press, Cambridge (1988). ISBN 0521594464
33. Ulrich, K.T., Eppinger, S.D.: Product design and development. McGraw-Hill, New York (1995). ISBN 978-0071137423
34. Vişa, I., Comsit, M.: Tracking systems for solar energy conversion devices, Proceedings of the 14th conference Eurosun'04, vol. 2, pp. 143–148 (2004)
35. Vişa, I., Alexandru, P., Talaba, D., Alexandru, C.: Mechanisms functional design. Modern and traditional methods (in Romanian language), Editura LuxLibris, Brasov (2004). ISBN 973-9240-60-7
36. Vişa, I., Antonya C.S.: Modeling the structure of mechanical multybody systems. Proceedings of the 4th international conference IDMME (Integrated Design and Manufacturing in Mechanical Engineering). Clermond Ferrand, France, 1–10 (2002)
37. Vişa, I., Antonya, C.S.: Structural modeling of planar linkages as multybody systems. Proceedings of the 11th world congress in mechanisms and machine science. Tianjin, China (2003)
38. Vişa, I., Antonya, C.S.: Structural synthesis of planar linkages as multybody systems. Proceedings of the eighth IFToMM international symposium, vol. 1, pp. 329–334. Bucharest, Romania (2001)
39. Vişa, I., Antonya, C.S.: Structural synthesis of planarmultibody systems of linkage type with four bodies. Proceedings of international symposium on theoretical and applied mechanics, pp. 335–343. Iasi, Romania (2001)
40. Vişa, I.: Aspects of multibody used in kinematic-dynamic analysis of linkages by performant software. Proceedings of the mechanisms and mehanical transmissions Romania Symposium, vol. I, pp. 111–118. Resita, Romania (1996)
41. Vişa, I., Ciobanu, D.: Structural synthesis of mechanisms type linkage as multybody systems. Proceedings of PRASIC'02, vol. 1, pp. 228–234. Brasov, Romania (2002)
42. Vişa, I., Gavrila, C.: Structural synthesis method of mobile transversal coupling type linkages as multybody systems. Proceedings of PRASIC, vol. 1, pp. 235–238. Brasov, Romania (2002)
43. Vişa, I.: Mechanical systems modeling as multybody systems in product design. Proceedings of PRASIC'02, vol. 3, pp. 255–264. Brasov, Romania (2002)
44. Vişa, I.: Structural analysis of linkages as multybody systems. Proceedings of the 8th IFToMM international symposium, vol. 1, pp. 323–326. Bucharest, Romania (2001)
45. Wallrapp, O., Wiedemann, S.: Simulation of deployment of a flexible solar array. Multibody Syst. Dyn. 7(1), 101–125 (2002)
46 Yoo, W.-S., Kim, K.N., Kim, H.W., Sohn, J.H.: Developments of multibody system dynamics: Computer simulations and experiments. Multibody Syst. Dyn. 18(1), 35–58 (2007)

Helical Gear Dimensions in the Case of the Minimal Equalized Specific Sliding

A.T. Antal and A. Antal

Abstract The paper gives a new computational method for the determination of the geometrical dimensions of the helical gears with addendum modification based on the sliding equalization at the beginning and at the ending of the meshing. The sliding between the teeth's flanks during the meshing is used to increase the lifetime of the gears by equalization at the points where the differences are the highest. The variations of the addendum modification values, at different axis angles and axis distances, are determined using the MATLAB computing environment, while the equalization condition is maintained. Minimization of the equalized sliding is obtained using a genetic algorithm in order to have the least possible sliding between the teeth flanks at given work conditions.

Keywords Genetic algorithm · Helical gears · Lifetime · Sliding coefficients

1 Introduction

At planar gears several methods and criteria of choosing the addendum modification are known in order to determine the geometrical dimensions of the wheels [1–4]. This paper extends the criterion of the equalized specific sliding used at planar gears, to the spatial gears that is, at helical gears. Based on this criterion the paper gives a methodology of obtaining the geometrical dimensions of the helical gears, with specific addendum modifications. The input data consists of the number of the teeth z_1 and z_2, the normal module mn, the distance between the axes a, and

A.T. Antal (✉)
Department of Mechanics and Programming, Faculty of Machine Building, Technical University of Cluj-Napoca, Cluj-Napoca, Romania

I. Vişa (ed.), *SYROM 2009*,
DOI 10.1007/978-90-481-3522-6_5,

the angle between the axes Σ. Making equal the sliding coefficients at the beginning and the ending of the meshing the specific addendum modifications x_1 and x_2, together with the helix angles on the pitch cylinders β_1 and β_2 are obtained. A MATLAB application was conceived to compute the geometrical dimensions of the gears as the numerical results involve solving a nonlinear system of equations. When equalization is omitted the differences between the sliding coefficients are highest at the points where the meshing ends and begins. One of the wheels will always deteriorate faster then the other. The equalized sliding coefficients will make the wearing the same in these two special points and the lifetime of the gear will increase this way. Further, the equalized sliding in these two points is minimized using a genetic algorithm is order to decrease even more the wearing between the teeth flanks.

2 Sliding Coefficients at Helical Gears

Considering the drawing from Fig. 1, the meshing line is obtained by the intersection of the P_1 and P_2 tangent planes to the base cylinders. On this line, we have the A point, where the meshing begins, and the E point where the meshing ends. During the meshing process between the teeth flanks, on the meshing line, the relative velocity of the 1 tooth is varying in regard to the 2 tooth. Because of this the sliding comes between the teeth flanks. The sliding between the teeth flanks

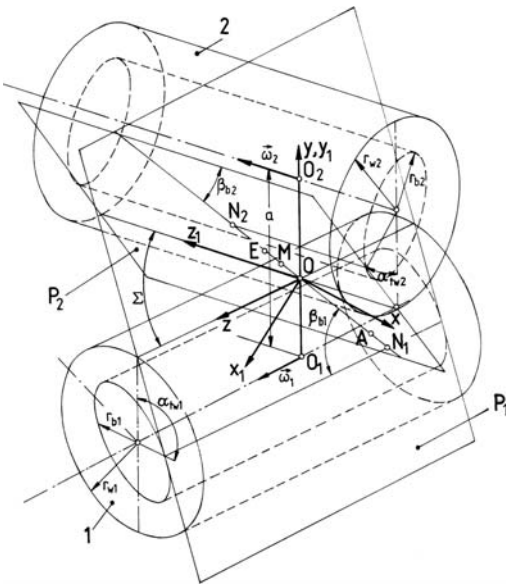

Fig. 1 The helical gear schema

can be evaluated with the help of the ζ_{12} and the ζ_{21} sliding coefficients. ζ_{12} measures the sliding of the 1 flank in regard to the 2 flank, while ζ_{21} measures the sliding of the 2 flank in regard to the 1 flank. The sliding coefficients are determined at A and E points which are the most far meshing points from the C point (pitch point) as here the sliding coefficients have the highest values. The determination of the sliding coefficients for the helical gear from Figure 1 at the point A, where the meshing begins, and at point E, where the meshing ends, was proved in [5].

$$\left.\begin{aligned} A_A &= y_A[1 - u_{21}\cos(\Sigma)] + r_{w1} + r_{w2}u_{21}\cos(\Sigma) \\ B_A &= x_A[1 - u_{21}\cos(\Sigma)] + z_A u_{21}\sin(\Sigma) \\ C_A &= (y_A - r_{w2})u_{21}\sin(\Sigma) \\ A_E &= y_E[1 - u_{21}\cos(\Sigma)] + r_{w1} + r_{w2}\cos(\Sigma) \\ B_E &= x_E[1 - u_{21}\cos(\Sigma)] + z_E u_{21}\sin(\Sigma) \\ C_E &= (y_E - r_{w2})u_{21}\sin(\Sigma) \\ u_{21} &= \frac{\omega_2}{\omega_1} = \frac{z_1}{z_2} \end{aligned}\right\} \quad (1)$$

$$\begin{aligned} x_A &= r_{b2}\cos(\alpha_{tw2})[\tan(\alpha_{ta2}) - \tan(\alpha_{tw2})]\frac{\tan(\alpha_{tw2})}{\tan(\alpha_{tw1})} \\ y_A &= -r_{b2}\sin(\alpha_{tw2})[\tan(\alpha_{ta2}) - \tan(\alpha_{tw2})] \\ z_A &= -r_{b2}\cos(\alpha_{tw2})[\tan(\alpha_{ta2}) - \tan(\alpha_{tw2})]\frac{\tan(\alpha_{tw1}) + \cos(\Sigma)\tan(\alpha_{tw2})}{\sin(\Sigma)\tan(\alpha_{tw1})} \end{aligned} \quad (2)$$

$$\begin{aligned} x_E &= r_{b1}\cos(\alpha_{tw1})[\tan(\alpha_{ta1}) - \tan(\alpha_{tw1})] \\ y_E &= r_{b1}\sin(\alpha_{tw1})[\tan(\alpha_{ta1}) - \tan(\alpha_{tw1})] \\ z_E &= r_{b1}\cos(\alpha_{tw1})[\tan(\alpha_{ta1}) - \tan(\alpha_{tw1})]\ \frac{\tan(\alpha_{tw1}) + \cos(\Sigma)\tan(\alpha_{tw2})}{\sin(\Sigma)\tan(\alpha_{tw2})} \end{aligned} \quad (3)$$

$$\varsigma_{12A} = \frac{A_A^2 + B_A^2 + C_A^2}{(y_A + r_{w1})A_A + x_A B_A} \quad (4)$$

$$\varsigma_{21E} = \frac{A_E^2 + B_E^2 + C_E^2}{C_E^2 - (y_E + r_{w2})\ u_{21}A_E\cos(\Sigma) - u_{21}[x_E\cos(\Sigma) - z_E\sin(\Sigma)]B_E} \quad (5)$$

Considering the expressions from (1–3), the sliding coefficients ζ_{12A} and ζ_{21E} are determined as in [5] with the (4) and the (5) expressions. In the (1–5) expressions:

- x_A, y_A, z_A and the x_E, y_E, z_E are the coordinates of the A and E points from Figure 1.
- r_{b1} and r_{b2} are the base circles radii.
- α_{tw1} and α_{tw2} are the pressure angles in the frontal planes of the gear wheels.
- α_{ta1} and α_{ta2} are the pressure angles in the frontal planes on the addendum circles determined by the expressions α_{ta1}=arcos(rb1/ra1) and αta2=arcos(r_{b2}/r_{a2}).
- r_{a1} and r_{a2} are the radii of the teeth head circles.
- Σ the angle between the helical gears axes.

3 Determination of the Geometrical Dimensions of the Helical Gears

The geometrical relations used to compute the dimensions of the one and the two helical wheels are, [6]:

– The diameters of the pitch circles:

$$\begin{aligned} d_1 &= m_n \frac{z_1}{\cos(\beta_1)} \\ d_2 &= m_n \frac{z_2}{\cos(\beta_2)} \end{aligned} \tag{6}$$

– The teeth declination angles on the base cylinders:

$$\begin{aligned} \sin(\beta_{b1}) &= \sin(\beta_1)\cos(\alpha_n) \\ \sin(\beta_{b2}) &= \sin(\beta_2)\cos(\alpha_n \end{aligned} \tag{7}$$

– The number of the teeth of the equivalent wheels:

$$\begin{aligned} z_{n1} &= \frac{z_1}{\cos^2(\beta_{b1})\cos(\beta_1)} \\ z_{n2} &= \frac{z_2}{\cos^2(\beta_{b2})\cos(\beta_2)} \end{aligned} \tag{8}$$

– The meshing angle at the normal plane:

$$\begin{aligned} inv(\alpha_{nw}) \approx 2\frac{x_1 + x_2}{z_{n1} + z_{n2}} \tan(\alpha_n) + \\ + inv(\alpha_n) \end{aligned} \tag{9}$$

– The teeth declination angles on the rolling cylinders:

$$\begin{aligned} \sin(\beta_{w1}) &= \frac{\sin(\beta_{b1})}{\cos(\alpha_{nw})} \\ \sin(\beta_{w2}) &= \frac{\sin(\beta_{b2})}{\cos(\alpha_{nw})} \end{aligned} \tag{10}$$

– The meshing angles at frontal planes:

$$\begin{aligned} \cos(\alpha_{tw1}) &= \cos(\alpha_{nw})\frac{\cos(\beta_{w1})}{\cos(\beta_{b1})} \\ \cos(\alpha_{tw2}) &= \cos(\alpha_{nw})\frac{\cos(\beta_{w2})}{\cos(\beta_{b2})} \end{aligned} \tag{11}$$

– The specific cutback of the tooth head:

$$k = x_1 + x_2 + \frac{\dfrac{d_1}{\cos^2(\beta_{b1})}\left(1 - \dfrac{\cos(\alpha_n)}{\cos(\alpha_{nw})}\right)}{2m_n} + \frac{\dfrac{d_2}{\cos^2(\beta_{b2})}\left(1 - \dfrac{\cos(\alpha_n)}{\cos(\alpha_{nw})}\right)}{2m_n} \tag{12}$$

– The profile angles of the basic rack at frontal planes of the 1 and 2 helical wheels:

$$\begin{aligned} \cos(\alpha_{t1}) &= \cos(\alpha_n)\frac{\cos(\beta_1)}{\cos(\beta_{b1})} \\ \cos(\alpha_{t2}) &= \cos(\alpha_n)\frac{\cos(\beta_2)}{\cos(\beta_{b2})} \end{aligned} \tag{13}$$

– The diameters of the base circles for the 1 and the 2 wheel:

$$\begin{aligned} d_{b1} &= d_1\cos(\alpha_{t1}) \\ d_{b2} &= d_2\cos(\alpha_{t2}) \end{aligned} \tag{14}$$

– The diameters of the rolling circles for the 1 and the 2 wheel:

$$\begin{aligned} d_{w1} &= d_1\frac{\cos(\alpha_{t1})}{\cos(\alpha_{tw1})} \\ d_{w2} &= d_2\frac{\cos(\alpha_{t2})}{\cos(\alpha_{tw2})} \end{aligned} \tag{15}$$

– The diameters of the head circles for the 1 and the 2 wheel:

$$\begin{aligned} d_{a1} &= m_n\left(\frac{z_1}{\cos(\beta_1)} + 2h_a^* + 2x_1 - 2k\right) \\ d_{a2} &= m_n\left(\frac{z_2}{\cos(\beta_2)} + 2h_a^* + 2x_2 - 2k\right) \end{aligned} \tag{16}$$

4 Equalization of the Specific Sliding

In order to equalize the specific sliding at the A and the E meshing points of the helical gear the (4) and (5) expressions will be used. As the equalization criterion must be obtained for different Σ angles and different a distances between the wheels, we obtain the following system of nonlinear equations:

$$\left.\begin{aligned} \varsigma_{12A}(x_1, x_2, \beta_1, \beta_2) &= \varsigma_{21E}(x_1, x_2, \beta_1, \beta_2) \\ \beta_{w1}(x_1, x_2, \beta_1, \beta_2) + \beta_{w2}(x_1, x_2, \beta_1, \beta_2) &= \Sigma \\ r_{w1}(x_1, x_2, \beta_1, \beta_2) + r_{w2}(x_1, x_2, \beta_1, \beta_2) &= a \end{aligned}\right\} \tag{17}$$

The second equation from the system is based on the (10) expressions, while the third is based on the (15) expressions. In order to solve the (17) nonlinear system the formulas from (1) to (16) must be computed. (17) allows computing the variations of the helix angles on the pitch cylinders β_1 and β_2 with respect of the specific addendum modifications x_1 and x_2 at given values of the Σ and a. If the x_1, z_1, z_2, α_n, h_a^*, c^*, m^n, Σ and a values are given, a set of the x_2, β_1 and β_2 values are obtained while the ζ_{12A} and ζ_{21E} specific sliding are the equal, the sum of β_{w1} and β_{w2} is equal to Σ, and the distance between the axis is a. (see the columns 5–10 from Tables 1–4). (17) is solved using MATLAB's *fsolve()* function from MATLAB's Optimization Toolbox. *fsolve()* implements an iterative method that needs staring values for the computations. If the equalization criterion is left out only the last two equations are forming the system. The data from Table 1 are obtained in this case for: $z_1 = 20$, $z_2 = 30$, $\Sigma = 900$, $a = 89$mm (distance between the helical gears axis), $\alpha_n = 200$ (the profile angle of the basic rack), $h_a^* = 1$ (the height coefficient from head of the tooth), $c^* = 0.25$ (the clearance coefficient from the head of the tooth), $m_n = 2.5$mm. The initial conditions for the *fsolve()* are: $\beta_1 = 450$, $\beta_2 = 450$. When the x_1 and x_2 values are given (the values for the specific addendum modifications were chosen so that no interferences would appear at the head and at the based of the teeth), as shown in Table 1, the sliding coefficients are different (columns 5 and 6), so the wearing of the two wheels in the two points is not the same, and one wheel will deteriorate faster. Also, there are cases when the solutions the system, the β1 and β2 angles, are found with a great loss of the precisions (see the shaded lines from Table 1).

When solving (17) the domain for the Σ value is varying between 0° and 900. The domain variation for the a values are restricted by standards. As the integer values of a are easier to manufacture, one way of determining the domain would be the condition of obtaining integer values. This domain is important because choosing a value outside it will lead to a (17) system that has no solutions. The domain values for the specific x_1 and x_2 addendum modifications are $[-0.2, 0.8]$ in order to avoid interferences. The x_1 value is given and the domain is walked through a 0.1 step, while x_2, β_1 and β_2 are obtained as solutions of (17). The x_2

Table 1 Variation of the specific sliding when no equalization is made

x_1	x_2	β_1 [°]	β_2 [°]	ζ_{12A}	ζ_{21E}	β_{w1} [°]	β_{w2} [°]	Σ [°]	a [mm]
−0.2	−0.4	42.232	48.837	2.5627	1.9913	41.759	48.241	90	89
−0.1	−0.2	42.75	47.784	2.4770	2.0471	42.507	47.493	90	89
0	0	43.369	46.631	2.3862	2.1100	43.369	46.631	90	89
0.1	0.2	44.148	45.319	2.2872	2.1855	44.409	45.591	90	89
0.2	0.4	45.25	43.683	2.1699	2.2889	45.798	44.202	90	89
0.3	0.6	47.978	40.369	1.9505	2.5555	48.887	41.064	89.951	89
0.4	0.8	47.431	39.844	1.9554	2.5208	48.633	40.760	89.393	89
0.5	0.25	46.112	42.554	2.0394	2.4425	46.821	43.179	90	89
0.6	0.3	47.978	40.369	1.8962	2.6553	48.887	41.064	89.951	89
0.7	0.35	47.705	40.106	1.8897	2.6536	48.761	40.912	89.673	89
0.8	0.4	47.431	39.844	1.8829	2.6516	48.633	40.760	89.393	89

solutions outside the accepted domain will not be considered technically as correct results.

As shown in Table 2 solutions of the (17) system can be found, and a domain can be established for the a values between 88 and 91 mm. Here the equalization is made with success (columns 5 and 6 are equal), while the angle between the axes is 90° (the sum of columns 7 and 8 is equal to column 9) and the distance between the axis is an integer value. The shaded values are outside the accepted domain for x_2. We will now pick $a = 90$ mm from this domain and solve again the (17) system. The obtained results are shown in Table 3. Again, the shaded results are not considered as x_2 is outside the accepted domain. For $a = 90$ mm and $\Sigma = 90°$ more technical solutions can be obtained however, the equalized sliding are not the same. From the acceptable solutions the one with the minimum values of the equalized sliding coefficients will be the best, as in this case the wearing will be uniform at the A and the E points and minimized. When the equalization is made, the equalized values of the sliding coefficients are lower then the maximum values of the sliding coefficients when no equalization is made (compare ζ_{12A} and ζ_{21E} values for $a = 89$ mm from Table 1 with those from Table 2).

Table 2 Variation of the specific sliding when the equalization is made

x_1	x_2	β_1 [°]	β_2 [°]	ζ_{12A}	ζ_{21E}	β_{w1} [°]	β_{w2} [°]	Σ [°]	a [mm]
−0.2	−0.021	45.47	44.94	2.24035	2.24035	45.263	44.737	90	88
−0.1	0.738	45.44	43.43	2.22288	2.22288	46.024	43.976	90	89
0	0.571	45.12	43.87	2.22675	2.22675	45.637	44.363	90	89
0.1	0.393	44.80	44.32	2.23028	2.23028	45.242	44.758	90	89
0.2	0.205	44.48	44.80	2.23339	2.23339	44.839	45.161	90	89
0.3	1.014	44.52	43.20	2.20588	2.20588	45.686	44.314	90	90
0.4	0.828	44.18	43.70	2.21028	2.21028	45.247	44.753	90	90
0.5	0.628	43.83	44.22	2.21440	2.21440	44.796	45.204	90	90
0.6	0.414	43.48	44.77	2.21815	2.21815	44.334	45.666	90	90
0.7	1.278	43.59	43.06	2.18240	2.18240	45.278	44.722	90	91
0.8	1.067	43.21	43.64	2.18756	2.18756	44.775	45.225	90	91

Table 3 Variation of the specific sliding when the equalization is made and $a = 90$mm

x_1	x_2	β_1 [°]	β_2 [°]	ζ_{12A}	ζ_{21E}	β_{w1} [°]	β_{w2} [°]	Σ [°]	a [mm]
−0.2	−0.021	45.47	44.94	2.24035	2.24035	45.263	44.737	90	88
−0.1	0.738	45.44	43.43	2.22288	2.22288	46.024	43.976	90	89
0	0.571	45.12	43.87	2.22675	2.22675	45.637	44.363	90	89
0.1	0.393	44.80	44.32	2.23028	2.23028	45.242	44.758	90	89
0.2	0.205	44.48	44.80	2.23339	2.23339	44.839	45.161	90	89
0.3	1.014	44.52	43.20	2.20588	2.20588	45.686	44.314	90	90
0.4	0.828	44.18	43.70	2.21028	2.21028	45.247	44.753	90	90
0.5	0.628	43.83	44.22	2.21440	2.21440	44.796	45.204	90	90
0.6	0.414	43.48	44.77	2.21815	2.21815	44.334	45.666	90	90
0.7	1.278	43.59	43.06	2.18240	2.18240	45.278	44.722	90	91
0.8	1.067	43.21	43.64	2.18756	2.18756	44.775	45.225	90	91

5 Minimization of the Equalized Sliding Coefficients

While solving the (17) nonlinear system several problems might appear. The transcendent equation at (9) solved with the *fzero()* MATLAB function might not have solutions: there are no solutions; the numerical method won't converge to the solution; the solution is a complex value, instead of real one. When solving (17) using *fsolve()*: the system might not have solutions; depending on the start points, the numerical method may converge to a nonzero point; the obtained values are correct however, from a technical point of view are not acceptable. Genetic Algorithms (GAs) are a category of evolutionary algorithms well known to find approximate solutions to the optimization problems of difficult functions. A penalty function is used to convert the constrained optimization problem into an unconstrained problem for the GA-based optimization. The *gatool* function from MATLAB's Genetic Algorithm and Direct Search Toolbox is used to find the minimum of the equalized specific sliding. The objective function is the unpenalized function to which is added a constant penalty for the solutions that violate in some way the feasibility.

$$\varsigma_{12A\,\min} = \varsigma_{12A} + \sum_{i=1}^{k} C_i \delta_i \tag{18}$$

In (18) δ_i is 0 if constraint i is 0, otherwise is 1 and Ci is a constant imposed for the violation. For a set of x_1, x_2, β_1, β_2 violations are considered if any of the three equations from (17) are not zero (no convergence to the solution) or if x_1 or x_2 are outside the allowed domains (a solution is found but it's not acceptable from a technical point of view) or the computations are not possible (no convergence or complex values are obtained). The x_1, x_2, β_1, β_2 are the parameters used in the *gatool* and the codification of the parameters is of real type. The numerical results are given in Table 4 with higher decimal precision. The GA obtains with success equalized values for the specific sliding with values that are lower that those obtained in Tables 2–3. For example in Table 2, if a = 89 mm, then the minimum value for ζ_{12A} is 2.22288, while in Table 4 is 2.221345.

6 Conclusions

The results from Tables 2–4 are showing the equalization of the specific sliding succeeds. Assessing the equalization of the specific sliding criterion at the points where the meshing stars and ends causes the limitation of the values given for a and Σ.

Table 4 Variation of the minimized equalized specific sliding for Σ = 900

x_1	x_2	β_1 [°]	β_2 [°]	ζ_{12A}	ζ_{21E}	β_{w1} [°]	β_{w2} [°]	a [mm]
−0.2000	−0.02068	45.4673	44.9369	2.240345	2.240345	45.26331	44.73669	88
−0.1375	0.79842	45.5552	43.2693	2.221345	2.221345	46.16664	43.83336	89
0.4250	0.77954	44.0880	43.8263	2.211341	2.211341	45.13568	44.86432	90

Based on the given x_1 and the x_2, β_1, β_2 values obtained by solving (17) system the geometrical dimensions of the increased lifetime helical wheels can be obtained. The minimal equalized specific sliding are found using a GA, as the function to be minimized is nonlinear and with problems during the computations. This minimization succeeds and the obtained values, as shown in Table 4, are better then those obtained by a systematic search of the solutions domain. Lower equalized values of the sliding coefficients could be obtained by the GA if the values of the x_1 and x_2 addendum modifications obtained from the equalization criterion would have a wider domain, however in this case the values must be tested against interference conditions, which are the conditions concerning the cut and the undercut of the teeth.

References

1. Bolotovskii, I.A.: Spravocinik po gheometriceskomu rasciotu evolvent-nih zubciatih i cerviacinih peredaci. Moskva, Masinostroenie (1986)
2. Maros, D.: Cinematica roţilor dinţate. Editura Tehnică, Bucureşti (1958)
3. Niemann, G., Winter, H.: Maschinenelemente. Band III. Springer-Verlag, Berlin (1983)
4. MAAG – Taschenbuch. MAAG – Zahnräder. Aktiengesellschaft CH – 8023, Zürich, Schweiz (1985)
5. Antal, A., Antal, T.A.: A computer program for the calculus of the sliding at the helical gears. Prasic '98 – national symposium with international participation, vol. II – Machine elements. Braşov, Romania. Mechanical Transmissions, 5–7 November 1998, pp. 235–238
6. Antal, T.A., Antal, A., Arghir, M.: Determination of the addendum modification at helical gears, at the points where the meshing starts and ends, based on the relative velocity equalization criterion. Proceedings in applied mathematics and mechanics – PAMM J. 8(1), 10965-10966 (Dec. 2008) (10003-10988). Published Online: Feb 26 2009 1:06AM, DOI: 10.1002/pamm.200810965, ISSN: 1617-7061. Copyright © 2008 WILEY-VCH Verlag GmbH & Co. KGaA, Weinheim (2009)

Mathematical Model for Two Degree of Freedom Motion

I. Ardelean

Abstract The paper presents the conceive of control function for mechanisms following a planar contour of an object. The manipulator moves along the contour of the object is considered a problem of keeping a manipulator in contact with an object. Such motion allows one to determine an object contour that is a priori unknown. The design control is useful for tracking part joist in welding, grinding or polishing. By following an object contour, it is possible to avoid obstacles. Such motion may be considered as a motion along a mechanical constraint.

Keywords Degree · Freedom · Mechanism · Motion

1 Introduction

The contour following motion of a mechanism is studied in papers [1, 2, 3, 5, 7], among many others. In this paper, a control for such motion is built on the basis of a systematic approach to the problem control synthesis for robotic systems with force sensing. This approach designs robotic systems motions along constraints by representing complex motions as a superposition of primitive (basic) ones. The control – keeping motion is a basic motion and it can be controlled as described is the preceding paper.

2 Mathematical Model

We shall study a two-degree-of-freedom translational motion in the horizontal plane of the spatial mechanism arm. A force sensor measuring two horizontal components of the force vector is attached to the lower end of the mechanism

I. Ardelean
Technical University of Cluj-Napoca, Cluj-Napoca, Romania

I. Vişa (ed.), *SYROM 2009*,
DOI 10.1007/978-90-481-3522-6_6,

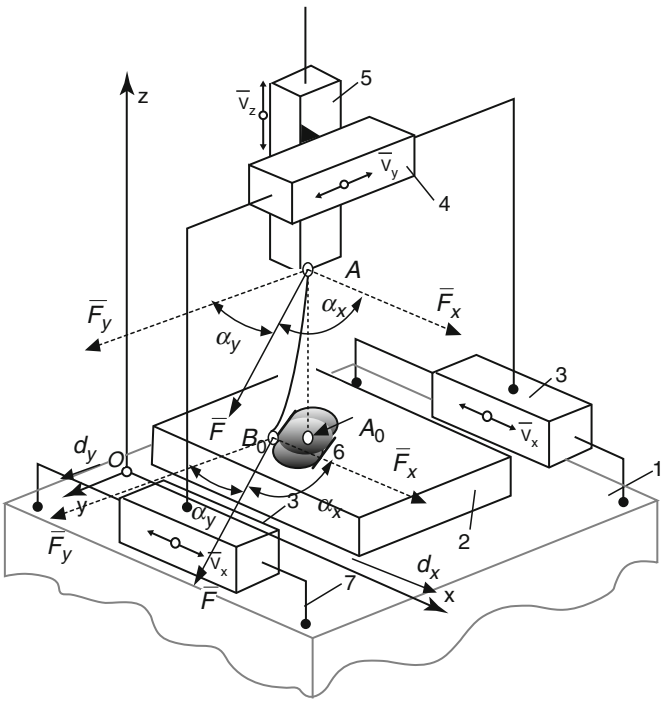

Fig. 1 Schematics of mechanism with two degree of freedom and two columns

arm. Let us introduce a stationary orthogonal coordinate system OXY in the horizontal plane (mechanism base plane). The translational motion of the mechanism arm along the axes OX and OY involves two respective degrees of freedom.

The motion along each axis is actuated by a separated electric motor. Figure 1 illustrates the schematics of the spatial mechanism with two degree of freedom and two columns. Figure 2 illustrates the schematics spatial mechanism with two degree of freedom and four columns, [4].

In the two figures significances note de are: 1 – table set, 2 – table for positioning the source of information to measure, 3, 4, 5 – the translation module on the axis Ox, Oy, Oz, 6 – source of information to measure.

Denote by A the point where the palpable is attached to the mast, by A_0, the projection of the point A onto the plane xOy, Fig. 1. Let x, y be the coordinates of the point A_0. By neglecting the inductance of the motor armature, can write the equations of motions for the two – degree – of –freedom system in hand in the form:

$$\begin{aligned} m_x \cdot \ddot{x} + d_x \cdot \dot{x} &= \alpha_x \cdot u_x + F_x, \\ m_y \cdot \ddot{y} + d_y \cdot \dot{y} &= \alpha_y \cdot u_y + F_y. \end{aligned} \tag{1}$$

In the above equations, $m_x$and m_y are equivalent masses of the moving parts (the mechanism arm, motor rotor, couple de translation) for the respective degree of

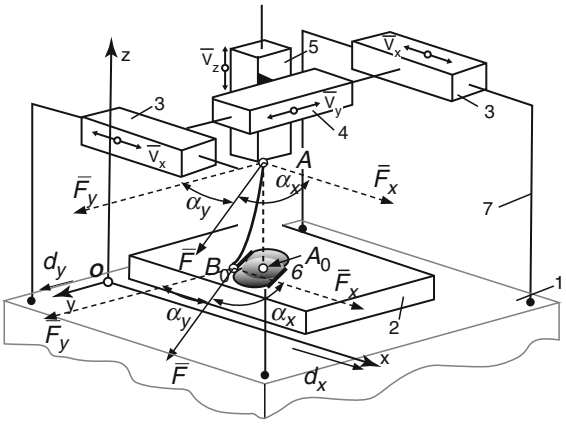

Fig. 2 Schematics of mechanism with two degree of freedom and four columns

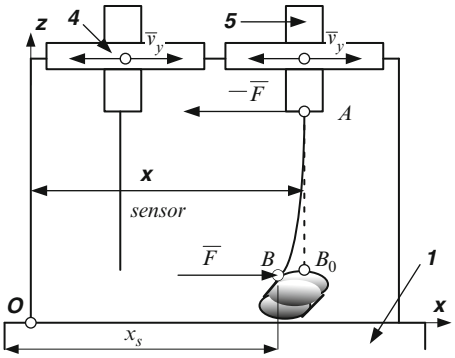

Fig. 3 Schematics for one – dimensional motion of the mechanism

freedom $d_x \cdot \dot{x}$ and $d_y \cdot \dot{y}$ are combined forces of viscous friction and back e.m.f. in the drives; u_x and u_y are voltages supplied to the motors; d_x, d_y, α_x, α_y are positive constants dependent on the drive characteristics; $\bar{F}_x$ and $\bar{F}_y$ are components of the horizontal force $\bar{F}$ exerted by the force sensor/palpable on the mechanism mast.

Each equation in (1) is analogous to:

$$m \cdot \ddot{x} + d_2 \cdot \dot{x} = d_1 \cdot u + F_a, \tag{2}$$

and can be derived in the similar way, Fig. 3, with same notates that Figs. 1 and 2.

A sensor/palpable probe, a finger sensor, or a wrist sensor may be used for the force measurement, [6, 8]. We used sensor of each type in different experiments. Each of the used sensors had two channels with orthogonal sensitivity axes in the horizontal plane. Through we refer to a probe – type force sensor below, the derived equations may also be used for other sensor types. In this paper, shall model the force sensor as an infinitely thin elastic mass less rod, Fig. 1, with a uniform bending stiffness in

all directions. The rod is vertical when under formed. As noted above, it is attached to the mechanism arm at the point A.

In the absence of contact between the force sensor and the object, the force acting on the arm is $F = 0$, as the sensor is assumed to be mass less. When the contact is established at the point B, the sensor bends, Fig. 1. Denote the projection of the point B overlaid with A, onto the plane xOy by B_0. The force exerted by the object on the sensor is applied at the point B. The horizontal component of this force is collinear to the vector A_0B_0. Since the rod is assumed to be mass less, this component is equal to the horizontal force $\bar{F}$ applied from the sensor to the mechanism at the point A. If the sensor stiffness is high and its deformations are small, then, in accordance with, [9, 10] the model adopted in for displacement sensors, consider the force $\bar{F}$ to be proportional to the length of the segment A_0B_0:

$$F = k \cdot A_0B_0. \tag{3}$$

The coefficient k = *constant* > *0* defines the sensor stiffness. Herein ignore energy dissipation in the sensor. For simplicity sake, assume that the object is a right cylinder. The object lateral surface is orthogonal to the plane xOy, and the top and bottom flanges are parallel to this plane. The sensor contact the object at the point B overlaid with A of the flange. Let us write an equation for the flange, Fig. 1 contour projection onto the plane xOy in the parametric form, [11]:

$$x = x(s); \quad y = y(s), \tag{4}$$

Where s the length of the contour is are measured from a certain point on it, Figs. 3 and 4.

Let s_B be a parameter (arc length) corresponding to the point B_0. The vector equality may be rewritten as two scalar ones:

$$\begin{aligned} F_x &= k \cdot [x(s_B) - x], \\ F_y &= k \cdot [y(s_B) - y]. \end{aligned} \tag{5}$$

The expressions for the tangent τ and the normal n to the contour (4) at the point B_0 have the form:

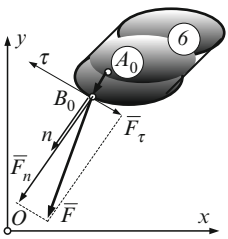

Fig. 4 Object 6 contour projections onto the plane xOy

$$\tau = \begin{bmatrix} x'(s_B) \\ y'(s_B) \end{bmatrix} = \begin{bmatrix} \cos\varphi \\ \sin\varphi \end{bmatrix},$$
$$n = \begin{bmatrix} -y'(s_B) \\ x'(s_B) \end{bmatrix} = \begin{bmatrix} -\sin\varphi \\ \cos\varphi \end{bmatrix}, \tag{6}$$

Where $\varphi = \varphi(s_B)$ is an angle measured in the positive between the axis Ox and the vector $\bar{\tau}$ at the point B_0.

The prime denotes differentiation with respect to$s$. It is assumed that the respective derivates exist. We consider $\bar{n}$ in (6) to be the vector of the normal that is external with respect to the object. Clearly, along with the vector $\bar{\tau}$ in (6), the vector $-\bar{\tau}$ is also a unit tangent vector.

The projections F_τ and F_n of the force (. . .0 onto the tangent and normal to the top contour at the point B0 (3) are given by:

$$F_\tau = F \cdot \tau = k \cdot \left\{ x'(s_B) \cdot [x(s_B) - x] \right\} + k \cdot \left\{ y'(s_B) \cdot [y(s_B) - y] \right\},$$
$$F_n = F \cdot n = k \cdot \left\{ -y'(s_B) \cdot [x(s_B) - x] \right\} + k \cdot \left\{ x'(s_B) \cdot [y(s_B) - y] \right\}, \tag{7}$$

Where F_τ is fractional force between the sensor and the object, and F_n is a force of normal pressure.

If the contact point B_0 moves along the contour, i.e. $s_B \neq 0$, then the force F_τ is directed against the contouring velocity vector, and the force vector F is on the boundary of the cone of friction:

$$F_\tau = -f \cdot F_n \cdot \operatorname{sgn} \dot{s}_B \quad if \quad F \rangle 0. \tag{8}$$

In the above equation, $f = const. \rangle 0$ is a Coulomb friction coefficient? Denote a friction angle by $\beta :\ \tan\beta = f$. From (7) and (8) for $\dot{s}_B \neq 0$, we obtain:

$$\{x'(s_B) \cdot [x(s_B) - x] + y'(s_B) \cdot \cdot [y(s_B) - y]\} = f\left\{ y'(s_B) \cdot [x(s_B) - x] - \right.$$
$$\left. -x'(s_B) \cdot [y(s_B) - y] \right\} \cdot \operatorname{sgn} \dot{s}_B. \tag{9}$$

If $\dot{s}_B = 0$ then the force vector F lies in the cone of friction:

$$|F_\tau| \ \leq f \cdot F_n. \tag{10}$$

If the equation for the contour (4) are given, then, provided the arm coordinates x, y are known, one can find the coordinate s_B of the contact point B from (9) or (10). Once s_B is known, one can find the coordinates $x(s_B),\ y(s_B)$ of the point B from (4).

Then we find the components (5) of the force F, so as to close the system of equations of motion (1). If the friction coefficient $f = 0$, then the relationships (9), (10) are replaced by only one equation:

$$x^{'}(s_B) \cdot [x(s_B) - x] + y^{'}(s_B) \cdot [y(s_B) - y] = 0 \tag{11}$$

The equation (11) is an orthogonally condition for the vectors of contact force F and contour tangent τ.

The relationships (1), (4), (5), (9), (10) present a closed form description for a two degree of freedom mechanism in contact whit on object 6.

In the absence of contact, one should only use the equations (1), assuming $F_x = F_y = 0$.

These relationships also define moments of establishing and losing contact.

3 Control Problem Statement

Let us assume that a force sensor is in contact with an object at the initial time, see Figs. 1 and 2.

The object contour is unknown a priori, i.e., the equations (4) are not given.

It is desired to design control of the drive, such that the force sensor keeps contact with an object and moves along its contour, i.e., along a unilateral constraint, [12, 13].

We shall consider a mechanisms motion along an object contour as a superposition of two motions – at a normal and at a tangent to the contour.

Accordingly, we define the "desired"

Velocity vector $\bar{V}_d$ as a sum of two terms:

$$\bar{V}_d = \bar{V}_n + \bar{V}_\tau = g \cdot (F_n - F_d) \cdot \bar{n} + v \cdot \bar{n}. \tag{12}$$

In the above equation, $F_d = const. \rangle 0$ is desired value of the normal force component exerted on the force sensor by the object, $g \rangle 0$ is a constant feedback gain, $v = const. \rangle 0$ and is a desired value of the mechanism velocity along a tangent to the object contour, the desired contour velocity.

The first term V_n in (1) is a vector directed towards the object if $F_n \langle F_d$ and form the object if $F_n \rangle F_d$.

One can consider the expression (1) for the commanded velocity as an extension of

$$V_d = g \cdot (F_d - F). \tag{13}$$

For $v = 0$, (12) is an extension of (13) for the case of a two degree of freedom mechanism keeping contact with an object.

Using this method the computer receives a measurement F from the force sensor and calculates V_d by formula (13).

In the case of $v \neq 0$, (1) extends (13) for a mechanism keeping contact with an object and simultaneously moving along its contour.

If the mechanism is required to move in the opposite direction along the contour, one should substitute $-\tau$ for τ in (12), [12, 13].

We design the mechanism control as a linear feedback of the velocity

$$K = Q \cdot (V_d - V), \tag{14}$$

Where:

$$K = \begin{bmatrix} K_x \\ K_y \end{bmatrix}, Q = \begin{bmatrix} q_x & 0 \\ 0 & q_y \end{bmatrix} \tag{15}$$

$$V = \begin{bmatrix} \dot{x} \\ \dot{y} \end{bmatrix} = \begin{bmatrix} V_x \\ V_y \end{bmatrix}, V_d = \begin{bmatrix} V_{xd} \\ V_{yd} \end{bmatrix}, \tag{16}$$

and q_x, q_y are positive constants.

In the absence of friction, i.e., for $f = \beta = 0$,

$$F = F_n = \sqrt{F_x^2 + F_y^2}. \tag{17}$$

For $f = 0$, F_n can be found and the vector of normal $\bar{n}$ from (17) by using a force sensor to measure the force vector $\bar{F}$.

By setting the desired direction of the mechanism motion, we can uniquely define the vector $\bar{\tau}$, for example, by rotating the vector $\bar{n}$ clockwise through an angle $\pi/2$.

Thus, we can compute all terms in (12). Therefore, in the absence of friction, the control laws (14), (15) can be implemented by using the information from force sensors and velocity sensors measuring the components $\dot{x}$ and $\dot{y}$ of the vector V.

In reality, friction is always present and $\beta \neq 0$. Let a force sensor move in contact with an object. Then force vector $\bar{F}$ is on the boundary of the friction cone, Fig. 4, [15].

4 Conclusions

Suppose that control voltages u_x, u_y are given as functions of time and/or phase coordinates. Also, let the initial conditions $x(0)$, $y(0)$, $\dot{x}(0)$ *and* $\dot{y}(0)$ be given.

If for $t = 0$ the sensor contacts the object, then we assume that the coordinates $x(s_B)$, $y(s_B)$ of the contact point B, which satisfy the relationships (9), (10), are known as well.

Under these conditions, the solutions to the equations (1), (4), (5), (9), (10) Describe the manipulator motion for $t \rangle 0$. When solving the equations, in principle, one may obtain several solutions for s_B from (9), (10).

In this case, to find a unique solution, it is necessary to introduce additional conditions such as the requirement that the function $s_B(t)$ is continuous.

References

1. Abele, E., Boley, D., Sturz, W.: Interactive programming of industrial robots for debarring. In: 14th International Symposium on Industrial Robots, pp. 505–516 (1984)
2. Aner, M.: Fügemechanismen mit Sensorik in der automatischen Montage. Robotersysteme 8, 101–106 (1992)
3. Arai, H., Tachi, S.: Position control system of a two degree of freedom manipulator with a passion joint. IEEE Trans. Ind. Electron. IE 38–1, 15–20 (1991)
4. Asada, H., Slotin, J.J.: Robot Analysis and Control. Wiley, New York (1986)
5. Asada, H., Yang, B.-H.: Skill acquisition from human experts through pattern processing of teaching data. In: Proceedings of the 1989 IEEE International Conference on Robotics and Automation, pp. 1302–1307 (1989)
6. Ashhab, M., Stefanopoulu, A.G., Cook, J.A., Levin, M.B.: Control of camels intake process (Part II). Proceedings of the Dynamic Systems and Control Division, DSC 67, Nashville, TN, pp. 187–194 (1999)
7. Barbashin, E.A.: Introduction to the Theory of Stability. Wolters-Noordhoff, Groningen (1970)
8. Berkof, R.S., Lowen, G.G.: A new method for completely force balancing simple linkages. Trans. ASME J. Eng. Ind. 91(B), 21–26 (1969)
9. Chetaev, N.G.: The Stability of Motion. Pergamon Press, New York (1961). Translation from the Russian
10. Chong, N.Y., Kotoku, T., Ohba, K., Tanie, K.: Virtual repulsive force field guided coordination for multitelerobot collaboration. In: Conference Proceeding IEEE International, Conference on Robotics and Automation, Seoul, Korea, 21–26 May 2001, pp. 1013–1018
11. Gorinevsky, D.M., Formalsky, A.M., Schneider, A.Y.U.: Force Control of Robotics Systems. CRC Press LLC, Boca Raton (1997)
12. Mills, J.K., Goldenberg, A.A.: Force and position control of manipulators during with the aid of industrial robots. Ann CIRP 34(1), 49–52 (1985)
13. Tarn, T.J., Wu, Y., Isidori, A.: Force regulation and contact transition control. IEEE Control Syst. 16(1), 32–40 (1996)
14. Van Brussel, H., Belien, H., Thielemans, H.: Force sensing for advanced robotic control. Robotics 2(2), 139–148 (1986)
15. West, H., Asada, H.: A method for the design of hybrid position/force control for manipulators constrained by contact with the environment. In: IEEE International Conference on Robotics and Automation, pp. 251–259 (1985)

Design and Simulation of Kursk Robot for In-Pipe Inspection

G. Carbone, A. Malchikov, M. Ceccarelli, and S. Jatsun

Abstract In this paper a design of robot for in-pipe inspection is discussed as based on the principle of using vibration for locomotion action. The original design of asymmetrical dry friction mechanisms is proposed through a mathematical model of robot that has been developed also for the equations of motions. In addition, an analysis of robot movement has been investigated with different parameters also with the aim to present design improvements.

Keywords Design · In-pipe robots · Modelling · Robotics · Simulation

1 Introduction

Different types of robots for in pipe inspection have been widely investigated in the literature has reported, for example in [1–19].

Vibration driven robots have simple design and they don't need any special actuators such as wheels, caterpillars or legs as discussed for example in [20–23]. Therefore, mobile vibration robots can move not only on space, and also in environments with dense materials, which are not available for wheeled or legged robots. Vibrating motion allows moving on rough surfaces and in liquid environments.

G. Carbone (✉), M. Ceccarelli and S. Jatsun
Department of Theoretical Mechanics and Mechatronics, University of Cassino, Cassino, Italy
A. Malchikov
Kursk State Technical University, Kursk, Russia

I. Vişa (ed.), *SYROM 2009*,
DOI 10.1007/978-90-481-3522-6_7,

In the simplest case robot's body moves in one dimension, on a line or in a pipe. The motion is achieved by use of changing a shape of the robot by using the concept of worm-like motion. The typical biologic examples can be recognized in insects as caterpillars and flatworms.

However, a robot design is complicated as a mechatronic system, which consists of mechanic, electronic, and control sub-systems. Mechanical vibration can influence on the internal masses of the robot, and the robot body interacts with an environment with some force. Robot can be equipped of electronic control system with feedback module, which allows to run an optimal motion and to keep given parameters of working element even when different external forces will act on the system.

The parameters of the working element and of motion depend on robot task and environment conditions. In order to perform a one-direction motion an asymmetrical dry friction force is needed among robot bodies and surface. This nonlinear friction force can be obtained by special form of needles or guidelines on the contact place or by special one-way clutch mechanisms.

2 Kursk Robot for In-Pipe Inspection

In Kursk State Technical University a prototype of Robot for In-Pipe Inspection has been designed and built [17, 18]. This robot moves by using vibrations of the robot body. The robot can be a general platform for traveling along pipes and returning along the same route. It has the possibility to drive in horizontal and inclined directions of straight pipes in addition; it can be stably positioned in each position without power supply. A user can be able to remotely control the robot by using wires or wireless communication.

In this paper the pipe structure is considered as rigid body. Robot consists of two solid bodies that are connected between each other by visco-elastic element and an electro actuator. The actuator is composed of a DC-motor with rack and pinion; it provides a linear motion of the working element. The actuator provides a double-direction linear motion and acts as external force to each robot body. The robot includes a special asymmetric friction mechanism in order to provide different friction forces between robot's body and the internal pipe wall.

A general scheme of the robot is presented on Fig. 1. The robot body consists of two main masses 1 and 2 (see Fig. 1), which are connected by spring 5 and electro-actuator 3. Each body has one-direction motion mechanism 4, which gives asymmetrical friction force between robot and supporting pipe surface.

The 1-D motion of the robot can be obtained by periodical relative vibration motion of two parts of robot body along the line. In this case, it is necessary that the characteristic of friction force between robot body and the supporting surface is asymmetric as pointed out in [8, 11]. In this paper we propose an original design for the mechanism with one-direction motion.

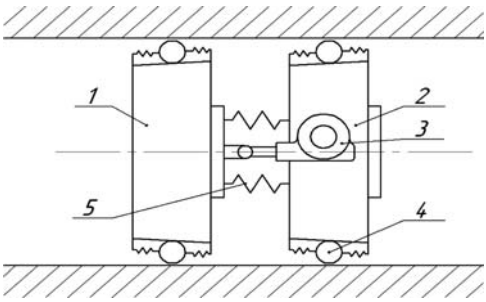

Fig. 1 A scheme of double-mass vibrating robot in a pipe: 1 – front body of the robot, 2 – second body of the robot, 3 – actuator, 4 – one-direction motion mechanism, 5 – springs

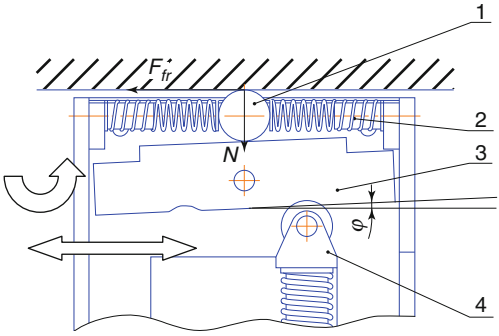

Fig. 2 A design of a new asymmetric friction mechanism

The asymmetric friction mechanism has dominant influence on motion performance. This mechanism creates force feedback between robot and internal pipe wall. The aim is to design the one-direction mechanism with maximum difference friction force for forward and backward slip. Up to now bristles or flexible blades were used with different shape. Their disadvantage consists of a significant difference of friction forces as depending on roughness and hardness of pipe wall. An original asymmetric friction mechanism has been designed to eliminate this disadvantage with the solution in Fig. 2. Main elements of the friction mechanism are listed in Table 1.

The asymmetric friction force F_{fr} is generated by the special mechanism with ball 1, springs 2 and inclined plane 3, which can change the angle of slope φ, so that it generate a different friction force as depending on direction of motion. If the robot has forward displacement, ball 1 move on the plane 3. In this case, the force between ball and plane is small. If robot changes the direction of motion, ball collides with pipe's wall and robot cannot move. Thus, the angle between surface of plane and pipe surface is smaller than friction angle.

A one-direction mechanism motion is obtained through the two phases:

First phase – forward motion with the minimal friction force

Table 1 Main elements of the friction mechanism in Fig. 2

Components	Denomination
1	Ball
2	Spring
3	Inclined plane
4	Switcher

Fig. 3 A 3D CAD model of robot with two masses and electrical drives inside a pipe

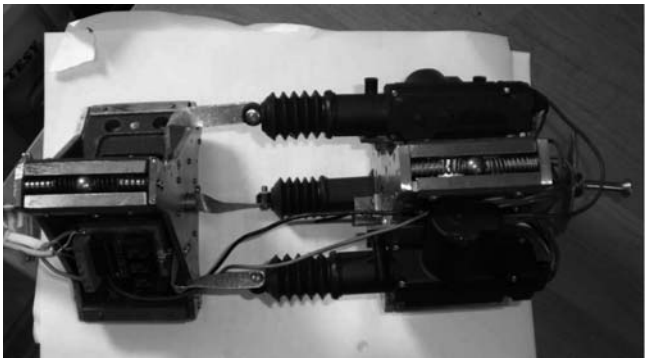

Fig. 4 A photo of the built prototype t with two masses and electrical drives

Second phase – backward motion with jamming mode of operation, by which movement is stopped

Mechanical properties of this mechanism have been tested with an experimental prototype. The results of experiment have confirmed the difference of friction force for forward and backward motion.

In order to reverse the direction of robot motion a control system changes the inclination angle of the ball supporting surface by using an electromagnet. A 3D CAD model and the robot prototype are shown in Figs. 3 and 4.

3 Mathematic Model of Robot's Motion

In order to characterize the parameters of the robot moving inside a pipe, a mathematical model has been formulated with the aim to describe the interaction of the moving parts with a technological load and the vibration-driven actuator.

The electrical drive periodically moves each mass as depending on the control program. Relative motion of two parts of robot body provides 1-D motion of the robot, but in this case, it is necessary that the characteristic of friction force between robot body and the supporting surface is asymmetric. A scheme of robot which has used in numerical simulation in the form presented in Fig. 5.

In the Fig. 5 the parameters are indicated as m_1, which is mass of the front part of the robot; m_2, which is mass of the rear part; Q_1, which is electro drive force; P_1, which is a restoring spring force proportional to relative displacement; R_1, which is the viscosity damping force proportional to the velocity. Similarly forces Q_2, P_2, R_2 act on the mass m_2. Nonlinear dry friction forces are indicated as F_1 and F_2. A mathematical model of friction force can be formulated in the form

$$F_i \begin{cases} F_i & if \quad \dot{X}_i < 0, \\ 0 & if \quad \dot{X}_i > 0, \quad i = 1,2 \\ F_i^* & if \quad \dot{X}_i = 0; \end{cases} \tag{1}$$

where F_i^* is the static friction force, which is defined from a condition of a force balance acting on the ith mass; and $\dot{X}_i$ is the velocity of ith mass. The force $F_1{}^*$ can be calculated by the formula

$$F_1{}^* = R_1 + P_1 + Q_1. \tag{2}$$

and the viscosity damping force can be expressed as

$$R_1 = \mu(V_1 - V_2). \tag{3}$$

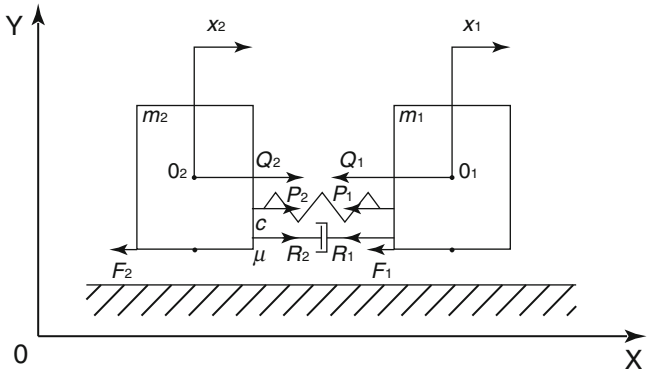

Fig. 5 A scheme for numerical simulation of the robot

With, $R_2 = -R_1$, where μ is the damping coefficient; $V_i = dX_i/dt$ is the velocity of masses m_1 and m_2.

The restoring force can be computed as

$$P_1 = c(X_1 - X_2). \tag{4}$$

Where, c is the spring coefficient.

4 A Numerical Characterization of Operation Features

This subchapter describes results of modeling and simulating in-pipe robot in COSMOS Motion Solid Works, [24, 25].

In a first step of modeling we have calculated the value of the friction force between robot's body and pipe's wall (F_1 and F_2, see Fig. 6). The scheme of modeling is shown in Fig. 6. For control of motion of robot we use force Q_i.

The computed relative displacement of two bodies is presented on Fig. 7. The normal reaction force between the wall of pipe and robot's body (N_i, see Fig. 6) is computed as constant. This force provides friction and is applied to the bodies are shown in the results in Figs. 8 and 9.

In this plots the difference between friction force for forward and backward motion are evident. For backward movement, in the first body a friction force (ΔF_{1max}) has been computed as approximately equal to 7.7 N. For forward movements force (ΔF_{1min}) has been computed as approximately equal to 2.4 N. In the

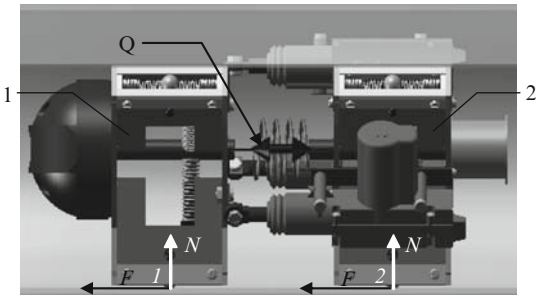

Fig. 6 A general scheme for robot simulation: Q – electro drive force, F1, F2 – dry friction forces (1 – the first robot body, 2 – the second robot body)

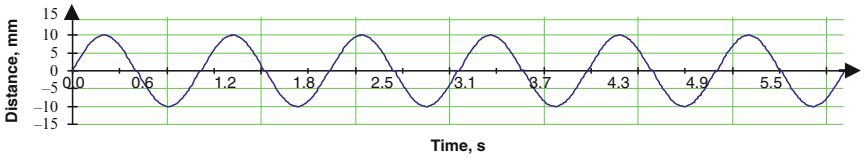

Fig. 7 The dependence of attached interaction on time (displacement)

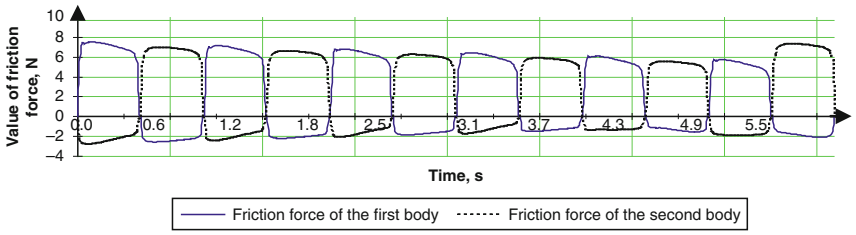

Fig. 8 Value of friction force between robot and pipe

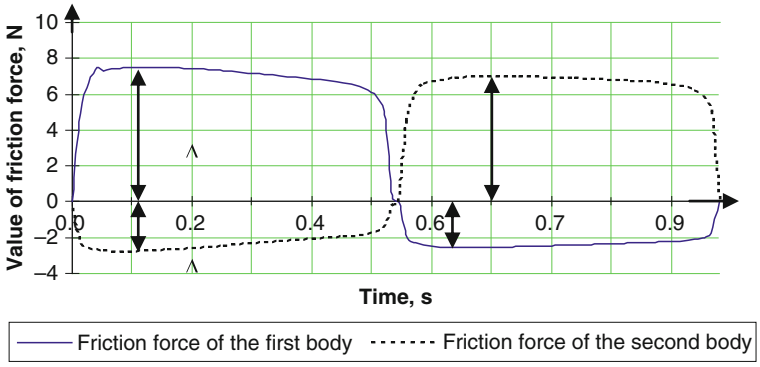

Fig. 9 Changing of friction force during one period

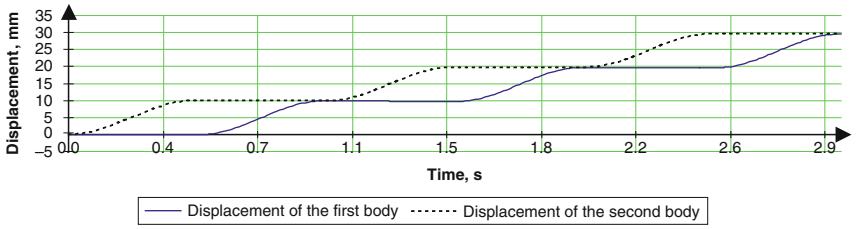

Fig. 10 The robot's displacement (with nominal parameters: k_{fr} = 0.120 – for forward motion body; k_{fr} = 0.600 – for backward motion)

second body friction force has been computed as approximately equal to 2.6 N for forward movements (ΔF_{2min}) and equal to 7 N for backward movements (ΔF_{2max}).

The value of friction force for forward motion is bigger than friction force for backward motions by four times. This result is feasible and it show that robot can move.

Figures 10, 11, 12 and 13 show the results of simulation for the motions of robot bodies with different parameters. In the first plot the results are related with nominal parameters. The magnitude of relative oscillation has been computed as 10 mm and the backward displacement of the bodies is negligible.

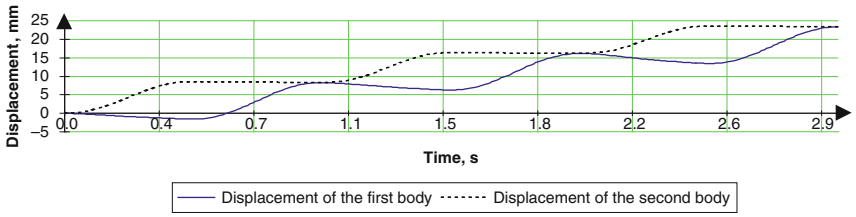

Fig. 11 The robot's displacement (with $k_{fr} = 0.120$ – for forward motion body; $k_{fr} = 0.400$ – for backward motion)

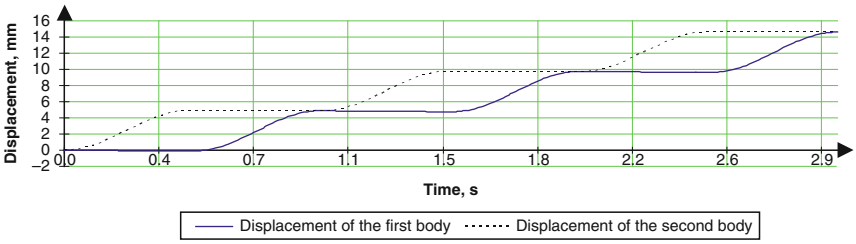

Fig. 12 The robot's displacement (with decreased value of setting interaction)

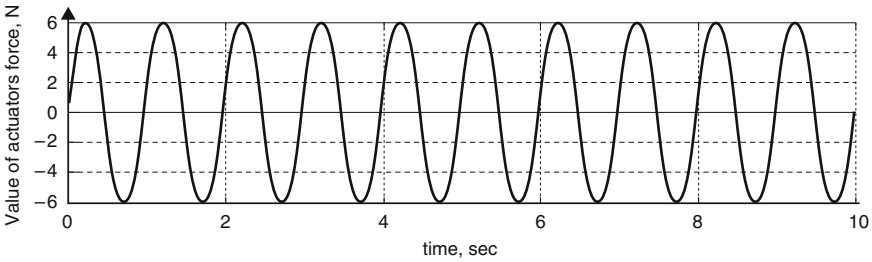

Fig. 13 The dependence of attached interaction on time (actuators force)

This simulation has been computed with a reduced value of the friction coefficient of first body (0.4 – for backward motion). The backward motion has been computed with about 3 mm. The result of this simulation show that small change of parameters provide significant decrease of robot movements. In Fig. 12 the displacement of robot's bodies with decreased value of setting interaction are shown. We can see that movement of robot strongly depends on value of actuator force. Therefore, it is very important to provide constant actuator forces by using of control program.

In addition, simulation has been carried out for a characterization of dynamic parameters by using proper codes in MATLAB environment, [26].

According to scheme of the mathematic robot model in Fig. 5, a program for determining value of the friction force and value of displacement has been elaborated.

The graph of input force (actuator force) is presented in Fig. 13. Initially, we have used sinusoidal signal as input force.

The force N between wall of pipe and robot's body has been computed constant as shown in Fig. 6. The computed friction force applied to first body is shown in Figs. 14 and 15. For forward movements the first body exerts a friction force, which has been computed equal to 8.64 N; while for backward movements force has been computed equal to 1.7 N. The second body exerts a friction force approximately equal to 1.7 N for forward movements and 8.64 N for backward movements.

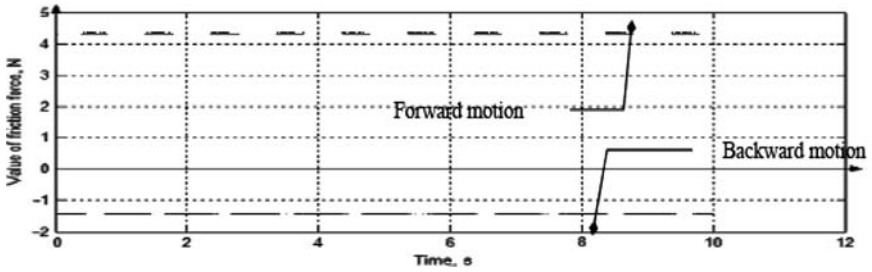

Fig. 14 Value of friction force between first robot body and wall of pipe

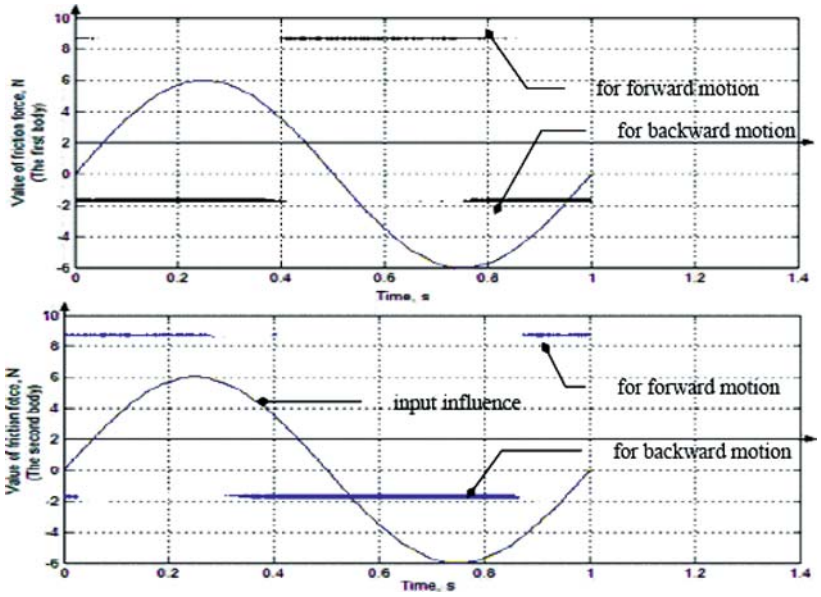

Fig. 15 Changing of friction force during one period for first and second body

Figures 16, 17, and 18 show results for the displacements of the robots bodies with different system parameters. In Fig. 16 the results are related with nominal value of the parameters and it is to note that the backward displacement of bodies is negligible.

We can see that decrease of friction coefficient for backward movements provide diminution of total displacement of robot; also in this case robot has backward drive. The backward motion is of about 5 mm. In Fig. 18 the displacement of robot bodies has been computed with decreased value of setting. Figure 18 shows that robot displacement strongly depends on value of actuators force. Decrease of magnitude of input force provides diminution of total displacement of robot.

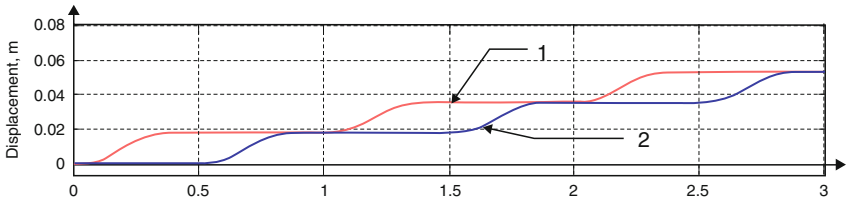

Fig. 16 The graph of robot's displacement: 1 – the first body, 2 – second body (with nominal parameters: kfr = 0.120 – for forward motion body; kfr = 0.600 – for backward motion)

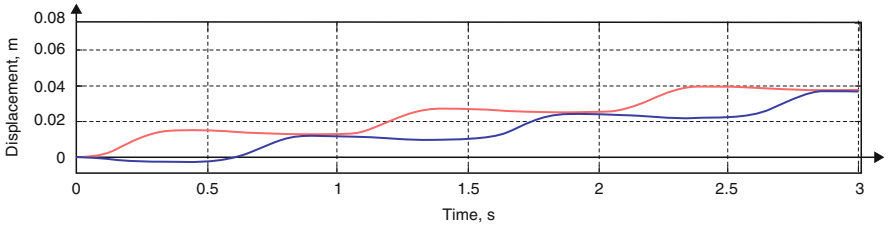

Fig. 17 The graph of robot's displacement: 1 – the first body, 2 – second body (with $k_{fr} = 0.120$ – for forward motion body; $k_{fr} = 0.400$ – for backward motion)

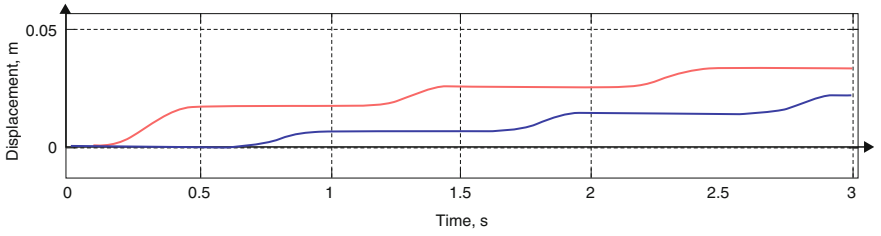

Fig. 18 The graph of robot's displacement: 1 – the first body, 2 – second body

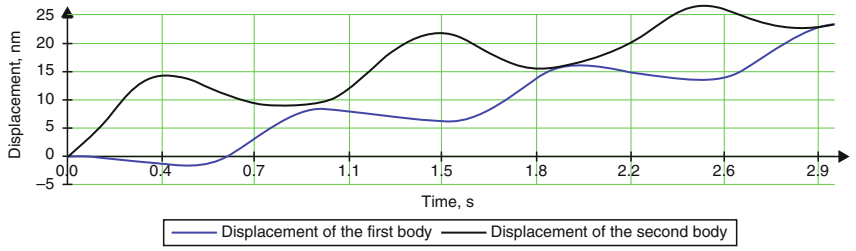

Fig. 19 The graph of robot's experimental displacement

5 Result of Experimental Testing

For investigation of locomotion of Kursk robot for In-Pipe Inspection the experimental tests are carryout. A glass plump pipe has been used for these experiments. The diameter of pipe is equal 140 mm. The graph with the measured results for robot's displacement for parameters is shown in Fig. 19.

We can see that robot has stable movements of robot bodies. It can be explain by uneven surface of pipe.

6 Conclusion

In this paper an original new design of robot is presented whose operation is based on a vibration principle of locomotion. An original asymmetrical dry friction mechanism is discussed with simulation results as to provide different value of friction force for locomotion. Numerical analysis of robot movement with different parameters and results of experimental tests are presented.

Acknowledgments Part of this work has been developed during the visit of second author at LARM in Cassino in 2008 with support of MIUR project of Italy-Russia Program. This work has been also supported by grant of RFBR 08-08-00438.

References

1. Hirose, S., Ohno, H., Mitsui, T., Suyama, K.: Design of In-Pipe Inspection Vehicles for ø25, ø 50, ø 150 Pipes. J. Robot. Mechatronics 12(3), 310–317 (2000)
2. Tatar, O., Mandru, D., Ardelean, I.: Development of mobile minirobots for in pipe inspection tasks. Mechanika J. 68(6), 60–64 (2007)
3. Moghaddam, M., Hadi, A.: Control and guidance of a pipe inspection crawler (PIC). 22nd International Symposium on Automation and Robotics in Construction, Ferrara (2008)

4. Carnegie Mellon University the Robotics Institute, State-Of-The-Art Review (In-Pipe-Assessment Robot Platforms) (2004)
5. Ragulskis, L., Spruogis, B., Mistinas, V., Matuliauskas, A.: Investigation of dynamics of a pipe robot of advanced type. J. Vibroengineering 8(3), 79–84 (2006)
6. Kothari, K., Pittard, G.: Sealing Large-Diameter Cast-Iron Pipe Joints Under Live Conditions. http://www.osti. gov/bridge/servlets/purl/842636-T4m 7n5/native/842636.pdf (2009)
7. Versatrax 100 pipe Inspection system. http://www.inuktun.com/versatrax100.htm (2009)
8. Horodinca, M., Doroftei, I., Mignon, E., Preumont, A.: A simple architecture for in-pipe inspection robots. International Colloquium on Mobile and Autonomous Systems, Magdeburd (2002)
9. Horodinca, M., Preumont, A., Burda, I., Mignon, E.: The heli-pipe inspection robots architecture for curved pipes. International Conference of Manufacturing Systems, Iasi (2003)
10. Robinson, N., Spencer, A.: Get inside robot to impel normal pipe operation. International Conference Underwater Intervention, New Orleans (2005)
11. Martinson, E., Miller, M., Wasi, S.: The pipe crawler. 16th Florida Conference on Recent Advances in Robotics, Dania Beach (2003)
12. Tache, F., Fischer, W., Caprari, G., Moser, R., Mondada, F., Siegwart, R.: Magnebike: a magnetic wheeled robot with high mobility for inspecting complex shaped structures. J. Field Robot. 26, 453–476 (2009)
13. Gambao, E., Hernando, M., Brunete, A.: Multiconfigurable inspection robots for low diameter canalizations. 22nd International Symposium on Automation and Robotics in Construction, Ferrara (2005)
14. Brunete, A., Hernando, M., Gambao, E.: Drive modules for pipe inspection microrobots. IEEE International Conference on Mechatronics and Robotics, Aachen (2004)
15. Dovica, M., Gorzas, M., Kovač, J., Ondočko, Š.: In-pipe passive smart bristled micromachine. 2nd Slovakian – Hungarian Joint Symposium on Applied Machine Intelligence, Herľany (2004)
16. Choi, H.R., Roh, S.-g.: In-pipe robot with active steering capability for moving inside of pipelines. In: Habib, M.K. (ed.) Bioinspiration and Robotics: Walking and Climbing Robots. I-Tech Education and Publishing, Vienna (2007)
17. Jatsun, S., Zimmerman, K., Zeigis, I., Jatsun, A.: Vibration driven robots for in pipe inspection. International Conference on Mechatronics, Kumamoto, pp. 237–249 (2007)
18. Jatsun, S., Bobotnik, N., Zimmerman, K., Zeigis, I.: Modeling of motion of vibrating robots. 12 IFToMM World Congress, Besancon, 2007, pp. 171–188
19. Ceccarelli, M.: Design and operation of in-Pipe Robot for cutting tacks. LARM internal report, Cassino (2005)
20. Dovica, M., Slosarčik, S.: A contribution to the study of microactuators. Bulletin of National University Lviv Polytechnic, Solid State Electronics: Theory and Applications, pp. 55–66 (2001)
21. Bolotnik, N., Tsimmerman, K., Zejdis, I., Jatsun, S.: Mobile vibrating robots. 9th International Conference on Climbing and Walking Robots, Brussels, pp. 558–563 (2006)
22. Bolotnik, N., Jatsun, S., Tcherepanov, A.: Automatically controlled vibration-driven. International Conference on Mechatronics, Budapest, pp. 438–441 (2006)
23. Hollinger, G., Gwaltney, D.: Evolutionary design of fault-tolerant analog control for a piezoelectric pipe-crawling robot. 8th Conference on Genetic and evolutionary computation, Seattle, pp. 761–768 (2006)
24. COSMOSMotion Overview, JEA. http://www.owlnet.rice.edu/~mech403/HelpFiles/Cosmos Motion_Overview2007.pdf (2007)
25. COSMOSMotion Overview. http://www.solidworksacademic.de/solidworks (2009)
26. MATLAB online help. http://www.mathworks.com/access/helpdesk/help/techdoc/matlab. html (2009)

Conceptual Design of an Omni-directional Mobile Robot

I. Doroftei

Abstract In order to move in tight areas and to avoid obstacles mobile robots should have good mobility and maneuverability. These capabilities mainly depend on the wheels design. Research is continuously going on in this field, to improve the autonomous navigation capability of mobile robotic systems. This paper provides some information about the mechanical design of an omni-directional robot, about its kinematics, as well as about its electronics and control strategies. This report is the result of a research conducted at the Robotics Laboratory of the Mechanical Engineering Faculty, "Gh. Asachi" Technical University of Iasi, Romania.

Keywords Design · Kinematics · Mobile robot · Omni-directional wheel

1 Introduction

Industrial and technical applications of mobile robots are continuously gaining in importance. They are already widely used for surveillance, inspection and transportation tasks. A further emerging market is that of mobile entertainment robots.

One of the main requirements of an autonomous mobile robot is its ability to move through the operational space, avoiding obstacles and finding its way to the next location, in order to perform its task, capabilities known as localization and navigation. In order to know where to go, the robot must have accurate knowledge of its current location. It means, it should use a great variety of sensors, external references and algorithms.

In order to move in tight areas and to avoid obstacles mobile robots should have good mobility and maneuverability. These capabilities mainly depend on the

I. Doroftei
"Gh. Asachi"-Technical University of Iasi, Iaşi 700050, România

I. Vişa (ed.), *SYROM 2009*,
DOI 10.1007/978-90-481-3522-6_8,

wheels design. Research is continuously going on in this field, to improve the autonomous navigation capability of mobile robotic systems.

This paper introduces a mobile robot with omni-directional motion capabilities, thanks to its special Mecanum wheels. The present paper provides some information about the mechanical design of an omni-directional robot, about its kinematics, as well as about its electronics and control strategies. This report is the result of a research conducted at the "Gh. Asachi" Technical University of Iasi, Theory of Mechanisms and Robotics Department.

2 Previous Work

The Mecanum wheel was invented in 1973 by a Swedish engineer (Mecanum Company), named Ilon [7]. This is why it is called Mecanum or Swedish wheel. Using four of these wheels provides omni-directional movement for a vehicle without needing a conventional steering system [2, 3, 11].

The first mobile robot with Mecanum wheels, called "Uranus", was designed and constructed in Carnegie Mellon University [9, 10]. It had not a suspension system, which is absolutely necessary if the ground is not completely flat.

The benefits of a vehicle with Mecanum wheels relative to one with steered wheels have been presented by [3]. [9] and [10] introduced the kinematics of Uranus robot and developed an algorithm for feedback control of it.

Many other projects with four Mecanum wheels have been presented by [4, 8, 13].

Omni-directional vehicles with Mecanum wheels have some shortcomings. According to [12], a vehicle with Mecanum wheels is susceptible to slippage, and as a result, with the same amount of wheel rotation, lateral traveling distance is different from longitudinal traveling distance. In addition, the ratio of longitudinal traveling distance over lateral traveling distance with the same amount of wheel rotation, changes with ground condition. The second drawback is that the contact point between the wheel and the ground moves along a line parallel to the wheel axis, even though the wheel is always in contact with the ground. The lateral movement produces horizontal vibrations. The last drawback is that its ability to overcome obstacles is not independent of travel direction.

The slippage of the wheels prevents the most popular dead-reckoning method, using rotary shaft encoders [1, 5], from being performed well on a vehicle with Mecanum wheels. In order to solve the problem, visual dead-reckoning was used as a slip-resilient sensor [6, 12].

3 Mecanum Wheel

A Swedish omni-directional wheel has three DOFs composed of wheel rotation, roller rotation, and rotational slip about the vertical axis passing through the point of contact (see Fig. 1). In the omni-directional wheel, its velocity can be divided

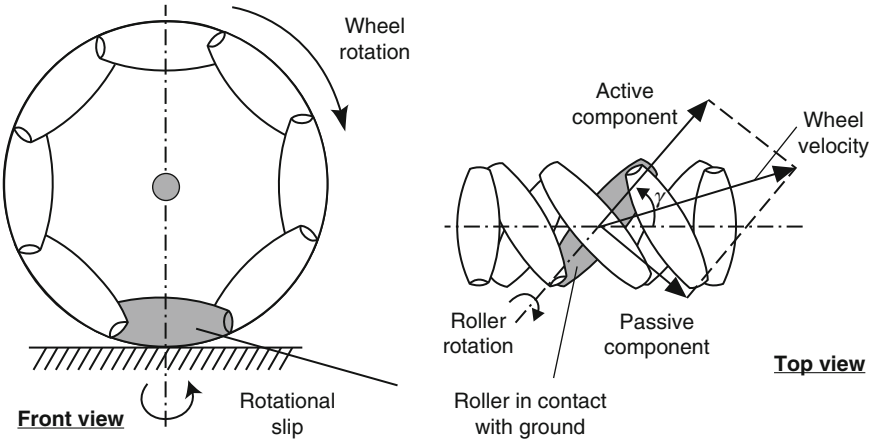

Fig. 1 DOFs in a Mecanum wheel [14]

Fig. 2 Wheel kinematics

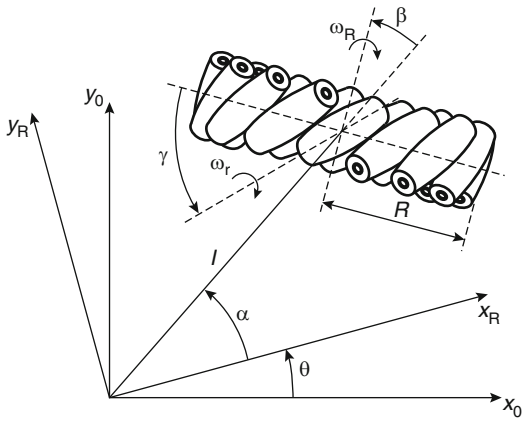

into the components in the active direction and in the passive direction. The active component is directed along the axis of the roller in contact with the ground, while the passive one is perpendicular to the roller axis.

In order to avoid the wheel rolling slippage, next condition should be respected (see Fig. 2) [13]

$$[\sin(\alpha+\beta+\gamma)-\cos(\alpha+\beta+\gamma)-l\cdot\cos(\beta+\gamma)]\cdot\mathbf{R}^{-1}(\theta)\cdot\left[v_x v_y \omega\right]^{-1}- \\ -R\cdot\omega_R\cdot\cos\gamma=0 \tag{1}$$

where

$$\mathbf{R}^{-1}(\theta)=\begin{bmatrix}\cos\theta & \sin\theta & 0\\ -\sin\theta & \cos\theta & 0\\ 0 & 0 & 1\end{bmatrix}, \tag{2}$$

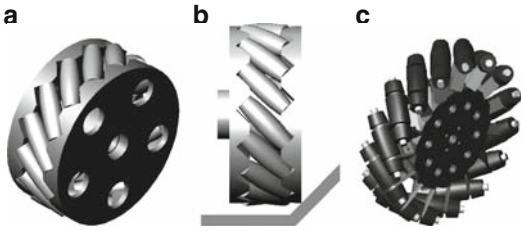

Fig. 3 Wheel designs

v_x,v_y,ω are the linear and rotational robot velocities.

On the lateral side the wheel will not slip because the rollers are freely rotating around their axes [13]

$$[\cos(\alpha+\beta+\gamma) \quad \sin(\alpha+\beta+\gamma) \quad l\cdot\sin(\beta+\gamma)]\cdot\mathbf{R}^{-1}(\theta)\cdot[v_x \quad v_y \quad \omega]^{-1}- \\ -R\cdot\omega_R\cdot\cos\gamma - r\cdot\omega_r = 0 \tag{3}$$

Two wheel designs have been used for our platform. The first wheel solution was based on a traditional Mecanum wheel (Fig. 3a). This design, though having a good carrying capacity, has the disadvantage that, when encountering an inclined or an uneven work surface, the rim of the wheel can make contact with the surface instead of the roller, thus preventing the wheel form operating correctly (Fig. 3b).

Another simple alternative design, which alleviates this problem, consists in having the rollers spit in three and mounted as shown in Fig. 3c. This design ensures that the rollers are always in contact with the work surface, thus allowing for better performance on uneven surfaces.

4 Robot Design

Typical Mecanum-wheel based vehicles have a square or rectangular configuration, with two wheels on each side of the chassis. Using four of these wheels provides omni-directional movement for a vehicle without needing a conventional steering system. In our case, we have chosen a square configuration, in order to simplify the mathematical model and, obviously, the motion control of it.

The first prototype is based on conventional Mecanum wheels (Fig. 4a). The second one is based on the wheel shown in Fig. 3c.

Because the omni-directional capability of the robot depends on each wheel resting firmly on the ground, some are equipped with suspension systems. Even if these designs are for indoor applications (this means they are moving on flat

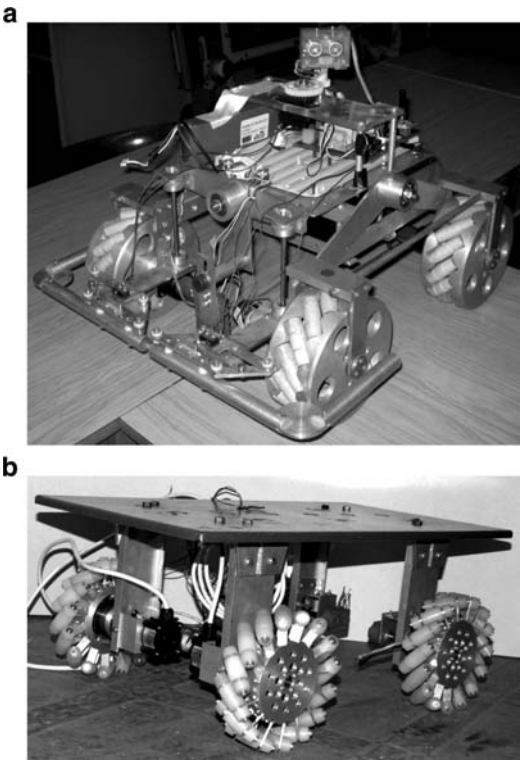

Fig. 4 Robot prototypes

surfaces), having four wheels, they need a suspension system just in case of small waves that could exist on the ground. For the first prototype, a passive suspension system with two spatial four-bar mechanisms (serial connected) is used, in order to easy adapt the system to the ground.

The trajectories of the contact points between rollers and work surface in vertical plane will be circular segments, when the robot is moving on uneven terrain. It means that the contact surface will not be a square in such cases, as it is when the robot works on flat terrain. This fact will introduce some errors in the trajectory control of the robot.

In order to avoid these problems, the second prototype (Fig. 4b), based on Mecanum wheels with centrally mounted rollers, will use a suspension based on two double Lambda mechanisms (Fig. 5), which give straight line trajectories on vertical plane. The two double Lambda mechanisms will be connected by a double conical gear.

This design balances the reaction forces on each wheel; therefore the traction force remains same for each wheel whether one wheel is on upper position.

The second suspension mechanism was not yet implemented.

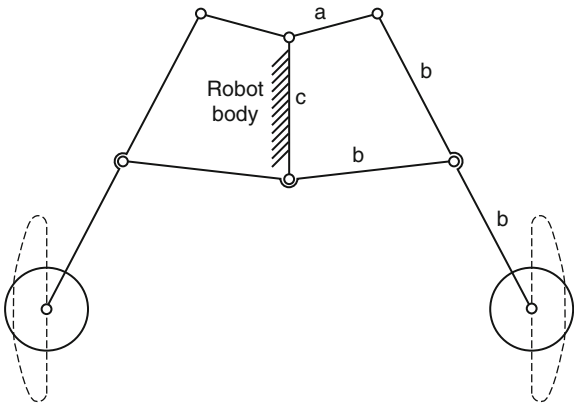

Fig. 5 Suspension based on double Lambda mechanism

5 Robot Kinematics

When Mecanum wheels are actuated, the angled peripheral rollers translate a portion of the force in the rotational direction of the wheel to a force normal to the wheel direction. Depending on each individual wheel direction and velocity, the resulting combination of all these forces produce a total force vector in any desired direction thus allowing the platform to move freely in the direction of the resulting force vector, without changing of the wheels themselves.

If we consider a fixed world frame $x_W O_W y_W$ and a mobile frame $x_R O_R y_R$ attached to the robot chassis (see Fig. 6), we can write direct kinematics equation as follow

$$\begin{bmatrix} v_x^W(t) \\ v_y^W(t) \\ \Omega_z^W(t) \end{bmatrix} = \begin{bmatrix} \cos\phi(t) & -\sin\phi(t) & 0 \\ \sin\phi(t) & \cos\phi(t) & 0 \\ 0 & 0 & 1 \end{bmatrix} \cdot \begin{bmatrix} v_x(t) \\ v_y(t) \\ \omega_z(t) \end{bmatrix}, \tag{4}$$

with

$$\begin{bmatrix} v_x(t) \\ v_y(t) \\ \omega_z(t) \end{bmatrix} = \frac{R}{4} \cdot \begin{bmatrix} 1 & -1 & -1 & 1 \\ 1 & 1 & 1 & 1 \\ -\frac{1}{l_1+l_2} & \frac{1}{l_1+l_2} & -\frac{1}{l_1+l_2} & \frac{1}{l_1+l_2} \end{bmatrix} \cdot \begin{bmatrix} \omega_1(t) \\ \omega_2(t) \\ \omega_3(t) \\ \omega_4(t) \end{bmatrix}, \tag{5}$$

where: R is the wheel radius; ω_i is the angular velocity of the wheel i ($i = 1..4$); l_1, l_2 are the distances between wheel axis and body center (see Fig. 5).

Robot coordinates according to the fixed world coordinate $x_W O_W y_W$ will be:

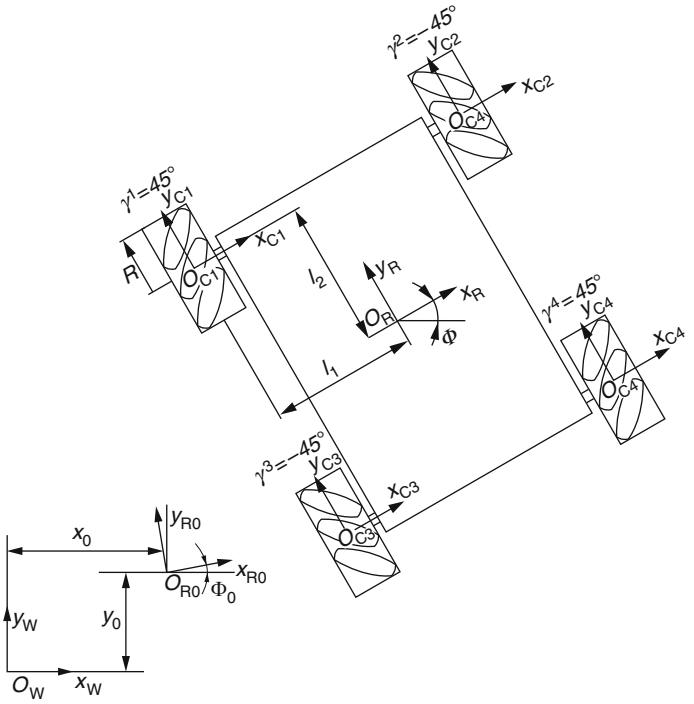

Fig. 6 Robot kinematics

$$\begin{cases} x^W(t) = \int_0^t v_x^W(t) \cdot \mathrm{d}t + x_0 \\ y^W(t) = \int_0^t v_y^W(t) \cdot \mathrm{d}t + y_0 \\ \phi^W(t) = \int_0^t \Omega_z^W(t) \cdot \mathrm{d}t + \phi_0 \end{cases} . \tag{6}$$

Inverse robot kinematics is described by:

$$\begin{aligned} \begin{bmatrix} \omega_1(t) \\ \omega_2(t) \\ \omega_3(t) \\ \omega_4(t) \end{bmatrix} &= \frac{1}{R} \begin{bmatrix} 1 & 1 & -(l_1+l_2) \\ -1 & 1 & l_1+l_2 \\ -1 & 1 & -(l_1+l_2) \\ 1 & 1 & l_1+l_2 \end{bmatrix} \cdot \begin{bmatrix} v_x(t) \\ v_y(t) \\ \Omega_z(t) \end{bmatrix} = \\ &= \frac{1}{R} \begin{bmatrix} 1 & 1 & -(l_1+l_2) \\ -1 & 1 & l_1+l_2 \\ -1 & 1 & -(l_1+l_2) \\ 1 & 1 & l_1+l_2 \end{bmatrix} \cdot \begin{bmatrix} \cos\phi(t) & \sin\phi(t) & 0 \\ -\sin\phi(t) & \cos\phi(t) & 0 \\ 0 & 0 & 1 \end{bmatrix} \cdot \begin{bmatrix} v_x^W(t) \\ v_y^W(t) \\ \Omega_z^W(t) \end{bmatrix}, \end{aligned} \tag{7}$$

6 Robot Control

The first prototype can be remote controlled, using a command system (Fig. 7), or it can follow a line or to be autonomous, using an ultrasonic sensor for obstacle avoidance.

In order to receive commands from the system presented in Fig. 7, or to detect obstacles and to drive the motors, an electronics board based on a PIC16F876 microcontroller, and placed on the robot, is used (Fig. 8).

The aim of this project was to provide the platform with motion control that could be programmed to accommodate various robotic behaviors specified.

6.1 Line Follower Mode

Fixed line following is the simplest and most reliable solution, yet is also the most limiting. A physical line is marked on the ground along the path which the robot is to follow. For a robot that is set up in a fixed location for a set task this system is effective but for a research robot with omni-directional capability this approach is seen to be a primitive, though still viable, option. The main application of this platform being education, line following remain interesting for the students. We have used two OPB704 infrared sensors for the first prototype of the robot.

6.2 Remote Control Mode

This prototype can be also remote controlled, using a command system (Fig. 7), and the electronic board (Fig. 8). A steering wheel set is used as a main driving element

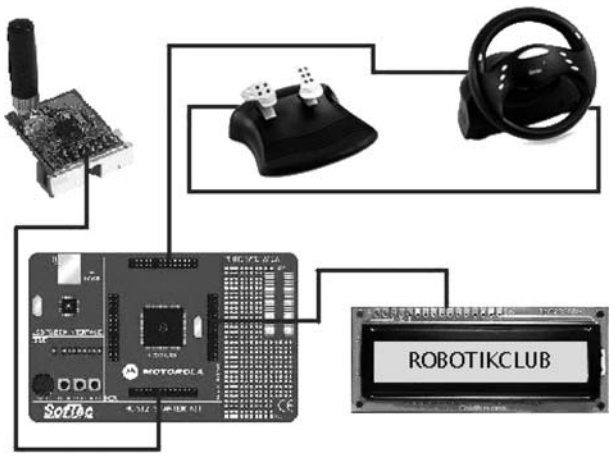

Fig. 7 Command system of the first prototype

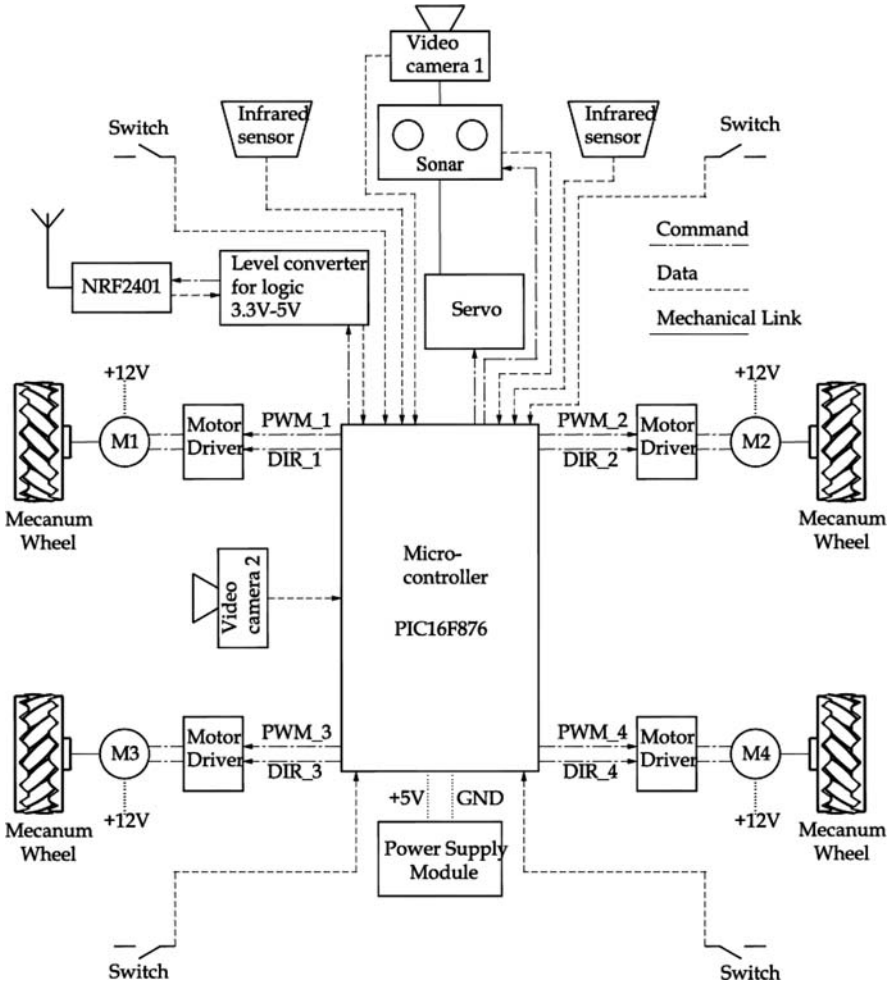

Fig. 8 Electronic board of the first prototype

and two transmitters/receivers based on the NRF2401 circuit, in order to transmit commands to the robot and to receive data from it. Because the robot can be controlled outside the room where we have the fixed command system, a video camera (video camera *1* in Fig. 8) will transmit images from the robot working space during its movement.

6.3 Autonomous Mode

To avoid obstacles in autonomous mode, a pair of ultrasonic sensor and two contact switches (two in the front and two in the back) have been used for the first

prototype. Because a single pair of ultrasonic sensors is used, the module sonar-camera is always swinging using a servo and a supplementary gear transmission, mounted on the top of the robot. Even if the servo has an angular stroke of 180°, thanks to the gear transmission, the sensor is able to scan an angle of 360°.

To simplify the control and to reduce the time for the distance measuring procedure, the ultrasonic sensor is swinging between two limits, $-\alpha_{max}$ and $-\alpha_{min}$ (Fig. 9). The robot velocity along x_S axis depends on $\sum D_i p_v$ and its angular velocity depends on $\sum D_i p_\omega$, where: D_i is the distance measured to the obstacle, for α_i angular position of the servo (Fig. 9); p_v and p_ω are the computing coefficients for linear and angular speed, respectively. If the distance to the obstacle becomes smaller than a minimum imposed value, the linear speed will be zero (the robot stops) and the vehicle will turn, finding an "exit". If this turning motion takes a long time (this time becomes bigger than a maximum imposed value), the servo will swing for the maximum limits (from −180° to +180°) finding a faster solution. This could happen when the robot is entering in a closed space.

If during the robot movement it will get an impact with an obstacle (one of the front switches is ON), the vehicle will go backward and will continue turning, and then it will try again to go forward.

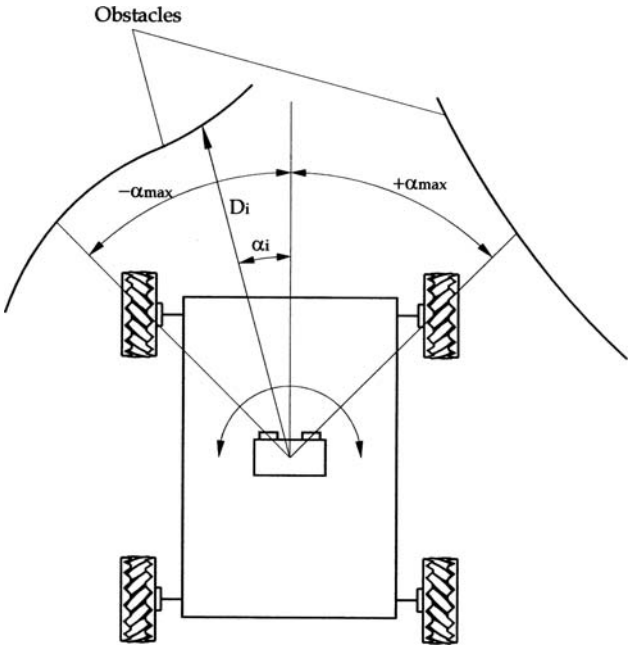

Fig. 9 Obstacle avoidance

6.4 The Second Prototype

The electronic board of the second prototype is more complex, based on a FPGA control board and on using more sensors, in order to get the position (robot odometry) of the robot during its movement and also to correct it (Fig. 10).

A hierarchical algorithm will be used in order to control the robot motion, based on three levels: level 0 – master level or human operator (the right side of electronics board); level 1 – global robot goal will be transformed in motor sub-goals); level 2 – motor control. Level 1 and level 2 are integrated into the FPGA board. For an efficient result at the level 1, a GPS and inertial sensors have been used (accelerometer and gyroscope). The encoders and current sensors will serve the level 2.

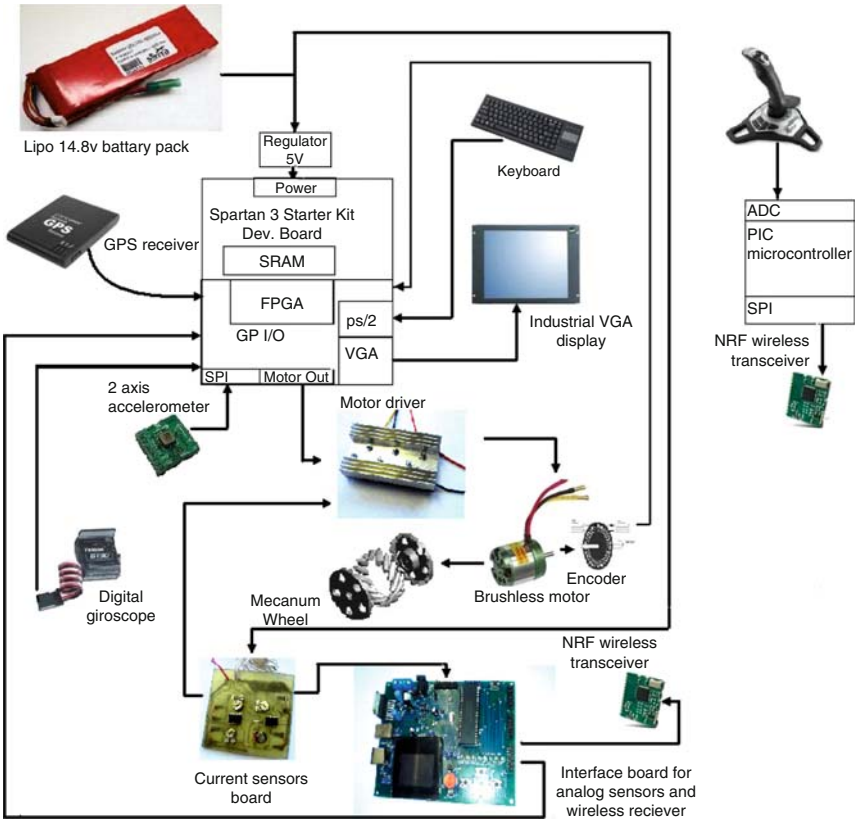

Fig. 10 Electronics of the second prototype

7 Conclusion

Omni-directional vehicles have great advantages over conventional (non-holonomic) platforms, with car-like Ackerman steering or differential drive system, for moving in tight areas. They can crab sideways, turn on the spot, and follow complex trajectories. These robots are capable of easily performing tasks in environments with static and dynamic obstacles and narrow aisles. Such environments are commonly found in factory workshop offices, warehouses, hospitals, etc.

The development of an omni-directional vehicle was pursued to further prove the effectiveness of this type of architecture and to add a ground vehicle platform that is capable of exceptional maneuverability.

In this paper, design aspects of Mecanum wheels and, also, of mobile robots based on such wheels have been presented. Two practical solutions of Mecanum wheels and two mobile platforms have been described. Thanks to its motion capabilities and to its different control possibilities, the robots discussed in this chapter could be used as interesting educational platforms.

Acknowledgments This paper is supported by The National University Research Council, through the PNII-IDEI research grant, No. 84/01.10.2007.

References

1. Borenstein, J., Everett, H.R., Feng, L.: Navigating Mobile Robots: Sensors and Techniques. A K Peters, Wellesley, MA (1996)
2. Bräunl, T.: Eye-Bot: a family of autonomous mobile robots. In: Proceedings of 6th International Conference on Neural Information Processing, Perth, Australia, November 1999, pp. 645–649 (1999)
3. Dickerson, S.L., Lapin, B.D.: Control of an omni-directional robotic vehicle with Mecanum wheels. In: National Telesystems Conference Proceedings, Atlanta, USA, 26–27 March 1991, pp. 323–328 (1991)
4. Diegel, O., Badve, A., Bright, G., Potgieter, J., Tlatle, S.: Improved Mecanum wheel design for omni-directional robots. In: Proceedings of 2002 Australian Conference on Robotics and Automation, Auckland, 27–29 November 2002, pp. 117–121 (2002)
5. Everett, H.R.: Sensors for Mobile Robots: Theory and Application. A K Peters, Wellesley, MA (1995)
6. Giachetti, A., Campani, M., Torre, V.: The use of optical flow for road navigation. IEEE Trans. Robot. Automation 14(1), 34–48 (1998)
7. Ilon, B.E.: Wheels for a course stable selfpropelling vehicle movable in any desired direction on the ground or some other base. US Patent (1975)
8. Koestler, A., Bräunl, Th.: Mobile robot simulation with realistic error models. In: 2nd International Conference on Autonomous Robots and Agents, Palmerston North, New Zealand, 13–15 December 2004, pp. 46–51 (2004)
9. Muir, P.F., Neuman, C.P.: Kinematic modeling for feedback control of an omnidirection wheeled mobile robot. In: IEEE International Conference on Robotics and Automation (1987)
10. Muir, P.F., Neuman, C.P.: Kinematic modeling of wheeled mobile robots. Journal of Robotic Systems 4(2), 281–340 (1987)

11. Muir, P.F., Neumann, C.P.: Kinematic modeling for feedback control of an omnidirectional wheeled mobile robot. In: Coxy, I.J., Wilfong, G.T. (eds.) Autonomous Robot Vehicles, pp. 25–31. Springer, Berlin (1990)
12. Nagatani, K., Tachibana, S., Sofne, M., Tanaka, Y.: Improvement of odometry for omnidirectional vehicle using optical flow information. In: IEEE/RSJ International Conference on Intelligent Robots and Systems (2000)
13. Siegwart, R., Nourbakash, I.R.: Introduction to Autonomous Mobile Systems. MIT Press, Cambridge, MA (2004)
14. Song, J.B., Byun, K.S.: Design and control of a four-wheeled omnidirectional mobile robot with steerable omnidirectional wheels. J. Robot. Syst. 21(4), 193–208 (2004)

Structural Design of the Fundamental Plane Kinematic Chains

B. Grecu, G. Adîr, V. Adîr, and V.G. Adîr

Abstract In this paper is introduced a method which allows establishing of the structural schemes of the kinematic chains, based on the degree of freedom (L) or on the degree of mobility (M) and number of the outlines (N). Starting from the kinematic chains solutions with one outline and degree of mobility $M1$ ($L4$) and using the notion of "connection", it is established an algorithm allowing to obtain the structural solutions of the complex kinematic chains with $N \geq 2$ and ordered according to the degree of mobility.

Keywords Connection · Kinematic chain · Outline · Structural scheme

1 Introduction

The plane kinematic chains allow to study the structural characteristics of the plane mechanisms and their synthesis represents a first phase of the mechanisms design. Evaluation of all alternatives of mechanical structures, having the same topological features, gives the possibility for a best choice of the constructive and kinematic solutions.

Grounding of the structural synthesis has concerned many specialists belonging to the mechanisms field. Some papers tackle both numerical solutions and structural ones [4–6, 8], and others tackle aspects of structural synthesis, based on notions of kinematic couple [2], driving group [1], connect [3]. The structural solutions obtained by using the outlines method [5] have a direct efficiency for the kinematic calculus and the structural solutions based on connection notion [3] facilitate the dimensional synthesis.

B. Grecu (✉) G. Adîr, V. Adîr, and V.G. Adîr
University Politehnica of Bucharest, Bucharest, Romania

I. Vişa (ed.), *SYROM 2009*,
DOI 10.1007/978-90-481-3522-6_9,

The algorithm that will be presented is based on connection notion [3] and establishes the possibilities to obtain the complex structural schemes by connections between the outlines of the simple kinematic chains.

2 Outlines Connections. Calculus

In [3] is grounded the connection notion which appears between the elements: driving, driven and frame. We consider a kinematic chain with "n" elements and "c" couples, ordered on a single outline of class VI, with the structural scheme in Fig. 1a.

The degree of freedom "L" of the chain coincides with the outline class. A kinematic chain that appears between two elements of the given outline, defines a simple connection (Fig. 1b), characterized by c^* couples, n^* elements ($n^* = c^*–1$) and degree of freedom L^*:

$$L^* = 3n^* - 2c^* = c^* - 3 \tag{1}$$

Besides the connections of type A,B,C [3], it is considered, also, the connection with $c^* = 0$, that we call of type "O" (Fig. 2).

By introduction of a connection it is obtained the structural scheme which suits to a kinematic chain with two independent outlines and whose degree of freedom is given by the relation:

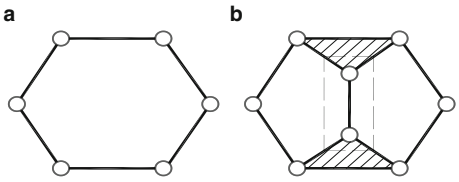

Fig. 1 One outline structural scheme (**a**); connection (**b**)

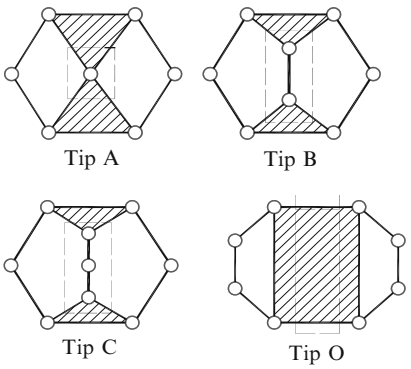

Fig. 2 Connections in structural schemes with $N = 2$

$$L = L_e + L^* \tag{2}$$

where L_e is the degree of freedom of the outside outline.

It is noticed that between the degrees of freedom L_i of the independent outlines and that of the outside outline, there is the relation:

$$2c = \sum L_i + L_e \tag{3}$$

And because the degree of freedom of an outline coincides with its class, the relation (3) is written under the appearance:

$$2c = \sum jN_j + k \tag{4}$$

From the equations system (2) and (3), it is established the number of couples $c^*$of the connection:

$$c^* = \sum L_i - L - 3;\ c^* = \sum M_i - M \tag{5}$$

If between two, three or four elements from the outside outline, there are introduced two connections, the structural scheme established suits to a kinematic chain with three outlines (Fig. 3).

Connections can be simple (Fig. 3a, b) or complex (Fig. 3c). The degree of freedom of the complex connection is obtained by addition of the degrees of freedom of the applied simple connections [3]. The complex connection appears when a second connection includes couples of an element from the outside outline of rank bigger than two (involved in a previous connection).

So, there can be made the following appreciations:

(a) As regards the structural schemes of the kinematic chains with two independent outlines, the connection results by crossing of the two constitutive outlines and for the chains with three outlines, the connection appears as a crossing between the outside outline of the structural scheme with two outlines with a third outline.
(b) Connection of type "O" allows obtaining of the structural schemes of the mechanisms with fragmented degree of mobility.

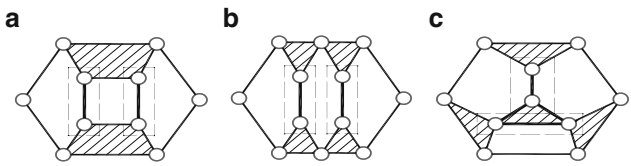

Fig. 3 Connections in structural schemes with $N = 3$

(c) The couples of the structural scheme with an independent outline form one single equivalence class and those belonging to the outside outline of the structural scheme with more outlines, can form more equivalence classes, according to the elements rank which form the couple and the symmetry of the outline.
(d) To one simple connection is assigned a dimension "d" which corresponds to its number of couples. Connections are identified thru "dimension" on the outside outline of the structural scheme and includes couples of different equivalence classes. In Table 1 there are examples of connections for outside outlines of class 5, 6, 7 and 8.
(e) The structural schemes with more outlines are established by superposition of the connections of same dimension identified on the constitutive outlines.
(f) The elements from both outlines which compete in the potentional couples of the superposition connection, increase their class (rank) by one unit. In case of

Table 1 Examples of connections

Schema structurală	Clase de echivalentă	Conexiuni identificate			
		Tip A	Tip B	Tip C	Tip O
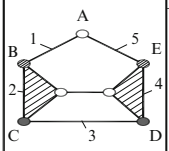	λ_1 λ_2 λ_3 A B C (E) (D)	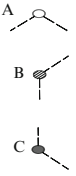	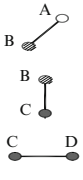	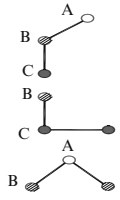	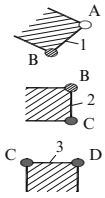
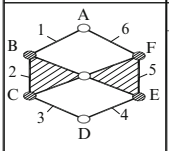	λ_1 λ_2 A B, C (D) (F, E)	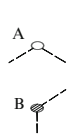	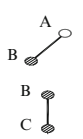	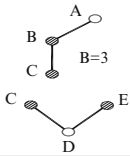	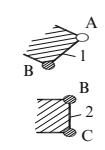
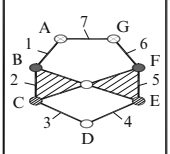	λ_1 λ_2 λ_3 λ_4 D A B C (G) (F) (E)	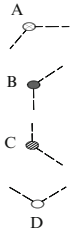	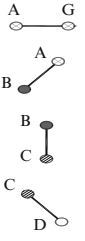	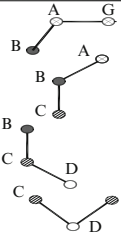	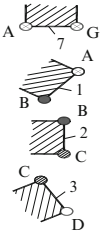
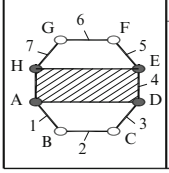	λ_1 λ_2 A B (D) (C) (E) (F) (H) (G)	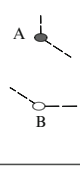	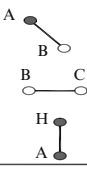	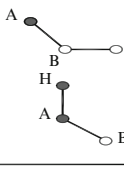	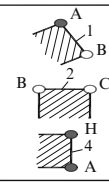

"O" connection, the rank is given by addition of the ranks of the respective elements.

3 Algorithm for Establishing of the Structural Schemes

(a) Establishing of the number of elements and kinematic couples when they are imposed as input parameters: L – degree of freedom (or M – degree of mobility) and N – outlines number of the kinematic chain, based on the relations:

$$\begin{aligned} n &= L + 2N - 2 \\ c &= L + 3N - 3 \end{aligned} \tag{6}$$

$$\begin{aligned} n &= M + 2N + 1 \\ c &= M + 3N \end{aligned} \tag{6'}$$

(b) Establishing of the structural schemes of the chains with $N = 1$ and $M \geq 1$, when $n = c$.

(c) Establishing of the outside outline class of the structural schemes, characterized thru the same value of M (or L), according to the classes sum of the constitutive outlines and explanation of the extreme values, based on the relations:

$$\begin{aligned} k &= 2(N + n - 1) - \sum_{j \geq 4} jN_j \quad k_{\max} = 2(N + n - 1) - \sum_{j_{\min}} j_{\min} N_{j_{\min}} \quad k_{\min} \\ &= 2(N + n - 1) - \sum_{j_{\max}} j_{\max} N_{j_{\max}} \end{aligned} \tag{7}$$

The class of the outside outline has to be greater or equal to the greatest class of the constitutive outlines [6]. In Table 2 there are presented the results obtained for the degree of mobility $M = 1, 2, 3$ with $N = 2$ and $N = 3$.

(d) Establishing of the number of couples c^* and of elements n^* of the connection by the relations:

$$c^* = \sum_{i=2}^{N} M_i - M; n^* = c^* - 1 \tag{8}$$

For the kinematic chains with $M = 1, 2, 3$ and $N = 2, 3$, the number of couples and elements are specified in Table 3, being delimited the solutions for the mechanisms with fragmented M, [7].

Table 2 Results obtained for M = 1, 2, 3 and $N = 2$, $N = 3$

$N = 2$						$N = 3$						
ΣjN_j	outline		k			ΣjN_j	outline			K		
	I	II	M = 1	M = 2	M = 3		I	II	III	M = 1	M = 2	M = 3
8	4	4	6	8	–	12	4	4	4	8	10	12
9	4	5	5	7	9	13	4	4	5	7	9	11
10	4	6	–	6	8	14	4	4	6	5	8	10
10	5	5	–				4	5	5			
11	4	7	–	–	7	15	5	5	5	5	7	9
11	5	6	–	–			4	5	6	–		
12	6	6	–	–	6		4	4	7	–		
						16	4	6	6	–	6	8
							5	5	6	–		
							4	5	7	–	–	
							4	4	8	–	–	
						17	4	6	7	–	–	7
							5	5	7	–	–	
							5	6	6	–	–	
						18	6	6	6	–	–	6

Table 3 Number of couples and elements

$N = 2$							$N = 3$						
ΣjN_j	M = 1		M = 2		M = 3		ΣjN_j	M = 1		M = 2		M = 3	
	n^*	c^*	n^*	c^*	n^*	c^*		n^*	c^*	n^*	c^*	n^*	c^*
8	0	1	–1	0	–	–	12	0	2	–1	1	–2	0
9	1	2	0	1	–1	0	13	1	3	0	2	–1	1
10	–	–	1	2	0	1	14	2	4	1	3	0	2
11	–	–	–	–	1	2	15	3	5	2	4	1	3
12	–	–	–	–	2	3	16	–	–	3	5	2	4
							17	–	–	–	–	3	5
							18	–	–	–	–	4	6

(e) Establishing of the structural schemes of the kinematic chains with two outlines and establishing of the connections of different types (different dimensions).
(f) Establishing of the kinematic chains schemes with three outlines, by identifying of the connections on the outside outline of the structural scheme with two outlines and an outline scheme.

4 Application

To illustrate this, there are presented the structural schemes of the kinematic chains with $M = 1$ ($L = 4$) and $N = 3$. According to the algorithm, it is established the number of elements n and couples c with relations (6') and results $n = 8$, $c = 10$. Based on relations (7), it is established the maximum and minimum class of the

Table 4 Structural schemes of kinematic chains with three outlines

Σ_j	I, II, III	k	Schema structurală M=1 (L=4); N=3; n=8; c=10
12	4 4 4	8	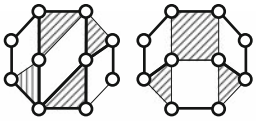
13	4 4 5	7	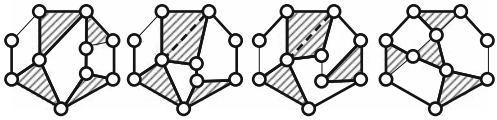

outside outline, $k_{max} = 8$, $k_{max} = 5$ and k for private solutions of the outlines in the sum ΣjN_j (Table 2). There are calculated c^* şi n^* by using the relations (8), the values being written in Table 3. The structural schemes of kinematic chains with three outlines are obtained by connections between the outside outlines of the schemes with two outlines and simple outlines of different classes (Table 4).

5 Conclusions

In the paper, it has been introduced the notion of connection "O", as a contribution of the authors, through this, including also the mechanisms with factioned degree of mobility. The connections method eliminates the solutions of the complex mechanisms with rigid outlines.

References

1. Duca, C.: Sinteza structuralã a grupelor conducãtoare plane. SYROM'73, Bucureşti (1973)
2. Dudiţã, Fl.,ş.a.: Optimizarea structuralã a mecanismelor, Ed. Tehnicã, Bucureşti (1987)
3. Kovacs, Fr., Perju, D., Savii, G.: Metode noi în sinteza mecanismelor, Ed. Facla (1976)
4. Manolescu, I.N.: Contribuţii la sinteza numericã, structuralã şi cinematicã a gupelor Assur, alanţurilor cinematice, a mecanismelor şi mecanismelor motor plane articulate,Tezã de doctorat, I.P. Bucureşti (1969)
5. Pelecudi, Chr.: Bazele analizei mecanismelor, Ed. Academiei R.S.R., Bucureşti (1967)
6. Pelecudi, Chr.: Teoria mecanismelor spaţiale, Ed. Academiei R.S.R., Bucureşti (1972)
7. Pelecudi, Chr., Grecu, B.: Caracteristicile schemelor structurale ale roboţilor şi manipulatoarelor cu M = 3;N = 3, Al V-lea Simpozion de roboţi industriali, Braşov (1986)
8. Tempea, I.: Contribuţii la sinteza numericã şi structuralã a lanţurilor cinematice plane cu ajutorul teoriei grafelor, Tezã de doctorat, Institutul Politehnic Bucureşti (1973)

Structural Design of the Plane Mechanisms with Linkages and Gears

B. Grecu, G. Adir, A. Adir, and V. Adîr

Abstract The paper presents the structural characteristics of mechanisms with linkages and gears. It is presented the interdependence relation which is the base for the numerical solutions. For structural representations, there were used symbols that characterize the mechanisms with linkages and gears. A computing programme was elaborated to establish the numerical solutions for different input parameters.

Keywords Algorithm · Degree of mobility · Gears · Linkage

1 Introduction

The plane mechanisms with linkages and gears (written down as MeBaRd) are part of the category of general plane mechanisms. Whether upon these ones have been achieved structural synthesis studies [10], the structural synthesis of linkages and gears mechanisms can be analyzed like a distinct problem [9, 11].

Some papers refer directly to a certain class of mechanisms, such as planetary mechanisms [1, 2, 4] some others refer to some subsystems with zero mobility, called structural groups with cogged elements [6, 8].

In this paper, by developing some ideas from [3, 5, 6, 8], it has be achieved a general algorithm for the unitary design of MeBaRd, having as input parameters: M degree of mobility and N – outlines number.

B. Grecu (✉)
Department of Mechanisms & Robots, High School Grigore Cerchez, University Politehnica of Bucharest, Bucharest, Romania

I. Vişa (ed.), *SYROM 2009*,
DOI 10.1007/978-90-481-3522-6_10,

2 The Structural Magnitudes of MeBaRd

In the structure of linkages and gears mechanisms can be found as kinematic elements, as well, bars (with rotation couples c_{bb} between them) (Fig. 1a) and gears (with upper couples – s between them). Good running of a mechanism involves to assure the constant distance between the gears axis, so, the existence of a bar and two rotation couples c_{bd} (Fig. 1b).

Between the kinematic elements, bars (b) and gears (d), intervene the following connections types [8]: rotation couples $(c = c_{bb} + c_{bd})$, upper couples (s) and rigid links $(r = r_{bd} + r_{dd})$ (Fig. 2).

To represent the structure of the kinematic chains with linkages and gears there are used conventional symbols that underline the connections between elements (Table 1).

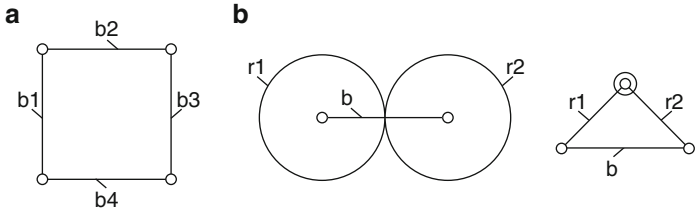

Fig. 1 Kinematic chains: (**a**) with linkages; (**b**) with gears

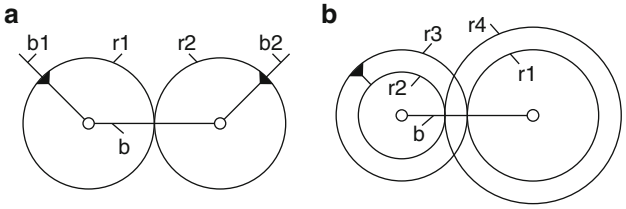

Fig. 2 Rigid links (**a**) between bars and gears; (**b**) between two gears

Table 1 Structural symbols for MeBaRd

Conventional symbol	Significance	Described connections
	2 gears	One upper couple Two rotation couples
	2 gears	One upper couple One rotation couple One rigid link
	2 gears	One upper couple Two rigid links

There are identified the outlines (N_b) – ascertained by bars, of class $j \geq 4$ and the outlines (N_d) – ascertained by gears $(N_d = s)$, of class j = 3.

Between the structural magnitudes: bars, gears, upper couples, rigid links, outlines and the degree of mobility, it has been established the interdependence relation:

$$(b + d) - (s + r) = M + 2 \cdot N_b + 1 \tag{1}$$

3 Structural Synthesis Criteria of MeBaRd

MeBaRd are established from plane kinematic chains. The combination between gears and bars represents a parallel assembly, in which gears are working and don't represent isolated elements. The upper couple is established by the gears positioned on the couples axles of a bar (bar is representing the centers line).

The rigid link between bar and gear is possible if the gear is not working with other gears positioned on the couples axles of the bar and the rigid link between two gears is possible when these ones are positioned on the same axis.

4 Numerical and Structural Solutions of MeBaRd

By taking into consideration the degree of mobility M and the outlines number as input parameters [7], it is established the number of elements and rotation couples with the relations:

$$\begin{aligned} n &= M + 2 \cdot N_b + s + 1 \\ c &= M + 3 \cdot N_b + s \end{aligned} \tag{2}$$

Using (1) there are established the numerical solutions of the structural synthesis that are valid for integer and positive values of the magnitudes b, d, s, M, N_b.

It is considered b and d, respectively s and r, as classes of the A and respectively B sets and it is established number of types of A and B partitions in two classes.

According to the outlines number of bars$(N_b)$and of their classes, it is established the minimum and maximum number for bars:

$$\begin{aligned} b_{\min} &= j_{\min} \cdot N_{b,j\min} \\ b_{\max} &= j_{\max} \cdot N_{b,j\max} \end{aligned} \tag{3}$$

where $j_{\min} = 4$.

The number of upper couples on an outline of bars is $s_{\min} \leq s \leq s_{\max}$, the limit values being:

$$s_{\min} = 1;\ s_{\max} = 2 \cdot j \tag{4}$$

According to the outlines number N_d, it is established the minimum and maximum number of gears:

$$\begin{aligned} d_{\min} &= s + 1 \\ d_{\max} &= 2 \cdot s \end{aligned} \tag{5}$$

The number of rigid links is limited by kinematic elements, $r_{\min} \leq r \leq r_{\max}$, the limits values being:

$$r_{\min} = b + d - n;\ r_{\max} = d \tag{6}$$

So, there are established the limits of A and B the sets:

$$\begin{aligned} A_{\min} &= b_{\min} + d_{\min} \\ A_{\max} &= b_{\max} + d_{\max} \end{aligned} \tag{7}$$

$$\begin{aligned} B_{\min} &= s_{\min} + r_{\min} \\ B_{\max} &= s_{\max} + r_{\max} \end{aligned} \tag{8}$$

The numerical solutions are obtained by using the computing programme SIMeBaRd. The programme delivered results for different values of M and N_b, useful in establishing of the limits of A and B sets.

To one numerical solution it suits one or more structural solutions. To introduce the structural solutions it has to apply the simple structural schemes of bars and gears. The limitation of solutions is given by the term that the frontier outline be of maximum class, namely:

$$k = 2(N + n - 1) - \sum j \cdot N_j \tag{9}$$

The number of inner rotation couples (c^*) and the number of inner elements (n^*) are established with the relations:

$$\begin{aligned} c^* &= c - k \\ n^* &= n - k \end{aligned} \tag{10}$$

In the structural schemes the upper couples are represented by two concentric circles, to underline the outlines of class three. The structural solutions can be represented by structural schemes MeBaRd [3], the symbols being describes in Table 1.

In Table 2 there are presented the numerical solutions for M = 1 and $N_b = 1$, for $j = 4 \div 6$ ($j_{\min} = 4$; $j_{\max} = 6$).

Table 2 Numerical solutions for M = 1 and $N_b = 1$, $N_d = s$

A	b	d	B	s	r	c	c_{bb}	c_{bd}
6	4	2	2	1	1	5	4	1
7	4	3	3	2	1	6	4	2
7	5	2	3	1	2	5	5	0
8	4	4	4	2	2	6	4	2
8	4	4	4	3	1	7	4	3
8	5	3	4	2	2	6	5	1
9	4	5	5	3	2	7	4	3
9	4	5	5	4	1	8	4	4
9	5	4	5	3	2	7	5	2
10	4	6	6	3	3	7	4	3
10	4	6	6	4	2	8	4	4
10	5	5	6	3	3	7	5	2
10	5	5	6	4	2	8	5	3
10	6	4	6	2	4	6	6	0

In Table 3 there are presented the structural schemes MeBaRd for M = 1; $N_d = 2$and 3;$N_b = 0$ and the kinematic schemes of the linkages and gears chains.

In Table 4 there are presented the structural schemes MeBaRd for M = 1; $N_d = 2$;$N_b = 1$ (class j = 4) and the kinematic schemes of the linkages and gears chains.

SIMeBaRd – PROGRAMME FOR THE STRUCTURAL SYNTHESIS OF LINKAGES AND GEARS MECHANISMS

```
50 INPUT "Amin = ", Amin: INPUT "Amax = ", Amax: INPUT "Nb = ", Nb
60 INPUT "bmin = ", bmin: INPUT "bmax = ", bmax: INPUT "dmin = ", dmin
70 FOR M = 1 TO 3
75 PRINT "M = ", M: PRINT "Nb = ", Nb
80 DEL = M + 2 * Nb + 1
100 FOR I = Amin TO Amax
110 A = I: b = bmin: d = A – b: rmin = 2 * (b − DEL)
135 IF rmin > 0 THEN GOTO 140
137 rmin = 0: smax = b + 2 * (Nb - 1)
150 IF d < dmin THEN GOTO 440
160 L = d
170 FOR K = 1 TO L
180 PAR = 2 * K: IMR = 2 * K − 1
190 IF PAR = d THEN GOTO 220
200 IF IMR > = d THEN GOTO 240
210 NEXT K
220 s = d/2
230 GOTO 250
240 s = d/2 + 5: r = A − s − DEL
260 FOR K = 1 TO L
270 IMR = 2 * K − 1
280 IF IMR > d THEN GOTO 320
```

Table 3 Structural schemes MeBaRd for M = 1; $N_d = 2$ şi 3; $N_b = 0$

Structural solution MeBaRd	General structural scheme	Kinematic chain MeBaRd	Kinematic chain MeBaRd (reduced appearance)
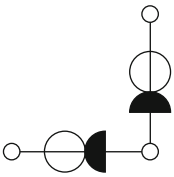	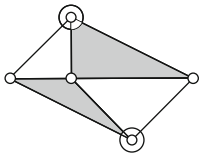	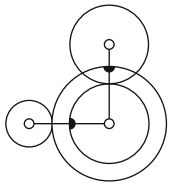	-
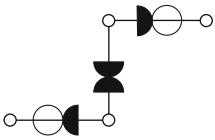	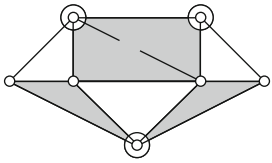	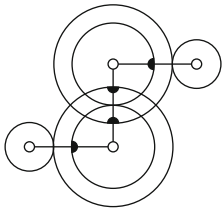	-
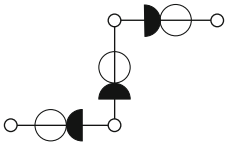	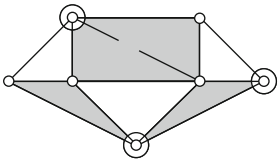	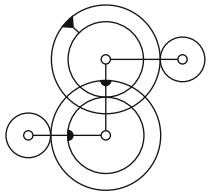	-

```
300 IF IMR > = r THEN GOTO 320
310 NEXT K
320 spr = A − DEL
330 IF r > d THEN GOTO 410
340 IF r < rmin THEN GOTO 410
350 IF s > smax THEN GOTO 410
360 cbb = Nb + b − 1: cbd = d − r: c = cbb + cbd
365 PRINT USING "##"; A;
370 PRINT USING "#######"; b; d; spr; s; r; c; cbb; cbd
380 IF s > = (d − 1) THEN GOTO 410
390 s = s + 1
400 GOTO 250
410 IF b > = bmax THEN GOTO 440
```

Table 4 Structural schemes and Kinematic chains MeBaRd for $N_b = 1$, with j = 4

Structural solution MeBaRd	General structural scheme	Kinematic chain MeBaRd	Kinematic chain MeBaRd (reduced appearance)
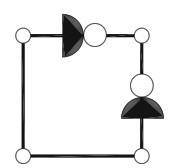	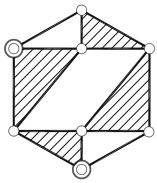	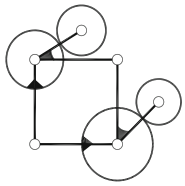	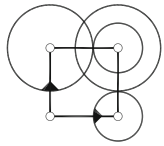
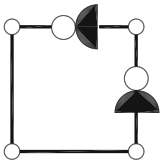	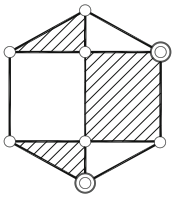	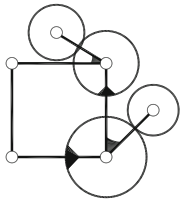	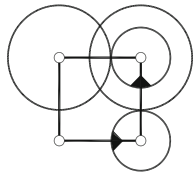
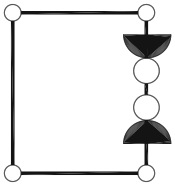	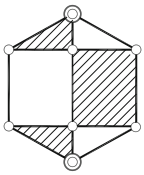	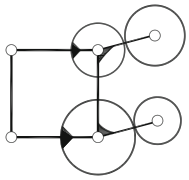	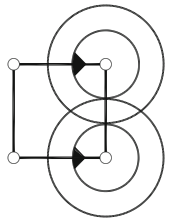
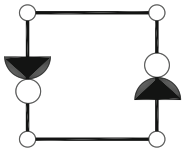	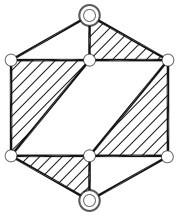	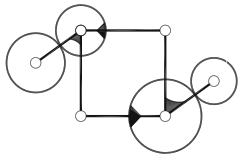	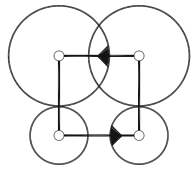
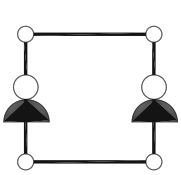	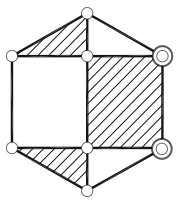	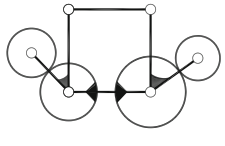	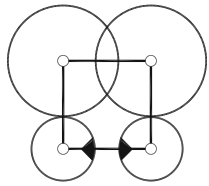

```
420 b = b + 1
430 GOTO 120
440 NEXT I
485 NEXT M
495 STOP
```

5 Conclusions

The computing structural algorithm of MeBaRd is applicable for different values of the input structural parameters. The structural schemes MeBaRd facilitate to obtain easily the kinematic schemes and eliminate the possibility of serial link of gears and bars. It can be used for: planetary mechanisms, orientation mechanisms for industrial robots, generating mechanisms for plane trajectories,positioning mechanisms for robots.

The computing programme in QBASIC can be easily transform in another computing language.

References

1. Bugaevschi, E.: Consideraţii structurale privind mecanismele cu cuple superioare. SYROM'73, vol. C, Bucureşti, 1973
2. Bobancu, S.: Contribuţii la structura mecanismelor biplanetare, multiplanetare. SYROM'73, vol. C, Bucureşti (1973)
3. Grecu, B.: Sistematizarea lanţurilor cinematice cu bare articulate şi roţi dinţate, referat de doctorat. Bucureşti (1978)
4. Margine, Al.: Contribuţii la sinteza geometrico-cinematică şi dinamică a mecanismelor planetare cu roţi dinţate, Teză de doctorat, UPB (1999)
5. Niţu, I.: Contribuţii la cinematica roboţilor industriali cu module cinematice diferenţiale de orientare, Teză de doctorat, UPB (1998)
6. Ocnărescu, C.: Cercetări teoretice şi experimentale în domeniul roboţilor poliarticulaţi. Teză de doctorat, UPB (1996)
7. Pelecudi, Chr.: Metoda contururilor în sinteza numerică şi structurală a lanţurilor cinematice, St.cerc.mec.apl., nr.3 (1967)
8. Pelecudi, Chr., Grecu, B.: Asupra sistematizării mecanismelor plane cu bare articulate şi roţi dinţate, SYROM ' 81, vol. 3, Bucureşti (1981)
9. Rooney, G.T., Zamfir,V.: Sinteza structurală a lanţurilor cinematice plane cu bare şi elemente dinţate cu $L_3 = 4$, $l = 5$, $c_5 = 4$, $c_4 = 1$; SYROM'73, vol. A, Bucureşti (1973)
10. Tempea, I.: Sinteza structurală a lanţurilor cinematice plane generale cu N = 1,2,3, contururi deformabile şi grad de libertate L3 = 4, St.cerc. mec. aplic., nr.1 (1972)
11. Zamfir, V.: Asupra analizei şi sintezei structurale a lanţurilor cinematice cu bare şi elemente dinţate, SYROM'73, vol. A, Bucureşti (1973)

Design of LegVan Wheel-Legged Robot's Mechanical and Control System

A. Gronowicz and J. Szrek

Abstract The wheel-legged robot is a vehicle with many degrees of freedom. Thanks to its peculiar design, depending on the need the vehicle will use one of its ways of moving: travelling on wheels or walking, which enhances its locomotive properties. This paper presents a novel solution of the wheel-legged robot equipped with special designed limb kinematic system. Moreover, an idea of the control system design is sketched and selected results of the tests carried out on the robot prototype are reported.

Keywords Control system · Geometry · Robot's Limb · Topology

1 Introduction

Among mobile land robots one can distinguish legged robots and wheeled robots.

The way in which legged robots move is inspired by nature. Thanks to their design the robots can negotiate obstacles, adjusting the distribution of mass among the individual limbs.

Since they move on wheels, wheeled robots are capable of higher speeds than legged robots. But they cannot negotiate obstacles as well as legged robots.

The merits of the two types of robots can be combined in a hybrid wheel-legged robot. This design is based on wheels mounted on a special system enabling large movements. When the terrain allows this, the robot moves on wheels, but when it encounters an obstacle, it surmounts it by walking (raising its limb).

A. Gronowicz (✉)
Division of Machine Theory and Mechatronical Systems, Wroclaw University of Technology, Wrocław, Poland
e-mail: Antoni.gronowicz@pwr.wroc.pl

I. Vişa (ed.), *SYROM 2009*,
DOI 10.1007/978-90-481-3522-6_11,

Table 1 Parameters of robot

Robot Mass	35 kg
Length	0.75 m
Width	0.45 m
Height	(0.35–0.65) m
Max obstacle height	0.30 m

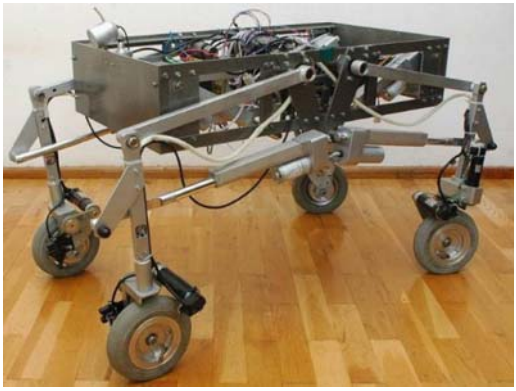

Fig. 1 Mobile wheel-legged robot LegVan

Mobile robots are investigated in many research centres. The papers on wheel-legged robots typically present the suggested control system, robot functions and control algorithms. The wheel-legged robots moving on wheels but also able to negotiate obstacles, known from the literature are: Hylos [3, 4] WorkPartner [5] and Roller-Walker [1]. Each of them has four wheels and is able to walk. Other robots [6, 10] and robots with more than four legs like Athlete [9], are also known.

This paper presents the LegVan wheel-legged robot built in the Division of Machine Theory and Mechatronical Systems at Wroclaw University of Technology (Poland).

The robot has four limbs with a wheel attached to each (some parameters of the robot are listed in Table 1). All the wheels are driven wheels, two of them being also turn wheels. The robot's (Fig. 1) functions are: platform levelling (keeping in horizontal position) in uneven terrain and negotiating obstacles by walking (raising the limbs).

The robot's special feature is the wheel suspension system enabling levelling by means of only one limb drive. As a result, the control system has been simplified and robot operation improved without limiting the ability to negotiate obstacles by walking.

2 Wheel-Legged Robot's Suspension System

The LegVan robot has a special suspension system designed to best perform the levelling and walking functions by means of a minimum number of drives. The kinematic system design was sought in three stages. First, the motion requirements

were defined, i.e. the kinematic system's number of DOFs needed to perform the assumed function was determined. This is closely connected with the required number of drives.

Then a structure (a set of members connected together by kinematic pairs) was sought for the suspension system. Usually there are many possible structural kinematic system designs ensuring the defined motion properties. Therefore a suitable design should be selected from a set of possible designs. Such a set can be easily created using the structural synthesis of mechanisms [2].

In the third stage of searching for a kinematic system the geometric dimensions of the members are determined. For this purpose one can employ the numerous methods of geometric synthesis. However, for some systems, as is the case here, the requirements and constraints are formulated in such a way that the well-known methods cannot be applied.

2.1 Structure of Robot Suspension System

It is assumed that the robot will move in urbanized terrain where it can encounter terrain unevenness in the form of slopes, steps and thresholds. It is allowed that a pair of wheels on the robot's one side moves on a horizontal plane while the other pair of wheels encounters a slope, a threshold or a step.

It is also assumed that the robot will encounter obstacles which will have to be surmounted by walking over them.

It follows from the above requirements that each of the four wheels should be capable of large movements. In addition, when negotiating thresholds, steps or walking over an obstacle, programmable curvilinear trajectory μ of the wheel centre (Fig. 2) should be maintained. Altogether, the wheel should have four degrees of freedom (walking f_1 and f_2, turn f_3, travel f_4 – Fig. 2). The missing intermediate chain U can be obtained using the structural synthesis methods [2].

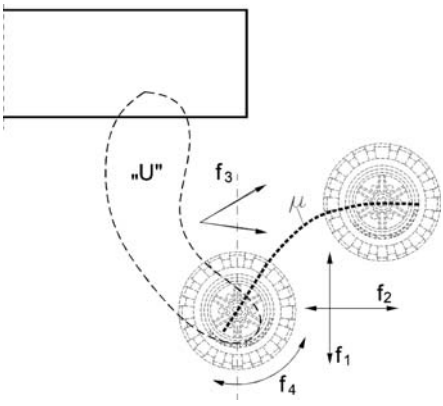

Fig. 2 Required number of DOFs

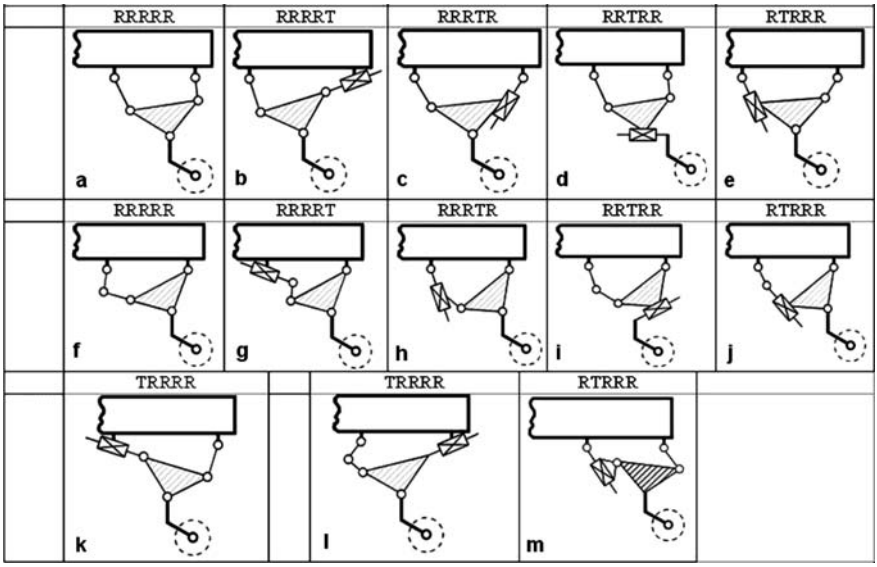

Fig. 3 Examples of possible kinematic suspension system designs

Examples of possible kinematic system (without travel and turn) designs, consisting of five links, are shown in Fig. 3.

2.2 Geometric Synthesis

The geometric synthesis of kinematic systems boils down to the determination of the linear and angular dimensions of their members so as to obtain the required properties.

In the considered case, a special wheel centre trajectory is required of the wheel guidance system. The system shown in Fig. 3m has been selected from the obtained set of possible limb designs.

Then appropriate dimensions were selected for the individual components (Fig. 4) to enable levelling motion (best along trajectory E_pE_k) by means of only one drive in each limb.

The shape of trajectory μ depends on linear dimensions: a, b, c, x_D, z_D, e and angles β and γ. In the assumed motion range, angle δ should be larger than certain minimum value δ_{min} in order to protect the system against reaching singular positions A geometric synthesis method of searching for a proper geometry had been developed (Fig. 5) [7, 8].

The method was applied whereby limb dimensions ensuring wheel axis displacement along a nearly rectilinear trajectory by means of only one drive q_1 (Fig. 6) were determined.

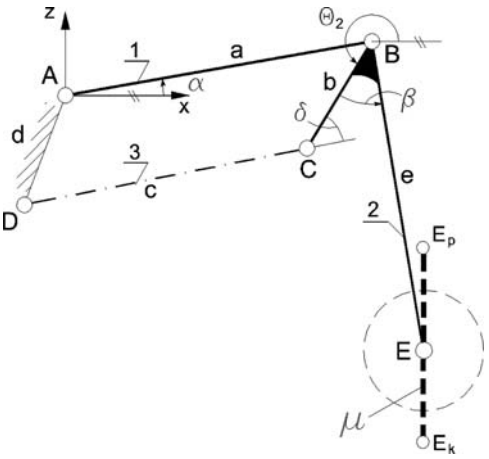

Fig. 4 Parameters of robot limb

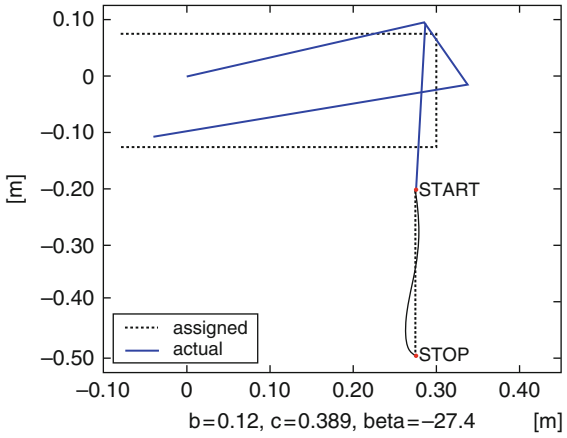

Fig. 5 Robot limb trajectory

The suspension kinematic system is also characterized by a linear dependence of drive servomotor (q_1) elongation on vertical wheel centre (E) displacement.

3 LegVan's Control System

The LegVan robot uses 14 drive motors. Because of the considerable number of drives and the robot's peculiar functions, its control system was divided into blocks.

In the robot one can distinguish drive modules responsible for the motion of the individual groups of motors, and measuring modules. One group, comprising four drive motors and two turn motors, is responsible for robot travel on wheels. Another

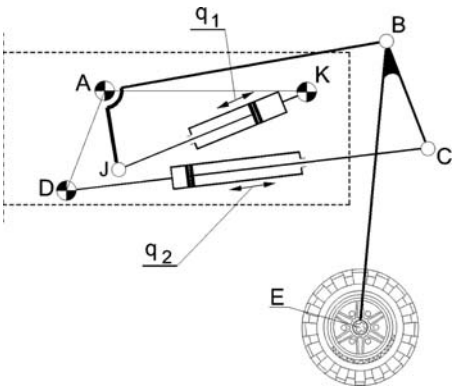

Fig. 6 LegVan robot's limb

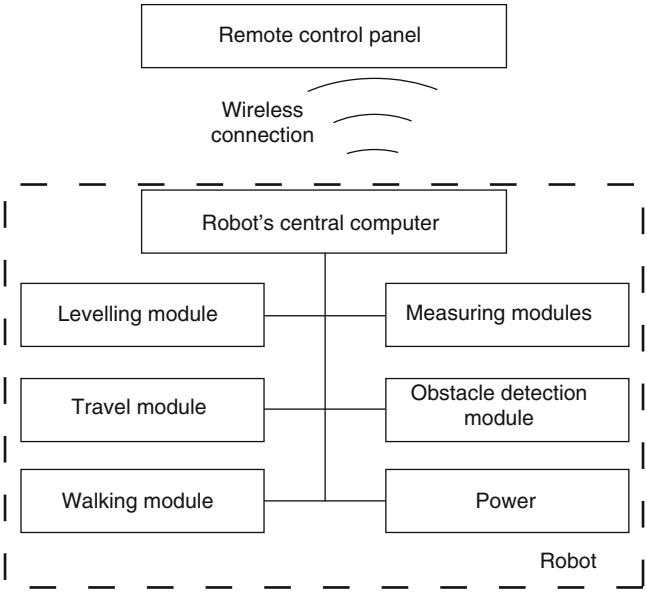

Fig. 7 Control system diagram

four drives are used to keep the platform level. The remaining four motors are employed only for walking. A schematic diagram of the robot's control system is shown in Fig. 7.

Each of the drive blocks has its own microcontroller ensuring feedback-based adjustment to the assigned position or speed. The modules are based on the MC68332 microcontroller.

The measuring modules and the power control module are responsible for the processing of signals coming from the robot's surroundings. The distance from the obstacle, the pressures exerted by the wheels on the base, the deviations of the

platform from the horizontal, etc., are measured. The measuring modules are based on the Atmega8 microcontroller.

The measuring modules and the motor control are connected with the robot's main computer – a PC104 unit with the LX800 processor. All the measurement data and control signals are transmitted via the central computer to a remote control computer. The robot's central and remote computers have a wireless network connection. In the remote computer the measurement data are visualized and the robot control commands are read.

3.1 Robot's Software

The flow of the particular data coming from the environment to the user is shown in Fig. 8. The flow chart shows the individual modules, their hardware location and the path of data flow in the software hierarchy. The main, robot control application (MRCA), which contains all the robot parameters and visualizes the measurement data, runs on the external computer. The application window is shown in Fig. 9.

MRCA communicates with the robot via the "Controller" application running on the robot's central computer.

The communication with the local modules, and so the interaction with the environment (data reading and action), is handled by the "Controller". The robot can be controlled in the manual mode and in the automatic mode. Manual control is effected by means of a joystick connected to the external control computer (Fig. 10).

In addition, the picture from the camera mounted on the robot is displayed in the control application.

In the automatic mode the robot autonomously executes the given task.

3.2 Robot Functions

The robot has been designed to operate in uneven terrain with obstacles. The robot's main functions are: keeping the platform level and negotiating encountered obstacles by walking. The robot performs both functions autonomously using the information coming from its sensors, and the control algorithms.

Since the platform levelling function is continuously performed while the robot operates, the suspension system design is such that the levelling motion of each limb is executed by a single motor. This has been achieved through appropriate selection of dimensions for the particular members.

The walking function, i.e. negotiating obstacles by raising a limb, is also performed autonomously. The operation algorithms have been developed for a specific group of obstacles (a step, a threshold) which can be localized by distance sensors situated in front of the robot's wheels.

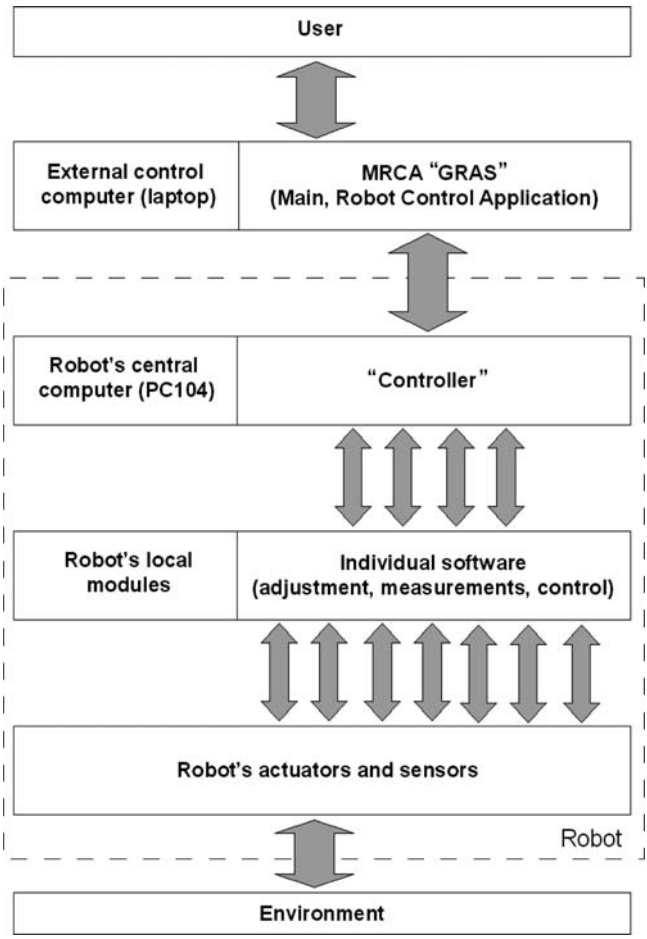

Fig. 8 Architecture of robot software

4 Experimental Results

Experiments were carried out to test the LegVan robot's active suspension system, control system, communication system and two main functions: levelling and walking. The levelling function was tested on the obstacle course shown in Fig. 11 on which several robot runs at different speeds were carried out.

The levelling function consists in compensating terrain unevenness by manipulating the suspension system. The information about the deviation of the platform comes from the inclinometers located on it. Exemplary traces of robot operation with the levelling function turned off (the wheels then do not move relative to the

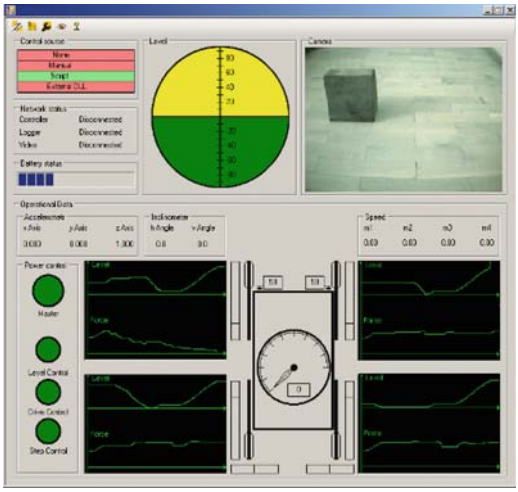

Fig. 9 Window of robot controlling application

Fig. 10 External control computer

platform) are shown in Fig. 12. When the levelling function is off, the platform changes is orientation relative to the base whereby operation safety decreases.

Figure 13 shows a situation when levelling is on. Then obstacle course unevenness is compensated by the suspension system and the platform deviation error oscillates around zero, which can be seen in Fig. 14.

Then the negotiation of obstacles situated in front of one and two wheels was tested. An obstacle is located and its height determined on the basis of the signal

Fig. 11 Obstacle course for robot

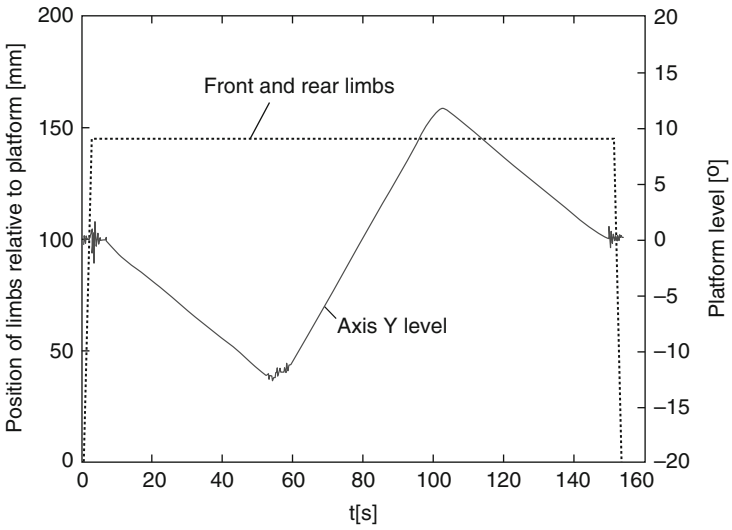

Fig. 12 Levelling turned off

received from the distance sensor. The robot travelling at a certain speed encounters an obstacle, reduces its speed and stops in front of the obstacle. Then it carries out the walking procedure to get over the obstacle. The particular stages are shown in Fig. 15 and the traces of the signals coming from the sensors are shown in Fig. 16.

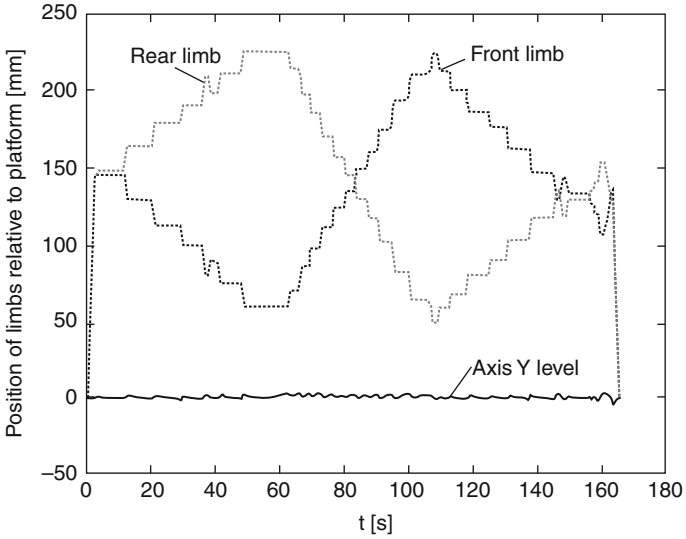

Fig. 13 Levelling turned on

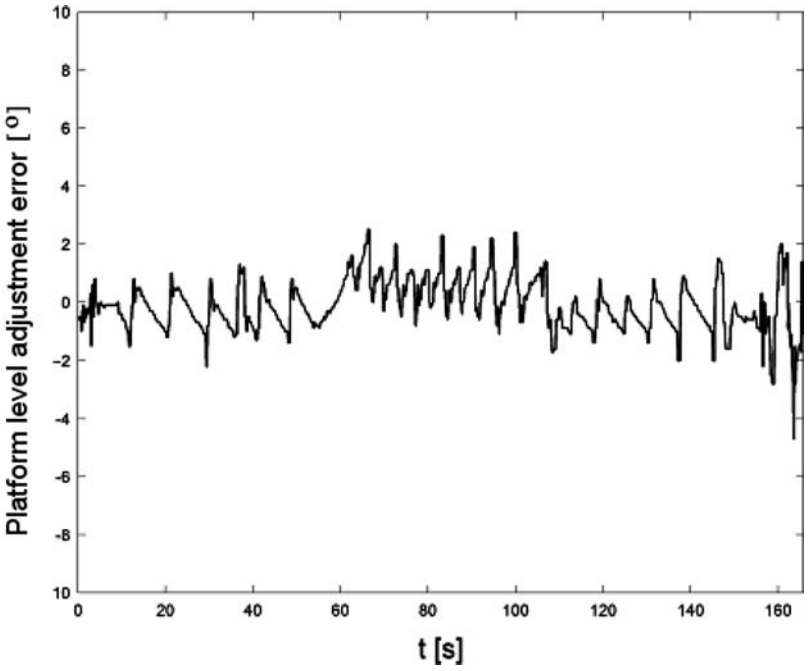

Fig. 14 Level deviation error

Fig. 15 Walking function tests

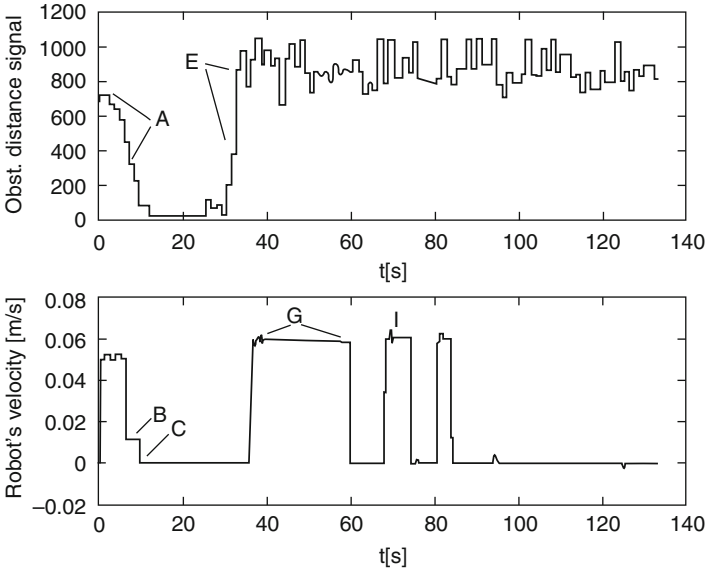

Fig. 16 Signals coming from robot's sensors during walking

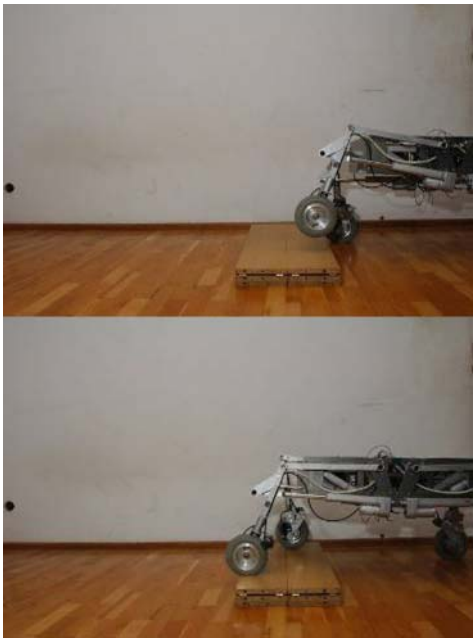

Fig. 17 Walking function tests v2

Also the behaviour of the robot when the obstacle was situated in front of two wheels (Fig. 17) was tested.

5 Conclusions

The idea of a design of the LegVan wheel-legged robot's mechanical part (including the suspension system) and its control system and selected experimental test results have been presented. The robot's distinguishing feature is its ability to negotiate obstacles by walking and levelling its platform, using only one drive in a limb. This is possible thanks to the special geometry of the suspension system.

References

1. Endo G., Hirose S.: Study on Roller-Walker (System Integration and Basic Experiments). Proceedings of the 1999 IEEE International Conference on Robotics and Automation, Detroit (1999)
2. Gronowicz A., Miller S.: Mechanisms (in Polish). Wroclaw University of Technology Publishing House (1997)

3. Grand Ch., BenAmar F., Plumet F., Bidaud Ph.: Stability control of a wheel-legged mini-rover. Proceedings of the CLAWAR 2002 Conference (2002)
4. Grand Ch., BenAmar F., Plumet F., Bidaud Ph.: Decoupled control of posture and trajectory of the hybrid wheel-legged robot Hylos. Proceedings of the 2004 IEEE International Conference on Robotics and Automation, New Orlean (2004)
5. Halme A., Leppänen I., Salmi S., Ylönen S.: Hybrid locomotion of wheel-legged machine. Proceedings of the CLAWAR 2000 Conference (2000)
6. T. Ishimatsu, M. J. Lawn: Modeling of a Stair-Climbing Wheelchair Mecha-nism With High Single-Step Capabi-lity. IEEE Transactions on Neural Systems and Rehabilitation Engineering, vol. 11, no. 3, September (2003)
7. Szrek J.: Method of synthesizing mobile wheel-legged robot's suspension system (in Polish). 20th Polish Conference on TMM, Zielona Góra (2006)
8. Szrek, J.: Synthesis of kinematic and control systems of a four wheel-legged robot (in Polish). PhD thesis, Wroclaw University of Technology (2008)
9. Tristan B. Smith, Javier Barreiro, David E. Smith, Vytas SunSpiral, Daniel Chavez-Clemente: ATHLETE's Feet: Multi-Resolution Planning for a Hexapod Robot. Proceedings of the International Conference on Automated Planning and Scheduling (ICAPS), Sydney, Sept. (2008)
10. Tadakuma, K., Masatsugu, M., Hirose, S.: Mechanical Design of Horizontal Polyarticular Expandable 3-wheeled Planetary Rover; "Tri-Star3". Proceedings of the IEEE International Conference on Mechatronics & Automation, Niagara Falls, Canada, July (2005)

Mathematical and Virtual Modelling of a Spur Gear

G. Haraga

Abstract This paper is based on a spur gear modelling from a mathematical and virtual point of view. In the first part of the paper are presented the geometrical calculation elements of the spur gear. In the second part of the paper we point out aspects about a spur gear modelling by using CAD systems. Gears are mechanism which transmit force from one part of a machine to another and are present in virtually all machines that have spinning parts. Nowadays, gears are used on a large scale from aerospace industry to toy manufacturing. They have a variety of forms to suit any mechanical need.

Keywords Calculation geometry · Engineering reference · Solid edge · Spur gear

1 Introduction

In this paper we have presented some 3D models concerning spur gears using Engineering Reference function in Solid Edge software.

Gears can be used to reverse rotational direction, increase or decrease speed of rotation, transfer rotation to a different axis, or to synchronize rotation across two or more axes in a machine or engine.

An essential benefit of gears is their ability to utilize the mechanical principles of ratios to turn speed into power, otherwise referred to as gear reduction.

G. Haraga
Department of Descriptive Geometry and Engineering Graphics, Politehnica University of Bucharest, Bucharest, Romania

I. Vişa (ed.), *SYROM 2009*,
DOI 10.1007/978-90-481-3522-6_12,

The gears can also be used between shafts, which can be parallel or inclined to one another. They are used to transmit power between shafts rotating usually at different speeds. There are many types of gears, but the most popular gear types:

Spur gear is the simplest and most common type of gear and can be characterized by their straight cogs, these gears are mounted on parallel shafts [5].

2 Geometric Parameters of a Spur Gear

In this section, we are presented the geometric parameters of a spur gear, as shown in Fig. 1.

Pitch surface – the surface of the imaginary rolling cylinder that the toothed gear may be considered to replace.

Pitch circle – a right section of the pitch surface.

Addendum – the radial distance between the pitch circle and the addendum circle.

Addendum circle – a circle bounding the ends of the teeth, in a right section of the gear.

Dedendum – the radial distance between the pitch circle and the root circle.

Root circle – the circle bounding the spaces between the teeth, in a right section of the gear.

Clearance – the difference between the dedendum of one gear and the addendum of the mating gear.

Face – That part of the tooth surface lying outside the pitch surface.

Flank – The part of the tooth surface lying inside the pitch surface.

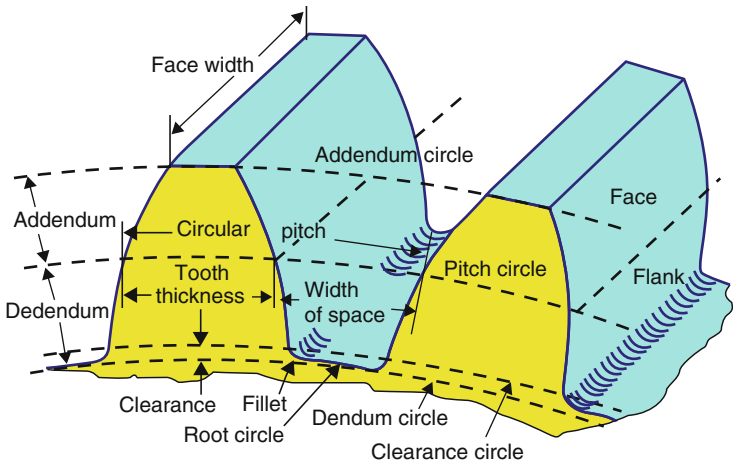

Fig. 1 Geometric parameters of a spur gear

Tooth thickness – the thickness of the tooth measured on the pitch circle. It is the length of an arc and not the length of a straight line.

Circular pitch – the width of a tooth and a space, measured on the pitch circle.

Diametral pitch – the number of teeth of a gear per inch of its pitch diameter. A toothed gear must have an integral number of teeth[7].

That is,

$$p = \frac{\pi d}{z}; P = \frac{z}{d}; \tag{1}$$

According to the previous relation (1):

$$pP = \pi \tag{2}$$

where:
p = circular pitch;
P = diametral pitch;
z = number of teeth;
d = pitch diameter.
The *module* (m) – is the number of millimetres of pitch circle diameter per tooth.

$$m = \frac{1}{P} = \frac{p}{\pi} \tag{3}$$

2.1 The Involute Function

In this paragraph we will present the parametric equations of involute curve gear.

The involute gear profile is the most familiarly used system for gearing today. In an involute gear, the profiles of the teeth are involutes of a circle. In involute gear design, all contact between two gears occurs in the same fixed, flat plane namily the plane of action, even as their teeth mesh in and out. The contacting surfaces are always perpendicular to the plane of contact, so the dominant contact forces are always parallel to the plane (Fig. 2) [6, 8].

From definition:

$$KT = \overline{KM} \tag{4}$$

$$KT = r_b \cdot (\alpha + \theta); \tag{5}$$

$$\overline{KM} = r_b \cdot \tan\alpha; \tag{6}$$

Using the relations (4), (5) and (6),

$$\Rightarrow r_b \cdot (\alpha + \theta) = r_b \cdot \tan\alpha \tag{7}$$

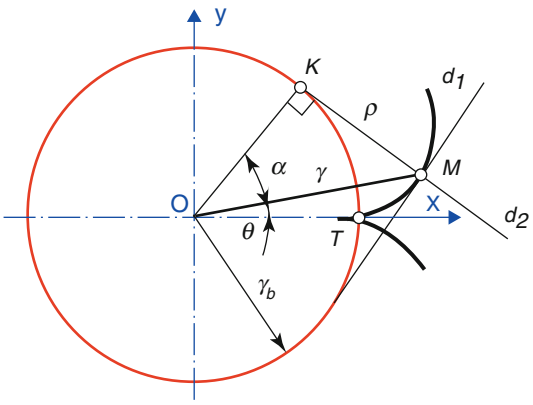

Fig. 2 The involute curve gear

From (7), results:

$$\theta = \tan\alpha - \alpha = inv\alpha. \tag{8}$$

The parametric equations of involute, are:

$$\begin{cases} inv\alpha = \tan\alpha - \alpha \\ r = \dfrac{r_b}{\cos\alpha} \end{cases} \tag{9}$$

where: $\rho = MK$; $d_1 \perp d_2$.

Two involute gears can mesh together (Fig. 3) if they have the same base circle pitch [9]. Other parameters of a gear mesh are: Center distance a_w;

Operating pitch diameters d_{w1} and d_{w2} (diameters with pure rolling action and zero sliding);

Tooth thicknesses on the operating pitch diameters S_{w1} and S_{w2};

Operating pressure angle α_w (involute profile angle on the operating pitch diameters);

Contact ratio ε_α.

3 Spur Gears with Solid Edge Software

In this part of the paper we point out aspects about a spur gear modelling by using Solid Edge software. Gears are mechanism which transmit force from one part of a machine to another and are present in virtually all machines that have spinning parts. They have a variety of forms to suit any mechanical need.

In order to maintain precise gear ratios and output speeds, gears have specially designed cogs. The most popular design used to achieve this is the involutes'

Fig. 3 Mesh parameters

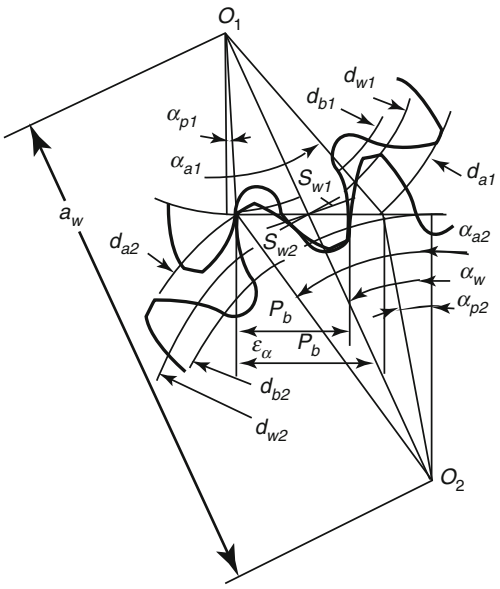

profile. It uses the mathematical concept of the involutes' curve to space gear cogs in a manner that efficiently keeps gear rotation perpendicular to a flat plane.

The gears can also be used between shafts, which can be parallel or inclined to one another. They are used to transmit power between shafts rotating usually at different speeds [3, 8]. Thus, can be mentioned such as spur gear used at trains, in watches and clocks.

A gear is a component within a transmission device that transmits rotational force to another gear or device. A gear is different from a pulley in that a gear is a round wheel that has linkages *teeth* or *cogs* that mesh with other gear teeth, allowing force to be fully transferred without slippage. Depending on their construction and arrangement, geared devices can transmit forces at different speeds, torques, or in a different direction, from the power source.

The most common situation is for a gear to mesh with another gear, but a gear can mesh with any device having compatible teeth, such as linear moving racks.

The gear's most important feature is that gears of unequal sizes – *diameters* – can be combined to produce a mechanical advantage, so that the rotational speed and torque of the second gear are different from those of the first.

In the context of a particular machine, the term *gear* also refers to one particular arrangement of gears among other arrangements such as *first gear*. Such arrangements are often given as a ratio, using the number of teeth or gear diameter as units [6].

The majority of engineers either design from experience and after that they test their designs with prototypes, or they use engineering calculations and formulas to see design suitability.

No matter what approach they use the Engineering Reference feature in Solid Edge makes powerful calculation driven design tools more accessible which

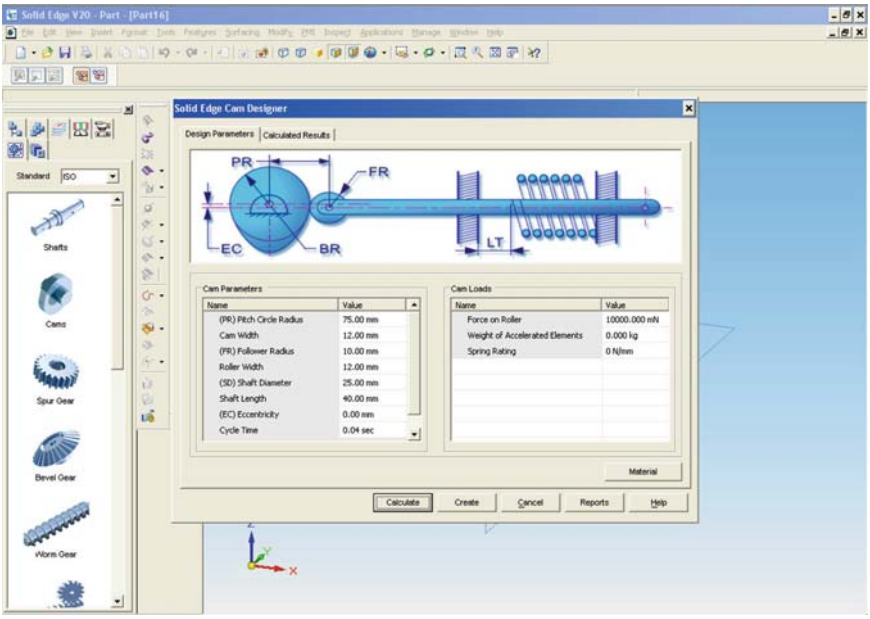

Fig. 4 The Engineering Reference box dialog

reduces the need for expensive physical prototypes. Thus, using engineering costs from a very early stage in the product lifecycle can reduce production costs.

Engineering Reference is a calculation- and formula-driven design tool for engineers and designers of machinery with design components such as shafts, cams, gears and springs (Fig. 4).

Engineering Reference will introduce engineering reference information within Solid Edge to help engineers design by function as well as form.

Even if totally integrated with Solid Edge, it is designed to preserve the engineer's design intent. It is this feature allows Solid Edge users to employ engineering calculations to create mechanically correct parts in an automatically way and reuse engineering principles based on knowledge.

There are a large variety of gears and they are used in many kinds of machines. Gears are astonishing things that can speed things up, slow things down, change direction of movement and transfer energy.

Systems design places additional emphasis on the function of a product and how its components interact with each other, which enhances productivity by reusing knowledge already captured during the design process or within existing engineering design principles [1, 2].

Engineering Reference is accessible through a new tab on the EdgeBar. The tool uses mechanical engineering rules that encapsulate machine design theory to generate parametric 3D parts. It automatically creates Solid Edge part models based on engineering formulas and application service conditions of the components.

If a design change is required, users edit the part by returning to the Engineering Reference where the operating conditions and parameters are changed and the model automatically updates. Knowledge captured in the component design is then used to quickly update the model. We can simply choose the component type from the EdgeBar and enter the relevant design parameters in dialog box [4].

Engineering Reference supports industry standards including ANSI, DIN and JIS, and it helps engineers design, select and strength-check a broad range of common machinery components, including: Cams, Shafts, Spur gears, Bevel gears, Extension springs and Compression springs.

At a simple look a gear is made up of a number of teeth, but when we take a closer look a gear is a complicated component. We will create a new part or assembly. Engineering Reference can be accessed with the help of button . When activating the Engineering Reference button, we open the Solid Edge Spur Gear Designer dialog box which has three sections.

In Fig. 5 is presented the Design Parameters section from Engineering Reference dialog box.

In Figs. 6 and 7 are presented the Calculated Results and Calculated Geometry sections from Engineering Reference dialog box.

Thus, we will activate the Create button and Solid Edge will automatic generate the spur gear 1 and spur gear 2 from Figs. 8 and 9:

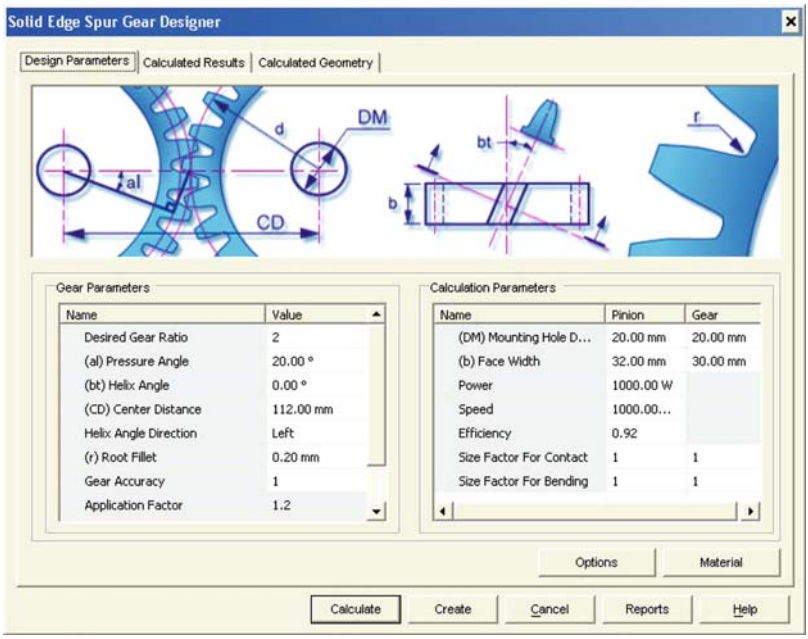

Fig. 5 The Design Parameters section

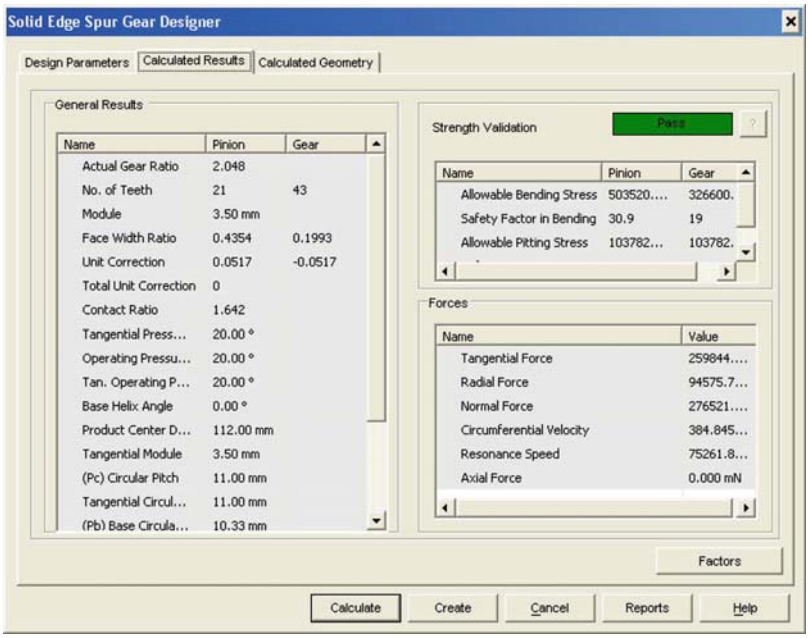

Fig. 6 The Calculated Results section

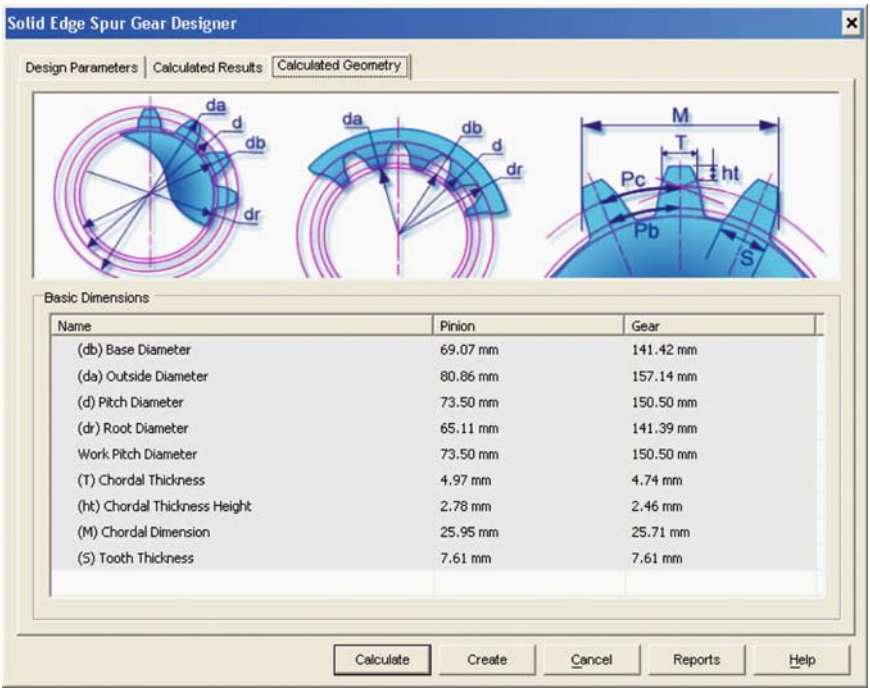

Fig. 7 The Calculated Geometry section

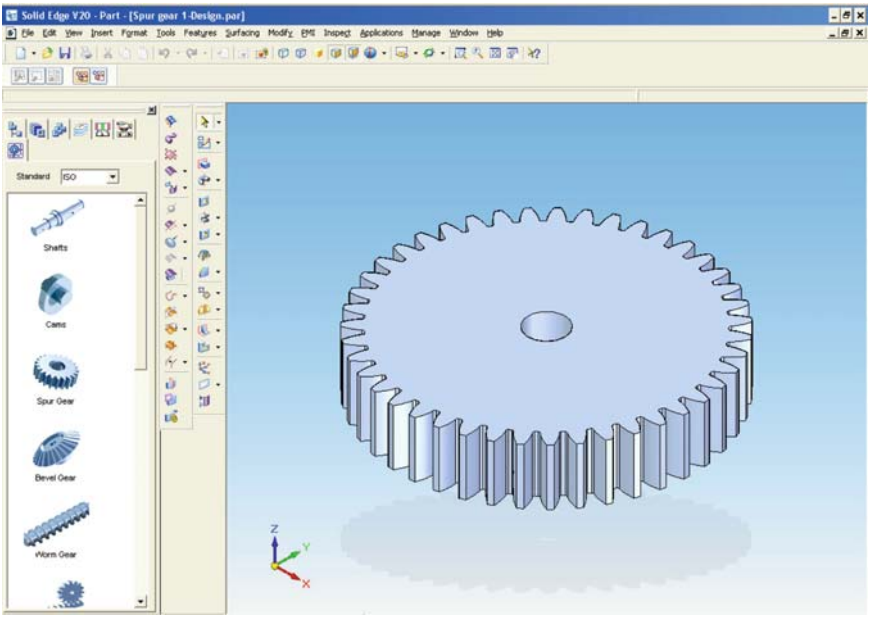

Fig. 8 The spur gear 1

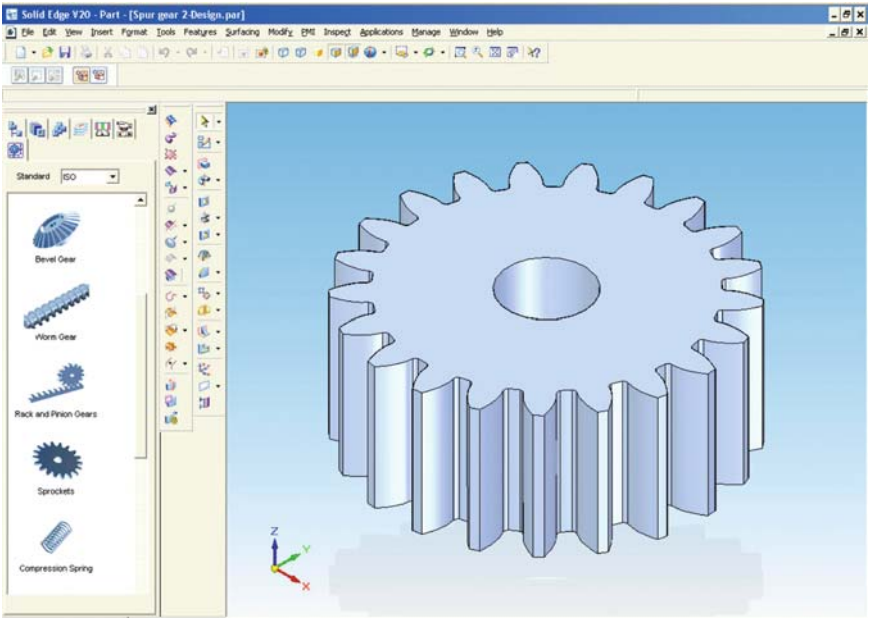

Fig. 9 The spur gear 2

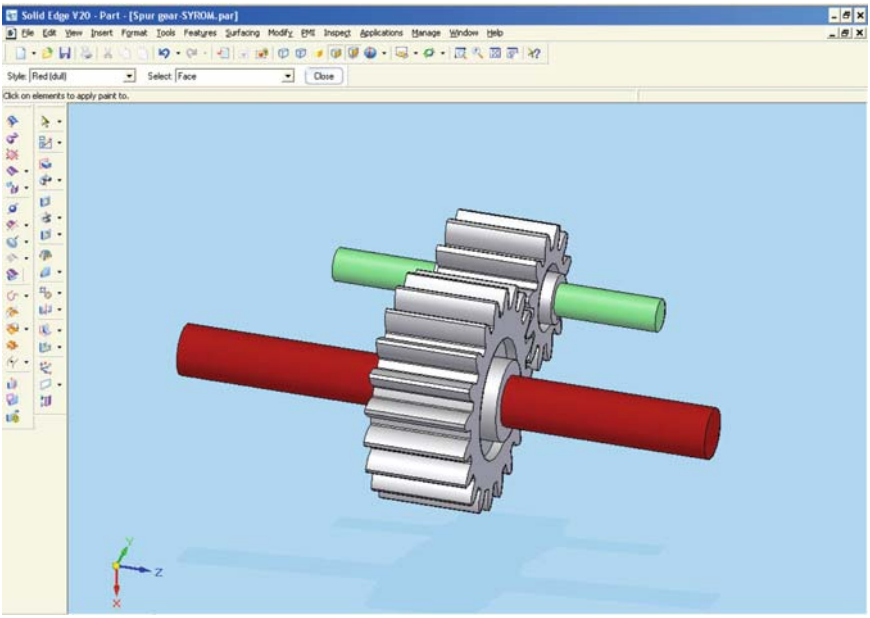

Fig. 10 The modeling of a spur gearing

When there are two gears, the former gear is called the *driver* and latter one is the *driven* gear. The *driver* gear gives the energy into the system and the *driven* gear is subject to the *driver* gears energy.

In Fig. 10 we can present the modelling of the spur gearing using Solid Edge software.

The virtual models presented, are used to investigate gear mesh. The tool uses mechanical engineering rules that encapsulate machine design theory to generate parametric 3D parts. It automatically creates Solid Edge part models based on engineering formulas and application service conditions of the components.

4 Conclusions

This paper is based on a spur gear modelling from a mathematical and virtual point of view. In the first part of the paper are presented the geometrical calculation elements of the spur gear. In the second part of the paper we point out aspects about a spur gear modelling by using CAD systems.

Solid Edge is a powerful program of graphics from CAD systems, and its results can be seen in the 3D models presented in this paper. We have also presented aspects concerning spur gear using Engineering Reference function. Even if totally integrated with Solid Edge, Engineering Reference is designed to preserve the

engineer's design intent. It is this feature allows Solid Edge users to employ engineering calculations to create mechanically correct parts in an automatically way and reuse engineering principles based on knowledge.

References

1. Ghelase, D., Daschievici, L., Haraga, G.: On the amplitudine of rigidity of worm-gearing tooth. XIV International Science and Engineering Conference Machine-Building and Technosphere of the XXI Century, ISBN 966-7907-22-8, pp. 34–38, Sevastopol, Ukraine, 17–22 September, 2007. Dieter, G.: Engineering Design. Boston. McGraw Hill (2000)
2. Ghelase, D., Daschievici, L., Haraga, G.: Optimal design of the worm-gearing with circular profil rigidity variation criterion. XIV International Science and Engineering Conference Machine-Building and Technosphere of the XXI Century, ISBN 966-7907-22-8, pp. 38–41, Sevastopol, Ukraine, 17–22 September (2007)
3. Haraga, G.: 3D Modelling a spur gearing with Solid Edge. The Annals of Dunarea de Jos University of Galati, Fascicle XIV, Mechanical Engineering (nivel B+), ISSN 1224-5615, pp. 92–95 (2006)
4. Russell Brook: Calculation-driven design tools remove the guesswork. Cadalyst (2006).
5. www.machines-direct.com
6. http://en.wikipedia.org/wiki/Gear
7. http://www.cs.cmu.edu/~rapidproto/mechanisms
8. Constantin, V., Palade, V.: Organe de maşini şi mecanisme, Vol. 2, Transmisii mecanice, Editura fundaţiei universitare "Dunărea de jos" Galaţi, ISBN 973-627-164-1
9. http://www.thermotech.com/pdf/Gears_Powertrain_Congress_Paper.pdf

Conceptual Synthesis of Speed Increasers for Renewable Energy Systems

C. Jaliu, D. Diaconescu, M. Neagoe, R. Săulescu, and M. Vatasescu

Abstract Usually, the drive trains for most of the renewable energy systems include a gearbox to increase up to 30 times the speed of the turbine shaft to the generator. The speed increasers for this kind of applications must have an acceptable efficiency, reduced overall dimensions and complexity and, therefore, a reduced technological cost. The paper objective is to develop innovative solutions of speed increasers that fulfil these requirements, by applying a conceptual design algorithm based on the VDI model. The principle solution developed in this manner is an innovative concept of the speed increaser and represents the input data for the embodiment design phase.

Keywords Conceptual design · Efficiency · Speed increaser

1 Introduction

Most small renewable energy systems drive trains include a gearbox to increase the speed of the turbine shaft to the generator. The range in which the input angular speed must be increased is 3–30. The speed increasers for wind and hydro applications must have an acceptable efficiency, reduced overall dimensions and complexity and, therefore, a reduced technological cost.

Two basic types of gearboxes are used in wind turbines applications: parallel-shaft gearboxes and planetary gearboxes [8]. In the first case, in order to obtain higher values of the transmission ratio, multiple stages are placed in series. This arrangement increases the multiplication ratio but, in the same time, increases the

C. Jaliu (✉)
Product Design and Robotics Department, Transilvania University of Braşov, Braşov, Romania

I. Vişa (ed.), *SYROM 2009*,
DOI 10.1007/978-90-481-3522-6_13,

overall dimension. Unlike the parallel-shaft gearboxes, the planetary gearboxes have some significant differences: the input and output shafts are coaxial, that reduces the radial and axial dimensions; there are sometimes multiple power branches, so the loads on each gear are reduced; the gearboxes are relatively light and compact.

The solutions for coupling the generator to the turbine in hydro systems [3] that allow an increase in speed are: belts, chains and gears. They are used with standardized turbines in the small-hydropower range where gearing is required but where other drives lack the capacity to handle the power and their cost becomes an insignificant component of total plant cost. Each type has its advantages and disadvantages:

1. Spur gears, used mainly in low power applications; there are characterized by relatively small transmission ratio, imposed by the overall dimensions.
2. Orthogonal bevel gears, used in low power applications; they can be used only with small transmission ratios; while the ratio increases the systems overall size increases, too.
3. Belt transmission, used in applications of low power; have a simple maintenance; the trapezoidal belt transmission is the most used in hydropower units, but its efficiency is relatively small. The transmissions with gear belts are efficient mainly for very small units, with capacities under 3 kW, at which the efficiency haves critical values.
4. Planetary transmission: the planetary transmission applied in precessional variant is compact and with a medium efficiency; it is used in the small hydro developed on Prut river.

The paper objective is to develop innovative solutions of speed increasers that reduce the disadvantages of the existent options. The concept of the speed increaser is developed using a conceptual design algorithm [1]. The algorithm is based on the VDI model [7] and consists in the following steps: (1) Requirements list establishment; (2) Global function establishment; (3) Global function description by structures of sub-functions; (4) Solving structures generation by: solving the sub-functions, sub-solutions composition and elimination of inadequate solution; (5) The best solving structure selection by evaluation. The final solution is an innovative concept of speed increaser, which is intended to be used in a small hydropower station. Similar, the algorithm can be applied to develop a speed increaser for wind turbines.

2 Requirements List

The first step in the design process is establishment of the list of requirements, taking into account the turbine and the generator prerequisites. From the requirements list of the hydropower station [3], the following requirements (main objectives) regarding the speed increaser come out [4, 5]:

1. Multiplication ratio of 10 ± 10%
2. Efficiency over 80%
3. Energy source: water
4. Not requiring a particular manufacturing process

These four main requirements are associated to the following optimization objectives, listed in the order of importance:

(A) Minimization of friction losses
(B) Minimization of radial overall dimension
(C) Minimization of axial overall dimension
(D) Minimization of complexity degree
(E) Minimization of manufacturing costs

These optimization (secondary) objectives are the technical-economic evaluation criteria needed in the identification of the principle solution.

3 Identification of the Speed Increaser Function

The speed increaser global function is a sub-function of the small hydropower station global function; its VDI symbolical structure (of 7M-6E-8I order), illustrated in Fig. 1, contains the following sub-functions:

M – input material (water/stream)
M* – output material (water/stream)
E_1* – lost mechanical energy
E_2* – lost electric energy
Eutila* – useful electric energy

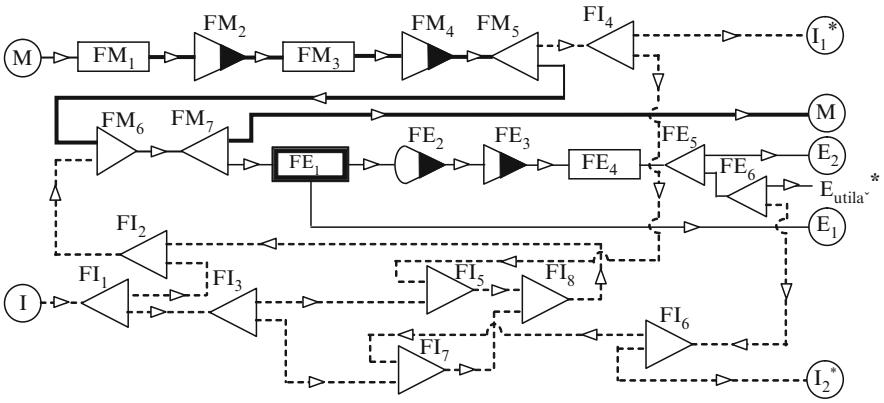

Fig. 1 The global function of a small hydropower station. The structure of functions of 7M-6E-8I order, in a symbolic representation

I – input information (instructions for use, command-control programs, critical values of the characteristic quantities etc.)

I_1* – output information regarding the material flow

I_2* – output information regarding the energy flow

FM_1 – material transmission

FM_2 – transformation of kinetic energy into potential energy

FM_3 – material transmission

FM_4 – incomplete transformation of potential energy into kinetic energy

FM_5 – material flow ramification

FM_6 – material – information connection of stop-start command type

FM_7 – transmission of material flow with its ramification in output material and mechanical energy

FE_1 – transmission of mechanical energy with speed multiplication

FE_2 – transformation of mechanical energy into electric energy

FE_3 – modification of electric energy parameters

FE_4 – transmission of electric energy

FE_5 – electric energy ramification into useful electric energy and lost energy

FE_6 – electric energy ramification into energy and information regarding the electric energy state parameters

FI_1 – ramification of information available in start command (when the instructions of use are fulfilled) and critical values of the parameters that command the system stopping

FI_2 – connection of start – stop commands with the execution of the last command

FI_3 – ramification of information into the material critical value (water pressure) and critical value of the provided electric energy

FI_4 – ramification of the information regarding the material flow into registered information (output) and the current value of the characteristic state quantity

FI_5 – connection and comparison of critical and current values for the state quantity of the material flow and the stop command issuing when the two values become equal

FI_6 – ramification of information regarding the current value for the state quantity of the energy flow into current value and registered value (output)

FI_7 – connection and comparison of the critical and current values for the state quantity of the energy flow and stop command issuing when the two values become equal

FI_8 – connection of stop commands and the system stop signal issuing

4 Detailing of the Speed Increaser Function

The main function of the speed increaser is to transmit and to modify the parameters of the mechanical energy. The FE_1 sub-function (Fig. 1), which designates the speed increaser global function, is illustrated, in detail, in Fig. 2.

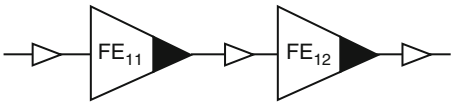

Fig. 2 The speed increaser structure of functions, in a symbolic representation

The speed increaser structure of functions contains the following sub-functions:

$FE_{1.1}$ and $FE_{1.2}$ – transmission and modification of mechanical energy parameters.

The speed increaser solving structures will be generated based on the structure from Fig. 2; this stage contains: (1) generation of the solving structural variants and (2) establishment of the solving structures, by the kinematical configuration (synthesis) of the obtained variants and by the elimination of the variants whose technical characteristics don't fulfil the requirements list, quantitatively.

5 Development of the Solving Structures

Further, the sub-functions of the speed increaser will be analyzed in order to generate the solving structures.

The development of reliable structures assumes the existence of two essential phases, as follows:

5.1 Development (Synthesis) of the Structural Solving Variants

The technical solutions [1, 2, 6] that accomplish the sub-functions from Fig. 2 are systematized in the morphological matrix from Table 1. By means of this matrix, there can be generated the solving structural variants, through a compatible composition of the potential solutions from Table 1.

Twenty-five distinct structural solving variants are obtained combining the solutions from Table 1. Five examples of structural variants with technical application are systematized in Table 2: SR1, . . ., SR25.

The structural schemes of the five variants identified in Table 2 are represented in Fig. 3. The internal transmission ratio (i_0) and the internal efficiency (η_0) for each of the five variants are also presented in Fig. 3. The solving variants developed by means of the morphological matrix fulfil only qualitatively the criteria imposed by the requirements list. Obviously, the solving structures of the function FE1 will be nominated by the variants that achieve the requirements, quantitatively.

In order to establish the solving structures, the technical characteristics of the developed solutions are further determined. The solving variants that fulfil the requirements become solving structures.

Table 1 Morphological matrix for the development of solving structural variants

Sub-function	Potential principle solutions				
$FE_{1.1}$ transmission	1.1 Internal involute gear pair	1.2 External involute gear pair	1.3 Internal cycloid gear pair	1.4 External cycloid gear pair	1.5 Harmonic gear pair
$FE_{1.2}$ modification	2.1 Internal involute gear pair	2.2 External involute gear pair	2.3 Internal cycloid gear pair	2.4 External cycloid gear pair	2.5 Harmonic gear pair

Table 2 Examples of structural solving variants

Solving variant	Speed increaser solution
SR1	1.1 + 2.2
SR2	1.1 + 2.1
SR18	1.4 + 2.3
SR19	1.4 + 2.4
SR25	1.5 + 2.5

5.2 Establishment of the Solving Structures

In order to establish the solving structures, firstly it is made the synthesis of the number of teeth from the condition of fulfilling the transmission ratio i. Then, the efficiencies of the proposed speed increasers are obtained on the basis of the gear pairs internal efficiencies.

The synthesis of the teeth numbers is performed imposing the value of the multiplication ratio i (10, ±10%); afterwards, the set of teeth numbers that correspond to the multiplication ratio is identified.

The following assumptions are considered in the synthesis of the teeth numbers: the teeth number of one sun gear is maintained constant; the direct relations between the satellite gears and the sun gear with constant teeth number is imposed (Figs. 3b and d); different values are given to the teeth numbers of the second sun gear in order to get a value of the multiplication ratio (i) closer to the imposed one.

The following relations for the multiplication ratio and efficiency can be written:

- For the variant from Fig. 3a:
- The multiplication ratio (i) is:

$$i = i_{H1}^{3} = \frac{\omega_{H3}}{\omega_{13}} = \frac{-\omega_{3H}}{\omega_{1H} - \omega_{3H}} = \frac{1}{1 - i_0} \tag{1}$$

- The efficiency (η) is:

$$\eta = \eta_{H1}^{3} = \frac{-\omega_{13} T_H}{\omega_{H3} T_1} = \frac{-\frac{T_1}{T_H}}{i_{H1}^{3}} = \frac{1 - i_0}{1 - i_0 \eta_0^{x}} \tag{2}$$

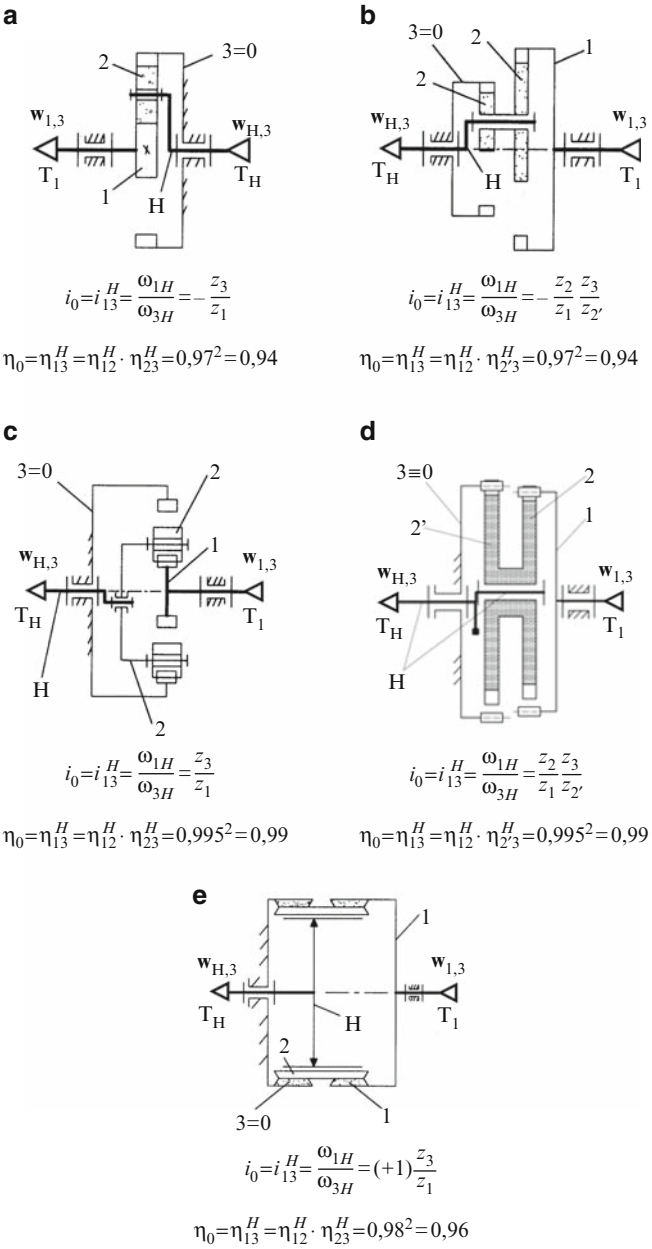

Fig. 3 Development of the solving structures through a combination of the two sub-functions (see Table 1)

where

$$x = \text{sgn}(\omega_{1H} T_1) = \text{sgn}\left(\frac{\omega_{1H} T_1}{-\omega_{13} T_1}\right) = \text{sgn}\left(\frac{\omega_{1H}}{\omega_{3H} - \omega_{1H}}\right) = \text{sgn}\left(\frac{i_0}{1 - i_0}\right) \quad (3)$$

- Taking into account that the input and output parameters of each solving variant from Fig. 3b–e correspond, the multiplication ratio (i) and the efficiency are given by the following relations:

$$i = i_{1H}^3 = \frac{\omega_{13}}{\omega_{H3}} = \frac{\omega_{1H} - \omega_{3H}}{-\omega_{3H}} = 1 - i_0 \quad (4)$$

$$\eta = \eta_{H1}^3 = \frac{-\omega_{H3} T_H}{\omega_{13} T_1} = \frac{-\frac{T_H}{T_1}}{i_{1H}^3} = \frac{1 - i_0 \eta_0^x}{1 - i_0} \quad (5)$$

where

$$x = \text{sgn}(\omega_{1H} T_1) = \text{sgn}\left(\frac{\omega_{1H} T_1}{\omega_{13} T_1}\right) = \text{sgn}\left(\frac{\omega_{1H}}{\omega_{1H} - \omega_{3H}}\right) = \text{sgn}\left(\frac{i_0}{i_0 - 1}\right) \quad (6)$$

The results of the numerical simulations for the multiplication ratios and efficiencies of the structural solving variants (Fig. 3) are presented in Fig. 4. The curves representing the multiplication ratio are obtained for different values of the gears teeth numbers. The grey areas from Fig. 4 represent the requirements regarding the multiplication ratio (i = 10 ± 10%).

6 Evaluation of the Solving Structures

Taking into account the results of the numerical simulations from Fig. 4 and the evaluation criteria included in the requirements list, two of the structural variants (Fig. 3b and e) can be eliminated due to their efficiency, which is smaller than 80%.

The technical characteristics of the remaining solving structures and the technical-economic criteria are systematized in Table 3. The fulfilment of these criteria by each structure is appreciated with ratings from 1 to 10.

According to the evaluation ratio R, obtained by shifting (see Table 3), all the analyzed solving structures have the same score. In the premise that the five criteria are of different weights (fine evaluation), the structures are reordered; with this aim, the absolute (W_k) and relative (w_k) weight coefficients were calculated by means of FRISCO formula (see Fig. 5) [1, 2]

From these evaluations and based on Table 3 and Fig. 5, it obviously outcomes that the principle solution of the speed increaser is designated by the structure SR19 (its technical performances are presented in Fig. 7).

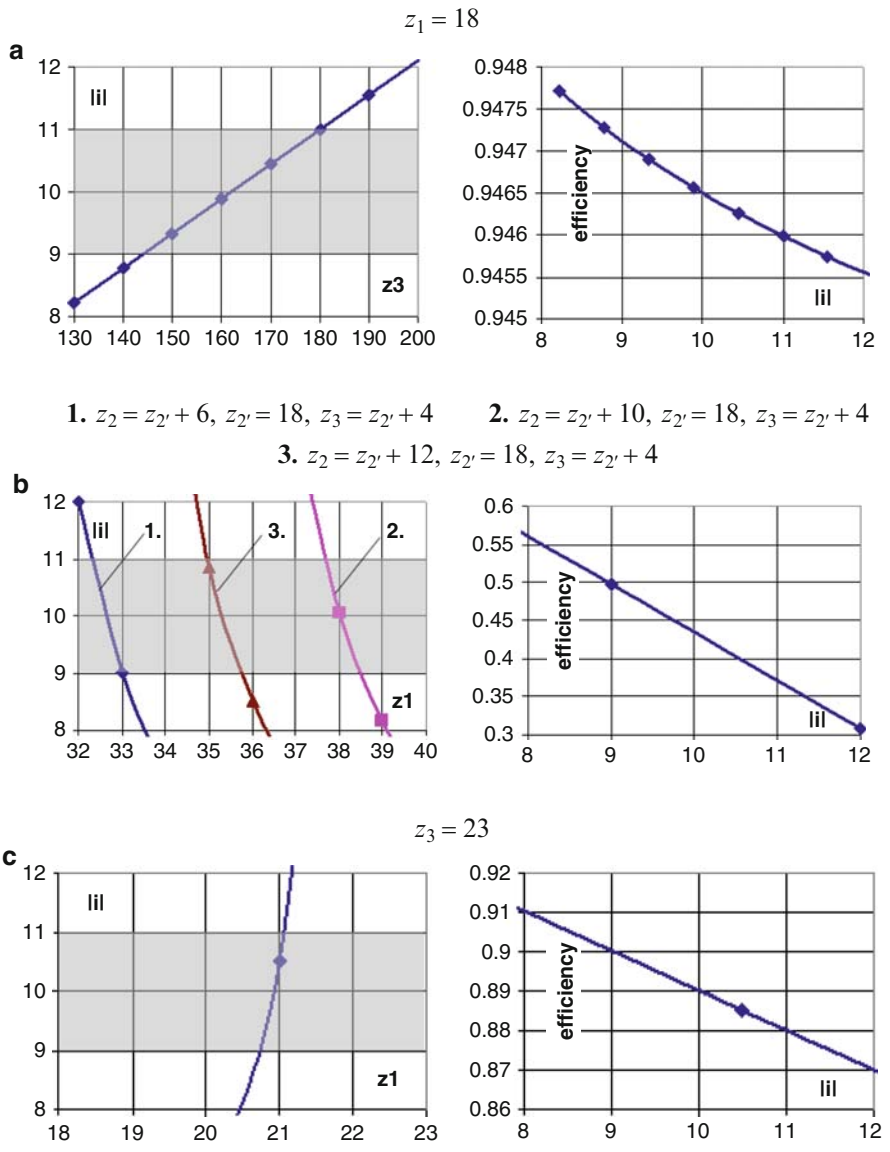

Fig. 4 (continued)

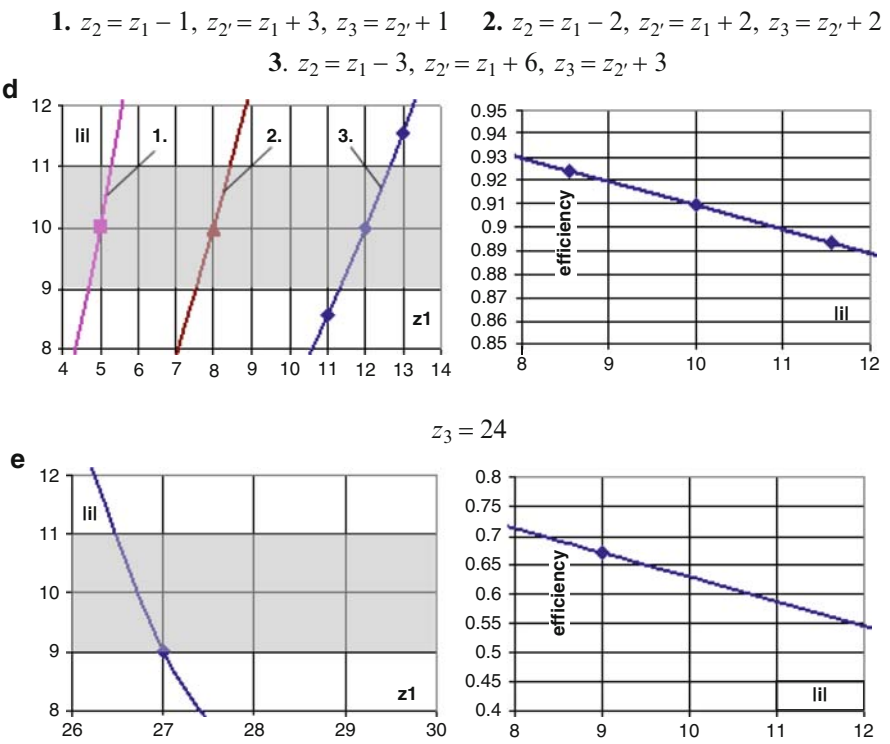

Fig. 4 Numerical simulations of the multiplication ratios and efficienies considering different values of the gears teeth numbers (1, 2, 3), for the 5 solving variants from Fig. 3

Table 3 Ordering the solving structures

Solving structure	SR1	SR18	SR19		
Fig. 3	a	c	d		
			I	II	III
TECHNICAL CHARACTERISTICS					
Teeth numbers			$z_1 = 5$	$z_1 = 8$	$z_1 = 12$
	$z_1 = 18$	$z_1 = 21$	$z_2 = 4$	$z_2 = 6$	$z_2 = 9$
	$z_3 = 160$	$z_3 = 23$	$z_{2'} = 8$	$z_{2'} = 10$	$z_{2'} = 15$
			$z_3 = 9$	$z_3 = 12$	$z_3 = 18$
Multiplication ratio (lil)	10	10.5		10	
Efficiency of the fixed axes gear pair (η_0)	0.94	0.99		0.99	
Transmission efficiency (η)	0.946	0.885		0.91	
TECHNICAL-ECONOMIC CRITERIA					
Minimization of the friction losses	7	9		9	
Minimization of the radial overall dimensions	7	8		9	
Minimization of the axia; overall dimensions	9	8		7	
Minimization of the complexity degree	9	8		8	
Minimization of the costs	9	8		8	
$\Sigma = 41$		41		41	
$R = \Sigma/(5 \times 10) = 0,82$		0.82		0.82	
Place 1		1		1	

k	Criterion / Criterion	A	B	C	D	E	P_k	L_k	S_k	W_k	w_k
1	A	0,5	1	1	1	1	4,5	1	4	5,2	0,5
2	B	0	0,5	1	1	1	3,5	2	3	2,85	0,27
3	C	0	0	0,5	1	1	2,5	3	2	1,55	0,15
4	D	0	0	0	0,5	1	1,5	4	1	0,73	0,07
5	E	0	0	0	0	0,5	0,5	5	0	0,15	0,01
									Sum	10,48	1,00

Fig. 5 Establishment of the absolute (W_k) and relative (w_k) weight coefficients by means of FRISCO formula

Fig. 6 Reordering of the solving structures

		SR1		SR18		SR19	
Crit.	w_K	N_K	$w_K \cdot N_K$	N_K	$w_K \cdot N_K$	N_K	$w_K \cdot N_K$
A	0,5	7	3,5	9	4,5	9	4,5
B	0,27	7	1,89	8	2,16	9	2,43
C	0,15	9	1,35	8	1,2	7	1,05
D	0,07	9	0,63	8	0,56	8	0,56
E	0,01	9	0,09	8	0,08	8	0,08
Sum		41	7,46	41	8,5	41	8,62
Place			3		2		1

Fig. 7 The speed increaser developed using the proposed conceptual design algorithm

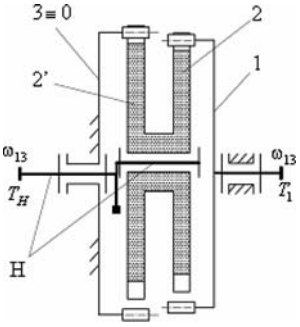

Fig. 8 The efficiencies of the solving variants from Fig. 3a, c and d

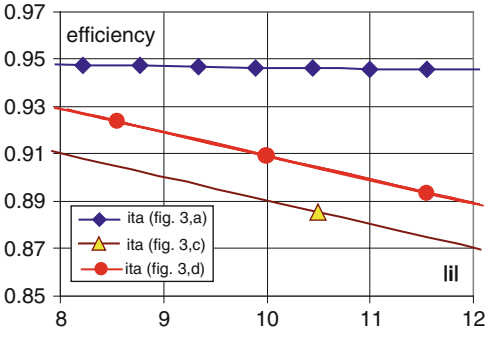

Due to the fact that the difference between the first and the second place (see Fig. 6) is of only 0,12 points and that all variants fulfil the requirement regarding the multiplication ratio, the efficiencies of the remaining three variants were analyzed comparatively; thus, the diagrams representing the efficiencies of variants SR1, SR18 and SR19 in terms of the multiplication ratio are presented in Fig. 8.

From Fig. 8 it outcomes that the best efficiency is obtained by SR1 (Fig. 3a), but its radial dimensions are too big and, therefore, the variant can be eliminated (see Table 3).

The efficiency of the other two solutions SR18 and SR19 fulfil the requirement (efficiency over 80%), SR19 being characterized by a better efficiency, reduced complexity and low manufacturing costs.

7 Conclusions

- An algorithm for conceptual design is presented in the paper, based on the requirements list and the global function of the small hydropower station. The algorithm is applied with the aim to identify the solving structures and, thus, to develop a transmission to be used as speed increaser.
- The structure of the algorithm contains:
- Requirements list establishment
- Global function establishment
- Global function description by structures of sub-functions
- Solving structures generation by: solving the sub-functions, sub-solutions composition and elimination of inadequate solution
- The best solving structure selection by evaluation
- In order to establish the solving structures, the synthesis of the gears teeth numbers and the transmission efficiency are presented in the paper. The numerical simulations made for the five solving variants form a data base that can be used in choosing the proper solution for given values of the multiplication ratio, efficiency and overall dimensions.
- The developed principle solution of the speed increaser represents an input data for the embodiment design phase.
- As for the concept developed using this algorithm, the same multiplication ratio and efficiency can be obtained for different combinations of gears teeth numbers, the most appropriate solution for a specific application has to be chosen in a subsequant step, namely in the embodiment design stage.

References

1. Diaconescu, D.: Products Conceptual Design (Romanian). Transilvania University of Brasov, Romania (2005)

2. Dieter, G.: Engineering Design. McGraw Hill, Boston (2000)
3. Harvey, A.: Micro-hydro Design Manual. ITDG Publishing House, London (2005)
4. Jaliu, C., Diaconescu, D., Săulescu, R.: Speed multipliers for renewable energy systems-hydro and wind. In: ICREPQ'08, Santander, Spania (2008)
5. Jaliu, C., Diaconescu, D.V., Neagoe, M., Săulescu R.: Dynamic features of speed increasers from mechatronic wind and hydro systems. In: EUCOMES 08, Casino, Italia, pp. 355–373. Springer, The Netherlands (2008)
6. Neagoe, M., Diaconescu, D.V., Jaliu, C., Pascale, L., Săulescu, R., Siscă, S.: On a new cycloid planetary gear used to fit mechatronic systems of RES. In: OPTIM 2008, IEEE Catalogue Number 08EX1996, Braşov, pp. 439–449 (2008)
7. V.D.I. (Verein Deutscher Ingenieure)-Richtlinien 2221 and 2222
8. Manwell, J.F., a.o.: Wind Energy Explained. Wiley, New York (2005)

Mobile Minirobots Structures

O. Tătar, D. Mândru, and A. Aluţei

Abstract In this paper, the author's most representative contributions in the field of mobile minirobots mobility structures are emphasized. The first part of the paper presents an in-pipe inspection and exploration minirobot. The main characteristic of the mentioned minirobot is an adaptable structure, based on linkage mechanisms. The second part of the paper presents an omnidirectional minirobot with conventional wheels. For each one of the three sets of wheels, the omnidirectional minirobot uses a synchronous transmission that allows a 360° rotation around its vertical axis. Movement transmission from the DC motors to the wheels is accomplished using gear mechanisms – three for steering and three for movement. The control and steering of the minirobot can be done from a PC or by using a joystick.

Keywords In-pipe minirobot inspection · Mobile minirobots · Omnidirectional minirobot

1 Introduction

Over the last decade, mobile robots have demonstrated the ability to operate in severe environments and perform hazardous tasks. The inspection of pipes may also be relevant for improving security and efficiency in industrial plants. The specific operations as inspection, maintenance, cleaning etc. are expensive thus the application of the robots appears to be one of the most attractive solutions [2, 3].

The term omnidirectional is used to describe the ability of a system to move instantaneously in any direction from any configuration. Omnidirectional robotic

O. Tătar (✉)
Department of Mechanisms, Precision Mechanics and Mechatronics, Technical University of Cluj-Napoca, Cluj-Napoca, Romania

I. Vişa (ed.), *SYROM 2009*,
DOI 10.1007/978-90-481-3522-6_14,

platforms have vast advantages over a conventional design in terms of mobility in congested environments. They are capable of easily performing tasks in environments congested with static and dynamic obstacles and narrow aisles. These environments are commonly found in factory workshops, offices, warehouses, hospitals and elderly care facilities. A large variety of omnidirectional robots are presented in specialized literature [1]. These robots can be divided in two categories: robots with special wheels and robots with conventional wheels. Usually, an omnidirectional robot has three or more of these types of wheels.

2 The In-Pipe Developed Minirobot

In Fig. 1, it's given the first constructive version of an in-pipe inspection minirobot, which was designed, modeled and developed.

The minirobot contains three linkage mechanisms (Fig. 2a), symmetrically placed along the longitudinal axis of the minirobot [4].

In the minirobot's structure, there is a mechanism (Fig. 2b), composed of a translation input element, and two structural (Assur) groups RRR (EmT(1) + RRR (2,3) + RRR(4,5)). The components of the minirobot are (Fig. 3a): 1 – helical spring, 2 – translation element, 3 – worm wheel, 4 – worm gear, 5 – worm, actuator support, 6 – actuator.

The force that the minirobot's mechanisms exert on the pipe walls is generated using an extensible spring. The helical spring placed on the central axis assures the repositioning of the structure, in case of pipe diameter variation.

The weight of the minirobot (the weight of the power feeding wires is also considered) is 978 g. The wheels have a radius of $r = 50$ mm and a length of 17 mm; the linkage elements have the following lengths: $h_1 = 30$ mm, $h_2 = 70$ mm, $h_3 = 135$ mm. The rear wheels are driven by three DC SANKO motors, through reduction transmissions. The actuation of the drive wheels is done using three worm gears with the number of teeth $z_1 = 1$, $z_2 = 52$, the module m = 0.6 mm, the worm gear thread inclination angle $\theta = 4°$, the normal gears and the inclination angle of the gear's teeth $\beta = 4°$. The drive DC motors can be powered with a voltage

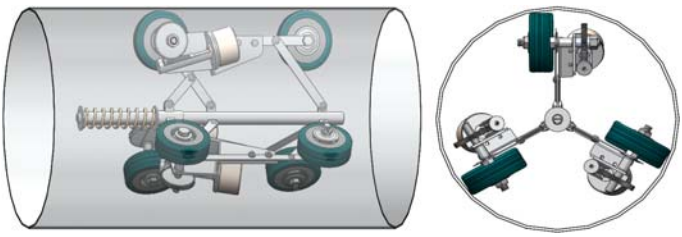

Fig. 1 The 3D model of the in pipe minirobot

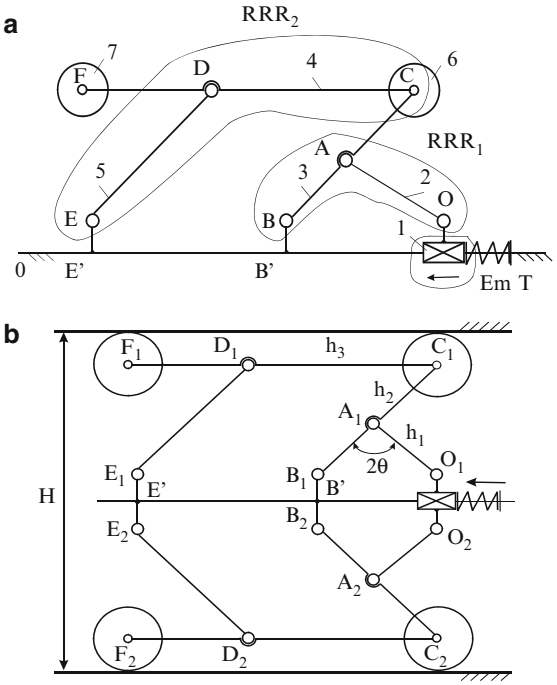

Fig. 2 The elementary mechanism (**a**) and the structural scheme of the minirobot (**b**)

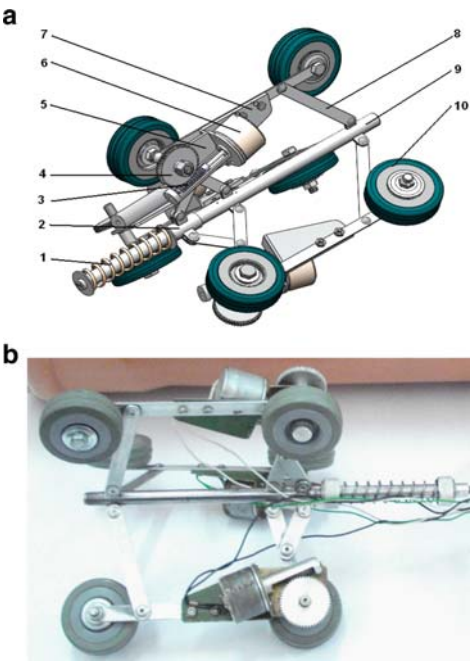

Fig. 3 The components of the minirobot (**a**) and the photography of the minirobot (**b**)

between 3–12 V. At a supply of 4 V the drive wheel's speed is of 40 rot/min and for 6 V is 60 rot/min.

A very important design feature of this minirobot is it's adaptability to the inner diameters of the pipes. This minirobot has movement capacities for inspection in pipes with diameters ranged between 140 and 200 mm, placed in horizontal or vertical configurations. The adaptability of the in-pipe minirobot to different pipe diameters is due to the mechanisms from it's structure. Figure 4 presents the testing of the in-pipe minirobot with diameters between Φ150 and Φ190 mm.

The structure presented above allows the use of a CCD camera or other devices needed for pipe inspection (remote-controlled laser measuring systems, sensors).

In Fig. 5 the minirobot uses a wireless video mini-camera for in-pipe inspection mounted inside of a protection system composed of a case with reels and two led's for light generation inside a pipe (Fig. 5b).

Depending on the applications, to ensure a bigger torque, the minirobot's motor and transmission can be easily changed (Fig. 6).

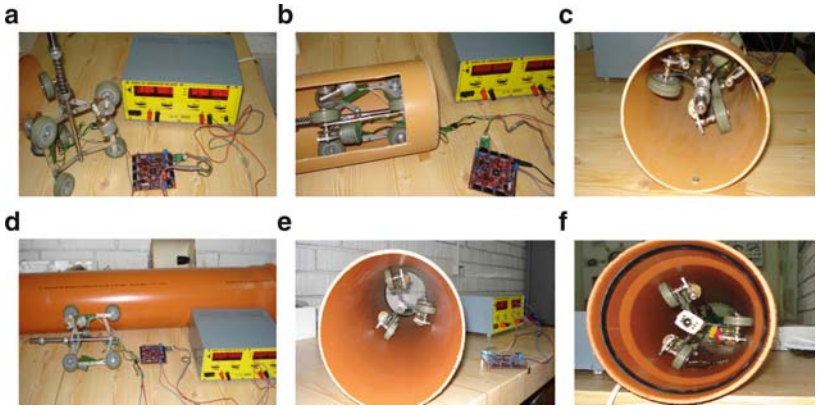

Fig. 4 The in-pipe minirobot with diameters of Φ150 and Φ190 mm testing of the prototype -

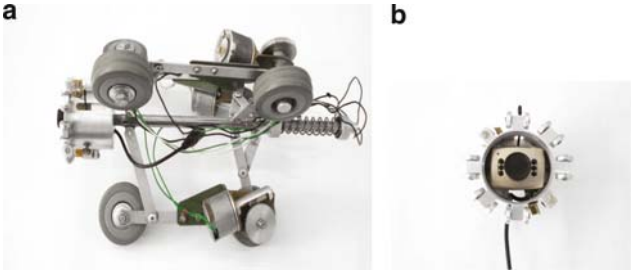

Fig. 5 The minirobot using the video mini-camera (**a**) and the protection system (**b**)

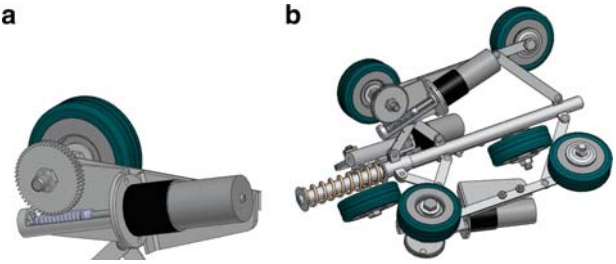

Fig. 6 The 3D model of the minirobot in pipe using a motor and reducer

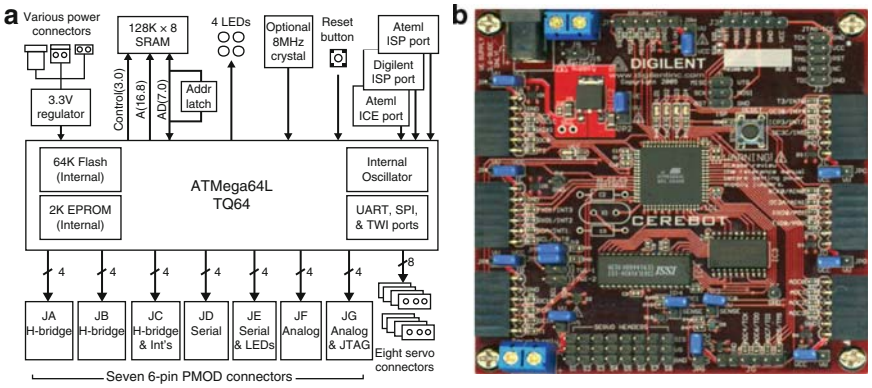

Fig. 7 The CEREBOT platform: (**a**) block sketch; Photo of the circuit board (**b**)

2.1 The Power and Control System

The hardware component consists of a CEREBOT motherboard (Fig. 7) and a few additional peripheral modules, all developed by Digilent [7].

3 The Developed Omnidirectional Minirobot

The omnidirectional minirobot presented in this part has three pairs of conventional wheels. The transmission from the D.C. motors to the robot's wheels is done using geared mechanisms: three for steering and another three for displacement. The steering of the minirobot can be done from a computer or using a joystick.

The minirobot has a platform placed on three supporting elements. At the base of each supporting element there is a pair of conventional wheels driven by a worm gear. Two D.C. motors are placed on the platform: for driving and steering; the motors use geared systems composed of cylindrical gears with straight teeth.

The minirobot weights 900 g, has a high of 200 mm, a width of 160 mm and the wheels have a radius of 45 mm.

The 3D model of the omnidirectional minirobot is presented in Fig. 8a [5, 6]. A picture of the developed prototype is presented in Fig. 8b.

For driving, the minirobot has in its structure three identical geared mechanisms. The kinematics scheme of one of this mechanism is presented in Fig. 9. The following annotations are used in the said scheme: n_{M1} – the motor's maximum rpm ($n_{M1} = 4{,}750$ rpm); n_R – wheel rpm, $Z_1 = 10$; $Z_2 = 50$; $Z_3 = 20$; $Z_4 = 40$; $Z_5 = 40$; $Z_7 = 20$ – gear number of teeth, $Z_6 = 1$ – worm gear number of threads. Another

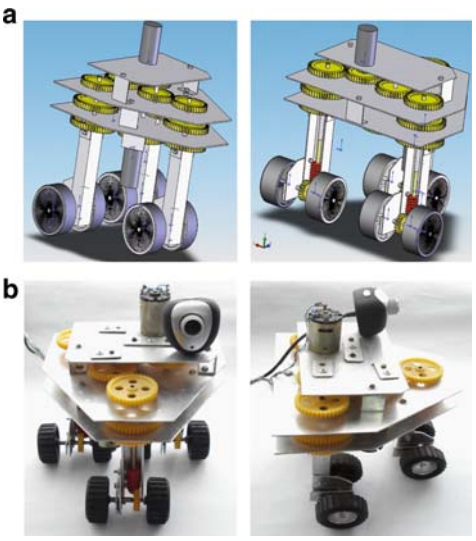

Fig. 8 The 3D Solid Works model of the designed minirobot (**a**); The picture of the omnidirectional minirobot (**b**)

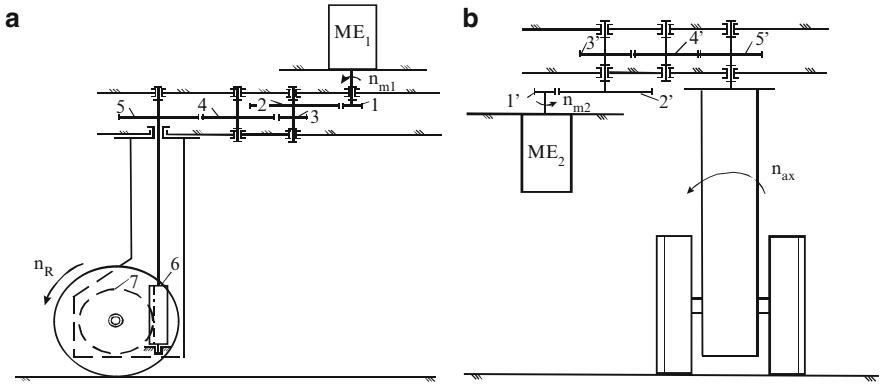

Fig. 9 The structural scheme of a drive mechanism (**a**) The structural scheme of a steering mechanism (**b**)

three identical geared mechanisms are used for steering. The kinematics scheme of one of this mechanism is presented in Fig. 9b. The following annotations are used in the said scheme: n_{M2} – the maximum rpm of the steering motor (n_{M2} = 4,750 rpm); n_{ad} – steering axle rpm; $Z'_1 = 10$; $Z'_2 = 50$; $Z'_3 = 10$; $Z'_4 = 30$; $Z'_5 = 50$; gear number of teeth.

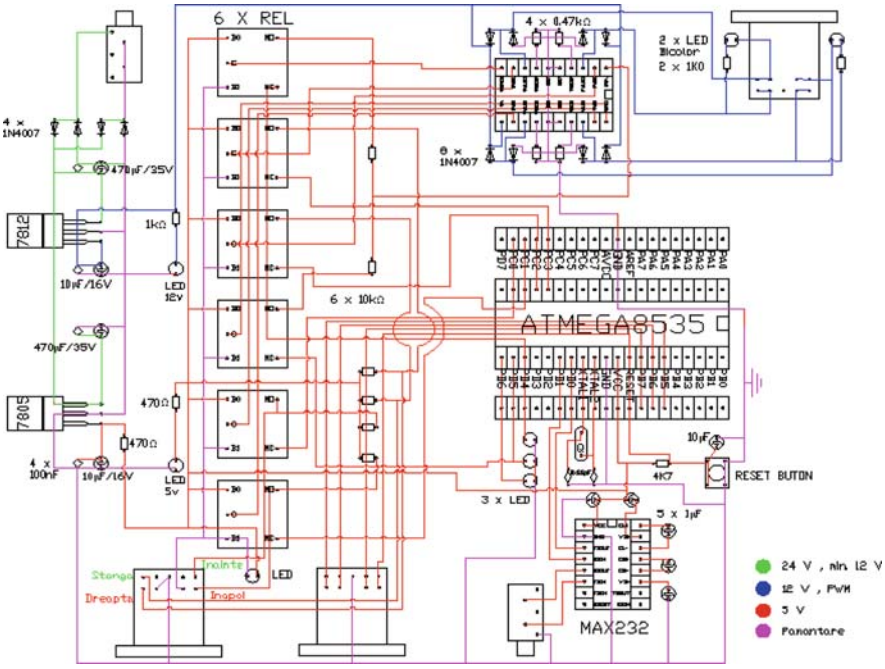

Fig. 10 Control system scheme

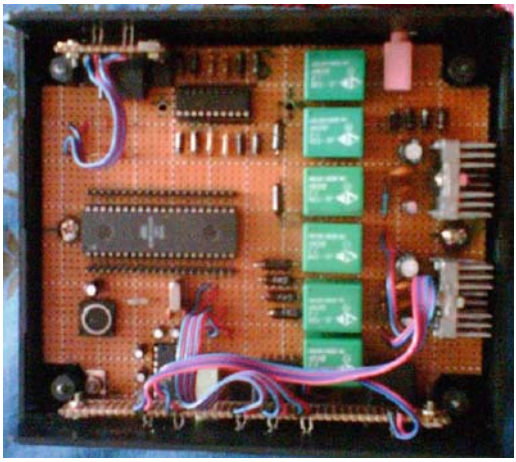

Fig. 11 The control system photography

The steering of the minirobot can be done from a PC or by using a joystick. These minirobots are not energetically autonomous, being powered from a voltage source trough wires. The minirobot's autonomy can be increased by eliminating the wires used for power supply and replacing them with accumulators.

The scheme of the control system used for the minirobot is presented in Fig. 10 and a picture of this system is given in Fig. 11 [6].

4 Conclusion

In the present paper, we proposed a wheeled type in-pipe minirobot defined by an adaptable structure based on linkage mechanisms and an omnidirectional minirobot.

The In-pipe minirobot is defined by a simple structure and kinematics, small number of actuators, light weight, low power consumption.

The omnidirectional minirorobot has conventional wheels and uses a synchronous geared transmission. In the future, the in-pipe inspection minirobot will be used as a driving module, part of modular inspection and exploring systems. Also, for the omnidirectional minirobot the problem of the energetic autonomy and control will be resolved.

Acknowledgments This work is supported by PNII – IDEI Project, ID 1056: *Modelling, simulation and development of robotic system families used for inspection and exploration.*

References

1. Diegel, O., Badve, A., Bright, G., Potgieter, J., Tlale, S.: Improved Mecanum wheel design for omnidirectional robots. Proceedings of 2002 Australasian Conference on Robotics and Automation, Auckland, 27–29 November 2002, pp. 117–122
2. Doroftei, I., Horodincă, M., Mignon, E., Preumont, A.: A new concept of in-pipe robot. Proceedings of the 8th IFToMM International Symposium on Theory of Machines and Mechanisms, Bucharest, Romania, August 28–September 1, 2001, pp. 83–88
3. Roh, S.G., Ryew, S.M., Choi, H.R.: Development of differentially driven in-pipe inspection robot for underground gas pipelines. In: Proceedings of International Symposium on Robotic, pp. 65–170 (2001)
4. Tătar, O., Mândru, D., Roş, V.: Agricultural pipe networks maintenance using robotic systems. Proceedings of the 35 International Symposium Actual Tasks On Agricultural Engineering, Opatija, Croatia, 2007, pp. 187–197
5. Tătar, O., Mândru, D.: Design of the mobile minirobots structures. Proceedings of IEEE International Conference on Automation, Quality and Testing, Robotics (AQTR 2008), paper R-M1-2, Cluj-Napoca, 2008, 1-4244-2577-8/08 IEEE, IEEE Catalog number CFP08AQT-CDR, ISBN: 978-1-4244-2577-8, Library of Congress 2008904446
6. Tătar, O., Mândru, D., Lungu, I.: Minirobot omidirectional. The 2nd International Conference Computational Mechanics and Virtual Engineering COMEC 2007, Brasov, Romania, 11–13 October 2007, pp. 203–206
7. http://www.digilentinc.com/

Synthesis of Linkages for Tracking Systems with Increased Angular Stroke

I. Vişa, D. Diaconescu, V. Popa, and B. Burduhos

Abstract Bi-axial Sun tracking systems are used to maximize the amount of the solar direct radiation that falls normally on the photovoltaic modules. Depending on the angular stroke, the axes of these systems can be driven by mechanical transmissions such as a worm-gear speed reducer, triangle linkages with linear actuators, rotary actuators etc. Considering the specific kinematical requirements and the minimum transmission angles, the paper presents the synthesis of two four-bar linkages that can be successfully used to increase the angular stroke of linear actuator. The proposed system is composed of a planar linkage and a spatial four-bar linkage for an azimuth tracking PV platform and a proper synthesis algorithm is proposed.

Keywords Angular stroke · Azimuthally tracked PV platform · Four-bar linkage · Solar tracking system · Transmission angle

1 Introduction

Mechanical Sun tracking systems, single-axis or dual-axis type, are used for maximizing the solar direct radiation that falls normally on the photovoltaic modules. Thus a 20%...50% energetic gain can be achieved as outlined in [2–4, 6, 7].

In the case of usual dual-axis azimuth tracking PV systems, one axis (of *type I*) has an angular stroke below 90° and the other one (of *type II*) has an angular stroke much higher than 90° the axis of type I consists in a revolute joint driven by a triangle linkage with linear actuator, that is further named *deformable triangle linkage*.

I. Vişa (✉)
Department of Product Design and Robotics, Transilvania University of Braşov, Braşov, Romania

I. Vişa (ed.), *SYROM 2009*,
DOI 10.1007/978-90-481-3522-6_15,

The axes of type II imply driving a revolute joint usually by a worm speed reducer or other gear reducer with a high speed ratio. Though it ensures larger angular strokes, azimuth tracking by a gear reducer has still significant disadvantages, namely: difficult control of the backlashes and stability, lower efficiency of the worm reducer (Figs. 1, 2, and 3), higher technological cost and complexity.

Fig. 1 A Deger azimuth tracker [10]

Fig. 2 An Imo Slew Drive [11]

Fig. 3 Feina SF20 azimuth tracker [12]

At the same time, *the deformable triangle linkages*, used to drive axes of type II, provide a relative reduced angular stroke (mostly about 120°...130°), due to the transmission angles limitation [5, 9].

The paper presents the kinematical synthesis of two azimuth tracking linkages that can increase the tracking angular stroke up to about 240°, using a linear actuator. The analytical synthesis of a planar linkage is firstly presented, than a spatial linkage is derived from the planar variant.

2 The Tracking Requirements

In PV tracking systems, the angular system used in modelling the current angular position of the sun-ray plays a key role in the design of the tracking mechanism. Thus, the *azimuth PV tracker* results from the *azimuth angular system* (consisting of the angles: *azimuth* ψ and *altitude* α, Fig. 4b), as a serial connection of the two rotations (Fig. 4a).

In Fig. 4c, the variations of the sun-ray angles during the Summer Solstice are presented considering the 45.65° N latitude (Brasov/Romania): $\psi = +127° \div -127°$ and $\alpha = 0° \div 68°$. The tracker's angles are marked with asterisk: ψ^*, α^*.

Due to the excessive drop in the transmission angle, the use of deformable *triangle linkage* reduces the tracking angular stroke, as presented in [8]; as Fig. 5 shows, the balance of the resistant moment $T = Q \cdot AB$ compels the actuator to give a force: $Q_1 = Q \cdot (1/\sin\gamma_B)$, where $\gamma = \gamma_B$ represents the transmission angle from the joint B.

The variation of the *amplification factor* $1/\sin\gamma_B = Q_1/Q$ (Fig. 5) results in a limitation of the γ_{min} minimum value to 30°, 20° or 10°, which implies a 2, 3 and about 6 times force amplification (Fig. 5).

In the next chapters (3 and 4), the paper proposes the geometrical generation followed by the analytical synthesis of a planar four-bar linkage that can amplify the output angle of a *deformable triangle linkage* at values above 180°.

3 Geometrical Generation of the Planar Four-Bar Linkage

The chapter presents the geometric generation of a planar linkage, with a linear actuator, able to reach an angular stroke in the daily movement of an azimuth tracked PV platform with values above $\Phi \geq 180°$.

This geometrical generation starts from the following data:

- The length of the AB side.
- Reduced radius e = AE/AB (of the circle which prevents the interference between joint A and crank CD); the value e = 0.2 was further considered.

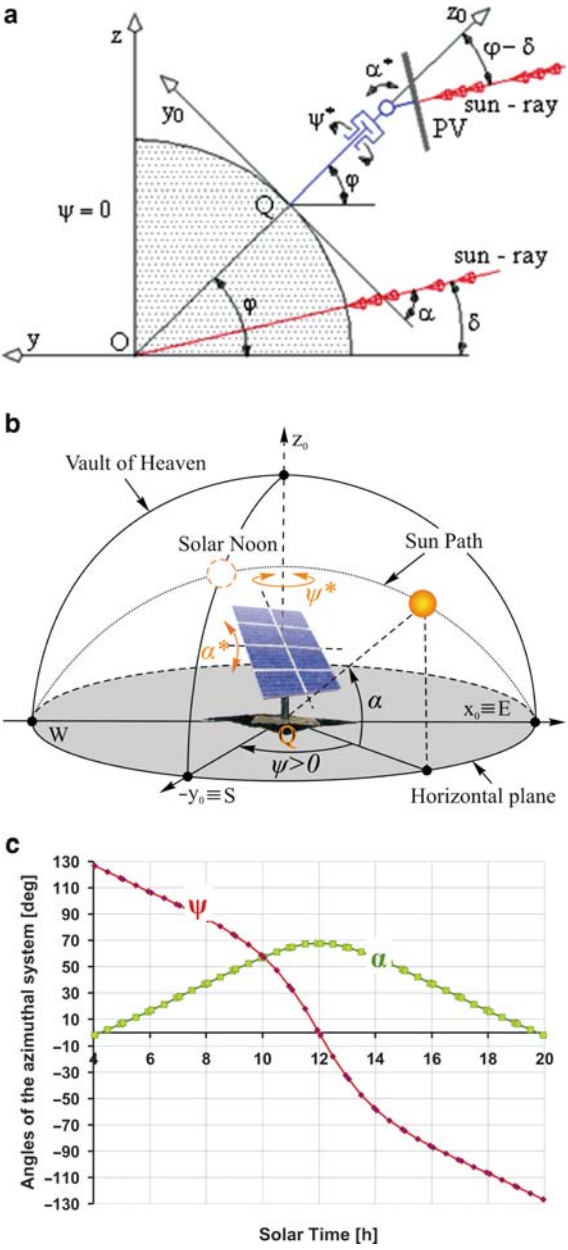

Fig. 4 (**a**) Azimuth Dual-Axis Tracker at the noon position; (**b**), (**c**) Sun-ray azimuth angles and their variations during the Summer Solstice at Brasov/Romania

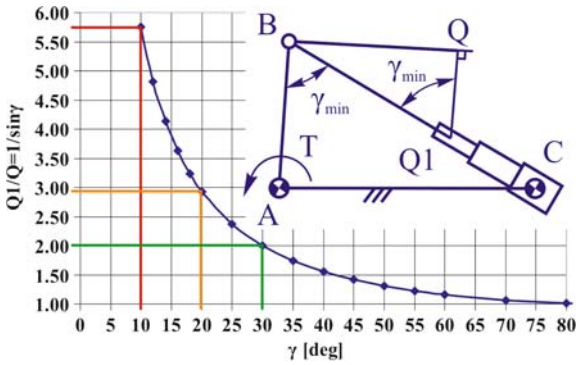

Fig. 5 Variation of the amplification factor with. the transmission angle

- The *minimum transmission angle* ($\gamma_{min} = \gamma_m$) *admitted* between the crank AB and the connecting rod BC, respectively the connecting rod BC and the crank CD; the value: $\gamma_{min} = \gamma_m = 20^\circ$ was used.

The linkage synthesis follows the main rule: *the minimum admitted value of the transmission angle* $\gamma_{min} = \gamma_m = 20^\circ$ *must be reached for both extreme linkage positions*, as described in Fig. 6a.

The parameters Φ, φ, BC/AB, CD/AB, AD/AB can be determined following four steps, as described in Fig. 7:

– The circle of radius el_1, with centre in A is drawn. The line AB is traced through point A and point B_1 is considered based on the crank AB length.
– A straight line goes through point B_1, under the circle of radius el_1, making the angle γ_{min} with B_1A.
– Tangent to the circle of radius el_1, a line is traced, under a γ_{min} angle; its intersection with previous line gives the point C_1 and so, the first extreme (blue) contour with γ_{min} is obtained.
– From this contour, changing the angle position from joint B, the second (red) contour with γ_{min} is derived; this represents the other extreme linkage positions obtained by turning around the point A, until C_2D_2 crosses C_1D_1 in a point $D \equiv D_1 \equiv D_2$, and C_1D_1 equals C_2D_2.

As result, for $\gamma_{min} = \gamma_m = 20^\circ$ and $e = 0.2$, the following main values of the linkage are obtained: $\Phi \approx 260^\circ$ (between AB_2 and AB_1), $\varphi \approx 120^\circ$ (between C_1D_1 and C_2D_2) and BC/AB ≈ 2.5, CD/AB ≈ 2.6 and DA/AB ≈ 1.1; so that, when a linear actuator rotates the big crank CD with the angular stroke $\varphi \approx 120^\circ$, the smaller crank, AB, makes a stroke $\Phi \approx 260^\circ$ (Fig. 7d).

Based on this graphical modelling, the analytical synthesis will be further approached.

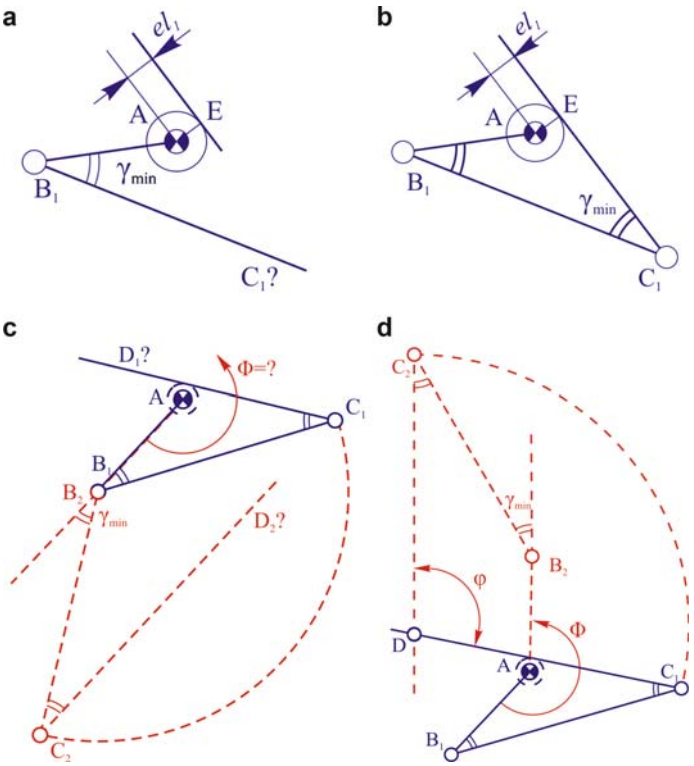

Fig. 6 (**a**) Scheme and notations used in the analytical kinematics; (**b**) The tracking linkage scheme with the extreme positions and the angular strokes of the crank

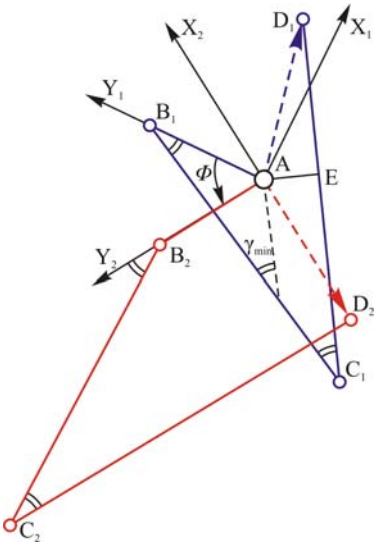

Fig. 7 Steps for generating a planar azimuth tracking four-bar linkage

4 Analytical Synthesis of the Tracking Planar Linkage

The analytical synthesis of the tracking planar linkage uses the same data: (a) the smaller crank length: $AB = AB_1 = AB_2 = l_1$; (b) the reduced eccentricity, $e = AE/AB$; (c) the minimum transmission angle admitted, $\gamma_{min} = \gamma_m$.

The parameters Φ, l, b and l_0 and φ will be established from the condition $D_1 \equiv D_2 \equiv D$ (Fig. 8), where:

$$\begin{aligned} AB &= l_1; \\ BC/AB &= B_1C_1/AB = B_2C_2/AB = l; \\ CD/AB &= C_1D_1/AB = C_2D_2/AB = b; \\ AD/AB &= AD_1/AB = AD_2/AB = l_0; \\ \varphi &= < C_2DC_1. \end{aligned} \tag{1}$$

There are considered the initial ($AB_1C_1D_1$) and final positions ($AB_2C_2D_2$) of the tracking four-bar linkage and their reference systems: AX_1Y_1, respectively AX_2Y_2, as presented in Fig. 8. The following relations are than valid:

$$l = 2 \cdot \cos\gamma_m + \frac{e}{\sin\gamma_m}; \tag{1'}$$

$$[AD_1] = \begin{bmatrix} 0 - l \cdot \sin\gamma_m + b \cdot \sin 2\gamma_m \\ 1 - l \cdot \cos\gamma_m + b \cdot \cos 2\gamma_m \end{bmatrix}_{X_1Y_1}; \tag{2}$$

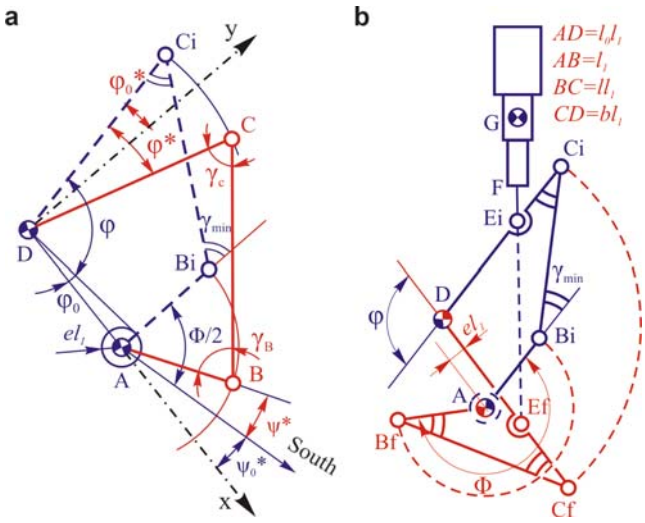

Fig. 8 Linkage geometrical scheme used in the analytical synthesis

$$[AD_2] = \begin{bmatrix} 0 - l \cdot \sin\gamma_m \\ 1 - l \cdot \cos\gamma_m - b \end{bmatrix}_{AX_2Y_2}; R_{2\to 1} = \begin{bmatrix} \cos\phi & -\sin\phi \\ \sin\phi & \cos\phi \end{bmatrix}; \quad (3,\ 4)$$

$$[AD_2] = R_{2\to 1}[AD_2]_{AX_2Y_2} = \begin{bmatrix} -l \cdot \sin(\phi + \gamma_m) + b \cdot \sin\phi - \sin\phi \\ l \cdot \cos(\phi + \gamma_m) - b \cdot \cos\phi - \cos\phi \end{bmatrix}_{AX_1Y_1}; \quad (5)$$

The condition $D_1 \equiv D_2 \equiv D \Leftrightarrow [AD_1] = [AD_2]$ leads to the following system of equations with the b and Φ unknowns:

$$\begin{cases} b \cdot (\sin 2\gamma_m - \sin\phi) = l \cdot [\sin\gamma_m - \sin(\phi + \gamma_m)] - \sin\phi \\ b \cdot (\cos 2\gamma_m + \cos\phi) = l \cdot [\cos\gamma_m + \cos(\phi + \gamma_m)] + \cos\phi - 1 \end{cases}; \quad (6)$$

Solving the system results in the Eq. (7) and the solutions (8) (where $\gamma_m = \gamma_{min}$):

$$\begin{aligned} a_1 \cdot \sin\phi \cdot + b_1 \cdot \cos\phi = c_1 \Rightarrow \\ \sin(\phi + \varepsilon) = (c_1/a_1) \cdot \cos\varepsilon; \varepsilon = \tan^{-1}(b_1/a_1); \end{aligned} \quad (7)$$

$$\begin{cases} 1 + \cos 2\gamma_m + l \cdot (\cos 3\gamma_m - \cos\gamma_m) = a_1 \\ \sin 2\gamma_m + l \cdot (\sin 3\gamma_m - \sin\gamma_m) = b_1 \\ \sin 2\gamma_m - 2l \cdot \sin\gamma_m = c_1 \end{cases}; \quad (7')$$

$$\begin{cases} \phi = \sin^{-1}((c_1/a_1) \cdot \cos\varepsilon) - \tan^{-1}(b_1/a_1) \\ b = \dfrac{l \cdot [\sin\gamma_m - \sin(\phi + \gamma_m)] - \sin\phi}{\sin 2\gamma_m - \sin\phi} \\ l_0 = \sqrt{l^2 + (1-b)^2 + 2l(1-b) \cdot \cos\gamma_m} \\ \varphi = (< C_1DC_2) = \phi + 2\gamma_m - 180^o \end{cases}; \quad (8)$$

The analytical expressions of the smaller crank displacement, ψ^*, and the transmission angles γ_B and γ_C, depending on the big crank displacement φ^*, can be obtained, as Fig. 6a shows:

$$\begin{cases} \varphi_0 = \sin^{-1}(e/l_0); \\ \varphi_0^* = \varphi + \varphi_0 - 90^o; \psi_0^* = \varphi + \varphi_0 - \Phi/2; \\ \varphi_L = \varphi^* - \varphi_0^*; \psi_L = \psi^* + \psi_0^*; \end{cases} \quad (9)$$

$$\begin{cases} [AB] = l_1 \begin{bmatrix} \cos\psi_L \\ \sin\psi_L \end{bmatrix}; \\ [CB] = l_1 \begin{bmatrix} l_0 + \cos\psi_L - b\sin\varphi_L \\ \sin\psi_L - b\cos\varphi_L \end{bmatrix}; CB = l.l_1; \\ [CD] = b.l_1 \begin{bmatrix} -\sin\varphi_L \\ -\cos\varphi_L \end{bmatrix}; \end{cases} \quad (9')$$

$$\begin{aligned}
\gamma_B &= \cos^{-1}\left(\frac{\overrightarrow{AB}}{l_1}\cdot\frac{\overrightarrow{CB}}{ll_1}\right) = \cos^{-1}\left(\frac{1+l_0\cos\psi_L - b\sin(\psi_L+\varphi_L)}{l}\right)\\
\gamma_C &= \cos^{-1}\left(\frac{\overrightarrow{CD}}{bl_1}\cdot\frac{\overrightarrow{CB}}{ll_1}\right) = \cos^{-1}\left(\frac{b-l_0\sin\varphi_L - \sin(\psi_L+\varphi_L)}{l}\right);\\
\psi^* &= \sin^{-1}(t.\cos\mu) - \mu - \psi_0^*
\end{aligned} \tag{9''}$$

$$\begin{cases} t = \dfrac{l_0^2 - l^2 + b^2 + 1 - 2l_0 b\sin\varphi_L}{2b\cos\varphi_L}; \\ \mu = \tan^{-1}((b\sin\varphi_L - l_0)/(b\cos\varphi_L)) \end{cases} \tag{9'''}$$

The variations of the main linkage parameters, resulted by applying the analytical correlations are presented in Figs. 9, 10, and 11 (the same notations

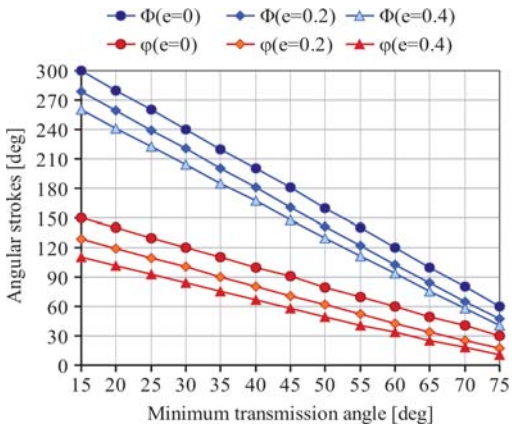

Fig. 9 The crank's strokes vs. minimum transmission angle γ_{min}

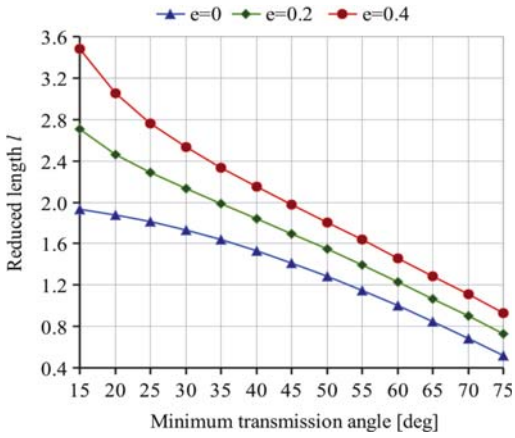

Fig. 10 Reduced length *l*

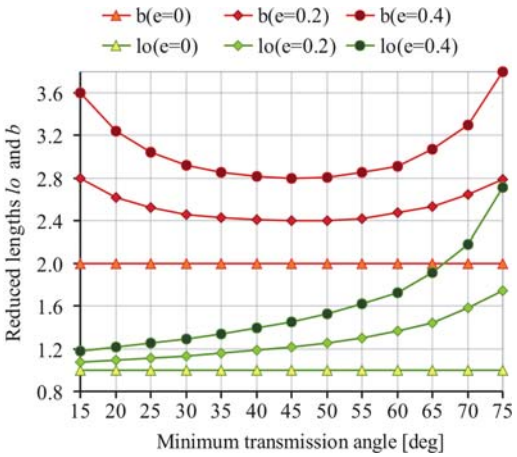

Fig. 11 Reduced lengths l_0 and b

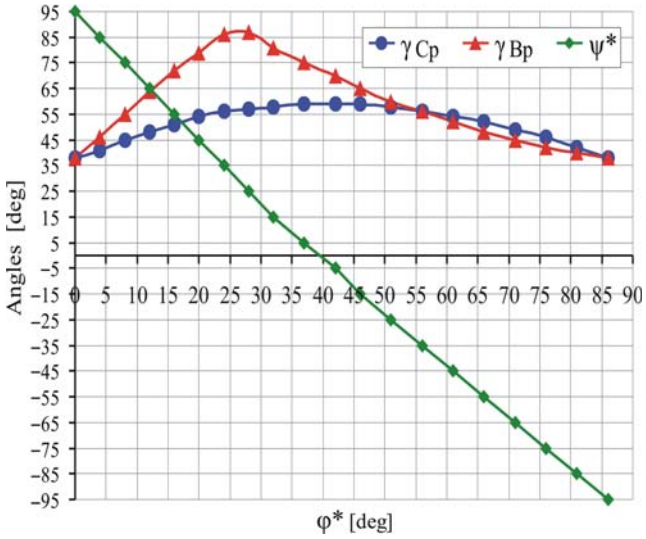

Fig. 12 Azimuth tracking linkages: (**a**) planar linkage; (**b**) spatial linkage derived from the planar version by DC_iC_f triangle rotation with 90° around the axis Δ

as in Fig. 6a and b are used).The angular stroke Φ increases when the e value increases and γ_{min} decreases; also, the linkage overall size increases when the size e increases.

Previous results, graphically obtained in Fig. 7d (see Chapter 3), can now be directly obtained, from Figs. 9 through 11, for e = 0.2 and $\gamma_{min} = 20°$. Another planar example (see Figs. 6 and 12a), with $e = 0.2$ and $\gamma_{min} = 38°$, is further used to generate and analyse comparatively an equivalent spatial linkage (see Figs. 12a and 13); for this planar linkage, the following main sizes are obtained from Figs. 9

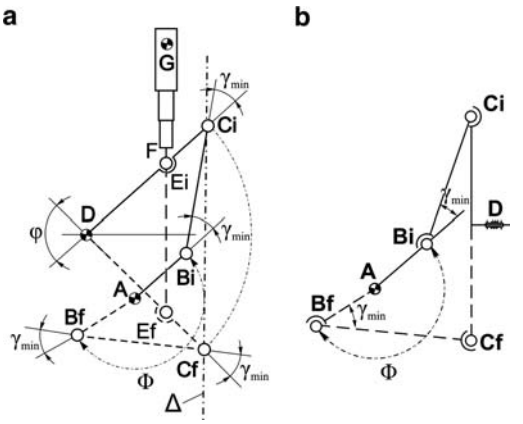

Fig. 13 (**a**) Two 2D schemes of a spatial tracking four-bar linkage (the BC connecting rod real reduced length is *l*); (**b**) Variations of the angles γ_B, γ_C and φ*, depending on the azimuth displacement ψ*, for a planar and an equivalent spatial linkage (*P* = planar; S = spatial)

through 11 (see Figs. 6 and 12a): Φ = 190°; φ = 86°; BC/AB = 1.90; CD/AB = 2.41 and DA/AB = 1.17. The corresponding variations of this planar linkage, for the current angles ψ*, γ_B and γ_C (see Figs. 6 and 12a), depending on the current big crank displacement φ*, are presented in Fig. 14.

5 Generation and Analysis of an Equivalent Spatial Linkage

Using the example of the planar tracking linkage from the previous chapter, with $e = 0.2$ and $\gamma_{min} = 38°$ (see Fig. 12a), an equivalent four-bar spatial linkage (i.e. with the same stroke Φ and the same reduced lengths of the mobile elements) is further generated (see Fig. 12b); then, the transmission angles of the spatial linkage and of its equivalent planar variant are comparatively analysed.

Starting from the planar tracking linkage (Fig. 12a) and turning the triangle C_iC_fD with 90° around the line Δ, a spatial linkage, as shown in Fig. 12b, is generated (in this process, the revolute joints B and C become spherical joints and the basis dimensions are changed).

In this case (see Fig. 12b), the value $\gamma_{min} = 38°$ of the transmission angles from the extreme positions of joint B remain unchanged, while the transmission angle from the f extreme position of joint C becomes too small; this last angle can be increased by decreasing the transmission angles from the i and f extreme positions of joint B. A solution of compromise is given in Fig. 13a and b, in which: Φ = 190°; $\gamma_{min} = 20°$; φ = 72°; BC/AB = 2; CD/AB = 2.4 and the base configuration (AD) is described by (see Fig. 13a): the reduced distance between the axes A and D: 1.16, the reduced distance from the vertical articulation A to the vertical median plane of the crank CD: 1.667 and the reduced distance from the horizontal articulation D to the horizontal median plane of the crank AB: 1.746.

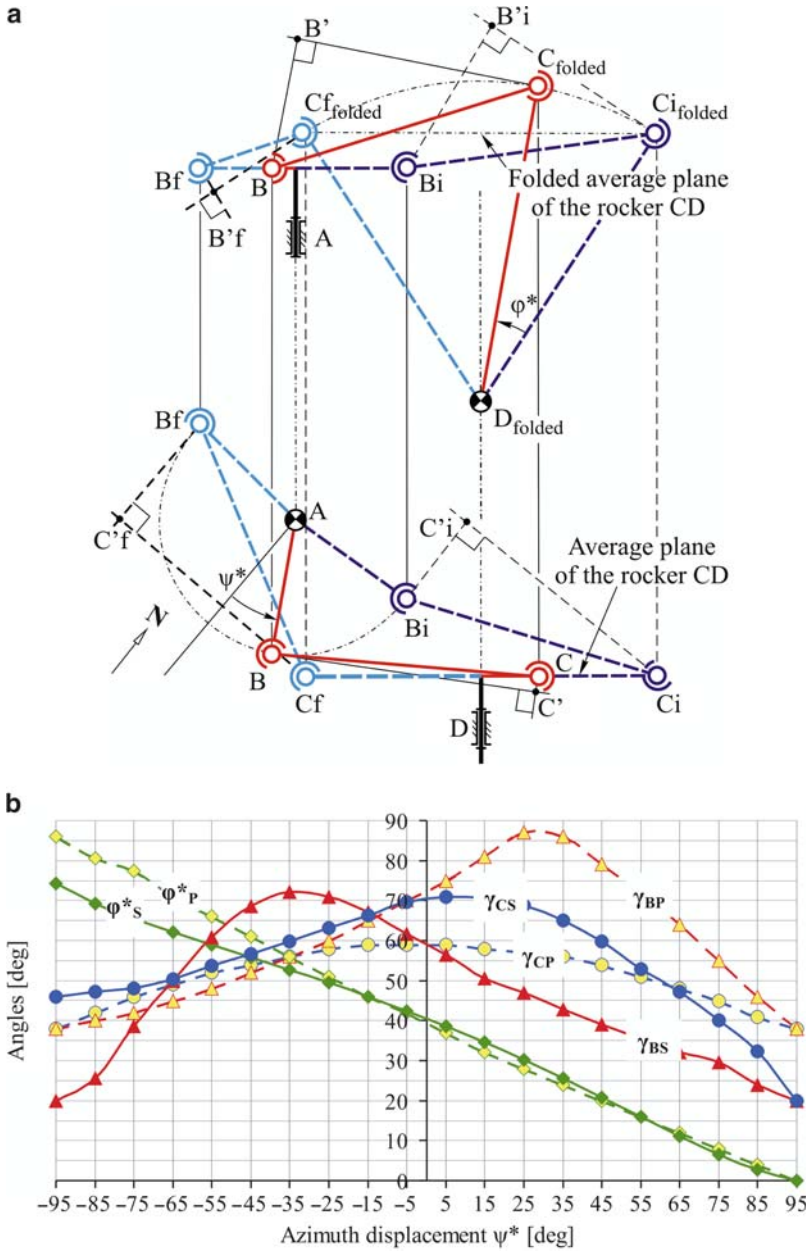

Fig. 14 Variation of angles ψ^*, γ_B, γ_C for: $e = 0.2$ and $\gamma_{min} = 38°$

A current position, the extreme positions and the relevant geometrical parameters of this spatial linkage are illustrated in Fig. 13a; because the connecting rod BC (of real reduced length l) does not appear in its real size, the calculus of the

Fig. 15 An application example of the spatial tracking linkage with linear actuator at the University Transilvania of Brasov/ Romania

transmission angles γ_B and γ_C can be made using the theorem of the three perpendiculars (see Fig. 13a):

$$\sin\gamma_B = \frac{BC'}{ll_1}; \sin\gamma_c = \frac{CB'}{ll_1}; \tag{10}$$

Further, there are comparatively analyzed the variations of the transmission angles γ_B, γ_C and the angular displacement φ^*, depending on the angular displacement ψ^* (see Figs. 6a and 13a), in the two situations: the planar linkage from Fig. 12a and the spatial linkage from Fig. 13a; these variations, presented in Fig. 13b, were obtained using the MBS (Multi-Body Systems) Method [1, 9].

According to Fig. 13b, although the homologous mobile sides have similar values, the planar linkage has better transmission angles than the spatial linkage. Even if the spatial solution has smaller transmission angles, it provides some advantages compared to the planar one: (1) the overall horizontal size of the spatial solution is smaller; (2) the amplification ratio (for the same relative sizes) is higher; (3) its actuator has better mounting and better working conditions.

Based on these results, the analytical synthesis of the spatial tracking four-bar linkage will be approached into a next paper.

A spatial tracking linkage, like that from Fig. 13a, is already used for an azimuth tracker at the University Transilvania of Brasov (Fig. 15).

6 Conclusions

(a) A gear speed reducer ensures angular strokes no matter how large, but is usually less economical than a linkage with a linear actuator; still, the use of a simple triangle linkage with linear actuator reduces the angular stroke of the tracking axis, due to the transmission angle limitation.
(b) The increase of the trackers' angular stroke, using a linear actuator, is presented in the paper by synthesis of the linkages consisting of a triangle linkage with a

linear actuator and a four-bar linkage that can *amplify* the output angle of the first linkage over 180°. Based on the analytical synthesis, with imposed minimum transmission angle, the linkage parameters are developed; using the diagrams, the suitable planar *angular amplifier* to drive the daily motion ψ^* of an azimuth tracker is obtained.

(c) Starting from a planar tracking linkage (obtained by analytical synthesis), an equivalent four-bar spatial linkage (i.e. with the same azimuth stroke and the same reduced lengths of the mobile elements) was graphically generated.

(d) The 190° azimuth angular stroke is achieved by the planar linkage for a minimum transmission angle of $\gamma_{\min} = 38°$ and an amplification ratio of $190°/86° = 2.20$. The same azimuth angular stroke is reached by a spatial linkage for $\gamma_{\min} = 20°$ and an amplification ratio of $190°/72° = 2.64$.

(e) Although the spatial solution has smaller transmission angles, it presents some advantages vs. the planar solution: smaller overall size, higher amplification ratio, better mounting and working conditions for the linear actuator. Analytical synthesis of the spatial linkage will be developed in a future paper.

(f) If the angular strokes must be higher than 190°, then only planar solution (that has higher transmission angles) can be used.

References

1. Haug, J.E.: Computer Aided Kinematics and Dynamics of mechanical Systems. Allyn and Bacon, Boston (1989)
2. Luquea, A., Marti, A., Bettb, A., Andreevc, V.M.: Full spectrum: a new PV wave making more efficient use of the solar spectrum. Solar Energy Materials & Solar Cells 87, 467–479 (2005)
3. Abu-Khadera, M.M., Badranb, O.O., Abdallah, S.: Evaluating multi-axes sun-tracking system at different modes of operation in Jordan. Renewable and Sustainable Energy Reviews 12, 864–873 (2008)
4. Messenger, R., Ventre, J.: Photovoltaic System Engineering. CRC Press, London (2000)
5. Norton, R.L.: Design of Machinery. Mc Graw Hill, Boston (1999)
6. Olchowik, J.M., Tomaszewski, R., Adamczyk, J., Gulkowski, S., Cieslak, K., Zabielski, K.: Four years exploitation analysis of the hybrid solar system in South-Eastern Poland conditions. Proceedings of 23rd European Photovoltaic Solar Energy Conference and Exhibition, Valencia, pp. 3084–3087 (2008)
7. Tafticht, T., Agbossou, K., Doumbia, M.L., Cheriti, A.: An improved maximum power point tracking method photovoltaic systems. Renewable Energy 33(7), 1508–1516 (2007)
8. Vişa, I., et al.: The synthesis of a linkage with liner actuator for solar tracking with large angular stroke. In: Proceedings of EUCOMES 08, ISBN 978-1-4020-8914-5, pp. 457–464 (2008)
9. Vişa, I.: Design of Mechanisms (Romanian language). Lux Libris, ISBN 973-9458-17-3 (2004)
10. www.degerenergie.de
11. www.goimo.com
12. www.tracker.cat

Upon Applying Closed Contours Method in Plane Mechanisms with Higher Pairs

S. Alaci, F.C. Ciornei, D. Amarandei, and D.A. Cerlincă

Abstract The study of plane mechanisms having in the structure higher pairs presents a series of particular aspects concerning the position of the points where the higher pair appears from the contacting curves. Using the closed contours method applied to the equivalent mechanism with lower pairs, the authors obtained analytical expressions for relative velocity and relative acceleration from higher pair, these expressions depending on the local geometry of the contact.

Keywords Equivalent linkage · Higher pair · Kinematics analysis · Plane linkage

1 Introduction

The bulk papers from literature regarding this issue refer to cam mechanisms. In the case of translating or oscillating knife-edge follower, when the trajectory of the tip is known, according to Pelecudi [1], the kinematics analysis can be made via vector equations. These equations express relationships between velocities and accelerations, respectively, of the contacting points. Assuming a general form of the follower, the kinematics analysis becomes more intricate. Pelecudi [1], suggests the use of relations of relative motion characteristics for the points from the cam and from the follower superimposing in the curvature centre of the follower. Therefore, the absolute motion of the follower can be obtained, but for the relative motion from higher pair cumbersome calculus are required.

The paper deals with the relative kinematics occurring in higher pairs contained in the structure of plane mechanisms. The solving approach is the method of vector

S. Alaci (✉)
Faculty of Mechanical Engineering, Mechatronics and Management, University of Suceava, Suceava, Romania

I. Vişa (ed.), *SYROM 2009*,
DOI 10.1007/978-90-481-3522-6_16,

loop-closure equation, applied to the equivalent linkage. The method is particularly efficient in the case of cam mechanisms, as for the other class of mechanisms with higher pairs, namely the geared mechanisms, the solving methods are completely found and specified in the literature; although, the method is useful for non-involute gear teeth profile.

2 Theoretical Remarks

The vector loop-closure equation method is an approach specific to kinematics of plane linkages. The closed plane linkages can form a plane mechanism of the third family, Dobrovolsky [2], whose mobility can be found with the following relation (Kutzbach criterion), from Uicker [3]:

$$M_3 = 3(n-1) - c_4 - 2c_5 \tag{1}$$

where n represents the number of the links, c_4 is the number of higher pairs and c_5 is the number of lower pairs from the structure of the linkage. It is aimed that the study of plane mechanisms should be generalized, and therefore, the c_4 term from Eq. (1) must be eliminated. This implies the replacement of higher pairs from the plane linkage. This operation is allowed, as mentioned in Hunt [4], if the following two conditions are fulfilled:

- *Structural condition*, which requires that the initial and final linkages should have the same mobility
- *Kinematics condition*, imposing an unmodified relative motion between the links that form the higher pair

The first condition leads to the observation that from structural point of view, a higher pair can be replaced by a link with two related lower pairs.

Concerning the second condition, one consider a higher pair, Fig. 1, resulting from contacting links *1* and *3*, hinged to the ground through revolute pairs, $O_1$and O_3 respectively. The higher pair appears in the point M, where the curves Γ_1 and Γ_3 are tangent.

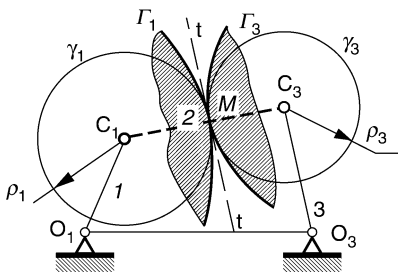

Fig. 1 Actual and equivalent lower pairs mechanism

In order to find the position of point M, it can be noted: in the case of mechanisms obtained from plane linkages, the closed contour method allows finding, on the first step, the position of the mechanism, but for the present study mechanism, the above method is inapplicable because the higher pair requires at least two conditions to be satisfied (presence of a common point of the two elements and the common tangent in this point, too). In Appendix, the methodology of finding the contact point M is presented. In the vicinity of contact point, the curves Γ_1 and Γ_3 can be replaced with osculating circles γ_1 and γ_3 respectively.

From the kinematics condition, it results that the length of the replacing element *2* must be equal to the $\rho_1 + \rho_3$ sum, representing the sum of curvature radii of the contacting elements in the contact point.

The equivalent mechanism is the articulated quadrilateral, $O_1C_1C_3O_3$, under the assumption that the curvature radii are finite. Two special problems of replacing operation occur:

- The substitute linkage $O_1C_1C_3O_3$ corresponds to all mechanisms with the same $\rho_1 + \rho_3$.
- On the substitute linkage, the relative motion (the translational motion between the overlaid points M_1 and M_3 from elements *1* and *3*, respectively) from higher pair does not appear.

Hartenberg şi Denavit [5], gave a more precise but complicated form of equivalence conditions for higher pair. They proved that for a correct equivalence, it is sufficient and necessary that the relation between the movement of one of the elements and the second element should remain unchanged for three infinite closed positions.

Voinea [6], gave a general method for kinematics analysis of the linkages only for velocities and accelerations. The aim of the present paper is to obtain the characteristics of the relative motion between the elements of the higher pair with respect to the local geometry of the two elements.

The corresponding vector contour to the substitute linkage, $O_1C_1C_3O_3$, is shown in Fig. 2.

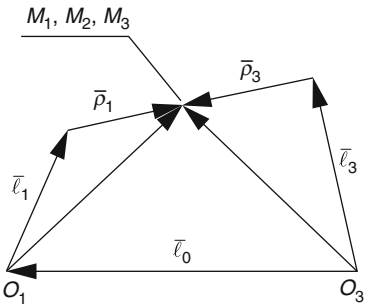

Fig. 2 Geometrical characteristics of equivalent mechanism

The closure equation for the vector contour $O_1C_1C_3O_3$ is:

$$\bar{\ell}_1 + \bar{\rho}_1 + (-\bar{\rho}_3) + (-\bar{\ell}_3) + \bar{\ell}_0 = 0 \tag{2}$$

3 Solution for Velocities

By differentiating with respect to time the Eq. (2), one obtains:

$$\bar{\omega}_1 \times \bar{\ell}_1 + \bar{\omega}_2 \times \bar{\rho}_1 + (-\bar{\omega}_2 \times \bar{\rho}_3) + (-\bar{\omega}_1 \times \bar{\ell}_3) = 0\,, \tag{3}$$

from which result the angular velocities, $\bar{\omega}_3$, of the driven element and $\bar{\omega}_2$, of the substitution element. The Eq. (3) can be written:

$$\begin{gathered} \bar{\omega}_1 \times (\bar{\ell}_1 + \bar{\rho}_1) + (\bar{\omega}_2 - \bar{\omega}_1) \times \bar{\rho}_1 + \\ +[-(\bar{\omega}_2 - \bar{\omega}_3) \times \bar{\rho}_3] + [-\bar{\omega}_3 \times (\bar{\ell}_3 + \bar{\rho}_3)] = 0 \end{gathered} \tag{4}$$

The absolute velocity of the point M_2 from the substituting element is given by the following relations, resulting:

- Directly from definition:

$$\begin{gathered} \bar{v}_{M_2} = \frac{d\bar{r}_1}{dt} = \frac{d(\bar{\ell}_1 + \bar{\rho}_1)}{dt} = \bar{\omega}_1 \times \bar{\ell}_1 + \\ + \bar{\omega}_2 \times \bar{\rho}_1 = \bar{\omega}_1 \times (\bar{\ell}_1 + \bar{\rho}_1) + (\bar{\omega}_2 - \bar{\omega}_1) \times \bar{\rho}_1. \end{gathered} \tag{5.a}$$

- And as a compound velocity:

$$\bar{v}_{M_2} = \bar{v}_{M_1} + \bar{v}^r_{M_2M_1}. \tag{5.b}$$

Comparing the Eq. (5.a) with (5.b), it results:

$$\begin{aligned} \bar{v}_{M_2} &= \bar{\omega}_1 \times (\bar{\ell}_1 + \bar{\rho}_1), \\ \bar{v}^r_{M_2M_1} &= (\bar{\omega}_2 - \bar{\omega}_1) \times \bar{\rho}_1. \end{aligned} \tag{6}$$

It can be observed that the relative velocity $\bar{v}^r_{M_2M_1}$ is normal to the substituting element and therefore, aligned along the tangent line *tt* from the contact point. On the other hand, the velocity of the point M_2 can be obtained by two ways:

- Directly from definition equation:

$$\begin{gathered} \bar{v}_{M_2} = \frac{d\bar{r}_3}{dt} = \frac{d(\bar{\ell}_3 + \bar{\rho}_3)}{dt} = \bar{\omega}_3 \times \bar{\ell}_3 + \bar{\omega}_2 \times \bar{\rho}_3 = \\ = \bar{\omega}_3 \times (\bar{\ell}_3 + \bar{\rho}_3) + (\bar{\omega}_2 - \bar{\omega}_3) \times \bar{\rho}_3. \end{gathered} \tag{7.a}$$

- As a compound velocity:

$$\bar{v}_{M_2} = \bar{v}_{M_3} + \bar{v}^r_{M_2M_3} \tag{7.b}$$

From Eqs. (7.a) and (7.b) it results:

$$\begin{aligned} \bar{v}_{M_2} &= \bar{\omega}_3 \times (\bar{\ell}_3 + \bar{\rho}_3), \\ \bar{v}^r_{M_2M_3} &= (\bar{\omega}_2 - \bar{\omega}_3) \times \bar{\rho}_3. \end{aligned} \tag{8}$$

The relative velocity $\bar{v}^r_{M_2M_3}$ is aligned along the normal to the substituting element. The relative velocity from higher pair, $\bar{v}^r_{M_3M_1}$, is obtained with the equation:

$$\begin{aligned} \bar{v}^r_{M_3M_1} = \bar{v}_{M_3} - \bar{v}_{M_1} = (\bar{v}_{M_2} - \bar{v}_{M_1}) - \\ -(\bar{v}_{M_2} - \bar{v}_{M_3}) = \bar{v}^r_{M_2M_1} - \bar{v}^r_{M_2M_3} = \\ = (\bar{\omega}_2 - \bar{\omega}_1) \times \bar{\rho}_1 - (\bar{\omega}_2 - \bar{\omega}_3) \times \bar{\rho}_3. \end{aligned} \tag{9}$$

The relative velocity $\bar{v}^r_{M_2M_3}$ can also be found using the definition equation of relative velocity:

$$\begin{aligned} \bar{v}^r_{M_3M_1} &= \bar{v}_{M_3} - \bar{v}_{M_1} = \\ &= \bar{\omega}_3 \times (\bar{\ell}_3 + \bar{\rho}_3) - \bar{\omega}_1 \times (\bar{\ell}_1 + \bar{\rho}_1). \end{aligned} \tag{10}$$

However, using this form, the direction of the relative velocity can not be evidenced.

4 Accelerations Analysis

A differentiate with respect to time of Eq. (4) allows to solve the accelerations distribution. It is obtained:

$$\begin{aligned} \bar{\varepsilon}_1 \times (\bar{\ell}_1 + \bar{\rho}_1) + \bar{\omega}_1 \times (\bar{\omega}_1 \times \bar{\ell}_1 + \bar{\omega}_2 \times \bar{\rho}_1) + \\ (\bar{\varepsilon}_2 - \bar{\varepsilon}_1) \times \bar{\rho}_1 + (\bar{\omega}_2 - \bar{\omega}_1) \times (\bar{\omega}_2 \times \bar{\rho}_1) \\ -[\bar{\varepsilon}_3 \times (\bar{\ell}_3 + \bar{\rho}_3) + \bar{\omega}_3 \times (\bar{\omega}_3 \times \bar{\ell}_3 + \bar{\omega}_2 \times \bar{\rho}_3) + \\ (\bar{\varepsilon}_2 - \bar{\varepsilon}_3) \times \bar{\rho}_3 + (\bar{\omega}_2 - \bar{\omega}_3) \times (\bar{\omega}_2 \times \bar{\rho}_3)] = 0. \end{aligned} \tag{11.a}$$

The Eq. (11.a) can be simplified by keeping in mind that angular velocities are normal to the plane of the motion (a scalar product between an angular velocity and a vector from this plane is always zero). In order to illustrate the directions of the components of relative acceleration, $a_{M_3M_1}$, it is written under the form:

$$\bar{\varepsilon}_1 \times (\bar{\ell}_1 + \bar{\rho}_1) - (\bar{\omega}_1^2)\bar{\ell}_1 - (\bar{\omega}_1\bar{\omega}_2)\bar{\rho}_1 + (\bar{\varepsilon}_2 - \bar{\varepsilon}_1) \times \bar{\rho}_1 - (\bar{\omega}_2^2)\bar{\rho}_1 + (\bar{\omega}_1\bar{\omega}_2)\bar{\rho}_1 -$$
$$[\bar{\varepsilon}_3 \times (\bar{\ell}_3 + \bar{\rho}_3) - (\bar{\omega}_3^2)\bar{\ell}_3 - (\bar{\omega}_3\bar{\omega}_2)\bar{\rho}_3 + (\bar{\varepsilon}_2 - \bar{\varepsilon}_3) \times \bar{\rho}_3 - (\bar{\omega}_2^2)\bar{\rho}_3 + (\bar{\omega}_3\bar{\omega}_2)\bar{\rho}_3] =$$
$$= \bar{\varepsilon}_1 \times (\bar{\ell}_1 + \bar{\rho}_1) - (\bar{\omega}_1^2)(\bar{\ell}_1 + \bar{\rho}_1) + (\bar{\omega}_1^2)\bar{\rho}_1 - (\bar{\omega}_2^2)\bar{\rho}_1 + (\bar{\varepsilon}_2 - \bar{\varepsilon}_1) \times \bar{\rho}_1$$
$$- [\bar{\varepsilon}_3 \times (\bar{\ell}_3 + \bar{\rho}_3) - (\bar{\omega}_3^2)(\bar{\ell}_3 + \bar{\rho}_3) + (\bar{\omega}_3^2)\bar{\rho}_3 - (\bar{\omega}_2^2)\bar{\rho}_3 + (\bar{\varepsilon}_2 - \bar{\varepsilon}_3) \times \bar{\rho}_3] =$$
$$= \bar{\varepsilon}_1 \times (\bar{\ell}_1 + \bar{\rho}_1) - (\bar{\omega}_1^2)(\bar{\ell}_1 + \bar{\rho}_1) + 2\bar{\omega}_1 \times [(\bar{\omega}_2 - \bar{\omega}_1) \times \bar{\rho}_1] - (\bar{\omega}_2 - \bar{\omega}_1)^2\bar{\rho}_1$$
$$+ (\bar{\varepsilon}_2 - \bar{\varepsilon}_1) \times \bar{\rho}_1 - \{\bar{\varepsilon}_3 \times (\bar{\ell}_3 + \bar{\rho}_3) - (\bar{\omega}_3^2)(\bar{\ell}_3 + \bar{\rho}_3) + 2\bar{\omega}_3 \times [(\bar{\omega}_2 - \bar{\omega}_3) \times \bar{\rho}_3]$$
$$- (\bar{\omega}_2 - \bar{\omega}_3)^2\bar{\rho}_3 + (\bar{\varepsilon}_2 - \bar{\varepsilon}_3) \times \bar{\rho}_3\} = 0 \tag{11.b}$$

The acceleration of the point M_2 on the substituting element is obtained with the equation:

$$\bar{a}_{M_2} = \frac{d\bar{v}_{M_2}}{dt} = \underline{\bar{\varepsilon}_1 \times (\bar{\lambda}_1 + \bar{\rho}_1) - (\bar{\omega}_1^2)(\bar{\lambda}_1 + \bar{\rho}_1)} +$$
$$\underline{+2\bar{\omega}_1 \times [(\bar{\omega}_2 - \bar{\omega}_1) \times \bar{\rho}_1]} - \underline{(\bar{\omega}_2 - \bar{\omega}_1)^2\bar{\rho}_1} + \underline{(\bar{\varepsilon}_2 - \bar{\varepsilon}_1) \times \bar{\rho}_1} \tag{12.a}$$

The underlined terms from Eq. (12.a) represent:

$$\bar{a}_{M_1} = \bar{\varepsilon}_1 \times (\bar{\lambda}_1 + \bar{\rho}_1) - (\bar{\omega}_1^2)(\bar{\lambda}_1 + \bar{\rho}_1)$$

– The absolute acceleration of the point M_1;

$$\bar{a}^c_{M_2M_1} = 2\bar{\omega}_1 \times [(\bar{\omega}_2 - \bar{\omega}_1) \times \bar{\rho}_1],$$

– The Coriolis component of relative acceleration;

$$\bar{a}^{rv}_{M_2M_1} = -\left(\frac{v_{M_2M_1}}{\rho_1}\right)^2 \bar{\rho}_1,$$

– The normal component of relative acceleration of M_2 point with respect to M_1;

$$\bar{a}^{r\tau}_{M_2M_1} = (\bar{\varepsilon}_2 - \bar{\varepsilon}_1) \times \bar{\rho}_1,$$

– The tangential component of relative acceleration

Using the above notation and by substituting in Eq. (12.a), it results:

$$\bar{a}_{M_2} = \bar{a}_{M_1} + \bar{a}^c_{M_2M_1} + \bar{a}^{rv}_{M_2M_1} + \bar{a}^{r\tau}_{M_2M_1} \tag{12.b}$$

An analogous procedure can be applied in order to find the relations between the accelerations of the points M_2 and M_3. One obtains:

$$\bar{a}_{M_2} = \bar{a}_{M_3} + \bar{a}^c_{M_2M_3} + \bar{a}^{rv}_{M_2M_3} + \bar{a}^{r\tau}_{M_2M_3} \tag{13.a}$$

where:

$$\bar{a}_{M_3} = \bar{\varepsilon}_3 \times (\bar{\ell}_3 + \bar{\rho}_3) - (\bar{\omega}_3^2)(\bar{\ell}_3 + \bar{\rho}_3)$$

represents the absolute acceleration of the point M_3;

$$\bar{a}^c_{M_2M_3} = 2\bar{\omega}_3 \times [(\bar{\omega}_2 - \bar{\omega}_3) \times \bar{\rho}_3]$$

represents the Coriolis component of relative acceleration of point M_2 with respect to point M_3;

$$\bar{a}^{rv}_{M_2M_3} = -\left(\frac{v_{M_2M_3}}{\rho_3}\right)^2 \bar{\rho}_3$$

is the normal component of relative acceleration of M_2 point with respect to M_3;

$$\bar{a}^{r\tau}_{M_2M_3} = (\bar{\varepsilon}_2 - \bar{\varepsilon}_3) \times \bar{\rho}_3$$

is the tangential component of relative acceleration of point M_2 with respect to M_3.

Using the above notation and by substituting in Eq. (13.a), it results:

$$\bar{a}_{M_2} = \bar{a}_{M_3} + \bar{a}^c_{M_2M_3} + \bar{a}^{rv}_{M_2M_3} + \bar{a}^{r\tau}_{M_2M_3} \tag{13.b}$$

Equating the right members of Eqs. (12.b) and (13.b), one obtains:

$$\begin{aligned} &\bar{a}_{M_1} + \bar{a}^c_{M_2M_1} + \bar{a}^{rv}_{M_2M_1} + \bar{a}^{r\tau}_{M_2M_1} = \\ &= \bar{a}_{M_3} + \bar{a}^c_{M_2M_3} + \bar{a}^{rv}_{M_2M_3} + \bar{a}^{r\tau}_{M_2M_3} \end{aligned} \tag{14.a}$$

Or, by suitably rearranging the terms:

$$\begin{aligned} &\bar{a}_{M_3} - \bar{a}_{M_1} = (\bar{a}^{r\tau}_{M_2M_1} - \bar{a}^{r\tau}_{M_2M_3}) \\ &(\bar{a}^c_{M_2M_1} - \bar{a}^c_{M_2M_3} + \bar{a}^{rv}_{M_2M_1} - \bar{a}^{rv}_{M_2M_3}) \end{aligned} \tag{14.b}$$

The advantage of the form obtained for Eq. (14.b) consists in the fact that it reveals the components of the relative acceleration, $\bar{a}_{M_3} - \bar{a}_{M_1}$, along the normal and tangential directions in the contact point of the two curves. Consequently, the component on normal direction is:

$$\bar{a}^v_{M_3M_1} = \bar{a}^c_{M_2M_1} - \bar{a}^c_{M_2M_3} + \bar{a}^{rv}_{M_2M_1} - \bar{a}^{rv}_{M_2M_3} \tag{15.a}$$

and on tangential direction:

$$\bar{a}^\tau_{M_3M_1} = \bar{a}^{r\tau}_{M_2M_1} - \bar{a}^{r\tau}_{M_2M_3} \tag{15.b}$$

The relations (15.a) and (15.b) can be expressed as functions of the kinematic parameters of the substituting linkage, as follows:

$$\bar{a}^{v}_{M_3M_1} = -(\omega_2^2 - \omega_1^2)\bar{\rho}_1 + (\omega_2^2 - \omega_3^2)\bar{\rho}_3 \tag{16.a}$$

$$\bar{a}^{\tau}_{M_3M_1} = (\bar{\varepsilon}_2 - \bar{\varepsilon}_1) \times \bar{\rho}_1 - (\bar{\varepsilon}_2 - \bar{\varepsilon}_3) \times \bar{\rho}_3 \tag{16.b}$$

It can be seen, as Voinea shows [7], that the tangential component $\bar{a}^{\tau}_{M_3M_1}$ is the relative derivative $\partial \bar{v}_{M_3M_1} / \partial t$ of relative velocity from the higher pair.

A particular case appears when one of the two profiles is a straight line (for example, $\rho_3 = \infty$). This situation cannot be analyzed with the equations obtained above by direct substitution of radius, $\rho_3 = \infty$ and the authors have analyzed this special case [8].

5 Conclusions

The kinematic parameters of an actual plane mechanism with higher pairs are found by means of an equivalent mechanism – the substitute linkage.

Using the vector loop-closure equation for the equivalent mechanism, the vector relations for relative velocity and relative acceleration from higher pair are found, and also, mentioning their properties. It is shown that, by relative derivative with respect to time of relative velocity, the tangential component of relative acceleration is found.

The advantage of the deduced relations consists in expressing the characteristics of the relative motion between the elements of the higher pair with respect to the local geometry of the two elements.

Appendix

The position of contact point M for the mechanism containing a higher pair can be found following the next methodology.

One considers two mobile planes P_1 and P_2, both parallel to a fix plane P. On each of the two planes, there is a curve, embedded into the plane and considered about mobile co-ordinate systems $O_1x_1y_1$ and $O_2x_2y_2$.

The parametric equations of the two planes, Fig. A1, are:

$$x_1 = x_1(t_1), y_1 = y_1(t_1).$$

$$x_2 = x_2(t_2), y_2 = y_2(t_2)$$

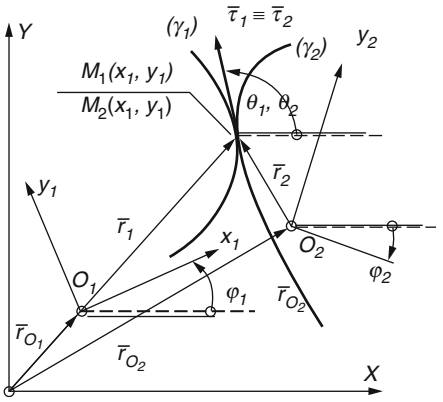

Fig. A1 A higher pair between two moving curves

The contact between the curves $(\gamma_1)$and (γ_2) implies:

- Coincidence of $M_2(x_1, y_1)$and $M_2(x_2, y_2)$ points
- The curves must have a common tangent in $M_2(x_1, y_1)$ and $M_2(x_2, y_2)$ points

The first condition is expressed as McCarthy proposed [9], by transforming the co-ordinates of the two points from mobile systems into fixed system, as a homogenous transform of plane co-ordinates, written under homogenous form. The transformation relation is written in matrix form:

$$\begin{bmatrix} A_1 & \mathbf{r}_{O_1} \\ 0 & 1 \end{bmatrix} \begin{bmatrix} \mathbf{r}_1 \\ 1 \end{bmatrix} = \begin{bmatrix} A_2 & \mathbf{r}_{O_2} \\ 0 & 1 \end{bmatrix} \begin{bmatrix} \mathbf{r}_2 \\ 1 \end{bmatrix} \tag{A.1}$$

where:

$$A_i = \begin{bmatrix} \cos(\varphi_i) & -\sin(\varphi_i) \\ \sin(\varphi_i) & \cos(\varphi_i) \end{bmatrix}, \quad \mathbf{r}_{O_i} = \begin{bmatrix} x_{O_i} \\ y_{O_i} \end{bmatrix}, \mathbf{r}_i = \begin{bmatrix} x_i(t_i) \\ y_i(t_i) \end{bmatrix}, \ i = 1, 2 \tag{A.2}$$

The A_i matrix and column vectors $\mathbf{r}_{O_i}$ define the displacement superimposing the fixed system XY over the mobile system $x_i y_i$ and the column vectors, $\mathbf{r}^t{}_i = [x_i(t_i), \quad y_i(t_i)]$, define the contact point position in mobile systems.

The second condition requires:

$$\varphi_1 + \theta_1 = \varphi_2 + \theta_2 + k\pi, k \in \mathbf{Z} \tag{A.3}$$

where: $\theta_i = atan[dy_i(t_i)/dx_i(t_i)]$, is calculated for the point where contact occur.

The Eq. (A.3) can lead to confusions due to $k\pi$ term. To avoid this inconvenience, the *tan(q)* function is applied to Eq. (A.3) and it results:

$$\frac{\tan\varphi_1 + \tan[\theta_1(t_1)]}{1 - \tan\varphi_1 \tan[\theta_1(t_1)]} = \frac{\tan\varphi_2 + \tan[\theta_2(t_2)]}{1 - \tan\varphi_2 \tan[\theta_2(t_2)]} \tag{A.4}$$

The following system results:

$$\begin{aligned}\cos(\varphi_1)x_1(t_1) - \sin(\varphi_1)y_1(t_1) + X_{O_1} &= \cos(\varphi_2)x_2(t_2) - \sin(\varphi_2)y_2(t_2) + X_{O_2}\\ \sin(\varphi_1)x_1(t_1) + \cos(\varphi_1)y_1(t_1) + Y_{O_1} &= \sin(\varphi_2)x_2(t_2) + \cos(\varphi_2)y_2(t_2) + Y_{O_2}\end{aligned}$$

$$\frac{\dot{x}_1(t_1)\sin\varphi_1 + \dot{y}_1(t_1)\cos\varphi_1}{\dot{x}_1(t_1)\cos\varphi_1 - \dot{y}_1(t_1)\sin\varphi_1} = \frac{\dot{x}_2(t_2)\sin\varphi_2 + \dot{y}_2(t_2)\cos\varphi_2}{\dot{x}_2(t_2)\cos\varphi_2 - \dot{y}_2(t_2)\sin\varphi_2} \tag{A.5}$$

where the upper dot point represents the derivative with respect to the parameter.

The system (A5) allows the finding of three of the parameters $X_{O_1}, Y_{O_1}, X_{O_2}, Y_{O_2}, \varphi_1, \varphi_2, t_1, t_2$ versus the remaining six parameters. For example, in the case of positional analysis of a rotating cam mechanism and oscillating follower, the positions of the joints are imposed via $X_{O_1}, Y_{O_1}, X_{O_2}, Y_{O_2}$, parameters, the position of the driving element, given by φ_1, and there are also known the equations of the curves (γ_1) and (γ_2).

The contact point between cam and follower is found, given by parameters t_1 and t_2, respectively, and the φ_2 angle, representing the angular movement of the follower.

References

1. Pelecudi, Chr, Maroş, D., Merticaru, V., Pandrea, N., Simionescu, N.: Mecanisme. E.D.P, Bucureşti (1985)
2. Dobrovolsky, V.V.: Theory of Mechanisms (in Russian). Maşghiz, Moscova (1953)
3. Uicker Jr., J.J., Pennock, G.R., Shigley, J.E.: Theory of Mechanisms and Machines, 3rd edn. Oxford University Press, New York (2003)
4. Hunt, K.H.: Kinematic Geometry of Mechanisms. Clarendon, Oxford (1978)
5. Hartenberg, R.S., Denavit, J.: Kinematic Synthesis of Linkage. McGraw-Hill, New York (1964)
6. Voinea, R., Atanasiu, M.: Metode analitice noi în teoria mecanismelor. Tehnică, Bucureşti (1964)
7. Voinea, R., Voiculescu, D., Ceauşu, V.: Mecanica. E.D.P, Bucureşti (1983)
8. Alaci, S., Ciornei, F.C.: Upon applying closed vector contours method for cam mechanisms with flat face follower. The Annals of "Dunărea de Jos" University of Galaţi, fascicle X, Appl. Mech. **XXIII**(XXVIII), 81–84 (2005)
9. McCarthy, J.M.: Introduction to Theoretical Kinematics. MIT Press, Cambridge, MA (1990)

Correlating Requirements Regarding the Command and the Mechanical Structure of the Automotive Steering System

P. Alexandru and C. Alexandru

Abstract The paper makes an analysis on the geometric and kinematic requirements of a steering system, and respectively the mechanical structure of the steering system which is able to meet those requirements. The paper refers to the requirement of achieving the correct steering law, the minimization of the rotation induced by the suspension displacement in the steering system, and the requirement concerning the angular capacity of the spherical joints. For the gear mechanisms of the steering box, the paper approaches the issue concerning the variable transmission ratio for both pinion – rack and rack – pinion variants.

Keywords Motor vehicle · Rack gear with variable ratio · Steering linkage

1 Introduction

Such important system for vehicle handling and safety (i.e., the steering system) must respond to multiple requirements [5–8], for which the automotive manufacturers developed sophisticated solutions at constructive and technological level. Certainly, the analysis of these solutions requires extremely large space.

As such, in this work, there are no references to the construction, either the hydraulic or electronic assistance, either direction or intelligent autonomous vehicle. We will refer to some basic requirements, say classical, and how to correlate them with the mechanical structure of the mechanisms from the steering system. Specifically, we refer to the requirement of achieving the correct steering law – a classical law which was intensively approached, the minimization of the steering induced by the suspension displacement – also a requirement much debated, the

P. Alexandru (✉)
Department of Product Design and Robotics, Transilvania University of Braşov, Braşov, Romania

I. Vişa (ed.), *SYROM 2009*,
DOI 10.1007/978-90-481-3522-6_17,

requirement of realizing variable transmission ratio – requirement that receives new solutions, and the requirement concerning the angular capacity of the spherical joints.

2 Functional Requirements for the Steering Linkage Mechanism (Steering Law, Induced Steering, Angular Capability)

Among the many requirements of the steering mechanism, we select as priority three of them, representing the fundamental kinematic functions.

- **The correct steering condition** considers that in turn the vehicle has an unique steering center for all wheels, and according with Ackerman equation (Fig. 1) this means

$$\mathrm{ctg}\theta_e - \mathrm{ctg}\theta_i = B_p/A_a. \tag{1a}$$

The equation can be modified by taking into account the lateral deviation of the elastic tires, as follows [1]:

$$\mathrm{ctg}\theta_e - \mathrm{ctg}\theta_i = B_p/kA_a. \tag{1b}$$

In equation (1), θ_e is the rotation angle of the wheel from the outside of the running curve, θ_i – the rotation angle of the wheel inside the curve, B_p – the distance between the wheels, A_a – the distance between the front and rear axes, $k = 1, 2\ldots 1$, 25 – the deviation coefficient of the tire.

Among the many linkage mechanisms presented in [1], which correlates the position of the two-wheel steering for the condition (1), we selected the two-loops mechanism with central pitman (Fig. 2a), and the variant with central rack (Fig. 2b).

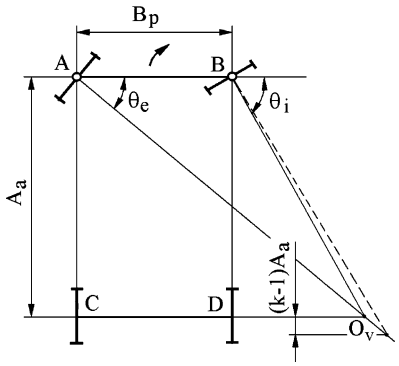

Fig. 1 The correct steering scheme

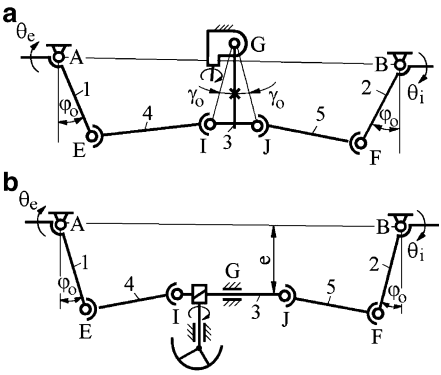

Fig. 2 Two-loops steering mechanisms

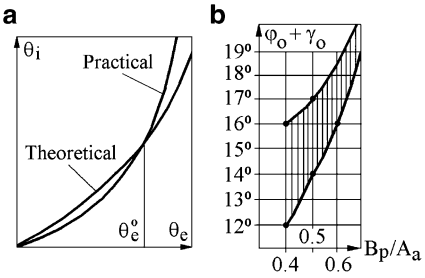

Fig. 3 The motion law θ_i (θ_e)

The motion law θ_i (θ_e) is graphically represented in Fig. 3a (the "practical" curve), while the "theoretic" curve represents the necessary condition (1).

The main parameter that influences the steering law θ_i (θ_e) is "$\varphi_{0,}$" This angle defines the positions of the steering knuckles levers 1–2, for the rectilinear displacement position (Fig. 2). The next parameter is the position/geometry of the central pitman arm 3, through the angle "$\gamma_{0,}$" or respectively the position of the rack 3, through the linear parameter "e."

Based-on these main parameters, the authors have developed the relations for obtaining the optimal values, so that the practical function to be closed-by the theoretic function θ_i (θ_e).

Generally, this condition can be obtained for an outside angle $\theta_e^{\circ} \approx 25–30°$, obtaining for beginning negative steering error, $\Delta\theta_i = \theta_i^{\,p} – \theta_i^{\,t}$, and then positive value. At the same time, we established the limit values, $\Delta\theta_i \approx -1.5° \ldots + 3...4°$ (Fig. 3a).

In this way, we can represent the optimal value field of these parameters (e.g., $\varphi_0 + \gamma_0$), also considering the characteristics of the vehicle, $B_p/A_{a,}$ and correlating these characteristics with other geometric parameters from the steering mechanism AEGFB, for instant the shaded field shown in Fig. 3b.

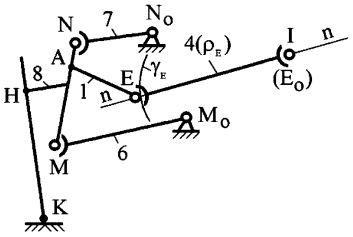

Fig. 4 The modeling of the rod curve

The usage of an optimization software do not always eliminate the major difficulty regarding the selection of the values for some geometric parameters, and the justified choice of the admissible steering error $\Delta\theta_i$; at the same time, there are problems concerning the theoretic steering function θ_i (θ_e).

• Other major problem of the linkage mechanisms used for the steering systems is **the induced steering**. When the wheel passes over a bump, there is the necessity for the wheel not to have oscillations from the running direction, in other words the suspension travel does not have influence on the steering system (does not generate "induced steering"). The phenomenon has negative influence on the vehicle behavior, and for this reason there is necessary to minimize the induced steering, $\theta_b^i \rightarrow 0$.

As you can see in Fig. 4, the pivot point A from the steering mechanism is located on the rod MN of the suspension mechanism. Therefore, at the wheel displacement KH, the joint E, which belongs to the rod (wheel carrier HMN), will describe a rod curve γ_E.

For avoiding the influence of the suspension travel on the steering position of the wheel, it is necessary for the joint I of the tie rod 4 to be located in the curvature centre of the rod curve γ_E described by E (for the rectilinear displacement). For this reason, the tie rod EI has the length equal with the curvature radius, $l_4 = \rho_E$, and the orientation is along the normal to γ_E. This problem is very complex from the mathematic (there is a spatial mechanical structure) and constructive point of view.

The relations obtained by I. Vişa [2] allow us to formulate a conclusion regarding the possibility of disposing the joint I not only in the curvature centre E_0, but on other axis passing through E_0 and normal on the plane of the curve γ_E. In this way, there are obtained supplementary variants for the optimum constructive design of the wheel guiding system (suspension – steering).

• Another important parameter is the **angular capability (capacity) of the spherical joints**. For avoiding blockings in the spherical joints of the mechanism, it is necessary to know exactly the relative motion between the bolt with spherical head and the carcass with spherical calotte, for the suspension travel as well as for the wheel steering motion.

In this way, the form, the dimensions and the location of the slot from the spherical carcass can be established. This is also a very complex problem because the mechanical system spatiality is defined by several parameters.

Thus, relative to the global reference frame xyz of the vehicle, the local reference frames $x_6y_6z_6/x_7y_7z_7$ attached to the suspension control arms 6, 7 are

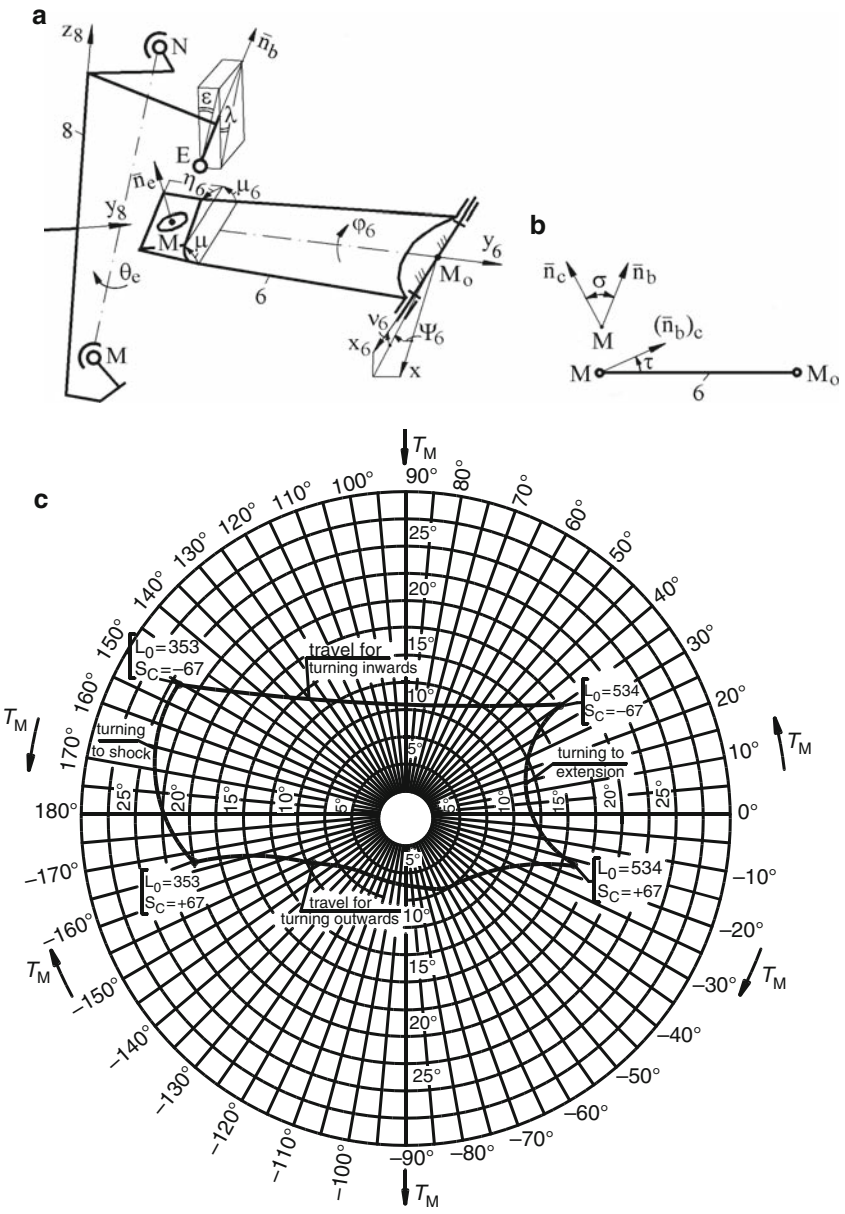

Fig. 5 The angular capacity of the joint

positioned by using two fixed angles (e.g., ψ_6 and ν_6), and the current motion angle, for example φ_6 (Fig. 5).

The carcass with spherical calotte is positioned relative to the plane of the control arm (Fig. 5a) by the angles μ_6 and η_6. The orientation of the bolt with

spherical head, which is connected to the wheel carrier 8, is defined in the local reference frame $x_8y_8z_8$, using the position angles λ and ε. At the same time, the wheel carrier reference frame $x_8y_8z_8$ is positioned by the pivot angles and by the current steering angle θ_e [2].

Therefore, the relations for computing the angles between the bolt axis and the normal axis to the plane of the carcass (σ), and respectively the projection of the bolt axis on the plane of the carcass (τ), are very complex. In fact, these angles define the angular capacity of the spherical joint (Fig. 5b).

An example for computing the angular capacity σ/τ is shown in the diagram from Fig. 5c (the diagram is represented in angular coordinates, σ/τ). The marked corners of the slot represent the extreme positions of the mechanical system in motion, namely for the maximum travel of the wheel (up/down), and the maximum steering motion (right/left).

3 Kinematic Requirement for the Steering Box with Rack (Variable Transmission Ratio)

Among the many requirements of operating the steering box, we refer only to the fundamental multiplier of effort by the driver at the steering wheel for an easy wheel steering. This multiplication, which is carried out in the transmission gears from the steering box, is defined by the transmission ratio. On vehicles which are not equipped with hydraulically assisted steering, the increasing of the steering effort with the actuating from the steering wheel can be compensated by increasing the transmission ratio of the box, thus making the boxes with variable ratios.

A special problem is to realize variable ratio for the pinion – rack or rack – pinion steering box, which is currently used.

- For the **pinion – rack** steering box (v. Fig. 2b), among the possible solutions for obtaining variable transmission ratio, $i \neq$ ct, we appreciate that a rack with variable profile angle is more realistic, the pinion being a classic one [3].

For obtaining symmetrical left/right motions, the rack is similar with the model shown in Fig. 6a. The rack contains the following zones: central zone, in which $i_{min} =$ ct, corresponding to the teeth profile angle α_1, intermediate left/right zones with variable ratio $i = i_{min}. . .i_{max,}$ corresponding to the profile angle $\alpha_1 \rightarrow \alpha_2$, end left/right zones with $i_{max} =$ ct, corresponding to the profile angle α_2 ($\alpha_2 < \alpha_1$).

The transmission ratio in the pinion – rack gear is defined by the angular velocity of the pinion and the linear velocity of the rack, as follows (r_p is the pinion radius):

$$i = \frac{\omega_p}{v_r} = \frac{1}{r_p}. \tag{2}$$

The obtaining of the variable ratio is justified by the property of the involute teeth profile, regarding the possibility to obtain different roll circles for the same

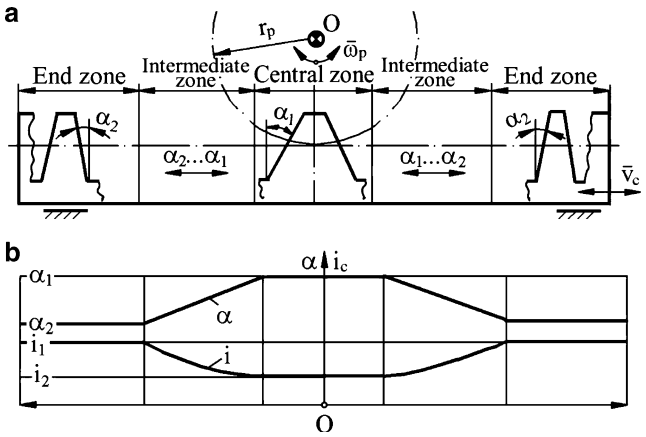

Fig. 6 The rack with variable profile angle

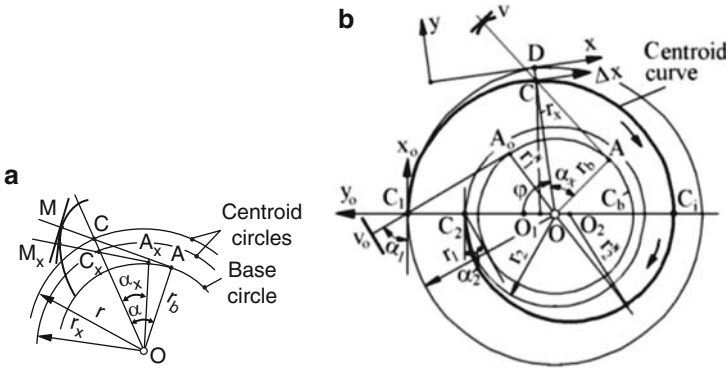

Fig. 7 The centroid circles and curve

teeth step p_b on the base circle, in other words, different gearing angles (Fig. 7a), according to the formula:

$$p_b = p_w \cos\alpha_w = p \cos\alpha = p_0 \cos\alpha_0. \quad (3)$$

Figure 7b presents a modeling scheme for the rack teeth with variable profile angle α and a classic pinion. There is a centroid by two eccentric circles (the centers O_1, and O_2), the gearing pole between pinion and rack traversing the centroid $c_1 c c_i c_2$ of the classic pinion. Obviously, for continuous variable ratio (in other words, a continuous centroid), the rack teeth profile is a curve (the difficulties are transferred to the manufacturing technology of the rack).

For obtaining a stepping variable ratio, the centroid (with jumps) of the pinion in gearing with the rack is shown in Fig. 8a, and this is possible if each teeth of the rack has its own profile angle (Fig. 8b). There is linear profile for the rack's teeth.

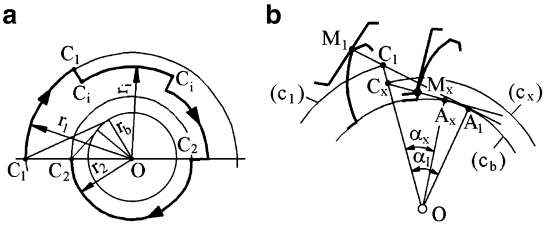

Fig. 8 The centroid with jumps

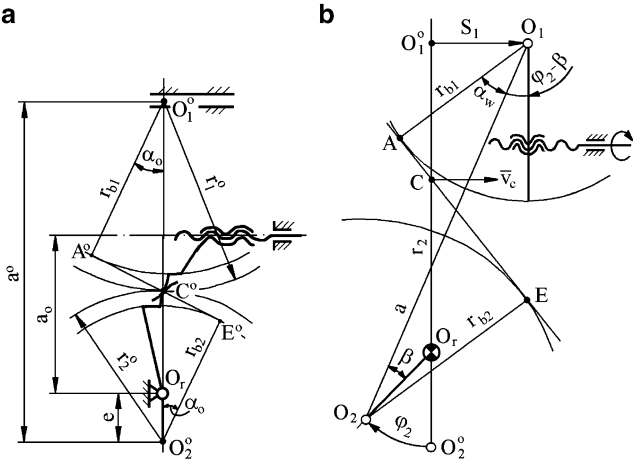

Fig. 9 The gearing scheme between the translated wheel and the eccentric sector

Since in this case can not exist simultaneously two pairs of teeth in gearing, there should be a single contact with degree of coverage $\varepsilon = 1$ (strictly), which is not acceptable, it is necessary to achieve "broken" profile, with two angles, which also generate technological problems (see Fig. 10).

Obviously, the transmission rate $i = 1/r_p$ will have a variation on the intermediary area of the rack, according with the variation of the division radius corresponding to the centroid curve $C_1CC_iC_2$ shown in Figs. 7b or 8a.

- For **the rack – pinion** steering box, which is practically realized by a screw – teethed nut – teethed sector group, a technological solution for obtaining variable transmission ratio is the transformation of the rack's nut in a **translated wheel** [4]. In this case, for realizing the necessary stroke of the steering system (regarding the vehicle functionality), there is necessary the gearing with an **eccentric sector** (Fig. 9a). The revolution centre O_r is not coincident with the pinion centre O_2 (there is the eccentricity "e").

According with the kinematic modeling shown in Fig. 9b, for the linear stroke S_1 of the wheel, the rotation φ_2 of the eccentric sector is obtained, the gearing pole moving from C^0 in C, and respectively the gearing angle α_0 (for the rectilinear displacement of the vehicle) will have the current value α_w. The notations with "0"

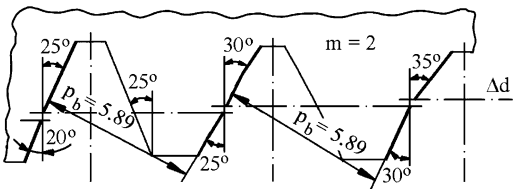

Fig. 10 Rack with "broken" profile

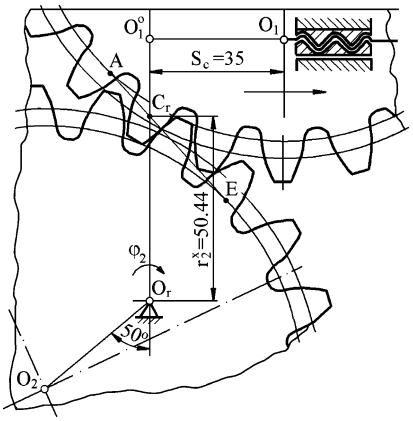

Fig. 11 Translated wheel and eccentric sector

exponent correspond to the initial position – for rectilinear displacement of the vehicle (Fig. 9a).

Obviously, the transmission ratio $i = 1/r_2$ will have a variation according with the variation of the sector's radius $r_2 = O_rC$.

Certainly, the correlation between the geometric parameters is very important for both pinion – rack and rack (wheel) – sector with variable transmission ratio.

Different computing examples performed by authors are shown in Fig. 10 (rack with "broken" profile) and Fig. 11 (translated wheel & eccentric sector), in the limited position.

4 Conclusions

All the five issues examined in the paper are decisive for the proper functioning of the mechanisms from the steering system of the motor vehicles. The paper highlightens the major solutions which are recommended usage in designing steering mechanisms from the geometric and kinematic point of view, as well as for the rack gearbox with variable ratio.

References

1 Alexandru, P., Vişa, I.: Modelarea structural-cineamtică a mecanismelor de ghidare a roţilor autovehiculelor rutiere. Lux Libris, Braşov (2001)
2 Alexandru, P., Vişa, I., Talabă, D., Alexandru, C., Antonya, C.S.: Modelarea statico-dinamică a mecanismelor de ghidare ale roţilor automobilelor. Lux Libris, Braşov (2005)
3 Alexandru, P.: The design of the pinion-rack steering gear with variable ratio. Proceedings of the 10th international conference TMM. Barcelona, 753–756 (2006)
4 Alexandru, P.: The rack-pinion gears for steering gearbox with variable ratio. Proceedings of the 12th IFToMM world congress. Besancon, 353–358 (2007)
5 Jin, Z.L., Weng, J.S., Hu, H.Y.: Rollover stability of a vehicle during critical driving manoeuvres. J. Automob. Eng. 221(9), 1041–1049 (2007)
6 Maclaurin, B.: Comparing the steering performances of skid – and Ackermann-steered vehicles. J. Automob. Eng. 222(5), 739–756 (2008)
7 March, C., Shim, T.: Integrated control of suspension and front steering to enhance vehicle handling. J. Automob. Eng. 221(4), 337–391 (2007)
8 Simionescu, P.A., Tempea, I., Loch, N.E.: Kinematic analysis of a two-degree-of-freedom steering mechanism. J. Automob. Eng. 215(7), 803–812 (2001)

Optimal Design of a Low-Mobility Schönflies Parallel Manipulator

O. Altuzarra, B. Sandru, C. Pinto, and O. Salgado

Abstract The optimal design of a Low-Mobility Parallel Manipulator with Schönflies motion is the subject of this paper. First, a general description of the manipulator is presented. Next, the discretized volume workspace is obtained making use of various circular trajectories. Further, the volume variation with dimensional parameters is purposed for optimal design. Similarly, the dispersion of the manipulator's dexterity based on the Frobenius norm is found and weighted. Next, the inverse dynamic problem is solved and, finally, kinematic and dynamic optimal functions are proposed in a multiobjective optimization. The results are shown as a set of Pareto-optimal solutions for the optimal design.

Keywords Multiobjective optimization · Parallel manipulators · Pareto front

1 Introduction

The parallel manipulators are mechanisms with two or more kinematic chains composed of a moving platform (MP) linked to a fixed base platform (BP) by several limbs. They are low-mobility manipulators if poses less than six degrees-of-freedom (dof) [4]. Several architectures of parallel robots for Schönflies-motion generation have been proposed during the last decade. An extensive list of this kind of manipulators is presented in [5].

The optimal design has been considered an important issue for achieving desired performances. For the optimization, various kinematic and dynamic functions have been used as performance criteria, e.g., workspace volume, dexterity, payload etc. Optimizing various objective functions at the same time converts the optimal

O. Altuzarra (✉)
Bilbao Department of Mechanical Engineering, University of Basque Country, Spain

I. Vişa (ed.), *SYROM 2009*,
DOI 10.1007/978-90-481-3522-6_18,

design in a mixed multiobjective optimization [6]. Often, optimum design problems imply a general conflicting in nature of several objectives. Thus, the best result with respect to all objectives is a set of optimal solutions which is called the Pareto optimal or non-dominated set.

Various techniques have been proposed to find the best compromise of a multi-objective optimization problem. Comparative studies between different methods have been presented during the years. However, some of these methods do not guarantee a Pareto optimal solution. An interval analysis based approach was proposed in [3] where all possible solutions are obtained as a set of regions in the parameter space.

In this paper a new multiobjective optimum design of the 4-dof Schönflies parallel manipulator is proposed. New objective functions related to the actuator's performance are proposed. First, a briefly description of the manipulator and its kinematics is recall. The first objective function to optimize is the workspace volume which is numerically discretized according to various circular trajectories. Then, the dexterity analysis, with the local distribution of the dexterity index on the workspace, is obtained which is also subject of the optimization. Next, the manipulator's inverse dynamic problem is solved in order to compute the energy consumption within the workspace which is also an optimization objective. Finally, the multiobjective results are obtained as a Pareto-optimum set.

2 Manipulator's Description

The parallel robot [7] presented in Fig. 1 is optimized in this paper. Designed for pick-and-place operations, the displacements involved are those of the four-dimensional Schönflies subgroup [2].

Four identical prismatic legs of the *PRΠRR* type supply the robot, namely: *P*, the actuated prismatic joint, in the direction of the unit vector **i** for $j = 1, 3$, and of **j** for $j = 2, 4$; *R*, of axis normal to the previous unit vectors and passing through B_j; the parallelogram joint Π, of plane normal to $\mathbf{n}_j$; *R*, of axis parallel to **j** for $j = 1, 3$, and to **i** for $j = 2, 4$; and *R*, of axis parallel to **k**.

2.1 Kinematics

The position vector of *P* can be expressed for limb *i* as

$$\mathbf{x}_P = \mathbf{x}_{A_i} + \mathbf{x}_{A_iB_i} + \mathbf{x}_{B_iC_i} + \mathbf{x}_{C_iD_i} - \mathbf{x}_{PD_i}, i = 1, ..., 4 \tag{1}$$

where the position vector of a given point X_i is denoted by the corresponding vector $\mathbf{x}_i$. Moreover, the position vectors of points A_i belongs to the base platform (BP).

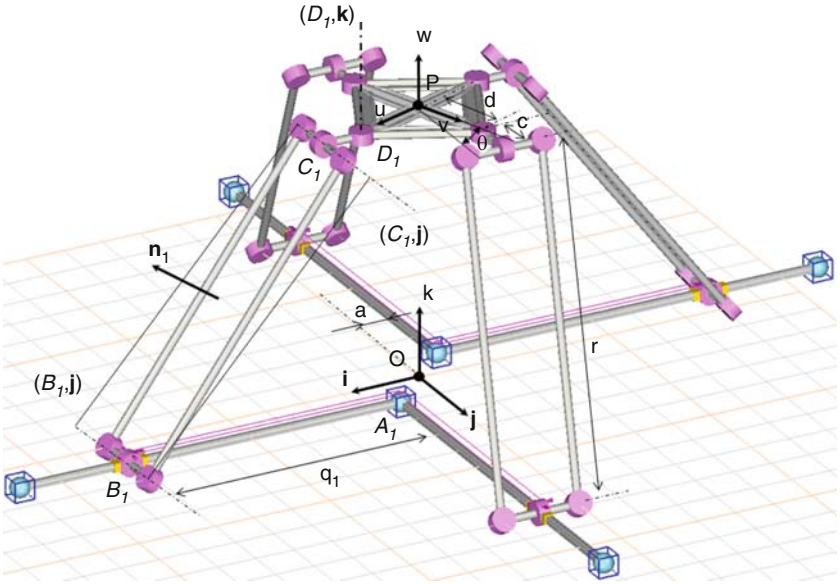

Fig. 1 Parallel manipulator in use

The vectors A_iB_i are expressed in terms of the actuated-joint variables q_i; vectors C_iD_i are constant throughout the robot workspace, e.g., have translational motion.

These vectors belong to the moving platform frame M (P, **u**, **v**, **w**) and, thus, the transformation to the frame B (O, **i**, **j**, **k**) is given by the rotation of angle θ around the z axis, where θ is the orientation angle of the MP with respect to the BP.

As vectors B_iC_i must satisfy the constraints

$$\|\mathbf{x}_{B_iC_i}\|^2 = r^2, i = 1, ..., 4 \tag{2}$$

with r representing the norm of B_iC_i, the values of the joint variables q_i are found upon substitution of equation (1) into equation (2) with the vectors described above as

$$\begin{aligned} q_1 &= x_P + d\cos\theta - a + c \pm \sqrt{\Delta_1} \\ q_2 &= x_P + d\cos\theta - a + c \pm \sqrt{\Delta_2} \\ q_3 &= -x_P + d\cos\theta - a + c \pm \sqrt{\Delta_3} \\ q_4 &= -x_P + d\cos\theta - a + c \pm \sqrt{\Delta_4} \end{aligned} \tag{3}$$

where Δ_i, for i = 1, ..., 4 are expressed by the next expressions:

$$\begin{aligned}\Delta_1 &= r^2 - (y_P + d\sin\theta - a)^2 - z_P^2\\ \Delta_2 &= r^2 - (x_P - d\sin\theta - a)^2 - z_P^2\\ \Delta_3 &= r^2 - (y_P - d\sin\theta + a)^2 - z_P^2\\ \Delta_4 &= r^2 - (x_P + d\sin\theta + a)^2 - z_P^2\end{aligned} \tag{4}$$

where x_P, y_P and z_P are the coordinates of the output point P of the (MP), a, c, d, r are the manipulator's design parameters and corresponding to the vectors described above, e.g., $\mathbf{x}_{A_i}$, $\mathbf{x}_{C_iD_i}$, $\mathbf{x}_{PD_i}$ respectively.

The existence of the 2^4 different solutions of $\mathbf{q}$ for a given pose depends on the equations (4) which also represent the cylinder's bounds for every kinematic chain of the manipulator. The working mode chosen is the one shown in Fig. 1.

Henceforth, for a refined further optimization, we introduce the actuator's path limits as

$$q_{\min} \leq q \leq q_{\max} \tag{5}$$

where $\mathbf{q}_{\min}$ and $\mathbf{q}_{\max}$ are the minimal and the maximal path of the actuators. Differentiating equation (1) with respect to time, and cancelling passive-joint-rate terms, the velocity equation is obtained as

$$J_v\dot{x} = J_q\dot{q} \tag{6}$$

where $\dot{x} = \begin{bmatrix}\omega_z & \dot{p}^T\end{bmatrix}^T$ is the four-dimensional MP twist, the actuated-joint-rate vector is $\dot{\mathbf{q}} = [\dot{q}_i]$, for $i = 1, ..., 4$, and the Jacobian matrices $\mathbf{J}_v$ and $\mathbf{J}_q$ are expressed by the equation (8). The vector $\mathbf{r}_i$ is defined as the unit vector directed from B_i to C_i, and vector $\mathbf{s}_i$ is a cross product, namely

$$\mathbf{r}_i = \frac{1}{r}\mathbf{x}_{B_iC_i}, \mathbf{s}_i = \mathbf{x}_{PD_i} \times \mathbf{r}_i, i = 1, ..., 4 \tag{7}$$

$$J_v = \begin{bmatrix} s_1^T k & r_1^T \\ s_2^T k & r_2^T \\ s_3^T k & r_3^T \\ s_4^T k & r_4^T \end{bmatrix}, \qquad J_q = \begin{bmatrix} r_1^T i & 0 & 0 & 0 \\ 0 & r_2^T j & 0 & 0 \\ 0 & 0 & -r_3^T i & 0 \\ 0 & 0 & 0 & -r_4^T j \end{bmatrix} \tag{8}$$

Further, by differentiating the equation (6) with respect to time we obtained acceleration equation as

$$J_v\ddot{x} + J_q\ddot{q} = h \tag{9}$$

where $\ddot{x} = \begin{bmatrix}\dot{\omega}_z & \ddot{p}^T\end{bmatrix}^T$ is the output acceleration vector and $\ddot{q} = [\ddot{q}_i]$, for $i = 1, ..., 4$, is actuated-joint-rate acceleration vector; $\mathbf{h}$ is a vector dependent of the position and velocity of the output vector $\mathbf{x} = [\theta \quad x_P \quad y_P \quad z_P]$, the passive coordinates and the Corriolis accelerations.

2.2 Dynamics

The inverse dynamics of the manipulator is also needed in the presented work. Thus, taking advantage of equations (6) and (9) and using a Lagrangian approach with dependent coordinates, we introduced the Lagrange multipliersλ. The end-effector dynamic contribution has been found with the output coordinates x, while the contribution of each limb has been stated as a function of input and passive coordinates, **q** and **f** respectively. All coordinates are related among them through the twelve scalar equations in equation (1), i.e., $\mathbf{\Gamma}$. The Lagrange equations for output and passive coordinates produce a linear system of equations in $\boldsymbol{\lambda}$, namely

$$\frac{d}{dt}\left(\frac{\delta L}{\delta \dot{x}}\right) - \frac{\delta L}{\delta x} - \tau_x = \left[\frac{\delta \Gamma}{\delta x}\right]^T \lambda \qquad \frac{d}{dt}\left(\frac{\delta L}{\delta \dot{f}}\right) - \frac{\delta L}{\delta f} = \left[\frac{\delta \Gamma}{\delta f}\right]^T \lambda \tag{10}$$

where $\boldsymbol{\tau}_\mathbf{x}$ is the given load of the output motion requirement.

Once the $\boldsymbol{\lambda}$ are solved, input forces $\boldsymbol{\tau}_\mathbf{q}$ can be solved in the linear system given by the Lagrange equations for input coordinates

$$\tau_q = \frac{d}{dt}\left(\frac{\delta L}{\delta \dot{q}}\right) - \frac{\delta L}{\delta q} - \left[\frac{\delta \Gamma}{\delta q}\right]^T \lambda \tag{10'}$$

3 Trajectory Based Criteria

The evaluation of the actuation system implies the use of different kinds of trajectories upon the manipulator's operational space. Some researchers have used the so called Adept cycle for pick and place manipulators. However, this type of trajectory is very specific, usually placed in a reduced part of the operational workspace, and do not evaluate the global manipulator's performance.

In the following, we will use circular trajectories, with a discretization pattern, centered in the Z axis, horizontal at a varying position in Z, and with a changing radius from zero to the maximum allowed by the inverse position problem. We will evaluate which radiuses are completely included in the workspace, and with this information an operational volume will be found. Jacobian analysis will be performed at postures in those circles to get dexterity measures. Actuator's variables will be evaluated for given motion requirements and performance indicators will be defined. Inverse dynamics will be solved to get power requirements to trace those paths. Finally, related indicators are sought.

The parameters design a, c, d and r shown in Fig. 1 are used for the optimization and we will take the constant value $r = 1$as a scale factor. Actuator's path limits or secondary geometrical parameters can be added to this list. For the time being, we will focus to the main geometrical parameters above and the limits of the actuator's path.

3.1 Workspace and Volume

In order to obtain the manipulator's workspace numerically, we proceeded to find a number of points within the workspace. This consist in setting first the actuator's limits q_{min} and q_{max}, then, obtaining the inverse kinematic problem (IKP) in the analytic way, and, finally, test each point for solution. Thus, every reachable point within the circular trajectories described above is inside the workspace if it accomplishes with equation (3) and equation (5). Further, all the points of such trajectories are added to the operational workspace. Hence, the manipulator's workspace volume is end-effector orientation dependent, being bigger for values of θ in the proximity of zero and, not only smaller for different values of θ but also included in the former.

For constructive reasons this orientation angle will vary within a range of $\pm\pi/6$. In our case, we have chosen to identify the largest dexterous workspace accessible. Hence, the circular trajectories defined will be performed with a constant orientation $\theta = \pi/6$ that guarantees that all values of θ inside the range of $\pm\pi/6$ are accessible.

It is obvious that it must be assume a certain error in the calculus of the volume, knowing that the discretization simplifies the continuous space. This error depends of the incrementation in r and Z that is used to define the manipulator's workspace. One can take into account that the operational workspace (see Fig. 2) leave outside points from the maximal reached workspace also.

In Fig. 3a the volume function is depicted varying a, c and d within a given range. It has been produced sections of this function for several values of a, in Fig. 3b, where the variation with c and d can be easily observed. These results indicate that a, is a parameter predominant in the volume function.

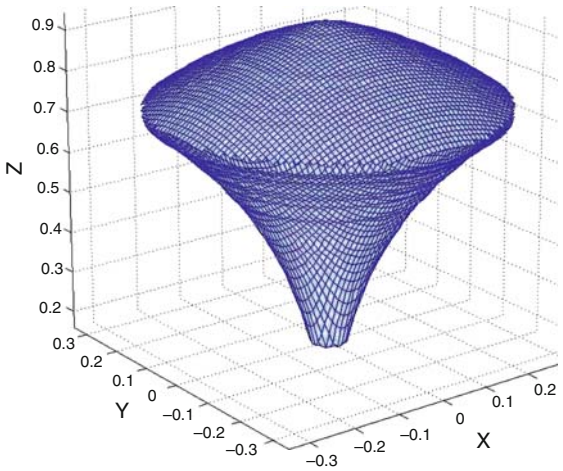

Fig. 2 Operational workspace

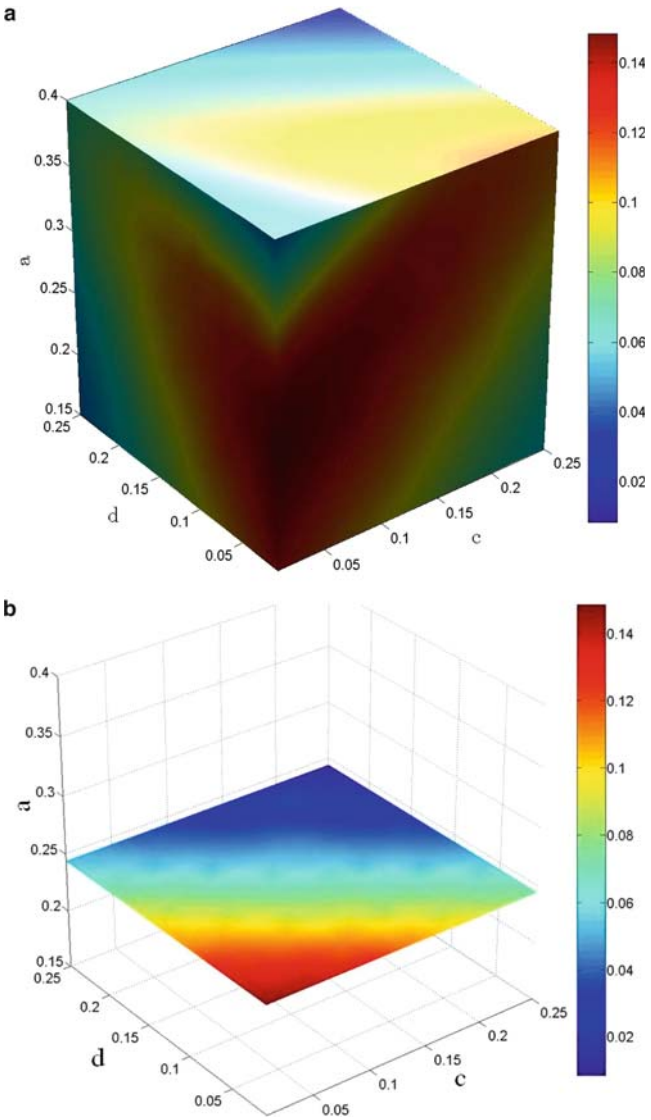

Fig. 3 Volume function

3.2 Dexterity

Two kinds of kinematic singularities where their controllability is lost are present, namely, the direct singularities pertaining to $\mathbf{J}_v$, and the Increased Instantaneous

Mobility (IIM) singularities [1]. In the case of the robot at hand, only singularities of the Jacobian matrix $\mathbf{J}_v$ are related, as no IIM singularities exist inside the robot.

The position accuracy is measured by implementing performance indices, e.g., the condition number. In order to obtain meaningful assessments, the Jacobian matrices must be dimensionally homogeneous [8], which is possible if one resorts to the concept of characteristic length.

The 2-norm condition number $\kappa_2$is frequently used in robotics. However, this condition number is not an analytic function of the robot posture, which can be a serious concern when gradient evaluations of the index are needed.

A performance index can be used instead, as the condition numberκ_F, based on the weighted Frobenius norm and defined as

$$\kappa_F(\bar{J}_v) = \|\bar{J}_v\|_F \left\|\bar{J}_v^{-1}\right\|_F \tag{11}$$

where $\bar{J}_v$ is the Jacobian $J_v$with a characteristic length introduced to make term homogenous. The weighted Frobenius norm is defined as

$$\|\bar{J}_v\|_F = \sqrt{\frac{1}{4} tr\left(\bar{J}_v \bar{J}_v^T\right)} \tag{12}$$

However, this performance index only shows the local robot performance at a given posture. Thus, a global value for the whole workspace, which provides only one value of the robot performance, is needed. This is to be used as an objective for the optimum design and is expressed by a global index as

$$\varepsilon_g = \frac{1}{N} \sum_{i=1}^{N} \left(\frac{1}{\kappa_F}\right)_i \tag{13}$$

where $N$is the number of points within the discretized workspace and $\varepsilon_g \in [0; 1]$.

For the manipulator in Fig. 1, a distribution of the global dexterity was obtained for constant orientations $\theta = 0$, $\theta = \pi/12$ and $\theta = \pi/6$. This distribution have been depicted in Figs. 4a, b, c respectively, for the previous range of the geometric parameters a, c and d. In this case, it was observed a notorious variation of the global dexterity. Therefore, we have obtained a mean value for θ between $-\pi/6$ and $\pi/6$, analyzing for several values of θ.

The designer should also take care of the distribution of local indices, so that the distribution is smooth in the workspace. On the contrary, many peak values on the workspace could provide the same global index, thereby indicating an unsuitable workspace.

We have plotted in Fig. 5 the percentage of points of the discretized workspace as a function of their local dexterity for two different manipulator's configurations. In Fig. 4a the design parameters are $a = 0.125$ m, $c = 0.102$ m, $d = 0.070$ m while in Fig. 4b the design parameters are $a = 0.35$ m, $c = 0.155$ m, $d = 0.082$ m corresponding to a maximal volume.

Fig. 4 Dexterity function

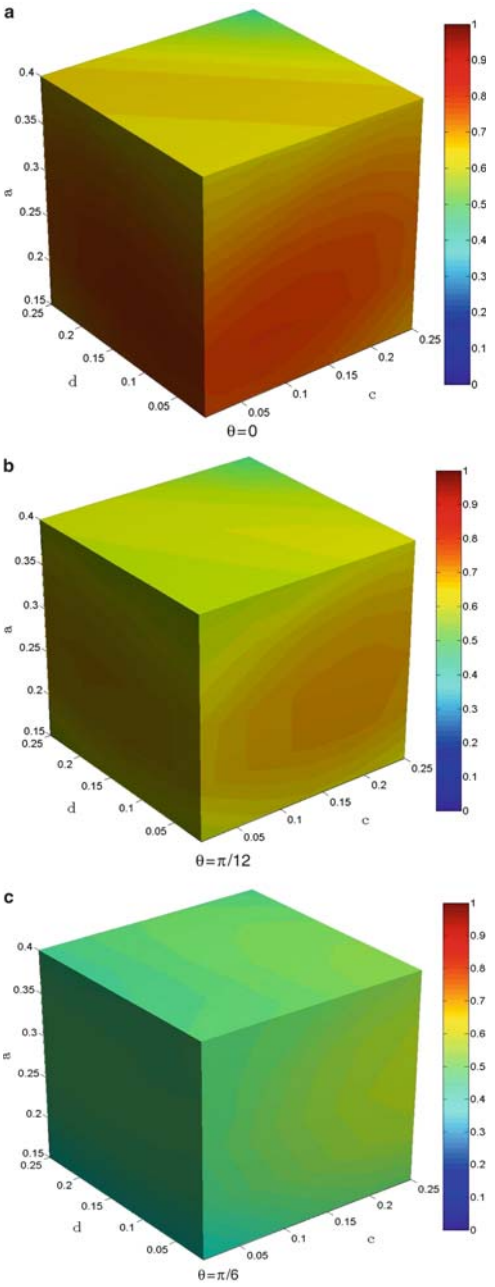

The value of standard deviation σ obtained in the distribution of local dexterity values above, can be used as a measure of the dispersion about the mean value. Then, this can be used to weight the global dexterity value and take into account the dispersion on the workspace accordingly.

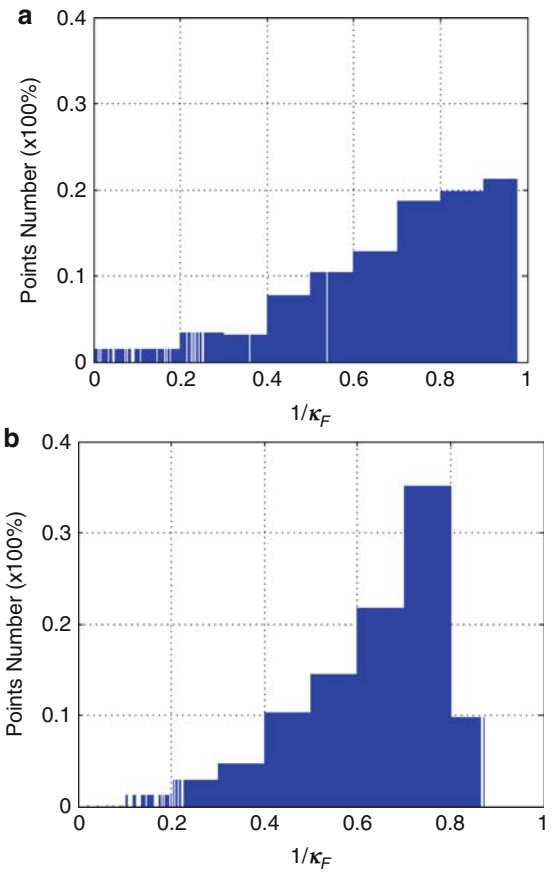

Fig. 5 Local dexterity distribution

In Fig. 6 we have plotted the modified value of the weighted global dexterity $\varepsilon_g - \sigma$ in the dexterous operational workspace taking into account the dispersion.

3.3 Input Energy Per Output Cycle

The energetic demand of the manipulator is one of the most important issues in the optimization design. By taking the advantage of the inverse dynamic problem, the input forces needed for each trajectory traced can be evaluated. Using the kinematic results for the inputs mentioned above, it is possible to find the power needed at the actuators in such motions. Again, these results are fully dependent on the motion demands, and not comparable if different circles are considered. Therefore, we need to relativize the power consumed with the circle traced.

The first attempt has been to make a ratio of the input energy per output cycle. In the dynamic analysis, link masses are proportioned to its length dimensions when

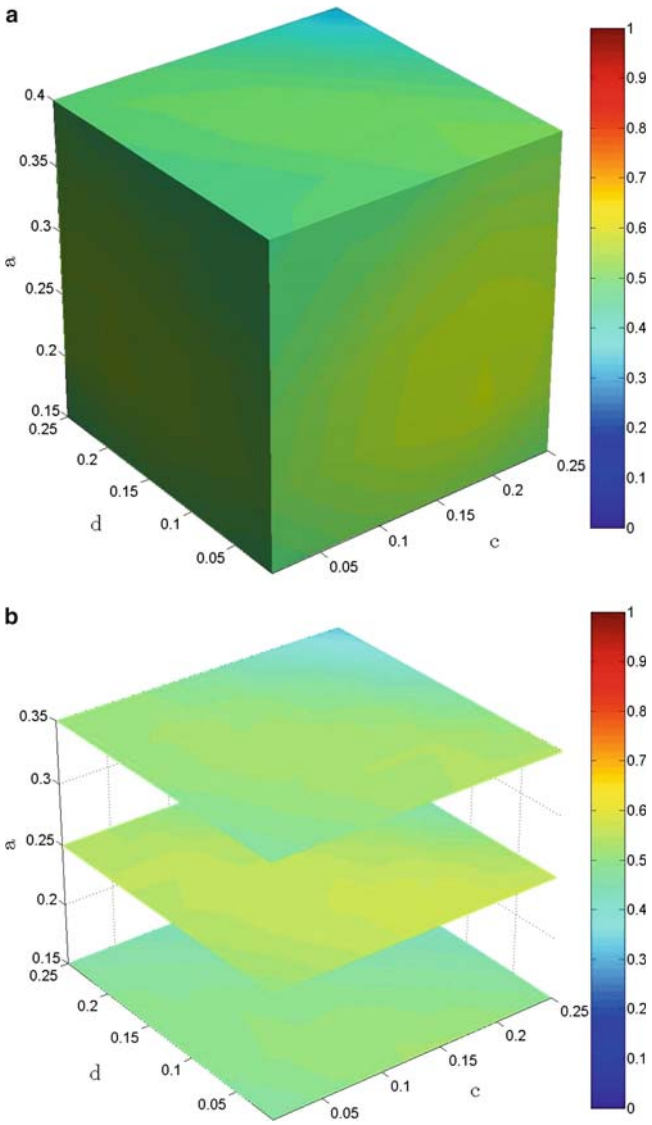

Fig. 6 Weighted dexterity function

varying geometric parameters c and d. As a first objective, the power needed for each actuated joint was computed as

$$P^j_{q_i} = \tau^j_{q_i} \cdot \dot{q}^j_i, \begin{array}{l} \forall j = 1, \ldots, n \\ \forall i = 1, \ldots, 4 \end{array} \tag{14}$$

where $P^j_{q_i}$ represents the power needed for ith actuated joint at the jth output position in a single circular trajectory, n is the discrete points number that generate a circular trajectory. Then, the energy of each actuator is computed as

$$E_i = \int_0^t P_{q_i} dt = \sum_{j=1}^{n} P^j_{q_i} \Delta t \tag{15}$$

with E_i being the energy of the ith actuated joint and t the motion time per a single circular trajectory. However, the closed-form integral of equation (15) turns to be a difficult task, knowing that the power, in this case, was numerically computed and does not have a continuous form. Thus, an easily approach was to numerically approximate the sum of each area of the power in the unit time interval Δt. Then, a ratio between the sums of the four input joints energy per trajectory cycle is obtained. Finally, various ratios are obtained for all the computed output trajectories within the operational workspace and a mean is calculated as a global ratio for each set of values a, c and d. The result is plotted in Figs.7a, b.

4 Pareto-Optimally Based Multiobjective

Pareto efficiency is a way of finding the optimal allocation subject to several objective functions that does not use a minimization procedure. The procedure leans on an iterative solution of the objective functions over a parameter's range of values, and a representation of the results on the space of the objectives. Then, the set of results with better values of the objectives is easily appreciated as an extreme manifold called Pareto front. On this Pareto front, the definite optimal solution is chosen upon additional considerations defined by the user.

In our case, we will use the parameters space [a, c, d] and the objective functions space [V, ε_g, E] defined by the dexterous operational workspace volume, dexterity weighted with the standard deviation, and input energy per output cycle. Thus, these objective functions were normalized to a non-dimensional range with their maximum values so the unity is the best result.

By extracting and scaling the values of the objective functions in Figs. 3a, 6a, and 7a, and their representation on the objectives space, we get Fig. 8. In this figure, the Pareto front is represented by a surface whose points fit best the input multiobjective requirements.

Finally, an optimal point was chosen in Fig. 8 with dimensional values [$a = 0.15$ m, $c = 0.07$ m, $d = 0.07$ m], whose scaled objectives are 0.58 in V, 0.89 in ε_g, and 0.85 in E, i.e., volume 0.84 m^3, dexterity 0.6 and input energy per output cycle 25.5 J/m.

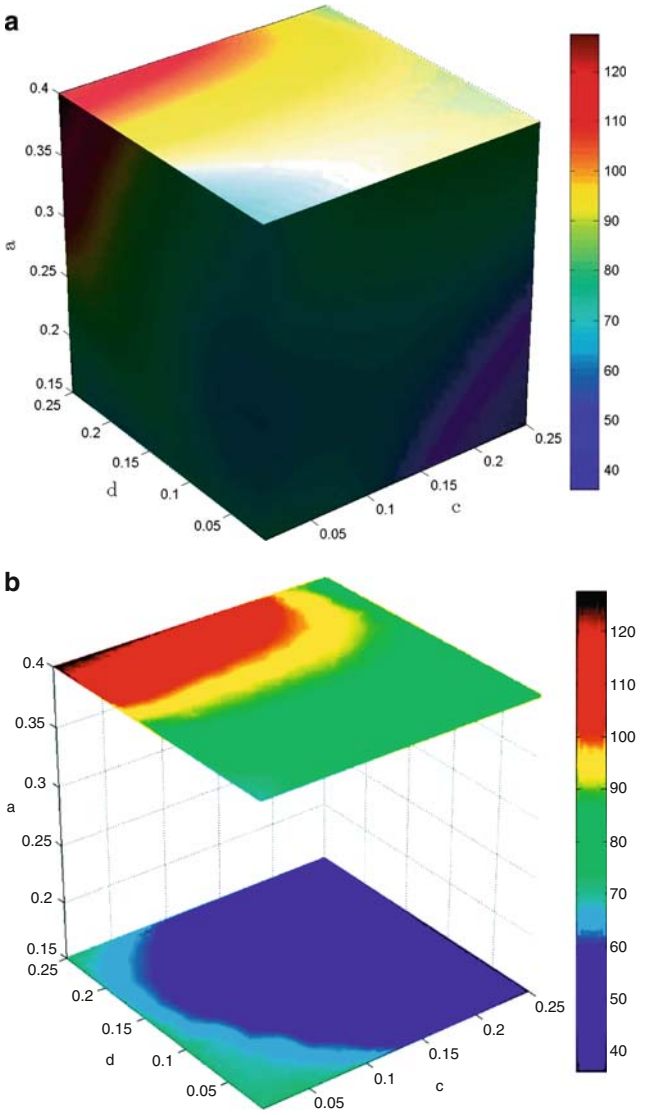

Fig. 7 Input energy per output cycle

5 Conclusions

In this paper, the Pareto efficiency concept has been applied to the multiobjective optimization of a parallel manipulator with three objective functions. First, kinematic functions of volume and dexterity have been used. However, the volume considered is the one obtained of a dexterous workspace, being closer to the

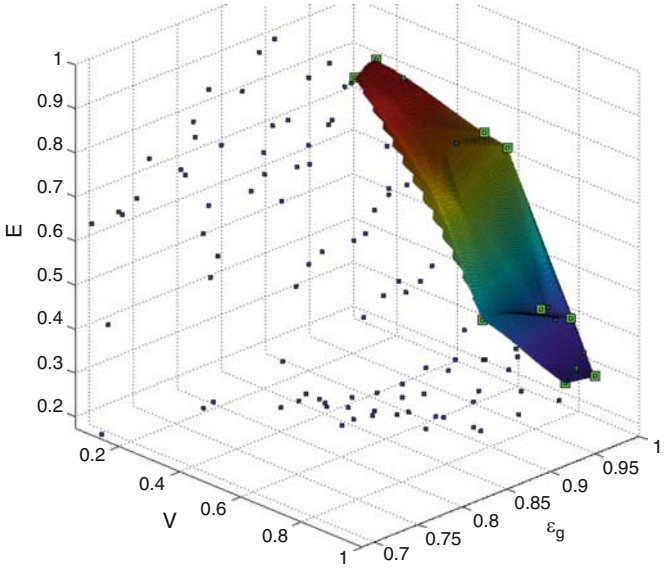

Fig. 8 Pareto front and Pareto index

operational workspace. Moreover, the dexterity has been found as a mean value of the dexterous workspace and weighted with a measure of the local dispersion of dexterity. Second, a dynamic function has been used to assess the power requirement of the manipulator. Finally, these functions have been scaled to be used in the transformation from the dimensional space to the objective functions space, in order to assess the Pareto front and to choose the optimal solution upon the designer judgment.

Acknowledgments The authors of this paper wish to acknowledge the finance received from the Spanish Government via the Ministerio de Educación y Ciencia (Project DPI2008–00159), the FEDER founds of the European Union and the University of the Basque Country (Project GIC07/78).

References

1. Altuzarra, O., Pinto, C., Avilés, R., Hernández, A.: A practical procedure to analyze singular configurations in closed kinematic chains. IEEE T. Robotic. 20(6), 929–940 (2004)
2. Angeles, J.: The degree of freedom of parallel robots: A group-theoretic approach. Proceedings of IEEE international conference on robotics and automation,1017–1024 (2005)
3. Hao, F., Merlet, J.-P.: Multi-criteria design of parallel manipulators based on interval analysis. Mecha. Machi. Theory 40, 157–171 (2005)
4. Huang, Z., Li, Q.: General methodology for type synthesis of symmetrical lower-mobility parallel manipulators and several novel manipulators. Int. J. Robot. Res. 21(2), 131–145 (2002)

5. Kong, X., Gosselin, C.: Type synthesis of 3T1R 4-DOF parallel manipulators based on screw theory. IEEE Trans. Robot. Autom. 20(2), 181–190 (2004)
6. Liu, X.-J., Guan, L., Wang, J.: Kinematics and closed optimal design of a kind of PRRRP parallel manipulator. ASME J. Mech. Design 129(5), 558–563 (2007)
7. Salgado, O., Altuzarra, O., Petuya, V., Hernández, A.: Synthesis and design of a novel 3T1R fully-parallel manipulator. ASME J. Mech. Design 130(3) (March 2008)
8. Schwartz, E., Manseur, R., Doty, K.: Noncommensurate systems in robotics. Int. J. Robot. Autom. 17(2), 1–6 (2002)

Dynamic Transmission Error Prediction of Spur Gear Pairs with Friction Consideration

V. Atanasiu, D. Leohchi, and C. Rozmarin

Abstract The paper presents an analytical and computer-aided analysis of the dynamic transmission error of spur gear mechanisms. The dynamic analysis of geared systems is difficult to accurately investigate due to the nonlinear characteristics accounting for periodic changes of tooth stiffness and sliding friction. A comparative study has been performed to investigate the effects of the mesh stiffness variation and sliding friction between contacting teeth on the dynamic transmission error of gear systems.

Keywords Dynamic transmission error · Friction · Spur gear

1 Introduction

The geared servomechanisms are used in many applications to transmit power and motion. The dynamic transmission error is considered as a relevant parameter in the dynamic behavior of geared systems [10, 12, 13]. Accurate dynamic modeling of these devices becomes important in order to reduce the undesired vibrations [13, 14].

Usually, dynamic models of spur gear pairs are based on the assumption that the load is equally shared among the tooth pairs in contact [4, 10–12]. In these models, Coulomb friction is assumed with a constant coefficient of friction μ. These assumptions not lead to a realistic dynamic model of gear pairs.

In order to obtain a realistic dynamic model, two main nonlinearities, sliding friction and variable mesh stiffness are considered in the paper.

V. Atanasiu (✉)
Department of Mechanisms Theory and Robotics, Technical University "Gheorghe Asachi" Iasi, Iasi, Romania

I. Vişa (ed.), *SYROM 2009*,
DOI 10.1007/978-90-481-3522-6_19,

Both, the average and the instantaneous friction coefficient are difficult to calculate. The existing equations for these coefficients [3–6,11] cannot be used with good results in the case of dynamic analysis.

An alternative calculus methodology for the instantaneous friction coefficient of spur gear pairs is proposed in the paper. The frictional forces on the gear tooth surfaces are computed by considering instantaneous friction coefficient and the dynamic normal load of the meshing cycle in relation to the variable mesh stiffness.

The frictional forces is then incorporated into a nonlinear dynamic model of the spur gear with the contribution of the time-varying mesh stiffness. The mesh stiffness along the path of contact is found by using an exact analytical model.

It can be expected that the improved dynamic model will provide an accurate prediction of the dynamic of the dynamic transmission error of spur gear pairs.

2 The Dynamic Model of Spur Gear

The dynamic model for a gear pair in mesh is shown in Fig. 1. In this model, the teeth are considered as springs and the gear blanks as inertia masses. The gear mesh interface is represented by the time-varying mesh stiffness $k_i(t)$ and the viscous damper c. The composite tooth profile error $e_i(t)$ represents the manufacturing errors and modifications of the involute tooth profile.

Figure 2 presents the distribution of the dynamic normal forces F_d^i and friction forces F_f^i among the pairs of teeth in contact, where $i = I, II$ represents the pair of contacting teeth I and II, respectively.

Referring to Fig. 2, the following mesh points were used to represent the successive positions of contact point of a tooth as it passes through the zone of loading: the initial point of engagement, A; the lowest point of single-tooth contact, B; the highest point of single-tooth contact, D; and the final point of engagement, E.

Section AB and DE are double – tooth contact zone and section BD is the single tooth – contact zone.

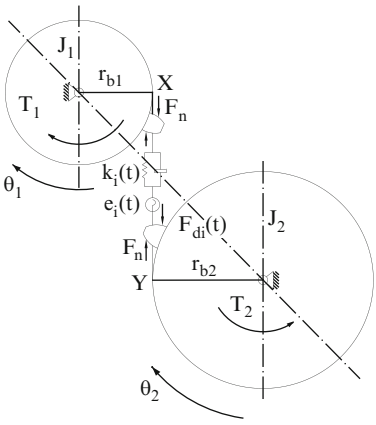

Fig. 1 Dynamic model of a spur gear pair

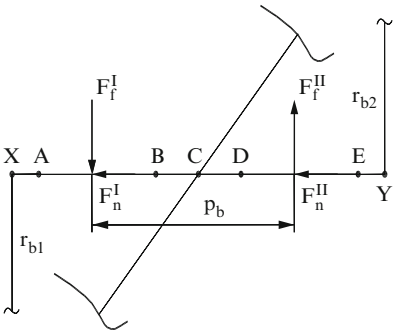

Fig. 2 Normal and friction forces

The differential equations of motion can be expressed as

$$J_1\ddot{\theta}_1 = T_1 - \sum_{i=I}^{II} r_{b1}F_d^i + \sum_{i=I}^{II} l_1^i F_f^i \tag{1}$$

$$J_2\ddot{\theta}_2 = -T_2 + \sum_{i=I}^{II} r_{b2}F_d^i + \sum_{i=I}^{II} l_2^i F_f^i \tag{2}$$

where $\theta_1,\ \theta_2$ are the rotation angle of the pinion and the driven gear, respectively. J_1 and $J_2$are the mass moments of inertia of the gears. T_1 and T_2 denote the external torques applied on the gear system and $r_{b1},\ r_{b2}$ are the base circle radii of the gears, l_1^i represents the distance measured from the point X to the mesh point and l_2^i is the distance measured from the point Y.

The dynamic normal load between two meshing gear teeth is expressed as

$$F_d^i = k_i(t)(r_{b1}\theta_1 - r_{b2}\theta_2 + e_i(t)) + c(r_{b1}\dot{\theta}_1 - r_{b2}\dot{\theta}_2) \tag{3}$$

where c is the damping coefficient calculated by

$$c = 2 \cdot \xi \cdot \sqrt{m_e \cdot k_m} \tag{4}$$

where m_e represents the equivalent inertia mass, k_m is the average mesh stiffness of the gear pair and t shows the meshing time. In the dynamic analysis, the amount of the damping ratio ξ= 0.1 is considered.

The dynamic transmission error (DTE) along the line of action is defined as

$$\delta_d = r_{b1}\theta_1 - r_{b2}\theta_2 \tag{5}$$

The specifications of the gear pairs which are selected in these illustrations are shown in Table 1, where x_1, x_2 are the addendum modification coefficients and ε_α is the contact ratio. These characteristics are for spur gear pairs having face-width of gears $b = 20[mm]$, tooth module $m = 2.5[mm]$, center distance $a = 90[mm]$, number of pinion teeth $z_1 = 18$, number of gear teeth $z_2 = 54$.

Table 1 Specifications of the gear pairs

Gear specifications	Gear Pairs	
	GA 1	GA 2
x_2	0	+0.5
x_2	0	−0.5
ε_α	1.65	1.53
AB, $[mm]$	4.79	3.92
AC,$[mm]$	6.52	3.43
BD,$[mm]$	2.59	3.46
DE,$[mm]$	3.92	5.28
Elastic modulus, $[GPa]$	210	210
Poisson's ratio	0.3	0.3

The segments AB, AC, BD, DE are the geometrical parameters of the analyzed gear pairs

3 Friction Force

3.1 Instantaneous Coefficient of Friction

It is generally agreed that the coefficient of friction does not remain constant during a meshing cycle. The experimental values of the instantaneous coefficient of friction at the meshing teeth were obtained by Radzimovsky [7] and Rebbechi [9]. On this basis, the curve drawn in Fig. 3 is considered in the analytical model for the evaluation of the instantaneous coefficient of friction. This model satisfies the boundary conditions of the sliding friction. The pitch point C is taken as origin and the curve corresponding to the recess path can be approximately represented by the following expression proposed by Rao [8]

$$\mu = a_1 \frac{y}{l} + a_2 \frac{y^2}{l} \tag{6}$$

where y and l are shown in Fig. 3.

The constants a_1 and a_2 can be established by considering Equation (6) and the boundary conditions for the equation.

From these conditions results $a_1 = 3\ \mu_m$, $a_2 = -1.5\ \mu_m$. This methodology is also fully valid for the approach length, by considering the specific geometrical parameters of this meshing zone.

The analytical relation for determining the average coefficient of friction μ_m in gear teeth are derived from roller and gear tests. Thus, in [15], the formula for calculation the coefficient of friction be used especially for spur gear pair with the pitch point in the middle of the path of contact. When $l_a \neq l_g$ it is necessary to consider the specific geometry parameters of the gear pair which is analyzed, where $l_a = AC$ and $l_g = CD$. In this way, it is better to use the average coefficient of friction μ_{ma} and μ_{mg} which are calculated in the middle length of the approach path and of the recess length, respectively. The numerical results obtained by using the equation (6) are in good agreement with the experimental results of the average coefficient of friction obtained in [9].

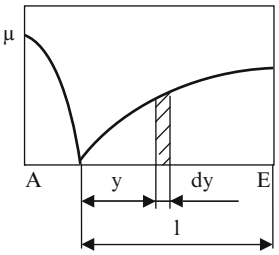

Fig. 3 Variation of coefficient of analytical spur gear model friction

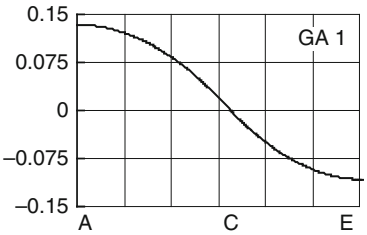

Fig. 4 Variation of the coefficient of friction for gear pair GA1

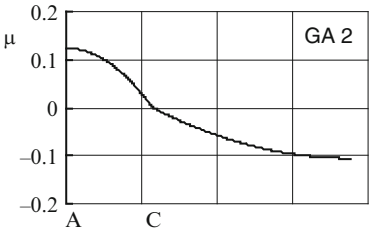

Fig. 5 Variation of the coefficient of friction for gear pair GA1

The friction coefficient μ changes its sign with direction of relative sliding, i.e.,

$$\mu = \mu \text{sgn}(y) \tag{7}$$

where sgn is the signum function defined as

$$\begin{aligned} \text{sgn}(y) &= 1, \ \textit{if} \ V_s > 0 \\ \text{sgn}(y) &= -1, \ \textit{if} \ V_s < 0. \end{aligned} \tag{8}$$

where V_s represents the sliding speed between mating teeth.

The rolling friction coefficient can be calculated by the method of Crook [6]. It is practically negligible compared to the sliding friction coefficient. The only point of exception is the pitch point.

Figures 4 and 5 show the numerical values of the instantaneous coefficient of friction along the line action in terms of the addendum modification coefficients for a pinion speed $\omega = 300s^{-1}$.

3.2 Friction Forces

Usually, the distribution factor of the friction force corresponding to a single tooth pair is defined as

$$c_f^I = \frac{\mu_m F_n^I}{F_n} \tag{9}$$

In Equation (9), F_n^I represents the static normal force corresponded to a single gear pair I, and F_n is the total normal force, where $F_n^I = 0.5F_n$ for double-tooth contact and $F_n^I = F_n$ for single-tooth contact.

Under dynamic condition, the instantaneous friction force for a single tooth pair i is expressed as follows

$$F_f^i = \mu_i F_d^i \tag{10}$$

where μ represents the instantaneous coefficient of friction and F_d^i is the dynamic normal load.

4 Mesh Stiffness

The time-varying mesh stiffness is mainly caused by the following factors: (i) the variation of the single mesh stiffness along the line of action; (ii) the fluctuation of the total number of total pairs in contact during the engagement cycle.

The gear tooth is modeled to be a nonuniform cantilever beam supported by a flexible fillet region and foundation [1,2] as shown in Fig. 2. The total deflection f_j of a pair of meshing teeth is expressed as

$$f_j = \sum_{j=1}^{2} f_{bj} + \sum_{j=1}^{2} f_{fj} + f_H \tag{11}$$

where f_b – the deflection due to bending, shear and axial deformation of the tooth corresponding to the involute profile;

f_f – the deflection due to the flexibility of the tooth foundation and fillet; f_H – the local compliance of the Hertzian contact.

The individual tooth mesh stiffness is defined in the normal direction to the contact surface as

$$k_j = \frac{F_n}{f_j} \tag{12}$$

where F_n is the normal tooth load.

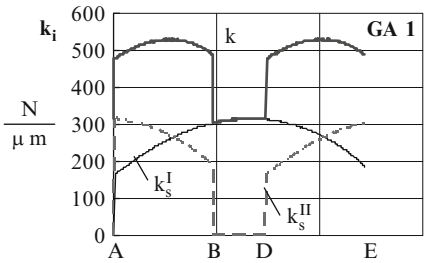

Fig. 6 Variation of the mesh stiffness components along the path of contact

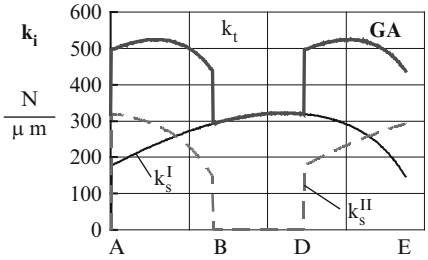

Fig. 7 Variation of the mesh stiffness components along the path of contact

The teeth pairs in contact act like parallel springs. Therefore, the total mesh stiffness during each engagement cycle can be written as a function of the position of contact point on the action line

$k_t = k_s^I + k_s^{II}$, for double-tooth contact
$k_t = k_s^I$, for single-tooth contact

where I and II are the mating points of the teeth pairs (Fig. 2).

Figures 6 and 7 show the variation of individual and total mesh stiffness from the starting to ending of contact in relation to the addendum modification coefficients.

These examples illustrate the effect of the change of the number of meshing teeth pairs on the amount of the total mesh stiffness.

5 Case Illustrations

In the analysis of dynamic transmission errors, the transmitting load is defined as F_n/b, where F_n represents the external static load transmitted by the gear teeth that is proportional to the applied torque T_1. The nominal specific load is $F_n/b = 200[N/mm]$. In the present study, the component of the static transmission error due to profile modification is not considered.

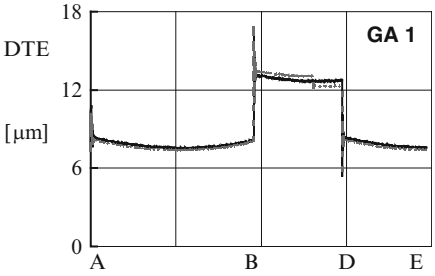

Fig. 8 Effect of the coefficient of friction $\mu = 0.1$ on δ_d

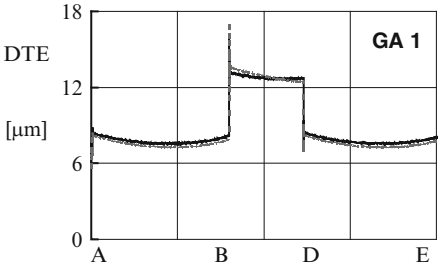

Fig. 9 Effect of the instantaneous coefficient of friction on δ_d

A computer program was developed for simulating the dynamic characteristics of spur gear pairs. The equations of motion are solved by the fourth-order Runge-Kutta method. Computer analysis of dynamic characteristics includes different gear pairs with combination of addendum modifications.

In Fig. 9 is presented the effect of the friction force on the shape of the dynamic transmission error curve for a friction coefficient μ computed by. Equation (6) at a pinion speed $\omega = 5s^{-1}$.

These transmission errors are almost identical to the static transmission errors.

The dynamic transmission error *DTE* are considered in the analysis. Figures 8 through 11 show the variation of dynamic response of spur gear systems with different operation conditions.

The effects of sliding friction and variable mesh stiffness on the amplitude and the variation of dynamic displacement can be analyzed from these data.

Figure 8 shows the variation of the dynamic transmission errors along the line of action at a very low speed ($\omega = 5s^{-1}$), where red dotted line is for $\mu = 0.1$ and blue solid line is for $\mu = 0$. When the sliding friction is included, an additional discontinuity in the shape is introduced at the transitions from AC zone to CE.

Figures 10 and 11 present the effect of the friction force on the shape of the dynamic transmission error curve for a friction coefficient μ computed by. equation (6) at a pinion speed $\omega = 300s^{-1}$, where blue solid line is for $\mu = 0$ and dotted red line is for a friction coefficient μ computed by equation (6).

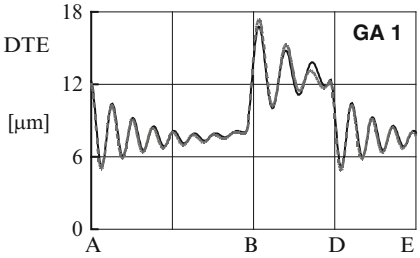

Fig. 10 Predicted dynamic transmission error for gear pair GA1

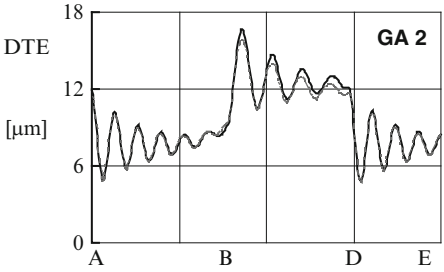

Fig. 11 Predicted dynamic transmission error for gear pair GA2

The sliding friction changes the slopes of the DTE corresponding to the single-tooth contact zone BD, while such effect does not seem to be significant for the DTE response at the AB and DE zones.

6 Conclusion

Dynamic transmission error is a result of the instantaneous contact conditions between active tooth profiles.

An analytical procedure for calculating dynamic characteristics of spur gear pairs with addendum modifications and sliding friction between contacting teeth is presented. This procedure predicts the effects of the time-varying mesh stiffness and sliding friction between meshing teeth on the variation of the dynamic transmission error during the meshing cycle of the gear pairs. The time-varying mesh stiffness along the path of contact is found by using an exact analytical model. An alternative methodology to evaluate friction forces as a function of dynamic normal load and instantaneous friction coefficient of contacting teeth.

The comparisons of the effect of friction coefficient on the variation of the dynamic transmission errors for a mesh cycle are presented for different pinion speeds.

The effects of addendum modification coefficients and pinion speed on the variation of the DTE are included in the analysis.

Acknowledgments This paper is based on the financial support of the National University Research Council of Romania, grant ID_296.

References

1. Atanasiu, V.: An analytical investigation of the time-varying mesh stiffness of helical gears. Buletinul I.P.Iasi, Gh. Asachi Technical University, Tomul XLIV, 1–2, s.V, pp.7–17 (1998)
2. Atanasiu, V.: Dynamic analysis of spur gears with tooth profile modifications. Proceedings of the ninth IFToMM international symposium on theory of machines and mechanisms. Bucharest, 2005, pp. 313–318
3. Benedict, G.H.: Instantaneous coefficients of gear tooth friction. ASLE Trans. 4, 57–70 (1961)
4. Gunda, R.: Dynamic analysis of sliding friction in a gear pair. Proceedings of DETC'03, ASME design engineering technical conferences and computers and information in engineering conference. Chicago, IL, 2–6 September 2003, pp. 1–8
5. Martin, K.F.: A review of friction predictions in gear tooth. Wear 49(2), 201–238 (1978)
6. Martin, K.F.: The efficiency of involute spur gears. ASME Trans., J. Mech. Design 103, 160–169 (1981)
7. Radzimovsky, E.I.: Dynamic behavior of gear systems and variation of coefficient of friction and efficiency during the engagement cycle. ASME J. Eng. Ind. 97(4), 1247–1281 (1975)
8. Rao, A.C.: Gear friction coefficient and forces. Wear 53, 87–93 (1979)
9. Rebbechi, B., Townsend, D.P.: Measurement of gear tooth dynamic friction. Power transmission and gearing conference, DE-vol. 88, pp.355–363. ASME (1996)
10. Vaishya, M.: Modeling and analysis of sliding friction in gear dynamics. ASME 2000 design engineering technical conferences and computers and information in engineering conference. Baltimore, Maryland, 10–13 September 2000, pp. 601–610
11. Vaishya, M.: Sliding friction-induced non-linearity and parametric effects in gear dynamics. J. Sound Vib. 248, 671–694 (2001)
12. Vaishya, M.: Strategies for modeling friction in gear dynamics. ASME Trans, J. Mech. Design 125, 383–393 (2003)
13. Velex, P.: An analytical study of tooth friction excitations in errorless spur and helical gears. Mech. Mach. Theory 37, 641–658 (2002)
14. Waiboer, R.: Velocity dependence of joint friction in robotic manipulators with gear transmissions. Multibody dynamics 2005, ECCOMAS thematic conference. Madrid, Spain, 21–24 June 2005, pp.1–19
15. Wink, H.C.: Performance assessment of solutions methods for load distribution problem of gear teeth. Mech. Mach. Theory 43, 80–94 (2008)
16. Calculation of load capacity of spur and helical gears. Calculation of scuffing load capacity. ISO 6336/4, DIN 3990/4

Designing Aspects of Differential Transmission with Balls

M. Bara, E. Teutan, and S. Stan

Abstract This paper represents a study concerning the kinematics an kinetostatics of a differential transmission with balls. In first parts of paper is present the same aspects of kinematics, determining the transmission ratios. In second parts of paper is present the kinetostatics study of cell SBS (sinusoidal channel – ball – sinusoidal channel) and for the entire transmission, determining in this way the force that act upon these, forces which are necessary in the constructive dimensioning.

Keywords Manufacturing process · Mechanisms · Mechanical transmissions

1 Introduction

The component parts of a differential frontal sinusoidal transmission (Fig. 1) are: the driving element which has profiled on its frontal side a closed sinusoidal channel with Z_1 periods (Fig. 2); the driving element 2 which has also profiled on the frontal side a sinusoidal channel with Z_2 periods; the follower (driven element) 3 which is provided with radial channels [1, 2, 3, 4]. Between the two disks profiled through the channels of disk 3 the linking elements are interposed – the balls 4. The role of balls 4 can be taken up by the conical rollers of the sinusoidal channels have the corresponding section for their profiles. When assembling a third of the diameter of the balls gets in the channel on disk 1, a third gets in the channel of disk 2 and the middle part gets in the radial channels of disk 3. The inertial effects are neglected.

For this kind of transmission in which the element 2 is fixed there are two elementary transmission ratios:

M. Bara (✉)
Department of Mechanisms, Precision Mechanics and Mechatronics, Technical University of Cluj Napoca, Cluj Napoca, Romania

I. Vişa (ed.), *SYROM 2009*,
DOI 10.1007/978-90-481-3522-6_20,

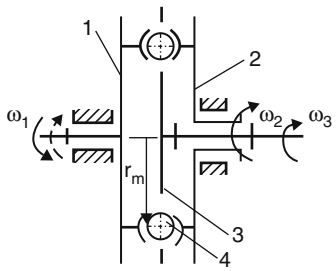

Fig. 1 The diagram of the differential frontal transmission

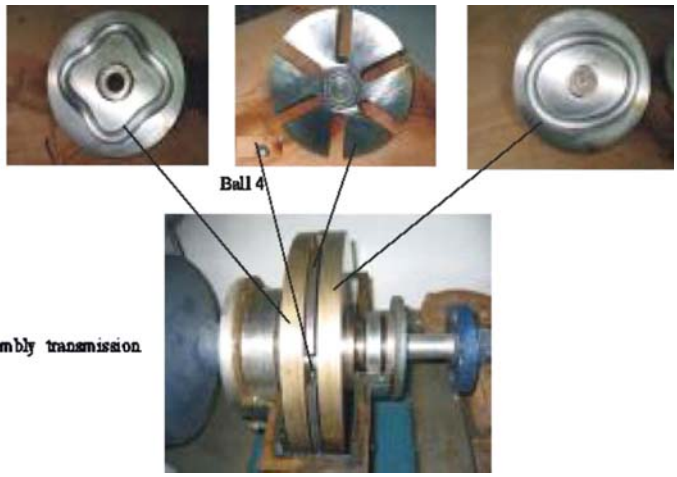

Fig. 2 The component parts of a differential frontal transmission

$$u_{13} = \frac{Z_2 + Z_1}{Z_1} \tag{1}$$

respectively,

$$u'_{13} = -\frac{Z_2 - Z_1}{Z_1} \tag{2}$$

2 The Determination of Transmission Ratio

The initial positions of elements no. 1, 2, 3 are definite when $OO_1^0 = OO_2^0 = A_0 = C_0$

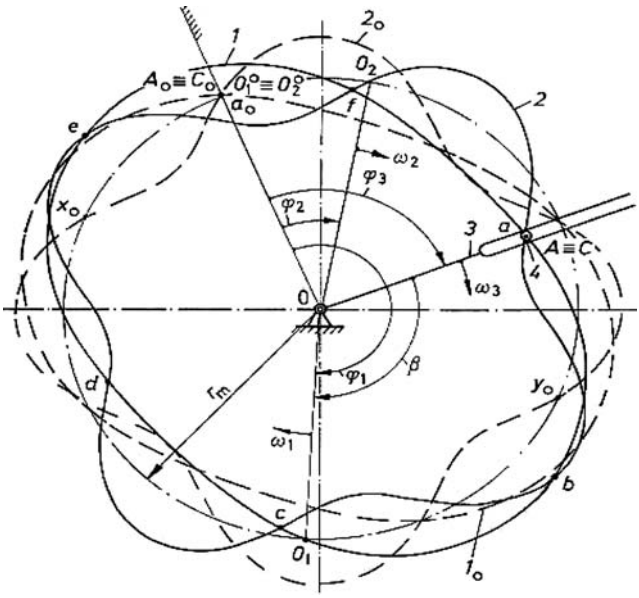

Fig. 3 The geometry of the differential transmission

It is considered that the medial fiber of the channel Z_1 (Fig. 3) is given by the equation [5, 6, 7, 8, 9]:

$$r_1 = r_m + \frac{h}{2}\sin Z_1\beta \tag{3}$$

and the medial fiber of the channel Z_2 is given by the equation:

$$r_2 = r_3 = r_m + \frac{h}{2}\sin Z_2(\varphi_3 - \varphi_2) \tag{4}$$

where: $r_1, r_2 = r_3$ – they are coordinate which position at the points A and C on the curves Z_1 and Z_2;

r_m – the medial ray of the channels;

h – the maximal longitudinal motion of the elements 4;

β – the angle between the current ray

$r_1 = OA$ and the line OO_1^0 (in the initial position);

φ_2 – the rotation angle of the driving element 2 compared to the reference line OC_0;

φ_3 – the angle between the current ray

$r_1 = OA$ and the reference straight line

OC_0 (this one determines also the position of the driven element 3);

Z_1, Z_2 – the number of periods of the profiles from the two cylindrical elements 1 and 2.

From the condition:

$$r_1 = r_2 \tag{5}$$

it results follows:

$$\sin Z_2(\varphi_3 - \varphi_2) - \sin Z_1\beta = 0 \tag{6}$$

The angles $\varphi_1, \varphi_2, \beta, \varphi_3$ are considered to be positive if they are measured in the hour sense.

So, between these angles it is true the equation:

$$\varphi_3 + \beta = \varphi_1 \tag{7}$$

where φ_1 is the rotation angle of the driving element 1.

With the help of the relation (7) the equation (6) can be written like this:

$$\sin Z_2(\varphi_3 - \varphi_2) - \sin Z_1(\varphi_1 - \varphi_3) = 0 \tag{8}$$

with the results:

$$\varphi_3 = \frac{Z_1}{Z_2 + Z_1}\varphi_1 + \frac{Z_2}{Z_2 + Z_1}\varphi_2 + \frac{2k\pi}{Z_2 + Z_1} \tag{9}$$

where: $k = 0, 1, ..., Z_2 + Z_1 - 1$, or

$$\varphi_3 = \frac{Z_1}{Z_2 - Z_1}\varphi_1 + \frac{Z_2}{Z_2 - Z_1}\varphi_2 + \frac{(2k' + 1)\pi}{Z_2 - Z_1} \tag{10}$$

where: $k' = 0, 1, ..., Z_2 - Z_1 - 1$.

By deriving proportional to the time the relation (9) and (10) it is obtained:

$$\vec{\omega}_3 = \frac{Z_1}{Z_2 + Z_1}\vec{\omega}_1 + \frac{Z_2}{Z_2 + Z_1}\vec{\omega}_2 \tag{11}$$

respectively:

$$\vec{\omega}_3' = -\frac{Z_1}{Z_2 - Z_1}\vec{\omega}_1 + \frac{Z_2}{Z_2 - Z_1}\vec{\omega}_2 \tag{12}$$

where:

$\vec{\omega}_1$ is the angular speed of the driving element 1:

$\vec{\omega}_2$ is the angular speed of the driving element 2:

$\vec{\omega}_3$ is the angular speed of the driven element 3:

$\vec{\omega}_3'$ is the angular speed of the conducted element 3 for the second group of solutions when the jumper elements 4 are placed in the points x_0 and y_0.

3 The Kinetostatic Study of the One Cell SBS

For the analysis of a frontal-sinusoidal transmission with balls one needs to make a sectioning of the cell SBS (sinusoidal channel – ball – sinusoidal channel) through the center of the ball with the help of three planes (Fig. 3). Element no. 3 (the radiating slotted disk) is cut with a plane parallel with the axis of rotation of the shaft, and the sinusoidal rolling channels (slots) are cut by normal planes to the sinusoidal on them [7].

As a result of the sectioning the following characteristics are put in light:

- The contact lines of the balls are AEF, HGM, LQK corresponding to the race-ways on the sinusoidal disks 1 or 2, and the slotted disk 3 respectively.
- The reactions between the ball and the three disks are noted with $\mathbf{f}_1$, $\mathbf{f}_2$ and $\mathbf{f}_3$ and have the points of application in E, G, and Q (Fig. 4).
- OX, OY and OZ are orthogonal axes.

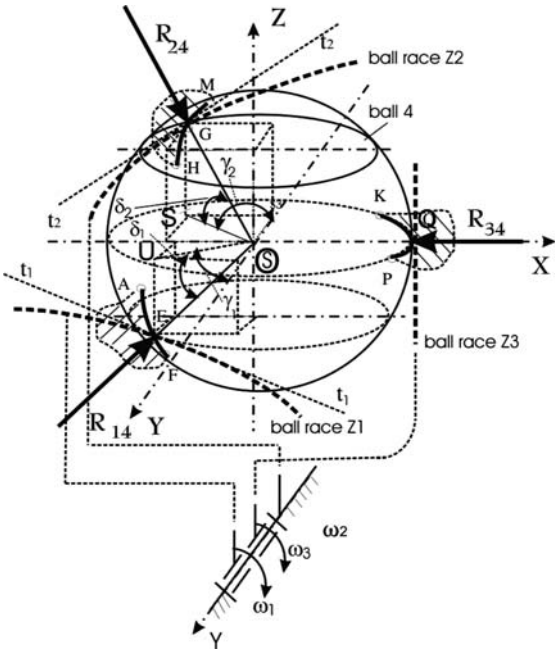

Fig. 4 Section of the cell SBS through the center of the ball

- OX, the axis perpendicular on the current radius $\mathbf{r}_0$ which positions the center of ball.
- OZ, the axis which passes through the center of the ball and is parallel to the axis of rotation of the transmission.
- δ_1 is the angle between the normal and the line OU which results from the intersection of the plane XOY with the plane $[P_1]$ which passes through point O and is normal on the sine curve Z_1 in point E.
- δ_2 is the angle between the reaction $\mathbf{f}_2$ and the line OS which results from the intersection of the plane XOY with the plane $[P_2]$ which passes through point O and is normal on the sine curve Z_2 in point G.
- γ_1 is the angle between the axis OY and the intersection line OU.
- γ_2 is the angle between the axis OY and the intersection line OS.

Next we are going to determine the relations between the modules of the reactions $\mathbf{f}_1$, $\mathbf{f}_2$ and $\mathbf{f}_3$.

The grip resistances and the forces of inertia are considered to be negligible because of their low value as compared to the three reactions. At the same time it is considered that the reaction $\mathbf{f}_3$ acts in the plane XOY and is directed along the axis OX.

Each of the forces $\mathbf{f}_1$, $\mathbf{f}_2$ and $\mathbf{f}_3$ will be written in decomposed form , in 3 components with the help of the unit vectors $\mathbf{i}$, $\mathbf{k}$ and of the axes OX, OY and OZ , in the following way :

$$\begin{aligned} f_1 &= f_1(\cos\delta_1 \sin\gamma_1 \mathbf{i} - \cos\delta_1 \cos\gamma_1 \mathbf{j} + \sin\delta_1 \mathbf{k}) \\ f_2 &= f_2(\cos\delta_2 \sin\gamma_{21} \mathbf{i} + \cos\delta_2 \cos\gamma_2 \mathbf{j} + \sin\delta_2 \mathbf{k}) \\ f_3 &= f_3 \mathbf{i} \end{aligned} \tag{13}$$

we get the relations

$$\frac{\mathrm{tg}\delta_1}{\mathrm{tg}\delta_2} = \frac{\cos\gamma_1}{\cos\gamma_2} \tag{14}$$

$$\frac{f_1}{f_3} = \frac{\mathrm{tg}\delta_1 \mathrm{tg}\gamma_1}{\sin\delta_1 \sin\gamma_1 (\mathrm{tg}\gamma_1 + \mathrm{tg}\gamma_2)} \tag{15}$$

and

$$\frac{f_2}{f_3} = \frac{\mathrm{tg}\delta_2 \mathrm{tg}\gamma_2}{\sin\delta_2 \sin\gamma_2 (\mathrm{tg}\gamma_1 + \mathrm{tg}\gamma_2)} \tag{16}$$

In the relations above it is considered that the angles δ_1 , δ_2 and γ_1, γ_2 don't exceed 90°.

The distance along the circumference of the sine curve from its starting point up to the current radius which positions the center of the ball is to be noted with q and it is to be called the circumference coordinate of the center of the ball.

Taking into account the dependence between the length of the circumference curve , the radius of the average fiber r_m and the central angle β for element 1, φ_3 respectively for element 2, on which the corresponding curve leans, one can determine the distance $y_{1,2}$ from the sine curve , with the help of the following relations:

for the sine curve Z_1 at which

$$q_1 = r_m\beta, y_1 = \frac{h\sin\left(\frac{Z_1 q_1}{r_m}\right)}{2}$$

and for the sine curve Z_2 at which

$$q_2 = r_m\varphi_3, y_2 = \frac{h\,\sin\left(\frac{Z_2 q_2}{r_m}\right)}{2}$$

Because

$$\frac{dy_1}{dq_1} = \mathrm{tg}\,\gamma_1 \quad \text{and} \quad \frac{dy_2}{dq_2} = \mathrm{tg}\,\gamma_2$$

one can write that

$$\mathrm{tg}\,\gamma_1 = \frac{hZ_1}{2r_m}\cos\left(\frac{Z_1 q_1}{r_m}\right)$$

respectively

$$\mathrm{tg}\,\gamma_2 = \frac{hZ_2}{2r_m}\cos\left(\frac{Z_2 q_2}{r_m}\right) \tag{17}$$

On the condition that $y_1 = y_2$ one obtains

$$\mathrm{tg}\gamma_1 = \frac{Z_1}{Z_2}\mathrm{tg}\gamma_2 \tag{18}$$

If one notes with $p_2 = \frac{\pi r_m}{Z_2}$ the semiperiod of the sine curve (the circumferencial semistep) one can write that:

$d_2 = \frac{2r_m}{p_2}$ is the inclination of the sine curve and

$\varepsilon_2 = \frac{q_2}{p_2}$ is the relative circumferencial coordinate of the ball.

With the notations above, the relations (14), (15), and (16) can be written under the form:

$$\frac{\mathrm{tg}\delta_1}{\mathrm{tg}\delta_2} = \sqrt{\frac{Z_2\left[2 + (\pi d_2)^2\cos^2(\pi\varepsilon_2)\right]}{2Z_2 + (Z_1\pi d_2)^2\cos^2(\pi\varepsilon_2)}} \tag{19}$$

$$\frac{f_1}{f_3} = \frac{Z_2}{Z_2 + Z_1} W \tag{20}$$

where

$$W = \sqrt{\frac{2Z_2 + (Z_1 \pi d_2)^2 \cos^2(\pi \varepsilon_2) + \mathrm{tg}^2 \delta_2}{Z_2 (\pi d_2)^2 \cos^2(\pi \varepsilon_2)} + \mathrm{tg}^2 \delta_2}$$

$$\frac{f_2}{f_3} = \frac{Z_2}{Z_2 + Z_1} Q \tag{21}$$

where

$$Q = \sqrt{\frac{(\pi d_2)^2 \cos^2(\pi \varepsilon_2) + 1}{(\pi d_2)^2 \cos^2(\pi \varepsilon_2)} (1 + \mathrm{tg}^2 \delta_2)}$$

$$\frac{f_1}{f_2} = \frac{1}{\sqrt{1 + \mathrm{tg}^2 \delta_2}} G \tag{22}$$

where

$$G = \sqrt{\mathrm{tg}^2 \delta_2 + \frac{2Z_2 + (Z_1 \pi d_2)^2 \cos^2(\pi \varepsilon_2)}{Z_2 + Z_2 (\pi d_2)^2 \cos^2(\pi \varepsilon_2)}}$$

The relations (20), (21), and (22) are valid for any point on the sinusoidal channels with Z_1, Z_2 periods.

4 Transmission of Forces and Torques

Next we are going to determine the forces and the moments that appear in a frontal transmission that has $Z_1 = 2$, $Z_2 = 4$, n = 6 (number of balls) and m_1 – the input torque .In this purpose will be projected the three reactions $\mathbf{f}_1$, $\mathbf{f}_2$ and $\mathbf{f}_3$ in XOY plane (Fig. 3) in adequate mode for each of the six cells SBS (sinusoidal channel-ball-sinusoidal channel) located in the points a, b, . . ., f.

For each cell SBS one gets in the plane XOY three forces $\mathbf{f}_{14}$, $\mathbf{f}_{24}$ and $\mathbf{f}_{34}$ which are coplanar and concurrent in the centre of the respective ball. These three forces insure the transmission of the input torque $\mathbf{m}_1$ so that it equilibrates the resistant torque $\mathbf{m}_3$.

The notations are: $\mathbf{f}_{14}$ – (the projection of the reaction $\mathbf{f}_1$ in the plane XOY) represents the force from this plane with which the leading element 1 acts upon ball 4 and is normal to curve 1;

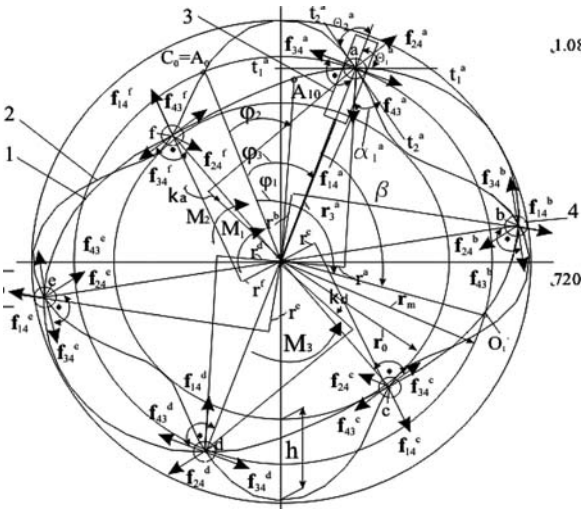

Fig. 5 The forces that act upon the elements of transmission

$\mathbf{f}_{24}$ – (the projection of the reaction in the plane XOY) represents the force from this plane with which the leading element 2 acts upon ball 4 and is normal to curve 2 (Fig. 5);

$\mathbf{f}_{34}$ – (the projection of the reaction $\mathbf{f}_3$ in the plane XOY) represents the force from this plane with which the led element 3 acts upon ball 4 and is normal to the direction of the radial channel 3.

It is obvious that upon the led element 3 will act the forces $\mathbf{f}_{43}$, equal and opposite sense with the forces $\mathbf{f}_{34}$ corresponding to the six points a, b, c, d, e, f.

If one notes with θ_1 and θ_2 the angles that – the position vectors $\mathbf{r}_1$ and $\mathbf{r}_2$ do with the tangents t_1–t_1, t_2–t_2 to curves 1, 2 in point a, than the following relations subsist:

$$\operatorname{tg}\theta_1 = \frac{r_1}{r_1'} = \frac{r_m + \frac{h}{2}\sin Z_1(\varphi_3 - \varphi_1)}{\frac{h}{2} Z_1 \cos Z_1(\varphi_3 - \varphi_1)} \tag{12}$$

$$\operatorname{tg}\theta_2 = \frac{r_2}{r_2'} = \frac{r_m + \frac{h}{2}\sin Z_2\varphi_3}{\frac{h}{2} Z_2 \cos Z_2\varphi_3} \tag{13}$$

The relations (12) and (13) are valid for any point on the curves 1 and 2.

On the basis of Fig. 3 the following relations can be written in order to:

(a) Determine the angle α

for $\theta_1, \theta_2 < 90^0$

$$\alpha = \theta_1 + \theta_2 - 90^0 \tag{14}$$

for $\theta_1, \theta_2 > 90^0$

$$\alpha = 270^0 - \theta_1 - \theta_2 \tag{15}$$

(b) Determine the angle
for $\theta_2 < 90^0$

$$\gamma_2 = 90^0 - \theta_2 \tag{16}$$

for $\theta_2 > 90^0$

$$\gamma_2 = \theta_2 - 90^0 \tag{17}$$

(c) Determine the angle γ_1
for $\theta_1 < 90^0$

$$\gamma_1 = 90^0 - \theta \tag{18}$$

for $\theta_1 > 90^0$

$$\gamma_1 = \theta_1 - 90 \tag{19}$$

The relations (14–19) are valid in all the six cells SBS so that they will have the following form:
for $\theta_1, \theta_2 < 90^0$

$$\begin{aligned} \alpha^{\mathrm{a}} &= \theta_1^{\mathrm{a}} + \theta_2^{\mathrm{a}} - 90^0 \\ \alpha^{\mathrm{f}} &= \theta_1^{\mathrm{f}} + \theta_2^{\mathrm{f}} - 90^0 \end{aligned} \tag{20}$$

$$\begin{aligned} \gamma_2^{\mathrm{a}} &= 90^0 - \theta_2^{\mathrm{a}} \\ \gamma_2^{\mathrm{f}} &= 90^0 - \theta_2^{\mathrm{f}} \end{aligned} \tag{21}$$

$$\begin{aligned} \gamma_1^{\mathrm{a}} &= 90^0 - \theta_1^{\mathrm{a}} \\ \gamma_1^{\mathrm{f}} &= 90^0 - \theta_1^{\mathrm{f}} \end{aligned} \tag{22}$$

for $\theta_1, \theta_2 > 90^0$

$$\begin{aligned} \alpha^{\mathrm{a}} &= 270^0 - \theta_2^{\mathrm{a}} - \theta_1^{\mathrm{a}} \\ \alpha^{\mathrm{f}} &= 270^0 - \theta_2^{\mathrm{f}} - \theta_1^{\mathrm{f}} \end{aligned} \tag{23}$$

$$\begin{aligned}\gamma_2^{\mathrm{a}} &= \theta_2^{\mathrm{a}} - 90^0\\ \gamma_2^{\mathrm{f}} &= \theta_2^{\mathrm{f}} - 90^0\end{aligned} \tag{24}$$

$$\begin{aligned}\gamma_1^{\mathrm{a}} &= \theta_1^{\mathrm{a}} - 90^0\\ \gamma_1^{\mathrm{f}} &= \theta_1^{\mathrm{f}} - 90^0\end{aligned} \tag{25}$$

From the equilibrium condition of the leading element 1, upon which acts the motor moment m_1 there results:

$$m_1 = f_{14}^{\mathrm{a}} r^{\mathrm{a}} + f_{14}^{\mathrm{b}} r^{\mathrm{b}} + f_{14}^{\mathrm{c}} r^{\mathrm{c}} + f_{14}^{\mathrm{d}} r^{\mathrm{d}} + + f_{14}^{\mathrm{e}} r^{\mathrm{e}} + f_{14}^{\mathrm{f}} r^{\mathrm{f}} \tag{26}$$

where, $f_{14}^{\mathrm{a}}, \ldots, f_{14}^{\mathrm{f}}$ represent the forces with which the leading element 1 acts upon balls 4 in the points a, b, c, d, e, f and they are determinated with the relations :

$$\begin{aligned}f_{14}{}^{\mathrm{a}} &= f_1^{\mathrm{a}} \cos\delta_1^{\mathrm{a}}\\ f_{14}{}^{\mathrm{f}} &= f_1^{\mathrm{f}} \cos\delta_1^{\mathrm{f}}\end{aligned} \tag{27}$$

and r^{a}, r^{b},.....r^{f} represent distances from the centre of revolution O to the force vectors $\mathbf{f}_{14}^{\mathrm{a}} \ldots \mathbf{f}_{14}^{\mathrm{f}}$.

On the basis of Fig. 2 it can be noticed that:

$$\begin{aligned}r^{\mathrm{a}} &= r_1^{\mathrm{a}} \cos\theta_1^{\mathrm{a}}\\ r^{\mathrm{f}} &= r_1^{\mathrm{f}} \cos\theta_1^{\mathrm{f}}\end{aligned} \tag{28}$$

where:

$$r_1{}^{\mathrm{a}} = r_2^{\mathrm{a}} = r_3^{\mathrm{a}}, r_1{}^{\mathrm{b}} = r_2^{\mathrm{b}} = r_3^{\mathrm{b}}, r_1{}^{\mathrm{f}} = r_2^{\mathrm{f}} = r_3^{\mathrm{f}}$$

represent distances from the centre of revolution O to the centers of balls 4 in the points a, b, ..., f.

From the equilibrium condition of the led element 3 upon which acts the resistant moment m_3 results:

$$m_3 = f_{34}^{\mathrm{a}} r_3{}^{\mathrm{a}} + f_{34}^{\mathrm{b}} r_3{}^{\mathrm{b}} + f_{34}^{\mathrm{c}} r_3{}^{\mathrm{c}} + f_{34}^{\mathrm{d}} r_3{}^{\mathrm{d}} + f_{34}^{\mathrm{e}} r_3{}^{\mathrm{e}} + f_{34}^{\mathrm{f}} r_3{}^{\mathrm{f}} \tag{29}$$

where:

$f_{34}^{\mathrm{a}}, \ldots, f_{34}^{\mathrm{f}}$ represent the forces with which the led element 3 acts upon balls 4 from the points a, b, ..., f and it is determinated with the relations:

$$\begin{aligned}f_{34}^{\mathrm{a}} &= f_{14}^{\mathrm{a}} \sin\gamma_1^{\mathrm{a}} + f_{24}^{\mathrm{a}} \sin\gamma\\ f_{34}^{\mathrm{f}} &= f_{14}^{\mathrm{f}} \sin\gamma_1^{\mathrm{f}} + f_{24}^{\mathrm{f}} \sin\gamma_2^{\mathrm{f}}\end{aligned} \tag{30}$$

and $r_3{}^{a}$, $r_3{}^{b}$,. . ....$r_3{}^{f}$ represent distances from the centre of revolution O to the force vectors $\mathbf{f}_{34}^{a}, \ldots, \mathbf{f}_{34}^{f}$.

In the relations (30) the forces are defined in the following way:

$$\begin{aligned} f_{24}^{a} &= f_2 \cos\delta_1^{a} \\ f_{24}^{f} &= f_2 \cos\delta_1^{a} \end{aligned} \tag{31}$$

From the equilibrium conditions of the balls 4 in the points a, b, ..., f written under the form of projections on the directions of the tangents t_2–t_2 to the curve 2 and of their normals the following relations can be written:

$$\begin{aligned} f_{14}^{a} \cos\alpha^{a} &= f_{34}^{a} \cos\gamma_2^{a} \\ f_{14}^{f} \cos\alpha^{f} &= f_{34}^{f} \cos\gamma_2^{f} \end{aligned} \tag{32}$$

respectively

$$\begin{aligned} f_{24}^{a} &= \mathrm{f}_{14}^{a} \sin\alpha^{a} + f_{34}^{a} \sin\gamma_2^{a} \\ f_{24}^{f} &= \mathrm{f}_{14}^{f} \sin\alpha^{f} + f_{34}^{f} \sin\gamma_2^{f} \end{aligned} \tag{33}$$

From the equilibrium condition of the led element 2 upon which acts the resistant moment m_2 results:

$$m_2 = f_{24}^{a} k_2{}^{a} + f_{24}^{b} k_2^{b} + f_{24}^{c} k_2^{c} + f_{24}^{d} k_2{}^{d} + f_{24}^{e} k_2{}^{e} + f_{24}^{f} k_2{}^{f} \tag{34}$$

where:

$f_{24}^{a}, \ldots, f_{24}^{f}$ represent the forces with which the led element 2 acts upon balls 4 from the points a, b, ..., f and it is determinated with the relations:

$$\begin{aligned} f_{24}{}^{a} &= f_{12}^{a} \cos\delta_2^{a} \\ f_{24}{}^{f} &= f_2^{f} \cos\delta_2^{f} \end{aligned} \tag{35}$$

and r^{a}, r^{b},. . ...r^{f} represent distances from the centre of revolution O to the force vectors $\mathbf{f}_{24}^{a} \ldots \mathbf{f}_{24}^{f}$.

On the basis of Fig. 2 it can be noticed that:

$$\begin{aligned} k^{a} &= r_2^{a} \cos\theta_2^{a} \\ k^{f} &= r_2^{f} \cos\theta_2^{f} \end{aligned} \tag{36}$$

where:

$$r_1{}^{a} = r_2^{a} = r_3^{a}, r_1{}^{b} = r_2^{b} = r_3^{b}, r_1{}^{f} = r_2^{f} = r_3^{f}$$

As in this case the number of the balls is even the forces are two and two equal and of opposite sense and the angles $\alpha^a, \ldots, \alpha^f$ and $\gamma_2^a, \ldots, \gamma_2^f$ are also equal two and two.

Between input powers p_1, p_2 and output power p_3 can be written a following relation.

$$p_3 = (p_1 + p_2)\eta \tag{37}$$

where η_{12}^3 is a efficiency transmission in this case.

The relation between m_1, m_2, m_3 is:

$$m_3\omega_3 = (m_1\omega_1 + m_2\omega_2)\eta_{12}^3 \tag{38}$$

or

$$m_3\left[\left(\frac{z_1}{z_2 + z_1}\right)\omega_1 + \left(\frac{z_2}{z_2 + z_1}\right)\omega_2\right] = (m_1\omega_1 + m_2\omega_2)\eta_{12}^3 \tag{39}$$

5 Conclusions

The relations (9), (10) and (11) express the relations between the reactions that appear between the three raceways and the ball interposed between them and they are valid for the *n* intersection points of the sine curves in which the *n* balls are placed.

From (39) we can draw the conclusion that, if the input torques m_1, m_2 are constants then the out torque m_1 is constant.

References

1. Akturk, N.: The effect of waviness on vibration associated with ball bearings. ASME, J. Tribol. 121, 667–677 (October 1999)
2. Bara, M.: Sinusoidal transmission with balls. Todesco, Cluj- Napoca (2001)
3. Bara, M.: Designing aspects of a frontal-sinusoidal transmission with balls, 2004 ASME international mechanical engineering congress. Anaheim, CA, 13–19 November 2004. No. IMECE 2004-59309, ISBN 0-7918-4179-0.
4. Bara, M.: The dynamic study of a frontal-sinusoidal transmission with balls, 2005 ASME international mechanical engineering congress. Orlando, FL, 5–10 November 2005. No. IMECE 2005-79048, ISBN 1-3517-2568-0
5. Bostan, I.A.: s.a., Transmisii planetare, precesionale si armonice. Ed. Tehnica, Bucuresti (1997)

6. Handra-Luca, V., Bara, M.: Geometrie und Kinematik des Reduktionsgetriebes mit Ubertragungskugeln, Konstruktion 44, 150–160. Springer-Verlag, Berlin (1992)
7. Ignatiscev, E.M.: Sinusosaricovii reductor, Mehanika masin, vipuse 58. Iz-vo Nauka, Moscova (1981)
8. Johnson, K.L.: Contact mechanics. Cambridge University Press, Cambridge (1985)
9. Kleine Enzyklopadie. Mathematik, VEB Verlag

Meshing Forces Distribution Analysis on Gearing Teeth with Precession Movement

A. Bruja, M. Dima, and C. Francu

Abstract In this report is presented a study of how geometrical parameters influences the distribution of meshing forces of harmonical gearing with rigid frontal element. Geometrical parameters that were studied are: angle between the axes, number of teeth of the wheels, median radius of the wheels (radius of the sphere where takes place the meshing), vertex angle of the satellite's rolls and profile's angular displacement. The values were obtained by using a computer software written by the authors which allows to compute the forces by modifying one parameter at a time and maintaining the others constant.

Keywords Central wheel · Harmonical · Mesh forces

Harmonical gearings with rigid frontal element are used in designing of frontal harmonical transmissions with rigid elements, which can be: gear reductors, differential gears, gearboxes and continuously variable transmissions. In Fig. 1a is represented a harmonical reductor with double sattelite and in Fig. 1b is represented the kinematic diagram.

Satellite toothing is realized in shape of conical rolls disposed regularly on the lateral surface of the rolling cone and which has the cone-points at the intersection of the axes of gear wheels.

The fixed central wheel's toothing flank has the mating profile shape of conical rolls. The number of teeth of the satellite is greater by 1 than the central wheel's number of teeth.

Figure 2 presents the harmonic gearing's conjunction with the sphere on which the meshing takes place and points out the central wheel's profile, the satellite's rolls and the line of contact [1]. The line of contact's parametric equation was determined based on fundamental law of meshing:

A. Bruja (✉)
Department of Technical Mechanics and Mechanisms, Faculty of Technological Equipment, Technical University of Civil Engineering Bucharest, Bucharest, Romania

I. Vişa (ed.), *SYROM 2009*,
DOI 10.1007/978-90-481-3522-6_21,

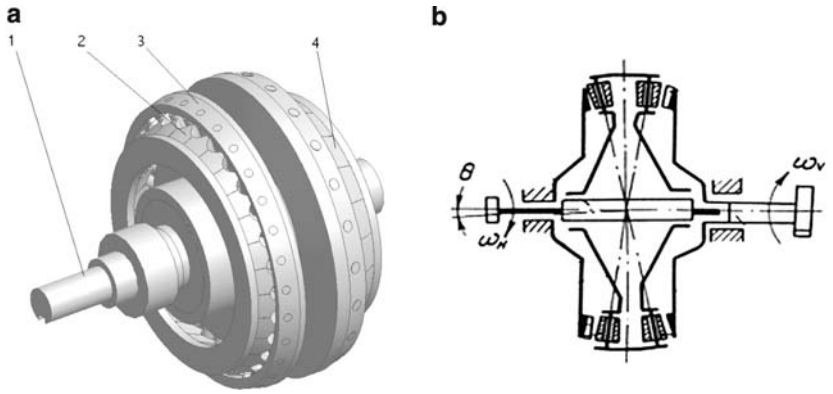

Fig. 1 Harmonical reductor with rigid frontal element with double sattelite. 1 – input shaft, 2 – fixed central wheel, 3 – double satellite, 4 – driven central wheel (fixed with output shaft)

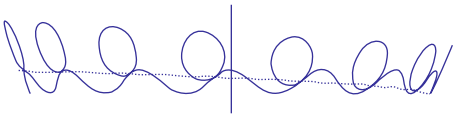

Fig. 2 Intersection with a sphere of a frontal harmonical transmission mesh rigid element

$$z_l = \frac{-b - \sqrt{b^2 - 4ac}}{2a}; y_l = \frac{2z_l(n_z x_1 - n_x z_1) + n_x(x_1^2 + y_1^2 + z_1^2 + r^2 - \rho'^2)}{2(n_x y_1 - n_y x_1)}; \quad (1)$$

$$x_l = -\frac{n_z z_l + n_y y_l}{n_x}, \varphi_s \in (0,\ 2\pi),\ \text{and } r = ct.$$

where

$$a = 4(n_x^2 + n_y^2)(n_z x_1 - n_x z_1)^2 + 4(n_x^2 + n_z^2)(n_x y_1 - n_y x_1)^2 + 8n_y n_z(n_z x_1 - n_x z_1)^2$$

$$\begin{aligned} b = {} & 4n_x(n_x^2 + n_y^2)(n_z x_1 - n_x z_1)(x_1^2 + y_1^2 + z_1^2 + r^2 - \rho'^2) \\ & + (4n_x n_y n_z)(n_x y_1 - n_y x_1)(x_1^2 + y_1^2 + z_1^2 + r^2 - \rho'^2) \end{aligned} \quad (2)$$

$$c = n_x^2(n_x^2 + n_y^2)(n_z x_1 - n_x z_1)(x_1^2 + y_1^2 + z_1^2 + r^2 - \rho'^2)^2 - 4r^2 n_x^2(n_x y_1 - n_y x_1)^2$$

where

- x_1, y_1, z_1 represents the coordinates of center of satellite's roll
- n_x, n_y, n_z are the parameters of the common normal $\vec{n}$ of the flanks in the point of contact
- r – radius of the sphere on which takes place the meshing
- ρ' – radius of the satellite's roll

As you can see in Fig. 2 during operation all the teeth are in contact and half of those are transmitting the motion. As of this, the problem of determining the forces that appear in the points of contact of the teeth, on the line of contact, is a redundant problem, and the degree of indeterminacy, is equal with the number of meshing teeth decreased by 1. The problem can be solved taking into account the elastic deformations of the teeth flanks in the points of contact, assuming that these deformations are proportional with the values of those forces [3, 4, 5]. Expression of the force can be determined, for every point of contact, p.

$$F_p = \frac{M_c \cdot \left(x_l n_{ry} - y_l n_{rx}\right)_p^n}{\sum_{p=1}^{m} \left(x_l n_{ry} - y_l n_{rx}\right)_p^{n+1}} \tag{3}$$

where

- M_c transmitted moment of twisting
- $x_l,\ y_l$ – the coordinates of points of contact (placed on the line of contact)
- n_{rx}, n_{ry} – parameters of direction of force in meshing
- $n = 10/9$
- m – number of pairs of teeth that are transmitting the motion; numbering of the pairs of teeth starts from the roll that is on the bottom between 2 teeth of central wheel.

Values of the $\bar{F}_p$ forces and their number depend by the values of geometrical and kinematical parameters of the gearing: angle between the axes, number of teeth of the wheels, median radius of the wheels (radius of the sphere where takes place the meshing), vertex angle of the satellite's rolls and profile's angular displacement (defined as the difference of the half vertex angles of cone's surface on which are disposed satellite's rolls [2]).

For a frontal harmonical reducer, having the following parameters: angle between the axes $\theta = 2.5°$, number of teeth of the central wheel $z_c = 29$, number of rolls of the satellite $z_s = 30$, median radius of meshing sphere $r = 85mm$, vertex angle of the satellite's rolls $\alpha = 2,4°$ and profile's angular displacement $\delta = 2,4°$, maximum transmitted torsion moment at the output shaft $M_c = 240Nm$, was written a computer program that can determine the values of forces in meshing and the modification of the geometrical and kinematical parameters.

For a clear interpretation of the results each of the five parameters taken into account was modified.

Next is presented the influence of every parameter.

For the angle between the axes θ, were taken into account: 2°, 2.5° and 3°, results are presented both as a chart and as a table in Fig. 3. You can observe that the values for the angle θ of 2° and 2.5° are meshing 15 pairs of teeth and for the value of θ of 3° are meshing 13 pairs of teeth. This fact happens because for an angle greater than θ = 2.5°, interference is showing up at the top of the teeth, which decreases the number of pairs of teeth in contact [6]. We can observe that for $\theta = 2.5°$ values of meshing forces are smaller than for θ = 2°.

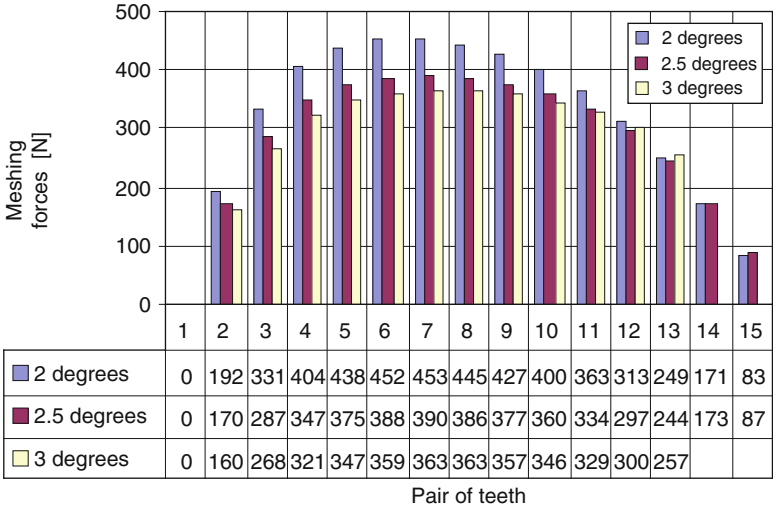

	1	2	3	4	5	6	7	8	9	10	11	12	13	14	15
2 degrees	0	192	331	404	438	452	453	445	427	400	363	313	249	171	83
2.5 degrees	0	170	287	347	375	388	390	386	377	360	334	297	244	173	87
3 degrees	0	160	268	321	347	359	363	363	357	346	329	300	257		

Fig. 3 Variation of the meshing forces by the angle between the axes

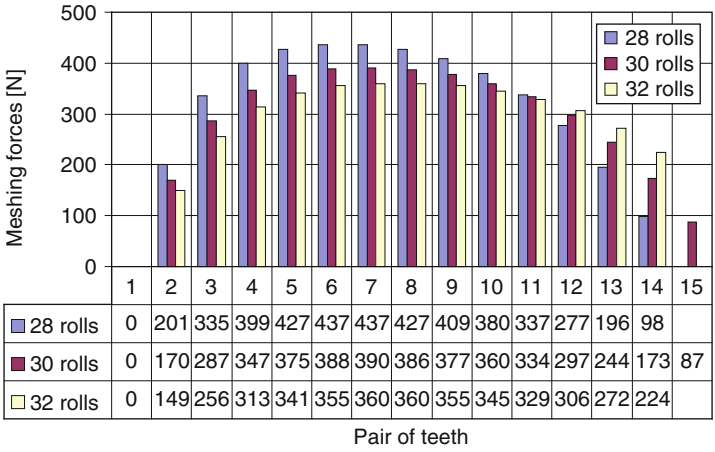

	1	2	3	4	5	6	7	8	9	10	11	12	13	14	15
28 rolls	0	201	335	399	427	437	437	427	409	380	337	277	196	98	
30 rolls	0	170	287	347	375	388	390	386	377	360	334	297	244	173	87
32 rolls	0	149	256	313	341	355	360	360	355	345	329	306	272	224	

Fig. 4 Variation of the meshing forces by the number of satellite's rolls

Figure 4 represents distribution of the meshing forces by the number of satellite's rolls. The analysis of Fig. 4 returns as expected the fact that the meshing forces are decreasing when the number of the teeth is increasing with the restriction that the interference would not show up (32 rolls case [6]).

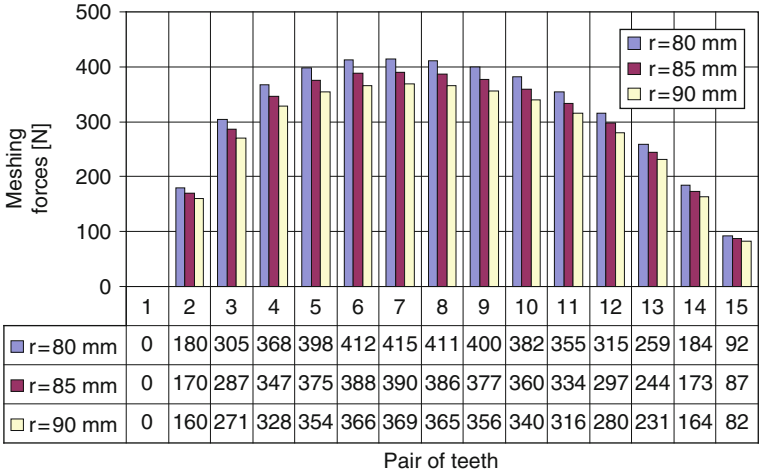

	1	2	3	4	5	6	7	8	9	10	11	12	13	14	15
r=80 mm	0	180	305	368	398	412	415	411	400	382	355	315	259	184	92
r=85 mm	0	170	287	347	375	388	390	386	377	360	334	297	244	173	87
r=90 mm	0	160	271	328	354	366	369	365	356	340	316	280	231	164	82

Fig. 5 Meshing forces variation by sphere's meshing radius

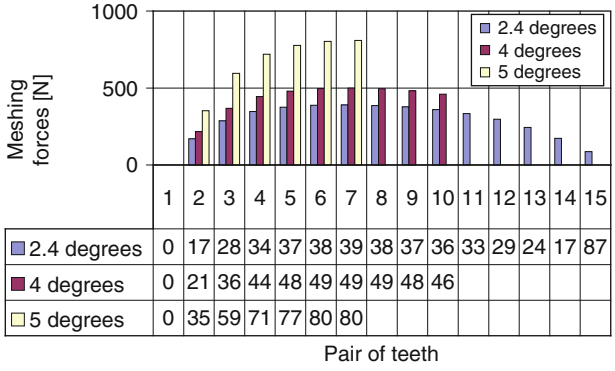

	1	2	3	4	5	6	7	8	9	10	11	12	13	14	15
2.4 degrees	0	17	28	34	37	38	39	38	37	36	33	29	24	17	87
4 degrees	0	21	36	44	48	49	49	49	48	46					
5 degrees	0	35	59	71	77	80	80								

Fig. 6 Meshing forces variation by vertex angle of the satellite's rolls

In Fig. 5, sphere's meshing radius growth indicates a decrease in meshing forces because of the fact that moment arms to the central wheel's axis of rotation are increasing. We can observe that variation of the force is strictly proportional with the variation of the parameter, for every tooth.

Vertex angle of the satellite's rolls has the greatest influence over the distribution of meshing forces in the frontal harmonical reducer Fig. 6. Increasing the vertex angle of the satellite's rolls over $\theta = 2.5^\circ$ makes the interference to show up, and this wears the teeth, and therefore number of pairs of teeth in contact is decreasing [6].

Profile's angular displacement influences the conditions in which meshing takes place and therefore influences the distribution of the meshing forces on every pair

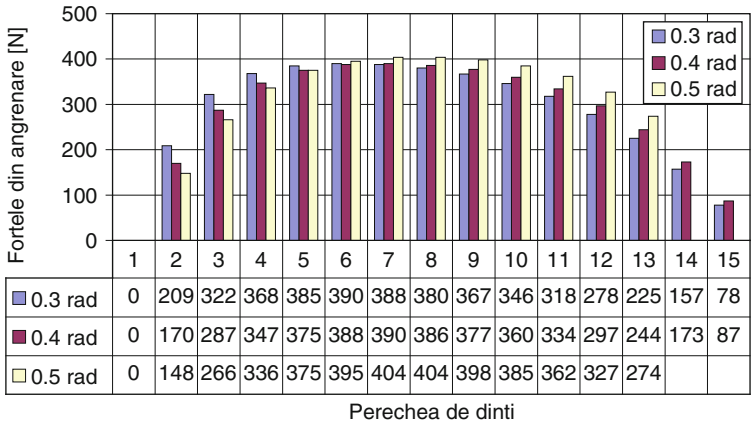

	1	2	3	4	5	6	7	8	9	10	11	12	13	14	15
0.3 rad	0	209	322	368	385	390	388	380	367	346	318	278	225	157	78
0.4 rad	0	170	287	347	375	388	390	386	377	360	334	297	244	173	87
0.5 rad	0	148	266	336	375	395	404	404	398	385	362	327	274		

Fig. 7 Meshing forces variation by profile angular displacement

of teeth in contact. We can see in Fig. 7 that a smaller value of angular displacement makes the distribution of the meshing forces more asymmetrical, and a higher value may have negative consequences by decreasing the pairs of teeth in contact.

By looking at the Figs. 3–7 some conclusions arise:

– For a gearing with a known reduction ratio, we can choose values for geometrical parameters, to distribute the meshing forces over the highest number of pairs of teeth in contact; The maximum number of teeth in contact is half of central wheel's number of teeth.
– Distribution of the meshing forces in points of contact has the shape of a second-degree curve slightly asymmetrical, values being higher when the contact is on the bottom of the tooth, and smaller when the contact is on the top of the tooth.

References

1 Adrian, B., Marian, D.: La détermination de la ligne d'action pour l'angrenage avec mouvement de précession. Articol, Analele Universităţii "Dunărea de Jos," Fascicola XIV, 17–20. Galaţi (1999). ISSN 1224–5615
2 Adrian, B., Marian, D.: L'influence des paramètres de la transmission par mouvement de précession sur le profil des dents de la roue centrale. Articol, Analele Universităţii "Dunărea de Jos", Fascicola XIV, 17–20. Galaţi (1999). ISSN 1224–5615
3 Adrian, B., Marian, D.: La cynétostatique de l'engrenage avec mouvement de précession. Articol, Analele Universităţii "Dunărea de Jos", Fascicola XIV, Galaţi (2000). ISSN 1224–5615
4 Adrian, B., Marian, D.: La repartition de la charge sur les dents des engrenages et la determination des forces qui agissent sur les elements composant de la transmissions harmonique frontale avec element rigide. Comunicare, XVI International conference on "Material

Flow, Machines and Devices in Industry," University of Belgrade, 7–8 December 2000, pp. 5.57–5.60
5 Bruja, A., Dima, M.: La détermination des forces qui agissent sur les dents de l'engrenage harmonique avec élément frontal rigide. Articol. Al VIII-lea Simpozion Internaţional de Teoria Maşinilor şi Mecanismelor IFToMM, SYROM 2001, vol. III, pp. 91–96. Bucureşti, 28 August–1 September 2001. ISBN 973-8143-38-1, ISBN 973-8143-27-6
6 Bruja, A., Dima, M.: Ascuţirea dinţilor şi interferenţa în cazul angrenajului armonic frontal cu element rigid. Articol, Sesiunea de comunicări ştiinţifice a Catedrei de Mecanică Tehnică şi Mecanisme, SIMEC 2002, 29 Martie 2002, pp. 23–26. ISBN 973-8165-20-2

Basic Aspects Concerning Development of the Hybrid Road and Driving Simulator

A. Capustiac and C. Brisan

Abstract The aims of this paper is to implement the quarter car model in Matlab/Simulink and study the system's response in case of applying different input function for the system.

Keywords Quarter car model · Road roughness · Simulator

1 Introduction

This paper deals with studying the modelled system's response in case of applying different input function for the system for the **Hy**brid **Roa**d and **D**riving **S**imulator (**HyRoaDS**). HyRoaDs wants to bring into the same hardware and software architecture both road and dynamics vehicle simulation.

There are different models used in vehicle dynamics: quarter car, half car [1] and full car model [2].

Quarter car model consists of the wheel, unsprung mass, sprung mass and suspension components. The suspension system is responsible for the ride quality and driving stability. There are three types of suspensions that can be designed: passive, semi-active and active. The passive one uses spring and damper and the advantages are simplicity and cost as shown in [2] and the second one uses a variable damping constant. Usually the active suspension demands complex design and bigger costs. It is recognized that the quarter-car representation is too simple for performing a comprehensive analysis of the ride motions of the vehicle [3]. However, even with this simplified representation, significant insight into the problem can be gained without greatly complicating the analysis.

Figure 1 presents different quarter car models, with 1 degree of freedom (DOF) and 2 DOF [4].

A. Capustiac (✉)
Department of Mechanisms, Precision Mechanics and Mechatronics, Technical University of Cluj Napoca, Cluj Napoca, Romania

I. Vişa (ed.), *SYROM 2009*,
DOI 10.1007/978-90-481-3522-6_22,

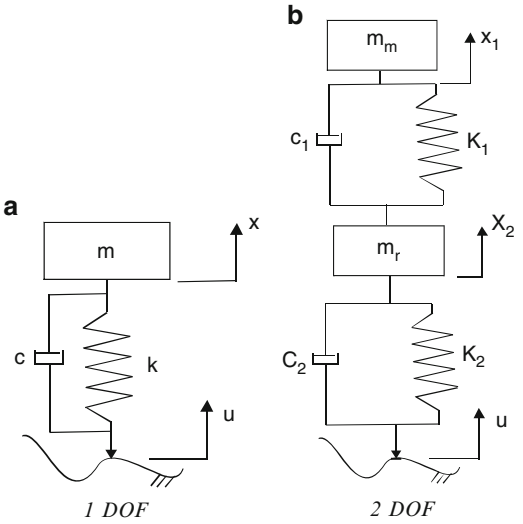

Fig. 1 Quarter car model

The full car model considers the links between sprung masses to be solid rods.

This model is more complex than the quarter car, yaw, pitch and roll oscillations are taken in consideration. Also the dynamic forces that act directly on the car body are introduced. In order to study the response and behavior of the suspension to different inputs and build a simple dynamic model, the two mass quarter car model was used for studying the road-wheel phenomena, giving good results in the low frequencies domain (0–10 Hz) [5]. The validity of the two mass quarter car model was demonstrated by Kim and Ro [6]. Thus, it is assumed that all suspensions are passive McPherson type (Fig. 2b). Non linearity of the springs and especially of the shock absorbers was taken into account when building the model

2 The Model and the Equations of the Vertical Oscillations

The elastic model for evaluating the vertical oscillations studied in this paper is the linear elastic model with two concentrated masses (Fig. 2a).

Since damping in the tire is typically very small, it is neglected in this study. In this model, the sprung and un-sprung masses corresponding to the one corner of the vehicle are denoted respectively by m_m and m_r The un-sprung mass m_r (Fig. 2a) represents the mass of the wheel, element 6 in Fig. 2b and the sprung mass, m_m (Fig. 2a) is one quarter of the total mass of the vehicle. The suspension system is represented by a linear spring of stiffness k_a and a linear damper with a damping rate c while the tire is modeled by a linear spring of stiffness k_r. The values of the suspension parameters are shown in Table 1 [7].

The differential equations of the model of the two masses are described in (1). The reference position for the displacements is the static equilibrium point.

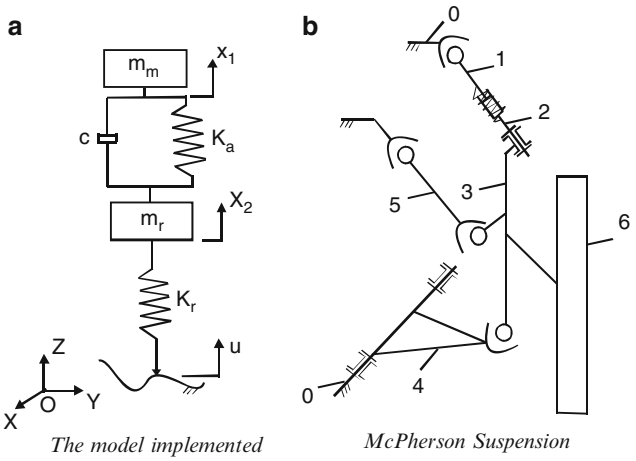

Fig. 2 Quarter car model studied

Table 1 Quarter car model parameters

Sprung mass	m_m	290 kg
Unsprung mass	m_r	59 kg
Damper	C	1,000 Ns/m
Suspension spring	k_a	16,182 N/m
Tyre spring	k_r	1,90,000 N/m

$$\begin{aligned}\ddot{x}_1 &= -\frac{1}{m_m}\left[k_a(x_1 - x_2) + c(\dot{x}_1 - \dot{x}_2)\right] \\ \ddot{x}_2 &= \frac{1}{m_r} * \left[k_a(x_1 - x_2) + c(\dot{x}_1 - \dot{x}_2) + c(\dot{x}_1 - \dot{x}_2) - k_r(x_2 - u)\right]\end{aligned} \tag{1}$$

In order to study the oscillations of the suspension, the model of the quarter car with 2 DOF was implemented in Matlab/Simulink. The system was solved using the state space. The state variables chosen are the positions and the velocities of the two masses, and the input is the road excitation or roughness – u(t) and the outputs are x_1 and x_2, the displacement of the car body and the displacement of the wheel.

The state equations are easily derived as follows

$$\begin{aligned}x_3 &= u \\ \dot{x}_1 &= x_3 \\ \dot{x}_2 &= x_4 \\ \dot{x}_3 &= -\frac{k_a}{m_m}x_1 + \frac{k_a}{m_m}x_2 - \frac{c}{m_m}x_3 + \frac{c}{m_m}x_4 \\ \dot{x}_4 &= \frac{k_a}{m_r}x_1 + \frac{(k_a - k_r)}{m_r}x_2 + \frac{c}{m_m}x_3 - \frac{c}{m_m}x_4 + \frac{k_r}{m_m}u\end{aligned} \tag{2}$$

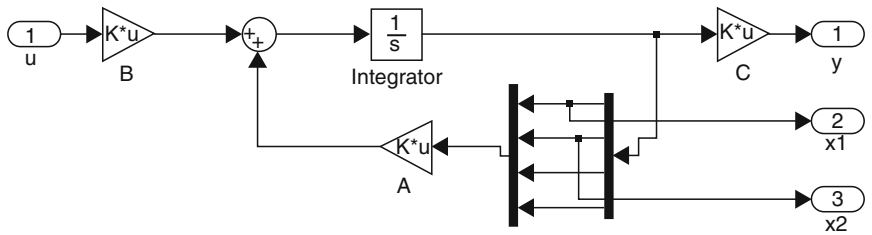

Fig. 3 The quarter car model with 2 DOF implemented in Matlab/Simulink

where:

x_1 is the distance between the sprung and the un-sprung masses (suspension travel);

x_2 is the distance between the un-sprung mass and the road surface (tire deflection);

x_3 is the sprung mass absolute velocity;

x_4 is the un-sprung mass absolute velocity.

In order to use state equations in Matlab/Simulink, equations (2) were written using matrixes (3).

The state and output equations were introduced in matrix form and the substituting the physical parameters for the suspension coefficients [8].

$$A = \begin{bmatrix} 0 & 0 & 1 & 0 \\ 0 & 0 & 0 & 1 \\ -\frac{k_a}{m_m} & \frac{k_a}{m_m} & -\frac{c}{m_m} & \frac{c}{m_m} \\ \frac{k_a}{m_r} & \frac{k_a - k_r}{m_r} & \frac{c}{m_r} & -\frac{c}{m_r} \end{bmatrix}; \quad B = \begin{bmatrix} 0 \\ 0 \\ 0 \\ \frac{k_r}{m_r} \end{bmatrix}; \quad C = [1 \quad 0 \quad 0 \quad 0]; \quad D = [0] \tag{3}$$

The simplified form of the equations (3):

$$\begin{aligned} \dot{x} &= A \cdot x + B \cdot u \\ y &= C \cdot x + D \cdot u \end{aligned} \tag{4}$$

where A, B, C and D are the coefficient matrixes and u is the input excitation and y is the output. These equations, the positions and the initial velocities are describing the elastic quarter car model.

Figure 3 presents the schematic drawing of the model implemented in Simulink.

While the input u(t) is constant, the system is in equilibrium and the values of x_1 and x_2 are constant. The initial conditions on the input and response variables are taken to be zero.

3 The Time Response of the Linear Model of the Suspension

To be able to analyze the time response of the elastic quarter car model, the values from the Table 1 were used in the four matrixes A, B, C and D. Using the values from the Table 1, and applying different inputs the time response was analyzed.

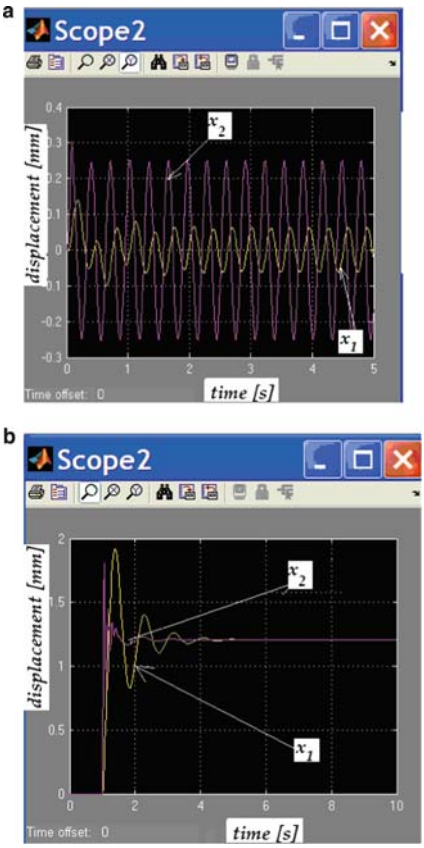

Fig. 4 Quarter car model with 2 degrees of freedom output

First a sinus wave with 0.2 amplitude and 20 rad/s frequency (Fig. 4a) was applied and then a step signal (Fig. 4b).

4 The Oscillations and Vibrations

The quality of the ride is associated with the vehicle's response to shocks and is a factor of the low frequency bounce of the suspension system. Following a bump, the un-damped suspension of a vehicle will experience a series of oscillations that will cycle according to the natural frequency of the system. According to the causes, the shocks and the vibrations can be: caused by the road's irregularities, wind, braking, and caused by engine, steering and the tyre-wheel-road system.

According "DIN 4150" [9] vibrations are:

- Barely perceptible vibrations <5 pali
- Well perceptible vibrations 5–10 pali

– Strong perceptible vibrations 10–20 pali
– Annoying vibrations 20–40 pali

Ride is perceived as most comfortable when the natural frequency is in the range of 1–1.5 Hz. When the frequency approaches 12 Hz, occupants perceive the ride as harsh. A high-performance sports car will have a stiffer suspension with a natural frequency of about 2–2.5 Hz [3]. The head and neck regions are especially sensitive to vibrations of 18–20 Hz. A realistic road model has to take into account the correlation between the different axles and the correlation between parallel tracks. The spectral description of the road, together with a knowledge of traversal velocity and of the dynamic properties of the vehicle, provide a response analysis which will describe the response of the vehicle expressed in terms of displacement, acceleration, or stress [10]. The spectral density with respect to displacement is given by:

$$\phi_h = \lim_{X\to\infty} \frac{4 \cdot \Pi \cdot}{T} b^2(\Omega) \tag{5}$$

where X is the road section analyzed, b is the irregularities amplitude, T is the time range and Ω is the space dependent pulsation.

5 Simulation of the Road Roughness

In order to be able to have a simulation with different outputs, the roughness of the road was simulated in Matlab/Simulink. One of the most useful tools to describe the stationary road roughness is the power spectral density (PSD) [11]. The vehicle is assumed to travel at a constant forward speed denoted by v (m/s) over a random road surface. It is also assumed that the tire behaves as a point-contact follower that is in contact with the road at all times. When a car moves at a constant velocity, the PSD of the road disturbance input is expressed:

$$G_q(n) = G_q(n_0)\left(\frac{n}{n_0}\right)^{-w} \tag{6}$$

where $G_q(n)$ is the road PSD, n is the spatial frequency, n_o is the reference spatial frequency, defined as 0.1 cycle/m, $G_q(n_0)$ is the road roughness coefficient, w is called waviness and has a general value of 2. The relationship between the time frequency f and the vehicle forward constant velocity v is defined by:

$$f = v * n \tag{7}$$

Derived from equation (6), the PSD of ground displacement has the following general form:

$$G_q(f) = \frac{G_q(n_0)n_0^2 v}{f^2} \tag{8}$$

The road roughness can be obtained with the following equation:

$$\dot{z}_r(t) + \omega_0 z_r(t) = vw(t) \tag{9}$$

where z_r (t) is the road roughness, w(t) is a white noise signal whose power spectral density is 1, ω_0 is the lowest angular frequency (rad/s) and Ω is the spatial angular frequency (rad/sec).

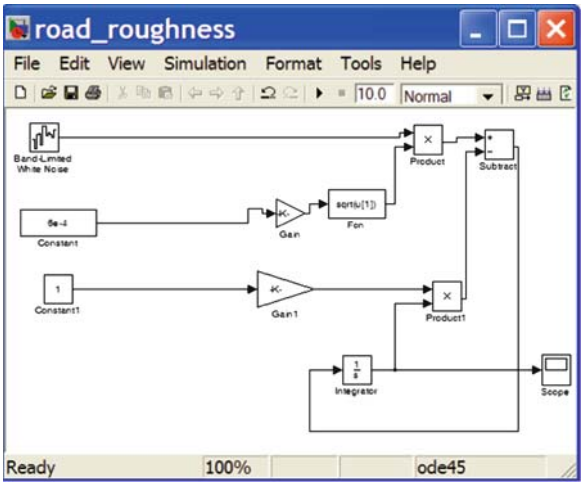

Fig. 5 Simulink model for road roughness

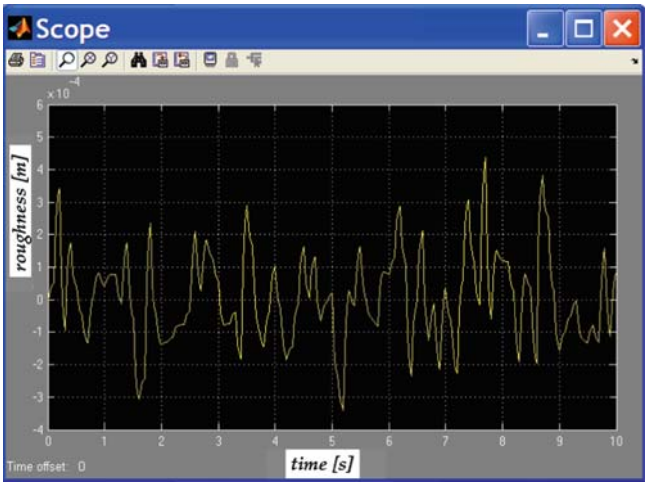

Fig. 6 Road roughness obtained from the model

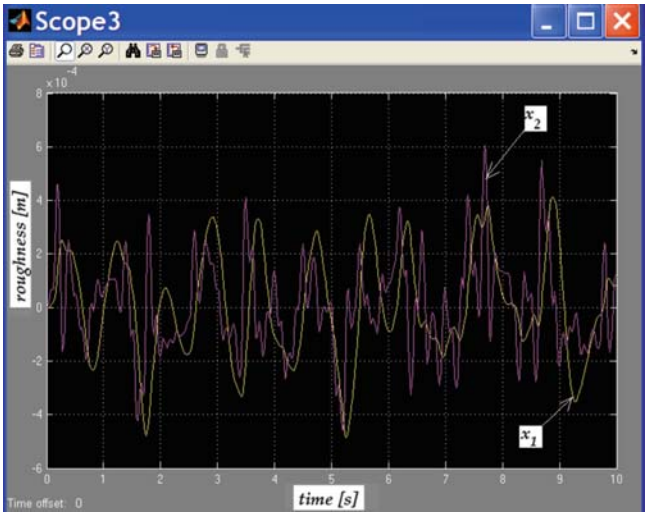

Fig. 7 Road roughness input for the quarter car model

For a constant velocity of 40 m/s the equations were implemented in a Simulink model (Fig. 5).

Figure 6 presents the roughness of the road (m).

The next step was to introduce in the 2 DOF quarter car model the road roughness as in input and study the results. Figure 7 presents the output of the model.

6 Conclusions

A quarter car model was designed in Simulink and validated on a simulated road using PSD. It was built to analyze the response of the vehicle to the excitation of the road profile. After building the two masses quarter car model and studying the frequency range, and the influences in case of a car ride, the road roughness was simulated. Then the roughness function was introduced as an input for the quarter car model and the outputs – the two displacements were studied. This experiment helped studying and observing the influence of the road roughness in case of a suspension for a constant velocity of the car.

References

1. Giua, A., Seatzu, G., Usai, G.: A mixed suspension system for a half car vehicle model. Dyn. Contr. 10(4), 375–397 (December 2000)
2. Liang, Yu., LI, Jun.: A study of active suspension based on full DOF vehicle model. J. Chongqing Univ. (English edition) 4(2), June 2005

3. Turkay, S., Akcay, H.: A study of random vibration characteristics of the quarter-car model. J. sound Vib. 282, 111–124 (12 October 2004)
4. Brandon, P., White, N.: Sensitivity of damper valve architecture to changes in mount stiffness/damping/hysteresis and the subsequent combined damping characteristics. Kingston University, Vehicle Dynamics Expo, 9 May 2006
5. Alexandru, P., Vişa, I., Talaba, D., Alexandru, C., Antonia, C.S.: Modelarea statico-dinamica a mecanismelor de ghidare ale rotilor automobilelor, pp. 235–240. Editura Lux Libris, Brasov (2005)
6. Kim, C., Ro, P.I.: A sliding mode controller for vehicle active suspension systems with nonlinearities. Proceedings Institution of Mechanical Engineers, Part D, vol. 212, pp. 79–92 (1998)
7. Mathworks: http://www.mathworks.fr/products/simulink/demos.html
8. Yahada, M.D., Hudha, S.K.: PI/PISMC control of hydraulically actuated active suspension system. Proceedings the 1st international conference on natural resources engineering and technology INRET2006. Marriot, Putrajaya, Malaysia, 24–25 July 2006
9. Verein Deutscher Ingenieure, VDI [Mitarb. u.a.: Fritz M]: *Einwirkung mechanischer Schwingungen auf den Menschen: Hand-Arm-Schwingungen. VDI-Richtlinien*, VDI 2057, Blatt 2, Stand: 09/2002
10. Rill, G.: The influence of correlated random excitation processes on dynamics of vehicles. In: Hedrick, J.K. (ed.) Proceedings of the eighth IAVSD symposium on the dynamics of vehicles on roads and on railway tracks, pp. 449–459 (1983)
11. He, Li., Qin, G., Zhang, Y., Chen, L.: Non-stationary random analysis of vehicle with fractional damping. International conference on intelligent computation technology and automation (2008)

On Link Effects of Ring Workspace of Three-Revolute Manipulators

Hao Gu and Marco Ceccarelli

Abstract A formulation for the ring workspace of three-revolute open chain manipulators is proposed through an algebraic expression of its boundary surface. The ring equations are deduced by considering the geometric process of generation of a solid ring and by expressing the ring boundary as an envelope surface. The algebraic nature of the formulation has been useful to develop direct analysis on workspace characteristics, which may be also useful in synthesis procedures. Moreover, a straightforward analysis has been developed to investigate link effects on the workspace shape and volume by considering some typical structural designs of three-revolute open chain manipulators.

Keywords Kinematics · Manipulators · Robotics · Workspace

1 Introduction

Workspace analysis of open chain robotics is a research topic of still great interest, since it is a fundamental issue for manipulator design.

Some early studies on the subject of manipulator performance in terms of workspace were developed in [1, 2]. Then, a great attention has been addressed to the topic in a very rich literature. An important breakthrough on the algebraic formulation to determine the workspace of revolution manipulators has been presented by Ceccarelli in [3, 4]. The algebraic nature of the formulation leads to more researches in terms of analysis on workspace characteristics [5, 6], and also synthesis procedures [7–9].

H. Gu (✉)
Laboratory of Robotics and Mechatronics, University of Cassino, Cassino, Italy

I. Vişa (ed.), *SYROM 2009*,
DOI 10.1007/978-90-481-3522-6_23,

In this paper, a straightforward analysis has been developed to investigate the effect of the chain parameters on the workspace shape and volume by considering different structural designs of three-revolute open chain manipulators.

2 The Workspace Boundary Envelope

The workspace of a manipulator is defined as the region of reachable points by a reference point H attached to the manipulator end-effecter [10]. As shown in Fig. 1, the workspace for a three-revolute manipulator is a ring, which is generated by the revolution of a tours about Z_1 axis, [3].

An algebraic formulation has been proposed for the determination of workspace boundary of three-revolute manipulators in [3]. The workspace boundary envelope is traced by the reference point H for different values of angle θ_3 because of the revolution about Z_1 and Z_2 axes. A formulation can be derived, with the hypotheses C_1 and E_1 are different from zero, and expressed through the radial reach r_1 and the axial reach z_1 of the workspace boundary points with respect to reference frame attached to the base in the form [3]

$$r_1 = \left[A_1 - z_1^2 + \frac{(C_1 z_1 + D_1)G_1 + F_1}{E_1}\right]^{1/2},$$

$$z_1 = \frac{-L_1 \pm Q_1^{1/2}}{K_1 C_1} - \frac{D_1}{C_1} \tag{1}$$

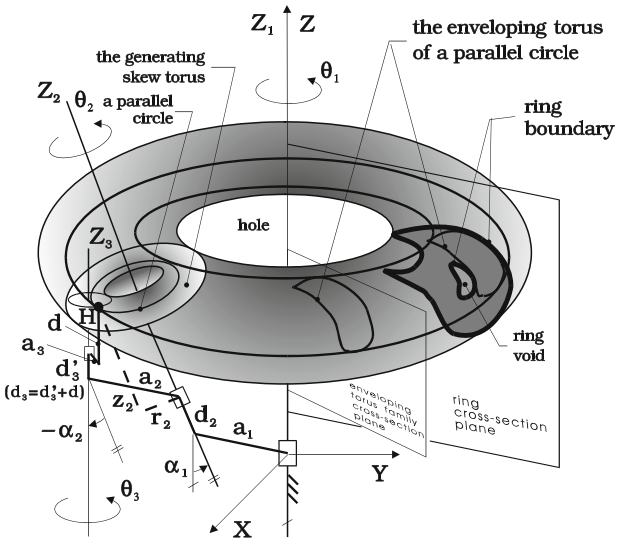

Fig. 1 The envelope geometry in a ring generation with a three-revolute open chain

where the so-called structural coefficients can be computed as functions of Denavit-Hartenberg parameters

$$A_1 = a_1^2 + r_2^2 + (z_2 + d_2)^2$$

$$\mathrm{B_1} = -4a_1^2\ \mathrm{r_2^2}$$

$$\mathrm{C_1} = 2\frac{\mathrm{a_1}}{\mathrm{s}\alpha_1}$$

$$\mathrm{D_1} = -2\mathrm{a_1}(\mathrm{z_2} + \mathrm{d_2})\frac{c\alpha_1}{s\alpha_1}$$

$$\mathrm{E_1} = -2\mathrm{a_3}\ (\mathrm{d_2}\ \mathrm{s}\alpha_2\ \mathrm{c}\theta_3 + \mathrm{a_2}\ \mathrm{s}\theta_3) \tag{2}$$

$$\mathrm{F_1} = 4a_1^2\ \mathrm{a_3}\ (\mathrm{a_3}\ \mathrm{s}\alpha_2^2\ \mathrm{s}\theta_3\ \mathrm{c}\theta_3 + \mathrm{a_2}\ \mathrm{s}\theta_3 - \mathrm{d_3}\ \mathrm{s}\alpha_2\ \mathrm{c}\alpha_2\ \mathrm{c}\theta_3)$$

$$\mathrm{G_1} = 2\mathrm{a_1}\ \mathrm{a_3}\ \frac{\mathrm{c}\alpha_1}{\mathrm{s}\alpha_1}\ \mathrm{s}\alpha_2\ \mathrm{c}\theta_3$$

$$L_1 = F_1 G_1$$

$$K_1 = {G_1}^2 + {E_1}^2$$

$$\mathrm{Q_1} = E_1^2\ \left[\mathrm{F_1^2} +\ \mathrm{B_1}\ (\mathrm{E_1^2} + G_1^2)\right]$$

in which $\mathrm{c}\alpha_\mathrm{i}$, $\mathrm{s}\alpha_\mathrm{i}$, $\mathrm{c}\theta_3$, and $\mathrm{s}\theta_3$ denote $\cos\alpha_\mathrm{i}$, $\sin\alpha_\mathrm{i}$, $\cos\theta_3$ and $\sin\theta_3$ respectively.

The reach distances $\mathrm{r_2}$ and $\mathrm{z_2}$ can be expressed from the link geometry as

$$\mathrm{r_2} = [(\mathrm{a_3}\ \mathrm{c}\theta_3 + \mathrm{a_2})^2 + (\mathrm{a_3}\ \mathrm{s}\theta_3\ \mathrm{c}\alpha_2 + \mathrm{d_3}\ \mathrm{s}\alpha_2)^2]^{1/2} \mathrm{z_2} = \mathrm{d_3}\ \mathrm{c}\alpha_2 - \mathrm{a_3}\ \mathrm{s}\theta_3\ \mathrm{s}\alpha_2. \tag{3}$$

Thus the workspace boundary can be obtained from equations (1–3) by scanning the angle θ_3, and plotting $\mathrm{r_1}$ and $\mathrm{z_1}$.

3 Effect of Chain Parameters on Shapes

The structural parameters can affect the workspace characteristics directly, since equations (1) are functions of them. There are seven parameters in total, and they are $\mathrm{a_1}$, $\mathrm{a_2}$, $\mathrm{a_3}$, $\mathrm{d_2}$, $\mathrm{d_3}$, α_1, α_2.

In order to make the analysis clear, we can consider the other length parameters as the ratio compared with $\mathrm{a_1}$. Thus, the problem becomes: how the parameters $\mathrm{a_2/a_1}$, $\mathrm{a_3/a_1}$, $\mathrm{d_2/a_1}$, $\mathrm{d_3/a_1}$, α_1, α_2 effect the workspace.

3.1 Tables of Workspace Topology

One group of d_2/a_1, d_3/a_1, α_1, α_2 can be fixed and the effect of a_2/a_1, a_3/a_1 is observed by using a two dimension table as shown in Table 1, in which the nine positions are defined as P1–P9. We have named this table as the Table of Workspace Topology (TWT).

In this paper, TWT is the basic unit to study the effect of parameters. Other tables can be determined by changing the values for d_2/a_1, d_3/a_1, α_1, α_2.

With the concept of TWT, the way to analyse the effect of parameters can be clear and efficient, because TWT arrange the workspace topology information as:

- One table express the effects of a_2/a_1 and a_3/a_1 readably.
- From table to table, the effects of d_2/a_1, d_3/a_1, α_1, α_2 can be detected by comparing the differences.

As shown in Table 2, the available values for α_1, α_2 are given to be 30° and 75°, while for d_2/a_1, d_3/a_1 are given to be 0.5, 1, 1.5.

Thirty-six TWTs can be derived and they are defined as T1–T36. Each of them has the structure that is shown in Table 1. Examples of T1, T10, T19, T28 can be found in Figs. 2–5.

3.2 Effect of Twist Angles

It has been found that thirty-six TWTs in Table 2 can be classified into four types named TYPE1 to TYPE4 by their shape characteristics. Furthermore, TWTs with

Table 1 Table of workspace topology

a_3/a_1 / a_2/a_1	0.5	1	1.5
0.5	P1	P2	P3
1	P4	P5	P6
1.5	P7	P8	P9

Table 2 TWTs for analysis

α_2	30°				75°			
α_1								
30°	d_3/a_1 / d_2/a_1	0.5	1	1.5	d_3/a_1 / d_2/a_1	0.5	1	1.5
	0.5	T1	T2	T3	0.5	T10	T11	T12
	1	T4	T5	T6	1	T13	T14	T15
	1.5	T7	T8	T9	1.5	T16	T17	T18
75°	d_3/a_1 / d_2/a_1	0.5	1	1.5	d_3/a_1 / d_2/a_1	0.5	1	1.5
	0.5	T19	T20	T21	0.5	T28	T29	T30
	1	T22	T23	T24	1	T31	T32	T33
	1.5	T25	T26	T27	1.5	T34	T35	T36

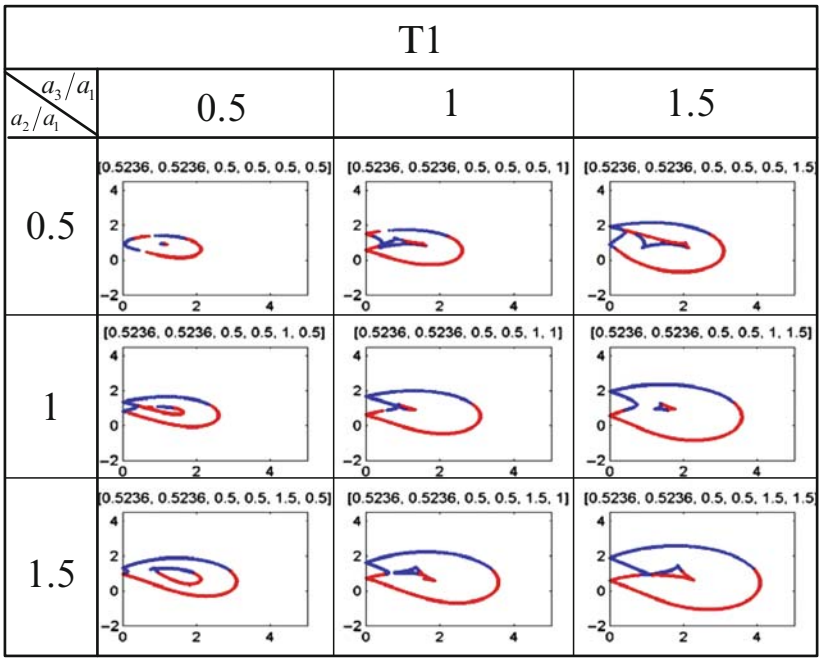

Fig. 2 Computed TWT of T1as in Table 2

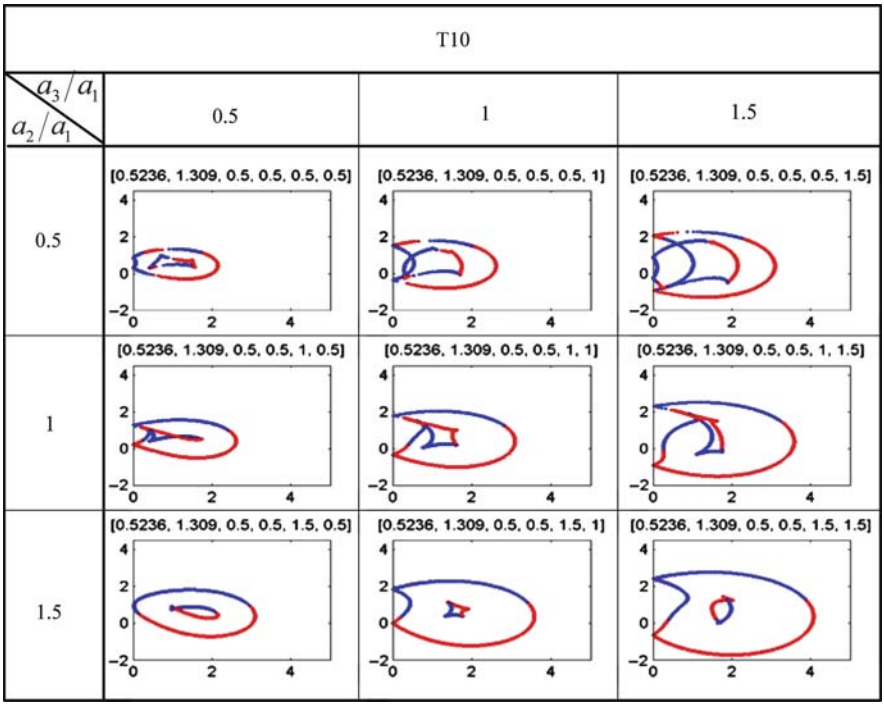

Fig. 3 Computed TWT of T10 as in Table 2

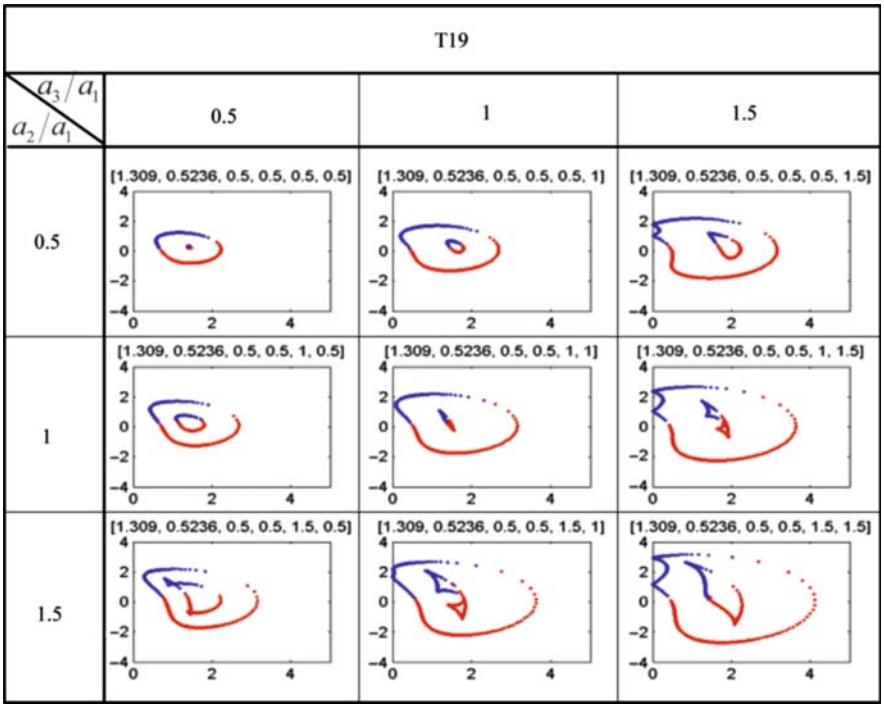

Fig. 4 Computed TWT of T19 as in Table 2

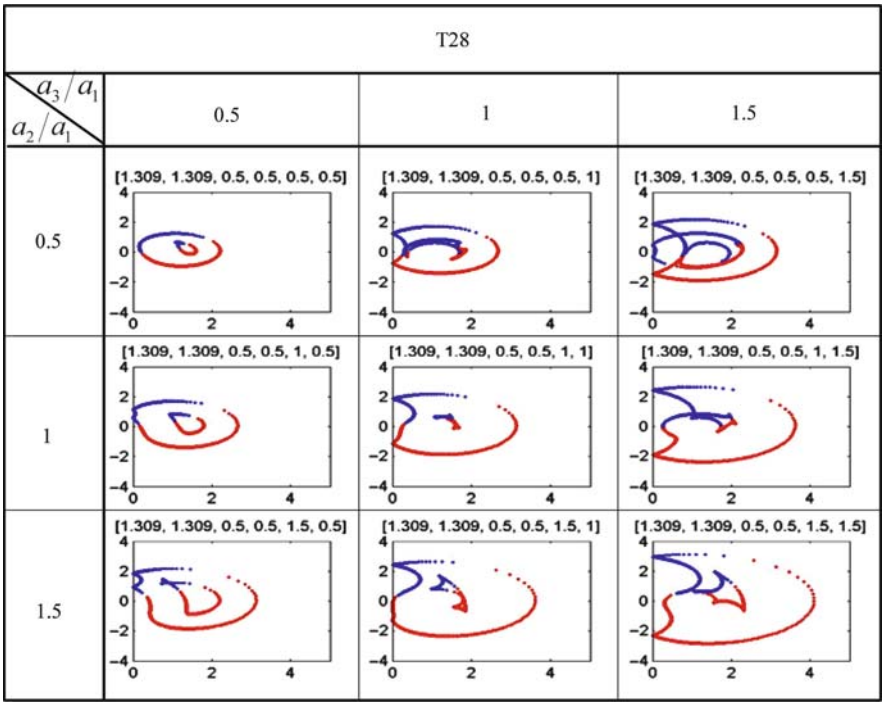

Fig. 5 Computed TWT of T28 as in Table 2

Table 3 The main shape characteristics for four types of TWT

Type of TWT	Characteristic	
	Regular shapes	Irregular shapes
TYPE1 ($\alpha_1 = 30°, \alpha_2 = 30°$)	Banana-like shapes. Most of them have the external boundary with cusps	None exists
TYPE2 ($\alpha_1 = 30°, \alpha_2 = 75°$)		Irregular shapes appear while $a_3 > a_2$
TYPE3 ($\alpha_1 = 75°, \alpha_2 = 30°$)	Pear-like shapes with smooth external boundary	None exists
TYPE4 ($\alpha_1 = 75°, \alpha_2 = 75°$)		Irregular shapes appear while $a_3 > a_2$

same values of α_1, α_2 belong to the same type of TWT. Therefore, types of TWT are decided by twist angles α_1, α_2, and the effect of twist angles on workspace shape can be outlined through types of TWT.

According to Table 2, TWTs T9(i−1) + 1 to T9(i−1) + 9 belong to TYPEi (i = 1–4). Figures 2–5 show the first TWT of each type, namely, T1, T10, T19, T28. The six dimension vector above the workspace shape in Figs. 2–5 indicates values of α_1, α_2, d_2/a_1, d_3/a_1, a_2/a_1 and a_3/a_1.

The main characteristics for four types of TWT are summarized in Table 3. It shows that twist angles can affect workspace shapes significantly. Particularly, α_1 affects the general shape characteristics of the workspace shape and α_2 effects the intersecting of envelope branches, which is characterized as the irregular shape in Table 3.

3.3 Effect of Link Offsets

The classifying of TWTs in Section 3.2 also hints that link offsets d_2, d_3 do not affect the workspace shape significantly, since T9(i−1) + 1 to T9(i−1) + 9 (i = 1–4) with different d_2, d_3 belong to the same type and have common characteristics.

A close view on the effect of link offsets has been investigated in Fig. 6, which shows workspace shapes of T10–T18 in TYPE2 at P3 position.

As shown in Fig. 6, it can be recognized that nine workspace shapes with different d_2, d_3 are similar. Particularly, those in a column with changes of d_2 have almost the same shape, while those in a row with changes of d_3 change the shape gradually. It means that d_2 almost has no effect on the workspace shape, while d_3 can effect the shape slightly.

3.4 Effect of Link Lengths

The effect of link lengths a_2, a_3 is expressed in each TWT directly. As Figs. 2–5 show, a_2, a_3 have considerable effect on the workspace shape.

Firstly, their effect on the shape scale is very obvious in the TWT. The longer link lengths are, the bigger the workspace becomes. A numerical evaluation of this effect is discussed in Section 4.

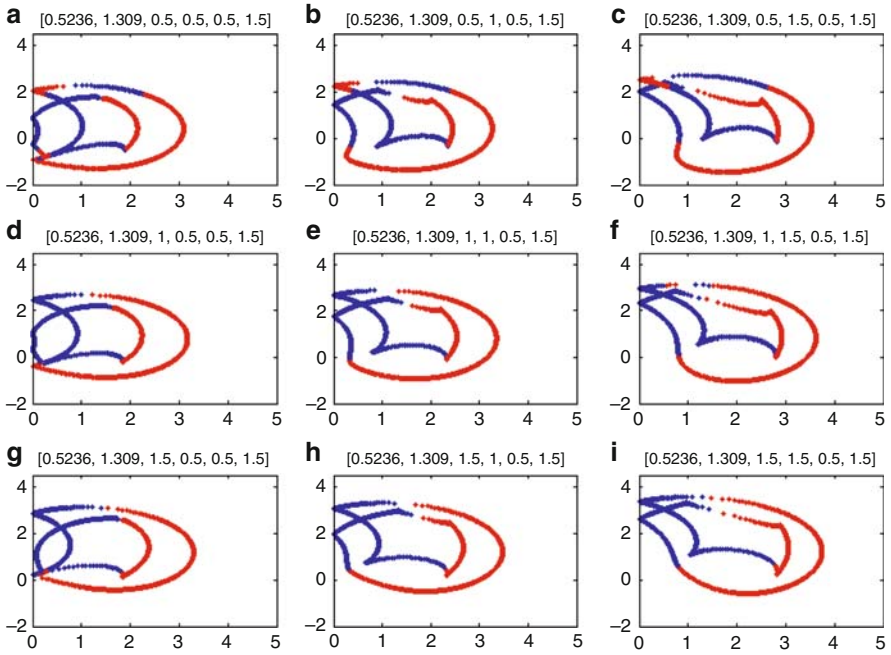

Fig. 6 Workspace shapes of T10–T18 at P3 position for indication the effect of link offsets: (**a**) T10; (**b**) T11; (**c**) T12; (**d**) T13; (**e**) T14; (**f**) T15; (**g**) T16; (**h**) T17; (**i**) T18

Secondly, link lengths can affect the ring void of the workspace. The ring void is a region of unreachable points within the workspace [10]. For the derived TWTs in Table 2, the first column of the TWT with $a_3/a_1 = 0.5$ always have workspace with a ring void.

Finally, for TWTs of TYPE2 and TYPE4 having irregular shapes, the effect of link lengths is more significant. Taking T31 in TYPE4 for example, the TWT can be divided into three zones, as shown in Fig. 7. Z1, Z2 and Z3 are the zones including workspace shapes with $a_2 > a_3$, $a_2 = a_3$, and $a_2 < a_3$ respectively. Irregular shapes appear in Z3 while in Z1 shapes are regular. Z2 is the transition zone between Z1 and Z3, where shapes have ambiguous characteristics like those in Z1 and Z3.

Table 4 summarizes the effect of all the above mentioned chain parameters on workspace shapes.

4 Volume Evaluation

The value of workspace volume is one of the fundamental characteristics of manipulator workspace [10]. The volume evaluation can give a numerical view of the chain parameters' effect.

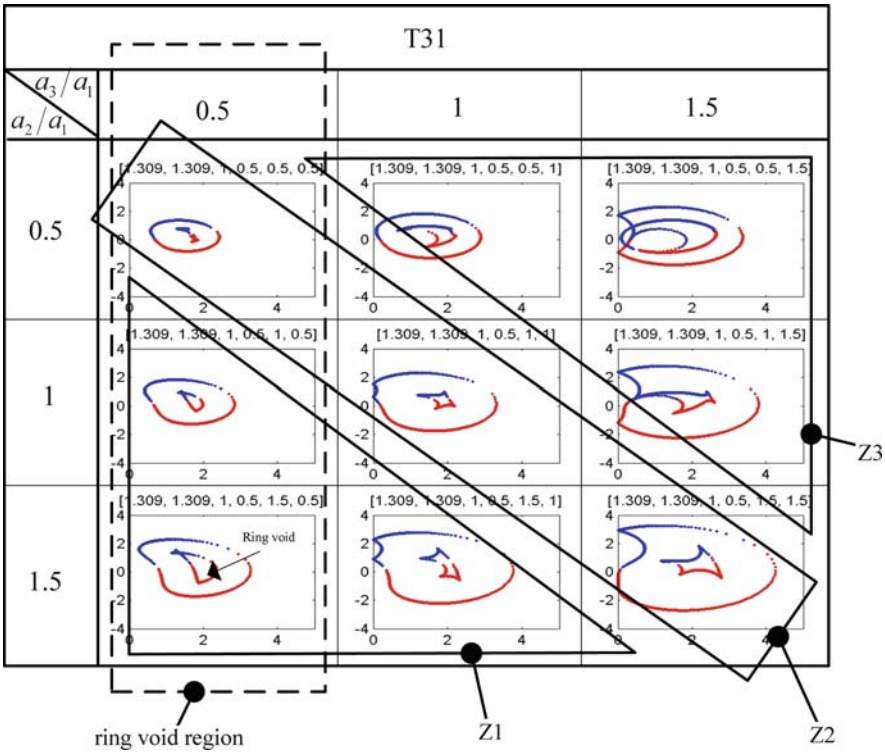

Fig. 7 Zones for analysing the effect of link lengths on workspace shapes

Table 4 The effect of chain parameters on workspace shapes

Parameter	Effect	Main character
a_2	Significant	Increase of the shape scale when α_2 is large, can generate envelope branches with intersection (irregular shape) a_3 can effect the existence of a ring void
a_3		
d_2	No significant	Almost no effect
d_3	Poor	Slightly changes of the shape scale
α_1	Very significant	The shape changes from banana to pear and versa vice
α_2		When $a_3 > a_2$, can generate envelope branches with intersection (irregular shape)

4.1 Numerical Algorithm

As suggested in [10], one can use the workspace points of the boundary contour to compute the cross-section area A and the workspace bulk volume V.

As shown in Fig. 8, the cross-section area has been scanned horizontally by lines with different values of z. From z_{min} to z_{max}, there must be intersections of the

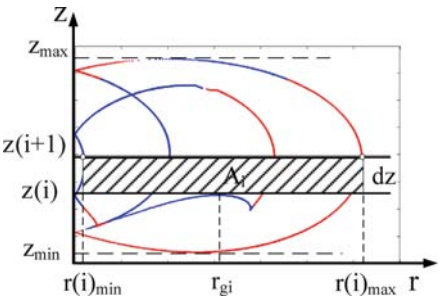

Fig. 8 A scheme for computing the workspace volume

scanning line and the ring workspace boundary, and $r(i)_{min}$, $r(i)_{max}$ can be derived from the intersections.

Thus, the bulk area can be evaluated by summing up the rectangle areas A_i in the form

$$A = \sum_{i=1}^{N} A_i \tag{4}$$

with

$$A_i = dz(r(i)_{max} - r(i)_{min}) \tag{5}$$

The workspace bulk volume V can be evaluated by means of formula as

$$V = \sum_{i=1}^{N} V_i \tag{6}$$

with

$$V_i = 2\pi A_i r_{gi} \tag{7}$$

in which r_{gi} is the radial reach of A_i's centre according to the Pappus-Guldino Theorem.

It is worth to note that, this horizontal scanning algorithm is suitable for all possible shapes of workspace, including the cases with intersecting envelope branches as shown in Fig. 8, that have been commented in [11].

4.2 Effect of Chain Parameters on Volume

By using the algorithm in 4.1, all the workspace volume of thirty-six TWTs can be computed.

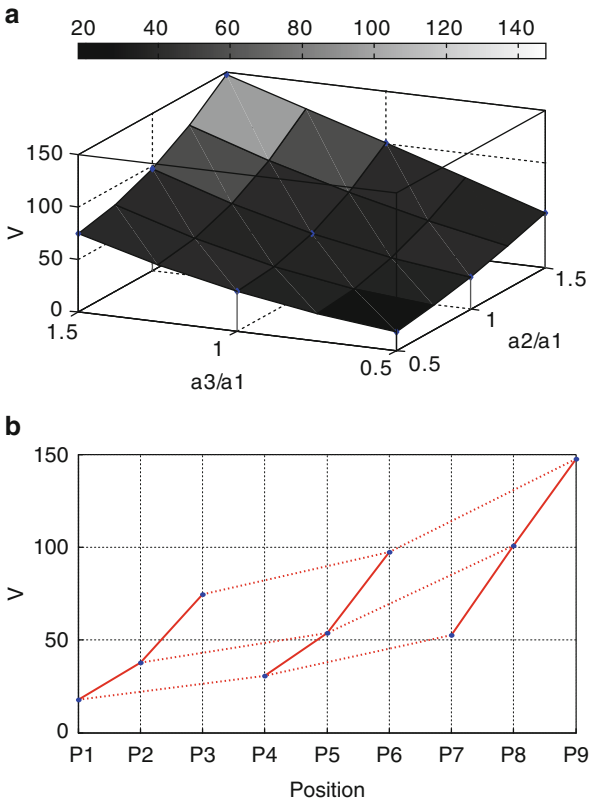

Fig. 9 Workspace volume for T10 in Table 2: (**a**) 3D evaluation as function of a_2 and a_3 (**b**) 2D evaluation as function of the position in TWT as given in Table 1

Taking T10 for example, the link lengths a_2 and a_3 are recognised to have a direct effect on the workspace volume, as illustrated in Fig. 9.

Figure 9a shows a 3D evaluation by considering two variables a_2 and a_3; the slope of the interpolating surface illustrates that the workspace volume has a positive relation with a_2 and a_3, namely, the longer link lengths are, the larger the volume becomes. More exactly, the effect of a_2 and a_3 on the workspace volume can be considered as a cubic-like function.

Figure 9b shows a 2D view for the volume evaluation by considering position in T10 as a variable. In fact, solid lines passing the volume values of P3i + 1, P3i + 2 and P3i + 3 (i = 0, 1, 2) express the effect of a_3 on the workspace volume, while dotted lines passing the volume values of Pi + 1, Pi + 4, Pi + 7 (i = 0, 1, 2) express the effect of a_2. From Fig. 9b it can also be detected that the workspace volume is positively affected by the link lengths a_2 and a_3.

For analyzing the effect of link offsets, Fig. 10 shows the plots of the workspace volumes of T10–T18 in P1 position as in Table 1, which is related to the fixed design configuration with a_2, a_3, α_1, α_2.

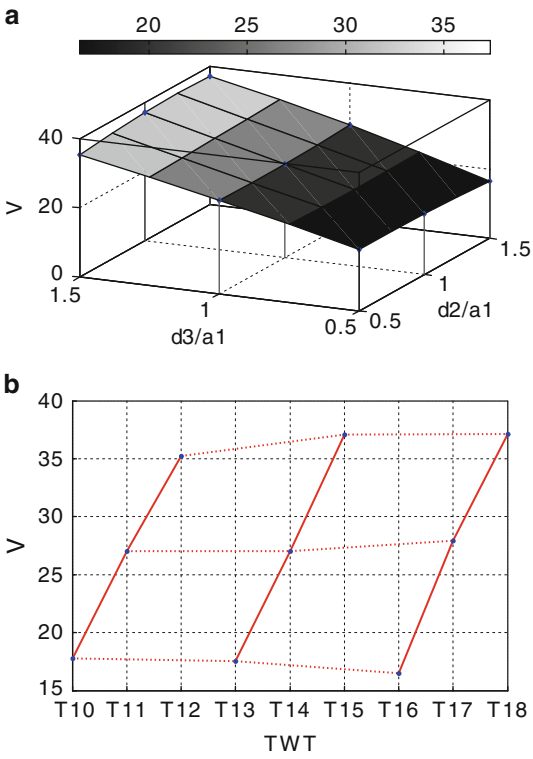

Fig. 10 Workspace volume for cases in T10–T18 at P1 position: (**a**) 3D evaluation as function of d_2 and d_3; (**b**) 2D evaluation as function of TWTs T10–T18

Similarly, both 3D and 2D view are used for evaluation. Particularly, variables for 2D view in Fig. 10b are the nine tables T10–T18, which indicate the change as function of d_2 and d_3. The solid and dotted lines express the effect of d_3 and d_2 respectively.

The interpolating surface of Fig. 10a is a plane which has a slope along the direction of d_3 only. It means that the volume is proportional to d_3, but is not affected by d_2 significantly.

Figure 10b illustrates the same fact, since gradients of the solid lines are positive while the dotted lines are almost horizontal.

The effect of twist angles has been evaluated by plotting the workspace volume of T1, T10, T19, T28 at P1 position, as shown in Fig. 11, which is related to a fixed design configuration of d_2, d_3, a_2, a_3.

Figure 11 shows results that are similar to Figs. 9 and 10. In particular, variables for the 2D view in Fig. 11b are four TYPEs, which actually indicate the change as function of α_1, α_2.

From Fig. 11, it can be deduced that twist angles α_1, α_2 have a quasi-proportional effect on the workspace volume.

Table 5 summarizes the effect of chain parameters on workspace volume for three-revolute manipulators.

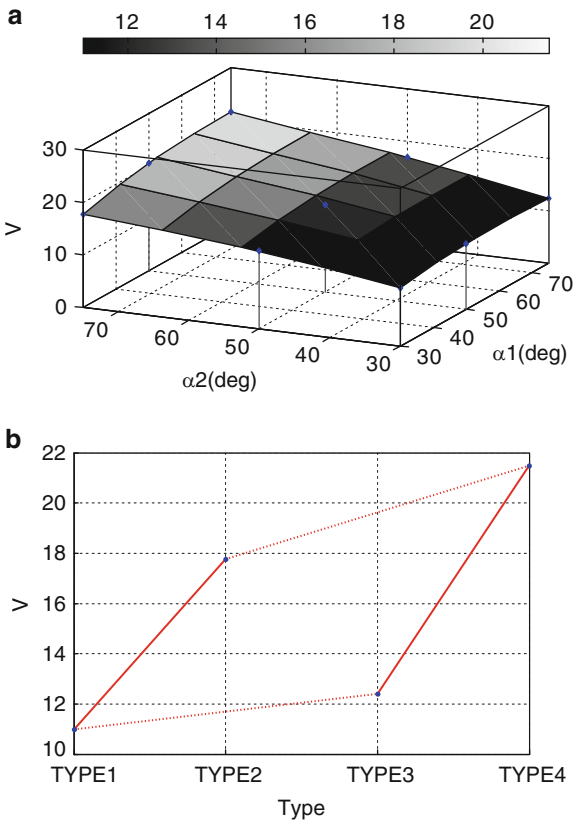

Fig. 11 Workspace volume for the cases of the TYPE characters in T1, T10, T19, T28 at P1 position: (**a**) 3D evaluation as function of α_1 and α_2; (**b**) 2D evaluation as function of TYPE

Table 5 The effect of chain parameters on workspace volume

Parameter	Effect	Function
a_2	Very significant	Quadratic-like
a_3		Cubic-like
d_2	No significant	Almost constant
d_3	Significant	Proportional
α_1		Quasi-proportional
α_2		

5 Conclusion

In this paper we have used the ring equations to investigate and characterize the effect of link parameters on the shape and volume of three-revolute open chain manipulators. In particular, some typical configurations that are indicative of the

continuous evaluation of workspace characteristics have been computed and computed results are reported to show both characteristic shapes and volume values, which indicate the design possibility as function changes in their values.

Acknowledgments The first author would like to acknowledge China Scholarship Council (CSC) for supporting his Ph.D. study and research at LARM in the University of Cassino, Italy, for the years 2008–2010.

References

1 Roth, B.: Performance evaluation of manipulators from a kinematic viewpoint. Natl. Bureau. Stand. (special publication) 459, 39–61 (1975)
2 Freudenstein, F., Primrose, E.J.F.: On the analysis of the workspace of a three-link, turning-pair connected robot arm. J. Mech. Transm-T. ASME 106, 365–370 (1984)
3 Ceccarelli, M.: On the workspace of 3R robot arms. Proceedings of 5th IFToMM international symposium on theory and practice of mechanism. Bucharest, pp. 39–46 (1989)
4 Ceccarelli, M.: A formulation for the workspace boundary of general N-revolute manipulators. Mech. Machi. Theory 106, 365–370 (1996)
5 Ottaviano, E., Ceccarelli, M., Lanni, C.: A characterization of ring void in workspace of three-revolute manipulators. Proceedings of 10th world congress on the theory of machines and mechanisms. Oulu 3**,** 1039–1044 (1999)
6 Saramago, S.F.P., Ottaviano, E., Ceccarelli, M.: A characterization of the workspace boundary of three-revolute manipulators. Proceedings of DETC'02. ASME 1, 34342–34352 (2002)
7 Ceccarelli, M.: A synthesis algorithm for three-revolute manipulators by using an algebraic formulation of workspace boundary. J. Mech. Design ASME 117, 298–302 (1995)
8 Ceccarelli, M.: Designing two-revolute manipulators for prescribed feasible workspace regions. J. Mech. Design ASME 124(3), 427–434 (2002)
9. Ceccarelli, M., Lanni, C.: A multi-objective optimum design of general 3r manipulators for prescribed workspace limits. Mech. Mach. Theory 39, 119–132 (2004)
10 Ceccarelli, M.: Fundamentals of mechanics of robotic manipulation. Kluwer, Dordrecht (2004)
11 Bergamaschi, P.R., Nogueira, A.C., Saramago, S.F.P.: Design and optimization of 3r manipulators using the workspace features. Appl. Math. Comput. 172, 439–463 (2006)

Contributions to the Dynamic Study of a Modular Serial Industrial Robot of TRTRR Type

V. Ispas, Vrg. Ispas, M. Simion, and O.A. Detesan

Abstract The paper presents an algorithm of determination of the dynamic equations of an industrial robot with five degrees of freedom. The robot consists in: the vertical translation module, the arm rotation module, the translation module from the arm structure and the orientation module of the gripper, which has two degrees of freedom. After presenting the structural kinematic scheme of the robot, the Lagrange's equations of the second kind are used, for the dynamic study. In this regard, the kinetic energy of the robot and the generalized driving forces are determined, which introduced into Lagrange's equations, lead to the differential equations of the robot.

Keywords Dynamics · Lagrange · Serial modular robots

1 Introduction

In the design stage of the industrial robots, an estimation of some amounts is necessary, like: the number of degrees of freedom, the shape and the dimensions of the working space, the mobility, the load capacity, the working coefficient etc. Also, in this stage, the choosing of the architectural structure of the robot, as well as the actuators, is imposed. Such estimation is possible only by accomplishing the dynamic study of the robot.

V. Ispas (✉)
Department of Applied Mechanics and Computer Programming, Technical University of Cluj-Napoca, Cluj-Napoca, Romania

I. Vişa (ed.), *SYROM 2009*,
DOI 10.1007/978-90-481-3522-6_24,

2 The Dynamic Equations

The following notations are made:

$l_i,\ i = 1 \div 5,$ the constructive parameters of the robot; $q_k,\ k = 1 \div 5,$ the geometrical parameters which constitute the generalised coordinates; $\bar{P}_i,\ i = 1 \div 5,$ the gravity forces of the modules, the dimension l_5 positioning the mass centre of the assemble consisting in the module 5, the gripper, and the object manipulated by the robot;

$\bar{F}_i,\ i = 1, 3,$ the driving forces including the passive forces from the modules 1 and 3; $\bar{M}_i,\ i = 2, 4, 5,$ the driving moments including the passive moments from the modules 2, 4 and 5; $m_i,\ i = 1 \div 5,$ the masses of the modules; $\dot{q}_k,\ \ddot{q}_k,$ the linear and angular velocities and accelerations corresponding to these modules; $J^{(i)}_{\Delta_2}$, $i = 2, 3, 4, 5,$ the mechanical moments of inertia of the modules 3, 4 and 5 and of the mobile equipment of the module 2 determined with respect to the axis of rotation (Δ_2); $J^{(i)}_{\Delta_4}$, $i = 4, 5,$ the mechanical moments of inertia of the mobile equipment of the module 4 and 5 (together with the gripper and the object to be manipulated), determined with respect to the axis of rotation (Δ_4); $J^{(5)}_{z_5} \equiv J^{(5)}_{\Delta_5},$ the mechanical moment of inertia of the mobile equipment of the module 5, together with the gripper and with object manipulated by the robot, determined with respect to the axis of rotation (Δ_5); $J^{(4)}_{x_4}$, $J^{(4)}_{z_4}$, the mechanical moments of inertia of the mobile parts of the module 4 determined with respect to the axis O_4x_4 and O_4z_4; $J^{(5)}_{x_5}$, $J^{(5)}_{y_5}$, the mechanical moments of inertia of the mobile assembly: module 5, the gripper and the object manipulated by the robot, determined with respect to the axis O_4x_5 and O_5y_5.

In Fig. 1 the following Cartesian reference frames were introduced:

- The fixed Cartesian frame $O_0x_0y_0z_0$, having the origin in the fixed point O_0 which belongs to the fix axis (Δ_1); – the mobile Cartesian frames $O_ix_iy_iz_i,\ i = 1 \div 5,$ with the origins $O_1 \div O_5$; – the mass centres of the modules $1 \div 4$and O_5 in the mass centre of the assembly module 5
- The gripper and the object to be manipulated.

In order to determine the dynamic equations of the robot, the Lagrange's equations of the second kind are used, written, regarding to [1], as:

$$\frac{d}{dt}\left(\frac{\partial E_c}{\partial \dot{q}_k}\right) - \frac{\partial E_c}{\partial q_k} = Q_k, \quad k = 1 \div 5. \tag{1}$$

In the equations (1) E_c represents the kinetic energy of the robot and Q_k represent the generalized forces.

The kinetic energy of the robot is equal to the sum of the kinetic energies of the composing elements, that is

$$E_c = \sum_{i=1}^{5} E_{c_i}. \tag{2}$$

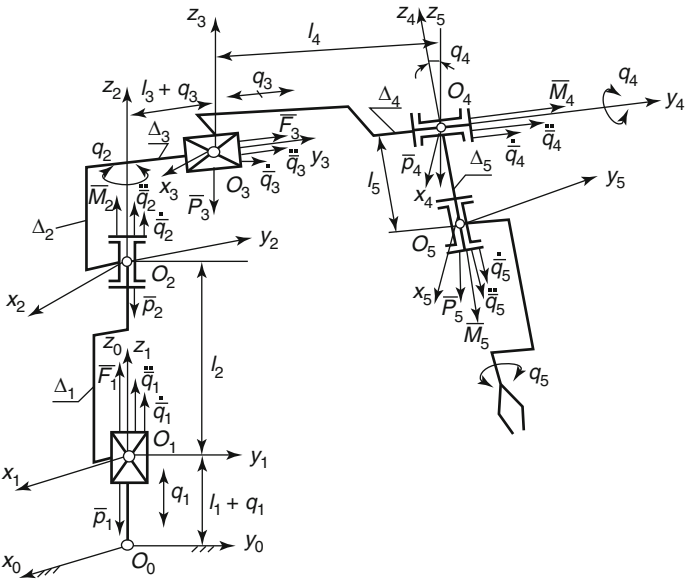

Fig. 1 The kinematics scheme of the modular robot TRTRR

According to [3], the kinetic energy of an element "*i*," considered as rigid body, can be determined with the relation:

$$\begin{aligned} E_{c_i} = &\frac{1}{2}\left[m \cdot \left(v_{ox}^2 + v_{oy}^2 + v_{oz}^2\right) + J_x \cdot \omega_x^2 + J_y \cdot \omega_y^2 + J_z \cdot \omega_z^2\right]_i \\ &+ \left[m \cdot x_c \cdot \left(v_{oy} \cdot \omega_z - v_{oz} \cdot \omega_y\right) + m \cdot y_c \cdot \left(v_{oz} \cdot \omega_x - v_{ox} \cdot \omega_z\right) + \right. \\ &\left. + m \cdot z_c \cdot \left(v_{ox} \cdot \omega_y - v_{oy} \cdot \omega_x\right)\right]_i - \left(J_{xy} \cdot \omega_x \cdot \omega_y + \right. \\ &\left. + J_{yz} \cdot \omega_y \cdot \omega_z + J_{zx} \cdot \omega_z \cdot \omega_x\right)_i. \end{aligned} \tag{3}$$

In relation (3), "*m*" is the mass of the body (module), x_c, y_c, z_c are the coordinates of the mass centre recorded in a Cartesian frame $Oxyz$, invariably attached to the body (module), having the origin in a point "O" belonging to that, $J_x, J_y, J_z, J_{xy}, J_{yz}, J_{zx}$ represent the mechanical axial and centrifugal moments of inertia of the rigid, v_{ox}, v_{oy}, v_{oz} are the Cartesian components of the instantaneous velocity of the point "O," ω_x, ω_y, ω_z represent the projections on the axis of the mobile frame $Oxyz$ of the angular instantaneous velocity vector $\bar{\omega}$ of the rigid revolving around the point "O."

For simplifying reasons, in Fig. 1 the reference frames $O_i x_i y_i z_i$, $i = 1 \div 5$, had been introduced, with the origins O_i placed in the mass centre of the modules, where the axis of these frames coincide with the principals directions of inertia corresponding to the mass centres.

$$E_{c_i} = \frac{1}{2}\left[m \cdot \left(v_{ox}^2 + v_{oy}^2 + v_{oz}^2\right) + J_x \cdot \omega_x^2 + J_y \cdot \omega_y^2 + J_z \cdot \omega_z^2\right]_i \tag{4}$$

The kinetic energies corresponding to the modules of the robot can be successively written, starting from the robot's base, with respect to the Fig. 1 and the relation (4).

Thus, for the module 1 of vertical translation, knowing that $\omega_{x1} = \omega_{x1} = \omega_{x1} = 0$, $v_{x_1} = 0,\ v_{y_1} = 0,$ and $v_{z_1} = \dot{q}_1$, the kinetic energy is obtained with relation:

$$E_{c_1} = \frac{1}{2} m_1 \cdot \dot{q}_1^2. \tag{5}$$

The kinematic parameters which characterise the motion of the second module of rotation of the robot arm are the following:

$$\omega_{x_2} = 0, \quad \omega_{y_2} = 0, \quad \omega_{z_2} = \dot{q}_2, \quad v_{x_2} = 0,\ v_{y_2} = 0,\ v_{z_2} = \dot{q}_1 \tag{6}$$

Having in view the equations (4) and (6), the kinetic energy corresponding to the module of rotation 2 has the expression:

$$E_{c_2} = \frac{1}{2} m_2 \cdot \dot{q}_1^2 + \frac{1}{2} J_{\Delta_2}^{(2)} \cdot \dot{q}_2^2. \tag{7}$$

In the equation (7), $J_{\Delta_2}^{(2)}$ represents the mechanical moment of inertia determined with respect to the axis of rotation (Δ_2) of the mobile equipment of the module of rotation 2.

The motion of the module of translation 3 from the robot's arm is characterised by the following kinematic parameters:

$$\begin{aligned} \bar{v}_{0_3} &= \dot{\bar{q}}_1 + \dot{\bar{q}}_2 \times \bar{r}_3 + \dot{\bar{q}}_3, \\ \omega_{x_3} &= \omega_{y_3} = 0, \quad \omega_{z_3} = \dot{q}_2 \end{aligned} \tag{8}$$

The square of the velocity $\bar{v}_{0_3}$ is

$$v_{0_3}^2 = \dot{q}_1^2 + (l_3 + q_3)^2 \cdot \dot{q}_2^2 + \dot{q}_3^2, \tag{9}$$

because, observing the Fig. 2,

$$\dot{\bar{q}}_1 \cdot \left(\dot{\bar{q}}_3 \times \bar{r}_3\right) = 0, \quad \dot{\bar{q}}_3 \cdot \left(\dot{\bar{q}}_2 \times \bar{r}_3\right) = 0, \quad \dot{\bar{q}}_1 \cdot \dot{\bar{q}}_3 = 0,$$

the respective vectors being perpendicular.

Denoting by $J_{z_3}^{(3)} = J_{0_{3_2}}^{(3)}$ the mechanical moment of inertia of the module 3 determined with respect to the axis $O_3 z_3$ which passes through O_3 and it is parallel with the axis of rotation 2, using (4) and (9), the kinetic energy of the module 3 is determined. Thus,

$$E_{c_3} = \frac{1}{2} m_3 \cdot \left(\dot{q}_1^2 + \dot{q}_3^2\right) + \frac{1}{2}\left[J_{0_{3_2}}^{(3)} + m_3 \cdot (l_3 + q_3)^2\right] \cdot \dot{q}_2^2. \tag{10}$$

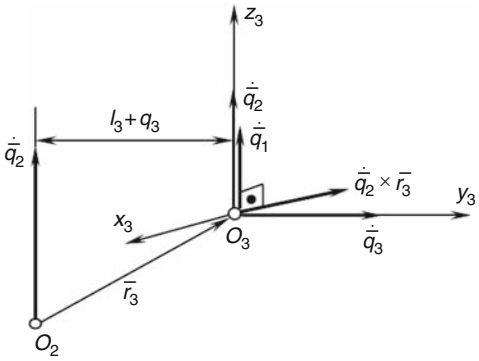

Fig. 2 The velocity of O_3 point (below the drawing)

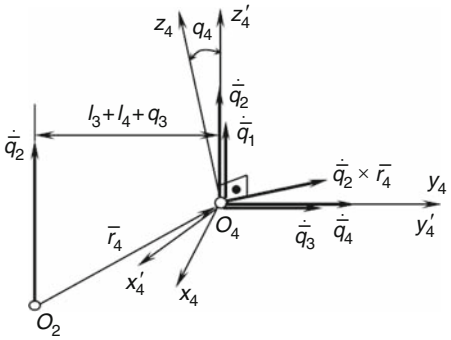

Fig. 3 The velocity of O_4 point (below the drawing)

The parameters which characterise the motion of the module 4 are:

$$\begin{aligned} &\bar{v}_{0_4} = \dot{\bar{q}}_1 + \dot{\bar{q}}_2 \times \bar{r}_4 + \dot{\bar{q}}_3, \quad \omega_{x_4} = \dot{q}_2 \cdot sq_4, \\ &\omega_{y_4} = \dot{q}_4, \quad \omega_{z_4} = \dot{q}_2 \cdot cq_4 \end{aligned} \tag{11}$$

Analyzing the Fig. 3, the velocity $\bar{v}_{0_4}$ is squared, and the following equation is obtained:

$$v_{0_4}^2 = \dot{q}_1^2 + (l_3 + l_4 + q_3)^2 \cdot \dot{q}_2^2 + \dot{q}_3^2, \tag{12}$$

because the scalar products $\dot{\bar{q}}_1 \cdot \left(\dot{\bar{q}}_2 \times \bar{r}_4\right)$, $\dot{\bar{q}}_3 \cdot \left(\dot{\bar{q}}_2 \times \bar{r}_4\right)$, $\dot{\bar{q}}_1 \cdot \dot{\bar{q}}_3$ are null, the respective vectors being perpendicular.

The significance of the following amounts is: $J_{y_4}^{(4)} = J_{\Delta_4}^{(4)}$ represents the mechanical moment of inertia of the module 4 determined with respect to the axis of rotation (Δ_4) of the module 4; $J_{x_4}^{(4)}$, $J_{z_4}^{(4)}$ represent the mechanical moment of inertia of the module 4 with respect to the axes O_4x_4, O_4z_4 which are contained in a perpendicular plane in O_4 on the axis(Δ_4).

Introducing in relation (4) the parameters expressed by relations (11) and (12), the kinetic energy of the module 4 is obtained, having the expression:

$$E_{c_4} = \frac{1}{2} m_4 \cdot \left(\dot{q}_1^2 + \dot{q}_3^2\right) + \frac{1}{2} m_4 \cdot (l_3 + l_4 + q_3)^2 \cdot \dot{q}_2^2 + \\ + \frac{1}{2}\left[J_{x_4}^{(4)} \cdot s^2 q_4 + J_{z_4}^{(4)} \cdot c^2 q_4\right] \cdot \dot{q}_2^2 + \frac{1}{2} J_{\Delta_4}^{(4)} \cdot \dot{q}_4^2. \tag{13}$$

The module 5 is characterized by following kinematic parameters:

$$\bar{v}_{0_5} = \dot{\bar{q}}_1 + \dot{\bar{q}}_2 \times \bar{r}_5 + \dot{\bar{q}}_3 + \dot{\bar{q}}_4 \times \bar{r}_6, \\ \bar{\omega}_5 = \dot{\bar{q}}_2 + \dot{\bar{q}}_4 + \dot{\bar{q}}_5. \tag{14}$$

Following the Fig. 4 and the first relation (14), the square of the velocity $\bar{v}_{0_5}$ is obtained. The expression of this amount is written as:

$$v_{0_5}^2 = \dot{q}_1^2 + \left[(l_3 + l_4 + q_3)^2 + l_5^2 \cdot s^2 \cdot q_4\right] \cdot \dot{q}_2^2 + \dot{q}_3^2 + l_5^2 \cdot \dot{q}_4^2 + 2 \cdot l_5 \cdot sq_4 \cdot \dot{q}_2 \cdot \dot{q}_3 + \\ + 2 \cdot l_5 \cdot (l_3 + l_4 + q_3) \cdot \dot{q}_2 \cdot \dot{q}_4, \tag{15}$$

because:

$$\dot{\bar{q}}_2 \times \bar{r}_5 = \dot{\bar{q}}_2 \times \bar{r}_4 + \dot{\bar{q}}_2 \times \bar{r}_6, \ \left(\dot{\bar{q}}_2 \times \bar{r}_5\right)^2 = \left[(l_3 + l_4 + q_3)^2 + l_5^2 \cdot s^2 q_4\right] \cdot \dot{q}_2^2; \\ \left(\dot{\bar{q}}_4 \times \bar{r}_6\right)^2 = l_5^2 \cdot \dot{q}_4^2; \\ \dot{\bar{q}}_1 \cdot \left(\dot{\bar{q}}_2 \times \bar{r}_4\right) = 0, \ \dot{\bar{q}}_1 \cdot \left(\dot{\bar{q}}_2 \times \bar{r}_6\right) = 0, \ \dot{\bar{q}}_1 \cdot \dot{\bar{q}}_3 = 0, \ \dot{\bar{q}}_1 \cdot \left(\dot{\bar{q}}_4 \times \bar{r}_6\right) = 0, \\ \dot{\bar{q}}_3 \cdot \left(\dot{\bar{q}}_2 \times \bar{r}_4\right) = 0, \\ \left(\dot{\bar{q}}_2 \times \bar{r}_6\right) \cdot \left(\dot{\bar{q}}_4 \times \bar{r}_6\right) = 0, \ \dot{\bar{q}}_3 \cdot \left(\dot{\bar{q}}_4 \times \bar{r}_6\right) = 0,$$

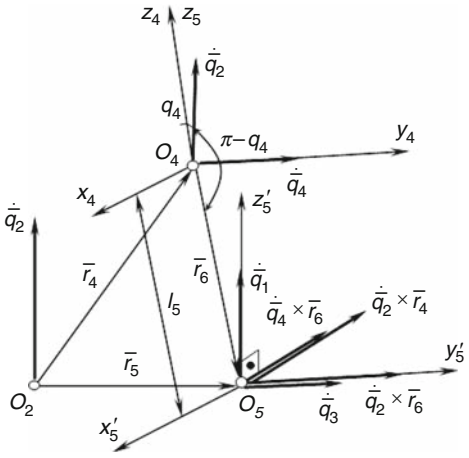

Fig. 4 The velocity of O_5 point

the respective vectors being perpendicular;

$$\left(\dot{\bar{q}}_2 \times \bar{r}_5\right) \cdot \dot{\bar{q}}_3 = \dot{q}_2 \cdot \dot{q}_3 \cdot l_5 \cdot sq_4;$$
$$\left(\dot{\bar{q}}_2 \times \bar{r}_5\right) \cdot \left(\dot{\bar{q}}_4 \times \bar{r}_6\right) = l_5 \cdot (l_3 + l_4 + q_3) \cdot \dot{q}_2 \cdot \dot{q}_4.$$

Analyzing the Fig. 5 and the second relation (14), the projections of the absolute angular velocity $\bar{\omega}_5$ are obtained, on the axis of the reference Cartesian frame $O_5x_5y_5z_5$ and they are:

$$\begin{aligned} \omega_{x_5} &= \dot{q}_4 \cdot sq_5 - \dot{q}_2 \cdot sq_4 \cdot cq_5 \\ \omega_{y_5} &= \dot{q}_4 \cdot cq_5 + \dot{q}_2 \cdot sq_4 \cdot sq_5 \\ \omega_{z_5} &= \dot{q}_2 \cdot cq_4 - \dot{q}_5. \end{aligned} \tag{16}$$

Introducing (15) and (16) into (4), the kinetic energy of the module 5 is obtained, having the expression:

$$\begin{aligned} E_{c_5} = {} & \frac{1}{2} m_5 \cdot \dot{q}_1^2 + \frac{1}{2}\left\{ m_5 \left[(l_3 + l_4 + q_3)^2 + l_5^2 \cdot s^2 q_4 \right] + J_{x_5}^{(5)} s^2 q_4 \cdot c^2 q_5 + \right. \\ & \left. + J_{y_5}^{(5)} s^2 q_4 \cdot s^2 q_5 + J_{z_5}^{(5)} c^2 q_4 \right\} \dot{q}_2^2 + \frac{1}{2} m_5 \cdot \dot{q}_3^2 + \\ & + \frac{1}{2}\left(m_5 \cdot l_5^2 + J_{x_5}^{(5)} s^2 q_5 + J_{y_5}^{(5)} c^2 q_5 \right) \cdot \dot{q}_4^2 + \frac{1}{2} J_{z_5}^{(5)} \dot{q}_5 + m_5 \cdot l_5 \cdot sq_4 \cdot \dot{q}_2 \cdot \dot{q}_3 \\ & + \left[m_5 \cdot l_5 (l_3 + l_4 + q_3) - J_{x_5}^{(5)} sq_4 \cdot sq_5 + J_{y_5}^{(5)} sq_4 \cdot sq_5 \right] \cdot \dot{q}_2 \cdot \dot{q}_4 \\ & - J_{z_5}^{(5)} cq_4 \cdot \dot{q}_2 \cdot \dot{q}_5. \end{aligned} \tag{17}$$

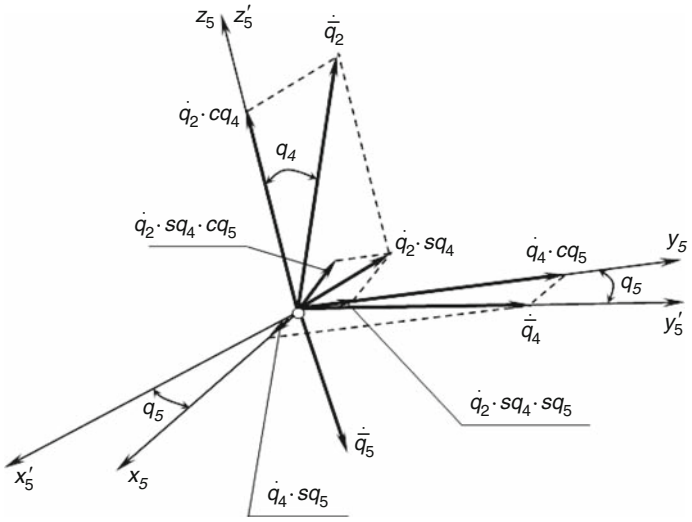

Fig. 5 The determination of the cartesian components of the angular velocity

The kinetic energy of the robot is obtained introducing in (2), the expressions (5), (7), (10), (13), and (17) of the kinetic energies of the robot's module. Thus,

$$\begin{aligned}E_c = &\frac{1}{2}m_1\cdot\dot{q}_1^2+\frac{1}{2}\{J_{\Delta_2}^{(2)}+J_{0_{3_2}}^{(3)}+m_3(l_3+q_3)^2+\left(\sum_{i=1}^{4}m_i\right)\left[(l_3+l_4+q_3)^2+l_5^2\cdot s^2q_4\right]+\\&+J_{x_4}^{(4)}s^2q_4+J_{z_4}^{(4)}c^2q_4+J_{x_5}^{(5)}s^2q_4\cdot c^2q_5+J_{y_5}^{(5)}s^2q_4\cdot s^2q_5+J_{z_5}^{(5)}c^2q_4\}\cdot\dot{q}_2^2+\\&+\frac{1}{2}\left(\sum_{i=3}^{5}m_i\right)\cdot\dot{q}_3^2+\frac{1}{2}[J_{\Delta_4}^{(4)}+m_5\cdot l_5^2+J_{x_5}^{(5)}s^2q_5+J_{y_5}^{(5)}c^2q_5]\cdot\dot{q}_4^2+\\&+\frac{1}{2}J_{z_5}^{(5)}\dot{q}_5+m_5\cdot l_5\cdot sq_4\cdot\dot{q}_2\cdot\dot{q}_3+[m_5\cdot l_5(l_3+l_4+q_3)-\\&-J_{x_5}^{(5)}sq_4\cdot sq_5\cdot cq_5+J_{y_5}^{(5)}sq_4\cdot sq_5\cdot cq_5]\cdot\dot{q}_2\cdot\dot{q}_4-J_{z_5}^{(5)}cq_4\cdot\dot{q}_2\cdot\dot{q}_5.\end{aligned}\tag{18}$$

For a compact writing, the notations (19) are made in the relation (18). Thus, the kinetic energy of the robot is expressed by the equation (20).

$$\begin{aligned}c_{11} = &\frac{1}{2}\left(\sum_{i=1}^{5}m_i\right);\ c_{22}=\frac{1}{2}\{J_{\Delta_2}^{(2)}+J_{0_{3_2}}^{(3)}+m_3\cdot(l_3+q_3)^2\\&+\left(\sum_{i=4}^{(4)}m_i\right)\left[(l_3+l_4+q_3)^2+l_5^2\cdot s^2q_4\right]+\\&+J_{x_4}^{(4)}\cdot s^2q_4+J_{z_4}^{(4)}\cdot c^2q_4+J_{x_5}^{(5)}\cdot s^2q_4\cdot c^2q_5+J_{y_5}^{(5)}\cdot s^2q_4\cdot s^2q_5+J_{z_5}^{(5)}\cdot c^2q_4\};\end{aligned}$$

$$\begin{aligned}c_{33} &= \frac{1}{2}\left(\sum_{i=3}^{5}m_i\right);\\c_{44} &= \frac{1}{2}\left[J_{\Delta_4}^{(4)}+m_5\cdot l_5^2+J_{x_5}^{(5)}\cdot s^2q_5+J_{y_5}^{(5)}\cdot c^2q_5\right];\\c_{55} &= \frac{1}{2}J_{z_5}^{(5)};\ c_{23}=m_5\cdot l_5\cdot sq_4;\\c_{24} &= m_5\cdot l_5\cdot(l_3+l_4+q_3)-J_{x_5}^{(5)}\cdot sq_4\cdot sq_5\cdot cq_4+J_{y_5}^{(5)}\cdot sq_4\cdot sq_5\cdot cq_5;\\c_{25} &= -J_{z_5}^{(5)}\cdot cq_4.\end{aligned}\tag{19}$$

$$\begin{aligned}E_c = &\ c_{11}\cdot\dot{q}_1^2+c_{22}\cdot\dot{q}_2^2+c_{33}\cdot\dot{q}_3^2+c_{44}\cdot\dot{q}_4^2+c_{55}\cdot\dot{q}_5^2+\\&+c_{23}\cdot\dot{q}_2\cdot\dot{q}_3+c_{24}\cdot\dot{q}_2\cdot\dot{q}_4+c_{25}\cdot\dot{q}_2\cdot\dot{q}_5\end{aligned}\tag{20}$$

The first member of the relation (1) contains the derivates of the kinetic energy with respect to the generalised coordinates and velocities, and with respect to the time.

From the relations (19) and (20), the following expressions can be written successively:

$$\frac{\partial E_c}{\partial q_1} = 0, \quad \frac{\partial E_c}{\partial q_2} = 0, \frac{\partial E_c}{\partial q_3} = \frac{\partial c_{22}}{\partial q_3} \cdot \dot{q}_2^2 + \frac{\partial c_{24}}{\partial q_3} \cdot \dot{q}_2 \cdot \dot{q}_4 =$$

$$= \left[m_3 \cdot (l_3 + q_3) + \left(\sum_{i=4}^{5} m_i (l_3 + l_4 + q_3) \right) \right] \cdot \dot{q}_2^2 + m_5 \cdot l_5 \cdot \dot{q}_2 \cdot \dot{q}_4;$$

$$\frac{\partial E_c}{\partial q_4} = \frac{\partial c_{22}}{\partial q_4} \cdot \dot{q}_2^2 + \frac{\partial c_{23}}{\partial q_4} \cdot \dot{q}_2 \cdot \dot{q}_3 + \frac{\partial c_{25}}{\partial q_4} \cdot \dot{q}_2 \cdot \dot{q}_5$$

$$= \left[\left(\sum_{i=4}^{5} m_i \right) \cdot l_5^2 + J_{x_4}^{(4)} - J_{z_4}^{(4)} + J_{x_5}^{(5)} \cdot c^2 q_5 + J_{y_5}^{(5)} \cdot s^2 q_5 - J_{z_5}^{(5)} \right]$$

$$\cdot sq_4 \cdot cq_4 \cdot \dot{q}_2^2 + m_5 \cdot cq_4 \cdot \dot{q}_2 \cdot \dot{q}_3 + J_{z_5}^{(5)} \cdot sq_4 \cdot \dot{q}_2 \cdot \dot{q}_5; \frac{\partial E_c}{\partial q_5}$$

$$= \frac{\partial c_{22}}{\partial q_2} \cdot \dot{q}_2^2 + \frac{\partial c_{44}}{\partial q_5} \cdot \dot{q}_4^2 + \frac{\partial c_{24}}{\partial q_5} \cdot \dot{q}_2 \cdot \dot{q}_4$$

$$= \left[J_{y_5}^{(5)} - J_{x_5}^{(5)} \right] \cdot s^4 q_4 \cdot sq_5 \cdot cq_5 \cdot \dot{q}_2^2 + \left[J_{x_5}^{(5)} - J_{y_5}^{(5)} \right] \cdot sq_5 \cdot cq_5 \cdot \dot{q}_4^2 +$$

$$+ \left[J_{y_5}^{(5)} - J_{x_5}^{(5)} \right] \cdot sq_4 \cdot c2q_5 \cdot \dot{q}_2 \cdot \dot{q}_4;$$

$$\frac{\partial E_c}{\partial \dot{q}_1} = 2 \cdot c_{11} \cdot \dot{q}_1 = \left(\sum_{i=1}^{5} m_i \right) \cdot \dot{q}_1;$$

$$\frac{d}{dt} \left(\frac{\partial E_c}{\partial \dot{q}_1} \right) = \left(\sum_{i=1}^{5} m_i \right) \cdot \ddot{q}_1; \frac{\partial E_c}{\partial \dot{q}_2} = 2 \cdot c_{22} \cdot \dot{q}_2 + c_{23} \cdot \dot{q}_3 + c_{24} \cdot \dot{q}_4 + c_{25} \cdot \dot{q}_5;$$

$$\frac{d}{dt} \left(\frac{\partial E_c}{\partial \dot{q}_2} \right) = 2 \cdot c_{22} \cdot \ddot{q}_2 + c_{23} \cdot \ddot{q}_3 + c_{24} \cdot \ddot{q}_4 + c_{25} \cdot \ddot{q}_5 + 2 \frac{dc_{22}}{dt} \cdot \dot{q}_2$$

$$+ \frac{dc_{23}}{dt} \cdot \dot{q}_3 + \frac{dc_{24}}{dt} \cdot \dot{q}_4 + \frac{dc_{25}}{dt} \cdot \dot{q}_5 = \{ J_{\Delta_2}^{(2)} + J_{0_{3_2}}^{(3)} + m_3 \cdot (l_3 + q_3)^2 +$$

$$+ \left(\sum_{i=4}^{5} m_i \right) \left[(l_3 + l_4 + q_3)^2 + l_5^2 \cdot s^2 q_4 \right] + J_{x_4}^{(4)} \cdot s^2 q_4 + J_{z_4}^{(4)} \cdot c^2 q_4 +$$

$$+ \left[J_{x_5}^{(5)} \cdot c^2 q_5 + J_{y_5}^{(5)} \cdot s^2 q_5 \right] \cdot s^2 q_4 + J_{z_5}^{(5)} \cdot c^2 q_4 \} \cdot \ddot{q}_2 + m_5 \cdot l_5 \cdot sq_4 \cdot \ddot{q}_3$$

$$+ \{ m_5 \cdot l_5 \cdot (l_3 + l_4 + q_3) + \frac{1}{2} \left[J_{x_5}^{(5)} - J_{y_5}^{(5)} \right] \cdot sq_4 \cdot s2q_5 \} \cdot \ddot{q}_4$$

$$- J_{z_5}^{(5)} \cdot cq_4 \cdot \ddot{q}_5 + 2 \left[m_3 \cdot (l_3 + q_3) + \left(\sum_{i=4}^{5} m_i \right) (l_3 + l_4 + q_3) \right] \cdot \dot{q}_2 \cdot \dot{q}_3$$

$$+ \{ l_5^2 \cdot cq_4 + [J_{x_4}^{(4)} - J_{z_4}^{(4)} + J_{x_5}^{(5)} \cdot c^2 q_5 + J_{y_5}^{(5)} \cdot s^2 q_5 - J_{z_5}^{(5)}] \cdot sq_4 \} \cdot \dot{q}_2 \cdot \dot{q}_4$$

$$+ \left[J_{y_5}^{(5)} - J_{x_5}^{(5)} \cdot sq_4 \right] \cdot sq_4 \cdot s2q_5 \cdot \cdot \dot{q}_2 \cdot \dot{q}_5 + m_5 \cdot l_5 \cdot (1 + cq_4) \cdot \dot{q}_3 \cdot \dot{q}_4$$

$$+\frac{1}{2}\left[J_{y_5}^{(5)}-J_{x_5}^{(5)}\right]\cdot cq_4\cdot s2q_5\cdot\dot{q}_4^2$$

$$+\left\{\frac{1}{2}\left[J_{y_5}^{(5)}-J_{x_5}^{(5)}\right]c2q_5+J_{z_5}^{(5)}\right\}\cdot sq_4\cdot\dot{q}_4\cdot\dot{q}_5;$$

$$\frac{\partial E_c}{\partial\dot{q}_4}=2\cdot c_{44}\cdot\dot{q}_4+c_{24}\cdot\dot{q}_2;$$

$$\frac{d}{dt}\left(\frac{\partial E_c}{\partial\dot{q}_4}\right)=2\cdot c_{44}\cdot\ddot{q}_4+c_{24}\cdot\ddot{q}_2+\frac{dc_{24}}{dt}\cdot\dot{q}_2+2\frac{dc_{44}}{dt}\cdot\dot{q}_4$$

$$=[m_5\cdot l_5\cdot(l_3+l_4q_3)+\frac{1}{2}\left(J_{y_5}^{(5)}-J_{x_5}^{(5)}\right)\cdot sq_4\cdot s2q_5]\cdot\ddot{q}_2$$

$$+\left[J_{\Delta_4}^{(4)}+m_5\cdot l_5^2+J_{x_5}^{(5)}\cdot s^2q_5+J_{y_5}^{(5)}\cdot c^2q_5\right]\cdot\ddot{q}_4+m_5\cdot l_5\cdot\dot{q}_2\cdot\dot{q}_3$$

$$+\frac{1}{2}\left(J_{y_5}^{(5)}-J_{x_5}^{(5)}\right)\cdot(cq_4\cdot s2q_5\cdot\dot{q}_2\cdot\dot{q}_4+2sq_4\cdot c2q_5\cdot\dot{q}_2\cdot\dot{q}_5)$$

$$+\frac{1}{2}\left(J_{y_5}^{(5)}-J_{x_5}^{(5)}\right)\cdot s2q_5\cdot\dot{q}_4\cdot\dot{q}_5;$$

$$\frac{\partial E_c}{\partial\dot{q}_5}=2\cdot c_{55}\cdot\dot{q}_5+c_{25}\cdot\dot{q}_2;$$

$$\frac{d}{dt}\left(\frac{\partial E_c}{\partial\dot{q}_5}\right)=c_{25}\cdot\ddot{q}_2+2\cdot c_{55}\cdot\ddot{q}_5+\frac{dc_{25}}{dt}\dot{q}_2$$

$$=-J_{z_5}^{(5)}\cdot cq_4\cdot\ddot{q}_2+J_{z_5}^{(5)}\cdot\ddot{q}_5+J_{z_5}^{(5)}\cdot cq_4\cdot\dot{q}_2\cdot\dot{q}_5 \tag{22}$$

The generalized forces Q_k, $k=1\div 5,$ are obtained by giving virtual displacements so that to vary successively the parameters q_k, respectively with the virtual displacements $\delta q_1,\delta q_2,\delta q_3,\delta q_4,\delta q_5$. According to [2], the generalised forces Q_k are obtained with the relation:

$$Q_k=\frac{\delta L}{\delta q_k},\ k=1\div 5. \tag{23}$$

The virtual elementary mechanical work corresponding to the external generalised forces and moments and to some elementary virtual displacements, has the expression:

$$\delta L=\sum_{i=1}^{n}\bar{F}_i\cdot\delta\bar{r}_i+\sum_{i=1}^{n}\bar{M}_i\cdot\delta\bar{\theta}_i, \tag{24}$$

where, in the case of the robot presented in Fig. 1, it becomes:

$$\begin{aligned}\delta L = {} & (\bar{F}_1 - \bar{P}_1)\cdot\delta q_1 + \bar{P}_2\cdot\delta\bar{r}_2 + (\bar{P}_3 + \bar{F}_3)\cdot\delta q_3 + \bar{P}_4\cdot\delta\bar{r}_4 \\ & + \bar{P}_5\cdot\delta\bar{r}_5 + M_2\delta q_2 + M_4\delta q_4 + M_5\delta q_5.\end{aligned} \tag{25}$$

Considering that:

$$\begin{aligned}&\delta\bar{r}_3 = \delta q_1\cdot\bar{k}_2, \quad \delta\bar{r}_3 = \delta q_1\cdot\bar{k}_2 + \delta q_3\cdot\bar{j}_3,\\ &\delta\bar{r}_4 = \delta q_1\cdot\bar{k}_2 + \delta q_3\cdot\bar{j}_3,\end{aligned}$$

$$\delta\bar{r}_5 = \delta q_1\cdot\bar{k}_2 + \delta q_3\cdot\bar{j}_3,$$

the expression (25) of the virtual elementary mechanical work will be

$$\delta L = \left(F_1 + \sum_{i=1}^{5} P_i\right)\cdot\delta q_1 + M_2\cdot\delta q_2 + F_3\cdot\delta q_3 + M_4\cdot\delta q_4 + M_5\cdot\delta q_5. \tag{26}$$

Dividing successively the relation (26) with $\delta q_1, \delta q_2, \delta q_3, \delta q_4, \delta q_5$, regarding (23), the following generalized forces are obtained:

$$\begin{aligned}&Q_1 = F_1 - \sum_{i=1}^{5} P_i, \quad Q_2 = M_2,\\ &Q_3 = F_3, \quad Q_4 = M_4, \quad Q_5 = M_5.\end{aligned} \tag{27}$$

The dynamic equations of the robot, having in view (1), (21), (22) and (27), are:

$$\left(\sum_{i=1}^{5} m_i\right)\cdot\ddot{q}_1 = F_1 - \sum_{i=1}^{5} P_i$$

$$\begin{aligned}&\{J^{(2)}_{\Delta_2} + J^{(3)}_{0_{3_2}} + m_3\cdot(l_3+q_3)^2 + \left(\sum_{i=4}^{5} m_i\right)\left[(l_3+l_4+q_3)^2 + l_5^2\cdot s^2q_4\right]\\ &\quad + J^{(4)}_{x_4}\cdot s^2q_4 + J^{(4)}_{z_4}\cdot c^2q_4 + \left[J^{(5)}_{x_5}\cdot c^2q_5 + J^{(5)}_{y_5}\cdot s^2q_5\right]\cdot s^2q_4 + J^{(5)}_{z_5}\cdot c^2q_4\}\cdot\ddot{q}_2\\ &\quad + m_5\cdot l_5\cdot sq_4\cdot\ddot{q}_3 + \{m_5\cdot l_5\cdot(l_3+l_4+q_3) +\\ &\quad + \frac{1}{2}\left[J^{(5)}_{x_5} - J^{(5)}_{y_5}\right]\cdot sq_4\cdot s2q_5\}\cdot\ddot{q}_4 - J^{(5)}_{z_5}\cdot cq_4\cdot\ddot{q}_5\\ &\quad + 2\left[m_3\cdot(l_3+q_3) + \left(\sum_{i=4}^{5} m_i\right)(l_3+l_4+q_3)\right]\cdot\dot{q}_2\cdot\dot{q}_3 +\\ &\quad + \{l_5^2\cdot cq_4 + [J^{(4)}_{x_4} - J^{(4)}_{z_4} + J^{(5)}_{x_5}\cdot c^2q_5 + J^{(5)}_{y_5}\cdot s^2q_5 - J^{(5)}_{z_5}]\cdot sq_4\}\cdot\dot{q}_2\cdot\dot{q}_4\end{aligned}$$

$$+\left[J_{y_5}^{(5)}-J_{x_5}^{(5)}\cdot sq_4\right]\cdot sq_4\cdot\cdot s2q_5\cdot\cdot\dot{q}_2\cdot\dot{q}_5+m_5\cdot l_5\cdot(1+cq_4)\cdot\dot{q}_3\cdot\dot{q}_4$$

$$+\frac{1}{2}\left[J_{y_5}^{(5)}-J_{x_5}^{(5)}\right]\cdot cq_4\cdot s2q_5\cdot\dot{q}_4^2+\left\{\frac{1}{2}\left[J_{y_5}^{(5)}-J_{x_5}^{(5)}\right]c2q_5+J_{z_5}^{(5)}\right\}\cdot sq_4\cdot\dot{q}_4\cdot\dot{q}_5$$

$$=M_2\left(\sum_{i=3}^{5}m_i\right)\cdot\ddot{q}_3+m_5\cdot l_5\cdot sq_4\cdot\ddot{q}_2$$

$$-\left[m_3\cdot(l_3+q_3)+\left(\sum_{i=4}^{5}m_i\right)\cdot(l_3+l_4+q_3)\right]\cdot\dot{q}_2^2$$

$$+m_5\cdot l_5\cdot(cq_4-1)\cdot\dot{q}_2\cdot\dot{q}_4=F_3$$

$$\left\{m_5\cdot l_5\cdot(l_3+l_4+q_3)+\frac{1}{2}\left[J_{y_5}^{(5)}-J_{x_5}^{(5)}\right]\cdot sq_4\cdot s2q_5\right\}\cdot\ddot{q}_2$$

$$+\left[J_{\Delta_4}^{(4)}+m_5\cdot l_5^2+J_{x_5}^{(5)}\cdot s^2q_5+J_{y_5}^{(5)}\cdot c^2q_5\right]\cdot\ddot{q}_4$$

$$-\left[\left(\sum_{i=4}^{5}m_i\right)\cdot l_5^2+J_{x_4}^{(4)}-J_{z_4}^{(4)}+J_{x_5}^{(5)}\cdot c^2q_5+J_{y_5}^{(5)}\cdot s^2q_5-J_{z_5}^{(5)}\right]\cdot sq_4\cdot cq_4\cdot\dot{q}_2^2$$

$$+m_5\cdot l_5(1-cq_4)\cdot\dot{q}_2\cdot\dot{q}_3+\frac{1}{2}\left[J_{y_5}^{(5)}-J_{x_5}^{(5)}\right]\cdot cq_4\cdot s2q_5\cdot\dot{q}_2\cdot\dot{q}_4$$

$$+\left\{\left[J_{y_5}^{(5)}-J_{x_5}^{(5)}\right]\cdot c2q_5-J_{z_5}^{(5)}\right\}\cdot sq_4\cdot\dot{q}_2\cdot\dot{q}_5+\frac{1}{2}\left[J_{x_5}^{(5)}-J_{y_5}^{(5)}\right]\cdot s2q_5\cdot\dot{q}_4\cdot\dot{q}_5=M_4 \tag{28}$$

$$-J_{z_5}^{(5)}\cdot cq_4\cdot\ddot{q}_2+J_{z_5}^{(5)}\cdot\ddot{q}_5+\frac{1}{2}\left[J_{x_5}^{(5)}-J_{y_5}^{(5)}\right]\cdot s^2q_4\cdot s2q_5\cdot\dot{q}_2^2$$

$$+\frac{1}{2}\left[J_{y_5}^{(5)}-J_{x_5}^{(5)}\right]\cdot s2q_2\cdot\dot{q}_4^2+\left[J_{x_5}^{(5)}-J_{y_5}^{(5)}\right]\cdot sq_4\cdot c2q_5\cdot\dot{q}_2\cdot\dot{q}_4$$

$$+J_{z_5}^{(5)}\cdot sq_4\cdot\dot{q}_2\cdot\dot{q}_5=M_5.$$

3 Conclusions

The system (28) of differential equations of the robot allows the solving of the two reciprocal fundamental problems of the dynamics of the systems, according to [2] and [4], namely the direct and the inverse problem. In the case of the direct problem the motion of the robot is determined, if the forces and moments which acting to the robot are known. In the case of the inverse problem, the laws of variation of the driving forces and moments are determined, if the motion of the robot is known.

The numerical values for the particular application are:

$$l_1 = 0,5\ [m];\ \ l_2 = 0,5\ [m];\ \ l_3 = 0,1\ [m];\ \ l_4 = 0,6\ [m];\ \ l_5 = 0,2\ [m];$$
$$q_1 = 0,3\ [m];\ \ q_2 = \frac{3\pi}{4}\ [rad];\ \ q_3 = 0,5\ [m];\ \ q_4 = \frac{3\pi}{4}\ [rad];\ \ q_5 = \frac{3\pi}{4}\ [rad];$$
$$m_1 = 60\ [Kg];\ \ m_2 = 30\ [Kg];\ \ m_3 = 50\ [Kg];\ \ m_4 = 5\ [Kg];\ \ m_5 = 12\ [Kg];$$

$$J^2_{\Delta_2} = 0,064\ \left[Kg \cdot m^2\right];\ J^{(3)}_{0_{3_2}} = 0,075\ \left[Kg \cdot m^2\right];\ J^{(4)}_{x_4} = 0,002\ \left[Kg \cdot m^2\right];$$
$$J^{(4)}_{z_4} = 0,003\ \left[Kg \cdot m^2\right];\ J^{(5)}_{x_5} = 0,0025\ \left[Kg \cdot m^2\right];\ J^{(5)}_{y_5} = 0,0028\ \left[Kg \cdot m^2\right];$$
$$J^{(5)}_{z_5} = 0,01\ \left[Kg \cdot m^2\right];\ J^4_{\Delta_4} = 0,02\ \left[Kg \cdot m^2\right];\ \dot{q}_1 = 0,1\ \left[{}^{m}/_{s}\right];\ \dot{q}_2 = 0,785\ \left[{}^{rad}/_{s}\right];$$
$$\dot{q}_3 = 0,1\ \left[{}^{m}/_{s}\right];\ \dot{q}_4 = 0,785\ \left[{}^{rad}/_{s}\right];\ \dot{q}_5 = 0,785\ \left[{}^{rad}/_{s}\right];\ \ddot{q}_1 = 0,2\ \left[{}^{m}/_{s^2}\right];$$
$$\ddot{q}_2 = 1,33\ \left[{}^{rad}/_{s^2}\right];\ \ddot{q}_3 = 0,2\ \left[{}^{m}/_{s^2}\right];\ \ddot{q}_4 = 1,33\ \left[{}^{rad}/_{s^2}\right];\ \ddot{q}_5 = 1,33\ \left[{}^{rad}/_{s^2}\right].$$

Replacing the numerical values in the set of equation (28), the following values are obtained:

$$F_1 = 31,4\ [N];\ M_2 = 25,27\ [Nm];$$
$$F_3 = -22,31\ [N];\ M_4 = 1,56\ [Nm];$$
$$M_5 = 0,027\ [Nm].$$

References

1. Ispas, V.: Manipulatoare şi roboţi industriali, Editura Didactică şi Pedagogică, Bucureşti (2004)
2. Schilling, I.R.: Fundamentals of robotics analysis and control. Prentice-Hall, Englewood Cliffs, NJ (1990)
3. Voinea, R., Voiculescu, D., Ceauşu, V.: Mecanica. Editura Didactică şi Pedagogică, Bucureşti (1983)
4. Vukobratovic, M., Potkonjak, V.: Dynamics of manipulation robots. Scientific fundamentals of robotics 1. Springer-Verlag, Berlin-Heidelberg/New York (1982)

Contributions to the Palletization of Auto Batteries Using the Finite Displacements Theory

V. Ispas, l.C. Mic, R.M. Gui, and A.C. Horvat

Abstract After identifying the places in which the palletization of auto batteries from S.C. ROMBAT S.A. Bistrita can be done, the structural kinematic scheme of the articulated robot IGM RT 330.1/370.1 (which can be found in S.C. ROMBAT S.A.) was developed. Forwards, by using the finite displacements theory of a rigid solid, the paper presents an algorithm of calculation in order to establish the relations of dependency between the initial and the final positions of the batteries and the constructive parameters of the robot. The algorithm of calculation has a matrix form that is suitable for computer implementation.

Keywords Finite displacement · Industrial robot · Matrix

1 Introduction

The matrix relations for transforming the coordinates and the finite displacements theory can be applied in the geometric and kinematic study of industrial robots. The matrix approach of this study leads to algorithms easy to program.

The determination of the geometric and kinematic parameters is made so that the manipulated object reaches from an initial position to a final position. It is known that a body, free in space, is defined by six independent parameters that can be chosen in different ways. According to the Michel Chasles theorem, presented in [4] and [5], the most general finite displacement of a rigid body, from an initial position to a final position, is equivalent to a translation together with a simultaneous rotation about an axis parallel to the translation. This axis is called the rototranslation axis of movement. The mathematical expression of this movement is shown by matrix

V. Ispas (✉)
Department of Applied Mechanics and Computer Programming, Technical University of Cluj-Napoca, Cluj-Napoca, Romania

I. Vişa (ed.), *SYROM 2009*,
DOI 10.1007/978-90-481-3522-6_25,

relations that contain the screw matrix [S] = [r_0:C], with it's translation [T] and rotation [R] components.

2 Relations of Dependency Between the Initial and the Final Position of Auto Batteries and the Kinematic Parameters of the Robot that Manipulate Them

Forward is presented a computing example for the study of the positions occupied by the objects manipulated by the articulated robot IGM RT330 (Fig. 1.). Thus, the Fig. 2 presents the kinematic scheme of the robot with five degrees of freedom. The five independent motions of the robot are rotations because the robot has five revolute joints.

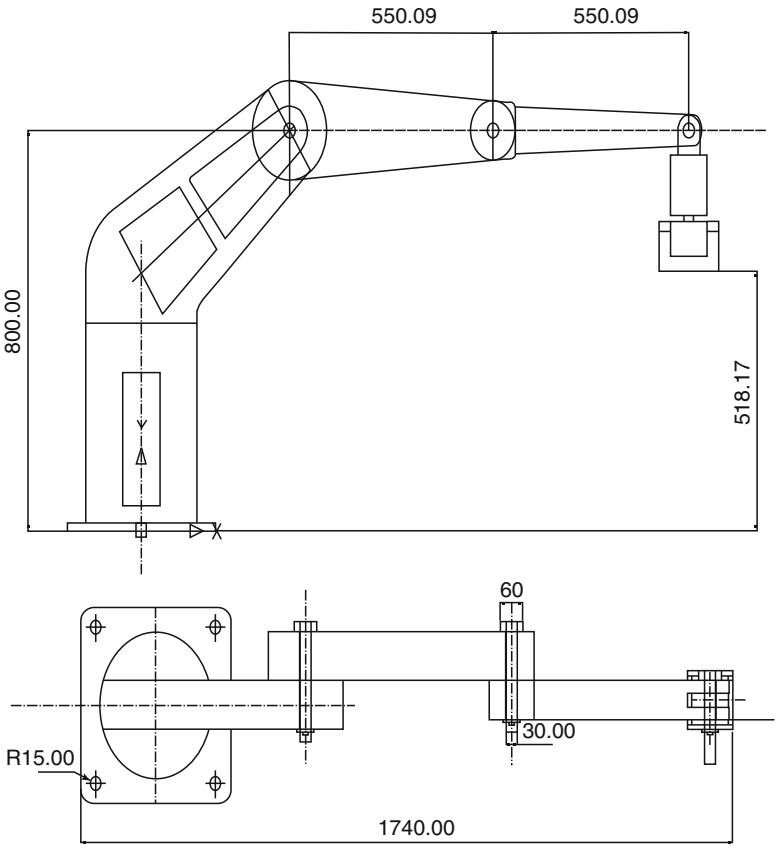

Fig. 1 The articulated robot IGM RT330

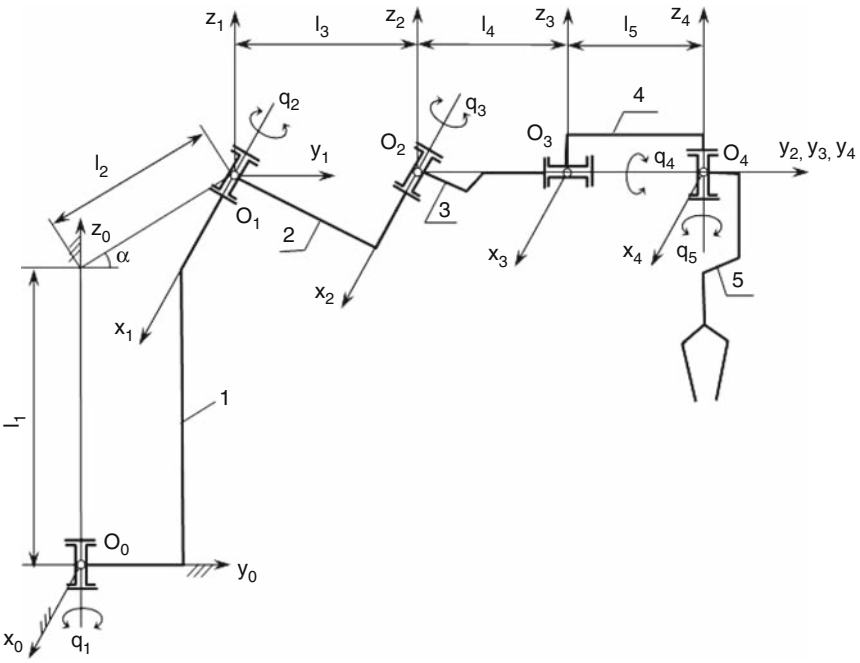

Fig. 2 The kinematic scheme of the robot

In the center of gravity of each kinematic joint, one Cartesian system of coordinates can be found, as it follows:

- in O_0 – the fixed frame $O_0x_0y_0z_0$, from the base of the robot, which has the O_0z_0 axis collinear with the rotation axis of the joint; the moving element of the rotation module from the base of the robot rotates around this axis;
- in O_1 – the mobile frame $O_1x_1y_1z_1$, parallel to $O_0x_0y_0z_0$; the O_1x_1 axis is along the rotation axis of the main arm 2. The position of the point O_1 is determined by the constructive parameters l_1, l_2 and α;
- in O_2 – the mobile frame $O_2x_2y_2z_2$, parallel to $O_1x_1y_1z_1$; the O_2x_2 axis is along the rotation axis of the secondary arm 3. The origin point of the frame is at l_3 distance from O_1;
- in O_3 – the mobile frame $O_3x_3y_3z_3$ is parallel to $O_2x_2y_2z_2$ and has the O_3x_3 axis along the rotation axis of element 4. The point O_3 is at distance l_4 from point O_2;
- in O_4 – the frame $O_4x_4y_4z_4$ is attached to the end-effector 5 and it is parallel to $O_3x_3y_3z_3$. The O_4x_4 axis is overlapped with the rotation axis of the end-effector. The position of the origin point O_4 is defined by the distance l_5.

The constructive parameters of the robot are l_i, $i = 1 \div 5$, α, and the geometrical parameters of movement are the generalized coordinates q_k, $k = 1 \div 5$.

Having the initial position of the auto battery, which is hold on by the gripper, by means of tree non-collinear points of the manipulated object, $x_1(i)_4$, $y_1(i)_4$, $z_1(i)_4$,

registered in the mobile frame $O_4x_4y_4z_4$, it is required to determine the coordinates $x_2(i)_0$, $y_2(i)_0$, $z_2(i)_0$, i = 1, 2, 3, of the three points in the final position. This problem can be solved only if the constructive and the kinematic parameters of the robot are known.

The manipulated object is a specific type of auto battery manufactured by S.C. ROMBAT S.A. Bistriţa. The batteries are transported on a band conveyor to the working place of the robot where they are loaded on a stock pallet.

According to [1], by applying gradually the matrix transfer relations from one frame to another and the finite displacements theory, the final position of the auto battery on the stock pallet is obtained. The final position results from a matrix relation between the initial and the final position of the battery manipulated by the robot.

To apply the finite displacements theory it is necessary to record the two positions of the manipulated object in the same frame. This thing can be done by using matrix relations which transform the points coordinates from one system to another.

From Fig. 2 it can be seen that the final position of the battery on the stock pallet can be obtained by applying gradually, from the end-effector to the base of the robot, the finite displacements theory and the matrix relations for transforming the coordinates.

Therefore, according to [2] and [3], by applying the computing algorithm from the inverse problem of finite displacements we obtain the coordinates, $x_2(i)_4$, $y_2(i)_4$, $z_2(i)_4$, of the points P(i), (i = 1, 2, 3) that belong to the battery after it was rotated around O_4z_4 axis with the angle q_5. Taking into account that the subscript 1 refers to the initial position and the subscript 2 refers to the final position, the following matrix relations can be written:

$$[r_2(i)]_4 = [R]_4 \cdot [r_1(i)]_4, i = 1, 2, 3, \tag{1}$$

where

$$[r_1(i)]_4 = \begin{bmatrix} 1 \\ x_1(i)_4 \\ y_1(i)_4 \\ z_1(i)_4 \end{bmatrix}, i = 1,\ 2,\ 3, \tag{2}$$

$$[r_2(i)]_4 = \begin{bmatrix} 1 \\ x_2(i)_4 \\ y_2(i)_4 \\ z_2(i)_4 \end{bmatrix}, i = 1,\ 2,\ 3, \tag{3}$$

represents the column matrix of the points coordinates P_i, in the initial and the final position, registered in the frame $O_4x_4y_4z_4$, and

$$[R]_4 = \begin{bmatrix} 1 & 0 & 0 & 0 \\ 0 & cq_5 & -sq_5 & 0 \\ 0 & sq_5 & cq_5 & 0 \\ 0 & 0 & 0 & 1 \end{bmatrix} \tag{4}$$

is the rotation matrix (the rotation axis is O_4z_4). In relation (4) sq_5 means $sin\ q_5$ and cq_5 means $cos\ q_5$.

Following the kinematic chain (Fig. 2.) from the end-effector to the base of the robot, the rotation motion around the $O_3x_3y_3z_3$ axis (defined by the parameter q_4) will take place, after, previously, the battery position was registered with respect to the frame $O_3x_3y_3z_3$. Therefore,

$$[r_1(i)]_3 = [r_0 \vdots C]_{34} \cdot [r_2(i)]_4, i = 1, 2, 3 \tag{5}$$

$$[r_2(i)]_3 = [R]_3 \cdot [r_1(i)]_3, i = 1, 2, 3 \tag{6}$$

relations in which

$$[r_1(i)]_3 = \begin{bmatrix} 1 \\ x_1(i)_3 \\ y_1(i)_3 \\ z_1(i)_3 \end{bmatrix}, i = 1, 2, 3, \tag{7}$$

$$[r_2(i)]_3 = \begin{bmatrix} 1 \\ x_2(i)_3 \\ y_2(i)_3 \\ z_2(i)_3 \end{bmatrix}, i = 1, 2, 3 \tag{8}$$

represent the column matrix of the points coordinates P_i, i = 1, 2, 3, belonging to the battery after the rotation with the angle q_5, respectively, after the rotations with q_5 and q_4 registered to the frame $O_3x_3y_3z_3$, while

$$\left[r_0 \vdots C\right]_{34} = \begin{bmatrix} 1 & 0 & 0 & 0 \\ 0 & 1 & 0 & 0 \\ l_5 & 0 & 1 & 0 \\ 0 & 0 & 0 & 1 \end{bmatrix} \tag{9}$$

and

$$[R]_3 = \begin{bmatrix} 1 & 0 & 0 & 0 \\ 0 & cq_4 & 0 & sq_4 \\ 0 & 0 & 1 & 0 \\ 0 & -sq_4 & 0 & cq_4 \end{bmatrix} \tag{10}$$

according to [7], are the matrix for transforming coordinates of points from frame $O_4x_4y_4z_4$ to the frame $O_3x_3y_3z_3$, respectively, the rotation matrix corresponding to the rotation motion of link 4 around O_3y_3 axis.

Thus, the battery position is registered, after the rotation motion characterized by the parameters q_4 and q_5 to the reference system $O_2x_2y_2z_2$ and a rotation motion is performed, around the axis O_2y_2, characterized by the parameter q_3. The mathematical expressions of these are illustrated below:

$$[r_1(i)]_2 = [r_0 \vdots C]_{23} \cdot [r_2(i)]_3, i = 1, 2, 3 \tag{11}$$

$$[r_2(i)]_2 = [R]_2 \cdot [r_1(i)]_2, i = 1, 2, 3 \tag{12}$$

In relations (11) and (12) the matrices:

$$[r_1(i)]_2 = \begin{bmatrix} 1 \\ x_1(i)_2 \\ y_1(i)_2 \\ z_1(i)_2 \end{bmatrix}, i = 1, 2, 3, \tag{13}$$

and

$$[r_2(i)]_2 = \begin{bmatrix} 1 \\ x_2(i)_2 \\ y_2(i)_2 \\ z_2(i)_2 \end{bmatrix}, i = 1, 2, 3, \tag{14}$$

are the column matrices of points coordinates P_i, registered in the frame $O_2x_2y_2z_2$, before and after the rotation motion around O_2x_2 axis, and

$$[r_0 \vdots C]_{23} = \begin{bmatrix} 1 & 0 & 0 & 0 \\ 0 & 1 & 0 & 0 \\ l_4 & 0 & 1 & 0 \\ 0 & 0 & 0 & 1 \end{bmatrix}, \tag{15}$$

$$[R]_2 = \begin{bmatrix} 1 & 0 & 0 & 0 \\ 0 & 0 & 0 & 0 \\ 0 & cq_3 & -sq_3 & 0 \\ 0 & sq_3 & cq_3 & 1 \end{bmatrix}, \tag{16}$$

represent the matrix for transforming the coordinates of points P_i, from the frame $O_3x_3y_3z_3$, according to [8], to the frame $O_2x_2y_2z_2$, respectively, the rotation matrix corresponding to the rotation of third link around O_2x_2 axis.

Carrying on, from Fig. 2, the battery position can be recorded, after making the rotation movements characterized by the parameters q_3, q_4, q_5, to the frame

$O_1x_1y_1z_1$. Afterwards, the rotation of second link around O_1x_1, characterized by the parameter q_2, is performed.

The mathematical expressions of these operations are:

$$[r_1(i)]_1 = [r_0 \vdots C]_{12} \cdot [r_2(i)]_2, i = 1, 2, 3 \tag{17}$$

$$[r_2(i)]_1 = [R]_1 \cdot [r_1(i)]_1, i = 1, 2, 3, \tag{18}$$

in which

$$[r_1(i)]_1 = \begin{bmatrix} 1 \\ x_1(i)_1 \\ y_1(i)_1 \\ z_1(i)_1 \end{bmatrix}, i = 1, 2, 3 \tag{19}$$

and

$$[r_2(i)]_1 = \begin{bmatrix} 1 \\ x_2(i)_1 \\ y_2(i)_1 \\ z_2(i)_1 \end{bmatrix}, i = 1, 2, 3, \tag{20}$$

are the column matrices of points coordinates P_i, registered with respect to the frame $O_1x_1y_1z_1$, before and after the rotation with q_2 around O_1x_1 axis. Also,

$$[r_0 \vdots C]_{12} = \begin{bmatrix} 1 & 0 & 0 & 0 \\ 0 & 1 & 0 & 0 \\ l_3 & 0 & 1 & 0 \\ 0 & 0 & 0 & 1 \end{bmatrix}, \tag{21}$$

$$[R]_1 = \begin{bmatrix} 1 & 0 & 0 & 0 \\ 0 & 0 & 0 & 0 \\ 0 & cq_2 & -sq_2 & 0 \\ 0 & sq_2 & cq_2 & 1 \end{bmatrix}, \tag{22}$$

represent the matrix for transforming the coordinates of points P_i from the frame $O_2x_2y_2z_2$ to $O_1x_1y_1z_1$ and the rotation matrix for the rotation of link 2 around axis O_1x_1.

To reach the final position of the auto battery on the stock pallet, first at all, the position of the battery after making the rotations characterized by the parameters q_3, q_4, q_5 to the frame $O_0x_0y_0z_0$ from the base of the robot is recorded. After that, the link 1 rotates around the vertical axis O_0z_0, the movement being characterized by the parameter q_1. Mathematically, these remarks are expressed in the following relations:

$$[r_1(i)]_0 = [r_0 \dot{:} C]_{01} \cdot [r_2(i)]_1, i = 1, 2, 3 \tag{23}$$

$$[r_2(i)]_0 = [R]_0 \cdot [r_1(i)]_0, i = 1, 2, 3. \tag{24}$$

In this expressions,

$$[r_1(i)]_0 = \begin{bmatrix} 1 \\ x_1(i)_0 \\ y_1(i)_0 \\ z_1(i)_0 \end{bmatrix}, i = 1,\ 2,\ 3, \tag{25}$$

and

$$[r_2(i)]_0 = \begin{bmatrix} 1 \\ x_2(i)_0 \\ y_2(i)_0 \\ z_2(i)_0 \end{bmatrix}, i = 1, 2, 3, \tag{26}$$

are the column matrices of points coordinates P_i, registered in the frame $O_0x_0y_0z_0$, before and after the rotation around the axis O_0z_0, while

$$[r_0 \dot{:} C]_{01} = \begin{bmatrix} 1 & 0 & 0 & 0 \\ 0 & 1 & 0 & 0 \\ l_2 c\alpha & 0 & 1 & 0 \\ l_1 + l_2 s\alpha & 0 & 0 & 1 \end{bmatrix}, \tag{27}$$

and

$$[R]_0 = \begin{bmatrix} 1 & 0 & 0 & 0 \\ 0 & cq_1 & -sq_1 & 0 \\ 0 & sq_1 & cq_1 & 0 \\ 0 & 0 & 0 & 1 \end{bmatrix}, \tag{28}$$

represent the matrix for transforming the coordinates of points P_i from $O_1x_1y_1z_1$ to the frame $O_0x_0y_0z_0$, respectively, the rotation matrix around O_0z_0 axis.

Being given equations (23), (18), (17), (12), (11), (6), (5), (1), the matrix relations (24) will have the next form:

$$[r_2(i)]_0 = [R]_0 \overset{8}{[}\, [r_0 \dot{:} C]_{01} \overset{7}{[}\, [R]_1 \overset{6}{[}\, [r_0 \dot{:} C]_{12} \overset{5}{[}\, [R]_2 \overset{4}{[}\, [r_0 \dot{:} C]_{23} \overset{3}{[}\, [R]_3 \overset{2}{[}\, [r_0 \dot{:} C]_{34} \overset{1}{[}\, [R]_4 [r_1(i)]_4 \overset{1\ 2\ 3\ 4\ 5\ 6\ 7\ 8}{]\ ]\ ]\ ]\ ]\ ]\ ]\ ]}. \tag{29}$$

The final position of the points coordinates registered to the fixed frame $O_0x_0y_0z_0$ from the base of the robot, is obtained from relation (29) in which the matrices from equations (2), (3), (4), (9), (10), (15), (16), (21), (22), (27), (28) are replaced. After doing the calculation and knowing that $[r_2(i)]_0 = \begin{bmatrix} 1 \\ x_2(i)_0 \\ y_2(i)_0 \\ z_2(i)_0 \end{bmatrix}$, $i = 1, 2, 3$, we have the relations for the final points of the auto battery placed on the stock pallet:

$$\begin{aligned} x_2(i)_0 = {} & (sq_1 \cdot sq_2 \cdot cq_3 \cdot cq_4 \cdot cq_5 - sq_1 \cdot sq_2 \cdot sq_3 \cdot sq_5) \cdot x_1(i)_4 \\ & - (sq_1 \cdot sq_2 \cdot sq_5 \cdot cq_3 \cdot cq_4 + sq_1 \cdot sq_2 \cdot sq_3 \cdot cq_5) \cdot y_1(i)_4 \\ & + sq_1 \cdot sq_2 \cdot sq_4 \cdot cq_3 \cdot z_1(i)_4 + l_3 \cdot sq_1 \cdot sq_2 \\ & - l_4 \cdot sq_1 \cdot sq_2 \cdot sq_3 - l_5 \cdot sq_1 \cdot sq_2 \cdot sq_3 - sq_1 \cdot l_2 c\alpha \end{aligned} \tag{30}$$

$$\begin{aligned} y_2(i)_0 = {} & (-sq_2 \cdot cq_1 \cdot cq_3 \cdot cq_4 \cdot cq_5 + sq_2 \cdot sq_3 \cdot sq_5 \cdot cq_1) \cdot x_1(i)_4 \\ & + (sq_2 \cdot sq_5 \cdot cq_1 \cdot cq_3 \cdot cq_4 + sq_2 \cdot sq_3 \cdot cq_1 \cdot cq_5) \cdot y_1(i)_4 \\ & - sq_2 \cdot sq_4 \cdot cq_1 \cdot cq_3 \cdot z_1(i)_4 - l_3 \cdot cq_1 \cdot sq_2 \\ & + l_4 \cdot sq_2 \cdot sq_3 \cdot cq_1 + l_5 \cdot sq_3 \cdot sq_2 \cdot cq_1 + cq_1 \cdot l_2 c\alpha \end{aligned} \tag{31}$$

$$\begin{aligned} z_2(i)_0 = {} & \begin{bmatrix} (cq_2 \cdot cq_3 \cdot cq_4 \cdot cq_5 - cq_2 \cdot sq_3 \cdot sq_5) + \\ + (sq_3 \cdot cq_4 \cdot cq_5 + cq_3 \cdot sq_5 - sq_4 \cdot cq_5) \end{bmatrix}. \\ x_1(i)_4 - {} & \begin{bmatrix} (cq_2 \cdot cq_3 \cdot cq_4 \cdot sq_5 + sq_3 \cdot cq_2 \cdot cq_5) + \\ + (sq_3 \cdot sq_5 \cdot cq_4 - cq_3 \cdot cq_5 - sq_4 \cdot sq_5) \end{bmatrix}. \\ y_1(i)_4 + {} & [(sq_4 \cdot cq_2 \cdot cq_3) + (sq_3 \cdot sq_4 + cq_4)] \cdot z_1(i)_4 + l_3 \cdot cq_2 + \\ & + (cq_3 - cq_2 \cdot sq_3) \cdot l_4 + (cq_3 - sq_3 \cdot cq_2) \cdot l_5 + l_1 + l_2 s\alpha \end{aligned} \tag{32}$$

3 Numerical Application

Imposing the design and kinematic parameters of the robot:

$l_1 = 0.333$ [m], $l_2 = 0.492$ [m], $l_3 = 0.55$ [m],

$l_4 = 0.55$ [m], $l_5 = 0.17$ [m], $\alpha = 35$,

and the values of the coordinates $x_1(i)_4$, $y_1(i)_4$, $z_1(i)_4$, $i = 1, 2, 3$ (Table 1) for the initial position of the battery, registered to the mobile frame $O_4x_4y_4z_4$, by using the expressions (30), (31) and (32), the final position of the auto battery can be found.

The values of the parameters q_k, $k = 1 \div 5$ are given as:

$q_1 = 70°$, $q_2 = 75°$, $q_3 = 30°$, $q_4 = 0°$, $q_5 = 90°$.

Table 1 The initial position of the battery

$P_1(i)_4$			
i	1	2	3
$x_1(i)_4$	1.5875	1.5875	1.4125
$y_1(i)_4$	0.0875	−0.0875	0.0875
$z_1(i)_4$	0.3	0.4	0.4

Table 2 The final position of the battery

$P_2(i)_0$			
i	1	2	3
$x_2(i)_0$	−0.9952	−0.8578	−0.9158
$y_2(i)_0$	0.3623	0.3123	0.3334
$z_2(i)_0$	2.6937	2.9203	2.6648

After doing the calculation, the final points of the auto battery, placed on the stock pallet, were summarized in Table 2.

4 Conclusions

The matrix relations for transforming the coordinates and the finite displacements theory can be applied at the geometric and kinematic study of the industrial robots, carrying on to algorithms easy to program.

Using the inverse problem of the finite displacements theory, this paper presents an application of the study of the positions occupied by the objects manipulated by the articulated robot IGM RT330.1/370.1 with five degrees of freedom.

The calculation procedure shown in this paper can be applied analogously to any kinematic scheme of a robot.

References

1. Khalil, W., Dombre, E.: Modeling, identification and control of robots. Taylor & Francis, Bristol, PA, USA (2002)
2. Ispas, V.: Calculation algorithm for the problem of finite displacements of a solid rigid body. Art in Construction, Manufacturing and Exploitation of Cars Symposium, vol. II, part I, pp. 41–46. Piteşti (1979)
3. Ispas, V.: Contributions to the study of finite displacements of a solid rigid body. Art in Construction, Manufacturing and Exploitation of Cars Symposium, vol. II, part I, pp. 87–92. Piteşti (1979)

4. Ispas V (1990) Kinematic applications in the construction of manipulators and industrial robots. Romanian Academy Press, Bucharest
5. Ispas, V.: Manipulators and industrial robots. E. D. P., Bucharest, RA (2004)
6. Plitea, N.: Study of the finite displacements of a board in plane motion, when are known the positions of a two points of the board. Guide for papers, pp. 90–94. I.P. Cluj-Napoca (1984)
7. Popescu, P.: Mechanics. Kinematics, Lito I.P. Cluj-Napoca (1978)
8. Popescu, P., Ispas, V.: Study of the finite displacements of a solid rigid body. Guide for papers, pp. 95–104. Lito I.P. Cluj-Napoca (1984)

Unconventional Mathematical Model for Complex Mechanical Structures

E. Mereuta, G. Ciubucciu-Ionete, M. Rus, and S. Veresiu

Abstract The paper presents an unconventional mathematical model, originally built to simulate the motion of mechanical structures with rigid bodies, which is now rewritten with different assumptions regarding the deformations of kinematic elements. The steps to be followed are also described, considering a particular mechanical system. Virtual models are created, using programming languages, aiming to enable the proposed mathematical model and to simulate the kinematics of mechanical structure.

Keywords Computer program · Mathematical model · Unconventional model

1 Introduction

The dynamic equations of motion are often used to solve computational dynamics of complex mechanical structure. Many different forms were developed, most of them using elementary Newtonian mechanics [1, 2, 8]. Thus, we can point out: the augmented formulation and the embedding technique [12] which lead to a large number of equations or to sparse matrix structure, often difficult to solve, as more elaborate numerical algorithms are needed.

Another approach widely used for constructing and describing complex mechanical structures is system high level modelling method, which use interdisciplinary models and provide all responses to any external conditions. Due to its complexity, it is often difficult to create the virtual prototypes [13].

E. Mereuta (✉)
GMT Department, Dunarea de Jos University of Galati, Romania

I. Vişa (ed.), *SYROM 2009*,
DOI 10.1007/978-90-481-3522-6_26,

The proposed mathematical model is considered unconventional as it describes the motion in a compact structure, using symbolical notations, based on modern algebra principles consisting of a new approach regarding the correlation: modern algebra – mechanics – mechanisms (introducing a new concept namely dynamical bijection), on an axiomatic system tailor made for iterative mathematical models and on Leapunov's theorem of stability [11].

The direct mathematical models used for describing the mechanical structure motion, provide the state parameters assuming the forces and torques fields [5, 6]. The unconventional direct mathematical model proposed, is an iterative one, based on differential equations. The Cauchy parameters are considered as input data, for position and velocity; the number of such groups is equal to D.O.F. The Cauchy groups are arbitrarily considered, as long as the continuity of the domain of movement is not exceeded [3]. An important criterion to be taken into account refers to Leapunov's stability of motion [4], as the disturbances can be given by an improper choice of input data.

In order to express the mathematical model in a compact structure, the symbolical notations used are in fact the transmitting functions for positions, velocities, accelerations and dynamics [7, 11].

For example: the symbolical equation

$$[1,2,3,4] \rightarrow \left[\mu'_C, \varphi_1^0, \varphi_2^0\right] \rightarrow [C] \rightarrow [A,B,C,D,C_1,C_2,C_3,C_4\varphi_4]^0$$

states that using the input parameters $\left[\mu'_C, \varphi_1^0, \varphi_2^0\right]$, we can determine the configuration [C] and the positions of all characteristic points (including kinematic pairs, centers of gravity etc.).

2 General Structure of Mathematical Models

The general structure of mathematical models for simulation the motion of mechanical structure consists of: constants, input parameters (according to Cauchy's conditions), state parameters on iteration (0) determined using inverse mathematical models, the unconventional mathematical model, the output data (the velocity or acceleration field).

The general structure is shown in Fig. 1, where the symbolic notations are: MS – the mechanical structure, CID – constants and input data, MM – the unconventional mathematical model, OD – the output data [8].

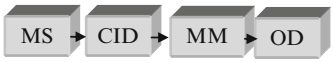

Fig. 1 General structure of mathematical models

3 The Mathematical Model [A ∩ C]

This unconventional mathematical model for simulating the motion of mechanical structures is based on the intersection of the acceleration field with the reactive forces field [6]. In order to illustrate this method, let's consider the mechanical structure shown in Fig. 2, a five-bar linkage with two input motor torques: Mm1 and Mm4.

The mechanical structure is used for lifting the weight $\overline{G}$. We have to analyze the motion of the mechanical structure in order to get a required dependency of the angular velocity of linkage 2 with respect to time variable: $\omega_2 = F(t)$. The mechanical characteristic of the motor torque on element 4 is known: $M_{m4} = M_{m4}(\omega_4)$ [11].

In this case, we assume that only one motor torque has a conditional mechanical characteristic [4], the other one is not controlled.

For the time variable t = 0, the Cauchy-Kovalevskaia's parameters are: $\varphi_1^0, \varphi_2^0, \omega_1^0, \omega_2^0$.

The following symbolic equations are written:

For the positions:

$$\begin{aligned}[1,2,3,4] \rightarrow \left[\mu'_C, \varphi_1^0, \varphi_2^0\right] \rightarrow \\ [C] \rightarrow [A,B,C,D,C_1,C_2,C_3,C_4\varphi_4]^0\end{aligned} \tag{1}$$

For the velocity field:

$$\begin{aligned}[1,2,3,4] \rightarrow \left[\omega_1^0, \omega_2^0\right] \rightarrow [v] \\ \rightarrow [\omega_3, \omega_4, \overline{v_A}, \overline{v_B}, \overline{v_C}, \overline{v_D}]^0\end{aligned} \tag{2}$$

The [A∩C] mathematical model develops as follows:

$$\begin{aligned}\overline{\varepsilon_{1,l}} \times \overline{OA} - \omega_1^2 \cdot \overline{OA} + \overline{\varepsilon_2} \times \overline{AB} \\ -\omega_2^2 \cdot \overline{AB} + \overline{\varepsilon_{3,l}} \times \overline{BD} - \omega_3^2 \cdot \overline{BD} \\ +\overline{\varepsilon_{4,l}} \times \overline{DE} - \omega_4^2 \cdot \overline{DE} = 0\end{aligned} \tag{3}$$

- The accelerations field and the inertia field are expressed literally.
- The equations for the counteracting forces are written as follows.

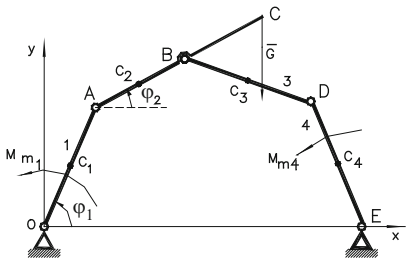

Fig. 2 Five-bar linkage

$$\begin{gathered}\left(1-\sum \overline{F}=\overline{0}\cap 1-\sum M_0=0\right)\cap \\ \left(2-\sum \overline{F}=\overline{0}\cap 2-\sum M_A=0\right)\cap \\ \left(3-\sum \overline{F}=\overline{0}\cap 3-\sum M_B=0\right) \\ \left(4-\sum \overline{F}=\overline{0}\cap 4-\sum M_D=0\right)\end{gathered} \tag{4}$$

The total number of equations is 14, the undetermined parameters are:

$$\left[\varepsilon_1,\varepsilon_3,\varepsilon_4,\overline{F_{01}},\overline{F_{21}},\overline{F_{32}},\overline{F_{43}},\overline{F_{04}},M_{m1}\right]^0 \tag{5}$$

The input values for next iterations are the velocities, obtained from the following equations:

$$\begin{gathered}\varphi_1^1=\varphi_1^0+\omega_1^0\cdot\Delta t;\varphi_2^1=\varphi_2^0+\omega_2^0\cdot\Delta t \\ \omega_1^1=\omega_1^0+\varepsilon_1^0\cdot\Delta t;\omega_2^1=\omega_2^0+\varepsilon_2^0\cdot\Delta t\end{gathered} \tag{6}$$

We can now get the M_{m1}^i time variation $M_{m1}(t)$, or angular velocity variation $M_{m1}(\omega_1)$, or position variation $M_{m1}(\varphi_1)$.

Considering the mechanical structure shown in Fig. 3, also a five-bar linkage, but now the kinematic linkage is undetermined [6], due to the fact that the input torque M_{m4} is missing. In order to get the stability of motion [4] the spring R was added (the possibilities if motion are now limited).

We include the output motor torque M_{u4}, among the input data and we assume it to be constant: $M_{u4}=-k,\ k>0$.

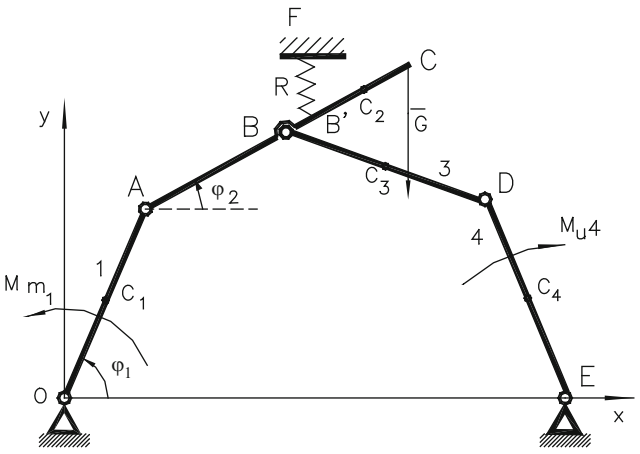

Fig. 3 The undetermined five-bar linkage

Now, the symbolical equations are:

$$[1,2,3,4] \rightarrow \left[\mu'_C, \varphi_1^0, \varphi_2^0\right] \rightarrow [C] \rightarrow \left[A, B, C, D, C_1, C_2, C_3, C_4, \overline{R}\right]^0 \tag{7}$$

$$[1,2,3,4] \rightarrow \left[\omega_1^0, \omega_2^0\right] \rightarrow [v] \rightarrow \left[\omega_3, \omega_4, \overline{v_A}, \overline{v_B}, \overline{v_C}, \overline{v_D}\right]^0 \tag{8}$$

$$[1,2,3,4] \rightarrow \left[\varepsilon_{1,l}^0, \varepsilon_2^0\right] \rightarrow \cap \rightarrow [1,2,3,4,0] \rightarrow \left[M_{u4}, \overline{G}, M_{m1,l}, \tau\left(\overline{F}_{ip}\right), \overline{R}, p = 1,2,3,4\right] \rightarrow \rightarrow \left[p - \sum \overline{F} = 0, p - \sum M_k = 0, p = 1...5\right] \rightarrow \left[M_{m1}, \varepsilon_1, \varepsilon_3, \varepsilon_4, \overline{F}_{01}, \overline{F}_{12}, \overline{F}_{23}, \overline{F}_{34}, \overline{F}_{04}\right]^0 \tag{9}$$

Another example of mechanical structure which is analyzed using the proposed mathematical model is the crank – connecting rod assembly (Fig. 4), with significant stability of motion, actuated by an asynchronous electrical engine [11]. In order to determine the state variables and to simulate the motion on computer, the following input data are assumed:

- The mechanical characteristics of the kinematic elements (lengths, masses, inertia moments etc.).
- The fixed kinematic pairs.
- The input independent parameters: φ_1, ω_1 (according to Cauchy-Kovalevskaia theorem).
- The mechanical characteristic of the engine: $M_m = M_m(\omega_1)$.
- The actual load $\overline{F_u} = \overline{F_u}(t, s_3, \dot{s}_3)$.
- The friction torques is assumed to be insignificant to the applied forces torque.
- The time increment Δt.

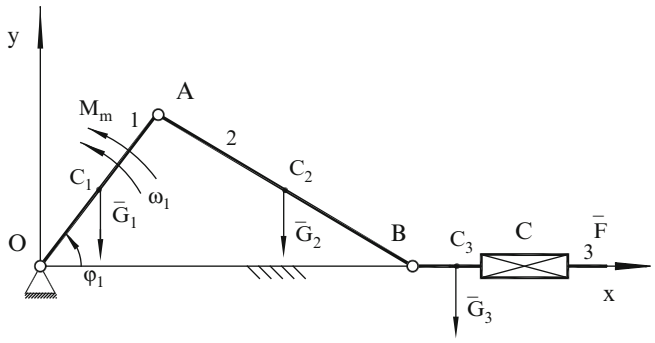

Fig. 4 The crank – connecting rod assembly

For this mechanical structure, we can write nine dynamic equilibrium equations (three for each kinematic element), with nine unknown variables (two components for each reactive force in kinematic pairs and the angular acceleration of input crank ε_1).

To solve the nine-equation system, the following steps are to be followed:

Iteration 0 (i)

The equations for positions are written symbolically [7], as follows:

$$\begin{aligned}(0,\varphi_1,A) &\Rightarrow A\\ (A,B)\cap(y_B=0) &\Rightarrow B\\ (0,\varphi_1,C_1) &\Rightarrow C_1\\ (A,C_2)\cap(B,C_2) &\Rightarrow C_2\\ (B,C_3)\cap(C,C_3) &\Rightarrow C_3\end{aligned} \tag{10}$$

The symbolic equations for velocity field are:

$$\begin{aligned}(v_O=0,\omega_1,v_A) &\Rightarrow \overline{v_A}\\ (v_A,\omega_2,v_B)\cap\left(v_{By}=0\right) &\Rightarrow \omega_2, v_{Bx}\end{aligned} \tag{11}$$

$$\begin{aligned}2-\sum\overline{F}=\overline{0} \Leftrightarrow -\overline{F_{21}}&\\ +\overline{F_{i2}}+\overline{G_2}+\overline{F_{32}}=\overline{0}&\end{aligned} \tag{12}$$

$$\begin{aligned}3-\sum\overline{F}=\overline{0} \Leftrightarrow -\overline{F_{32}}+\overline{F_{i3}}+\overline{G_3}&\\ +\overline{F_{03}}+\overline{F_u}=\overline{0}&\end{aligned} \tag{13}$$

$$\begin{aligned}1-\sum M_O=0 \Leftrightarrow \overline{OA}\times\overline{F_{21}}+\overline{OC_1}&\\ \times\left(\overline{F_{i1}}+\overline{G_1}\right)+\overline{M_m}+\overline{M_{i1}}=\overline{0}&\end{aligned} \tag{14}$$

$$\begin{aligned}2-\sum\overline{M_B}=\overline{0} \Leftrightarrow -\overline{BA}\times\overline{F_{21}}+\overline{BC_2}&\\ \times\left(\overline{F_{i2}}+\overline{G_2}\right)+\overline{M_{i2}}=\overline{0}&\end{aligned} \tag{15}$$

$$\begin{aligned}3-\sum\overline{M_B}=\overline{0} \Leftrightarrow \overline{BC}\times\overline{F_{03}}&\\ +\overline{BC_3}\times\overline{G_3}+\overline{M_{03}}=\overline{0}&\end{aligned} \tag{16}$$

The unknown variables are:

$$\overline{F_{21}},\overline{F_{32}},M_{03},F_{03y},\varepsilon_1.$$

As for the angular acceleration ε_1, we can consider it as an implicit one, being included in inertia torques.

The dependencies can be revealed if the angular acceleration of element 2 (ε_2) is expressed as a function of angular velocity ε_1:

$$(a_A, \varepsilon_2, a_B) \cap \left(a_{By} = 0\right) \Rightarrow \varepsilon_2 = f(\varepsilon_1) \tag{17}$$

$$\varepsilon_2 = \frac{1}{AB_x}(\omega_1^2 OA_y + \omega_2^2 AB_y - \varepsilon_1 OA_x) \tag{18}$$

The inertia torques of mobile elements can be also expressed as functions of angular acceleration ε_1, as follows:

$$\begin{cases} \overline{F_{i1}} = -m_1 \cdot \overline{a_{C1}} = \overline{f_1}(\varepsilon_1) \\ M_{i1} = -\varepsilon_1 \cdot J_{C1} = f_2(\varepsilon_1) \end{cases} \tag{19}$$

$$\begin{cases} \overline{F_{i2}} = -m_2 \cdot \overline{a_{C2}} = \overline{f_3}(\varepsilon_1) \\ M_{i2} = -\varepsilon_2 \cdot J_{C2} = f_4(\varepsilon_1) \end{cases} \tag{20}$$

$$\begin{cases} \overline{F_{i3}} = -m_3 \cdot \overline{a_{C3}} = \overline{f_5}(\varepsilon_1) \\ M_{i3} = -\varepsilon_3 \cdot J_{C3} = 0 \end{cases} \tag{21}$$

Iteration 1 (i + 1)

In order induce the next iteration, Eq. (22) are used, considering a suitable value for the time increment Δt, according to the desired accuracy [7].

$$\begin{aligned} \omega_1^{1(i+1)} &= \omega_1^{0(i)} + \varepsilon_1^{0(i)} \cdot \Delta t \\ \varphi_1^{1(i+1)} &= \varphi_1^{0(i)} + \omega_1^{0(i)} \cdot \Delta t \end{aligned} \tag{22}$$

These are the new input data for iteration (1) or (i + 1). The angular acceleration ε_1^i is the variable that allows the building-up transient process.

4 Numerical Example

In order to illustrate the mathematical model described above, a computer programme was developed, tailor made for the mechanical structure shown in Fig. 2, considering the following input data:

$$\begin{aligned} l_1 &= 0.3m; l_2 = 0.46m; l_3 = 0.4m; \\ l_4 &= 0.51m; l_5 = 1m; \\ m_1 &= 2kg; m_2 = 3.06kg; \\ m_3 &= 2.7kg; m_4 = 3.4kg \\ \varphi_1 &= 108^0; \varphi_4 = 126^0; \\ \omega_1 &= 10s^{-1}; \omega_4 = 10s^{-1} \end{aligned}$$

The time dependencies of angular accelerations, of angular velocities and positions parameters for both linkages 1 and 4 results are shown in Fig. 5 .

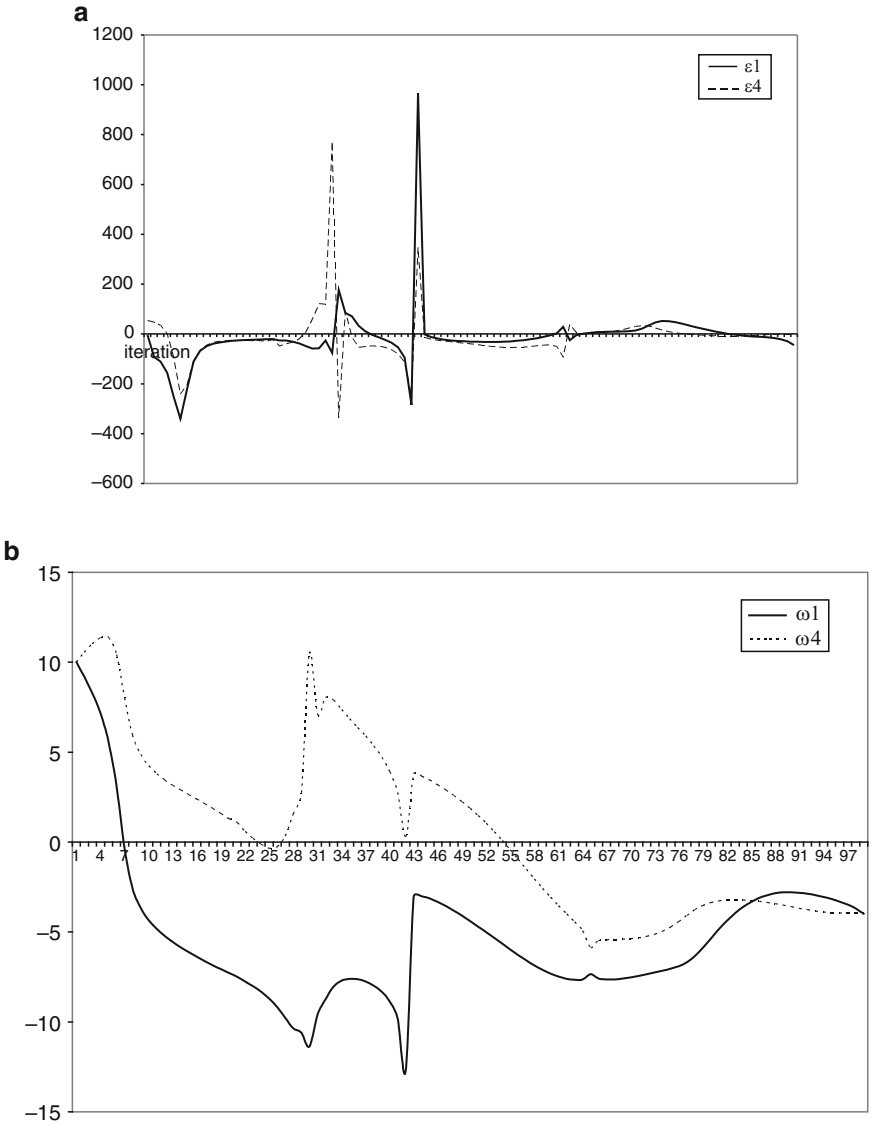

Fig. 5 (Continued)

5 Unconventional Mathematical Model for Deformable Elements

In order to extend the proposed algorithm to flexible mechanical structure, we can rewrite the symbolic equations, assuming that only the input linkage is deformable, along its axis.

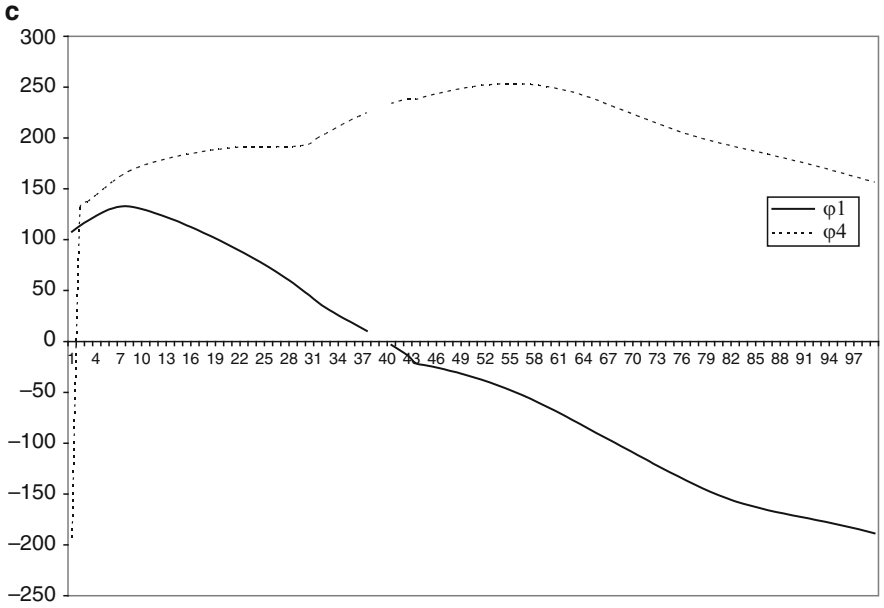

Fig. 5 (**a**) Time fluctuation for angular acceleration. (**b**) Time fluctuation for angular velocity. (**c**) Time fluctuation for angular parameters

As the algorithm provides the reactive forces for each step, we can determine the lengthening, as follows:

$$\Delta l = \frac{F \cdot l}{E \cdot A} \tag{23}$$

where F is the axial force on linkage 1.

$$\overline{F} = F_{21x} \cdot \cos \varphi_1 + F_{21y} \cdot \sin \varphi_1 \tag{24}$$

The computer programme is augmented with supplementary instructions, which modify the length of linkage, after each iteration.

$$l_1^{i+1} = l_1^i + \Delta l_1^i \tag{25}$$

The comparative results are shown in Fig. 6, where the kinematic parameters for the deformable mechanical structure are noted with *.

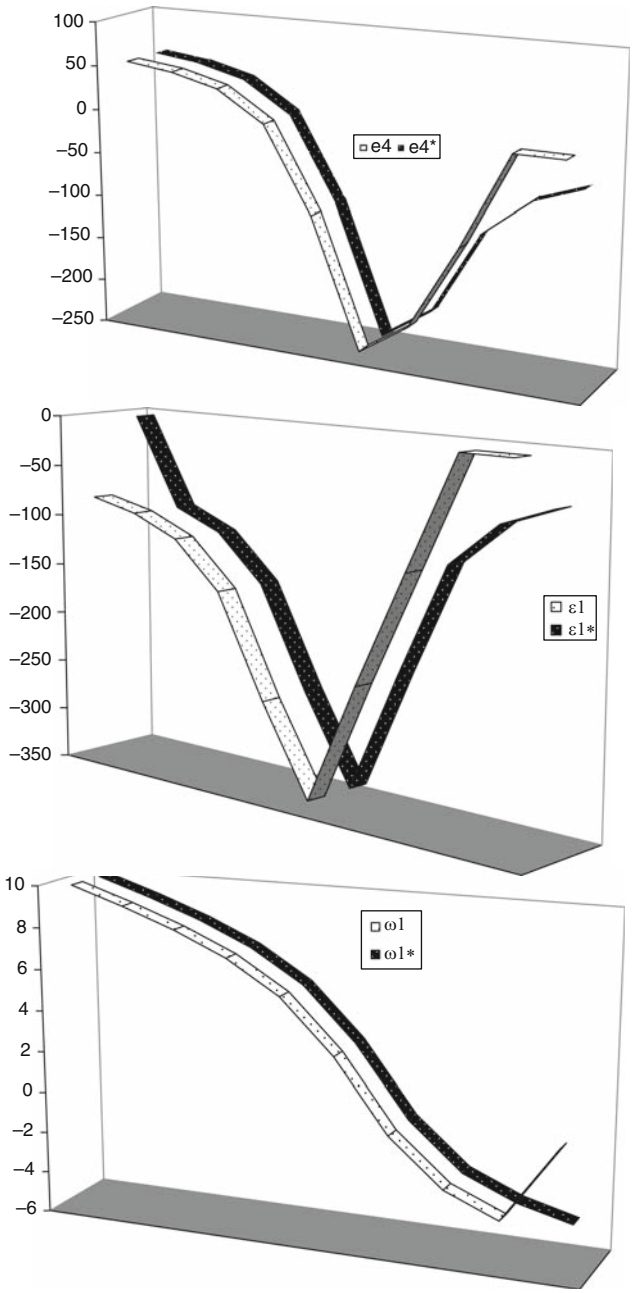

Fig. 6 Comparative diagrams for kinematic parameters

6 Conclusions

The mathematical model proposed is based on an axiomatic system [4] which allows extending its assumptions to both undetermined mechanical structures and flexible ones [9, 10].

The algorithm can be also extended to a more complex situation, when all the linkages are considered deformable, as the mathematical model provides all the reactive forces.

We can also take into account the frictions in rotational joint, which are neglected in this paper.

Further papers will reveal the influence of friction and flexibility of all linkages.

References

1. Featherstone, R.: Rigid body dynamics algorithms. Springer Science Business Media, LLC, The Australian National University, Canberra, ACT, Australia (2008)
2. Hibbeler, R.C.: Engineering mechanics – dynamics, 11th edn. Prentice-Hall, NJ (2006)
3. Mereuta, E.: Abstract Algebra structures regarding the mathematical models for kinematic chains, pp. 51–54. In: The Annals of "Dunărea de Jos" University, Fascicle X Applied Mechanics (1999). ISSN 1221–4612
4. Mereuta, E.: Mechanical system stability related to the axiomatic system proposed, pp. 47–50. In: The Annals of "Dunărea de Jos" University, Fascicle X Applied Mechanics (1999). ISSN 1221–4612
5. Mereuta, E., Chirica, R.: Mathematical models for stimulating the determined mechanical structures motion, pp. 15–18. In: The Annals of "Dunarea de Jos" University of Galati, Fascicle X – Applied Mechanics (2000). ISSN 1221–4612
6. Mereuta, E.: Unconventional algorithm analysis of output kinematic element motion, pp. 47–52. In: The Annals of "Dunarea De Jos" University of Galati, Fascicle X Applied Mechanics (2004). ISSN 1221–4612
7. Mereuta, E.: Equivalence mathematical relationships in the analysis of complex mechanical structures, pp. 13–16. In: The Annals of "Dunarea De Jos" University Of Galati, Fascicle X Applied Mechanics (2006). ISSN 1221–4612
8. Meriam JL, Kraige LG (2006) Engineering Mechanics: Dynamics, 6th edn. Wiley, New York
9. Oranescu, A., Mereuta, E., Stroe, S.: New principles on the equivalence classes of the topologies of rigid multibody systems. In: Huang, T. (ed.) Proceedings of the 11th World Congress in Mechanism and Machine Science, pp. 999–1003. China Machinery Press, Tianjin, China. ISBN7-89492-107-6/TH-14
10. Oranescu, A., Mereuta, E., Bejenaru, S., Rus, M.: Sur la dynamique des structures mécaniques mobiles. The 12th IFToMM World Congress. Besançon, France, 18–21 June 2007
11. Oranescu, A.: Prioritatile patrimoniului stiintific ale scolii de mecanisme din Galati. Galati University Press, Galati (2008)
12. Shabana, A.: Computational Dynamics, 2nd edn., p. 188. Wiley-Interscience, New York (2001)
13. Wang, P.B., Li, B.H., Chai, X., Yanqiang, D.: Research on high level modeling method for complex simulation system. In: Systems Modeling and Simulation, Theory and Applications, Asia Simulation Conference, p. 93. Springer (2006)

On the Power Losses of Cylindrical and Bevel Gears Used in Wind Turbines and Tracking Systems for Photovoltaic Platforms

Gh. Moldovean, B.R. Butuc, and C.A. Bozan

Abstract Wind turbines and tracking systems for photovoltaic platforms have as component parts cylindrical and bevel gears. The electrical energy quantity given by these systems can be improved through minimizing running power losses. By means of a computing program has been analyzed the influence of the main geometrical parameters of external and internal cylindrical gears and bevel gears used for wind turbines and tracking system for photovoltaic platforms, on the specific sliding losses.

Keywords Bevel gears · External gears · Internal gears · Power losses

1 Introduction

According to the state of the art, energy saving is one of the priorities of machinery and equipments manufacturers. Until recently, gears were considered having high efficiency in transmitting load, but according to the state of the art, efficiency increasing has become a very important issue [10]. Gears efficiency importance led ISO to develop two standards relating to the method of calculating gears friction losses. One of these standards was proposed by American scientists (AGMA) [15, 16] and the other by German scientists [17].

In gears assemblies, reducers, gear boxes and feed boxes each item causes power losses. The most important power losses are given by gears, rolling bearings and sealing [4, 5]. Power losses can be divided in: no-load losses and load-dependent losses. The most important no-load losses are: gears windage losses, gears and rolling bearings, oil churning losses and the seal system losses given by its friction

Gh. Moldovean (✉)
Department of Product Design and Robotics, Transilvania University of Braşov, Braşov, Romania

I. Vişa (ed.), *SYROM 2009*,
DOI 10.1007/978-90-481-3522-6_27,

with the shaft [5, 12, 17]. Gears mesh load-dependent mechanical power losses incorporate sliding friction loss and rolling friction loss. Sliding friction appears as a result of the relative sliding between two contacting teeth surfaces. During load transmission teeth deform creating a contact band. The resultant of the distributed force is shifted so that force acting distance increases [6].

The moment given by the normal force and the increasing distance of the normal force arm generates rolling friction between teeth. At the pitch-point rolling friction reaches the maximum. By contrast, sliding is zero at the pitch point and reaches maximum values at the start of the approach and at the end of the recess.

Total power losses are achieved by adding all of the mentioned losses.

This paper analyzes the influence of the geometrical parameters on the external and internal cylindrical gears as well as bevel gears used in wind turbines and tracking systems of photovoltaic platforms, on specific sliding friction power losses.

2 Theoretical Basis

Instantaneous power lost by sliding friction during gear mesh is dependent of teeth contact point. It is determined with relation [16]

$$P_f(x) = \mu(x)F_n(x)\upsilon_{al}(x), \tag{1}$$

where μ is the sliding friction coefficient; F_n – normal force between teeth, measured in N; υ_{al} – sliding velocity measured in m/s.

Sliding velocity in the contact point is determined with relation (see Fig. 1)

$$\upsilon_{al} = \overline{CY}(\omega_1 \pm \omega_2) = x(\omega_1 \pm \omega_2), \tag{2}$$

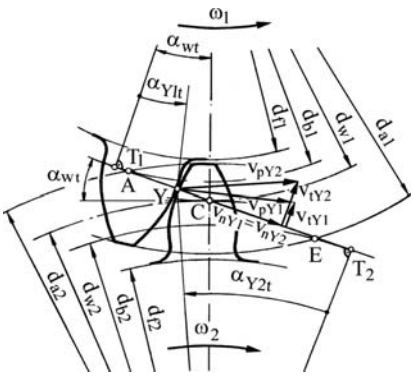

Fig. 1 Relative velocity scheme

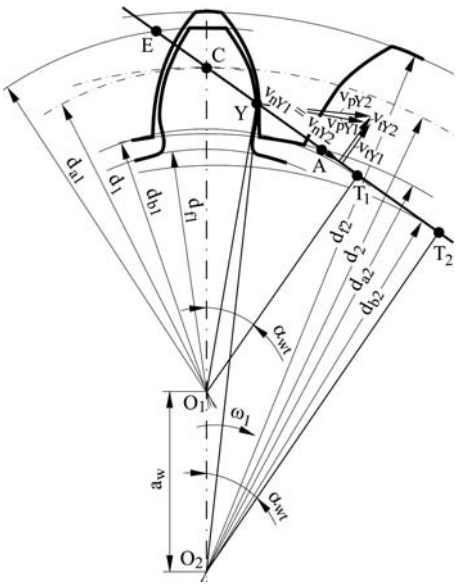

Fig. 2 Internal cylindrical gear

along pitch path, ISO [17] where ω_1 and ω_2 are the angular velocities of pinion and wheel, and x is the distance between pitch point C and contact point Y. The superior sign corresponds to external cylindrical gear while the inferior sign corresponds to internal cylindrical gear (see Fig. 2).

Since the friction coefficient varies slightly the usage of an average value for this coefficient is recommended. This coefficient is determined with relation

$$\mu_{mz} = 0.048\left(\frac{F/b}{\upsilon_{\Sigma}\rho}\right)^{0.2}\eta_{oil}^{-0.05}R_a^{0.25}X_L, \tag{3}$$

where: F is the tangential force at the base circle; b – gear width; υ_{Σ} – the sum of the tangential velocities corresponding to pitch point; ρ – reduce curvature in the pitch point; η_{oil} – dynamic viscosity at the running temperature, in mPa.s; R_a – average roughness of the pinion and driven wheel teeth surfaces, in μm; X_L – lubricant factor.

Instantaneous specific power lost by friction $P_{sf}(x)$ is defined as a ratio between power $P_f(x)$ and the input power $P_1(x)$. At a real gear there are areas with one pair of teeth in contact and areas with two pairs of teeth in contact (see Fig. 3).

In single contact situation (on BD segment) the instantaneous friction power loss is determined with relation (1), and the input power with relation

$$\begin{aligned} P_1(x) &= T_1\omega_1 = \\ &= F_n\left[\frac{d_{b1}}{2} - \mu_{mz}\left(\frac{d_{b1}}{2}\tan\alpha_{wt} - x\right)\right]\omega_1\,, \end{aligned} \tag{4}$$

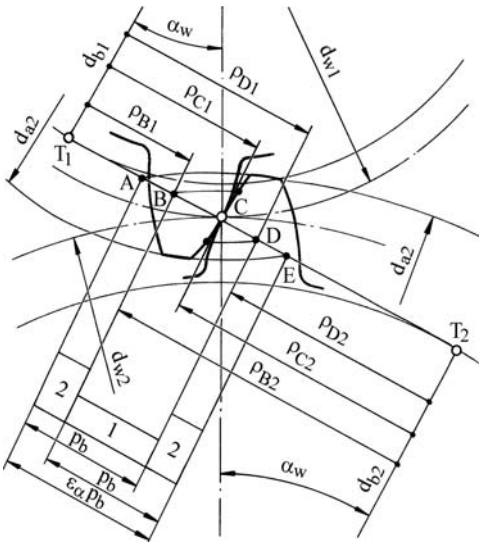

Fig. 3 Contact ratio scheme

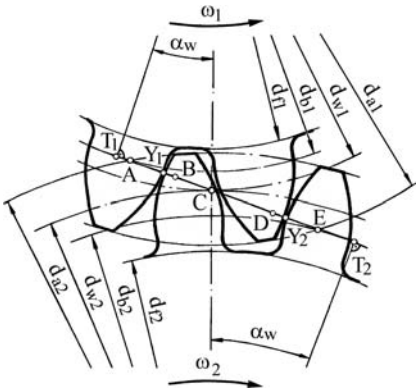

Fig. 4 Double contact mesh

resulting by neglecting the low value terms

$$P_{sfY}(x) = \frac{2\mu_{mz}x}{m\cos\alpha_t}\,\frac{u+1}{z_1 u}. \tag{5}$$

In double contact situation, on segments AB and DE, specific power losses are different from single contact situation because of the load distribution on teeth and of the different relative sliding of teeth pairs. Considering the commonly case met in practice when pitch point C is situated between contact points Y_1 and Y_2 (Fig. 4), and, in the hypothesis of uniform distribution on the two pairs of teeth [5, 11], the following relations can be drawn:

• Instantaneous friction power losses

$$\begin{aligned} P_{f\,Y1Y2}(x) &= 0.5\mu_{mz}F_n(|v_{alY1}| + |v_{alY2}|) = \\ &= 0.5\mu_{mz}F_n p_b(\omega_1 + \omega_2)\,; \end{aligned} \tag{6}$$

• Input power

$$P_{1Y1Y2}(x) = 0.5F_n(d_{b1} + \mu_{mz}p_b)\,\omega_1; \tag{7}$$

• Instantaneous specific power lost by friction (it is considered $\pi\mu_{mz}/z_1 << 1$)

$$P_{sf\,Y1Y2}(x) = \pi\mu_{mz}\frac{u+1}{z_1 u}. \tag{8}$$

Instantaneous specific power lost by friction has a reduced importance for gears, the most important being the medium friction power losses, according to which the gear efficiency is calculated. During the gearing process, the contact point of each teeth pair is repeatedly shifted along a length equal to p_b [11].

Thus, the medium friction power loss is determined by integration of the instantaneous specific friction power losses on the length on the base circle pitch using the relation

$$\begin{aligned} P_f &= \tfrac{1}{p_b}\int_0^{p_b} P_{sf}(x)\,dx = \\ &= \tfrac{1}{p_b}\left(\int_0^{AB} P_{sfY}(x)dx + \int_0^{BD} P_{sfY1Y2}(x)\,dx\right) \end{aligned}. \tag{9}$$

In this paper, the medium friction power losses is determined taking into consideration that the contact point is positioned between B and D points, so $\overline{AC} < p_b$ and $\overline{CE} < p_b$. So, the contact ratio of the tooth head of the pinion is $\varepsilon_1 = \overline{CE}/p_b < 1.0$ and contact ratio of the tooth head of the driven wheel is $\varepsilon_2 = \overline{CA}/p_b < 1.0$.

The first term of the expression (9) can be wrote as

$$\begin{aligned} \int_0^{AB} P_{sf\,Y}(x)\,dx &= \pi\mu_{mz}\frac{u+1}{z_1 u}x|_0^{AB} = \\ &= \pi\mu_{mz}\frac{u+1}{z_1 u}p_b(\varepsilon_1 + \varepsilon_2 - 1), \end{aligned} \tag{10}$$

where $AB = AC - BC = p_b\varepsilon_2 - p_b(1 - \varepsilon_1)$.

The second term can be wrote as

$$\int_0^{BD} P_{sf\,Y1Y2}(x)\,dx = \\ = \frac{2\mu_{mz}}{m\cos\alpha_t}\,\frac{u+1}{z_1 u}\left(\int_0^{BC} x\,dx + \int_0^{CD} x\,dx\right) = \\ = \frac{\mu_{mz}p_b^2}{m\cos\alpha_t}\left[(1-\varepsilon_1)^2 + (1-\varepsilon_2)^2\right]\frac{u+1}{z_1 u}. \tag{11}$$

Finally, relation for the determination of the medium friction power losses in the cylindrical gear is

$$P_f = \pi\mu_{mz}\frac{u\pm 1}{z_1 u}\left(1-\varepsilon_\alpha+\varepsilon_1^2+\varepsilon_2^2\right). \tag{12}$$

For the straight bevel gear, the reasoning presented for the external cylindrical gear, is applied to the virtual gear corresponding to external frontal cone [7]. The geometrical elements involved are presented in Fig. 5; relation for calculating the power lost by friction being

$$P_f = \pi\mu_{mz}\frac{u_v-1}{z_1 u_v}\left(1-\varepsilon_{v\alpha}+\varepsilon_{v1}^2+\varepsilon_{v2}^2\right). \tag{13}$$

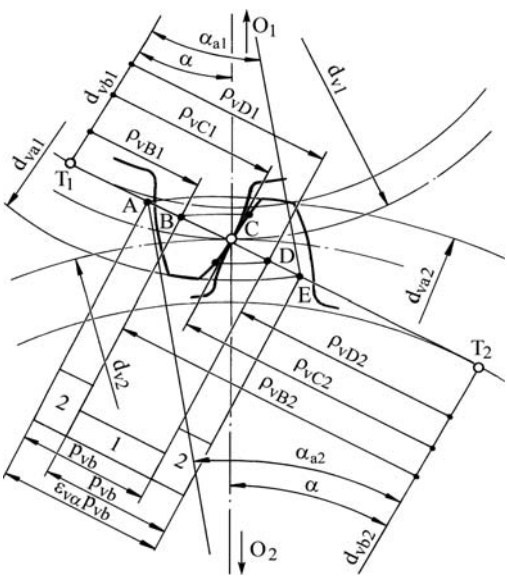

Fig. 5 Virtual gear

Table 1 Relations used for calculus of the geometrical elements

Cylindrical gear	Straight bevel gear
Gear ratio $u = z_2/z_1$	Virtual gear ratio $u_v = u^2 = (z_2/z_1)^2$
Addendum contact ratio of the pinion $\varepsilon_1 = \frac{z_1}{2\pi}(tg\,\alpha_{at1} - tg\,\alpha_{wt})$	Virtual addendum contact ratio of the pinion $\varepsilon_{v1} = \frac{z_1}{2\pi}\frac{\sqrt{u^2+1}}{u}(tg\,\alpha_{va1} - tg\,\alpha)$
Addendum contact ratio of the wheel $\varepsilon_2 = \frac{z_2}{2\pi}(\pm tg\,\alpha_{at2}\ mtg\,\alpha_{wt})$	Virtual addendum contact ratio of the wheel $\varepsilon_{v2} = \frac{z_2}{2\pi}\sqrt{u^2+1}(tg\,\alpha_{va2} - tg\,\alpha)$
Transverse contact ratio $\varepsilon_\alpha = \varepsilon_1 + \varepsilon_2$	Transverse contact ratio of a virtual spur gear $\varepsilon_{v\alpha} = \varepsilon_{v1} + \varepsilon_{v2}$

The geometrical elements of the external and internal cylindrical gears as well as bevel gears, involved in the calculus of medium friction power losses are presented in Table 1.

The pressure angle on the tip circle of the pinion, respectively of the driven wheel for external cylindrical gear is determined taking into consideration the shortening of the tooth from the condition of maintaining the tooth head clearance [2]. In the case of the internal cylindrical gear the pressure angle on the tooth head takes into consideration the modification of the tooth head height to maintain a normal tooth head clearance [8] and also from the condition of avoiding interference between the pinion tooth foot and the driven wheel tooth head [3, 9].

3 Results and Discussions

To highlight the influence of the geometrical parameters of the gears on power lost by friction, the authors have developed a computing program, the results being presented below in the form of diagrams.

In Fig. 6 it is presented the power lost by friction, in percent, for cylindrical gear as a function of the pinion's teeth number and the coefficient of fraction μ.

From Fig. 6 we can see a substantial increase of the power lost by friction with the increase of the coefficient of friction and a reduction of the power lost through friction by increasing the pinion's teeth number. The advantage of the internal cylindrical gear in comparison with the external one is obvious, even for a low number of teeth.

Figure 7 presents the power lost by friction, in percent, as a function of gear ratio.

Following the curves in Fig. 7 we can notice a difference between the external and the internal cylindrical gear. The power lost by friction for the external gear decreases with the increase of the gear ratio. Compared to the external gear the power lost by friction increases for the internal gear. The increasing of the power lost by friction for the internal gear is greater compared to the decrease of the power lost by friction for the external gear.

Concluding, the power losses for the internal gear are reduced comparing to the external gear power losses, thus emphasizing the advantages of using internal gear.

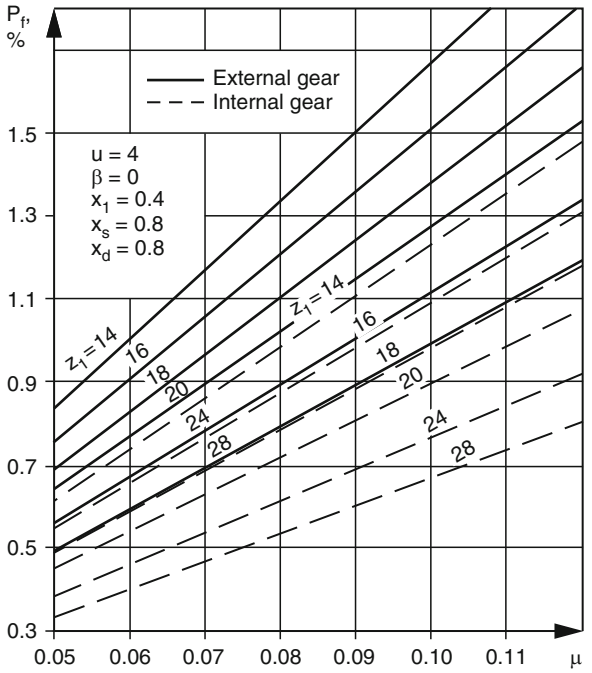

Fig. 6 $P_f = f(\mu, z_1)$ for cylindrical gear

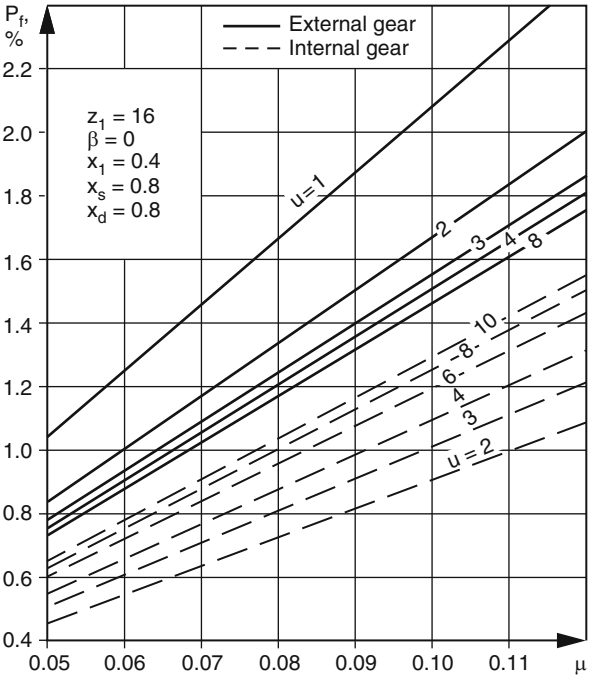

Fig. 7 $P_f = f(\mu, z_1)$ for cylindrical gear

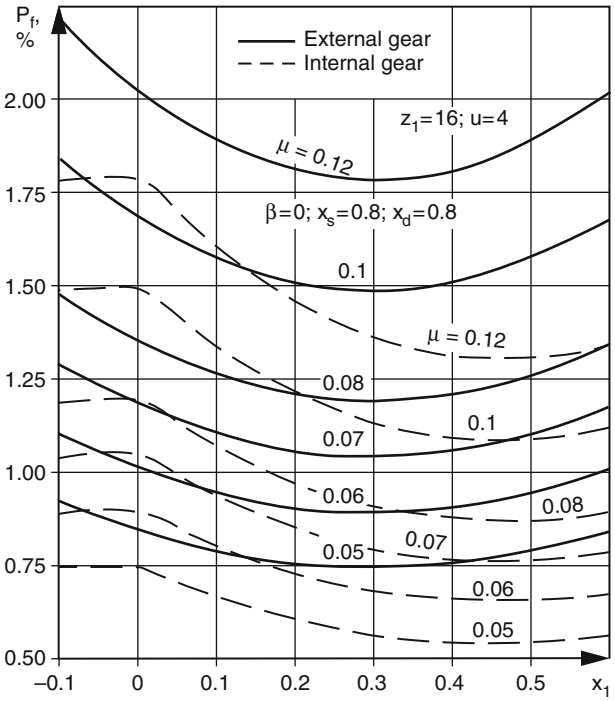

Fig. 8 $P_f = f(x_1, \mu)$, for $x_s = 0.8$

The influence of the profile shift coefficient x_1 and of the coefficient of friction μ on the power lost by friction for the external and internal gears is presented in the next figures. Figure 9 shows these influences for a profile shift coefficient of $x_s = 0.8$ and Fig. 9 for a profile shift coefficient of $x_s = 0$.

A first observation coming from the analysis of diagrams of Figs. 8 and 9 is that, for cylindrical external gear, the influence of the profile shift coefficient on the power lost by friction is almost zero.

The power lost by friction decreases in the middle zone of the range of values comparing to the extremities range of values.

The variation of the power lost by friction for the internal gear is different from the variation of the external gear. This difference is explained by the influence of two imposed conditions: one is to avoid interference between the dedendum of the tooth and the addendum of the pinion's tooth of the internal gear [1], and the second condition relates to the modification of the tooth addendum in order to maintain a normal clearance to head tooth [8, 9].

The variation of the power lost by friction as a function of the helix angle and of the friction coefficient, for external and internal gear is represented in Fig. 10.

The first observation drawn from the analysis of the diagrams is related to the power losses for external cylindrical gear versus the internal gear. The power losses for internal gear are substantially lower compared to the power losses of the

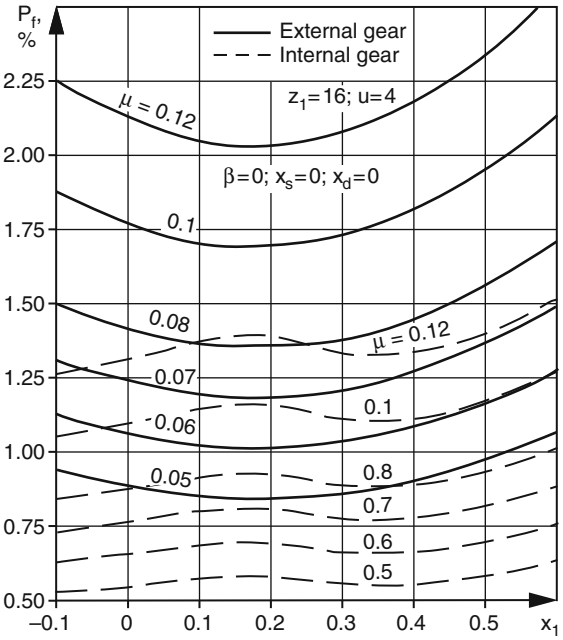

Fig. 9 $P_f = f(x_1, \mu)$, for $x_s = 0$

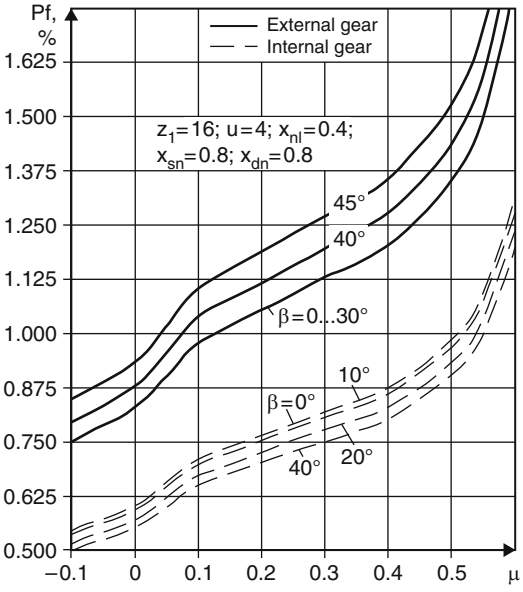

Fig. 10 $P_f = f(\mu, \beta)$, for cylindrical gear

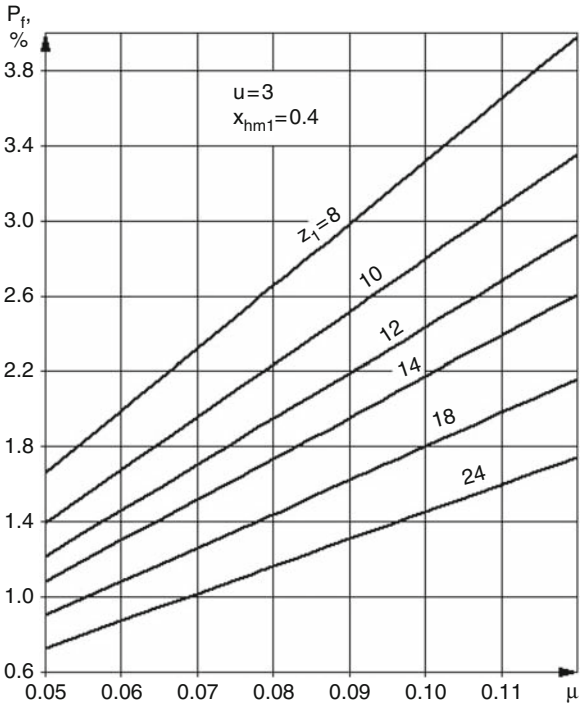

Fig. 11 $P_f = f(\mu, z_1)$ for straight bevel gear

external gear. Another difference relates to the fact that the external gear power loss by friction decreases along with decreasing helix angle, unlike internal gear where losses decrease when the helix angle increases.

Figure 11 is presenting the power lost by friction, in percent, for straight bevel gear, depending on the number of teeth of the pinion and the coefficient of friction μ.

The decreasing of power lost by friction by increasing the number of teeth and a significant increase in power losses with increasing the coefficient of friction μ, regardless of the number of pinion's teeth can be seen by analyzing the diagram from Fig. 11. The increase in power losses by an increase coefficient of friction is more visible for a reduced number of pinion's teeth.

In practice it is recommended the usage of straight bevel gears with increased number of teeth in order to reduce power losses. By dimensioning bevel gears from condition of teeth resistance at contact and bending stress in order to determine the minimum module, a reduced power losses by friction is obtained.

The influence of the straight bevel gear ratio on the power losses is presented in Fig. 12. Analysis of this diagram highlights that increasing gear ratio, power lost by friction decreases, but it increases with the increase of the friction coefficient, regardless of the chosen gear ratio.

Diagram drawn in Fig. 13 is presenting the power losses for straight bevel gear in relation to profile shift coefficient and coefficient of friction μ.

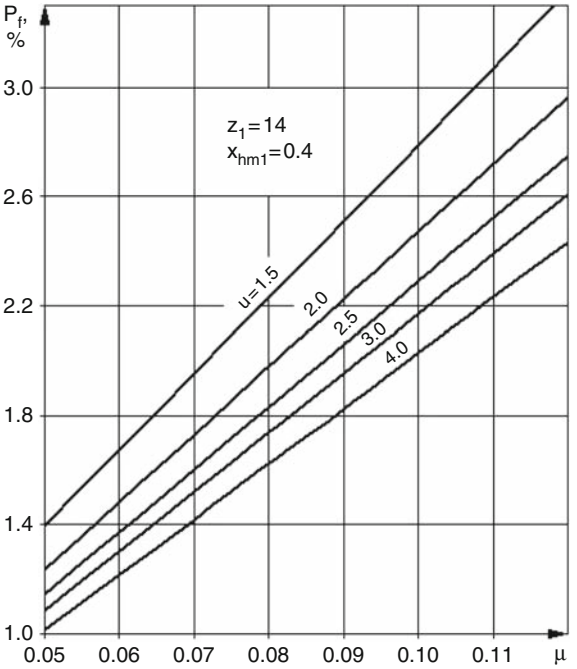

Fig. 12 $P_f = f(\mu, u)$, for straight bevel gear

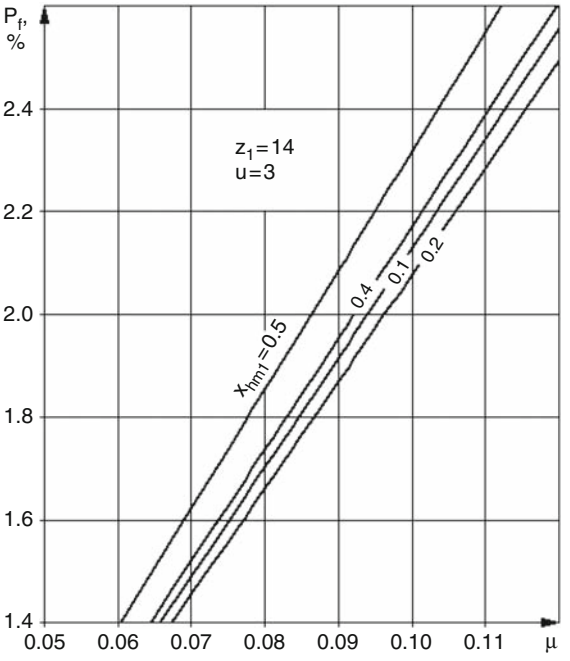

Fig. 13 $P_f = f(\mu, x_{hm1})$, for bevel gear

The analysis takes into consideration the producers and branch literature recommendations relating to profile shift coefficients for bevel gears [13, 14]. Profile shift coefficients are chosen to avoid teeth undercutting and sharpening. As a result, for reduced number of teeth and large gear ratio, the profile shift coefficient increases. By contrast, for large teeth number and reduced gear ratio, the profile shift coefficient decreases. A first observation for bevel gears refers to the variation of the power lost by friction depending on values of profile shift coefficients on a restricted domain.

A second observation is related to the fact that, for values of shift coefficients higher than 0.4, the power lost by friction considerably increases.

4 Conclusions

The analysis presented by means of the diagrams led to the following conclusions:

- From the analysis of these three types of gears (external and internal cylindrical gears and straight bevel gear) it is clearly shown that internal gear has the most reduced power lost by friction, therefore the highest efficiency. The gear with the lowest efficiency is the straight bevel gear.
- The reduction of the power losses can be achieved by increasing the number of pinion's teeth, by increasing the gear ratio for external cylindrical gears and straight bevel gears, or by decreasing the gear ratio for internal cylindrical gears.
- The shift coefficient value has also an influence on the power lost by friction; therefore, a shift coefficient value of $x_1 \approx 0.1$–0.4 (see Figs. 8 and 9) is recommended for the pinion of the external cylindrical gear; for internal cylindrical gear a shift coefficient value of $x_1 \approx 0.3$–0.6 (see Fig. 8) or $x_1 \approx -0.1$–0 and $x_1 \approx 0.3$–0.5 is recommended (see Fig. 9); for straight bevel gear the value of the shift coefficient should be near 0.2.
- By comparing external and internal cylindrical gears, it can be seen that the helix angle has different influence on the power losses; therefore, the power lost by friction has a reduced value at reduced helix angles (minimum for spur gear) for external cylindrical gears, while for internal cylindrical gears the power lost by friction decreases by increasing the helix angle (see Fig. 10).

As a general conclusion, by adequate selection of the geometrical parameters of the cylindrical or bevel gear, the power lost by friction can be reduced, without extra costs. The authors will go further with researches related to the analyses of the factors that have influence on the friction coefficient in order to minimize it.

References

1 Bozan, C.A., Gavrila, C.: Tooth addendum modification to avoid the interference between the pinion dedendum and internal wheel addendum. Proceedings of the 5th KOD international symposium, p. 85. Novi Sad, Serbia (2008)

2 Deaky, B., Gavrilă, C.: Influenţa deplasărilor de profil asupra scurtării dinţilor angrenajelor cilindrice. Buletinul Simpozionului PRASIC'06, p. 25. Brasov (2006)
3 Florea, R., et al.: Organe de masini. Editura tehnica, Bucuresti (2007)
4 Heingartner, P., Mba, D.: Determining power losses in the helical gear mesh. A case study. Gear Technol. (September/October), p. 32 (2007)
5 Hohn, B.R., Michaelis, K., Wimmer, A.: Low loss gears. Gear Tehnol. (June), p. 28 (2007). Available at: http://www.geartechnology.com
6 Michlin, Y., Myunster,V.: Determination of power losses in gear transmissions with rolling and sliding friction incorporated. Mech. Mach. Theory 37, p. 167 (2002)
7 Moldovean, Gh., et al.: Angrenaje cilindrice şi conice. Metodici de proiectare. Editura Lux Libris, Braşov (2002)
8 Moldovean, Gh., Huidan, L., Coman, A.: Profile modification influence on the tooth addendum extension of internal gear. Proceedings of the 2nd ICEGD international conference, p. 163. Galaţi, Romania (2007)
9 Moldovean, Gh., Bozan, C.A., Huidan, L.: Profile modification influence on the contact ratio of internal gear. Proceedings of the 5th KOD international symposium, p. 91. Novi Sad, Siberia (2008)
10 Petry-Johnson, T.T., et al.: Experimental investigation of spur gear efficiency. Proceedings of the ASME IDETC/CIE conference. Las Vegas (2007). Available at: http://www. cryogenic-superfinish.com/pdf/GM_OSU%209.27.07.pdf
11 Sauer, L., et al.: Angrenaje. Proiectare. Materiale. Editura Tehnică, Bucuresti (1970)
12 Velex, P., Cahonwet, V.: Experimental and numerical investigations of the influence of tooth friction in spur and helical gear dynamics. J. Mech. Design ASME 122, p. 515 (2000)
13 Velicu, D., Moldovean, Gh., Velicu, R.: Proiectarea angrenajelor conice si hipoide. Ed. Universitatii Transilvania din Brasov, Brasov (2004)
14 Velicu, D., Moldovean, Gh.: Profile modification influence on the contact ratio for straight bevel gear. Proceedings of the 2nd ICEGD international conference, p. 229. Galaţi, Siberia (2007)
15 AGMA 14179-1. Gear reducers – thermal capacity based on ISO/TR 14179-1. AGMA information sheet (2001)
16 ISO 14179-1. Gear thermal capacity – Part 1: Rating gears drives with thermal equilibriumat 95°C sump temperature. Technical Report (2001)
17 ISO 14179-2. Gear thermal capacity – Part 2: Thermal load-carrying capacity. Technical Report (2001)

New Formulations on Acceleration Energy in the Robot Dynamics

I. Negrean, A. Duca, C. Negrean, and K. Kacso

Abstract Based on formulations developed in this paper, a few important notions in the dynamics of robot mechanical systems are analyzed. Using some differential transformations as well as matrix exponentials the expressions for acceleration energy will be determined, in an explicit form and then in matrix form. The expressions for acceleration energy will lead into determining control functions for any mechanical robot structure (MRS).

Keywords Acceleration energy · Dynamics · Matrix exponentials · Robotics

1 Introduction

The matrix transfer equations for any kinematical chain, with *(R)-rotation* or *(T)-prismatic* driving joints, corresponding to the mechanical robot structure (MRS), are established by means of locating transformations, according to [2] and [3]. *The locating term* (position and orientation) substitutes the position and orientation between two adjoining kinetic links. In order to determine the transfer equations, the (MRS) will be represented into the initial configuration. Using the equations of Forward Kinematics (direct model), the linear and angular transfer matrices are defined using *the matrix exponentials*. As a result, *the forward kinematics equations* answerable to linear and angular velocities and accelerations will be presented by their defining expressions. The study with matrix exponentials will be extended in the robot dynamics to the level of robot structures with rigid and flexible links.

I. Negrean (✉)
Department of Mechanics and Computer Programming, Technical University of Cluj-Napoca, Cluj-Napoca, Romania

I. Vişa (ed.), *SYROM 2009*,
DOI 10.1007/978-90-481-3522-6_28,

2 The Forward Kinematics Equations

This section is devoted to the finding of forward kinematics equations that can be applied in case of any robot structure. The forward kinematics equations are developed using the matrix exponentials. In the first part of this section are presented, in an exponential form, the forward kinematics equations (linear and angular velocities and accelerations) and then, this equations are applied to determine the acceleration energy.

2.1 Matrix Exponentials in the Forward Kinematics

According to [1, 3], will be presented some important expressions which results mainly from applying the *Algorithm of Matrix Exponentials in Kinematics (MEK)*. The first variant of this algorithm aims to the direct application of matrix exponentials obtaining the expression for the Jacobian matrix, which is described by the matrix:

$$ {}^0J\ \left(\bar{\theta}\right) = \left\{\ \left[{}^0J_{iv}\ \left(\bar{\theta}\right)\right]^T\ \left[{}^0J_{i\Omega}\ \left(\bar{\theta}\right)\right]^T\ \{i=1\rightarrow n\}\ \right\}^T \tag{1} $$

The components of the Jacobian matrix can be written in an explicit form, such as follows:

$$ \begin{aligned} &\left\{\left[{}^0J_{iv}\left(\bar{\theta}\right)\right]\{i{=}1{\rightarrow}n\}\right\}= \\ &= \left(\begin{array}{l} \exp\left\{\sum_{j=0}^{i-1}\left\{\bar{k}_j^{(0)}\times\right\}q_j{\cdot}\Delta_j\right\}{\cdot}\bar{v}_i{+}\exp\left\{\sum_{k=i}^{n}\left\{\bar{k}_k^{(0)}\times\right\}q_k{\cdot}\Delta_k\right\}{\cdot}\bar{p}_n^{(0)}+ \\ +\Delta_i{\cdot}\exp\left\{\sum_{j=0}^{i-1}\left\{\bar{k}_j^{(0)}\times\right\}q_j{\cdot}\Delta_j\right\}{\cdot}\left\{\bar{k}_i^{(0)}\times\right\}\left\{\sum_{k=i}^{n}\left\{\exp\left\{\sum_{m=i-1}^{k-1}\left\{\bar{k}_m^{(0)}\times\right\}q_m{\cdot}\delta_m\right\}{\cdot}\bar{b}_k\right\}\right. \end{array}\right) \end{aligned} \tag{2} $$

$$ \left\{\begin{array}{c}\left[{}^0J_{i\Omega}\ \left(\bar{\theta}\right)\right] \\ \{i=1\rightarrow n\}\end{array}\right\} = \left(\exp\left\{\sum_{j=0}^{i-1}\left\{\bar{k}_j^{(0)}\times\right\}q_j\cdot\Delta_j\right\}\cdot\ \bar{k}_i^{(0)}\cdot\Delta_i\right) \tag{3} $$

where $\bar{k}_j^{(0)}$ represents the unit vector, which describes the orientation of each driving axis of the robot structure;

q_j represents the generalized coordinate, (the geometrical control functions) for any kinematical driving axis, $\bar{p}_n$ describes the position of the end-effector with respect to $\{0\}$ fixed system, and the parameters $\bar{k}_i^{(0)}$ and $\bar{v}_i^{(0)}$ are the screw parameters, $\bar{v}_i^{(0)}$ being expressed in the following form:

$$\bar{v}_i^0 = \bar{p}_i^{(0)} \times \bar{k}_i^{(0)} \cdot \Delta_i + (1 - \Delta_i) \cdot \bar{k}_i^{(0)} \tag{4}$$

where $\bar{p}_i^{(0)}$ is the position vector that gives the final position of $\{i\}$ moving system with respect to $\{0\}$ fixed system.

In the expressions above, Δ_i represents a matrix operator that depends on the type of motion performed around and along the driving axis. According to *MEK Algorithm*, in order to apply the second or third variant for the calculus of the *Jacobian Matrix*, an external loop $(i = 1 \rightarrow n)$ is opened. Inside this loop, some matrix exponentials are determined:

$$\underset{(3\times3)}{ME}\,(V_{i1}) = \exp\left\{\sum_{j=0}^{i-1}\left\{\bar{k}_j^{(0)}\times\right\} q_j \cdot \Delta_j\right\} \tag{5}$$

$$\underset{(3\times6)}{ME}\,(V_{i2}) = \left[\begin{array}{cc} I_3 & \Delta_i \cdot \left\{\bar{k}_i^{(0)}\times\right\} \end{array}\right] \tag{6}$$

$$\left\{\begin{array}{c} \underset{\{6x[9+3\cdot(n-i)]\}}{ME\,(V_{i3})} \equiv \\ \left[\begin{array}{cc} I_3 & [0] \\ [0] & \left[\exp\left\{\sum_{m=i-1}^{k-1}\left\{\bar{k}_m^{(0)}\times\right\} q_m \cdot \delta_m \cdot \Delta_m\right\}\right] \\ [0] & \exp\left\{\sum_{k=i}^{n}\left\{\bar{k}_k^{(0)}\times\right\} q_k \cdot \Delta_k\right\} \end{array}\right] \end{array}\right\} \tag{7}$$

Applying a few transformations, from the expressions (5–7) are finally obtained:

$$\underset{(6\times6)}{ME}\,\{J_{i1}\} = \left[\begin{array}{cc} ME\{V_{i1}\} & [0] \\ [0] & ME\{V_{i1}\} \end{array}\right] \tag{8}$$

$$\underset{(6\times9)}{ME}\,\{J_{i2}\} = \left[\begin{array}{cc} ME\{V_{i2}\} & [0] \\ [0] & I_3 \end{array}\right] \tag{9}$$

$$\underset{\{9\times[12+3\cdot(n-i)]\}}{ME\{J_{i3}\}} = \left[\begin{array}{cc} ME\{V_{i3}\} & [0] \\ [0] & I_3 \end{array}\right] \tag{10}$$

The matrix exponential described by Eqs. (8–10), are included in a matrix written as:

$$\underset{\{6\times[12+3\cdot(n-i)]\}}{ME\{{}^0J_i\}} = ME\{J_{i1}\} \cdot ME\{J_{i2}\} \cdot ME\{J_{i3}\} \tag{11}$$

The column vector of the Jacobian matrix is determined using the expression bellow:

$$\left\{ \begin{array}{c} M_{iv\omega} \\ \{\,[12+3\cdot(n-i)]\times 1\,\} \end{array} = \left[M_{iv}^{T} \quad M_{i\omega}^{T} \right]^{T} = \right\} \\ \left\{ \left[\bar{v}_i^{(0)T} \quad \bar{b}_k{}^{T} \quad \bar{p}_n^{(0)T} \quad \Delta_i \cdot \bar{k}_i^{(0)T} \right]^{T} \right\} \tag{12}$$

So, the (i) column and obviously the Jacobian matrix as well, can be determined by using the following matrix expression:

$$\left\{ {}^{0}J\left(\bar{\theta}\right) \underset{(6\times n)}{\equiv} \left[\begin{array}{c} {}^{0}J_i \\ {\scriptstyle (6\times 1)} \\ (i=1\rightarrow n) \end{array} \right] \right\} \equiv \left\{ \begin{array}{c} ME\left\{ {}^{0}J_i \right\} \cdot M_{iv\omega} \\ \text{second variant} \end{array} \right\} \tag{13}$$

In above expression, $ME\left\{ {}^{0}J_i \right\}$ is the result of the product between Eqs. (8–10):

$$\left\{ \begin{array}{c} \left\{ {}^{0}J\left(\bar{\theta}\right) \underset{(6\times n)}{\equiv} \left[\begin{array}{c} {}^{0}J_i \\ {\scriptstyle (6\times 1)} \\ (i=1\rightarrow n) \end{array} \right] \right\} \equiv \\ ME\{J_{i1}\} \cdot \left[\begin{array}{cc} ME\{V_{i2}\} ME\{V_{i3}\} & [0] \\ [0] & I_3 \end{array} \right] \cdot \{M_{iv\omega}\} \end{array} \right\} \tag{14}$$

In order to determine the expressions for transfer operators and Jacobian matrix with respect to the moving system$\{n\}$, the following expressions are to be applied:

$$\left\{ {}^{n}R = \left[\begin{array}{cc} R_{n0}^{-1} & [0] \\ [0] & R_{n0}^{-1} \end{array} \right] \equiv ME\ ({}^{n}R) \right\} \tag{15}$$

Within Eq. (15), the components of the matrix are expressed in an exponential form, as:

$$R_{n0}^{-1} = \left\{ R_{n0}^{(0)} \right\}^{-1} \cdot \prod_{i=n}^{1} \exp\ \left\{ -\left\{ \bar{k}_i^{(0)} \times \right\} q_i \cdot \Delta_i \right\} \tag{16}$$

where R_{n0} represents the rotation matrix between moving frame $\{n\}$ and $\{0\}$

The expression for the Jacobian matrix, with respect to$\{n\}$ moving frame is given:

$${}^{n}J\left(\bar{\theta}\right) = ME\ ({}^{n}R)\ \cdot {}^{0}J\left(\bar{\theta}\right) \tag{17}$$

$ME\ ({}^{n}R)$ and ${}^{0}J\left(\bar{\theta}\right)$ are substituted by Eqs. (15) or (16), previously determined. The next steps consist in determining the Jacobian matrix time derivative. For this, an external loop $(i=1\rightarrow n)$ is opened. By applying any of the two calculus variants, are obtained the components of the column vectors that form the Jacobian matrix time derivative, projected on the fixed frame$\{0\}$:

$$\left\{\begin{array}{c} {}^{0}\dot{J}_{i} \\ {}_{(i=1\to n)} \end{array} = \prod_{j=1}^{4} M\{\dot{J}_{ij}\} \equiv \right.$$
$$\left. \equiv \left\{\begin{array}{c} ME\{\dot{J}_{i1}\} \cdot ME\{J_{i2}\} \cdot ME\{J_{i3}\} \cdot M_{iv\omega} + \\ +ME\{J_{i1}\} \cdot ME\{J_{i2}\} \cdot ME\{\dot{J}_{i3}\} \cdot M^{*}_{iv\omega} + \\ +ME\{J_{i1}\} \cdot ME\{J_{i2}\} \cdot ME\{J_{i3}\} \cdot \dot{M}_{iv\omega} \end{array}\right\}\right\}$$

The Jacobian matrix time derivative with respect to $\{n\}$ moving frame can be also determined in an exponential form, such as:

$$^{n}\dot{J}(\bar{\theta}) = ME(^{n}R) \quad \cdot {}^{0}\dot{J}(\bar{\theta})$$

In keeping with *MEK Algorithm*, the matrix that achieves the transfer from the fixed frame $\{0\}$ to the moving frame$\{n\}$ of the Jacobian matrix and of its derivative is:

$$\left\{\begin{array}{c} \left[{}^{n}J(\bar{\theta}) \quad {}^{n}\dot{J}(\bar{\theta})\right]^{T} \equiv \\ \begin{bmatrix} ME\{^{n}R\} & [0] \\ [0] & ME\{^{n}R\} \end{bmatrix} \cdot \begin{bmatrix} {}^{0}J(\bar{\theta}) \\ {}^{0}\dot{J}(\bar{\theta}) \end{bmatrix} \end{array}\right\}. \tag{18}$$

$^{n}J(\bar{\theta})$ and $^{n}\dot{J}(\bar{\theta})$ from Eq. (18) represents the Jacobian matrix and its derivative with respect to moving frame $\{n\}$.

The differential matrices of first and second order denoted with A_{ki} and A_{kjm} that characterize the homogenous transformations are also determined by means of the expressions presented bellow.

$$\left\{\begin{array}{c} A_{ki} \equiv \\ \exp\left\{\sum_{j=0}^{i-1} A_j \cdot q_j\right\} \cdot A_i \cdot \exp\left\{\sum_{l=i}^{k} A_l \cdot q_l\right\} \cdot T_{k0}^{(0)} \end{array}\right\} \tag{19}$$

where $T_{k0}^{(0)}$ expresses the locating (homogenous transformation) between $\{k\}$ and frames $\{0\}$, in initial robot configuration.

$$\left\{\begin{array}{c} A_i = \\ \begin{bmatrix} \{{}^{i}\bar{k}_i \cdot \Delta_i \times\} & \{\bar{p}_i \times\}{}^{i}\bar{k}_i \cdot \Delta_i + {}^{i}\bar{k}_i \cdot (1-\Delta_i) \\ 0 \quad 0 \quad 0 & 0 \end{bmatrix} \end{array}\right\} \tag{20}$$

$$\begin{array}{l} A_{kjm} = \left\{\exp\left\{\sum_{l=0}^{m-1} A_l \cdot q_l\right\}\right\} \cdot A_m \cdot \\ \cdot \left\{\exp\left\{\sum_{i=m}^{j-1} A_i \cdot q_i\right\} \cdot A_i \cdot \exp\left\{\sum_{p=i}^{k} A_p \cdot q_p\right\}\right\} \cdot \cdot T_{k0}^{(0)} \end{array} \tag{21}$$

$$\left\{\begin{array}{l} \exp\left\{\sum\limits_{j=0}^{i-1} A_j \cdot q_j\right\} \equiv \\ \equiv \left[\begin{array}{cc} \prod\limits_{j=0}^{i-1} \exp\left\{\left\{\bar{k}_j^{(0)}\times\right\} q_j \Delta_j\right\} & \sum\limits_{j=0}^{i-1}\left\{\prod\limits_{k=0}^{i-1}\exp\left\{-\left\{\bar{k}_k^{(0)}\times\right\} q_k \Delta_k\right\}\right\}\cdot \bar{b}_{j+1} \\ 0\quad 0\quad 0 & 1 \end{array}\right] \end{array}\right\} \tag{22}$$

The *absolute* values for *angular velocities* and *accelerations*, corresponding to any kinetic link $i = 1 \to n$ from the mechanical robot structure (MRS), can be determined on the basis of the expressions (23–26). These are projected onto the systems $\{0\}$ and $\{i\}$.

$$^0\bar{\omega}_i \equiv \sum_{j=1}^{i}\left\{\exp\left\{\sum_{k=1}^{j-1}\left\{\bar{k}_k^{(0)}\times\right\} q_k \Delta_k\right\}\right\}\bar{k}_j^{(0)}\dot{q}_j\Delta_j \tag{23}$$

$$^0\dot{\bar{\omega}}_i \equiv \sum_{j=1}^{i}\left\{ME\left\{V_{j1}\right\}\ddot{q}_j + ME\left\{\dot{V}_{j1}\right\}\dot{q}_j\right\}\bar{k}_j^{(0)}\Delta_j \tag{24}$$

$$^i\bar{\omega}_i = \left\{\left\{R_{i0}^{(0)}\right\}^{-1}\exp\left\{-\left\{\sum_{j=i}^{1}\left\{\bar{k}_j^{(0)}\times\right\} q_j\Delta_j\right\}\right\}\right\}\cdot {}^0\bar{\omega}_i \tag{25}$$

$$^i\dot{\bar{\omega}}_i = \left\{\left\{R_{i0}^{(0)}\right\}^{-1}\exp\left\{-\left\{\sum_{j=i}^{1}\left\{\bar{k}_j^{(0)}\times\right\} q_j\Delta_j\right\}\right\}\right\}\cdot {}^0\dot{\bar{\omega}}_i \tag{26}$$

The linear velocities and accelerations of the origin$\{O_i\}$, associated to any kinetic element(i), can be determined as it follows:

$$^0\bar{v}_i \equiv \sum_{j=1}^{i} ME\left\{J_{j1}\right\}\cdot ME\left\{J_{j2}\right\}\cdot ME\left\{J_{j3}\right\}\cdot M_{jv}\cdot\dot{q}_j \tag{27}$$

$$\left\{\begin{array}{l} {}^0\dot{\bar{v}}_i \equiv \sum\limits_{j=1}^{i}\left\{{}^0\dot{J}_{i\,(i=1\to n)}\cdot\dot{q}_j\right\} + \\ +\sum\limits_{j=1}^{i}\left\{ME\left\{J_{j1}\right\}\cdot ME\left\{J_{j2}\right\}\cdot ME\left\{J_{j3}\right\}\cdot M_{jv}\cdot\ddot{q}_j\right\} \end{array}\right\} \tag{28}$$

$$\left\{\begin{array}{l} {}^0\dot{J}_{i\,(i=1\to n)} = \\ Tr.\left\{\left[\begin{array}{c} ME\left\{\dot{J}_{j1}\right\}\cdot ME\left\{J_{j2}\right\}\cdot ME\left\{J_{j3}\right\} \\ ME\left\{J_{j1}\right\}\cdot ME\left\{J_{j2}\right\}\cdot ME\left\{\dot{J}_{j3}\right\} \\ ME\left\{J_{j1}\right\}\cdot ME\left\{J_{j2}\right\}\cdot ME\left\{J_{j3}\right\} \end{array}\right]\cdot\left[\begin{array}{c} M_{jv} \\ M_{jv}^{*} \\ \dot{M}_{jv} \end{array}\right]^T\right\} \end{array}\right\}$$

In the expression above, $Tr.() = Trace()$

$$ {}^{i}\bar{v}_i = \left\{ \left\{ R_{i0}^{(0)} \right\}^{-1} \exp\left\{ -\left\{ \sum_{j=i}^{1} \left\{ \bar{k}_j^{(0)} \times \right\} q_j \Delta_j \right\} \right\} \right\} \cdot {}^{0}\bar{v}_i; \tag{29} $$

$$ {}^{i}\dot{\bar{v}}_i \equiv \left\{ \left\{ R_{i0}^{(0)} \right\}^{-1} \exp\left\{ -\left\{ \sum_{j=i}^{1} \left\{ \bar{k}_j^{(0)} \times \right\} q_j \Delta_j \right\} \right\} \right\} \cdot {}^{0}\dot{\bar{v}}_i; \tag{30} $$

The expressions for the Jacobian matrix exponentials are substituted in the generalized expression for determining the operational velocities and accelerations.

$$ \left\{ \begin{array}{l} \left[{}^{(n)0}\dot{\bar{X}} \quad {}^{(n)0}\ddot{\bar{X}} \right]^T = \\ \left\{ \begin{array}{l} = \left[\begin{array}{cc} \left[{}^{(n)0}\bar{v}_n^T \quad {}^{(n)0}\bar{\omega}_n^T \right]^T \\ \left[{}^{(n)0}\dot{\bar{v}}_n^T \quad {}^{(n)0}\dot{\bar{\omega}}_n^T \right]^T \end{array} \right] = \\ = \left[\begin{array}{cc} [0] & {}^{(n)0}J\left(\bar{\theta}\right) \\ {}^{(n)0}J\left(\bar{\theta}\right) & {}^{(n)0}\dot{J}\left(\bar{\theta}\right) \end{array} \right] \cdot \left(\begin{array}{c} \ddot{\bar{\theta}} \\ \dot{\bar{\theta}} \end{array} \right) \end{array} \right\} \end{array} \right\} \tag{31} $$

In the expression (31), $\left({}^{(n)0}\bar{v}_n^T, \ {}^{(n)0}\dot{\bar{v}}_n^T \right)$ are the linear velocity and acceleration of the end-effector with respect to $\{0\}$fixed and $\{n\}$ moving frames and $\left({}^{(n)0}\bar{\omega}_n^T, \ {}^{(n)0}\dot{\bar{\omega}}_n^T \right)$ describes the angular velocity and acceleration of the end-effector.

The kinematical control function matrix results from applying the polynomial interpolation functions, and is written as:

$$ M_{\theta n}^{CF} = \left\{ \begin{array}{l} \left[\begin{array}{lll} \dot{\theta}_k(\tau) & \dot{\bar{\theta}}_k(\tau) & \ddot{\bar{\theta}}_k(\tau) \\ k = 1 \rightarrow m & & \end{array} \right]^T \\ \left[\begin{array}{l} \left[\begin{array}{lll} q_{jk}(\tau) & \dot{q}_{jk}(\tau) & \ddot{q}_{jk}(\tau) \end{array} \right] \\ j = 1 \rightarrow n \end{array} \right]^T \end{array} \right\} \tag{32} $$

where τ represents the time variable and $k = 1 \rightarrow m$ the number of robot configuration.

Remarks: The matrix exponentials enjoy important advantages due to their compact form, easy geometric visualization and especially they avoid the frames typical to every kinetic link. The matrix exponentials stay at the basis of the dynamic control functions that characterize robot structures.

3 The Acceleration Energy in the Robot Dynamics

The dynamics equations which characterize any robot mechanical system with $(n\ d.o.f)$, subjected to holonomic or non-holonomic relation, can be determined on the basis of a fundamental dynamics quantity, known as *acceleration energy*.

3.1 The Explicit Expression of the Acceleration Energy

In this section according to [2] and demonstrations from [3] is presented the expression for the acceleration energy, in an explicit form and then in a matrix form.

First, the explicit form of the defining expression for acceleration energy is determined. For this purpose, is considered a kinetic element(j), represented within Fig. 1.

The geometrical and kinematical modeling and mass distribution has been performed. According to [4], the starting expression for the acceleration energy is given by:

$$E_A = \left\{ \frac{1}{2} \int \dot{v}_j^2 \cdot dm = \frac{1}{2} \int {}^j\dot{\bar{v}}_j^T \cdot {}^j\dot{\bar{v}}_j \cdot dm \right\} \tag{33}$$

In keeping with the expression for ${}^j\dot{\bar{v}}_{C_j}$:

$${}^i\dot{\bar{v}}_{C_i} = {}^i\dot{\bar{v}}_i + {}^i\dot{\bar{\omega}}_i \times {}^i\bar{r}_{C_i} + {}^i\bar{\omega}_i \times {}^i\bar{\omega}_i \times {}^i\bar{r}_{C_i}, \tag{34}$$

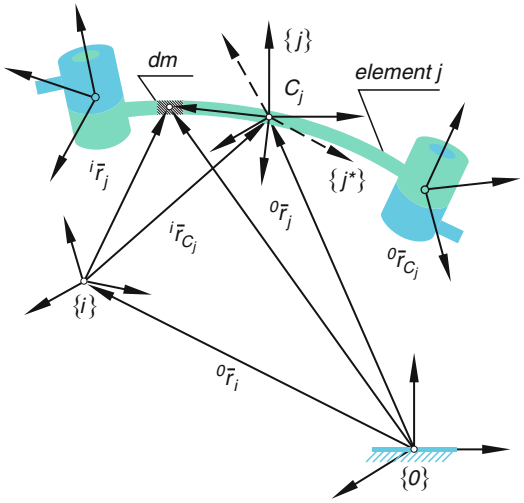

Fig. 1 The representation of the kinetic element (j)

it results the following expression for ${}^{j}\dot{\bar{v}}_j$:

$$ {}^{j}\dot{\bar{v}}_j = {}^{j}\dot{\bar{v}}_{C_j} + {}^{j}\dot{\bar{\omega}}_j \times {}^{j}\bar{r}_j + {}^{j}\bar{\omega}_j \times {}^{j}\bar{\omega}_j \times \bar{r}_j \tag{35} $$

In the above expression, the parameters $\left\{{}^{j}\dot{\bar{v}}_{C_j}; {}^{j}\bar{\omega}_j; {}^{j}\dot{\bar{\omega}}_j\right\}$ are the acceleration of the mass center, the angular velocity and acceleration that expresses the absolute rotation of the kinetic element(j). Substituting (35) into (33), it results an expression that can be developed resulting in this way six terms. The first term is represented by the following integral form:

$$ \left\{\frac{1}{2}\cdot\int {}^{j}\dot{\bar{v}}^{T}_{C_j}\cdot{}^{j}\dot{\bar{v}}_{C_j}\cdot d\,m \equiv \frac{1}{2}\cdot M_j\cdot{}^{j}\dot{\bar{v}}^{T}_{C_j}\cdot{}^{j}\dot{\bar{v}}_{C_j}\right\} \tag{36} $$

The first term from the expression (35) describes the component of acceleration energy corresponding to translational motion, a part of general motion described by the kinetic assembly. The next term obtained from Eq. (33), is given by the relation:

$$ \left\{\begin{array}{l} \dfrac{1}{2}\displaystyle\int \left({}^{j}\dot{\bar{\omega}}_j \times {}^{j}\bar{r}_j\right)^{T}\cdot\left({}^{j}\dot{\bar{\omega}}_j \times {}^{j}\bar{r}_j\right)\cdot d\,m \equiv \\ \equiv \dfrac{1}{2}\cdot{}^{j}\dot{\bar{\omega}}^{T}_j\cdot{}^{j}I^{*}_j\cdot{}^{j}\dot{\bar{\omega}}_j \end{array}\right\} \tag{37} $$

where ${}^{j}I^{*}_j$ represents the axial-centrifugal, inertial tensor, corresponding to the (j) kinetic element, with respect to $\{j\}$ frame.

The following two terms are identical:

$$ \left\{\begin{array}{l} \dfrac{1}{2}\cdot\displaystyle\int \left({}^{j}\dot{\bar{\omega}}_j \times {}^{j}\bar{r}_j\right)^{T}\cdot\left({}^{j}\bar{\omega}_j \times {}^{j}\bar{\omega}_j \times {}^{j}\bar{r}_j\right)\cdot d\,m = \\ = \dfrac{1}{2}\cdot\displaystyle\int \left({}^{j}\bar{\omega}_j \times {}^{j}\bar{\omega}_j \times {}^{j}\bar{r}_j\right)^{T}\cdot\left({}^{j}\dot{\bar{\omega}}_j \times {}^{j}\bar{r}_j\right)\cdot d\,m \end{array}\right\} \tag{38} $$

Performing a series of mathematical transformations in the equations above, (38), the result will be the following expression:

$$ \left\{\begin{array}{l} \left\{\dfrac{1}{2}\cdot\displaystyle\int \left({}^{j}\dot{\bar{\omega}}_j \times {}^{j}\bar{r}_j\right)^{T}\cdot\left({}^{j}\bar{\omega}_j \times {}^{j}\bar{\omega}_j \times {}^{j}\bar{r}_j\right) d\,m\right\} \equiv \\ \equiv \left\{\dfrac{1}{2}\cdot{}^{j}\dot{\bar{\omega}}^{T}_j\cdot\left[{}^{j}\bar{\omega}_j \times {}^{j}I^{*}_j\cdot{}^{j}\bar{\omega}_j\right]\right\} \end{array}\right\} \tag{39} $$

The last term of the acceleration energy is expressed by means of a matrixequation, as presented within the following expression:

$$ \left\{\begin{array}{l} \dfrac{1}{2}\cdot\displaystyle\int \left({}^{j}\bar{\omega}_j \times {}^{j}\bar{\omega}_j \times {}^{j}\bar{r}_j\right)^{T}\cdot\left({}^{j}\bar{\omega}_j \times {}^{j}\bar{\omega}_j \times {}^{j}\bar{r}_j\right)\cdot d\,m \equiv \\ \equiv \dfrac{1}{2}\cdot\bar{\omega}^{T}_j\cdot\left[{}^{j}\bar{\omega}^{T}_j\cdot Tr.\left({}^{j}I_{pj}\right)\cdot{}^{j}\bar{\omega}_j - {}^{j}\bar{\omega}^{T}_j\cdot{}^{j}I_{pj}\cdot{}^{j}\bar{\omega}_j\right]\cdot{}^{j}\bar{\omega}_j \end{array}\right\} \tag{40} $$

Substituting the above expression as well as (39) in the starting equation, is obtained:

$$\left\{\begin{array}{l} E_A^j(q_k\,;\ \dot{q}_k\,;\ \ddot{q}_k;\quad k=1\to j)= \\ =(-1)^{\Delta_M}\dfrac{1-\Delta_M}{1+3\cdot\Delta_M}\cdot\left\{\dfrac{1}{2}\cdot M_j\cdot{}^j\dot{\bar{v}}_{C_j}^T\cdot{}^j\dot{\bar{v}}_{C_j}\right\}+ \\ +\Delta_M^2\left\{\dfrac{1}{2}\cdot{}^j\dot{\bar{\omega}}_j^T\cdot\left\{{}^jI_j^*\cdot{}^j\dot{\bar{\omega}}_j+\left[{}^j\bar{\omega}_j\times{}^jI_j^*\cdot{}^j\bar{\omega}_j\right]\right\}+\right. \\ +\dfrac{1}{2}\cdot{}^j\dot{\bar{\omega}}_j^T\cdot\left[{}^j\bar{\omega}_j\times{}^jI_j^*\cdot{}^j\bar{\omega}_j\right]+ \\ +\dfrac{1}{2}\cdot\bar{\omega}_j^T\cdot\left[{}^j\bar{\omega}_j^T\cdot Tr.\left({}^jI_{pj}\right)\cdot{}^j\bar{\omega}_j-\right. \\ \left.\left.-\left[{}^j\bar{\omega}_j^T\cdot{}^jI_{pj}\cdot{}^j\bar{\omega}_j\right]\cdot{}^j\bar{\omega}_j\right]\right\} \end{array}\right\} \tag{41}$$

In the expression (41), ${}^jI_{pj}$ represents the so called *planar-centrifugal inertial tensor*.

The final expression, presented above, represents *the generalized and explicit form of the acceleration energy*. In the explicit form, of the acceleration energy, the following matrix operator will be applied:

$\Delta_M=\{-1;\ \ 0;\ \ 1\}$, where it takes the value $\Delta_M=-1$ in case the kinetic link is in a *General Motion*, $\Delta_M=0$ when the link is performing a *Translational Motion*, and $\Delta_M=1$ for the *Rotational Motion*.

3.2 The Matrix Expression of the Acceleration Energy

In keeping with [2, 3] it will be determined the *matrix expression* for the acceleration energy. For this, it is considered a kinetic link (i), represented in Fig. 1. The kinetic element, seen as a rigid body is divided into an infinite number of elementary masses, (dm), continuously distributed and positioned relative to$\{i\}$ and $\{0\}$ by position vectors presented in Fig. 1. The differential expression of the acceleration energy can be also written in the form presented bellow, such as:

$$\left\{\begin{array}{l} dE_A^i\equiv\left\{\dfrac{1}{2}\cdot Tr.\left\{\begin{pmatrix}{}^0\ddot{\bar{r}}_i\\0\end{pmatrix}\cdot\left({}^0\ddot{\bar{r}}_i^T\ \ 0\right)\right\}\cdot dm\right\}\equiv \\ \equiv\left\{\dfrac{1}{2}\cdot Tr.\left\{{}_i^0\left[\ddot{T}\right]\cdot\begin{pmatrix}{}^i\bar{r}_i\\1\end{pmatrix}\cdot\left({}^i\bar{r}_i^T\ \ 1\right)\cdot dm\cdot{}_i^0\left[\ddot{T}\right]^T\right\}\right\} \end{array}\right\}$$

The integral expression for the acceleration energy is obtained from applying the mass integral in the following equation:

$$E_A^i\equiv\frac{1}{2}\cdot Trace\left[{}_i^0\left[\ddot{T}\right]\cdot{}^iI_{psi}\cdot{}_i^0\left[\ddot{T}\right]^T\right] \tag{42}$$

${}^{i}I_{psi}$ represents the pseudoinertial tensor, which includes all masic moments of zero, first and second order. The second time derivative of locating matrix ${}^{0}_{i}\left[\ddot{T}\right]^{T}$ can be determined as follow:

$$ {}^{0}_{i}\left[\ddot{T}\right]^{(T)} \equiv \sum_{j=1}^{i} A_{ij}^{(T)} \cdot \ddot{q}_j + \sum_{j=1}^{i}\sum_{k=1}^{i} A_{ijk}^{(T)} \cdot \dot{q}_j \cdot \dot{q}_k \tag{43} $$

The differential matrices of first and second order are substituted by the exponential functions. The expressions are rewritten as:

$$ \left\{ \begin{array}{l} A_{ij} = A_{ij}\left[q_j(t); j = 1 \rightarrow i\right] \equiv \\ \equiv \left\{ \exp\left\{ \sum_{k=0}^{j-1} A_k \cdot q_k \right\} \right\} \cdot A_j \cdot \left\{ \exp\left\{ \sum_{l=j}^{i} A_l \cdot q_l \right\} \right\} \cdot T_{i0}^{(0)} \end{array} \right\} $$

$$ \left\{ A_{ijk} \equiv \left\{ \exp\left\{ \sum_{l=0}^{k-1} A_l \cdot q_l \right\} \right\} \cdot A_k \cdot A_{ijk}^{11} \cdot T_{i0}^{(0)} \right\}; $$

where A_{ijk}^{11} has the following expression:

$$ A_{ijk}^{11} = \left\{ \exp\left\{ \sum_{m=k}^{j-1} A_m \cdot q_m \right\} \cdot A_m \cdot \exp\left\{ \sum_{p=m}^{i} A_p \cdot q_p \right\} \right\} $$

Substituting the expressions for the differential matrices of first and second order presented above into the integral form of the acceleration energy, defined by means of the relation (42), it finally results a new explicit expression for the acceleration energy, that can be written in the following form:

$$ \left\{ \begin{array}{l} E_A\left(\bar{\theta}; \dot{\bar{\theta}}; \ddot{\bar{\theta}}\right) = \frac{1}{2} \sum_{i=1}^{n}\sum_{j=1}^{i}\sum_{m=1}^{i} Tr\left[A_{ij} \cdot {}^{i}I_{psi} \cdot A_{im}^{T}\right] \cdot \ddot{q}_j \cdot \ddot{q}_m + \\ \quad + \frac{1}{2} \sum_{i=1}^{n}\sum_{j=1}^{i}\sum_{k=1}^{i}\sum_{m=1}^{i} Tr\left[A_{ij} \cdot {}^{i}I_{psi} \cdot A_{ikm}^{T}\right] \cdot \ddot{q}_j \cdot \dot{q}_k \cdot \dot{q}_m + \\ \quad + \frac{1}{2} \sum_{i=1}^{n}\sum_{j=1}^{i}\sum_{k=1}^{i}\sum_{m=1}^{i} Tr\left[A_{ijk} \cdot {}^{i}I_{psi} \cdot A_{im}^{T}\right] \cdot \ddot{q}_m \cdot \dot{q}_j \cdot \dot{q}_k + \\ + \frac{1}{2} \sum_{i=1}^{n}\sum_{j=1}^{i}\sum_{k=1}^{i}\sum_{l=1}^{i}\sum_{m=1}^{i} Tr\left[A_{ijk} \cdot {}^{i}I_{psi} \cdot A_{ilm}^{T}\right] \cdot \dot{q}_j \cdot \dot{q}_k \cdot \dot{q}_l \cdot \dot{q}_m \end{array} \right\} $$

According to same [3] a set of notations of the dynamics matrices, are implemented:

$$ M\left(\bar{\theta}\right) = \left[M_{ij} \quad \begin{array}{l} i = 1 \rightarrow n \\ j = 1 \rightarrow n \end{array} \right] $$

$$\left\{ M_{ij} \equiv \sum_{k=\max(i;j)}^{n} Tr\left\{ M_{ij}^{11} \right\} \cdot T_{k0}^{(0)} \cdot {}^{k}I_{psk} \cdot A_{kj}^{T} \right\}; \tag{44}$$

$$M_{ij}^{11} \equiv \left\{ \exp\left\{ \sum_{j=0}^{i-1} A_j \cdot q_j \right\} \right\} \cdot A_i \cdot \left\{ \exp\left\{ \sum_{l=i}^{k} A_l \cdot q_l \right\} \right\};$$

$$V\left(\bar{\theta};\dot{\bar{\theta}}\right) = \left\{ \dot{\bar{\theta}}^{T} \cdot \begin{bmatrix} V_{ijm} & j = 1 \to n \\ & m = 1 \to n \end{bmatrix} \cdot \dot{\bar{\theta}} \; i = 1 \to n \right\}^{T}$$

$$V_{ijm} = \sum_{k=\max\,(i;j;m)}^{n} Tr\left\{ V''_{ijm} \right\} \cdot \left\{ \cdot T_{k0}^{(0)} \cdot {}^{k}I_{psk} \cdot A_{kjm}^{T} \right\} \tag{45}$$

$$V''_{ijm} \equiv \left\{ \exp\left\{ \sum_{j=0}^{i-1} A_j \cdot q_j \right\} \right\} \cdot A_i \cdot \left\{ \exp\left\{ \sum_{l=i}^{k} A_l \cdot q_l \right\} \right\}$$

$$C\left(\bar{\theta}\right) = \left\{ \begin{array}{c} V_{ijj} = \sum\limits_{k=\max\,(i;j)}^{n} Tr\left[A_{ki} \cdot {}^{k}I_{psk} \cdot A_{kjj}^{T} \right] \\ i = 1 \to n; \quad j = 1 \to n \end{array} \right\} \tag{46}$$

$$\left\{ \begin{array}{l} D\left(\bar{\theta};\dot{\bar{\theta}}\right) = \\ \left\{ \dot{\bar{\theta}}^{T} \cdot \begin{bmatrix} D_{ijlm} & l = 1 \to n \\ & m = 1 \to n \end{bmatrix} \cdot \dot{\bar{\theta}} \begin{array}{l} i = 1 \to n \\ j = 1 \to n \end{array} \right\} \end{array} \right\} \tag{47}$$

$$D_{ijlm} = \sum_{k=\max\,(i;j;l;m)}^{n} Tr\left\{ A_{kij} \cdot {}^{k}I_{psk} \cdot A_{klm}^{T} \right\} \tag{48}$$

$$A_{kij} = \left\{ \exp\left\{ \sum_{l=0}^{j-1} A_l \cdot q_l \right\} \right\} \cdot D_{ijlm}^{11} \cdot T_{k0}^{(0)}; \tag{49}$$

$$D_{ijlm}^{11} = A_j \cdot \left\{ \exp\left\{ \sum_{m=j}^{i-1} A_m \cdot q_m \right\} \cdot A_m \cdot \exp\left\{ \sum_{p=i}^{k} A_p \cdot q_p \right\} \right\}$$

The dynamics matrix, written above has the following significance: $V(\bar{\theta};\dot{\bar{\theta}})$ represents the column *vector* which contains the matrix of *Coriolis terms* $B\left(\bar{\theta}\right)$ and the matrix of *centrifugal terms* denoted $C\left(\bar{\theta}\right)$. The matrix $D(\bar{\theta};\dot{\bar{\theta}})$, represents the *pseudoinertial* or *pseudomass matrix* of acceleration energy. Substituting the

dynamics matrices in the expression of acceleration energy and performing the transformations, it results:

$$\left\{\begin{array}{l} E_A\left(\bar{\theta};\dot{\bar{\theta}};\ddot{\bar{\theta}}\right)=\frac{1}{2}\cdot\left[\ddot{\bar{\theta}}^T\cdot M\left(\bar{\theta}\right)\cdot\ddot{\bar{\theta}}+\right. \\ \left.+\ddot{\bar{\theta}}^T\cdot V\left(\bar{\theta};\dot{\bar{\theta}}\right)+\dot{\bar{\theta}}^T\cdot D\left(\bar{\theta};\dot{\bar{\theta}}\right)\cdot\dot{\bar{\theta}}\right] \end{array}\right\}; \tag{50}$$

$$\left\{\begin{array}{l} E_A\left(\bar{\theta};\dot{\bar{\theta}};\ddot{\bar{\theta}}\right)\equiv\frac{1}{2}\cdot\ddot{\bar{\theta}}^T\cdot\left\{M\left(\bar{\theta}\right)\cdot\ddot{\bar{\theta}}+\right. \\ \left\{+B\left(\bar{\theta}\right)\cdot\left[\dot{\bar{\theta}}\cdot\dot{\bar{\theta}}\right]\right\}+\frac{1}{2}\cdot\left\{+\ddot{\bar{\theta}}^T\cdot C\left(\bar{\theta}\right)\cdot\left[\dot{\bar{\theta}}^2\right]+\right. \\ \left.\left.+\dot{\bar{\theta}}^T\cdot D\left(\bar{\theta};\dot{\bar{\theta}}\right)\cdot\dot{\bar{\theta}}\right\}\right\}. \end{array}\right.$$

As it was presented in the third part of the paper, the expression in the generalized form (40) characterizes the acceleration energy answerable to every kinetic link. This equation contains all the *mass properties*, as well as the acceleration of the mass center, angular rotation velocity and acceleration respectively. But, the acceleration energy can be also determined by means of (41) which represent the integral expression of the acceleration energy obtained by applying the mass integral properties. Finally, extending the study about the mechanical system with n d.o.f., and then applying a few remarkable differential transformations, according to [1–8], it is obtained a new expression for the acceleration energy in a matrix form. The expression (50) represents the acceleration energy written in a matrix form based on dynamics matrices. The terms of this expression are developed in the expressions (44–49). As a conclusion, it comes to highlight the great advantages of using the matrix exponentials that refers to their compact form as well as the easy geometric visualization, and finally the fact that the results are not dependent on the moving frames attached to each kinetic link.

4 Conclusions

Based on the formulation within this paper, a fundamental notion in the robot dynamics has been analyzed. Using differential transformations and matrix exponentials, the acceleration energy has been developed in an explicit and matrix form. The explicit form can be applied in case of any rigid body regardless of motion performed by the kinetic link. The acceleration energy represents an important dynamic notion that can be further applied in order to determine the generalized inertia forces and dynamics equations for holonomic or non holonomic robotic systems, with rigid and elastic structure.

References

1. Negrean, I., Negrean, D.C.: Matrix exponentials to robot kinematics. 17th International Conference on CAD/CAM, Robotics and Factories of the Future, CARS&FOF 2001, vol. 2, pp. 1250–1257. Durban (2001)
2. Negrean, I., Negrean, D.C.: The acceleration energy to robot dynamics. Proceedings of A&QT-R (THETA 13) International Conference on Automation, Quality and Testing, Robotics, Tome II, pp. 59–64. Cluj-Napoca, Romania (May 2002)
3. Negrean, I., Duca, A., Negrean, D.C., Kacso, K.: Mecanica avansată în robotică. UT Press, Cluj-Napoca (2008). ISBN 978-973-662-420-9
4. Yuan, B.S., Huggins, J.D.: Dynamics of flexible manipulator arms: Alternative derivation, verification, and characteristics for control. ASME J. Dyn. Syst. Meas. Control 115, 394–404 (1993)
5. Li-Sheng, W., Yih-Hsing, P.: Appell's equation of motion for nonholonomic dynamical systems. Am. J. Phys 71(1), 72–82 (2003)
6. Ardema, M.D.: Analytical dynamics theory and applications, pp. 225–243/245–259. Springer, USA (2006). ISBN 978-0-306-48681-4
7. Chuev, M.A.: Differential equations of program motions of a mechanical system. Mech. Solids 43(1), 153–164 (2008). Allerton Press, Springer Science + Business Media LLC
8. Zhong, W.X.: Advances in Mechanics and Mathematics, vol.5. Springer, USA (2004). ISBN 978-1-4020-7880-4

Dynamics of a Parallel Platform for Helicopter Flight Simulation Considering Friction

D.L. Pisla, T.P. Itul, A. Pisla, and B. Gherman

Abstract In the paper the inverse dynamical model with friction of a 6-DOF parallel structure destined to helicopter flight simulation is presented using the Newton-Euler equations. The obtained dynamical algorithms offer the possibility of a complex study of the parallel structure in order to evaluate the dynamic capabilities and to generate the control algorithms. Using a numerical and graphical simulation the diagrams for the dynamics representation are computed and represented. The influence of the friction on the joint generalized forces is also studied in the paper.

Keywords Dynamics · Parallel platform · Flight simulator

1 Introduction

Parallel robots have some advantages over serial ones such as higher stiffness, very good precision, high speeds and accelerations, a better weight over payload rate. However, kinematic and dynamic analysis of the parallel structures is much more complicated due to the constraints and singularities presence [10].

Dynamics effects and analysis are the basis of design specification and advanced control of parallel mechanical systems. To establish the equations of motion, there exist essentially four methods: Newton-Euler equations; Lagrange equations of first kinds with so-called LAGRANGE multipliers; Lagrange equations of second kind with a minimum number of system coordinates; Virtual work formulation.

Until now, in the most existing papers, the experimental identification of dynamics for the parallel robots is restricted to simple models in combination

D.L. Pisla (✉)
Department of Mechanics and Computer Programming, Technical University of Cluj-Napoca, Cluj-Napoca, Romania

I. Vişa (ed.), *SYROM 2009*,
DOI 10.1007/978-90-481-3522-6_29,

with adaptive control algorithms [5, 7, 11, 20]. The most important force source which is not included is the friction.

A new approach was presented in [4], where Grotjahn et al. develop a complex dynamic model including friction, which uses Jourdain's principle of virtual power and is suited for the parallel robot control of the innovative hexapod PaLiDA. The friction model includes friction in both active joints as well in passive joints. Poignet et al. [17] deal with the application of the interval analysis to estimate the four-degrees of freedom parallel robot dynamic parameters. Yiu et al [20] developed the dynamics with friction for a planar redundant parallel robot.

Riebe et al. [19] present a dynamic model for a Stewart platform with six DOF, based on Newton-Euler equations including the frictional behavior. The parameters describing the friction model are identified and optimized. Chen et al. [2] present a dynamic model of a Cartesian guided tripod including the nonlinear compliance and mechanical friction. Quantitative analysis and comparison of the variation friction sources from the actuated joints and passive joints have been conducted. In [8, 9] different solutions for solving the dynamical model with friction for the guided in three points parallel robots are presented.

In [6] an analytical study of the kinematics and dynamics for the Stewart platform-based machine tool structures is presented.

It is estimated that the forces due to the friction could represent a certain part from the forces/torques which are necessary for the manipulator movement in typical situations. Thus it is necessary to model these friction forces in order to reflect in the dynamic equations the physical reality.

Generally, in the above mentioned contributions, the experimental identification of dynamics for the parallel robots is restricted to simple models in combination with adaptive control algorithms.

Flight simulators are extensively used by the aviation industry and the military for pilot training, disaster simulation and aircraft development. The different types of flight simulators range from video games up to full-size cockpit replicas mounted on hydraulic, electric or electromechanical actuators [1, 12].

Contrary to popular belief, flight simulators are not used to train pilots how to fly aircraft. Today's modern simulators are used by commercial airlines and the military alike, to familiarize flight crews in normal and emergency operating procedures. Using simulators, pilots are able to train for situations that they are unable to safely do in actual aircraft. These situations include loss of flight surfaces and complete power loss etc. In all cases **dynamics** plays a very important role for the behavior of parallel structures used as flight simulators.

It is widely acknowledged that the cues provided by a good visual system offer the bulk of realism in a flight simulator. It has also been shown that pilots consider the provision of consistent motion cues to add substantially to the realism of the simulation and to be helpful in the piloting task [18].

Thus, motion platforms are used on modern high-end flight simulators in order to provide motion cues consistent with the visual, auditory and control-feel cues to which the pilot is also subjected.

Within the motion-related subsystems, the most consistent research effort is over the washout subsystem which takes the motions generated by the aircraft equations including large displacements and filters to provide simulator motion-base commands. These commands must provide the pilot with realistic motion cues, while remaining within the simulator's motion limits [12].

In the paper the inverse dynamical model with friction of a 6-DOF parallel structure for helicopter flight simulation is presented using the Newton-Euler equations.

The paper is organized as follows: Section 2 is dedicated to the geometric model of the studied 6-DOF parallel structure; Section 3 deals with the kinematic modeling; Sections 4 and 5 present the dynamics without and with friction using Newton-Euler equations; Section 6 presents some simulation tests on a parallel platform; the conclusions of this work are detailed in the Section 7.

2 Geometrical Model

The general scheme of the parallel platform is presented in the Fig. 1 and the kinematic scheme of one chain in the Fig. 2.

In order to solve inverse geometric model, the positions of guiding points A_i (i = 1, 2, . . ., 6) are computed:

$$\bar{P}_i = \bar{P} + [R] \cdot \bar{p}_i; \quad i = 1, 2, ..., 6 \tag{1}$$

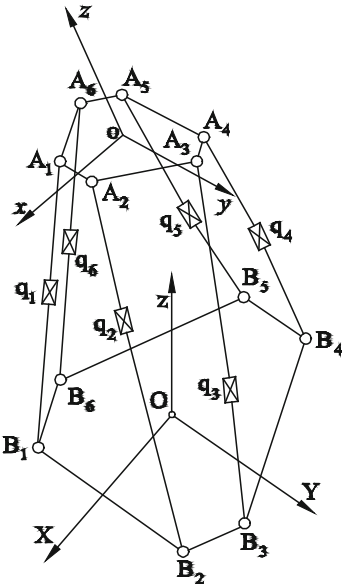

Fig. 1 The parallel platform

Fig. 2 One kinematic chain

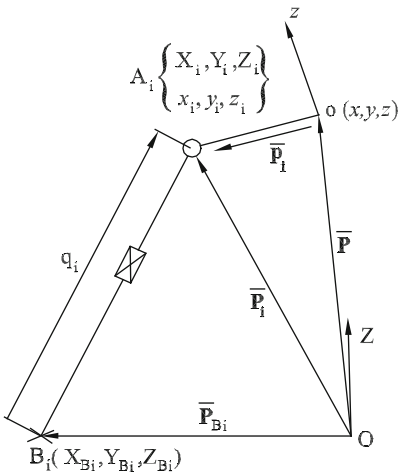

where [R] is the rotation matrix.

The generalized coordinates q_i of the mechanism could be considered even the leg lengths B_iA_i:

$$q_i = |\bar{P}_i - \bar{P}_{Bi}| \tag{2}$$

The direct geometric model is solved with the input-output equations:

$$(\bar{P} + [R] \cdot \bar{p}_i - \bar{P}_{Bi})^2 = q_i^2; \quad i = 1, 2, ..., 6 \tag{3}$$

The equations which express the constant distance between the guiding points are:

$$|\bar{P}_j - \bar{P}_i| = |\bar{p}_j - \bar{p}_i|; \; i, j = 1, 2, ..., 6, \; i \neq j \tag{4}$$

Using the Eqs. (2) together with (4), it yields a 18 equations system for the direct geometric model, which has as unknowns the absolute coordinates of points A_i.

The singularities of this parallel structure have been extensively discussed in [13].

3 Kinematic Model

The kinematic model yields through the differentiating of the input-output equations of the mechanism:

$$[A] \cdot \dot{\bar{X}} = [B] \cdot \dot{\bar{q}} \tag{5}$$

where:

$$[A] = \begin{bmatrix} \bar{e}_1^T & [(\bar{P}_1 - \bar{P}) \times \bar{e}_1]^T \\ \bar{e}_2^T & [(\bar{P}_2 - \bar{P}) \times \bar{e}_2]^T \\ \vdots & \vdots \\ \bar{e}_6^T & [(\bar{P}_6 - \bar{P}) \times \bar{e}_6]^T \end{bmatrix}; \; [B] = [I_6]$$

$$\dot{\bar{X}} = [\, \bar{v} \quad \bar{\omega} \,]^T = [\, \dot{X} \quad \dot{Y} \quad \dot{Z} \quad \omega_X \quad \omega_Y \quad \omega_Z \,]^T$$

$$\dot{\bar{q}} = [\, \dot{q}_1 \quad \dot{q}_2 \quad \dots \quad \dot{q}_6 \,]^T$$

$\bar{e}_i$ – the unit vector of the A_iB_i direction leg.
The relation (5) could be written in form:

$$\bar{v} = [J_v] \cdot \dot{\bar{q}}; \; \bar{\omega} = [J_\omega] \cdot \dot{\bar{q}} \tag{6}$$

In Fig. 3 an upper view of the parallel mechanism is illustrated with the geometric parameters and the axes unit vectors $\bar{u}_i$, $\bar{u}_i'$, $\bar{e}_i$.

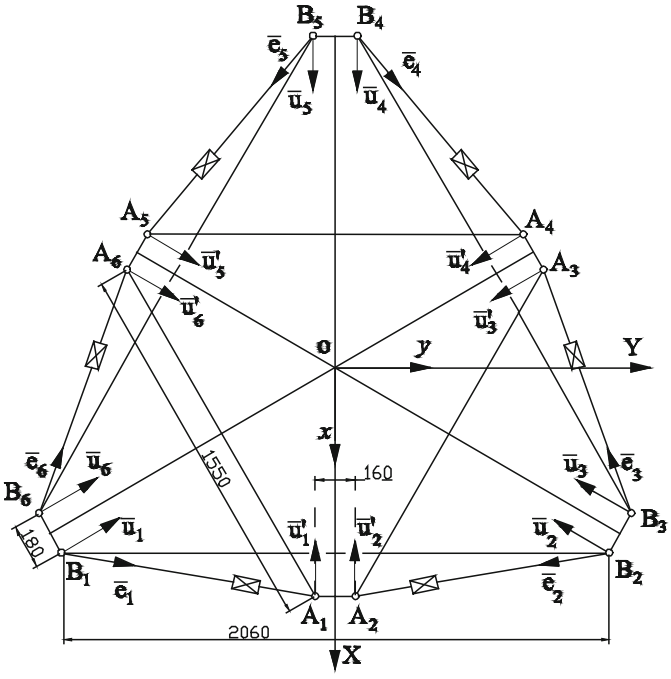

Fig. 3 Upper view of the platform

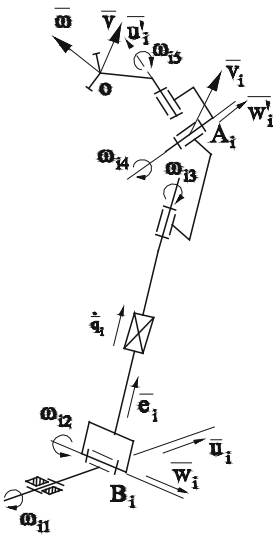

Fig. 4 "i"kinematic chain

The kinematic scheme of the "i" chain with joints representation is illustrated in Fig. 4.

The unit vectors of the joints 2 and 4 for the "i" chain have the expressions with respect to the OXYZ fixed system:

$$\bar{w}_i = \frac{\bar{u}_i \times \bar{e}_i}{|\bar{u}_i \times \bar{e}_i|};\ \bar{w}_i' = \frac{\left([R] \cdot \bar{u}_i'\right) \times \bar{e}_i}{\left|\left([R] \cdot \bar{u}_i'\right) \times \bar{e}_i\right|} \tag{7}$$

The relative velocities from passive joints of each chain will be computed. The first two relative rotation velocities are:

$$\bar{v}_i = \dot{q}_i \bar{e}_i + (\omega_{i1} \bar{u}_i + \omega_{i2} \bar{w}_i) \times q_i \bar{e}_i \tag{8}$$

and the other three from the equality:

$$\sum_{j=1}^{5} \bar{\omega}_{ij} = \bar{\omega} \tag{9}$$

It yields:

$$\omega_{ij} = \bar{a}_{ij} \cdot \bar{v} + \bar{b}_{ij} \cdot \bar{\omega}\,; \mathrm{i} = 1, 2, ..., 6;\ j = 1, 2, ...5 \tag{10}$$

where:

$$\bar{a}_{i1} = \frac{\bar{w}_i}{q_i|\bar{u}_i \times \bar{e}_i|};\ \bar{b}_{i1} = \frac{([R]\cdot\bar{p}_i)\times\bar{w}_i}{q_i|\bar{u}_i \times \bar{e}_i|};$$

$$\bar{a}_{i2} = \frac{\bar{w}_i \times \bar{e}_i}{q_i};\ \bar{b}_{i2} = \frac{([R]\cdot\bar{p}_i)\times(\bar{w}_i \times \bar{e}_i)}{q_i};$$

$$\bar{a}_{i3} = c_{i3}\bar{a}_{i1} + d_{i3}\bar{a}_{i2};\ \bar{b}_{i3} = \bar{e}_{i3} + c_{i3}\bar{b}_{i1} + d_{i3}\bar{b}_{i2};$$

$$c_{i3} = \frac{\left(\left([R]\cdot\bar{u}_i^{'}\right)\cdot\bar{u}_i\right)\cdot\left(\left([R]\cdot\bar{u}_i^{'}\right)\cdot\bar{e}_i\right) - \bar{u}_i\cdot\bar{e}_i}{1-\left(\left([R]\cdot\bar{u}_i^{'}\right)\cdot\bar{e}_i\right)^2};$$

$$d_{i3} = \frac{\left(\left([R]\cdot\bar{u}_i^{'}\right)\cdot\bar{w}_i\right)\cdot\left(\left([R]\cdot\bar{u}_i^{'}\right)\cdot\bar{e}_i\right)}{1-\left(\left([R]\cdot\bar{u}_i^{'}\right)\cdot\bar{e}_i\right)^2};$$

$$\bar{e}_{i3} = \frac{\bar{e}_i - \left(\left([R]\cdot\bar{u}_i^{'}\right)\cdot\bar{e}_i\right)\cdot\left([R]\cdot\bar{u}_i^{'}\right)}{1-\left(\left([R]\cdot\bar{u}_i^{'}\right)\cdot\bar{e}_i\right)^2};$$

$$\bar{a}_{i4} = c_{i4}\bar{a}_{i1} + d_{i4}\bar{a}_{i2}$$

$$\bar{b}_{i4} = \bar{e}_{i4} + c_{i4}\bar{b}_{i1} + d_{i4}\bar{b}_{i2}$$

$$c_{i4} = -\bar{u}_i\cdot\bar{w}_i^{'};$$

$$d_{i4} = -\bar{w}_i\cdot\bar{w}_i^{'};\ \ \bar{e}_{i4} = \bar{w}_i^{'};$$

$$\bar{a}_{i5} = c_{i5}\bar{a}_{i1} + d_{i5}\bar{a}_{i2}$$

$$\bar{b}_{i5} = \bar{e}_{i5} + c_{i5}\bar{b}_{i1} + d_{i5}\bar{b}_{i2}$$

$$c_{i5} = \frac{(\bar{u}_i\cdot\bar{e}_i)\left(\left([R]\cdot\bar{u}_i^{'}\right)\cdot\bar{e}_i\right) - \left([R]\cdot\bar{u}_i^{'}\right)\cdot\bar{u}_i}{1-\left(\left([R]\cdot\bar{u}_i^{'}\right)\cdot\bar{e}_i\right)^2};$$

$$d_{i5} = \frac{-\bar{w}_i\cdot\left([R]\cdot\bar{u}_i^{'}\right)}{1-\left(\left([R]\cdot\bar{u}_i^{'}\right)\cdot\bar{e}_i\right)^2}$$

$$\bar{e}_{i5} = \frac{[R]\cdot\bar{u}_i^{'} - \left(\left([R]\cdot\bar{u}_i^{'}\right)\cdot\bar{e}_i\right)\cdot\bar{e}_i}{1-\left(\left([R]\cdot\bar{u}_i^{'}\right)\cdot\bar{e}_i\right)^2};$$

4 Dynamic Model Without Friction

To study the dynamics without friction two simplifying hypothesis where adopted: all joints frictionless, the inertia of guiding legs B_iA_i is neglected.

For establishing the relationships between the drive generalized forces and the kinematic parameters of the mobile platform (on which the simulation cockpit is fixed) the Newton-Euler formalism is used (Fig. 5):

$$\begin{bmatrix} Q_1 \\ Q_2 \\ \vdots \\ Q_6 \end{bmatrix} = [A]^{-T} \cdot \begin{bmatrix} m\bar{a} + M\bar{a}_c - (m+M)\bar{g} \\ ([I_o] + [I_c]) \cdot \dot{\bar{\omega}} + \\ +\bar{\omega} \times (([I_o] + [I_c]) \cdot \bar{\omega}) + \\ +([R] \cdot \bar{p}_c) \times M(\bar{a}_c - \bar{g}) \end{bmatrix} \tag{11}$$

where:

Q_i – the drive generalized force from the B_iA_i leg;

m, M – the mass of the mobile plate, respectively of the (helicopter cockpit and pilots;

$\bar{g} = [\,0 \quad 0 \quad -9.806\,]^T$ – the gravitational vector;

$\bar{p}_c = \overline{oc}$ – position vector of the cockpit mass centre;

$\bar{a}_c = \bar{a} + \dot{\bar{\omega}} \times ([R] \cdot \bar{p}_c) + \bar{\omega} \times (\bar{\omega} \times [R] \cdot \bar{p}_c)$ – acceleration of the cockpit mass centre;

$[I_o]$ – inertia tensor of mobile platform about point "o";

$[I_c]$ – inertia tensor of the cockpit about point "c."

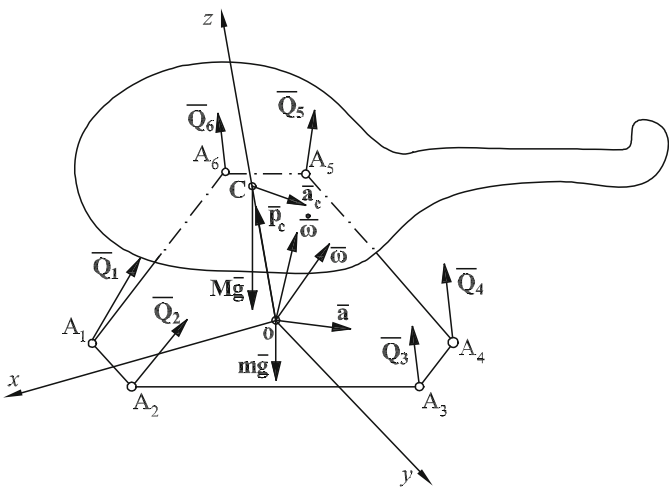

Fig. 5 Dynamic modeling of the parallel platform

5 Dynamic Model with Computation of Additional Drive Generalized Forces Caused by Friction

For the friction forces or torques evaluation the model of the viscous friction together with the model of Coulomb friction is chosen [3]. It is considered that the necessary torque from a rotation passive joint to win the friction has the relative velocity sense:

$$\begin{gathered} Mf_{ij} = c_j\omega_{ij} + \mu_j\frac{d_j}{2}|Q_i|\text{sgn}(\omega_{ij}); \\ i = 1,2,...,6;\ j = 1,2,...,5 \end{gathered} \tag{12}$$

where:

c_j – the viscous coefficient from rotational joint "j"; μ_j – the Coulomb friction coefficient from rotational joint "j"; d_j – the diameter of the "j" joint pin.

In the active prismatic joint the necessary force for win the friction could be given through the relation:

$$Qf_i^m = c_t\dot{q}_i + \mu_t|Q_i|\text{sgn}(\dot{q}_i);\ i = 1,2,...,6 \tag{13}$$

where: c_t – the viscous coefficient from active joint; μ_t – the Coulomb friction coefficient from the same joint.

In order to get the generalized drive forces which are necessary to overcome the friction from the passive joints, the principle of virtual power is applied:

$$\overline{Qf^p}\cdot\dot{\bar{q}} = \sum_{i=1}^{6}\sum_{j=1}^{5} Mf_{ij}\cdot\omega_{ij} \tag{14}$$

Taking into account from (6) and (10), it yields finally:

$$\begin{bmatrix} Qf_1^p \\ Qf_2^p \\ \vdots \\ Qf_{61}^p \end{bmatrix} = [J_v]^T\cdot\left(\sum_{i=1}^{6}\sum_{j=1}^{5} Mf_{ij}\cdot\bar{a}_{ij}\right) + [J_\omega]^T\cdot\left(\sum_{i=1}^{6}\sum_{j=1}^{5} Mf_{ij}\cdot\bar{b}_{ij}\right) \tag{15}$$

The total active generalized forces are:

$$Q_i^m = Q_i + Qf_i^m + Qf_i^p + m_s\ddot{q}_i \tag{16}$$

where $m_s$is the leg upper part mass.

6 Simulation Results

The achieved kinematic and dynamic algorithms have been implemented in the developed simulation system [14–16]. It consists of five main modules: Kinematics; Singularities; Workspace; Trajectory, Dynamics. Within the system the virtual graphical model was created, the 3D functional model allows the designer to understand its functionality (Fig. 6). The geometric parameters can be modified within the 3D modeling software influencing the simulation environment. The assembly relations between the parts, subassemblies and between parts and sub-assemblies can be also modified. These facilities enable the possibility to develop complex relations between the shape of the workspace, links and geometrical dimensions in order to optimize the parallel structure. The obtained results are useful for the designers in understanding the workspaces characteristics distribution and parallel robots optimization.

For the simulation have been considered six simple motions along and around the reference system axes with the harmonic laws: X, Y, Z - $1.8 = 0.3 \cos(\pi \cdot t)$, respectively α, β, $\gamma = \frac{\pi}{9} \cos(\pi \cdot t)$ and the following input inertia and friction data for the parallel mechanism, which correspond to the real Stewart platform, which is located at the Systems Dynamics Simulation Laboratory Technical University of Cluj-Napoca [21] (Fig. 7):

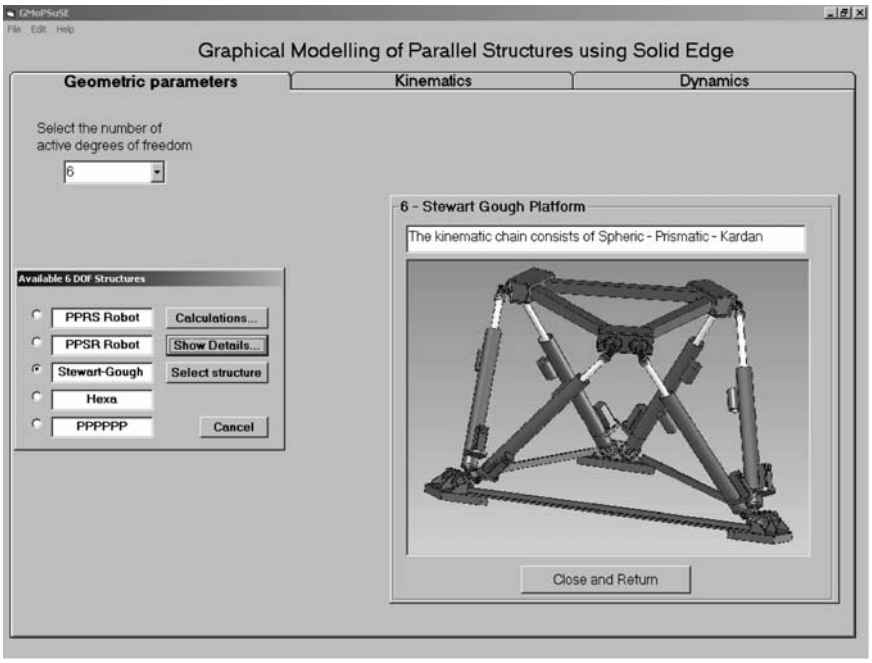

Fig. 6 The developed simulation program

Fig. 7 The parallel platform

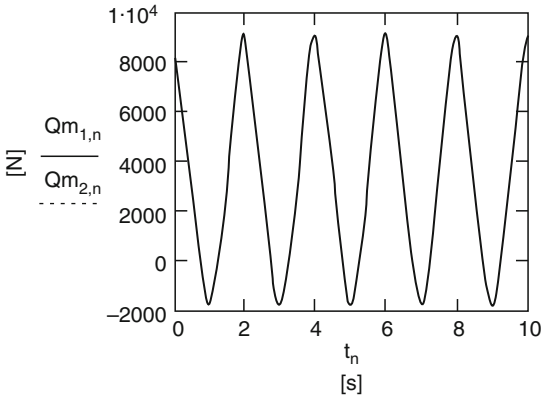

Fig. 8 The total generalized active forces

$$m = 300\,kg;\ M = 1500kg;\ m_s = 25\,kg;$$

$$d_j = 0,024\,m;\ I_x = I_y = 37,5\,kg\,m^2;$$

$$I_z = 75\,kg\,m^2;\ I_{xc} = 384\,kg\,m^2;$$

$$I_{yc} = I_{zc} = 624\,kg\,m^2;\ c_t = 0,005\,\frac{N\,s}{m};$$

$$\mu_t = \tan(3^0) = 0,05241;\ c_j = 0,003\,\frac{N\,m\,s}{rad};\ \mu_j = \frac{4}{\pi}\,\mu_t.$$

In Fig. 8 the diagrams of the total generalized forces from the legs 1 and 2 for the pitch motion (around the OY axis) are presented.

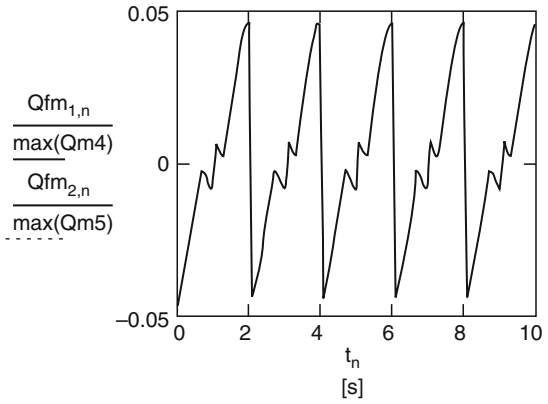

Fig. 9 The fraction of generalized forces due by the friction

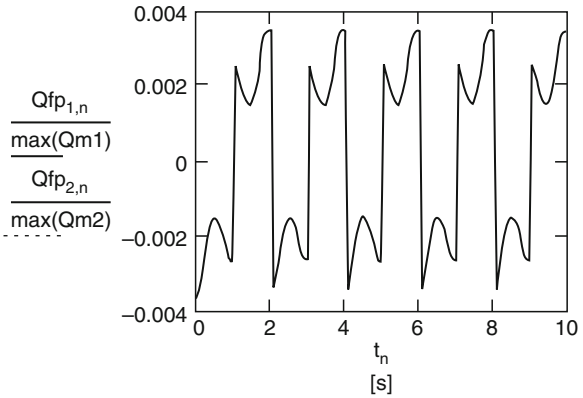

Fig. 10 The fraction of generalized forces due by the friction from passive joints

In the Fig. 9 the fraction between the generalized forces due to the friction and the maximal total generalized forces from the same legs are illustrated. In the Fig. 10 the time history of the fraction between generalized forces due to the friction from the passive joints and the maximal total generalized forces are shown.

7 Conclusions

This paper presents the dynamics of a parallel platform for helicopter flight simulation. The dynamic models without and with friction are obtained. Using a numerical and graphical simulation, the diagrams for the dynamics representation

are computed. The results have shown that the total friction effect is about 5% and the friction from the passive joints is under 0.4%. It is happened for all studied parallel platform motions. The dynamical algorithms offer the possibility of a more complex dynamic study in comparison with existing simple dynamic models.

Acknowledgments This research was financed from the research grants awarded by the Romanian Ministry of Education and Research.

References

1. Andreev, A. N., Danilov, A. M.: Information models for designing, conceptual broad-profile flight simulators. Meas. Tech. 43(8), 2000
2. Chen, J.-S., Yao-Hung, K., Hsu, W.-Y.: The influence of friction on contouring accuracy of a Cartesian guide tripod machine tool. Int. J. Adv. Manuf. Technol 30, 470–478
3. Craig, J.J.: Introduction to Robotics. Mechanics and Control. Addison-Wesley, New York (1989)
4. Grotjahn, M., Heimann, B., Abdellatif, H.: Identification of friction and rigid-body dynamics of parallel kinematic structures for model-based control. Multibody Syst Dyn. 11(3), 273–294 (2004)
5. Guégan, S., Khalil, W.: Dynamic modeling of the orthoglide. In: Lenarcic, J., Thomas, F. (ed.) Advances in Robot Kinematics, pp. 387–396. Kluwer, Netherlands (2002)
6. Harib, K., Srinivasan, K.: Kinematic and dynamic analysis of Stewart platform-based machine tool structures. Robotica 21(5), 541–554 (2003)
7. Honneger, M., Codourey, A., Burdet, E.: Adaptive control of the Hexaglide, a six d.o.f. parallel manipulator. IEEE International Conference on Robotics and Automation, pp. 543–548. Albuquerque (1997)
8. Itul, T., Pisla, D., Pisla, A.: Dynamic model of a 6-DOF parallel robot by considering friction effects. 12th IFToMM World Congress. Besançon, France, 18–21 June 2007
9. Itul, T., Pisla, D.: The influence of friction on the dynamic model for a 6-DOF parallel robot with triangular platform. J. Vibroeng. 9, 24–29 (2007)
10. Itul, T., Pisla, D.: Kinematics of a three degrees of freedom parallel structure with applications for the satellite antenna orientation, pp. 197–202. RAAD2005, Bucharest (2005)
11. Merlet, J.-P.: Parallel robots. Kluwer, Dordrecht (2000)
12. Nahon, M.A., Gosseli: A comparison of flight simulator motion – base architectures. J. Mech. Design 122, 17–24 (2000)
13. Pernkopf, F., Husty, M.L.: Singularity analysis of spatial Stewart-Gough platforms with planar base and platform. Proceedings of ASME Design Engineering Technology Conference. Montreal, Canada (2002)
14. Pisla, D. L.: Kinematic and dynamic modeling of parallel robots. Dacia, Romania (2005)
15. Pisla, A., Plitea, N., Prodan, B.: Modeling and simulation of parallel structures used as flight simulators. Proceedings of TMT2007. Tunisia (2007)
16. Plitea, N., Pisla, A., Pisla, D., Prodan, B.: Dynamic modeling of a 6-dof parallel structure destinated to helicopter flight simulation. Proceedings of ICINCO 2008. Madeira (2008)
17. Poignet, Ph., Ramdani, N., Vivas, O.A.: Robust estimation of parallel robot dynamic parameters with interval analysis, pp. 6503–6508. 42nd IEEE Conference on Decision and Control. Hawaii USA (2003)
18. Reid, L.D., Nahon, M.A.: Response of airline pilots to variations in flight simulator motion algorithms. J. Aircraft 25(7), 639–646 (1998)

19. Riebe, S., Ulbrich, H.: Modeling and online computation of the dynamics of a parallel kinematic with six degrees-of-freedom. Arch. Appl. Mech. **72**, 817–829 (2003)
20. Yiu, Y.K., Li, Z.X.: Dynamics of a plannar 2-dof redundant parallel robot, pp. 339–343. International Conference on Mechatronics Technology. Singapore (2001)
21. Motion Technology. Available at: http://www.boschrexroth.com/business_ _units/bri/sub-websites/ systems_engineering/ en/ Industry_ Segments/ Motion_ Technology / index.jsp.

One D.O.F. Parallel Manipulator Based on Bricard Rectangular Mechanism

L. Racila

Abstract A new application of Bricard rectangular mechanism is being presented in this paper. If three of the six revolute joints are imposed to remain in a fixed horizontal plane, a translation movement is obtained for the plane defined by the other three joints. For this spatial disposition, an analytical analysis is presented and the variation of the distance between the horizontal plane and the mobile plane is studied according to the input parameters.

Keywords Overconstrained mechanism · Kinematics · Translator · Industrial application

1 Introduction

Overconstrained mechanisms with revolute joints are composed by four, five or six joints. A mechanism with six revolute joints is considered in this paper, more precisely Bricard rectangular mechanism.

Bricard mechanisms are the only ones to be independent, the other overconstrained mechanisms with revolute joints are combinations of the mechanisms with four, five or six revolute joints. In 1897, three types of octahedral linkages: the line-symmetric, the plane-symmetric and the double collapsible octahedral linkages are described by Raoul Bricard in his paper [2]. Thirty later years, he makes the point on "paradoxical" mechanisms [3] and three mechanisms with six revolute joints: the line-symmetric, the plane-symmetric and the trihedral (rectangular) mechanism are being presented. An analyze of these mechanisms has been made by J. E. Baker

L. Racila
Department of Applied Mechanics, University of Craiova, Craiova, Romania

I. Vişa (ed.), *SYROM 2009*,
DOI 10.1007/978-90-481-3522-6_30,

in 1980 [1], who gives the closure equations for all these mechanisms [4, 7, 11, 13]. In 1987, a new mechanism is presented by K. Wohlhart that is considered as a generalization of Bricard rectangular mechanism, called Wohlhart mechanism [12].

Overconstrained mechanisms have always been studied by researchers, but only for its kinematical properties. From the industrial point of view, excepting the "Turbula" mechanism [10] that is inspired from Bricard rectangular mechanism and deployable structures of Gan and Pellegrino [6], overconstrained mechanisms with six revolute joints have not found places in industry.

In this paper, Bricard rectangular mechanism is shown in a new spatial disposition. The mechanism base for this translator is the Bricard rectangular mechanism in a particular case where all links are the same length. We call this mechanism Bricard symmetric rectangular mechanism (or Wohlhart symmetric mechanism). In this case, three joints will be constrained to remain in a fixed plane, the horizontal plane. By imposing a linear movement to these three joints from the center of the circumscribed circle, a movement for the three others joints is obtained, in a plane that will remain parallel with the horizontal plane.

Such a mobile platform was presented by Racila and Dahan [9], having as input parameter the movement of the actuated joints in the fixed horizontal plane. In this paper the input parameter is the movement of the intersecting point of actuated joints axes, this new configuration giving much precision then others.

2 Closure Equations

The Denavit-Hartenberg terminology [5] for a mechanism with revolute joints (Fig. 1) is being used.

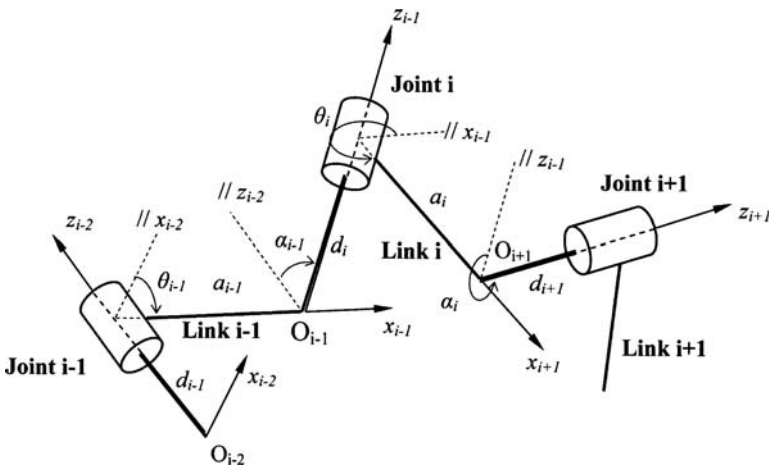

Fig. 1 Denavit – Hartenberg parameters

The following geometrical conditions are considered, in the particular case of Bricard symmetric rectangular mechanism:

$$\begin{cases} d_1 = d_2 = d_3 = d_4 = d_5 = d_6 = 0 \\ \alpha_1 = \alpha_3 = \alpha_5 = \dfrac{\pi}{2} \\ \alpha_2 = \alpha_4 = \alpha_6 = \dfrac{3\pi}{2} \\ a_1 = a_2 = a_3 = a_4 = a_5 = a_6 = a \end{cases} \tag{1}$$

A 12 equations system can be obtained from the closure of the kinematics chain, which can be reduced to a single one [8], between the input angle θ ($\theta_1 = \theta_3 = \theta_5 = \theta$) and the output angle φ ($\theta_2 = \theta_4 = \theta_6 = \varphi$):

$$\cos\theta \cdot \cos\varphi + \cos\theta + \cos\varphi = 0 \tag{2}$$

Is interesting to be noted the fact that the input-output equation is symmetrical in θ and φ, so the output angle can also serve as input angle.

3 New Spatial Disposition

A Bricard symmetric rectangular mechanism is now considered, but not in its classical position, with one fixed element, but in a new one, with no fixed elements.

In this new position, three revolute joints O_1, O_3 and O_5 are constrained to remain in the horizontal plane (Fig. 2).

It will be shown that the three odd joints O_1, O_3 and O_5 have movements on the heights of their circumscribed circle, the others three joints O_2, O_4 and O_6 always being in a parallel plane with the horizontal plane.

For clarity, the horizontal plane of the movement (Fig. 3) is being presented.

Is noted:

– By subscript of the letter O – the number of the joint;

– By superscript of the letter O – the joint position in its displacement.

The mechanism in its first position (in initial position the input angle is $\theta = 0°$, noted here with superscript 1) is represented by the triangle $O_1^1O_3^1O_5^1$ and by the $O_2^3O_4^3O_6^3$ triangle for its final position (in this position the input angle is $\theta = 120°$, noted here with superscript 3). An intermediary position is represented by the triangle $O_1^2O_3^2O_5^2$ (superscript 2).

In the positions 1 and 3, all the points of mechanism are in the same horizontal plane. In the intermediary position 2, the mechanism has a spatial position. The movement of actuated joints O_1, O_3 and O_5 is symmetrical; the three joints have the equal displacement in equal time.

The movement began in the first position (Fig. 3 – superscript 1), when the input angle is $\theta = 0°$ and all the six links are in the horizontal plane, making an equilateral

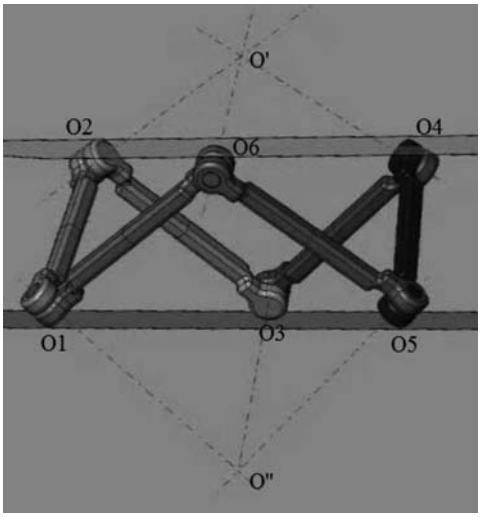

Fig. 2 CAD simulation of manipulator in intermediary position

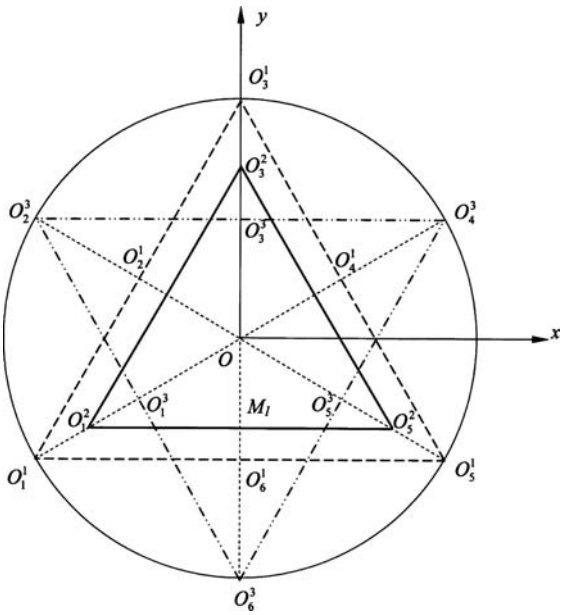

Fig. 3 Horizontal plane of movement

triangle. When the input angle θ is increased, the even joints start their movement and the planes that these joints make are always parallel with the horizontal one. Continuing the movement, the even joints attempt a maximum height (Figs. 2 and

3 – superscript 2) and then it follows the descending one, when the even joints attempt finally the horizontal plane (Fig. 3 – superscript 3) in the final position 3, when the input angle is $\theta = 0^\circ$.

OO" distance is considered as input parameter, between the intersecting point of actuated joint axes and the horizontal plane. This distance is noted by z. The equality of $O''O_1^2$, $O''O_5^2$ and $O''O_3^2$, segments is proven by the mechanisms' symmetry and some elementary calculus [8].

So, when OO" distance varies, the $O''O_1^2$, $O''O_5^2$, and $O''O_3^2$ distances vary, giving a movement to the actuated odd joints and so the b distance will be varying also (Fig. 4).

But when the b distance is varying, the even joints make displacements in parallel planes with the horizontal plane.

The distance h_{246} between the two planes, the horizontal plane (135) and the mobile plane (246) according to the input parameters z is [8]:

$$h_{246} = \sqrt{\frac{[m(z) - 2 \cdot a^2] \cdot [8 \cdot a^2 - m(z)]}{6 \cdot m(z)}} \tag{3}$$

with the notation $m(z) = a^2 - 3 \cdot z^2 + \sqrt{(a^2 - 3 \cdot z^2)^2 + 48 \cdot a^2 \cdot z^2}$

The curves of variation for h_{246} according to the distance z are given in the Fig. 5 for three values of the links length a (a = 40, a = 80, a = 120).

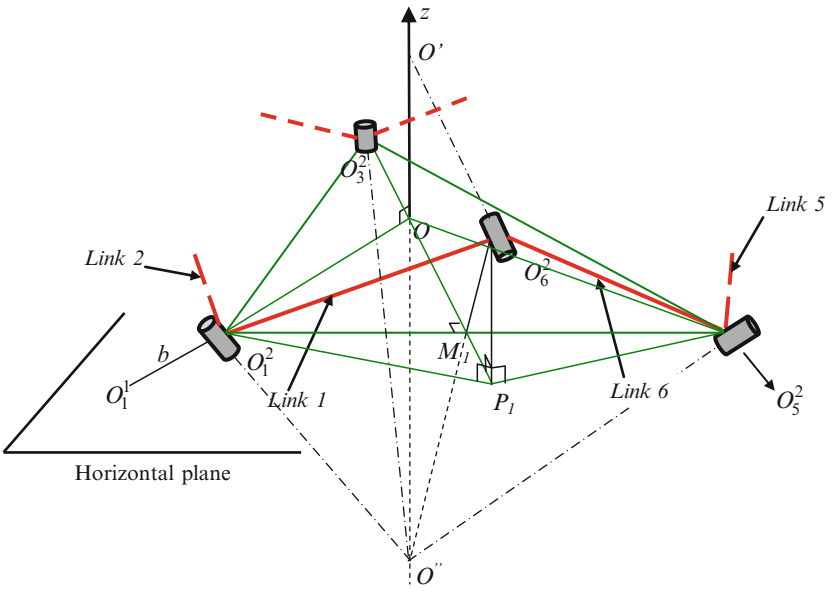

Fig. 4 Intermediary position

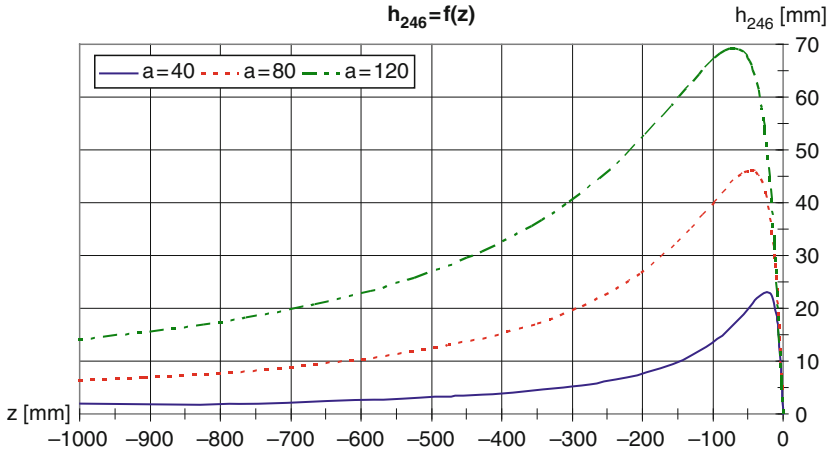

Fig. 5 Variation of the distance h_{246} according to z

Fig. 6 First prototype of translator

4 Conclusion

New perspectives for industrial applications based on overconstrained mechanisms are given by this one d.o.f. translator. This device can be used with a good precision in optical devices, for example. Such a mobile platform has a good precision to the order of 1:100–1:1000 (depending of the links length and O"O_i segments). A great advantage of this 6R translator is given by an important surface in translation defined by the three support points.

Two prototypes have been realized until now. For these prototypes the input parameter is the distance b (Figs. 6 and 7).

Fig. 7 Second prototype of translator

To increase the precision it must be considered, as input parameter, the distance z.

Of course, in this second case, it remains the delicate technological aspects to make from this device a real application capable to assure a given task in a production chain.

References

1. Baker, J.E.: An analysis of the Bricard linkages. Mech. Mach. Theory **15**, 267–286 (1980)
2. Bricard, R.: Mémoire sur la théorie de l'octaèdre articulé. J. de Mathématiques pures et appliquées, Liouville 3, 113–148 (1897)
3. Bricard, R.:"Leçons de Cinématique," Tome II – Cinématique Appliquée. Gauthier–Villars, Paris (1927)
4. Dietmaier, P.: A new 6R space mechanism. Proceedings of 9th world congress on the theory of machines and mechanisms, vol. 1, pp. 52–56. Milano, Italy (1995)
5. Denavit, J., Hartenberg, R.S.: A kinematic notation for lower–pair mechanism based on matrices. J Appl. Mech. **22**, 215–221 (1955)
6. Gan, W.W., Pellegrino, S.: "Closed-loop deployable structures," AIAA 2003–1450. Proceedings of 44th AIAA/ASME/ASCE/AHS/ASC structures. Structural dynamics, and materials conference, Norfolk, 7–10 April 2003
7. Mavroidis, C., Roth, B.: Analysis and synthesis of overconstrained mechanisms. Proceedings of the 1994 ASME design technical conferences, vol. DE-70, pp. 115–133. Minneapolis (September 1994)
8. Racila, L.: Existence et cinématique des mécanismes articulés spatiaux à six barres. Ph.D. dissertation, University of Franche-Comte, Besançon (2006)
9. Racila, L., Dahan, M.: Bricard mechanism used as translator. Proceedings of 12th world congress IFToMM, vol. 3, pp. 337–341. Besançon, France (Juin 2007)
10. Schatz, P.: Rhytmusforschung und Technik. Verlag freies Geistesleben, Stuttgart (1975)

11. Waldron, K.J.: Overconstrained linkages. Environment and planning B, vol. 6, pp. 393–402, 1979
12. Wohlhart, K.: A new 6R space mechanism. Proceedings of the 7th world congress IFToMM, vol. 1, pp. 193–198. Sevilla, Spain (1987)
13. Wohlhart, K.: The two types of the orthogonal Bricard linkage. Mech. Mach. Theory **28**, 809–817 (1993)

Theoretical and Experimental Research on the Dynamics of a 4DOF Isoglide 4-T3R1 Parallel Robot

N. Rat, M. Neagoe, and G. Gogu

Abstract The paper deals with the theoretical and experimental study of the kinematic and dynamic behaviour of a four DOF Isoglide4-T3R1 parallel robot with decoupled translation motions. The Lagrange with multipliers method was successfully applied to derive the closed-form dynamic model using the Maple software. Next, an equivalent dynamic virtual model of the Isoglide4-T3R1 parallel robot was developed and simulated in ADAMS program on different established trajectories. The theoretical dynamic models (closed-form model and ADAMS numerical approach) were validated through dynamic experimental testing carried out on the Isoglide4-T3R1 parallel robot prototype developed at French Institute of Advanced Mechanics (IFMA), France. Finally, relevant conclusions regarding the Isoglide4-T3R1 dynamic behaviour are presented.

Keywords Experimental research · Kinematic and dynamic analysis · Modelling and simulation · Parallel robot

1 Introduction

In the last years, the parallel robots used like tackle machines, manipulators, etc., began to have a great industrial importance. In comparison with serial robots, the parallel robots have some advantages like: high rigidity, good rapport payload/masse of the robot, high mechanical stiffness, etc.

The parallel robots have begun to make the object of study in priority at the last three decades. In this period, important contributions were done specially on the parallel robot modelling: kinematics [1–4] and dynamics [5].

N. Rat (✉) and M. Neagoe
Department of Product Design and Robotics, Transilvania University of Braşov, Braşov, Romania
G. Gogu
French Institute of Advanced Mechanics, Clermont-Ferrand, France

I. Vişa (ed.), *SYROM 2009*,
DOI 10.1007/978-90-481-3522-6_31,

Because the parallel robots are closed kinematics chains, constituted by a mobile platform with *n* degree of freedom, connected to the fixed base by serial or complex kinematics chains, the dynamic modelling proves to be complex even in the rigid body hypothesis.

Regarding the dynamic modelling of the parallel robots, different methods can be applied. A method using the Lagrange – D'Alembert formulation has been applied by Yen and Lai [11] for obtaining the dynamic equations of a 3-DOF translational parallel robot.

The virtual work principle was usefully applied by Wu et al. [12] for obtaining the dynamic equation for a 3DOF parallel robot and the obtained driving forces were optimized by applying the least-square method.

Li and Xu [13] derived the analytical dynamic model of a translational parallel robot using the dynamic equations obtained via the virtual work principle and validated on a virtual prototype with the ADAMS software.

In this paper, a kinematic and dynamic modelling for the Isoglide4-T3R1 parallel robot is presented [14]. The Lagrange method with multipliers was used to derive the closed form dynamic model in the rigid links hypothesis. Based on numerical examples, the dynamic closed form models were validated through MBS prototyping in ADAMS environments.

2 On the Kinematics of the Isoglide4-T3R1 Parallel Robot

The parallel robot Isoglide4-T3R1 (Fig. 1) has four degrees of freedom (DOF) and uncoupled translational motions. This parallel robot has four elementary legs A, B, C and D (Fig. 1), connected to the mobile platform by revolute joints and to the fixed base by linear motors (translational joint). Each elementary leg has four passive rotational joints and one active translational joint.

This parallel robot is one of a family of parallel robot with N = 2 number of overconstraints [6].

More details concerning the calculation of mobility, spatiality and number of overcontraints for this type of parallel robots are presented in [7] and [8].

The formulae for mobility calculation founded on Chebychev – Grübler-Kutzbach's criterion do not work for this parallel robot [9,10]. More general formulae, applicable to the parallel robots, have been recently proposed and demonstrated in [7] and [8].

The mobile platform has three uncoupled translations ($v_x = \dot{q}_1, v_y = \dot{q}_2, v_z = \dot{q}_3$) and one coupled rotation $\omega_y = a(\dot{q}_4 - \dot{q}_3)$ where $a = 1/r\cos(\varphi_y)$ and $r = \mathrm{HG}$ is the length of the mobile platform.

The variable angle φ_y (Fig. 1) depends on the difference between the position of the two z axis vertical motors (q_3 and q_4).

The moving platform velocities are related to the velocities $[\dot{q}]$ of the actuated joints by the general equation:

$$ {}^{p}\begin{bmatrix} v \\ w \end{bmatrix}_{H} = [J] \cdot \begin{bmatrix} \dot{q} \end{bmatrix} \tag{1} $$

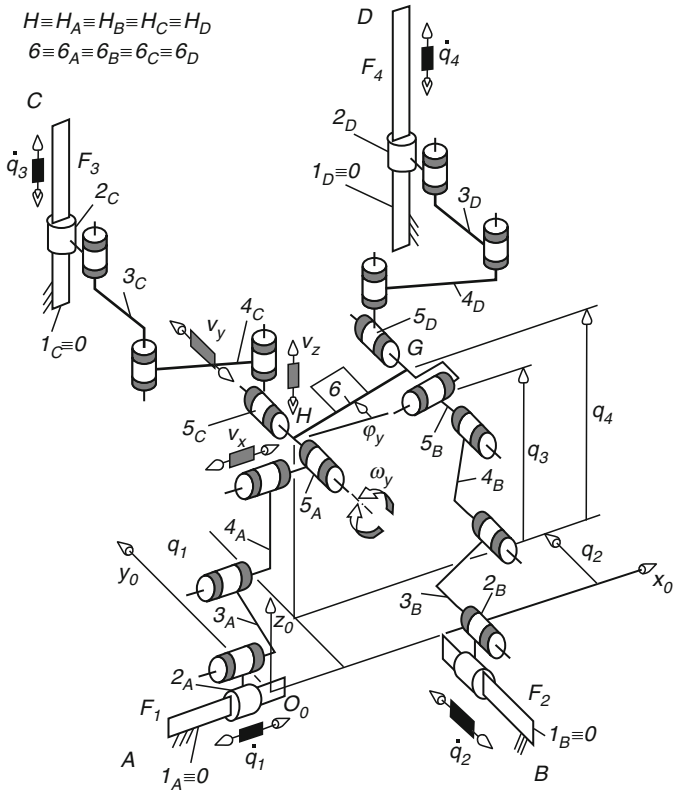

Fig. 1 The kinematical structure of Isoglide4-T3R1 parallel robot [8]

where : $[v] = [\, v_x \quad v_y \quad v_z \,]^T$ is the velocity of the point H belonging to the moving platform; $[w] = [\, w_x \quad w_y \quad w_z \,]^T$ is the angular velocity of the moving platform; $[J]$ is the Jacobian matrix and p is the coordinate system in which the velocities of the moving platform with respect to the fixed platform are expressed.

For the studied parallel robot the kinematical model is given by:

$$p \begin{bmatrix} v_x \\ v_y \\ v_z \\ w_y \end{bmatrix}_H = [J] \begin{bmatrix} \dot{q}_1 \\ \dot{q}_2 \\ \dot{q}_3 \\ \dot{q}_4 \end{bmatrix}, \tag{2}$$

where:

$$[J] = \begin{bmatrix} 1 & 0 & 0 & 0 \\ 0 & 1 & 0 & 0 \\ 0 & 0 & 1 & 0 \\ 0 & 0 & 0 & \frac{1}{r\cos(\varphi)} \end{bmatrix}$$

3 Dynamic Modelling of the Isoglide4-T3R1 Parallel Robot

The dynamic modelling has been done in the premises of: (a) the gravity vector is oriented in negative sense of the z axis, and (b) no external load on the moving platform.

Considering rigid elements with distributed masses, the dynamic model was derived using the Lagrange multipliers method:

$$\sum_{i=1}^{k} \lambda_i \frac{\partial \Gamma_i}{\partial q_j} = \frac{d}{dt}\left(\frac{\partial L}{\partial \dot{q}_j}\right) - \frac{\partial L}{\partial q_j} - \hat{Q}_j, \tag{3}$$

Where λ_I are the Lagrange multipliers;
q_j – displacement of the actuators;
$\hat{Q}_j$ – generalized external forces;
L – parallel robot Lagrangean:

$$L = \sum_{i=1}^{n} K_i + \sum_{i=1}^{n} P_i, \tag{4}$$

where: K_i is the kinetic energy of the link i; P_i – the potential energy of the link i.

The Lagrange multipliers λ_i are identified introducing a set of 13 geometric equations with 17 kinematic parameters (13 dependent joint variable and four independent joint variables):

- The position of the characteristic point H(X_H, Y_H, Z_H) of the mobile platform (element 6) must be the same for the arms A and C (three equations);
- The position of the point G (X_G, Y_G, Z_G) must be the same for the arms B and D (three equations);
- The distance between the point H and G is a constant r (one equation);
- The points H and G have the same coordinate Y (one equation);
- The sum of the first three rotational dependent joint variables of each of the A, C and D arms is zero (three equations);
- The sum of the first three rotational joints variables of the B arm must be equal with angle φ (one equation);
- The orientation angle φ is done by: $\sin(\varphi) = \frac{q_3 - q_4}{r}$ (one equation).

Finally, the analytical expression of the driving forces F_1, F_2, F_3 and F_4 (Fig. 1) are obtained applying the dynamic algorithm into a specific Maple application;

4 Virtual Model and Experimental Testing of the Isoglide4-T3R1 Parallel Robot

Starting from the prototype of Isoglide4-T3R1 (Fig. 2a) accomplished at LaMI laboratory of IFMA, France, a virtual ADAMS model was obtained (Fig. 2b).

Fig. 2 The prototype (**a**) and the virtual model (**b**) of the Isoglide4 – T3R1 parallel robot

4.1 Isoglide4-T3R1 CAD Model

The real prototype was made using the parts designed in CATIA software.

The virtual prototype (Fig. 3) was developed in ADAMS software using the parts imported from CATIA. For each part, the same inertial proprieties were taken in consideration (masses and inertial moments). In this way, the same forms, the same materials and the same proprieties for each part from the CAD model and real prototype are maintained.

The CAD model has the same reference coordinate system as the physical prototype, with the origin O_0 placed at intersection of the axes of the motors M_1 and M_2 (Fig. 3).

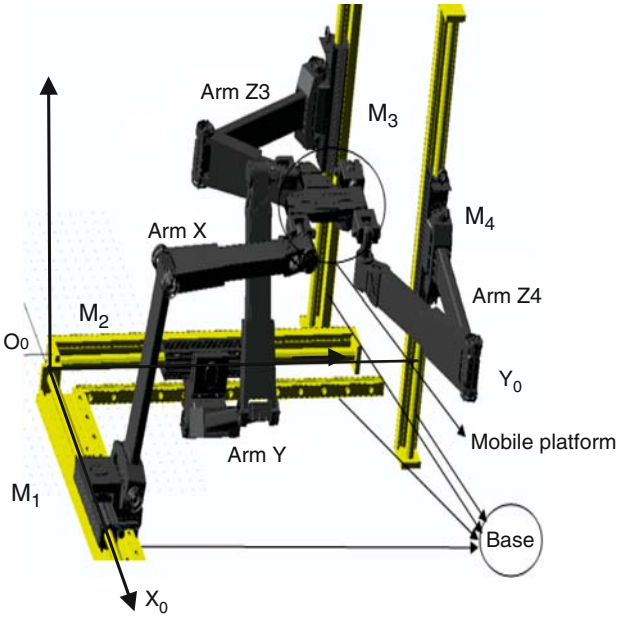

Fig. 3 ADAMS model of the Isoglide4 – T3R1 parallel robot: general view and parameterization

4.2 Dynamic Experimental Testing of the Isoglide4-T3R1 Parallel Robot

An experimental testing was made with physical prototype (Fig. 2a). In parallel, a CAD model (in ADAMS) was developed for comparing the obtained results.

For testing the robot, a linear trajectory (with fifths degree polynomial law of time) was taken into consideration. The choice displacement is of 0.2 m for motor M_1 with acceleration maximum of 1 m/s^2 during 1.062 s.

The experimental displacement of the motor M_1, presented in Fig. 4, follows closely the commanded displacement. The perturbation effects of the system become perceptible for the speed and acceleration (obtained by numerical derivation), presented in Figs. 5 and 6.

For comparison with the ADAMS model, the next steps are taken in consideration:

1. Filtration of the obtained acceleration from experimental tests – Fig. 6, using MATLAB software;
2. Integration of the filtered acceleration (Fig. 7) to obtain filtered speed and displacement (Fig. 8);
3. The filtered displacements are inserted in ADAMS model as movement law of time for the motors;

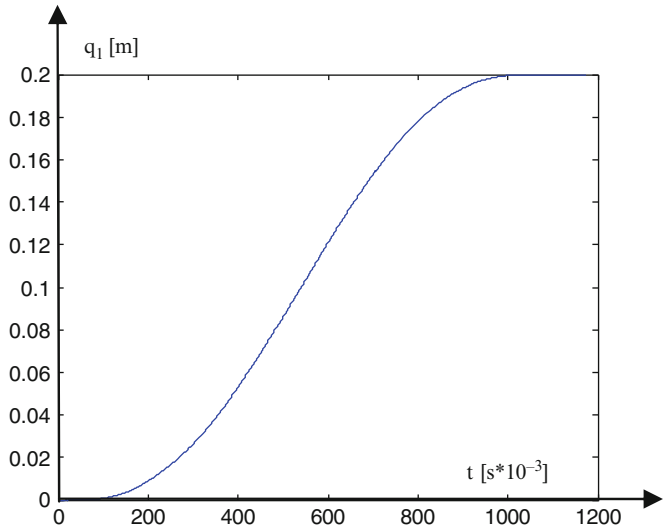

Fig. 4 The experimental obtained displacement for the linear motor M_1

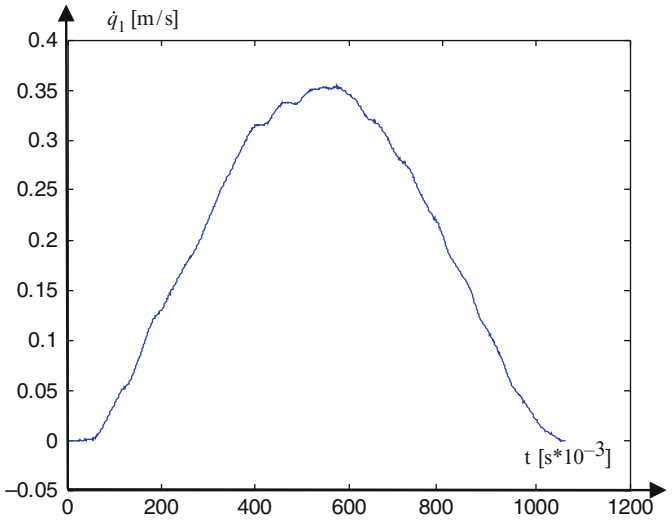

Fig. 5 The experimental obtained speed for the linear motor M_1

4. Establishing of the experimental force F_1 = ct*U(t), where U(t) is the measured tension;
5. The filtration of the obtained driving force F_1 (Fig. 9);
6. Comparing the obtained results from experimental tests and ADAMS model (Fig. 10).

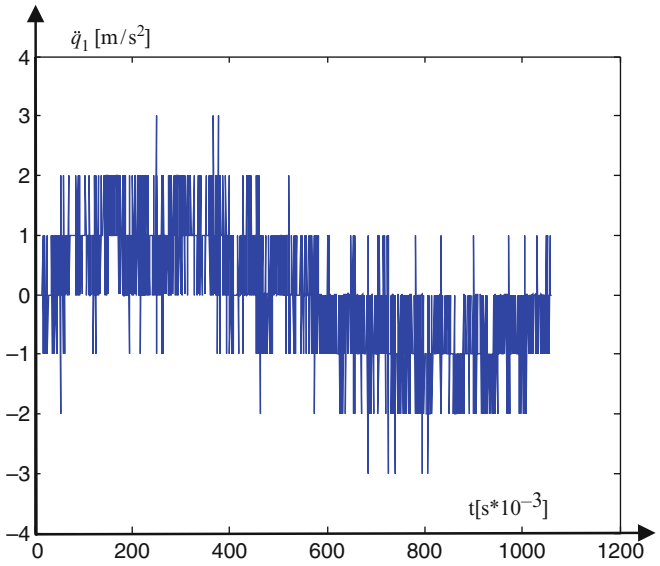

Fig. 6 The experimental obtained acceleration for the linear motor M_1

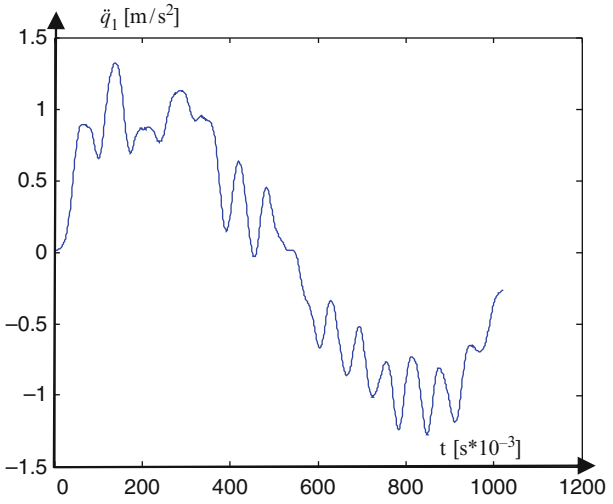

Fig. 7 The filtrated acceleration of the linear motor M_1

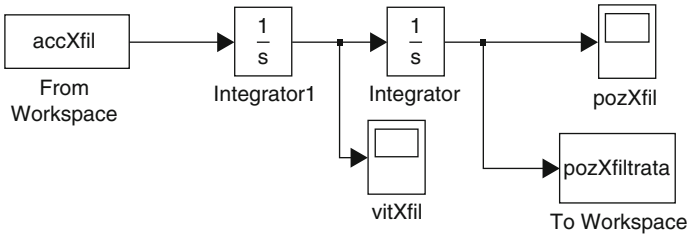

Fig. 8 The integration of the filtered acceleration

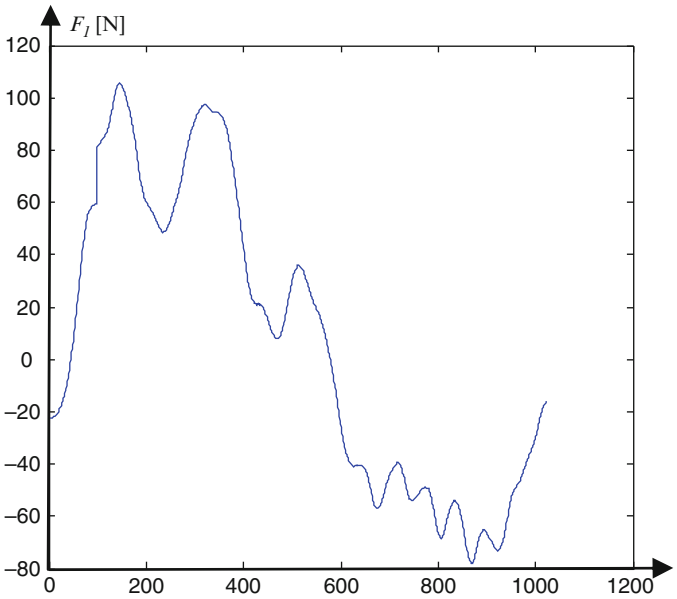

Fig. 9 The experimental filtered driving force F_1

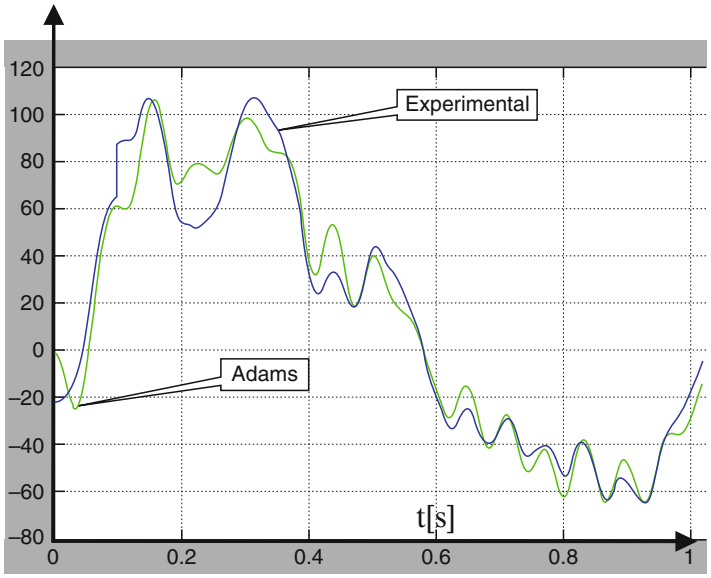

Fig. 10 The driver force F_1 obtained experimentally (see also Fig. 9) and using ADAMS simulation

5 Conclusions

The study highlights the following conclusions:

- An analytical dynamic model was obtained using Maple software;
- Even the analytical dynamic model is complex, the method used can be usefully applied to derive the dynamical model of any parallel robots;
- A virtual CAD model was done in ADAMS environment, obtaining a CAD model in concordance with the physical model;
- Dynamic experimental testing was done on a physical prototype from IFMA, France, obtaining a good concordance with the results of the theoretical close-form and virtual CAD models.

References

1. Hunt, K.H.: Constant-velocity shaft couplings: A general theory. Transactions of the ASME, J. Eng. Ind. 95B, 455–464 (1973)
2. Hunt, K.H.: Structural kinematics of in-parallel-actuated robot arms. Transactions of the ASME, J. Mech. Design 105, 705–712 (1983)
3. Hunt, K.H.: Kinematic Geometry of Mechanisms. Oxford University Press, Oxford (1978)
4. Merlet, J.-P.: Les robots parallèles. Hermès, Paris (1990, 1st edn; 1997, 2nd edn)
5. Tsai, L.-W.: Mechanism Design: Enumeration of kinematic structures according to function. CRC Press, Boca Raton, FL (2000)
6. Rat, N.R., Dudita, F., Gogu, G., Neagoe, M.: Dynamic study of parallel robots with decoupled motions: Isoglide4 – T3R1. COMEFIM 2006, Act on CD-ROM.
7. Gogu, G.: Mobility and spatiality of parallel robots revisited via theory of linear transformations. Eur. J. Mech./A – Solids 24, 690–711 (2005)
8. Gogu, G.: Structural Synthesis of Parallel Robots. Part 1: Methodology. Springer, Dordercht (2008)
9. Gogu, G.: Chebychev-Grubler-Kutzbach's criterion for mobility calculation of multi-loop mechanisms revisited via theory of linear transformations. Eur. J. Mech./A – Solids 24, 427–441 (2005)
10. Gogu, G.: Mobility of mechanisms: A critical review. Mech. Mach. Theory 40, 1068–1097 (2005)
11. Yen, P.-L., Lai, C.-C.: Dynamic modeling and control of a 3-DOF Cartesian parallel manipulator. Mechatronics 19, 390–398 (2009)
12. Wu, J., Wang, J., Wang, L., Li, T.: Dynamics and control of a planar 3-DOF parallel manipulator with actuation redundancy. Mech. Mach. Theory 44, 835–849 (2009)
13. Li, Y., Xu, Q.: Dynamic modeling and robust control of a 3-PRC translational parallel kinematic machine. Robot. Cim-Int. Manuf. 25, 630–640 (2009)
14. Gogu, G.: Structural synthesis of fully-isotropic parallel robots with Schönflies motions via theory of linear transformations and revolutionary morphology. Eur. J. Mech./A – Solids 26, 242–269 (2007). ISSN 0997-7538, 2007

The Monitorisation of the Motion of Differential Gears

M. Rus, S. Veresiu, E. Mereuta, and L. Mihaescu

Abstract This paper offers a research on the possibility to monitorise the kinematics of the motion of a differential gear by using the mathematical models of computer simulation. As an example, we consider a differential gear having the mobility M = 2 which works by means of two engines: a monitorised engine M_{m1} and an engine that works at normal range $M_{m3.}$ An angular speed having a linear variation is obtained for the planet carrier arm of M_{m3}. At the end, the paper describes some of the results (engine torque, angular accelerations, and reactions) obtained by running the program achieved in the Visual Basic language and by means of the Matlab soft.

Keywords Differential gear · Kinematic monitorisation · Mathematical model

1 Introduction

This paper will describe the mathematical model (A∩C) (the correlation between the field of the accelerations and the kinetostatic field) for the computer simulation of the motion produced by a differential gear having imposed kinematics.

The mathematical models having monitored kinematics supposes the solving of the force field applied to a structure of rigid bodies and the defining of the driving module of the field, when a certain kinematics is required.

The monitorisation of an engine means that its working is conditioned by the fact that, the speed (in a given area of the mobile system) and its electrical engine torque (that produces the kinematic field) are listed in time.

M. Rus (✉)
GMT Department, "Dunărea de Jos" University of Galaţi, Galaţi, Romania

I. Vişa (ed.), *SYROM 2009*,
DOI 10.1007/978-90-481-3522-6_32,

The correlation "kinematics – engine torque(s)" of driving is an unreal feature of each mobile gear.

The necessity of the technical usage of an equipment having monitorised kinematics is essential to the implementation of the modern technique in practical usage, such as: machine-tools, pumps, transport and elevating machines, gears having kinematic functions that are imposed to the output wheel [1].

The model described can be applied to the structures having unitary, suprauni-tary, plane or spatial mobility [2].

This paper studies the usability of the kinematic monitorisation aiming at the possibility of monitoring the kinematics of a point from the rotating motion.

2 The Description of the Mathematical Model (A∩C) Having Monitored Kinematics

The algorithm $(A \cap C)$ is based on the correlation between the field of accelerations and the kinetostatic field.

This model can be applied to the determined structures (the number of the scalar parameters to be monitored, corresponds to the number of the driving engines whose dynamics has to be monitored) as well as to the undetermined structures, the motions in R^2 or R^3 [2].

The mathematical model is shown in Fig. 1.

where: φ_1^i, φ_S^i – input (Cauchy) parameters – angles (see Fig. 2);

ω_1^i, ω_S^i – input (Cauchy) parameters for speeds (see Fig. 2);

$\varepsilon_1^i, \varepsilon_S^i$ – input (Cauchy) parameters for accelerations (see Fig. 2).

The following iterations will be set in by the relations:

$$\begin{aligned} \varphi_1^{i+1} &= \varphi_1^i + \omega_1^i \Delta t \\ \varphi_S^{i+1} &= \varphi_S^i + \omega_S^i \Delta t \\ \omega_1^{i+1} &= \omega_1^i + \varepsilon_1^i \Delta t \\ \omega_S^{i+1} &= \omega_S^i + \varepsilon_S^i \Delta t \end{aligned} \tag{1}$$

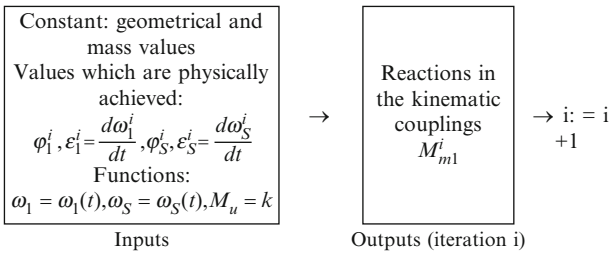

Fig. 1 The simplified lay-out of the algorithm (A∩C)

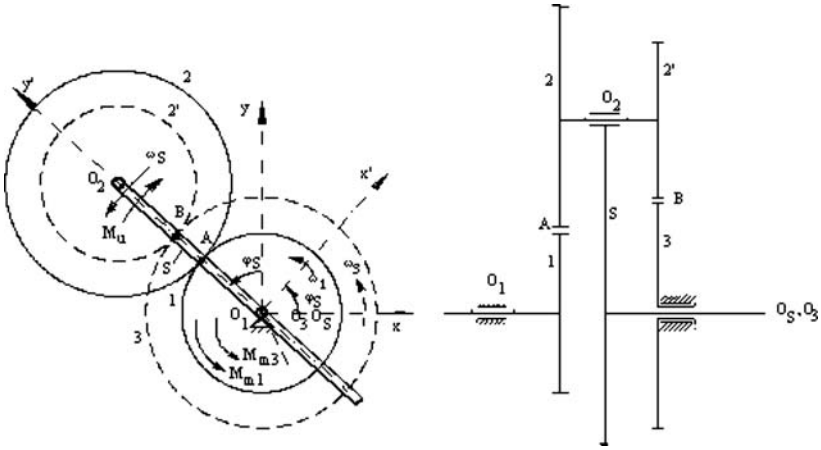

Fig. 2 The differential gear

where: Δt – the time increment chosen depending on the imposed error for the response.

A curved variation as described in (2) can be accepted in order to have a greater precision:

$$\begin{aligned}
\varphi_1^{i+1} &= \varphi_1^i + \omega_1^i \Delta t + \varepsilon_1^i \frac{\Delta t^2}{2} \\
\varphi_S^{i+1} &= \varphi_S^i + \omega_S^i \Delta t + \varepsilon_S^i \frac{\Delta t^2}{2} \\
\omega_1^{i+1} &= \omega_1^i + \varepsilon_1^i \Delta t \\
\omega_S^{i+1} &= \omega_S^i + \varepsilon_S^i \Delta t
\end{aligned} \tag{2}$$

One can calculate the entire configuration and kinetostatics of the mechanical system by knowing the input Cauchy parameters.

As an example, we shall consider the differential gear from Fig. 2, with the development radii r_1, r_2, $r_{2'}$, r_3 (the wheels r_2 and $r_{2'}$ are in solidarity). The motion for these radii will be studied so that the angular speed for the planet carrier has a parabolic variation of the type: $\omega_S = C_1 t^2 + C_2$, where C_1 and C_2 are positive constants imposed by the following conditions:

$$\begin{aligned}
t = 0s &\rightarrow \omega_S = 0,25 s^{-1} \\
t = 9s &\rightarrow \omega_S = 9,25 s^{-1}
\end{aligned}$$

The following values are obtained by solving the linear system: $C_2 = 0.25$ and $C_1 = 0.11$.

The imposed kinematic equation for angular speed is:

$$\omega_S = 0,25 + 0,11 t^2 \tag{3}$$

The system works with two engines: M_{m1} = monitored and M_{m3} = normally working [1]:

$$M_{m3}^{i} = \frac{3663,9}{3,85 - 0,37 \cdot \omega_3^i + \frac{1}{3,85-0,37\cdot\omega_3^i}} \tag{4}$$

Relation (4) was obtained from the expression of the electric engine torque supplied by the short-circuit engines, considering Kloss's relation [3]:

$$M_m = \frac{2M_{\max}}{\frac{s}{s_k} + \frac{s_k}{s}} \tag{5}$$

where: M_{max} is the maximum engine torque in point s_k;

s_k is the short-circuit slipping;

s is the customary slipping.

The following values were accepted in order to calculate the relation of the engine torque: ω_0 is the network's angular frequency corresponding to the pull-in torque's speed ($\omega_0 = \frac{\pi \cdot n_0}{30}$), the pull-in speed – $n_0 = 1000$ r.p.m, and thus $\omega_0 = 104,7197\text{s}^{-1}$, the rated speed – $n_n = 950$ r.p.m, normal angular frequency – $\omega_n = 99,4838\text{s}^{-1}$, the nominal torque calculated from the rated output (in KW) – $M_n = \frac{1000 \cdot P_n}{\omega_n} = 10,0519 \cdot P_n$ (Nm), the overload coefficient – $\lambda = \frac{M_k}{M_n} = 2,7$ and thus $M_k = 2,7 \cdot 10,0519 \cdot P_n = 27,1401 \cdot P_n$, the nominal slipping

$s_n = \frac{\omega_0 - \omega_n}{\omega_0} = \frac{n_0 - n_n}{n_0} = 0,05$, the short-circuit slipping

$$s_k = s_n(\lambda + \sqrt{\lambda^2 - 1}) = 0,26.$$

Using these values, relation (5) becomes:

$$M_m = \frac{54,2802 \cdot P_n}{\frac{104,7197-\omega}{104,7197\cdot 0,26} + \frac{104,7197\cdot 0,26}{104,7197-\omega}} \Rightarrow$$

$$M_m = \frac{54,2802 \cdot P_n}{3,85 - 0,037 \cdot \omega + \frac{1}{3,85-0,037\cdot\omega}} \tag{6}$$

If we consider that:

1. A reductor having the gear reduction rate $r = 10$ is inserted between the engine and differential gear.
2. The overall efficiency of the entire aggregate is $\eta \cong 0,7$.
3. The engine's rated output is $P_n = 7,5kW$,

then, relation (6) would be:

$$M_{m3}^{i} = \frac{3663,9}{3,85 - 0,37 \cdot \omega_3^i + \frac{1}{3,85-0,37\cdot\omega_3^i}} \tag{4}$$

Note: The abrasions in the kinematic couplings are not taken into consideration.

The mathematical model (A∩C) having monitored kinematics is structured by means of the following relations which are written using the level 2 symbolic notations [4,5]:

$$\begin{aligned} &[1, S, 2, 3] \rightarrow [\mu_{C'}, \omega_1, \omega_S] \rightarrow \\ &[\overline{v}] \rightarrow [\omega_2, \omega_3]^0 \end{aligned} \tag{7}$$

$$\begin{aligned} &[1, S, 2, 3] \rightarrow [\mu_{C''}, \tau(\overline{F}_i)^0, M_u^0, \\ &M_{m3}^0, \varepsilon_S^0] \rightarrow [A \cap C] \rightarrow [\varepsilon_1, \varepsilon_2, \\ &\varepsilon_3, \overline{F}_{O1}, F_{21}, M_{m1}, \overline{F}_{S2}, F_{32}', \\ &\overline{F}_{O3}, \overline{F}_{OS}]^0 \end{aligned} \tag{8}$$

where: [1, S, 2, 3] – a linkage containing the elements: 1, S, 2, 3;

$\mu_{C'}$ – mass constants used to determine the speeds field;

$\mu_{C''}$ – mass constants used to determine the accelerations and the kinetostatic fields;

$\tau(\overline{F}_i)$ – the running torque of inertia;

$[\overline{v}], [A \cap C]$ – the mathematical model;

$[\omega_2, \omega_3]$ – the speeds field;

$[\varepsilon_1, \varepsilon_2, \varepsilon_3, \overline{F}_{O1}, F_{21}, M_{m1}, \overline{F}_{S2}, F_{32}', \overline{F}_{O3}, \overline{F}_{OS}]$ – the accelerations and kinetostatic fields;

$$i = 0, ..., 90.$$

By applying the Willis theorem given the points A and B, we obtain:

$$\begin{aligned} \omega_2^0 &= \frac{1}{r_2}[\omega_S^0(r_1 + r_2) - \omega_1^0 r_1] \\ \omega_3^0 &= \frac{\omega_1^0 - (1 - R)\omega_S^0}{R} \\ R &= \frac{r_2 r_3}{r_{2'} r_1} \end{aligned} \tag{9}$$

By deriving the angular speed ω_S, we obtain the following angular acceleration ε_S:

$$\varepsilon_S^0 = \frac{d\omega_S^0}{dt} = 1 \Rightarrow M_{iS}^0 = -\varepsilon_S^0 J_{OS} \tag{10}$$

$$\varepsilon_1^0 \text{ - unknown} \Rightarrow M_{i1}^0 = -\varepsilon_1^0 J_{O1} \tag{11}$$

$$\begin{aligned} \varepsilon_2^0 &= \frac{1}{r_2}[\varepsilon_S^0(r_1 + r_2) - \varepsilon_S^0 r_1] \Rightarrow \\ M_{i2}^0 &= -\varepsilon_2^0 J_{O2} \end{aligned} \tag{12}$$

$$\varepsilon_3^0 = \frac{\varepsilon_1^0 - (1-R)\varepsilon_S^0}{R} \Rightarrow M_{i3}^0 = -\varepsilon_3^0 J_{O3} \tag{13}$$

where: $M_{ij}^0 (j = \overline{1,S})$ – the motion of inertia forces;

J_{Oj} $(j = \overline{1,S})$ – the axial moment of inertia.

The following equations can be written in order to calculate the kinetostatic field:

$$\begin{cases} \overline{F}_{O1}^i + \overline{F}_{21}^i = \overline{0} \\ \overline{M}_{m1}^i + \overline{M}_{i1}^0 + \overline{O_1 A}^i \times \overline{F}_{21}^i = \overline{0} \\ \overline{F}_{S2}^i + \overline{F}_{i2}^i + \overline{F}_{21}^i + \overline{F}_{32'}^i = \overline{0} \\ \overline{M}_{i2}^0 - \overline{O_2^i A^i} \times \overline{F}_{21}^i + \\ \overline{O_2^i B^i} \times \overline{F}_{32'}^i = \overline{0} \\ \overline{F}_{O3}^i + \overline{F}_{32'}^i = \overline{0} \\ \overline{M}_{m3}^i + \overline{M}_{i3}^i - \overline{O_3 B^i} \times \overline{F}_{32'}^i = \overline{0} \\ \overline{F}_{OS}^i + \overline{F}_{S2}^i = \overline{0} \\ \overline{M}_u^i + \overline{M}_{iS}^i - \overline{O_1 O_2^i} \times \overline{F}_{S2}^i = \overline{0} \end{cases} \tag{14}$$

where: $\overline{F}_{O1}^i, \overline{F}_{O3}^i, \overline{F}_{OS}^i$ – the reactions in the kinematic couplings;

$F_{21}^i, F_{32'}^i$ – the reactions on the teeth (see Fig. 3) for which the relations (15), (16) can be written:

$$\begin{aligned} \overline{F}_{21}^i = {} & F_{21}^i(\cos\alpha_0 \cos\varphi_S^i \\ & + \sin\alpha_0 \sin\varphi_S^i)\bar{i} + F_{21}^i(\cos\alpha_0 \sin\varphi_S^i \\ & - \sin\alpha_0 \cos\varphi_S^i)\bar{j} \end{aligned} \tag{15}$$

$$\begin{aligned} \overline{F}_{32'}^i = {} & -F_{32'}^i(\cos\alpha_0 \cos\varphi_S^i \\ & + \sin\alpha_0 \sin\varphi_S^i)\bar{i} + F_{32'}^i(\cos\alpha_0 \sin\varphi_S^i \\ & - \sin\alpha_0 \cos\varphi_S^i)\bar{j} \end{aligned} \tag{16}$$

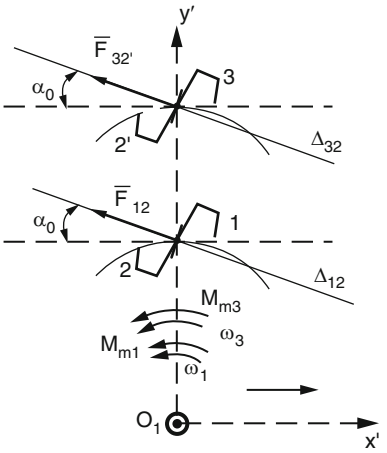

Fig. 3 The reactions on the teeth

The system described by (14) together with the Eqs. (12) and (13) form a linear system containing 14 equations having 14 unknowns:

$$[\varepsilon_1, \varepsilon_2, \varepsilon_3, \overline{F}_{O1}, F_{21}, M_{m1}, \overline{F}_{S2}, F_{32}{}', \overline{F}_{O3}, \overline{F}_{OS}]$$

The following iterations are set in by means of the following relations:

$$\begin{aligned} \varphi_1^i &= \varphi_1^{i-1} + \omega_1^{i-1}\Delta t \\ \varphi_S^i &= \varphi_S^{i-1} + \omega_S^{i-1}\Delta t \\ \omega_1^i &= \omega_1^{i-1} + \varepsilon_1^{i-1}\Delta t \\ \omega_S^i &= 0,25 + 0,11 \cdot (i \cdot \Delta t)^2 \end{aligned} \tag{17}$$

where, $i = 0, ..., 90$.

3 The Experimental Results

The program made for the motion's simulation is achieved by means of the Visual-Basic language [6], and the linear system was solved by means of the Matlab soft [7].

The input values (see Fig. 2) are:

$r_1 = 0,3m; r_2 = 0,3m; r_3 = 0,4m; r_2{}' = 0,2m$ – the development radii;

$m_2 = 10kg$ – the weight of the element 2;

$\alpha_0 = 20^\circ$ – the gearing angle;

$J_{O1} = 20kgm^2, J_{O2} = 30kgm^2,$
$J_{O3} = 15kgm^2, J_{OS} = 5kgm^2$ – the axial moments of inertia;

$M_u = -1000Nm$ – the effective moment;

$$\varphi_1^0 = 10^\circ, \varphi_S^0 = 30^\circ, \omega_1^0 = 0,15s^{-1}, \omega_S^0 = 0,25s^{-1}$$

– Cauchy parameters;

$$O_1(0,0), O_3(0,0), O_S(0,0), \Delta t = 0,1s;$$

$$\varphi_1^i = \varphi_1^{i-1} + \omega_1^{i-1}\Delta t$$
$$\varphi_S^i = \varphi_S^{i-1} + \omega_S^{i-1}\Delta t$$
$$\omega_1^i = \omega_1^{i-1} + \varepsilon_1^{i-1}\Delta t$$
$$\omega_S^i = 0,25 + 0,11 \cdot (i \cdot \Delta t)^2$$

$$O_2^i(-(r_1 + r_2)\sin\varphi_S^i, (r_1 + r_2)\cos\varphi_S^i,$$
$$A^i(-r_1\sin\varphi_S^i, r_1\cos\varphi_S^i), B^i(-r_3\sin\varphi_S^i, r_3\cos\varphi_S^i)$$

The following values are obtained as a result of the running of the two programs: (a) Angular speeds and accelerations (Table 1 and 2) (Figs. 4–6):

Table 1 The results of kinematics

It.	ω_S	ω_1	ω_2	ω_3
0	0.25	0.15	0.35	0.2
1	0.25	1.12	−0.62	0.69
2	0.25	2.06	−1.56	1.16
3	0.26	2.98	−2.46	1.62
4	0.27	3.85	−3.32	2.06
5	0.28	4.7	−4.14	2.49
...	...	...	...	...
90	9.16	156.27	−137.95	82.72

Table 2 The results of kinematics

It.	ε_S	ε_1	ε_2	ε_3
0	0	9.72	−9.72	4.86
1	0.02	9.42	−9.38	4.72
2	0.04	9.11	−9.02	4.58
3	0.07	8.78	−8.65	4.42
4	0.09	8.44	−8.26	4.26
5	0.11	8.08	−7.86	4.1
...	...	...	...	...
90	1.98	23.65	−19.69	12.82

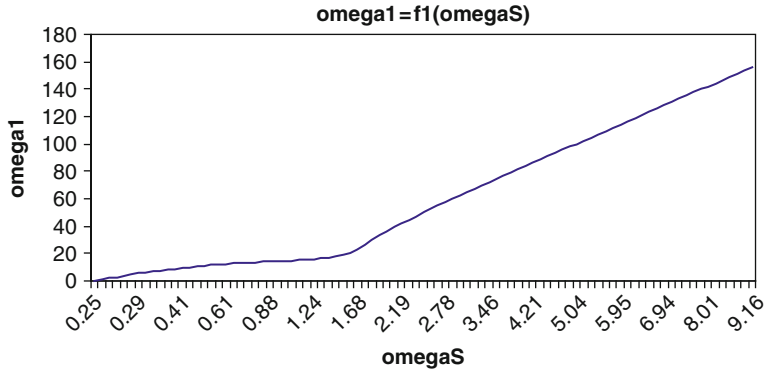

Fig. 4 Diagram 1

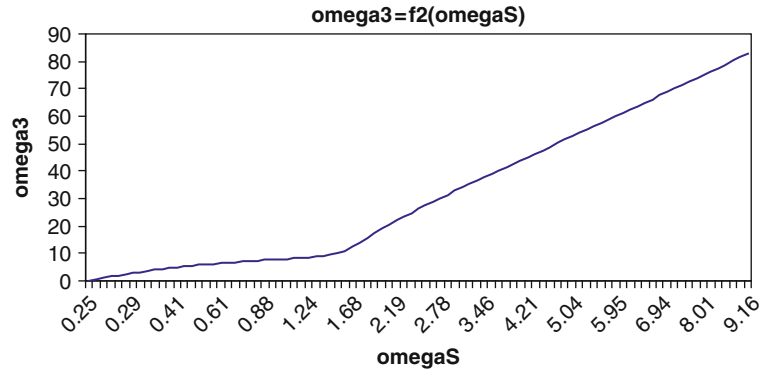

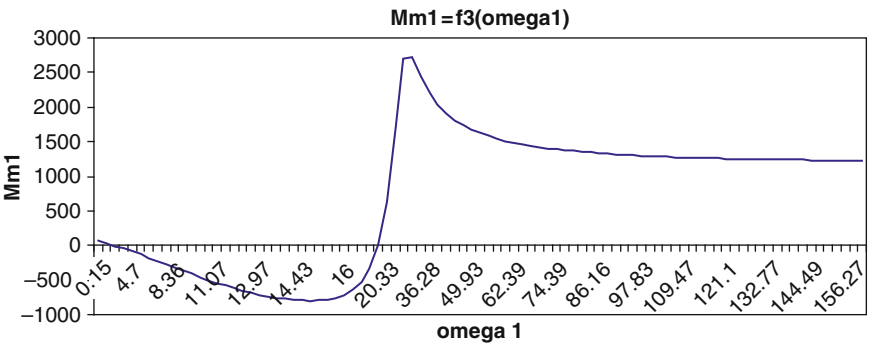

Fig 5 Diagrams 2 and 3

$\omega_1 = f_1(\omega_S)$ – diagram 1;
$\omega_3 = f_2(\omega_S)$ – diagram 2.
(b) Reactions and M_{m1} (Table 3):

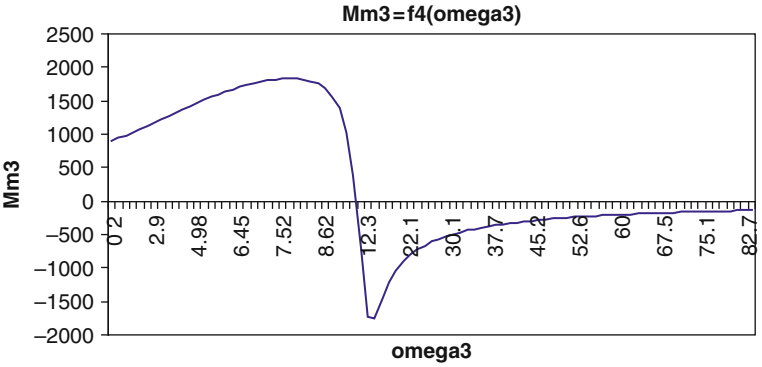

Fig. 6 Diagram 4

Table 3 The results of kinetostatic field

It.	F_{O1x}	F_{O1y}	F_{O3x}	F_{O3y}
0	437.98	77.23	−738.16	−385.22
1	542.69	109.74	−776.84	−461.37
2	651.24	148.81	−817.35	−544.05
3	763.12	194.92	−859.63	−634.12
4	877.65	248.64	−903.61	−732.47
5	993.89	310.53	−949.13	−839.98
...	...	...	...	...
90	2428.06	1132.28	−36.13	−369.92

Table 3 – Continuation

It.	F_{OSx}	F_{OSy}	F_{S2x}	F_{S2y}
0	1746.87	307.66	1746.87	307.66
1	1738.85	351.23	1738.85	351.23
2	1729.71	394.77	1729.71	394.77
3	1719.33	438.64	1719.33	438.64
4	1707.58	483.16	1707.58	483.16
5	1694.28	528.67	1694.28	528.68
...	...	...	...	...
90	−1982.4	−397.99	−1982.4	−397.99

Table 3 – Continuation

It.	F_{21}	$F_{32'}$	M_{m3}	M_{m1}
0	−444.74	2218.37	906.72	68.99
1	−553.67	2327.64	945.74	32.37
2	−668.02	2442.32	986.67	−6.1
3	−787.62	2562.26	1029.46	−46.39
4	−912.19	2687.16	1073.99	−88.39
5	−1041.27	2816.58	1120.11	−131.94
...	...	...	...	...
90	2679.09	−875.26	−136.75	1228.3

$M_{m1} = f_3(\omega_1)$ – diagram 3;
$M_{m3} = f_4(\omega_3)$ – diagram 4.

4 Conclusions

1. It can be observed that in the case of monitored kinematics a kinematic parameter disappears from the field of the unknowns, being replaced by M_{m1} (the electric engine motor).
2. It can be observed that in the case of kinematic monitorisation the listing in time is allowed for the angular rotation speed as well as for the electric engine torque.
3. It can be seen that the curves having almost identical radii of curvature are obtained by drawing the diagrams $\omega_1 = f_1(\omega_S)$ and $\omega_3 = f_2(\omega_S)$.
4. Some complementary curves with increased hollowing are obtained as a result of the graphical representation of the diagrams $M_{m1} = f_3(\omega_1)$, $M_{m3} = f_4(\omega_3)$.

These curves correspond to the working diagram of the triphases non-synchronous motor (the engine torque according to the slipping$s = \frac{\omega_0 - \omega}{\omega_0}$, as in Kloss's relation).

5. In the model shown above, the abrasions from the kinematic couplings and those between the teeth were not taken into consideration, because they can be determined by means of the subprogram of successive approximations.
6. The paper presented an example of a differential gear having imposed kinematics for the planet carrier arm ($\omega_S = C_1 t^2 + C_2$)
7. The kinematic restriction can be imposed on the speed or acceleration of a point belonging to the structure.
8. The mathematical relation which describes the motion's restriction can have any kind of variance law.

References

1. Rus, M.: Monitorizarea mişcărilor nestaţionare a angrenajelor. Teza de doctorat, Galati (2007)
2. Orănescu, A., Bejenaru, S., Rus, M.: Prioritèes de patrimoine de l'école de mécanismes de Galati, pp.135–140. A-IX-a Conferinţă Internaţională de Mecanisme şi Transmisii Mecanice, MTM, Bucureşti (2004)
3. Bivol, I., Vasilache, C.: Utilizarea convertizoarelor statice în procesul de conversie a energiei. Editura Secorex, Bucureşti (2001)
4. Rus, M.: The mathematical model of the computer simulation of the motion produced by a gear having fixed axes with monitored kinematics pp. 41–46. The Annals of "Dunarea de Jos" University of Galati Fascicle X Applied Mechanics (2005). ISSN 1221 - 4612
5. Rus, M.: The computer simulation of the motion produced by a differential gear having imposed kinematics, vol. I – Mecanisme şi Tribologie, pp. 155–160. Al 8 – lea Simpozion naţional cu participare internaţională, PRoiectarea ASIstată de Calculator "PRASIC '06," Braşov (2006)
6. Microsoft Visual Basic 6.0 Programmer's Guide. Ed. Teora (1999)
7. Ghinea, M., Fireţeanu, V.: MATLAB. Calcul numeric. Grafică. Aplicaţii. Ed. Teora (1997)

Structure, Kinematics and CAD Model of a Mobile Telethesis

I. Staretu

Abstract In the paper it is presented first the structure of a reference telethesis, on the basis of which then it is proposed a structure for a mobile telethesis. For this telethesis it is presented succinctly the structural characterization and the forward and inverse kinematic analysis of the telethesis arm. For the kinematic analysis the method of homogeneous operators is used. Based on the kinematic scheme it is implemented the 3D model in CATIA, of the telethesis. Based on the CAD model one can get the technical project and subsequently one can be done the telethesis prototype, which is the focus of the authors during the next period.

Keywords CAD model · Constructive design · Mobile telethesis · Structure

1 Introduction

A telethesis is mechatronic equipment used to help persons with handicap, around them or at distance [2–4]. There are fixed teletheses, which can be mounted around the persons with handicap (on the table, on the bedside table or on the wheelchair).

There are as well mobile teletheses, which can perform different activities at distance (in the same room with the person with handicap, in another room or at longer distance, for example: in the garden etc.).

Teletheses have a complex mechanical structure and, in general, their main part is a robotic arm, similar to the human arm. In the paper, a mobile reference telethesis is presented with its structural peculiarities, calculation for forward and inverse kinematic for the robotic arm, used the method of the homogeneous operators, kinematic calculation for the gripper – mechanical hand, a constructive project for the telethesis, a CAD model and a CAD simulation.

I. Staretu
Department of Product Design and Robotics, Transilvania University of Braşov, Braşov, Romania

I. Vişa (ed.), *SYROM 2009*,
DOI 10.1007/978-90-481-3522-6_33,

2 Structure for a Reference Telethesis

A telethesis must be, theoretically, similar to the human arm regarding the dimensions and the degree of freedom. A similar structure to the human arm, without the palm and the fingers, must have three movements of rotation (I, II, III), similar to the movements of the shoulder joint, one movement of rotation (IV), similar to the movement of the elbow joint and three movements of rotation (V, VI, VII), similar to the joint of the palm (Fig. 1) [6, 7].

The third part of a mobile telethesis is the mobile platform, which usually has two degrees of mobility (forward – backward movement and right – left movement). As a result the total mobility of a mobile telethesis will be Mtot = 7 (for the arm) + 1 or 5 (for the gripper) + 2 (for the platform) = 10 or 14.

This structure is very complex and it is difficult to achieve. Consequently a more simplified structure with M = 9 (M = 6 for the arm and M = 1 for the gripper and M = 2 for the mobile platform) is preferred (Fig. 2 – the mobility of the gripper is not shown).

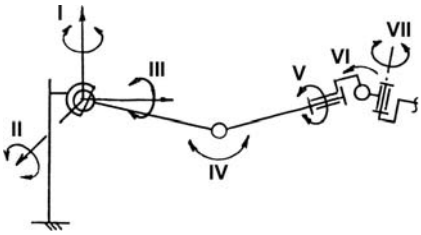

Fig. 1 Reference telethesis

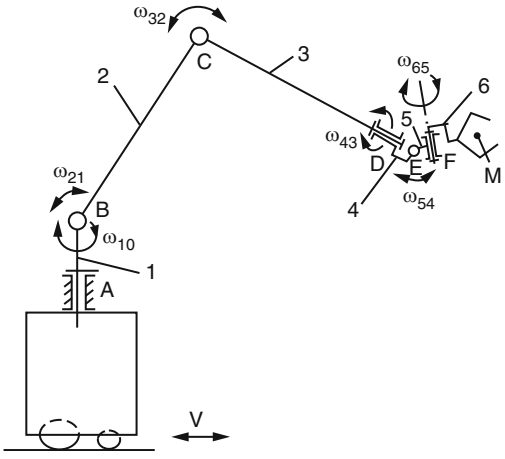

Fig. 2 Simplified structure of the telethesis

3 The Kinematics for the Reference Telethesis

The area accessed by the robotic arm is essential to the utility of the telethesis. (the possibility of movement in the area closer or farther from the working point is provided by the mobile platform, as in the case of any mobile robot, which does not involve specific issues in the case of a telethesis).

Therefore, the solution of its forward and inverse kinematic problem is summarized here. These, for the reference telethesis, can be solved through different methods, well known in the theory of the mechanisms [1, 2].

3.1 Forward Kinematics

With the forward kinematics, it can be obtained the position of the characteristic point M (in the reference system $O_o x_o y_o z_o$).

The local reference systems attached to the structure of the telethesis are placed in every joint (Fig. 3).

In this figure, the distances and the angles between the reference local systems are represented too. The position of the characteristic point M is obtained with the method of the homogeneous operators [1].

Regarding this method, for a translation from the reference system "m" to the reference system "n," the matrix of the translation operator is:

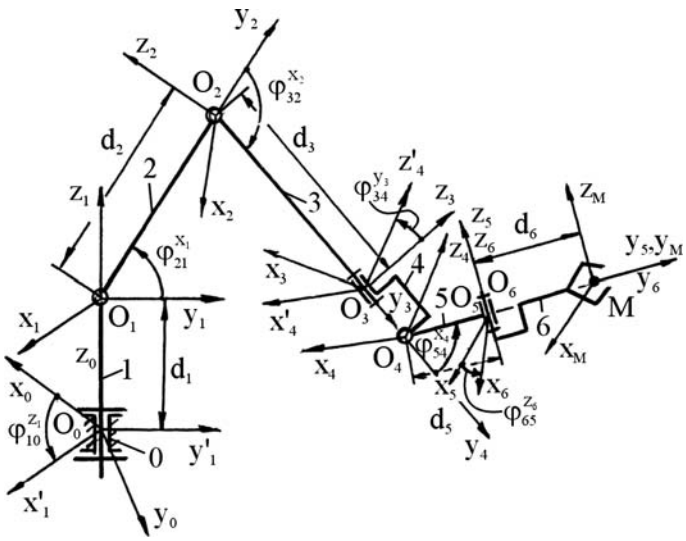

Fig. 3 Kinematic scheme of the telethesis

$$A_{mn} = T_{mn}^{x} = \begin{bmatrix} 1 & 0 & 0 & 0 \\ d_{nm} & 1 & 0 & 0 \\ 0 & 0 & 1 & 0 \\ 0 & 0 & 0 & 1 \end{bmatrix} \tag{1}$$

The matrix for the rotation operator around x-axis is :

$$A_{mn} = R_{mn}^{x} = \begin{bmatrix} 1 & 0 & 0 & 0 \\ 0 & 1 & 0 & 0 \\ 0 & 0 & C_{nm} - S_{nm} & \\ 0 & 0 & S_{nm} & C_{nm} \end{bmatrix} \tag{2}$$

The matrix for the rotation operator around y-axis is:

$$A_{mn} = R_{mn}^{y} = \begin{bmatrix} 1 & 0 & 0 & 0 \\ 0 & C_{nm} & 0 & S_{nm} \\ 0 & 0 & 1 & 0 \\ 0 - S_{nm} & 0 & C_{nm} & \end{bmatrix} \tag{3}$$

And around z-axis is:

$$A_{mn} = R_{mn}^{z} = \begin{bmatrix} 1 & 0 & 0 & 0 \\ 0 & C_{nm} - S_{nm} & 0 & \\ 0 & S_{nm} & C_{nm} & 0 \\ 0 & 0 & 0 & 1 \end{bmatrix} \tag{4}$$

In these matrices $S_{nm} = \sin\varphi_{nm}$, and $C_{nm} = \cos\varphi_{nm}$.

The position of the characteristic point M in the reference system $O_0x_0y_0z_0$ is: $A_{0M} = A_{01}\ A_{12}\ A_{23}\ A_{34}\ A_{45}\ A_{56}\ A_{6M}$, where: $A_{01} = R_{01}^{z} \cdot T_{01}^{z}$; $A_{12} = R_{12}^{x} \cdot T_{12}^{y}$; $A_{23} = R_{23}^{x} \cdot T_{23}^{y}$; $A_{34} = R_{34}^{y} \cdot T_{34}^{y}$; $A_{45} = R_{45}^{x} \cdot T_{45}^{y}$; $A_{56} = R_{56}^{z}$; $A_{6M} = T_{6M}^{y}$.

These matrices are:

$$R_{01}^{z} = \begin{bmatrix} 1 & 0 & 0 & 0 \\ 0 & C_{10} - S_{10} & 0 & \\ 0 & S_{10} & C_{10} & 0 \\ 0 & 0 & 0 & 1 \end{bmatrix};\ T_{01}^{z} = \begin{bmatrix} 1 & 0 & 0 & 0 \\ 0 & 1 & 0 & 0 \\ 0 & 0 & 1 & 0 \\ d_1 & 0 & 0 & 1 \end{bmatrix};$$

$$R_{12}^{x} = \begin{bmatrix} 1 & 0 & 0 & 0 \\ 0 & 1 & 0 & 0 \\ 0 & 0 & C_{21} - S_{21} & \\ 0 & 0 & S_{21} & C_{21} \end{bmatrix};\ T_{12}^{y} = \begin{bmatrix} 1 & 0 & 0 & 0 \\ 0 & 1 & 0 & 0 \\ d_2 & 0 & 1 & 0 \\ 0 & 0 & 0 & 1 \end{bmatrix};$$

$$R_{23}^{x} = \begin{bmatrix} 1 & 0 & 0 & 0 \\ 0 & 1 & 0 & 0 \\ 0 & 0 & C_{32} - S_{32} & \\ 0 & 0 & S_{32} & C_{32} \end{bmatrix}; \; T_{23}^{y} = \begin{bmatrix} 1 & 0 & 0 & 0 \\ 0 & 1 & 0 & 0 \\ d_3 & 0 & 1 & 0 \\ 0 & 0 & 0 & 1 \end{bmatrix};$$

$$R_{34}^{y} = \begin{bmatrix} 1 & 0 & 0 & 0 \\ 0 & C_{43} & 0 & S_{43} \\ 0 & 0 & 1 & 0 \\ 0 - S_{43} & 0 & C_{43} & \end{bmatrix}; \; T_{34}^{y} = \begin{bmatrix} 1 & 0 & 0 & 0 \\ 0 & 1 & 0 & 0 \\ d_4 & 0 & 1 & 0 \\ 0 & 0 & 0 & 1 \end{bmatrix};$$

$$R_{45}^{x} = \begin{bmatrix} 1 & 0 & 0 & 0 \\ 0 & 1 & 0 & 0 \\ 0 & 0 & C_{54} - S_{54} & \\ 0 & 0 & S_{54} & C_{54} \end{bmatrix}; \; T_{45}^{y} = \begin{bmatrix} 1 & 0 & 0 & 0 \\ 0 & 1 & 0 & 0 \\ d_5 & 0 & 1 & 0 \\ 0 & 0 & 0 & 1 \end{bmatrix};$$

$$R_{56}^{z} = \begin{bmatrix} 1 & 0 & 0 & 0 \\ 0 & C_{65} - S_{65} & 0 & \\ 0 & S_{65} & C_{65} & 0 \\ 0 & 0 & 0 & 1 \end{bmatrix}; \; T_{6M}^{y} = \begin{bmatrix} 1 & 0 & 0 & 0 \\ 0 & 1 & 0 & 0 \\ d_6 & 0 & 1 & 0 \\ 0 & 0 & 0 & 1 \end{bmatrix}.$$

In these matrices : $C_{10} = \cos\varphi_{10}^{z}$; $S_{10} = \sin\varphi_{10}^{z}$; $d_1 = \overline{O_0O_1}$; $C_{21} = \cos\varphi_{21}^{x}$; $S_{21} = \sin\varphi_{21}^{x}$; $d_2 = \overline{O_1O_2}$; $C_{32} = \cos\varphi_{32}^{x}$; $S_{32} = \sin\varphi_{32}^{x}$; $d_3 = \overline{O_2O_3}$; $C_{43} = \cos\varphi_{43}^{y}$; $S_{43} = \sin\varphi_{43}^{y}$; $d_4 = \overline{O_3O_4}$; $C_{54} = \cos\varphi_{54}^{x}$; $S_{54} = \sin\varphi_{54}^{x}$; $d_5 = \overline{O_4O_5}$; $C_{65} = \cos\varphi_{65}^{z}$; $S_{65} = \sin\varphi_{65}^{z}$; $d_6 = \overline{O_6M}$ $(O_5 \equiv O_6)$; i = 0, 1, 2, 3, ... 6, M; the angles φ_{ij}^{k} are the angles between the reference systems i and j and d_i are the distances between the reference systems with parallel axes.

3.2 Inverse Kinematics

With the inverse kinematics, the rotation of the pivot joints for a position of the characteristic point M can be obtained.

If we know the elements of the A0M matrix:

$$A_{0M} = T_{mn}^{x} = \begin{bmatrix} 1 & 0 & 0 & 0 \\ b_{21} & b_{22} & b_{23} & b_{24} \\ b_{31} & b_{32} & b_{33} & b_{34} \\ b_{41} & b_{42} & b_{43} & b_{44} \end{bmatrix}; \tag{5}$$

for inverse kinematics, the following equation is used:

$$A_{01}A_{12}A_{23}A_{34}A_{45}A_{56}A_{6M} = A_{0M} \tag{6}$$

With inverse operators, $A_{01}^{-1}, A_{12}^{-1}, A_{23}^{-1}, \ldots,$ a system is obtained and then its solutions, depending on the matrices: $A_{01}, A_{12}, A_{23} \ldots A_{45}, A_{56}, A_{6M}$.

4 Structure and Kinematic for the Gripper of the Telethesis

4.1 Structural Synthesis

The structural synthesis is made similar with the biomechanism of the human hand and the mechanism of the finger too (Fig. 4a).

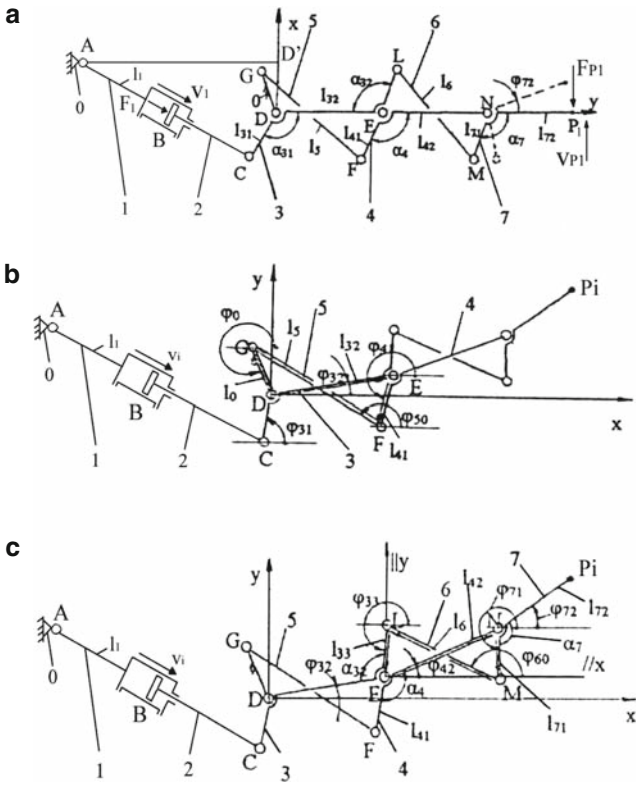

Fig. 4 The cinematic schemes

4.2 Structural Analysis

The mechanism of the finger (Fig. 4a) is a polycontour mechanism with two outside connections L = 2 (v1, F1; vP1, FP1) and degree of freedom M = 1.

The degree of freedom is obtained with $M = \sum M_i - \sum f_c$, where Mi is the degree of freedom for monocontour i mechanism and $\sum f_c$is the degree of freedom for common joints .

For each monocontour mechanism the degree of freedom is obtained with $M = \sum f_i - \chi_K$ (where $\sum f_i$ is the degree of freedom of the joints and χ_K is kinematic degree of the monocontour k mechanism [1]).

For the mechanism of the finger (Fig. 4a) the following relations are obtained:

$$\begin{aligned} M_I &= f_A + f_B + f_C + f_D - \chi_I = 1 + 1 + 1 + 1 - 3 = 1 \\ M_{II} &= f_D + f_E + f_F + f_G - \chi_{II} = 1 + 1 + 1 + 1 - 3 = 1 \\ M_{III} &= f_L + f_M + f_N + f_E - \chi_{III} = 1 + 1 + 1 + 1 - 3 = 1, \end{aligned} \tag{1}$$

and $\Sigma f_C = f_D + f_E = 1 + 1 = 2$.

The degree of freedom will be:

$$M = M_I + M_{II} + M_{III} - \Sigma f_C = 1 + 1 + 1 - 2 = 1 \tag{2}$$

M = 1 has the following significance: one independent movement (speed): $v_1 = \dot{s}_1$ and one function of the external forces: $F_1 = F_1(F_{P1})$. L−M = 1 represents one function of movement: $v_{P1} = v_{P1}(v_1)$ and one independent force: F_{P1} – the contact force between fingers and grasped object.

4.3 Kinematic Synthesis

The kinematic synthesis is used to obtain a correct closing of the finger and of the gripping mechanism. This situation is obtained with a good correlation between the dimensions of the phalanxes and a good relative position of the fingers.

4.4 Kinematic Analysis

The function of position, the function of speed and the function of acceleration for characteristic P_i points are obtained from the kinematic analysis. The vectorial close chain method is used successively for each monocontour mechanism. The vectorial equations are:

$\overrightarrow{AC} + \overrightarrow{CD} + \overrightarrow{DD'} + \overrightarrow{D'A} = 0$ (Fig. 4a), $\overrightarrow{DE} + \overrightarrow{EF} + \overrightarrow{FG} + \overrightarrow{GD} = 0$ (Fig. 4b) and $\overrightarrow{EN} + \overrightarrow{NM} + \overrightarrow{ML} + \overrightarrow{LE} = 0$ (Fig. 4c) [5].

The implicit form for the equation of position is: φ72i = φ72i(s1), i – the number of the finger: i = 1, 2, 3, 4.

The functions for speeds are the derivative function of time of the functions for positions and the functions for accelerations are the derivative of the functions for speed:

$$v_{Pi} = \dot{\varphi}_{72i}, a_{Pi} = \dot{v}_{Pi}\,. \tag{3}$$

5 Static Synthesis and Analysis

The static synthesis solves the problem to obtaining the necessary gripping force on each finger and the total gripping force.

The function of the external forces is obtained from the theorem of balance between the powers of entrance and emergence of mechanism: $v_i \cdot F_i + v_{Pi} \cdot F_{Pi} = 0$, and

$$F_i = -\frac{v_{Pi} \cdot F_{Pi}}{v_i} \tag{4}$$

The internal forces are calculated using the theorem of the joints and, afterwards, with the balance static equations of the mobile elements [1].

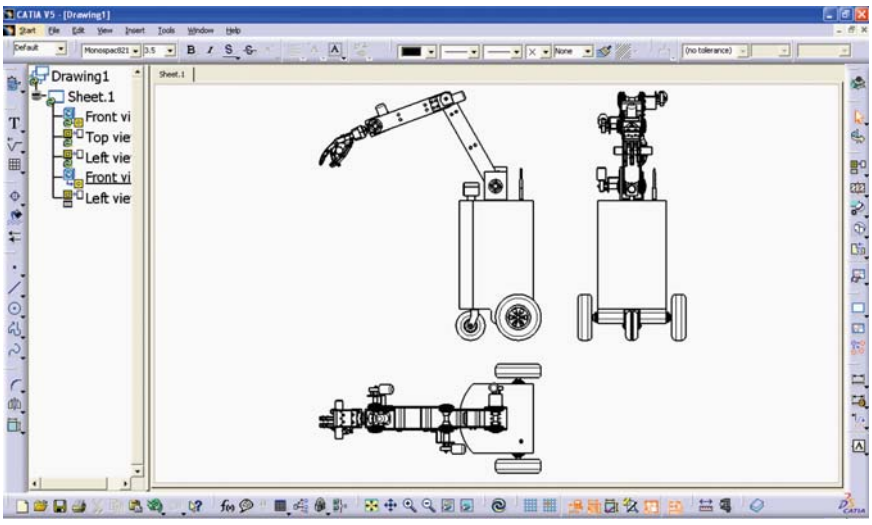

Fig. 5 Constructive design of the telethesis

6 Constructive Design, CAD Model and CAD Simulation

Based on the structural-kinematic layout, the technical design of the telethesis was done (Fig. 5). It has a robotic arm with the main dimensions of the "arm and forearm" similar to the human upper member, it is equipped with an anthropomorphic gripper with five mono mobile fingers (Fig. 6), at this stage, with the possibility

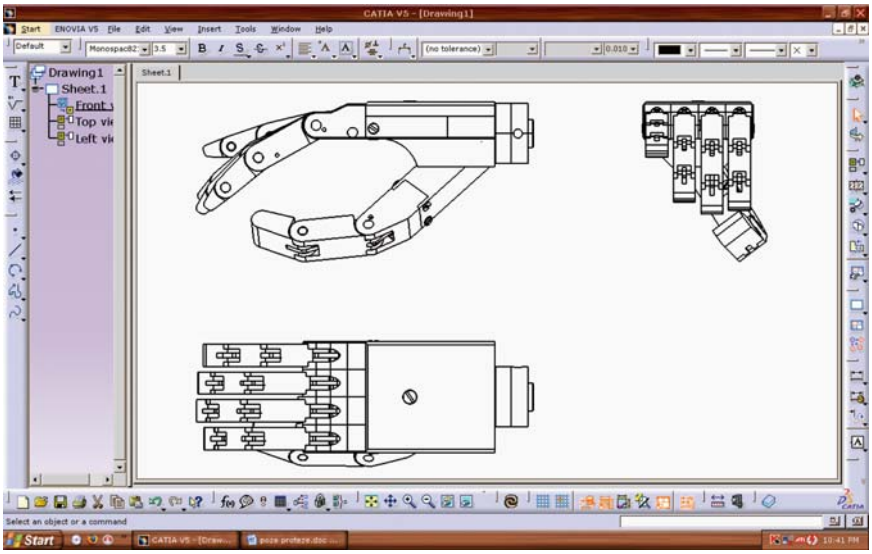

Fig. 6 Constructive design of the gripper

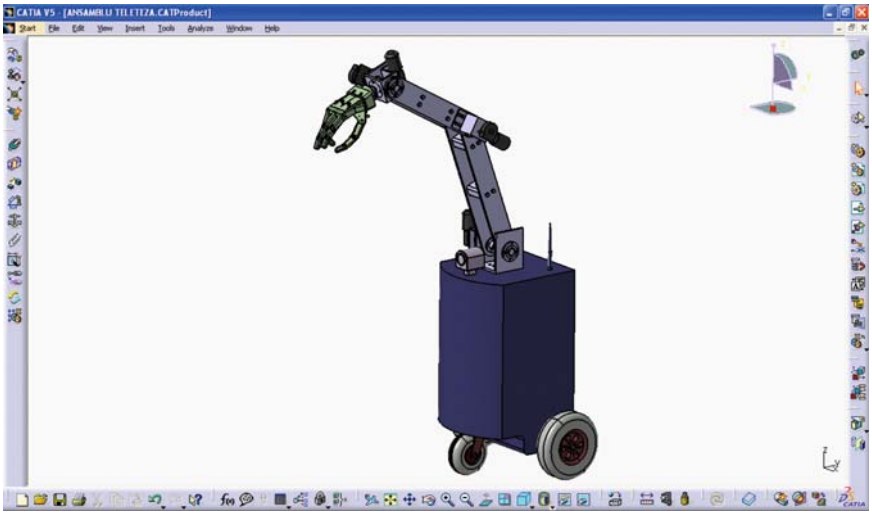

Fig. 7 CAD model of the telethesis

of transforming it into a pentamobile gripper at a subsequent version and a mobile platform [7].

In addition, the telethesis is equipped with cameras and a system for receiving the command signal by radio waves and obviously, with appropriate command equipment, but it is not the subject of this paper.

Based on the technical project the CAD model was created in the CATIA software(Fig. 7).

To optimize constructively and for the identification of certain constructive and technical differences, the functional simulation in CATIA was done, without an object to be gripped (Fig. 8a) and with an object grasped (Fig. 8b). Through this

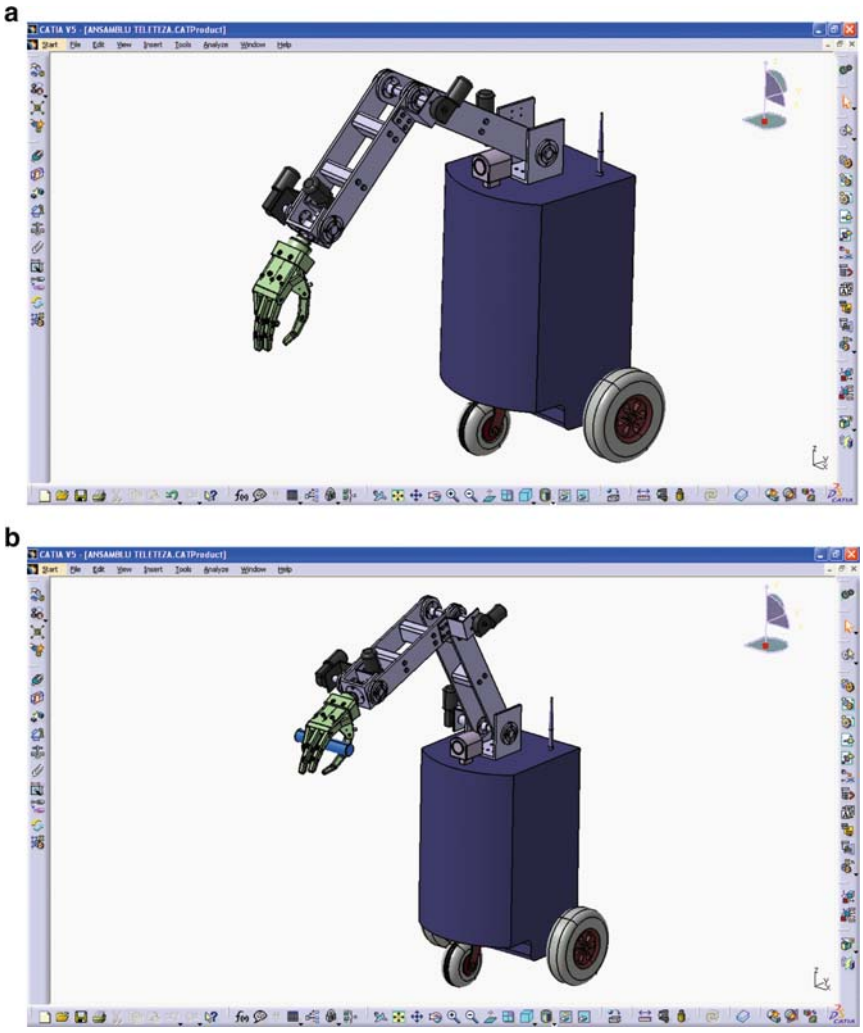

Fig. 8 CAD simulation

simulation there can be highlighted the work area of the telethesis, and by default the limit positions, and there can be identified locations of other auxiliary components so that they are accessible and the objects to be manipulated can be gripped and brought to the utility area of the beneficiary.

7 Conclusions

Regarding the aspects presented in this paper, the following conclusions can be formulated:

- Telethesis is a mechatronic structure and it is a complex equipment fixed or mobile, which can be used to substitute one or both human arms.
- The main parts of the mobile telethesis are: a mobile platform; a robotic arm, which can be kinematically analyzed (forward and inverse kinematics) similar to kinematic analysis of the industrial robots and a gripper.
- A functional simulation in CAD space are useful stages to obtain better constructive and functional versions of the teletheses.

Acknowledgments This work was supported thorough the national project CNCSIS: *Constructive Optimization and Virtual Simulation of the Mechatronical Modular Structures Usable as Prostheses and Teletheses for the Human Hand,* founded by Ministry of Education, Research and Innovation of Romania, in the period 2007–2008.

References

1 Dudita, Fl., a.o.: Linkages mechanisms (in Romanian). Tehnica Press, Bucuresti (1987)
2 Coiffet, Ph.: La Robotique. Hermes Press, Paris (1993)
3 Guittet, I.: La Robotique medicale.Hermes Press, Paris (1988)
4 Hillman, M.: Rehabilitation robotics from past to present – A historical perspective. In: Proceedings of the ICORR. Daejeon, Korea (2003)
5 Stareţu, I.: Elements of medical robotics and prostheses (in Romanian). Lux Libris Press, Brasov (2004)
6 Staretu, I.: Fixed telethesis – structure kinematics and simplified prototype, pp. 207–212. In: Proceedings of the 3rd International Conference on Robotics. Iasi (2006)
7 Staretu, I.: Constructive optimization and virtual simulation of the mechatronical modular structures usable as prostheses and teletheses for the human hand. National Romanian Grant 894 (2007–2008)

Asymptotic Analysis of Parametrically Excited Spring Pendulum

R. Starosta and J. Awrejcewicz

Abstract The weakly non-linear 2-DOF mechanical system parametrically and externally excited is studied. It may serve as a model for a variety of engineering systems, including ship motions with nonlinear coupling between pitching and wave loadings. The transfer of energy from one to another mode of vibrations is illustrated and analyzed. Multiple scales method application allows reducing the original nonautonomous system to an approximate autonomous system regarding amplitude and phase variables in order to find steady state solutions and verify their stability.

Keywords Discrete dynamics · Multiple scale method · Parametric resonance

1 Introduction

The parametrical nonlinear systems are of great interest of many researches. We are focused on analysis of dynamics of 2-DOF (two-degree-of-freedom) flexible pendulum. The pendulum with changing length moving on circular path is investigated (Fig. 1). Dynamical systems including pendulum play significant role in technology. Discussion on such models regarding damping of vibrations may be found in [2–5]. In such systems one can observe an auto-parametric resonance phenomena, because of the coupling occurring in the equations of motion. The phenomenon of energy transfer in such systems was also widely discussed in [3].

The system investigated in the paper can model a various elements of engineering machines or can simulate the motion of a floating body.

R. Starosta (✉)
Institute of Applied Mechanics, Poznan University of Technology, Poland

I. Vişa (ed.), *SYROM 2009*,
DOI 10.1007/978-90-481-3522-6_34,

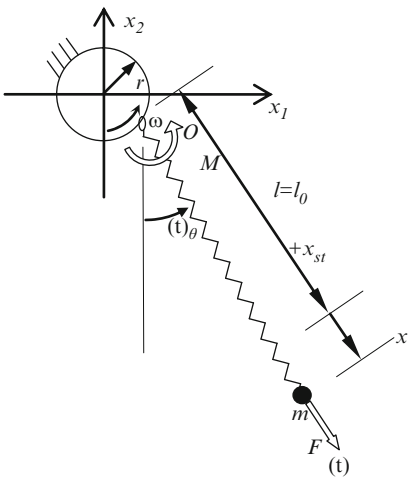

Fig. 1 Spring pendulum moving on circular path

The applied multiple scale method allows for identification of the system parameters being dangerous due to the resonance and yields time histories for the assumed generalized co-ordinates. Also stability of the steady state solution can be carried out after transferring the modulation equations into an autonomous form.

Several procedures in the computer algebra system *Mathematica* are prepared in order to automatizing most of the algebraic transformations [6].

2 Formulation of the Problem

The kinetic and potential energy of the examined system have the form:

$$\begin{aligned} T &= \frac{1}{2}m\Big(\Big(r\omega\cos\omega t + \dot{\bar{x}}\sin\phi + (l+\bar{x})\dot{\theta}\cos\theta\Big)^2 \\ &\quad + \Big(r\omega\sin\omega t + \dot{\bar{x}}\cos\theta + (l+\bar{x})\dot{\theta}\sin\theta\Big)^2\Big), \\ V &= \frac{1}{2}k\Big(\frac{gm}{k}+\bar{x}\Big)^2 + \\ &\quad + gm(-r\cos\omega t - (l+\bar{x})\cos\theta), \end{aligned} \tag{1}$$

where m – mass of the pendulum, l – statically stretched length, k – stiffness of the spring, g – Earth's acceleration, and $\bar{x}$ and θ are the generalized co-ordinates (see Fig. 1.). The moment M(t) acts around a point O and the force F(t) acts on the mass along the pendulum length. Forces of linear viscous damping are considered to be present in both longitudinal and swing motions of the pendulum (c_1 and c_2 are viscous coefficients).

The governing equations of our system follow:

$$\begin{aligned}
&\Big(\omega_2^2(1-\cos\theta)-\rho\omega^2\cos(\omega t-\theta)-\dot\theta^2+\ddot x\Big)\\
&\quad+x\Big(\omega_1^2-\dot\theta^2\Big)+c_1\dot x=f_1\cos\Omega t,\\
&(1+x)\Big(-\rho\omega^2\sin(\omega t-\theta)+\omega_2^2\sin\theta+2\dot x\dot\theta\\
&\quad+(1+x)\ddot\theta\Big)+c_2\dot\theta=f_2\cos\Omega t,
\end{aligned}\tag{2}$$

where

$$f_1\equiv\tfrac{F}{lm},f_2\equiv\tfrac{M}{l^2m},\ \omega_1^2\equiv\tfrac{k}{m},\ \omega_2^2\equiv\tfrac{g}{l},\ \rho\equiv\tfrac{r}{l},\ x\equiv\tfrac{\bar x}{l}.$$

Since a motions in some small neighborhood of a static equilibrium position are considered, the amplitude of vibrations is assumed to be of order of a small parameter $0<\varepsilon<<1$, i.e., $x=\varepsilon\tilde x,\ \theta=\varepsilon\tilde\theta$. In addition we apply the following scaling:

$$\rho=\varepsilon\tilde\rho\,f_i=\varepsilon^2\tilde f_i,\ c_i=\varepsilon\tilde c_i,\ i=1,2,$$

and the following approximations

$$\sin\theta\cong\theta-\frac{1}{3!}\theta^3\ \text{and}\ \cos\theta\cong1-\frac{1}{2}\theta^2.$$

Eq. (2) can be cast into the form:

$$\begin{aligned}
&\ddot{\tilde x}+\varepsilon\tilde c_1\dot{\tilde x}+\omega_1^2\tilde x-\varepsilon^2\tilde x\dot{\tilde\theta}^2+\omega_2^2\varepsilon\frac{\tilde\theta^2}{2}-\varepsilon\dot{\tilde\theta}^2-\\
&\quad-\tilde\rho\varepsilon\omega^2\Big(\cos\omega t+\sin\omega t+\varepsilon\tilde\theta\Big)=\varepsilon\tilde f_1\cos\Omega t,\\
&(1+\varepsilon\tilde x)\Big((1+\varepsilon\tilde x)\ddot{\tilde\theta}+\omega_2^2\ddot\theta+2\varepsilon\dot{\tilde x}\dot{\tilde\theta}\Big)+\varepsilon\tilde c_2\dot{\tilde\theta}\\
&\quad-(1+\varepsilon\tilde x)\tilde\rho\varepsilon\omega^2\Big(\sin\omega t-\varepsilon\tilde\theta\cos\omega t\Big)=\varepsilon\tilde f_2\cos\Omega t.
\end{aligned}\tag{3}$$

In order to simplify the notation, the sign – tilde will be further omitted.

The solution of (3) is sought in the following form

$$\begin{aligned}
x(t;\varepsilon)&\approx x_0(T_0,T_1)+\varepsilon\,x_1(T_0,T_1)+O(\varepsilon^2),\\
\theta(t;\varepsilon)&\approx\theta_0(T_0,T_1)+\varepsilon\,\theta_1(T_0,T_1)+O(\varepsilon^2),
\end{aligned}\tag{4}$$

where $T_0=t$ and $T_1=\varepsilon t$.

The original set of equations will be transformed to the set of partial differential equations owing to the following relations:

$$\begin{aligned}\frac{d}{dt} &= \frac{\partial}{\partial T_0} + \varepsilon \frac{\partial}{\partial T_1},\\ \frac{d^2}{dt^2} &= \frac{\partial^2}{\partial T_0^2} + 2\,\varepsilon\,\frac{\partial^2}{\partial T_0\,\partial T_1}.\end{aligned} \tag{5}$$

Substitution of (4) and (5) to (3) yields the equations:
(order ε^0)

$$\begin{aligned}\frac{\partial^2 x_0}{\partial T_0^2} + \omega_1^2 x_0 &= 0,\\ \frac{\partial^2 \theta_0}{\partial T_0^2} + \omega_2^2 \theta_0 &= 0;\end{aligned} \tag{6}$$

(order ε^1)

$$\begin{aligned}&\frac{\partial^2 x_1}{\partial T_0^2} + c_1 \frac{\partial x_0}{\partial T_0} + \omega_1^2 x_1 + 2\frac{\partial^2 x_0}{\partial T_0\,\partial T_1} - \left(\frac{\partial \theta_0}{\partial T_0}\right)^2\\ &\quad + \frac{1}{2}\omega_2^2\theta^2 - \rho\omega^2 \cos\omega T_0 = f_1 \cos(\Omega T_0),\\ &\frac{\partial^2 \theta_1}{\partial T_0^2} + \omega_2^2 \theta_1 + c_2 \frac{\partial \theta_0}{\partial T_0} + 2\frac{\partial^2 \theta_0}{\partial T_0\,\partial T_1} + 2x_0 \frac{\partial^2 \theta_0}{\partial T_0^2}\\ &\quad + 2\frac{\partial x_0}{\partial T_0}\frac{\partial \theta_0}{\partial T_0} + \omega_2^2 x_0 \theta_0 - \rho\omega^2 \sin T_0\omega = f_2 \cos\Omega T_0.\end{aligned} \tag{7}$$

The solution of (6) may be found as follows

$$\begin{aligned}x_0 &= A(T_1)\, e^{i\,\omega_1 T_0} + \bar{A}(T_1)\, e^{-i\,\omega_1 T_0},\\ \theta_0 &= B(T_1)\, e^{i\omega_2 T_0} + \bar{B}(T_1)\, e^{-i\omega_2 T_0}.\end{aligned} \tag{8}$$

Substitution of (8) to (7) gives the first order equation in the form:

$$\begin{aligned}\frac{\partial^2 x_1}{\partial T_0^2} + \omega_1^2 x_1 &= \frac{1}{2} F e^{iT_0\Omega} - e^{2iT_0\omega_2}\left(G_1 + \omega_2^2\right)B^2\\ &\quad + \omega_2^2 B\bar{B} - \frac{3}{2}e^{2iT_0\omega_2}\omega_2^2 B^2 + \frac{1}{2}e^{iT_0\omega}\rho\omega^2 +\\ &\quad - i\omega_1 e^{iT_0\omega_1}\left(c_1 A + 2\frac{dA}{dT_1}\right) + c.c.,\end{aligned} \tag{9}$$

$$\begin{aligned}\frac{\partial^2 \theta_1}{\partial T_0^2} + \omega_2^2 \theta_1 &= -e^{iT_0(\omega_1+\omega_2)}\left(-2\omega_1\omega_2 - \omega_2^2\right)AB\\ &\quad + -ie^{i\omega_2 T_0}\omega_2\left(c_2 B + 2\frac{dB}{dT_1}\right) + \frac{1}{2}e^{iT_0\Omega}f_2 - \frac{1}{2}e^{iT_0\omega}\omega^2 + c.c,\end{aligned}$$

were A and B are functions of T_1.

Removal of secular terms in (9), requires

$$c_1 A + 2\frac{dA(T_1)}{dT_1} = 0,\ c_2 B + \frac{dB(T_1)}{dT_1} = 0, \tag{10}$$

and then the solution of (9) is follows

$$\begin{aligned} x_1 = &-\frac{e^{iT_0\Omega} f_1}{2\left(\Omega^2 - \omega_1^2\right)} - \frac{e^{iT_0\omega}\rho\omega^2}{2\left(\omega - \omega_1^2\right)} + \\ &+ e^{2iT_0\omega_1}\frac{3\omega_2 B^2}{2\left(4\omega_2^2 - \omega_1^2\right)} + c.c., \\ \theta_1 = &-\frac{\omega_2(2\omega_1 + \omega_2)}{\omega_1(\omega_1 + 2\omega_2)} AB e^{i(\omega_1+\omega_2)T_0} + \frac{ie^{iT_0\omega}\rho\omega^2}{2\left(\omega^2 - \omega_2^2\right)} \\ &\frac{(2\omega_1 - \omega_2)}{\omega_1(\omega_1 - 2\omega_2)} A\bar{B} e^{i(\omega_2-\omega_1)T_0} - \frac{f_2 e^{iT_0\Omega}}{2\left(\Omega^2 - \omega_2^2\right)} + c.c. \end{aligned} \tag{11}$$

The above solution becomes singular when the primary, parametric or internal resonances occur, i.e., when $\omega_1 = \Omega$, $\omega_2 = \Omega$, $\omega_1 = \omega$, $\omega_2 = \omega$ and/or $\omega_1 = 2\omega_2$. Note that the system behavior is very complex, especially when the natural frequencies satisfy certain resonance conditions. In order to study the resonances, we can introduce the new so-called detuning parameters. Let us examine parametric and internal resonances appeared simultaneously, i.e., $\omega \approx \omega_1,\ 2\omega_2 \approx \omega_1$. Detuning parameters σ_1 and σ_2 are introduced into (9) in the form:

$$\omega = \omega_1 + \varepsilon\sigma_1,\ 2\omega_2 = \omega_1 + \varepsilon\sigma_2. \tag{12}$$

This substitution gives the solvability conditions:

$$\begin{aligned} &-\frac{1}{2}e^{iT_1\sigma_1}\rho\omega^2 + \frac{3}{2}e^{iT_1\sigma_2}\omega_2^2 B^2 \\ &+ 2i\omega_1\frac{dA}{dT_1} + ic_1\omega_1 A = 0, \\ &2e^{-iT_1\sigma_2}\omega_1\omega_2 A\bar{B} - e^{-iT_1\sigma_2}\omega_2^2 A\bar{B} \\ &+ 2i\omega_2\frac{dB}{dT_1} + ic_2\omega_2 B = 0. \end{aligned} \tag{13}$$

In order to obtain the solution of (13) in the form:

$$\begin{aligned} x &= a\cos(\omega_1 t + \alpha) \\ \theta &= b\cos(\omega_2 t + \beta) \end{aligned}, \tag{14}$$

the following scaling is introduced [1]:

$$A \to \frac{a}{2} e^{i\alpha}, \qquad B \to \frac{b}{2} e^{i\beta}. \tag{15}$$

Note that the introduced amplitudes a and b and phases α and β depend on T_1. Introduction of (15) into (13) yields:

$$\begin{aligned}
\frac{da}{dT_1} &= -\frac{4c_1\omega_1 a - 4\rho\omega^2 \sin\xi + 3\omega_2^2 b^2 \sin\eta}{8\omega_1}, \\
\frac{d\alpha}{dT_1} &= \frac{-4\rho\omega^2 \cos\xi + 3\omega_2^2 b^2 \cos\eta}{8\omega_1 a}, \\
\frac{db}{dT_1} &= \frac{1}{4} b(2c_2 - (2\omega_1 - \omega_2) a \sin\eta), \\
\frac{d\beta}{dT_1} &= \frac{1}{4}(2\omega_1 - \omega_2) a \cos\eta,
\end{aligned} \tag{16}$$

where:

$$\begin{aligned}
\xi &= T_1 \sigma_1 - \alpha(T_1), \\
\eta &= T_1 \sigma_2 - \alpha(T_1) + 2\beta(T_1).
\end{aligned} \tag{17}$$

Equations (16) are non-autonomous because their right-hand sides depend on the independent variable T_1. They can be transformed into autonomous system of equations by presenting $\frac{d\alpha}{dT_1}$ and $\frac{d\beta}{dT_1}$ in terms of $\frac{d\xi}{dT_1}$ and $\frac{d\eta}{dT_1}$. After some transformations we get

$$\begin{aligned}
\frac{d\xi}{dT_1} &= \frac{\left(4\rho\omega^2 \cos\xi - 3\omega_2^2 b^2 \cos\eta\right)}{4\omega_1 a} + \sigma_1, \\
\frac{d\eta}{dT_1} &= \sigma_2 + \frac{1}{2}(2\omega_1 - \omega_2) a \cos\eta \\
&\quad + \frac{4\rho\omega^2 \cos\xi - 3\omega_2^2 b^2 \cos\eta}{8\omega_1 a}
\end{aligned} \tag{18}$$

instead of $(16)_2$ and $(16)_4$.

Now equations $(16)_1$, $(16)_3$ and (18) form an autonomous system of equations. Fixed points of these equations are defined by the following relations

$$\frac{da}{dT_1} = 0, \ \frac{db}{dT_1} = 0, \ \frac{d\xi}{dT_1} = 0, \ \frac{d\eta}{dT_1} = 0,$$

which can be written in the form:

$$
\begin{aligned}
0 &= -\frac{4c_1\omega_1 a - 4\rho\omega^2 \sin\xi + 3\omega_2^2 b^2 \sin\eta}{8\omega_1},\\
0 &= \frac{\left(4\rho\omega^2 \cos\xi - 3\omega_2^2 b^2 \cos\eta\right)}{4\omega_1 a} + \sigma_1,\\
0 &= \frac{1}{4} b(2c_2 - (2\omega_1 - \omega_2)a \sin\eta),\\
0 &= \sigma_2 + \frac{1}{2}(2\omega_1 - \omega_2)a\cos\eta\\
&\quad + \frac{4\rho\omega^2 \cos\xi - 3\omega_2^2 b^2 \cos\eta}{8\omega_1 a}.
\end{aligned}
\tag{19}
$$

3 Stability of the Fixed Points

In order to study the fixed points stability we use the following

$$
\begin{aligned}
a &= a_0 + a_1,\ \xi = \xi_0 + \xi_1,\\
b &= b_0 + b_1,\ \eta = \eta_0 + \eta_1,
\end{aligned}
\tag{20}
$$

where $a_0,\ \xi_0\,, b_0,\ \eta_0$ are solutions to Eq. (19), and $a_1,\ \xi_1\,, b_1,\ \eta_1$ are perturbations (assumed to be small compared to $a_0,\ \xi_0\,, b_0,\ \eta_0$). Now (20) are substituted into $(16)_{1,\,3}$ and (18), and the resulting equations are linearized. Taking into account that steady state values satisfying Eq. (19), we get

$$
\begin{aligned}
\dot{a}_1 &= \frac{c_1}{2} a_1 + D_1 \cos(\xi_0)\,\xi_1\\
&\quad + 2D_2 b_0 \sin(\eta_0) b_1 + D_2 b_0^2 \cos(\eta_0)\,\eta_1\\
a_0\dot{\xi}_1 &= \sigma_1 a_1 - 2D_1 \sin(\xi_0)\,\xi_1\\
&\quad - 4D_2 b_0 \cos(\eta_0)\,b_1 - 2D_2 b_0^2 \sin(\eta_0)\,\eta_1,\\
\dot{b}_1 &= D_3 b_0 \sin\eta_0\, a_1\\
&\quad + \left(D_3 a_0 \sin(\eta_0)\,\frac{c_2}{2}\right) b_1 + D_3 a_0 b_0 \cos(\eta_0)\,\eta_1\\
a_0\dot{\eta}_1 &= (\sigma_2 - 4D_3 a_0 \cos(\eta_0))\,a_1\\
&\quad + 2D_1 \sin(\xi_0)\,\xi_1 - 2D_1 b_0 \cos(\eta_0)\,b_1\\
&\quad + \left(-D_2 b_0^2 \sin(\eta_0) + 2D_3 a_0^2 \sin(\eta_0)\right)\eta_1,
\end{aligned}
\tag{21}
$$

where:

$$
D_1 = \frac{\rho\omega^2}{2\omega_1},\ D_2 = -\frac{3\omega_2^2}{8\omega_1},\ D_3 = -\frac{2\omega_1 - \omega_2}{4}.
$$

If the steady state solution $a_0,\ \xi_0\ , b_0,\ \eta_0$ is asymptotically stable, then the real parts of the roots of the characteristic equation

$$\lambda^4 + \Gamma_1\lambda^3 + \Gamma_2\lambda^2 + \Gamma_3\lambda + \Gamma_4 = 0 \tag{22}$$

should be negative. $\Gamma_1, \Gamma_2, \Gamma_3, \Gamma_4$ are functions of the parameters $a_0, b_0,$ $\xi_0, \eta_0, \omega_1, \omega_2,\ \sigma_1, \sigma_2, F$. According to the Routh-Hurwitz criterion the necessary and sufficient conditions of stability is as follows:

$$\begin{aligned} &\Gamma_1 > 0, \Gamma_3(\Gamma_1\Gamma_2 - \Gamma_3) - \Gamma_4\Gamma_1^2 > 0, \\ &\Gamma_3 > 0, \Gamma_4 > 0 \end{aligned} \tag{25}$$

4 Example

The parametric and internal resonances occurring simultaneously and defined by (12) are studied for the following fixed parameters:

$$\omega = 2.6,\ \omega_1 = 2.6,\ \omega_2 = 1.3, \Omega = 1.67,$$

$$c_1 = 0.01, c_2 = 0.01,\ \rho = 0.01, \varepsilon = 0.1,$$

$$\sigma_1 = 0, \sigma_2 = 0, f_1 = 0.01, f_2 = 0.01,$$

The modulations of amplitudes and phases (for the initial conditions $a(0) = 0.1,$ $b(0) = 0.1,\ \alpha(0) = 0,\ \beta(0) = 0$) yielded by (16) are presented in Figs. 2–5.

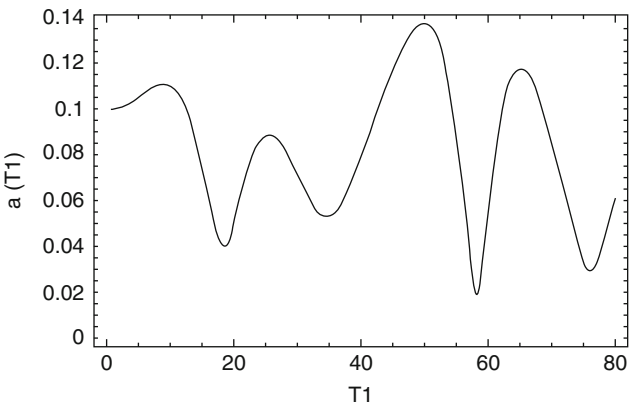

Fig. 2 Modulation of amplitude a(T_1)

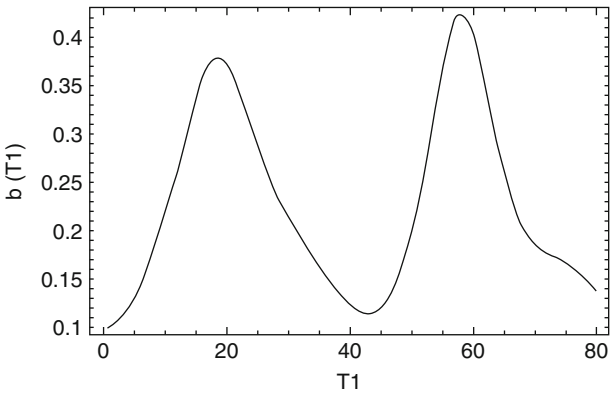

Fig. 3 Modulation of amplitude $b(T_1)$

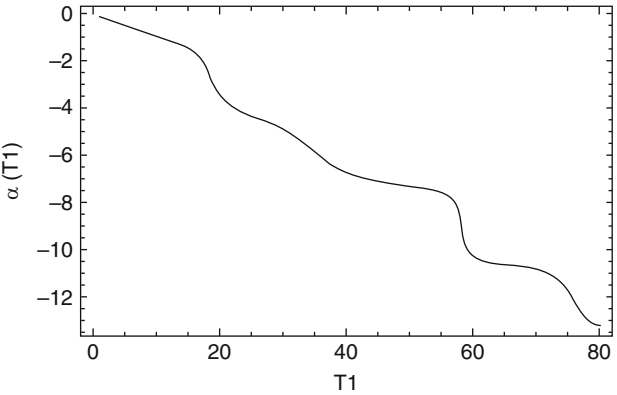

Fig. 4 Modulation of phase $\alpha(T_1)$

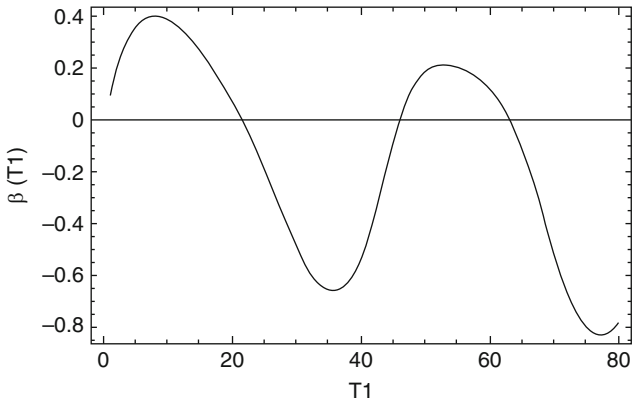

Fig. 5 Modulation of phase $\beta(T_1)$

Time history of motion is reported in Figs. 6 and 7. In Fig. 6 the solution is obtained by multiple-scale-method whereas in Fig. 7 by numerical solution of Eq. (3). The obtained results coincide very well.

In the Figs. 8 and 9 the Poincaré maps are presented in the chosen phase planes.

Time history diagrams and Poincaré maps suggest that the motion has chaotic character.

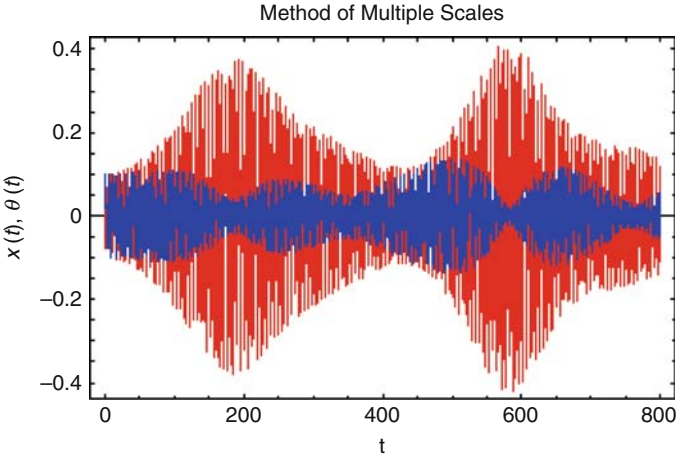

Fig. 6 Time history of $x(t)$ and $\theta(t)$

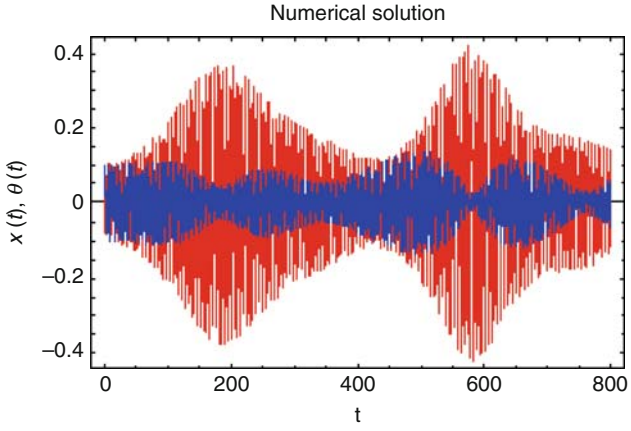

Fig. 7 Time history of $x(t)$and $\theta(t)$

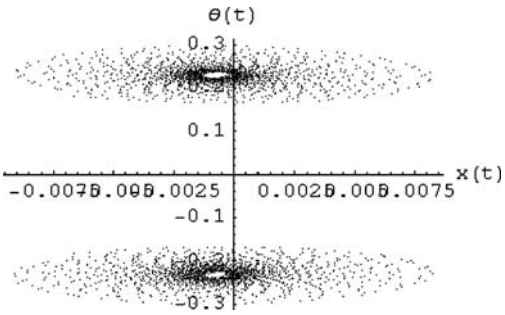

Fig. 8 Projection of the Poincaré map on plane (x, θ)

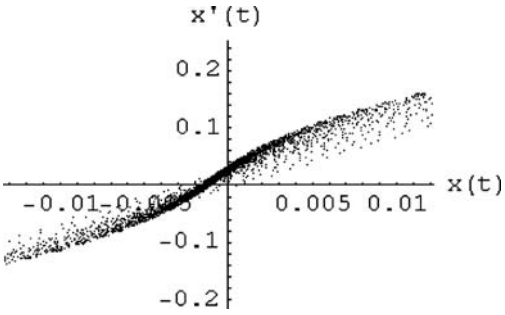

Fig. 9 Projection of the Poincaré map on plane (x,x').

5 Conclusions

Our results show that both quantitative and qualitative analyses of parametrical systems can be successfully carried out by the multiple-scale-method. The method allows to detect the most dangerous parameters of the system with respect to occurring resonances. One may observe energy transfer in the presented diagrams. The transformations were carried out automatically with the use of interactive procedures within *Mathematica*. Analytical results were confirmed numerically, and stability of the fixed points were defined.

References

1. Awrejcewicz, J., Krysko, V.A.: Introduction to Asymptotic Methods. Chapman and Hall, Boca Raton (2006)
2. Genin, M.D., Ryabow, V.M.: Elastic-Internal Vibroisolating Systems. Nauka, Moskwa (1988) (in Russian)

3. Karamyskin, V.V.: Dynamiceskoje gasenie kolebanii. Maszinostrojenie, Leningrad (1988)
4. Sado, D.: Energy Transfer in Two Degree of Freedom Coupled Systems (in Polish). OWPW, Warszawa (1997)
5. Shivamoggi, B.K.: Perturbation methods for differential equations. Birkhauser, Boston (2002)
6. Starosta, R., Awrejcewicz, J.: Asymptotic Solution and Stability of Autoparametrical Systems. ENOC-2008. Saint Petersburg, Russia, 30 June–4 July 2008

Simple Mechanical Clutch with Multiple Functions

I. Stroe

Abstract The paper presents a new type of clutch named "Elastic and Safety Clutch," that can accomplish the functions of the elastic and those of the safety clutches, but that is not a combined clutch. The strict systematization of the extant clutches, as well the simple functions' combinations lead to new types of clutches. The paper presents the constructive solution of this new type of clutch, the analytical determination of the torque, the cinematic modeling and the theoretical and experimental researches concerning the dynamic testing. The clutch presented is an elastic and safety clutch with metallic intermediate elements. There are also presented the simple function of the clutch, the operating principle and the specific characteristics.

Keywords Clutch · Functions multiple · Mechanism with cam

1 Introduction

A condition imposed to the elastic clutches is that at the breakage of an element, the clutch does not failure immediately. If there is only an elastic element, the total breakage of the clutch has to be inferred in case of partial fractures or the fissures. Another condition imposed to elastic clutches is that the elastic elements that can rapidly be destroyed, to be easily replaced – if it is possible without the clutch disassembling or the axial displacement of the axle stubs [1, 2].

The elastic clutch could take over, overloads up to a certain torque value. Over this value, when the transmission is not provided with a load disengagement

I. Stroe
Department of Product Design and Robotics, Transilvania University of Braşov, Braşov, Romania

I. Vişa (ed.), *SYROM 2009*,
DOI 10.1007/978-90-481-3522-6_35,

system, the elastic elements of the clutch are destroyed, this corresponding with the placing of transmission out of the operation.

The safety clutch fulfills (besides the main function of the torque transmission) the function of torque limitation or automatic interruption of the connection between the coupled shafts, in the case of some overloads' occurrence, during the performance.

The safety clutches assure the transmission performance up to the limit torque value, for what the safety elements are designed. Over this value, it appears the relative slipping between the semi-clutches that involves the mechanical transmission protection. Taking the data above into consideration, it results the necessity of some clutches, that by the associated functions to allow the load disengagement before that the elastic elements to be destroyed. In the case of diverse applications, when the mechanical transmission imposes it, there can be combined the simple functions of one clutch type with the simple functions of another clutch type, obtaining a combined coupling. In this case, the combined coupling is obtained by the connection, of two or more simple clutches, in a certain manner, on purpose to accomplish accordingly the imposed complex functional role of mechanical transmission. [1, 2].Taking the data above into consideration, this paper will present a new type of clutch, whose component elements can accomplish the functions of a combined clutch. It will be presented by the name "Elastic and Safety Clutch" [3].

In the first Fig. 1 there is presented a classification of the mechanical clutch which includes also the new type of the elastic and safety clutch [3, 4].

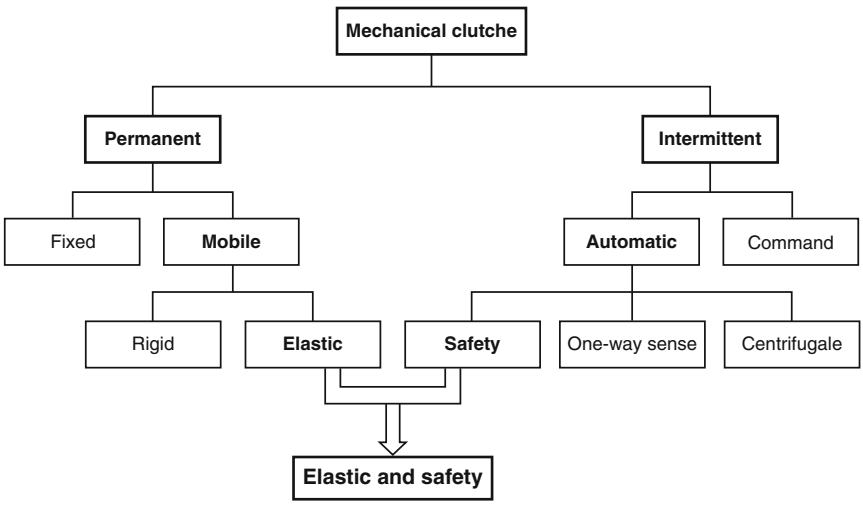

Fig. 1 The classification the mechanical clutches

2 Elastic and Safety Clutch

The paper presents a new type of clutch named "Elastic and Safety Clutch," that can accomplish the functions of the elastic and those of the safety clutches, but that is not a combined clutch [4]. The angle of relative rotation between the two semi-clutches depends on the number of cam prominences. The strict systematization of the extant clutches, as well as the simple combination of functions lead to new types of clutches.

2.1 Derivation Proceeding from the Structural Schemes

Beginning with the topological study of the elastic and safety clutches, there are tackled, further on, two important problems [1, 4]:

a. A proceeding proposal widely allows the derivation of the structural scheme frame of the topological variant we have obtained [1].
b. The identification and the systematization is based on the proceeding, we have proposed the most representative and usable elastic and safety clutch structure.

The elastic and safety clutches are characterized by the following functions (functional and technical criteria):

- They make the bundle between two shafts.
- (With relatively fix variable position) and ensure the moment transmission and the rotation motion between the shafts (according to the general definition).
- The power transmission is braked off when the resistive moment outruns an imposed limit value.
- The braking off of the energy flux is realized on the basis of an elastic element deformation.

Out of the analysis of the properties corresponding to the elastic and safety clutches, a distinctive importance goes to the elastic element modeling, to ensure the automated braking off every flux, at the torque limit value.

From their use within technique, the critical analysis [2, 4] of the mechanism leads to the conclusion that the cam mechanism (Fig. 2) lends oneself (the best) to the demands previously formulated, thus.

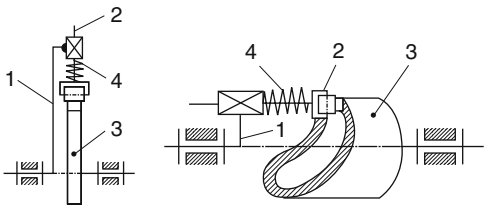

Fig. 2 Structural scheme

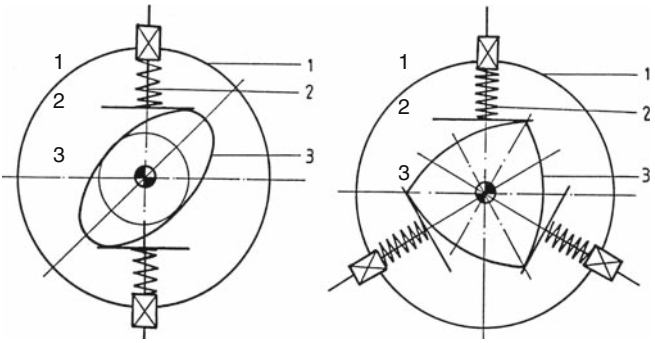

Fig. 3 Structural scheme with flat translation followers

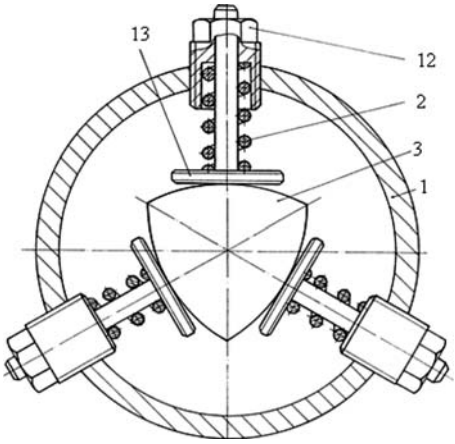

Fig. 4 The design of the clutch

Figure 3 presents the structural schemes of the elastic and safety clutch with flat translation followers [3].

2.2 Construction of the Clutch

The constructive solution allows the pretension adjustment without taking to pieces the clutch, Figs. 3 and 4. The clutch contains the equiangular cam 3, with three prominences, which represents one of the semi-clutches and the flange 1 represents the second semi-clutch. On this flange there are mounted the three flat translation followers 13 – that are equiangularly disposed – as well as the fastening and adjusting elements 12, that are required for the pretension of the compression spiral springs 2 [5].

The driving semi-clutch 1 transmits the torsion moment by means of the equiangular cam 3, that are in contact with the three flat translation followers 13, due to the pressing force of the compression spiral springs 2.

Knowing the elastic characteristic of the compression springs, the pressing force necessary for the torque transmission can be adjusted by means of the special screws 12, [3, 4].

2.3 The Torque Moment and Its Elastic Characteristics

Starting from the structural scheme in Fig. 5 the geometrical models for the determination of torsion moment are presented. The moment can be transmitted by the clutch on the curved radius M_0M_1 and M_1M_2:

$$T* = [k_a(s_2 + \delta)] \cdot OB, \tag{1}$$

$$T = n[k_a(s_2 + \delta)] \cdot OB \tag{2}$$

where by T^* it had been written down the moment that corresponds to a single proeminence ($T* = T/n$, n – the number of the prominences of the cam and the number of the flat translation followers), φ_1 is the relative angular displacement, μ is the friction coefficient between the cam and the follower, k_a is the rigidity of the coiled spring, δ is the initial curving of the spring and s_2 is the displacement of the follower.

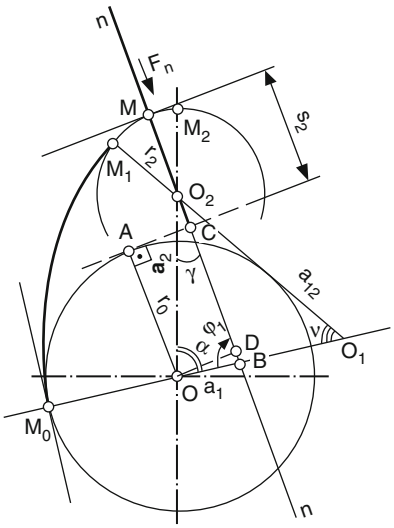

Fig. 5 Geometrical model for the torque determination

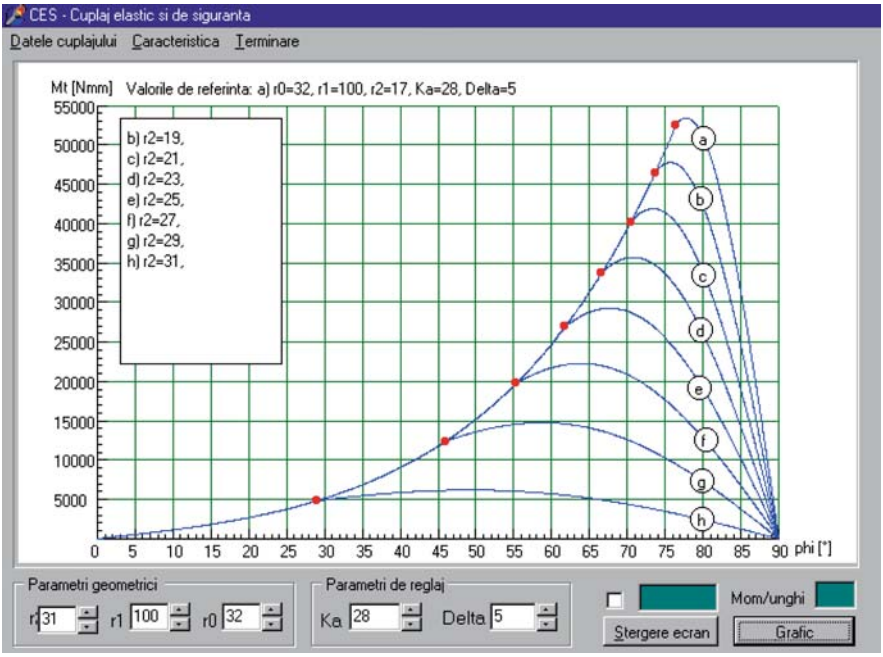

Fig. 6 The elastic characteristic of the clutch

The determination of the s_2 – change of place will be performing distinctly, for each circle arc of the cam profile.

The elastic characteristic of the clutch is given by the relation (3) and is presented in Fig. 6, through the derivation of the Eq. (4), for different values of the radius of curvature r2 other parameters remain constant Figs. 5 and 6.

$$K(\varphi) = \frac{dT(\varphi)}{d(\varphi)}, \tag{3}$$

$$\begin{aligned} T &= nT \\ &= nk_a\{[(r_1 - r_0)(1 - \cos\varphi_1) + \delta] \cdot \sin\varphi + \mu[(r_1 - r_0)(1 - \cos\varphi_1) + r_0]\} \end{aligned} \tag{4}$$

3 Theoretical and Experimental Researches

The determination of the force transmission functions, for the equivalent mechanism with two degrees of freedom (that models the elastic and safety clutch working) will be achieved using the Lagrange equations of the second species.

Along the way there are necessary the expressions of the relative rotation angle, the angular velocities and the accelerations functions Fig. 7 [2, 4].

The dynamic study of the clutch we propose will be achieved on the basis of an equivalent plane mechanism with two degrees of freedom and with three external connections, namely the input ($\varphi_1 M_1$) the output ($\varphi_3 M_3$) and the contact cam – flat translation follower (s_a, F_a); the motion of the semi-clutches φ_1 and φ_3 are considered the independent parameters. The adopted mechanism model is defined taking into consideration the following assumptions: the kinematic elements are rigid; the kinematic pairs are permanent, geometrical, and stationary.

Figure 8 represents the cam positions for the first and the second uncoupling stages, considering both semi-clutches moving; thus the angular relative displacement between the two semi-clutches is $\varphi = \varphi_1 - \varphi_3$ [3].

The movement conduction equations are:

$$S_a = S_a(\varphi_1, \varphi_3), \tag{5}$$

$$M_1 = M_1(\varphi_1, \varphi_3, F_a), \tag{6}$$

$$M_3 = M_3(\varphi_1, \varphi_3, F_a), \tag{7}$$

Knowing the geometry of the cam (Fig. 8) there can be determined the transmission function $Ss_a = s_a(\varphi_1, \varphi_3) = s_{23}\varphi_3$, as well as the relative and absolute position functions of the flat translation followers 2, s_{21}, s_2. Differentiating these position functions, there can be also determined the velocity and acceleration functions of

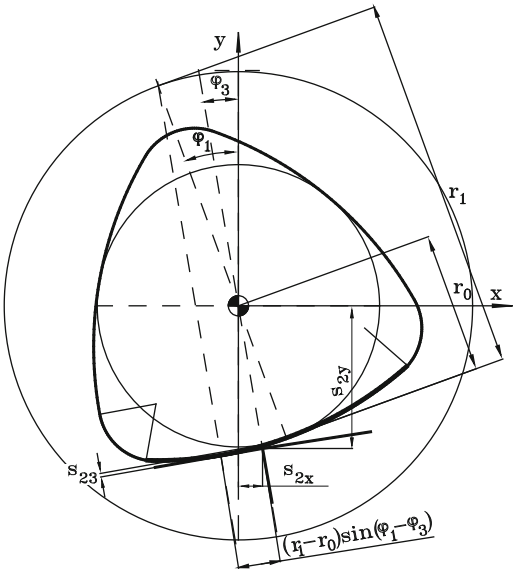

Fig. 7 Definition scheme for the position function

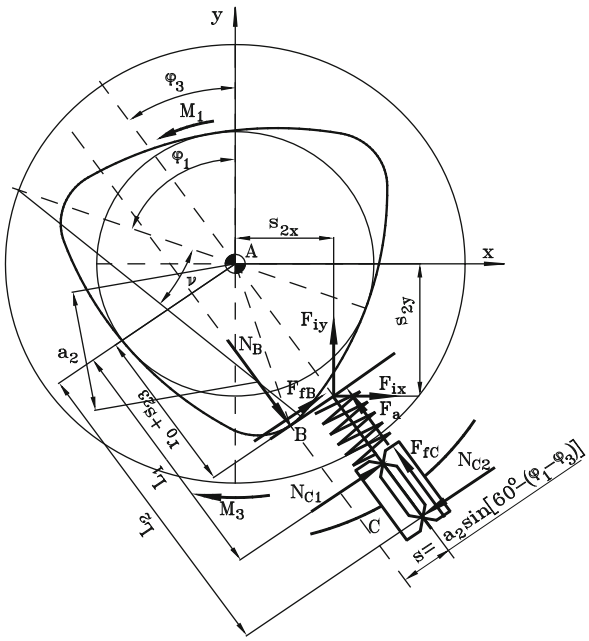

Fig. 8 The scheme force for the first and the second stage

the flat translation follower 2 (13), depending on the relative rotation angle between the semi-clutches. The determination of the force transmission functions, for the equivalent mechanism with two degrees of freedom (that models the elastic and safety clutch working) will be achieved using the Lagrange equations of the second species. This way there are necessary the expressions of the relative rotation angle, the angular velocities and the acceleration functions. These functions are presented in equations:

The relative rotation angle (absolute co-ordinates)

$$\varphi_1 - \varphi_3 \in [0, \varphi_{\max}] \tag{8}$$

This stage intents to determine the expressions of the friction forces F_{fB} and F_{fC}, their expressions being necessary for the determination of the generalised forces Q_1, and Q_3 [3, 4].

Using the force scheme presented (Fig. 4), it can be written the equilibrium equation system of the element 2. The mechanism presented is bimobile and it has two unknown motions $(\varphi_1, \dot{\varphi}_1, \ddot{\varphi}_1)$ and $(\varphi_3, \dot{\varphi}_3, \ddot{\varphi}_3)$.

For the determination of the two motions, there will be use the two transmission functions of the external forces; these functions are described by two Lagrange equations of the second species (9).

By means of the motion Eq. (9), it can be simulate the clutch working. In this way Fig. 9 presents the dynamic diagrams for a situation when the resistant moment

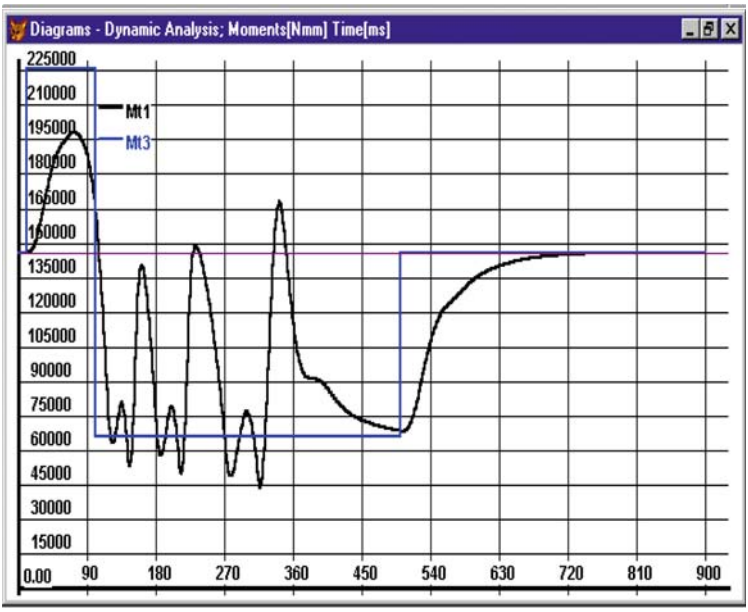

Fig. 9 Dynamic diagrams for a medium shock value

has a variation corresponding to a medium shock for a short period of time, followed by a decrease of this under the initial value (the moment for what the clutch was designed) [3, 4].

$$\begin{cases} \dfrac{d}{dt}\left(\dfrac{\partial E_c}{\partial \dot{\varphi}_1}\right) - \dfrac{\partial E_c}{\partial \varphi_1} = Q_1 \\ \dfrac{d}{dt}\left(\dfrac{\partial E_c}{\partial \dot{\varphi}_3}\right) - \dfrac{\partial E_c}{\partial \varphi_3} = Q_3 \end{cases}, \tag{9}$$

$$Q_1 = M_1 - 3\,(F_a - F_{fC})k_1 - 3\,F_{fB}k_2, \tag{10}$$

$$Q_3 = -M_3 + 3\,(F_a - F_{fC})k_1 + 3\,F_{fB}k_2, \tag{11}$$

The resistant moment increase leads at its beginning to the decrease of the angular velocity, the motor moment increases; at the resistant moment decrease takes also place the motor moment decrease, that leads to repeated uncoupling, until its stabilisation. After the return of the resistant moment to the initial value, the clutch returns to the nominal working point (the initial angular velocity for the two semi-clutches and the initial value for the motor moment).

Figure 10 presents the testing dynamic diagram of the elastic and safety clutch on a testing stand. The testing regime corresponds to the shock moment increase up

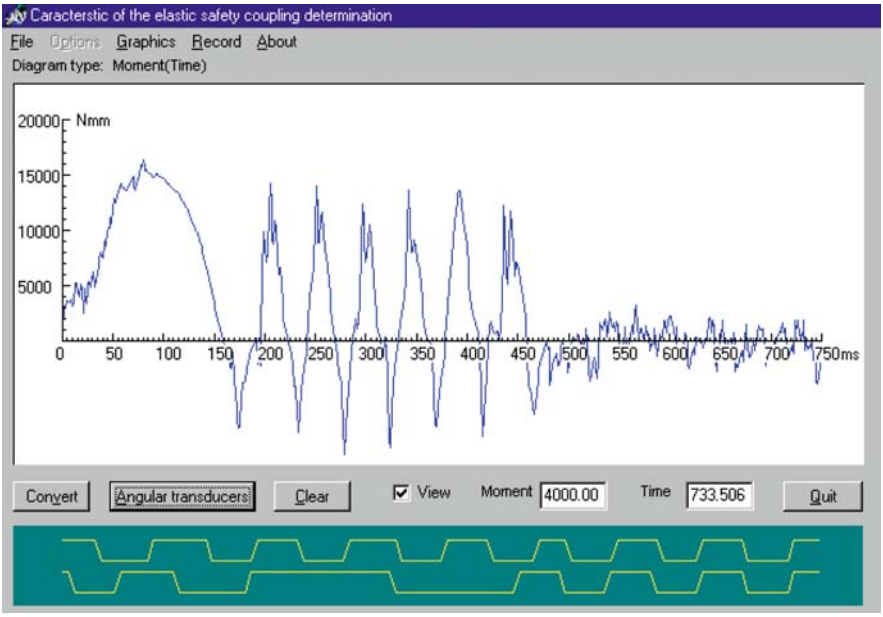

Fig. 10 Dynamic diagrams for a big shock value

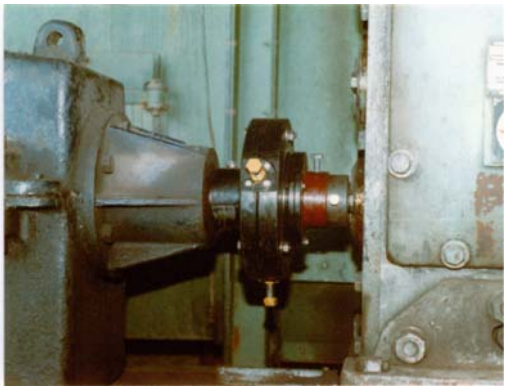

Fig. 11 The implementation of the clutch

to a value corresponding to the repeated uncoupling situation, followed be the return to the normal working after the elimination of the shock moment. The analysis of the diagrams presented leads to the following conclusions: the clutch characteristics are progressive; the clutch has an important capacity of elastic deformation, determining the torsion shocks damping; the uncoupling is made without the elastic elements destroying and without any further shocks [3–5].

Figure 11 presents the implementation of the clutch

The elastic and safety clutches of the [3] mechanisms with cam and flat translation type follower present the following advantages:

- The clutches have a simple construction, cabaret reduced dimension, cheap price.
- The clutches ensure the compensation of axial, radial and angular deviation in relatively large limits.
- The clutches ensure the a relative movement between the semi – clutches, according to the nature and to the disposing mode of the component elements; above the accepted limits, the elastic clothe becomes a safety one.
- The clutches ensure the limitation and the adjustment of the transmitted moment.

References

1. Drăghici, I.: ş.a. Calculul şi construcţia cuplajelor. Editura Tehnică, Bucureşti (1978)
2. Pampel, W.: Kupplungen. Band I Berlin, VEB Verlag Technik (1958)
3. Stroe, I.: Theoretical and experimental contribution regarding the conceiving and modulations of a new class of clutches with multiples functions Elastic and Safety Clutches. Ph.D. Thesis, Transilvania University of Braşov, Braşov (1999)
4. Stroe, I., Eftimie, E.: Elastic and Safety Clutch. Editura Ecran Magazin, Braşov (2001)
5. Stroe, I.: Design procedure of elastic and safety clutches using cam mechanisms. In Proceeding on CD-ROM of Twelfth World Congress in Mechanism and Machine Science. Besancon – France, 17–21 June 2007

Analysis of the Direct Kinematic Problem in 3-DOF Parallel Manipulators

M. Urizar, V. Petuya, O. Altuzarra, E. Macho, and A. Hernandez

Abstract In this paper, the authors will show a methodology for computing the configuration space with one constant input, basing on the principles of the discretization methods. Taking chance of an entity called the reduced configuration space, the Direct Kinematic Problem will be solved. Moreover, this entity allows the transition between different solutions to be performed, with the purpose of enlarging the range of motion of the manipulator.

Keywords Dkp solutions · Parallel manipulator · Path planning · Reduced configuration space

1 Introduction

Parallel manipulators are an interesting alternative to serial manipulators given the important mechanical and kinematics advantages offered, i.e., better stiffness, high accuracy, higher velocity and acceleration of the end-effector, etc. Nevertheless, in counterpart they present limited and complex workspaces with internal singularities. Thus, the workspace size and shape, as well as the singularity loci are considered the main design criteria of these robots. The representation of the workspace normally stands for the reachable volume of the end-effector.

Concerning the workspace obtaining methods, there exist several viewpoints; discretization methods, geometric methods and analytical methods can be distinguished. Discretization methods [1, 7], consist in establishing a mesh of nodes with end-effector's positions and orientations. Each node is checked to find whether it

M. Urizar (✉)
Faculty of Engineering in Bilbao, Department of Mechanical Engineering, University of the Basque Country, Basque Country, Spain

I. Vişa (ed.), *SYROM 2009*,
DOI 10.1007/978-90-481-3522-6_36,

belongs or not to the workspace, normally by means of solving the Inverse Kinematic Problem (IKP).

In general, parallel manipulators have multiple DKP and IKP solutions, called assembly modes and working modes respectively. Some applications are trying to show the practicability of changing between different DKP solutions, whereby the workspaces associated to each solution are joined to get a larger practical workspace. Nevertheless, in these approaches DKP singularities are crossed making use of additional strategies, such as redundant actuators in passive joints or making use of physical effects like gravity [4], which may imply a certain risk of uncontrollability.

Although initially it was a common belief that DKP solutions are always separated by DKP singularities [2], afterwards in [3] it was showed this assumption is not always verified. Dealing with this topic, other authors have managed to demonstrate that it is possible to join different DKP solutions via paths totally free of singularities [6]. This fact suggests the possibility of a wider use of the workspace.

The configuration space is a concept used by several researches [6, 8], to get direct visualizing and analysis of all assembly modes and working modes simultaneously. It will be shown in this paper that computing and making use of a particularization of the configuration space, called the reduced configuration space, it is possible to obtain all DKP solutions and maximize the manipulator's motion by means of path planning.

2 Computing Workspace with One Input Constant

The target manipulators in the present research are three-degree-of-freedom (DoF) planar or spatial parallel manipulators formed by three kinematic chains or limbs (not necessary the same type), being each limb actuated by just one input actuator. Also, the kinematic joints in each limb must be lower pairs as revolute (R), prismatic (P) and so on.

The process for obtaining the workspace with one constant input is based on the procedure consisting in discretizing the workspace obtaining discrete poses of the manipulator. The moving platform's location is defined by the location of a moving frame attached to it. As an example, in the planar cases depicted in Fig. 1, the moving frame is (P, **X0**, **Y0**) being (0, **X0**, **Y0**) the fixed frame.

In the three examples represented in Fig. 1, the constant input stands for the parameter L in the R$\underline{\text{P}}$R limb, the angle α in limb $\underline{\text{R}}$RR, and the parameter s in $\underline{\text{P}}$RR. In the three cases, the constant input restricts the moving frame motion to a circular motion round a fixed node denoted as (xa,ya). Thus, the positional discretization algorithm locates the moving frame (P, **X0**, **Y0**), in position and also with several orientations, into discrete poses that meet the constant input constraint.

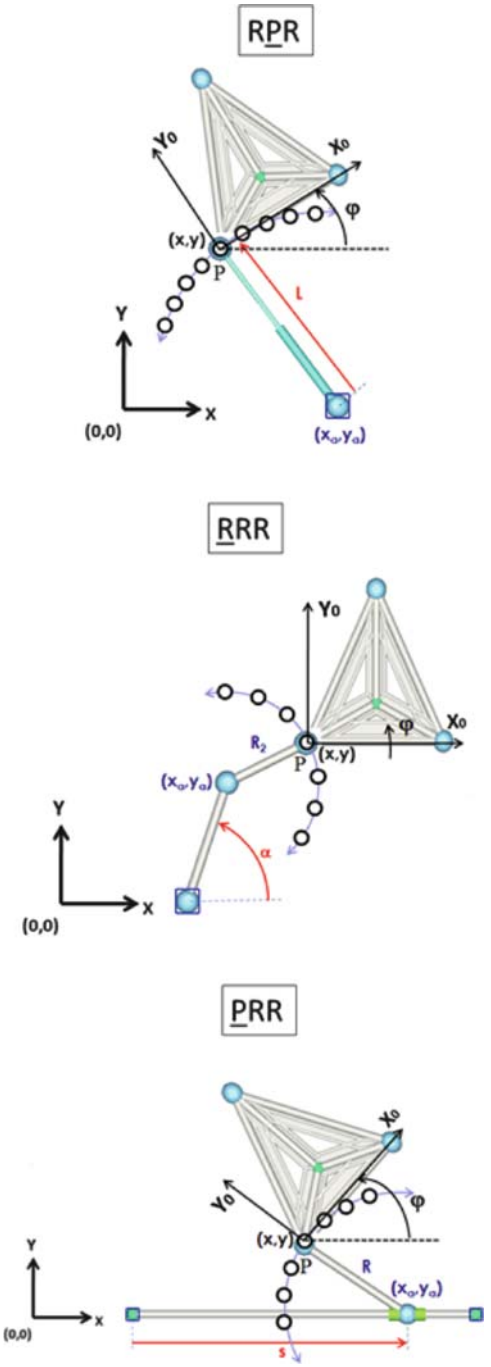

Fig. 1 Positional discretization algorithm

Subsequently, the verification of which discrete pose constitutes a solution is carried out analytically, by solving the IKP of the remaining kinematic chains separately. One pose will belong to the workspace when the three kinematic chains can be assembled. The discrete poses belonging to the workspace are joined in an interpolation process, hence, obtaining a continuous surface.

The kinematic analysis is carried out by evaluating the DKP and IKP Jacobian matrices' determinants for each pose. One position equation for each limb is set up, called the characteristic equation (*fi* for $i = 1, 2, 3$). Mathematical assembly is performed expressing in the characteristic equations, *fi*, each limb joining-node coordinates as a function of the output variables. Then, the system governing the velocity problem is obtained and can be expressed in matrix form as follows:

$$\begin{bmatrix} \frac{\partial f_1}{\partial x_1} & \frac{\partial f_1}{\partial x_2} & \frac{\partial f_1}{\partial x_3} \\ \frac{\partial f_2}{\partial x_1} & \frac{\partial f_2}{\partial x_2} & \frac{\partial f_2}{\partial x_3} \\ \frac{\partial f_3}{\partial x_1} & \frac{\partial f_3}{\partial x_2} & \frac{\partial f_3}{\partial x_3} \end{bmatrix} \begin{Bmatrix} \dot{x}_1 \\ \dot{x}_2 \\ \dot{x}_3 \end{Bmatrix} = - \begin{bmatrix} \frac{\partial f_1}{\partial q_1} & 0 & 0 \\ 0 & \frac{\partial f_2}{\partial q_2} & 0 \\ 0 & 0 & \frac{\partial f_3}{\partial q_3} \end{bmatrix} \begin{Bmatrix} \dot{q}_1 \\ \dot{q}_2 \\ \dot{q}_3 \end{Bmatrix} \tag{1}$$

where *xk* and *qk*, for $k = 1, 2, 3$, are the manipulator's output and input variables respectively. Jacobian matrices' terms are the partial derivatives of the characteristic equations, *fi*, with respect to each of the output variables, *xk*, in the DKP Jacobian (**J**DKP) and with respect to each input variable, *qk*, in the IKP Jacobian (**J**IKP).

The mapping of the determinants |**J**DKP| and |**J**IKP| is carried out for each pose obtaining all the singularity loci.

3 Visualizing the Reduced Configuration Space

The reduced configuration space constitutes a three-dimensional surface that relates one output variable against the two input variables that are not constant. This entity allows the relation between input and output variables to be visualized.

The parallel manipulator represented in Fig. 2 is a 3-DoF planar parallel manipulator with three limbs, one R<u>P</u>R kinematic chain and two P<u>R</u>R kinematic chains. The input variable of the first limb R<u>P</u>R is defined by the parameter *L1*, and the angles $\alpha 2$ and $\alpha 3$ correspond to the inputs of the second and third limbs respectively. The geometric parameters of the manipulator are: *a*, *b* (that define the moving platform's dimensions), *R2* and *R3*.

For the example, a constant value to the <u>R</u> joint of limb three will be given, i.e., $\alpha 3$. Thus, the moving frame (P, **X0**, **Y0**) is located attached to the platform joining-node *B3* that links to limb three. The three characteristic equations, as explained in Section 2, are as follows:

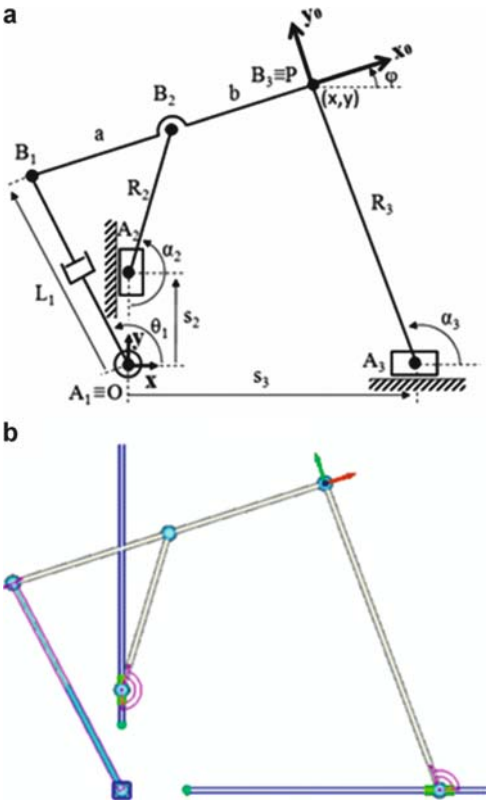

Fig. 2 (**a**) Parallel manipulator RPR-2PRR; (**b**) Software representation

$$\begin{cases} f_1 : (x-(a+b)\cos\varphi)^2 + (y-(a+b)\sin\varphi)^2 \\ \quad -L^2{}_1 = 0 \\ f_2 : (x - b\cos\varphi) - R_2 \sin\alpha_2 = 0 \\ f_3 : y - R_3 \sin\alpha_3 = 0 \end{cases} \tag{2}$$

The dimensional values are: $a = b = R2 = 2.5$ and $R3 = 2a = 5$. Fixing input angle $\alpha 3$ constrains the moving platform's motion to a constant value of the output variable y. Thus, both the reduced configuration spaces representing output variable φ or x can be depicted, obtaining different surfaces for each case, and having each one of them the same information related to the motion capacity analysis.

Selecting constant input $\alpha 3 = 170°$ and representing, i.e., output variable φ yields the reduced configuration space shown in Fig. 3. Note that it is not a closed surface due to the angular character of input $\alpha 2$ and output φ.

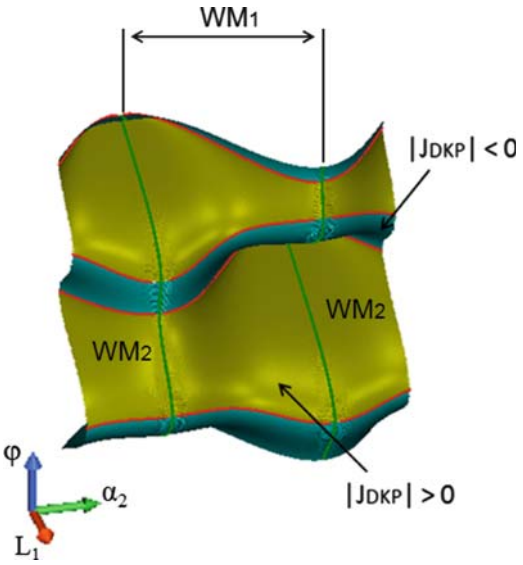

Fig. 3 Reduced Configuration Space for $\alpha 3 = 170°$

In Fig. 3, the different regions associated with the positive and negative sign of the |**J**DKP| are shown, separated between them by the DKP singularity curves depicted in red colour. Besides, the two regions associated with the two possible configurations of limb two are separated by the IKP singularity curves, plotted in green.

The two possible configurations of limb two establish the two working modes of this limb. The manipulator is in its WM1 when $-90° \leq \alpha 2 \leq 90°$, WM2 being associated with the range $90° \leq \alpha 2 \leq 270°$.

3.1 Finding All DKP Solutions

The DKP consists in obtaining the output variables for specific input values. For a given input, the reduced configuration space can be computed, and the two remaining inputs represent a vertical line in the reduced configuration space that intersects the surface at several points. Each of these intersection points will belong to triangles made up by the three closer exact solutions. Hence, it is feasible to make an interpolation among those point values to obtain the approximate solution (x,y,ϕ) of the intersection point, as it is shown in Fig. 4. The solutions of all the intersection points will bring out all the DKP solutions.

To clarify the procedure, the example under study will be used. Being the input values: $L1 = 4$, $\alpha 2 = 21°$ and $\alpha 3 = 170°$, it yields the four DKP solutions represented in Fig. 5. At the left side of Fig. 5, both the reduced configuration space at the top and its projection onto the joint space $(L1,\alpha 2)$, underneath, are depicted. The

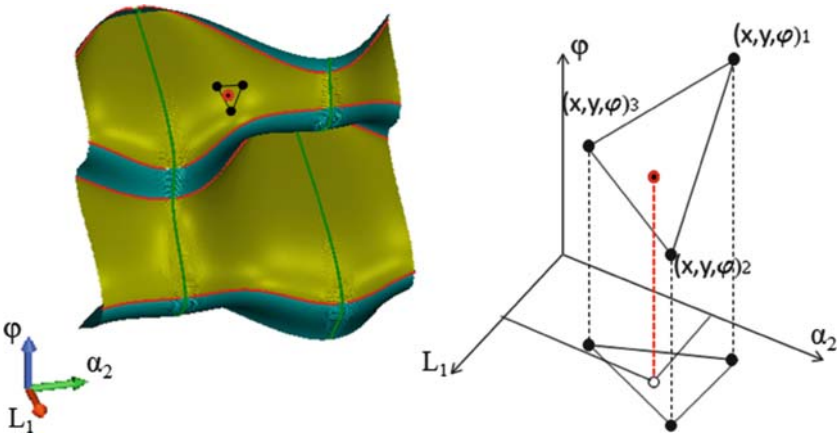

Fig. 4 Interpolation process for obtaining the DKP solutions

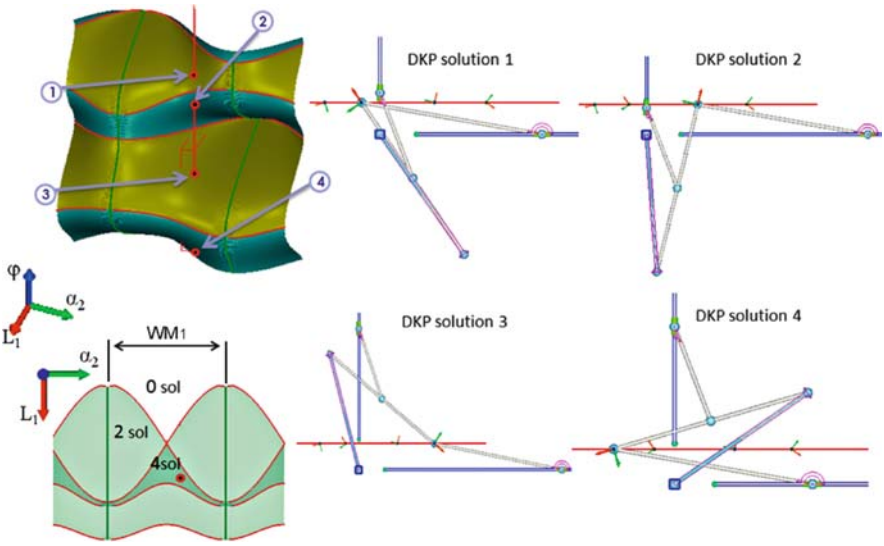

Fig. 5 Four DKP solutions for inputs: L1 = 4, α2 = 21° and α3 = 170°

selected inputs correspond to one point in the joint space inside the region with four DKP solutions, meanwhile this point represents a vertical line in the 3D plot.

The four solutions represented on the right hand side of Fig. 5 have a constant value of output variable *y*, due to the constraint of fixing input α3. Hence, the moving frame's origin lies in a horizontal line plotted in red colour.

By varying the point in the joint space, the DKP solutions for any input values can be obtained.

4 Path Planning Between Different DKP Solutions

The aim of this section is to take advantage of the reduced configuration space with the purpose of path planning between different DKP solutions.

Representing the reduced configuration space implies that one of the input variables remains constant. Nevertheless, applying iteratively the procedure, for different input values, the corresponding reduced configuration spaces can be depicted. This allows us to analyze the optimum constant input for making non-singular transitions between DKP solutions, thus, enlarging the manipulator's motion ability.

In Fig. 6, the reduced configuration space for constant $\alpha 3 = 160°$ is depicted. Comparing this case with the one obtained previously for $\alpha 3 = 170°$ (Fig. 5), it can be observed the region with four DKP solutions has been reduced, and also, special points, called cusp points, appear in the projected DKP singularity curves onto the joint space.

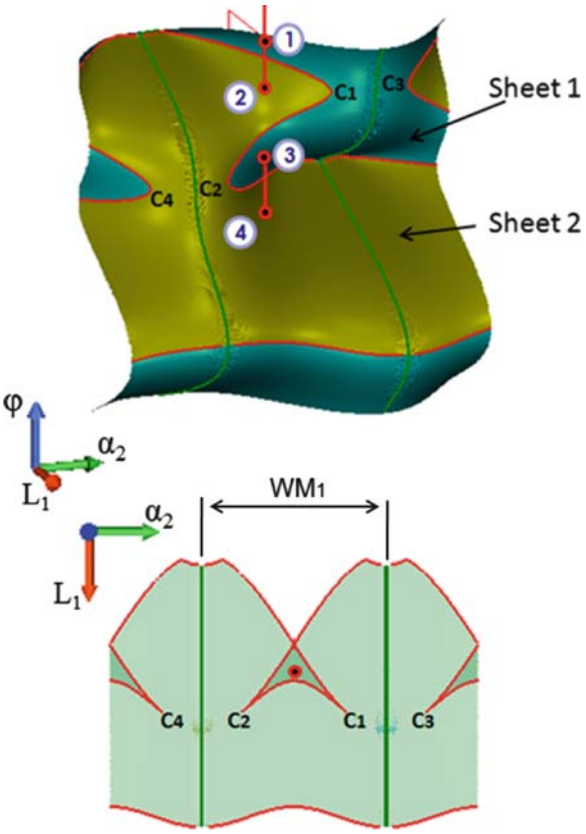

Fig. 6 Reduced configuration space for constant $\alpha 3 = 160°$ and DKP solutions

Cusp points correspond to points in the DKP singularity curves where three DKP solutions coalesce. It has been researched in previous papers [5], that encircling cusp points permits making non-singular solution changes between different solutions or assembly modes.

Let us demonstrate these affirmations in the example under study. Focusing on the DKP solutions' location for constant $\alpha 3 = 170^{\circ}$ (Fig. 5), it can be observed that there are four regions associated to $|\mathbf{J}DKP| < 0$ (plotted in blue, two regions) or $|\mathbf{J}DKP| > 0$ (plotted in green, two regions) which are separated between them by the DKP singularity curves. Besides, as explained previously, the IKP singularity curves divide the reduced configuration space into two regions associated to the two working modes of the manipulator.

In this case (for $\alpha 3 = 170^{\circ}$), the DKP solutions lie one in each singularity-free region and the impossibility exists for finding a path or trajectory to move from one solution to another without crossing any singularity.

Nevertheless, focusing on Fig. 6, which corresponds to $\alpha 3 = 160^{\circ}$, the reduced configuration space has acquired a shape such that there are only two singularity-free regions, separated between them by the DKP singularity curves. These two regions are called 'sheets' of the reduced configuration space, and define the maximum region free of any singularity.

Yet again, similarly to the previous case for $\alpha 3 = 170^{\circ}$, the IKP singularity curves divide the reduced configuration space into two regions according to each working mode. Thus, for each working mode, there are two sheets free of internal singularities.

Due to the existence of only two singularity-free sheets, in each of them lie two different DKP solutions. Solutions (1–3) are located on the region with $|\mathbf{J}DKP| < 0$ (sheet1), meanwhile solutions (2–4) lie on the region with $|\mathbf{J}DKP| > 0$ (sheet2). Hence, it is feasible to search for paths inside the singularity-free sheets so as to move from one solution to another.

In fact, the existence of the aforementioned cusp points is the key factor for planning transitions between solutions. In Fig. 7, the paths joining the two pairs of solutions in each sheet, by encircling cusp points *c1* and *c2*, are shown. Each one of these paths remains completely inside each singularity-free sheet associated with WM1. Thus, the transitions between solutions can be performed in a completely safety way.

Working now with the first of the sheets, i.e., the one associated to $|\mathbf{J}DKP| < 0$ (sheet1), the singularity-free path joining the two DKP solutions 1 and 3 is shown in Fig. 8, which does not cross at any time neither the DKP nor the IKP singularity curves.

This path encircles cusp point *c1*, standing for a circular trajectory in the joint space. Poses correspondent to solutions 1 and 3, and two intermediate poses *pi*, along the path, have been represented in Fig. 8.

Therefore, visualizing the reduced configuration space for different input values, allows searching for the optimal input for non-singular transitions to be possible, thus, getting a wider operational workspace.

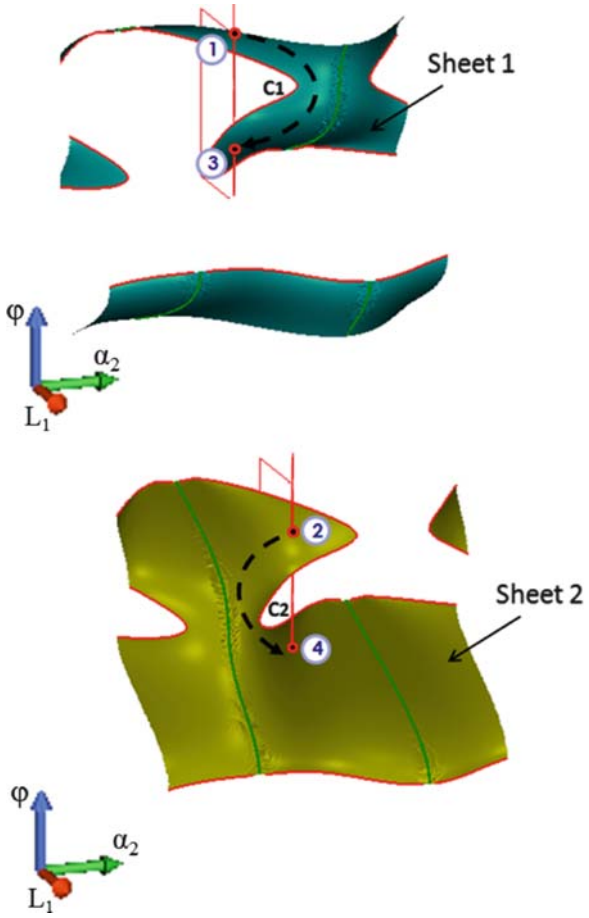

Fig. 7 Singularity-free paths encircling cusp points

It must be emphasized that the reduced configuration space has all the information of the configuration space. However, as it has been explained, one of the inputs must remain constant and depending on the selected value of the input it is feasible or not to perform non-singular transitions.

5 Conclusions

In this paper, a useful computational tool for obtaining the reduced configuration space with constant input has been presented. It allows the Direct Kinematic Problem to be solved, and the locations of the solutions across the different surfaces visualized. In addition, the reduced configuration space permits searching for

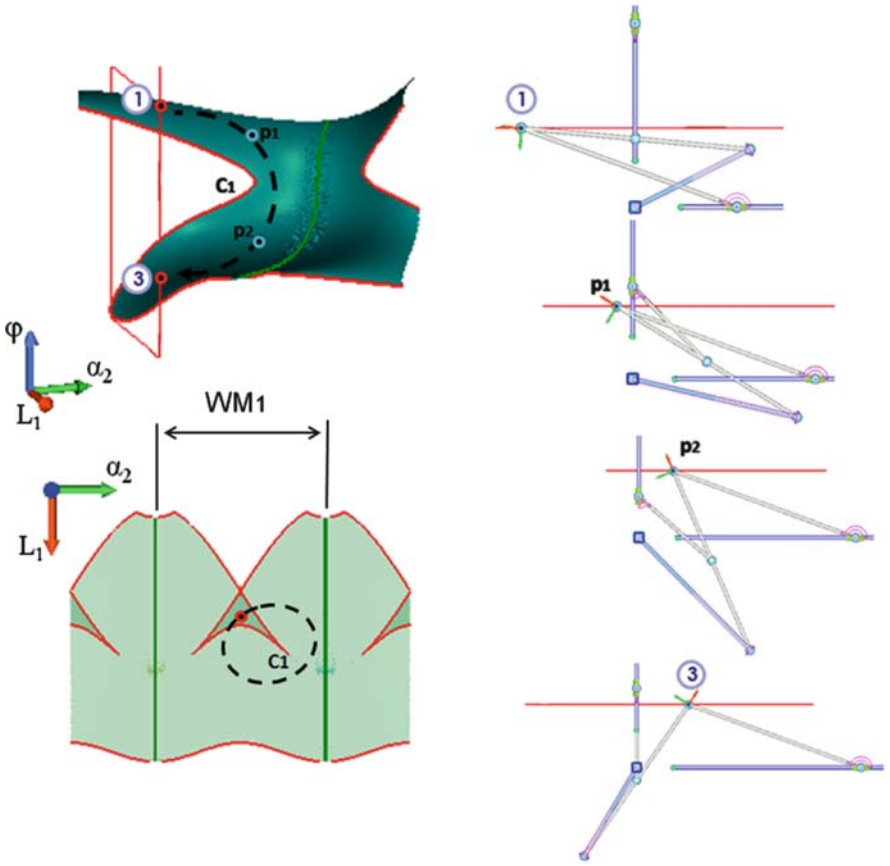

Fig. 8 Path planning between solutions 1 and 3

trajectories joining different solutions so as to enlarge the manipulator's range of motion.

Acknowledgments The authors of this paper wish to acknowledge the financial support received from the Spanish Government via the Ministerio de Educación y Ciencia (Project DPI2008-00159) and the University of the Basque Country (Project GIC07/78).

References

1. Dash, A.K., Yeo, S.H., Yang, G., Chen, I.-M.: Workspace analysis and singularity representation of three-legged parallel manipulators. In: ICARCV 02, pp. 962–967 (2002)
2. Hunt, K., Primrose, E.: Assembly configurations of some in-parallel-actuated manipulators. Mech. Mach. Theory 28(1), 31–42 (1993)

3. Innocenti, C., Parenti-Castelli, V.: Singularity free evolution from one configuration to another in serial and fully-parallel manipulators. J. Mech. Des. 120(1), 73–79 (1998)
4. Maass, J., Kolbus, M., Buddle, C., Hesselbach, J., Schumacher, W.: Control strategies for enlarging a spatial parallel robot's workspace by change of configuration. In: Proceedings of the 5th Chemnitz Parallel Kinematics Seminar, pp. 515–530 (2006)
5. Macho, E., Altuzarra, O., Pinto, Ch., Hernández, A.: Transitions between multiple solutions of the Direct Kinematic Problem. In: 11th International Symposium Advances in Robot Kinematics, Batz-sur-mer (2008)
6. McAree, P., Daniel, R.: An explanation of never-special assembly changing motions for 3–3 parallel manipulators. Int. J. Robot. Res. 18(6), 556–575 (1999)
7. Pott, A., Franitza, D., Hiller, M.: Orientation workspace verification for parallel kinematic machines with constant length. In: Mechatronics and Robotics Conference, Aachen (2004)
8. Zein, M., Wenger, P., Chablat, D.: Non-singular assembly mode changing motions for 3-RPR parallel manipulators. Mech. Mach. Theory 43(4), 480–490 (2007)

Kinematical Analysis of Mechanical Systems by Results of Digital Video Recording

A. Vukolov and E. Kharitonov

Abstract There is an actual problem in computational mechanics to explore the kinematics of mechanical and biological systems "as is", in normal working environment. One way to solve the problem is usage of digital video recording with analysis of results. In this work, the treatment process of sheet stamping press DV recordings was described. The video was taken during normal process of production, the errors originated from production conditions was considered and properly compensated. The phase trajectory of the system may easily be recovered with this method.

Keywords Coupler curve · Kinematics · Press · Video

1 Target Setting

The target of the work was to develop the methodology of mechanical and biological systems exploration by results of digital video recording. Here the many error-making factors of recording conditions and real production process must be considered. As an example for practical methodology application, the sheet stamping press working process analysis was described. The results of the work were:

- Cycle and speed plots of slider and coupler motion
- Slider phase trajectory plot

A. Vukolov (✉)
Russian Federation, Bauman Moscow State Technical University, Moscow, Russia

I. Vişa (ed.), *SYROM 2009*,
DOI 10.1007/978-90-481-3522-6_37,

2 Peculiarities of Digital Video Recording Process and the Subject of Inquiry

2.1 Peculiarities of Digital Video Recording Process

Usage of photo shooting as the auxiliary method of linkage motion exploration was presented in [1]. It was natural to use this method to explore the multibar linkages with unknown structure using a multiframe video recording. Some info about usage of video recording devices and techniques was taken from [2–4]. However, the video equipment that was suggested in [3, 4] (motion capture equipment with rayover optical registration targets) is very expensive for us. To perform this work, we tried to use cheap widespread video equipment to obtain admissible results.

Video recording was performed under difficult conditions during simple industrial process of production, without any specific lighting equipment, optical registration targets and frame exchanging synchronization techniques. The main equipment was:

1. Panasonic NV-GS180 digital video camera with built-in DV streamer, 3x CCD matrices, prismatic color separation. Objective of the camera is Panasonic Video Lens 17 mm – high range zoom lens with reduced geometrical distortion.
2. Photo tripod with 160 cm maximum height.
3. Three kilograms self-made counterweight that was used to stabilize the tripod while the basis is oscillating.

The camera makes output video in DVSD PAL 4:3 Interlaced Screener format, with lossless compression, 720 × 576 pixels resolution. To make it possible to perform the analysis, the video stream was deinterlaced using freeware TomsMoComp filter. The final output (for demonstration) was MPEG1, 2,000 Kb/s data rate. All intermediate treatment was performs using Pinnacle Systems Pinnacle Studio 10.7 Titanium video editing program. All measurements were made in Cartesian video frame-based coordinate system (X-axis is frame width measure, and Y-axis is frame height measure).

2.2 Subject of Inquiry Peculiarities Description

The subject of inquiry was IHI double-action sheet stamping press, and its drawing slider motion specifically (as it is marked on Fig. 1).

Main peculiarity of the drawing coupler and slider point motion exploration was the press parts arrangement: the drawing coupler locates at the secondary viewing plane rather the clamping one.

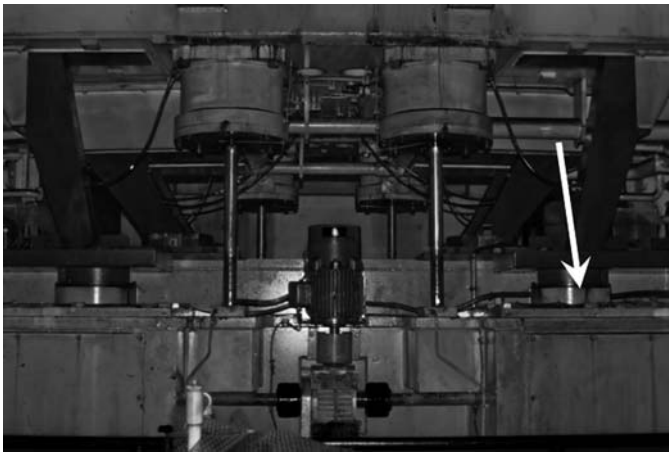

Fig. 1 The visible parts of sheet stamping press linkage. The couplers are darkened while editing. The drawing slider is marked with white arrow

2.3 Sources of Errors of the Recording Process

There are two main sources of errors while video recording were discovered: The first one is video equipment setup and hardware problems, the second one is linked to stamping process entirely. In whole, the reliability of results strongly depends of global error amount estimation.

Below the video equipment setup error-making factors are listed:

- Low image contrast. Error value depends of lighting conditions. Handling with intermediate contrast correction.
- Input device (CCD matrix) noise. Depends of lighting conditions and image colorimetry (the noise amount grows while blue color predominance). Maximum noise amount was accurately measured; its value is 3.7 pixels per basic compressible fragment (16×16).
- Frame fields reading time difference (on interlaced video transportation stream) and deinterlacing errors. This error value depends of axis (near zero on X [width measure] axis of the frame) and speed of an object. Maximum interlacing error amount registered during slider speed measurement is 1% of slider speed. On coupler, this type of errors compensates automatically by X-axis displacement measure precision.
- Optical distortion. This type of errors was disregarded in this work because of tracking point's allocation on frame field.
- Compression and intermediate video treatment process errors. This type of errors is not necessary to handle due to very small values on used equipment.

Below the stamping process-linked error-making factors are listed:

- Camera viewpoint displacement due to press basis amenability. The maximum error amount exists near bottom dead center of the linkage.
- Camera viewpoint displacement due to vibrations. The frequencies of perturbations are estimated as below 10 Hz. Handling of these errors is disregarded in this work, due to very small real error amount values.
- Influence of slider load to shape of resulting curves due to viscose-elastic characteristic of the press basis. The real influence appears while load slump just after stamping operation. It is impossible to handle this error due to experimental equipment.

There are different error-making factors for speed and geometrical parameters measurement. The real error amounts for geometrical parameters measurement are presented in Table 1.

Table 1 Real error amounts estimation on geometrical parameters measurement

Error-making factor	Error amount estimation [%]	
	By X-axis (frame width)	By Y-axis (frame height)
1. Low image contrast	0.1	0.1
2. Input device noise	2.5	2.5
3. Frame field reading time difference	Without influence	
4. Optical distortion	Without influence	
5. Compression and intermediate video treatment process errors	Without influence	
6. Camera viewpoint displacement due to press basis amenability	5.8	7.2
7. Camera viewpoint displacement due to vibrations	Without influence	
8. Influence of slider load	Impossible to handle	

Table 2 Real error amounts estimation on speed measurement

Error-making factor	Error amount estimation [%]	
	By X-axis (frame width)	By Y-axis (frame height)
1. Low image contrast	Without influence	
2. Input device noise	Without influence	
3. Frame field reading time difference	0	1.0
4. Optical distortion	Without influence	
5. Compression and intermediate video treatment process errors	Without influence	
6. Camera viewpoint displacement due to press basis amenability	5.8	5.8
7. Camera viewpoint displacement due to vibrations	Without influence	
8. Influence of slider load	Impossible to handle	

The real error amounts for speed measurement are presented in Table 2.

The full possible error amount estimation (according to known issues) was performed as described in [6].

Full possible error amount was estimated about:

- 9.89% on geometrical parameters measurement
- 8.2% on speed measurement

3 Data Analysis Methodology Description

While the video frames treatment, the kinematical characteristics of visible moving parts of the linkage must be obtained. In case of special optical registration targets absence, the only method of solving this problem is to select easy-tracking characteristic points on moving parts of the linkage, and track its displacement within frame sequence to determine the vectors of point speed and transference (Fig. 2).

To perform more accurate definition, the motion characteristics were treating statistically, and the average result in actual frame sequence was used. Maximum length of the frame sequence was accepted at ten frames. Inside the sequence, the values of kinematical characteristics were accepted as constants. The geometrical measurement method was examined; as it's described in [5]. It was interesting to extend the method of phase trajectory recovery to experimental kinematical (non geometrical) data treatment. Precision of the results was recognized as acceptable is the presence of good camera optics, sensitiveness, focusing and object tracking.

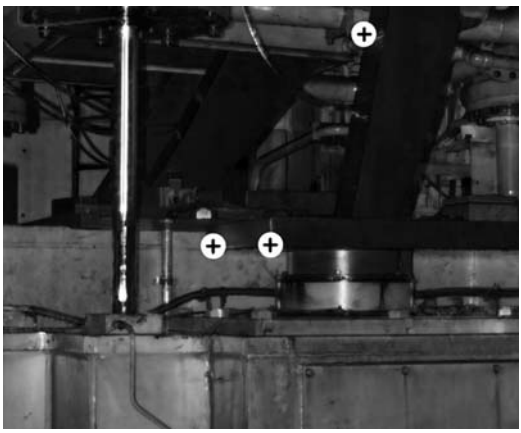

Fig. 2 Tracking points definition sample

4 Results of Experimental Data Treatment. Slider Phase Trajectory Plotting

The method of slider phase trajectory recovery is evident as described in [5]. It requires transference ($S(t)$) and speed ($v(t)$) functional dependence arrays of the slider. Next step of an algorithm is parametric conversion of arrays to phase trajectory ($S(v)$). This step was performed using MathCAD 14 symbolic processor. The graph plot of slider transference is presented on Fig. 3.

Slider speed graph plot is presented on Fig. 4. The recognizable oscillations near an just after $t = 4.9$ was be considered as results of influence of secondary (clamping) press slider motion.

The clamping slider occupies near bottom dead center at that time.

While bottom dead center passage, the clamping slider produces elastic waves in press basis. It is possible to observe these waves as oscillations on the graph plots.

Parametric conversion of the presented graph plots (and its functional arrays) was performed using MathCAD. The result of conversion is phase trajectory graph plot.

The phase trajectory of drawing slider is presented on Fig. 5.

5 Conclusions

- The method of mechanical systems kinematics exploration was proposed. The experiment with real machine was conducted to approve the method and the possibilities of its real application.

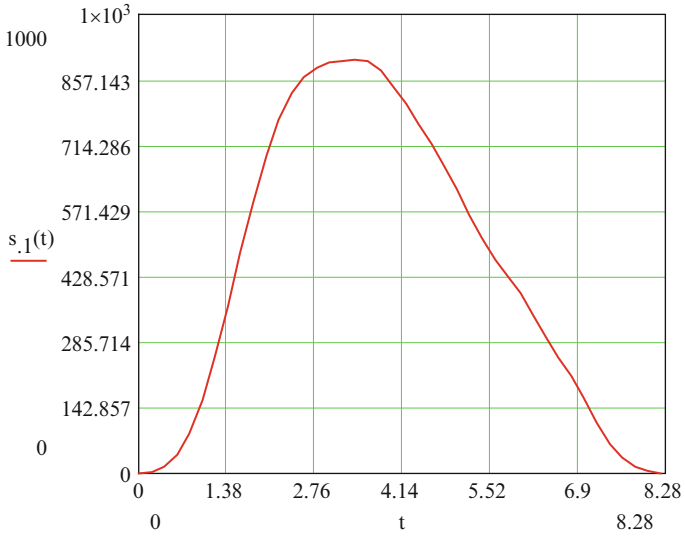

Fig. 3 Slider transference graph plot (within single production cycle)

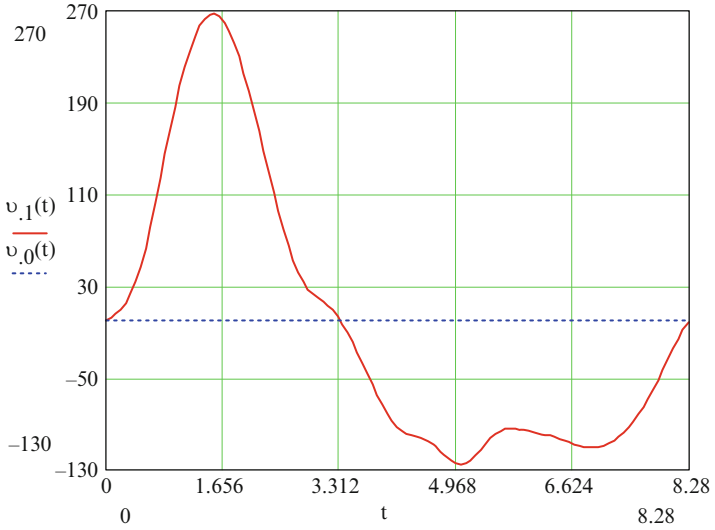

Fig. 4 Slider speed graph plot (within single production cycle)

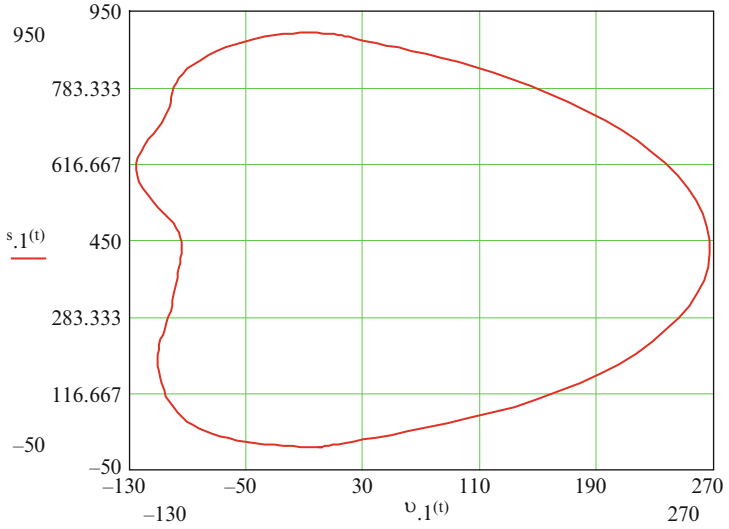

Fig. 5 Slider phase trajectory plot

- The experimental- and environmental-defined error amounts were examined and treated where possible.
- As the results of experimental data treatment, the kinematical characteristics (slider transference and speed graph plots) and cycle characteristic (slider motion phase trajectory) obtained.

The proposed method is perspective thing for exploration of mechanical systems with unknown (inc. changing) structure. Also it is possible to use the method to explore biological systems and remote diagnostic processes. As a continuation of this work, the paper [7] was developed.

References

1. Golovin, A., Lafitsky, A., Simuskhin, A.: Experimental and theoretical research of Cams wearing of Cams mechanism. In: Ceccarelli, M. (ed.) Proceeding of 2nd International Conference EuCoMeS-2008, pp. 107–119. Springer, Netherlands (2008)
2. De Aguiar, E., Theobalt, C., Magnor, M., Theisel, H., Seidel, H.-P.: M^3: marker-free model reconstruction and motion tracking from 3D voxel data. Proceedings of 12th Pacific Conference on Computer Graphics and Applications, 2004. PG 2004, 6–8 October 2004, pp. 101–110
3. Cheung, K.M.G., Baker, S., Kanade, T.: Shape-from-silhouette of articulated objects and its use for human body kinematics estimation and motion capture. Computer Vision and Pattern Recognition, 2003. Proceedings of 2003 IEEE Computer Society Conference on Volume 1, vol. 1, pp. I-77–I-84, 18–20 June 2003
4. Todorov, E.: Probabilistic inference of multijoint movements, skeletal parameters and marker attachments from diverse motion capture data. IEEE Trans. Biomedical Engineering 54(11), 1927–1939 (2007)
5. Golovin, A.: Design of Multibar Linkages (in Russian). BMSTU, Moscow (1995)
6. Zaidel, A.: Errors of Physical Values Measurement (in Russian). ISBN 5-8114-0643-6 S-Pb.: Lan' (2005)
7. Golovin, A., Guryanova, E., Labanova, N.: Coupler curve area of existence definition for linkage by results of digital video recording. Proceedings of SYROM'09 (2009)

Dynamics of Mobile Vibration-Driven Robots

K. Zimmerman, I. Zeidis, N. Bolotnik, and S. Jatsun

Abstract Design of mobile robots that can move without wheels or legs is an important engineering and technological problem. Self-propelling mechanisms that consist of a body that has contact with a rough surface and internal masses are considered. Asymmetry in friction that is necessary for the robot to move can be provided in several ways. First, the robot can be equipped with specific contact devises that provide anisotropy for the coefficient of friction, i.e., the coefficient of friction depends on the direction of motion. For example, the contact surface of the robot can be covered with needles. Second, this asymmetry can be provided for isotropic friction by changing the normal pressure of the robot on supporting surface. A number of mathematical models of such systems are presented in the paper.

Keywords Design · In-pipe robots · Modelling · Vibration-driven robots

1 Introduction

In the present paper, the concept of vibration-driven robots is developed. Such robots can move in various media without wheels, caterpillars or leg. The propulsion of the robot is provided, on the one hand, due to vibration of internal masses in the robot and, on the other hand, due to interaction of the robot's body with the environment. The robots under consideration move without separation from the supporting surface (Fig. 1). The following notation is used: F_x and F_z are the inertial

K. Zimmerman (✉), I. Zeidis
Technical Mechanics Department, Faculty of Mechanical Engineering, TU Illmenau, Illmenau, Germany
N. Bolotnik
Institute for Problems in Mechanics of the Russian Academy of Sciences, Moscow, Russia
S. Jatsun
Kursk State Technical University, Kursk, Russia

I. Vişa (ed.), *SYROM 2009*,
DOI 10.1007/978-90-481-3522-6_38,

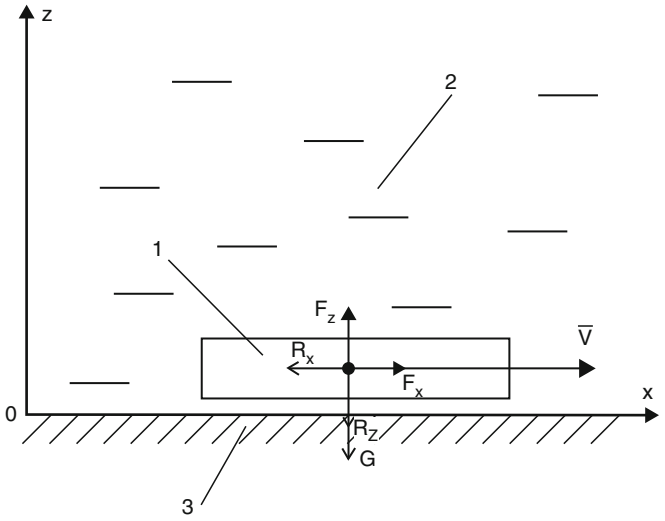

Fig. 1 Motion of a vibration-driven robot without separation from the surface. 1 – robot's body, 2 – environment, 3 – supporting surface

forces produced by the motion of the internal masses, R_x and R_z are the longitudinal and transverse components of the force applied to the robot by the environment and the supporting surface, G is the weight of the robot, and V is the velocity of the robot

The vibration-driven robot is designed as a mechatronic system consisting of mechanical, electrical, and electronic (microcomputer) components. The mechanical vibration is transmitted from the vibration exciter to the robot's body, which interacts with the environment with some force. The robot is equipped with a feedback microcontroller to maintain an efficient operation mode and to provide prescribed characteristics for the motion of the end-effector under the action of various disturbances. The characteristics of the vibration exciter should be tuned to a specific task to be executed by the robot. This tuning can be performed on the basis of the parametric optimization in which an operating characteristic of the robot (e.g., the average velocity) is used as the objective function.

A classification of vibration-driven robots according to the dimension of the space in which the robots and/or their parts move is proposed (Fig. 2). The simplest robots are 1-D robots that move in a one-dimensional space. The motion of such robots is provided by either longitudinal redistribution of mass of the robot's body (worm-like motion [1–9]) or vibratory motion of internal masses in the direction of the motion of the robot [10–14]. More complicated are 2-D robots that move in a two-dimensional space (along a surface). Such a motion can be performed, for example, by changing the shape of the robot's body (snake-like motion [15]) or by means of internal masses moving in a plane parallel to the plane of motion of the robot. Robots that move along a line but the internal masses move in two dimensions (e.g., along the horizontal and along the vertical) are also classified as 2D robots [16–19]. An important type of these robots are the robots with rotating internal masses [17–19]. Most complicated are 3-D robots that can move in a

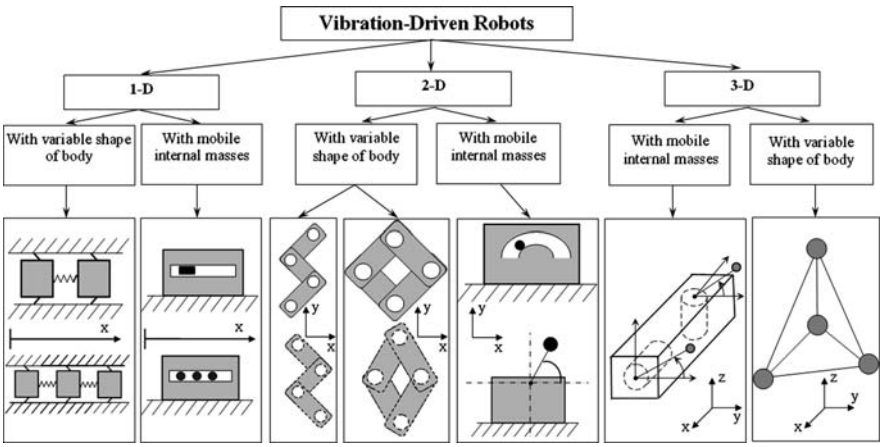

Fig. 2 Classification of vibration robots

three-dimensional space. Three-dimensional motion of the robot can be provided by changing the shape of the robot's body or by means of movable internal masses.

2 Mathematical Model of a 1-D Robot with a Vibrating Internal Mass

The schematic of a simple 1-D robot is shown in Fig. 3. The internal mass of this robot can move periodically along a straight line parallel to the line of motion of the robot.

The dynamics of the robot is governed by the differential equation

$$(\mathrm{m} + \mathrm{M}) \cdot \mathrm{x_e} = \mathrm{F_{fr}} - \mathrm{m} \cdot \mathrm{x_r}, \tag{1}$$

where m is the magnitude of the internal mass, M is the mass of the robot's body, $\mathrm{x_r}$ is the relative acceleration of mass m, $\mathrm{x_e}$ is the acceleration of the robot's body, and F_{fr} is the friction force between the robot's body and the supporting surface.

The friction between the robot's body and the supporting surface is assumed to be Coulomb's dry friction. Therefore,

$$F_{fr} = \begin{cases} -F_{fr}^{+}, & \dot{x} > 0, \\ F_{fr}^{0}, & \dot{x} = 0, \\ F_{fr}^{-}, & \dot{x} > 0, \end{cases} \tag{2}$$

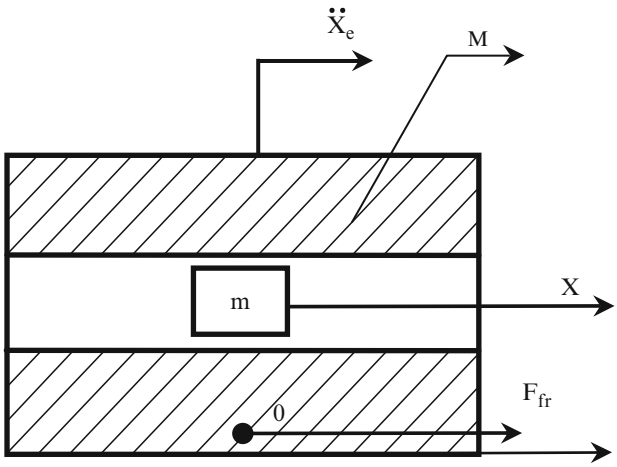

Fig. 3 Schematic of a simple 1-D robot

where $\dot{x}$ is the velocity of the robot's body and $F_{fr}^0 \in \left[-F_{fr}^+,\ F_{fr}^-\right]$. The parameter

$$a = \frac{F_{fr}^- - F_{fr}^+}{2} \tag{3}$$

characterizes asymmetry of the friction relative to the direction of motion. For $a = 0$, we have a symmetric model of friction. The parameter a can be changed by using a special cover for the contact surface of the robot's body. Figure 4 shows different types of the contact surfaces for the robot's body. One of them provides a symmetric friction force ($a = 0$) and the other, an asymmetric friction force ($a \neq 0$).

Some examples of the solutions of Eq. (1) are shown in Figs. 5 and 6. The curves in these figures correspond to symmetric friction ($a = 0$). The motion of the internal mass is asymmetric. During time T_1 the internal mass moves with lower acceleration equal to -5, and during time T_2 it moves with higher acceleration equal to 20. Analysis shows that the ratio $T = T_1/T_2$ influences the average velocity of the robot. It is rather theoretical case, because it is impossible to implement the ideal bang-bang acceleration law for the internal mass using a realistic drive. Figure 7 demonstrates the time histories of motion of the robot for the case where the acceleration of the internal mass relative to the robot's body changes harmonically. This law of motion can be ensured by an electromagnetic drive or a DC motor drive. The minimum and maximum values of the relative acceleration of the internal mass coincide with those of Fig. 6. However, the average velocity of the robot's body for the case shown in Fig. 7 is substantially lower than for the case shown in the previous figure.

General view of a 1-D robot with one internal mass is depicted in Fig. 8. This prototype has one electromechanical drive with a DC motor and a gearbox that provides a rectilinear motion for the mass in accordance with an asymmetric

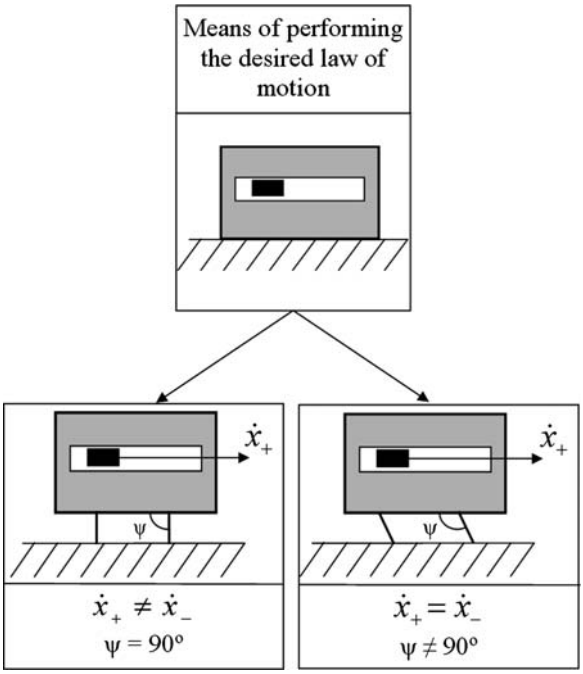

Fig. 4 Different types of contact

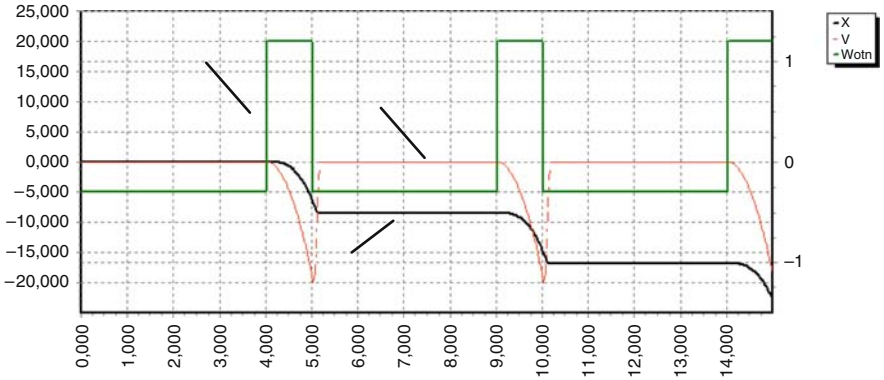

Fig. 5 Time history of the robot's motion for T = 4. 1: Relative acceleration of the internal mass. 2: Velocity of the robot's body. 3: Displacement of the robot

vibration law. The internal mass is wheeled to reduce friction losses. Vibration-driven robots with a one-coordinate vibration exciter can move along a rough surface only if the friction between the robot's body and the supporting surface or/and the exciter vibrations have asymmetric characteristics.

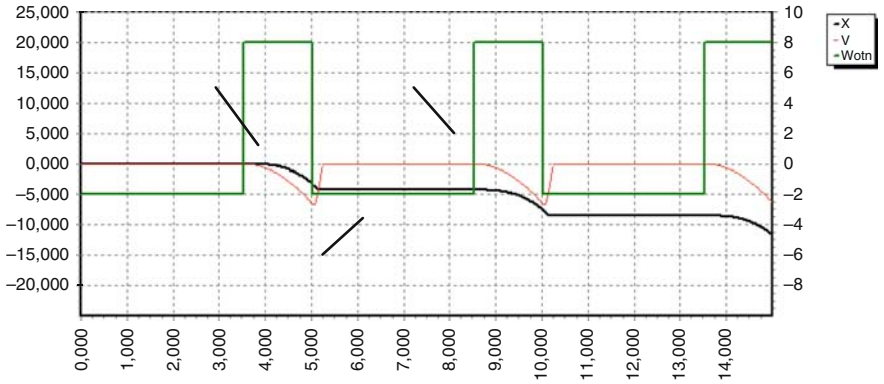

Fig. 6 Time history of the robot's motion for $T = 2.33$. 1: Relative acceleration of the internal mass. 2: Velocity of the robot's body. 3: Displacement of the robot

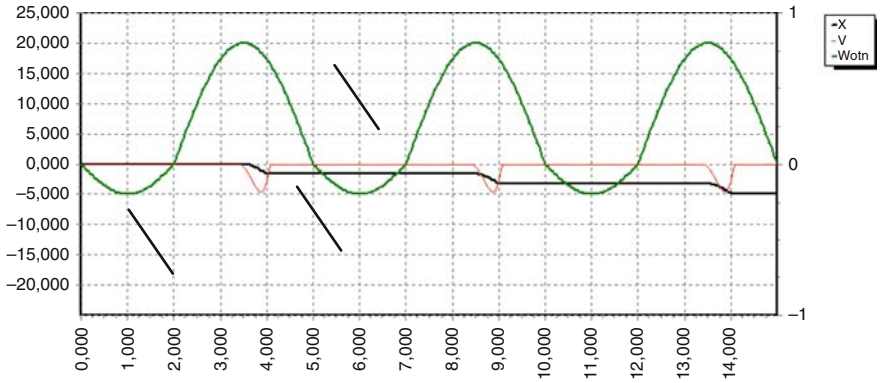

Fig. 7 Time history of the robot's motion for the harmonic law of motion of the internal mass. 1: Relative acceleration of the internal mass. 2: Velocity of the robot's body. 3: Displacement of the robot

Fig. 8 General view of the prototype of a 1-D robot with one internal mass Fig. 9 Cleaner mini-robot with an electromagnetic actuator and two asymmetric friction elements: (**a**) general view of the cleaner: 1 – first body; 2 – electromagnet; 3 – armature; 4 – second body; 5 – asymmetric friction mechanism; 6 – elastic element; (**b**) design schematic of the cleaner: m_1 and m_2 – masses of the robot's components

3 Mathematical Model and Design of a 1-D Robot with Variable Shape of the Robot's Body

This robot consists of two components (rigid bodies) that are connected by a spring-and-dashpot element and can move relative to each other. Both the components have contact with a rough surface along which the robot moves. These two components can be regarded as parts of the robot's body. The relative motion of these parts changes the distribution of mass in the robot's body. One-dimensional motion of the robot can be provided by a periodic relative motion of the two parts of the robot's body along a line (Fig. 9). In this case, it is necessary that the

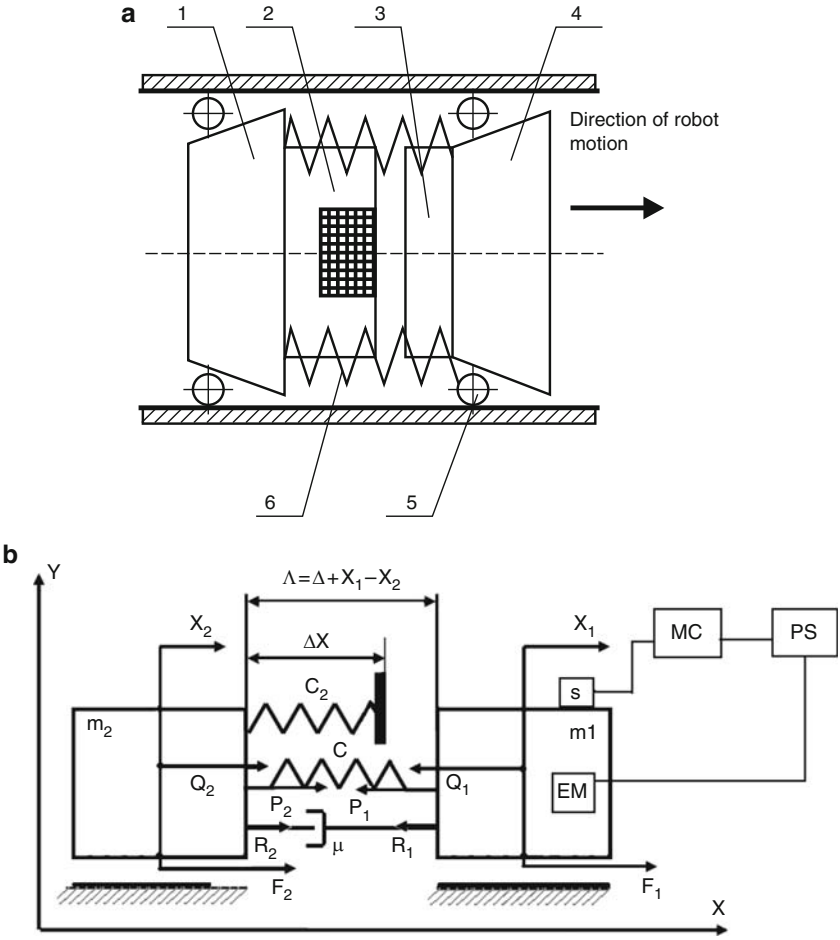

Fig. 9 Cleaner mini-robot with an electromagnetic actuator and two asymmetric friction elements: (**a**) general view of the cleaner: 1 – first body; 2 – electromagnet; 3 – armature; 4 – second body; 5 – asymmetric friction mechanism; 6 – elastic element; (**b**) design schematic of the cleaner: m_1 and m_2 – masses of the robot's components

characteristic of the friction force between the robot's body and the supporting surface be asymmetric. The robot under consideration was designed for cleaning pipelines from solid deposits. To determine the parameters of the cleaner robot, we developed a mathematical model that described the interaction of the end-effector with the technological load (due to the resistance of the solid deposits) and the electromagnetic vibration actuator. This robot has a control system that provides an appropriate voltage applied across the electromagnet (EM). The control system consists of a sensor (S), a microcontroller (MC), and a source of electric power supply (PS).

To characterize the dynamic behavior of the robot, introduce the following notation: X_1 and X_2 are the coordinates of the robot's components relative to a fixed (inertial) reference frame; C and μ are the spring rate and the damping coefficient of the element that connects the components; C_2 and μ are the spring rate and the damping coefficient of the limiter; $Q_{1,2}$ are the forces generated by the electromagnetic exciter; $P_{1,2}$ are the spring forces acting on the robot's components; $R_{1,2}$ are the damping forces acting on the robot's components; ΔX is the length of the unstrained spring of the limiter; Δ is the distance between the robot's components when the spring that connects these components is unstrained.

The non-dimensionalized differential equations that govern the dynamics of the robot with an electromagnetic vibration actuator can be represented as follows:

$$\begin{cases} \dot{\bar{\Phi}} = \varepsilon \cdot \bar{u}(\tau)\varepsilon - \beta\left(\bar{\Delta} + (\mathrm{X}_1 - \mathrm{X}_2)\right)\bar{\Phi}, \\ \ddot{\bar{X}}_1 = -\varsigma(\mathrm{X}_1 - \mathrm{X}_2) - P_1 - \chi \cdot \bar{\Phi}^2 + \bar{F}_1, \\ \ddot{\bar{X}}_2 = m\,\varsigma(\mathrm{X}_1 - \mathrm{X}_2) - P_2 - m\,\chi \cdot \bar{\Phi}^2 + m\bar{F}_2, \end{cases} \tag{4}$$

$$\varepsilon = \frac{U_0}{\Phi_0 \cdot \omega},\ \beta = \frac{2X_0 \cdot R}{\mu_0 \cdot S \cdot \omega},$$

$$\xi = \frac{\mathrm{C}}{\omega^2 \cdot \mathrm{m}_1} = \frac{\lambda_1^2}{\omega^2},\ \chi = \frac{(\Phi_0)^2}{\mu_0 \cdot S \cdot X_0 \cdot \omega^2 \cdot m_1},$$

$$\bar{m} = \frac{m_1}{m_2},\ \bar{\Delta} = \frac{\Delta}{X_0},\ \varsigma = \frac{\mu}{m_1 \omega},$$

where ω is the vibration excitation frequency of the electromagnetic drive, U_0, Φ_0, X_0 are the scales of voltage, magnetic flux, and length, respectively; Φ is the magnetic flux; R is the active electric resistance of the electromagnet's coil; $U(t)$ is the input voltage, S is the area of the air gap in the electromagnet; μ_0 is the electromagnetic constant.

The system of nonlinear differential equations governing the motion of the robot is solved by numerical methods. Based on the simulation results, we determined the parameters of the electromagnetic vibration exciter and analyzed the motion of the robot for various values of the power supply parameters. Figure 10 shows the

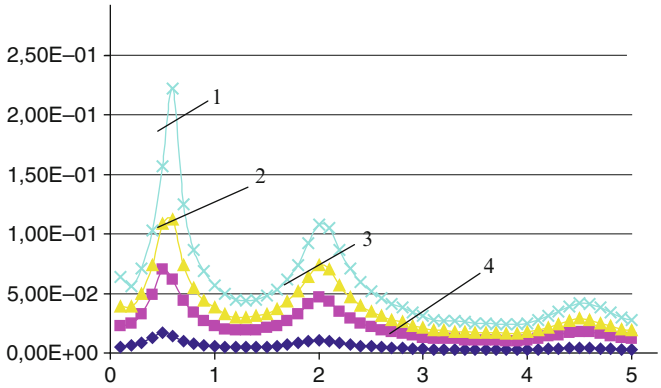

Fig. 10 The average velocity of the robot as a function of the excitation frequency for various power supply parameters. 1: $\varepsilon = 6$, 2: $\varepsilon = 4$, 3: $\varepsilon = 3$, 4: $\varepsilon = 2$

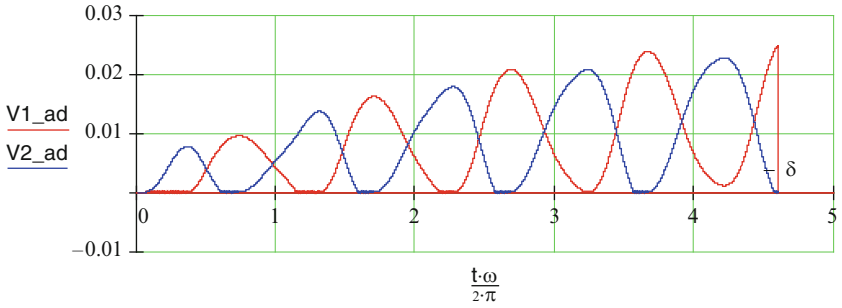

Fig. 11 Time histories of the velocities of the robot's components for $\varepsilon = 0.5$ and $\xi = 1$

average velocity of the steady motion of the robot as a function of the parameter ξ. The curves of these figure have a "resonant" character; at certain values of ξ, peaks of the average velocity are observed.

Figures 11, 12, and 13 show the behavior of the robot for various modes of motion. Figures 11 and 13 correspond to "resonant" modes for $\xi = 1$ and $\xi = 2$, respectively. Figure 12 demonstrate a non-resonant mode for $\xi \approx 1.3$. Not that in all modes there no reversal modes of motion, the velocities of the robot's components never become negative. This means that both components of the robot do not change the direction of motion. In some intervals, the velocity of each body vanishes and remains zero for some time, that is a stick-slip effect is observed. A similar robot was considered in [20]. However, in the cited paper, the dynamics of the drive was not taken into account and the force acting between the robot's components was used as the control variable. In additional, the model of [20] did not have an additional elastic element that limited the relative motion of the components.

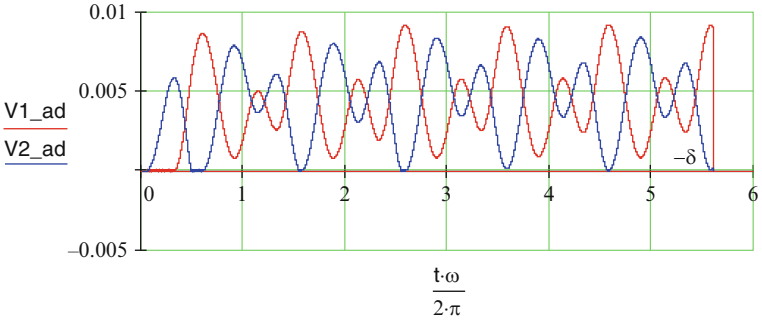

Fig. 12 Time histories of the velocities of the robot's components for $\varepsilon = 2$ and $\xi = 1.3$

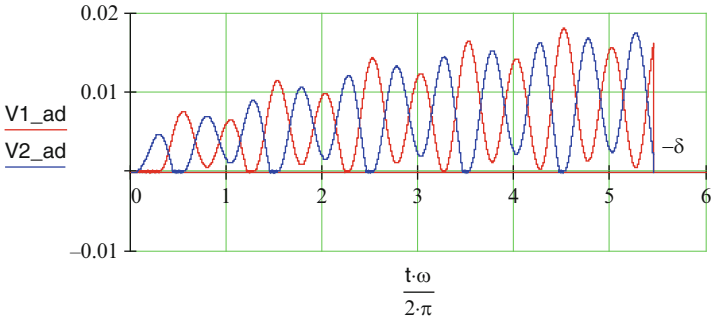

Fig. 13 Time histories of the velocities of the robot's components for $\varepsilon = 2$ and $\xi = 2$

4 Vibration-Driven Robot with Two Rotating Masses

This system (Fig. 14) consists of two identical modules connected by a spring. Each module contains an unbalance vibration exciter. The vibration exciters rotate in the same direction at the same frequency but these rotations are shifted in phase (there is a nonzero angle between the rays from the axes of rotation to the centers of mass of the exciters). The near-resonant mode of motion of this system is studied for the case where the friction force and the excitation force have the same order of magnitude and are small in comparison with the maximum force developed in the spring. The method of averaging is used in this study. It is shown that by changing the off-resonance frequency detuning in sign one can control the direction of motion of the system. The speed of motion can be controlled by changing the magnitude of the phase shift between the rotations of the vibration exciters.

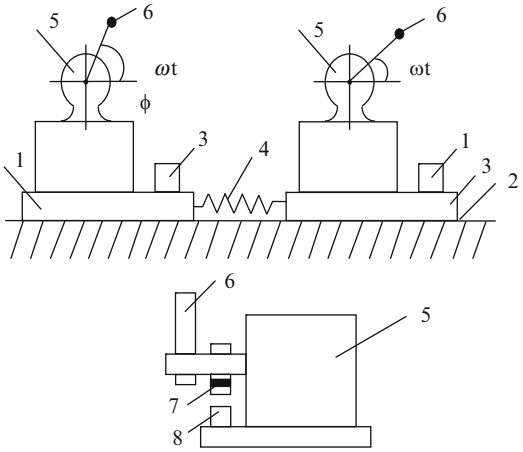

Fig. 14 Schematic of a two-module vibration-driven robot: 1 and 2 are the modules of the robot, 3 is the control system, 4 is a spring, 5 are DC motors, 6 are the rotors of the vibration exciters, 7 and 8 are the components of the sensor for measuring the angular velocity of the exciter's rotation

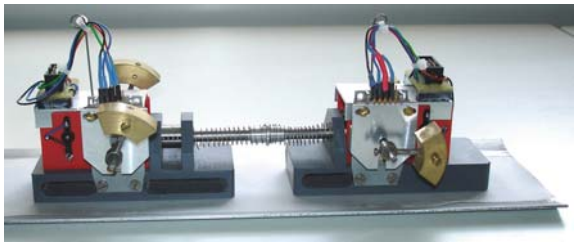

Fig. 15 Physical model of the two-module system with two vibration exciter

5 Experimental Studies

For all systems considered in this paper, experimental physical models were designed and built. The physical model of the two-module system the schematic of which is shown in Fig. 14 is depicted in Fig. 15. The experiments show acceptable agreement of the behavior of the physical systems with the theoretical predictions.

6 Conclusions

Vibration-driven robots with a one-coordinate vibration exciter can move along a rough surface only if the friction between the robot body and the supporting surface or/and the exciter vibrations have asymmetric characteristics. Robots with a one-coordinate exciter that provides the motion of an internal mass along a straight line

can move along the supporting surface in the case of symmetric friction. Such robots can be utilized for cleaning pipelines from solid deposits if the resistance caused by the deposits is low.

The system that consists of two identical modules connected by a spring and is driven by two vibration exciters can be controlled by varying the excitation frequency and the phase shift between the rotations of the exciters. The direction of motion can be reversed by changing between the pre-resonant and post-resonant excitation modes, while the speed can be controlled by changing the magnitude of the phase shift between the rotations of the exciters.

Acknowledgments This study was supported by the Russian Foundation for Basic Research (projects 08-08-00438 and 09-01-91330) and the German Research Society (DFG) (projects Zi 540-12/1 and SFR 622).

References

1. Aoshima, S., Tsujimura, T., Yabuta, T.: A miniature mobile robot using piezo vibration for mobility in a thin tube. J. Dynamic Syst. Meas. Control 115, 270–278 (1993)
2. Ma, J., Lo, M., Bao, Z., Wang, A.: Micro peristaltic robot simulating earthworm and its control system. J. Shanghai Jiao tong Univ. 33(7) (1999)
3. Jatsun, S.F., Safarov, J.: Vibrating engine for robots. In: Proceedings of CLAWAR, Madrid, pp. 1016–1021 (2000)
4. Jatsun, S.F., Vorontsov, R.: Dynamics of vibrating robot for in pipe inspection. In: International Symposium – SYROM, Bucharest, pp. 205–209 (2001)
5. Zimmermann, K., Zeidis, I., Steigenberger, J., Jianjun, H.: An approach to the modelling of worm-like motion systems with a finite number of degrees of freedom, First Steps in Technical Realization. In: Proceedings of the 4th International Conference of Climbing and Walking Robots, Karlsruhe, pp. 561–568 (2001)
6. Yeh, R., Hollar, S., Pister, K.S.J.: Design of low-power silicon articulated microrobots. J. Micromechatronics 1(3), 191–203 (2001)
7. Gradetsky, V.G., Knyazkov, M.M., Kravchuk, L.N., Solovtsov, V.N.: Microsensor control of motion of compact robots inside tubes (in Russian). Mikrosistemnaya Tekhnika, No. 8, pp. 11–19 (2002)
8. Zimmermann, K., Zeidis, I., Steigenberger, J.: Mathematical model of worm-like motion systems with finite and infinite numbers of degrees of freedom, Theory and Practice of Robots and Manipulators. In: Proceedings of the 14th CISM IFToMM Symposium (RoManSy 14), pp. 7–16 (2002)
9. Zimmermann, K., Zeidis, I., Pivovarov, M.: Dynamics of a nonlinear oscillator in consideration of non-symmetric Coulomb dry friction. In: Book of Abstracts Fifth Euromech. Nonlinear Dynamics Conference, Eindhoven, Netherlands, 7–12 August 2005, p. 308
10. Chernousko, F.L.: On the motion of a body containing a movable internal mass. Dokl. Phys. 50(11), 593–597 (2005)
11. Chernousko, F.L.: Analysis and optimization of the motion of a body controlled by means of a movable mass. J. Appl. Math. Mech. 70(6), 819–842 (2006)
12. Chernousko, F.L.: Optimal periodic motions of a two-mass system in a resistive medium. J. Appl. Math. Mech. 72(2), 202–215 (2008)
13. Chernousko, F.L.: On the optimal motion of a body with an internal mass in a resistive medium. J. Vib. Control 14(1–2), 197–208 (2008)

14. Figurina, TYu: Optimal control of the motion of a two-body system along a straight line. J. Comput. Syst. Sci. Int. 46(2), 227–233 (2007)
15. Chernousko, F.L.: Snake-like locomotions of multilink mechanisms. J. Vib. Control 9(1–2), 235–256 (2003)
16. Bolotnik, N.N., Figurina, TYu: Optimal control of the rectilinear motion of a rigid body on a rough plane by means of the motion of two internal masses. J. Appl. Math. Mech. 72(2), 126–135 (2008)
17. Chernousko, F.L., Zimmermann, K., Bolotnik, N.N., Yatsun, S.F., Zeidis, I.: Vibration-driven robots. The Workshop on Adaptive and Intelligent Robots: Present and Future. In: Proceedings, Vol. 1, The Institute for Problems in mechanics RAS, Moscow, pp. 26–31 (2005)
18. Bolotnik, N.N., Jatsun, S.F., Jatsun, A.S., Cherepanov, A.A.: Automatically controlled vibration-driven robots. In: Proceedings of the International Conference on Mechatronics ICM, Budapest, pp. 438–441 (2006)
19. Bolotnik, N.N., Zeidis, I., Zimmermann, K., Yatsun, S.F.: Dynamics of controlled motion of vibration-driven systems. J. Comput. Syst. Sci. Int. 45(5), 831–840 (2006)
20. Chashchukhin, V.G.: Simulation of dynamics and determination of control parameters of inpipe minirobot. J. Comput. Syst. Sci. Int. 47(5), 806–811 (2008)

Experimental Aspects Concerning Self-locking Angle

S. Alaci, F.C. Ciornei, L. Irimescu, and D. Amarandei

Abstract Self-locking is a phenomenon that occurs both in lower pairs and higher pairs, being quantified by the self-locking angle; it occurs due to friction forces, depending directly on normal forces from mechanism pairs. The paper presents some preliminary experimental aspects regarding the influence of different parameters (bushing geometry and material, shaft heat treating, gap dimension and friction type, rolling/sliding for dry/lubricated contact) upon the self-locking angle, carried out on test rigs specially designed and constructed by the authors.

Keywords Friction · Kinematics pairs · Self-locking angle

1 Introduction

Self-locking is a phenomenon that occurs both in lower pairs and higher pairs, and especially in cam mechanisms [1]. It is defined as the phenomenon of impossible motion of a mechanism despite the value of motor forces or moments [2]. This phenomenon occurs due to friction forces from kinematic pairs, depending directly on normal forces from mechanism pairs.

Kostitin, quoted by Artobolevski [1], proposed that for cam mechanisms, the self-locking angle should be named critical pressure angle. Duca [2], presents a more general definition of the pressure angle, as the angle between the direction of the velocity of the point where the force is applied and the direction of the force. This definition assimilates the maximum pressure angle to self-locking angle.

S. Alaci (✉)
Faculty of Mechanical Engineering, Mechatronics and Management, University of Suceava, Suceava, Romania

I. Vişa (ed.), *SYROM 2009*,
DOI 10.1007/978-90-481-3522-6_39,

The pressure distribution has a shape directly related to the shape of the filleted curve of the bushed bearing, always being greater at the edges of the bearing and therefore named "edge effect". Another important parameter for proper working of a cylindrical pair is correct length implementation. A kinematical pair is more efficient as the locking angle is greater.

Two different situations are observed: in the first case, the self-locking angle depends on the geometry of the pair and on the mechanism's position; in the second case, the self-locking angle depends only on the dry friction coefficient. The present paper presents a rig designed to determine the self-locking angle from a prismatic pair.

2 Theoretical Consideration

Self-locking happens both in lower pairs and higher pairs. In the case of lower pairs, it can manifest both in revolute and prismatic pairs. From the two mentioned cases, the self-locking effect occurs strongly in prismatic and cylindrical pairs. An analysis of self-locking phenomenon is made by Artobolevski [1], only for the case when the direction of the force crosses the axis of the pair outside the contact region. Duca [2], applies a similar procedure, for the case of a prismatic (or cylindrical) pair, regardless of the position of the crossing point. A section of this pair is shown in Fig. 1, where:

- a is the shaft diameter
- v_{12} is the velocity of shaft 1 with respect to bushing 2
- $\bar{R}_{12}$ is reaction force from the pair, considered applied in the centre of the pair (vector)
- $\tilde{M}_{12}$ is reaction momentum from the pair (scalar)
- $\tilde{M}_{f_{12}}$ is friction momentum from the pair (scalar)
- $\bar{F}_{f_{12}}$ is friction force from the pair (vector)

One considers that the reaction momentum M_{r12} can be replaced by a couple made of $\bar{R}_c$ forces acting symmetrically from the centre of the pair, in the points A and B, being oriented normal to the translation direction. Therefore, the following relation is valid:

$$M_{r12} = c\,R_c \tag{1}$$

where c is a feature with length dimension and its value depends on contact pressure distribution in the pair. For typical cases, the value of c parameter is indicated in Fig. 2. The assumptions made and shown in Fig. 2 regarding the contact pressure distribution in cylinder pair are far from true. Actually, as Shtaerman [3], and McEwen [4] and Johnson [5], show, the pressure distribution has a shape directly related to the shape of the filleted curve of the bearing, always being greater to the edges of

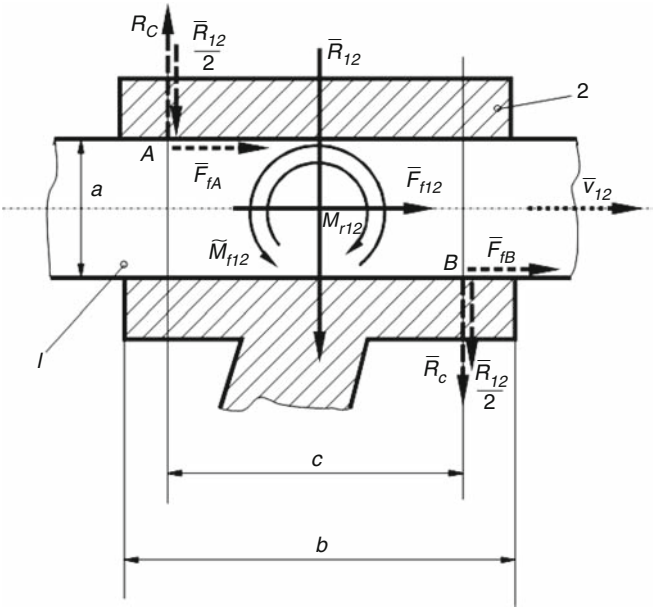

Fig. 1 Forces and torques from prismatic pair [2]

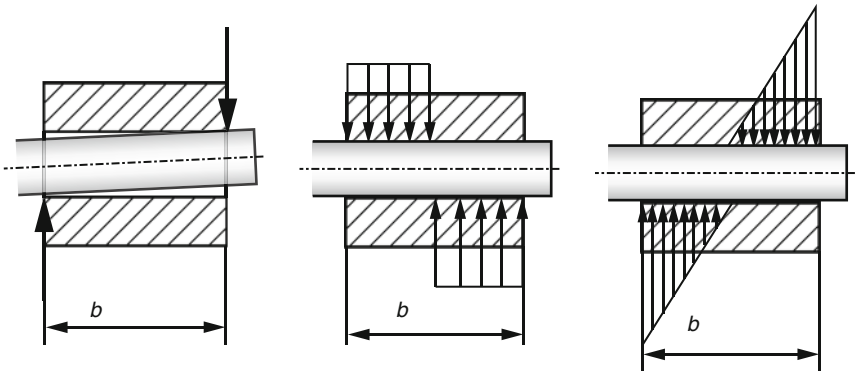

Fig. 2 Various pressure distribution in the prismatic pair

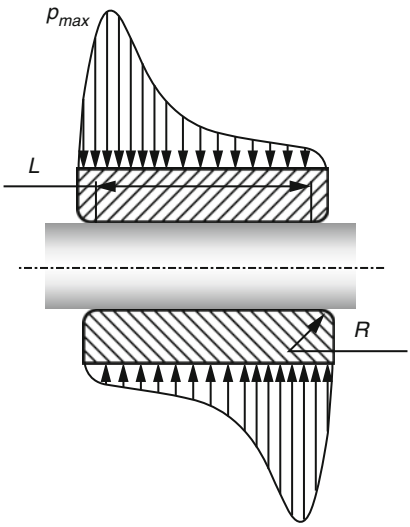

Fig. 3 Influence of fillet radius upon contact pressure distribution

the bearing and consequently named "edge effect", Fig. 3. In order to reduce the stress concentrators in the edge zones of the bearing, the transition from the front face of the bearing to the cylinder region must be made by a revolving surface having a generating line chosen as to diminish the edge effect. Technology imposes the choice upon the fillet surface either conical or doughnut-shaped. The last situation is more favourable and was adopted for guiding element (bolster) construction. The fillet radii were $R2 \div R2.5$. Another important parameter for proper working of a cylindrical pair is correct length implementation. This is necessary for two considerations:

(a) *Structural*, as the contact surface between shaft and bushed bearing must take four of the six DOF of the shaft (the shaft must only rotate around and translate along its axis). For a too short length bearing, only two DOF would be eliminated: the translations on directions normal to shaft axis and the pair would function as a two class pair.

(b) *Dynamic*, with the purpose of reducing the mean contact pressure.

The reaction force $\bar{R}_{12}$ is replaced by the force system $\bar{R}_{12}/2$ applied in A and B. The normal resulting forces and friction forces from points A and B, have, respectively, the expressions:

$$R_A = |R_c - R_{12}/2\,|\,;\;\; R_B = R_c + R_{12}/2 \tag{2}$$

$$F_{fA} = \mu|\,R_c - R_{12}/2|\;\;;\; F_{fB} = \mu(R_c + R_{12}/2) \tag{3}$$

The above forces are replaced in the centre of the pair by a friction force and a resulting friction torque:

$$F_{f12} = \mu[|\,R_c - R_{12}/2| + (R_c + R_{12}/2)] \tag{4}$$

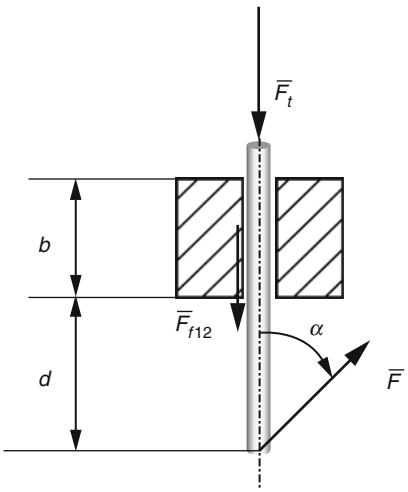

Fig. 4 Shaft balance in revolute pair [2]

$$M_{f12} = [(R_c + R_{12}/2) - |R_c - R_{12}/2|] = \\ = \mu \frac{a}{2}[(R_c + R_{12}/2) - |R_c - R_{12}/2|]. \quad (5)$$

Considering the revolute pair, the forces acting on the shaft, Fig. 4, are:

- F_t – technological force (must be balanced)
- F – active force, forming the angle α with the sliding direction from the pair
- $F_{f_{12}}$ – friction force acting on the shaft

From the torques equilibrium equation on the shaft for the centre of the pair, it results the force necessary to action the shaft. Two situations emerge:

$$\text{(a)} \quad \frac{M_{r12}}{c} > \frac{R_{21}}{2} \quad ; \text{(b)} \quad \frac{M_{r12}}{c} < \frac{R_{21}}{2}$$

(a) The case is characterised by the fact that the point of application of force $\bar{F}$ is outside the contact region and it results:

$$F = \frac{F_t}{\cos\alpha - \mu \frac{2d+b-\mu a}{c} \sin\alpha} \quad (6)$$

(b) The second case is characterised by the fact that the point of application of force $\bar{F}$ is inside the contact zone; it is given by:

$$F = \frac{F_t}{\cos\alpha - \mu \sin\alpha} \tag{7}$$

The mechanism will not self-lock if the following relation is valid:

$$F > 0 \tag{8}$$

From this condition, the extreme values of pressure angle for which the self-locking phenomenon is avoided, result:

$$\alpha_{bl} = \operatorname{atan}\frac{c}{\mu(2d + b - \mu a)}, \quad \frac{M_{r21}}{c} > \frac{R_{21}}{2}; \tag{9}$$

and

$$\alpha_{bl} = \operatorname{atan}\frac{1}{\mu}, \quad \frac{M_{r21}}{c} < \frac{R_{21}}{2} \tag{10}$$

respectively.

A kinematical pair is more efficient as the locking angle is greater. From relations (9) and (10), two different situations are observed: in the first case, the self-locking angle depends on the geometry of the pair and on the position of the mechanism by a and d parameters; in the second case, the self-locking angle depends only on the dry friction coefficient, μ.

Fig. 5 RCCC mechanism from lab [10]

Fig. 6 Larochelle's RCCC mechanism [11]

3 Experimental Evidences

During experimental researches in the laboratory, the authors met the self-locking phenomenon after constructing a *RCCC* spatial type mechanism, Fig. 5.

The constructive elements calculus was made after kinematics study, following the method described by Yang [6, 7], McCarthy [8], and Fisher [9]. This mechanism presents mobility only for certain positions of the leading element. The revolute pairs of the mechanism were made from steel cylinders introduced in bushing with free running fit, $H8/f8$ [10]. The same mechanism is presented on the site of Larochelle from Florida University [11], shown in Fig. 6. Despite the general image, one can observe that the cylindrical pairs were made using linear ball bearings.

4 Test Rig Design and Testing Method

The authors designed, Fig. 7, and employed a first test rig, as seen in Fig. 8, presented in [12]. At the end of a shaft, a cable passing over a roller pulls under a variable angle, due to an overhanging weight. The self-locking phenomenon was identified when the contact between the shaft and a limit stop element opened and the electrical power of the driving motor was thus switched off. At this moment, the angle between the cable and the shaft axis reached the self-locking value. Two main limits of the presented test rig were observed: first, the actual self-locking angle was limited by design as the cable touched the case of the bushing; secondly, the situation when the direction of the force from the shaft crosses the inside of the bushing-shaft contact cannot be studied. As a consequence, a new test rig was designed, presented in Fig. 9. The shaft *1* is guided by two identical bushings, *2*.

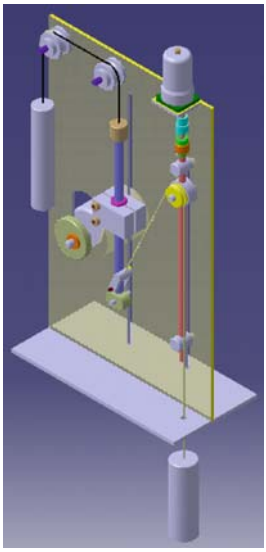

Fig. 7 Initial design of test rig

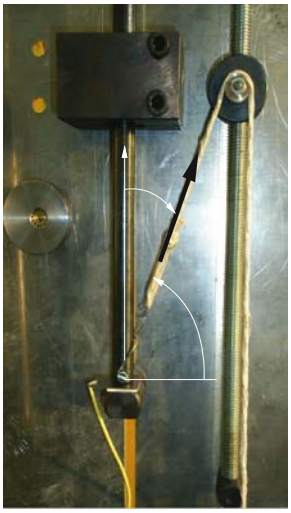

Fig. 8 Initial rig for self-locking tests

The bushings are half-split to ensure changeability of the bushings during tests. The bushing cases, *3*, are fixed to the holed column *4*, the distance between bushings being modifiable, meaning a variable *b* parameter. A half-split bushing *13* is fitted to the shaft, ensuring the value for *y* parameter. On this bushing, two pins *12* are built in, together with a bevel angle, *7*. A cable *5*, fastened on the two pins, is rolled over two pulleys *14*, from the mobile nut *6*. When the driving screw is rotating, the

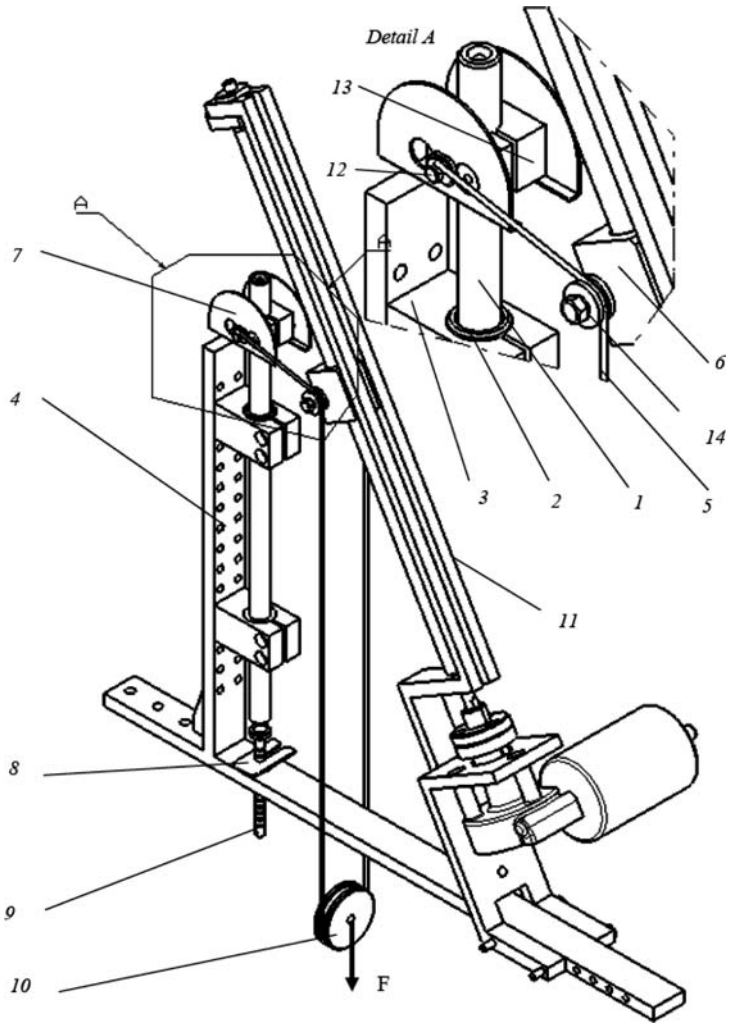

Fig. 9 Test rig for self-locking angle study

mobile nut translates and the angle of the cable can reach any values in the range $0 \div 90°$.

In the lower part of the rig, a roller (with diameter greater than the base element) is hanged on the cable and can support the loading weight. The inferior end of the shaft rests on grooved pin, *9*, playing the role of limit stop element. This pin is electrically insulated and the electrical circuit can be turned off when the mechanical contact is broken. The *y* distance can be rapidly be modified using the pocketed plate, *8*. In the initial position, the α angle between the cable and the shaft must be around 90°, for a firm contact shaft-grooved pin.

Fig. 10 Test rig from the lab

Fig. 11 Detail of the rig

When the screw rotates, the mobile nut slides ascending along the guide and the angle of the cable decreases until the shaft-grooved pin contact is released. This unfastening produces the switching off of the rig power and corresponds to the self-locking moment. The angle α can thus be measured on the bevel angle.

To model the situation for the force acting inside the contact region, the half-split bushing *13* must be fitted to the shaft between the two bushings *3*.

The actual test rig built in the lab is presented in Figs. 10 and 11. The friction type influence upon self-locking angle can be studied by changing the sliding bushings with linear ball bearing bushings, Fig. 12. The study of fillet radius influence is made using a set of bushings, with various filleting radii or chamfered, Fig. 13.

The most complex phase of the tests refers to finding the c parameter from Eq. (1).

Fig. 12 Sliding and linear ball bearing bushings

Fig. 13 Bushings with various filleting radii and chamfered

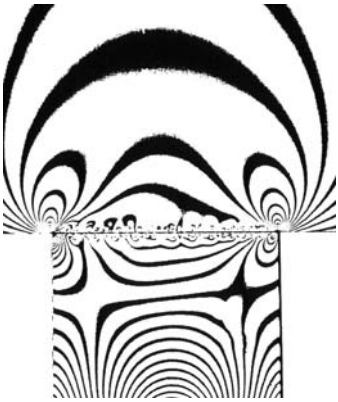

Fig. 14 Photoelastic isochromatics for an unchamfered bushing [13]

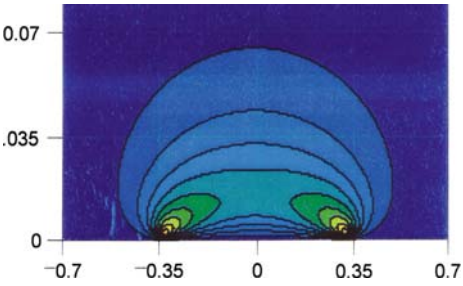

Fig. 15 Theoretical isochromatics patterns for unchamfered bushing

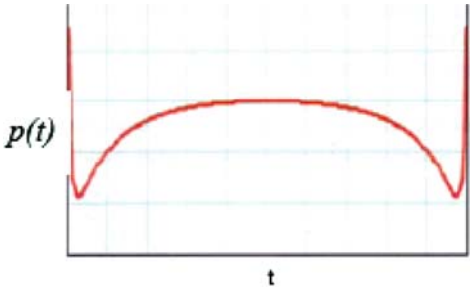

Fig. 16 Pressure distribution

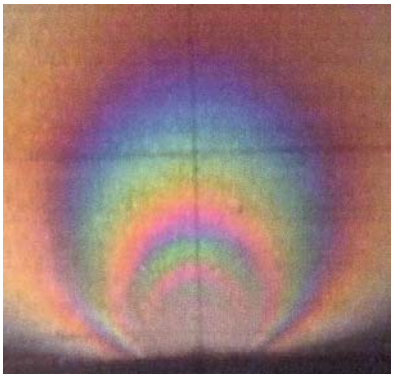

Fig. 17 Experimental isochromatics for a higher pair disc-half-plane [14]

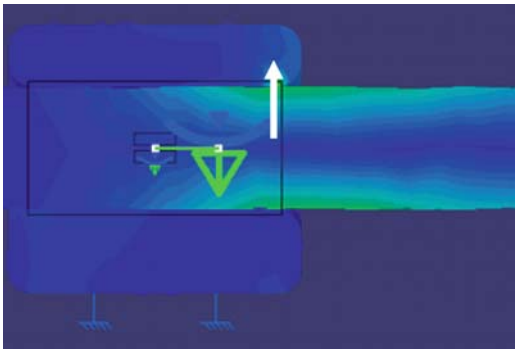

Fig. 18 FEA stress state, filleted bearing and small normal force on the shaft

The actual situations range in a domain characterised by the fillet radius of the bushing, namely from zero, when the edge is knife-type (unchamfered), to a radius conducting to torus shape for the bushing (Fig. 13).

The limit aspects, with zero fillet radius were studied by Alaci [14], and Figs. 15 and 16 present the theoretical isochromatics and pressure distribution, respectively.

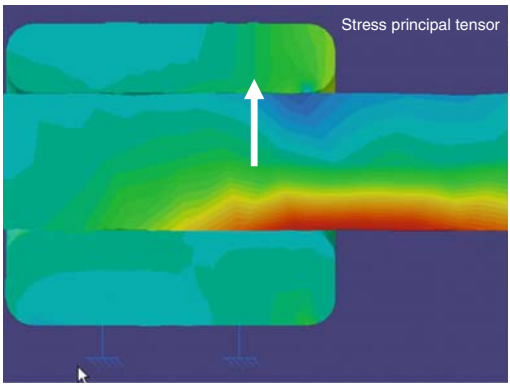

Fig. 19 FEA stress state for a bigger force

The other limit case, for torus bushing, can be equivalent to the plane problem of the contact between a half-plane and a disc. The experimental photoelastic results obtained in [14] are presented in Fig. 17.

The pressure distribution is half-elliptical and it is applied on a narrow strip symmetrical to the initial contact line. For a specific situation, the stress state and pressure distribution cannot be found analytically and therefore, a numerical method should be applied. In Figs. 18 and 19, the principal normal stresses for a shaft-filleted bushing are presented. Figure 18 shows the stress state for small normal load (small self-locking angle) and Fig. 19, corresponds to a greater normal force (large self-locking angle).

5 Experimental Work and Conclusions

Experimental tests were carried out in order to validate Eqs. (9) and (10). From test rig design, the constructive parameters a, b and d were identified. The only unknown parameter required to apply the mentioned relations was the friction coefficient, μ, between shaft and bushing. Using a device presented in Fig. 20, experimental test conducted to the value $\mu = 0.27$ for friction coefficient. The bushing and the shaft of the rig were used on a device where the transitory times, t_1, t_2, when the bushing passes through two gates, 1 and 2, were measured.

The friction coefficient is found using Galilei's formula:

$$\mu = \frac{v_1^2 - v_2^2}{2gL}, \quad v_i = \frac{b}{t_1}, \; i = 1, 2 \tag{11}$$

where: $b = 32\,mm$, $L = 130\,mm$, $t_1 = 0.024s$ and $t_2 = 0.031\,s$. Preliminary experimental results are given in Table 1.

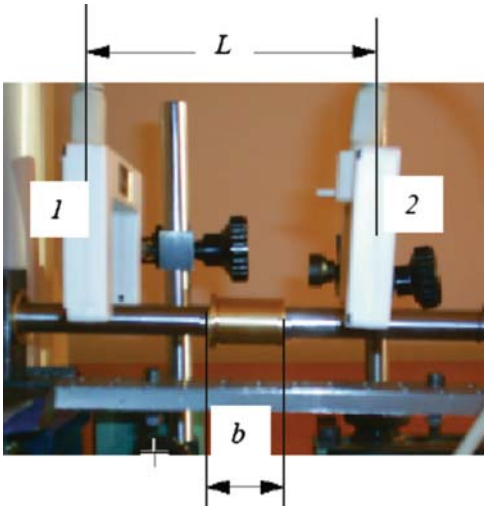

Fig. 20 Device for friction coefficient measurements

Table 1 Experimental results

d (mm)	b (mm)	R (mm)	μ	α (deg)	α_{th} (deg)
43	124	4	0.27	33	65
66	92	4	0.27	32	57

For the case when the direction of the force crosses the bushing axis inside the contact area, theoretical values for self-locking angle is $\alpha_{th} = 74.89°$and the measured values are in the range $\alpha = 48° \div 57°$. The discrepancies between theoretical and experimental results show the necessity of extra research work. Possible causes of the errors could be:

- The micro-welding points for the un-heat treated materials.
- The approximation of the prismatic pair of arbitrary width with a cylindrical one with blocked revolving motion.
- The coaxiality constraints between the two bushings ends suggest the necessity of one-piece bushing, with simultaneous machining of the two holes.

References

1. Artobolevski, I.I.: Teoria mecanismelor şi maşinilor. Tehnică, Bucureşti (1955)
2. Duca, C.: Mecanisme. Rotaprint I.P, Iasi (1983)
3. Shtaerman, I.: Contact Problems in the Theory of Elasticity (in Russian). Gostehizdat, Moscow (1949)

4. McEwen, E.: Stresses in elastic cylinders in contact along a generatrix. Philos. Mag. 40, 454 (1949)
5. Johnson, K.L.: Contact Mechanics. Cambridge University Press, Cambridge (1985)
6. Yang, A.T., Freudenstein, F.: Application of dual-number quaternion algebra to the analysis of spatial mechanisms. ASME J. Appl. Mech. 31, 300–308 (June 1964)
7. Yang, A.T.: Application of quaternion algebra and dual numbers to the analysis of special mechanisms. Ph.D. Thesis, Columbia University (1963)
8. McCarthy, J.M.: An Introduction in Theoretical Kinematics. Massachusetts Institute of Technology, Cambridge, MA (1990)
9. Fischer, I.: Dual Number Methods in Kinematics, Statics and Dynamics. CRC Publication, New York (1999)
10. Alaci, S., Ciornei, F.C., Pătraş-Ciceu, S.: Aspects concerning RCCC Spatial Mechanisms Kinematics. 3rd International Conference on Advanced Concepts in Mechanical Engineering, Bulletin of the Polytechnic Institute of Jassy, Tome LIV(LVIII), Fasc.1, Section Machine Construction, ISSN 1011-2855, pp. 411–422 (2008)
11. http://www.fit.edu/faculty/profiles/profile.html
12. Alaci, S., Ciornei, F.C., Irimescu, L., Cerlincă, D.A.: Test rig for self-locking study. Proceedings of 14th Conference on Elastohydrodynamic Lubrication and Traction, Varehd 14 (on CD), Suceava University (2008)
13. Frocht, M.M.: Photoelasticity. Wiley, New York (1953)
14. Alaci, S.: The effect of internal hole type discontinuities upon stress state in elastic plane contact (in Romanian). Ph.D. Thesis, Suceava University (2002)

Strategy for Optimizing the Synchronous Belt Drives Design

S. Butnariu

Abstract The present method of synchronous belt drives design assumes step-by-step procedures for selecting acceptable components for a desired application. Otherwise, for special applications, the selection of the belt drives components (pulleys, tensioner device and belt), performed now using algorithms, nomograms, equations, coefficients, can be optimized by simulating the drive tests under different loading. For this we propose to use different CAE methods, such as Multi-Body Analysis. This paper presents a model developed for the characterization of the behaviour of synchronous belt transmissions, with the final goal of predicting the load distribution on the contact arc.

Keywords Belt · Design · Drive · Multi-body · Synchronous · Timing

1 Introduction

Synchronous belts provide ideal solutions for power transmission and linear drive applications because they offer high accuracy, lower maintenance and can accommodate many different product-conveying requirements.

Synchronous belt drives have significant advantages when compared to chain drives. Some examples are excellent elongation behaviour and good damping characteristics under load. Synchronous belts are frequently used in combustion engines (about one-third of industrial motors) for driving the timing/injection system as well as various accessories.

Irregularities of crankshaft's rotary speed and alternating driving torques of timing/injection components lead to excitation of belt-system's natural frequencies.

S. Butnariu (✉)
Transilvania University of Brasov, Brasov, Romania

I. Vişa (ed.), *SYROM 2009*,
DOI 10.1007/978-90-481-3522-6_40,

As a consequence, resonance effects will appear within the operating speed range causing significant rise in system's forces, lateral vibrations, wear, and noise [1].

Most manufacturers' manuals contain step-by-step procedures for selecting acceptable belts for an application, considering factors such as speed, horsepower requirements, size limitations, duty cycle and environmental conditions.

2 Tooth Loading

In contact with a pulley, each tooth is exposed to a certain load. The distribution of the tooth load varies during the contact and depends among other variables on the elastic and frictional properties of the belt.

The most loaded tooth puts a limit on the transmitted torque of a drive. The teeth of the belt are indexed from the tight to the passive side. When the torque is transmitted, the belt tension changes from F_t to F_s; this means that there must be a certain distribution of the tooth load [5].

Many applications with synchronous belts drive imposes particulars conditions regarding transmitted torque, speeds, meshing and noises.

Current literature (technical books and design manuals, most of them imposing by belts manufacturers) still does not provide all the necessary information on belt and tooth forces and belt material properties, which would enable engineers to optimize the drive for a special case of application.

In order to study the load distribution and to enhance its performance, it is important to have the availability of measurement instruments capable of measuring this characteristic under operating conditions.

So, for solve these problems, a new method it must to develop.

3 Multi-body Based Model of the Belt Drive

Based on a discretization of the belt, a multi-body model has been defined to emulate the behaviour of the transmission [3]. A rigid body represents each pulley.

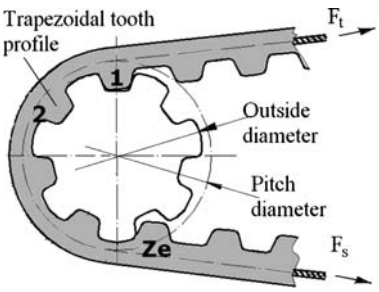

Fig. 1 Synchronous belt drive meshing mechanism

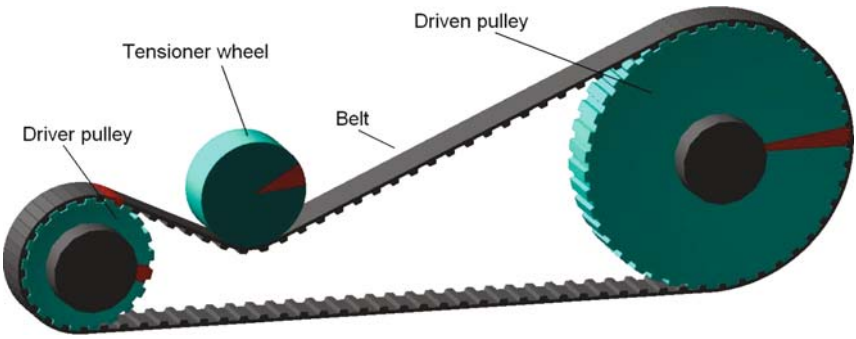

Fig. 2 Synchronous belts transmission basic structure

In order to manage the meshing phase and the polygonal effect, the geometry of the teeth has been duly reproduced (Fig. 1).

Figure 2 presents the components of a distributor mechanism of a FIAT 1300 engine (a typical drive arrangement for a single overhead cam – SOHC), with 21 teeth sprocket and 42 teeth pulley. The centre distance of this drive is 300 mm.

The model is composed of the following bodies: a driving sprocket, responsible for motion generation; a driven pulley, responsible for brake torque; a tensioner device (wheel diameter 50 mm); a belt, profile L, ISO 5296, composed by a number of 97 teeth which can be joined each other.

The tension is set after the belt is installed by moving the adjustable idler [2].

In order to simulate the motion of this complex mechanical system, it was chosen a version of ADAMS, because this software is able to manage the contact between bodies and the properties of various materials such steel, rubber and glass fibber.

On the other hand, ADAMS has a specialized module for engine components, inclusive belt transmission and a detailed template builder.

Some of the parameters were known at beginning from manufacturer's data or obtained by experimental tests. The model can be driven by external dynamic or kinematic constraints. The model, composed by two pulleys, one tensioning device and a 97 teeth belt, has 294° of freedom.

4 Description Test and Results

Multi-body model was run several times on the ADAMS software, changing some parameters. The results presented below are part of a larger set of determinations made on this model. Table 1 below lists the experiments carried out, with the parameters which were modified.

The distribution of the teeth loading was measured in the test rig fitted. At the end of dynamic simulation it was possible to obtain detailed information on system behaviour. Figures 3, 4, 5, 6, 7, 8, and 9 have on abscissa the rotation angle

Table 1 Used experimental values

Determination no.	Angular velocity (grd/s)	Torque (Nm)	Tooth stiffness (N/m)	Pre-tensioning force (N)
Det_01	12	20	10^3	200
Det_02			10^4	
Det_03			10^5	
Det_11	12	10	10^4	50
Det_12				200
Det_13				350
Det_21	12	10	10^4	200
Det_22		20		
Det_23		30		
Det_31	12	10	10^4	200
Det_32	24			
Det_33	36			

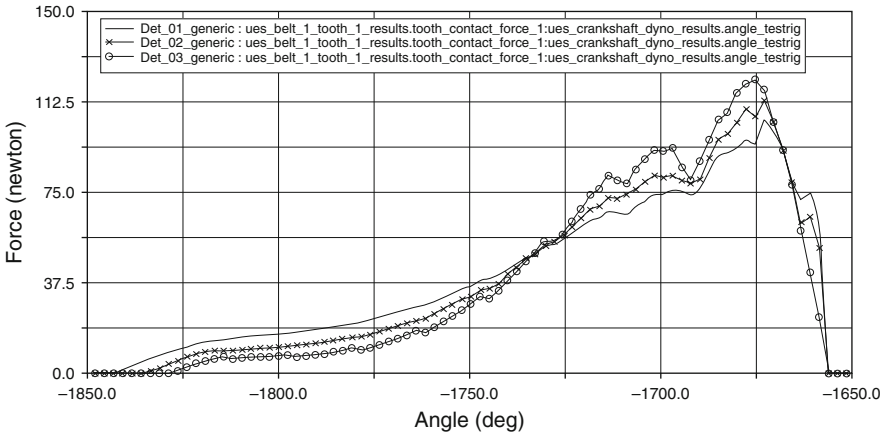

Fig. 3 Load distribution on driver pulley (cases 01. . .03)

corresponding driver or driven pulley, respectively and on ordinate line the values of tooth load.

Figure 3 shows the output of the ADAMS software for the first layout (Det_01. . .03), when it was modified the teeth stiffness. The equivalent tooth stiffness introduced in a dynamic model permit to give a lot of informative results. Note that, for the driver pulley, with increasing tooth stiffness, the torque will be transmitted by the first teeth come in contact with pulley teeth.

Similar results were obtained at the driven pulley, shown in Fig. 4, were a large part of the torque is transmitted over by teeth being at the end of contact arc, toward the tight side of belt. It may be said that, with increasing teeth stiffness, belt behaviour is closely by chain behaviour.

In Fig. 5 is presented the load distribution on driver pulley teeth taking in consideration pre-tensioning force variation. Increasing the pre-tensioning value, the load distribution on pulley teeth get to a uniform shape.

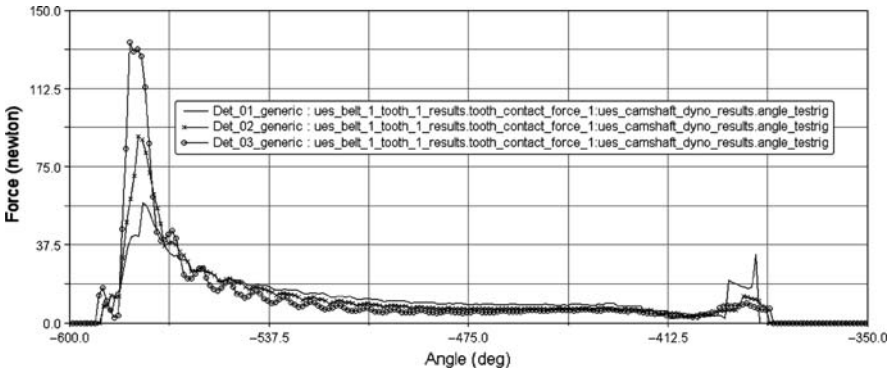

Fig. 4 Load distribution on driven pulley (cases 01. . .03)

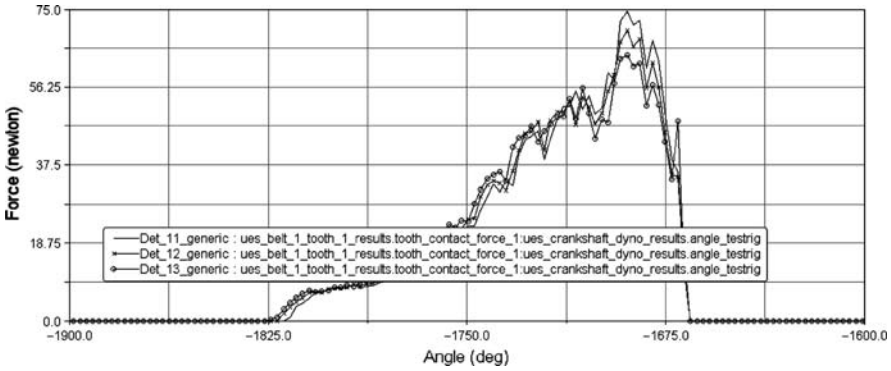

Fig. 5 Load distribution on driver pulley (cases 11. . .13)

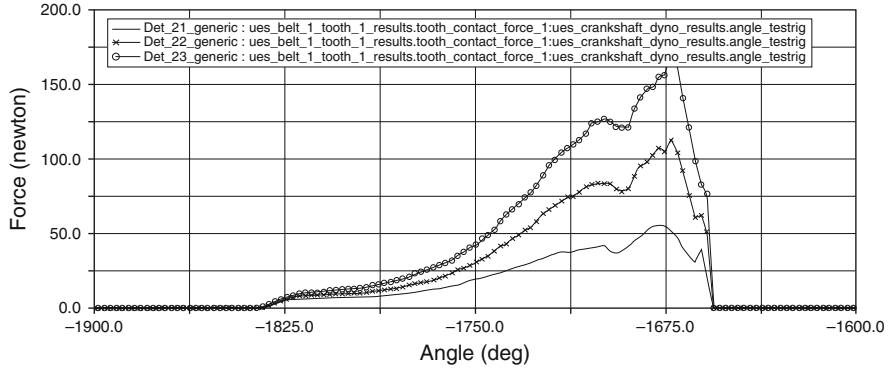

Fig. 6 Load distribution on driver pulley (cases 21. . .23)

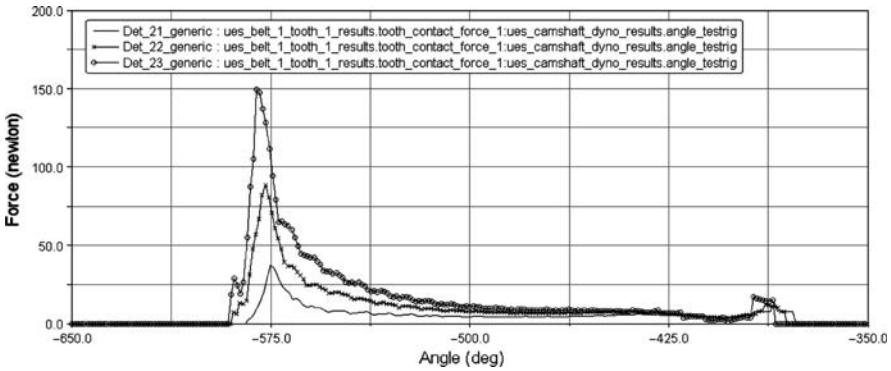

Fig. 7 Load distribution on driven pulley (cases 21. . .23)

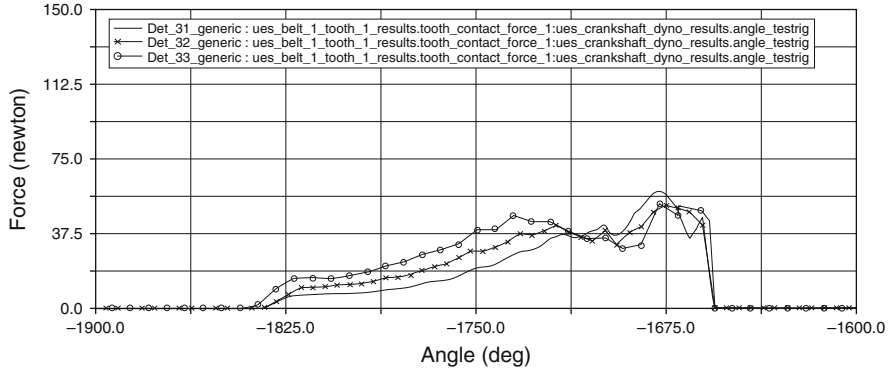

Fig. 8 Load distribution on driver pulley (cases 31. . .33)

Figures 6 and 7 show the same kind of data for the second layout (Det_21. . .23), with three distinct cases for the brake torque. It can see that for small values of the torque, all the teeth which are in contact with pulley can transmit the torque. Increasing the brake torque, the teeth loading is moving to the tight side of the belt were the belt teeth are much stressed.

Observe how easily it is to upload belt teeth, depending on the position that it occupies at a time by arc of circle. For the teeth, the stress peaks are situated near the tight load side where the tooth load distribution is highest. The maximum loads decrease along the rest of the contact arc in the slack load side [4].

In Det_31...33 determinations we modified the angular velocity values of driver pulley, keeping constant braking torque, tooth stiffness and pre-tensioning values.

It observes that, for driver pulley, increasing angular velocity of driver pulley, the tooth load is going to an equal distribution on wrapping arc (Fig. 8). For the driven pulley (Fig. 9), increasing velocity, it observes that the load is transfer to firsts and lasts teeth on wrapping arc.

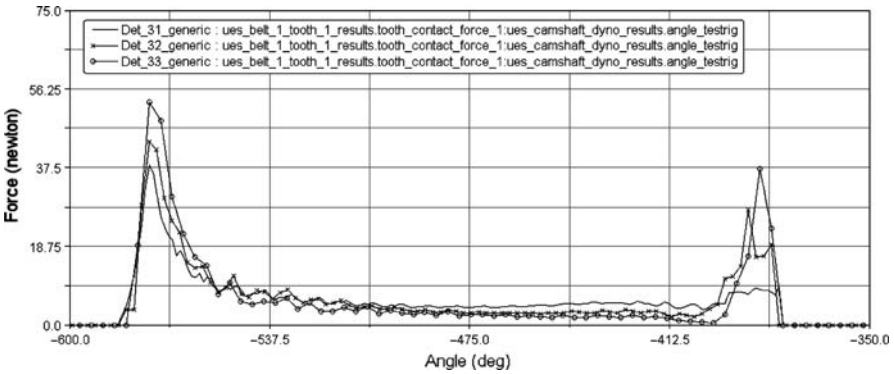

Fig. 9 Load distribution on driven pulley (cases 31. . .33)

5 Conclusion

This paper has described a detailed model developed for the characterization of the behaviour of synchronous belt transmissions, with the final goal of predicting the load distribution on the contact arc of a given design and suggesting possible design changes, in order to avoid the improper structure of the transmission.

The presented design method was developed just for these types of situations, when classical methods and available components aren't enough.

The present study has demonstrated the ability of Multi-Body method to simulate the transmission of torque between pulleys and belt.

This analysis method involves a subjectivity degree during its deployment: materials and their properties choice, joints and applications choice or defining areas of contact.

References

1. Batchelar, P.H.: A practical guide to synchronous belts. Mach. Des. Wilson Appl. Sci. Technol. Abstr. 68(8), 100–103 (1996)
2. Butnariu, S.: Theoretical and experimental researches on synchronous belts. Ph.D Thesis, Transilvania University of Brasov (2004)
3. Callegari, M., Cannella, F., Ferri, G.: Multi-body modelling of timing belt dynamics. In: Proceedings of the Institution of Mechanical Engineers, vol. 217, Part K, pp. 63–75 (2003)
4. Childs, T.H.C., Dalgarno, K.W., Parker, I.K., Hojjati, M.H., Tutt, M.J., Day, A.J.: The meshing of timing belt teeth in pulley grooves. In: Proceedings of the Institution of Mechanical Engineers, vol. 211, Part D, pp. 205–218 (1997)
5. Gerbert, G., Johnsson, H., Persson, U., Stensson, G.: Load distribution in timing belts. J. Mech. Des. 100, 208–215 (1978)

Control Design and Simulations of the Linear Actuator LX-80-L

I.A. Cosma, V. Mătieş, and C. Rusu

Abstract The aim the paper is to simulate and control the high precision linear actuator provided by Parker, LX-80L-T14MPS. In the first part of the paper are studied and simulated the actuator's response to a Proportional-Integrative-Derivative controller using Matlab Simulink software. After turning the PID controller's constants, these are introduced using a interface in the real time controller VIX-500-CH. By establishing and introducing these parameters in the controller, a set of commands is executed to verify the accuracy and behaviour of the linear actuator.

Keywords Linear actuator · PID control · Simulation

1 Introduction

A linear actuator is a device that develops force and motion, from an available energy source, in a linear manner, as opposed to rotationally like an electric motor. There are various methods of achieving this linear motion.

Controlling linear actuators has a very important significance in designing positioning production systems in industry worldwide. For a high accuracy of positioning, these linear actuators must have a very high precision and good repeatability rate. There have been developed a large variety of linear actuators, variety which includes: mechanical actuators, hydraulic actuators, piezoelectric actuators, electromechanical actuators a.o. This paper takes in consideration one of these types of actuators, the electro-mechanical one.

I.A. Cosma (✉)
Department of Mechanisms, Precision Mechanics and Mechatronics, Technical University of Cluj-Napoca, Cluj-Napoca, Romania

I. Vişa (ed.), *SYROM 2009*,
DOI 10.1007/978-90-481-3522-6_41,

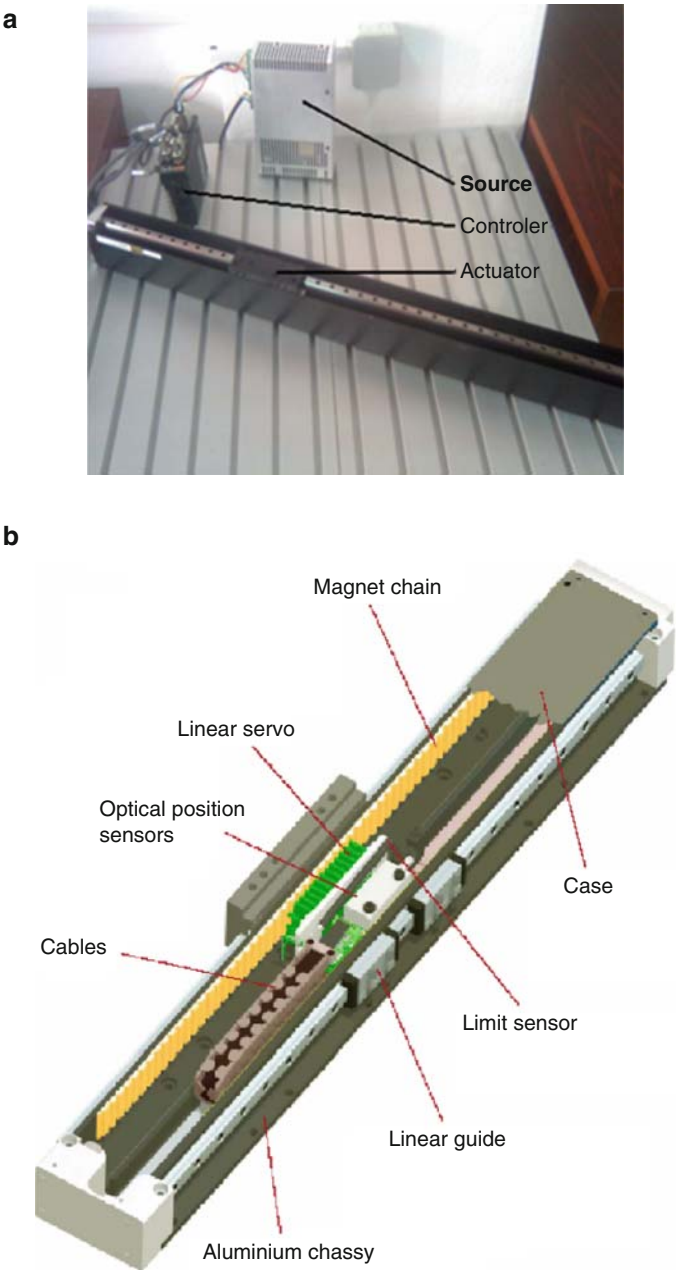

Fig. 1 (**a**) Experimental stall: the linear actuator, with controller and power source; (**b**) Structure of the linear actuator

The actuator presented in Fig. 1 [4] is an integration of more components: the mechanical component (represented by the moving cart and the sliding mechanism on which the cart is attached), the electrical component (the three phases of the electrical circuit and the power source) and the informational one (the Vix-500CH controller).

2 Linear Actuator Parker LX-80L-Mechatronics Laboratory

The linear actuator presented in Fig. 1 is able to achieve speeds up to 3 m/s and accelerations up to 7 m/s^2. With a maximum stroke of 750 mm, the actuator can be implemented and successfully applied in a large variety of robotic systems, positioning systems or magnetic levitation systems. The positioning precision of the actuator reaches 5 μm and the generated force 19 N.

The source is represented by the power supply XL-PSU generating a tension of 80 V d.c. and a maximum current flow of 8 A.

2.1 Mathematical Model

The equivalent electrical circuit of the linear actuator is presented in Fig. 2 (according to Magnetics Devision 2002) [2],
where the constants for a typical actuator are:

R_c = 1.95 ... 2.93 [Ω];
L_c = 739 ... 639 [μH] and
K_F = 2.98 ... 3.83 [N/A]
and the relation between them:

$$U = u_R + u_L + u_{EMF} = R_c i_a + L_c \frac{dI_a}{dt} + K_B \Delta v$$

The model of the system which stays at the basis of the response simulation to the PID controller is based on system of equation (1), which completely describes the running of the linear actuator. The equilibrium of the voltages is written:

$$U = I_a R + E,$$

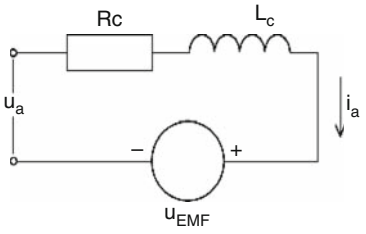

Fig. 2 Equivalent circuit for the electromechanical actuator

where $E = Blv$ is the electromotor induced voltage. U will become:

$$U = I_a R + Blv$$

Dividing by $Bl = K_f$ we obtain first equation of system (1):

$$v = \frac{U}{K_F} - \frac{R_a I_a}{K_F}$$

$$\begin{cases} v = \frac{U}{K_F} - \frac{R_a i_a}{K_F} \\ F = K_F i_a \\ E = K_F v \\ F - m\frac{d^2x}{dt^2} - F_R - F_F - C_V \frac{dx}{dt} = 0 \end{cases} . \quad (1)$$

where:

U – voltage through circuit (80 V max)
$v = dx/dt$ -speed of the moving cart (3 m/s max)
i_a – current through the circuit (3.90 A-peak)
E – induced electromotor voltage
m – mass of the moving cart (287 g)
F_R – resistant force (accord.with. appl.)
F_f – static friction (2 N)
F_v – viscous damping (1 N/m/s)

The last equation of the system (1) takes in consideration all forces that are acting at the level of the moving part (active and resistant forces). The system of equation (1) is implemented using Matlab-Simulink software, in order to simulate the actuators response to a step signal using a PID controller.

2.2 *Implementation of the Mathematical Model in Matlab-Simulink*

The need to implement the mathematical model in Matlab-Simulink (Figure 3) software is given by the necessity to calibrate the real time PID controller of the mechatronic platform, so that the actuator should achieve prescribed performances (overshoot, settling time and steady-state error), according to the application in which it is implemented (Figure 4). The parameters which are ruling the process in which is involved a PID controller are represented by: proportional gain (K_p), integrative gain (K_i) and derivative gain (K_d) [3].

The response of the subsystem to a PID controller is presented in Fig. 5. The first part of the figure shows the variation of the cart velocity. The second part of the figure illustrates the position of the moving cart according to the set value. There can be observed the performance of the positioning act using the PID controller

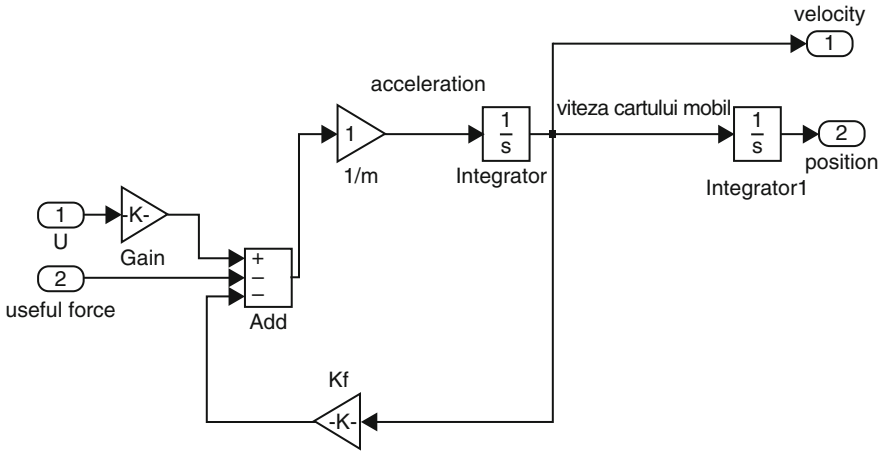

Fig. 3 Simulink actuator model as subsystem

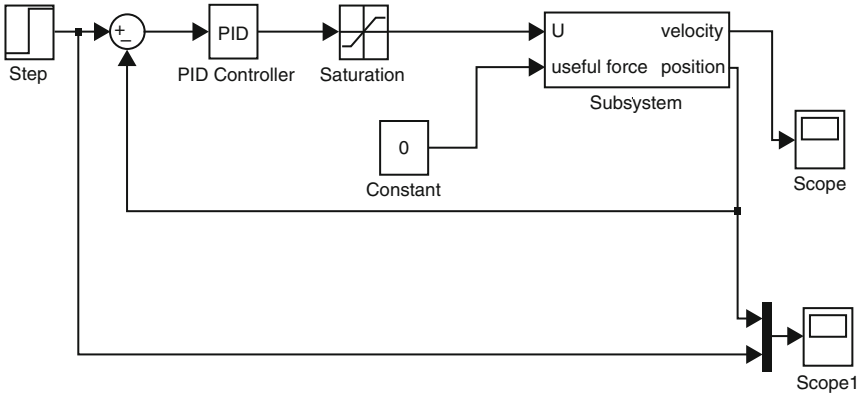

Fig. 4 Subsystem controlled by PID-controller

(part two of the figure – overshoot, settling time and steady state error). In order to minimize those parameters, the PID controller has to be calibrated. After according constants of PID controller, the obtained response of the system is presented in Fig. 5b. For this response there were found the following constants: $K_p = 10$, $K_i = 2$, $K_d = 35$.

2.3 *Testing the System Using Determined K_p, K_i, K_d Parameters*

The parameters determined during the simulation and optimization of the actuator response can be easy implemented using the special interface. After connecting the controller through the serial cable to a personal PC, this interface lets us to

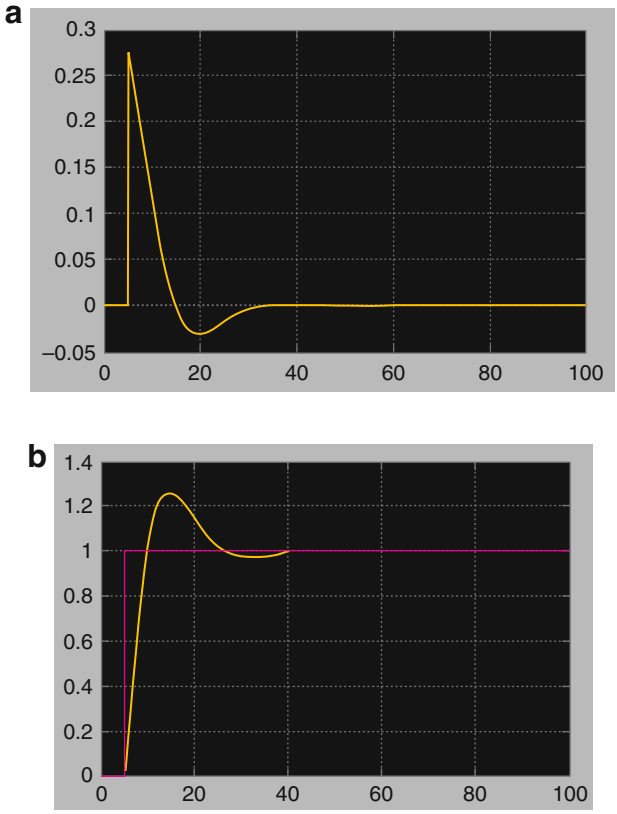

Fig. 5 (**a**) Step response of the actuator using PID controller (velocity); (**b**) Step response of the actuator using PID controller (displacement)

configure the parameters of the real time controller. After configuring these parameters, they are loaded into the controller via the serial connection.

The response of the actuator is then analyzed and there are drawn conclusions about the behaviour of the actuator. A set of moving profiles of the mobile cart is given and then the response is then analyzed. One of the sets of moving profiles is given by command [6]:

1PROFILE2(2000, 3000, 12000, 220);

where the parameters of the moving profile are: 1 – the address of the axis

2 – number of the defined profile

2000 – acceleration of the cart

3000 – deceleration of the cart

12000 – number of desired steps

220 – velocity of execution

Easi-V interface displays the data collected from the actuator's sensors through the serial connection and displays it for the analyzing the behaviour concerning the

actuator's response. According to the maximum precision the actuator can achieve, the steady state error, the overshoot and settling times are analyzed.

3 Conclusions

The positioning error according Easi-V interface is zero (taking in consideration the precision of the encoder-5μm). At high velocities (2–3 m/s) of the moving cart, the parameters like overshoot and settling time cannot be observed, but at slower speeds (0.05–0.1 m/s) all these parameters can be easy observed. The settling time is according to the set speed of the cart, and the overshoot can be evaluated to be 150 steps of the encoder's resolution –corresponding to a maximum of 0.75 mm.

Acknowledgments The financial support was ensured based on PN-II project Nr. 71129/2007

References

1. Liang, Y., I-Ming, C., a.o.: Torque modeling of a spherical actuator based on lorentz force law. Proceedings of the 2005 IEEE International Conference on Robotics and Automation, Barcelona, Spain, April 2005
2. Schneiders, M., Makarovic, J., a.o.: Design considerations for electromechanical actuation in precision motion systems. In: 16th IFAC World Congress, Prague (2005)
3. Szabo, F.: Contributii privind studiul procesului de integrare în mecatronica. PhD Thesys, Universitatea Tehnica din Cluj-Napoca, Cluj-Napoca (2006)
4. Parker Automation, VIX series digital drives, User guide (June 2005)
5. Sisteme Mecatronice de acţionare realizate cu noi tipuri de actuatori pentru aplicaţii în robotică şi în alte domenii. Project PN-II 71-129/2007, Director Prof. V. Măţieş
6. http://www.maccon.de/FTPROOT/ViX_IE_quickstart.pdf

The Analysis of a Dwell Mechanism for Alpha -Stirling Engine

N.M. Dehelean and V. Ciupe

Abstract All engineers who work to improve the work efficiency of the α Stirling engine try to replace the crank mechanism of compression cylinder by another one. It could be useful a mechanism able to perform a dwell during the whole period of expansion. This stop of the compression piston has to enlarge the active area of the PV diagram. As consequence it is expected an efficiency improvement. This request could be very well accomplish by a cam mechanism. But this one is too large, too complicate, expansive and unreliable for solar systems as shown in [1]. Hence, the paper tries to find out a linkage able to perform an equivalent dwell as a cam mechanism. The purpose of the analysis is to find out the movement functions yC(t) and yE(t) to reveal if there are in a proper phase relation between them or not. The proper phase relation demonstrates that the mechanism is good for the application. Second, it must show that yE(t) has a large enough dwell, in accordance with the expansion stroke time of the expansion cylinder.

Keywords Bar mechanism · Crank rod mechanism · Dwell mechanism · Movement law · Stirling engine

1 On the Working Cycle of Stirling Engine

The PV diagram of α-Stirling engine it is far away from an ideal PV diagram. The principle schema of a α-Stirling engine is shown in Fig. 1. As seen the engine has two crank rod mechanisms, one for the compression cylinder and the other for the expansion cylinder. The movement functions for both pistons are sinusoidal, as shown in Fig. 2.

N.M. Dehelean (✉)
Department of Mechatronics, "Politehnica" University of Timişoara, Timişoara, Romania

I. Vişa (ed.), *SYROM 2009*,
DOI 10.1007/978-90-481-3522-6_42,

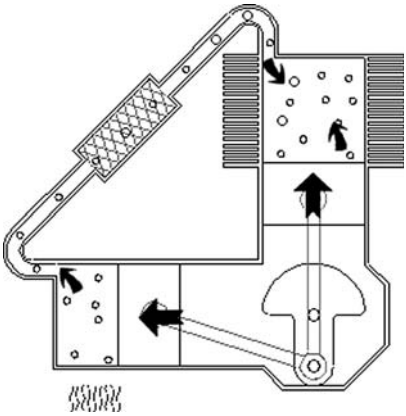

Fig. 1 The standard α-Stirling engine

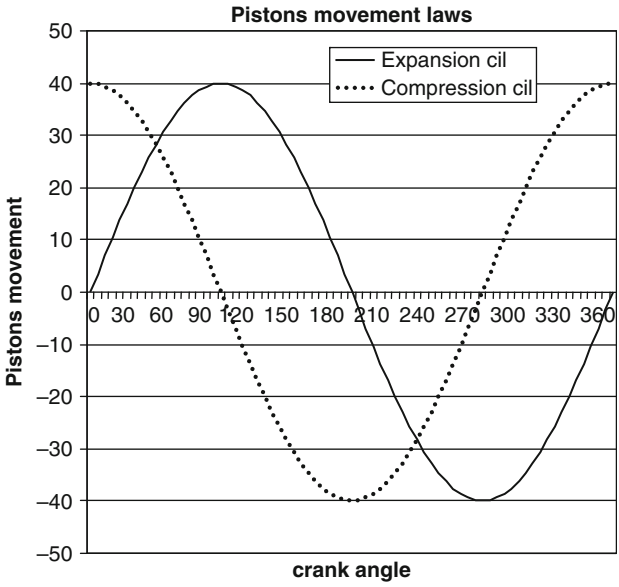

Fig. 2 Piston movement functions

Therefore, all the engineers who struggle to improve the work efficiency of the engine try to replace the crank mechanism of the compression cylinder by another one. It could be useful a mechanism able to perform a stop during the whole period of expansion. This stop of the compression piston has the role to enlarge the active area of the PV diagram shown in [2] and as a consequence it is expected an efficiency improvement in [4]. This request could be very well accomplish by a cam mechanism. But this one is too large, too complicate, expensive and unreliable. Hence, we try to find out a bar mechanism able to perform an equivalent stop as a cam mechanism.

In order to reach the dwell displacement function, without using a cam mechanism, the authors try to create a new bar mechanism.

2 A New Dwell Mechanism Dedicated to a-Stirling Engine

In [3] an acceptable dwell mechanism is expressed, able to be used in a α-Stirling engine. But this one is not good enough regarding the phases of the two pistons (Fig. 3). In order to improve this situation it is necessary to change the position of the articulation B between bars 2 and 3. It is preserved the relative position of the cylinder axis parallels. Hence the mechanism will become like the schema presented in Fig. 4.

The same reference *xoy* axes are placed in accordance with the Schmidt Analysis (Gustav Schmidt has made the classical Stirling Analysis in 1871).

Using the same reference we can replace the pseudo-sin function of compression cylinder, in Schmidt analysis by the new space function, in order to develop a new isothermal analysis of the engine.

3 On the Movement Functions of the Mechanism

The purpose of the analysis is to find out the movement functions yC(t) and yE(t) to reveal if there is a proper phase relation between them or not. The proper phase relation demonstrates that the mechanism is good for the application. Second, it must show that yE(t) has a large enough stop level, in accordance with the expansion stroke time of the expansion cylinder.

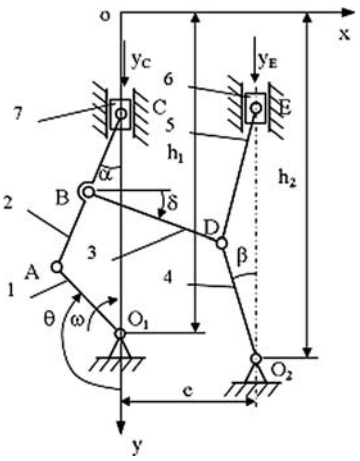

Fig. 3 General bar mechanism

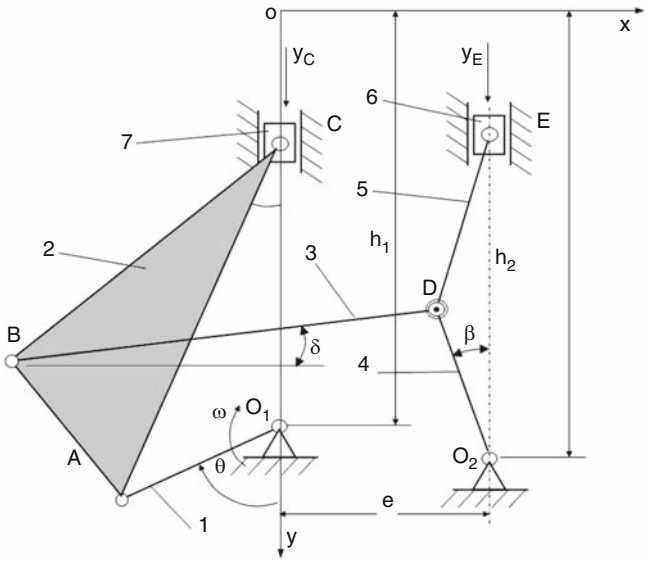

Fig. 4 The modified bar mechanism

The new displacement function yE(t) will be inserted in Schmidt analysis, instead of sin relation.

Notations used:

O1A = Rc rod

AC = b; BB' = h; AB' = b1

O2D = R2

BD = K

The point A(xA, yA) has a position expressed by the equation system (1). The angle θ = θ(t) and θo = 0o when the rod O1A is oriented to *oy* axis.

$$\begin{cases} x_A = -R_{c\,rod}\ \sin(\theta) \\ y_A = h_1 + R_{c\,rod}\ \cos(\theta) \end{cases} \tag{1}$$

Using the *sin* theorem equation (2) can be written as follows:

$$\frac{b}{\sin(\pi - \theta)} = \frac{R_{c\,rod}}{\sin(\alpha)} \tag{2}$$

resulting the angle α = α(t):

$$\alpha = \arcsin\left(\frac{R_{c\,rod}}{b}\sin\theta\right) \tag{3}$$

The point B(x_b, y_b) has a position expressed by the equation system:

$$\begin{cases} x_b = (b_1 - b)\ \sin\alpha - h\ \cos\alpha \\ y_b = h_1 + R_{c\,rod}\ \cos(\theta) - b_1\ \cos\alpha - h\ \sin\alpha \end{cases} \tag{4}$$

where b_1, b, h are the geometrical parameters of the crank (Fig. 5).

The point C(x_C, y_C) has a position expressed by the equation system:

$$\begin{cases} x_c = 0 \\ y_c = h_1 + R_{c\,rod}\ \cos(\theta) - b\ \cos\alpha \end{cases} \tag{5}$$

The point D(x_D, y_D) has a position expressed by the equation system:

$$\begin{cases} x_D = e - R_2\ \sin\beta \\ y_D = h_2 + R_2\ \cos\beta \end{cases} \tag{6}$$

The point E(x_E, y_E) has a position expressed by the equation system:

$$\begin{cases} x_E = e \\ y_E = h_2 - 2\,R_2\ \cos\beta \end{cases} \tag{7}$$

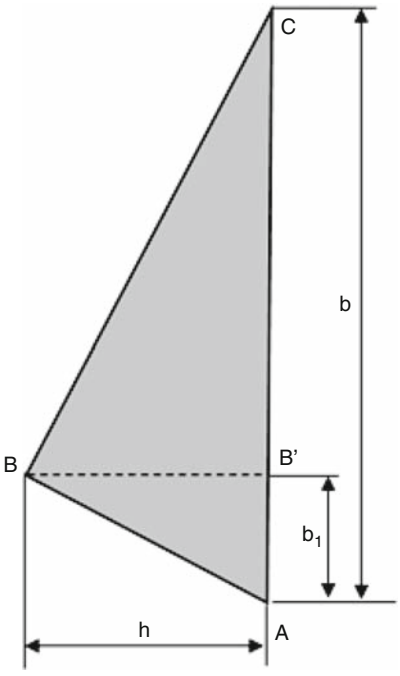

Fig. 5 Compression piston rod

In order to solve $y_E(t)$ the expression of $\beta(t)$ is needed. To obtain the function $\beta(t)$ the equation system of the BD element must be written:

$$\begin{cases} x_B + K\ \cos\delta + R_2\ \sin\beta - e = 0 \\ y_B - K\ \sin\delta + R_2\ \cos\beta - h_2 = 0 \end{cases} \tag{8}$$

The equation system (8) has two variables: β and δ. The variable δ is not needed, so it can be eliminated.

$$\begin{cases} x_B + R_2\ \sin\beta - e = -K\ \cos\delta \\ y_B + R_2\ \cos\beta - h_2 = K\ \sin\delta \end{cases} |\hat{2}\ and\ + \tag{9}$$

resulting the equation:

$$\begin{aligned} &x_B^2 + y_B^2 + R_2^2 + e^2 + h_2^2 + 2R_2(x_B - e)\sin\beta \\ &+ 2R_2(y_B - h_2)\cos\beta - 2x_B e - 2y_B h_2 = K^2 \end{aligned} \tag{10}$$

It must be applied the next substitution:

$$\left| \begin{aligned} A &= 2R_2(x_B - e) \\ B &= 2R_2(y_B - h_2) \\ C &= K^2 + 2x_B e + 2y_B h_2 - x_B^2 - \\ &\quad - y_B^2 - R_2^2 - e^2 - h_2^2 \end{aligned} \right.$$

The equation (10) becomes simpler:

$$A\sin\beta + B\cos\beta = D \tag{11}$$

$$A\sqrt{1 - \cos^2\beta} + B\cos\beta = D \tag{12}$$

$$1 - \cos^2\beta = \frac{D^2}{A^2} + \frac{B^2}{A^2}\cos^2\beta - 2\frac{B\,D}{A^2}\cos\beta \tag{13}$$

$$\cos^2\beta\left(\frac{B^2}{A^2} + 1\right) - 2\frac{B\,D}{A^2}\cos\beta + \frac{D^2}{A^2} - 1 = 0 \tag{14}$$

The second substitution will be:

$$\left| \begin{aligned} P &= \frac{B^2}{A^2} + 1 \\ Q &= 2\frac{B\,D}{A^2} \\ R &= \frac{D^2}{A^2} - 1 \end{aligned} \right.$$

resulting an algebraic equation:

$$P\,X^2 - Q\,X + R = 0 \tag{15}$$

where $X = \cos\beta$

The equation that remains, gives the β values (16) because β = β(θ) or β = β(t).

$$\beta = arc\,\cos\left[\frac{Q + \sqrt{Q^2 + 4\,P\,R}}{2\,P}\right] \tag{16}$$

The roots with negative sign are not practical for the mechanism; they are however in the field of *arcos* function.

Replacing β into y_E expression provides the function $y_E = y_E(t)$. There is impossible to obtain $y_E = y_E(t)$ as an analytical expression. Hence, we need to calculate y_C and y_E position point by point.

Using a computer program the moving functions $y_C = y_C(t)$ and $y_E = y_E(t)$ can be obtained. The two functions are shown in Fig. 6, y_C as y-expansion and y_E as y-compression.

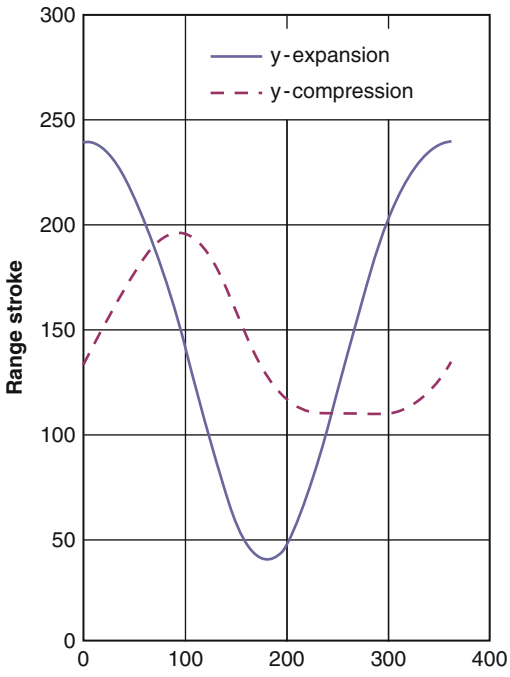

Fig. 6 Piston strokes

4 The Schmidt Analysis Insertion Paragraph

From the Schmidt analysis only the paragraphs where it is necessary to replace the old values by the new ones are shown. The original calculus presented in [5] is preserved and marked.

Therefore the mass of gas inside the regenerator space is given by:

$$\text{(S6)}\ m_r = p.V_r.\ln(T_h/T_c)/(R(T_h - T_c))$$

The volume of the compression space varies in sinusoidal fashion:

$$\text{(S7)}\ V_c = V_{clc} + 0.5.V_{swc}(1 + \cos(\theta))$$

θ = crank angle, proportional to time
V_{clc} = clearance volume = minimum of V_c
V_{swc} = swept volume, $\max\{V_c\} = V_{clc} + V_{swc}$
The volume of the expansion space varies in sinusoidal fashion:

$$\text{(S8)}\ V_e = V_{cle} + 0.5.V_{swe}(1 + \cos(\theta + \delta))$$

The equation (S8) has to be improved by replacing: $0.5.V_{swe}.\cos(\theta + \delta)$ with $y_E(t)$.
The same operation has to be done with the equation. (S13) in Schmidt Analysis.

$$\text{(S13)}\ p = \frac{m_{tot}RT_h}{V_{ref}} \frac{1}{(e + c + d) + c\ \cos\theta + e\ \cos(\theta + \delta)}$$

Equation (S13) allows to determine the pressure p at any angle θ for given volumes and temperatures T_h and T_c.

By differentiating equation (S8) with respect to θ, the following equation from paragraph 3.1 in [5] are obtained:

$$dVe = -0.5.V_{swe}.\sin(\theta + \delta).d\theta$$

Expression "$-0.5.V_{swe}\ .sin(\theta + \delta).d\theta$" must be replaced with a numeric differentiation of $y_E(t)$.

One has to note that the sense of the crank rotation is in accordance with the classical Schmidt analysis calculus.

5 Conclusion

The low efficiency of an α-Stirling engine drives us to improve on its work characteristics in order to enhance its efficiency. The main way to achieve this is to improve on the engine characteristics [6]. There are a lot of mechanisms species that could be used to obtain a stop movement necessary for the compression cylinder. A bar mechanism could be more reliable than a cam mechanism despite that the cam mechanism is more precise.

The bar mechanism presented in this paper has seven bars but seems to be reliable enough for this application.

There are, also, other ways to improve the efficiency, like changing the working gas in the cylinders. A good efficiency is obtained using a gas that has a high specific heat, like hydrogen or helium.

References

1. Ciupe, V., Dehelean, N.M., Maniu, I.: Distributed concentrator for solar power generation. In: Proceedings of the 19th DAAAM, Trnava, pp. 279–280, ISSN: 1726–9679 (2008)
2. Dehelean, N.M., Ciupe, V., Maniu, I.: Modified mechanism of a Stirling engine for use with solar power generation. In: Proceedings of the 19th DAAAM, Trnava, pp. 369–370, ISSN: 1726–9679 (2008)
3. Dehelean, N.M., Ciupe, V., Maniu, I.: A new mechanism to syncrhonize α-Stirling Engine. In: Scientific Bulletin of the "Politehnica" University of Timisoara, Transactions on Mechanics, Tom 53, Fasc. S1, pp. 81–84, ISSN: 1224–6077 (2008)
4. Herzog, Z.: The ideal Stirling Cycle and heat load on the regenerator. Available at: http:// mac6. ma.psu.edu/stirling/ideal_stirling_cycle/index.html (2008)
5. Herzog, Z.: The Schmidt analysis of Stirling engines. Available at: http://mac6.ma.psu.edu/ stirling/simulations/isothermal/schmidt.html (2008)
6. Wikipedia: The Stirling engine. Available at http://en.wikipedia.org/wiki/Stirling_engine (2008)

A Digital Model of a Dwell Mechanism for Alpha-Stirling Engine

N.M. Dehelean, V. Ciupe, and E.C. Lovasz

Abstract The paper shows a digital model of a dwell mechanism dedicated to an α-Stirling Engine. The low efficiency of an α-Stirling Engine drives us to improve on its work characteristics in order to rise-up its efficiency [2]. The main way to achieve this is to improve the engine characteristics. There are a lot of mechanisms species that could be used to obtain a dwell movement function that is necessary to the compression cylinder. A bar mechanism could be more reliable than cam mechanism despite that the cam mechanism is more precise. The bar mechanism presented in this paper has seven bars but seems to be reliable enough for this application. There are other ways to improve the efficiency, to change the working gas from the cylinders. A good efficiency is obtained using a gas that has a high specific heat, like hydrogen or helium.

Keywords Bar mechanism · Dwell mechanism · Simulation · Stirling engine

1 Introduction

The first stage of movement function evaluation starts from the mechanism configuration that is shown in paper [1]. In order to evaluate the active and resistant torque at the compression rod it is necessary to reveal the reduced torque expression coming from the movement function and estimated forces applied on the piston in the compression cylinder. The real torque will be obtained using the pressure diagram acquired from a physical model.

N.M. Dehelean (✉)
Department of Mechatronics, "Politehnica" University of Timişoara, Timişoara, Romania

I. Vişa (ed.), *SYROM 2009*,
DOI 10.1007/978-90-481-3522-6_43,

2 The Kinetostatic Analysis of the Mechanism

In order to be able to perform an appropriate simulation, the mechanism described in [1] must be further analysed. The active and reactive forces that appear in the mechanism are represented in Fig. 1. Active forces appearing in the compression cylinder are displayed in Fig. 2, where:

F_7 – active force provide by expansion cylinder
F_6 – passive force provide by compression cylinder
M_1 – active torque
M_2 – resistant torque

From the above graphics some relations can be deduced in order to extract the movement functions of both expansion and compression cylinder (y_E and y_C) and also for the torque present at the crank of the expansion cylinder:

$$M = M_1 + M_2 \tag{1}$$

$$M_1 = F_7' \, a \tag{2}$$

$$F_7' = \frac{F_7}{\cos \alpha} \tag{3}$$

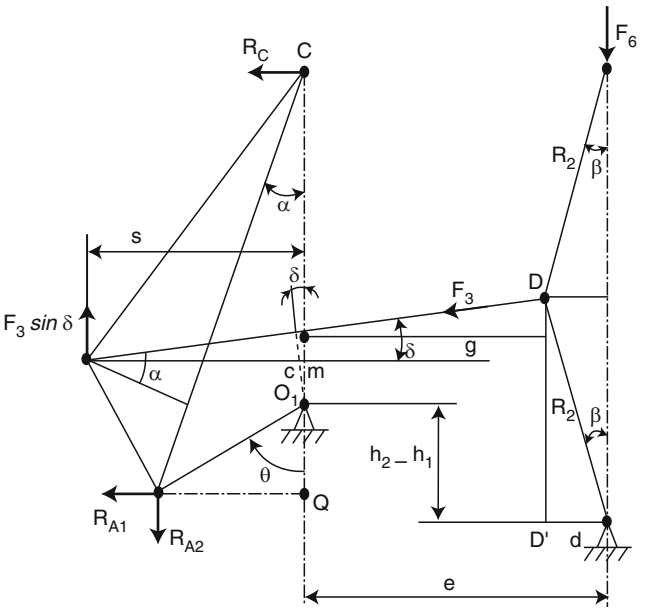

Fig. 1 Kinetostatics of the mechanism

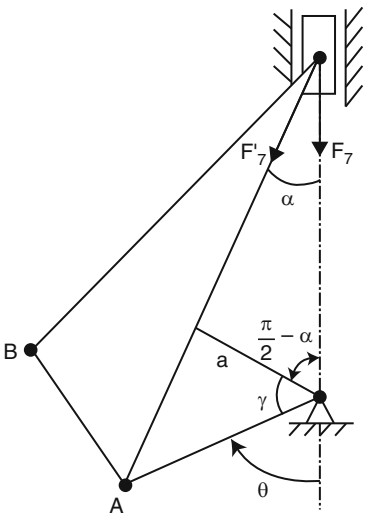

Fig. 2 Forces in the compression cylinder

$$\gamma = \frac{\pi}{2} + \alpha - \theta \tag{4}$$

$$a = r_{c\,rod}\ \cos\gamma \tag{5}$$

$$M_1 = \frac{F_7}{\cos\alpha}\ r_{c\,rod}\ \cos\left(\frac{\pi}{2} + \alpha - \theta\right) \tag{6}$$

and resulting from the force equilibrium in joint 'D:

$$F_3 = \frac{2\,F_6\ \tan\beta}{\cos\delta} \tag{7}$$

From the equation system (9), presented in [1] the angle δ can be determined:

$$\tan\delta = \frac{h_2 - y_B - R_2\ \cos\beta}{x_B + R_2\ \sin\beta - e} \tag{8}$$

$$d = R_2\ \sin\beta\ ; \quad DD' = R_2\ \cos\beta \tag{9}$$

$$m = DD' - (h_2 - h_1) - (e - d)\ \tan\delta \tag{10}$$

$$m = R_2\ \cos\beta - h_2 + h_1 - (e - d)\ \tan\delta \tag{11}$$

$$M_2 = R_{A2}\,R_{c\,rod}\ \sin\theta - R_{A1}\,R_{c\,rod}\ \cos\theta \tag{12}$$

$$\begin{cases} R_{A1} + R_C = F_3 \cos\delta \\ F_3 \cos\delta \ (m + R_{c\,rod} \cos\theta) - \\ -R_C(b \cos\alpha - m - R_{c\,rod} \cos\theta) = 0 \end{cases} \tag{13}$$

Some substitutions must be applied:

$$p = m + R_{c\,rod} \cos\theta \ ; \quad F_{3H} = F_3 \cos\delta \tag{14}$$

and the system becomes:

$$\begin{cases} R_{A1} + R_C = F_{3H} \\ F_{3H}\, p - R_C \ (b \cos\alpha - p) = 0 \end{cases} \tag{15}$$

$$R_{A1} = F_{3H} - R_C \tag{15'}$$

The joint 'C' does not support load on the 'o-y' (vertical) direction, so the following equation can be expressed:

$$F_3 \sin\delta \left(\frac{b_1}{\cos\alpha} + (b \cos\alpha - p) \tan\alpha \right) = R_{A2}\, R_{c\,rod} \sin\theta \tag{16}$$

The right hand term being a component of M_2, the equation of M_2 is:

$$\begin{aligned} M_2 = F_3 \sin\delta \left(\frac{b_1}{\cos\alpha} + (b \cos\alpha - p) \tan\alpha \right) - \\ - R_{A1}\, R_{c\,rod} \cos\theta \end{aligned} \tag{17}$$

3 Digital Simulations of the Dwell Mechanism

By making use of the relations obtained above, a numeric simulation of the mechanism can be conducted. Figure 3 shows the movement functions and phases of the two cylinders and also the torque obtained at the crank of the expansion cylinder. The known parameters, forces, dimensions and compression ratio are imposed for this simulation.

The torque diagram shows that the mechanism provides an active torque on an angle sweep from 0° to 32° (detail D in Fig. 3). This offers an advantage to move out the engine from top dead center.

Integrating the both areas under the torque curve it obtains a ratio between the active and the resistant torque on a work cycle. This ratio is only an evaluation that could be used further on (Fig. 4).

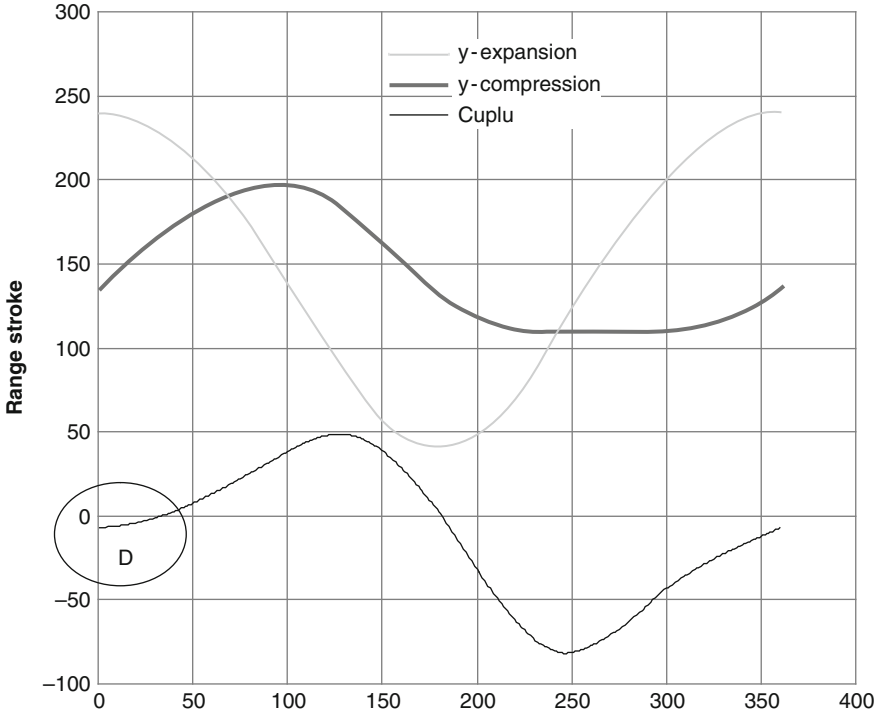

Fig. 3 Piston movement functions

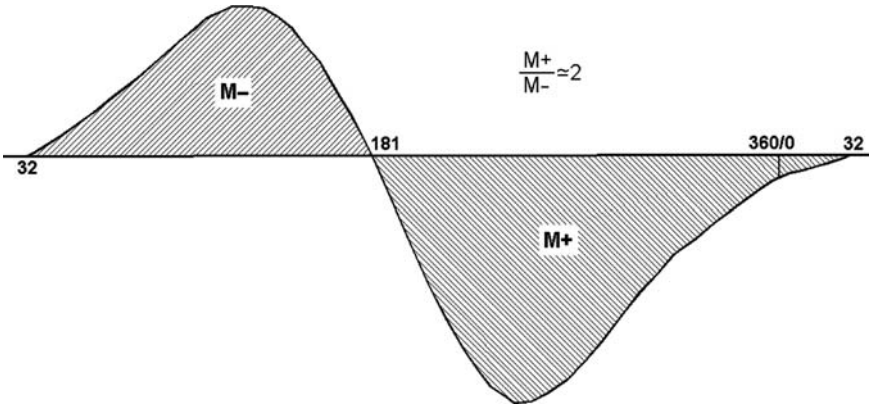

Fig. 4 Compression piston's crank torque

According to the paper intention, accuracy improvement of the mechanism simulation, it was used a specialized German simulation software ("Kosim") that provides displacement, speed, acceleration and force function graphs for a full turn of the mechanism (Figs. 5, 6, and 7).

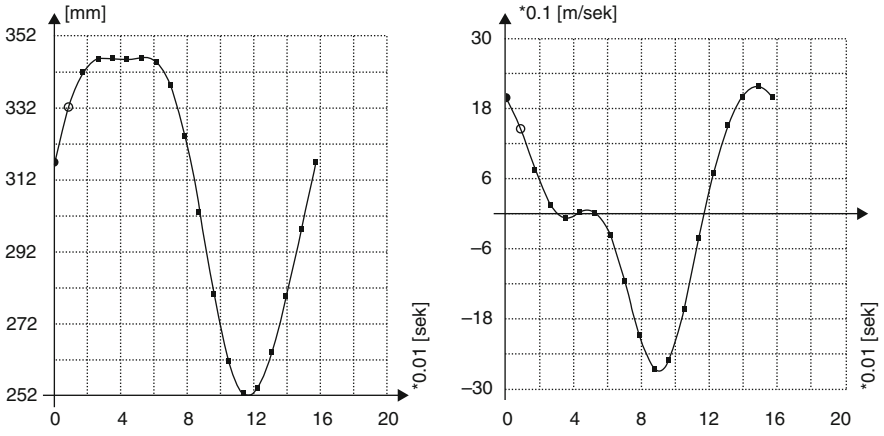

Fig. 5 Expansion piston displacement and velocity functions

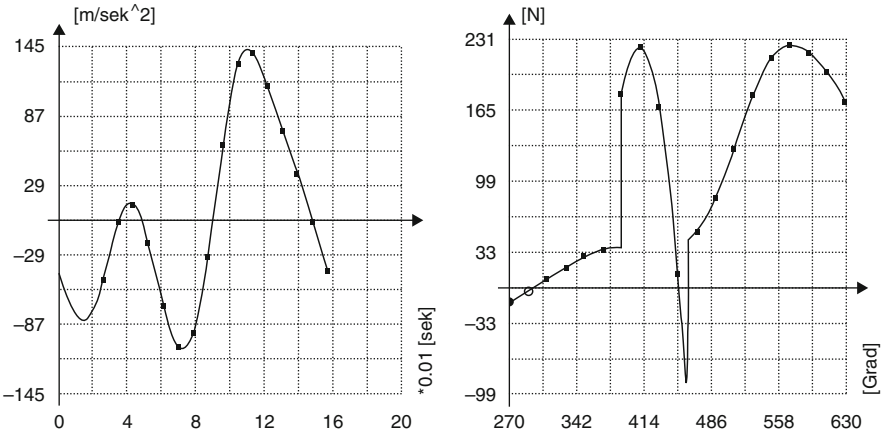

Fig. 6 Expansion piston acceleration and reactive force

It can be observed that velocity is not strictly 0 on the dwell angle period. That is true because the dwell is not strictly a stop displacement and could be observed if it increases the scale of diagram representation.

The target of the paper is to evaluate that the new mechanism is better then a classic crank-shaft one for the use in Stirling engines. Therefore it is necessary to evaluate the forces, torques, mechanical work on a complete work cycle [3]. For this reason Fig. 7 contains a complete working cycle representation, not only the dwell period.

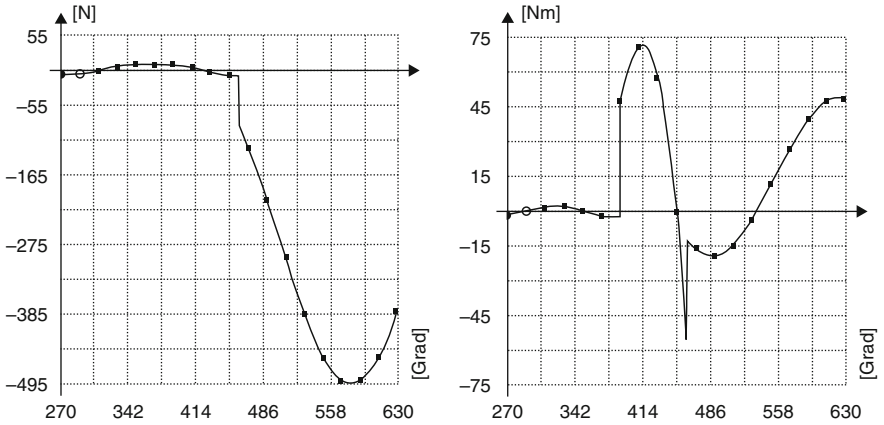

Fig. 7 Compression piston reactive force and crank torque

4 Conclusion

The simulations of the mechanism prove that the proposed technical solution is appropriate to be embedded in an α-Stirling engine structure. This is expected to provide a better displacement, speed and acceleration functions than cam mechanisms. The accuracy of the deduced relations is sustained by the use of mechanism dedicated software also the movement function graphs based on these calculations. Also the high amount of positive torque obtained brings up the advantages of the proposed mechanism design and drives us into further research in this field. The full validation of the mechanism will be revealed on the real prototype.

References

1. Dehelean, N.M., Ciupe, V.: The analysis of a dwell mechanism for α-Stirling Engine. In: Proceedings of the 10th International Symposium on Science of Mechanisms and Machines, Syrom'09, pp. 511–519 (2009)
2. Dehelean, N.M., Ciupe, V., Maniu, I.: A new mechanism to syncrhonize α-Stirling Engine. In: Scientific bulletin of the "Politehnica" University of Timisoara, Transactions on Mechanics, Tom 53, Fasc. S1, pp. 81–84, ISSN: 1224-6077 (2008)
3. Herzog, Z.: The Schmidt Analysis of Stirling engines. Available at: http://mac6.ma.psu.edu/stirling/simulations/isothermal/schmidt.html (2008)

AutoCad Simulations and Experiments on the Manufacturing of Gears

V.F. Duma and V. Patrusel

Abstract The paper presents some of the results of two student projects regarding the experimental and theoretical simulations of the manufacturing process of gears with different profile displacements. A dedicated experimental stall with a toothed rack (Maag) tool was achieved. The experimental simulations of the manufacturing process were matched by the theoretical calculus using the classical equations of teeth with evolventic profile and, more interesting, by the results obtained performing an AUTOCAD simulation of the process. The paper also stresses on the fine performances of undergraduate students involvement in research groups, with stimulating results for their career-to-be.

Keywords AUTOCAD · Gears · Manufacturing process · Simulation

1 Introduction

The importance of mechanical transmission in machines that use sprocket wheels [4] is well-known in mechanical engineering. The mechanical transmissions perform by example [3, 5]: (i) the connection between the main shaft of the power machines and the main shaft of the work machine or between the shafts of different machines, in order to achieve the transmission of power or movement; (ii) the change of the rotation sense or of the velocity from one shaft to another with a given ratio, e.g., using a gearbox; (iii) the amplification of the rotation movement for increasing the sensitivity, in measuring systems and apparatuses [7].

V.F. Duma (✉)
Department of Product Design, Aurel Vlaicu University of Arad, Arad, Romania

I. Vişa (ed.), *SYROM 2009*,
DOI 10.1007/978-90-481-3522-6_44,

A myriad of studies exist on the geometry of the various gears [2], from their profile design [9] to dynamic problems [8], e.g., with regard to the errors of manufacturing the gears [1].

Our study is a contribution to this complex problem. Our scope is to offer a tool for simulating the manufacturing process of gears with the classical but most used evolventic profile [2, 7]. We start from the experimental method of simulating the manufacturing process for different profile displacements, and we reach for a much more precise method, using AUTOCAD in order to simulate the process and ascertain the characteristic parameters of the gear to be produced.

The paper summarizes some of the main results of two student projects focused on this theme, one involving the experimental part, the other one the AUTOCAD simulations. Their work has been performed in the Mechanism and Mechatronics Student Research Group that involves mostly 2nd (but also 3rd and 4th) year students, passionate about these subjects, asking for a more extended activity that may have as outcome original results. These are a source of satisfaction for such students and a good hint for them regarding what a future career in research and/or engineering design may be. As a first communication of these results is achieved in the yearly Scientific Student Conference, held every May in Arad, a synthesis of the most interesting ones is the subject of more elaborate papers, such as this one.

2 Experimental Simulations

2.1 Experimental Stall

The geometric elements of a rack are highlighted in Fig. 1. Out of the different manufacturing methods of gears, we shall use such a rack tool in order to obtain its corrugated gear. The manufacturing process usually involves a rotating cylindrical piece and a translating tool, the rack with the shape presented in Fig. 2, commonly known as the Maag 'comb.' We shall simulate the process by moving the piece (3) and maintaining the tool (2), characterized by a module m = 10 mm, stationary, thus reproducing the actual relative movement between them. In order to avoid slip, a guiding rack (5), with an m = 1 mm module is used.

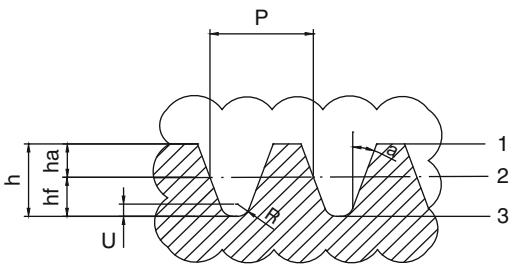

Fig. 1 Geometric elements of the teeth: height h = 2.25 m; top height h_a = 1 m; foot height h_f = 1.25 m; c = 0.25 m (head move); ρ_f = 0.38 m (radius of curvature)

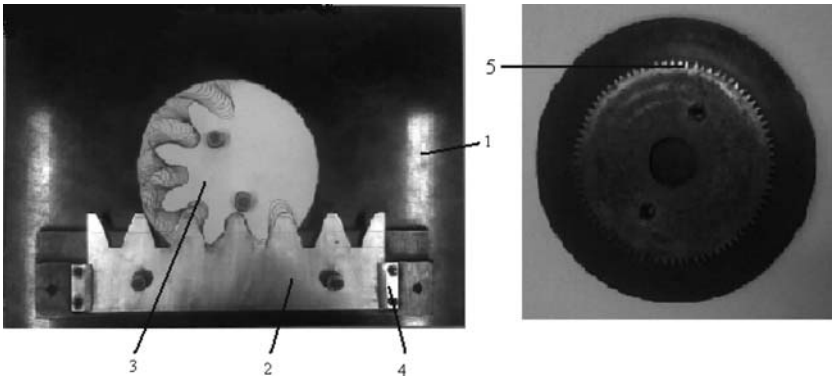

Fig. 2 Experimental stall: (1) Support plate; (2) generating toothed rack (module m = 10 mm); (3) half-finished product; (4) scale; (5) guiding denture (module m = 1 mm)

For obtaining gears with different profile movements, the generating toothed rack has the possibility of position adjustment before the beginning of the process, using the gradual scale (4). The distance between the rack and the center of the product-to-be-made may thus be adjusted in a maximum ±10 mm scale.

2.2 Results

The distance between the reference axis and the division axis defines the profile movement. This is equal to X = xm, where x represents the profile displacement coefficient and m [mm] is the module of the gear to be obtained. Depending on the values of X, one of the three following cases may be reached (Fig. 3):

(i) $X < 0$ – the reference axis intersects the division circle and we shall obtain the minus well
(ii) $X = 0$ – the reference axis is over the division axis and we shall obtain the zero well
(iii) $X > 0$ – the reference axis intersects the division circle and we shall obtain the plus well

By moving the toothed rack, the thickness of the teeth obtained will thus be different (Fig. 3). For positive movements (iii) this thickness decreases at the top, and this shortcut has to be limited at an admissible value. For sprockets with a small number of teeth, in the process of tooth making the phenomenon of undercutting (i) may appear, and a positive profile movement becomes necessary.

As the work method to be used, we set the profile movement with the help of the gradual scale (4), Fig. 2. Five chosen profile movements will be presented in this study, with X = −4; −2; 0; 2; 4 mm. Three of these results are presented in Fig. 3,

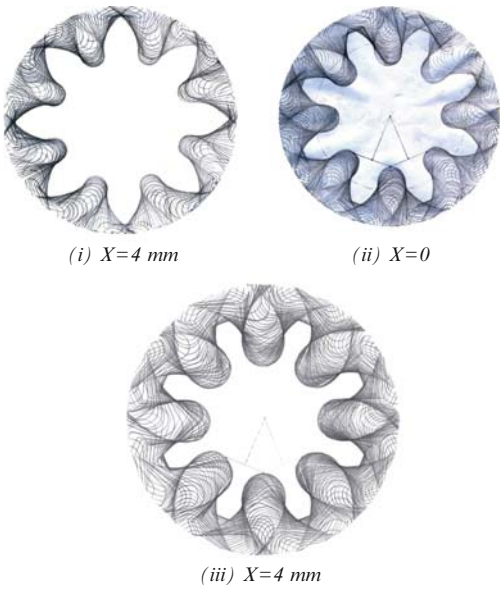

Fig. 3 Gears obtained with the experimental simulation; examples for three profile movements: (i) X = 4 mm; (ii) X = 0; (iii) X = −4 mm

only for these extreme and the center values of X, in order to remark the differences obtained in the profiles of the tooth.

For each profile displacement the disc that represents the semi-finished product (3) is moved incrementally on the guiding denture (5). A line is ruled in each position on the disc on the edge of the toothed rack. Then the semi-finished product (3) is rotated with a small angle (some 2°–3°). This procedure is repeated until the cylinder has completed a full rotation.

A comparison of the experimental and calculated parameters of the produced gear has been performed [6]. However, in order to obtain high precisions, the experimental stall and the manufacturing method can and will be simulated in AUTOCAD, which is much more interesting, as we shall conclude from the following paragraph. The comparison mentioned above will be therefore demonstrated between the results obtained in AUTOCAD and by calculus, with the remark that experimental results are well matched by the AUTOCAD ones that, however, provide better precision.

3 AUTOCAD Simulations of the Manufacturing of Gears

For every one of the five cases in Fig. 4, but also for the experimentally achieved ‘gears,’ as those in Fig. 3, the following steps were followed:

– The center of the gear has been found.
– The roll circle has been drawn, with the radius:

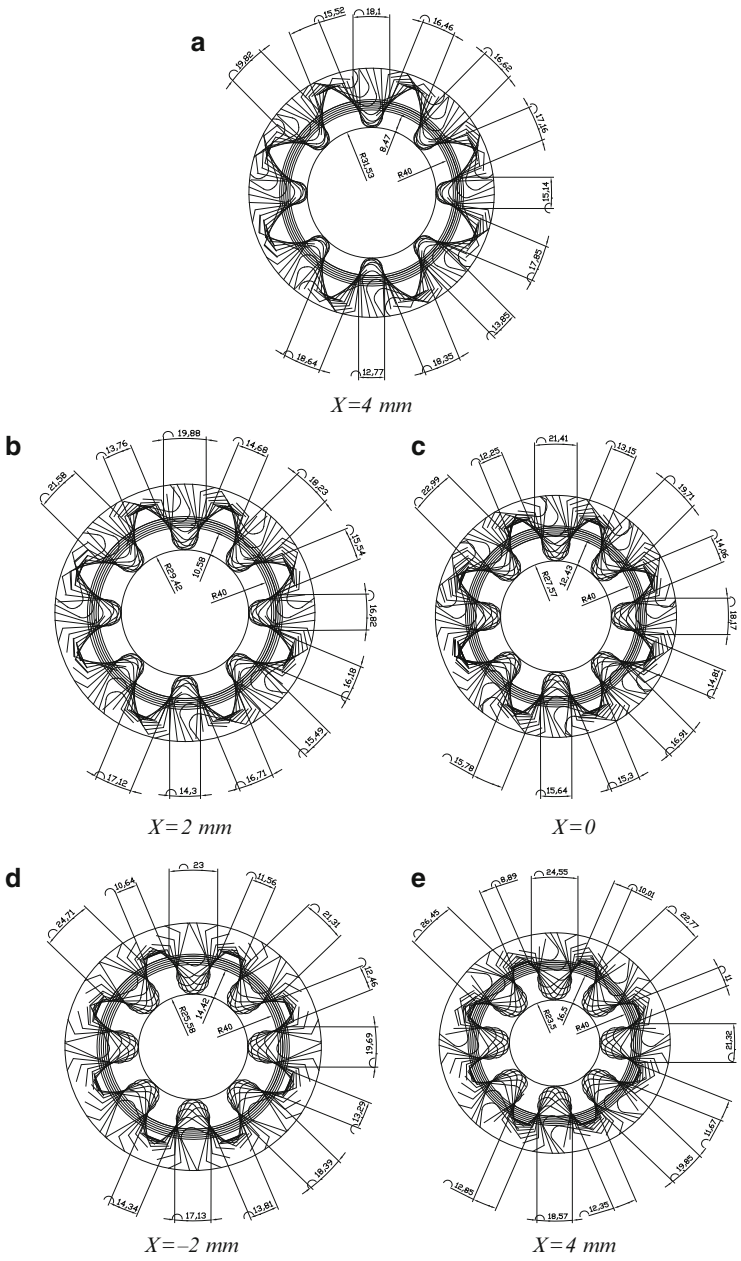

Fig. 4 AutoCAD simulations of the manufacturing process of a gear with z = 8 teeth and module m = 10 mm, for different values of the profile movement X.

$$r = \frac{mz}{2} = 40mm \tag{1}$$

- The thickness "s" of the tooth has been measured, and so has been the empty space "e" on the roll circle.
- The thickness s_y of the tooth has been measured, and so has been the empty space e_y on a circle with a certain, chosen radius r_y.
- The foot height h_f of the tooth has been measured.
- The radius r_f of the foot circle has been determined.

In order to verify the geometrical characteristics in Fig. 1, all of these parameters have to be calculated, as well.

The thickness of the tooth and of the empty space in-between, on the rolling circle, will be respectively [2, 7]:

$$s = m\left(\frac{\pi}{2} + 2xtg\alpha\right); \tag{2}$$

$$e = m\left(\frac{\pi}{2} - 2xtg\alpha\right) \tag{3}$$

The height of the tooth foot and the radius of the foot circle will be respectively:

$$h_f = h_{0f} - xm; \tag{4}$$

$$r_f = r - h_f, \tag{5}$$

where, as m = 10 mm, h_{of} = 12.5 mm was obtained (a rack with α = 20 is used).

The results of this calculus are presented in Table 1, in a comparison between the characteristic parameters of the teeth with those of the different 'gears' obtained in AUTOCAD and presented in Fig. 4 (which are, as pointed out previously, a good match with those obtained experimentally using the stall in Fig. 2, and presented in Fig. 3).

Table 1 Match of the calculated and experimental parameters of the teeth

Parameters (mm) X (mm)	s^{calc}	s^{exp}	e^{calc}	e^{exp}	h_f^{calc}	h_f^{exp}	r_f^{calc}	r_f^{exp}
4	18.60	18.64	12.79	12.77	8.5	8.47	31.5	31.53
2	17.16	17.12	14.25	14.30	10.5	10.58	29.5	29.42
0	15.70	15.78	15.70	15.64	12.5	12.43	27.5	27.57
−2	14.25	14.34	17.16	17.13	14.5	14.42	25.5	25.58
−4	12.79	12.85	18.60	18.57	16.5	16.5	23.5	23.5

The width of the tooth and the empty thickness on a current circle (of a chosen radius r_y = 44 mm) are respectively:

$$s_y = d_y\left[\frac{1}{z}\left(\frac{\pi}{2} + 2xtg\alpha\right) + inv\alpha - inv\alpha_y\right]$$

$$e_y = d_y\left[\frac{1}{z}\left(\frac{\pi}{2} - 2xtg\alpha\right) - inv\alpha + inv\alpha_y\right] \tag{5}$$

where:

$$\alpha_y = \arccos\left(\frac{r}{r_y}\cos\alpha\right) = 31.32^\circ,$$

$$inv\alpha = tg\alpha - \alpha^{rad} = 0.0149;$$

$$inv\alpha_y = tg\alpha_y - \alpha_y{}^{rad} = 0.0618.$$

The ascertainment of the pace p_y is then performed and the overall results are presented in Table 2:

$$p_y = \frac{pr_y}{r}, \text{ where } p = s + e \tag{6}$$

The width of the tooth has a variation law with regard to the chosen radius r_y of the circle the measurement is performed on. In Fig. 5 this variation of the width with regard to the current radius r_y is presented.

For X = 0 the width of the tooth is ascertained with regard to the radius r_y of the circle the measurement is performed on, where $r_y \in \{40, 41, 42, 43, 44, 45\}$. This width is also ascertained experimentally (measured) with regard to the same radius r_y – on the gears obtained using the experimental stall in Fig. 2 and the AUTOCAD simulation. The match of the two series of data (X = 0 calculated and X = 0 experimental) is demonstrated in Fig. 6. This match proves: (i) the evolventic profile of the gear teeth thus obtained; (ii) the good precision of the experimental simulation

Table 2 Width of the tooth and of the empty space on a circle of a given radius r_y

Parameters (mm) X (mm)	r_y	s_y^{calc}	s_y^{exp}	e_y^{calc}	e_y^{exp}	p_y^{calc}	p_y^{exp}
4	44	16.35	16.46	18.20	18.10	34.52	34.56
2	44	14.75	14.6	19.80	19.88	34.55	34.56
0	44	13.15	13.15	21.40	21.41	34.54	34.56
−2	44	11.55	11.56	23.00	23.00	34.55	34.56
−4	44	9.94	10.01	24.60	24.55	34.5	34.56

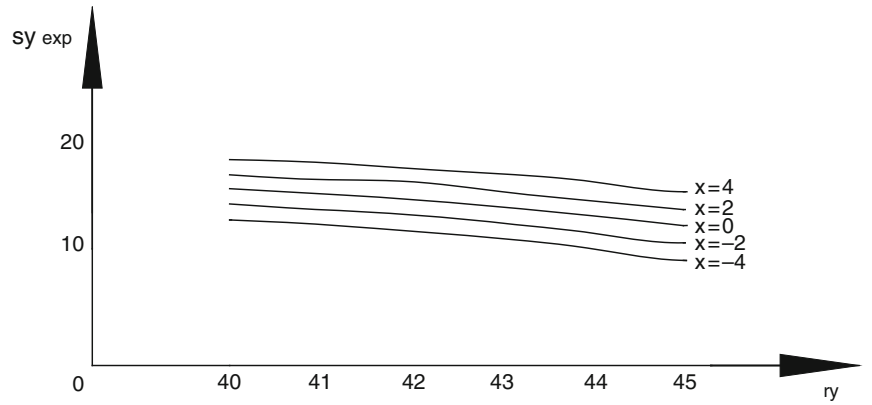

Fig. 5 Graphs of the width of the gear tooth with regard to the current radiuses considered – for different profile movements (X)

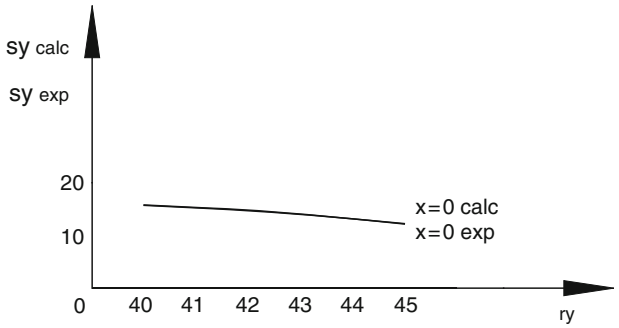

Fig. 6 Width of the gear tooth – for X = 0 profile movement – calculated and experimental

of the manufacturing process and of the control method used – for the ascertainment of each characteristic dimension, e.g. the widths s_y and e_y.

4 Conclusions

The work performed demonstrates the good capabilities of the method used for the precise simulation of the manufacturing process of gears. The good match between the experimental results and those obtained using AUTOCAD allows for the extensive use of this program in simulating any manufacturing process, regardless of: (i) the manufacturing method (with toothed rack or with the corrugated gear); (ii) the parameters of the gear (m, z, X); (iii) the particular profile of the tooth, yet taking into account the method of obtaining each profile (e.g., for cycloid profiles of the teeth, by rolling two circles of different radiuses).

The built of a dedicated experimental stall is thus demonstrated to be less necessary, especially as the precision of the AUTOCAD simulations in the detailed study of the gear obtained has proven superior to the experimental method.

A fine, fast comparison between the product-to-be-obtained is thus achieved, while choosing different parameters of the process – see Fig. 4, for the comparison of the gears to be manufactured, with regard to the different profile displacements. Practical applications of this proposed method, using AUTOCAD, involve the most different types of mechanical transmissions, in particular those with cylindrical gears for which the present study has been performed.

References

1. Li, S.: Finite element analyses for contact strength of a pair of spur gears with machining errors, assembly errors and tooth modifications. Mech. Mach. Theory 42, 88–114 (2007)
2. Litvin, F.L.: Gear Geometry and Applied Theory. Prentice-Hall, New Jersey (1994)
3. Maros, D.: Theory of Mechanisms and Machines. Kinematics of Gears (in Romanian). Tehnica, Bucharest (1958)
4. Mott, R.L.: Machine Elements in Mechanical Design, 3rd edn. Prentice-Hall, New Jersey (1999)
5. Panait, G.: Theory of Mechanisms and Machines (in Romanian), vol. I. Universal Cartfil, Ploiesti (1998)
6. Patrusel, V., Duma, V.F.: Simulation of the manufacturing process of gears using toothed rack tools (MAAG). Sci. Tech. Bull. of the Aurel Vlaicu University of Arad, Series: Mech. Eng. 3(2), 41–51 (2007)
7. Perju, D.: Mechanisms for Fine Mechanics (in Romanian), vol. I, II. Politehnica, Timisoara (1990)
8. Wink, C.H., Serpa, A.L.: Performance assessment of solution methods for load distribution problem of gear teeth. Mech. Mach. Theory 43, 80–94 (2008)
9. Yang, D.C.H., Tong, S.-H.: On the profile design of transmission splines and keys. Mech. Mach. Theory 42, 82–87 (2007)

Modeling a Galvoscanner with an Optimized Scanning Function

V.F. Duma, A.G. Podoleanu, and M. Nicolov

Abstract The paper presents the modeling of a galvanometer-based scanning device with an increased duty cycle, i.e. a high efficiency of using the available time for the scanning process. From the basic dynamic equations of the oscillating element, the active torque and the command function that have to be used are derived. An analytical study is performed on the possible profiles of the scanning function, and an optimum solution is demonstrated, in order to obtain an as small as possible inertia torque and an as high as possible duty cycle. The active torque and the command functions are deduced for this optimum scanning law. A MathCAD study of the command function with regard to the desired scanning (oscillating) frequency completes the modeling process.

Keywords Galvanometer scanners · Modelling · Oscillating elements

1 Introduction

The scanning techniques have a large range of applications [2, 6], from commercial ones, with average performances (i.e., speed and resolution), e.g., barcode scanning or laser printers, to industrial systems, e.g., for dimensional measurements [19] or P.I.V. (particle instantaneous velocity) techniques, and to high end fields in full development, i.e., medical imaging for confocal microscopy [18, 23] and/or optical coherence tomography (OCT) [17, 18, 22].

V.F. Duma (✉) and M. Nicolov
Faculty of Engineering, Aurel Vlaicu University of Arad, Arad, Romania
V.F. Duma
The Institute of Optics, University of Rochester, Rochester, N.Y., USA
A.G. Podoleanu
Applied Optics Group, University of Kent, Canterbury, UK

I. Vişa (ed.), *SYROM 2009*,
DOI 10.1007/978-90-481-3522-6_45,

The scanning devices developed since the 1970s [4], in order to meet the requirements of a certain application are using rotating mirrors (monogon [6, 7], polygonal [3, 8] or pyramidal scanners), oscillating mirrors (resonant or galvanometer-based [1, 9–15, 20, 21] scanners), or are holographic, electro-optical or acusto-optical devices [2].

The most used nowadays are the galvanometer-based scanners (GS), for both uni-dimensional (1D) and 2D systems suitable for a large range of applications, with an advantage on the polygon scanners in most domains, except those where a fast scan rate is compolsory, e.g., OCT, but also in industrial systems, as we have approached in several studies [6, 7].

The wide spread of GS devices is due to the fact that monogon (plane mirror) scanners [7], although simple and versatile, have a low duty cycle η, i.e., a low efficiency of using the available time for the scanning process. The polygon scanner has a much improved η, and one can also obtain a reciprocal compensation of some of its main sources of errors. However, there are certain disadvantages, e.g., the high angular velocity required in order to obtain a high scanning frequency, necessary especially for on-line applications; also its sources of errors that may be, however, considered for obtaining superior performances in certain applications [8].

The oscillating mirror scanner has a much higher duty cycle η than the rotating mirrors scanners [2, 11], and high scanning frequencies and velocities in compact solutions [15]. Positioning speeds as fast as 150 μs, and positioning resolutions of 1 μrad are achievable [1]. Fundamental studies on the design and characteristics of the galvoscanners (GS) were developed [12, 13], while the technology also improved both regarding their construction [1, 5], testing [20] and control [21].

This paper is part of our approach on the possibility of obtaining, using a GS device (Fig. 1), an optimum (with regard to the users' demands) oscillating law for the scanning mirror (Fig. 1), using a command function easily achievable electronically. Such a study is necessary in order to develop high performance 1D scanners, which we have already used extensively for OCT systems and applications, with centric or eccentric [17] galvoscanner mirror, in a on-going direction of research.

It is also necessary for achieving 2D scanning systems, e.g. with two orthogonal galvanometers [10] or with combinations of polygon and galvo scanners (Fig. 2) [2].

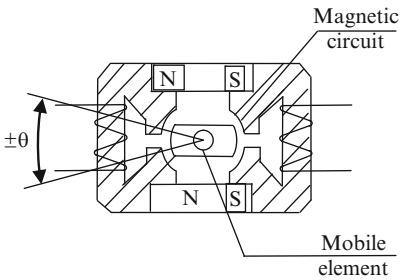

Fig. 1 Galvanometer-based scanner. The mobile element comprises the oscillating mirror. The device is placed to an L distance from the actual object to be scanned (not marked in the figure)

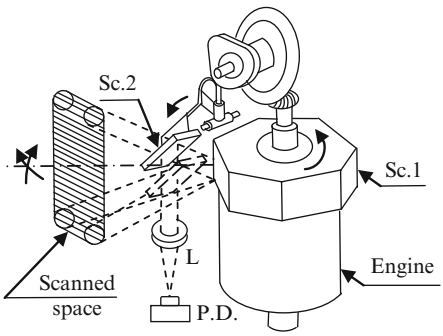

Fig. 2 2D scanner with a polygonal and a galvanometer scanning head

2 Equations of the Galvoscanners

Several solutions of GS devices, with regard to the generated scanning function x(t) are presented in the state-of-the-art: (i) sawtooth profile for x(t) [11], with a linear, active portion, and a faster returning one; this may however causes significant mechanical problems, i.e., undesired vibrations and overheating of the system, as often experienced in practice; (ii) convenient, easy-to-generate profile of the command current function i(t) of the galvanometer for which an angular θ(t) function is obtained and x(t) results non-linear; (iii) proposed scanning function [9, 10], symetrical and linear on both portions, which requires an appropriate command function i(t), that can achieve an active torque $M_a(t)$ able to produce this x(t) function. To determine this i(t) function is the scope of our studies.

For the functions in the state-of-the-art, the duty cycle η reaches 66% for (i), and 70% for (ii) [2, 11]. Solution (iii) which we propose and explore analitically in this study, may reach theoretically a value of η much closer to 100%. The mechanical functioning of the device is also smoother, due to the symetrical oscillating law. The study has to be performed with regard to the required oscillating frequencies, in relationship with the scanning velocity.

The ideal scan is linearly, i.e., with a constant scanning velocity v. However, curved turning portions have to be provided (Fig. 3) for x(t), with a minimum duration 2τ with regard to $2t_a$ (the active time interval) in order to maximize the duty cycle. We have previously discussed [9] several possible expressions of the x(t) scanning function. In the present study, one of these most promising profiles will be considered: with convenient sinusoidal stop-and-turn portions.

In order to determine the x(t) function, the oscillating mirror will be considered as a cam, while the laser beam will play the role of the follower. Methods specific to the theory of mechanisms will be used [16] for the ascertainment of the moving law of the follower, as it is well known from the design of cam mechanisms.

The angular scanning function is obtained, with the angular velocity and acceleration, from the equation of the scanning function, written using the distance L to the plane or to the lens the scanning system may use for projecting the laser beam deflected by the oscillating mirror:

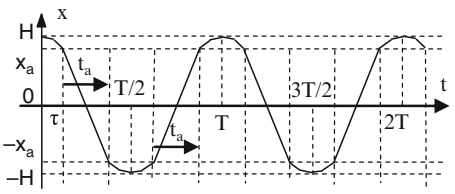

Fig. 3 Proposed scanning function of the galvanometer-based scanner, symmetrical and linear on both active portions

$$\theta(t) = +\frac{1}{2}\arctan\frac{x(t)}{L} \tag{1}$$

In order to obtain a linear expression for x(t) in this case, the θ(t) function has to result with a controllled non-linearity. The profiles of both these functions have to be determined in order to fulfill this requirement.

The equation of the mobile element of the galvanometer scanner (Fig. 1) is:

$$\ddot{\theta} + 2\xi\omega_0\dot{\theta} + \omega_0^2\theta = \frac{M_a(t)}{J}, \tag{2}$$

with

$$\omega_0 = \sqrt{\frac{k}{J}};\ \xi = \frac{c}{2\sqrt{Jk}}, \tag{3}$$

where J is the inertia momentum of the mobile element, c is the damping coefficient of the galvanometer, k is the elastic coefficient of the springs, and $M_a(t)$ is the magneto-electric active torque applied in order to produce the desired movement. The natural pulsation (ω_0) and the unitless damping factor (ξ) of the system are thus also defined.

The magneto-electric active torque is provided by the current i(t) and by the constant magnetic flux Φ=BNS that passes through the coil:

$$M_a(t) = \Phi(t)\cdot i(t) \tag{4}$$

where B is the magnetic induction, N is the number of spires, and S is the area of the surface of the mobile coil.

The necessary active torque results from equation (2), due to the imposed profile of the θ(t) function:

$$\begin{aligned} M_a(t) &= \frac{-J}{L^3}\cdot\frac{x\dot{x}^2}{\left[1+(x/L)^2\right]^2} + \\ &+ \frac{1}{2L}\cdot\frac{c\dot{x}+J\ddot{x}}{1+(x/L)^2} + \frac{k}{2}\arctan\frac{x}{L} \end{aligned} \tag{5}$$

Therefore, the neccesary i(t) command function for obtaining the required scanning function x(t) results with equation (4).

3 Linear and Sinusoidal Scanning Function

We have explored quit a complicated expression for the linear + sinusoidal scanning function in [10], which resulted in solving numerical equations in order to determine the coefficients of the function. In the present study, we shall consider a much simpler expression of x(t), which will have as consequence an easier way of solving the problem, i.e. the possibility of obtaining analytically the functioning parameters.

(a) For t∈[0, τ], a sinusoidal portion of the function will be considered in this case:

$$x(t) = a\sin(\omega t + \varphi)$$

$$\dot{x}(t) = a\omega\cos(\omega t + \varphi). \tag{6}$$

where *a, b, c* are the constants to be ascertained from the functioning conditions (Fig. 3):

$$x(0) = H; x(\tau) = x_a;$$

$$\dot{x}(0) = 0; \dot{x}(\tau) = -v. \tag{7}$$

From equations. (6) and $(7)_{3,1}$, the coefficients result:

$$a = H;\ \varphi = \pi/2, \tag{8}$$

while from $(7)_{2,4}$, one has:

$$\omega = \frac{v}{\sqrt{H^2 - x_a^2}} \tag{9}$$

$$\tan\omega\tau = \frac{v}{\omega x_a} \tag{10}$$

From this second equation, the half-time interval of the return portion is obtained:

$$\tau = \frac{\sqrt{H^2 - x_a^2}}{v}\arctan\frac{\sqrt{H^2 - x_a^2}}{x_a^2}. \tag{11}$$

(b) For t∈[τ, T/2–τ], the first linear portion of x(t) is achieved. From

$$x = at + b, \tag{12}$$

with the functioning conditions

$$x(\tau) = x_a;\ x(T/4) = 0;$$

$$\dot{x}(t) = v = ct. \tag{13}$$

one obtains

$$x(t) = -v(t - T/4), \tag{14}$$

where the scanning velocity obtained

$$v = \frac{x_a}{T/4 - \tau} \tag{15}$$

represents the second designing equation.

(c) For t∈[T/2–τ, T/2+τ], x(t) also has Eq. (6), but in this case with the conditions (Fig. 3):

$$x\left(\frac{T}{2} - \tau\right) = x\left(\frac{T}{2} + \tau\right) = -x_a;$$

$$x\left(\frac{T}{2}\right) = -H;\ \ \dot{x}\left(\frac{T}{2}\right) = 0;$$

$$-\dot{x}\left(\frac{T}{2} - \tau\right) = \dot{x}\left(\frac{T}{2} + \tau\right) = v. \tag{16}$$

therefore:

$$a = -H;\quad \varphi = \pi/2 - \omega T/2, \tag{17}$$

while ω and τ result with equations (9) and (10), respectively.

(d) For t∈[T/2+τ, T-τ] the function x(t) has the second linear portion. Similar to case (b) and with the same velocity v,

$$x(t) = v(t - 3T/4). \tag{18}$$

(e) For t∈[T-τ, T], equation (6), with conditions (7), has the coefficients:

$$a = H;\ \varphi = \pi/2 - \omega T, \tag{19}$$

with the same equations for ω and τ.

The equations of the device are thus completely deduced. Whatever the profile of the scanning function, with steep portions for $\dot{x}(t)$ and $\ddot{x}(t)$ [9], the angular scanning function $\theta(t)$ results with a graph that has only non-linear, curved portions. This conclusion can be reached both with graphical or analitical methods.

4 Active Torque and Command Function

For the linear + sinusoidal scanning function, in Table 1 the expressions of the M(t) function are derived using equation. (5) for each charateristic time interval pointed out in the previous section.

The active torque has to be studied on time intervals with regard to the parameters that characterize it: (i) the natural pulsation ω_0 and the unitless damping

Table 1 Active torque M(t) for the linear and sinusoidal scanning function

Time interval	Active torque $M(t) \propto i(t)$
(a)	$\frac{-J\omega^2H^3}{L^3}\cdot\frac{\cos\omega t\sin^2\omega t}{\left[1+(H^2\cos^2\omega t)/L^2\right]^2}-\frac{\omega H}{2L}\cdot\frac{c\sin\omega t+J\omega\cos\omega t}{1+(H^2\cos^2\omega t)/L^2}+$ $+\frac{k}{2}\arctan\frac{H\cos\omega t}{L}$
(b)	$\frac{Jv^2}{L^3}\cdot\frac{t-T/4}{\left[1+v^2(t-T/4)^2/L^2\right]^2}-\frac{v}{2L}\cdot\frac{c}{1+v^2(t-T/4)^2/L^2}-$ $-\frac{k}{2}\arctan\frac{v(t-T/4)}{L}$
(c)	$\frac{J\omega^2H^3}{L^3}\cdot\frac{\cos\omega(t-T/2)\sin^2\omega(t-T/2)}{\left[1+(H^2\cos^2\omega(t-T/2)/L^2\right]^2}-\frac{k}{2}\arctan\frac{H\cos\omega(t-T/2)}{L}+$ $+\frac{\omega H}{2L}\cdot\frac{c\sin\omega(t-T/2)+J\omega\cos\omega(t-T/2)}{1+(H^2\cos^2\omega(t-T/2)/L^2}$
(d)	$-\frac{Jv^2}{L^3}\cdot\frac{t-3T/4}{\left[1+v^2(t-3T/4)^2/L^2\right]^2}+\frac{v}{2L}\cdot\frac{c}{1+v^2(t-3T/4)^2/L^2}+$ $+\frac{k}{2}\arctan\frac{v(t-3T/4)}{L}$
(e)	$-\frac{J\omega^2H^3}{L^3}\cdot\frac{\cos\omega(T-t)\sin^2\omega(T-t)}{\left[1+(H^2\cos^2\omega(T-t)/L^2\right]^2}+\frac{k}{2}\arctan\frac{H\cos\omega(T-t)}{L}+$ $+\frac{\omega H}{2L}\cdot\frac{c\sin\omega(T-t)-J\omega\cos\omega(T-t)}{1+(H^2\cos^2\omega(T-t)/L^2}$

factor ξ; (ii) the linear scanning domain H, in relationship with the useful domain x_a; the distance L from the pivot of the scanner to the lens or to the projection plane; (iii) the scanning velocity v and the scanning frequency f_s, that are usually a requirement of the users, thus of the designing theme.

From this rather complex study, in the present paper we shall consider some of its most essential aspects. In Fig. 4 the graphs of each of the portions of the reduced moment $M_a(t) = M(t)/J$ are ascertained in MathCad for a numerical example suitable for lower frequencies, i.e., industrial applications: v = 200 mm/s, L = 150 mm,

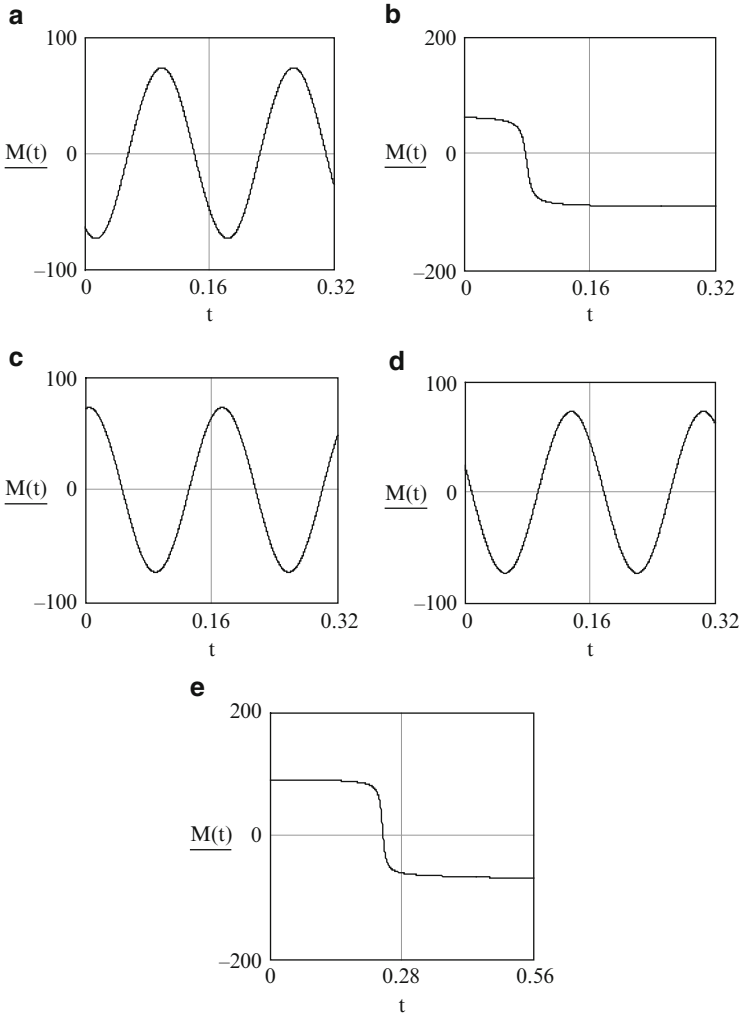

Fig. 4 Reduced active moment M [Nmm] on time intervals t [s] (see Section 3) *for v = 200 mm/s, L = 150 mm, H = 15 mm, x_a = 14 mm*

H = 15 mm, x_a = 14 mm, therefore the characteristic ration of the galvanometer-based scanner is $r = x_a/H = 0.93$.

As studied previously [9], the ratio r has the highest impact on the duty cycle of the scanner, i.e., on its efficiency in using the available time for the scanning process. This is due to the fact that, as r is closer to 1 (for x_a as close as possible to H), this means a smaller available angle for the stop-and-turn portion of the scanning function.

From equation (11) the stop-and-turn interval is $\tau = 0.009887$ s, while from equation (15)

$$T = 4(x_a/v + \tau), \tag{20}$$

therefore T = 0.319548 s. From equation (9), $\omega = 0.9285 \times 10^{-3}$ rad/s. Values of $\omega_0 = 10$ rad[1] and $\xi = 1$ (critical damping) were also considered, after a numerical study of the functions that may be obtained in MathCad, as the preferred parameters of the device.

The time interval in Fig. 4 has been extended to the entire period T for each function deduced in Table 1, in order to better visualize their graphs, although smaller time intervals (see Section 3) have to be considered for each portion of the function $M(t) \propto i(t)$ that provides with equation (4) the command function.

A problem that remains for future study is to determine the optimum generating the M(t) function that is numerically obtained (Fig. 4) by considering each of its five time portions. Both conventional and fuzzy approches are currently considered in order to achieve this scope, and to make the device functional.

5 Conclusions

The paper has developed a solution of galvanometer-based scanner with an optimized scanning function, with symmetrical linear portions and fast stop-and-turn sinusoidal portions. The oscillating law of the device was determined using the theory of mechanisms, while the applications span a large domain, from industrial to biomedical. The study was achieved up to the active/driving moment, proportional to the command function/the current input that has to be provide to the device in order to obtain the required scanning function/oscillating law.

Future theoretical work remains, for the study of this active moment with regard to its parameters. The main problem is to be able to achieve as high as possible scanning frequencies, i.e. as high as possible scanning velocities, while the duty cycle has to remain with sufficient values. Experiments are expected to be fulfilled considering also a closed loop for the device, in order to provide controlled oscillations.

The study will then be continued with the development of 2D scanners, for which the necessary theoretical functions have already been achieved [10].

Acknowledgments The research is supported by the Romanian Education and Research Ministry Grant, PN II Ideas Grant, CNCSIS/NURC (National University Research Council) code 1896/2008.

References

1. Aylward, R.P.: Advances and technologies of galvanometer-based optical scanners. Proc. SPIE 3787, 158–164 (1999)
2. Bass, M.: Handbook of Optics. McGraw-Hill, New York (1995)
3. Beiser, L.: Design equations for a polygon laser scanner. Proc. SPIE 1454, 60–66 (1991)
4. Beiser, L.: Fundamental architecture of optical scanning systems. Appl. Optics 34, 7307–7317 (1995)
5. Coleman, S.M.: High capacity aerodynamic air bearing (HCAB) for laser scanning applications. Proc. SPIE 5873, 56–64 (2005)
6. Duma, V.F.: Scanning. Politehnica, Timisoara (2004)
7. Duma, V.F.: On-line measurements with optical scanners: metrological aspects. Proc. SPIE 5856, 606–617 (2005)
8. Duma, V.F.: Novel approaches in the designing of the polygon scanners. Proc. SPIE 6785, 6785–1Q (2006)
9. Duma, V.F., Podoleanu, A.Gh.: Theoretical approach on a galvanometric scanner with an enhanced duty cycle. Proc. SPIE 7139, 71390D (2008)
10. Duma, V.F.: Mathematical functions of a 2-D scanner with oscillating elements. In: Awrejcewicz, J. (ed.) Modeling, Simulation and Control of Nonlinear Engineering Dynamical Systems, pp. 243–253. Springer, Berlin (2009)
11. Gadhok, J.S.: Achieving high-duty cycle sawtooth scanning with galvanometric scanners. Proc. SPIE 3787, 173–180 (1999)
12. Li, Y., Katz, J.: Laser beam scanning by rotary mirrors. I. Modeling mirror-scanning devices. Appl. Opt. 34, 6403–6416 (1995)
13. Li, Y.: Laser beam scanning by rotary mirrors. II. Conic-section scan patterns. Appl. Opt. 34, 6417–6430 (1995)
14. Li, Y.: Beam deflection and scanning by two-mirror and two-axis systems of different architectures: a unified approach. Appl. Opt. 47, 5976–5985 (2008)
15. Marshall, G.F., Montagu, J.I.: Advances in oscillatory optical scanners. Proc. SPIE 2383, 440–448 (1995)
16. Perju, D.: Mechanisms for fine mechanics (in Romanian). Politehnica, Timisoara (1991)
17. Podoleanu, A.G., Dobre, G.M., Jackson, D.A.: En-face coherence imaging using galvanometer scanner modulation. Opt. Lett. 23, 147–149 (1998)
18. Podoleanu, AGh, Dobre, G.M., Cucu, R.G.: Sequential optical coherence tomography and confocal imaging. Opt. Lett. 29(4), 364–366 (2004)
19. Richter, B.: Laser scan devices for industrial application. WIRE 42(6) (1992)
20. Rohr, B.E.: Testing high-performance galvanometer-based optical scanners. Proc. SPIE 2383, 460–469 (1995)
21. Sabo, D.A., Brunner, D., Engelmayer, A.: Advantages of digital servo amplifiers for control of a galvanometer based optical scanning system. Proc. SPIE 5873, 113–120 (2005)
22. Yun, S.H., Boudoux, C., Tearney, G.J., Bouma, B.E.: High-speed wavelength-swept semiconductor laser with a polygon-scanner-based wavelength filter. Opt. Lett. 28, 1981–1983 (2003)
23. http://www.olympusfluoview.com/products/index.html

Simulation of a Pressure Controlled Hose Type Joint Using F.E.M.

N. Dumitru, M. Negru, and S. Dumitru

Abstract The paper presents a hose type joint which is controlled by pneumatic pressure. The joint is made by a special type of hose with 2 or 4 pneumatic chambers. The hose has a particular construction in order to assure a strength discontinuity of the hose structure. That feature permits the bending of the hose proportional with the pneumatic pressure value. The bending of this hose joint can be made in different planes by controlling the pressure in the hose chambers. This kind of joint can be used in many multi-body mobile systems which necessitate the control over every joint. The main advantage is that it's not using elements in motion and the friction phenomenon is eliminated.

Keywords Finite element method · Hose · Joint · Pneumatic pressure

1 Introduction

Many robots mechanisms are very complex and their capacity of performing various motions has increase.

The purpose of this paper is to propose a hose type joint controlled by pneumatic pressure, with a special structure, which can be used in multi-body systems.

Other pneumatic rubber joints were theoretical and practical analyzed in several papers, with the most interesting utility domains in medicine like MacKibben artificial muscle developed in 1950s [2], Romac actuator [3], Flexible micro actuator [4, 8], Pneumatic planar soft actuator [5], and colonoscopy insertion actuator [6].

The paper [1] shows a new design and prototyping method for a bending pneumatic rubber joint and its application to a soft-bodied manta swimming robot.

N. Dumitru (✉)
Faculty of Mechanics, University of Craiova, Craiova, Romania

I. Vişa (ed.), *SYROM 2009*,
DOI 10.1007/978-90-481-3522-6_46,

The design is based on optimal design using non-linear finite element method, in which geometrical and material non-linearity are considered and fabrication process is based on a rapid and efficient prototyping system using a CAD/CAM based rubber modelling process.

The hose type joint proposed in this paper has a special structure which permits special types of motion if it is used as a mechanism joint.

2 Hose Design

In order to create a pressure controlled hose type joint we have analyzed and conceive different types of hose designs.

This type of hose must have 2 or 4 pneumatic chambers which permit the bending of the hose in different planes (Figs. 1 and 2).

The hose with at least four chambers permits many bending planes by controlling the values of the pressures in all four pneumatic chambers (Fig. 3).

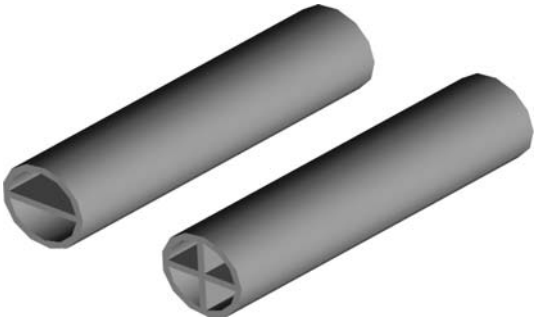

Fig. 1 Hoses with 2 and 4 pneumatic chambers

Fig. 2 Bending types of 2 chambers hose

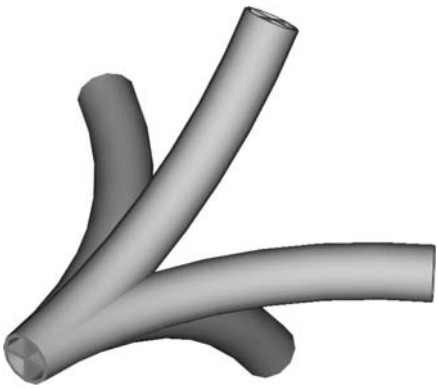

Fig. 3 Bending types of 4 chambers hose

One of the designs that we have conceive, consists in creating the structure of the hose by two materials: rubber and metal because a hose made only by rubber will only inflate and the bending phenomenon is nil.

These two materials must be positioned in hose structure in a particular way in order to achieve an optimum bending phenomenon.

This particular way consist in a series of metallic rings with 2 or 4 interior walls, covered by a layer of rubber which made the transition between these rings.

The rubber part of the hose is intended to permit the longitudinal stretch of the walls of active pneumatic chambers. The rubber part it is positioned between the metallic rings and also is covering them.

The metallic rings are used for constraining the transversal inflation of the hose walls. The number of rings and the distance between them are influencing the bending of the joint (Figs. 4, 5, 6, and 7).

3 Mathematical Model

In order to explain the deformation of the two chamber hose under air pressure applied in one of the chamber, we propose to analyze what happen in a planar section of this hose. The planar section is positioned along longitudinal axis of the hose and it is perpendicular to the transversal wall of the hose (Fig. 8).

The system equilibrium equations are (1):

$$\begin{aligned} &\sum Y = 0 \Leftrightarrow V_1 + V_2 + V_3 = p \cdot R \\ &V_2 \cdot R + V_3 \cdot 2 \cdot R - p \cdot R \cdot \left(R + \frac{R}{2} \right) = 0 \\ &\Rightarrow V_2 + 2 \cdot V_3 = \frac{3}{2} \cdot p \cdot R \end{aligned} \tag{1}$$

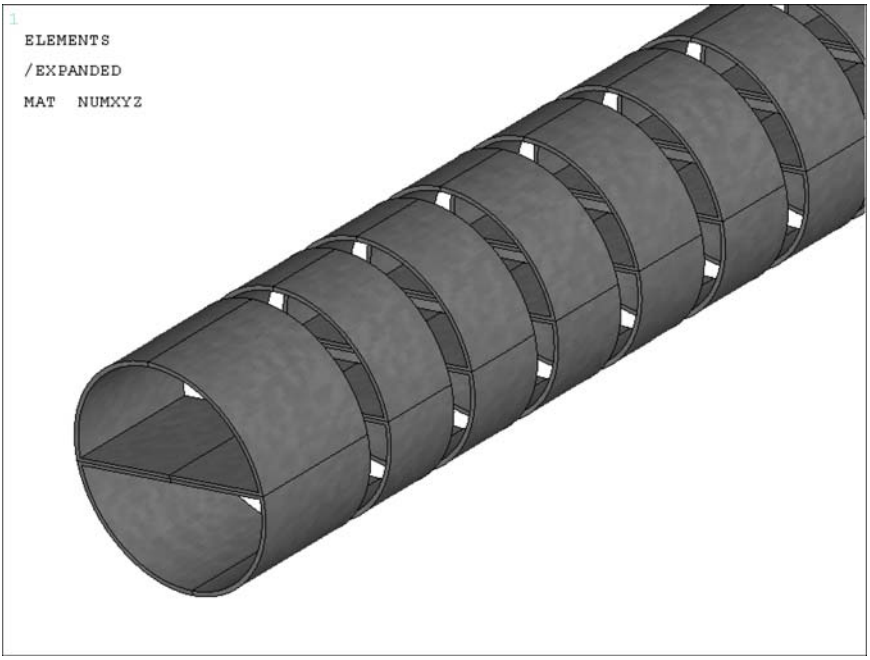

Fig. 4 Metallic part of 2 chambers hose

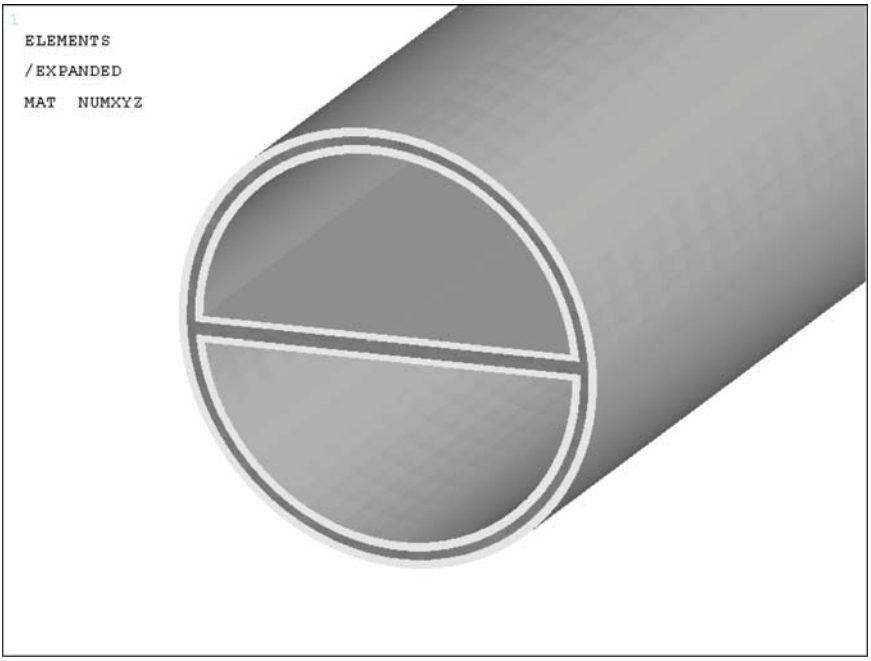

Fig. 5 Rubber part of 2 chambers hose

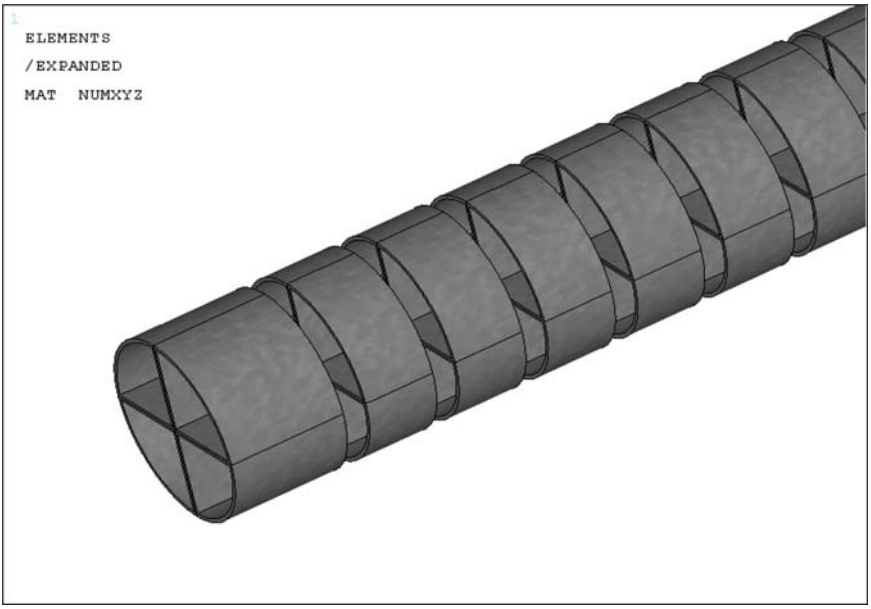

Fig. 6 Metallic part of 4 chambers hose

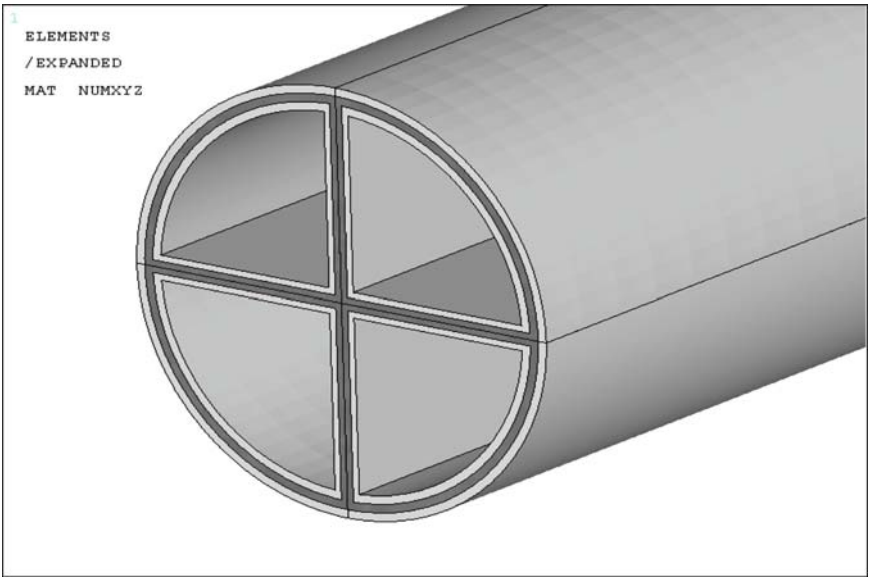

Fig. 7 Rubber part of 4 chambers hose

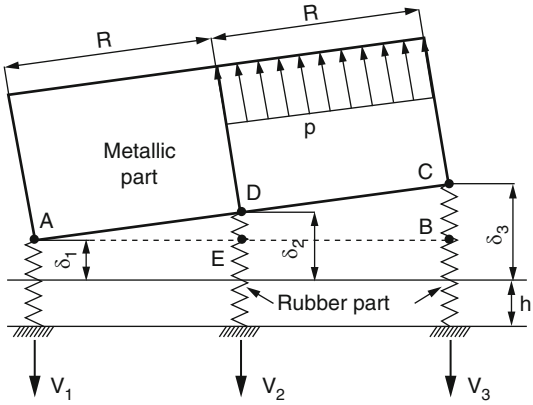

Fig. 8 Planar section of the hose

In order to resolve the system and determine the reaction forces V_1, V_2, and V_3, we need a third equation which is the condition that the metallic part of the hose will remain undeformed after the deformations of the rubber part of the hose. In this case, in the triangle ABC we have:

$$\begin{aligned} &AD = DC \\ &CB = 2 \cdot DE \\ &CB = \delta_3 - \delta_1,\ DE = \delta_2 - \delta_1 \end{aligned} \tag{2}$$

The displacements of the rubber parts caused by axial loads V_1, V_2, and V_3 are:

$$\begin{aligned} \delta_1 &= \frac{V_1 \cdot h}{E \cdot A} \\ \delta_2 &= \frac{V_2 \cdot h}{E \cdot A} \\ \delta_3 &= \frac{V_3 \cdot h}{E \cdot A} \end{aligned} \tag{3}$$

where:
h – the height of the rubber walls between two metallic parts of the hose
A – area of the rubber walls section
Replacing relations (3) in relation (2), we have:

$$\begin{aligned} &\frac{\frac{V_3 \cdot h - V_1 \cdot h}{E \cdot A}}{\frac{V_2 \cdot h - V_1 \cdot h}{E \cdot A}} = 2 \\ &\Rightarrow V_3 + V_1 - 2 \cdot V_2 = 0 \end{aligned} \tag{4}$$

The system equations are:

$$\begin{aligned} &V_1 + V_2 + V_3 = p \cdot R \\ &V_2 \cdot R + V_3 \cdot 2 \cdot R - p \cdot R \cdot \left(R + \frac{R}{2}\right) = 0 \\ &V_3 + V_1 - 2 \cdot V_2 = 0 \end{aligned} \tag{5}$$

and the solution is:

$$\begin{aligned} V_1 &= \frac{p \cdot R}{12} \\ V_2 &= \frac{4 \cdot p \cdot R}{12} \\ V_3 &= \frac{7 \cdot p \cdot R}{12} \end{aligned} \tag{6}$$

We can observe that V_3 is seven times bigger then V_1, so the displacement δ_3 is seven times bigger then δ_1.

If the mathematical model is adapted for tridimensional analysis the result is that δ_3 is five times bigger then δ_1.

This conclusion explain the deformation of this special type of hose under air pressure applied in one of the hose chamber.

4 Numerical Simulation

The numerical simulation was realised using ANSYS program [7].

We have used two finite elements models, for two hoses with two and four pneumatic chambers. Both models were designed with hexahedral elements and two different materials:

- Metallic rings – steel with:
  - E = 2.1 × 10^5 MPa
  - ν = 0.3
- Rubber with:
  - E = 8 MPa
  - ν = 0.49

In order to achieve a good convergence of solution, the mapped mesh process was used for both finite elements models of the joint hose (Fig. 9).

We have considered for simulation a hose of 400 mm length and 40 mm in diameter. The width of the hose walls is 3 mm and the width of the steel rings is 1 mm. The height of the steel rings is 30 mm.

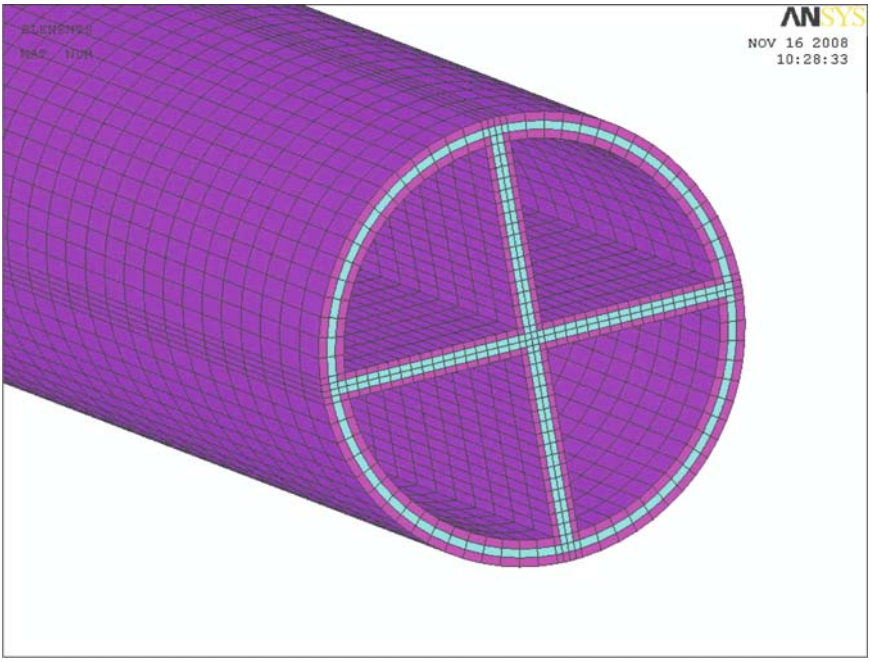

Fig. 9 Meshing of 4 chambers hose

The boundary conditions for both models are the same and consists in:

- All six degrees of freedom are restricted for the nodes at the bottom of the hose models.
- Pressure of 1 MPa (10 bar) is applied on all surfaces of the chamber hose.

First we have analysed the model with two pneumatic chambers in order to determine the displacement of the end part of the hose and the value of steel rings stresses.

In this case the pressure "p" is applied in the upper pneumatic chamber of the hose model. The results are presented in the Figs. 10, 11, 12, 13.

As we can observe, under the pneumatic pressure in one chamber, the maximal displacement of the end part of the hose is 203 mm and the maximal Von Mises Stress on the steel rings is 131.75 MPa, which is smaller then the admissible stress of the steel.

The second hose model has four chambers. We have used two load cases: first when pressure "p" is in one chamber and second with pressure "p" in two hose chambers (Figs. 14, 15, 16, and 17).

We can observe that for load case 1, when pressure "p" is applied in one hose chamber, the maximal displacement is 127 mm at the end of the hose and the maximal Von Mises stress is 57.6 MPa. For the second load case when pressure "p" is applied in two hose chambers, the maximal displacement is 180.5 mm and the maximal Von Mises stress is 53.5 MPa.

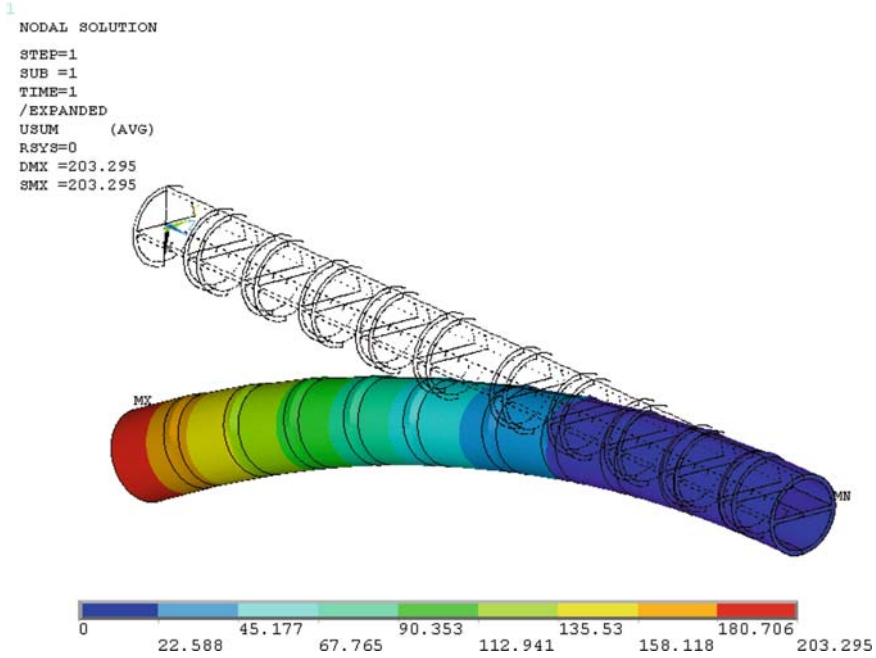

Fig. 10 Displacements (mm)

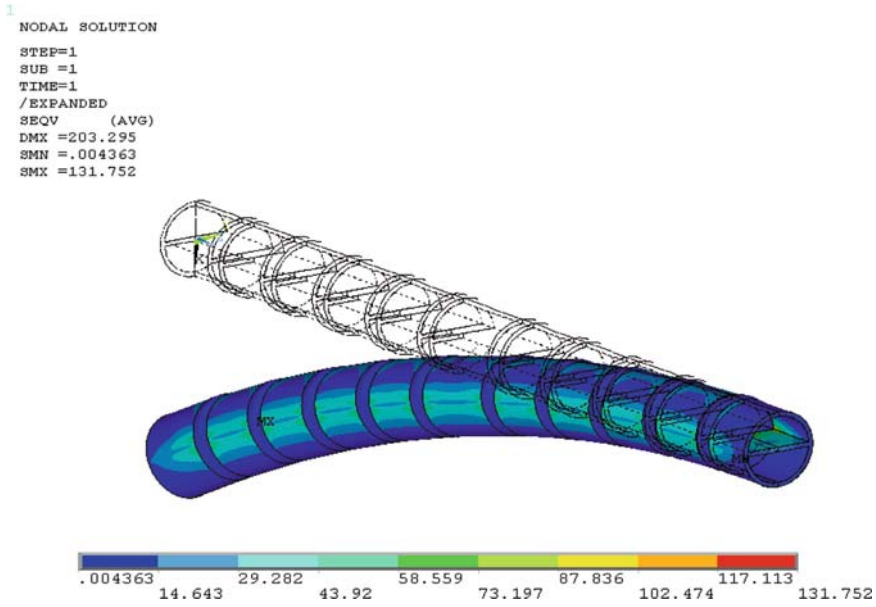

Fig. 11 Von Mises Stresses (MPa)

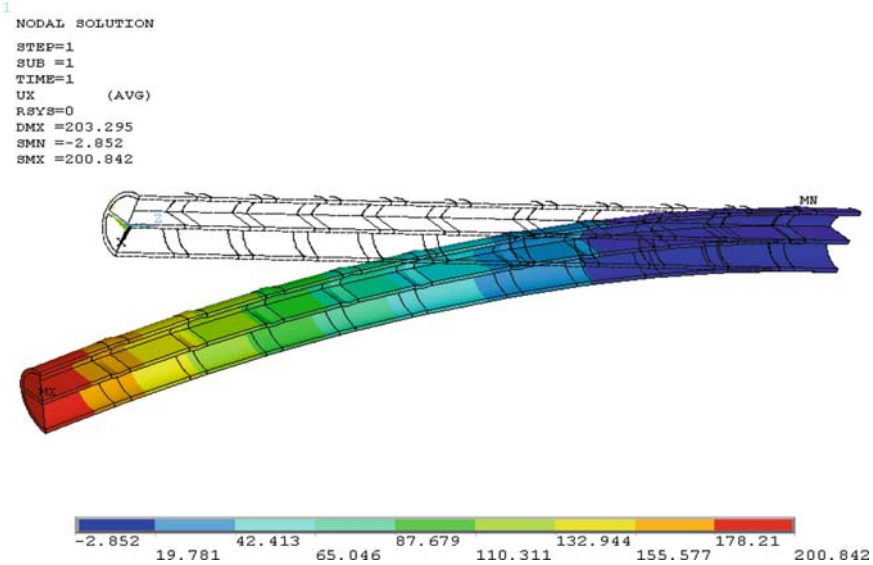

Fig. 12 Section displacements (mm)

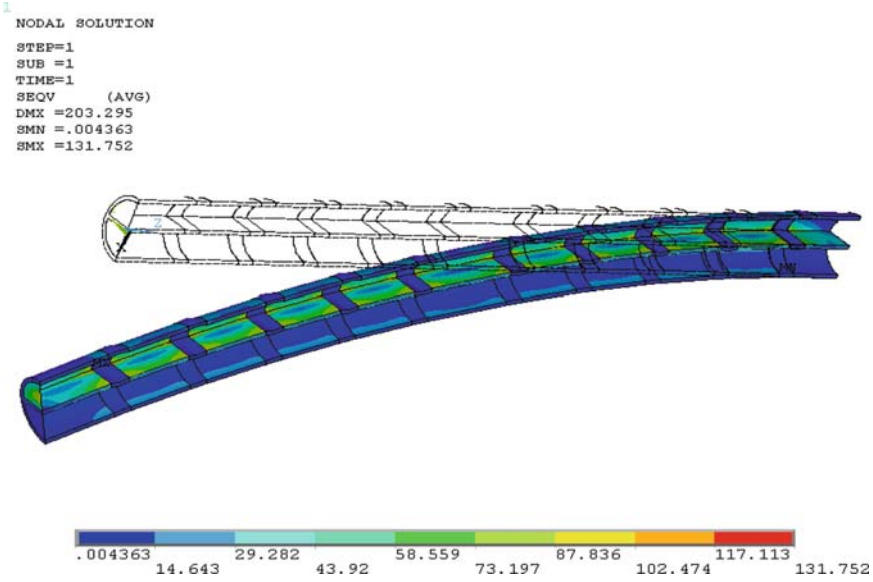

Fig. 13 Section Von Mises Stresses (mm)

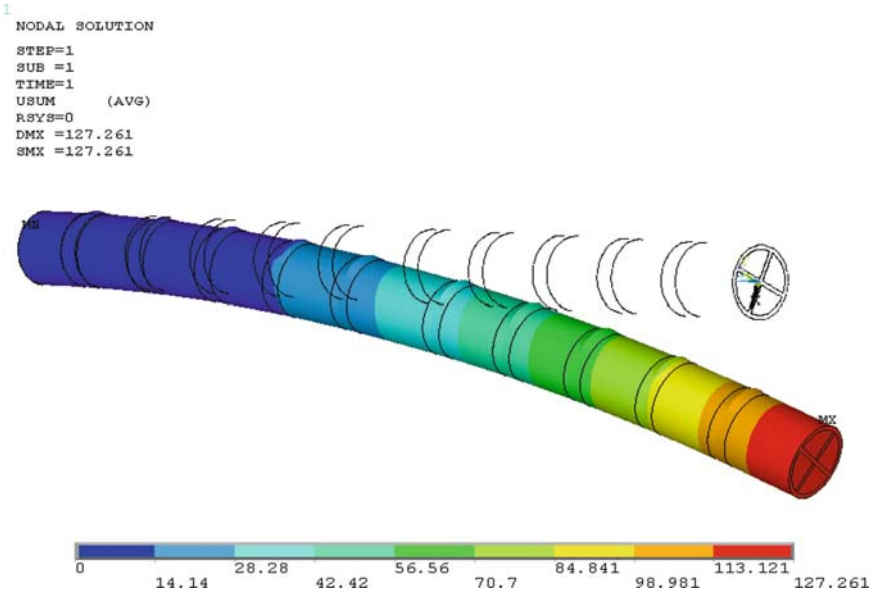

Fig. 14 Displacement (mm) – load case 1

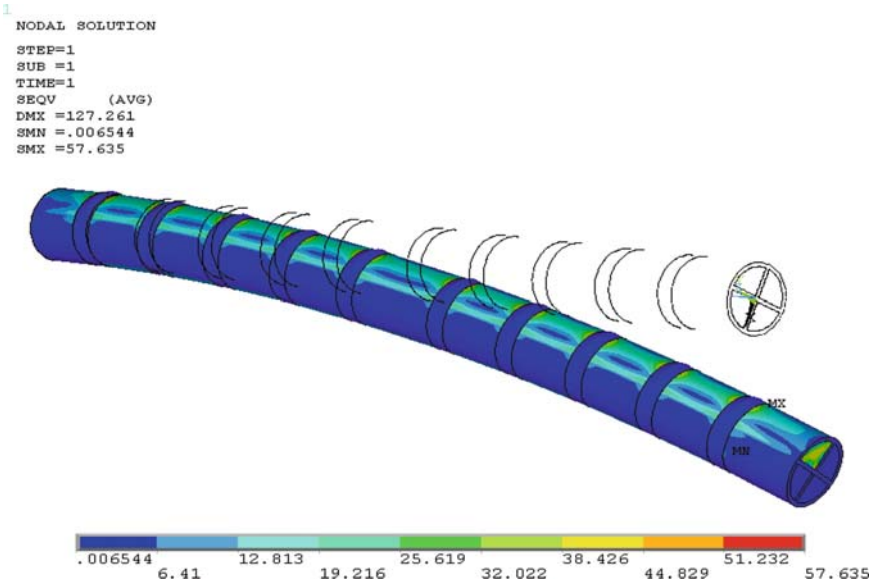

Fig. 15 Von Mises Stress (MPa) – ldcase 1

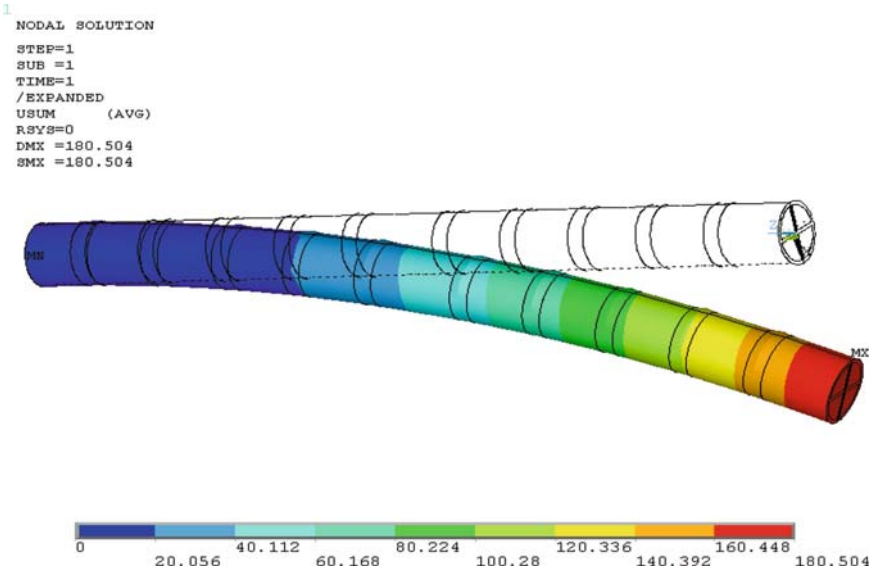

Fig. 16 Displacement (mm) – load case 2

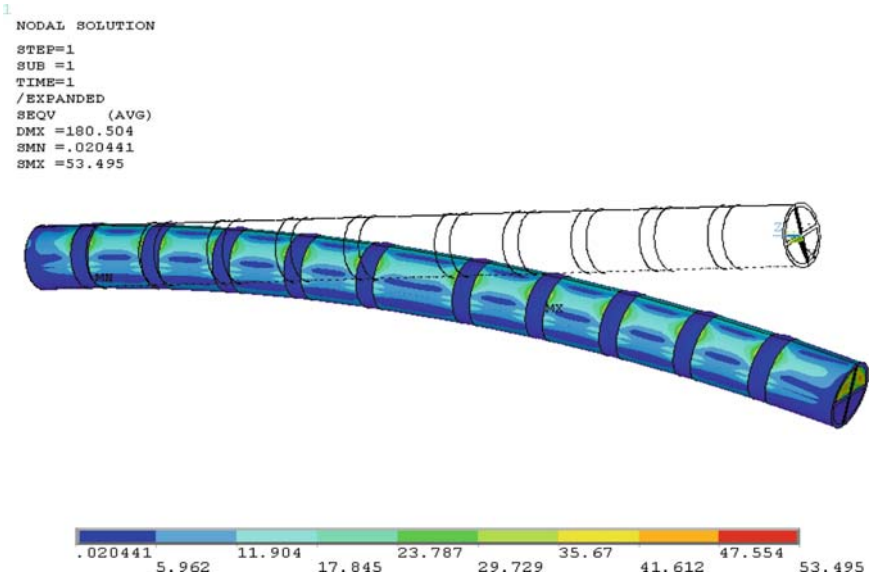

Fig. 17 Von Mises Stress (MPa) –ldcase 2

5 Conclusions

The idea of making two or more pneumatic chambers hoses can transform a simple hose into a special type of joint which can be controlled by the pressures in these pneumatic chambers.

An ordinary type of hose under pneumatic pressure applied in the hose chambers, will just inflate and no bending will result. So, it is necessary to use a special type of hose in order to permit the bending phenomenon.

This particular type of hose we suggest in this paper blocks the inflation of the hose and permit the longitudinal stretch of the pneumatic chambers walls. As result the hose will bend proportionally with the value of the pressure applied in the hose chambers. As we can see in the numerical simulation we have obtain displacements of 200 mm at values of 1 bar pneumatic pressure for a hose of 400 mm long.

The pressure can be applied in one or more pneumatic chambers of the hose with different values, making the bending phenomenon to appear in different planes.

The hose with four or more chambers can bend in many ways depending of the values of the pressures applied in those pneumatic chambers of the hose.

The advantages of this type of joint are:

- Is not using elements in motion, so the friction is almost not present
- Is an active joint between the elements of the multi-body systems and can control the motion of these elements
- The range of bending motion is very large
- The control of bending motion is precise
- The hose joint is elastic

This study will be followed up by integrating this type of joint in some multi-body systems in order to simulate his functionality.

References

1. Suzumori, K., Endo, S., Kanda, T.: A bending pneumatic rubber actuator realizing soft-bodied manta swimming robot. In: IEEE Roma, Italy, 10–14 April 2007
2. Schulte, H. F., Jr.: The characteristics of the Mckibenn artificial muscle. In: The Application of External Power in Prothetics and Orthetics. National Academy of Sciences, National Research Council, Washington, DC, pp. 94–115 (1961)
3. Immega, G. B.: Romac actuator for micro robot. In: Proceedings of MicroRoboticsand Teleoperators Workshop by IEEE Robotics and Automation Council (1987)
4. Susuzmori, K., Iikura, S., Tanaka, H.: Applying a flexible microactuator to robotic mechanisms. IEEE Control Syst. 12(1), 21–27 (1992)
5. Noritsugu, T., Sasaki, D., Matsuo, S., Kusunoki, I., Mitsumine, Y.: Development of medical care assist bed using pneumatic planar soft actuator. J. Robot. Mechatronics 14(6), 547–556 (2002)

6. Suzumori, K., Hama, T., Kanda, T.: New pneumatic rubber actuators to assist colonoscope insertion. In: IEEE 2006, pp. 1824–1829 (2005–2006)
7. Ansys 12User's Guide
8. Suzumori, K., Abe, A.: Applying flexible microactuators to pipeline inspection robots. In: Transactions of IMACS/SICE, North-Holland, pp. 515–520 (1993)

Workspace and Singularity Analysis for a Reconfigurable Parallel Robot

N. Plitea, D. Pisla, A. Vidrean, C. Vaida, and B. Gyurka

Abstract In this paper several aspects regarding the workspace analysis and singularity identification of a reconfigurable parallel robot are presented. Using the developed kinematic model, the reconfigurable parallel robot singularities within the generated workspace are identified. The simulation results for the workspace and singularities generation are also presented.

Keywords Reconfigurable parallel robots · Singularities · Workspace

1 Introduction

A multitude of industrial applications require different solutions for obtaining the desired results. For solving certain tasks should be developed a special mechanism for each application. Reconfigurable robots can be defined as a specific category of robots in which their components (individual joints and links) can be assembled in different configurations and geometries.

A modular reconfigurable robot consists of a collection of individual link and joint components that can be assembled into a number of differing robot geometries. Compared to a conventional industrial robot with fixed geometry, such a system can provide flexibility to the user, enabling it to cope with a wide spectrum

N. Plitea (✉)
Department of Mechanics and Computer Programming, Technical University of Cluj-Napoca, Cluj-Napoca, Romania
IPA R&D Institute for Automation, Cluj Subsidiary, Cluj-Napoca, Romania

I. Vişa (ed.), *SYROM 2009*,
DOI 10.1007/978-90-481-3522-6_47,

of tasks through proper selection and reconfiguration of a large inventory of functional components [4].

It was shown that a modular robot can be configured as a serial manipulator to accomplish assembly tasks or as a parallel rigid manipulator to accomplish precise tasks [2, 14].

A modular reconfigurable parallel robot can be rapidly constructed and its workspace can be varied by changing the leg positions, joint types, and link lengths for a variety of tasks. Modularity has many advantages. This kind of parallel robot comprises components built with standardized units or dimensions.

This leads to flexibility, variety in use, rapid changeover and ease of maintenance. For a modular reconfigurable parallel robot system to be deployable and effective in performing its assigned tasks, certain issues must be addressed. These fundamental issues include parallel robot configuration design, kinematics analysis, workspace analysis, kinematic calibration, singularity analysis and dynamics analysis.

Reconfigurable robots have been studied and developed in research institutes around the world [3, 5–8, 17, 28].

The problem of studying the workspace of parallel mechanisms has attracted the attention of many researchers. The main difficulty of the workspace analysis for parallel robots arises from the fact that a complete representation of the workspace should be embedded in a six-dimensional workspace for which there is no possible graphical illustration. The most investigated workspace is the 3D *constant orientation workspace*, which describes the possible location of the end-effecter origin for a constant orientation: geometric or algebraic approaches may be used [9, 10, 15, 20].

In [16] geometrical algorithms to determine various workspaces of planar manipulators are presented.

A well-known method used to determine the workspace was the determination of cross sections in the workspace, parallel to the base. These cross sections are determined for different z values and if the step between these values is small enough, the obtained workspace may have a good approximation.

In [1] the interval analysis for workspace generation is used.

Husty analyzed the workspace of planar three-legged platforms with joint limits [12]. He investigates the kinematical image of the workspace in the image space using a planar mapping technique. In [18] an analysis of the reachable workspace of a spatial Stewart-Gough-Platform with planar base and platform is presented. The complete workspace (position and orientation) taking into account active and passive joints is computed.

Itul presents a method that generates the graphical visualization and the analysis elements for a defined parallel robot working space [13].

Pisla presents a new simulation program for the workspace analysis of parallel robots. The simulation program enables to establish the relationships between the workspace shape, elements links and geometrical parameters of the structure [23]. In [22] the workspace analysis of a new parallel robot for minimally invasive surgery is presented.

For workspace generation there are essentially three methods:

1. Method which uses the inverse geometrical model
2. Method which uses the direct geometrical model
3. Method which uses the Cartesian workspace results as an intersection of the workspace for each kinematic chain

The paper is organized as follows: Section 2 is dedicated to the kinematics and the singularity analysis of the studied reconfigurable parallel robot. Section 3 describes the workspace generation of the studied reconfigurable parallel robot. The graphical results of the simulation are also illustrated and interpreted. The conclusions of this work are presented in Section 4.

2 Kinematics of the ROPAR4 Parallel Robot

2.1 The Reconfigurable Parallel Robot

The studied 4-DOF parallel robot derives from a 6-DOF reconfigurable parallel robot, based on the patent, following the co-operation between Technical University of Braunschweig, Germany and Technical University of Cluj-Napoca, Romania [11, 24, 26].

The 6-DOF reconfigurable parallel robot consists of three identical kinematic chains, connected to the mobile platform through spherical joints and to the base through prismatic joints (Figs. 1 and 2). In each chain two linear drives with identical linear axis in the z direction are integrated. This 6-DOF reconfigurable parallel robot is characterized by a robust mechanical structure and high dynamic performance, a good ratio between the manipulated mass and the own mass and modularity construction.

The use of this reconfigurable parallel kinematic mechanism could be motivated due to the practical need to develop different mechanisms having different degrees of freedom with minimum investment. The major disadvantage of the 6-DOF reconfigurable parallel robot consists in higher cost of production caused by the

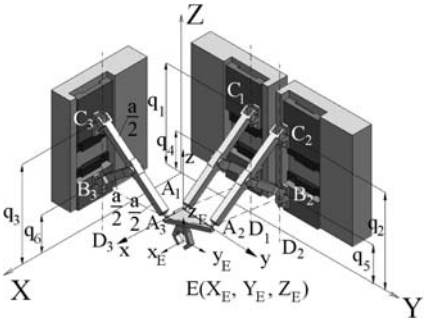

Fig. 1 The parallel robot with 6-DOF

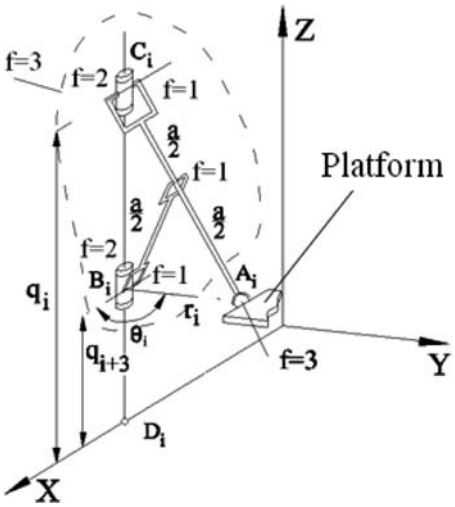

Fig. 2 One kinematic chain

number of motors and the number of modules necessary for the robot construction. The large number of motors increases the complexity of robot control. The achievement of a complex control leads to higher production costs. In many fields of activity in which the parallel robots are used, it is not necessary to use all six degrees of freedom, as solutions of robots with two, three, four or five degrees of freedom are more suitable. As applications and fields of utility for these robots can be mentioned: accuracy assembly tasks, laser processing of materials and water jet cutting tasks.

Some cases of reconfigurable parallel robots which derive from the 6-DOF robot are presented below:

Case 1: The 5-DOF reconfigurable parallel robot [19, 24]:

$$q_1 \rightarrow q_1,\ q_2 \rightarrow q_2,\ q_3 \rightarrow q_3,$$
$$q_4 = q_5 \rightarrow q_4,\ q_6 \rightarrow q_5$$

The platform performs translations along the OX, OY and OZ axes and two rotations (precession and nutation angles).

The input data for the inverse geometrical model are:

$$X_E, Y_E, Z_E,\ \psi,\ \theta, \varphi = 0$$

Case 2: The 4-DOF reconfigurable parallel robot [19, 24]:

$$q_1 \rightarrow q_1,\ q_2 \rightarrow q_2,\ q_3 \rightarrow q_3,$$
$$q_4 = q_5 = q_6 \rightarrow q_4$$

The platform performs translations along the OX, OY and OZ axes and a rotation around the OZ axis.

The input data for the inverse geometrical model are:

$$X_E,\ Y_E,\ Z_E,\ \varphi,\ \ \psi = 0,\ \ \theta = 0$$

Case 3: The 3-DOF reconfigurable spatial parallel robot [24]:

$$q_1 = q_2 \rightarrow q_1,\ q_3 \rightarrow q_2,$$
$$q_4 = q_5 = q_6 \rightarrow q_3$$

The platform performs translations along the OX, OY and OZ axes.

The input data for the inverse geometric model are:

$$X_E,\ Y_E,\ Z_E,\ \psi = 0,\ \theta = 0,\ \varphi = 0$$

Case 4: The 3-DOF reconfigurable planar parallel robot [24]:

$$q_1 \rightarrow q_1,\ q_2 \rightarrow q_2,\ q_3 \rightarrow q_3,$$
$$q_4 = q_5 = q_6 = Z_0(const)$$

The platform performs translations along the OX and OY axes and a rotation around the OZ axis.

The input data for inverse geometric model are:

$$X_E,\ Y_E,\ \varphi,\ \ Z_E = C\,(const),\ \psi = 0,\ \theta = 0$$

Case 5: The 2-DOF reconfigurable parallel robot [24]:

$$q_1 = q_2 \rightarrow q_1,\ q_3 \rightarrow q_2,$$
$$q_4 = q_5 = q_6 = Z_0\ \ (const)$$

The platform performs translations along the OX and OY axes in the plane $Z = Z_0 = C\,(const.)$

The input data for the inverse geometric model are:

$$X_E,\ Y_E,\ Z_E = C\,(const)$$

The present paper focuses on the workspace and singularity analysis of 4-DOF reconfigurable parallel robot (**ROPAR4**) It should be mentioned that ROPAR4 is also reconfigurable, and other robots could be designed originating in it.

2.2 Kinematics

The geometrical analysis of the ROPAR4 reconfigurable parallel robots is presented below.

The following constant geometrical parameters have been considered [25, 26]:

$$a, b, d, h, k, x_E = \frac{h}{3},\ y_E = \frac{b}{3},\ z_E = -d$$

$$x_{A_1} = 0,\ y_{A_1} = 0,\ z_{A_1} = 0,\ X_{B_1} = 0,\ Y_{B_1} = Y_{D_1} = k$$

$$x_{A_2} = 0,\ y_{A_2} = b,\ z_{A_2} = 0,\ X_{B_2} = 0,\ Y_{B_2} = k + b$$

$$x_{A_3} = h,\ y_{A_3} = 0,\ z_{A_1} = 0,\ X_{B_3} = X_{D_3} = h,\ Y_{B_3} = 0 \tag{1}$$

The constant geometrical parameters are presented in Figs. 2 and 3.

In the inverse geometrical problem case of ROPAR4 robot, the generalized coordinates of the end-effector X_E, Y_E, Z_E, φ are given and the driving coordinates q_1, q_2, q_3, q_4 of the robot are analytically computed:

$$X_E,\ Y_E, Z_E,\ \varphi \ \rightarrow\ q_1,\ q_2,\ q_3,\ q_4 \tag{2}$$

$$q_4 = Z_{A_i} = Z_E + d$$

$$q_i = q_4 + \sqrt{a^2 - r_i^2}\ \ i = 1, 2, 3 \tag{3}$$

In the ROPAR4 direct geometric modeling case the input data are the driven coordinates q_i, $i = 1,\ 2,\ 3,\ 4$, while the generalized coordinates of the end-effector X_E, Y_E, Z_E, φ are required.

The equations for the determination of the direct geometric modeling of the ROPAR4 are [19, 25]:

$$r_i = \sqrt{a^2 - (q_i - q_{i+3})^2}, \quad i = 1, 2, 3 \tag{4}$$

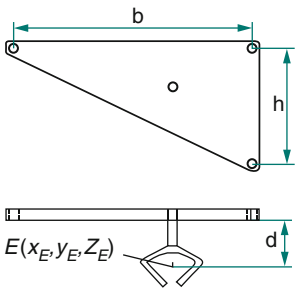

Fig. 3 Platform geometrical parameters

$$\begin{aligned}[X_{A_i}(X_E, Y_E, \varphi) - X_{B_i}]^2 + [Y_{A_i}(X_E, Y_E, \varphi) - Y_{B_i}]^2 \\ - r_i^2(q_i, q_4) = 0, \quad i = 1, 2, 3\end{aligned} \tag{5}$$

$$\begin{cases} f_1(X_E, Y_E, Z_E, \varphi) \\ \equiv [X_E + (x_{A_1} - x_E)\, c\varphi - (y_{A_1} - y_E)\, s\varphi - X_{B_1}]^2 \\ \quad + [Y_E + (x_{A_i} - x_E)\, s\phi + (y_{A_i} - y_E)\, c\varphi - Y_{B_1}]^2 - r_1^2 = 0 \\ f_2(X_E, Y_E, Z_E, \varphi) \\ \equiv [X_E + (x_{A_2} - x_E)\, c\varphi - (y_{A_2} - y_E)\, s\varphi - X_{B_2}]^2 \\ \quad + [Y_E + (x_{A_2} - x_E)\, s\varphi + (y_{A_2} - y_E)\, c\varphi - Y_{B_2}]^2 - r_2^2 = 0 \\ f_3(X_E, Y_E, Z_E, \varphi) \\ \equiv [X_E + (x_{A_3} - x_E)\, c\varphi - (y_{A_3} - y_E)\, s\varphi - X_{B_3}]^2 \\ \quad + [Y_E + (x_{A_3} - x_E)\, s\varphi + (y_{A_3} - y_E)\, c\varphi - Y_{B_3}]^2 - r_3^2 = 0 \\ f_4(X_E, Y_E, Z_E, \varphi) \equiv q_4 - Z_E - d = 0 \end{cases} \tag{6}$$

The system (6) is a nonlinear equations system. The solutions of the system could be determined by means of Newton-Raphson method.

For the inverse kinematics, the end-effector velocities $\dot{X}_E$, $\dot{Y}_E$, $\dot{Z}_E$, $\dot{\varphi}$ in the inverse kinematic model case of ROPAR4 reconfigurable parallel robot, are given and the driving velocities $\dot{q}_1$, $\dot{q}_2$, $\dot{q}_3$, $\dot{q}_4$ of the robot are computed using equation (8):

$$A\dot{X} + B\dot{q} = 0 \tag{7}$$

$$\dot{q} = -B^{-1}A\dot{X} \tag{8}$$

For the forward kinematics, the driving velocities $\dot{q}_1$, $\dot{q}_2$, $\dot{q}_3$, $\dot{q}_4$ in the direct kinematic model case of ROPAR4 reconfigurable parallel robot are given and the end-effector velocities $\dot{X}_E$, $\dot{Y}_E$, $\dot{Z}_E$, $\dot{\varphi}$ of the robot are computed using the equation (7):

$$\dot{X} = -A^{-1} \cdot B \cdot \dot{q} \tag{9}$$

2.3 Singularities of the ROPAR4 Robot

The parallel structures are used in applications that require high precision, and thus errors and blockages are not allowed as they could affect the robot's working environment.

The kinematic precision increase and the parallel structure's stability assurance can be achieved through the identification and avoidance of possible singularities in the prescribed workspace [21].

To determine the ROPAR4 singularities the equation (7) is used.

A distinction can be made between three different types of singularities [27]:

Type I. Singularities occur when det(B) = 0. In these configurations, the platform is locally movable, even if the actuator leg lengths are fixed. In these situations, the system gains one or more degrees of freedom and it loses its rigidity.

Using equation (10), it yields:

$$\begin{aligned}\det B = &-8 \cdot (Z_E + d - q_1) \\ &\cdot (Z_E + d - q_2) \cdot (Z_E + d - q_3)\end{aligned}$$

From the constructive constraints and the actuator stroke values it yields there are no singularities of type I.

Type II. Singularities occur when det(A) = 0. The corresponding configurations are on the boundary of the manipulator workspace or on internal boundaries between regions of the workspace. In these cases, the end-effecter looses one or more degrees of freedom.

It was developed an algorithm which considers firstly a volume bigger then real workspace of the robot.

For solving the singularity problem the entire volume is covered and based on equations (2) and (3), the driving coordinates q_i, i = 1, 2, . . . , 4, are calculated for each point. To validate the driving coordinates, each point has been verified to be contented by the covered volume.

Applying this algorithm the resulting points of singularity of type II (det A = 0 from equation (11)) are presented in Fig. 4.

The parameters used for the simulation are: $x_{\min} = 25$, $y_{\min} = 50$, $z_{\min} = 90$, $x_{\max} = 165$, $y_{\max} = 290$, $z_{\max} = 400$, increment = 1 mm, epsilon = 0.0001.

Based on these parameters a number of 10,416,000 points have been evaluated.

Type III. Singularities, also known as architectural singularities, occur when A and B are simultaneously singular. If this occurs, finite output motion is possible even when the actuators are fixed.

The expressions for the ROPAR4 Jacobian matrices are:

$$B = \begin{pmatrix} 2 \cdot [Z_E + d - q_1] & 0 & 0 & 0 \\ 0 & 2 \cdot [Z_E + d - q_2] & 0 & 0 \\ 0 & 0 & 2 \cdot [Z_E + d - q_3] & 0 \\ 0 & 0 & 0 & -1 \end{pmatrix} \tag{10}$$

$$A = \begin{pmatrix} -2 \cdot a_{*1} & -2 \cdot b_{*1} & -2 \cdot [Z_E + d - q_1] & c_{*1} \\ -2 \cdot a_{*2} & -2 \cdot b_{*2} & -2 \cdot [Z_E + d - q_2] & c_{*2} \\ -2 \cdot a_{*3} & -2 \cdot b_{*3} & -2 \cdot [Z_E + d - q_3] & c_{*3} \\ 0 & 0 & 1 & 0 \end{pmatrix} \tag{11}$$

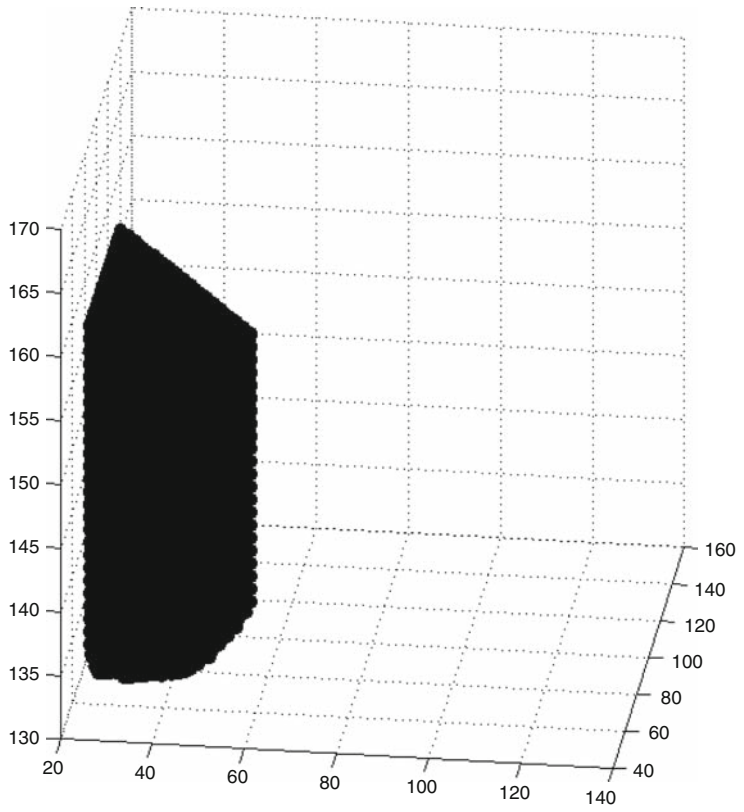

Fig. 4 Singularities points (Type II)

where:

$$a_{*i} = X_E + (x_{Ai} - x_E) \cdot c\varphi - (y_{Ai} - y_E) \cdot s\varphi - X_{Bi};$$

$$b_{*i} = Y_E + (x_{Ai} - x_E) \cdot s\varphi + + (y_{Ai} - y_E) \cdot c\varphi - Y_{Bi};$$

$$c_{*i} = (-2) \cdot a_{*i} \cdot \cdot [-(x_{Ai} - x_E) \cdot s\varphi - (y_{Ai} - y_E) \cdot c\varphi] - 2 \cdot b_{*i} \cdot [(x_{Ai} - x_E) \cdot c\varphi - (y_{Ai} - y_E) \cdot s\varphi]; \quad i = 1, 2, 3$$

Superposing the cases when the two determinants are equal with zero, it can be easily seen that in none of the above situations the determinants cannot be null in the same time. In conclusion, from the constructive point of view, for the

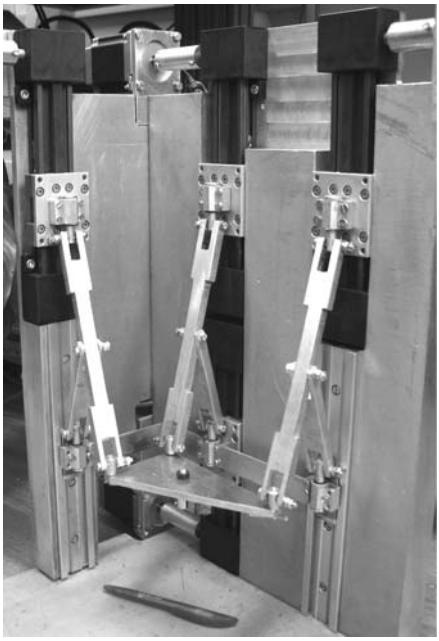

Fig. 5 The ROPAR4 robot

functioning conditions imposed, there are no singularity points of type III. These types of singularities can be easily avoided in the design stage.

An experimental model of ROPAR4 has been built-up at CESTER Research Center, Technical University of Cluj-Napoca, Romania (Fig. 5).

For the design of ROPAR4 parallel robot a modular structure has been chosen that leads to the reduction of the fabrication costs. The actuation is performed through linear motors with high resolution, to ensure a good positioning accuracy for the robot. In Fig. 5 the mechanical structure of ROPAR4 reconfigurable parallel robot is represented. Each of the three arms is a planar mechanism consisting of two elements.

Each arm of the ROPAR4 is connected to the mobile platform and to the carriages using universal joints. The constituent elements of each arm are the elements of a right-angled triangle, which can be rotated around the vertical cathetus.

3 Workspace of the ROPAR4 Robot

3.1 The Geometrical Method

The geometrical method for ROPAR workspace generation is based on the intersection of volumes for each identical kinematic chain.

In Fig. 6 is represented the total workspace of ROPAR4 parallel robot.

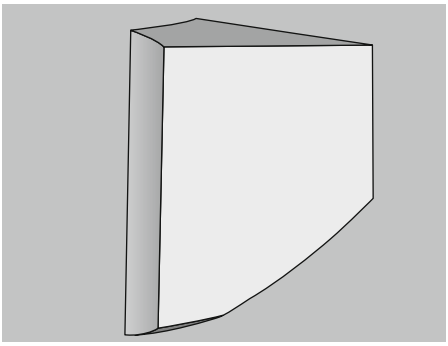

Fig. 6 The ROPAR4 robot workspace

3.2 The Analytical Method

The workspace of ROPAR4 was analytically generated using the MATLAB software.

For the workspace generation was considered initially a cuboid which encloses the workspace of the robot.

The cuboid is generated based on the geometry of the robot. For the workspace analysis the cuboid is approached as a three-dimensional matrix, or as a volume of points, each point having three coordinates (X, Y, Z).

For each point the inverse kinematic equations are used (with the coordinates of the point representing the end-effectors coordinates).

If the resulting data is a valid combination of the active joints (q_1, q_2, q_3 *and* q_4) the point is situated in the workspace of the robot.

Sequentially all the points within the cuboid are analyzed the resulting valid points representing the workspace of the robot. For these points the singularity algorithm is applied to determine the also the volume of singularities for ROPAR4.

Figure 7 illustrates the results, namely the workspace of the robot using two colors. The lighter one represents the volume occupied by singular points. The singularity points limit a compact volume situated on the boundary of the workspace of ROPAR4.

As there are no isolated points in other areas of the workspace (see Fig. 4) in the control algorithm of ROPAR4, the singularity zone can be easily eliminated from the workspace of the robot, thus obtaining a robot that can be used in a workspace without singularity points.

From the comparative analysis of both used methods, it yields the same shape respectively the same dimensions for the ROPAR4 workspace.

4 Conclusions

In the paper, the kinematic model for a 4-DOF reconfigurable parallel robot, its singularities and workspace analysis have been presented. The analysis and the graphical visualization of the singularities within the generated workspace offers

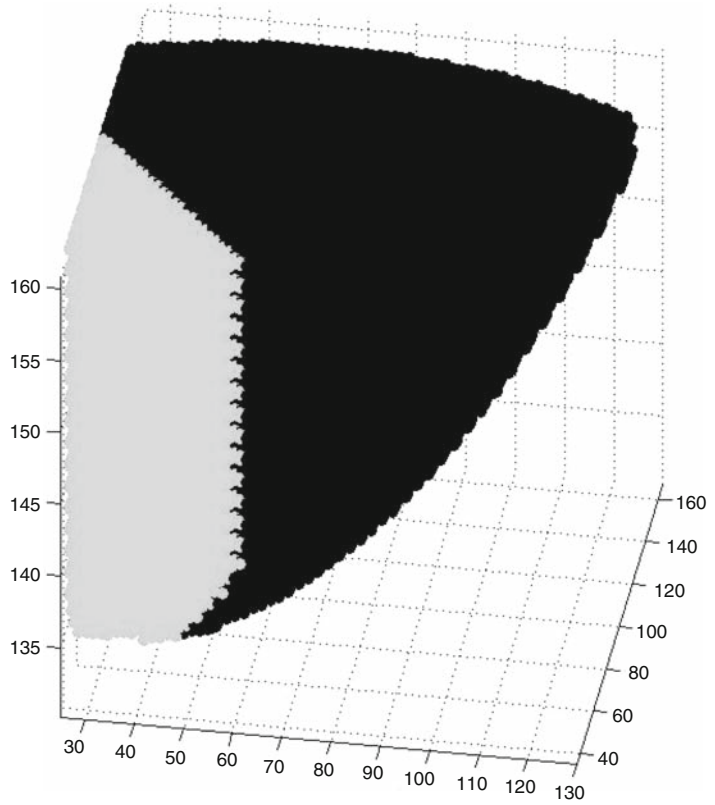

Fig. 7 The workspace of the ROPAR4 with singular points

multiple advantages: the identification of the optimal working zone; the identification of singularities and structures verification before a parallel robot is built. The obtained simulation results are useful for the designers not only to understand the distribution of characteristics of the workspaces for various geometrical parameters of reconfigurable robot, but also to optimize the ROPAR4 parallel robot.

Acknowledgments This research was financed from the research grants awarded by the Romanian Ministry of Education and Research.

References

1. Chablat, D., Wenger, Ph.: Workspace analysis of the orthoglide using interval analysis. In: Lenarčič, J., Thomas, F. (eds.) Advances in Robot Kinematics, Kluwer, Norwell, pp. 397–406 (2002)
2. Chen, I.M.: Theory and applications of modular reconfigurable robotic systems. Ph.D thesis, California Institute of Technology, Pasadena, CA (1994)

3. Chen, I.-M., et al.: Architecture for rapidly reconfigurable robot workcell. In: 5th International Conference of Control, Automation, Robotics and Vision, Singapore, pp. 100–104 (1998)
4. Chen, I.-M., Yang, G., Yeo, S.: Automatic modelling for modular reconfigurable robotic systems – theory and practice. In: Industrial Robotics: Theory, Modelling and Control, pp. 43–81 (2006)
5. Chen, I.M.: A rapidly reconfigurable robotics workcell and its applications for tissue engineering. Report: Innovation in Manufacturing Systems and Technology (IMST), January 2003
6. Choi, J., et al.: Dynamic and stable reconfiguration of self-reconfigurable planar parallel robots. Adv. Robot. 18(6), 565–582 (2004)
7. Dash, A.K., et al.: Task-oriented configuration design for reconfigurable parallel manipulator systems. Int. J. Comput. Integr. Manufacturing 18(7), 615–634 (2005)
8. Fassi, I., et al.: Design and control issues for reconfigurable parallel mechanisms. In: 35th CIRP International Seminar on Manufacturing Systems, Seoul, Korea, 13–15 May 2002
9. Gao, F., Liu, X.-J., Chen, X.: The relationships between the shapes of the workspaces and the link lengths of a 3-DOF symmetrical planar parallel manipulators. Mech. Mach. Theory 36, 205–220 (2001)
10. Gosselin, C.: Determination of the workspace of 6-dof parallel manipulators. ASME J. Mech. Des. 112–113, 331–336 (1990)
11. Hessebach, J., Plitea, N., Kerle, H., Thoben, R.: Manipulator mit Parallelstruktur, Patenschrift DE 197.10.171.C2, Deutsches Patent-und Markenamt, Bundesrepublik Deutschland, 07.02.2002 (2002)
12. Husty, M.: On the workspace of planar three-legged platforms. In: World Automation Congress, Montpelier, vol. 3, pp. 339–344 (1996)
13. Itul, T.-P., Pisla, D.L.: Workspace analysis of a Three Degrees of Freedom Parallel Robot. In: Automation, Quality and Testing, Robotics, 2006 IEEE International Conference on May 2006, vol. 2, pp. 290–295. Digital Object Identifier: 10.1109/AQTR.2006.254647 Posted online: 2006-12-11 09:18:09.0 (2006)
14. Kiat, L.W.: Kinematic analysis and calibration of modular parallel robots. School of Mechanical & Production Engineering, Master of Engineering thesis, Nanyang Technological University (2000)
15. Kumar, V.: Characterization of workspaces of parallel manipulators. In: ASME Proceedings of the 21th Biennial Mechanisms Conference, Chicago, pp. 321–329 (1990)
16. Merlet, J.-P.: Parallel robots. Kluwer, Norwell (2006)
17. Negri, S., et al.: Improvement and optimization of a reconfigurable parallel kinematic machine. In: 2002 Japan-USA Symposium on Flexible Automation (2002 JUSFA), Hiroshima, Japan, 15–17 July 2002
18. Pernkopf, F., Husty, M.: Reachable workspace and manufacturing errors of Stewart-Gough manipulators. In: Proceedings of MUSME 2005, Brazil (2005)
19. Pisla, D., Nicolae, P., Anneline, V., Bogdan, P., Bogdan, G., Dorin, L.: Kinematics and design of two variants of a reconfigurable parallel robot. In: Proceedings of ASME/IFToMM ReMAR2009, London (2009)
20. Pisla, D., Pisla, A.: The relationships between the shape of the workspace and geometrical dimensions of parallel manipulators. PAMM 4(1), 167–168 (2004)
21. Pisla, D., Itul, T., Vaida, C.: On singularities analysis for the 3-DOF parallel mini-robots. In: Acta Technical Napocensis, Series Applied Mathematics and Mechanics 50, vol. I, Technical University of Cluj-Napoca, Romania (2007)
22. Pisla, D., Plitea, N., Vaida, C.: Kinematic modeling and workspace generation for a new parallel robot used in minimally invasive surgery. In: Advances in Robot Kinematics: Analysis and Design, Springer, Heidelberg (2008)
23. Pisla, D., Pisla, A.: The relationships between the shape of the workspace and geometrical dimensions of parallel manipulators. PAMM 5, 213. DOI: 10.1002/pamm.200510084 (2004)
24. Plitea, N., Hesselbach, J., Pisla, D., Raatz, A., Vaida, C., Simnofske, M., Prodan, B., Burisch, A., Vidrean, A.: Modeling of parallel microrobots with two to six degrees of

freedom. In: Acta Technica Napocensis, Series: Machines Construction Materials, vol. 50, Technical University of Cluj-Napoca, Romania (2007)
25. Plitea, N., Vidrean, D., Pisla, D., Vaida, C., Gherman, B., Prodan, B.: Modeling and design of a mini parallel robot with four degrees of freedom. In: Acta Technica Napocensis, Series: Applied Mathematics and Mechanics 51, Vol. II, Technical University of Cluj-Napoca, Romania (2008)
26. Raatz, A.: Stoffschüssige Gelenke aus pseudoelastischen Formgedechniss-legierungen für Parallelroboter. Ph.D. Thesis, Technical University Braunschweig, Vulkan Verlag, Essen (2006)
27. Sefrioui, J., Gosselin, C.M.: Singularity analysis and representation of planar parallel manipulators. Robot. Autonomous Syst. 10, 209–224 (1992)
28. Yang, G., et al.: Design and kinematic analysis of modular reconfigurable parallel robots. In: SIMTech Technical Report (AT/01/010/AMS) (2001)

Kinematics and Movement Control of a Six-Legged Mobile Robot

V. Adîr, G. Adîr, and V. G. Adîr

Abstract The paper presents the kinematics of the movement for a six-legged mobile robot, inspired from the living world, as well as the command and control system, which allow the robot to move on different surfaces with different speeds. The stability of the robot during movement is assured by the tripod system. For generating the movement, through a command and control system, there are used stepping motors, bars and steel cables.

Keywords Command and control system · Mobile Robot · Tripod system

1 Introduction

The researchers from different corners of the world, study the biological models offered by the living world, trying to find the best solution [3, 4, 7, 8]. Their studies examine the component elements, the connection between these ones and the parameters which determine their characteristics. Many researches have shown that insects are moving just using their six or eight articulated legs [6]. As regards the relative position of legs with respect to the body, they are placed on the lateral parts of the body (arthropodes) or below the body (quadruped and biped vertebrates) [5, 6]. By making an analyze regarding insects, there can be seen some important characteristics, as: bilateral symmetry, poly-segmented body, even number of legs (four, six, eight, etc.)

V. Adîr (✉)
Department of Graphical Engineering, Department of Mechanisms and Robots, Department of Aerospace Engineering, University Politehnica of Bucharest, Bucharest, Romania

I. Vişa (ed.), *SYROM 2009*,
DOI 10.1007/978-90-481-3522-6_48,

2 Kinematics of the Mobile Robot

The experimental six-legged mobile robot that we have achieved [1], called RP 2000, represented in Fig. 1, has three systems: mechanical, driving and command and control system.

The *mechanical system* has a modular structure, consisting of a steel body, where six identical legs are driven by using bars and steel wires. Every leg is connected to the body by a rotational joint (G). The foot (A) is connected to the leg thru a spherical joint (B), that allows to maintain the stability of the mobile robot when moving on different kind of terrain. To support the movement, each leg is tight to the body structure thru a spring connected between C and D points. So, the leg has the So, the leg has the possibility to move back and forward, up and down (Fig. 2).

The *driving system* allows three functions:

- To command the impulses (to control the frequency of these impulses)
- To distribute the impulses according to the number of phases and the direction of the movement
- To raise the legs in an established order

The driving system includes eight stepping motors which act the mechanisms of the mobile robot.

The movement of the six-legged robot is done by using two phases:

- Raising and descent of the legs on the ground (supporting phase)
- Translation motion – forward and back (transfer phase)

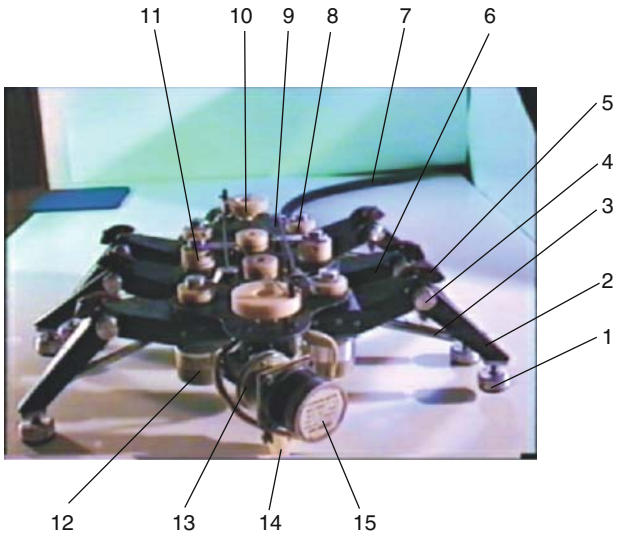

Fig. 1 Six-Legged Mobile Robot 1. Instep; 2. Leg segment I; 3. Spring; 4. Joint; 5. Wire; 6. Leg segment II; 7. Cable for power supply and command; 8. Fixing part I; 9. Rod; 10. Fixing part II; 11. Fixing part III; 12. Electric engine; 13. Reducer; 14. Wheel; 15. Electric motor

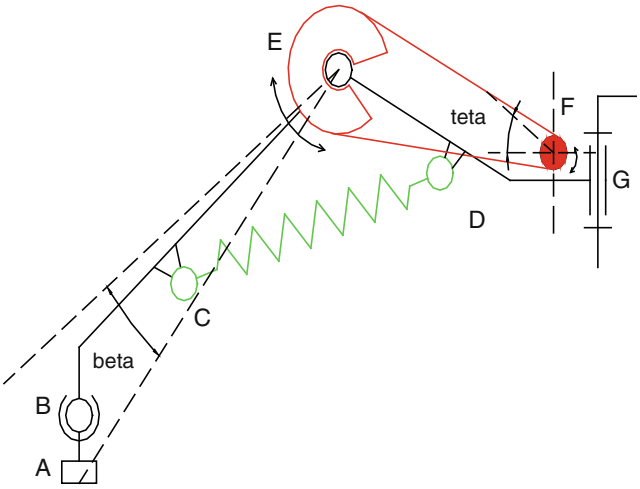

Fig. 2 Leg of the mobile robot

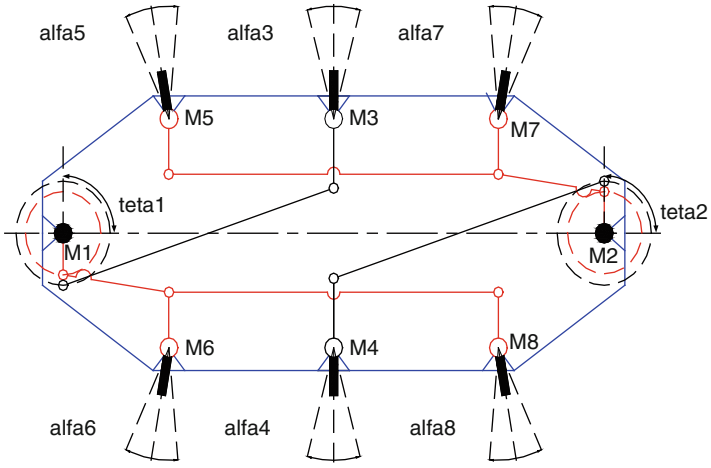

Fig. 3 Synchronization position of the robot

In the banned position, the mobile robot is sustained on the six legs. The legs will have a middle position. This position is well known as "synchronization position" of the mobile robot (Fig. 3).

The movement is achieved like this: the robot is successively sustained on three legs (acted by the stepping motors M4, M5, M7 or M3, M6, M8) and by acting the stepping motors M1, M2, it is obtained the shifting function (Fig. 3).

The *supporting phase* is achieved by using, at the beginning, the six legs of the mobile robot, and then, when starting the computing program, this phase is achieved by three legs, that assure the stability of the robot during movement.

The *transfer phase*, which make the robot to walk, has five sequences:

- Raising of three legs
- Rotation of these three legs (joint G), with a certain angle
- Descent of these three legs
- Supporting of the robot on three legs (base being a triangle) and the acting the motors to achieve the translation movement according to the computing program

To achieve the stability criterion, it is necessary to have, the same time, three legs on the soil, and the centre of gravity of the mobile robot has to be inside of the support triangle.

In Fig. 4 it is depicted the succession of the phases and sub-phases for achieving the movement of the mobile robot forward.

3 Command and Control System of the Six-Legged Mobile Robot

The *command and control system* contains the unit MINICONTROL, acting the eight axes of the stepping motors, according to a computer program. This system has all the necessary interfaces for acting the mobile robot (RP 2000), for connecting to an external process and to a data acquisition system. In Fig. 5 it is

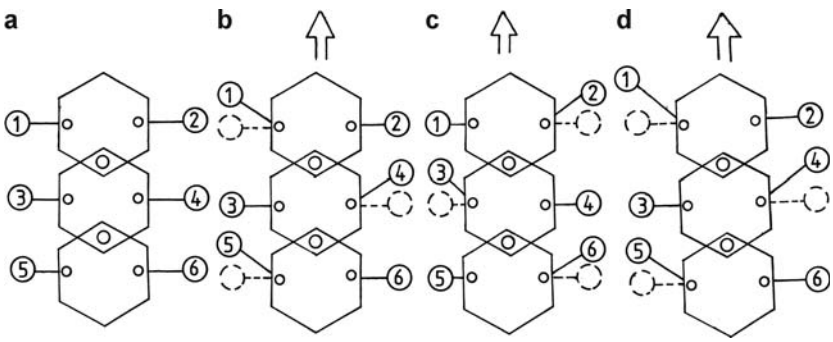

Fig. 4 Succession of the phases and sub-phases of the movement. Legend: (**a**) Initial position (Sustaining on the six legs); (**b**) Lifting of the legs 1, 4, 5, rotation forward and descent on soil; Lifting of the legs 2, 3, 6, acting of the electric motor for moving forward; (**c**) Rotation forward of legs 2, 3, 6, descent on soil; Lifting of the legs 1, 4, 5 and acting the electric motor for moving forward; (**d**) Rotation forward of the legs 1, 4, 5, descent on soil; Lifting of the legs 2, 3, 6 and acting the electric motor

depicted the connections scheme. In this figure there have been made the following notations:

M1, . . ., M8 – stepping motors; SSw – synchronization switch; LSw – limit switch; H/F – half/full step; E – enable; HP MON – display home position; PPI – programmable port interface; ADC ITF – analog digital conversion interface; PC – personal computer; MON – monitor.

The computer has a PCL 812 with the possibility of reading of 16 analog input of 12 bits resolution. The data transfer from PC to controller is accomplished on a parallel port.

By taking into consideration that the torque reserve of the stepping motors is limited by the rotational frequency and that the six-legged mobile robot could move, also, onto irregular surfaces, it is necessary to have an adaptable command [2, 4].

This command involves to have a permanent measurement of the torque in the motor shaft. This thing could be done by measuring the electric current into the reeling stator.

The electric current is measured as a medium value in the rotational period of the electromagnetic field in stator. The instantaneous maximum value of the current is limited by the protection circuits of the operating level to an adjustment value for each motor.

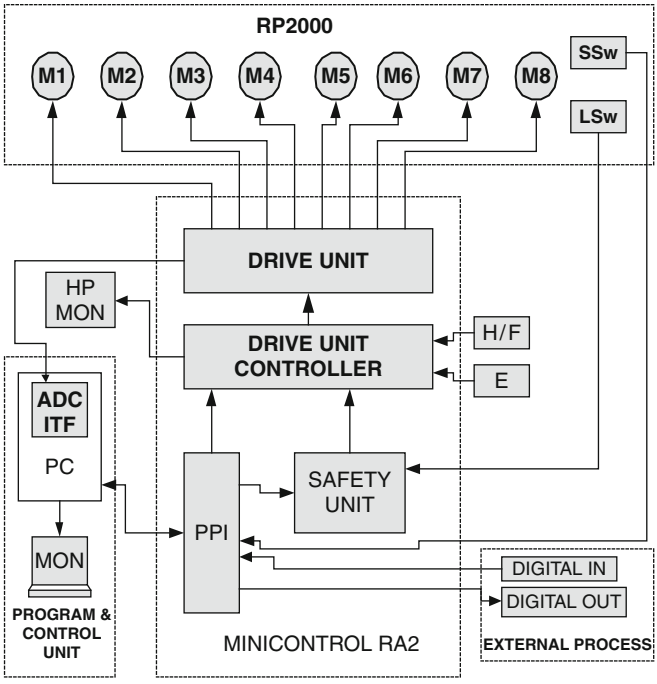

Fig. 5 Connections Scheme

With the view to have such command model, there have been achieved some measurements of the medium current (at the end of each eight steps), correlated to the open-loop programmed rotational frequency, when the walking robot is moving with different speed, on different surfaces of a variable inclination.

We have noticed that the torque value doesn't pass beyond the admissible maximum value for all motors, when the mobile robot is moving. This is possible because the testing conditions (surface, speed) have a necessary reserve, specifically to the open-loop command system.

The closed-loop shifting to the limit of the admissible parameters of the motor presume a higher shifting speed on irregular surfaces over the admissible limit of the mechanical compliance in the mechanisms of the mobile robot. In this case the real diagram will be located nearby the limit of the reference diagram, without passing beyond it and the reference torque diagram floats, depending on the variation of the frequency rotation of the engine.

4 Conclusions

The experimental six-legged mobile robot presented in this paper is designed to walk forward and backward, according to a computing program. The structure of this robot is based on biological principles, by copying the insects' locomotion. In spite of the fact that the action of the systems by using stepping motors has a low dynamics, it could be possible to test regulation algorithms to turn to maximum account resources, offered by one engine.

By continuous measurement of the torque, it is possible to increase the speed of motors till the maximum admissible value. Also, the torque motor is able to compensate the presence of some effort transducers, which is a very important fact for a mobile (walking) robot, especially when it is moving on an irregular terrain.

References

1. Adîr, V.: Ph.D Thesis, Contribuţii teoretice şi experimentale asupra analizei şi sintezei mecanismelor din construcţia roboţilor mobili. Politehnica University of Bucharest, Bucharest, Romania (2000)
2. Berns, K., Dillmann, R., Piekenbrock, S.: Neural networks for the control of a six-legged walking machine. Robot. Autonomous Syst. 14, 233–244 (1995)
3. Dudiţă, F., Gogu, Gr., Diaconescu, D.: Mecanisme articulate. Editura Tehnică, Bucureşti (1989)
4. Ferrell, C.: A comparison of three insects – inspired locomotion controllers. Robot. Autonomous Syst. 16, 135–159 (1995)
5. Gheţie, V.: Atlas de anatomie comparativă, vol. I. Editura Agro-Silvică de Stat (1954)
6. Grasse, P. P.: Traite de zoologie: Insectes, Tome IX. Mason et Cie Editors, Paris (1949)
7. Hasslacher, B., Tilden, M.W.: Living machines. Robot. Autonomous Syst. 15, 143–169 (1995)
8. Pfeiffer, F., Weidemann, H.J., Eltze, J.: Six-legged technical walking considering biological principles. Robot. Autonomous Syst. 14, 223–232 (1995)

LabView Based Control and Simulation of a Construction Robot

Th. Borangiu, F.D. Anton, and S. Anton

Abstract The paper describes a multiprocessor control system for construction robots integrated in a SOA designed as a layered CAD – CAE information structure. The motion control system addresses both the robot's mobile carrier and the partially closed-loop arm of cylindrical type; their motion control is embedded in a multiprocessor Motion Control system for which programming library was developed. Experimental results concerning the motion control of the 5-d.o.f. robot arm are reported.

Keywords Bricklaying robot · Embedded real time systems · KB Programming support · Multiprocessor systems · Robot motion control

1 Introduction

The nowadays demand on the manufacturing process in the building industry is constantly rising to enable competition for quality, standardization and decrease of production costs. The standardization is directly related both to replication of construction procedures (bricklaying, windows placing, application of mortar on walls, finishing operations – painting, polishing) and to increasing working productivity. These two objectives, subject to constraints of efficient use of materials resources and employment of workers, can be reached by using robots in the most common, monotonous, effort demanding building operations – from which the most representative is bricklaying for wall elevation [4].

Th. Borangiu (✉)
Department of Automatic Control and Industrial Informatics, University Politehnica of Bucharest, Bucharest, Romania

I. Vişa (ed.), *SYROM 2009*,
DOI 10.1007/978-90-481-3522-6_49,

Rationalisation efforts in the construction industry are more and more associated with the attempt to create information systems used to automate the building processes. Up to now, automated solutions are developed however in each case for each special building process. The repetition of development errors and the increased training expenditure for the users cause high development costs, which make an economic application of the automation systems often impossible. One possible solution for the above problems is an open and modular control for construction robots based on embedded systems operating in a Service Oriented Architecture (SOA), which means:

- Using autonomous guided vehicles as robotic arm carriers moving to pre planned locations in the building site [3, 6].
- Using the robot arm in working locations to perform various types of operations: bricklaying, finishing, etc.
- Using generic hardware modules (general purpose mathematic processors, motion controllers, universal motion interfaces, remote control and communication terminals) to build up embedded modular robot controllers adaptable to the working tasks and environment, external sensors, and material flow.
- Relying on open standard software (Linux-based real time operating system) and open solutions in software system design: the basic software system is created from a set of task-oriented modules and library functions such as: trajectory generator, motion tracking, end-effector set up, mobile platform navigator, inclination control, range finder and odometry localization, which are selected, attached and combined according to the set of particular services to be provided in a construction application, i.e. creating a Service Oriented Architecture (SOA) [4].
- Using a Knowledge Based Technology System (KBTS) to map technology specifications into production data and area robot work tasks and, by further access to a construction materials data base to automatically generate the parameters of application programs (base wall and brick stack locations, offsets in stacks, motion and grasping data (trajectory type, speed, pick offsets).

Research in control systems for construction robots is still seeking feasibility solutions and possibilities of large scale implementing, through integration with KBTS and databases on construction procedures and materials.

2 Robot Functionality and Operating Modes for Construction Tasks

Figure 1 presents the global robot system and its working environment with sensory control. The mechanical robot arm is a 5-d.o.f. partially closed-chain kinematic structure (with parallel linkages) of cylindrical type, carried by a 3-d.o.f. mobile wheeled platform. The resulting 8-d.o.f. mobile construction robot is able to move on quasi-horizontal prepared floors, and generates a 3.5 m-height workspace in 2D locations of the building site.

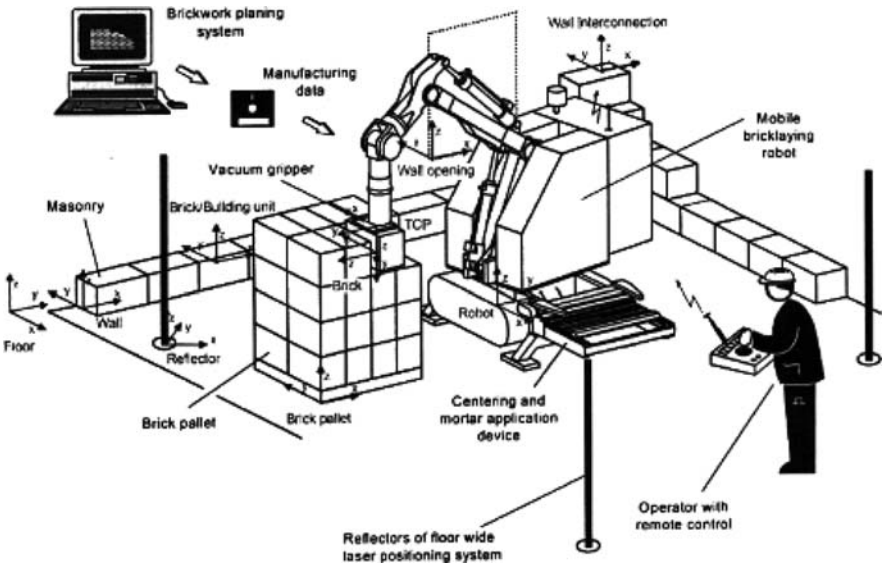

Fig. 1 The construction robot and its environment

The inclination of the mobile platform can be measured with inclinometers along two orthogonal symmetry axes and correspondingly corrected by means of a 4-d.o.f. mechanism electrically driven by four ac motors.

The mobile robot platform is a free-ranging (non-guided) wheeled vehicle, capable to avoid obstacles (e.g. brick pallets, walls) in a structured environment; its arm performs coordinated movements either in the Cartesian space or in the five-dimension joint space automatically at program execution or under manual control. A PC-based operator console is used both as teach pendant for robot point learning and as robot terminal for execution of monitor commands, program editing, debugging, execution start-up and monitoring.

The robot vehicle is a chassis with omni directional wheels. Two wheels (in diagonal locations) are driven by two asynchronous motors and generate respectively forward - backward displacements (when control signals are identical) and CW-CCW rotations (for opposite control signals); the remaining two are loose wheels – the angular displacement of one loose wheel being measured by an encoder. The third motor of the mobile robot platform drives turns simultaneously the four omni directional wheels via a common transmission mechanism.

In the most general situation, the displacement of the guided robot vehicle to a location within the building site is performed as a sequence of straight line displacements planned such that the contact with brick stacks of known location and dimension is avoided, whereas the shortest path is followed [6].

For each individual path segment, the four wheels of the robot's mobile platform are first turned along the direction towards the destination) point; then, the two actuated wheels drives the robot vehicle along this direction until the motion

program is completed. Brick pallets may be placed everywhere in (known locations) the building site; the robot will turn around them to avoid collision and then resume its planned path towards the destination.

Due to positioning errors of the robot vehicle (wheel slipping, different friction coefficients of the four omni directional wheels), an accurate auto locating procedure is started once the platform stops. This procedure is executed with a laser scanner mounted on the mobile platform, and three reflectors disposed in known locations $x_i, y_i, 1 \leq i \leq 3$ relative to the reference frame (x_0, y_0) of the building site. A range finder receives the distances $d_i, 1 \leq i \leq 3$ and computes by triangulation the Cartesian location $x_R, y_R$of the robot vehicle. For a (prepared) horizontal floor the reflectors are at the same height and are scanned by the laser beam in a 360° planar sweep.

3 Modeling and Embedded Motion Control of Robot Arm

3.1 Geometric Models of the Robotic Arm

The robot arm mounted on the wheeled platform is a 5-d.o.f. closed-chain (parallelogram linkage CDEF) mechanical structure of cylindrical type having the joint variables vector $\mathbf{q} = [\,\theta_1 \quad d_2 \quad d_3 \quad \theta_4 \quad \theta_5\,]^{\mathrm{T}}$. The point connecting the linkages CD and CF can be driven along two orthogonal (horizontal and vertical) directions, described by the joint variablesd_2, d_3. This means that the motion of point G is amplified by $\mathrm{k} = (\mathrm{L} + \mathrm{l})/\mathrm{l} \geq 1$ with respect to the motion of point C (Fig. 2). The end-effector wrist G is capable of two degrees of mobility: *pitch* (θ_4) and *roll* (θ_5).

Due to its closed structure, the Denavit-Hartenberg formalism and Luh-Paul-Walker Algorithm for Local Coordinate System Allocation cannot be used to get the implicit Direct Kinematics arm model, DKI. Due to this, a pure geometric approach was used to obtain the direct model: the location of an orthogonal frame is successively moved in important points of the arm structure, until the end-tip location P is reached. The DKI model is computed in two stages:

DK position model:

$$Pos(\ \theta_1, d_2, d_3, \theta_4, \theta_5) \rightarrow [X_H\, Y_H \quad Z_H\,]^{\mathrm{T}}$$

$$\begin{cases} X_P = X_H + g\cos\ \beta\sin(\ \theta_1 - \ \gamma) \\ Y_P = Y_H + g\cos\ \beta\cos(\ \theta_1 - \ \gamma) \\ Z_P = Z_H + g\sin\ \beta\left(1\ -\ 2\sin\left(\dfrac{\theta_5}{2}\right)\right) \end{cases}, \tag{1}$$

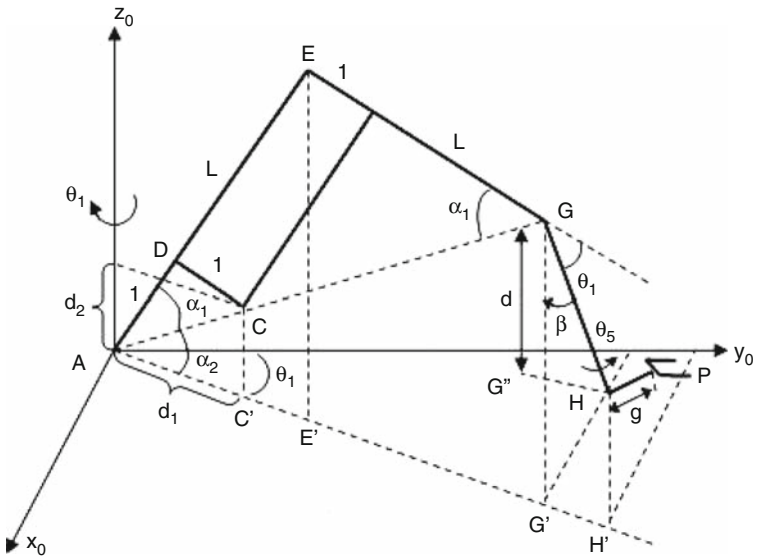

Fig. 2 The closed-chain kinematic structure of the 5-d.o.f. cylindrical robot manipulator

where

$$X_H = (kd_3 + G'H')\sin\ \theta_1$$
$$Y_H = (kd_3 + G'H')\cos\ \theta_1, \frac{l+L}{l} = k$$
$$Z_H = kd_2 - GG''$$

$$D = \sqrt{\frac{4l^2 - \left(d_2^2 + d_3^2\right)}{d_2^2 + d_3^3}},$$

$$\alpha_1 = \arccos\frac{\sqrt{\left(d_2^2 + d_3^2\right)}}{2l}, \alpha_2 = \arccos\frac{d_3}{\sqrt{d_2^2 + d_3^2}}$$

$$G'H' = \frac{d}{2l}[D(d_2\cos\theta_4 - d_3\sin\theta_4) + d_3\cos\theta_4 + d_2\sin\theta_4]$$

$$GH'' = \frac{d}{2l}[D(\ -\ d_2\sin\theta_4 + d_3\cos\theta_4) - d_3\sin\theta_4 - d_2\cos\theta_4], \theta_4\rangle\alpha_1 - \alpha_2$$

DK orientation model:

$$Orient(\theta_1, d_2, d_3, \theta_4, \theta_5) \rightarrow \mathbf{R}_5^0$$

The implicit homogenous orientation matrix $\mathbf{R}_5^0$ is derived below; its conversion to *rpy* minimal format is done at run time whenever relative transformations are used to plan arm motion.

$$\mathbf{R}_5^0 = \begin{bmatrix} s_1 \sin\beta & -c_1c_5 + s_1 \cos\beta s_5 & c_1s_5 + s_1 \cos\beta c_5 & 0 \\ -c_1 \sin\beta & -s_1c_5 - c_1 \cos\beta s_5 & s_1s_5 - c_1 \cos\beta c_5 & 0 \\ \cos\beta & -\sin\beta s_5 & -\sin\beta c_5 & 0 \\ 0 & 0 & 0 & 1 \end{bmatrix}$$

where

$$s_1 = \sin\theta_1, c_1 = cos\theta_1, s_5 = \sin\theta_5, c_5 = \cos\theta_5$$

$$\alpha_1 = ar\cos\frac{\sqrt{d_2^2 + d_3^2}}{2l}, \alpha_2 = ar\cos\frac{d_3}{\sqrt{d_2^2 + d_3^2}},$$

$$\beta = 90^\circ - \alpha_1 + \alpha_2 + \theta_4$$

The closed-loop Solution of the Inverse Kinematics problem is obtained using a combined algebraic and geometric computation [2]:

$$\mathbf{T}_5^0(\ \theta_1, d_2, d_3,\ \theta_4,\ \theta_5) = \begin{bmatrix} & \mathbf{R}_5^4 & & X_P \\ & & & Y_P \\ & & & Z_P \\ 0 & 0 & 0 & 1 \end{bmatrix} = \begin{bmatrix} n_x^* & s_x^* & a_x^* & X_P^* \\ n_y^* & s_y^* & a_y^* & Y_P^* \\ n_z^* & s_z^* & a_z^* & Z_P^* \\ 0 & 0 & 0 & 1 \end{bmatrix} \quad (2)$$

$$\begin{cases} \sin\ \beta = \sqrt{n_x^{*2} + n_y^{*2}} \\ \cos\ \beta = n_z^* \end{cases} \Rightarrow$$

$$\beta = \mathrm{a\,tan\,2}\left(n_z^*, \sqrt{n_x^{*2} + n_y^{*2}}\right)$$

$$(\ \beta = \ \beta^*) \Rightarrow \theta_4 - \alpha_1 + \alpha_2 = \beta^* - 90^0$$

$$\cos\ \beta = n^*$$

where

$$\theta_5 = a\tan 2\left(-\frac{a_z^*}{\sqrt{n_x^{*2} + n_y^{*2}}}, -\frac{s_z^*}{\sqrt{n_x^{*2} + n_y^{*2}}}\right)$$

$$\theta_1 = a\tan 2\left(-\frac{n_z^* s_z^* \left(a_x^* + a_z^*\right)}{\sqrt{n_x^{*2} + n_y^{*2}}}, \frac{a_z^* a_x^* - s_z^* s_x^*}{\sqrt{n_x^{*2} + n_y^{*2}}}\right)$$

$$\theta_4 = \beta^* + \alpha_1 - \alpha_2 - 90^0$$

$$d_2 = \frac{2(l+L)\cos\alpha_1 \sin\alpha_2}{k},\ \alpha_1 = ar\cos\frac{Y_H^* - d\sin\beta^*\cos\theta_1}{2(l+L)\cos\alpha_2\cos\theta_1}$$

$$d_3 = \frac{2(l+L)\cos\alpha_1\cos\alpha_2}{k}$$

where $\alpha_2 = a\tan 2\left(\frac{X_H^* - d\sin\beta^*\sin\theta_1}{\sin\theta_1}, Z_H^* + d\cos\beta^*\right)$

$$X_H = X_P^* - g\cos\beta^*\sin(\theta_1 - \chi^*) = X_H^*$$

$$Y_H = Y_P^* - g\cos\beta^*\cos(\theta_1 - \chi^*) = Y_H^*$$

$$Z_H = Z_P^* - g\sin\beta^*\sin\left[1 - \sin\frac{\theta_5}{2}\right] = Z_H^*$$

where $\chi = ar\sin\left[\frac{\sin\theta_5/2}{n_z^*}\right] = \chi^*$

Bricklaying tasks assume not only pick-and-place sequences, but also linear Cartesian motions whem mortar is applied to bricks held in the gripper.

Other construction tasks requiring the execution of linear Cartesian pats of the robot arm are: wall finishing, painting etc. In addition, all locations of interest in CAD files are specified in Cartesian coordinates and directly mapped to robot points as transformations relative to the world frame (reference frame attached to the building site) of the robot arm.

Consequently, the arm's trajectories are planified in the Cartesian space according to the algorithm:

$$t = t_0$$

loop:

Wait new control period (sample);

Update the end-effector's operational trajectory planner $\mathbf{TP}(t)$: computing the necessary position and velocity data $\{\ \mathbf{p}(t),\quad \phi(t),\quad \mathbf{p}(t), \omega(t)\ \}$ in Cartesian space at current time t;

Compute the closed form inverse kinematics solution in joint space, IK[$\mathbf{TP}(t)$], corresponding to $\mathbf{TP}(t)$;

IF $t = t_{\text{final}}$ exit;

ELSE go to *loop*.

The method consists in generating support points by linear interpolation along the imposed operational path, and adding a desired speed profile. Then **TP** converts then the Cartesian support points in joint representations and feds them to the trajectory tracking unit. The **TP** has been implemented using the RMRC technique:

$\delta\mathbf{q}_c(t) = \mathbf{J}^{-1}(\mathbf{q}_c(t))\delta\mathbf{X}_c(t)$, where

$$\delta\mathbf{q}_c(t) = \mathbf{q}(t_{k+1}) - \mathbf{q}(t_k)\ \delta\mathbf{x}_c(t) = I_{\text{OS}}(\mathbf{x}_d(t_{k+1}) - \mathbf{dk}(\mathbf{q}(t_k))$$

One can observe that both the interpolation for support points and their conversion from Cartesian to joint representation are incremental, which reduces the computation time and increases the band width of the **TP** [1].

3.2 Embedded Control of the Construction Robot

Motion tracking is performed with dual DSP-GPGA NI 735x motion controller with PID and feed forward laws; for linear Cartesian trajectories the contouring mode is used, according to which the computed joint-space support points are fed to a reference buffer as a set of relative values with respect to the initial point, followed by cubic spline interpolation between them subject to imposed speed and acceleration constraints.

The robot controller is designed as a ***multiprocessor structure***, including four interconnected processing areas (Fig. 3):

1. A real-time, embedded controller NI PXI 8196 acting as a mathematical processor for execution of application programs, motion planning and trajectory generation t centralized level):
   - Planning motion of the robot arm from trained or edited robot points and specified path types, and of the mobile vehicle by comparing site maps with path specifications (for collision avoidance with interior walls or brick stacks);

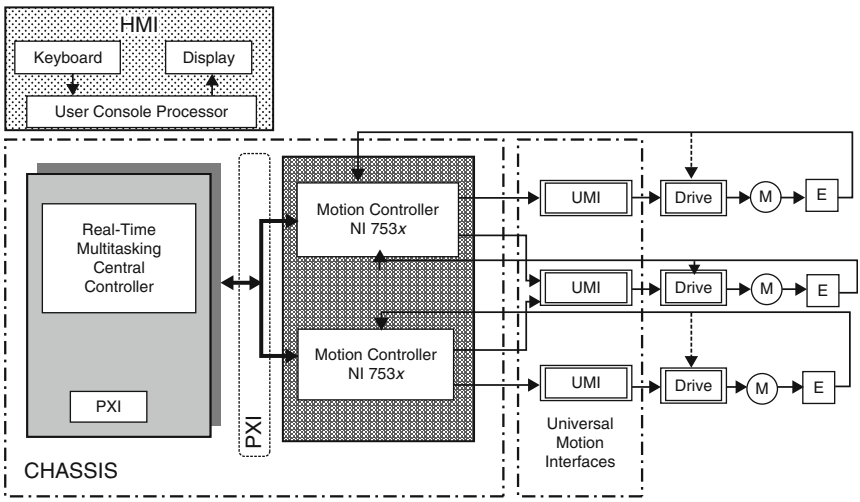

Fig. 3 Industrial implementing of the multiprocessor robot controller

- Generating linear Cartesian trajectories of the arm and vehicle, coordinate joint trajectories of the arm, single-axis platform displacements to compensate deviations from horizontality;
- Locating the mobile vehicle by triangulation from range finder data;
- Communication with the operator's console for data and program transfer, diagnosis and production reports.

2. Two NI 735x motion controllers addressing three groups of coordinated axes (group 1:5 axes of the cylindrical robot arm; group 2:3 axes of the robot vehicle; 4 axes of the platform inclination mechanism):

- Slave status for motion tracking in vector mode, i.e. coordinated motion in groups of axes configured by the PXI controller;
- Loop control and S-type speed profile are embedded at motion control level, with PID- (position and speed) and feed forward control;
- Arm and platform calibration using breakpoint modes (drive axis until occurrence of external event – limit switch);
- Monitoring encoders, limit switches, external devices, protections and sequencing commands

3. Twelve motor servo drive boards (power amplifiers) connected to the motion controllers through universal motion interfaces (UMI).
4. Operator console, acting both as robot terminal and teach pendant – a laptop wireless connected to the PXI real-time embedded central processor.

The system applications were developed differently: motion planning, kinematics model computation and trajectory generation are written as C++ routines, whereas the set of motion tracking routines: vector control (electronic gearing) – for coordinated joints motion, contouring – for traversing Cartesian support points along linear trajectories or breakpoint motion – for calibration were developed as LabVIEW applications with the NI LabVIEW Real-Time module, and downloaded in the embedded real-time PXI central controller via Ethernet.

The embedded code is run on a real-time, multitasking operating system.

Figure 4 shows the generic mechanism used to create, convert and transfer the application code to the hardware processing modules. This mechanism is based on integrated C support for developing multi-platforms of Motion Control type.

The system controlling the Windows application code programming tools (Visual C++ and LabVIEW) shares an *Application Programming Interface* – API with the Motion Control (MC) language.

The same software operations are in the MC programming language and in the function library, which simplifies program migration and reduces adaptation times for applications developed in different languages.

The Real Time Operating System of the robot controller is pre-emptive and re-entrant, having the capability to execute both on mono processor and multiprocessor architectures, and supporting Intel processors. The OS architecture is modular and consists of two main layers (Fig. 5):

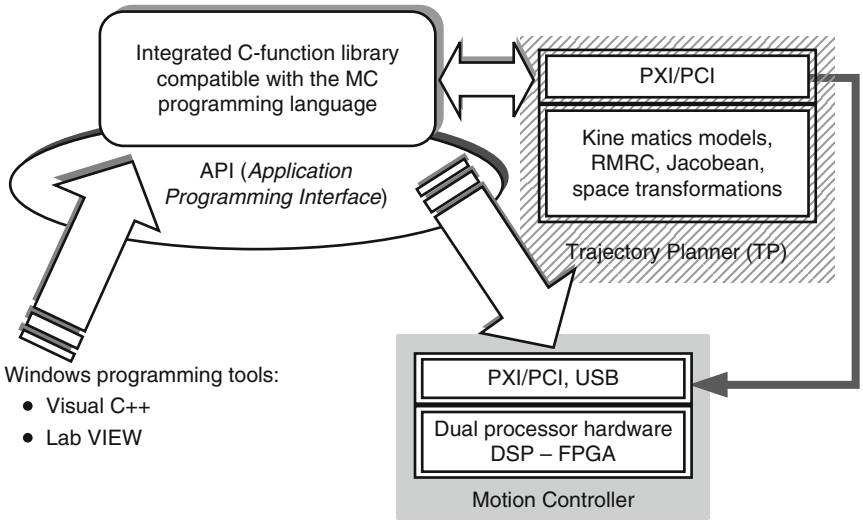

Fig. 4 Creating, converting and transferring motion control application code for MC hardware units

- A *user module* (with limitations to system resource access), and
- A *kernel module*, having unrestricted access to the system's memory and external devices.

The **User module** contains subsystems capable to pass I/O requests to suitable software drivers of the kernel module, by using the I/O manager.

Two subsystems are on the user module layer:

- The *Environment* subsystem (E_Ss) executing applications written for various types of OS,
- The *Integral* subsystem (I_Ss) operates specific system functions for the E_Ss.

The Executive interfaces and all subsystems in the User module deal with I/O, object management, security and process management.

The hybrid **Kernel** is positioned between the HAL (Hardware Abstraction Level) and the Executive, in order to provide multiprocessor synchronization, planning and interrupt- and execution threads resolution, as well as trap processing and exception solving. The Kernel module consists from executive services, in their turn composed from several modules performing specific tasks, kernel drivers, a Microkernel and HAL (*Hardware Abstraction Level*). HAL includes specific code for hardware controlling I/O interfaces, interrupt controllers and multiple processors [5].

The Microkernel is responsible for driver setup at the start moment. The drivers in the Kernel module are on three layers: high-, medium- and low level. Low level drivers are either inheritance drivers controlling directly a device, or busses for the PnP hardware. The PnP Manager is used to detect and initialize at system start

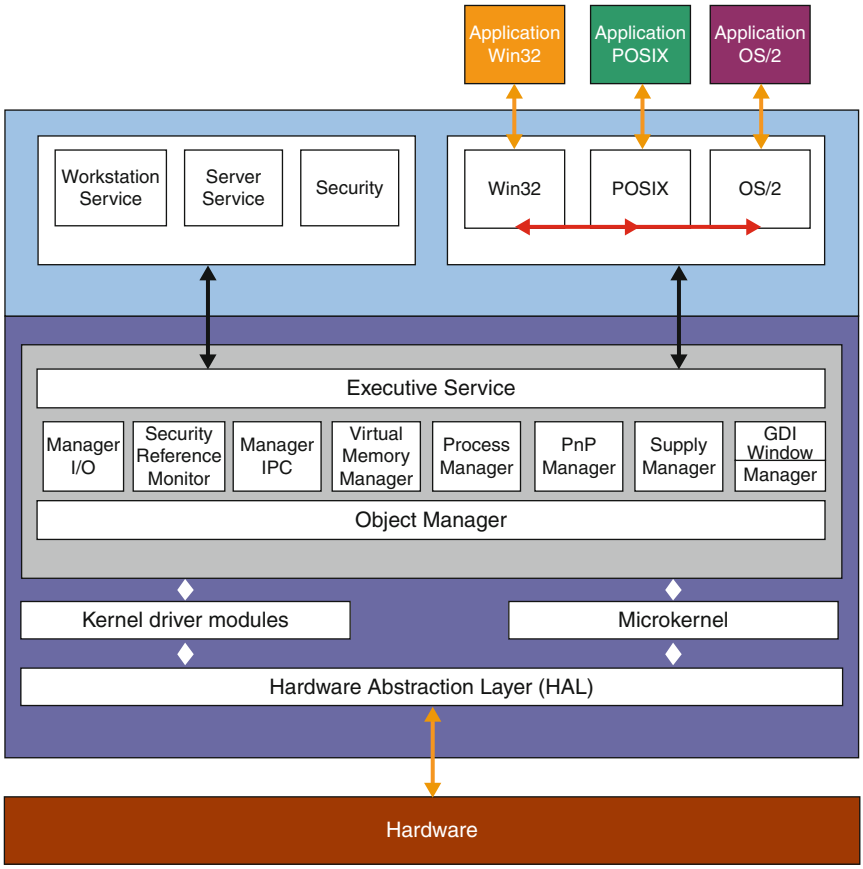

Fig. 5 The architecture of the operating system (OS)

up the Plug and Play devices. Low level drivers are either inheritance drivers controlling directly a device, or busses for the PnP hardware. The PnP Manager is used to detect and initialize at system start up the Plug and Play devices.

4 Experimental Work Conclusions

The reported research was carried out in the framework of a National CEEX Grant funded by the Ministry of Education and Research, and aims to develop a robot system and KBTS for automating construction tasks (Fig. 6).

On the test has been observed that the positioning precision of the entire structure is 0.2 mm due to mechanical movement transmission, also the robot needs to move using small accelerations and trapezoidal speed profile, on high accelerations/decelerations the mechanical structure starts to vibrate.

Fig. 6 The construction robot

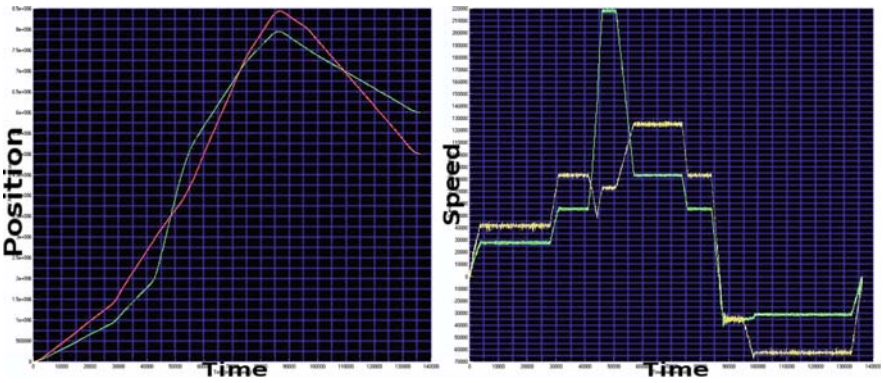

Fig. 7 Blending moves for two axes (position – left, and speed-right)

Another problem which we try to solve is that the motors are commanded by two different types of frequency converters which give two different types of speed control (Fig. 7.) (the KEB converters seems to be more stable – green line, the other converter is LS-600).

In Fig. 7 the internal PID loops of the converters are disabled and is used only the PID control loop of the NI controllers.

Figure 8 shows simulation results of RMRC motion control algorithms for linear paths in the joint space of the robot arm. In the left side is represented the

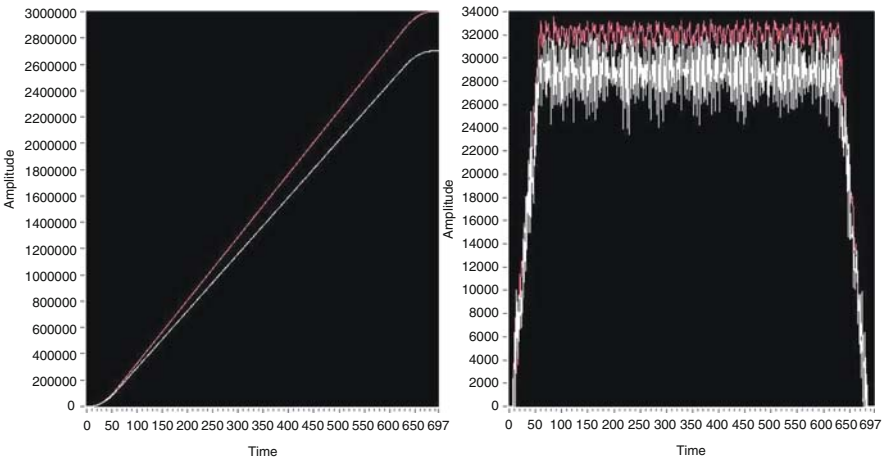

Fig. 8 RMRC and electronic gear path control results equal to 1 and the other values in the range (–1, 1)

Position/Time characteristic, and in the right side is presented the Speed/Time characteristic (Red – KEB, White – LS600). Linear joint space paths are done by the trajectory generator and motion tracking processor according to the "electronic gear" algorithm below:

1. Start from two trained robot joint configurations $\theta_1, d_2, d_3, \theta_4, \theta_5$: initial p_i and final p_f.
2. Compute the rotation/translation path differences between each element of p_f and p_i, as the difference array $\theta_{1\Delta}, d_{2\Delta}, d_{3\Delta}, \theta_{4\Delta}, \theta_{5\Delta}$.
3. Determine the axis maximum path difference

$$\Delta q_i = \max_{1 \le i \le 5} (\theta_{1\Delta}, d_{2\Delta}, d_{3\Delta}, \theta_{4\Delta}, \theta_{5\Delta}) \tag{3}$$

corresponding to the master axis (*MA*) motion for the current trajectory segment.

Compute the gear ratio between the maximum path difference and each element of the difference array; the *gear array* $GA = \theta_{1\delta}, d_{2\delta}, d_{3\delta}, \theta_{4\delta}, \theta_{5\delta}$ results. This array will have one value equal to 1 and the other values in the range (–1, 1).

4. The positions of the five axes are modified incrementally by adding the values from the gear array multiplied by a value obtained by dividing the maximum difference to the resolution of the motor mounted on this axis (the other slave axes (*SA*) will have at least the same resolution). The value of n in the equation below incrementally changes axes position along the linear joint path:

$$\begin{aligned} MA\_pos &= (MA\_pos - offset) + \Delta q_i / n \\ SA\_pos &= (MA\_pos - offset) \cdot GA \end{aligned} \tag{4}$$

5. Actions in step 5 are executed until the difference between p_i and p_f is small enough.

The parameters of the motion control algorithms were tuned to provide 1 mm worst error for Cartesian displacements and 0.2 mm worst positioning error.

In Fig. 8 we can see the big difference between the two converters; the LS-600 converter has problems in keeping the constant speed. The position is reached, but the speed has big variations which can lead to problems when the robot is loaded with high payload.

References

1. Borangiu, Th.: *Task-driven control of robots integrated in intelligent manufacturing systems*. In: Proceedings of 3rd IFAC Workshop Intelligence and Manufacturing Systems IMS'95, Pergamon Press, Oxford, pp. 79–89 (1995)
2. Borangiu, Th., Oltean, E.: *Multi-processor design of nonlinear robust motion control for rigid robots*. Lecture Notes in Computer Science, 1798, Springer, Berlin, pp. 224–238 (1999)
3. Nehmzow, U.: Mobile Robotics: A Practical Introduction. Springer, London (2003)
4. Pritschow, D., Kurz, J., Mc Cornack, S.E., Dalacker M.: *Practical sensor strategies for on-site positioning of a mobile bricklaying robot*. In: Proceedings of the 13th ISARC Symposium, Tokyo, Japan, pp. 281–290 (2006)
5. Tourassis, V., Tourassis, M., Ang, M.: *Task decoupling in robot manipulators*. J. Intell. Robot. Syst. 14, 283–302 (1995)
6. Zhao, Y.: *Kinematics, dynamics & control of wheeled mobile robot*. In: Proceedings of IEEE International Conference on Robotics and Automation, Nice, pp. 91–96 (1992)

Synthesis Method of Planar Mechanisms Approximating Open Paths

J. Buśkiewicz

Abstract The paper addresses synthesis of planar mechanisms approximating open paths. The technique is introduced and discussed on the example of the four-bar linkage, although it can be applied to a planar mechanism with four links as it does not refer to mathematical formulas describing the geometry of a mechanism. It suffices to know the trajectories of the joints of the coupler a point of which traces a required path. An objective function is proposed and minimized by the evolutionary algorithm. The synthesis of four-bar linkages generating arcs given parametrically including straight line and square angle are carried out. The results obtained prove that the method is effective.

Keywords Evolutionary algorithms · Path synthesis · Planar mechanisms

1 Introduction

Optimal synthesis of mechanisms is recently a subject of intensive studies. Most of the papers focus on seeking mechanisms approximating closed curves. Open path synthesis seems to be far more complex problem as the arc, that best fits the desired one, has to be extracted from the generated curve.

The geometrical adaptation technique [1] was proposed and used in open-path synthesis of the four bar linkage. This method reduces the number of optimized parameters to five as an objective function is independent of the position, orientation and size of a curve. The synthesis problem [2] was described as initial value problem of a system of ordinary differential equations. Four bar linkages generating straight line and square angle were synthesized for illustrative purposes. The present

J. Buśkiewicz
Institute of Applied Mechanism, Poznan University of Technology, Poznan, Poland

I. Vişa (ed.), *SYROM 2009*,
DOI 10.1007/978-90-481-3522-6_50,

paper utilizes the coupler angle function in open path synthesis. This function, but in a different way, was applied to optimal synthesis of four-bar linkages tracing closed curves [3]. The synthesis of a linkage approximating straight line has been widely concerned. Analytical techniques [4–9], e.g. geometric and displacement matrix methods, were elaborated to synthesize four-bar linkage generating coupler curve a part of which is an approximate straight line. To some extent the method considered in the present paper addresses the curvature theory introduced recently into mechanism theory as a tool for the kinematic design [10–12] providing a concise description of the geometric properties of planar mechanisms.

The presented method is universal and is not restricted to a specific planar mechanism as it does not refer to mathematical formulas describing the geometry of a mechanism. It suffices to know the trajectories of the joints of the coupler a point of which traces a given path. The idea of the method consists in determining coefficients of an approximation of the coupler angle function. As far as the synthesis is concerned, satisfactory results are obtained when the harmonic function, e.g. sine or cosine approximates the angular position of the coupler. Moreover, the lengths of the coupler have to be determined. The method reduces the number of optimized parameters to seven.

In case of the four bar linkage, the joints connecting the coupler with the crank and rocker move along either a circle or a circular arc. An objective function measures the deviation of the computed joints paths from ideal circles. The radiuses and centres of the circles are the lengths of the crank and rocker and the locations of their fixed ground pins, respectively. These dimensions are the secondary results of the method, i.e. they are not optimized parameters. The method can be easily extended to an arbitrary planar mechanism (e.g. the crank-slider mechanism) with three moveable links connected by revolute and/or prismatic joints. The objective function is minimized by the evolutionary algorithm. The method is applied to synthesize straight line, square angle as well as other shapes.

2 Method Description

The method is discussed and introduced on the example of the four bar linkage. The main idea is to determine coefficients of a function that approximates angular position of the coupler. The coupler point C traces an arc given parametrically in the coordinate system:

$$x = x(t), y = y(t) \tag{1}$$

Without loss in generality, it can be taken that$t \in \langle 0, 1 \rangle$. The coupler angle function α is measured anticlockwise from the positive direction of the horizontal axis to the first arm of the coupler, as is shown in Fig. 1.

The angle is expressed in terms of the linkage dimensions and the crank angle. The coupler angle function is periodical of period 2π, e.g. for a crank-rocker it takes

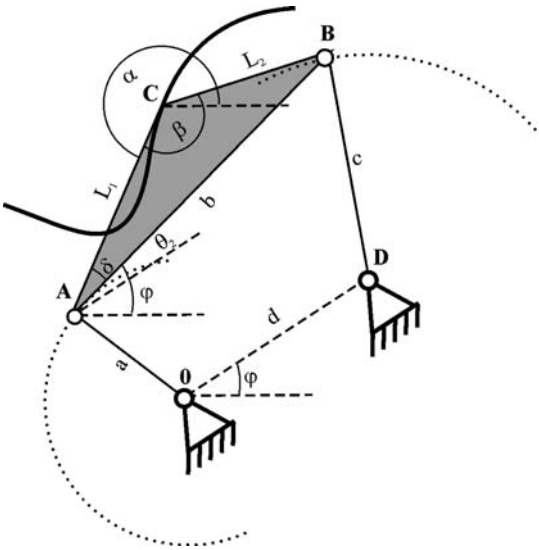

Fig. 1 The coupler angle function α for a four-bar linkage

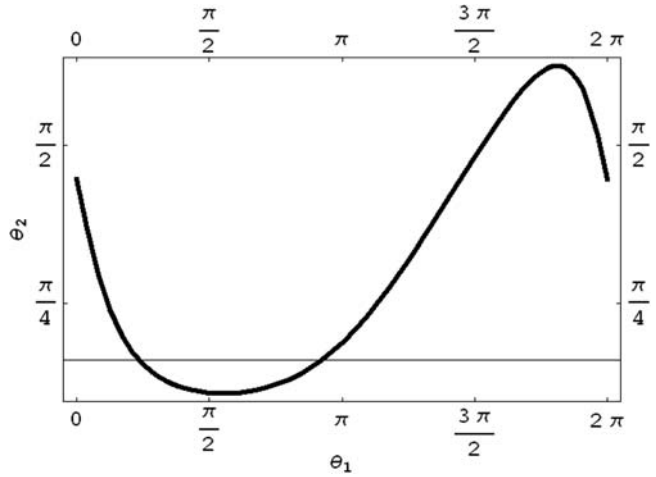

Fig. 2 The graph of θ_2 for a crank-rocker four-bar linkages with $a = 2$, $b = 3$, $c = 3$, $d = 3$

values in the interval $(0, 2\pi)$ (or $(-\pi, \pi)$), and each value is taken twice (Fig. 2). The angle α is related to the angle θ_2 by $\alpha = \theta_2 + \delta + \varphi + \pi$. Although θ_2 is frequently given in the formulae for the position of a four bar linkage, the method introduces the angle α not to associate the method with a particular mechanism or its specific position.

The description aims at minimizing the number of parameters optimized in search of an optimal solution. The maximum number of the parameters equals nine $(x_O, y_O, x_D, y_D, a, b, c, L_1, \delta)$ when the optimal synthesis of the four bar linkage generating closed curves is considered. Five parameters suffice to define the linkage when a description is invariant under translation, scaling, rotation, mirror reflection, change of the starting point, and direction reversal. Then, a curve is sought the shape of which best approximates the shape of a required curve. Scaling is a complex problem, that requires special attention in open path synthesis. In methods utilizing closed curves descriptions the curve length is normalized and taken as equal to 1. In open path synthesis an arc is a part of a closed path and its starting and ending points are not known. That is why two additional parameters have to be added in open path synthesis, namely the boundary positions θ_{10} and θ_{11} specifying the angle through which the crank rotates when an arc is traced. These two angles increase the number of the parameters to 11.

When geometric properties are extracted from an arc, the number of the parameters can be reduced to five [1]. But if the method processes parametrical equations, the minimum number of the parameters lies between 6 and 11.

To return to the method, when the coupler point moves along a given arc, the coupler angle function has to vary in such a way that the coupler joints A and B trace out arcs of circles. Hence, the optimized parameters are the coupler lengths L_1, L_2, b (or, which is more convenient, the angle β instead of b), and coupler angle function coefficients. Taking into account the information on the formula and the character in which the angle θ_2 varies, the following form of the approximation of the coupler angle function is proposed:

$$\alpha = A \sin(\omega t + \alpha_S) + \gamma \tag{2}$$

The angle α is allowed to vary in $\langle 0, 2\pi)$, hence, $A \in \langle 0, 2\pi)$. The crank angle $\theta_1 \in (\theta_{10}, \theta_{11}) \subset \langle 0, 2\pi)$ corresponds, but is not equal, to the argument of the sine function $(\omega t + \alpha_S)$ (analogy to the expression $\theta_1 = \theta_{10} + (\theta_{11} - \theta_{10})t$). Taking into account that$t \in \langle 0, 1\rangle$, ω belongs to $\langle -2\pi, 2\pi\rangle$. The negative values enable α both clockwise and anticlockwise rotations of the crank. The phase angle $\alpha_S \in \langle -2\pi, 2\pi)$ corresponds to the position of the crank $\theta_1 = \theta_{10}$ at which an arc starts to be traced. The coupler angle function is sensitive to rotation of a mechanism. When a mechanism is rotated through an angle $\gamma \in \langle -2\pi, 2\pi\rangle$, α is shifted by γ.

An important question to be discussed is the influence of the approximation of α on the method efficiency. In a four bar linkage θ_2 is given as

$$\theta_{2_{1,2}} = 2arctg \frac{-E \pm \sqrt{E^2 - 4DF}}{2D} \tag{3}$$

where $D = \cos\theta_1 + K_5 - K_1 + K_4 \cos\theta_1$, $E = -2\sin\theta_1$, $F = K_1 + K_5 + (K_4 - 1)\cos\theta_1$,

$$K_1 = \frac{d}{a}, K_4 = \frac{d}{b}, K_5 = \frac{-a^2 - b^2 + c^2 - d^2}{2ab}$$

For given dimensions of a four-bar linkage one can find the coefficients of α function so as to achieve an arbitrary value of θ_2. Then for a value of θ_1 there exists such t that

$$\theta_2(\theta_1) = \alpha - (\delta + \varphi + \pi) = \theta_2 *, \tag{4}$$

where right-hand side of equation (4) denoted as $\theta_2 *$ is the approximation of θ_2. It follows that $\theta_1(t)$ can vary in such a way that θ_2 varies like a sine function. The explicit form of the function $\theta_1(t)$ is not required, and the method does not impose any constraints on the angular velocity of the crank. The only requirement is that $\theta_1(t)$ has to be monotonic to ensure one direction of the crank rotation.

$$\frac{d}{dt}(\theta_2(\theta_1(t))) = \frac{d\theta_2}{d\theta_1}\frac{d\theta_1}{dt} = A\omega\cos(\omega t + \alpha_S) \tag{5}$$

If only θ_2 and α are monotonically decreasing or monotonically increasing in the same intervals (have extrema at the same points), the sign of the quotient of $\frac{d\alpha}{dt}$ and $\frac{d\theta_2}{d\theta_1}$ does not change. Thus $\frac{d\theta_1}{dt}$ has a constant sign, which means that $\theta_1(t)$ is monotonic. The above reasoning also shows that accuracy of the approximation of θ_2 is not so essential. The inaccuracy of this description arises from the fact that the arc equations (1) and α are coupled to each other by the argument t, i.e. the

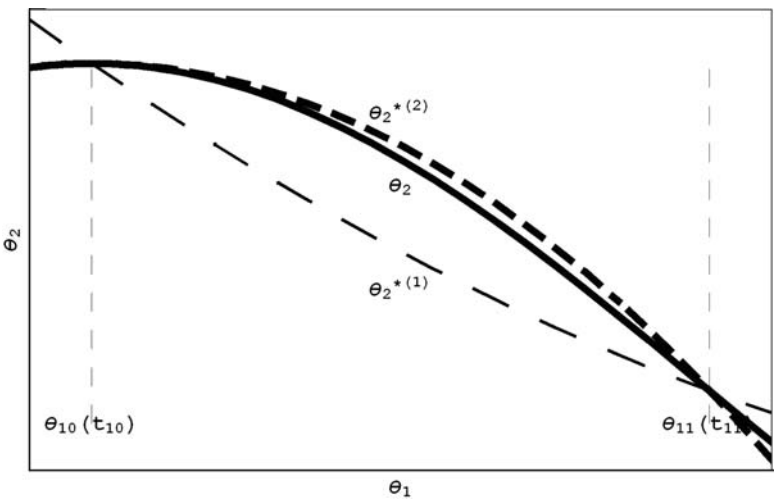

Fig. 3 Two exemplary functions $\theta_2^{*(1)} = \alpha_1 - (\delta + \varphi + \pi)$, and $\theta_2^{*(2)} = \alpha_2 - (\delta + \varphi + \pi)$ approximating the angle θ_2 over interval $(\theta_{10}, \theta_{11})$

argument of the sine has to change linearly as $(\omega t + \alpha_S)$ over $t \in \langle 0, 1\rangle$ while the arc is traced (Fig. 3). This is the main disadvantage of the method.

To sum it up, the method combines the general properties of the coupler angle function and the dimensions of the coupler. Seven parameters are optimized: L_1, L_2, β, A, ω, α_S and γ. This gives two parameters over the minimum number, but four below the maximum one, in the synthesis of four-bar linkage. The description is invariant under translation (i.e. the parameters defining the problem do not change when an arc is translated), which allows x_A, y_A to be excluded. The further reduction arises from the way in which the coupler angle function is approximated. α is expressed in terms of A, ω, α_S and γ instead of a, b, c, d, θ_{10} and θ_{11}.

Direction reversal and mirror reflection result in a change of ω, α_S signs, scaling affects L_1, L_2, and rotation γ.

An arc is traced during incomplete rotation of the crank. Numerical examples show that if the range of the crank angle, for which an arc is traced, is small, the parameter γ can be neglected. In these cases, the function (2) with $\gamma = 0$ gives a satisfactory approximation of the coupler angle function.

The paper discusses an analytical-numerical method to solve synthesis problem. The first approach consists in deriving explicit formulas for radiuses of curvature of the paths traced by the joints A and B:

$$\rho_{A,B} = \frac{\left(x''_{A,B}{}^2 + y''_{A,B}{}^2\right)^{\frac{3}{2}}}{y''_{A,B}x'_{A,B} - x''_{A,B}y'_{A,B}}, \tag{6}$$

where $x_A = x + L_1 \cos\alpha$, $y_A = y + L_1 \sin\alpha$,
$x_B = x + L_2 \cos(\alpha + \beta)$, $y_B = y + L_2 \sin(\alpha + \beta)$.

The mean radiuses are computed after integrating over $t \in \langle 0, 1\rangle$:

$$a = \rho_{AV,A} = \int_0^1 \rho_A dt,\ c = \rho_{AV,B} = \int_0^1 \rho_B dt \tag{7}$$

The expressions (7) are the lengths of the crank and coupler. The objective function is taken as follows:

$$E_\rho = \frac{\left|\rho_{A,\max} - \rho_{A,\min}\right|}{a} + \frac{\left|\rho_{B,\max} - \rho_{B,\min}\right|}{b} \tag{8}$$

The lengths should be placed in prescribed intervals. The other constraints specify permitted values of the coupler lengths. Moreover, the constraints are imposed to force that the crank rotates in one direction and that the angular displacement of the crank, during which an arc is traced, is greater than a prescribed value $\Delta\theta_1$.

$$a_S \le a \le a_E,\ b_S \le b \le b_E,\ L_{1S} \le L_1 \le L_{1E}, L_{2S} \le L_2 \le L_{2E}, \tag{9}$$

$$\forall t_1 > t_2,\ \theta_1(t_1) < \theta_1(t_2) \text{ or } \theta_1(t_1) > \theta_1(t_2),\ \theta_{11} - \theta_{10} \ge \Delta\theta$$

It may happen that a short part of a path, which diverges from a circle, significantly affects the mean value of the curvature. This results in a high value of the error and strongly aggravates the convergences of the algorithm minimizing the objective function. For this reason an approach less sensitive to local oscillations of the curvature has been elaborated.

For the sake of the implementation of the method as the computer algorithm realizing the synthesis task, the paths are discretized and given as a set of m points. With the curves x_A,y_A,x_B,y_B being generated, sets of the parameters x_{0i},y_{0i},a_i and x_{Di},y_{Di},c_i are determined. a_i is the radius of the circle located at (x_{0i},y_{0i}) and passing through three points $A_{1i}(x_A(t_{1i}),y_A(t_{1i}))$, $A_{2i}(x_A(t_{2i}),y_A(t_{2i}))$, $A_{3i}(x_A(t_{3i}),y_A(t_{3i}))$,

where $t_{1i} = i\Delta t$, $t_{3i} = 0.5 + i\Delta t$, $t_{2i} = 0.5(t_{3i} + t_{2i})$, $\Delta t = 1/m$ and $i = 1..m^* = \lfloor m/2 \rfloor$ (Fig. 4).

It is easy to show that for each triple of points:

$$x_{Oi} = \frac{b_1 a_{22} - b_2 a_{12}}{a_{11} a_{22} - a_{12} a_{21}},\ y_{Oi} = \frac{b_2 a_{11} - b_1 a_{21}}{a_{11} a_{22} - a_{12} a_{21}}$$
$$a_{Oi} = \sqrt{(x_A(t_{2i}) - x_{Oi})^2 + (y_A(t_{2i}) - y_{Oi})^2} \tag{10}$$

where: $a_{11} = 2(x_A(t_{1i}) - x_A(t_{2i}))$, $a_{12} = 2(y_A(t_{1i}) - y_A(t_{2i}))$, $a_{21} = 2(x_A(t_{1i}) - x_A(t_{3i}))$,

$$a_{22} = 2(y_A(t_{1i}) - y_A(t_{3i})),$$

$$b_1 = x_A^2(t_{1i}) + y_A^2(t_{1i}) - x_A^2(t_{2i}) - y_A^2(t_{2i}),$$

$$b_2 = x_A^2(t_{1i}) + y_A^2(t_{1i}) - x_A^2(t_{3i}) - y_A^2(t_{3i}).$$

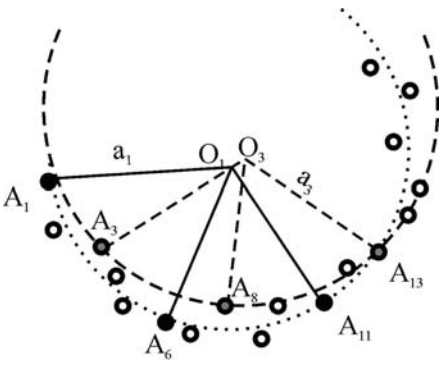

Fig. 4 An illustration of the method. Two chosen circles passing through points A_1, A_6, A_{11} and A_3, A_8, A_{13} of the radius a_1 and a_3, respectively

Averaging these values, one gets the coordinates of the ground pin of the crank and the crank length, respectively

$$x_O = \frac{\sum_{i=1}^{m^*} x_{0i}}{m^*}, y_O = \frac{\sum_{i=1}^{m^*} y_{0i}}{m^*}, a = \frac{\sum_{i=1}^{m^*} a_{Oi}}{m^*} \tag{11}$$

The same equations (10–11) enable the coordinates of the rocker ground pin (x_D, y_D) and the rocker length $c = |\mathrm{BD}|$ to be determined.

The objective function has a form:

$$E_\rho = \frac{\max|\mathrm{A_iO}| - \min|\mathrm{A_iO}|}{a} + \frac{\max|\mathrm{B_iD}| - \min|\mathrm{B_iD}|}{c} \tag{12}$$

Then, the remaining parameters are computed as follows:

$$b = L_1^2 + L_2^2 - 2L_1L_2\cos\beta, d = \sqrt{(x_O - x_D)^2 + (y_O - y_D)^2},$$

$$\varphi = arctg((y_D - y_O)/(x_D - x_O)).$$

It should be noted that these dimensions are the secondary results of the method, i.e. they are computed after the optimisation process.

Assuming that $\mathbf{p_i}$ is the vector between points A_{i-1} and A_i, the following condition allows to check whether the crank rotates in one direction:

$$\cos(\mathbf{p_i}, \mathbf{p_{i+1}}) = \frac{\mathbf{p_i} \circ \mathbf{p_{i+1}}}{|\mathbf{p_i}||\mathbf{p_{i+1}}|} < \pi \tag{13}$$

3 Numerical Solutions

Numerical simulations have been carried out in the search for an arc being a section of

- A closed coupler curve obtained during complete rotation of the crank and best fitted to a given arc
- An open curve obtained during incomplete rotation of the crank (Grashof condition are not met) and best fitted to a given arc

The following arcs are chosen:

- Straight line: $x = 4t$, $y = 0$,$t \in \langle 0, 1\rangle$
- Square angle: $x = 2t$, $y = 0$, $t \in \langle 0, 0.5\rangle$, $x = 1$, $y = 2t - 1$, $t \in (0.5,1\rangle$
- Parabola: $x = t$, $y = 3t(t - 1)$, $t \in \langle 0, 1\rangle$

- Sine: $x = 4t$, $y = \sin(2\pi t)$, $t \in \langle 0, 1 \rangle$
- Test: the arc is generated by the four-bar linkage: $a = 1$, $b = 2$, $c = 2$, $d = 2$, $L_1 = 3$, $\delta = 1$, $1.5 \leq \theta_1 \leq 4.5$

The cases comprise the arcs given parametrically and the arc precisely traced by the coupler point of the specified four bar linkage and for specified range of the angle through which the crank rotates. The latter case is chosen for verification purposes as many four-bar linkages drawing the same paths exist. This way, the influence of the coupler angle function approximation on accuracy of results may be verified on the example for which a precise solution exists.

Both crank-rocker and double rocker four-bar linkages are allowed. Most solutions neglect the parameter γ in the approximation (2) since the growth in computational cost resulting from optimizing one more parameter has not been compensated by a significant improvement of the results obtained. The explanation and condition for such a simplification is provided in Section 2. The objective function is minimized utilizing the evolutionary algorithm. It is not described in depth as the classical approach is applied. The optimal parameters obtained in the synthesis of the four bar linkage are collected in Table 1. The dimensions of the mechanisms generating given arcs are collected in Table 2. Table 3 presents the constraints imposed on mechanisms.

Good approximations are obtained for arcs given by 10 points. The square angle synthesis proves that a solution can be improved by increasing the number of points. Solutions are subject to some constraints. Except a few cases, the minimum angle $\Delta\theta_1$, through which the crank has to rotate the coupler point to draw an

Table 1 The optimal parameters

Arc/Error	Optimized parameters						
	L_1	L_2	β	A	ω	α_S	γ
Straight line $E_\rho = 0.019$	4.02	1.06	0.64	2.69	1.04	0.56	0 n.o.[a]
Square angle 1 $E_\rho = 0.09$	12.88	6.84	0.61	0.33	2.75	–4.66	0 n.o
Square angle 2 $E_\rho = 0.1$	14.42	10.27	0.44	0.26	2.14	1.74	0.13
Sine $E_\rho = 0.07$	5.11	3.52	1.32	1.41	0.84	0.01	0 n.o
Parabola $E_\rho = 0.017$	10.27	11.88	5.26	1.6	–0.34	1.02	0 n.o
Test $E_\rho = 0.054$	7.61	4.13	0.5	4.1	0.52	0.8	0 n.o

[a]n.o. – not optimized

Table 2 The parameters of the four-bar linkages

Arc	Four-bar linkage parameters							
	a	c	x_O	y_O	x_D	y_D	θ_{10}	θ_{11}
Straight line	1.14	5.54	0.22	2.89	2.83	5.34	0.55	4.096
Square angle1	6.92	7.12	6.94	-0.24	1.75	–1.18	–3.74	–2.61
Square angle2	5.6	9.21	9.44	0.95	3.36	–0.89	–3.55	–2.58
Sine	9.52	1.41	–3.01	5.11	2.2	3.63	–0.28	0.21
Parabola	4.99	39.32	5.6	13.63	48.4	16.67	3.87	4.81
Test	4.81	3.95	–0.38	2.26	–0.94	0.31	2.24	3.76

Table 3 The constraints imposed on the four-bar linkage parameters

Arc	Constraints					
	$L_{1E}L_1$	L_2L_{2E}	Max(a)	Max(c/a)	$\Delta\theta_1$	m
Straight line	20	30	5	5	π– c-r[a]	10
Square angle1	15	10	8	5	$\pi/8$ – c-r	30
Square angle2	15	15	5	5	$\pi/8$ – r-r[b]	10
Sine	20	30	10	5	$\pi/8$ – r-r	10
Parabola	20	30	5	10	$\pi/8$– c-r	10
Test	20	30	5	5	$\pi/4$ – c-r	10

[a]c-r – crank-rocker, [b]r-r – rocker-rocker four-bar linkage

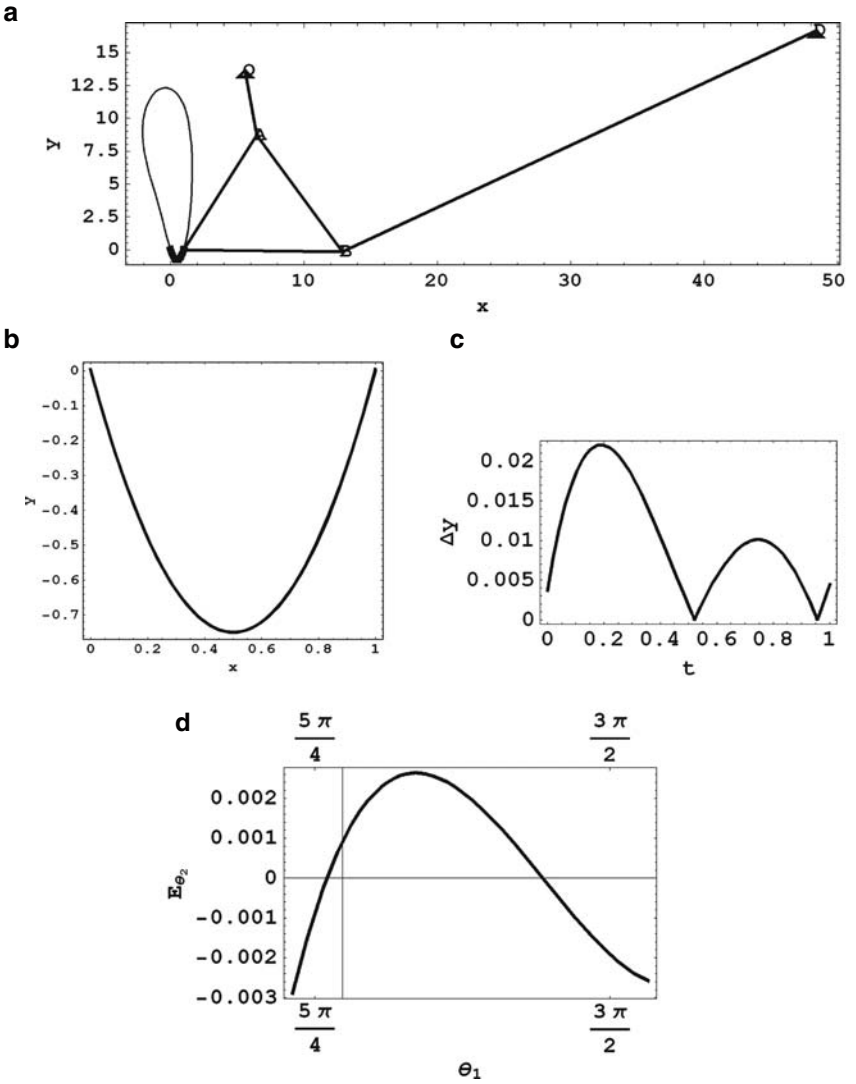

Fig. 5 The solutions for the parabola (**a**) the four-bar linkage obtained (**b**) comparison of the synthesized and given path (**c**) variation in y-value, (**d**) the error E_{θ_2}

arc, is $\pi/8$. This condition is imposed to reduce the workspace of a mechanism obtained, and is enhanced by specifying the maximum values of the coupler dimensions, crank length, and c/a. In general, the accuracy of approximation may be improved by decreasing $\Delta\theta_1$. Depending on accuracy obtained either the crank-rocker (or double crank) or double rocker mechanisms have been accepted (e.g. a double rocker mechanism approximates the sine much more accurately than

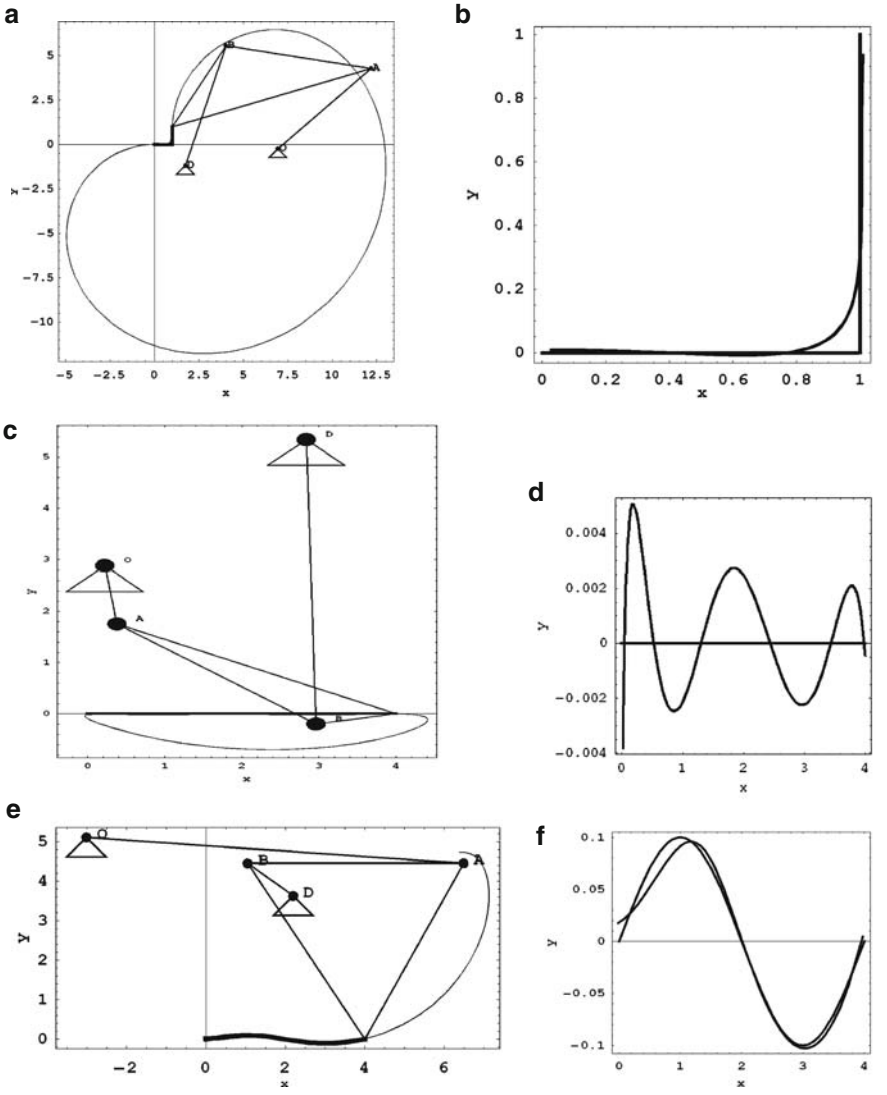

Fig. 6 The solutions for the square angle (**a**,**b**), straight line (**c**,**d**) and sine (**e**,**f**). The four-bar linkages obtained and comparisons of the synthesized and given paths

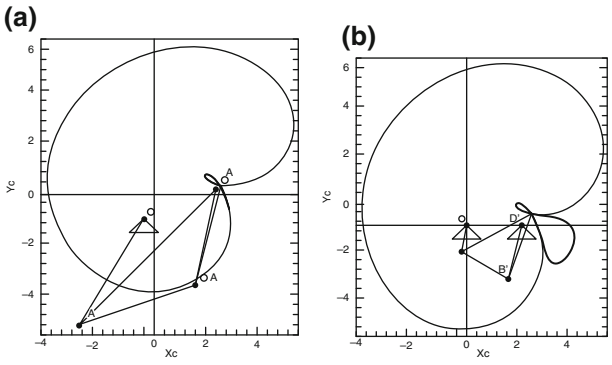

Fig. 7 The solution for the test arc (**a**) the four-bar linkage obtained, (**b**) the four-bar linkage generating the curve containing the test arc

a crank-rocker). To reject double rocker mechanisms, a penalty function is added to the objective function if Grashof conditions are not met. Two solutions for the square angle are presented. In the example square angle 2, γ is also optimized and Grashof conditions are not imposed on the four-bar linkage, nonetheless, the accuracy is not significantly improved in comparison with the case square angle 1 obtained for 30 points on the arc. The number of points should be taken carefully. An excessive number of points not only does not improve a solution but also increases the computational costs. The remaining examples are obtained under assumption that $\gamma = 0$. Figures 5 and 6 show the mechanisms obtained, a comparison of the arcs synthesized and given. The variation in y-value between the parabola and its approximation is presented in Fig. 5c. As the function (2) approximates the coupler angle function, it is obvious that for determined dimensions the actual angle function θ_2 varies from $\theta_2 *$. The graph 5d presents the error $E_{\theta_2} = \theta_2 - \theta_2 *$ and shows that the angles vary slightly. In Fig. 7 the curve is presented that the test arc is a part of. Although the synthesized mechanism differs from the one which precisely generates the test arc, their coupler curves have one common section – that is the test arc. In this case the solution approaches to a precise one.

4 Conclusions

The novel technique for open path synthesis has been introduced. The method proves to be effective in the synthesis of the four-bar linkage and can be easily applied to the planar mechanisms with four links connected by prismatic/revolute joints. The simplicity of the method makes it suitable for computer implementation. The author hopes that the idea enables elaborating analytical methods for specific arcs or mechanisms. The disadvantage is the dimensional form of the description, which prevents the number of the optimized parameters from being reduced.

References

1. Sanchez Marin, F.T., Gonzalez, A.P.: Open-path synthesis of linkages through geometrical adaptation. Mech. Mach. Theory 39, 943–955 (2004)
2. Lio, M.D., Cossalter, V., Lot, R.: On the use of natural coordinates in optimal synthesis of mechanisms. Mech. Mach. Theory 35(10), 1367–1389 (2000)
3. Hongying, Y., Dewei, T., Zhixing, W.: Study on a new computer path synthesis method of a four-bar linkage. Mech. Mach. Theory 42, 383–392 (2007)
4. Jianyou, H., Weixiang, Q., Huishe, Z.: Study on synthesis method of λ-formed 4-bar linkages approximating a straight line. Mech. Mach. Theory 44, 57–65 (2009)
5. Vidosic, J.P., Tesar, D.: Selections of four-bar mechanisms having required approximate straight-line outputs, Part I, II, III. J. Mech. 2, 23–44, 45–59, 61–76 (1967)
6. Karelin, V.S.: On the synthesis of the inverted slider-crank mechanisms for approximate straight line motion. Mech. Mach. Theory 21(1), 13–18 (1985)
7. Hodges, P.H., Pisano, A.P.: On the synthesis of straight line, constant velocity scanning mechanisms. J. Mech. Des. 113(12), 464–472 (1991)
8. Dijksman, E.A., Smails, A.T.J.M.: λ-formed 4-bar linkages set in a translation-position to design mechanisms approximating a straight line. Mech. Mach. Theory 31(8), 1033–1042 (1996)
9. Dijksman, E.A., Smails, A.T.J.M.: How to exchange centric inverted slider cranks with λ-formed four-bar linkages. Mech. Mach. Theory 35, 305–327 (2000)
10. Pennock, G.R., Kassner, D.J.: Kinematic analysis of a planar eight-bar linkage: application to a platform-type robot. J. Mech. Des. 114(1), 87–95 (1992)
11. Pennock, G.R., Sankaranarayanan, H.: Path curvature of a geared seven-bar mechanism. Mech. Mach. Theory 38(12), 1345–1361 (2003)
12. Pennock, G.R.: Curvature theory for a two-degree-of-freedom planar linkage. Mech. Mach. Theory 43(5), 525–548 (2008)

Kinematic Calculus Modelling of a Handling Arm Driving System

I. Daj

Abstract In the paper a calculus model of cinematic geometric analysis of a variant of mechanism actuated with hydraulic cylinder is derived and presented as a base of a synthesis CAD version for such a system. It is about a variant of the ranging arm cutting drum system as the working unit of the coal cutting shearer-loaders. On the basis of the derived model, a Mathcad application is used in order to interactively design the considered structure on the criterion of imposed limits for the connecting-rod oscillation angle and pressure angle.

Keywords Modelling · Kinematics · Analysis · Synthesis

1 Introduction

In the paper, the studied handling arm and ranging drum mechanism represents the active working part of the mining cutter-loaders, as it is shown in Fig. 1 [1, 3].

The handling and ranging removal $\varphi = \varphi(s)$ of the cutting drum D is realized by the ranging arm RA of l_b length.

This can be positioned on cutting height $H\ (\varphi(s))$, inside a specific $[\varphi\ ]$ angular interval of working, $\varphi \leq \varphi_{max.}$

The $\varphi = \varphi(s)$ positioning movement of the ranging arm RA, is developed by the hydraulic cylinder HC as driving element.

This is having linear actuating s motion as input quantity in the handling four-link device formed as shown in the structural design presented in Fig. 2 [4].

I. Daj
Department of Product Design and Robotics, Transilvania University of Braşov, Braşov, Romania

I. Vişa (ed.), *SYROM 2009*,
DOI 10.1007/978-90-481-3522-6_51,

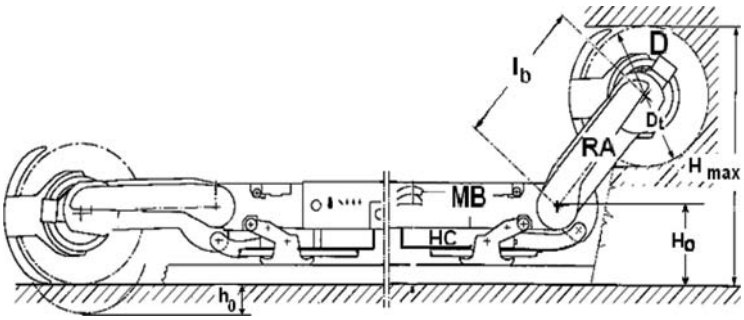

Fig. 1 The constructive variant of ranging drum cutter-loader system

Fig. 2 Structural, geometric and kinematic modelling

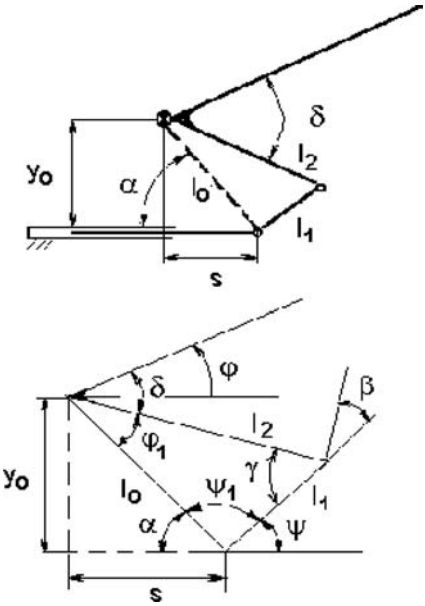

This mobile arm subassembly is jointed to the machine central body *MB* by swivel connections. The H_0 weight is a machine system constructive parameter, being generally a cutter loader specification.

In the paper it is about the version having the hydraulic cylinder fixed under the shearer-loader body. So, in this case a four-link mechanism is formed, in which the driving piston-rod is linked to the handling balancer-arm by an articulated connecting-rod (Fig. 1).

In this improved constructive variant the driving hydraulic cylinder works in more favourable conditions, being solidly mounted and better protected. In the same time, using the articulated connecting-rod, the pressure angle variation in the

active flexible joint on the arm, can be much improved by dimensioning and designing suitably the connecting-rod.

Coherently, that is solvable by an adequate synthesis calculus. The base of such a calculus version, shown below, is the possible correlation between this pressure angle variation $\beta = \beta(s)$, and the variation of the connecting-rod oscillation angle $\psi = \psi(s)$, the piston displacement s being the input quantity (Fig. 2).

2 Cinematic Analysis Modelling

A geometric and kinematic modelling of the driving mechanism, version presented, is proposed in Fig. 2.

The simplicity and efficiency of this modelling is based on the cinematic triangular contour, formed by two sides of constant length, l_1 and l_2 (as constructive dimensions) and the side of the variable length, l_0.

The handling-arm position is given by the $\varphi = \varphi\ (s,\ \delta)$ angle, having s as command input; δ is a specific constructive parameter.

The angles φ_1, Ψ_1 and the transmission angle $\gamma = \gamma(s)$, are auxiliary calculus quantities. These angles can be calculated directly by the cosine theorem, as internal angles defining the triangular configuration of the driving mechanism mobile contour, as it is shown in Fig. 2.

For the same configuration a right angle triangle is permanently defined by the sides $y_{0,}$, l_0 and s. This right angle triangle allows to define the variable angular quantity $\alpha = \alpha\ (s,\ y_0\ )$.

The position angle φ and the oscillating angle Ψ, are both variable: $\Psi = \Psi\ (s)$, being in correlation with $\varphi = \varphi\ (s)$, for $s \leq s_{max}$.

With all these calculus modelling specifications and in respect of geometrical configuration from Fig. 2, the functional quantities φ and Ψ can be expressed by the following simple formulas, as basic calculus relations:

$$\varphi = \varphi_1 + \ \delta - \ \alpha; \Psi = \ \pi - (\Psi_1 + \ \alpha). \tag{1}$$

At the same time, the H cutting height as operating coordinate of the machine can be expressed by a functional dependence:

$$\mathrm{H} = \mathrm{H}(\varphi(\mathrm{s}))\, \mathrm{S} \leq \mathrm{H}_{\max} \ \Leftrightarrow \mathrm{s} \leq \mathrm{s}_{\max,} \tag{2}$$

being influenced directly by the constructive parameters l_b – the arm length, and D_t – the drum diameter (Fig. 1).

Based on (1) and (2), using the cosine theorem and other mathematical formulas and models, the functional expressions and quantities of the calculus procedure can be well defined. The variable position of l_0, towards the base of four-link mechanism is given by the variable angle α.

These variable quantities are defined by the following relations:

$$l_0(s) = \left(y_0{}^2 + s^2\right)^{1/2};$$

$$\alpha(s) = \operatorname{atan}\left(y_0/s\right); \tag{3}$$

In the Eq. (3), y_0 is a constant geometrical parameter, as constructive dimension which marks the arm articulation fixed on the machine body.

The quantities l_1, l_2 and δ are also geometrical and constructive parameters of the system, as it is shown in Fig. 2.

The position of handling-arm is given by the angle $\varphi = \varphi\,(s,\delta)$, having s as input variable command and δ as constant constructive parameter.

The interior angles φ_1 and ψ_1 are auxiliary calculus quantities; γ is the transmission angle and β the pressure angle between connecting-rod and handling-arm, having the functional variation

$$\beta = \pi/2 - \gamma, \tag{4}$$

where γ can be calculated directly by the cosine theorem, as interiors angles of the variable cinematic contour, as mentioned above. With all these explanations, the relations and the quantities of computation are all well established.

Given this calculus modelling and based on real constructive dimensions as *input data,* a computation can be realised. The principal sections of this kind of application are presented in the Annex of calculus.

3 Synthesis Proposed Version

Referring to the quantities and to the relations of computation, mentioned above, for the efficiency and for generalisation of the calculus, the following relative values will be introduced:

$$\sigma = s/y_0; \quad \lambda_1 = l_1/l_0; \quad \lambda_2 = l_2/l_0; \; k = \lambda_2/\lambda_1. \tag{5}$$

In this way, on the base of (3) and (5), it results:

$$\alpha = \operatorname{atan} 1/\sigma; \; \lambda_2 = \lambda_1/k \tag{6}$$

So, keeping count of (1) and (6), the angles of oscillation of connecting-rod can be expressed as $\beta = \beta(\lambda_1', \lambda_2', k, \sigma)$.

The values of λ_1' and λ_2' are determined from the geometrical, constructive and functional conditions of the system, as *the triangle inequalities and a practical interval of variation for s.*

The limits of this interval of s variation are implicated as restrictions in calculus running.

Imposing certain limit values to ψ variation, we can obtain a corresponding variation for β.

By an adequate choice of the parameters l_1, l_2 and δ, oscillation angle ψ can attain the most possible value (90°, at limit) while β can take a minimum possible value (0° at limit), for a certain angular functional space $\varphi(s)$, of the handling-arm, with $s_{min} < s < s_{max}$.

The synthesis process is an iterative and interactive one, of CAD type application. Such a computing application variant – Mathcad session – is presented in calculus Annex enclosed below.

4 Conclusions

In respect to what is shown above, we can conclude that to a certain connecting-rod length l_2, in this constructive variant, the pressure angle $\beta(s)$ can take minimum values corresponding to a certain functional work space $\varphi(s)$ of the cutter-loader handling-arm.

On the other hand, the calculus modelling is contrived so that a flexible CAD process can be realized. This is realized efficiently by fructifying the designer contribution based on knowledge and experience.

Concretely, the contribution is based on real specific data interactively applied to design engineering process of a certain functional-constructive variant of such a specific mechanical system.

References

1 Daj, I.: Mecanismul brat-tambur al Combinelor miniere. Proiectare optimizare. Ed. Universitas, Petroşani (2000)
2 Daj, I., Stareţu, I., Ciobota, M.: Contributions to an optimal synthesis of a handling arm driving mechanism with hydraulic cylinder – CAD application. În: buletinul "The 8-th IFToMM International Symposium on Theory of Machines and Mechanisms," vol. I, pp. 89–94. Universitas Politehnica of Bucharest – SYROM (2001)
3 Daj, I.: Contribuţii la perfecţionarea concepţei constructive a asamblului braţ organ de lucru pentru maşinile tehnologice miniere. Teza de doctorat, Universitatea din Petroşani (1999)
4 Daj, I, Andras, I.: Model geometrico - cinematic generalizat privind subansamblul braţ mobil port-tambur al combinelor de extragere, ca mecanism de manevrare-poziţionare. În Buletinul Simpozionului naţional cu participare internaţională PRASIC 1998, vol. Mecanisme, pp. 55–60. Braşov (1998)
5 Boiko, N.G.: e.a.: Ispolnitelnie organi ocistnih combainov dlia tonkih pologih plastov. Donnecina, Donetsk (1996)

Synthesis of a Bi-Axial Tracking Spatial Linkage with a Single Actuator

D. Diaconescu, I. Vişa, M. Vatasescu, I. Hermenean, and R. Saulescu

Abstract Aiming to reduce the complexity of the solar tracking, this paper proposes a system based on R-R-S-S linkage, which acts only with the help of one actuator. The work presents the cinematic synthesis of a spatial linkage, based on the request of the solar direct radiation maximization falling perpendicularly upon the PV platform, in the case of Brasov's climatic conditions. The linkage can be adjusted during each season or it can be non-adjustable during the whole year. To compare these two situations, regarding the amount of received solar direct energy, this paper also includes numerical simulations made in two atmospheric conditions: clear sky and estimated real sky.

Keywords Adjustable tracking linkages · Azimuth tracking · Bi-axial tracking linkage · PV module · Received solar radiation

1 Introduction

The electrical energy delivered by a PV module depends on the degree of received direct solar radiation and on the PV efficiency. The maximum amount of solar energy can be obtained only when the solar rays are normal on the PV module surface [5, 7]. A method for increasing the amount of solar radiation can be achieved by using mechanical systems for the orientation of the modules in accordance with the path of the sun. Basically, the tracking systems are mechanical systems with M = 1 or M = 2 degrees of mobility [3] (corresponding with the number of revolute axes – mono-axial or bi-axial), driven by rotational or linear actuators which are

D. Diaconescu (✉)
Department of Product Design and Robotics, Transilvania University of Braşov, Braşov, Romania

I. Vişa (ed.), *SYROM 2009*,
DOI 10.1007/978-90-481-3522-6_52,

controlled in order to ensure the optimal positioning of the modules on each light day of the year [1].

A main part of today's researches and market trends focus on the bi-axial types of tracking systems. Also new on the research platform are the tracking mechanisms used for Concentrating PV systems (CPV), which require a high tracking accuracy, implicit a complex functional structure. Aiming to reduce the structural complexity of a tracking system, during the past years, bi-axial systems appeared, that use a mono-mobile mechanism with a single actuator.

One patented solution shows that the system adjustment can be conducted by means of a spatial cylindrical came with a complex mechanism including bars, see Fig. 1 [8, 9]. Another encountered solution is the one that uses only one actuator that accomplishes simultaneously the azimuth and elevation movement of the tracker; an example of such a patented system is presented in Fig. 2 [10].

The tracking system has only one actuator which accomplishes the PV platform's movement towards the vertical axis (*azimuth movement*), whereas the orientation movement towards the horizontal axis (*altitude movement*) is accomplished within dependence about the first one, through means of an ***R-R-S-S*** (***R*** = revolute joint; ***S*** = spherical joint) linkage, which can have one or more adjustable lengths.

This work presents the kinematical synthesis [11] of an ***R-R-S-S*** spatial linkage, based on the request of the *received direct radiation* maximization (solar direct radiation which falls perpendicularly upon the PV platform), in the case of Brasov's climatic conditions; it is studied the case of the linkage with adjustable device as well as the case of the linkage without adjustable device. In the last part of the paper, the behaviour of the synthesized linkages are established and analyzed comparatively by numerical simulations. The results will be direct implemented in the photovoltaic park development of the Transilvania University of Brasov.

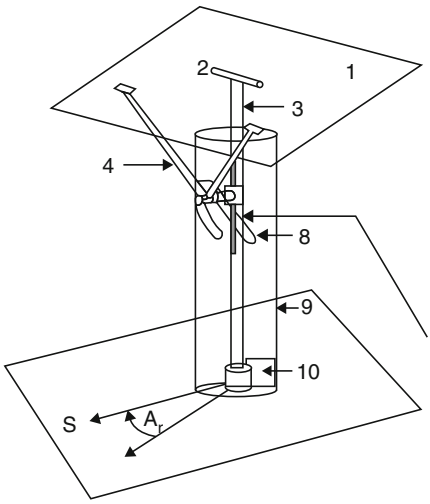

Fig. 1 Greek patented solar bi-axial tracking system with a single actuator

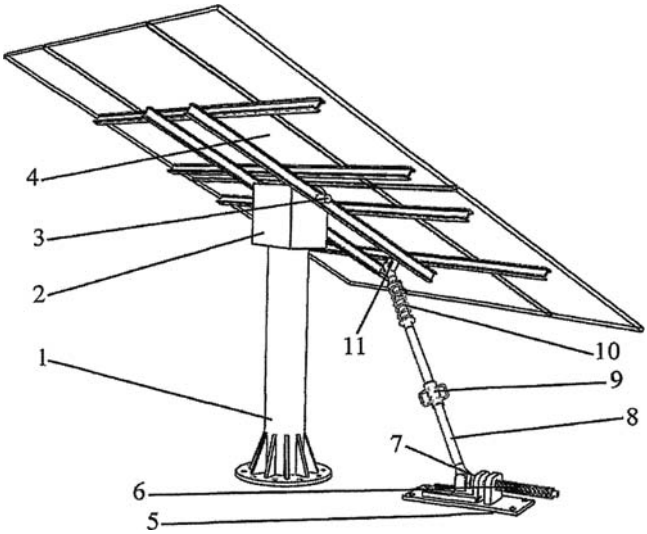

Fig. 2 Spanish patented solar biaxial tracking system with a single actuator

2 Kinematic Modelling of the *R-R-S-S* Linkage

The analyzed tracking system, shown in Fig. 3a, accomplishes the azimuth orientation movement (around the vertical axis, embodied by the 0–4 revolute joint) with the help of an actuator (of worm-gear type) placed at the top of the supporting pole; simultaneously the spatial linkage 0≡3-1-2-4-0 of ***R-R-S-S*** type accomplishes the PV's platform elevation movement (around a horizontal axis embodied by the 2–4 revolute joint). The auxiliary screw device 0-3-5-0 allows the vertical adjustment of the 1–3 spherical joint.

The ***R-R-S-S*** linkage (see Fig. 3b) is characterized by four geometric lengths: l_0 – the distance between the centre of the 1–3 spherical joint and the vertical axis of the 4–0 revolute joint, l – the swing arm length (the distance between the centres of the two spherical joints) , r – the frame radial dimension (the distance between the centre of the 1–2 spherical joint and the horizontal axis of the 2–4 revolute joint) , h – the distance between the centre of the 1–3 spherical joint and the horizontal plane which contains the axis of the 2–4 revolution joint. The geometrical synthesis of this linkage is based on the premises that the azimuth angle is a known input data (ψ^*), already optimized according to its sun homologous angle (ψ).

The approximation of the angle ψ^* was carried out in steps following the sun ψ path (see Figs. 6a, 7a, and 8a).

By means of the Fig. 3b, the platform altitude angle α^* can be determined.

Considering the notations from Figs. 3a, b it can be written the relations (1–4):

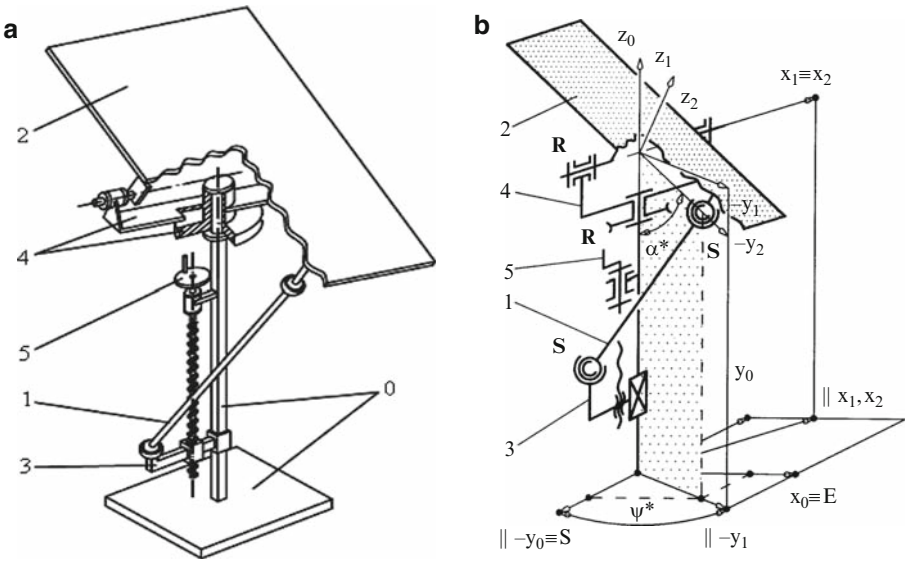

Fig. 3 The analyzed bi-axial azimuthal tracker with a single actuator: (**a**) Constructive scheme; (**b**) Kinematical scheme

$$\bar{r}_C = \vec{QC} = \begin{bmatrix} r \cdot \sin\alpha^* \cdot \sin\psi^* \\ -r \cdot \sin\alpha^* \cdot \cos\psi^* \\ h - r \cdot \cos\alpha^* \end{bmatrix}_{Qx_0y_0z_0} \tag{1}$$

$$\bar{r}_D = \vec{QD} = \begin{bmatrix} 0 \\ -l_0 \\ 0 \end{bmatrix}_{Qx_0y_0z_0}; \tag{2}$$

$$\bar{r}_C - \bar{r}_D = \vec{DC} = \begin{bmatrix} r \cdot \sin\alpha^* \cdot \sin\psi^* \\ l_0 - r \cdot \sin\alpha^* \cdot \cos\psi^* \\ h - r \cdot \cos\alpha^* \end{bmatrix}_{Qx_0y_0z_0} \tag{3}$$

$$|\bar{r}_C - \bar{r}_D|^2 = l^2 \tag{4}$$

By developing the relation (4), in accordance with previous relations, we can express the platform altitude angle depending on the platform azimuth angle as it follows:

$$2r(l_0 \cdot \sin\alpha^* \cdot \cos\psi^* + h \cdot \cos\alpha^*) = \left(r^2 + h^2 + {l_0}^2\right) - l^2 \tag{5}$$

$$\alpha^* = 2\tan^{-1}\frac{a \pm \sqrt{a^2 + b^2 - c^2}}{b + c} \tag{6}$$

where:

$$a = 2R \cdot \cos\psi^*; b = 2RH \tag{6'} (6'')$$

$$c = R^2 + H^2 + 1 - L^2 \tag{6'''}$$

$H = h/l_0$ is a ratio between the only adjustable length of the spatial quadrilateral mechanism and l_0.

$R = r/l_0$ is the ratio between radial dimension of the mechanism′ and l_0.

$L = l/l_0$ represents the ratio between the swing bar length and l_0.

In the synthesis and acting of a linkage an important role plays the pressure angle σ, between the swing arm 1 and the PV-platform frame 2; further, the expression of this pressure angle is determined by means of the Fig. 3b:

$$\cos\sigma = \bar{k}_2 \cdot vers\vec{D}C = \begin{bmatrix} \cos\alpha^* \cdot \sin\psi^* \\ -\cos\alpha^* \cdot \cos\psi^* \\ \sin\alpha^* \end{bmatrix}^t \cdot \frac{1}{L} \begin{bmatrix} R \cdot \sin\alpha^* \cdot \sin\psi^* \\ 1 - R \cdot \sin\alpha^* \cdot \cos\psi^* \\ H - R \cdot \cos\alpha^* \end{bmatrix} \tag{7}$$

$$\sigma = \cos^{-1}\left(\frac{H}{L}\sin\alpha^* - \frac{1}{L}\cos\alpha^* \cdot \cos\psi^*\right) \tag{8}$$

These parameters are used next for the geometric synthesis, where the pressure angle must not exceed 60°–65°.

3 Geometrical Synthesis

The purpose of a tracking system is to gain the maximum received solar direct radiation on the PV platform. First it was established the amount of solar radiation for the region of Brasov using the meteorological data from the University meteorological station. For the direct solar radiation computation, in the premise that the sky is clear, the following expressions are used [6]:

$$R_{DR} = R_0 \exp[-T_R/(0.9 + 9.4.\sin\alpha)] \tag{9}$$

$$R_0 = 1367.[1 + 0,0334 \cdot \cos(0,9856°N - 2,27°)][W/m^2] \tag{10}$$

where: R_{DR} is the direct solar radiation; N is the day number within a year, α is the sun altitude, T_R is the solar direct radiation loss coefficient in the Earth atmosphere (*without clouds*); the T_R coefficient [5] is determined for every month of the year and is specific for each geographic area.

The radiation computation was further on considered in two different atmospheric conditions: (1) permanent clear sky and (2) estimated real sky situation [2].

The synthesis and the simulations of the tracking system were carried on two premises: (1) considering an adjustable linkage depending on each season and (2) considering the mechanism not adjustable for a whole year period. In accordance with first premise, during a whole year three parameters (L, R, $L_0 = l_0/l_0 = 1$) of the linkage will be maintained constant while the forth (H) will be adjusted suitable for each season. The non-adjustable situation takes as premise the fact that the four parameters are constant throughout the year.

Starting from the relation (5), divided by l_0, the following relation can be obtained:

$$(\sin\alpha^* \cdot \cos\psi^* + H \cdot \cos\alpha^*) = \left(R^2 + H^2 + 1\right) - L^2]/(2R) = const. \tag{11}$$

From the correlation (11) the following equality results:

$$\sin\alpha^*_{Mi} \cdot \cos\psi^*_{Mi} + H_i \cdot \cos\alpha^*_{Mi} = \sin\alpha^*_{mi} \cdot \cos\psi^*_{mi} + H_i \cdot \cos\alpha^*_{mi} \tag{11'}$$

where $i =$ the summer solstice (ss), the equinox (eq) and the winter solstice (ws); $M =$ the light day noon $m =$ the light day morning/evening.

From expression (11′) results:

$$H_i \cong \frac{\sin\alpha^*{}_{Mi} \cdot \cos\psi^*{}_{Mi} - \sin\alpha^*{}_{mi} \cdot \cos\psi^*{}_{mi}}{\cos\alpha^*{}_{mi} - \cos\alpha^*{}_{Mi}} \tag{11''}$$

In the premise that during the equinox at noon the pressure angle is almost zero, the linkage has the configuration shown in Fig. 4; using the similitude of the two

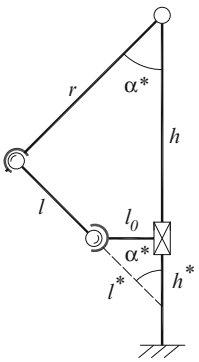

Fig. 4 Kinematical scheme of the solar tracker at the equinox noon

isosceles right-angled triangles from this figure, we can write the expression for R, knowing that $\alpha^* \approx 45^\circ$:

$$R \cong \cos\alpha * \cdot (H+1) = 0.7 \cdot (H+1) \tag{12}$$

In the premises that during the equinox $\psi_i^* = 90^\circ$ and $\alpha^* = \alpha_{mi}^*$ at the sunrise, from relation (5) results the expression for L:

$$L \cong \sqrt{H^2 + R^2 + 1 - 2RH\cos\alpha^*{}_m} \tag{13}$$

Based on the numerical simulations (see Fig. 5) and analysing the solar radiation in Brasov area the values from Table 1 were taken into consideration for solstices and equinoxes. Using these values it can be observed the optimum values for the linkage dimensions are during the equinox, as highlighted in the Table 1. So L remains constant during a year at a value of 2.02, R is constant at $R = 3.4$ for both adjustable and non-adjustable linkages. In accordance with (11′), the values of H during each season for the adjustable system become: $H_{SS} = 2.2$, $H_{EQ} = 3.8$,

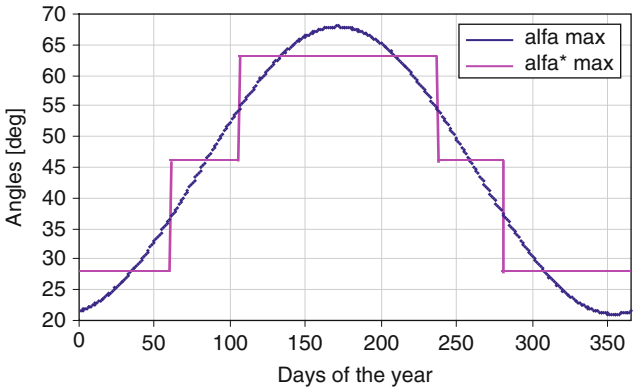

Fig. 5 Variations of the sun ray maximum altitude (continuous curve) and of the PV platform maximum altitude (step curve)

Table 1 The optimum values for the adjustable linkage dimensions during the equinox and the two solstices

i	Summer solstice	Equinox	Winter solstice
$\alpha^*{}_M$	63°	45.5°	28.5°
$\psi^*{}_M$	0°	0°	0°
$\alpha^*{}_m$	31°	27.5°	20°
$\psi^*{}_m$	90°	90°	56°
H_i	2.2	3.8	4.7
R		3.4	
L		2.02	

H_{WS} = 4.7; in the case of the non-adjustable linkage the value o H will be kept constant at the value during the equinox (H_{EQ} = 3.8).

The next chapter presents the numerical simulations regarding the response of a PV platform tracked by means of the obtained linkages in comparison with a fixed and tilted PV platform.

4 Numerical Simulations

Further on, the paper presents the numerical simulations for the cases of the two obtained tracking linkages (adjustable and non-adjustable) and also for the case of a fixed and tilted PV platform, in two premises: (1) permanent clear sky and (2) estimated real sky; for instance, in Figs. 6–9 there are graphically illustrated the simulation results from four main days, in the premise of the *clear sky*:

Then, using the direct radiation simulation results, the *daily average of the* received *direct solar energy is computed* (during a *season* and respectively during a *year*) for each of the previous situations; these results are graphically illustrated in Figs. 10 and 11 and numerically in Table 2.

The angular context of the four mentioned days is shown in Figs. 6a, 7a, 8a and 9a; these angles are the azimuth angle ψ, the altitude angle α, and the corresponding platform angles : ψ^*, α^*.

The incidence angle on the PV modules should be as small as possible so that more direct radiation falls on the PV platform; Figs. 6b, 7b, 8b and 9b presents the variation

of the incident angles (between the solar ray and the PV modules) and the pressure angles (between the swing arm 1 and the PV platform frame 2, Fig. 2b).

The variations of the available solar direct radiation and the direct radiation received by the PV modules, corresponding to the exemplified 4 days, there are illustrated in Figs. 6c, 7c, 8c and 9c, for the *clear sky*.

The diagrams from Fig. 10a shows the *average daily* variations of the *received solar direct energy* (during a *season* and respectively during a *whole year*) in the case of the PV platform orientated through non-adjustable linkage. Analogous, in Fig. 10b there are represented the same parameters in the case of a PV platform orientated through the adjustable linkage. For a better comparison in Fig. 11a there are systematized and graphically represented the *daily average* variations of the *solar direct energy* (during a *season* and respectively during a *whole year*), corresponding to the PV platform orientated with the non-adjustable linkage, with the adjustable linkage and not tracked system (fixed and tilted PV platform), in the premise of *clear sky*.

Analogous, in Fig. 11b there are illustrated the same parameters but in the premise of *estimated real sky* conditions; the transition from the *clear sky* conditions to the *estimated real sky* conditions was made by means of the *clouds crossing factor* (Fig. 12), established for the Brasov area in paper [2].

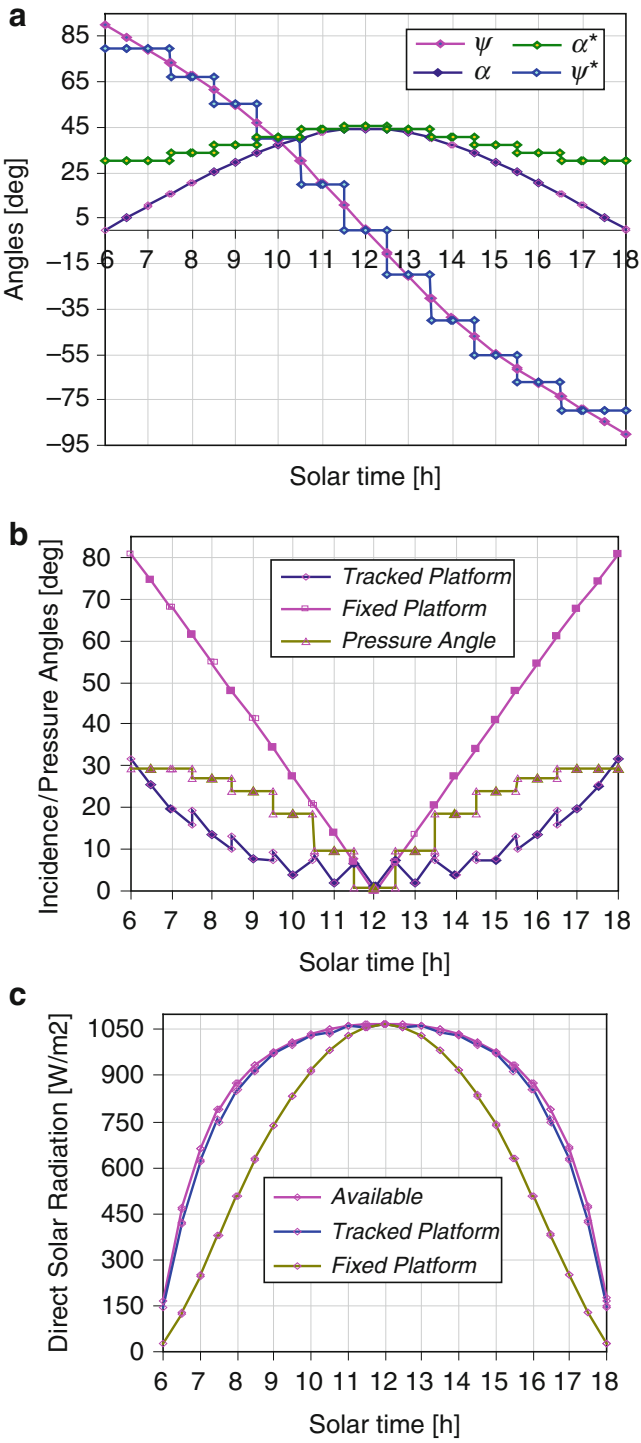

Fig. 6 Numerical simulations for the spring equinox: (**a**) Solar and platform angles (**b**) Incidence and pressure angles (**c**) Available and received direct solar radiation, when the sky is clear

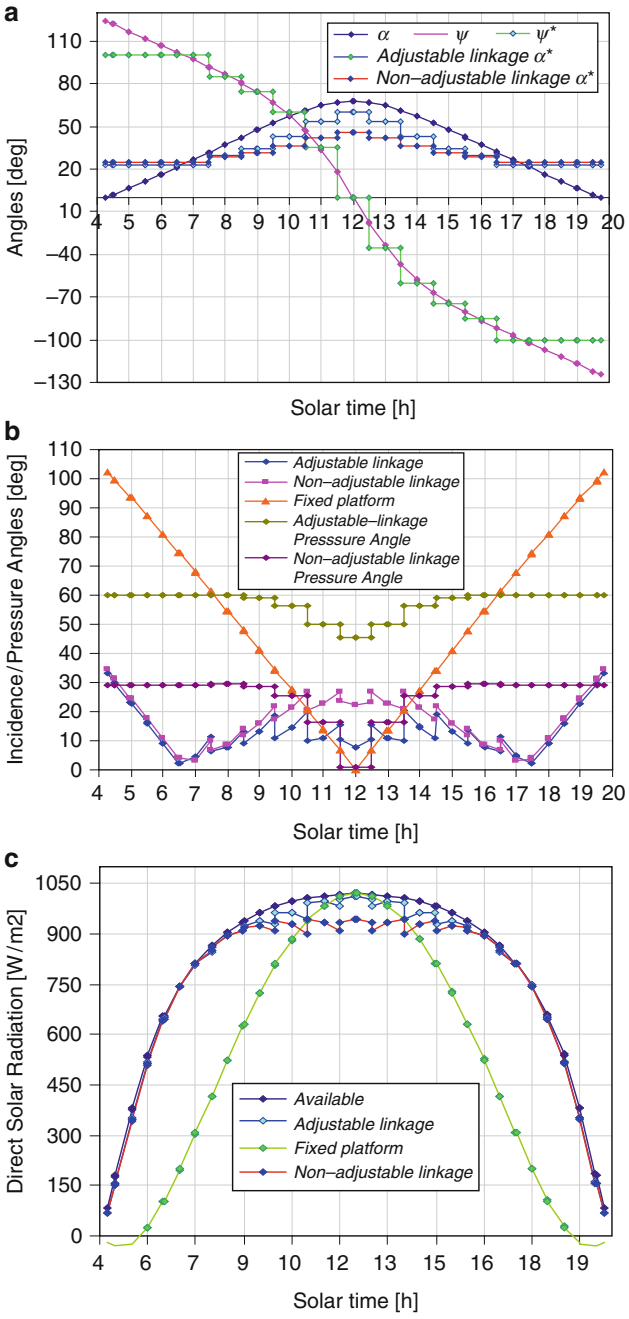

Fig. 7 Numerical simulations for summer solstice: (**a**) Solar and platform angles; (**b**) Incidence and pressure angles; (**c**) Available and received direct solar radiation, when the sky is clear

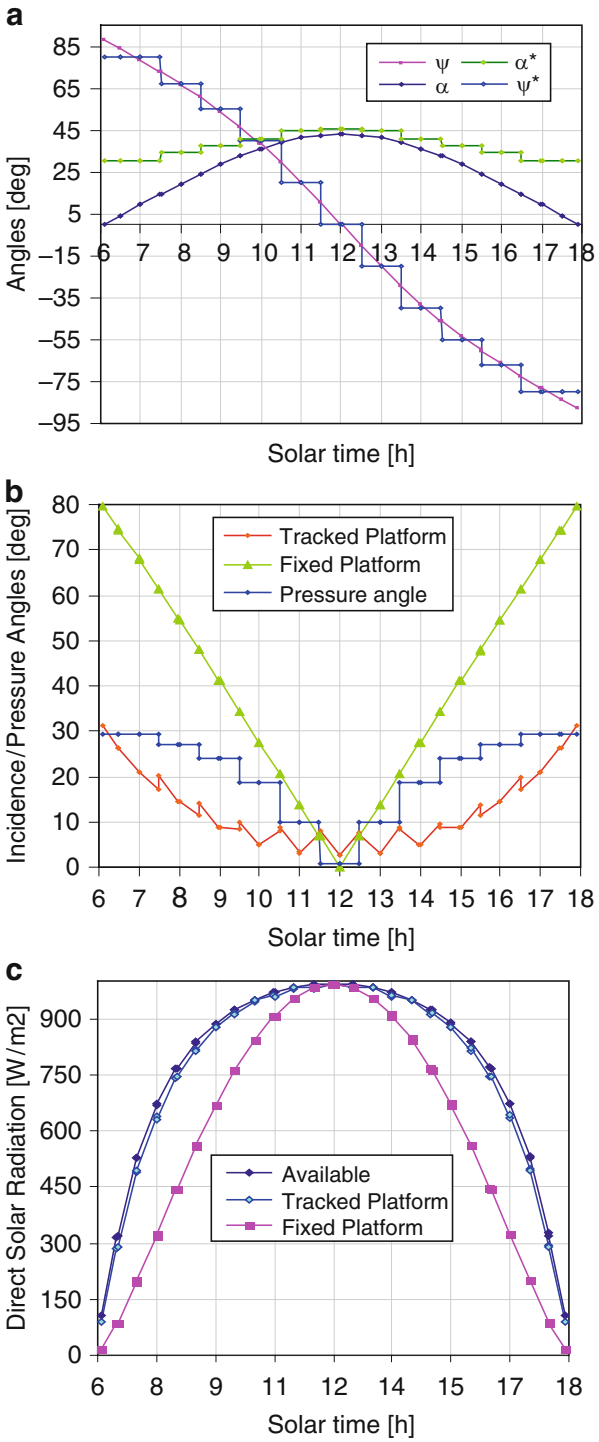

Fig. 8 Numerical simulations for autumn equinox: (**a**) Solar and PV panel angles; (**b**) Incidence and pressure angles; (**c**) Available and received direct solar radiation, when the sky is clear

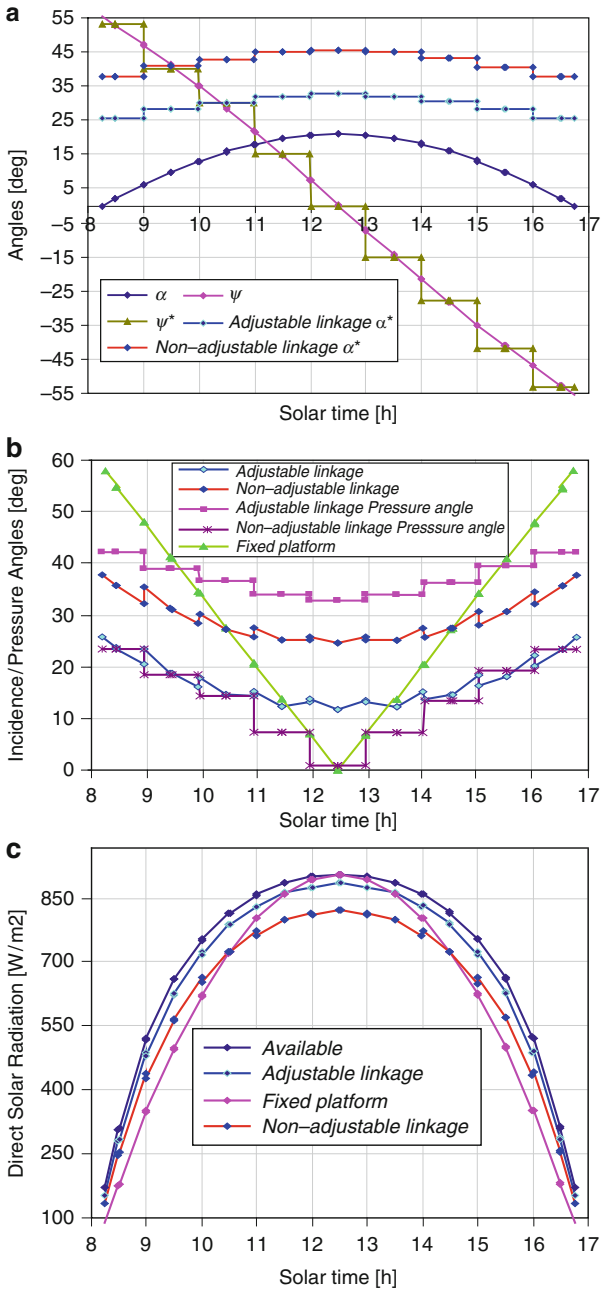

Fig. 9 Numerical simulations for winter solstice: (**a**) Solar and PV panel angles; (**b**) Incidence and pressure angles; (**c**) Available and received direct solar radiation, when the sky is clear

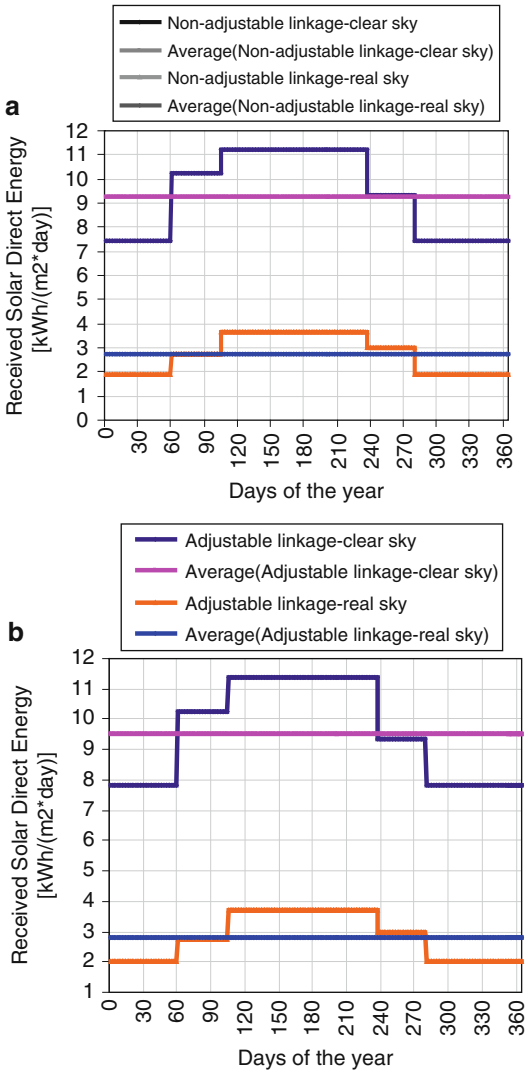

Fig. 10 Variations of the solar direct energy: (**a**) for non-adjustable and (**b**) for adjustable linkages

5 Conclusions

Based on the numerical simulations from the previous chapter, in the Table 2 there are established of the *average daily* values of the *solar direct energy* received by the PV platform in all acting situations.

Compared to the fixed and tilted PV platform, the tracked system represents a meaningful improvement, in the both considered premises: *clear sky* and respectively *estimated real sky*.

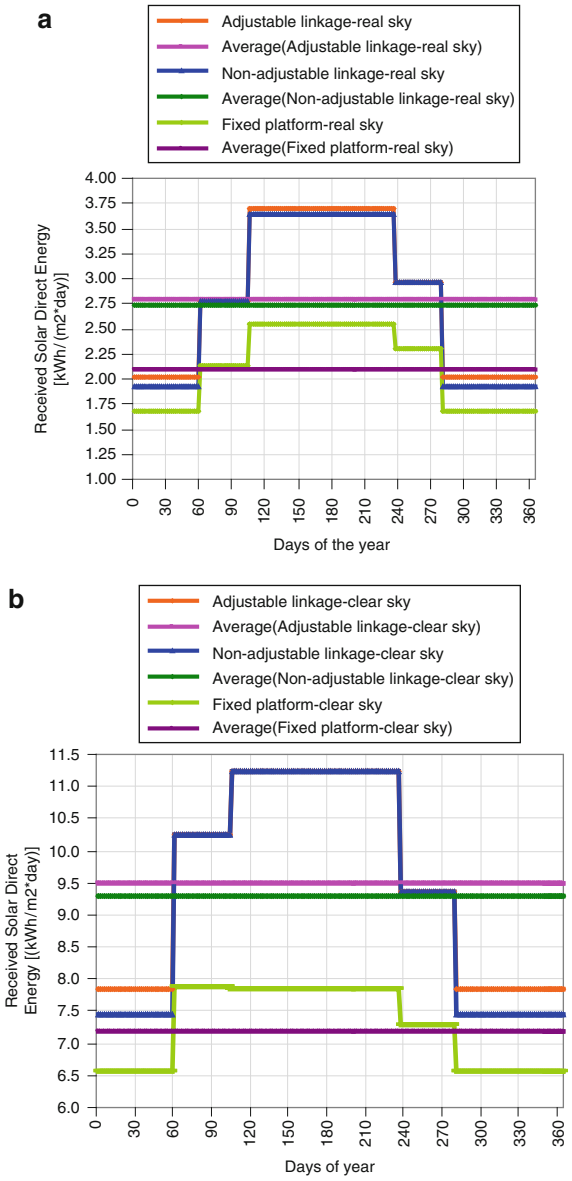

Fig. 11 Variations of the solar direct energy: (**a**) for clear sky and (**b**) for estimated real sky

In accordance with Figs. 10 and 11 and Table 2, the PV platform with *adjustable tracking linkage* is more efficient than the fixed and tilted PV platform with 31.9% in clear sky conditions, and with 33.25% in estimated real atmospheric conditions.

The adjustable linkage doesn't bring a significant gain compared to the non-adjustable linkage, the difference being just of 2.29% during the clear sky premises, and only 1.79% in estimated real atmospheric conditions.

Table 2 Daily average of the received solar direct energy during one year period considering the three types of tracking systems

	Fixed PV plat-form	PV plat-form with adjustable tracking linkage	PV plat-form with non-adjustable linkage
Daily average of the received solar direct energy during a whole year [kWh/(m^2-day)]			
Clear sky	7.2	9.49	9.28
Estimated real sky	2.1	2.79	2.74

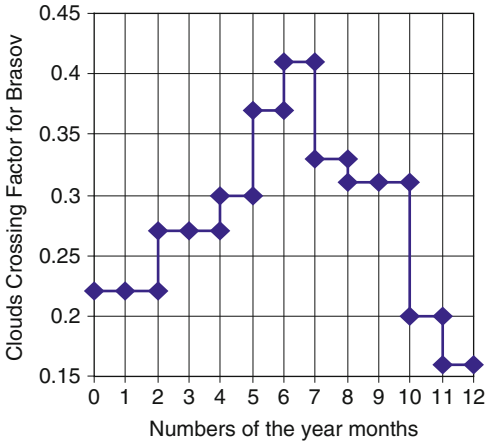

Fig. 12 Variation of the clouds crossing factor of the solar direct radiation for Brasov area (After [2]).

The small positive differences between the adjustable and the non-adjustable linkage highlight that the non-adjustable tracking linkage is rather recommended to be used in the Brasov atmospheric conditions.

In accordance with Figs. 6c, 7c, 8c, and 9c (valid in the premise of the *clear sky*), whereas for the equinox day the results are satisfactory and the summer solstice results can be accepted, the winter solstice results are far off the optimum ones.

In the premise of clear sky, Fig. 9c shows that the energy offered by the direct radiation received by the PV platform, in the case of the tracking with non-adjustable linkage and in the case of the fixed and tilted PV platform, is almost the same; on the other hand, considering that in Brasov the days with sun during the winter period are few, results that in this location the PV platform should be rather orientated with an non-adjustable linkage system in the spring, summer and autumn seasons and should be kept in a fix and tilted position in the winter season.

References

1 Diaconescu, D., Vişa, I., Burduhos, B., Popa, V.: On the Sun-Earth angles used in the solar trackers' design. Part 2: Simulations. In the Annals of the Oradea University, Fascicle of Management and Technological Engineering, CD-ROM Edition, vol. VI (XVI), pp. 842–849. ISBN: 1583-0691

2 Diaconescu, D., Vişa, I., Hermenean, I., Vatasesc, M.: Clouds influence o the solar radiation for a mountain location, pp.7–28. Proceedings of the BRAMAT Conference. Brasov (2009)
3 Dudiţă, F.L., Diaconescu, D., Gogu, G.R.: Mecanisme articulate. Ed. Tehnică, Bucureşti (1989)
4 Linke, F.: Die Sonnenstrahlung und ihre Schwachung in der Atmosphäre. Handbook der Geophysik. Borntrager, Berlin 8, 281–291 (1942)
5 Linke, F.: Transmissions-Koeffizient und Trübungsfaktor. Beitr. Phys. fr. Atmos. 10, 91–103 (1922)
6 Kleemann, M., Meliss, M.: Regenerative Energiequellen. Springer, Berlin (1993)
7 Meliss, M.: Renewable Energy Sources – Practice (in German). Springer, Berlin-Heidelberg (1997)
8 Norton, R.: Design of Machinery. McGraw-Hill, Boston (1999)
9 Patent: G.R.: 1006107B1: Innovative Azimuthal Solar Tracker. Greece (2009)
10 Patent: WO2008/000867 A1: *Solar Tracker with Movement in Two Axes and Actuation in Only One of Them*, Spain, 2008.
11 Vişa, I., Alexandru, P., Talaba, D., Alexandru, C.: Proiectarea Funcţională a Mecanismelor. Metode Clasice şi Moderne. Ed. Lux Libris, Brasov (2004)

Dimensional Synthesis of Suspension System of Wheel-Legged Mobile Robot

A. Gronowicz and P. Sperzyński

Abstract The objective suspension system has two DOF and is based on a four-bar linkage where one of rockers is replaced by linear actuator. The wheel is placed at a coupler point and the second linear actuator forces motion of the four-bar. The main goal of the synthesis is to obtain a linear dependency of displacement of second actuator with respect to vertical displacement of wheel which additionally should move along rectilinear trajectory while first actuator's length is a constant. For the objective system specific optimisation criteria were defined and a genetic algorithm has been applied as the method of optimisation. An example of synthesis has been included.

Keywords Genetic algorithm · Geometry · Two Dof System

1 Introduction

Recent years brought a significant progress in terms of new method appliance in the field of dimensional synthesis task. Increasingly often there are probabilistic optimisation methods to be used, developed on the ground of new research on artificial intelligence. A wide range of techniques has already been tested in the dimensional synthesis [2–7]. Fuzzy – logic, neural networks, optimisation algorithms like ant algorithms, not to mention simulated annealing or genetic algorithms which close the list. The latter are increasingly being used because of ease of implementation. Already mentioned approaches replace the classic deterministic methods of optimisation problem. One of the reasons is basically less computational

A. Gronowicz (✉)
Department of Machines Theory and Mechatronical Systems, Wroclaw University of Technology, Wroclaw, Poland

I. Vişa (ed.), *SYROM 2009*,
DOI 10.1007/978-90-481-3522-6_53,

complexity, undoubtedly advantage of the method, resulting from the fact that there is no longer need to calculate the derivatives of goal function.

2 Mechanism Structure

Scheme of the mechanism being a subject of this study (the suspension of wheel-legged robot Leg-Van [1]) is presented in Fig. 1.

It was built on the basis of four-bar mechanism. Its mobility equals two – driver q_1 (actuator) forces the change of link 1 orientation, causing the center of wheel E to move according to its designated trajectory μ_E. The second driver q_2 enables the change of already mentioned trajectory μ_E by the elongation or shortening the distance BD. Once the q_1 is fixed, the q_2 actuator causes the E point to move along the path designated by the circle centered at point C of radius l_3. As a result the mechanism has the ability to reach a desired point E (x_E, y_E) links in the *XY* coordinate system. All linear dimensions have been standardized so that the length of each designated trajectory μ_E (E point path) equals one.

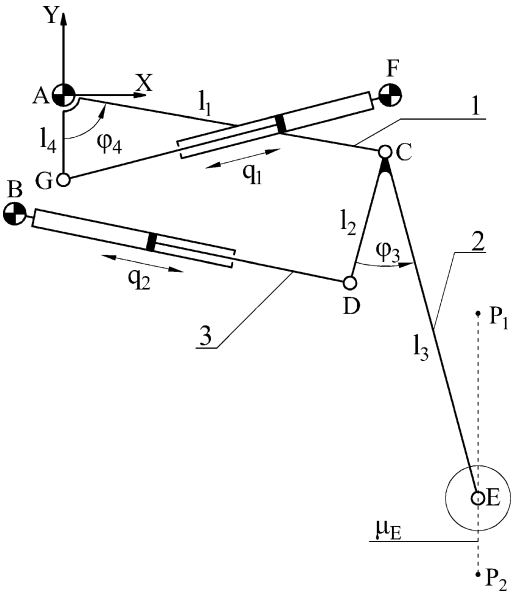

Fig. 1 Scheme of Leg-Van's suspension mechanism

3 Dimensional Synthesis

3.1 Formulation of the Problem

The subject of dimensional synthesis is determining all mechanism dimensions in a way enabling the execution of the movement according to the specified characteristic. The aforementioned may describe positions of particular device elements, trajectories of the points or define the movement dependencies between the input and output elements of the considered device. In some cases the requirements imposed on the device are very strict. In the case being a subject of this research (the suspension of wheel – legged robot Leg-Van) there are the following requirements to be met:

- The centre of E circle should move along a straight line in the direction of **Y** axis determined by two points $P_1(x_0, y_P)$ $P_2(x_0, y_K)$, denoting respectively the beginning and ending point.
- Dependence of the point E coordinate y_E on the drive q_1, should be a constant.
- The execution of a designated movement should not cause the internal variables of the mechanism to coincide with its singular positions.

The discussed movement (along straight line P_1P_2) is executed with the drive q_2 inactive (BD at a constant value). The main goal of optimisation process is achieving a function of rectilinear motion of considered point E along the vertical axis with respect to the q_1 drive. The optimisation of mechanism dimensions aiming at achieving a precise trajectory of point E becomes the issue of less importance. The already mentioned assumptions are expressed in a form of the following equations:

$$y_E(q_1) = a_1 q_1 + a_0,$$

$$x_E(q_1) = x_0 = const.$$

The task was made so as to simplify the platform positioning system of the balancing mobile robot. When attempted to change the platform orientation relative to the ground there is a location of the E wheel centre to be changed in each of the limbs (robot legs). Once all the imposed synthesis requirements are met a significant simplification of mechanism kinematics is achieved. Inverse or direct kinematics computation task transforms into solving a linear equation of the variable q_1 or y_E.

3.2 The Synthesis Method

The dimensional synthesis involves two stages. Each one determines particular mechanism dimensions. The block diagram of the considered synthesis is presented in Fig. 2. The following mechanism parameters should be determined in order to guarantee a task completion: l_1, l_2, l_3, l_4, q_2, $B(x_B, y_B)$, $F(x_F, y_F)$, φ_3 and φ_4.

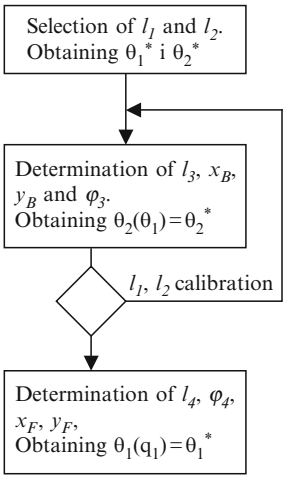

Fig. 2 Synthesis method diagram

First stage is to determine the length l_1 and l_3 which are the links between the wheel and platform. The next step is to define l_2 and q_2, point B position and finally φ_3 angle which altogether define ABCD mechanism.

The last stage focuses on choosing the exact F position and setting the l_4 length and φ_4 angle to an appropriate value. The last two stages of our synthesis are the subject of genetic algorithm action.

3.2.1 Stage One – Two-Link Chain ACE

This stage assumes that two-link chain ACE of arms l_1 and l_3 lengths (Fig. 3) creates a connection between the wheel and platform. The considered path length is equally divided into n (small enough) parts. Computation of inverse kinematics is performed in each of the points of division. It leads to $\theta_1^*(y_E)$ and $\theta_2^*(y_E)$ characterizing the degree of slope of mechanism bars with respect to the horizontal axis of the adopted reference frame. To meet a synthesis requirements, it is strictly required for suspension bars 1 and 2 to respect a designated characteristics $\theta_1^*(y_E)$ and $\theta_2^*(y_E)$. In order to achieve a linear characteristics $\theta_1^*(y_E)$ a complete search of the accuracy of Δl was made for the range of l_1 and l_3 values. Already made computations were used to determine a goal function in subsequent parts of the synthesis.

3.2.2 Stage Two – Four-Bar Mechanism

Stage two considers four-bar ABCD mechanism presented in Fig. 4. The task aims at determining mechanismparameters so that the angle $\theta_2(\theta_1)$ characteristics remains in line with previous stage results $\theta_2^*(y_E)$.

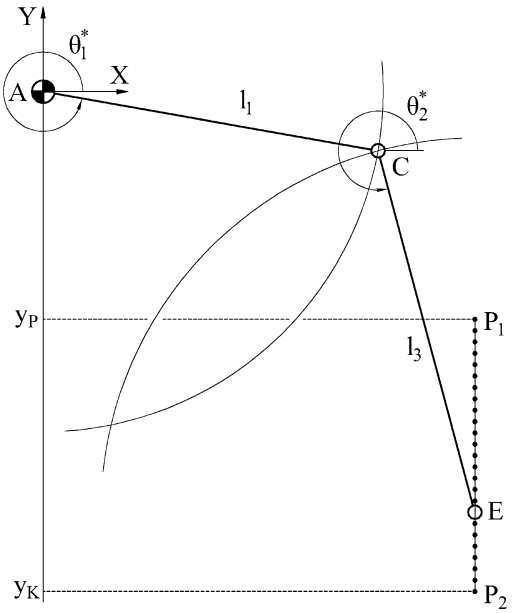

Fig. 3 Two link chain ACE

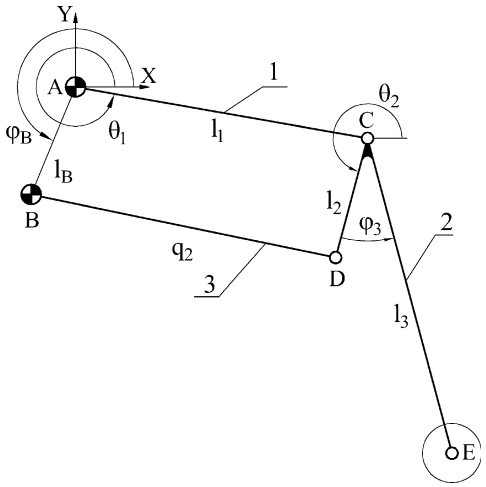

Fig. 4 Four-bar ABCD mechanism

The assumption is made that link 1 changes its orientation θ_1 according to the $\theta_1{}^*(y_E)$ function. On the basis of $\theta_1{}^*(y_E)$ characteristics the orientation θ_2 for each θ_1 value was calculated:

$$\theta_2(\theta_1) = 2arctg(\tau(\theta_1)), \tag{1}$$

where:

$$\tau(\theta_1) = \frac{-C_2 + \sqrt{C_1^2 + C_2^2 - C_3^2}}{C_3 - C_2},$$

$$C_1 = 2(l_1 l_3 \sin\theta_1 - l_3 l_B \sin\varphi_B),$$
$$C_2 = 2(l_1 l_3 \cos\theta_1 - l_3 l_B \cos\varphi_B),$$
$$C_3 = l_1^2 + l_3^2 + l_B^2 - q_2^2 - 2 l_1 l_B \cos(\theta_1 - \varphi_B).$$

Parameters φ_B and l_B indicate orientation and length of the AB vector which defines B point location in the assumed coordinate system. The goal function is expressed as follows:

$$F_1 = \sqrt{\sum_{i=1}^{n} \left(\theta_2\left(\theta_{1i}^*\right) + \varphi_3 - \theta_{2i}^*\right)^2}, \tag{2}$$

To solve this problem a genetic algorithm was used. The chromosome consists of the following parameters: x_B, y_B, l_2, q_2 and φ_3.

3.2.3 Calibration of l_1 and l_3

For the purpose of improvement of second stage results, all the values of parameters determined in a first stage were subject of the following change. For small Δl_1 and Δl_3 values the parameters $l_1 \pm \Delta l_1$ and $l_3 \pm \Delta l_3$ have been selected. Once the parameters changed, the characteristics θ_1 and θ_2 have been recalculated. If the new results were any better than the previous ones the whole process was repeated till the obtained mechanism parameters qualified as quasi-optimal.

3.2.4 Stage Three – Drive q_1 Parameters

The last stage of the studied synthesis determines the last four mechanism parameters. Those are the coordinates of point F connecting q_1 drive with the platform, length of l_4 and φ_4 angle. For optimisation purpose at this point (similarly to the previous stage) a genetic algorithm was used. The chromosome consists only of three parameters: length l_4 and point F coordinates x_F, y_F. The determination of φ_4 angle was carried out on the basis of other parameters. Additional restriction was imposed on the GF actuator. Namely it should be perpendicular to the AG once the q_1 middle position is achieved (Fig. 5).

In order that determine φ_4, it was necessary to set the link 1 orientation in the middle of the range defined by the $\theta_1^*(y_E)$ characteristic. Subsequently, on the basis of point F position and l_4 length the φ_4 angle was chosen so that to satisfy the following condition:

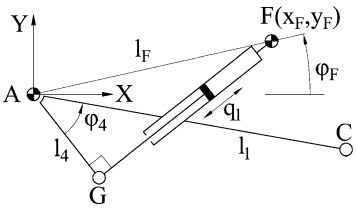

Fig. 5 Parameters of q_1 driver

$$\angle FGA = \frac{\pi}{2}, \Rightarrow GA \perp GF.$$

According to the assumption, the following restriction was imposed on the AC bar motion. Namely its range was defined by the boundary of $\theta_1^*(y_E)$ characteristic. For those two boundaries the lengths q_{1P} and q_{1K} (corresponds to P_1 and P_2 in Fig. 3) of drive q_1 were determined in such a way that the change of bar 1 orientation was in line with previously assumed angle values. Basically if q_1 changes its value in a range of $\Delta q_1 << |q_{1P} - q_{1K}|$, then the E point shift along the vertical axis should change at a constant rate according to the following equation:

$$\frac{\Delta y_E}{\Delta q_1} = a_1.$$

In other words, a derivative of vertical position E with respect to q_1 should be fixed as follows:

$$\frac{dy_E}{dq_1} = a_1. \tag{3}$$

The y_E coordinate of point E is expressed by the equation below:

$$y_E = l_1 \sin\theta_1 + l_3 \sin(\theta_2(\theta_1) + \varphi_3),$$

where:

$$\theta_1(q_1) = 2arctg\left(\frac{\sin\varphi_F - \sqrt{1 - C_0^2}}{C_0 + \cos\varphi_F}\right),$$

$$C_0 = \frac{l_F^2 + l_4^2 + q_1^2}{2 l_4 l_F}.$$

l_F and φ_F denote accordingly the length and orientation of vector AF. The characteristic $\theta_2(\theta_1)$ is given in a form of equation (1). Derivative of y_E position relative to the q_1 drive is :

$$\frac{dy_E}{dq_1} = \frac{dy_E}{d\theta_1}\frac{d\theta_1}{dq_1}.$$

Finally the following form of goal function was adopted:

$$F_2 = \sqrt{\sum_{i=1}^{n}\left(\frac{dy_E}{dq_{1i}} - a_1\right)^2}, \tag{4}$$

where q_I denotes the corresponding drive values within the range of $[q_{IP}, q_{IK}]$. The boundaries q_{IP} and q_{IK} were determined on basis of $q_I(\theta_1)$ relation:

$$q_1(\theta_1) = \left|\begin{pmatrix} x_F \\ y_F \end{pmatrix} - l_4\begin{pmatrix} \cos(\theta_1 - \varphi_4) \\ \sin(\theta_1 - \varphi_4) \end{pmatrix}\right|,$$

where θ_1 angle was replaced with the boundary values of $\theta_1^*(y_E)$ characteristic. The a_I parameter (equation (3)) was determined on the following basis:

$$a_1 = \frac{y_k - y_p}{q_{1K} - q_{1P}}. \tag{5}$$

3.3 Genetic Algorithm

Genetic algorithms are optimisation methods that have arisen with the development of artificial intelligence methods. These algorithms belong to a group of probabilistic methods of optimisation, which in its performance should reflect the natural evolution process. According to the literature a distinction between three main types of evolutionary algorithms is made. Evolutionary strategies (ES), evolutionary programming (EP) and a wide range of genetic algorithms (GA). The GA starts with selection of initial population χ_0. The aforesaid set consists of n – mechanisms randomly chosen from previously defined range. The values of these parameters were represented by real, floating point numbers in double precision in accordance with the IEEE 754 standard. Subsequently a goal function is determined for each and every initial population member. When taken into account that it seeks to minimize the objective function F, all the population members are subjected to sorting according to the value of individual objective function. For implementation purposes the appropriate methods of selection, crossing, mutation and reproduction were chosen. Once the initial set of n – chromosomes (each chromosome denotes an individual mechanism) is defined the main loop starts. The first step of the loop (selection) is to select $n/2$ pairs of individuals from the current population χ_i. Proportional selection was adopted, i.e., the measure of the likelihood of evolution

of each candidate is its position in population (individuals sorted according to the F_i function value (see Eqs. (2) and (4)). Subsequently considered population is subjected to so called crossing with probability p_x. Namely it is the exchange of genes between two selected individuals. During the execution of aforesaid process each gene is exchanged with likelihood p_{xx}. Evolving members are then liable to mutation with probability p_m. Similarly to crossing each gene of muting individual is transformed according to the probability p_{mm}. The considered process involves addition of a $\Delta \cdot U(0, 1)$, where $U(0, 1)$ is derived from uniform distribution and has values within the range of [0, 1]. Population is then expanded by addition of r new individuals randomly chosen from the expected solution set. The final stage of the algorithm is reproduction. New χ_{i+1} population is created and for this purpose a selection of n members takes place. Aforesaid selection is preceded by sorting the individuals from χ_i and $n + r$ set obtained in the process of evolution. New population is then created by n first candidates from the list and the best one ever determined. This particular method is called elite based reproduction strategy. Once a fixed number of step is achieved the algorithms stops. The solution is represented by mechanism with the best objective function value obtained in the process of evolution.

4 Results of Optimisation

The subject of calculations was segment P_1P_2 previously used to implement the Leg-Van robot [1]. The aforementioned is located between the points P_1 (275 mm, −200 mm) and P_2 (275 mm, −500 mm). The normalization was performed so that the length of the segment equals 1. The following new trajectory boundaries were obtained: P_1 (11/12, −2/3) and P_2 (11/12, −5/3). In the initial step, lengths of l_1 and l_3 were determined of the range [0.8; 1.4]. And there we have $l_1 = 1.0701$ and $l_3 = 0.9553$. Afterwards the dimensions of four-bar mechanism ABCD were defined (see Fig. 1) for the purpose of achievement a designated trajectory μ_E (Fig. 6)

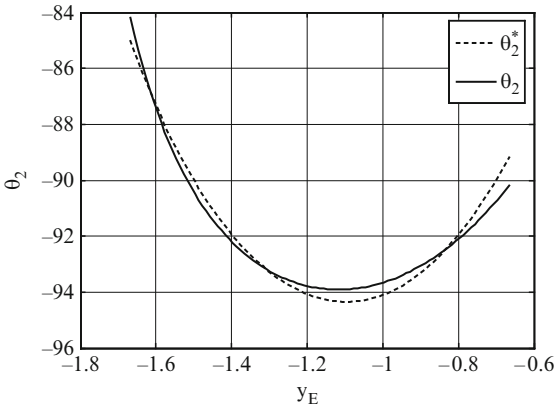

Fig. 6 Characteristics of angles θ_2

Respectively a genetic algorithm GA (described in the section above) was used. The best outcomes were obtained for the population of quantity $n = 30$. The experiments were stopped after 15,000 iterations. The likelihood of crossing and mutation amounted accordingly $p_x = 1$, $p_{xx} = 0.5$, $p_m = 0.5$ and $p_{mm} = 0.15$, $r = 5$ where r denotes the number of randomly chosen individuals in each iteration (Fig. 7).

The conducted experiments finally resulted in modification of AC and CE length, accordingly: $l_1 = 1$, $l_3 = 1.1$. In consequence the following values of parameters were obtained: B (−0.1463; −0.345), $l_2 = 0.3794$ and $\varphi_3 = 26.2587°$. The corresponding characteristics of angles $\theta_2^*(y_E)$ and $\theta_2(\theta_1^*)$ The final stage involved determination of point F position, length l_4 and φ_4 angle. Best results were achieved for the boundary values of the considered range.

The following values were determined: F(1; −0.4333), $l_4 = 0.4$ and $\varphi_4 = 87.2271°$. dyE/dq_1 derivative chart shown in Fig. 8. The average value of the

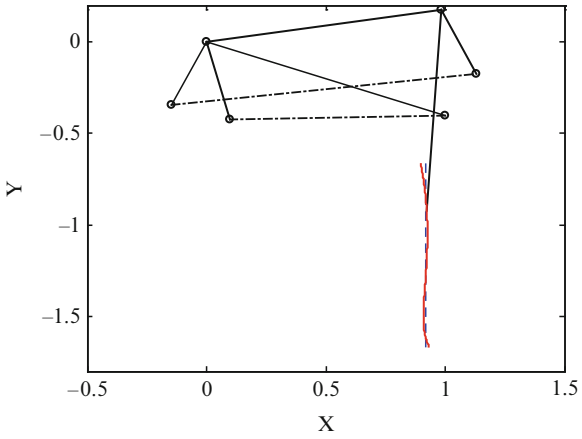

Fig. 7 Achieved suspension mechanism

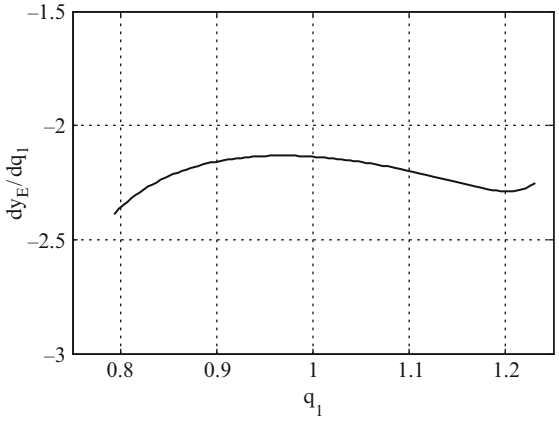

Fig. 8 Course of derivative dy_E/dq_1

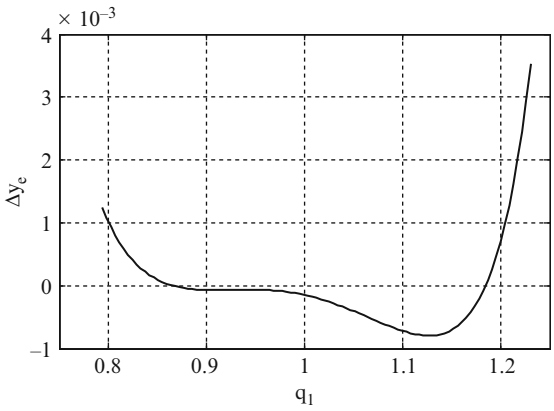

Fig. 9 Discrepancy between the $y_E(q_1)$ characteristic

derivative obtained was −2.2051, while the parameter a_1 (Eq. (5)) for the dimensions determined was −2.2911. Figure 9 reveals the discrepancy between the calculated characteristic $y_E(q_1)$ and previously assumed on the other side. It is important that small variance between point E trajectories is obtained. Mostly it does not exceed the value of 10^{-3} (Fig. 9).

5 Conclusions

The subject of this work is dimensional synthesis of the suspension mechanism of wheel-legged robot Leg-Van. The effort was concentrated on achieving the linear dependency between position y_E (centre of the wheel) and drive q_1. Problem of synthesis was initially decomposed. Each subtask was assigned a particular optimisation goal. As previously stated, the optimisation process was carried by genetic algorithm (GA). According to the experimental results, the considered method was proved effective in terms of optimising mechanism dimensions in an attempt to obtain a desired movement characteristic. Rectilinear performance $y_E(q_1)$ with the value of q_2 drive fixed at a constant rate enables the elimination of second drive q_2 from the performance of robot balancing task. This particular one concentrates only on walking task. The advantage of the applied genetic algorithms is the simplicity of implementation which allows rapid testing.

The method fault is a tendency to nesting in a local extreme causing difficulties when it comes to find a global extreme [2]. Whereas the necessity of repeatedly calculating objective function value doesn't give rise to any difficulties when taken into account a high efficiency of modern computers.

References

1 Szrek, J.: Synthesis of kinematic and control system of a four wheel-legged robot (in Polish). Ph.D. thesis, Wroclaw University of Technology (2008)
2 Kanarachos, A., Koulocheris, D., Vrazopoulos, H.: Evolutionary algorithms with deterministic mutation operators used for the optimization of the trajectory of a four-bar mechanism. Math. Comput. Simulat. 63, 483–492 (2003)
3 Laribi, M.A., Mlika, A., Romdhane, L., Zeghloul, S.: A combined genetic algorithm–fuzzy logic method (GA–FL) in mechanisms synthesis. Mech. Mach. Theory 39, 717–735 (2004)
4 Zhou, H.: Kwun-Lon Ting: Adjustable slider–crank linkages for multiple path generation. Mech. Mach. Theory 37, 499–509 (2002)
5 Zhou, H., Edmund, H.M.: Cheung: Analysis and optimal synthesis of adjustable linkages for path generation. Mechatronics 12, 949–961 (2002)
6 Affi, Z., EL-Kribi, B., Romdhane, L.: Advanced mechatronic design using a multi-objective genetic algorithm optimization of a motor-driven four-bar system. Mechatronics 17, 489–500 (2007)
7 Smaili, A., Diab, N.: Optimum synthesis of hybrid-task mechanisms using ant-gradient search method. Mech. Mach. Theory 42, 115–130 (2007)

Cam Mechanism with Flat/Tangential Translating Follower and Its Size

E.-C. Lovasz, D. Perju, K.-H. Modler, D.T. Mărgineanu, V. Văcărescu and E.S. Zăbavă

Abstract An important problem in the cam mechanisms synthesis is their total size as a minimization condition (criteria). Usual this condition is reduced to the cam size only, which may be partial accepted for cam mechanisms with oscillating follower ([1], [3], [4], [5]). The problem is quite different when the cam mechanism has a translating follower. In this case the length of follower's guiding is a very important contributor to the total size of the cam mechanism. This problem was presented in [2] for cam mechanisms with contact roll of the translating follower. The same problem will be presented in this paper but for cam mechanism with flat translating follower.

Keywords Cam mechanism · Flat translating follower · Minimal size

1 Introduction

As was presented in [2] the total size of a cam mechanism with translating follower and contact roll is decided by the basic (minimum) cam radius, the guiding length and, of course, by the follower's stroke (which has the most important weight).

The basic cam radius, as well as the follower's guiding length depend drastically on the pressure angle, so that this parameter cam be taken into account as the minimisation criteria.

E.-C. Lovasz (✉)
Department of Mechatronics, Politehnica University of Timişoara, Timişoara, Romania
K.-H. Modler
Lehrstuhl für Getriebelehre, Institut für Festkörpermechanik, Fakultät Maschinenwesen, Technische Universität Dresden, Dresden, Germany

I. Vişa (ed.), *SYROM 2009*,
DOI 10.1007/978-90-481-3522-6_54,

In the case of the cam mechanism with flat translating follower, the pressure angle is zero in most usual situations when follower's tangent line is perpendicular to its displacement direction. For this case other parameters for size minimization have to be taken into account.

2 The Forces' Equilibrium and Guiding's Size Establishment

The working condition of the cam mechanism is obviously (see Fig. 1):

$$F \geq F_T + \mu(R_1 + R_1), \tag{1}$$

where:

$$F_T = F_u + F_i + F_e \tag{2}$$

is the total force acting on follower with the components:

F_u – the useful (technological) force;

$F_i = -m_F \cdot a_F$ – the inertial force acting on the follower;

F_e – elastic force of a spring witch makes sure the permanent contact between cam and follower.

R_1 and R_2 are the reactions forces in the follower's guiding of length b (see Fig. 1) and μ is the friction's coefficient in guiding.

F – the acting force from cam to the follower

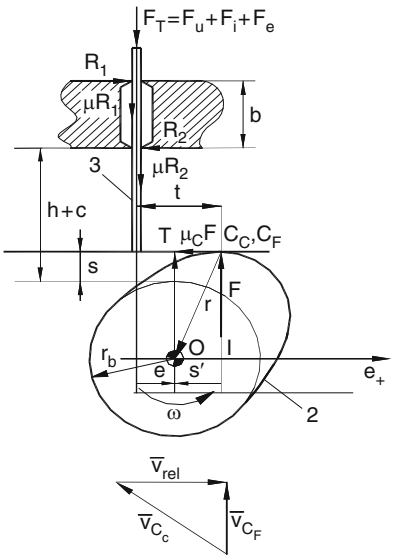

Fig. 1 Kinematics and forces' equilibrium of the cam mechanism

The follower's velocity can be written as:

$$\bar{V}_F = \bar{V}_{C_F} = \bar{V}_{C_C} + \bar{V}_{C_F C_C} \tag{3}$$

where: $\bar{V}_{C_C} = \bar{\omega} \mathrm{x} \bar{r}$ is the velocity of the contact point belong to the cam

$\bar{V}_{C_F C_C}$ – is the relative velocity between follower and cam.

If the relationship (3) is divided by cam's angular velocity ω and it is represented rotated (counter-clockwise) with 90° it is obtained:

$$\overline{CT} = \overline{CO} + \overline{OT} \tag{4}$$

where:

$$CT = \frac{V_F}{\omega} = \frac{ds/dt}{d\varphi/dt} = \frac{ds}{d\varphi} = s', OT = r_b + s \tag{5}$$

s being the current position of the follower for a current position of the cam (φ) and r_b is the basic (minimum) cam's radius.

By equilibrium condition of the follower it results:

$$R_1 = \frac{F}{b}[t - \mu(h + c - s)], R_2 = \frac{F}{b}[t - \mu(b + h + c - s)] \tag{6}$$

where:

$t = s' + e$, e is the eccentricity which is considered positive if the cam's centre O is on right-hand side in respect with the guiding line.

μ_C – the friction coefficient between cam and follower;

c is the clearance between follower's disc and the guiding; it also can be used for spring positioning.

With these values the condition (1) becomes:

$$F_T \leq F\left[1 - \frac{2\mu}{b}\left(s' + e - \mu_c\left(h + c - s + \frac{b}{2}\right)\right)\right] \tag{7}$$

Considering the ratio

$$\frac{F_T}{T} = \Phi \tag{8}$$

as a loading coefficient which can be considered as an instantaneous efficiency ($F_T ds/Fds$), the relationship (7) can be written as:

$$2\mu\left[\frac{s' + e - \mu_c(h + c - s)}{b} - \frac{\mu_c}{2}\right] \leq 1 - \Phi \tag{9}$$

from which, the minimum guiding length results:

$$b \geq 2\mu \frac{s'_{\max} + e - \mu_c(h + c_{\min} - s)}{1 - \Phi - \mu \cdot \mu_c} \tag{10}$$

or in nondimensional/relative expression:

$$\frac{b}{h} \geq \frac{2\mu}{1 - \Phi + \mu \cdot \mu_c} \left[\frac{s'_{\max}}{h} + \frac{e}{h} - \mu_c \left(1 + \frac{c_{\min}}{h} - \frac{s}{h} \right) \right] \tag{11}$$

For the particular case of an eccentric mechanism ($e \neq 0$), with $\mu = \mu_C$ and $s'_{\max} = s'|_{s=h/2}$ as for majority of the usual transmission functions, relationship (11) becomes:

$$\frac{b}{h} \geq \frac{2\mu}{1 - \Phi + \mu^2} \left[\frac{s'_{\max}}{h} + \frac{e}{h} - \mu_c \left(\frac{1}{2} + \frac{c_{\min}}{h} \right) \right]. \tag{12}$$

For a very well lubricated mechanism ($\mu < 0, 1$), $\mu^2 \rightarrow 0$ and a centric mechanism ($e = 0$) the relationship (12) is reduced to:

$$\frac{b}{h} \geq \frac{2\mu}{1 - \Phi} \frac{s'_{\max}}{h}. \tag{13}$$

3 The Total Size of a Cam Mechanism with Flat Translating Follower and the Influence's Factors of It

The total size of a cam mechanism on follower's translating direction can be deduced from Fig. 2, i.e.:

$$H = 3h + 2r_b + b + c_{\min}, \tag{14}$$

or in non-dimensional expression:

$$\frac{H}{h} = 3 + 2\frac{r_b}{h} + \frac{b}{h} + \frac{c_{\min}}{h} \tag{15}$$

where c_{min} is the minimum clearance necessary for the spring emplacement. It can be positioned under or above of the guiding and represents the compression spring's length for maximum elastic forces (F_e). This value it results from the condition of permanent contact between follower and cam:

$$F_e = F_{e0} + ks. \tag{16}$$

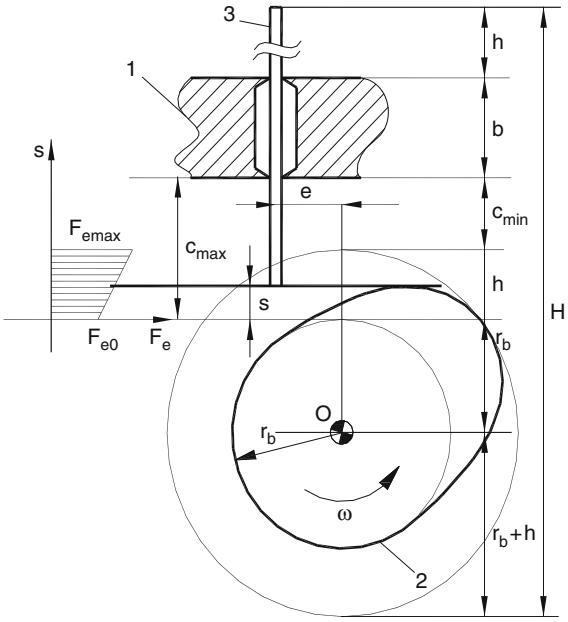

Fig. 2 The total size of the cam mechanism

The basic (minimum) radius of the cam, also in non-dimensional expression, is:

$$\frac{r_b}{h} = \left|\frac{s''_{\max}}{h}\right| - \frac{s}{h}\Big|_{s''_{\max}}. \tag{17}$$

As can be seen in relationship (15) the total relative size of the mechanism it depends on the cam's relative basic radius (r_b/h), the relative guiding length (b/h) and the minimum relative clearance (c_{min}/h). But the first two parameters and partial the third depend significantly on the mechanism's transmission function by its kinematical parameters. In the same time the guiding length depends also by the friction coefficients (μ and μ_c), by the loading coefficient (Φ) and by the mechanism's eccentricity (e).

4 Case Studies

It will be analyzed, from the mechanism's size point of view a couple of usual transmission functions and the specific mechanism's parameters.

The transmission functions taken into account as example and their specific non-dimensional maximum values are presented in Table 1, where:

$$y = \frac{s}{h}; x = \frac{\varphi}{\varphi_{a/p}} \tag{18}$$

Table 1 Some of transmission functions used for the case studies

No.	Transmission function	Equation	Maximum values and their positions			
			y'_{max}	$x\|_{y'_{max}}$	$\|y''_{max}\|$	y''/y''_{max}
1	Parabolic	$y = 2x^2$	2	1/2	4	1/2
2	Fifth order polynomial	$y = 2x^3 - 15x^4 + 6x^5$	1.87	1/2	5.77	0.78
3	Sine	$y = x - \frac{1}{2\cdot\pi}\sin 2\pi x$	2	1/2	2π	0.75
4	Cosine	$y = \frac{1}{2}(1 - \cos \pi x)$	$\pi/2$	1/2	$\pi^2/2$	1

$\varphi_{a/p}$ – is the cam's rotating angle for active and passive/returned stroke, respectively

$$s' = \frac{ds}{d\varphi} = \frac{h \cdot dy}{\varphi_{a/p} \cdot dx} \Rightarrow \frac{s'}{h} = \frac{1}{\varphi_{a/p}} \cdot y' \tag{19}$$

$$s'' = \frac{d}{d\varphi}\left(\frac{ds}{d\varphi}\right) = \frac{d}{\varphi_{a/p} \cdot dx}\left(\frac{h}{\varphi_{a/p}} \cdot \frac{dy}{dx}\right) = \frac{h}{\varphi_{a/p}^2} \cdot \frac{d^2y}{dx^2} \Rightarrow \frac{s''}{h} = \frac{1}{\varphi_{a/p}^2} \cdot y'' \tag{20}$$

4.1 Case Study 1

Let consider a cam mechanism with: $\mu = \mu_c = 0.1$, $e = 0$, $c_{min}/h = 1/2$ and $\Phi = 0.85$.

In this case, the relationship (12) for the active stroke becomes:

$$\frac{b}{h} \geq \frac{0,2}{0,16}\left(\frac{s'_{max}}{h} - 0,1\right) = 1,25\left(\frac{y'_{max}}{\varphi_a} - 0,1\right) \tag{21}$$

For this example the relative guiding length depends only on transmissions functions and its stroke's time (or corresponding rotating cam's angle).

The relative cam's basic (minimum) radius is given by relationship (17). Taking into account the relationship (20) it becomes:

$$\frac{r_b}{h} \geq \frac{y''_{max}}{\varphi_a^2} - y\Big|_{y''_{max}} \tag{22}$$

The total relative cam mechanism's size is obtained from the relationship (15), which, for this case, becomes:

$$\frac{H}{h} = 3,5 + 2\frac{r_b}{h} + \frac{b}{h} \tag{23}$$

The expressions (21), (22) and (23) are represented in Fig. 3 for the active cam's angle: $\varphi \in (0, \pi)$.

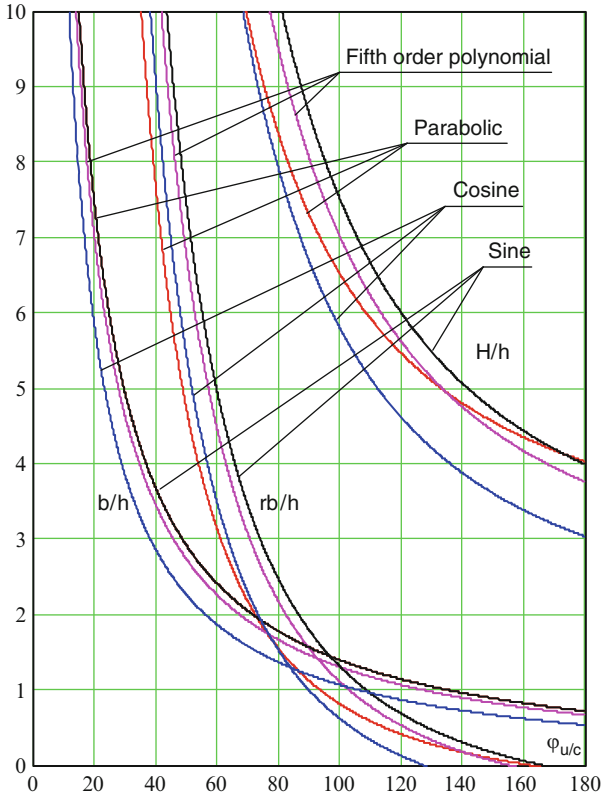

Fig. 3 The variations of relative basic radius, relative guiding's length and total relative longitudinal size of a cam mechanism in respect with active stroke angle

4.2 Case Study 2

For the same transmission functions (see Table 1) with $\varphi_a = \pi/2$, the variation of relative guiding length in respect with remained parameters Φ, μ, e/h, $c_{\min}/h$ are given in Figs. 4a, b, c and d respectively.

In Fig. 4a the variation of the relative guiding's length in respect with the loading coefficient Φ are represented, for a cam mechanism having $\mu = 0.1$; $e = h/10$ and $c_{\min} = h/2$. As can be seen for a loading coefficient greater than 0.9 the guiding length it increases abruptly, and the situation has to be avoided.

The influence of friction coefficient it is represented in Fig. 4b for a cam mechanism with $\Phi = 0.85$; $e = 0$ and $c_{\min} = h/2$. The guiding length increase with the friction coefficient but much slowly than a proportional variation.

The negative eccentricity it reduces the guiding length but not in an important ratio as can be seen in Fig. 4c for a cam mechanism with $\Phi = 0.85$; $\mu = 0.1$; and $c_{\min} = h/2$.

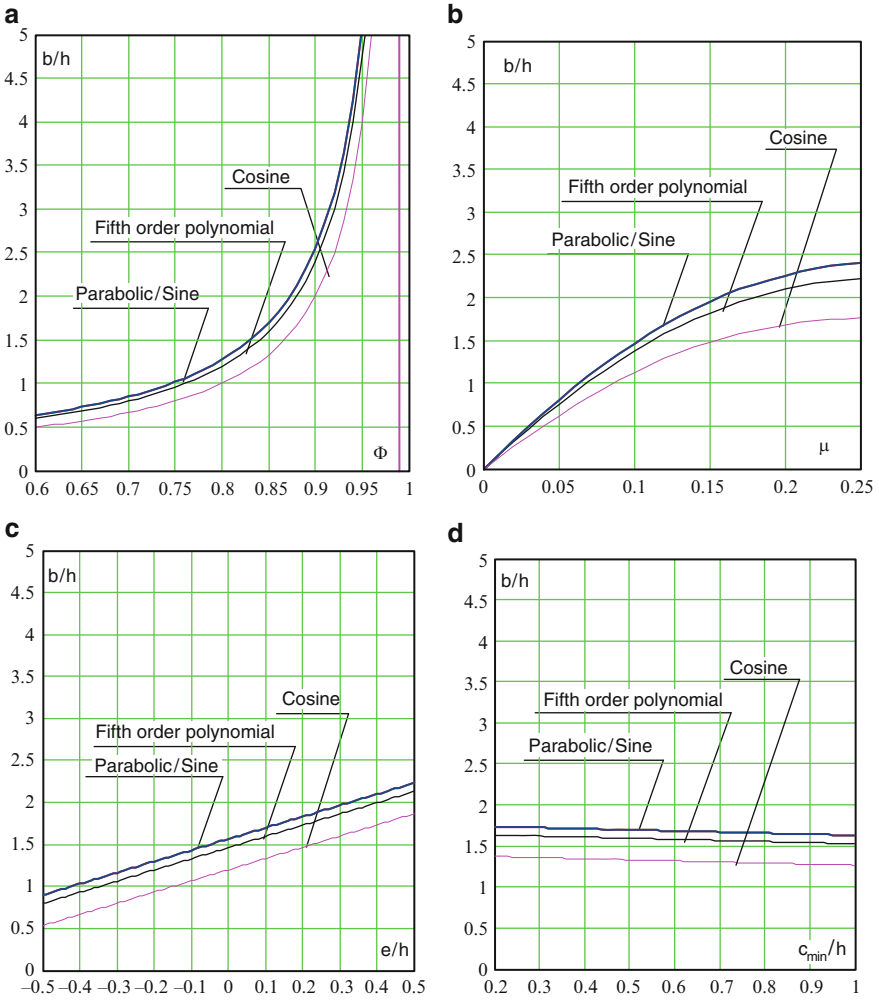

Fig. 4 The variations of the relative guiding's length in respect with the cam's mechanism parameters

The minimum clearance $c_{\min}$ has a very small influence on guiding's length as is presented in Fig. 4d for a cam mechanism with $\Phi = 0.85$; $\mu = 0.1$ and $e = h/10$.

5 Conclusions

In this paper as in [2] it is underlined that total size of a cam mechanism, even in the particular case of zero pressure angle, it depends not only of basic radius, but also by stroke, guiding's length and the minimum clearance of follower's disc to the

guide. The guiding's length also it depends of the loading coefficient, friction coefficient an eccentricity.

The most important factors are the stroke's length an the characteristics angles for active and returned strokes.

References

1 Duca, C., Popovici, A., Oprişan, C.: Bazele proiectării mecanismelor cu came. Ed. Ghe., Asachi Iaşi (1999)
2 Lovasz, E.-Ch., Perju, D., Modler, K.-H., Zăbavă, E.S., Hotea, A.: On the size of cam mechanism with translation follower. Mech. Manipulators 6(1) (2007)
3 Lovasz, E-Ch, Cărăbaş, I.: Principii de sinteza a mecanismelor cu roţi dinţate şi came. Ed. Politehnica, Timişoara (2006)
4 Luck, K., Modler, K.-H.: Getriebe-technik – Analyse, Synthese, Optimie-rung. Springer-Verlag, Wien, Ney York (1990), 1. Auflage
5 Perju, D.: Mechanisms for precision mechanics (in Romanian), vol. 1. Ed. Univ Politehnica Timisoara, Timisoara (1990)

A Design of Compliant Mechanism with Integrated Actuators

N. Modler, K.-H. Modler, W. Hufenbach, E.C. Lovasz, D. Perju, and D. Mărgineanu

Abstract The transmission of motion sequences especially is currently realized in most applications by classical mechanisms showing a high number of parts and high structural weight. The use of so-called compliant elements with specifically adjustable compliances offers the possibility to transmit motions just by structural deformations. Moreover, the composite design is predestined to integrate piezo-ceramic actuators into the laminate lay-up and thus rises the possibility to design structure-integrated drives. This paper makes a contribution to the efficient analysis and synthesis of such active compliant structures by developing new material-adapted analytical and numerical calculation models.

Keywords Compliant mechanisms · Piezo-ceramic actuator · Textile reinforced composite materials

1 Introduction

Compliant Mechanisms consist of special rigid elements, that are, according to their functional purpose, with higher rigidity (in the following, rigid elements) and with higher elasticity (compliant elements). Thus particular linkages as transmission and guiding mechanisms can be realized. The movement capability depends heavily on both the material used and the geometry of the rigid and elastic elements. Beyond that, the type, placement and value of the loads influence the transmission function and the trajectories [1].

N. Modler (✉), K.H. Modler and W. Hufenbach
Faculty of Mechanical Engineering, TU Dresden, Germany
E.C. Lovasz, D. Perju and D. Margineanu
Faculty of Mechanics, Politehnica University of Timisoara, Timisoara, Romania

I. Vişa (ed.), *SYROM 2009*,
DOI 10.1007/978-90-481-3522-6_55,

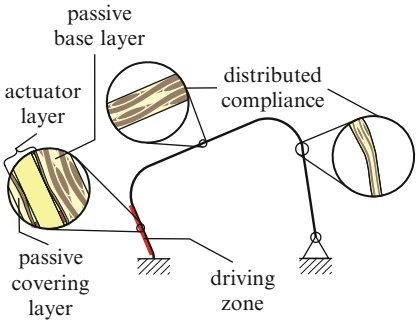

Fig. 1 Mono-element compliant mechanism with distributed compliance and integrated active elements as actuators

On the basis of the developed numeric model for the active textile reinforced compliant mechanisms (A-TCM), elastic links with piezoelectric actuators integrated in the textile reinforced material can be built (Fig. 1) [2].

As an example, a flap's mechanism as a transmission A-TCM is chosen here, as these linkages can be found in various domains of equipment, machine and automotive applications. The A-TCM building method with its high elastic potential based on the material offers, next to other advantages, a reduced part number and thus an assembly cost reduction, in particular the possibility to adjust on purpose the flaps system's opening behaviour and its energy consumption. Therefore new innovative solutions are available, that will be presented on the basis of the flaps mechanism demonstrator.

The demonstrator's conception covers a planar coupler A-TCM adapted to reduced space that, by an actuator integrated in the material with work ability adjusted to the flaps' weight, allows an opening angle up to 90°. The basis for a technical conversion is the choice of proper materials like glass or carbon fibre reinforced plastic materials, that allows high strength (e.g., tensile stress limit) having in the same time high elasticity. The structural pre-choice is done on the analytic equivalent model basis. Resulting from the identified basic geometric and material parameters of the mechanism, the detailed synthesis through the developed numerical calculus algorithm will be accomplished. Also similar hybrid and monolithic flaps A-TCM will be compared.

2 Design Study of a Flaps Mechanism Demonstrator

A fundamental task of a flaps mechanism is to realize an opening angle up to 90° (Fig. 2).

A typical complex requirement profile for a flap A-TCM is summarized in Table 1.

Considering such a complex requirement profile the drive and motion modes of operation were realized using compliant four bar linkages (Fig. 3). The flap's

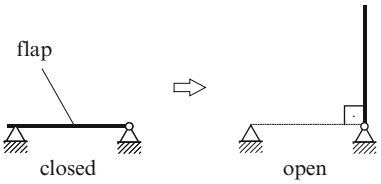

Fig. 2 Schematic of the initial and the final flap positions

Table 1 A range of the typical flap mechanisms demonstrator requirements

Type of Requirement	Requirement
Functional	Flap adjustment in the open state
	Inactive drive zone in the closed state
Technological	Reduced number of parts and decreased assembly effort
Relating to mechanism	Horizontal initial position
	Opening angle up to 90°
	High transmission ratio of drive angle φ to output angle ψ
Relating to drive	Material integrated actuator (embedded Macro Fibre Composite, Mfc)
	Realization of the maximum working capacity of the driving link
	Uncomplex type of driving link construction (mono element)
Geometrical	Small installation space of the closed state
Relating to material	Wide deformability (high strength/stiffness ratio)

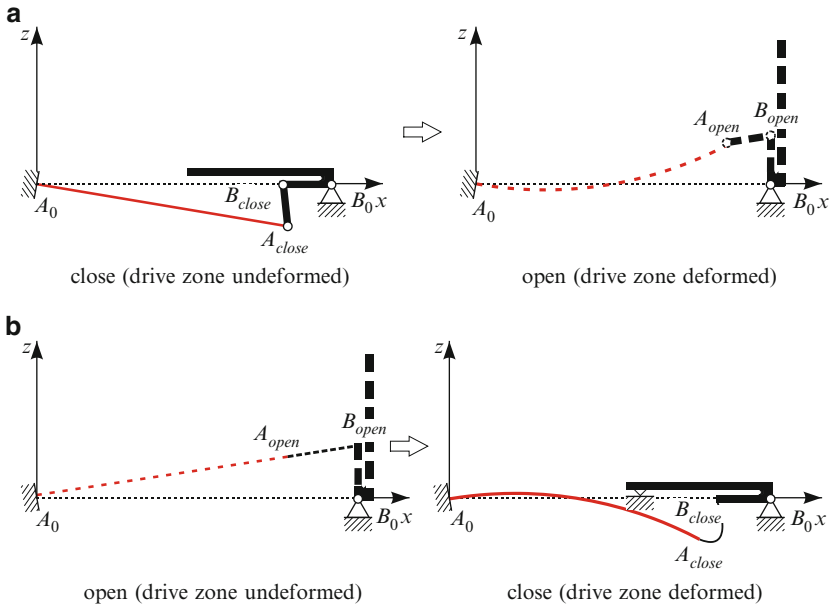

Fig. 3 Operating modes of flap A-TCM with 90° opening angle

mechanism is based on a driving link $\overline{A_0A}$, implemented by a bending actuator and connected by a rigid coupler $\overline{AB}$ (differential design, Fig. 3a) or by a compliant coupler (integrally design, Fig. 3b) with the output link $\overline{BB_0}$. The pure rotation without guiding function requires the flap tightly connected to the output link.

3 Analytically Based Structural Pre-Choice

The synthesis of compliant mechanisms is completely different to the design process of conventional kinematic systems. For compliant mechanisms the movement and deformation of the flexible elements depends on the elastic material parameters as well as the amplitude and direction of the applied forces. Therefore, the kinematic and kinetostatic characteristics of such mechanisms are coupled. This results in a complex and iterative synthesis process for compliant mechanisms, which also includes the materials design.

The identification of a suitable mechanisms configuration usually requires efficient search techniques like gradient methods or evolutions algorithms [3, 4].

For reduction of the feasible configurations an analytically based structural pre-choice was carried out. The calculation model had to define the number, the shape as well as the position of the particular links and joints.

The initial point of the calculation is the derivation of equivalent flaps A-TCM models [2].

3.1 Drive's Values

The drive's values result from the calculation of the free ends deflection (w_{end}^{max}) of the simply supported bi-layer driving link (Fig. 4a), representing the height of stroke, as well as from the blocking load force (F_z^{max}, Fig. 4c).

Furthermore the pre-design-relevant drive value $w_{end}^{max}/2$ at the maximum output or lift working capacity is obtained from (see Fig. 4b):

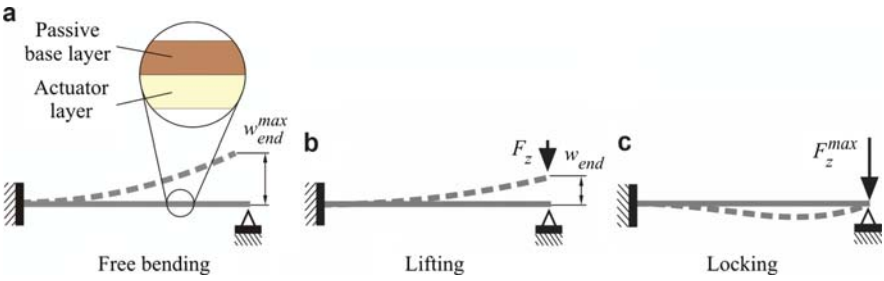

Fig. 4 Determination of the drives values w_{end}^{max} and F_z^{max}

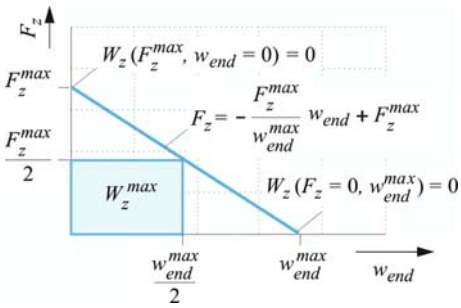

Fig. 5 Lift working capacity of a bi-layer bending actuator [5]

$$\begin{aligned} W_z &= F_z\, w_{end}, \\ &= w_{end}\,(-m\, w_{end} + n), \\ &= -m\, w_{end}^2 + n\, w_{end}. \end{aligned} \tag{1}$$

The first derivative of (1) with respect to w_{end} provides with $m = F_z^{max}/w_{end}^{max}$ and $n = F_z^{max}$ (q.v. Fig. 5):

$$\begin{aligned} W'_z &= 0 = -2\, m\, w_{end} + n, \\ w_{end} &= \tfrac{n}{2\,m} = \tfrac{w_{end}^{max}}{2} \end{aligned}. \tag{2}$$

Substitute $w_{end}^{max}/2$ into (1) we obtain

$$W_z^{max} = \frac{F_z^{max}}{2}\,\frac{w_{end}^{max}}{2}. \tag{3}$$

3.2 *Differential Design*

In the differential design case (hybrid compliant mechanism) the compliant driving link was replaced by rigid link (Fig. 6).

The length of the rigid replacement link $\overline{A_0 A_i}$ results from the distance from the fixed support to the tip of the deflected driving zone at $w_{end}^{max}/2$ (Fig. 7).

The drive angle φ_{12} is the angle between initial (position 1) and final position (position 2), given that the initial position marks the deformed state.

Moreover the initial driving angle φ_1 is specified to $-\varphi_{12}/2$. The initial output angle ψ_1 is here $\pi/2$ and ψ_{12} is the angle between initial and final position of the output link (Fig. 6).

Geometric relations of the equivalent four bar linkage have been used for the determination of the design parameters ℓ_1 (fixed link), ℓ_3 (coupler) and ℓ_4 (output link).

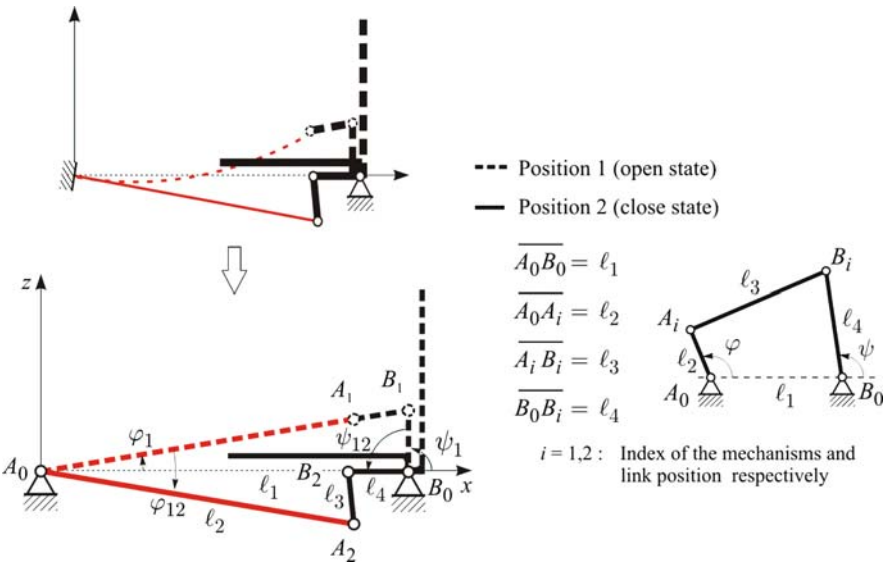

Fig. 6 Four-bar linkage equivalent model of the flaps A-TCM (differential design)

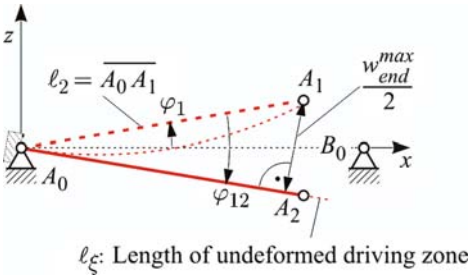

Fig. 7 Definition of the driving lengths and angles

Two transmission equations can be written for the initial position (φ_1, ψ_1) and the final position $(\varphi_1 + \varphi_{12}, \psi_1 + \psi_{12})$ respectively. Furthermore the instant centre initial position leads to $\psi'_{12} = 0$. This results in the conditional equations (q.v. [4]):

$$F(\varphi_1, \psi_1) = 0 = \ell_1^2 + \ell_2^2 - \ell_3^2 + \ell_4^2 - 2\ell_1\ell_2 cos\varphi_1 + 2\ell_1\ell_4 cos\psi_1 - 2\ell_2\ell_4 cos(\varphi_1 - \psi_1), \tag{4}$$

$$F(\varphi_1 + \varphi_{12}, \psi_1 + \psi_{12}) = 0 = \ell_1^2 + \ell_2^2 - \ell_3^2 + \ell_4^2 - 2\ell_1\ell_2 cos(\varphi_1 + \varphi_{12}) + 2\ell_1\ell_4 cos(\psi_1 + \psi_{12}) - 2\ell_2\ell_4 cos(\varphi_1 - \psi_1 + \varphi_{12} - \psi_{12}), \tag{5}$$

$$F'(\varphi_1, \psi_1, \psi'_{12} = 0) \quad = 0 = \ell_1 \sin\phi_1 + \ell_4 \sin(\varphi_1 - \psi_1). \tag{6}$$

From the equations (4–6) follow the conditional equations for ℓ_1, ℓ_3 and ℓ_4. In order to get explicit equations, ℓ_1 is normalised to $\ell_1^* = 1$. The calculation of ℓ_1, ℓ_3 and ℓ_4 result from

$$\ell_4^* = -\frac{\sin\varphi_1}{\sin(\varphi_1 - \psi_1)}, \tag{6}$$

$$\ell_2^* = \frac{\ell_4^*[\cos(\psi_1 + \psi_{12}) - \cos\psi_1]}{[\cos(\psi_1 + \psi_{12}) - \cos\psi_1] + \ell_4^*[\cos(\varphi_1 - \psi_1 + \varphi_{12} - \psi_{12}) - \cos(\varphi_1 - \psi_1)]}, \tag{7}$$

$$\ell_3^* = \sqrt{1 + \ell_2^{*2} + \ell_4^{*2} - 2\ell_2^* \cos\varphi_1 + 2\ell_4^* \cos\psi_1 - 2\ell_2^*\ell_4^* \cos(\varphi_1 - \psi_1)}. \tag{8}$$

Given ℓ_2, the real link lengths arise from $\ell_1 = \frac{\ell_2}{\ell_2^*}$, $\ell_3 = \ell_3^* \frac{\ell_2}{\ell_2^*}$ and $\ell_4 = \ell_4^* \frac{\ell_2}{\ell_2^*}$.

3.3 *Integrally Design*

As distinguished from the differantial design the monolithic flaps A-TCM is characterized by a compliant coupler tightly connected with the compliant driving and the rigid output link.

In the final position the flap's mass produces a deformation of the coupler resulting in a shorter distance $\overline{A_\xi B_1}$. This results in an equivalent model wherein the compliant coupler is substituted by two pin-jointed rigid links (Fig. 8).

Effectively $\ell_{coupler}$ results from $1,5\ \ell_{3_{\text{differntial design}}}$ (see Section 3.1.). The length of the driving zone is here ℓ_ξ (q.v. Fig. 9, $\ell_\xi = \ell_{2_{\text{differential design}}}$). Furthermore the other lengths arise out of the pseudo rigid body model according to [6] by $\ell_2 = \ell_\xi + \xi$ and $\ell_3 = 0,8\ \ell_{coupler}$ with $\xi = 0,2\ \ell_{coupler}$.

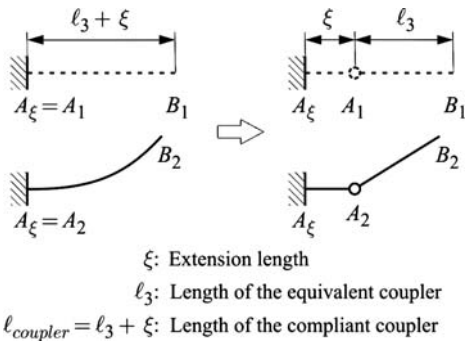

Fig. 8 Equivalent model of the compliant coupler

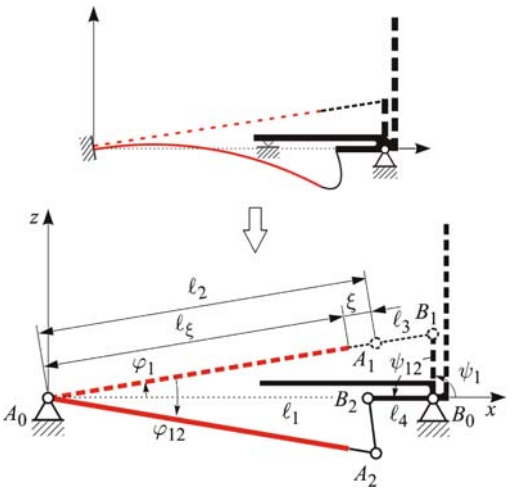

Fig. 9 Four-bar linkage equivalent model of the flaps A-TCM (integrally design)

To design an integral flaps A-TCM its recommended to dimension a differential flap A-TCM (see Section 3.2) first, using the equations (6–8) and the given length of the driving zone as well as the given driving and output angles (q.v. Section 4, Table 2).

4 Numerical Analysis

On the basis of a multi-physics finite element model, coupled field calculations (kinetostatic analysis) were performed in order to analyse the actuator-induced deformation fields of the compliant mechanism and the transfer function of output motion upon input motion (Fig. 10).

For that purpose the geometry was calculated from Sections 3.2 and 3.3. (see Table 2)

The analytical solution of the transfer function $\psi(\varphi)$ for the four-bar linkage described in Fig. 9 (kinematic pre-design) reads (q.v. [4]):

$$\psi = 2arctan\frac{I_B \pm (I_B^2 + I_A^2 - I_C^2)^{1/2}}{I_A - I_C} \quad \text{with} \quad \begin{aligned} I_A &= 2\ell_4(\ell_1 - \ell_2\, cos\varphi), \\ I_B &= -2\ell_2\ell_4\, sin\varphi, \\ I_C &= \ell_1^2 + \ell_2^2 - \ell_3^2 + \ell_4^2 - 2\ell_1\ell_2\, cos\varphi. \end{aligned} \tag{9}$$

These results were used to investigate the dependence of flaps opening angle upon flaps mass and therefore to optimise structurally relevant variables of the driving zone and of the compliant composite coupler.

Table 2 Design parameters of the integral flaps A-TCM used for numerically and analytical calculated transfer functions

Design parameter	Value	Remark
$\ell_{coupler}$	40,00 mm	Length of the compliant coupler, determined by $1,5\ \ell_{3_{\text{differntial design}}}$ (model material: polypropylene, thickness 0.2 mm)
ℓ_{flap}	249,23 mm	Rigid flap, length determined for demonstration porpuses
ℓ_{ξ}	211,00 mm	Length of the driving zone (actuator layer: 2 MFC P1 8557, Smart Material GmbH; passive base layer: unidirectional high tensile carbon fiber epoxy composite, thickness 0.25 mm, w_{end}^{max} = 49.61 mm)
ϕ_1°	6.80°	Initial driving angle, determined by symmectric open and close state (q.v. Section 3.1)
ϕ_{12}°	−13.60°	Driving angle, determined by the drives value $w_{end}^{max}/2$ (q.v. Fig. 7)
ψ_1°	90.00°	Initial output angle, determined by vertical open state
ψ_{12}°	90.00°	Output angle, demanded by 90° opening angle
ℓ_1	249.23 mm	Length of the base frame, calculated from (7)
ℓ_2	219.00 mm	Length of the equivalent drive link (Fig. 8, $\ell_2 = \ell_{\xi} + \xi$)
ℓ_3	32.00 mm	Length of the equivalent coupler ($\ell_3 = 0,8\ \ell_{coupler}$)
ℓ_4	29.74 mm	Length of the output link, calculated from (6)
ξ	8.00 mm	Extension length, $\xi = 0,2\ \ell_{coupler}$

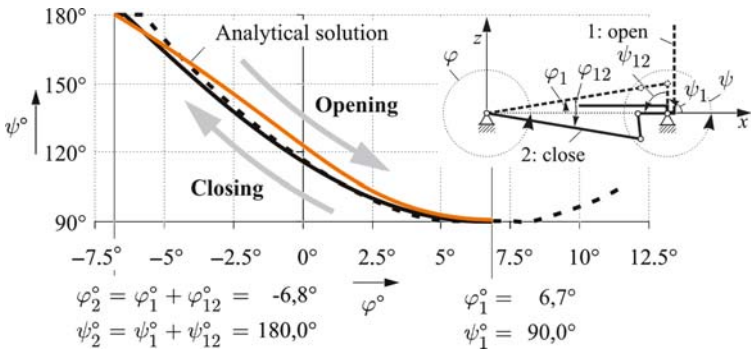

Fig. 10 Numerically calculated transfer function of a flaps A-TCM ($m_{flap} = 5,2$ g) in comparison to the analytical solution of the pre-design

5 Conclusions

The developed design concepts allow to fully exploit the high lightweight potential of active composite compliant mechanisms with integrated actuators. The special locally adapted composite lay-up rises the possibility to produce the entire mechanism as one piece . The driving link and the coupler can be designed as

compliant elements with a compliance-related stiffness concept. The integrally design has a number of properties, which make them really suitable for use in automotive mechatronics and mechanical engineering applications. They are free from friction and clearance as well as easy to assemble. Moreover, the performed composite-adapted embedding of piezo-ceramic actuators allows integrated drives.

Acknowledgments The authors would like to express their gratitude towards the Deutsche Forschungsgemeinschaft (DFG), which supports this research within the scope of the subproject D2 of the Collaborative Research Centre SFB 639 "Textile-Reinforced Composite Components in Function-Integrating Multi-Material Design for Complex Lightweight Applications."

References

1. Hufenbach, W., Modler, K.-H., Täger, O., Modler, N., Lovasz, E.-C.: Design and manufacturing of smart textile compliant hinges. Acta. Technica. Napocensis 2, 831–836 (2006)
2. Modler, N.: Nachgiebig keits mechanismen aus Textilverbunden mit integrierten aktorischen Elementen. Dissertation TU, Dresden (2008)
3. Hufenbach, W., Gude, M.: Analysis and optimisation of multi-stable composites under residual stresses. Compos. Struct. 55, 319–327 (2002)
4. Luck, K., Modler, K.-H.: Getriebetechnik – Analyse, Synthese, Optimierung. 2. Auflage, Springer-Verlag Berlin, Heidelberg, New York (1995)
5. Rau, G.: Thermo-Bimetalle – Thermobimetalle und ihre Anwendung. Grundlagen, Berechnung, Gestaltung, Auswahl. Pforzheim, Rau (1974)
6. Howell, L.L.: Compliant Mechanisms. Wiley, New York (2001)

Software Platform for Analyzing and Optimizing the Mechanical Systems

C. Alexandru

Abstract The paper presents a modern trend in education and scientific research in the field of the mechanical systems, approaching a unitary concept for the kinematic and dynamic analysis and optimization. This concept is based on the utilization of a complex software platform for testing in virtual environment. The components of the digital platform and the interactions between them (data transfer) are presented in paper, as well as the phases of the virtual prototyping process. At the same time, there is presented a complex application, which it was developed in the Centre Product Design for Sustainable Development from Transilvania University.

Keywords Analysis · Mechanical System · Optimization · Virtual prototyping

1 Introduction

As product complexity increases and competitive product development cycle times are reduced, hardware prototype creation and testing become major bottlenecks to successful new product launches. Due to these bottlenecks, leading global manufacturers are feeling increasing pressure to rapidly institute enterprise-wide, simulation-based design and virtual prototyping practices that can insure greater product performance and quality in a fraction of both the time and cost required with traditional approaches [3, 4].

Virtual prototyping is a software-based engineering discipline that entails modelling a mechanical system, simulating and visualizing its 3D motion behaviour under real-world operating conditions, and refining and optimizing the design

C. Alexandru
Centre "Product Design for Sustainable Development", Transilvania University of Braşov, Braşov, Romania

I. Vişa (ed.), *SYROM 2009*,
DOI 10.1007/978-90-481-3522-6_56,

through iterative design studies. This advanced simulation technique consists mainly in conceiving a detailed model and using it in a virtual experiment, in a similar way with the real case. An important advantage of this kind of analysis consists in the possibility of make virtual measurements in any point/area, and for any parameter.

By using various types of commercial software solutions (CAD – Computer Aided Design, MBS – MultiBody Systems, FEA – Finite Element Analysis, C&C – Command and Control), there can be created complex virtual prototypes, which means that accurate modeling of components and the specific operating conditions.

In this context, the paper presents the concept of integrated analysis – optimization – simulation of the mechanical systems using a digital platform for virtual test environment. The platform integrates software solutions for evaluating the form, the fitting, the functionality, and the durability of the mechanical systems.

2 Virtual Prototyping Concept

Traditional CAD/CAM/CAE practices used to evaluate the functional characteristics of the mechanical systems were focused on a concept referred to as art-to-part. Nearly all engineering software activity was oriented toward the design, development, and manufacturing of higher quality parts [7]. Unfortunately, optimal part design rarely leads to optimal system design. The interaction of form, fit, function, and assembly of all parts in a product is a major contributor to overall product quality. The big opportunity to increase quality and reduce time and cost has now shifted to the system level.

The system-focused approach involves the following software solutions: Digital Mock-Up (DMU) – to investigate product form and fit, Functional Virtual Prototyping (FVP) – to assess product function and operating performance, and Virtual Factory Simulation (VFS) – to assess assembly and manufacturability of the product. The integration of the system-focused tools provides a means for realizing the transition from physical to virtual prototyping, with all of the concomitant benefits.

The steps to create a virtual model (Fig. 1) mirror the steps to build a physical prototype. During the build phase, virtual prototypes are created of both the new product concept and any target products which may already exist in the market. The geometry and mass properties are obtained from component solid models. The structural, thermal and vibratory characteristics result from component finite element models or experimental tests.

One of the most important axioms for successful functional virtual prototyping is to simulate as test. Testing of hardware prototypes has traditionally involved both lab tests and field tests in various configurations, which are very expensive. With virtual prototyping, it is enough to create virtual equivalents of the lab and field tests (e.g. virtual tracks in automotive simulation).

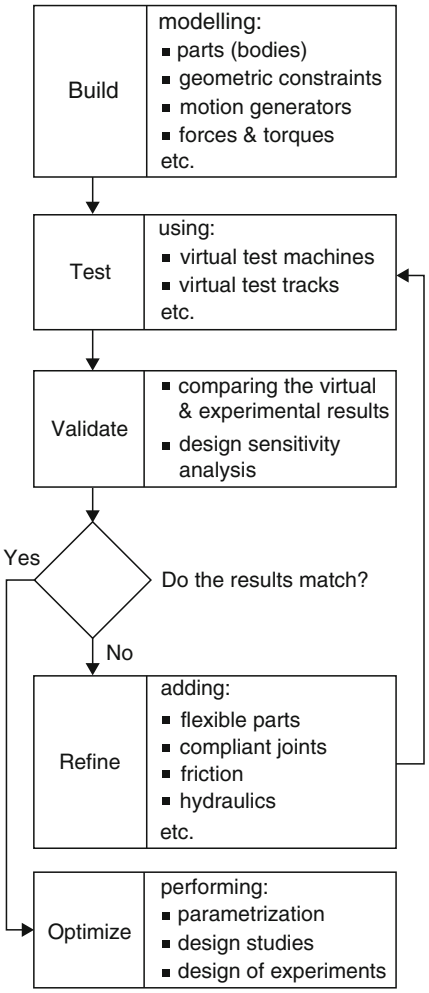

Fig. 1 Virtual prototyping phases

To validate the virtual prototype, the physical and virtual models are tested identically, using the same testing and instrumentation procedures. The results are compared, and design sensitivity analyses are performed to identify design parameters that have influence on the performance results that do not correspond. Afterwards, different changes on these parameters are realized in order to obtain an acceptable correlation.

Refining the virtual prototype involves the fidelity of the model. By replacing the rigid components with flexible counterparts, adding frictions, and representing the automatic systems that control the operating performance of the mechanical system, respectively, can make the improvement of the virtual prototype.

The optimization of the virtual prototype is made with the following steps: parameterizing the model; defining the design variables; defining the objective functions for optimization and the design constraints; performing design studies and design of experiments; optimizing the model on the basis of the main design variables. Parameterizing the model simplifies changes to model because it helps to automatically size, relocate and orient bodies. Design variables allow creating independent parameters and tie modelling objects to them. Design study describes the ability to select a design variable, sweep that variable through a range of values and then simulate the motion behaviour of the various designs in order to understand the sensitivity of the overall system to these design variations.

The objective function is a numerical quantification that distinguishes or rates candidate designs. The constraints are boundaries that directly or indirectly eliminate unacceptable designs; they often take the form of additional goals for the mechanism design. In general, the optimization problem is described as a problem to minimize or maximize the objective function over a selection of design variables, while satisfying various constraints on the design.

Part of the design process is to manipulate the unknowns (variables) in a design to arrive at a good design that satisfies all goals (objectives) and restrictions (constraints). If these features can be quantified, optimization techniques can be used to analytically arrive at the best theoretical solution.

3 Virtual Prototyping Platform

Generally, the virtual prototyping platform includes the following software products (Fig. 2): CAD – Computer Aided Design (ex. CATIA, PROENGINEER, SOLIDWORKS); MBS – MultiBody Systems (ex. ADAMS, SD-EXACT, PLEXUS); FEA – Finite Element Analysis (ex. NASTRAN/PATRAN, COSMOS, ANSYS); Command and Control (ex. MATLAB, EASY5, MATRIXx). The MBS software is the main component of the virtual prototyping platform, and it allows analyzing, optimizing, and simulating the system under real operating conditions [6].

The CAD software is used for creating the geometric (solid) model of the mechanical system. This model contains data about the mass and inertia properties of the rigid parts. The part geometry can be exported from CAD to MBS using standard format files, such as STEP or Parasolid. To import the geometry of the

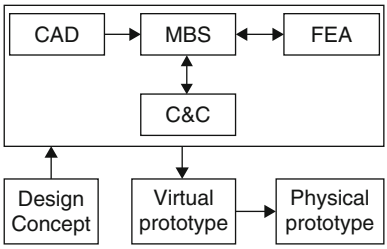

Fig. 2 Virtual prototyping platform

rigid parts, the MBS software reads the CAD file and converts the geometry into a set of MBS geometric elements.

The FEA software is used for modeling flexible bodies in mechanical systems. Integrating flexibilities into model allows to capture inertial and compliance effects during simulations, to study deformations of the flexible components, and to predict loads with greater accuracy, therefore achieving more realistic results. The flexible body characteristics are defined in a finite element modeling output file (MNF – Modal Neutral File). The information in a MNF includes location of nodes and node connectivity, nodal mass and inertia, mode shapes, generalized mass and stiffness for modal shapes. The MBS model transmits to FEA the motion and load states in the mechanical system, which can be defined using a FEA Loads format file.

In the modern concept, the mechanical systems are approached as mechatronic systems, which integrate mechanics, electronics, and information technology. The mechatronic systems are built-up with some units with basic functions, which are made to interact between them in order to form a complex system with a given functionality.

Integrating the control system in the mechanical model at the virtual prototype level, the mechanical designer and the controls designer can share the same model; they can also verify from one database the combined effects of a control system on a nonlinear, non-rigid model. In this way, the physical testing process is greatly simplified, and the risk of the control law being poorly matched to the physical (hardware) prototype is eliminated.

In these terms, the virtual prototyping platform has to include C&C (Command and Control) software, which directly exchanges information with the MBS software; the output from MBS is input for C&C and vice-versa. The mechanical model and the control system communicate by passing state variables back and forth. The analysis process creates a closed loop in which the control inputs from the control application affect the MBS simulation, and the MBS outputs affect the control input levels.

In the concurrent engineering concept, the simulation of the mechatronic system involves the following steps: designing the mechanical model (including bodies, joints, forces etc.), analyzing the dynamic model, identifying the inputs and outputs that complete a closed loop between the MBS model and the control application, explaining the trajectory and synthesizing the reference signals, defining the input block diagram, designing the control system diagram, designing the controller and the interface electric circuits, and simulating the mechatronic system.

In this approach, complex virtual prototypes for different mechanical and mechatronic systems (products) can be developed, which exactly replicate the structure (components) and the operating conditions of the product.

4 Case Study

The virtual prototyping has become very important in a lot of fields, for example automotive industry, aircraft industry, railway industry, robotics, biomechanics, mechatronic products, industrial machines, renewable energy systems and so on.

The researches in the field of the renewable energy represent a priority at global level because provides viable alternatives to a series of major problems that humanity is facing: the limited and pollutant character of the fossil fuels, global warming, and the greenhouse effect. In the design process of the renewable energy systems (RES), the virtual prototyping can be used to simulate the real behaviour of these complex systems, as well as for evaluating the durability, and the energetic and economic efficiency of the RES-based products.

To demonstrate the virtual prototyping capabilities, in the present paper, the virtual prototype of the mechatronic tracking system used for a photovoltaic panel is developed and analyzed. The study is made using a digital prototyping platform that integrates the following licensed software packages: CAD – CATIA, MBS – ADAMS/View, FEA – ADAMS/AutoFlex, C&C – EASY5 and ADAMS/Controls.

The solar energy conversion is one of the most addressed topics in the fields of renewable energy systems. The present-day techniques allow converting the solar radiation in two basic forms of energy: thermal and electric energy. The technical solution for converting the solar energy in electricity is well-known: the photovoltaic (PV) systems. For increasing the efficiency of the photovoltaic conversion, there are two ways [5]: increasing the efficiency at the absorber level; increasing the degree of use of the solar radiation, which can be maximized by tracking the Sun path.

Basically, the tracking systems are mechanical systems driven by electrical motors, which are controlled in order to ensure the optimal positioning of the PV module relatively to the Sun position, on the entire period of the day and also depending on the season. The orientation may increase the efficiency of the conversion system up to 50% [1, 2].

The photovoltaic system with tracking is efficient if the following condition is achieved, $\varepsilon = (E_T - E_F) - E_C >> 0$, where E_T is the electric energy produced by the photovoltaic panel with tracking, E_F – the energy produced by the same panel without tracking (fixed), and E_C – the energy consumption for orienting the panel. The maximization of the efficiency parameter ε by optimizing the tracking system became an important challenge.

The application in paper is made for a pseudo-equatorial tracking system, at which the daily motion is directly driven by a rotary motor, and the elevation motion is performed with a linear actuator (Fig. 3). The PV panel is mounted on the sustaining frame which is connected to a support that rotates around the horizontal axis for generating the elevation. The daily motion is made by rotating the panel (frame) relative to the support. The linear actuator that generates the elevation motion is disposed between support and base/pillar.

The solution for system used in the study was selected from the multitude of the structural solution by using of the Multi Criteria Analysis. The evaluation criteria of the solutions were referring to the tracking precision, the amplitude of the motion, and the complexity of the system from manufacturing and implementation point of view.

The virtual model of the tracking system is designed so that it has six parts, which are connected through the following geometric constraints: base/pillar fixed

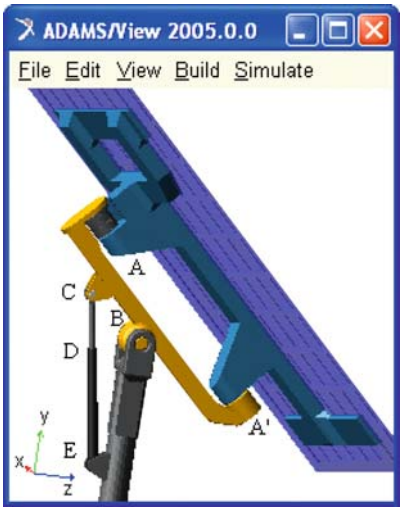

Fig. 3 Virtual model of the solar tracker

on ground; intermediary support mounted on base – revolute joint (B); actuator cylinder to base – revolute joint (E); actuator piston to support – revolute joint (C); cylinder to piston – translational joint (D); rotary motor fixed on support; panel frame to motor/support – revolute joint (A-A').

The model takes into consideration the mass forces, the reactions in joints, and the joint frictions. Joint reactions, bending moment, and torque preload determine the frictional torque in the revolute joints, while joint reaction force, bending moment, torsional moment, and force preload are used to compute the frictional force in the translational joint. For modeling the joint frictions there are considered the friction arm, the pin radius, the bending reaction arm, the coefficient of dynamic and static friction, the stiction transition velocity, and the maximum stiction deformation.

Using the MBS environment ADAMS, the geometric optimization of the tracking system is made in view to minimize the motor torque (for the daily motion), and the motor force (the elevation motion). The parameterization of the mechanism is made using the points that define the structural model, in fact the locations of the geometric constraints (see Fig. 3). The global coordinates of the design points (A, B, C, D, and E) were defined as design variables. The optimization was made, individually, for each motion, in the specific kinematic chain, considering the continuous orientation (without brakes).

In paper, the exemplification of the geometric optimization is made for the elevation (seasonal) motion chain. The numeric simulations correspond to the Braşov geographic area, considering the passing from the equinox position (45.55° – relative to the horizontal axis) to the summer solstice position (22.05°); therefore, the angular field of the elevation angle is 23.5°. The rotation is made in 0.1 h, the daily position of the panel being fixed at 0° (in the solar noon position).

The kinematic chain BCDE of the elevation motion is symmetrical disposed in the longitudinal – vertical plane (YZ). Maintaining this symmetry, we have taken into account for optimization the global coordinates of the joints on base (B, E). In this way, there are four design variables: $Y_B \rightarrow DV\_1$, $Z_B \rightarrow DV\_2$, $Y_E \rightarrow DV\_3$, and $Z_E \rightarrow DV\_4$.

In addition, for maintaining the relative location and orientation of the translational joint between cylinder and piston, the markers that define this joint were parameterized using the expressions: LOC_RELATIVE_TO({0,0,0}, point_D) – the function returns an array of three numbers representing a location, by transforming a specified location that is relative to a coordinate system object; ORI_ALONG_AXIS(point_E, point_C, "Z") – the function returns the alignment of a specified axis from one coordinate system object to another, and has an underlying parameter that allows it to express the resulting orientation in the proper coordinate system.

The design objective for optimizing the elevation motion is the minimization of the motor force for generating the imposed trajectory; the design objective value is the maximum absolute value of this measure during simulation. At the same time, we defined a design constraint that controls the pressure angle, measured between the vector of the linear force generated by actuator and the vector of the intermediary element's velocity in the point C. Theoretically, when the pressure angle is 90°, the system is blocked, because the piston cannot transmits the force to the intermediary support. Practically, considering the frictions, the self-blocking appears at values smaller than 90°, and for safety reasons, the maximum acceptable value of the pressure angle is 65°.

For evaluating the sensibility of the objective function on the modification of the design variables, design studies were performed. These studies are individually made for each variable, keeping the rest fixed at their nominal value. The results represent a summary of the sensitivity of the motor force to a given change in the geometric location, keeping all other locations fixed. We found sensitivities by using the plot statistics function and finding the slope of the design study curve for motor force plotted against design variable value. In this way, we identified the main variables, with great influence on the motor force, namely DV_1 and DV_3 (the vertical locations of the joints on base); the longitudinal coordinates (DV_2, DV_4) are secondary variables.

The results for the optimum mechanism, regarding the elevation motion, are presented in Fig. 4, with the following maximum values: motor force (a) – 137 N, pressure angle (b) – 46°. The results confirm the viability of the optimization algorithm, and this will have an important contribution for the energetic efficiency of the tracking system.

In the next step, for obtaining more realistic results, we have developed the control system of the tracking mechanism using ADAMS/Controls and EASY5. For connecting the mechanical model and the control system, the input and output parameters have been defined. The control torque (for the daily motion) and force (the elevation) represent the input parameters in the mechanical model. The outputs, transmitted to the controller, are the daily and elevation angles of the PV panel.

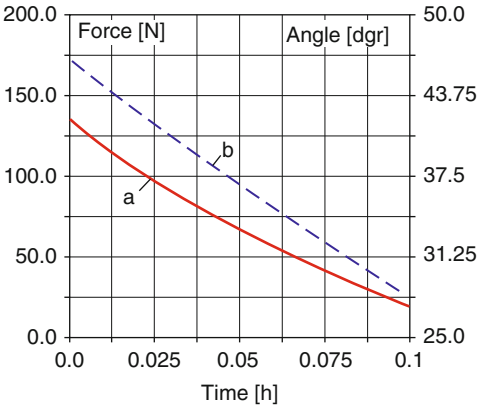

Fig. 4 Geometric optimization result

For the input state variables, the run-time functions are 0.0 during each step of the simulation, because the control torque and force will get their values from the control system. The run-time functions for the input variables are defined using a specific function that returns the variable value [8]: VARVAL(control_torque), respectively VARVAL(control_force). For the output variables, the run-time functions return the angles about the revolution axes, as follow: the daily angle – AZ(panel.MAR_1, support.MAR_2), which returns the rotation of one coordinate system marker attached to panel about the Z-axis of another marker attached to support; the elevation angle – AX(support.MAR_3, base.MAR_4), which returns the rotation of one marker attached to support about the X-axis of another marker to base.

The next step is facilitating the exporting of the ADAMS plant files for the control application. The input and output information are saved in a specific file for EASY5 (*.inf). There are also generated a command file (*.cmd), and a dataset file (*.adm), which are used during simulation; with these files, the control system diagram was created in EASY5. For example, in Fig. 5 there is shown the control system diagram for the daily motion, in which the input function generator represent the database of the daily angle. From controller point of view, for obtaining reduced transitory period and small errors, we used a PID controller.

The mechanical system sub-block includes the ADAMS Plant, which is used to simulate the mechanical model in ADAMS/Solver form (.adm file) and in ADAMS/View form (.cmd file). In the mechatronic model, ADAMS accepts the control torque and force from EASY5 and integrates the mechanical model in response to them. At the same time, ADAMS provides the current angles for EASY5 to integrate the control system model.

The second way for increasing the energetic efficiency of the PV system with tracking consists in the optimization of the motion law. The PV panel can be rotated without brakes during the day-light, or there can be a step-by-step motion. In paper, the strategy for optimizing the motion law aims to reduce the angular field of the daily motion and the number of actuatings, without significantly affecting the incoming solar energy, and to minimize the energy consumption.

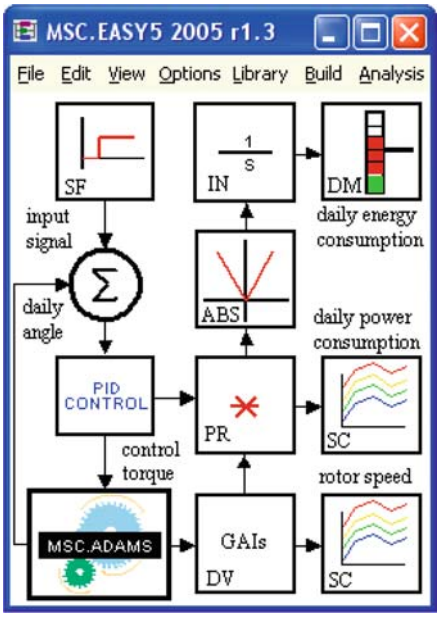

Fig. 5 Control system diagram

The energy produced by the PV panel depends on the quantity of incident solar radiation, and the module's efficiency. The incident radiation, which is normal to the active surface, depends on the direct terrestrial radiation and the angle of incidence. The direct radiation is empirical established, depending on the extraterrestrial radiation, the medium solar constant, the day number during a year, the distortion factor, the solar altitude angle, the solar declination, the latitude angle, the solar hour angle, and the local time [5]. The incidence angle is determined from the scalar product of the Sun's ray vector and the normal vector on panel, depending on the diurnal and seasonal angles of the Sun's rays, the daily and elevation angles of the module, and the azimuth angle [2]. In this way, we are able to estimate the incident radiation in every day, for different locations and tracking strategies.

In paper, the numeric simulations were performed for the summer solstice day, which is a relevant situation for evaluating the energetic efficiency, with the following input data: the location latitude, 45.633 North; the location longitude, 25.583 East; the solar declination, 23.45°; the solar time interval, $T \in [4.26, 19.74]$; the elevation (seasonal) angle, 22.05°.

For identifying the optimum motion field, we have considered the correlation between the motion amplitude and the solar time, for obtaining symmetric revolute motions relative to the solar noon position (the daily angle, $\beta = 0$). The analysis was performed for the following tracking cases: (a) $\beta \in [-90°, +90°]$, $T \in [4.26, 19.74]$ – the maximum interval; (b) $\beta \in [-60°, +60°]$, $T \in [6.84, 17.16]$; (c) $\beta \in [-30°, +30°]$, $T \in [9.42, 14.58]$; (d) $\beta = 0$, $T \in [4.26, 19.74]$ – the fixed panel. In this study, we considered that the panel in rotated without brakes.

For beginning, we obtained the incident radiation curve (using the mathematic algorithm described in [2]), for each tracking case (Fig. 6), and then, by integrating the radiation curves and taking into account the active surface (1.26 m^2) and the panel efficiency (15%), we determined the energy production. Afterwards, the energy consumption was obtained using the virtual prototype of the tracking system. For evaluating the energy consumption, there is also considered the return of the system in the initial position, after the sunset, in 0.2 h, T∈[19.74, 19.94].

In this way, the energy balance was performed, the results being systematized in Table 1 (the energy gain is computed relative to the fixed panel case). Analyzing these results, we identified the optimum motion field (i.e. the daily angle interval), β∈[–60°, +60°], in which there is the maximum energy gain.

In the next stage, considering the optimum motion field, we have evaluated different step-by-step tracking strategies. The key idea is to minimize the operating time, which is important for the system reliability. In these terms, we have developed and analyzed four tracking cases, depending on the number of steps (in consequence, the step dimension – Δβ) for realizing the optimum angular field: 8 steps (Δβ=15°), six steps (Δβ=20°), four steps (Δβ=30°), two steps (Δβ=60°).

One of the most important problems in the step-by-step tracking is to identify the optimum actuating moment. The solution to this problem is obtained in the following phases: the optimum angular field was segmented into the intermediary positions, depending on the step dimension for each case, and the incident radiation curves have been consecutively obtained considering the module fixed in these positions

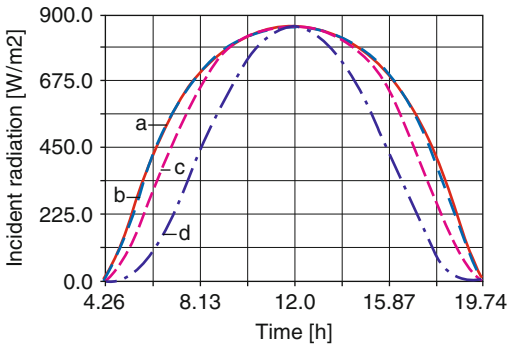

Fig. 6 Incident radiation curves

Table 1 Energy balance for the considered tracking cases

β [dgr]	E_T/E_F [Wh per day]	E_C	Gain [%]
[–90, +90]	1740.88	79.11	35.02
[–60, +60]	1726.44	39.86	37.04
[–30, +30]	1598.91	10.73	29.04
0	1230.73	–	–

Table 2 Energy balance for the step-by-step orientation

Number of steps	E_T [Wh per day]	E_C	Gain [%]
8	1718.35	43.79	36.06
6	1715.39	42.69	35.91
4	1706.92	40.93	35.36
2	1670.97	39.60	32.55

during the day-light; analyzing these curves, we have identified the moment in which the value of the incident radiation for a certain position "k" become smaller than the value in the next position "k + 1"; the analysis continues with the next pair of positions "k + 1", "k + 2", and so on.

For the considered step-by-step cases, the results of the energy balance are shown in Table 2, the energy gain being computed relative to the fixed panel. According with the results from Tables 1–2, we obtained values closed-by the continuous motion case, and this demonstrates the viability of the adopted step-by-step strategy. The consumptions for realizing the step-by-step motion are little greater than the consumption for the continuous motion, and this because of the over-shootings that appear when the motor is turned-on/off.

The final aspect for this study is to refine the tracking system by adding flexible parts. The modeling of the mechanical structure with finite elements has two main objectives: identifying the eigenshapes and eigenfrequencies of the system, which are useful to avoid the resonance phenomenon due to the action of the external dynamic loads (as wind or earthquake); identifying the maximum deformabilities and the equivalent stresses, depending on the action of the external factors and on the position of the structure.

In paper, the analysis of the structure is made for different values of the daily position of the panel, in the above-obtained optimum field, $\beta \in [-60^\circ, +60^\circ]$, the elevation being fixed at 22.05° (for the summer solstice day, in Braşov geographic area). The external load is materialized by forces and pressures which are produced by a 90 km/h wind speed which is acting on the structure; this speed generates a pressure of 1,200 MPa on the panel surface.

For creating the finite element model of the tracking system, we used the specific ADAMS/AutoFlex module, which automatically mesh the geometries imported from CAD system. In these terms, analyzing the refined virtual prototype of the tracking system, we obtained the following results: the variation of the eigenfrequencies with the daily position angle is insignificant from quantitative point of view; the maximum values of the equivalent stresses (von Misses), which appear in the rotational joints of the structure, are less than the admissible resistance values (90 ... 120 MPa), and this assures the mechanical resistance condition (the maximum value is 71 MPa); the maximum value of the deformability is small ($<$0.08 mm), and this ensures proper functioning of the system.

5 Final Conclusions

The application is a relevant example regarding the implementation of the virtual prototyping tools in the design process of the mechanic and mechatronic systems. One of the most important advantages of this kind of simulation is the possibility to perform virtual measurements in any point or area, and for any parameter (motion, force, energy). This is not always possible in the real case due to the lack of space for transducers placement, lack of appropriate transducers or high temperatures.

Integrating the finite element model in the multibody system analysis, we can quickly build a parametric flexible body representation of a component, analyze the system, make changes to the flexible body and evaluate the effect of the changes, all within the MBS environment.

These aspects help us to take quick decisions on any design changes without going through expensive hardware prototype building and testing. The behavioral performance predictions are obtained much earlier in the design cycle of the mechanic and mechatronic systems, thereby allowing more effective and cost efficient design changes and reducing overall risk substantially.

References

1. Abdallah, S.: Two-axis sun tracking. Energy Conversion & Manage. 45(11), 31–39 (2004)
2. Alexandru, C., Pozna, C.: Different tracking strategies for optimizing the energetic efficiency of a photovoltaic system. In: Proceedings of the 16-th IEEE International Conference AQTR, Cluj-Napoca, Vol. 3, pp. 434–439 (2008)
3. Bernard, A.: Virtual engineering: methods and tools. J. Eng. Manufacture 219(5), 413–421 (2005)
4. Haug, E.J.ao: Virtual prototyping simulation for design of mechanical systems. J. Mech. Des. 117(63), 63–70 (1995)
5. Meliß, M.: Regenerative Energie- quellen. Springer, Berlin (1997)
6. Orlandea, N.V.: ADAMS – theory and applications. Vehicle Syst. Dynamics 16, 121–166 (1987)
7. Ryan, R.: Functional Virtual Prototyping. MDI Press (2001)
8. Getting Started using ADAMS/View v2005 – Training Guide. MSC Software Corporation, Santa Ana, USA (2005)

Considerations Regarding the Transdisciplinary Nature of the Homeokinesis Concept, as a Result of Its Integration in the Theory of Complex Mechatronical Systems

S. Berian and V. Mătieş

Abstract The purpose of this paper is that of creating, in the context of a transdisciplinary approach to mechatronical education, a bridge between nonlinear thermodynamics, self-organized mechatronical complex systems and the homeokinetic principle. The systems described by non-linear thermodynamics become, near the bifurcation point, extremely sensitive to small external fluctuations, self-organizing themselves through symmetry-breaking. Simple learning rules, derived from the homeokinetic principle, realize a self-learning robotic system with an emergent explorative-predictable behaviour. The homeokinetic principle ensures the functioning of the mechatronical system on the "edge of chaos" regime, which corresponds to the T state from Lupascian logic and transdisciplinary methodology.

Keywords Autonomous robot · Homeokinesis principle · Mechatronics · Self organization · Transdisciplinarity

1 Introduction

Considering the absence of a universally-accepted definition of mechatronics or its specific curriculum, the identity of mechatronics is still an open subject. Craig claims that "mechanical engineering professors teaching design must teach an integrated approach to design – mechanical, electronic, controls and computers. . ." [7]. According to the Erkmen et al., "mechatronics has come to mean the synergistic use of precision engineering, control theory, computer science and sensor/actuator technology design to design improved products or processes" [14]. Chronologically, Harashima et al. were among the first [15] who emphasized that the terms *synergy* and *integration* are at the foundation of mechatronics, defined as "the

S. Berian (✉)
Baptist High School "Emanuel" Oradea, Technical University Cluj-Napoca, Cluj-Napoca, Romania

I. Vişa (ed.), *SYROM 2009*,
DOI 10.1007/978-90-481-3522-6_57,

synergistic integration of mechanical engineering and intelligent computer control in the design and manufacturing of industrial products and processes" [16]. Through its integrative and synergetic nature, mechatronics transcends the limits of a sole discipline [20]. Consequently, taking into account the consistency and, at the same time, the integrative and creative valencies of the transdisciplinary approach [2], we consider that the identity of mechatronics can be enriched through revealing its transdisciplinary character. The third postulate (the epistemological one) of the transdisciplinary approach, deeply rooted in the quantum mechanics' hypothesis of boot-strapping, reveals that complexity is an essential characteristic of the world [21, 22]. Hence, we consider that the transdisciplinary approach of mechatronics requires the study of complex systems, defined as a numerous ensemble of simple interactive entities which allow the appearance of emergent phenomena: global coherent patterns which, although being the result of the interactions between the system's components, cannot be deduced by studying these isolated parts apart from each other [4, 6]. The emergent proprieties of complex systems have a strong synergical character. The adaptable behaviour of mechatronical open systems, integrated in the world through continuous exchange of matter, energy and information with the environment is similar to that of the living systems [3]. The system's level of adaptivity is measured by the capacity of the system to self-organize itself. Self-organisation is an interdisciplinary key concept that describes the formation of specific patterns in the presence of unspecific driving forces [19]. Following the *principle of homeokinesis*, emergent behaviours can be generated by self-organizing autonomous robotic agents (situated in a complex external world) using nonlinear controllers [8–11, 19]. Further on, we will explain the meaning of central concepts previously mentioned, starting from the roots of self-organization: the nonlinear thermodynamics.

2 Self-organized Complex Systems

For an open thermodynamic system, the expression:

$$\frac{\partial(\rho s)}{\partial t} = -\nabla \vec{J}_s + \sum_i J_i X_i \tag{1}$$

plays the role of the second principle of classic thermodynamics [28]. $\vec{J}_s$ represents the total entropy flux/unity of volume/unity of time exchanged with the environment, while $\sum_i J_i X_i$ is the sum of all the products between generalized forces, X_i, and flows, J_i, of the irreversible internal processes. The significance of the left term of the equation (1) is given by:

$$S = \int_V \rho s \, dV, \tag{2}$$

where S represents the total entropy of the system.

If the system is near equilibrium, there is a linear dependence between the flows and the forces. In this region, according to Prigogine's theorem of the minimum production of entropy [25], any system evolves to a *non-equilibrium steady state* in which the production of entropy,

$$P = \int_V \sum_i X_i J_i \, dV, \tag{3}$$

reaches the minimum value. The steady state, in which the system transfers entropy to the environment, is stable with regard to the local perturbations, and therefore the system does not allow spontaneous manifestations which would enable patterns of increased complexity to appear.

For the systems from the linear region, whatever the limit conditions are, $\delta^2 S$ is a Liapunov function [25], namely it satisfies the two mathematical conditions which ensure the stability of the system, due to the amortization of the perturbations:

$$\delta^2 S < 0, \tag{4}$$

$$\frac{1}{2}\frac{\partial}{\partial t}\delta^2 S > 0. \tag{5}$$

In the case of thermodynamic systems far enough from equilibrium for the relations between the flows and the forces to become non-linear, the condition (5) is not satisfied, the system becoming unstable and is therefore lead by laws specific to itself [23]. The systems described by nonlinear thermodynamics become, near the *bifurcation point*, extremely sensitive to small external fluctuations, perceiving differences that are impossible to distinguish by systems that are in equilibrium or in its nearness. The bifurcation points are situated in the proximity of unstable regions in which the far-from-equilibrium open system 'chooses', through *symmetry-breaking*, between its multiple possible future evolutions. These small differences lead to the process of *self-organization*, by selecting, through *negative feed-back*, certain external perturbations which, through *positive feed-back*, are amplified, leading to *multistability*: the coexistence of stable spatio-temporal structures [3]. This phenomenon occurs, for instance, in autocatalytic chemical reactions, in the case of spontaneous magnetization or Bénard cells [26].

3 The Self-organization of the Behaviour of Complex Mechatronical System Through Homeokinetic Learning

The behaviour of a robot is a spatial-temporal pattern which is formed in the complex interaction between the robot and its environment. In the early days of cybernetics, homeostasis was considered the basic concept of self-organization [19].

Introduced by Canon [5], the term *homeostasis* initially referred to the self-regulating mechanism of an organism, which enables it to maintain its essential variables (i.e. blood pressure or body temperature) at a constant level. Cybernetics proposed the negative (self-correcting) feed-back loops as the mechanism that underlies homeostasis and adaptive behaviour in organism [27]. The concept of the *self-correcting system* was extended by Ashby [1], which defined an *ultrastable system* (particularly an ultrastable autopilot) as one that can adapt to radical disruptions, being able to plastically reconfigure itself when any of its essential variables would go outside their bounds. Such ultrastability (*higher-order stability*) requires a primary feed-back, between the sensorimotor system and the environment, and a secondary one, between the essential variables and the sensorimotor system. Although there are attempts to introduce the homeostatic principle in robotics [24], there aren't many practical applications [13] because this principle is very helpful in stabilising systems through the compensation of external perturbations, but, not being adapted to any specific process, it seems to be of limited for the construction of behaviour systems [17, 19]. As showed, self-organization is a result of the "compromise" between a driving force (positive feed-back) which amplifies external perturbations and a regulating force (negative feed-back) which tries to stabilise the system [19].

In the field of artificial intelligence, particularly in evolutionary robotics, the *adaptivity* is the main goal of an autonomous agent. Adaptivity means much more than stability: the system must operate in a regime situated somewhere between the chaotic behaviour and the ordered state of homeostatic equilibrium [3]. In this *edge of chaos* regime the robot is able to adapt his behaviour to changing external condition searching for new functionalities [12].

Shortly, true autonomy must involve the emergence of self-organized behaviours for robots, through symmetry-breaking [3, 10, 11]. The self-organization of the robot means that its evolution must not be driven into a desired direction by a semantic introduced from outside, like in supervised learning or in reinforcement learning. In other words, a self-organized robot must adapt to the environment by developing functional behaviours which do not depend on an imposed target or a reward signal.

The principle of *homeokinesis*, the "dynamical pendant of homeostasis" [8], provides a mechanism for the self-organization of the robot, in which the goal of the agent is not to remain in a stationary state (i.e. homeostatic equilibrium), but to attain a definite *internal kinetic regime*. Homeostasis and homeokinesis are not mutually exclusive, but are complementary [17].

The homeokinesis principle "is completely unspecific and yet induces specific, seemingly goal-oriented behaviours of an agent in a complex external world" [8]. The robot, endowed with an adaptive, internal representation of its behaviour (*self-model*), is able to discover its own semantics, using the *misfit* between the behaviour predicted by the model and the true behaviour as the *learning signal* for the adaptation of both the model and the controller.

If the robot has a controller (neural network) that generates motoric outputs:

$$y_t = K(x_t; c), \tag{6}$$

where $x_t \in \mathbf{R}^n$ are the sensory inputs observed at time t and c is the parameter vector, these outputs represent motor commands executed in the real world. Consequently, new sensor values appear: x_{t+1}. The robot is equipped with an internal adaptable *world model* which realizes a prediction function ψ, the predicted sensor values at $t + 1$.There's an unavoidable difference between sensor inputs and the predictions of the internal model [8]:

$$\psi(x_t) \approx x_{t+1}. \tag{7}$$

If $\hat{x}_t$ is the vector of the sensor values reconstructed by the model from the sensor values x_{t+1}, this reconstruction represents a step backward in time [17]:

$$\hat{x}_t = \psi^{-1}(x_{t+1}). \tag{8}$$

The sequence $x_t \rightarrow x_{t+1} \rightarrow \hat{x}_t$ was named by Der et al. the "time loop" [11], and the energy function:

$$E = \| u \|^2, \tag{9}$$

where $u_t = x_t - \hat{x}_t$, represents the *time loop error*. The error is used as a learning signal for the adaptation of both the model and the controller. Minimizing E minimizes the sensitivity of $\psi^{-1}$and maximizes the sensitivity of ψ. So, time reversal inverts instable behaviour into stable one and the stable behaviour into unstable one [17]. By the descent of E, the modelling error $x_{t+1} - \psi(x_t)$ is decreased and the sensitivity of the system is increased (the robot is unstable in the forward time direction) [10, 17].

In conclusion, "an increase in sensitivity will tend to lower predictability and vice versa, such that the actual behaviour can be expected to *oscillate between periods of exploration and stabilization* in a way which reflects the quality of the predictor and the complexity of the environment" [17]. Then, as a result of the nonlinearities of the world and of the controller, behavioural multistability emerges.

The computer simulations shows that, under control by homeokinetic principle, mechatronical complex systems (robots starting from *tabula rasa* initial conditions), learned a number of different behaviours which depends on the environmental conditions: Braitenberg vehicle develop a stable light following behaviour [8], Khepera robots learns to follow a wall, to balance a ball [9], to navigate through narrow corridors [10] or to move a little box in order to explore a larger arena [11], etc. Similar self-organized behaviours have been pointed out in the case of certain real robots, like Pioneer robot or rocking stamper [12, 13, 29].

It is remarkable that, if the environmental conditions drastically changes, the mechatronical system (i.e. Khepera robot) is able to switch, through symmetry breaking between different behaviours, leading to multistability (the coexistence of stable spatio-temporal behavioural patterns).

4 The Transdisciplinary Nature of the *Homeokinesis* Concept

The experiments show that the mechatronical complex system (the robot) governed by the homeokinetic principle *adapts its exploration according to the knowledge of the world*: as long as the error is small the knowledge is large, the prediction quality of the system increases, favouring the *explorative mode*. If the error increases, the predictability decreases and leads to the *avoidance behaviour*. In other words, the environmental changes generate changes in sensor values, which progressively destabilize the robot, leading it towards a chaotic regime. The time loop error keeps the robot in harmony with the environment, providing a counteracting effect: the requirement that the effects of the robot's actions must remain predictable.

In conclusion, learning under the principle of homeokinesis drives the mechatronical complex system (the robot) towards the *edge of chaos*, a working regime where the system is characterized by the "optimum payoff between creativity and stability" [12]. The mechatronical system's behaviour is *explorative* (the robot is creative, exploring sometimes risky regions) but remains, in the mean time, *predictable* (is able to adapt to slow environmental changes, keeping a stable, non-chaotic behaviour).

Using the Lupascian logic language [18], the *actualization* of the pure explorative behaviour means reaching maximum *heterogenisation*, and the robot will move chaotically. Reversely, the actualization of the pure *predictive* behaviour means reaching maximum *homogenisation*: the robot gets stuck in a sterile stable state. As Nicolescu noticed, both extreme, absolute heterogenisation and also absolute homogenisation would lead to an eternal immobility, to "cosmic death" [22].

For the mechatronical system to function the actualisation of explorative behaviour means the potentiation of predictive behaviour and reverse, without either one of them being able to reach absolute potentiation or actualisation. According to Lupascian logic [18], the maximum antagonism, or, informationally speaking, *the maximum complexity* is reached in *T state* in which the two behaviours are both semi-actual and semi-potential. Introducing the T state, the Lupascian logic replaced the Aristotelian principle of the excluded third with the *principle of the included third*, identified in Nicolescu's transdisciplinary methodology as *the principle of the Hidden Third* [18, 22]. Thus, we can now claim that the T state represents, in the case of the studied mechatronical systems, the edge of chaos, the state in which certain explorative-predictive behavioural patterns emerge.

The homeokinesis principle ensures the functioning of the mechatronical system on the edge of chaos, reaching its autonomy through realization of a dynamic harmony between the "interior" and the "exterior" world of the system. *Mutatis mutandis*, in Basarab Nicolescu's transdisciplinary approach [21, 22], knowledge is, simultaneously, external and internal, the study of the Universe and of the human being complementary supporting each other.

5 Conclusions

The contemporaneous growth of interest in mechatronics has identified a need for a new educational paradigm, which favours the formation of engineers and teachers endowed with a comprehensive, creative, integrative thinking in the technological area. In this context, the necessity to transcend the limits of a single discipline becomes an imperative educational request. Therefore, through the present paper we intend to emphasize the transdisciplinary nature of mechatronics, by creating links between nonlinear thermodynamics, the self-organization of complex systems and the emergent robots behaviour derived from the homeokinetic principle.

We consider that, using the Lupascian logic, through which we showed the link between the edge of chaos regime of a robot and the T state from transdisciplinary methodology, we emphasized the creative potential of a transdisciplinary approach to mechatronics.

References

1. Ashby, W.: Design for a Brain: The Origin of Adaptive Behaviour. Chapman and Hall, London (1960)
2. Berian, S., Mătieş, V.: Considerations regarding the process of stigmergic self-organization in the functioning of mechatronical systems. Scientific Bulletin of the "Politehnica" Institute of Timisoara 53(67), 219–224 (2008)
3. Berian, S., Mătieş, V.: Integrative valencies of the transdisciplinary approach. Scientific Bulletin of the "Petru Maior" Institute of Tg. Mureş 3(5), 1–8 (2007)
4. Boschetti, F., Prokopenko, M., Macreadie, I., Grisogono, A.M.: Defining and detecting emergence in complex networks. In: Proceedings of 9th KES Conference, Melbourne, pp. 573–580 (2005)
5. Canon, W.: The Wisdom of the Body. Norton, London (1939)
6. Casti, J.L.: Would-be Worlds: How Simulation is Changing the Frontiers of Science. Wiley, New York (1997)
7. Craig, K.: Is anything really new in mechatronics education? IEEE Robot. Automation Mag. 8(2), 12–19 (2001)
8. Der, R., Hesse, F., Liebscher, R.: Self-organized exploration and automatic sensor integration from the homeokinetic principle. In: Proceedings of Workshop on SOAVE'04, Düsseldorf, Fortschritt-Berichte VDI, 10(743), 220–230 (2004)
9. Der, R., Hesse, F., Martius, G.: Rocking stamper and jumping snake from a dynamical system approach to artificial life. Adaptive Behav. 14(2), 105–115 (2006)
10. Der, R.: Homeokinesis and the Moderation of Complexity in Neural Systems. Available at: http://www.informatik.uni-leipzig.de/~der/Veroeff/leakint.pdf (2005)
11. Der, R., Liebscher, R.: True Autonomy from Self-Organized Adaptivity. Available at: http://www.informatik.uni-leipzig.de/~der/Veroeff/bristol.pdf (2002)
12. Der, R., Pantzer, T.: Emergent robot behavior from the principle of homeokinesis. In: Proceedings of Workshop on SOAVE' 2000, Ilmenau, Fortschritt-Berichte VDI, 10(643), 39–46 (2000)
13. Der, R., Steinmetz, U., Pasemann F.: Homeokinesis - a new principle to back up evolution with learning. In: Computational Intelligence for Modelling, Control, and Automation, vol. 55 of Concurrent Systems Engineering Series. IOS Press, Amsterdam, pp. 43–47 (1999)

14. Erkmen, A.M., Tsubouchi, T., Murphy, R.: Mechatronics education. IEEE Robot. Automation Mag. 8(2), 4 (2001)
15. Grimheden, M.: Mechatronics engineering education. Doctoral Thesis, Royal Institute of Technology, Stockholm (2006)
16. Harashima, F., Tomizuka, M., Fukuda, T.: Mechatronics–what is it, why, and how? IEEE/ASME Trans. Mechatronics 1(1), 1–4 (1996)
17. Hesse, F., Der, R., Herrmann, J. M.: Reflexes from self-organizing control in autonomous robots. In: Berthouze, L., Prince, C.G., Littman, M., Kozima, H., Balkenius, K. (eds.) 7th International Conference on Epigenetic Robotics: Modelling Cognitive Development in Robotic Systems, Rutgers University, Piscataway, NJ, vol. 134 of Cognitive Studies, pp. 37–44 (2007)
18. Lupaşcu, Ş.: L'éxpérience microphysique et la pensée humaine. Rocher, Paris (1989)
19. Martius, G., Herrmann, J.M., Der, R.: Guided self-organisation for autonomous robot development. In: Costa, A., Francesco, M. (eds.) Advances in Artificial Life 9th European Conference, Lisbon, vol. 4648 of Lecture Notes in Computer Science, Springer, Berlin, pp. 766–775 (2007)
20. Mătieş, V., et al.: Tehnologie şi educaţie mecatronică. Ed. Economică Preuniversitaria, Bucureşti (2002)
21. Nicolescu, B.: La Transdisciplinarité. Manifeste. Rocher, Paris (1996)
22. Nicolescu, B.: Nous, la particule et le monde. Rocher, Paris (2002)
23. Nicolis, G., Prigogine, I.: Self-Organization in Non-equilibrium Systems. Wiley, New York (1977)
24. Paolo, E.D.: Organismically-inspired robotics: homeostatic adaptation and natural teleology beyond the closed sensorimotor loop. In: Murase, K., Asakura, T. (eds.) Dynamical Systems Approach to Embodiment and Sociality, Advanced Knowledge International, Adelaide, Australia, pp. 19–42 (2003)
25. Prigogine, I., Stengers, I.: Entre le temp et l',éternité. Flammarion, Paris (1993)
26. Prigogine, I.: Time, Structure and Fluctuations. Available at: http://nobelprize.org/nobel_prizes/chemistry/laureates/1977/prigogine-lecture.pdf (1977)
27. Rosenbleuth, A., Wiener, N., Bigelow, J.: Behaviour, purpose and teleology. Philos. Sci. 10(1), 18–24 (1943)
28. Vâlcu, R., Dobrescu, A.: Termodinamica proceselor ireversibile. Ed. Tehnică, Bucureşti (1982)
29. http://robot.informatik.uni-leipzig.de/research/videos/

Design of a Clamp Mechanism

A. Pozdîrcă

Abstract The paper is a study case for a clamp mechanism design, solving both analysis and synthesis problems. Starting form a realized clamp offered by Carr Lane Co. based on a smooth spiral cam, the author proposes a better cam profile, a more secure one. The problem of synthesis is to determine the new cam profile. The enveloped method presented, offers a compact way to determine the planar or spatial cam profile. The new profile was exported in CAD software for 3D modeling and complete analysis of the entire mechanism. The analyses problem is solved in the Autodesk Inventor environment for the cam clamp made by Carr Lane Co.

Keywords Autodesk Inventor · CAD · Cams · Enveloping · Equation of meshing · Parametric modelling

1 Introduction

In the design of a mechanism the first step is its definition in a sketch. Let there be the sketch in Fig. 1, associated to a simple clamp mechanism with cam, made of: ground 0, clamp 1 and handle 2. On the clamp we distinguish the profile of a cam, which is undetermined.

The mechanism is handled manually; by pressing the handle, the flat heel presses the cam, leading to closure of the piece with contact on the head of the clamp V. The sketch is defined within the following set of dimensional parameters:

- Distance between the joints of the handle and clamp, designate as a
- Coordinates of the clamp, head, designated as x_v and y_v
- Distance from the heel to its joint, designated as b

A. Pozdîrcă
CAD-CAM Department, "Petru Maior" University of Tîrgu Mureş, Tîrgu Mureş, Romania

I. Vişa (ed.), *SYROM 2009*,
DOI 10.1007/978-90-481-3522-6_58,

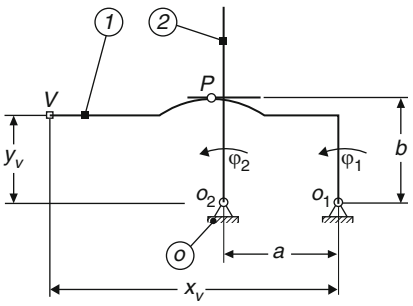

Fig. 1 Sketch of a clamp mechanism

The objectives are: (i) determine the profile of the cam; (ii) export this profile to a CAD environment; (iii) 3D modelling of the mechanism's parts and the adjustment check; (iv) optimization by the modification of the parameters associated to the 3D assembly.

2 Functional Diagram

Cam calculus is subjected to conditions of functional nature that allow precise definition of the functional diagram [4]. These conditions can be expressed as follows: the initial position of adjustment is when the handle is vertical. For an anticlockwise rotation of the handle with Φ_2, it is expected that the clamp head moves vertically at Δy. The vertical stroke of the clamp head V creates a rotation requirement of the collar Φ_1, given by the relation (Fig. 2):

$$\Phi_1 = \arctan\frac{y_v}{x_v} - \arcsin\frac{y_v - \Delta y}{r_v} \tag{1}$$

The functional diagram of the cam meets the functional requirements: in clamp rotation at angle Φ_1, the handle has to perform a stroke Φ_2. Transmission can be linear. It will determine dependence between the rotation angle of the cam and rotation angle of the handle, expressed mathematically in the formula:

$$\varphi_2 = \frac{\Phi_2}{\Phi_1} \cdot \varphi_1 \tag{2}$$

For this space function, the reduced speed of the handle is a constant:

$$\varphi_2' = \frac{d\varphi_2}{d\varphi_1} = \frac{\Phi_2}{\Phi_1} \tag{3}$$

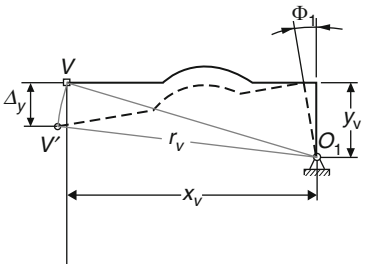

Fig. 2 Determination of cam stroke

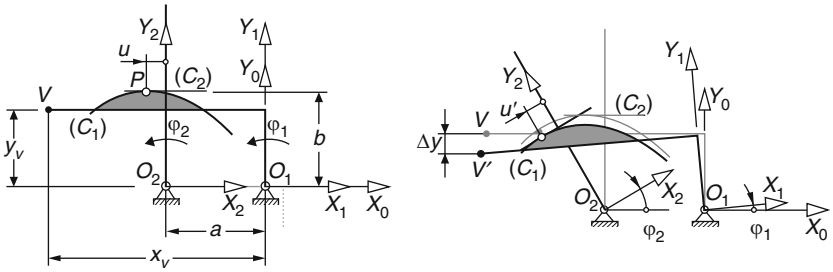

Fig. 3 Initial position and displacement of the cam mechanism

3 Profile of Cam

Determination of the profile of the cam is based on dimensional parameters give in Fig. 1 and the transmission function (2). The calculus is based on the theory of enveloping curves. Let there be the cam mechanism represented in initial position and displaced position (Fig. 3). Three systems of coordinates S_i are associated with indices corresponding to the individual bodies. A point P on the flat heel will have its own system of coordinates S_2 (Fig. 3):

$$\begin{cases} x_2(u) = u \\ y_2(u) = b \end{cases} \tag{4}$$

Coordinates of point P in the system S_1 associated to the cam can be obtained with a transformation of coordinates written as a matrix and scalar manner, respectively:

$$\begin{aligned} &\mathbf{r}_1 = \mathbf{M}_{1,2} \cdot \mathbf{r}_2 = \mathbf{M}_{1,0} \cdot \mathbf{M}_{0,2} \cdot \mathbf{r}_2 \\ &\begin{cases} x_1 = x_1(u, \varphi_1) \\ y_1 = y_1(u, \varphi_1) \end{cases} \end{aligned} \tag{5}$$

Equations (5) describe a lines family of type (C_2), who's enveloping (C_1) gives the profile of the wanted cam. The parameter of the generating curve is u and that of the family is φ_1. A connection is sought between the two parameters, according to the theory of enveloping curves.

In contact point P, the vector tangent to the straight line (C_2) in the family and the vector tangent to enveloping line (C_1) must be collinear; this requirement is expressed in a relation of the type [1, 3]:

$$\frac{\dfrac{\partial x_1}{\partial \varphi_1}}{\dfrac{\partial x_1}{\partial u}} = \frac{\dfrac{\partial y_1}{\partial \varphi_1}}{\dfrac{\partial y_1}{\partial u}} \tag{6}$$

Replacing the partial derivates of the parametric equations (5) in relation (6) and making calculations the relationship between the two parameters u and φ_1 can be obtained as illustrated here:

$$u = \frac{-a \cdot \cos \varphi_2}{\varphi'_2 - 1} \tag{7}$$

Introducing relation (7) in (5), we obtain the parametric equation of the cam profile.

The enveloping method for the cam profile determination is powerful and general. For the spatial cams, relations (5) and (6) can replace with [2]:

$$\begin{cases} x_1 = x_1(u, v, \varphi_1) \\ y_1 = y_1(u, v, \varphi_1) \\ z_1 = z_1(u, v, \varphi_1) \end{cases} \tag{8}$$

$$\left(\frac{\partial \mathbf{r}_1}{\partial u} \times \frac{\partial \mathbf{r}_1}{\partial v}\right) \cdot \mathbf{v_{12}} = 0 \tag{9}$$

An AutoLISP program was created for the profile calculation and representation as polyline in AutoCAD. The profile in .dwg format can be imported by the most popular 3D CAD platforms, such as Autodesk Inventor [6]. These 3D platforms include generators for common parts like spring, gears, cams etc.

But the generator included in Autodesk Inventor, called Design Accelerator, can't handle this type of cam, so an additional program is needed in conjunction with Autodesk Inventor. An AutoCAD drawing can be imported in the sketch environment, and based on that it can grow the 3D model of the mechanism.

After validation in the sketch of the clamp mechanism and determination of the cam profile, the entire assembly can be designed in Autodesk Inventor. Dynamic Simulation module of this software is a powerful tool for the mechanism analysis.

Next steps present how Autodesk Inventor software can solve 3D modeling, assembling and analyzing problem for a vertical handle cam clamp made by Carr Lane CO. This clamp is based on a circular cam and we prove that is less securely than our.

4 Assembly of Some 3D Components

The clamp mechanism starts from a model offered by Carr Lane CO [5]. 3D representation of the mechanism can be downloaded from www.carrlane.com in more types of files. A file type recognized by Autodesk Inventor is.SAT. The downloaded file represents five components assembly free of joints (Fig. 4).

Assembly of 3D components in Inventor use four types of constraints: Mate, Angle, Tangent and Insert (Fig. 5). The first step is to ad enough constraints and builds a consistent assembly. The applied constraints form an assembly of connected parts, which cannot be used identical to analysis specific of a mechanism with jointed parts.

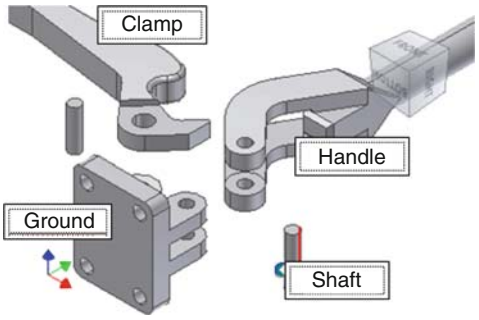

Fig. 4 Components of the mechanism

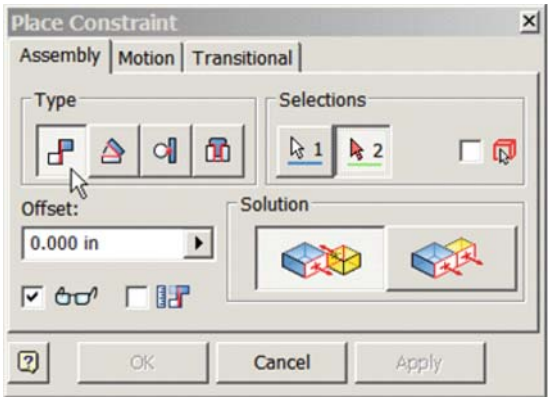

Fig. 5 Assembly constraints used by Autodesk Inventor

5 Assembly Preparation for Analysing

In Autodesk Inventor, the dedicated module for mechanisms analysis is Dynamic Simulation. For analysis, the clamp and the handle must be prepared as show in Fig. 6, with two axial sketches uses for contacts joints between clamp and handle.

Also, the piece that is fixed needs to be modelled for analysis reasons. A method for modelling in accordance with the rest of the assembly is called "adaptive". In the adaptive modelling, contours of the assembly components, they can be designed in work planes for the newly modelled part, and the modification of the "neighbours" leads to the modification of the adaptive part.

This type of modelling is appropriate for proper design of the handle and the clamp, so that the mechanism ensures the needed functionality for fix and quick opening of part.

6 Transformation of the Assembly into a Mechanism

There are some major differences between the Assembly environment and that of Dynamic Simulation. First, the applied constraints for relative positioning of the parts in the assembly are not cinematic joints, but Autodesk Inventor has functions of automatic conversion of constraints in joints/couples.

Implicitly, the assembly components in the analysis module have zero degree of freedom – they are grounded. In the assembly mode inserted pieces were free and then forced into particular positions – canceling relative freedom.

By automatic conversion, Inventor takes on joints formation and the intelligent formation of groups of parts. In this example, Inventor formed a group of four grounded elements (Fig. 7). Group formation and application of joints can be made also manually through commands of Dynamic Simulation module.

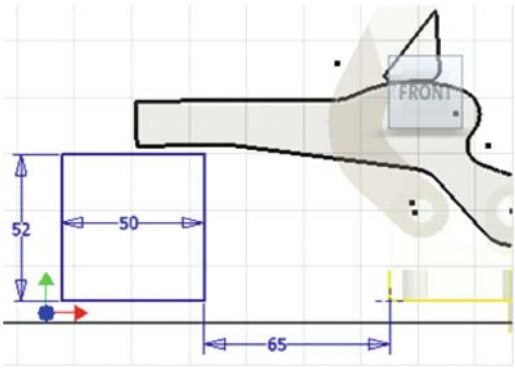

Fig. 6 Assembly preparation for the future mechanism analysis

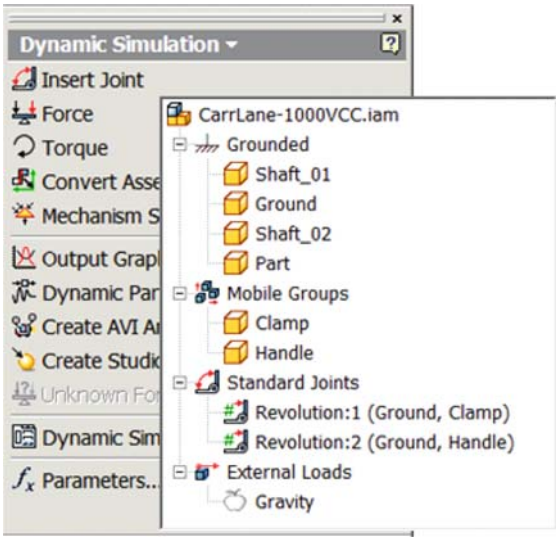

Fig. 7 Grouping of elements in the transformation of the assembly into a mechanism

7 A Contact Joint Creation

Autodesk Inventor classifies couples into: (i) Standard; (ii) Rolling; (iii) Sliding; (iv) Contact; (v) Force. Contact couples do not bring bodies into contact and do not clear degrees of freedom. They permit acknowledgement of hits and not allow interference of bodies. Thus, body movement is restricted until point of contact. Contacts include collisions with a restitution coefficient between 0 and 1, to situate them between the plastic and elastic limits. A friction coefficient can be also declared (Fig. 8).

The contact couple could block entry of the handle heel in the clamp; it could limit clamp movement to contact with the part or the descent of the handle until contact with the ground part.

Figure 9 shows contour selections required in acknowledgement of contact couples of handle and clamp, as well as clamp and fixed piece. Each couple is associated a pair of coordinate systems.

8 Insertion of a Force

The forces in the mechanism can be applied externally or in joints. In Fig. 10, the dialog box was modified for the Revolution couple: 2 (Ground, Handle), where for the arm of the handle and a manual acting force of 100 N, the corresponding moment introduced in the joint was 18,293 N·mm.

The dialog box associated with a joint allows for the introduction of a moment of action of constant or variable time value. Similarly, it allows for the introduction of a spring in the couple that will add controlled resistance through a parameter called

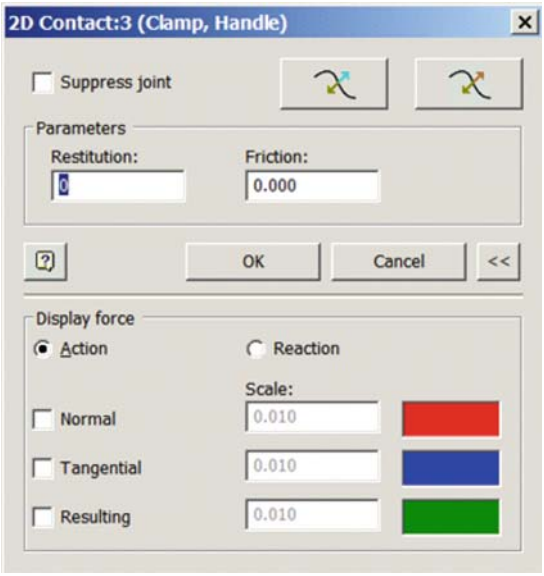

Fig. 8 Parameters of the contact joint: friction and restitution coefficient

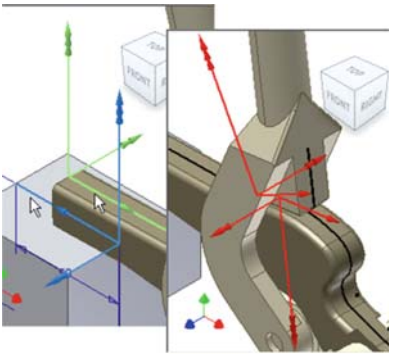

Fig. 9 Formation of contact couples and associated systems

Elastic stiffness. Last, but not least, if friction is considered in the couple, it will work as resistant moment, calculated on basis of the coefficient of friction in the parameter Coefficient and the radius of the couple under parameter Radius. Autodesk Inventor will multiply the normal force in the couple with the coefficient of friction and radius to take into account the effect of friction in the form of a resistant moment.

9 Analysis of the Mechanism

In analysis of the mechanism movement and developed forces are studied. For the cam mechanism analyzed, some practical questions can be asked, like: (i) what is the force of adjustment developed in manual action of the handle; (ii) where is the contact point Handle-Cam.

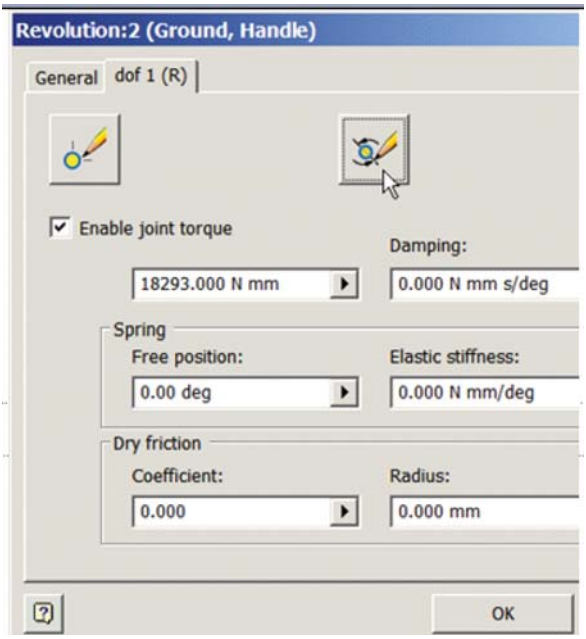

Fig. 10 Introduction of a moment of action in a couple

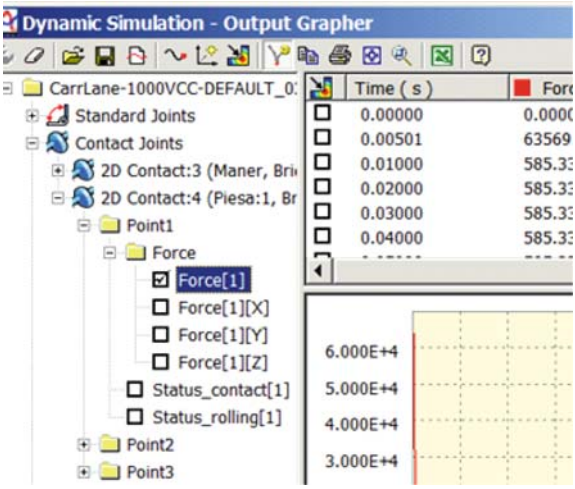

Fig. 11 Show results of the analysis

In Inventor the results of analysis can be asked using the command Output Grapher, which can report positions, speed, acceleration and forces. Figure 11 presents the situation of variation of the force in the contact couple Clamp-Part.

After collision moment, thrust stabilizes at 585 N, approximately six times higher than the action of the handle.

Maintaining on the screen the position corresponding to adjustment and canceling the action of moment in the Revolution couple:2 (Ground, Handle), displacement of the part can be checked for different values of the coefficient of friction. Each couple can be associated with a coefficient of friction. From the point of view of displacement, the friction in 2D Contact couple:3 (Handle, Clamp) is decisive.

For a coefficient equal to zero in this contact joint, by dragging the clamp the handle will move clockwise.

10 Profiles Comparison

Performances of the two cam profile can be measured through the limit of the coefficient of friction for which the clamp is displaced. These limits depend on the values of the parameter u corresponding to position of contact point Handle-Cam. The closer contact to the handle axis is safer. Values of parameter u for φ_1 chosen in the interval [0°, +4°] step of 0.5° are given in Fig. 12 as two graphics: for the circular cam (u_1) and for the non-circular one (u_2). Conclusion is: the non-circular cam is surer at the end of the course.

For the noncircular cam, the result is based on the relation (7); for the circular one, proposed by Carr Lane CO, Autodesk Inventor can solve the problem using the trace function.

In Inventor, each part has an associated coordinate system. The associated system of the handle has a Y axis aligned to the handle axis, and passed through the O_2 point. The distance from the contact point to the handle axis is equal with the coordinate X of the centre point of the circular cam in the handle's system (Fig. 13).

The application can rapport the trajectory of the interesting points, like centre of the circular cam, in the system desired. In Output Grapher, value of P[X] parameter in Trace:2 (Clamp)/Handle category, means the distance u_2. Value of P[1] parameter for Revolution:1 (Ground, Clamp) joint, correspond to the angle φ_1.

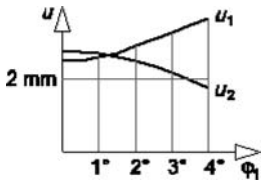

Fig. 12 Values of parameter u depend with angle of the clamp

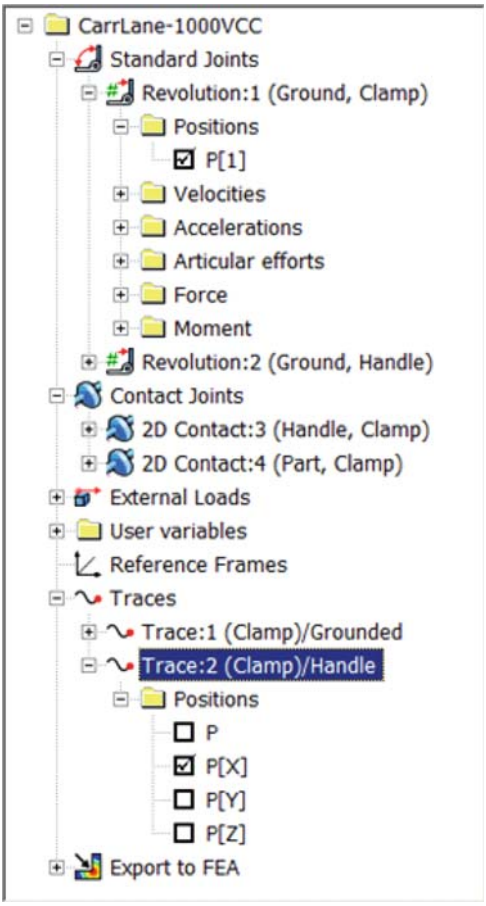

Fig. 13 The browser of the Output Grapher

11 Conclusions

In the cams synthesis, the Design Accelerator, as component generator of Autodesk Inventor software, is limited for two common types:

– Disc cam
– Linear cam

with the following type and following shape given in Fig. 14. None of these types covers our study case. So a profile calculus is needed.

The pair AutoCAD - Autodesk Inventor environments can solve the problem. By writing an AutoLISP program, a profile can be calculated and drawn in AutoCAD as polyline. Further more, the program counts the list of the u_1 parameter for each contact point. The next step is the import of the profile to Inventor for a complete 3D modeling of the entire assembly.

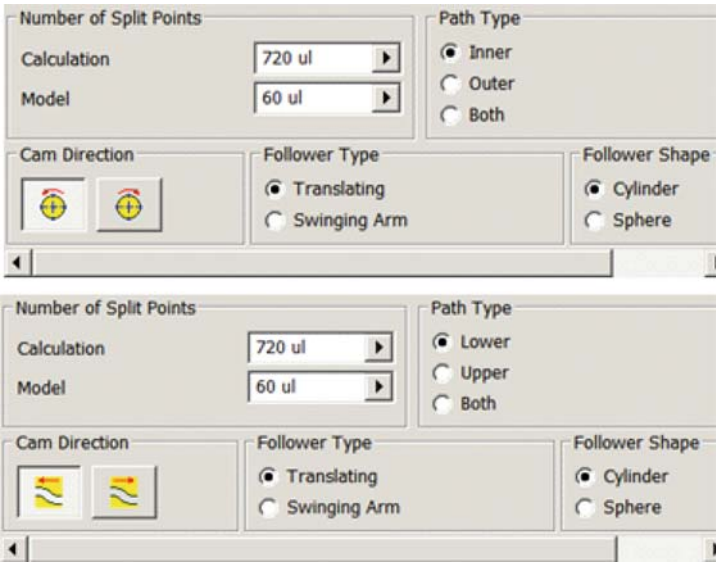

Fig. 14 Types of cams generated by Autodesk Inventor

Analysis of an existing mechanism can be made in Autodesk Inventor with the Dynamic Simulation application. In this application, Carr Lane's assembly can be transform in to a mechanism. The assembly constraints become joints. In the process of the analysis, the fixing force of a piece can be rapport for a given joint torque applied in Revolution (Ground, Handle) joint. Plus, it was compared the position of the contact point for the circular cam by the non-circular one.

With this study case, there were establish the analyzing and synthesis steps for a cam mechanism in a computer aided design manner, based on the Autodesk environment. For the cam profile determination the enveloping method, based on equation of meshing (9), is general and powerful.

References

1. Ionescu, Gh.D.: Teoria diferentiala a curbelor si suprafetelor cu aplicatii tehnice. Editura Didactica si Pedagogica, Bucuresti (1975)
2. Litvin, F.L.: Gear Geometry and Applied Theory, pp. 121–123. PTR Prentice Hall, Englewood Cliffs, NJ (1994)
3. Pelecudi, Chr.: Mecanisme. Editura Didactica si Pedagogica, Bucuresti, pp. 65–76 (1985)
4. Vişa, I.: Proiectarea functionala a mecanismelor. Editura LUX LIBRIS, Brasov, pp. 161–199 (2004)
5. http://www.carrlane.com
6. Autodesk Inventor Professional 2009, Dynamic Simulation and Stress Analysis, Autodesk Official Training Courseware (AOTC), Autodesk Inc., May 2008, 11 McInnis Parkway, San Rafael, CA 94903, USA

New Orientation Mechanism (Wrist) Used on the Industrial Robots

O. Antonescu and P. Antonescu

Abstract The paper presents a method of geometrical and kinematic synthesis of new orientation mechanisms (wrist) with three output rotations. A unitary kinematic synthesis is used for the main mechanical schemes of orientation mechanisms with three independent motions (d.o.f.). In the case of unitary kinematic method three criteria are considered, which correspond to the orientation mechanism with bevel gearings. In the case of direct kinematics, the movement is calculated into three sequences and the kinematic chains, specific for each mobility degree, are identified. The reverse kinematics is associated with the kinematic synthesis of the orientation mechanisms. This implies the calculus of the input parameters when three angular output displacements are imposed. A new kinematic schema together with the design schema and the practical stand of orientation mechanisms with decoupled movement is presented.

Keywords Bevel gearing · Functional model · Mobility degree · Orientation mechanism · Reverse kinematics

1 Introduction

The **Or**ientation **M**echanisms (OrM) of industrial robots have two or three output rotations (Fig. 1). In the case of OrM with cylindrical/conical gears, the kinematic chains are in correspondence with the known planetary mechanisms [2, 3]. While the partially coupled orientation mechanisms with two rotations (OrM-2R) are simple, those with three rotations (OrM-3R) have a complex structure [3, 5–7]. In most cases, into the structure of OrM-3Rs are present conical and cylindrical

O. Antonescu (✉)
"Politehnica" University of Bucharest, Bucharest, Romania

I. Vişa (ed.), *SYROM 2009*,
DOI 10.1007/978-90-481-3522-6_59,

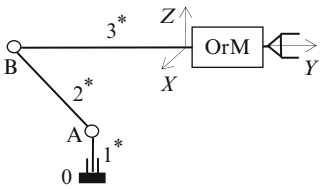

Fig. 1 Main kinematic chain of PsM *type* $R\perp R//R$

toothed elements. The input axes are parallel while the output axes are orthogonal (Fig. 1).

The three rotary orientation movements are usually performed around the axes of a Cartesian orthogonal system, which has the origin at the end of the last arm of the robot's **Pos**itioning **M**echanism (PsM).

In specialty literature, analytical methods of kinematic calculus are used, but in some cases these are not unitary while in other cases the calculus is unjustly simplified.

The latter case considers the output rotary movements of OrM-3R to be independent.

Starting with PsM-3Rs, methods of topological structural synthesis of the main kinematic chains from the serial industrial robots have been elaborated [1, 3, 4].

While the main chain of the robot with 3R + R has a limited usage, the main chain of the industrial robot with 3R + 2R can perform several operations such as: welding, flame cutting, spray painting, milling and assembling.

2 Unitary Kinematic Analysis Method

The method of kinematic analysis and synthesis of OrM-3R, with complex topological structure, consists in decomposing the real movement in three distinct phases corresponding to each independent input parameter.

The unitary solving of direct kinematics of OrM-3R with conical gears is based on three criteria established for the calculus of the transmission functions performed by the conical planetary mechanism [1, 5]. The three rotation axes have to be properly chosen.

The three criteria used for the kinematic calculus of bevel planetary gear-set are the following (Fig. 2):

(a) By taking into account the hypothesis of a immobilized planetary carrier (port-satellite), the operator $(-1)^k$ of the transmission ratio performed by a conical gear-set, can be negative or positive depending on the position of the common generatrix of the two conical gears in the quadrants I, III (k = 1) or II, IV (k = 2). The four quadrants are defined by choosing the axes orientation (Fig. 2a), according to the formula:

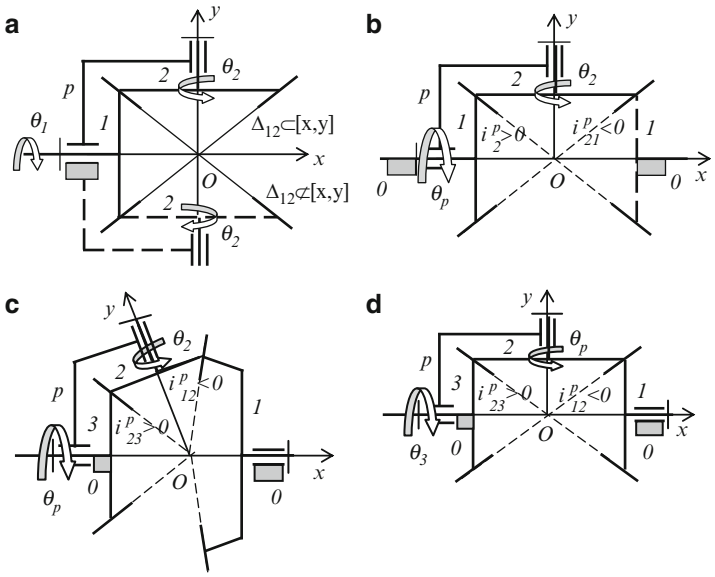

Fig. 2 (**a**) Conical planetary gear-set with locked p. (**b**) Conical planetary gear-set with locked sun gear 1. (**c**) Conical planetary mechanism with two sun gears 1 and 3. (**d**) Conical planetary mechanism with two orthogonal gearings

$$i^p_{21} = \frac{\theta_{2p}}{\theta_{1p}} = (-1)^k \frac{z_1}{z_2} \tag{2.1}$$

(b) The relative rotation of the planetary gear to the carrier, under the hypothesis of the sun gear locking, depends on the planetary carrier rotation and the conical gear transmission ratio (Fig. 2b), according to the formula:

$$\theta^1_{2p} = -\theta_p \cdot i^p_{21} \tag{2.2}$$

where i^p_{21} is calculated according to the first criterion (a).

(c) The carrier rotation of a conical planetary mechanism with two sun gears, one of them being blocked (Fig. 2c), is calculated according to the formula:

$$\theta^3_p = \frac{\theta_1}{1 - i^p_{13}} \tag{2.3}$$

where the transmission ratio i^p_{13} is calculated by

$$i_{13}^{p} = i_{12}^{p} \cdot i_{23}^{p} = -\frac{z_3}{z_1} \tag{2.4}$$

The transmission ratios $i_{12}^{p} < 0$, $i_{23}^{p} > 0$are calculated with the formula (2.1) for $k = 1$and $k = 2$ respectively.

In the case of orthogonal axes (Fig. 2d), $z_1 = z_3$, therefore $i_{13}^{p} = -1$ and formula (2.3) becomes:

$$\theta_{p3} = \frac{\theta_1}{2} \tag{2.5}$$

3 Symmetrical Kinematic Schema of OrM-3R

This kinematic schema is obtained from OrM-2R, where the parallel shafts Δ_1 and Δ_2, become planetary shafts (Δ'_3, Δ'_5). The planetary shafts are actuated by the gears 1 and 2 (Fig. 3) mounted on the coaxial shafts.

Two parts are distinguished: the proper OrM (Fig. 3) and the cylindrical planetary reducer for driving motors M1 and M3 (Fig. 4).

The movement of the planetary carrier p_1 is generated by the motor M2 operating directly without an intermediary gear, thus obtaining the rotation round the axis y, which is settled along the arm 3^* (Fig. 5).

The three input coaxial shafts with the rotations angles noted $\theta_1, \theta_2$and $\theta_3$are mounted in carcass 3^*. The carcass of the OrM-3R is solid with the forearm 3^* of a PsM-3R (Fig. 6).

Motors M1, M2 and M3 are set (in a vertical plane) at forearm 3^*, as additional mass (counterweight).

The mechanism with cylindrical gears (Fig. 6) allows three parallel input shafts and three coaxial output shafts. Output rotations θ_x, θ_y and θ_z (Fig. 7) are obtained depending on input rotations θ_1, θ_2 and θ_3.

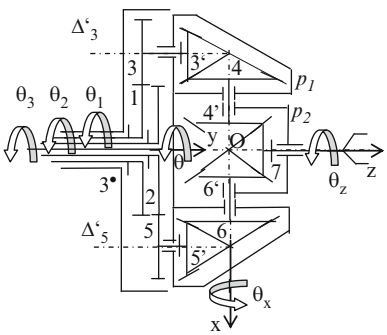

Fig. 3 Symmetrical schema of OrM-3R

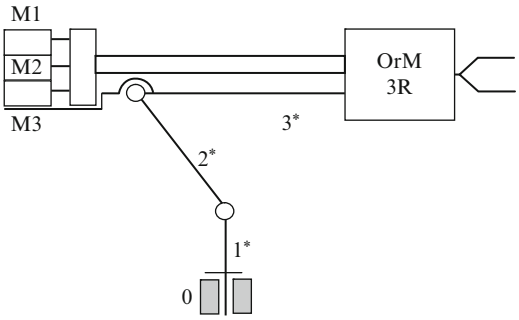

Fig. 4 Kinematic schema of PsM-3R + OrM-3R

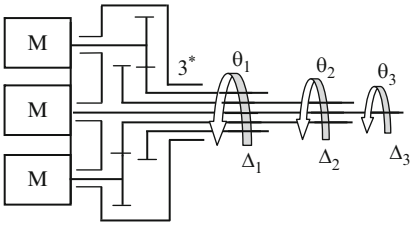

Fig. 5 Solutions from mounting of gears a and b

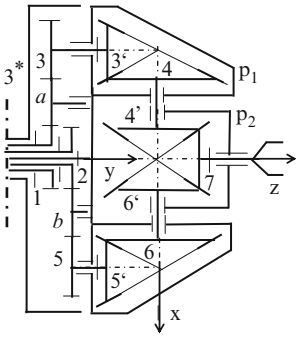

Fig. 6 Kinematic schema of the OrM-3R drive

It should be mentioned that the central shaft with the axis Δ_3 is solid with the carcass p_1, which becomes the planetary carrier for the bevel gears 3(3'), 4(4'), 5(5') and 6(6').

The application of the forward kinematics (Fig. 3) for each of the three kinematic chains, with d.o.f. of 1, gives the relations:

$$\text{(I)}\ \theta_1 \neq 0, \theta_2 = 0, \theta_3 = 0 \Rightarrow \theta_x^I = \theta_{p2}^I = \tfrac{1}{2}\theta_4^I = -\tfrac{1}{2}\theta_1 \cdot \frac{z_1 z_{3'}}{z_3 z_4} \tag{3.1}$$

$$\theta_z^I = \theta_{7p_2}^I = \theta_{p_2}^I \frac{z_{6'}}{z_7} = \tfrac{1}{2}\theta_1 \cdot \frac{z_1 z_{3'} z_{6'}}{z_3 z_4 z_7} \tag{3.2}$$

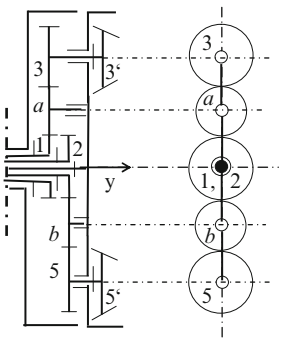

Fig. 7 (**a**) Didactic model of OrM-3R: Partialy view. Drive. (**b**) Didactic model of OrM-3R: Partialy view. Conical gears mechanism

$$(\text{II})\ \theta_1 = 0, \theta_2 \neq 0, \theta_3 = 0 \Rightarrow \theta_x^{II} = \theta_{p2}^{II} = \tfrac{1}{2}\theta_6^{II} = \tfrac{1}{2}\theta_2 \cdot \frac{z_2 z_{5'}}{z_5 z_6} \tag{3.3}$$

$$\theta_z^{II} = \theta_{7p_2}^{II} = \theta_{p_2}^{II} \cdot \frac{z_{4'}}{z_7} = -\tfrac{1}{2}\theta_2 \cdot \frac{z_2 z_{4'} z_{5'}}{z_5 z_6 z_7} \tag{3.4}$$

$$(\text{III})\ \theta_1 = 0, \theta_2 = 0, \theta_3 \neq 0 \Rightarrow \theta_x^{III} = \theta_{p2}^{III} = \tfrac{1}{2}(\theta_4^{III} + \theta_6^{III}) \tag{3.5}$$

$$\theta_y^{III} = \theta_{p_1}^{III} = \theta_3 \tag{3.6}$$

$$\theta_z^{III} = \theta_{7p_2}^{III} = (\theta_4^{III} - \theta_6^{III}) \cdot \frac{z_{4'}}{z_7} \tag{3.7}$$

where:

$$\theta_4^{III} = \theta_3 \cdot (1 + \frac{z_1}{z_3}) \cdot \frac{z_{3'}}{z_4} \tag{3.8}$$

$$\theta_6^{III} = -\theta_3 \cdot (1 + \frac{z_2}{z_5}) \cdot \frac{z_{5'}}{z_6} \tag{3.9}$$

In the case of forward kinematics, the starting point being the rotations θ_1, θ_2 and θ_3, the following output rotations can be obtained:

$$\theta_x = \theta_x^I + \theta_x^{II} + \theta_x^{III} = \tfrac{1}{2}(\theta_4^I + \theta_6^{II} + \theta_4^{III} + \theta_6^{III}) \tag{3.10}$$

$$\theta_y = \theta_y^I + \theta_y^{II} + \theta_y^{III} = \theta_3 \tag{3.11}$$

$$\theta_z = \theta_z^I + \theta_z^{II} + \theta_z^{III} = (\theta_4^I - \theta_6^{II} + \theta_4^{III} - \theta_6^{III}) \cdot \frac{z_{4'}}{z_7} \tag{3.12}$$

For the symmetrical OrM-3R (Fig. 3), with the geometrical conditions:

$$z_1 = z_2; z_3 = z_5; z_{3'} = z_{5'}; z_4 = z_6,$$

the formulas (3.10) and (3.12) become:

$$\theta_x = -\tfrac{1}{2}(\theta_1 - \theta_2) \cdot \frac{z_1 z_{3'}}{z_3 z_4} \tag{3.13}$$

$$\theta_z = -\tfrac{1}{2}(\theta_1 + \theta_2) \cdot \frac{z_1 z_{3'} z_{4'}}{z_3 z_4 z_7} + \theta_3 \cdot (1 + \frac{z_1}{z_3}) \cdot \frac{z_{3'} z_{4'}}{z_4 z_7} \tag{3.14}$$

In the particular case in which: $z_1 = z_3; z_{3'} = z_4; z_{4'} = z_7$, the results are:

$$\theta_x = -\tfrac{1}{2}(\theta_1 - \theta_2) \tag{3.13'}$$

$$\theta_z = -\tfrac{1}{2}(\theta_1 + \theta_2) + 4\theta_3 \tag{3.14'}$$

The two output rotations (θ_x, θ_z) may be partially decoupled only if $\theta_3 = 0$.

In the case of inverse kinematics the output rotations are given and, based on them, the input rotations will be calculated from (3.13'), (3.11), (4.14'):

$$\theta_1 = -\theta_x + 4\theta_y - \theta_z; \tag{3.15}$$

$$\theta_2 = \theta_x + 4\theta_y - \theta_z; \tag{3.16}$$

$$\theta_3 = \theta_y. \tag{3.17}$$

4 A New Kinematic Schema of OrM-3R

The new symmetrical schema of OrM-3R (Fig. 8) may perform the total decoupling of output rotations.

The main change of the symmetrical OrM-3R, presented above (Fig. 3), consists of the mounting the gears *a* and *b* (Figs. 5, 8) between the sun gears (1, 2) and planetary gears (3, 5).

With this symmetrical OrM-3R (Fig. 5) it is possible to obtain the rotations θ_x and θ_z (Fig. 8) as decoupled movements, only if motors M1 and M2 are driven simultaneously.

Thus, if the two motors M1 and M2 are driven in opposite directions, only the rotation θ_x is obtained.

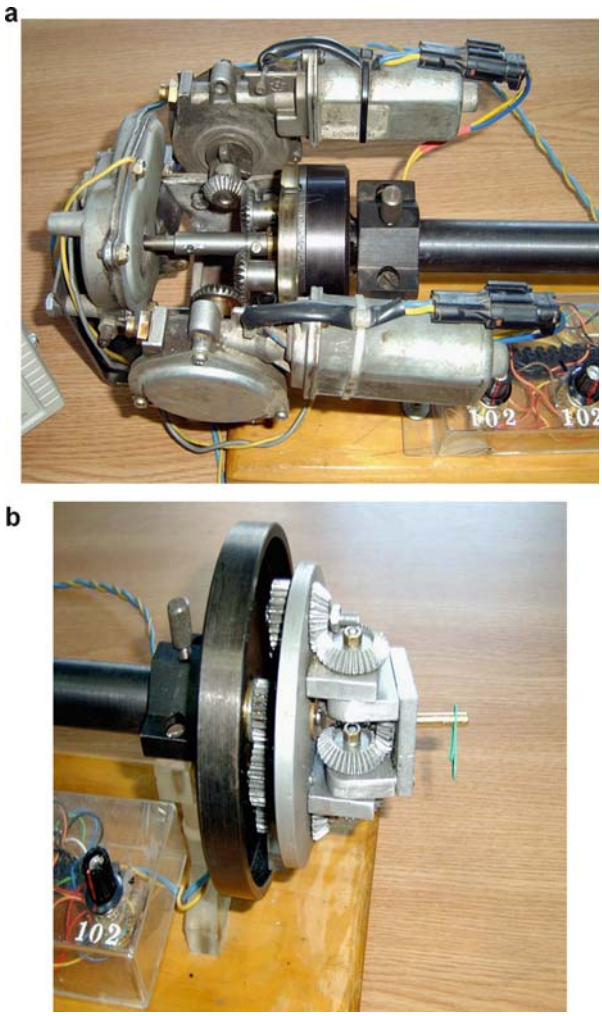

Fig. 8 Kinematic schema of OrM-3R with decoupled output rotations

Under the hypothesis $z_1 = z_3; z_2 = z_5$ (Fig. 5), this rotation may be calculated by the formula:

$$\theta_x = \tfrac{1}{2}(\theta_1 - \theta_2) \cdot \frac{z_{3'}}{z_4} \tag{4.1}$$

Also, if the two motors M1 and M2 are driven in the same direction, only the rotation θ_z is obtained from:

$$\theta_z = -\tfrac{1}{2}(\theta_1 + \theta_2) \cdot \frac{z_{3'} z_{4'}}{z_4 z_7} \tag{4.2}$$

In order to obtain the rotation θ_y as decoupled movement, the motor M3 is actuated. In this phase the gears 3 and 5 perform a circular translation movement according to the relation:

$$\theta_y = \theta_3 \tag{4.3}$$

The didactic model of the new constructive schema OrM-3R is realized, using three the electric motors having the reduction with worm gear (Fig. 7).

5 Conclusions

Three criteria are established as a unitary method for kinematic calculus specific to the bevel gears with movable axes of the planetary gearings (mechanism).

In order to obtain the synthesis of OrM-2R and OrM-3R with complex topological structure, specific kinematic chains are identified. These chains correspond to the two or three distinct phases corresponding to each independent parameter.

A new kinematic and constructive schema for symmetrical OrM-3R with decoupled movements is presented.

References

1. Yan, H.S., Hsiech, L.C.: Kinematic analysis of general planetary gears trains. In: Proceedings of 8th World Congress on TMM, Prague Czech Republic, pp. 153–157 (1991)
2. Antonescu, P., Antonescu, O.: Contributions to synthesis mechanisms of orientation of robots. In: Proceedings of 9th Congress TMM, Milano, pp. 1200–1204 (1995)
3. Antonescu, P.: Contributions to analysis and synthesis of robot's orientation mechanisms with conical gears (in Romanian). Robotica si management 7(2), 14–18 (2002)
4. Antonescu, P., Antonescu, O., Mihalache, D.: Contributions to Synthesis of the Orientation Mechanisms Used on Robots. In: Proceedings of 11th World Congress MMS, Tianjin, vol. 4, pp. 1786–1789 (2003)
5. Antonescu, O., Mihalache, D., Antonescu, P.: Synthesis of the orientation mechanisms (wrist) used on the industrial robots. In: Proceedings of Conference on Intelligent Manipulation and Grasping, Genova, pp. 296–301 (2004)
6. Antonescu, P.: Mechanism and Machine Science. Printech, Bucharest (2005)
7. Antonescu, P., Antonescu, O., Lung, I.: Synthesis and design of new orientation mechanisms (wrist). In: Proceedings of 4th Conference on Robotics, 13–14 November, Brasov, vol. 1, pp. 59–66 (2008)

Modular Orthopedic Devices Based on Shape Memory Alloys

D. Tarnita, D.N. Tarnita, N. Bizdoaca, D. Popa, C.E. Tarnita, and Fl. Cismaru

Abstract The main idea of this paper is related to design modular adaptive implants for fractured bones. In order to target the efficiency of medical treatment, the implant has to protect the fractured bone, for the healing period, undertaking much as is possible from the daily usual load of the healthy bones. Using implant modularity, the load is gradually transferred to bone, assuring in this manner a gradually recover of bone function. The proposed intelligent device has a network structure, with modules made out of Nitinol, especially designed in order to ensure a rapid connection and/or extraction of one or more MAI modules. We suggest a design for the unitary SMA module structure, a design which ensures not only the stability of the super-elastic network and constant force requirements, but also a rapid coupling/decoupling procedure. The adaptability of this design is related to medical possibility of the doctor to made the implant to correspond to patient specifically anatomy.

Keywords Bionics · Implants · Modularity · Numerical simulation

1 Introduction

Applications of Shape Memory Alloys to the biomedical field have been successful because of their advantages over conventional implantable alloys, enhancing both the possibility and the execution of less invasive surgeries.

Different applications exploit remarkable properties of Nitinol like: biocompatibility, superelasticity, force hysteresis, the shape memory effect (one-way or

D. Tarnita (✉)
University of Craiova, Faculty of Mechanics, Department of Applied Mechanics, Craiova, Romania

I. Vişa (ed.), *SYROM 2009*,
DOI 10.1007/978-90-481-3522-6_60,

two-way), the steerability, torquability, less sensitivity to magnetic resonance imaging, excellent corrosion resistance [2–10].

The shape memory alloys possess the ability to undergo shape change at low temperature and retain this deformation until they are heated, at which point they return to their original shape.

Typically, a fractured or cut bone is treated using a fixation device, which reinforces the bone and keeps it aligned during healing. Bone plates are sturdy internal devices, usually made of metal, that mount directly to the bone adjacent the fracture.

2 Modular Adaptive Implant

The design idea of modular adaptive implants results from the following observations:

- the doctors have a limited degree of freedom in selecting the proper dimensional apparatus for bones fractures;
- the current mechanical devices used in orthopedics lose some of their mechanical characteristics after some time (especially elasticity, which should ensure a constant tension that is mandatory for the correct anatomical healing of the fractured bones) [11];
- the process of fracture healing has a particular dynamic, which imposes the necessity of particular progressive tension or discharge to improve the recovery time, depending on the normal structure and function of the bone [11];
- to improve the healing process, the fractured parts have to be in permanent contact in order to ensure the proper conditions to develop bone calluses [4].

The direction of our study was focused on the external implants that ensure the protection and recovery of traumatized bones by absorbing the external forces and moments that the normal bone is subject to. This category of implants falls into the category of external attaching sub-systems.

This selection has the following advantages:

- minimal intervention and small size of the implanted foreign bodies – only the rods are introduced into the bone structure
- the small incisions mean smaller risk of infection
- the mechanical load of the system can be distributed according to a tensiometric map which optimally favors the healing process
- the possibility of dynamically modifying the load map by external intervention, without any other traumatizing interventions on the patient
- blood edema and improves bone recovery and vascularization of the region.

All these advantages are characteristic of external implants. The best known external implants are: fixators only with screws; external fixator with Schanz

screws; Iliazarov fixators (Fig. 1; hybrid fixators; pinless fixators (Zangenfixateur); Taylor Spatial Frame Fixator (Fig. 2).

The actual external fixators have to be manually adjusted with respect to the main axis of the bone. Unfortunately, the degrees of freedom of current devices are limited to three or four vertical screws.

The solution to these problems is the Modular Adaptive Implant – MAI.

The proper shape of MAI is related to the bones microscopic structure and to the numerical simulation presented in the previous chapter. As one can observe, comparing the structure of a healthy bone (Fig. 3) with that of an osteoporotic bone (Fig. 4), the internal architecture of the healthy bone has a regular modular structure [9].

A modular net, identical in structure with the bone and locally configurable in terms of tension and release, is best design solution in terms of biocompatibility. The identification of the mechanical solicitation of the particular bone structure, using finite element method, leads to the concept of the practical implementation of a feasible device able to undertake the functionality of normal bones. This device will partially discharge the tensions in the fractured bones (the fractured parts still need to be tensioned to allow the formation of the callus) improving the recovery time and the healing conditions.

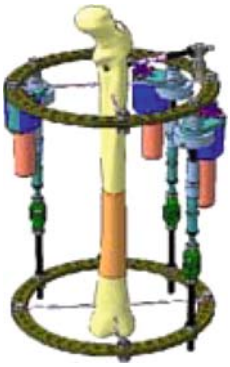

Fig. 1 Iliazov external apparatus

Fig. 2 Taylor spatial frame fixator

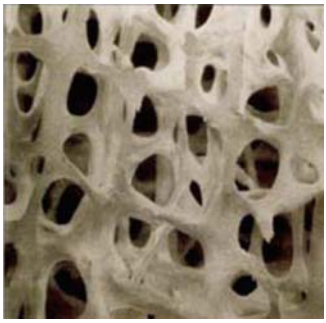

Fig. 3 Healthy bone

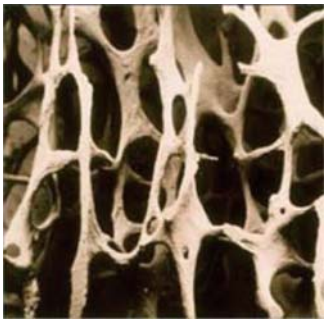

Fig. 4 Osteoporotic bone

The proposed intelligent device has a network structure, with modules made out of Nitinol, especially designed in order to ensure a rapid connection and/or extraction of one or more MAI modules. The binding of the SMA modules ensures the same function as other immobilization devices, but also respects additional conditions concerning variable tension and its discharge. Moreover, these modules allow little movement in the alignment of the fractured parts, reducing the risks of wrong orientation or additional bones callus.

In order to identify the optimal design, different implants were developed and experimented using numerical simulation.

We noticed that for all cases of attaching implants, the tensions system is ensured by screwing rods or parallel screws. For our research, we used a system that consisted of penetrating the bone and stabilizing the supporting rods using the same techniques as in the classic cases, the effort being geared towards replacing the rods, the tension screws with modular structures differently tensed. This ensemble creates a correcting and protecting tension bandage for the affected area. Also, studies conducted on corpses showed the fact that in the case of external attaching implants undergoing high tension forces the destruction of the implants is mainly caused by tension elements – columns or screws. These results indicate the fact that the solution suggested by our research has tremendous potential, because it can prevent such situations as a result of its modular adaptive characteristics.

Our research focused on identifying optimal shapes which would permit not only previous mechanical tensioning, but also a rapid change of modules tensed at a certain value with other modules with an elastic module that is superior or inferior to the previous one, depending on the desired protective or recovery-oriented tension map. We also designed and experimented numerically and physically a series of modules both individually and in a network.

The following figures (Figs. 5, 6, 7, 8 and 9) [1] show the main types of experimental modules, in a relative order of betterment of the concept and design.

Version 1, the triangular version represented the starting point for our experimental research. This was due to the already existing solutions of stabilizing fractured bones by using three stabilizing screws. This version of the module can be used not only as a bandage-like protective support, but also individually, as a fixation plate of larger segments of a big fracture. This approach was maintained in the case of the next versions, the coupling orifices being used to introduce the

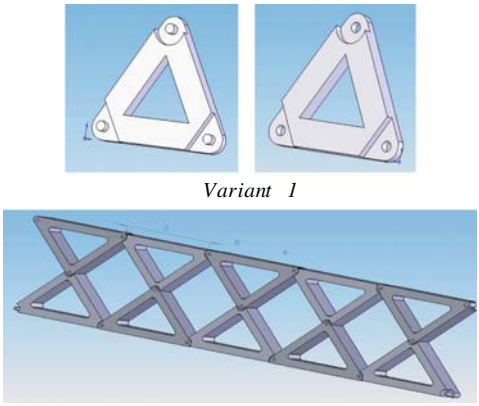

Fig. 5 The network for variant 1

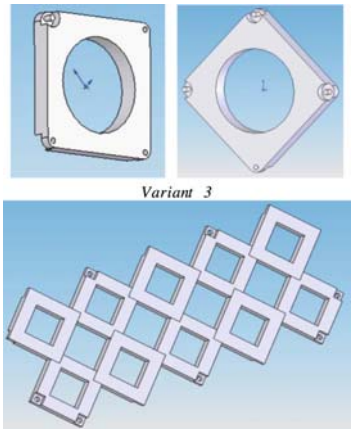

Fig. 6 The network for variant 2

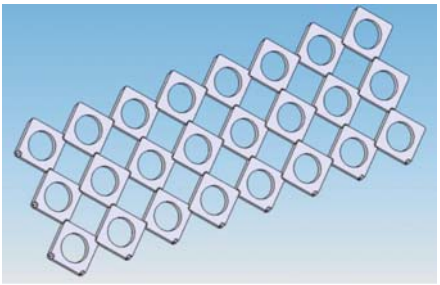

Fig. 7 The network for variant 3

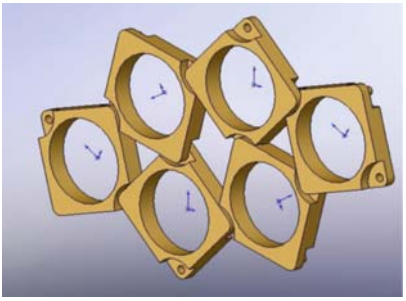

Fig. 8 *Other network for variant* 3

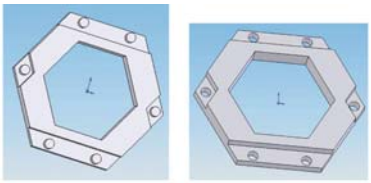

Variant 4

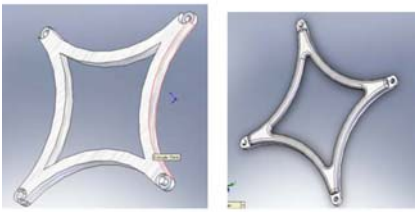

Variant 5 *Variant 6*

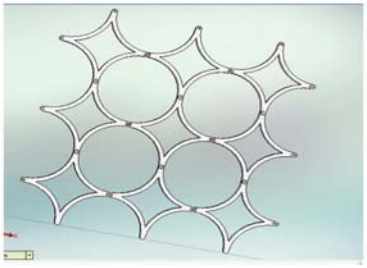

Fig. 9 The network for variant 6

fixation screws of the module utilized also as an internal implant with screw attachments. The biocompatibility of Nitinol and its super-elasticity allow better performance compared to other existing fixation plates.

We suggest the design shown in Fig. 9, Variant 5, for the unitary SMA module structure, a design which ensures not only the stability of the super-elastic network and constant force requirements, but also a rapid coupling/decoupling procedure. The second shape of the MAI is an improved solution (Variant 6), based on previous conclusions. This solution respects the protection of the patients for accidental unusual mechanical tension.

Using Solid Works package and COSMOS software [11, 12] we proceed to various numerical simulation of SMA module or networks, in order to test the proper mechanical design. In Fig. 10 are presented two successive stress diagrams obtained from a simulation by acting the network device presented in Fig. 8 with a force. With simulation helping we can observe that Variant 7 relives that applying high force equal with 30 N and torques to the MAI terminals, the coupling connectors will conduct to spike mechanical deformation (Fig. 11), potential dangerous for the patients. Variant 8 represents the optimal design for the network modules (Fig. 12).

Doctors can use SMA modules with different internal reaction tension, but all the modules will have same shape and dimension. The connection with affected bones and the support for this net are similar to those of a classic external fixator, but allowing for the advantages of minimal invasive techniques (Fig. 13).

The new device leads to a simple post-operatory training program of the patient. he relative advanced movement independence of patient with MAI network apparatus can lead to possibility of short distance walking. Actual devices are quite expensive and implies, for implementing, three persons: the patient, the current doctor and a kinetoterapeut (Fig. 14).

Figure 15 shows experimental modules physically created using infrastructure from the financial support of this project and from external sources interested in this domain.

Figure 16 shows experimental network versions obtained by modules created using a rapid prototyping technology – a 3D Zcorp Printer (Fig. 17).

3 Intelligent Coupling and Catching System in External Implants

External implants, being made of Nitinol, have specific advantages of this material. Each module developed in this project is made of Nitinol. The cost of shape memory alloy was the reason for that passed to shape optimization module, so it should be as easy as possible, with a simple geometry, but biocompatible – (presents similarities with the bone structure) and a price as lower. Local heating of module arms will lead to their constriction and quick declutch to total disconnection

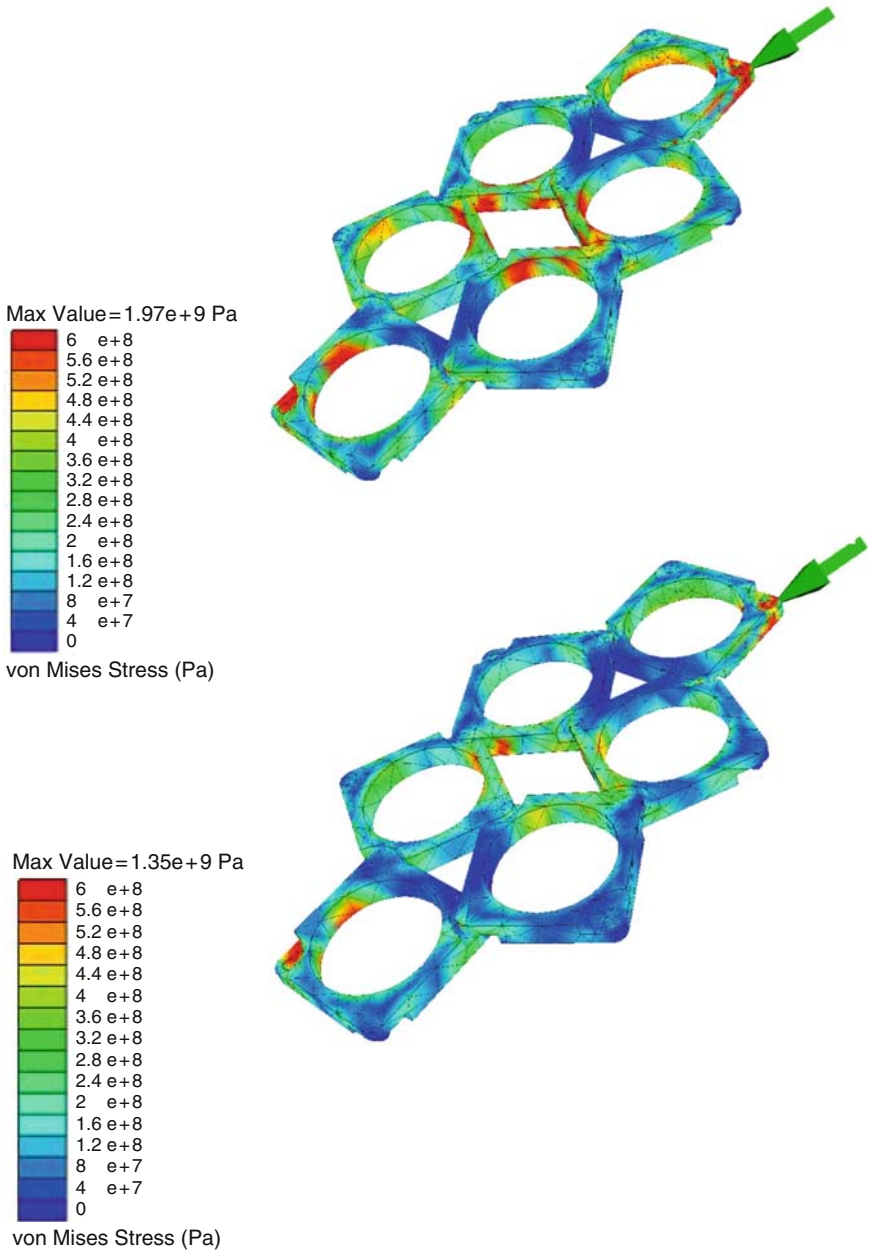

Fig. 10 Two successive stress diagrams

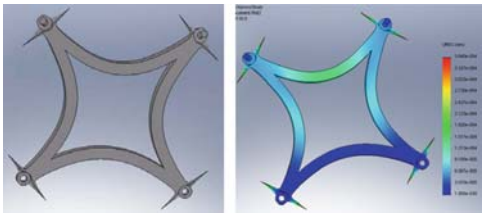

Fig. 11 Response of MAI – first design for accidental tension and forces

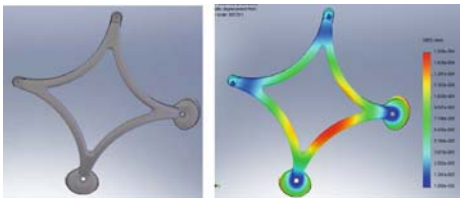

Fig. 12 Response of MAI – optimal design for accidental tension and forces

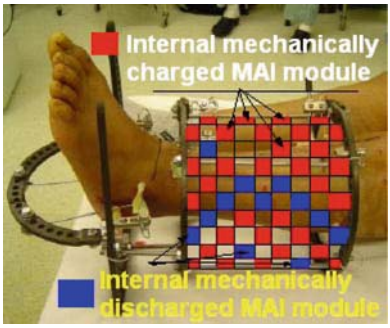

Fig. 13 MAI connection network

Fig. 14 KINETEK device for functional reduction type "continuous passive motion"

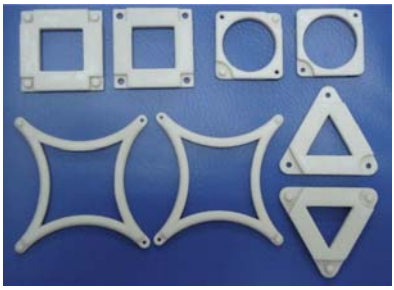

Fig. 15 Experimental modules

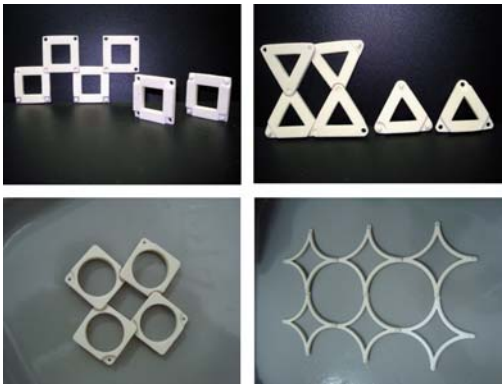

Fig. 16 Experimental network versions

Fig. 17 A rapid prototyping 3D printer Zcorp

or to the replacement of that module with a different strained one. As seen from previous paragraph, the optimization of module design has led to an optimum, not only in terms of the modules assembly which represents the protective bandage

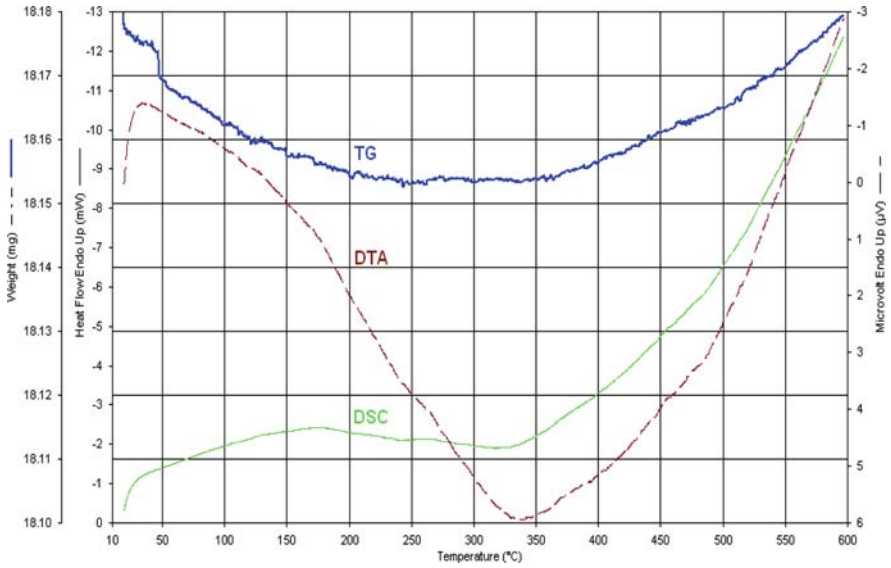

Fig. 18 The experimental diagrams obtained for a heating of SMA to a maximum temperature of 600°C

coupled to fixation rods from the support parts in traumatized bone, but also to an optimum in terms of mechanical wear and overstrains to that these modules can be exposed in time or accidentally.

All observations, numerical simulations and experiments so far could not constitute a proper basis for the development of the project without carrying out tests and experiments designed to study the Nitinol available to researchers in this project. Also, a particularly important aspect for implants and, especially, to their cost, is the reuse of their own, while ensuring the proper sterilization required. Sterilization, being made to high temperatures, the question arises how these temperatures affect the properties of modules made of SMA and used in the project proposed structures. Note the studies that extremely high temperatures, up to 600°C have major effects on the implant, which is an extra argument in further research.

The experiment was a simulation of the sterilisation of shape memory alloys, and it was identified a few of changes which could improve or not the biocompatible properties. The used method was **T**hermal **A**nalysis **M**ethods. The used technique was **T**hermo **G**ravimetric **A**nalysis. It can be observed that the TG graphic is almost constant (Fig. 18).

We also made studies of the structure of minimum energy required for decoupling implant modules, implant respectively, in the end, also the determination of best constructive solutions.

Tests carried out on Nitinol were aimed at identifying its compatibility with the required heat regime imposed by the sterilization process, along with energizing/

modular decoupling issues. To identify optimal constructive solutions, energy/decoupling solutions were analyzed for each proposed implants.

These implants being outside the body, are offering a big advantage about the fact that the material with shape memory no longer has to be compatible with the human body heat host, which leads to a reduction in the cost of implementing the implant. Modular structure can be externally energized using a heating system of the terminal point of a single/multiple module components. The structure of those terminals being denticulate, the terminals, by contraction, will involve relative movements of small amplitude, but will lead to create tension in the network after a certain direction desired/imposed by the physician. The stellar type for optimal implant will ensure the proper loading/unloading of the tensible patch made of these implants, both the transverse and longitudinal direction, corresponding to the stage of the patient's treatment.

4 Conclusions

The new device leads to a simple post-operatory training program of the patient. In the future, we want to realize different types of SMA modules and to experiment with them on real bones. At the same time the studies will be developed in the direction of numerical simulation of the complex ensemble made up of the bone and the MAI network for different functional regimes, for different weight, temperature and physical-chemical condition, for different types of bone fractures.

Acknowledgments This research activity was supported by Ministry of Education, Research and Innovations, Grant Idei_92- PNCDI 2.

References

1. Bîzdoacă, N., Tarniţă, D.N., Tarniţă, D., Bîzdoacă, E.: Application of smart materials: bionics modular adaptive implants. Advances in Mobile Robotics (Proceedings of the Eleventh International Conference on Climbing and Walking Robots – CLAWAR 2008, cotata ISI), Coimbra, Portugal, ISBN-13 978-981-283-576-5ISBN-10 981-283-576-8 World Scientific Publishing Co. Pte. Ltd pp. 190–198 – lucrare premiată cu The Industrial Robot Innovation Award 2008 Highly Commended (2008)
2. Duerig, T., Pelton, A., Stöckel, D.: Mater. Sci. Eng. A **273–275**, 149–160 (1999)
3. Friend, C.M., Morgan, N.B.: An overview of nitinol medical applications. Medical Applications for Shape-Memory Alloys (SMA). Professional Engineering Publishing Ltd., UK, p. 1 (1999)
4. Frank, T.G.: Medical Applications for Shape-Memory Alloys (SMA). Professional Engineering Publishing Ltd., UK, p. 31 (1999)
5. Funakubo, H.: Shape Memory Alloys. Gordon & Bleach, New York (1987)
6. van Humbeeck, J.: Shape memory materials: state of art and requirements for future applications. Journal de Physique IV **7**, 3–12 (1997)
7. Lagoudas, D.C., Rediniotis, O.K., Khan, M.M.: Applications of shape memory alloys to bioengineering and biomedical technology. In: Proceedings of the 4th International Workshop

on Mathematical Methods in Scattering Theory and Biomedical Technology, Perdika, Greece, 8–10 October, 1999
8. Pelton, A.R., Stöckel, D., Duerig, T.W.: Medical uses of nitinol. Mater. Sci. Forum **327–328**, 63–70 (2000)
9. Ryhänen, M., Kallioinen, J.: Medical Applications for Shape-Memory Alloys. Professional Engineering Publishing Ltd., UK, p. 53 (1999)
10. Shabalovskaya, S.A.: Biological aspects of TiNi alloys surfaces. Journal de Physique IV **5**, 1199–1204 (1995)
11. Tarnita, D., Tarnita, D., Bizdoaca, N., Negru, M., Copilus, C.: Modular orthopedic implants for forearm bones based on shape memory alloys. In: ISI Proceedings of the 19th International DAAAM Symposium, "Intelligent Manufacturing & Automation: Focus on Next Generation of Intelligent Systems and Solutions", October, Trnovo, Slovakia (2008)
12. Tarnita, D., Popa, D., Tarnita, D. N., Bizdoaca, N.: Properties and Medical Applications of Shape Memory Alloys. Romanian Journal of Morphology and Embriology **51**(1), Ed. Academiei Romane, ISSN 1220-0522 (2009)

Loading Cases and Forces on Azimuthal Solar Tracking Systems with Linear Actuators

R. Velicu, M. Lateş, and G. Moldovean

Abstract The paper is referring to azimuthal solar tracking systems, with two rotational axes: a vertical fixed axis and a horizontal mobile axis. The system is mobile and the loads on its elements are different depending on season or the moment of the day. The main loading cases are depending on the functional positions of the tracking system. Calculus relations have been drawn for the main forces acting on the elements considering different distributions of wind pressure. Conclusions and recommendations are based on the results established for two sizes of trackers.

Keywords Azimuthal tracker · Linear actuator · Wind load

1 Introduction

Two possibilities are available in order to improve the energy efficiency of fixed photovoltaic (PV) panels [1]. First option is to use materials with better solar absorbent properties and the second is to orientate the panels towards the sun, method called "tracking". As the first possibility is quite expensive and new materials need time to be developed, the second option can be reliable. An optimal design is improving a tracking system by diminishing the costs of building.

The subject of this paper is an azimuthal tracking system [2] (Fig. 1). It has two rotational axes: a vertical fixed axis (setting the ψ orientation angle) and a horizontal

R. Velicu (✉)
Centre "Product Design for Sustainable Development", Transilvania University of Braşov, Braşov, Romania

I. Vişa (ed.), *SYROM 2009*,
DOI 10.1007/978-90-481-3522-6_61,

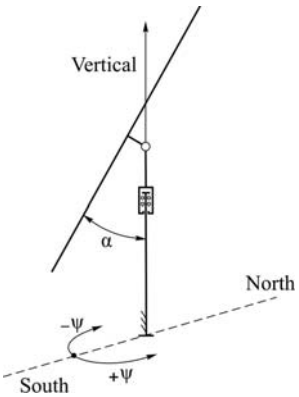

Fig. 1 General scheme of an azimuthal tracking system

mobile axis (setting α orientation angle). The system is using linear actuators in order to perform both movements.

A proper design must consider the loading cases depending on the functional positions of the tracking system (positions corresponding to minimum, medium and maximum rotational angles on the two main axes) and also the loads caused by own masses, wind, snow etc. (given by the specifics of the geographical region).

This paper is presenting a methodology of determining the loads involved in preliminary strength calculus of the elements of the tracking system. It also draws some conclusions on the loading cases and their involvement in the specific loading of elements.

2 External Loads and Loading Cases

2.1 Wind Load

The wind load is depending on the area of the panels (S) and on the maximum wind speed ($V_{\max}$), specifics of each geographical region (the maximum wind speed for the Braşov region is 30 m/s). Based on this, a maximum wind pressure (p_m) and a maximum wind force $W_{max} = p_m\, S$ can be determined [3, 4]. The wind direction can be considered towards the front of the panel (Fig. 2a–c) or towards the back of the panel (Fig. 2d–f). Different assumptions can be considered for the distribution of the wind pressure on the panels: uniform pressure [3] (Fig. 2a, d); vertical trapezoidal distribution, approximating the distribution presented in [5], reversed for opposite wind direction (Fig. 2b, e); vertical triangular distribution [6], reversed for opposite wind direction (Fig. 2c, f). For all six wind load cases presented in Fig. 2, the load can be reduced to a single wind force W and a moment M, placed on the axis of the panel, with values according to Table 1.

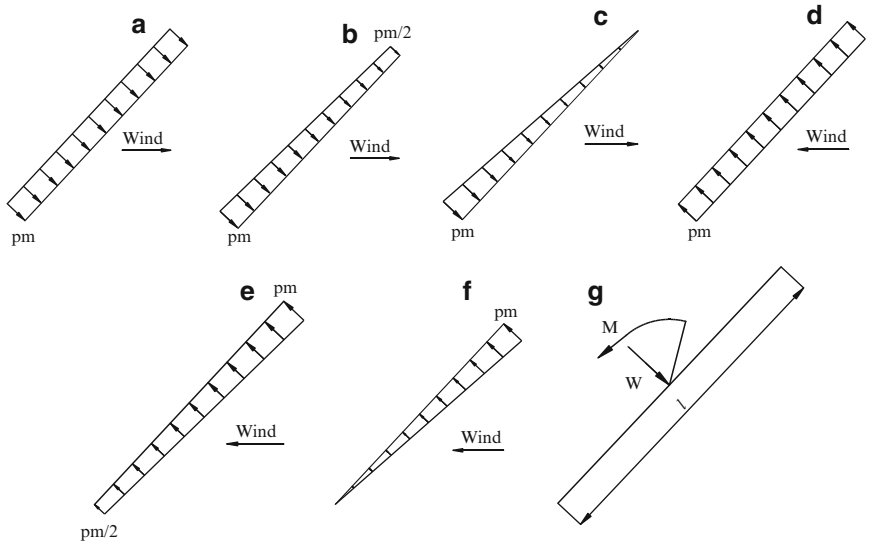

Fig. 2 Wind load cases ((**a**) – wind case 1; (**b**) – wind case 2; (**c**) – wind case 3; (**d**) – wind case 4; (**e**) – wind case 5; (**f**) – wind case 6; (**g**) – reduced model)

Table 1 Wind loads for wind loading cases

	Wind direction towards front of panel			Wind direction towards back of panel		
	Wind case 1	Wind case 2	Wind case 3	Wind case 4	Wind case 5	Wind case 6
W	W_{max}	$\frac{1}{2}W_{max}$	$\frac{3}{4}W_{max}$	$-W_{max}$	$-\frac{1}{2}W_{max}$	$-\frac{3}{4}W_{max}$
M	0	$\frac{1}{12}W_{max}l$	$\frac{1}{24}W_{max}l$	0	$\frac{1}{12}W_{max}l$	$\frac{1}{24}W_{max}l$

2.2 Weight

The weight of the panel together with all the parts (frame) directly attached to the panel (G) is considered. The weight of the other parts is not significant for preliminary design calculus and will not be considered.

2.3 Snow

Snow loads on sloped panels decrease as the tilt angles and slopes increase. Most PV or thermal collectors have glass surfaces that help the snow-shedding process. Since the tilt angles of a tracker during snow period are relatively big, there is a very small chance of snow load on panel. It can be neglected for Braşov region and it will not be considered in this paper.

2.4 Seismic Load

The seismic load is critical in earthquake-prone regions and the procedure for designing for seismic loads is standardized, mostly depending on the characteristics of the region. In this paper, the seismic load is not considered.

2.5 Loading Cases

In the case of azimuthal tracking systems, rotation around the vertical axis (ψ orientation angle) is not relevant for the loading of the structure. The geometry of the structure is mainly changed from the α orientation angle. The extreme positions of this movement must impose the loading cases that must be considered [2, 7]:

- *a – Loading case 1*: $\alpha = 67°$, corresponding to summer solstice at noon;
- *b – Loading case 2*: $\alpha = 9°$, corresponding to winter solstice at sunrise.

3 Preliminary Design Forces

3.1 Calculus Relations

Figure 3 presents the calculus diagram for the reactions in the seasonal rotational axis and in the linear actuator.

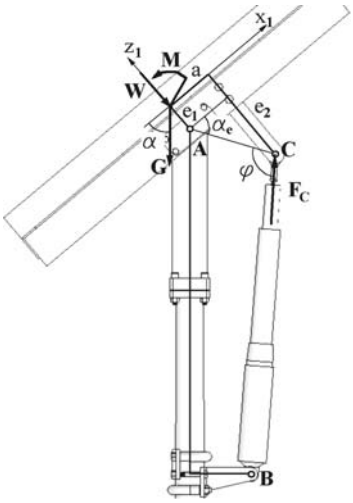

Fig. 3 Calculus diagram

The reaction in the linear actuator is calculated with relation

$$F_C = -\frac{(M + Ge_1 \cos\alpha)\cos\alpha_e}{a \sin\varphi}, \tag{1}$$

where $\alpha_e = \arctan\frac{e_2 - e_1}{a}$. Positive values mean compression of the actuator's screw and negative values mean tension on the actuator's screw.

The reactions in the A axis are:

$$F_{x1A} = G\cos\alpha - F_C\cos(\varphi - \alpha_e) \qquad F_{z1A} = W + G\sin\alpha - F_C\cos(\varphi - \alpha_e); \tag{2}$$

and the reactions in the bearings of the A axis are:

$$R_{A'} = R_{A''} = \frac{\sqrt{F_{x1A}^2 + F_{z1A}^2}}{2}; F_{aA} = 0. \tag{3}$$

Figure 4 presents the calculus diagram for the reactions in the bearings of the vertical axis.

The reactions in the vertical axis are:

$$R_D = \frac{W\cos\alpha(l_1 + l_2) - M - Ge_1\cos\alpha}{l_2};$$
$$R_E = \frac{W\cos\alpha l_1 - M - Ge_1\cos\alpha}{l_2}; F_{aD} = W\sin\alpha + G. \tag{4}$$

The optimal design of a linkage mechanism like the one involving the linear actuator is looking for symmetrical extreme positions C_1 and C_2 of the C link (see

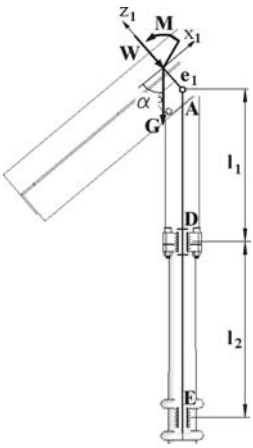

Fig. 4 Calculus diagram

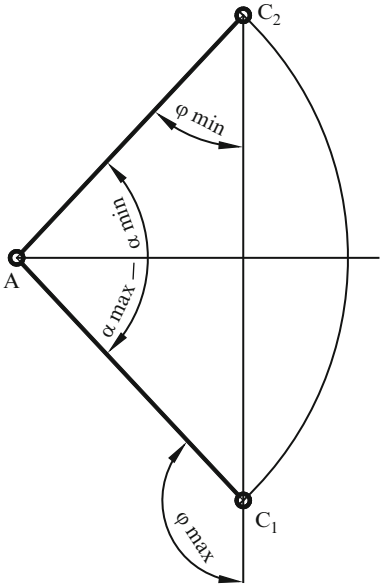

Fig. 5 Pressure angles

Fig. 3), relative to the less loaded position with $\varphi = 90°$, in order to obtain proper φ pressure angles.

Figure 5 presents the extreme positions of the linear actuator mechanism.

Based on Fig. 5, the following relations have been established:

$$\varphi_{\max} = 90° + \frac{(\alpha_{\max} - \alpha_{\min})}{2};$$
$$\varphi_{\min} = 90° - \frac{(\alpha_{\max} - \alpha_{\min})}{2}; \varphi \approx \varphi_{\min} + \alpha - \alpha_{\min}. \quad (5)$$

3.2 Numerical Results

Based on relations (1)–(5), the loads on the elements of the azimuthal tracking system with linear actuator have been calculated for the two loading cases and for the six wind cases. There have been considered two sizes of azimuthal trackers.

A *small size tracker* (developed at Transilvania University of Braşov) is equipped with a PV panel with a surface 1.48 × 0.67 m^2, approx. 1 m^2. The maximum wind speed for the Braşov region is 30 m/s resulting a maximum wind force on the panel $W_{max} = 580$ N for a maximum wind pressure $p_m = 580$ N/m^2. The dimensions of the tracking system are: $l = 670$ mm; $e_1 = 40$ mm; $e_2 = 140$ mm; $a = 80$ mm; $l_1 = 270$ mm; $l_2 = 340$ mm.

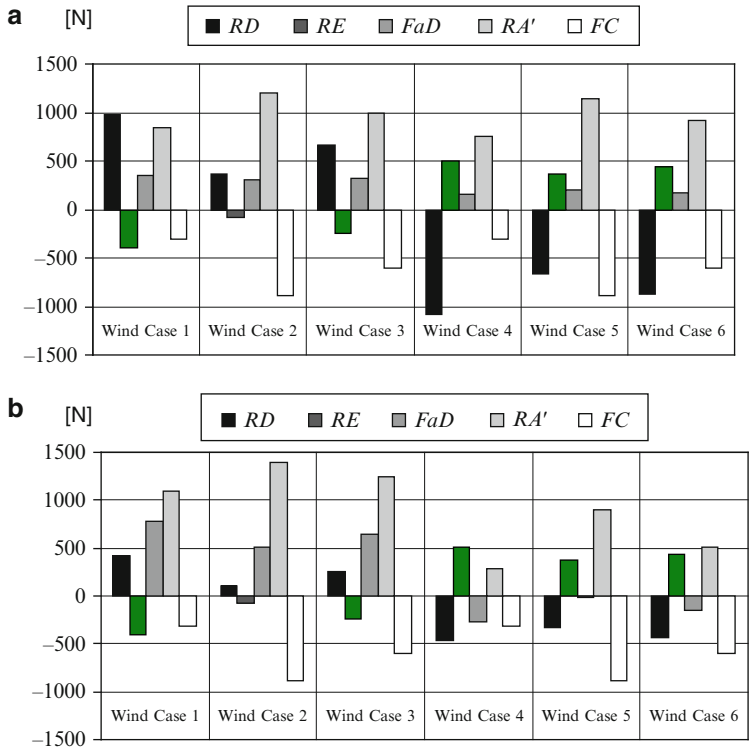

Fig. 6 Main reactions on bearings and linear actuator – small size tracker

Figure 6 presents the main reactions on the bearings of the mechanism and on the linear actuator for the two loading cases (a and b). There have been considered the possible wind cases, numbered from 1 to 6, presented in Table 1.

A *medium size tracker* (in process of development at Transilvania University of Braşov) is equipped with 8 PV panel with a total surface of $8 \times 1.64 \times 0.95$ m^2, approx. 12.5 m^2. It results a maximum wind force on the panel $W_{max} = 7{,}230$ N for a maximum wind pressure $p_m = 580$ N/m^2. The dimensions of the tracking system are: $l = 3{,}280$ mm; $e_1 = 420$ mm; $e_2 = 750$ mm; $a = 860$ mm; $l_1 = 1{,}100$ mm; $l_2 = 1{,}000$ mm.

Figure 7 presents the main reactions on the bearings of the mechanism and on the linear actuator for the two loading cases (a and b). There have also been considered the possible wind cases, numbered from 1 to 6, presented in Table 1.

4 FEM Analysis

The forces determined above are inputs for the stress or deformation analysis of each element of the tracker.

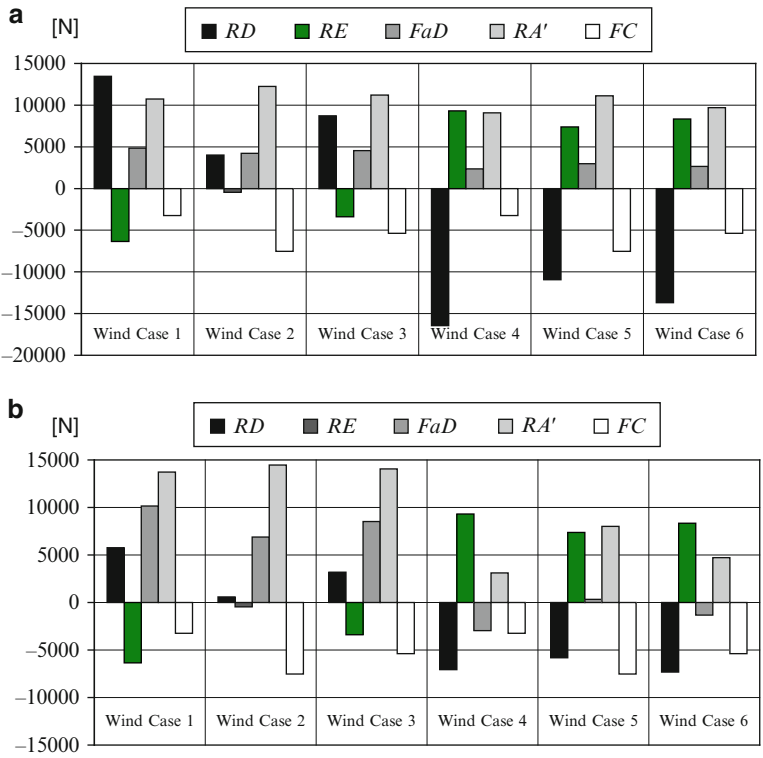

Fig. 7 Main reactions on bearings and linear actuator – medium size tracker

For the case of the small size tracker an FEM analysis has been performed for the vertical beam sustaining the tracker in bearings D and E.

Figure 8 presents the distribution of Von Misses stress along this part and Fig. 9 presents the translational displacements of the same part. There have been considered the maximum forces in the two bearings, corresponding to loading case 1 and wind case 2 (see Fig. 6a).

The values of both stresses and displacements are in the accepted range.

5 Conclusions

Based on the results presented above, the following conclusions can be drawn:

- The differences between the results on the two trackers (small and medium sizes) are mainly a problem of scale; the following conclusions are covering both size cases;

Fig. 8 Von Misses stress

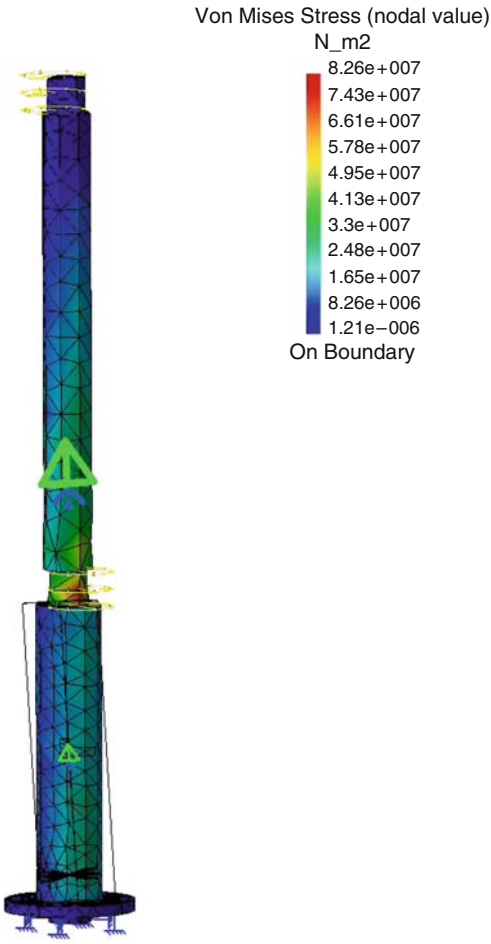

- The radial loads on the bearings of the vertical axis (R_D and R_E) are clearly depending on the wind case considered; biggest values are obtained for wind case 1 (for front wind), respectively wind case 4 (for back wind) and the smallest values are obtained for wind case 2 (for front wind), respectively wind case 5 (for back wind); Same observations are valid for the axial force on the vertical axis (F_{aD}) more clear for the loading case 2 (Fig. 8b);
- The force on the A bearings (R_A) is bigger for wind case 2 (for front wind), respectively wind case 5 (for back wind) and smaller for wind case 1 (for front wind), respectively wind case 4 (for back wind);
- The axial force in the actuator's screw is always negative meaning tension on the actuator and is bigger for wind case 2 (for front wind), respectively wind case 5 (for back wind) and smaller for wind case 1 (for front wind), respectively wind case 4 (for back wind);

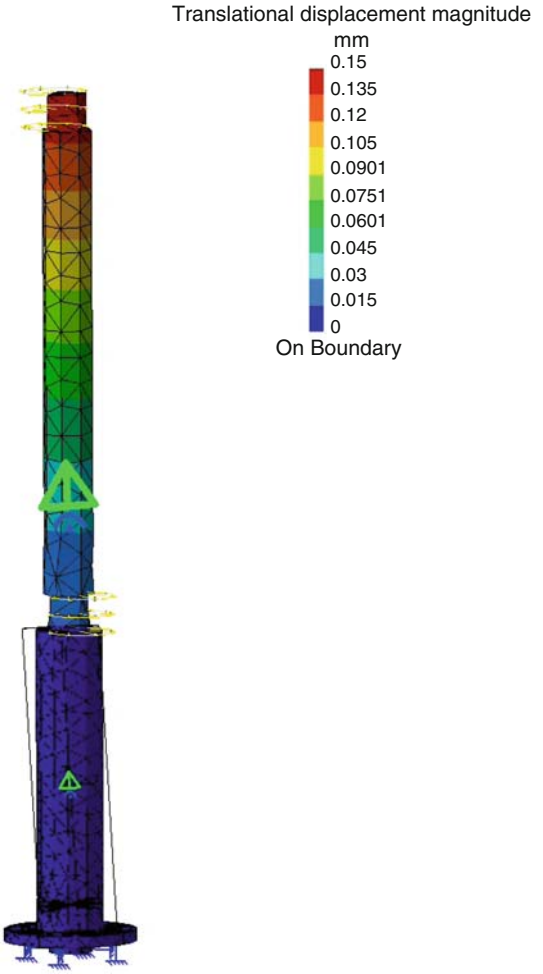

Fig. 9 Translational displacements

- Loading case 1 (summer solstice – noon) gives the biggest radial load R_D;
- Loading case 2 (winter solstice – sunrise) gives the biggest axial load F_{aD} and biggest force on the A bearings (R_A);
- Radial load R_D is slightly different between the two loading cases;
- Load on the screw's actuator is maximum for the two extreme loading cases;

The permissible axial load on the actuator is few times bigger than the maximum load for the extreme loading case, even if the actuator is the smallest of its class. Anyway, normal solar tracker systems have bigger dimensions than the tracker presented in this paper, using actuators at their permissible load [8]. Considering the geometry of the linkage mechanism with actuator, the axial load on the actuator's screw is increasing with the decrease of actuator stroke.

References

1. Clark, R.N., Vick, B.D.: Performance comparison of tracking and non-tracking solar photovoltaic water pumping systems. Presentation at the 1997 ASAE Annual International Meeting Minneapolis, Minnesota, 1997. http://www.cprl.ars.usda.gov/REMM Publishers.htm
2. Vişa, I., Diaconescu, D., Dinicu, V., Burduhos, B.: The incidence angles of the trackers used for the PV Panels' Orientation. Part I: azimuthally trackers. In: International Conference on Economic Engineering and Manufacturing Systems RECENT, vol. 10, Brasov (2007)
3. NP-082-04. Eurocode 1: Design Code. Bases of Design and Actions on Buildings. Action of Wind. Monitorul oficial al Romaniei
4. Roger, A., Messenger, J.: Photovoltaic Systems Engineering. CRC Press, Boca Raton (2004)
5. Coşoiu, C.I., Damian, A., Damian, R.M., Degeratu, M.: Numerical and experimental investigation of wind induced pressures on a photovoltaic solar panel. In: International Conference on Energy, Environment, Ecosystems and Sustainable Development, Algarve, Portugal (2008)
6. Sorensen, B.: Renewable Energy. Elsevier, Boston (2004)
7. Blackman, S., Popoli, R.: Design and Analysis of Modern Tracking Systems. Artech House, Boston (2000)
8. Velicu, R., Moldovean, G., Gavrilă, C.C.: Constructive aspects on the altitudinal system of a solar tracking PV Platform. In: International Conference on Sustainable Energy, Braşov, Romania (2008)

Index